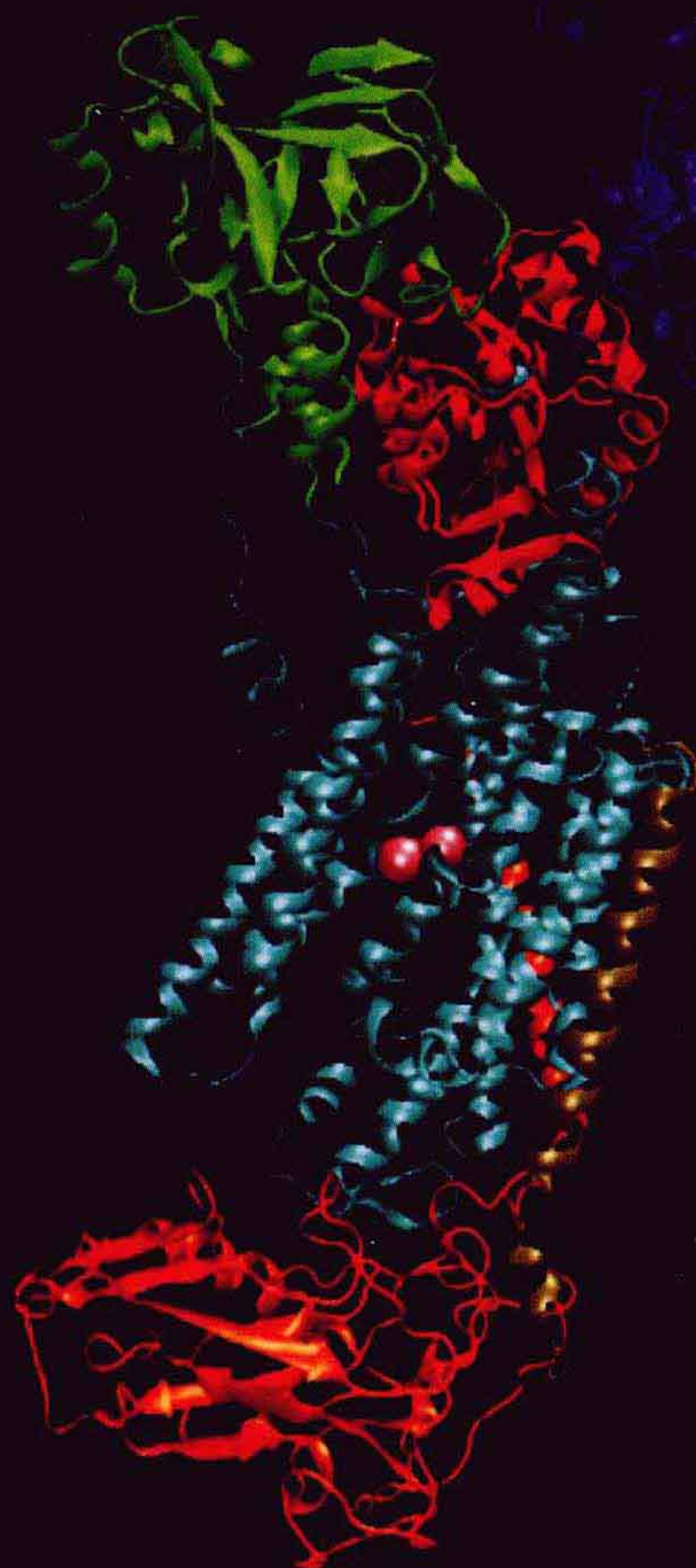
生命科学名著



细胞生理学手册（原书第四版）

——膜生物物理学

上册

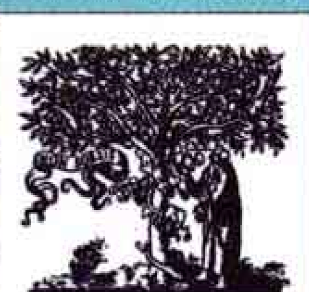
Cell Physiology Sourcebook:

Essentials of Membrane Biophysics

FOURTH EDITION

〔美〕N.斯皮尔莱克斯　主编

张志鸿　导读



原版引进



科学出版社

(Q-3128.0101)

封面设计 / 美光设计

本书的评价

《细胞生理学手册》于1996年（第一版）及1998年（第二版）被美国图书馆协会的期刊“精选”（CHOICE）列入优秀学术书籍的名单。

“细胞生理学领域的权威性书籍，无疑是当今最具综合性有效信息的手册之一。”

— CHOICE

“……一本细胞生理学的核心教科书……，有充分的理由表明拥有这样一本书很有必要，它实现了其客观的卓越性。在信号转导、膜生物学、离子通道、神经与肌细胞生理学等学科内容方面特别强……，它在其领域中是一本精深的教科书……”

— DOODY'S PUBLISHING REVIEWS

“第二版《细胞生理学手册》对学习细胞生理学、细胞生物物理学、电生理学的高年级本科生、研究生以及对众多领域中的生物科学家都非常有用。该书特别适合于引导接受物理科学训练的学生学习细胞生理学、引导生物学背景的学生学习细胞生物物理学。”

— BIOPHYSICAL JOURNAL

《细胞生理学手册》的特点

第四版《细胞生理学手册》提供了内容全面、权威性的信息。它是主要为高年级本科生和研究生编写的教材，也可供研究者做参考。此包含多种学科的出版物为对细胞生理学、膜生物物理学、电生理学和细胞信号感兴趣的科学家、研究者和学生提供了坚实的基础。本书在确立为该领域的一流教材的同时也是经典医学生理学教材的极好补充读物。

主要特色：

- 由多领域的一流研究者撰写
- 清晰、简明及全面地包含从基础概念到进展的细胞生理学所有方面

主要包含的论题：

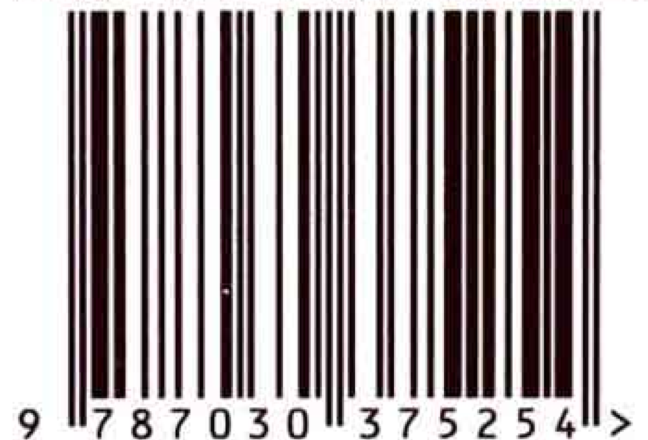
- 蛋白质的物理化学
- 膜的分子结构与特性
- 膜受体与第二信使
- 离子与非电解质的主动运输
- 离子通道的结构与运转
- 膜兴奋与传播
- 作为毒素、药物与疾病靶的离子通道
- 感觉转导机制
- 突触传递
- 光合作用与生物发光
- 原生动物与细菌的生理学



科学出版中心　生物分社
联系电话：010-64012501
E-mail：lifescience@mail.sciencep.com
网　址：http：//www.lifescience.com.cn

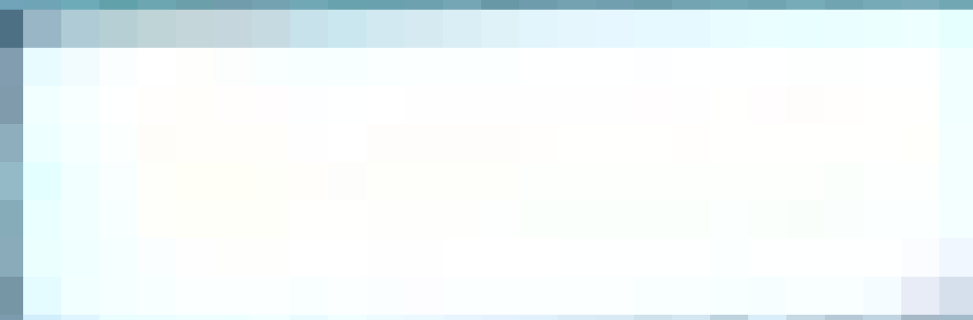
销售分类建议：生物学／生物物理

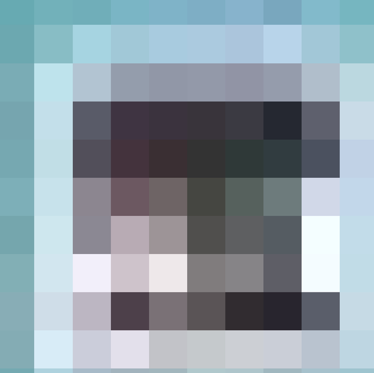
www.sciencep.com



ISBN 978-7-03-037525-4

定价：150.00元



生命科学名著

细胞生理学手册

——膜生物物理学精要（上）

（原书第四版）

Cell Physiology Sourcebook:

Essentials of Membrane Biophysics

(Fourth Edition)

〔美〕N. 斯皮尔莱克斯 主编

张志鸿 导读

科学出版社

北 京

图字：01-2012-5510 号

内 容 简 介

本书内容极其丰富，包含了动物、植物等各种细胞内发生的重要生命事件的分子基础、物理化学的机制、发现的历史渊源、数学上的定量描述、生理学功能、病理变化和疾病的关系，以及近代进展和展望等方面的详细内容和原始文献，具有作为“手册”的重要参考价值。全书分为七个部分，共 52 章 970 页。

本书内容适于作为高等院校和科研单位生理学、生物物理学、细胞生物学、分子生物学、生物化学、医学、药理学等学科研究生及高年级本科生的教材或阅读参考书，从事生命科学研究的工作者或其他交叉学科对生命科学感兴趣的师生和学者也可参考和阅读。

This is an annotated version of
Cell Physiology Sourcebook：Essentials of Membrane Biophysics（Fourth Edition）
Edited by Nicholas Sperelakis

ISBN：978-0-12-387738-3

图书在版编目(CIP)数据

细胞生理学手册：膜生物物理学精要（上）＝Cell physiology sourcebook：essentials of membrane biophysics：第 4 版：英文/（美）斯皮尔莱克斯（Sperelakis，N.）主编．张志鸿导读．—北京：科学出版社，2013.5

（生命科学名著）

ISBN 978-7-03-037525-4

Ⅰ.①细…　Ⅱ.①斯…②张…　Ⅲ.①细胞生理学－手册－英文
Ⅳ.①Q25－62

中国版本图书馆 CIP 数据核字（2013）第 106443 号

责任编辑：李　悦 / 责任印制：钱玉芬
封面设计：美光设计

科 学 出 版 社 出版
北京东黄城根北街 16 号
邮政编码：100717
http://www.sciencep.com
源海印刷有限责任公司 印刷
科学出版社发行　各地新华书店经销
*
2013 年 5 月第　一　版　开本：787×1092　1/16
2013 年 5 月第一次印刷　印张：37
字数：883 000

定价：150.00 元
（如有印装质量问题，我社负责调换）

导　读

张志鸿
（复旦大学生命科学学院，上海 200433；
E-mail：zhzhang@fudan. edu. cn）

细胞是生命的基本单元。单细胞是最简单的生命形式，高等生物则是多细胞的社会，依靠细胞之间在时间、空间上结构与功能的复杂、有序和动态的相互作用网络，展现出各种多姿多态的生命现象。虽然生命形式多种多样，但自然界的生物进化还是赋予所有生命具有共同的特性：都是由同样一些化学分子组成、细胞结构上有类似的组织原理、其行使类似功能的生物大分子往往有高度同源性的结构，更为重要的是这些生命活动都遵循同样的物理学和化学的基本定律。因而，虽然在自然界中它们表现出惊人的生物多样性，但基本的细胞功能，特别是细胞内外的物质交换、遗传规律、能量转换、细胞对内外环境的感受与响应、细胞内的信号转导、细胞间的通讯、细胞内各种内环境的恒定性、细胞运动等重要方面都有着同样的规律和基于类似的结构基础。其中的不少生命过程都是在生物膜（包括细胞表面的质膜和各细胞器上的内膜）的舞台上进行和展现的，本书即以此为出发点，根据这些重要生命活动的基本物理学和物理化学规律进行相当详实的阐述。

本书主编 Nicholas Sperelakis 教授现是美国辛辛那提大学医学院退休荣誉教授，曾长期担任该学院的主任和弗吉尼亚大学生理学教授，主要从事神经与肌肉的电生理学和生物物理学研究。他在膜生物物理学、磷酸化和环核苷酸等多种因子对离子通道的调控、离子通道的发育变化、心肌与平滑肌中兴奋的传播机制等方面开展了不少独创性研究，发表了 550 多篇科学论文。2002 年正式退休关闭实验室后，他用电子电路仿真软件 PSpice 继续深入进行研究。Nicholas Sperelakis 教授非常热爱和敬业于教学，他善于用容易理解的方式对学生讲授一些理解困难的概念。他的课程深受学生的欢迎，多次被学校学生评为“最佳讲授”。

本书的第一版出版于 1995 年，以后随着“细胞生理学”领域研究的快速发展以及新概念与成果的不断出现，至 2001 年又改版了 2 次。本书多年来已成为不少学校研究生和高年级本科生的教材以及生理学研究工作者经常查阅的范本。本书第四版则是 Nicholas Sperelakis 教授花费了一年半时间全身心集中编著而成。细胞生理学涵盖的内容极广，是我们了解“生命逻辑”、整合及系统生理学等方面的基础。这样一本巨著仅靠几位作者是难以完成的，因此 Nicholas Sperelakis 教授还邀请了其他 63 位具有不同专长的国际一流学者共同撰写了第四版《细胞生理学手册》。

本书内容极其丰富，包含了动物、植物等各种细胞内发生的重要生命事件的分子基础、物理化学的机制、发现的历史渊源、数学上的定量描述、生理学功能、病理变化和疾病的关系，以及近代进展和展望等方面的详细内容和原始文献，具有作为“手册”的重要参考价值。全书分为七个部分，共 52 章 970 页，各部分内容的简介如下。

第一部分　生物化学、代谢、第二信使与超微结构　根据生理溶液的物理化学特性

（热力学、化学平衡、反应动力学、运输过程、表面现象、分子结构与波谱学等），阐明活细胞中水分子的三种结构与功能、水与离子的相互作用、离子间的相互作用、溶质运输及膜电位等；蛋白质的分子结构、测定技术、结构与功能的关系；生物膜基本结构研究的历史沿革、膜脂质与膜蛋白、细胞膜的流动镶嵌模型、膜上脂质与蛋白质的相互作用、脂筏的膜微区结构、平面脂质双分子层膜上各种离子载体对离子选择性的通透；用多种光镜和电子显微镜技术获得的各种细胞器的超微结构；细胞内信号转导网络的普遍原理、19 种主要通过膜上 G 蛋白偶联受体和受体酪氨酸激酶介导的细胞内信号途径、调节生理学过程的主要几种信号途径；小分子化学介体（Ca^{2+}、cAMP、cGMP、DAG、IP_3等）的第二信使作用、质膜及细胞内膜上的膜蛋白（离子通道、运输交换体、离子泵）对细胞内 Ca^{2+} 的调节、Ca^{2+} 信号的产生、Ca^{2+} 主要通过细胞内三种分子（钙调蛋白、钙结合蛋白、蛋白激酶 C）的介导机制进行信号转导。

第二部分　膜蛋白、运输生理学、泵与交换体　物质跨膜扩散与通透的物理化学；决定细胞内离子浓度的主要因子（Na^+-K^+ 偶联泵、Ca^{2+}-Na^+ 交换反应、Ca^{2+} 泵）、细胞膜的等效电路分析、细胞静息膜电位的起源及定量描述（Goldman-Hodgkin-Katz 恒场方程、弦电导方程）；细胞内不通透性荷电大分子导致的跨膜 Gibbs-Donnan 平衡电位；膜上载体蛋白介导的运输（易化扩散、协同运输与逆向运输）及其热力学、动力学模型分析；跨膜主动运输离子泵（Na^+、K^+-ATPase、Ca^{2+}-ATPase、H^+、K^+-ATPase 等）的结构及其运输机制；膜上 Na^+-Ca^{2+} 交换体的结构、功能、系统发育及离子交换的乒乓机制；水跨膜通透及细胞内环境的恒定性（氯离子的调节、细胞容积的调节、细胞内 pH 的调节）。

第三部分　膜兴奋与离子通道　神经纤维、骨骼肌纤维等的生物电缆特性、动作电位通过膜上局部回路电流方式的快速传播；神经、肌肉和内分泌细胞的膜兴奋性；动作电位的产生机制及其特性、Hodgkin-Huxley 分析、膜片钳技术（常规膜片钳方法、自动膜片钳系统）；通过生物化学纯化方法、重组 DNA 技术、突变技术、X 射线晶体学等分子结构的测定技术，详细研究电压门控离子通道的结构及其功能；可兴奋细胞中的电突触、间隙连接的结构与特性；细胞膜上离子通道的各种调节机制：环核苷酸依赖性磷酸化的调节、GTP 结合蛋白的调节、与细胞骨架相互作用的调节；发育过程中离子通道的类型、数目和动力学特性的改变；众多离子通道呈现的机械敏感性。

第四部分　作为毒素、药物与遗传疾病靶的离子通道　用毒素分子探究不同组织中的特异性离子通道异构体、用行为分析确认可能有神经活性的新毒素；毒素分子和通道蛋白的相互作用；靶向 2 种心脏离子通道（电压门控 Ca^{2+} 离子通道和电压门控 Na^+ 离子通道）的分子药理学；基于离子通道分子结构设计的药物分子能特异性地和通道蛋白中关键的位点结合，从而起到对离子通道功能调节的作用；几种离子运输异常的遗传性疾病（家族性偏瘫偏头痛、囊性纤维化、长 QT 综合征、肌强直与骨骼肌周期性麻痹、恶性高热、利德尔综合征、巴特综合征）、基因突变对蛋白质结构与功能的影响、减轻或治愈病人症状的治疗方法。

第五部分　突触传递与感觉转导　神经递质配体（乙酰胆碱、谷氨酸、GABA、甘氨酸等）门控及细胞内配体（Ca^{2+}、环核苷酸、ATP、IP_3等）门控的 2 大类配体门控离子通道；配体门控离子通道的分子结构及三个基本特性：门控、电导及离子选择性通透；化

学突触的结构与功能、突触整合及放大、突触传递的调节；肽激素和神经递质分泌过程中的“兴奋一分泌偶联”、此过程中细胞骨架与跨膜信号的相互作用；依靠“刺激一响应偶联”，代谢感觉细胞中特化细胞内受体能感受循环代谢原料水平、代谢废物水平、细胞周围的离子组成、器官中张力等的变化，其中不少是通过 K^+ 通道的协调实施的；环核苷酸（cGMP 或 cAMP）门控离子通道在心脏起搏、视觉、嗅觉以及脑中突触可塑性等重要生理过程中起重要作用；一些感觉（电、机械力、盐觉、酸觉）受体是膜上的离子通道，另一些感觉（化学、光）则间接地通过特化的受体蛋白作用于离子通道；声转导与视觉转导；红外线感觉器官；通过受体系统动物有探测电场和磁场的能力。

第六部分　肌肉与其他收缩系统　骨骼肌和平滑肌细胞膜上离子通道的不同类型和不一样的兴奋性；心脏动作电位的产生、窦房结处起搏细胞的自发去极化；骨骼肌中兴奋一收缩偶联、T 管上的二氢吡啶受体（DHPR）和肌质网膜上雷诺定受体（RyR）之间的相互作用、三联体处 DHPR 四聚体的胞质段和 RyR1 四聚体物理相互作用以及相临 RyR1 彼此之间的协同作用、兴奋一收缩偶联的调节机制；肌肉收缩的滑动肌丝理论和横桥理论、肌肉能力学；非肌肉运动系统（鞭毛、纤毛、基于肌动蛋白和基于中心体蛋白）的运动、细胞迁移和黏着、生物弹簧；电鱼的电细胞中特化的膜蛋白不对称分布造成兴奋时的跨细胞不对称电流，这是电鱼的电器官产生强电发射的基础。

第七部分　原生动物与细菌　原生生物的生理学多样性、分子多样性、细胞器多样性、细胞多样性；一些未知功能的结构；原核生物细胞学、细菌细胞的能力学（底物水平磷酸化和化学渗透偶联）、细菌细胞中的物质运输与代谢策略、细菌对环境的响应及其机制、细菌致病的生理学。

第八部分　特化过程：光合作用与生物发光　光合细菌反应中心的组成及分子排列、反应中心的电子传递、光合作用的进化、叶绿体及碳同化的生物化学、叶绿体中光驱动的电子传递和质子跨膜运输、化学渗透假说及 ATP 的合成、光合作用的调节；生物发光的酶促机理、荧光素与萤光素酶、生物发光的意义（防御、进攻与通讯）、生物发光的调节机制。

本书内容的特点是：①以“手册”的要求，简明、全面地阐明了细胞内发生的重要生理学事件，介绍了其历史发展、近代进展和研究展望，同时对一些重要的方法学也进行了详细介绍。在知识水平上处于当前学科的最前沿；②侧重从膜生物物理学的角度、结构与功能的关系、仿真和数学定量等方面分析；③大多数章节开篇都有摘要，对公式和方程式有详细的由来说明、推导和演算，这些都大大方便了读者学习和理解；④主编 Nicholas Sperelakis 教授有长期教学的经验、本书的各撰写人也都是本学科相关领域的国际一流专家，经过四版修订后本书更趋完善。

目前，国际上已有几本在分子水平上介绍细胞内各种生命活动及其机制的细胞分子生物学教科书被广泛采用并得到一致的好评，它们主要是将近年来分子生物学、分子遗传学、结构生物学等学科迅猛发展取得的成果应用于阐述细胞生物学中的分子事件。本书则主要依据物理学和物理化学的概念和理论，从生物膜的舞台展示和分析分子水平上整个细胞全局的生理功能，其着眼点已从溶液中发生的生物化学变化拓展到一个活的生命机体。因此，在这个意义上本书和其他细胞分子生物学教科书在内容上能很好地互补和相互参

考。正是本书的这种有别于传统生理学和其他细胞分子生物学的新颖特点，自 1995 年第一版发行以来很快得到学术界和教育界的好评，次年即被美国图书馆协会评列为优秀学术教科书。时隔仅三年后的第二版几近一半的内容又得到了更新和补充，可见主编和撰写人的重视和努力。更令人赞叹的是当 Nicholas Sperelakis 教授 80 岁高龄时仍为了满足教学的需要，和出版社一起广泛听取社会的反馈意见和建议完成了这本第四版。在新一版中内容增加了许多重要的新材料，大多数章节进行了全面的修订，删除了一些在其他细胞生物学等教科书中常见的重复内容，各个章节的组织机构更为统一，同时为易于高年级大学本科生的理解而在正文中略微降低了水平（一些理解难度较大的热力学分析、重要方程的推导等内容放在相应章节后的附录中)。这些改进使得本书更加完善，特点更加突出。

本书内容适于作为高等院校和科研单位生理学、生物物理学、细胞生物学、分子生物学、生物化学、医学、药理学等学科研究生及高年级本科生的教材或阅读参考书，从事生命科学研究的工作者或其他交叉学科对生命科学感兴趣的师生和学者也可参考和阅读。

献　　辞

谨以本书献给地球及所有为拯救与保护环境，为使海洋、湖泊、河流、饮用水、空气及土壤免遭污染，为保护农田，为稳定世界人口，为保护野生生命，为保护动物生存权，以及为全球人权奋斗而孜孜不倦工作的机构。我也要感谢我的家庭给予的挚爱和支持，他们是我的夫人 Dolores，子女 Mark Demitri（已亡故）、Christine M.、Sophia A.、Thomas A.、Anthony J.，儿媳 Sherri，孙辈 Demetra、Gregory、Nina-Nicole。特别要感谢克利夫兰诊所的小儿科主任医学博士 David Magnuson 的贡献、技艺、智慧及博爱。非常感谢！

纪　念

Hugo Gonzalez-Serratos 博士于 2011 年 4 月 1 日逝世。Hugo 是位于巴尔的摩的马里兰大学生理学教授。他于 1960 年中期在伦敦大学学院是诺贝尔奖获得者 Andrew F. Huxley 教授的研究生。Gonzalez-Serratos 博士在肌肉生理学领域是公认的顶级科学家。我们大家都将永远怀念他。Gonzalez-Serratos 教授是本书的一名撰写人，永远缅怀他！

第一版序言

承蒙好意，我的朋友 Nicholas Sperelakis 的这本出色的书和本人的《普通生理学教材》(*A Textbook of General Physiology*) 很相近。在本人的书第一版的前言中，我表达了希望能和 Bayliss 的《普通生理学原理》(*Principles of General Physiology*) 相比较的愿望。本书的组织和部分撰写都是由像 William Bayliss 爵士和我一样与伦敦大学学院 (Sperelakis 教授在此度过一年学术休假) 有关联的学者完成的，因此若要做比较的话还是非常恰当的。我非常高兴地回忆起在伦敦大学学院初次遇见 Nicholas 时的情景，我还记得，我们讨论了关于他在眼睛跨晶状体电位方面的开拓性研究。

和内容不相关的是本书有着不一样的书名，我想这是因为“一般”与“普通”生理学之间的差别已变得界限模糊，以至需要更合适的书名。在本人所著教科书第一版的前言中，我提出普通生理学的定义应为：研究活体根据物理学和化学定律做出的即时反应。之后，我担忧该定义过于狭窄，于是提出可用“研究所有生命形式的共同特性”来取代。但无论我们选择何种定义，对我来说相当满意的是，实质上 Nicholas 这本新书的各部分标题都和我自己的书上基本一致。

如果让我进一步追忆，我经常怀疑一名积极从事研究的科学家如何能撰写这样一本内容广泛的新书。自第二次世界大战结束后 2 年我才开始写书的，此后有好几年（在英国长达 10 年）很少见到有原创性学术生理学和新研究结果的发表。这样，才有可能浏览相当长时期的原始文献，而不至于淹没在快速接连出现的新发现中，否则我的任务几乎是不可能完成的，其命运就像西西弗斯（古时希腊的暴君——译者注）一样。今天，这种任务更加难以完成，所以，我非常惊叹 Nicholas 只和几位合作者就写出了这本宏伟的书。

Hugh Davson

1995 年

第二版序言

在《细胞生理学手册》第一版序言中，Hugh Davson 认定该书与他本人众所周知、被高度赞誉的《普通生理学教材》为一个系列。仍由 Nicholas Sperelakis 主编的《细胞生理学手册》第二版继续着同样的传统。虽然第一版由于其内容的深度和广度受到了细胞生理学界的热烈欢迎，但自出版以来在此快速发展的领域出现了很多重要的进展。通过修订论题以及在第一版的所有部分中加入一些章节，第二版涉及了这些新进展。这些在各个部分加入的新论题包括：脂质结构、线粒体生理学、细胞对激素的响应、红细胞运输、神经细胞生理学、离子通道的发育变化、声转导、兴奋一收缩偶联、电板细胞。此外，新版还很有价值地增加了两部分新内容，其一是“原生动物与细菌”，内含两章有关这些有机体的生理学；另一部分是“细胞分裂与细胞凋亡”，包含的章节为细胞分裂的调节、癌细胞、细胞凋亡、电离辐射效应。第二版中这些大的修改及新材料的补充将本书提升到一个新的水平。

在生物学中具有重要地位的细胞生理学产生于许多更为传统的领域，因而其文献也涉及广泛。《细胞生理学手册》的重要价值在于它把该领域中内容丰富的诸种现代章节聚集在一起，各章都呈现统一的表现形式和写作水平，由此再加上内容清晰的表达，使得本书非常适于作为高年级学生或研究生水平的细胞生理学课程教材。第二版中更为广泛的内容也使它被选作为细胞生物物理学、膜生物学及生物医学工程等课程的教材很有吸引力，同样本书也可以作为教材用于离子通道结构及生理学的导论课程。

我非常高兴和荣幸应我同事 Nicholas Sperelakis 之邀写此《细胞生理学手册》第二版序言。本书清晰地给出了优秀的新标准。

Thomas E. Thompson
1997 年

第三版序言

当 Nicholas Sperelakis 诚邀我写此序言之时，我曾怀疑我是否能跟随 Hugh Davson 的脚步。我在伦敦大学学院学习生理学时正值他的不朽著作《普通生理学教材》一书出版之时。伦敦大学学院是那时身为一个学生的非凡之地。这不仅是因为 Hugh Davson 打下了他那特别的学科奠基石，而且也因为 Leonard Bayliss 那时也正在修订他父亲的著名《普通生理学原理》一书。这些书使我确信自己能成为生理学的研究学者，而细胞生理学是入门之地。同时，Davson 和 Bayliss 还担负着吸引医学学科的学生对生理学研究引起兴趣的责任。之后，我记得在成为伦敦大学学院的青年讲师时我曾问过 Hugh Davson 为何他未经常给学生讲授。他简单地作了这样的回答："Denis，我已将所有的都写下来了。告诉他们去阅读!"事实上也正是这句话唤起我阅读该书的兴趣。那本书现在仍在我的藏书室里，并且保存很好，还经常查阅。

本书亦将成为新一代生理学家经常查阅的范本，这将是对 Nicholas Sperelakis 和他同事们的工作的最大赞誉。新一代生理学家将踏入这门令人激动的学科，因为细胞生理学是我们了解整合与系统生理学所有方面的基础。因而，对所有想渴望了解终究何为"生理学"名词含意和根源的"生命逻辑"的我们来说，本书将是必不可少的资料源。当然，生命没有单一的"逻辑"。将一些其本质已被发现、公认的物理化学机制相互结合及交叉地用于阐明即使形成最简单细胞功能的各种缠绞在一起的过程时，我们惊奇地发现自然界的分子机制经常反复地在不同场合重现。基因密码能将与生命特性紧密相关的逻辑代代相传，因此我们称这种创新策略为"基因舞蹈"。逻辑是生理学的而非遗传学的。分子生理学家 Sydney Brenner 最近的文章（发表于诺华公司的题为"生物学中还原论的局限性"的学术讨论会）对此简明地阐述为："基因只是赋予它们编码蛋白质的特有性质，而系统的任何一种整合特性必须是它们之间的相互作用'计算'出来的。"我们正是认同了这样的观点：了解这些相互作用足以使生理学上升为能解决所遇到各种问题的定量分析科学。Brenner 意味深长地继续评论：这为仿真分析提供了框架。仿真实质上也已成为分析的一种必要工具，这是我们科学已走向成熟的标志。

这也是细胞生理学的范围现在更为广泛的标志。内容的广度是本书最大亮点之一，各个章节包含绝大多数重要的分子和细胞系统，因而它完全和其"手册"的书名相吻合。

Denis Noble

第四版序言

我很高兴为《细胞生理学手册》第四版写序言。Hugh Davson 教授在他的不朽著作《普通生理学教材》第四版后不再继续改版。可能，他意识到生理学的知识已变得太广，再要像以前那样单靠他一个人撰写出涵盖所有方面的受高度赞誉的教科书已不太可能了。

那么，什么原因使 Nicholas Sperelakis 教授能后继 Davson 写此教材巨著呢？他决定邀请更多的专家，这些人允诺与他合作，因为他们十分敬重他在细胞生理学领域中做出的重要贡献。虽然 2002 年 Sperelakis 教授关闭了实验室正式退休，但他还是和辛辛那提大学电子和计算机工程系的 L. Ramasamy 博士合作继续发表论文。Sperelakis 教授甚至花时间熟悉了 PSpice 中的技术，这是一种用以电路设计和分析的电子工程软件程序，其中的一些电学参量（如电阻、电容等）可用来代表生理学的参数。他在学习这一新方法时非常兴奋，并用 PSpice 仿真主要在《理论生物学和医学模型及生物医学工程》在线刊物上发表了约 10 篇论文。因第一篇论文概述了主要的概念，这里我仅列出这一篇完整的文献：N. Sperelakis and L. Ramasamy，*Propagation in Cardiac Muscle and Smooth Muscle Based on Electric Field Transmission at Cell Junctions：An Analysis by PSpice*. IEEE—EMB 21，177—190，2002。

Nicholas Sperelakis 教授在 20 世纪 60 年代有一些较有争论的研究发现。1977 年他与合作者数学家 James E. Mann 共同报道：心肌细胞之间闰盘的狭窄缝隙中产生的强电场能使兴奋从心肌中的一个细胞传递至下一个。由此，他们认为心肌中的兴奋传播可不必需要任何心肌细胞之间相连的间隙连接通道的参与。他们论证闰盘膜上快速 Na^{+} 通道的密度要大于表面肌纤维膜上的，这表明闰盘处的兴奋性同样地较大。我很高兴发现 Sperelakis 教授的电场假说已不再是孤立的，因为该假说已独立地被日本学者的论文所证实（K. Tsumoto，T. Ashihara，R. Haraguchi，K. Nagazawa，and Y. Kurachi，*Role of Subcellular Na Channel Distributions in the Mechanism of Cardiac Conduction*. Biophysical Journal 100，554—563，2011）。

本书第三版充实了有关细胞生理学和膜生物物理学领域各方面的重要信息。最为突出的是有多位在本人专长领域（收缩机制及兴奋—收缩偶联）中的著名专家的参与，这给我很深的印象。自《细胞生理学手册》第一版以来，以后的几个版本中接连有新的撰写人加入，我相信第四版亦是如此。我总是非常高兴接到 Nicholas Sperelakis 教授的电话，他是如此兴奋于研究、如此激动于发现。这种热忱也正是我们如此敬重他的一个原因。可能也正是这种热忱，他的妻子 Dolores 形容他仍似他们 51 年前结婚时那样的年轻和充满智慧。按弗吉尼亚医学院主任 Diomedes Logothetis 教授的说法，非常出色的学生是被生理学“病毒”过度兴奋的。因而，我想这也同样发生在如 Sperelakis 教授这样的成功科学家

身上。

当我写此序言之时，Nicholas Sperelakis 教授正在庆祝他的 81 岁生日。值此特殊的周年纪念日，许多希腊人会高喊“chronia polla”，它可不严格地翻译为“许多许多年”或“许多快乐再来”。我们不仅向 Sperelakis 个人，同时也为他的新版《细胞生理学手册》祝福。

Alexandre Fabiato

里士满，弗吉尼亚州

2011 年 3 月 8 日

第四版前言

从前，一位80岁退休的大学教授正过着安静和隐居的生活。然而，2010年春天的某一天，突然，Academic Press的高级策划Janice Audet联系他，她说许多学院仍使用我们第三版的“细胞生理学手册”作为他们细胞生理学课程的教科书，即使此第三版出版的年份（2001年）已久。

事实上，我已意识到第三版已被许多学院采用。大约2年前，一名佐治亚州立大学的研究生和我联系，告知他们将我的书作为他们细胞生理学课程的教材，然而他买不到新书，因为该书已不再印刷。他请求我能把本人的那本寄给他，他允诺会很好保护并在课程结束时返回给我。他甚至提出驱车到辛辛那提我的家来取。这位学生显然对该书非常渴望，因而就此问题我和我之前的编辑Noelle Gracy通了话。她安排了使用该教材的电子版作为替代品。问题解决了！

Janice想知道我是否对出第四版感兴趣。在我给她确切回复之前我请她在全国范围内向若干位课程负责人调查一下他们是否喜爱或不喜爱该书的第三版，理由是什么。从反馈来看，一致的意见是我们的书从总体上来说对于修读细胞生理学课程的低年级的研究生（或高年级大学本科生）来说水平过高；另一些建议是我们应该剔除前三版书中详述的有关细胞生物学的章节/论题，如细胞分裂、细胞凋亡等；我们应该采用彩图；应当在每一章加一个摘要的小节；虽然完成起来不易，但我们还是应当将这么多作者撰写的各章在格式上更趋一致。

我同意进行第四版的工作，重点集中在将这些建议采纳进新版。这一版的一些变化包括：删除约14章、合并几章，同时请撰写人将他们分担的章节内容定在研究生水平。新增了约10位新的撰写人负责一些专门的学科领域。我相信，最后定下的这些撰写人都是顶级的，我非常感谢他们的参与。

此项目需要我付出极大的努力，而且是在健康状况不是很好之时。那么我为何同意呢？是为了财富或金钱？绝对不是！那是微乎其微的。是为了名声或赞誉？不，现在要从这方面得益我已太老了。况且，我已主编了该书的三个版本。是对教学的奉献？是的，正是如此！我已将毕生奉献给教学，我相信我具有独到的能力可以将晦涩难懂的概念以容易理解的方式讲授出来。例如，我在伊利诺斯大学的学生时代，我们四名学生在一起学习准备隔天的遗传学考试。我解答了小组中提出的诸多问题，其中一位同学当时说：“Nick，你可以当这门课的老师了。”在我的教学生涯中，我也多次因最佳讲授被辛辛那提大学生理学系的研究生授予“金苹果”奖。

还有一个值得提及的例子。Michael Palmer是一位医学奥秘畅销书的作者，在他2009年发行的《二次诊断》小说中使用了我的姓。我的儿子Thomas问Palmer博士怎么会起“Sperelakis”的姓？要知道这在希腊后裔中它是非常少见的。Palmer博士的回答是：1960年代中期在他还是凯斯西储大学的一名医学学生时，他选读了我的神经与肌肉电生理学的课程。他说我是他上过的所有课程中最喜欢的基础科学教师，当时他们给我起了“spike”（神经动作电位的术语）的绰号。你能否相信经过约45年后Palmer博士仍记得我以及我

的绰号？奉献于教学！对此确有些不可思议，因为我自10岁至今有严重的口吃（虽然现在已轻得多）。

在本书第一版出版之前，我意识到在细胞生理学和膜生物物理学领域确实需要一本好的、权威性的教材。这样一本大学科范围的书要像我的朋友 Hugh Davson 那样单靠一人撰写的时代已过去。一本权威性教材要涵盖众多的学科专长，看来它只能由聚集一群分别涉及各个领域的专家的多作者撰写，在所有四个版本中我们都遵循这一原则。本教材的第一版、第二版及第三版分别出版于1995年、1998年和2001年。第一版和第二版因其优秀被美国图书馆协会授予“精选奖”。

伦敦大学学院的 Hugh Davson 写了第一版的序言。自他的《普通生理学教材》出版后 Davson 教授很有名，这本书多年来确实是所有研究生的“圣经”。我初次遇见 Hugh 是1965～1966年我在伦敦大学学院度学术休假时。他是一位迷人的家伙，我们间建立了亲近的友谊。那个时候，伦敦大学学院是非常合适之地。诺贝尔奖获得者 A. F. Huxley 是生理学系的主任，之后的诺贝尔奖获得者 Bernard Katz 是生物物理学系的主任。诺贝尔奖获得者 A. V. Hill 仍每周1～2次来到他在生物物理学系的办公室，他那时已90岁了！简直难以相信！顺便提及，伦敦大学学院也是我初次和本书的一位撰写人 Hugo Gonzalez-Serratos 相识之地。

Thomas E. Thompson 撰写了第二版的序言。他是我在弗吉尼亚大学工作时的生物化学系主任。他在平面及球形脂质双分子层膜领域是位一流的研究者。Tom 也是位出色的老师，我曾请他参与我的研究生课程。他曾任生物物理学会的主席。

牛津大学的 Denis Noble 撰写了第三版的序言。Denis 是心脏电生理学领域的一流研究者和理论家。一次，他请我在牛津举行的会议上作报告，诺贝尔奖获得者 Alan Hodgkin 爵士主持了那次分会。那时我双腿一直在打颤！

我决定请我长期的老友弗吉尼亚医学院的 Alexandre Fabiato 教授写此第四版的序言。Alex 是一位在心肌领域杰出的科学家。他在钙致钙释放机制上的研究非常有名，经常被引用。1989年他获得了声誉很高的美国心脏协会研究成就奖。他是在法国接受培养成为一名心脏病学家的，是 Edouard Coraboeuf 教授（法国，奥赛，巴黎大学）和 Silvio Weidmann 教授（瑞士，伯尔尼大学）的研究生，这二位导师都是心肌生理学领域的一流开拓者和巨匠。我很自豪和高兴，Alex 允诺写序言。

在准备本书的道路上不是没有一些大的颠簸的，有时似乎是难以克服的路障。对教学的奉献以及人们对本书的渴望，鼓舞着我去完成它。而且，我也感到这是一种对诸位撰写人的强烈责任心，一些撰写人在本修订版之初业已花费了时间和精力。再一次，我不知如何来强调我对他们努力的赞颂，以及我是多么自豪他们能参与本书的撰写。我们全体共同希望本教科书能深受欢迎、非常成功。

Nicholas Sperelakis

2011年5月

Dedication

This book is dedicated to Planet Earth and to all those organizations that are working tirelessly to save and protect the environment, to stop pollution of our oceans, lakes, rivers, drinking water, air, and soil, to preserve the farmlands, to stabilize world population, to protect and preserve wildlife, to promote animal welfare, and to fight for human rights around the globe.

I also want to acknowledge the love and support of my family: my wife Dolores and children Mark Demitri (deceased), Christine M., Sophia A., Thomas A., and Anthony J., daughter-in-law Sherri, and grandchildren Demetra, Gregory and Nina-Nicole.

A special thanks to David Magnuson, M.D., Chairman of Pediatric Surgery at Cleveland Clinic, for his great dedication, skills, wisdom and humanity. Efharisto para poli, aka "Εύχαριστω παρά πολύ".

In Memoriam

Dr Hugo Gonzalez-Serratos passed away on April 1, 2011. Hugo was Professor of Physiology at the University of Maryland in Baltimore. He was a graduate student of Professor Andrew F. Huxley, Nobel laureate, at University College London in the mid-1960s. Dr Gonzalez-Serratos achieved great recognition as a top scientist in the field of muscle physiology. He will be greatly missed by all of us. Professor Gonzalez-Serratos was a contributing author to this book. May his memory be eternal!

Contributors

Francisco J. Alvarez-Leefmans MD, PhD, Professor, Department of Pharmacology and Toxicology, Boonshoft School of Medicine, Wright State University, Dayton, Ohio, USA

Clive M. Baumgarten, Professor of Physiology and Biophysics, Biomedical Engineering and Medicine (Cardiology), School of Medicine, Virginia Commonwealth University, Richmond

Kenneth M. Blumenthal, Professor and Chairman, SUNY Department of Biochemistry, School of Medicine and Biomedical Sciences, Buffalo, New York, USA

John H.B. Bridge, Research Professor of Medicine, Division of Cardiology, University of Utah Health Sciences Center, Nora Eccles Harrison Cardiovascular Research and Training Institute, University of Utah, CVRTI, Salt Lake City, Utah, USA

Bruce A. Carlson, Washington University, St Louis, Missouri, USA

Laura Conforti, Department of Internal Medicine, University of Cincinnati, Cincinnati, Ohio, USA

John R. Dedman, Professor and Ohio Eminent Scholar, Department of Cancer & Cell Biology, Department of Molecular and Cell Biology, University of Cincinnati, Cincinnati, Ohio, USA

Neil D. Detweiler, Department of Pharmacology and Toxicology, University of Arkansas for Medical Sciences, Little Rock, Arkansas, USA

Istvan Edes, Institute of Cardiology, University of Debrecen, Debrecen, Hungary

Robert A. Farley PhD, Professor Physiology and Biophysics, Biochemistry and Molecular Biology, Departments of Physiology and Biophysics, and Biochemistry and Molecular Biology, Keck School of Medicine, University of Southern California, Los Angeles, California, USA

Joseph J. Feher PhD, Professor of Physiology and Biophysics, School of Medicine, Virginia Commonwealth University, Richmond, Virginia, USA

Darrell Fleischman, Adjunct Associate Professor, Department of Biochemistry and Molecular Biology, Boonshoft School of Medicine, Wright State University, Dayton, Ohio, USA

Michael S. Forbes Ph.D., Department of Pediatrics, University of Virginia School of Medicine, Charlottesville, Virginia, USA

Kenneth W. Foster, Professor, Physics Department, Syracuse University, Syracuse, New York, USA

Jeffrey C. Freedman, Associate Professor, Neuroscience and Physiology, SUNY Upstate Medical University, Syracuse, New York, USA

Andrew S. French, Professor of Physiology and Biophysics, Department of Physiology and Biophysics, Halifax, Nova Scotia, Canada

Nicole Gallo-Payet, Professor and Research Chair of the Faculty of Medicine and Health Sciences, Departments of Endocrinology, and Medicine, University of Sherbrooke, Sherbrooke, Quebec, Canada

Hugo Gonzalez-Serratos, Professor, Physiology, University of Maryland, School of Medicine, Baltimore, Maryland, USA

Anthony L. Gotter, Division of Human Genetics, The Children's Hospital of Philadelphia and the Joseph Stokes Jr Research Institute, Philadelphia, Pennsylvania, USA

Michael S. Grace, Associate Professor, Biological Sciences Department, College of Science, Florida Institute of Technology, Melbourne, Florida, USA

Steven M. Grassl, Associate Professor, Pharmacology, State University of NY Upstate Medical University, Syracuse, New York, USA

Dennis W. Grogan, Professor, Department of Biological Sciences, University, College of Arts and Sciences, University of Cincinnati, Cincinnati, Ohio, USA

Judith Heiny, Associate Professor, Department of Molecular and Cellular Physiology, University of Cincinnati, Cincinnati, Ohio, USA

Aldebaran M. Hofer, Associate Professor of Surgery & Research Health Scientist, VA Boston Healthcare System and the Department of Surgery, Brigham and Women's Hospital and Harvard Medical School, Massachusetts, USA

Atsushi Inanobe, Department of Pharmacology, Graduate School of Medicine and The Center for Advanced Medical Engineering and Informatics, Osaka University, Osaka, Japan

Marcia A. Kaetzel, Department of Cancer and Cell Biology, University of Cincinnati, Cincinnati, Ohio, USA

Robert S. Kass, Alumni and David Hosack Professor of Pharmacology and Chair, Columbia University College of Physicians and Surgeons, New York, USA

Sujay V. Kharade, Department of Pharmacology and Toxicology, University of Arkansas for Medical Sciences, Little Rock, Arkansas, USA

Takeshi Kobayashi, Assistant Professor, Department of Cellular Physiology and Signal Transduction, Sapporo Medical University School of Medicine, Sapporo, Japan

Evangelia G. Kranias, Chair, Department of Pharmacology & Cell Biophysics, Distinguished University Professor, Co-Director, Cardiovascular Center of Excellence, Department of Pharmacology and Cell Biophysics, University of Cincinnati, Cincinnati, Ohio, USA

Yoshihisa Kurachi, Department of Pharmacology, Graduate School of Medicine and The Center for Advanced Medical Engineering and Informatics, Osaka University, Osaka, Japan

Stephen Lambert, Associate Professor of Medicine, College of Medicine, University of Central Florida, Health Sciences Campus at Lake Nona, Orlando, Florida, USA

Michael Levandowsky, Research Scientist, Adjunct Professor of Biology, Haskins Laboratories, Pace University, New York, USA

Simon Rock Levinson, Professor, Department of Physiology and Biophysics, University of Colorado School of Medicine, Aurora, Colorado, USA

Daniel C. Marcus, Program Director, KSU COBRE grant; Professor, Anatomy and Physiology, College of Veterinary Medicine, Kansas State University, Manhattan, Kansas, USA

Gerhard Meissner, Professor, Departments of Cell and Molecular Physiology, and Biochemistry and Biophysics, The University of North Carolina at Chapel Hill School of Medicine, Chapel Hill, North Carolina, USA

Stan Misler, Associate Professor, Internal Medicine, Cell Biology and Physiology, Washington University in St Louis School of Medicine, St Louis, Missouri, USA

Catherine E. Morris, Senior Scientist, Neuroscience, Ottawa Hospital Research Institute; Professor, Department of Medicine, Division of Neurology, University of Ottawa, Ottawa, Ontario, Canada

Michela Ottolia, Department of Physiology, Cardiovascular Research Laboratories, David Geffen School of Medicine at UCLA, Los Angeles, California, USA

Richard J. Paul, Professor, Director, PhD Program in Systems Biology and Physiology, Department of Molecular and Cellular Physiology, College of Medicine, University of Cincinnati, Cincinnati, Ohio, USA

Asif R. Pathan, Department of Pharmacology and Toxicology, University of Arkansas for Medical Sciences, Little Rock, Arkansas, USA

Marcel Daniel Payet, Professor, Department of Physiology and Biophysics, Faculté de Médecine, Université de Sherbrooke, Sherbrooke, Quebec, Canada

Matthew Pincus, Professor, Clinical Pathology, SUNY Downstate Medical Center in Brooklyn; Chief, Department of Pathology & Laboratory Medicine, New York Harbor VA Medical Center, Brooklyn, New York, USA

Tracy J. Pritchard, Department of Pharmacology and Cell Biophysics, University of Cincinnati, Cincinnati, Ohio, USA

Robert W. Putnam, Professor, Department of Neuroscience, Cell Biology and Physiology, Boonshoft School of Medicine, Wright State University, Datyton, Ohio, USA

Seth Robey, Department of Pharmacology, College of Physicians and Surgeons, Columbia University, NY, New York, USA

Stephen D. Roper, Professor, Department of Physiology and Biophysics, University of Miami Miller School of Medicine, Miami, Florida, USA

Nancy J. Rusch, Professor and Chair, Department of Pharmacology and Toxicology, University of Arkansas College of Medicine, University of Arkansas for Medical Sciences, Little Rock, Arkansas, USA

Kevin J. Sampson, Department of Pharmacology, College of Physicians and Surgeons, Columbia University, NY, New York, USA

William A. Sather, Associate Professor, Department of Pharmacology, University of Colorado Denver, Aurora, Colorado, USA

Nicholas Sperelakis, Department of Physiology and Biophysics, College of Medicine and Division of Pharmaceutical Sciences, College of Pharmacy, University of Cincinnati, Cincinnati, Ohio, USA

Anup K. Srivastava, Department of Pharmacology and Toxicology, University of Arkansas for Medical Sciences, Little Rock, Arkansas, USA

Janusz B. Suszkiw, Professor, Department of Molecular and Cellular Physiology, University of Cincinnati, Cincinnati, Ohio, USA

Timothy C. Tricas, Professor, Department of Zoology & Hawaii Institute of Marine Biology, University of Hawaii at Manoa, Honolulu, Hawaii, USA

Noritsugu Tohse, Professor, Department of Cellular Physiology and Signal Transduction, Sapporo Medical University School of Medicine, Sapporo, Japan

Päivi H. Torkkeli, Professor of Physiology and Biophysics, Department of Physiology and Biophysics, Dalhousie University, Halifax, Nova Scotia, Canada

Natalia S. Torres, Nora Eccles Harrison Cardiovascular Research and Training Institute, University of Utah, Salt Lake City, Utah, USA

Kenneth R. Tovar, Vollum Institute, Oregon Health and Science University, Portland, Oregon, USA

Richard D. Veenstra, Department of Pharmacology, SUNY Upstate Medical University, Syracuse, New York, USA

Gordon M. Wahler, Professor, Physiology, Midwestern University, Downers Grove, Illinois, USA

Gary L. Westbrook, Senior Scientist and Co-Director, Vollum Institute Dixon, Professor of Neurology Oregon Health and Science University Portland, OR USA

J. Woodland Hastings, Professor of Natural Sciences, Department of Molecular and Cellular Biology, Harvard University, Cambridge, Massachusetts, USA

Hisashi Yokoshiki, Associate Professor, Department of Cardiovascular Medicine, Hokkaido University Graduate School of Medicine, Sapporo, Japan

Anita L. Zimmerman, Professor and Vice Chair, Molecular Pharmacology, Physiology and Biotechnology, Brown University, Providence, Rhode Island, USA

Foreword to the First Edition

It was kind and generous of my friend Nicholas Sperelakis to relate this excellent book so closely to my own, *A Textbook of General Physiology.* In the preface to the first edition of my book, I had expressed the hope that it might be compared with Bayliss' *Principles of General Physiology.* If this comparison is valid, it is very appropriate that the present book be organized and partly written by one who is, along with Sir William Bayliss and myself, associated with University College London (Professor Sperelakis having spent a sabbatical year there). It is a pleasure to recall that it was there that I first met Nicholas, and I remember discussing his pioneering study on the potentials across the crystalline lens of the eye.

For reasons that I think bear no relation to its scope, this book has a different title; I presume it is because the distinction between "ordinary" and "general" physiology has become sufficiently blurred to demand something more appropriate. The definition of general physiology that I had proposed in the preface to the first edition of my textbook was "the study of those aspects of living material that show some immediate prospect of being described in terms of the known laws of physics and chemistry." Later, I had misgivings as to the narrowness of this definition, and I then suggested that it might be replaced by "the study of those features of life that appear to be common to all forms." Whatever definition we choose, however, it is of immense satisfaction to me that this new book, essentially, has been fitted into the same sectional headings that I employed in my own book.

If I may be permitted to reminisce further, I have wondered frequently how a single scientist, actively engaged in research, could write a new book of such wide scope. The answer is that I wrote the book during the 2 years immediately following the end of World War II. Thus, for several years — in Great Britain for as many as 10 years — very little original academic physiology and new research had been published. This made it possible to survey the original literature of a lengthy period without being overwhelmed by a rapid succession of new discoveries that would have rendered my task nearly impossible, a fate similar to that of Sisyphus. Today, this task would be impossible, and it only surprises me that Nicholas has been able to produce this magnificent book with so few collaborators.

Hugh Davson
1995

Foreword to the Second Edition

In his Foreword to the first edition of the *Cell Physiology Sourcebook*, Hugh Davson established it as the lineal descendent of his own well-known and highly respected work *The Textbook of General Physiology*. The second edition of the *Cell Physiology Sourcebook,* again edited by Nicholas Sperelakis, continues in this same tradition. Although the first edition was enthusiastically received by the cell physiology community because of its depth and breadth of coverage, considerable important progress has been made in this rapidly developing area since its publication. The second edition deals with these new developments by a thorough reworking of topics and by the inclusion of new chapters in all sections covered in the first edition. The new topics introduced into the various sections include lipid structure, mitochondrial physiology, cell responses to hormones, red blood cell transport, neuron physiology, developmental changes in ion channels, sonotransduction, excitation-contraction coupling, and electroplax cells. In addition, the scope of the new edition has been valuably broadened by the inclusion of two entirely new sections. One titled *Protozoa and Bacteria* covers the physiology of these organisms in two chapters. In the other, *Cell Division and Programmed Cell Death*, there are chapters on the regulation of cell division, the cancer cell, apoptosis, and the effects of ionizing radiation. The extensive revisions and the new material in the second edition raise it to a new level.

Cell physiology, an area of central importance in biology, has grown out of a number of more traditional fields, and as a result, the literature continues to be widely dispersed. The great value of the *Cell Physiology Sourcebook* is that it gathers together under a single cover a broad range of up-to-date chapters that, taken together, define the field. The various chapters exhibit a uniformity of style and level of presentation that are a credit to the editor. Because of this and the scope and clarity of the presentations, this book can serve exceptionally well as an advanced undergraduate or graduate level text for cell physiology courses. The broad coverage of this second edition also makes it very attractive for use in cell biophysics, membrane biology, and biomedical engineering courses. It can serve equally well as a textbook for introductory courses in ion channel structure and physiology.

I was pleased, and indeed proud, to be asked by my colleague Nicholas Sperelakis to contribute the Foreword to the second edition of the *Cell Physiology Sourcebook*. This book clearly sets a new standard of excellence.

Thomas E. Thompson
1997

Foreword to the Third Edition

When Nicholas Sperelakis kindly invited me to write this foreword, I wondered how I could possibly follow in the footsteps of Hugh Davson. I studied physiology at University College London (UCL) at the time when his monumental *Textbook of General Physiology* was published. UCL was an extraordinary place in which to be a student at that time. Not only was Hugh Davson laying his particular cornerstone of the subject, but Leonard Bayliss was also reworking his father's famous *Principles of General Physiology*. These were the books that convinced me to become a research physiologist and that cell physiology was the place to begin. Between them, Davson and Bayliss were responsible for seducing generations of medical students to discover the challenge and delights of physiological research. Later, as a young lecturer at UCL, I remember asking Hugh Davson why he didn't lecture very much to the students. He simply replied: "Denis, I've written it all. Tell them to read!" Actually, that remark inspired me to reread his books. My copies are still in my library, and they are well and truly thumbed.

It will be the greatest tribute to the work of Nicholas Sperelakis and his colleagues that the pages of their book will also become the well-thumbed bible of a new generation of physiologists. They will be entering the discipline at an exciting time, for cell physiology is the base on which our understanding of all aspects of integrative and systems physiology must rest. This book, therefore, will be an essential source for all of us who aspire to understand the "logic of life," which is, after all, the meaning and origin of the word "physiology." Life has no single "logic," of course. Unraveling the physicochemical mechanisms that nature has discovered, fashioned, combined, and interwoven into the tangled skein of processes that form the function of even the simplest cell is a process full of surprises as we discover with awe the audacity with which nature's molecular mechanisms are reused again and again in different contexts. One might call this audacity the "dance of the genes" were it not for the inanimate and unthinking nature of these bits of code that transmit the logic from one generation to another. The logic is physiological, not genetic. The molecular biologist Sydney Brenner put the point succinctly when he wrote recently (in a Novartis symposium titled The Limits of Reductionism in Biology) that "Genes can only specify the properties of the proteins they code for, and any integrative properties of the system must be 'computed' by their interactions." We are approaching the point at which our understanding of those interactions is deep enough for physiology to aspire to become the quantitative analytical discipline it needs to be to solve the problems it tackles. Brenner went on to remark, significantly, "This provides a framework for analysis by simulation." It is a sign of the maturity of our science that simulation is indeed also becoming an essential tool of analysis.

It is further such a sign that the scope of cell physiology is now so wide. The breadth of this book is therefore one of its greatest strengths. The chapters encompass the great majority of important molecular and cell systems, so that it does indeed justify its title as a *sourcebook*.

Denis Noble

Foreword to the Fourth Edition

It is my pleasure to write a Foreword for the fourth edition of this textbook, entitled *Cell Physiology Sourcebook.* Professor Hugh Davson did not continue after the fourth edition of his monumental *A Textbook of General Physiology.* Perhaps he realized that the knowledge of physiology had become too broad for him to continue to cover the entire field alone, as he had done for his highly respected textbook.

So what permitted Professor Nicholas Sperelakis to write a noteworthy successor to Davson's formidable textbook? He decided to call upon an increasing number of specialists, and these prestigious specialists accepted to collaborate with him because they highly respected him as one of the major role models in Cell Physiology. Instead of really retiring when he closed his laboratory in 2002, Professor Sperelakis continued to publish articles, generally in collaboration with Dr L. Ramasamy from the Department of Electrical and Computer Engineering of the University of Cincinnati. Professor Sperelakis took the time to familiarize himself with the techniques used in PSpice, an electrical engineering software program (for circuit design and analysis), in which one substitutes electronic equivalents (e.g. resistances, capacitances, etc.) for physiological parameters. He was very excited while learning this new methodology. They have published about 10 articles using the PSpice simulations primarily in Theor Biol & Med Modelling and BioMed Eng Online. Since the first article summarizes the main ideas, I shall give complete reference only to this one, namely *N. Sperelakis and L. Ramasamy, Propagation in Cardiac Muscle and Smooth Muscle Based on Electric Field Transmission at Cell Junctions: An Analysis by PSpice. IEEE-EMB* **21**, *177-190, 2002.*

Professor Nicholas Sperelakis had some rather controversial research findings in the 1960s. In 1977, he reported with his mathematician collaborator, James E. Mann, that the transmission from one cell to the next one can occur in the myocardium by the development of an intense electric field in the narrow clefts of the intercalated disks. They stated, therefore, that propagation in myocardium can occur without the need of any gap-junction channels connecting the myocardial cells. They demonstrated that the density of fast Na^+ channels is greater in the intercalated-disk membrane than in the surface sarcolemma, which means that the excitability is likewise greater at the intercalated disks. I am glad to find that Professor Sperelakis is no longer alone in his Electric Field Hypothesis ever since that hypothesis was independently confirmed in the article by a Japanese group, namely *K. Tsumoto, T. Ashihara, R. Haraguchi, K. Nagazawa, and Y. Kurachi, Role of Subcellular Na Channel Distributions in the Mechanism of Cardiac Conduction. Biophysical Journal* **100**, *554-563, 2011.*

The third edition is packed with important information about the various aspects of the field of cell physiology and membrane biophysics. Most notably, I am impressed by the exceptional quality of the contributors relating to my field of expertise, namely the contractile mechanism and excitation–contraction coupling. Since the first edition of the *Cell Physiology Sourcebook*, new contributors were added for the subsequent editions, and I am certain that such will be the case for the fourth edition. It is always a pleasure to receive a telephone call from Professor Nicholas Sperelakis. He is so excited about his research, so vibrant with his passion for discovery. This enthusiasm is just one of the reasons why we respect him so much. Perhaps it is this passion to which his wife Dolores refers when she says that he is still as youthful and intellectually active as the young man she married 51 years ago. According to Professor Diomedes Logothetis, Chairman of our department at the Medical College of Virginia, the exceptionally good students are being hyperexcited by the "virus" of physiology, and I think that this happens also to established scientists such as Professor Sperelakis.

Professor Nicholas Sperelakis is celebrating his 81st birthday as I write this Foreword. For such a special anniversary, many Greeks add a "chronia polla" exclamation, which loosely translated is "many more years" or "with many happy returns". We wish that blessing, not only to Professor Sperelakis personally, but also for the new edition of his *Cell Physiology Sourcebook.*

Alexandre Fabiato
Richmond, VA
March 8, 2011

Preface

Preface to the Fourth Edition

Once upon a time, an 80-year-old retired university professor was leading a quiet and secluded life. Then one day in the spring of 2010, out of a clear blue sky, he was contacted by Janice Audet, Senior Acquisitions Editor for Academic Press. She said that a number of colleges were still using our third edition of *Cell Physiology Sourcebook* as the textbook for their courses in cell physiology, even though the third edition came out long ago, namely, in 2001.

In fact, I was aware of the use of the third edition in a number of colleges. About 2 years earlier, I was contacted by a graduate student from Georgia State University saying that they were using my book as the textbook for their class on cell physiology, but that he could not buy a copy because it was out of print. He asked me to send him my personal copy of the book. He said he would treat it well and return it to me at the end of the course. He even offered to drive to my home in Cincinnati to pick it up. This student was obviously desperate, so I talked to Noelle Gracy, my former editor, about the problem. She arranged for the class to have access to the e-book version of the textbook. Problem solved!

Janice wanted to know if I was interested in doing a fourth edition. Before I could give her a definitive answer, I wanted her to sample a number of course directors around the country to learn what they liked and what they didn't like about the third edition of the book. The consensus was that our book, in general, was pitched at too high a level for beginning graduate students (or senior undergraduates) taking a course in cell physiology. Some other suggestions were that we should eliminate some chapters/topics that are well-covered in the three textbooks available on cell biology, such as cell division, apoptosis, etc; we should improve the figures by using color; we should add a summary section at the beginning of each chapter; and, although difficult to achieve with so many contributing authors, we should try to make the various chapters more uniform in style.

I agreed to work on the fourth edition, and focused on incorporating the suggestions into the new edition. Some of the changes made to this edition include the omission of approximately 14 chapters, combining a few chapters, and asking contributors to try to pitch their chapters at the graduate student level. About 10 new contributors were recruited for specific expertise in the subject area. I believe that the final slate of contributors is top-notch, and I am extremely grateful for their participation.

So why did I agree to carry out this project that would require tremendous effort on my part, while in precarious health at that? Was it fortune/money? Absolutely not! That is miniscule. Was it fame/recognition? No, I'm too old to benefit from that now. Besides, I already edited three editions of the very same book. Was it dedication to teaching? Yes, that's what it was! I have dedicated my life to teaching, and I believe that I have the unique ability to present difficult concepts in an easily understandable way. For example, during my student days at the University of Illinois, four of us were studying together for an exam in genetics the next day. I was answering questions that the group had when one of them said, "Nick, you should be the one teaching this class." In the course of my career, I had also received multiple "golden apple" awards from graduate students in the Department of Physiology at the University of Cincinnati for the best teaching in our graduate courses.

One final example is worth mentioning. Michael Palmer, a best-selling author of medical mysteries, used my last name in one of his novels, "The Second Opinion", which came out in 2009. My son, Thomas, asked Dr Palmer how he came up with the name "Sperelakis", which is very uncommon in persons of Greek heritage. Dr Palmer replied that he was a medical student at Case-Western Reserve University in the mid-1960s, and he took my lectures on electrophysiology of nerve and muscle. He said that I was the favorite instructor in basic science of his entire class, and that they gave me the nickname of "Spike" which is jargon for a nerve action potential. Can you believe that Dr Palmer would remember me and my nickname after about 45 years? Dedication to teaching! My dedication to teaching is more amazing because I was a severe stutterer throughout my life, beginning at age 10 and continuing to the present (although now much less severe).

Before the first edition of this book was published, I saw a real need for a good, authoritative textbook in the area of cell physiology and membrane biophysics. The days when a single individual, like my friend Professor Hugh Davson, could cover such a broad area are gone. To cover the wide-ranging expertise necessary for an authoritative textbook, there seems to be no alternative other than arranging a multi-authored textbook by assembling a group of experts in the various topics to be covered. We used this principle in all four editions. The first edition, second edition, and third edition of this textbook came out in 1995, 1998, and 2001. The first and second editions received awards from the American Library Association for being outstanding, namely receiving their "Choice Award".

The Foreword to the first edition was written by Professor Hugh Davson of University College London (UCL). Professor Davson became very famous because of his textbook on cell physiology. It was indeed the "Bible" for all graduate students for a number of years. I first met Hugh when I was there on sabbatical leave in 1965–66. He was an amazing guy and we struck up an immediate friendship. In those days, UCL was quite the place. A.F. Huxley, Nobel Laureate, was head of the Physiology Department, and Bernard Katz, future Nobel Laureate, was head of the Biophysics Department. A.V. Hill, Nobel Laureate, was still coming to his office in the Biophysics Department about once or twice a week at age 90! Unbelievable! Incidentally, UCL is also where I first met Hugo Gonzalez-Serratos, a contributor to this book.

The Foreword for the second edition was written by Thomas E. Thompson. Tom was head of the Biochemistry Department at the University of Virginia while I was there. He was a leading investigator in the area of planar and spherical lipid bilayer membranes. Tom was an excellent teacher, and I had him participate in my graduate courses. Tom served as President of the Biophysical Society.

The Foreword for the third edition was written by Denis Noble of Oxford University. Denis became a leading investigator and theorist in the field of cardiac electrophysiology. One time, he asked me to give a lecture at a meeting being held at Oxford, and Sir Alan Hodgkin, Nobel Laureate, was chairing the session. I was shaking in my boots!

I decided to ask a long-time good friend, Professor Alexandre Fabiato of the Medical College of Virginia, to write the Foreword for this fourth edition. Alex is an outstanding scientist working on cardiac muscle. He is very well known and highly cited for his Ca-induced Ca release mechanism (CICR). He received the very prestigious Research Achievement Award from the national American Heart Association in 1989. Alex was trained as a cardiologist in France, and he was a graduate student with Professor Edouard Coraboeuf (University of Paris, Orsay, France) and Professor Silvio Weidmann (University of Bern, Switzerland), both leading pioneers and giants in the field of electrophysiology of cardiac muscle. I am proud and pleased that Alex agreed to do it.

The roadway along the book preparation trail was not without some large bumps and, at times, seemingly insurmountable roadblocks. Dedication to teaching, along with the great need for this textbook, kept me inspired to finish it. In addition, I felt a strong obligation to the Contributors, some of whom already had spent time and effort in beginning their revision. Again, I cannot stress how much I appreciate their efforts and how proud I am that they contributed to this book. We all hope that this textbook will be well received and highly successful.

Nicholas Sperelakis
May 2011

目　录

第三部分 膜兴奋与离子通道

第四部分 作为毒素、药物与遗传疾病靶的离子通道

第五部分　突触传递与感觉转导

第六部分　肌肉与其他收缩系统

Contents

Section I

Biophysical Chemistry, Metabolism, Second Messengers, and Ultrastructure

Chapter 1

Biophysical Chemistry of Physiological Solutions

Jeffrey C. Freedman

Chapter Outline

I. SUMMARY

This chapter describes the hydrogen-bonded structure of liquid water and its dipolar and dielectric properties. In salt solutions, water exhibits three regions of structure: oriented dipoles near ions; an intermediate structure-breaking region; and flickering clusters with short-range order characteristic of ice. Electrostatic interactions between ions and water based on Coulomb's law account for the enthalpy of hydration, as well as for the sequence of ionic mobilities of the hydrated alkali cations. Salts and non-electrolytes dissolve in cell water with nearly the same solubility and activity as in extracellular water; even the viscosities are similar. Protons in solution are hydrogen-bonded to water to form H_3O^+, which is further hydrated due to electrostatic forces. Protons migrate through water by a Grotthus chain mechanism; in contrast, other hydrated ions migrate through water as hard spheres that interact with water dipoles according to the ionic radius and charge. Non-specific ion–ion interactions reduce the activity coefficients of ions, as described by the Debye–Hückel theory, which conceptualizes a central ion surrounded by a cloud of counterions with smeared charge. Selective interactions of ions with sites on enzymes or on channel proteins occur in certain predictable specific patterns (Eisenman sequences) that depend on the energy of interaction between the ions and water dipoles, relative to that between ions and their binding sites.

All of the solutes in a cell contribute to the free energy of the intracellular solution. The Gibbs equation, which is derived in the Appendix by combining the first and second laws of thermodynamics, enables estimation of the changes in free energy when solutes cross cell membranes. The change in free energy is zero at equilibrium and negative for spontaneous processes. Solutes will redistribute until the electrochemical potential is the same in every compartment to which that solute has access. The Nernst equation (see Appendix), which follows from the Gibbs equation, relates the ratio of intracellular to extracellular ion concentrations at equilibrium to the membrane potential, and can be used to test whether a solute is in electrochemical equilibrium across a cell membrane.

II. INTRODUCTION

All living cells contain proteins, salts and water enclosed in membrane-bounded compartments. These biochemical and ionic cellular constituents, along with a set of genes, enzymes, substrates, and metabolic intermediates, function to maintain cellular homeostasis and enable cells to replicate and to perform chemical, mechanical and electrical work. *Homeostasis*, a term introduced by the physiologist Walter Cannon in *The Wisdom of the Body* (1932), means that certain parameters, including cellular volume, intracellular pH, the transmembrane electrical potential and intracellular concentrations of salts are maintained relatively constant in

Cell Physiology Sourcebook. DOI: 10.1016/B978-0-12-387738-3.00001-9

resting cells. Cellular homeostasis depends on a relative constancy of the extracellular fluids that bathe cells. The extracellular fluid compartment was termed the *milieu intérieur*, or internal environment, by Claude Bernard, who recognized around 1865 that "*La fixité du milieu intérieur est la condition de la vie libre*", that the constancy of the internal environment is the condition for independent life. In *An Introduction to the Study of Experimental Medicine* (see 1949 translation), Bernard wrote that "only in the physico-chemical conditions of the inner environment can we find the causation of the external phenomena of life". The development of cell physiology has been greatly influenced by the Bernard–Cannon theory of physical-chemical homeostasis.

Biophysical chemistry concerns the application of the concepts and methods of physical chemistry to the study of biological systems. Physical chemistry includes such physiologically relevant subjects as thermodynamics, chemical equilibria and reaction kinetics, solutions and electrochemistry, properties and kinetic theory of gases, transport processes, surface phenomena and molecular structure and spectroscopy. Throughout this book, it is seen that many cellular physiological phenomena are best understood with a rigorous and comprehensive understanding of physical chemistry. During the past 65 years, outstanding monographs on biophysical chemistry have been available: Höber (1945), Edsall and Wyman (1958), Tanford (1961), Cantor and Schimmel (1980), Silver (1985), Bergethon and Simons (1990), and Weiss (1996). To help the reader begin to understand how cellular homeostasis is achieved, this chapter will introduce some of the conceptual underpinnings of cell physiology by describing certain physicochemical properties of water and electrolytes that are relevant for understanding living cells.

III. STRUCTURE AND PROPERTIES OF WATER

Biological cells contain a large amount of water, ranging from 0.66 g H_2O/g cells in human red blood cells to around 0.8 g H_2O/g tissue in skeletal muscle. The amount of water in cells is determined by osmosis. Liquid water is a highly polar solvent, with a structure stabilized by extensive intermolecular *hydrogen bonds* (Fig. 1.1). The hydrogen bonds between adjacent water molecules are linear (O–H···O) but are able to bend by about 10°. From x-ray diffraction studies of ice crystals, it is known that each of the two covalent O–H bonds in water is 1 Å in length, that each of the two hydrogen bonds is about 1.8 Å in length and that these occur around each oxygen atom at angles of 104°30′ in a tetrahedral array.

The energy required to break hydrogen bonds in liquid water is 5 to 7 kcal/mol, much less than the 109.7 kcal/mol required to break the covalent O–H bond. A calorie is

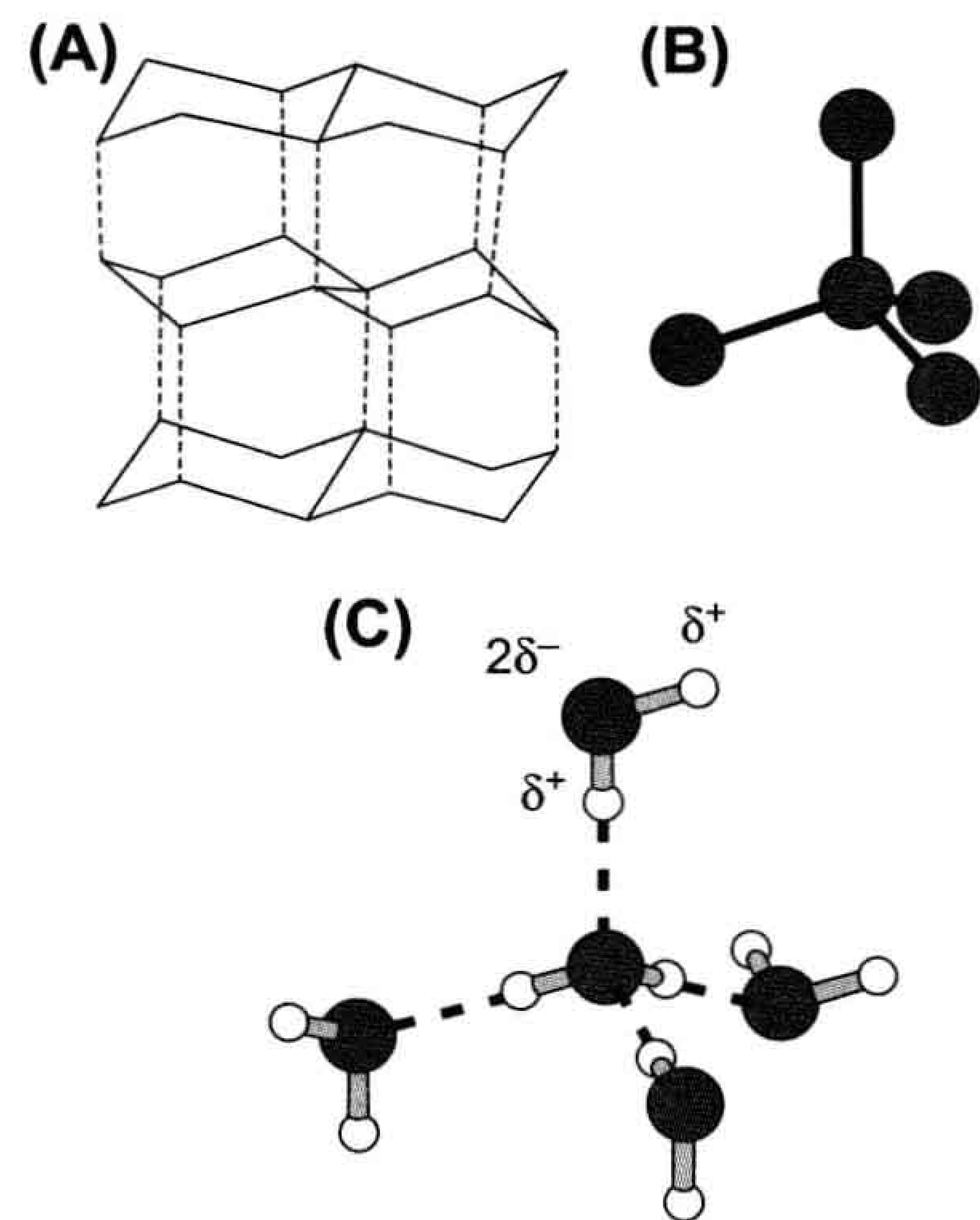


FIGURE 1.1 Hydrogen bonds in ice and liquid water. (A) Crystal structure of ice, showing the puckered hexagonal rings of oxygen atoms. (B) Each oxygen atom is connected to four others in a tetrahedron. (C) The linear hydrogen bonds are indicated by dotted lines between adjacent water molecules (O–H O). Two covalent bonds (O–H), indicated by solid lines, and two hydrogen bonds occur around each oxygen atom in a tetrahedral array. The partial charge separation of the O–H dipoles is indicated on the upper water molecule.

a unit of work equal to 4.18 J in the SI system of units, where 1 joule (J) equals 1 Newton·meter. The newton ($N = k \cdot gm/s^2$) is the unit of force in the International System of Units (SI); the dyne ($dyn = g \cdot cm/s^2$) is the corresponding unit of force in the older cgs system ($1\ N = 10^5$ dyn). Recall that, according to Newton's first law, the force (F) is mass times acceleration and that work is defined as force times distance. Because of the strength of hydrogen bonds, liquid water has unique physicochemical properties, including a high boiling point (100°C), a high *molar heat capacity* (18 cal/mol·K), a high *molar heat of vaporization* (9.7 kcal/mol at 1 atm) and a high *surface tension* (72.75 dyn/cm). As discussed by Bergethon and Simons (1990), all of these thermodynamic parameters are considerably higher for H_2O than for the analogous compound H_2S, which boils at −59.6°C. The outer electrons of the S atom shield its nuclear charge and reduce its electronegativity, making the S–H bond weaker, longer and less polar than the O–H bond. Also, the bond angle of H_2S is only 92°20′, an angle that does not form a tetrahedral array and thus H_2S does not form a hydrogen bonded network like water.

The extensive intermolecular association in liquid water is due to the geometry of the water molecule and also to its strong permanent *dipole moment*. Water molecules have no net charge, yet possess permanent charge separation along each of the two O–H bonds. Since oxygen is more *electronegative* than hydrogen, its electron density is preferentially

greater. Oxygen thus acquires a partial negative charge (δ^-), leaving the hydrogens with a partial positive charge (δ^+) (see Fig. 1.1C). The magnitude of the dipole moment (μ) of a chemical bond is computed as the product of the separated charge (q) at either end, and the distance (d) between the centers of separated charge ($\mu = qd$). The dipole moment of a molecule is the vector sum of the dipole moments of each bond. For water in the gaseous phase, the dipole moment is 1.85 debye, where 1 debye = 10^{-18} esu·cm. One esu (electrostatic unit), or stat-coulomb, equals 3.336×10^{-10} C, the coulomb (C) being a unit of electric charge. In liquid water, the dipole moment becomes even larger (2.5 debye) due to association with other water molecules. In comparison, the linear molecule carbon dioxide (O=C=O) also has a separation of charge, with a partial negative charge on each oxygen atom and a partial positive charge on the carbon atom. In this case, the oppositely directed dipole moments of the two C=O bonds sum to a zero dipole moment for the CO_2 molecule. In H_2S, the S—H bond has a smaller dipole moment (1.1 debye) than the O—H bond in water because sulfur is less electronegative than oxygen. Electrostatic attractions between opposite charges in adjacent water dipoles stabilize the hydrogen-bonded structure of liquid water.

Water strongly affects the forces between ions in solution by virtue of its high *dielectric constant*. The dielectric constant (ε) of a medium known as a *dielectric* is defined as the ratio of the coulombic force (F_{coul}) between two charges in a vacuum to the actual force (F) between the same two charges in the dielectric medium.

$$\epsilon = \frac{F_{coul}}{F}$$

In a vacuum, the coulombic force, Fcoul (newtons, N), between two ions with charges q^+ and q^- (C) separated by a distance d (meters, m) is given by Coulomb's law:

$$F_{coul} = \frac{q^+q^-}{4\pi\epsilon_0 d^2}$$

where ε_0 is the permittivity constant ($8.854 \times 10^{-12} C^2/N\,m^2$). Coulomb's law states that the force between two point charges is directly proportional to the magnitude of each charge and inversely proportional to the square of the distance between the charges. Substituting F_{coul} into the above expression and rearranging yields the following:

$$F = \frac{q^+q^-}{4\pi\epsilon_0\epsilon\, d^2}$$

The dielectric constant of a vacuum is unity and that of air is close to unity ($\varepsilon_{air} = 1.00054$). Increasing the dielectric constant of the solvent decreases the attractive force between oppositely charged ions. The force felt by a distant ion is reduced in a dielectric medium, such as water, as compared with a vacuum, because part of the interaction energy is spent aligning the intervening water dipoles and distorting their polarizable electron clouds. The dielectric constant of water at 25°C is 78.5, much greater than methanol ($\varepsilon = 32.6$), ethanol (24.0) or methane (1.7). In liquid water, the high dielectric constant weakens the coulombic attractive forces between oppositely charged particles and thus promotes dissociation and ionization of salts.

Although the thermodynamic properties of liquid water are explicable in terms of extensive hydrogen-bonding, the actual structure of water is complex. In the flickering cluster model, groups of 50—70 water molecules, resembling a slightly expanded broken piece of the ice lattice (icebergs), are continuously associating and dissociating on a picosecond time scale. This dynamic model contrasts with the extended order of solid ice. At a given instant, some water molecules are unattached to the clusters and are located in the interstitial regions of the network, but may attach and detach as the clusters continuously form and break down. Other theories treat water as a mixture of distinct states, or as a continuum of states, with considerable short-range order, characteristic of the crystalline lattice of ice.

Despite these uncertainties regarding the structure of liquid water and the influence of macromolecules on its properties in cells, the ability of water to act as a solvent inside cells closely resembles that of extracellular water. Thus, a variety of permeant, hydrophilic, non-metabolized non-electrolytes distribute at equilibrium across human red blood cell membranes with ratios of intracellular to extracellular concentrations that deviate from unity by less than 10% (Gary-Bobo, 1967). In mouse diaphragm muscle, Miller (1974) found that several alcohols, diols and monosaccharides exhibit distribution ratios within 2% of unity, whereas certain other sugars appear to be excluded from membrane-bounded intracellular compartments. The amount of solute that dissolves at equilibrium is also nearly normal in water that is constrained in gels, which are cross-linked networks of fibrous macromolecules. The diffusion of solutes within gels, however, may be hindered by collisions and interactions with the macromolecules and by the tortuosity of the diffusion paths.

Viscosity, another property of water, contributes to the resistance to flow. A fluid with a greater viscosity exhibits less flow under the influence of a given pressure gradient than a fluid with a lesser viscosity. For example, molasses, a concentrated sugar solution, is much more viscous than pure water. During *laminar flow*, a frictional force develops between adjacent layers (laminae) in the fluid and this force impedes the sliding of one lamina past its neighbor. In a *Newtonian fluid*, the frictional force per unit area, or shear stress (τ, dyn/cm^2), is proportional to the velocity gradient, or rate of strain (dv/dy, s^{-1}) between laminae,

$$\tau = \eta \cdot (dv/dy)$$

where the viscosity (η) is the proportionality constant with units of poise (=1 dyn s/cm^2), named after Poiseuille. The viscosity of H_2O at 20.3°C is 0.01 poise, or 1 centipoise (cp). In cultured fibroblasts, the fluid-phase cytoplasmic viscosity, as determined from rotational motions of fluorescent probes on a picosecond time scale, is only 1.2–1.4 times that of pure water (Fushimi and Verkman, 1991). Fluorescence studies also show that the viscosity is the same in the cytoplasm and nucleoplasm and is unaffected by large decreases in cell volume or by disruption of the cytoskeleton with cytochalasin B. The fluid-phase viscosity, as determined from fluorophore rotational motions, is not nearly as affected by macromolecules as is the bulk viscosity and it thus provides a more accurate view of the physical state of the aqueous domain of the cytoplasm. These and other studies (e.g. Schwan and Foster, 1977; Horowitz and Miller, 1984) set limits on the extent to which the physicochemical properties of intracellular water differ from those of extracellular water.

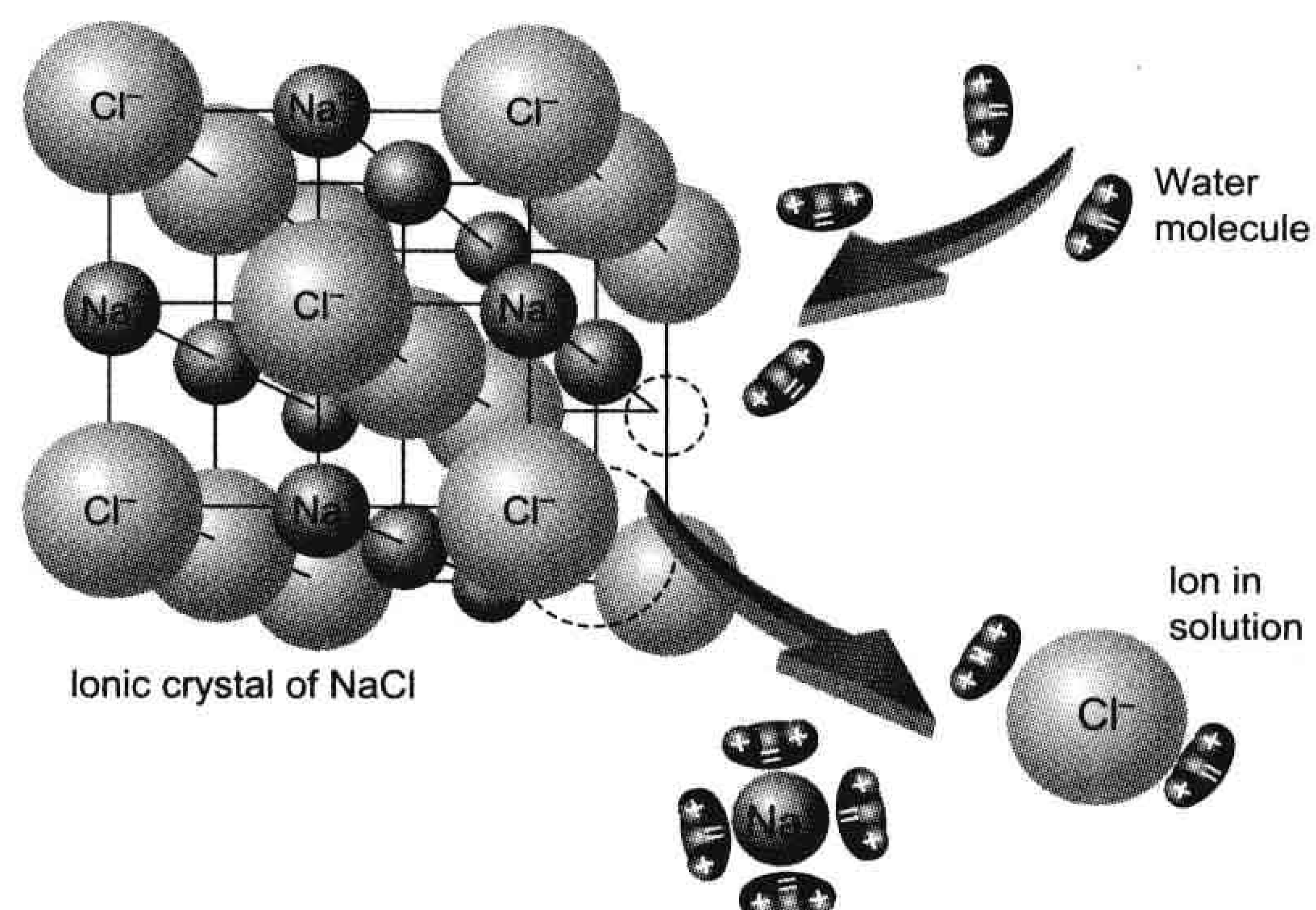


FIGURE 1.2 Dissociation of NaCl in water into hydrated Na^+ and Cl^- ions.

IV. INTERACTIONS BETWEEN WATER AND IONS

Ions in solution behave as charged, hard spheres that interact with and orient water dipoles. When crystals of sodium chloride are dissolved in water, the electrostatic attractive forces between water dipoles and ions in the crystal lattice overcome the inter-ionic attractive forces between oppositely charged ions in the crystal. The dissociated ions then acquire the freedom of translational motion as they diffuse into the solution accompanied by a layer of tightly associated *hydration water* (Fig. 1.2). *Ion* is the Greek word for "wanderer". The strength of the attraction between ions and water dipoles depends to a large extent on the ionic charge and radius. For the alkali metal cations, the force of attraction and the energy of interaction of ions with water, decreases according to the following series: $Li^+ > Na^+ > K^+ > Rb^+ > Cs^+$.

Li^+, being the smallest of the alkali metal cations, has the strongest interaction with water because its positively charged nucleus can approach most closely to the negative side of neighboring water dipoles. As the ionic radius increases with increasing atomic number in the alkali metal series, the filled outer shells of electrons effectively shield the cationic charge and reduce the distance of closest approach to water molecules. The smallest ion thus acquires the greatest degree of hydration and has the largest hydrated ionic radius.

According to Frank and Wen (1957), the orienting influence of ions on water dipoles results in three regions of water structure (Fig. 1.3). The electric field of an ion is sufficiently strong to remove water dipoles from the bulk water clusters and to attract to itself the oppositely charged ends of from one to five water dipoles. A certain number of these water dipoles, called the *hydration number*, then become trapped and oriented in the ion's electric field. The inner hydration shell includes water molecules that are aligned by the force field and in direct contact with the ion, 5 ± 1 for Li^+, 4 ± 1 for Na^+, 3 ± 2 for K^+ and Rb^+, 4 ± 1 for F^-, 2 ± 1 for Cl^- and Br^- and 1 ± 1 for I^-. Thus, in physiological saline at 0.15 M NaCl in water (55.5 M), about 1.6% ($=100 \times 0.15 \times 6/55.5$) of the water is located in the inner hydration shells of Na^+ and of Cl^-. Water in the inner hydration shells of Na^+, K^+ and Ca^{2+} rapidly exchanges with bulk water on a nanosecond time scale but, in contrast, the smaller divalent cation Mg^{2+}, with its high

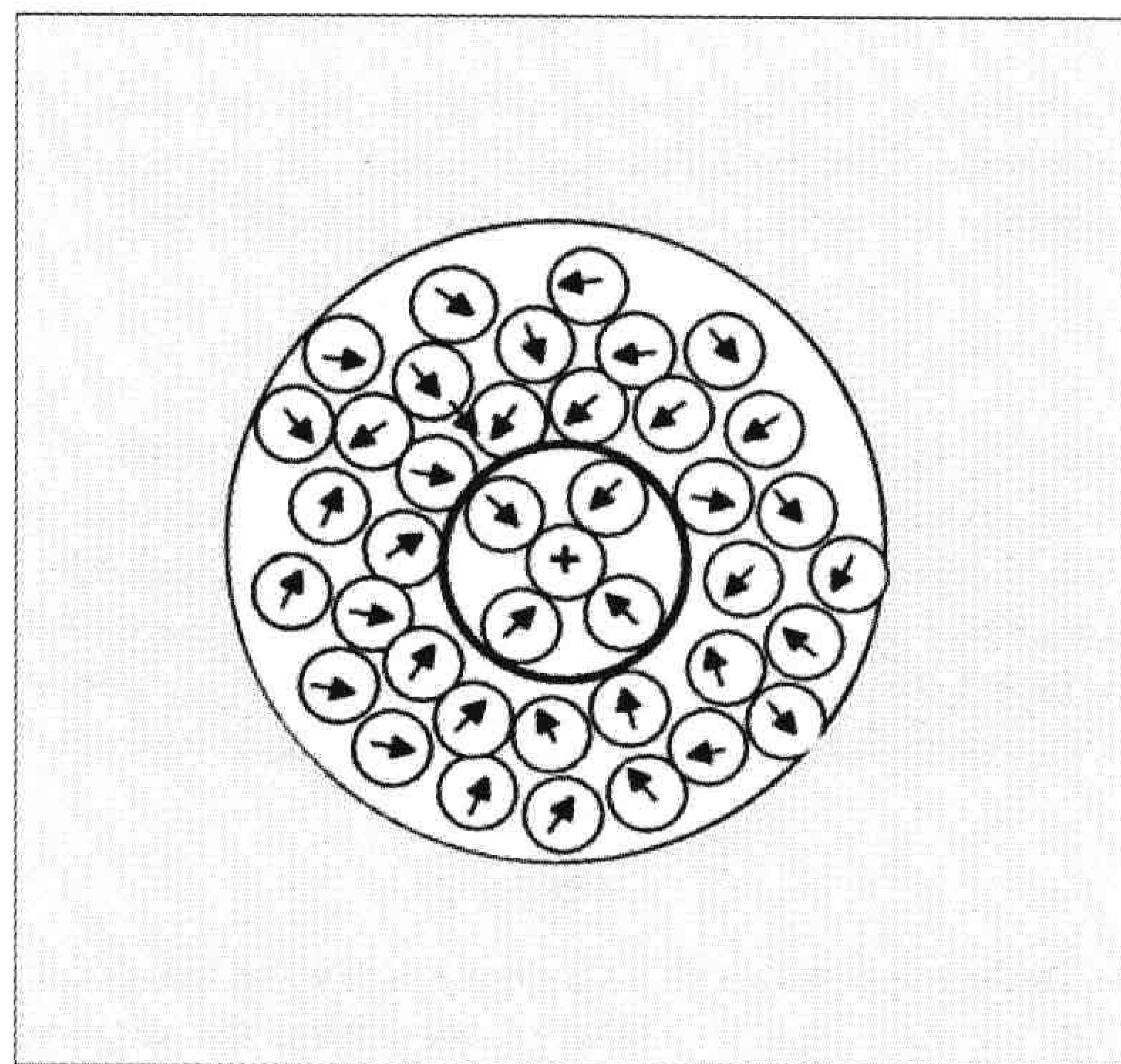


FIGURE 1.3 Three regions of water structure near an ion. A central cation is shown with a primary hydration shell of four oriented water dipoles, surrounded by a partially oriented secondary sheath. The gray region indicates the hydrogen-bonded structure of the bulk water.

charge density, is some four orders of magnitude slower in exchanging its inner hydration water. The inner hydration sheath of water molecules moves together with the ion as a distinct and single kinetic entity.

The mobilities of the alkali cations in water decrease as the non-hydrated ionic radius decreases, but as the hydrated ionic radius increases (Table 1.1; for discussion, see Hille, 2001). The ionic *mobility* (u) is defined as the proportionality constant that relates the velocity (v) of ionic migration to the force exerted by an external electric field E ($v = u \cdot E$); in other words, mobility is the velocity per unit electric field. Farther away from the ion, where the ion's electric field falls towards zero, water retains the structure of bulk water. In the region between the inner hydration sheath and the bulk water, the orienting influences of the ion and the bulk water network tend to compete and to disrupt the structure of water. In this intermediate structure-breaking region, the water dipoles are partially oriented toward the central ion, yet do not migrate with the ion, and they join only infrequently with the hydrogen-bonded clusters of the bulk water. If the net effect of an ion is to disorganize more water in the intermediate region than is found in the primary hydration shell, then the ion is termed a *structure-breaker*. Conversely, water may form a variety of hydrogen-bonded clathrate structures around apolar protein side chains, whose action resembles that of the class of solutes termed *structure-makers* (see Klotz, 1970, for review).

TABLE 1.1 Radii, Enthalpies of Hydration and Mobilities of Selected Ions

Ion	Non-hydrated Radius[a] (Å)	$\Delta H^0_{hydration}$[b] (kcal/mol)	Mobility[c] $10^{-4}\frac{cm/s}{V/cm}$
H^+	—	−269	36.25
Li^+	0.60	−131	4.01
Na^+	0.95	−105	5.19
K^+	1.33	−85	7.62
Rb^+	1.48	−79	8.06
Cs^+	1.69	−71	8.01
Mg^{2+}	0.65	−476	2.75
Ca^{2+}	0.99	−397	3.08
Sr^{2+}	1.13	−362	3.08
Ba^{2+}	1.35	−328	3.30
Cl−	1.81	−82	7.92

[a] *Radii are from Pauling (1960).*
[b] *Standard enthalpies of hydration at 25°C are from Edsall and McKenzie (1978).*
[c] *Mobilities in water at 25°C are from Hille (2001, p. 317).*

The *enthalpy of hydration* of an ion is a measure of the strength of the interaction between ions and water and is defined as the increase in enthalpy when one mole of free ion in a vacuum is dissolved in a large quantity of water. The enthalpy of hydration may be estimated from the heat released upon dissolving salts in water, usually less than 10 kcal/mol, taking into account the energy needed to dissociate the salt crystal and then to hydrate the ions. The enthalpy of hydration may be calculated using electrostatic theory. Accurate results are obtained if water is considered to be an electric quadrupole with four centers of charge, two partial positive charges near the hydrogen nuclei and two partial negative charges on the non-bonded electron orbitals near the oxygen nucleus. A further improvement in the calculated enthalpy of hydration is obtained when the polarizability (α) of the water dipole by the ion is taken into account. The electric field of the ion distorts the electron cloud of the hydration water along its permanent dipole axis, thus inducing an additional increment of charge separation and increasing the dipole moment. For small fields, this *induced dipole moment* (μ_{ind}) is proportional to the electric field strength (E) and the constant of proportionality is the *polarizability* ($\mu_{ind} = \alpha \cdot E$). In Fig. 1.4, the measured enthalpies of hydration for alkali metal cations and halides are compared with calculated values; the impressive agreement demonstrates the primary importance of electrostatic forces in determining the solvation of ions in water. The enthalpy of hydration for the smallest alkali metal cation Li^+ is quite large at −131 kcal/mol. With increasing ionic radius, the enthalpy falls progressively for Na^+, K^+ and Rb^+, reaching −71 kcal/mol for Cs^+, the largest non-hydrated but smallest hydrated ion in the series (see Table 1.1). For the divalent, alkaline earth

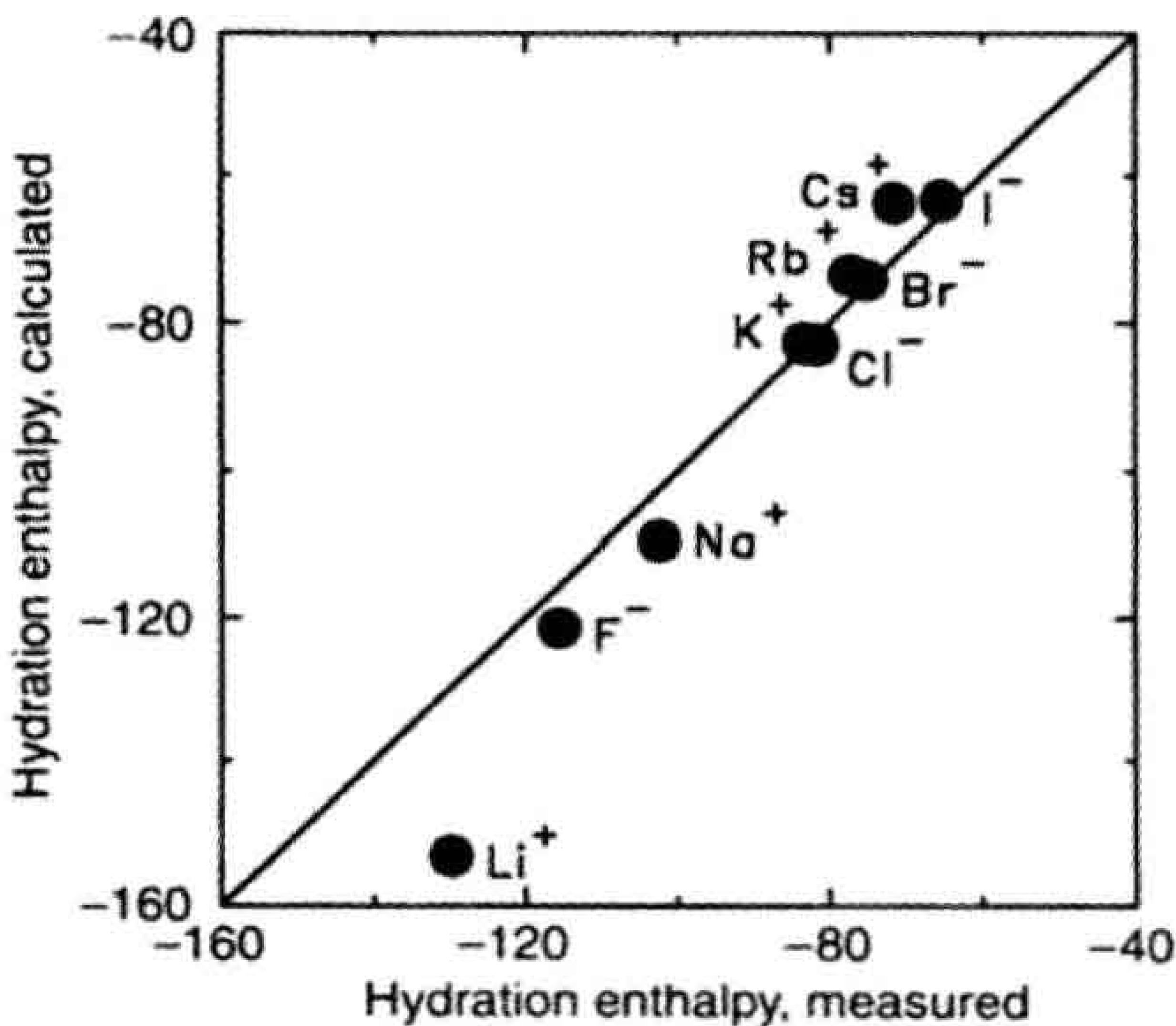


FIGURE 1.4 Comparison of measured enthalpies of hydration of alkali metal cations and halides in water (abscissa), with those calculated (ordinate) taking into account the Born charging energy, ion-dipole interactions, ion-quadrupole interactions and ion-induced dipole interactions *(data from Bockris and Reddy, 1970, p. 107).*

metal ions Mg^{2+} and Ca^{2+}, the enthalpies of hydration also follow the ionic radius but are considerably larger at −476 kcal/mol and −397 kcal/mol, respectively. As pointed out by Hille (2001), the magnitude of ionic hydration enthalpies approximates the cohesive strength of the ionic bonds in a crystalline salt lattice.

Physical chemical analyses show that, in small spaces that restrict the formation of tetrahedral water clusters, the dielectric constant will be reduced and electrostatic forces between ions will then be correspondingly increased. In the primary hydration shell of ions, the oriented water is polarizable but cannot be reoriented by applied fields and so the dielectric constant is reduced from its bulk value of 78 to a value of about 6, with intermediate values in the partially oriented structure-breaking region between the primary hydration shell and the bulk water. For this reason, the dielectric constant of a solution decreases with increasing salt concentration but, in protein-free solutions at physiological salt concentrations, the extent of the decrease is small due to the small fraction of hydration water.

V. PROTONS IN SOLUTION

The hydrogen-bonded structure of liquid water also contributes to high proton mobility by a mechanism that differs fundamentally from the migration of other hydrated ions. The proton is a highly reactive, positively-charged hydrogen nucleus, devoid of electrons. Whereas ions with electron shells typically have diameters in angstroms, the diameter of the proton is only about 10^{-5} Å. With such a small size, the proton has a strong attraction to electrons, as indicated by the high *ionization energy* of 323 kcal/mol needed to remove an electron from a hydrogen atom to form a proton. By comparison, the ionization energies for the alkali cations decrease with increasing atomic number in the series as follows:

$$\begin{aligned} \text{Li} + (124\ \text{kcal/mol}) &> \text{Na} + (118\ \text{kcal/mol}) \\ &> \text{K} + (100\ \text{kcal/mol}) \\ &> \text{Rb} + (96\ \text{kcal/mol}) \\ &> \text{Cs} + (90\ \text{kcal/mol}) \end{aligned}$$

As more filled electron shells separate and shield the outer shell from the positively charged atomic nucleus, it becomes easier to form a cation by removing an electron. The high affinity of the proton for electrons, and its small size, explain its tendency to form hydrogen bonds with the unshared electrons of oxygen in water. Infrared spectra indicate that protons in solution exist predominantly in the form of hydronium ions H_3O^+. Nuclear magnetic resonance (NMR) data are consistent with a flattened trigonal pyramidal structure, with O−H bond lengths of 1.02 Å and H−O−H bond angles of 115°, a structure resembling that of NH_3 but with a radius similar to that of K^+. The free energy of formation of H_3O^+ from H_2O and H^+ is about −170 kcal/mol, which corresponds to a hypothetical concentration of free protons in solution at room temperature of about 10^{-150} M − "about as zero as one can get" say Bockris and Reddy (1970). The heat of hydration of H_3O^+ is an additional −90 kcal/mol. The change in the density of water with temperature is consistent with the hydration of H_3O^+ with an additional three water molecules, forming the tetrahedral cluster $H_9O_4^+$ (Bockris and Reddy, 1970). The proton mobility in water is 36×10^{-4} $cm^2/s \cdot V$, much slower than expected on the basis of hydrodynamic theory if free protons were to carry the current, but curiously about seven times as fast as expected if H_3O^+ migrates like K^+. The abnormally high proton mobility in water (and also in ice) is consistent with a *Grotthus chain mechanism* (Fig. 1.5) in which the successive breakage and formation of hydrogen bonds, accompanied by proton jumps between neighboring water molecules, effectively results in the passage of H_3O^+ along a chain. This transport process is rate-limited by the time needed for each successive acceptor water molecule to rotate and reorient its non-bonded orbital into a suitable position to accept the donated proton. The Grotthus mechanism accounts for about 80% of proton mobility, with the remaining 20% due to H_3O^+ itself, as a single kinetic entity, undergoing a translational migratory movement through the solvent like other ions.

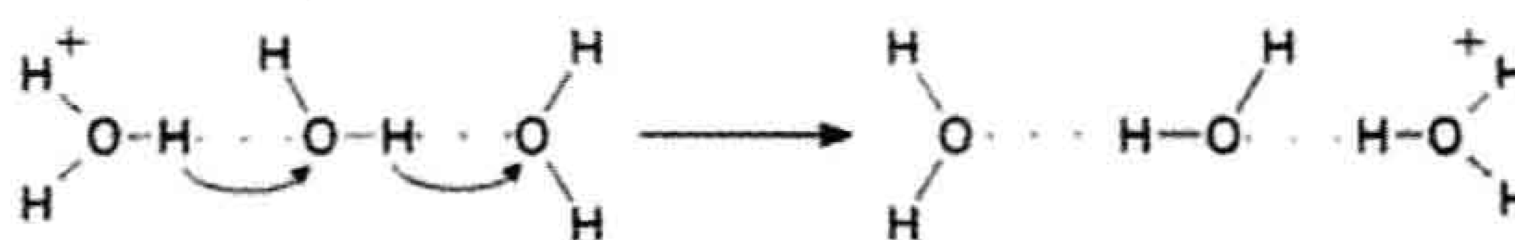


FIGURE 1.5 Grotthus chain mechanism for proton mobility in water.

VI. INTERACTIONS BETWEEN IONS

Interactions between ions may be weak or highly selective. Ions in solution attract ions of the opposite charge, in accordance with Coulomb's law. Since the long-range attractive forces are inversely proportional to the square of the distance between charges, the interaction energies are greater in more concentrated solutions. In a uni-univalent salt solution, defined as having monovalent cations and anions, of concentration *c* (mol/L), the average distance (*d*, angstroms or Å) between any two ions is given by:

$$d = (10^{27}/2N_A c)^{1/3}$$

where N_A is Avogadro's number (6.023×10^{23}). The factor 2 is included because the anions and cations are both counted and the factor 10^{27} is Å^3/L. For 0.15 M NaCl, the average distance between Na^+ and the nearest Cl^- is 17.7 Å, at which range coulombic forces are highly significant. At pH 7.4, where the concentration of "protons" (really

hydronium ions) is only 40 nM, the average distance between "protons" is 0.28 μm.

Attractive ion—ion interactions are stabilizing and they lower the chemical potential of an ion from its value in an ideal, infinitely-dilute solution. The *activity* (a) of an ion is defined in terms of its *chemical potential* (μ) as follows:

$$\mu = \mu^0(T,P) + RT \ \ln a$$

where $\mu^0(T, P)$ is the *standard-state chemical potential*, or the chemical potential when the activity is 1. Increases in chemical activity increase the chemical potential. The chemical potential of a solute in an ideal dilute solution, where the activity equals the chemical concentration (c), is:

$$\mu_{\text{ideal}} = \mu^0(T,P) + RT \ \ln c$$

In order to describe the properties of more concentrated non-ideal solutions, G.N. Lewis introduced the *activity coefficient* (γ), such that the activity is the product of the concentration (c) and the activity coefficient ($a=\gamma \cdot c$). The chemical potential of an ion in a non-ideal solution is:

$$\mu = \mu^0(T,P) + RT \ \ln c + RT \ \ln \gamma$$

where the term $RT \ln \gamma$ includes the effect of ion—ion interactions on the chemical potential.

When a salt (c_+c_-) is added to water, the cations and anions, at concentrations c_+ and c_- respectively, both contribute to the free energy of the solution. The chemical potentials of the cations and anions (μ_+ and μ_-, respectively) are given by:

$$\mu_+ = \mu_+^0 + RT \ \ln c_+ + RT \ \ln \gamma_+$$

$$\mu_- = \mu_-^0 + RT \ \ln c_- + RT \ \ln \gamma_-$$

Adding these two expressions and taking the average, gives:

$$\frac{\mu_+ + \mu_-}{2} = \frac{\mu_+^0 + \mu_-^0}{2} + RT \ \ln (c_+ \ c_-)^{1/2} + RT \ \ln (\gamma_+ \ \gamma_-)^{1/2}$$

The mean ionic activity coefficient $\gamma\pm$ is defined as:

$$\gamma_\pm = (\gamma_+ \ \gamma_-)^{1/2}$$

Mean ionic activity coefficients of salts have been estimated theoretically by the *Debye—Hückel theory*, which supposes that central ions attract oppositely-charged ions (or *counterions*) in a diffuse and structureless ion cloud (or atmosphere). The forces of coulombic attraction between the central ion and its cloud of counterions are opposed by the randomizing influence of the thermal motion of the ions. In dilute solutions, in which the theory treats central ions as point charges relative to the size of the ion cloud, the mean ionic activity coefficient ($\gamma\pm$) for salt ions with charges z_+ and z_-, is given by the limiting law as follows:

$$\log \ \gamma_\pm = -A|z_+ \ z_-| I^{1/2}$$

where I is the *ionic strength*, defined as:

$$I = \frac{1}{2}\sum_i c_i z_i^2$$

The constant A, which equals 0.5108 $\text{kg}^{1/2}\cdot\text{mol}^{-1/2}$ is given in terms of B, which equals 0.3287×10^8 $\text{kg}^{1/2}\cdot\text{mol}^{-1/2}\cdot\text{cm}^{-1}$, both at 25°C, as follows:

$$A = \frac{1}{2.303} \frac{N_A e_0^2}{2\epsilon RT} B$$

$$B = \sqrt{\frac{8\pi N_A e_0^2}{1000\epsilon kT}}$$

where N_A is Avogadro's number (6.023×10^{23} ions/mol), e_0 is the charge on an electron (4.80×10^{-10} stat-coul $= 1.60 \times 10^{-19}$ C), ε is the dielectric constant, R is the gas constant (8.32 J/mol·K), T is the absolute temperature (K) and k ($=R/N_A$) is Boltzmann's constant (1.38×10^{-23} J/K).

The derivation of the Debye—Hückel limiting law (see Bockris and Reddy, 1970) computes the spherically symmetric electric field around an ion, leading to an expression relating the charge density (ρ_r) of the ionic cloud to the electrostatic potential (ψ_r) at a distance r from the central point charge. The counterions, at concentration n_i for ionic species i at a distance r from the central ion, are considered to distribute in the electric field according to a *Boltzmann distribution*:

$$n_i = n_i^0 e^{-z_i e_0 \psi_r / kT}$$

where n_i^0 is the bulk ion concentration (ions/L). By linearizing the Boltzmann equation, using a Taylor series expansion and retaining only the first two terms, which assumes that $z_i e_0 \psi_r \ll kT$, a resulting expression shows how the electrostatic potential ψ decreases as a function of distance (r) from the central ion (Fig. 1.6A):

$$\psi_r = \frac{z_i e_0}{\epsilon} \frac{e^{-\kappa r}}{r}$$

where κ is given by:

$$\kappa = \sqrt{\frac{4\pi}{\epsilon kT} \sum_i n_i^0 z_i^2 e_0^2}$$

The charge density (ρ_r) of the ionic cloud also decreases with increasing distance from the central ion (see Fig. 1.6B) according to:

$$\rho_r = -\frac{r_i e_0}{4\pi} \kappa^2 \frac{e^{-\kappa r}}{r}$$

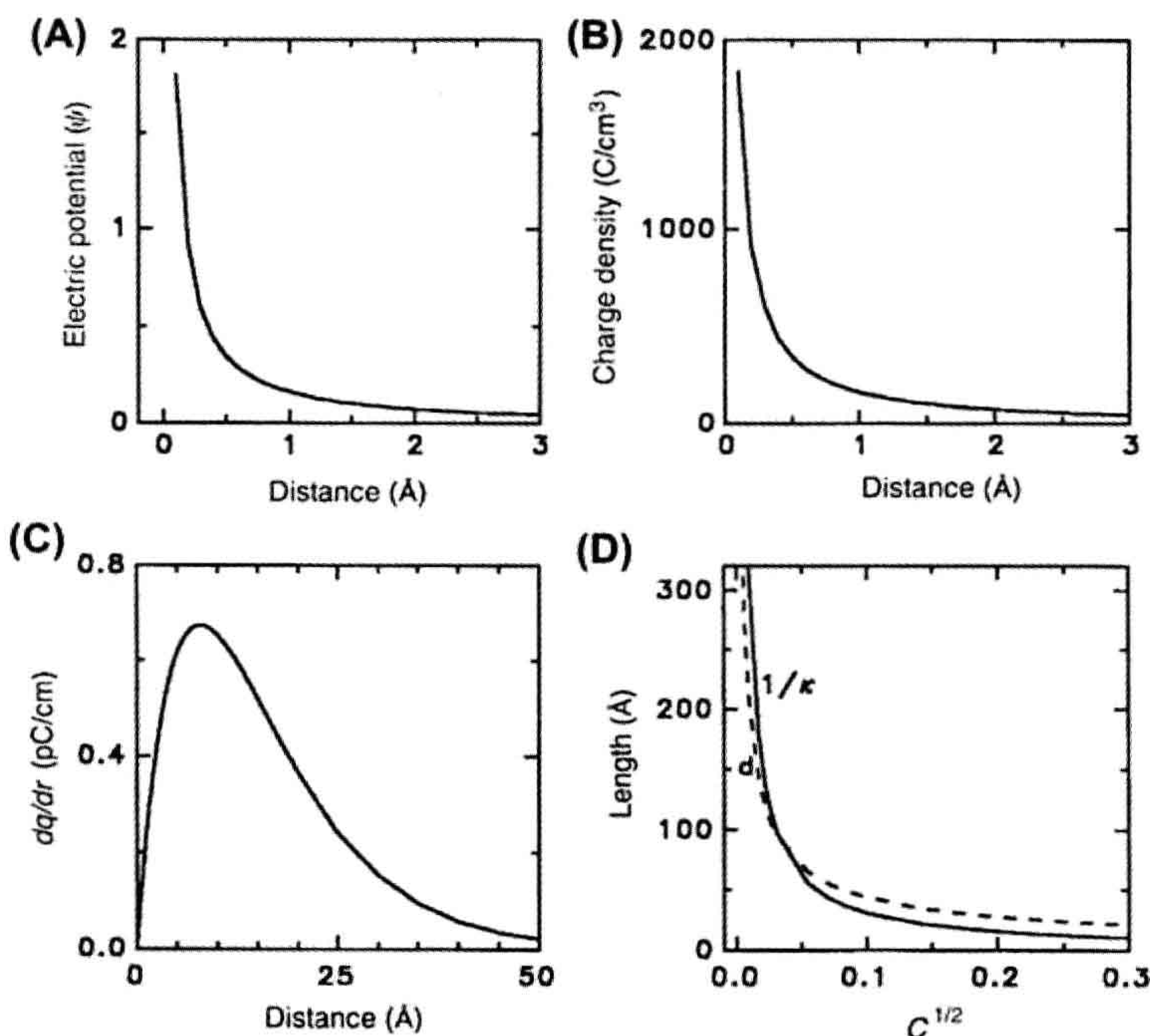


FIGURE 1.6 Debye–Hückel theory. (A) Electrostatic potential (ψ), (B) charge density (ρ) of the counterion cloud and (C) the charge (dq) enclosed in a spherical shell of thickness (dr), each calculated and plotted versus distance d from the central ion. (D) Debye length κ^{-1} (solid line) and average distance d between ions (dashed line) versus square root of ion concentration.

The amount of charge dq contained in a concentric spherical shell of thickness dr located at a distance r from the central ion (see Fig. 1.6C) is given by:

$$dq = -z_i e_0 e^{-\kappa r} \kappa^2 r dr$$

Furthermore, the maximum amount of charge contained in such a spherical shell occurs at a distance κ^{-1}, known as the *Debye length*, which defines the effective radius of the counterion atmosphere. It can also be shown that the Debye length is the distance away from the central ion where an ion of equal and opposite charge would contribute to the electrostatic field by an amount equivalent to that of the dispersed cloud of counterions (Bockris and Reddy, 1970). The Debye length decreases as the ionic concentration increases (see Fig. 1.6D).

The Debye–Hückel limiting law predicts activity coefficients accurately only to concentrations of about 0.01 M. In more concentrated solutions, the finite radius (a, in cm) of the ion is taken into account in the *extended Debye–Hückel equation*, given by:

$$\log \gamma_{\pm} = \frac{A|z_+ z_-|I^{1/2}}{1 + Ba\ I^{1/2}}$$

where the constants A and B are still 0.5108 $kg^{1/2}\,mol^{-1/2}$ and $0.3287 \times 10^8\ kg^{1/2}\,mol^{-1/2}\,cm^{-1}$, respectively, for water at 25°C. The ion-size parameter (a) is adjustable, but reasonable values extend the range of concentrations for which the Debye–Hückel theory accurately predicts ionic activity coefficients (Fig. 1.7).

At still higher salt concentrations above about 0.7 M, the activity coefficient stops decreasing and instead begins to increase with increasing salt concentration. This

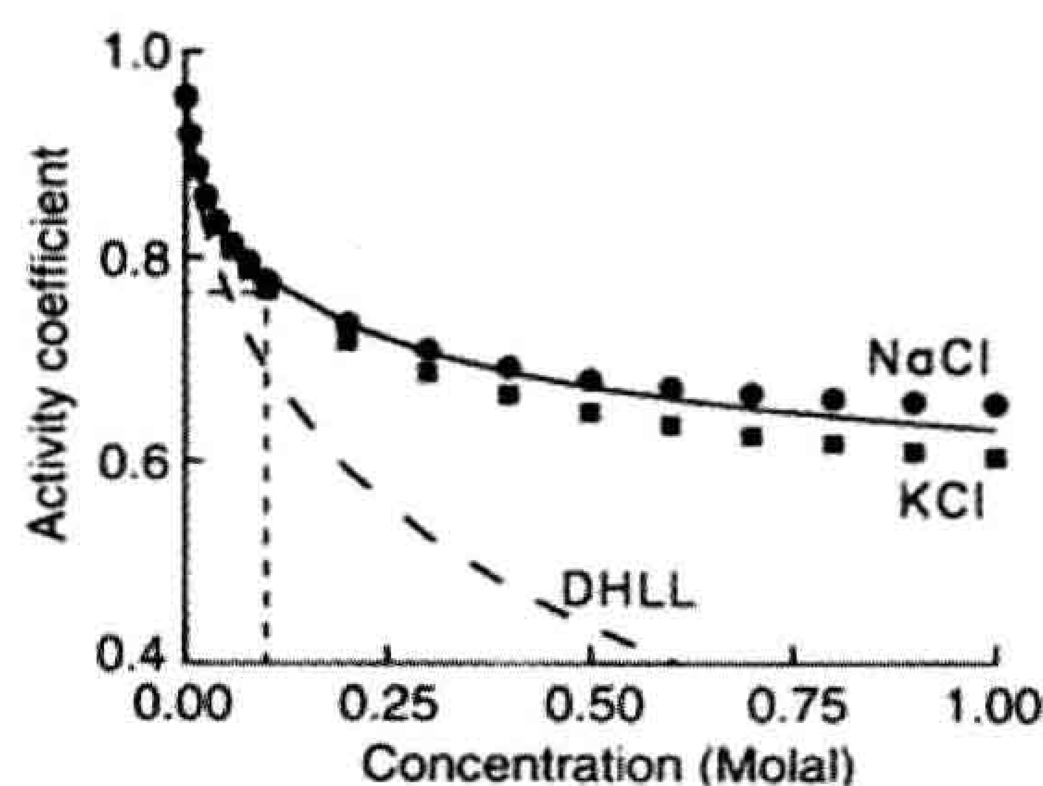


FIGURE 1.7 Activity coefficients of NaCl (circles) and KCl (squares). (*Data are from Robinson and Stokes (1959).*) The dashed curve represents the prediction of the Debye–Hückel limiting law. The solid line represents the prediction of the extended Debye–Hückel equation with an ion size parameter a of 4.7 Å. The dashed vertical line indicates that at 0.1 M, the activity coefficients of NaCl and KCl are 0.77 and 0.76, respectively.

behavior has been explained by the increasing fraction of hydration water, which both reduces the amount of free water in the solution and raises the effective concentration and, therefore, the activity, of the dissolved ions. Corrections for hydration enable prediction of the activity coefficient as a function of salt concentration over the full range of salt concentrations reaching to several molar. A related effect is that, in concentrated protein solutions, a certain shell of volume known as *excluded volume* around each protein is unavailable for solutes because the center of the solutes with their own finite size can only approach to within one solute radius of the protein surface. The fraction of excluded volume increases with increasing protein concentration and with increasing radius of the solutes which themselves may be proteins with enzymatic or regulatory activities. Such *macromolecular crowding* can dramatically increase activities of proteins in concentrated solutions.

The activity coefficients calculated by the Debye–Hückel theory indicate that the forces between ions in dilute solutions are weak and non-selective. The predicted activity coefficients depend on the ionic charge and the ionic strength of the solution and they are largely independent of the specific ion within, say, the alkali metal series. A very small degree of selectivity is introduced with the ion size parameter. The mean ionic activity coefficients for NaCl and KCl as a function of salt concentration are shown in Fig. 1.7. At 0.1 M concentrations, the activity coefficient of Na^+ is 0.77, whereas those of K^+ and Cl^- are both 0.76. These relatively high activity coefficients correspond to ion–ion interaction energies of only about −0.3 kcal/mol (see Hille, 2001).

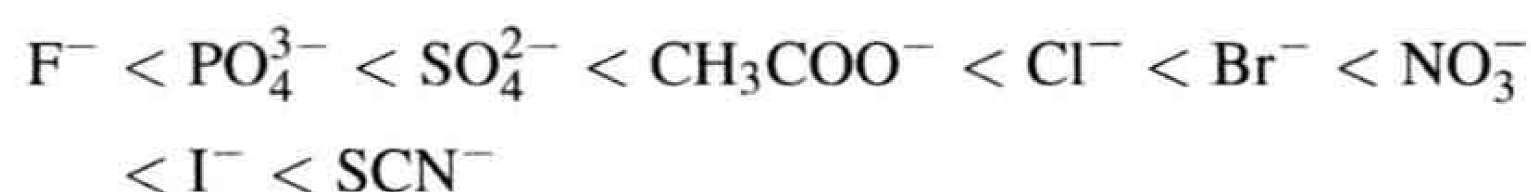
Agreement between theory and data, such as seen in Fig. 1.7 for the Debye–Hückel theory, does not necessarily imply the correctness of the theory, or of the model on which the theory is based. A fundamental criticism of the Debye–Hückel theory concerns the smeared charge model for the cloud of counterions (Frank and Thompson, 1960). Below a concentration of about 0.001 M, the Debye length κ^{-1} is greater than the average distance between ions in the solution (see Fig. 1.6D), in which case the counterions could reasonably appear as a cloud of smeared charge from the vantage point of the central ion. Above 0.001 M, however, the Debye length incongruously falls below the average distance between ions in the solution. Moreover, at only 0.01 M, just one ion is needed to account for 50% of the effect of the counterion cloud on the central ion, yet this ion must be smeared around the central ion in a cloud of spherically symmetric charge distribution located only 25 Å away from the central ion (Bockris and Reddy, 1970). Thus, well below physiological salt concentrations, the assumption of smeared charge in the Debye–Hückel theory is not in accord with the coarse-grained structure of salt solutions, despite the impressive ability of the theory to predict activity coefficients. A quasi-lattice approach to salt solutions minimizing the free energy using modern computational power would seem to be a preferable alternative (see Horvath, 1985, for references).

Intracellular solutions may be quite concentrated. The red-cell membrane and associated cytoskeleton enclose a viscous cytoplasmic solution of the oxygen-binding pigment *hemoglobin* at a concentration of 34 g/100 mL cells, corresponding to 5.2 mM, 7.3 millimolal, or 44 g Hb/100 g cell water. This concentration is near the threshold for gelation, but hemoglobin is one of the most soluble of all proteins and constitutes more than 98% of red-cell protein by mass. The hemoglobin $\alpha_2\beta_2$ tetrameters have a molecular weight of 64 373 Da and are approximately spheroidal with dimensions of 65 × 55 Å × 50 Å. In the interior of red blood cells, hemoglobin is nearly close-packed, with the distance between the surfaces of neighboring proteins averaging only about 20 Å. With the 86 carboxylates of aspartic and glutamic acids and with the 98 basic amino and amine groups of arginine, lysine and histidine per hemoglobin tetramer, the total cellular concentration of the titratable amino acids of human hemoglobin is around 0.9 M. Thus, hemoglobin contributes significantly, depending on intracellular pH, to a high intracellular ionic strength. Since the charged amino acids are located on the surface of hemoglobin and taking the radius of hemoglobin to be 28 Å, the average distance between charged sites is only about 7 Å. About 7600 water molecules per hemoglobin tetramer occupy the narrow interstices between the protein molecules. The hydration of hemoglobin in dilute solution is 0.2–0.3 g water/g Hb, representing about 15% of the intracellular water. When the tortuosity of the surface of soluble proteins is taken into account, as much as 30% of red-cell water could reside in the first monolayer around the protein surface.

To determine the *mean ionic activities* of the intracellular KCl and NaCl in the concentrated charged environment of human red blood cells, studies were conducted in which the red-cell membrane was rendered permeable to cations by exposure of the cells to the channel-forming antibiotic nystatin, thus allowing K^+, Na^+ and Cl^- to reach *Gibbs–Donnan equilibrium*. In these experiments, sufficient extracellular sucrose was added to prevent cell swelling by balancing the colloid osmotic pressure of hemoglobin and other impermeant cell solutes. The *mean ionic activity coefficient* of KCl and NaCl in the concentrated intracellular hemoglobin solution was found to be within 2% of that in the extracellular solution (Freedman and Hoffman, 1979a). In view of the high intracellular ionic strength and the high volume fraction of cell water in direct contact with hemoglobin, it is both curious and remarkable that intracellular salts and non-electrolytes appear to behave as if in dilute solution. Either the intracellular solution is indeed like a dilute solution or, alternatively, the

expected effect of protein–solvent interactions in altering the activity of intracellular solutes is offset by the effect of interactions between proteins and the solutes themselves.

Specific effects of small anions on the solubility, aggregation or denaturation of proteins often follow the *Hofmeister (lyotropic) series* in the following order of effectiveness:



$$F^- < PO_4^{3-} < SO_4^{2-} < CH_3COO^- < Cl^- < Br^- < NO_3^- < I^- < SCN^-$$

The ions to the right of Cl^- are referred to as *chaotropic*, since they tend to destabilize proteins (for review, see Collins and Washabaugh, 1985). Ions may also associate with sites on proteins, as exemplified by the binding to albumin of Ca^{2+} (Katz and Klotz, 1953), and of Cl^- (Scatchard et al., 1957; see ch. 8 in Tanford, 1961). Certain enzymes, ion channels and membrane transport proteins interact with the alkali cations with a high degree of *ionic selectivity*. Considering the five alkali metal cations, there are 5! (=120) possible orders of selectivity that might arise. However, only 11 cationic selectivity orders commonly occur in chemical and biological systems, as listed in Table 1.2. Eisenman (1967) predicted these selectivity orders by calculating the ion-site interaction energies. If the field strength of a negatively-charged site is weak, then an associated ion remains hydrated. In this case, Cs^+, having the smallest hydrated ionic radius, is favored (Sequence I) because it can approach most closely to the site and thus has the strongest coulombic force of attraction. If the field strength of the site is strong and the interaction energy between the ion and the site is stronger than the energy between the ion and water dipoles, then the ion is stripped of its associated water and becomes dehydrated. In this case, Li^+, having the smallest non-hydrated ionic radius, becomes favored (sequence XI). With intermediate field strengths, ions partially dehydrate, giving rise to the intervening selectivity sequences. For example, K^+ functions as a co-factor for the glycolytic enzyme pyruvate kinase, with the maximal catalytic velocity following Eisenman sequence IV. During in vitro protein synthesis, K^+ maintains an active conformation of 50S ribosomal subunits that catalyze peptide bond formation following Eisenman sequence III. Other sequences are possible when the sites are assumed to be polarizable (for review, see Eisenman and Horn, 1983).

TABLE 1.2 Eisenman's Selectivity Sequences for Binding of Alkali Cations to Negatively Charged Sites

Highest field strength of site	
Li > Na > K > Rb > Cs	Sequence XI
Na > Li > K > Rb > Cs	Sequence X
Na > K > Li > Rb > Cs	Sequence IX
Na > K > Rb > Li > Cs	Sequence VIII
Na > K > Rb > Cs > Li	Sequence VII
K > Na > Rb > Cs > Li	Sequence VI
K > Rb > Na > Cs > Li	Sequence V
K > Rb > Cs > Na > Li	Sequence IV
Rb > K > Cs > Na > Li	Sequence III
Rb > Cs > K > Na > Li	Sequence II
Cs > Rb > K > Na > Li	Sequence I
Lowest field strength of site	

VII. SOLUTE TRANSPORT: BASIC DEFINITIONS

In the intracellular or extracellular solutions, a solute is said to be at *equilibrium* when its concentration is constant in time without requiring the continuous input of energy from metabolism or other sources. In human red blood cells, for example, Cl^-, HCO_3^- and H^+ are at thermodynamic equilibrium, i.e. they are passively distributed. A solute is said to be at *steady-state* when its concentration is constant in time, but is dependent on the continuous input of energy from metabolism or other sources. *Active transport* utilizes energy and results in steady-state distributions that represent a deviation from equilibrium. In biological cells, the concentrations of Na^+, K^+ and Ca^{2+} are at a steady-state. Their concentrations are constant in time, but are dependent on the continuous hydrolysis of ATP by the Na^+-K^+ pump (for review, see Glynn, 1985) and the Ca^{2+} pump. With isolated red cell membranes ("ghosts"), active transport of Na^+ and K^+ against their respective concentration gradients has been observed directly by measurements of net fluxes (Freedman, 1976). The active production and maintenance of ion concentration gradients by membrane pumps, such as the Na^+, K^+-ATPase and the Ca^{2+}-ATPase, represent *chemical work* and *electrical work* done by the cell. The energy required for continuous pumping of Na^+ by resting frog sartorius muscles has been estimated to represent some 14–20% of the energy available from the hydrolysis of ATP and the value is similar in red blood cells.

Passive transport is the movement of solutes toward a state of equilibrium. Passive transport of *hydrophobic* substances across cell membranes usually occurs directly by diffusion across the lipid bilayer. Passive transport of *hydrophilic* substances is usually mediated by specific membrane proteins via a process known as *facilitated diffusion*. Passive ion transport may occur through pores or ion channels under the influence of concentration gradients and electrical forces by a process known as

electrodiffusion. The passive flow of ionic currents down their concentration gradients through specific ion channel proteins constitutes negative work done by the cell. The changes in free energy associated with ion transport and the Nernst equilibrium equation are described in the Appendix.

VIII. MEASUREMENT OF ELECTROLYTES AND MEMBRANE POTENTIAL

Ion concentrations in biological fluids may be expressed as millimoles per liter of solution (millimolar, or mM), or as millimoles per kilogram of water (millimolal). When a solution containing metallic ions is aspirated into a flame, each type of ion burns with a characteristic color, Na^+ giving a yellow flame, K^+ giving a violet flame and Ca^{2+} giving a red flame. In the technique of *flame photometry*, the intensity of the emitted light, in comparison with that produced by solutions containing known concentrations of ions, provides a convenient measure of ion concentration in extracellular fluids and in acid extracts of cells. With a uniform rate of aspiration, a flame photometer accurately measures the intensity of the emitted light, which is related linearly to the cation concentrations in suitably diluted standards and unknowns (see e.g. Funder and Wieth, 1966). *Atomic absorption spectroscopy* is an alternative technique that measures the light absorbed by ions during electronic excitation in a flame. Flame photometry and atomic absorption spectroscopy both measure total ionic concentrations in cell extracts irrespective of any intracellular compartmentation and they are sensitive in the millimolar range of cellular concentrations. K^+, Na^+, Ca^{2+} and other elements in single cells, or even in single cell organelles, may be measured by *electron probe microanalysis*, a technique that utilizes an electron beam to excite the emission of x-rays with energies characteristic of the various elements in cells.

The development of *ion-specific glass microelectrodes* by Eisenman (1967) and then of selective *liquid ion exchange microelectrodes*, made possible the direct determination of intracellular cation activities. Palmer and Civan (1977) found that for Na^+, K^+ and Cl^- of *Chironomus* salivary gland cells, the ion activities are the same in the nuclear and cytoplasmic compartments. In a related study, Palmer et al. (1978) found that during development of frog oocytes, the ratio of the cytoplasmic concentration of Na^+ to K^+ increases, while the corresponding ratio of ion activities decreases. This observation could reflect the development of yolk platelets and intracellular vesicles that contain ions at differing concentrations and activities than does the bulk cytoplasm. In frog skeletal muscle, the sarcoplasmic reticulum contains a solution enriched in calcium, whereas the ionic composition of the solution in the t-tubules is extracellular. The extracellular space, however, consists of the interstitial space between the muscle fibers as well as the vascular space; solutes leave these two extracellular compartments with differing rate constants, thus considerably complicating the interpretation of experiments that assess the rate of membrane transport with radioactive isotopes of Na^+, K^+ and other solutes (Neville, 1979; Neville and White, 1979).

To measure transient changes of intracellular Ca^{2+} in the micromolar and submicromolar range, *fluorescent chelator dyes* such as Quin-2, Fura-2, Indo-1 and Fluo-3 have been developed (Tsien, 1988). Quin-2, Fura-2, and Indo-1 are fluorescent analogs of ethylenediaminetetraacetic acid (EDTA), which contains four carboxylate groups that specifically bind two divalent cations. EGTA is a non-fluorescent analog with a higher binding affinity for Ca^{2+} as compared with its affinity for Mg^{2+} and it is thus quite useful in experiments where the extracellular concentration of Ca^{2+} is systematically varied. Fluo-3 is a tetracarboxylate fluorescein analog that exhibits a shift in the emission spectrum upon binding Ca^{2+}; in contrast, Fura-2 undergoes a shift in its excitation spectrum. By measuring the ratio of Fura-2 fluorescence upon excitation at two exciting wavelengths, changes in the concentration of Ca^{2+} may be monitored. The cells are incubated with a permeant ester form of the dye to enable the dye to permeate into cells; intracellular esterases then release the Ca^{2+}-sensitive chromophore. With video microscopy of cells stained with fluorescent Ca^{2+} indicators, it is also possible to obtain time-resolved and spatially-resolved light microscopic images of the changes in intracellular Ca^{2+}. Another fluorescent probe (SPQ), developed by Helsey and Verkman (1987), has been used to measure intracellular Cl^- and to study its transport across cell membranes.

The transmembrane electrical potential is usually measured by means of open-tipped microelectrodes such as those developed and used by Ling and Gerard (1949) to obtain accurate and stable measurements of the membrane potential of frog skeletal muscle. With human red blood cells, stable potentials have not been achieved with microelectrodes. As an alternative technique, Hoffman and Laris (1974) utilized fluorescent cyanine dyes to monitor and measure red cell membrane potentials. Fluorescent cyanines, merocyanines, oxonols, sytryls, rhodamines and other dyes have since been used in numerous electrophysiological studies of red blood cells, neutrophils, platelets and other non-excitable cells and organelles that are too small for the use of microelectrodes (for review, see Freedman and Novak, 1989a). The equilibrium distribution of permeant, lipophilic, radioactively labeled ions such as triphenylmethylphosphonium ($TPMP^+$) may also be used to assess the membrane potential using the Nernst equilibrium equation (see Freedman and Novak, 1989b).

APPENDIX: THERMODYNAMICS OF MEMBRANE TRANSPORT

AI. FREE ENERGY

When ions cross cell membranes, changes in free energy are involved. Consider a membrane permeable only to cations separating two solutions of KCl of differing concentrations, c_i and c_o, where the subscripts i and o represent the intracellular and extracellular compartments, respectively (Fig. 1A.1). If the intracellular concentration (c_i) is greater than the extracellular concentration (c_o), then potassium will tend to diffuse out of the cell down its concentration gradient. When only a very slight amount of potassium crosses the membrane (which for this example is assumed to be impermeable to chloride), the separation of charge creates a transmembrane electrical potential (E_m) that is negative inside, relative to outside. The resultant electrical force retards further efflux of potassium. An equilibrium is reached when the diffusion force favoring efflux of potassium exactly balances the electrical force, preventing efflux of potassium.

Prior to the attainment of equilibrium, the process of moving dn moles of K^+ ions out of the cell from compartment i to compartment o involves a change in *free energy* (dG) of the system. According to the laws of thermodynamics, the process will occur spontaneously only if $dG < 0$ and the system will be at equilibrium if $dG = 0$. Thus, in order to compute the change in free energy (dG), we need to review certain basic thermodynamic principles.

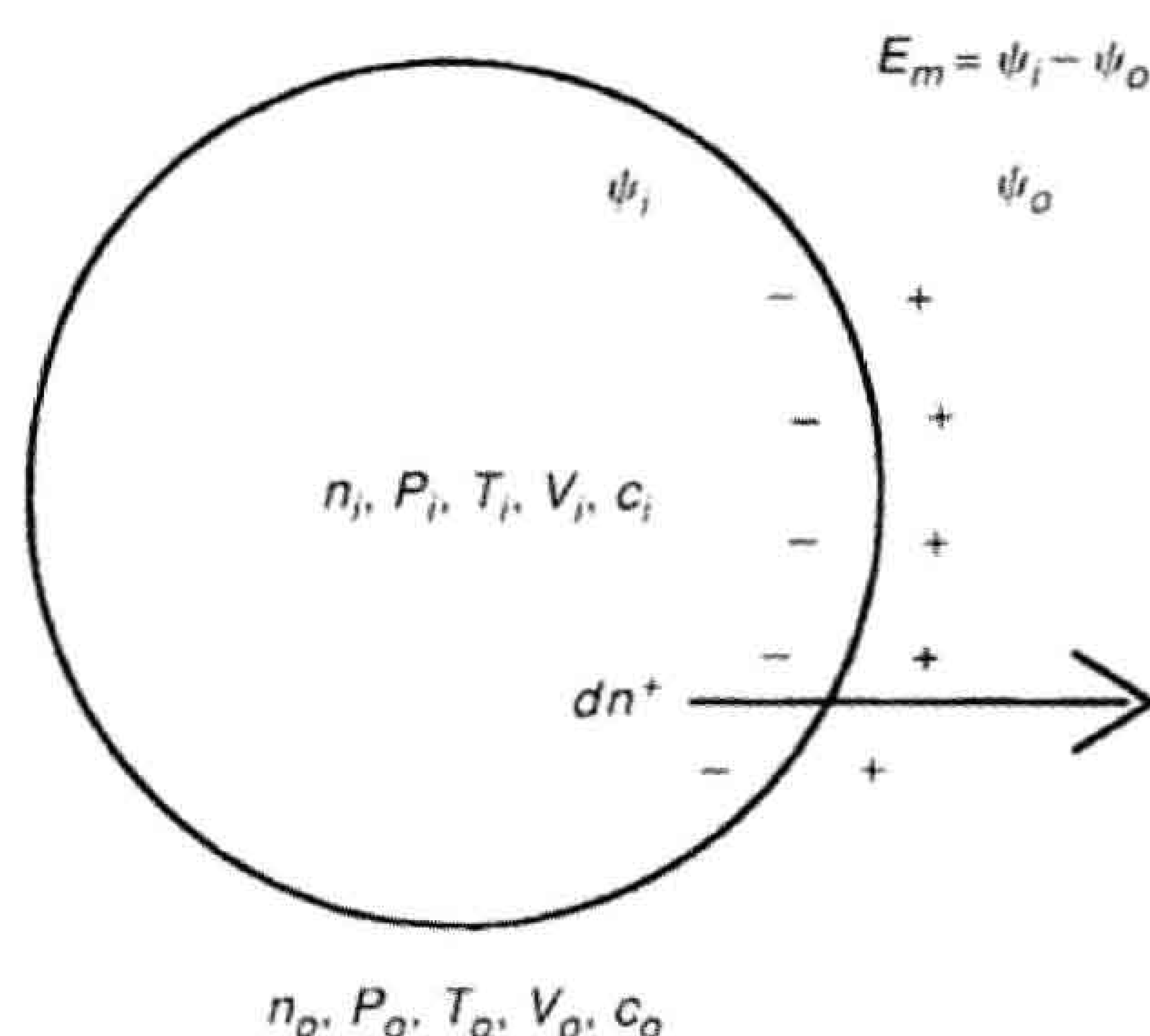


FIGURE 1A.1 Free energy of ion transport. A cell membrane separates the intracellular (subscript i) and the extracellular (subscript o). Each compartment is at pressure P and temperature T, has volume V and electrical potential ψ and contains solutes at concentration c. A free energy change is involved when dn^+ moles of cation leave the cell. The membrane potential E_m is $\psi_i - \psi_o$.

The *first law of thermodynamics*, also known as the law of conservation of energy, states that for any system, the increase in *energy* (dE) is the gain in *heat* (dQ) minus the *work* (dW) done by the system:

$$dE = dQ - dW$$

For reversible processes, the second law of thermodynamics defines the change in entropy (dS) of a system in terms of the heat gained (dQ) and the absolute temperature (T) as follows:

$$dS = \frac{dQ}{T}$$

Combining the first and second laws gives:

$$dE = TdS - dW$$

Since the difference in pressure (dP) between the internal and external solutions of animal cells is negligible, the work (dW) done by the system includes pressure–volume work, PdV, and electrical work, $zF\epsilon_m dn$, summed as follows:

$$dW = PdV + zF\epsilon_m dn$$

where P is the pressure, V is the total volume of the system, z is the ionic valence (eq/mol), F is the Faraday constant (=96 490 C/eq) and dn is the number of moles of solute crossing the membrane and leaving the cell. The transmembrane electrical potential (ϵ_m) is the difference in electrical potential (ψ, in volts or J/C), between the two compartments:

$$\epsilon_m = \psi_i - \psi_0$$

The electrical potential (ψ) represents the work done in moving a unit positive test charge from infinity to a point in the solution. Note that when the transmembrane electrical potential (ϵ_m) is negative inside, the electrical work done by the system is negative whenever Na^+ or K^+ leave the cell, but positive when K^+ or Na^+ enter the cell, irrespective of the mechanism of transport.

According to the first and second laws, the change in energy (dE) of the system is:

$$dE = TdS - PdV - zF\epsilon_m \, dn$$

For systems of variable chemical composition, the free energy (G) is by definition:

$$G = H - TS + \sum \mu_j n_j$$

where the enthalpy (H) is defined as;

$$H = E + PV$$

The *chemical potential* μ_j of the jth solute in the system at constant T, P, and n_k is defined by:

$$\mu_j = (\partial G / \partial n_j)_{T,P,n_k}$$

where n_j and n_k are the number of moles of the *j*th and *k*th solutes, respectively. The chemical potential, also called the *partial molar free energy*, represents the incremental addition of free energy to the system upon incremental addition of a solute. All solutes contribute to the free energy of a solution. While the free energy itself is a parameter of state for the whole system, the chemical potential refers to a particular solute. The free energy is thus given by:

$$G = E + PV - TS + \sum \mu_j n_j$$

Differentiating yields:

$$dG = dE + PdV + Vdp - TdS - SdT + \sum \mu_j dn_j$$

Substituting the expression for dE given previously and simplifying yields a form of the *Gibbs equation*,

$$dG = -SdT + VdP - zF\epsilon_m dn + \sum \mu_j dn_j$$

which states that the free energy of a system of variable chemical composition is a function of the temperature, the pressure and the number of moles of each component in the mixture, or $G = G(T, P, n_j)$. For processes that occur at constant temperature and pressure, where $dT = dP = 0$, the Gibbs equation simplifies to:

$$dG = -zF\epsilon_m dn + \sum \mu_j dn_j$$

which states that the increase in free energy of a system is equal to the sum of the electrical work done on the system plus the total change in free energy due to changes in chemical composition. Furthermore, when the system is at equilibrium, dG must equal zero. The second law of thermodynamics also implies that the change in free energy (dG) is negative for all spontaneous processes. Thus, the first and second laws of thermodynamics, when combined with the definitions of free energy and enthalpy, result in the Gibbs equation, which is the fundamental equation for the estimation of free energy changes when water, ions, or other solutes cross cell membranes.

AII. NERNST EQUILIBRIUM

The *Nernst equation* describes the relationship between voltage across a semipermeable membrane and the ion concentrations at equilibrium in the compartments adjacent to the membrane. The Nernst equation provides a simple method of testing whether or not a particular solute is at equilibrium.

Considering the example described in the previous section and using the Gibbs equation, the change in the free energy of the system that occurs when dn moles of K^+ ions move from compartment i containing K^+ at activity a_i to compartment o containing K^+ at activity a_o is given by:

$$dG = -zF\epsilon_m dn + \mu_i dn_i + \mu_o dn_o$$

where the change in free energy has been summed for the two compartments. For this process, the decrease in the number of moles of solute inside the cell ($-dn_i$) equals the increase outside the cell (dn_o), so that both may be represented by dn:

$$-dn_i = dn_o = dn$$

and therefore

$$dG = [-zF\epsilon_m - (\mu_i - \mu_o)]dn$$

The chemical potential in each solution is:

$$\mu_i = \mu_i^0 + RT \ln a_i$$

$$\mu_o = \mu_o^0 + RT \ln a_o$$

For the system under consideration, the intracellular and extracellular standard-state chemical potentials are assumed to be identical:

$$\mu_i^0 = \mu_o^0$$

and thus:

$$dG = [-zF\epsilon_m - RT \ln\ (a_i/a_o)]dn$$

At equilibrium, $dG = 0$ and, since, $dn \neq 0$ therefore

$$-zF\epsilon_m - RT\ln\ (a_i/a_o) = 0$$

Rearranging yields the Nernst equation for a cationic concentration cell,

$$\epsilon_m = -\frac{RT}{zF}\ln\frac{a_i}{a_o}$$

Converting the natural logarithm to base 10 yields:

$$\epsilon_m = -2.303\frac{RT}{zF}\log\frac{a_i}{a_o}$$

The value of $2.303RT/F$ is 58.7 mV at 23°C and 61.5 mV at 37°C.

For charged solutes, the *electrochemical potential* ($\mu_j = dG/dn_j$) of the *jth* solute is defined as the sum of a chemical and an electrical component. The electrical contribution to the electrochemical potential is $zF\psi$ and the chemical contribution is $RT \ln a$.

$$\mu_j = \mu_j^0(T, P) + RT \ln a_j + zF\psi$$

Note that a fundamental condition of equilibrium is that the difference in electrochemical potential between compartments i and o is zero. The electrochemical potential of the solute is the same in each compartment to which that solute has access.

The Nernst equation is independent of the mechanism of transport and is often used for ascertaining whether or not an intracellular ion is at electrochemical equilibrium. If so, then:

$$a_i = a_o e^{-zF\epsilon_m/RT}$$

Another way of understanding the Nernst equation is that, at equilibrium, ions distribute across the membrane electric field in accordance with a Boltzmann distribution.

If $z = 0$, as for non-electrolytes, then $a_i = a_o$, and the activities of the solutes will be the same at equilibrium on both sides of the membrane, as was found to be nearly the case for the distribution of non-electrolytes across the membranes of human red blood cells (Gary Bobo, 1967). If $z \neq 0$, as for electrolytes then, at equilibrium, each permeant monovalent ion will reach the same ratio of intracellular to extracellular activity. Such is the case for the passive distribution of Cl^-, HCO_3^- and H^+ in human red blood cells.

$$r = \frac{[Cl^-]_i}{[Cl^-]_o} = \frac{[HCO_3^-]_i}{[HCO_3^-]_o} = \frac{[H^+]_o}{[H^+]_i} = e^{F\epsilon_m/RT}$$

In red blood cells, Na^+, K^+ and Ca^{2+} deviate from this ratio due to the action of the Na^+-K^+ pump and Ca^{2+} pump. In skeletal muscle, K^+ and Cl^- have Nernst equilibrium potentials that are close to the actual measured resting potential, while Na^+ is far from equilibrium. In squid axons, the Nernst equilibrium potential for K^+ is closest to the resting potential, Cl^- is somewhat removed and, as in muscle and red blood cells, Na^+ is far from equilibrium.

BIBLIOGRAPHY

Bergethon, P. R., & Simons, E. R. (1990). *Biophysical Chemistry. Molecules to Membranes*. New York: Springer-Verlag.

Bernard, C. (1949). *An Introduction to the Study of Experimental Medicine*. (H.C. Green, translator). New York: Schuman.

Bockris, J. O'M., & Reddy, A. K. N. (1970). *Modern Electrochemistry*, Vol. (1). New York: Plenum Press.

Cannon, W. B. (1932). *The Wisdom of the Body*. New York: Norton.

Cantor, C. R., & Schimmel, P. R. (1980). *Biophysical Chemistry*. Parts I, II, III. San Francisco: W.H. Freeman.

Collins, K. D., & Washabaugh, M. W. (1985). The Hofmeister effect and the behavior of water at interfaces. *Q Rev Biophys, 18*, 323–422.

Cooke, R., & Kuntz, I. D. (1975). The properties of water in biological systems. *Ann Rev Biophys Bioeng, 3*, 95–126.

Debye, P. (1929). *Polar Molecules*. New York: Dover Publications.

Dick, D. A. T. (1959). Osmotic properties of living cells. *Internatl Rev Cytol, 8*, 387–448.

Edsall, J. T., & McKenzie, H. A. (1978). Water and proteins. I. The significance and structure of water; its interaction with electrolytes and nonelectrolytes. *Adv Biophys, 10*, 137–207.

Edsall, J. T., & Wyman, J. (1958). *Physical Biochemistry*. New York: Academic Press.

Eisenberg, D., & Kauzmann, W. (1969). *The Structure and Properties of Water*. Oxford: Oxford University Press.

Eisenman, G. (1967). *Glass Electrodes for Hydrogen and other Cations*. New York: M. Dekker.

Eisenman, G., & Horn, R. (1983). Ionic selectivity revisited: the role of kinetic and equilibrium processes in ion permeation through channels. *J Membr Biol, 76*, 197–225.

Frank, H. S., & Thompson, P. T. (1960). A point of view on ion clouds. In W. J. Hamer (Ed.), *The Structure of Electrolyte Solutions* (pp. 113–134). New York: John Wiley & Sons.

Frank, H. S., & Wen, W.-Y. (1957). Structural aspects of ion-solvent interaction in aqueous solutions: a suggested picture of water structure. *Disc Faraday Soc, 24*, 133–140.

Freedman, J. C. (1976). Partial restoration of sodium and potassium gradients by human erythrocyte membranes. *Biochim Biophys Acta, 455*, 989–992.

Freedman, J. C., & Hoffman, J. F. (1979a). Ionic and osmotic equilibria of human red blood cells treated with nystatin. *J Gen Physiol, 74*, 157–185.

Freedman, J. C., & Novak, T. S. (1989a). Optical measurement of membrane potentials of cells, organelles, and vesicles. *Meth Enzymol, 172*, 102–122.

Freedman, J. C., & Novak, T. S. (1989b). Use of triphenylmethylphosphonium to measure membrane potentials in red blood cells. *Meth Enzymol, 173*, 94–100.

Funder, J., & Wieth, J. O. (1966). Determination of sodium, potassium, and water in human red blood cells. Elimination of sources of error in the development of a flame photometric method. *Scand J Clin Lab Invest, 18*, 151–166.

Fushimi, K., & Verkman, A. S. (1991). Low viscosity in the aqueous domain of cell cytoplasm measured by picosecond polarization microfluorimetry. *J Cell Biol, 112*, 719–725.

Gary-Bobo, C. M. (1967). Nonsolvent water in human erythrocytes and hemoglobin solutions. *J Gen Physiol, 50*, 2547–2564.

Glynn, I. M. (1985). The Na^+, K^+-transporting adenosine triphosphatase. In A. N. Martonosi (Ed.) (2nd edn).*The Enzymes of Biological Membranes, Vol. 3* (pp. 35–114). New York: Plenum Press.

Heilbrunn, L. V. (1956). *The Dynamics of Living Protoplasm*. New York: Academic Press.

Helsey, N. P., & Verkman, A. S. (1987). Membrane chloride transport measured using a chloride-sensitive fluorescent probe. *Biochemistry, 26*, 1215–1219.

Hille, B. (2001). *Ion Channels of Excitable Membranes* (3rd ed.). Sunderland, MA: Sinauer Associates.

Höber, R. (1945). *Physical Chemistry of Cells and Tissues*. Philadelphia: The Blakiston Company.

Hoffman, J. F., & Laris, P. C. (1974). Determination of membrane potentials in human and Amphiuma red blood cells by means of a fluorescent probe. *J Physiol (London), 239*, 519–552.

Horowitz, S. B., & Miller, D. S. (1984). Solvent properties of ground substance studied by cryomicrodissection and intracellular reference-phase techniques. *J Cell Biol, 99*, 172s–179s.

Horvath, A. L. (1985). *Handbook of Aqueous Electrolyte Solutions. Physical Properties, Estimation and Correlation Methods*. New York: John Wiley and Sons.

Katz, S., & Klotz, I. M. (1953). Interactions of calcium with serum albumin. *Arch Biochem, 44*, 351–361.

Klotz, I. M. (1970). Water: its fitness as a molecular environment. In E. E. Bittar (Ed.), *Membranes and Ion Transport, Vol. 1* (pp. 93–122). New York: Wiley.

Läuger, P. (1991). *Electrogenic Ion Pumps*. Sunderland, MA: Sinauer Associates.

Ling, G. N., & Gerard, R. W. (1949). The normal membrane potential of frog sartorius fibers. *J Cell Comp Physiol, 34*, 383–396.

Miller, C. (1974). Nonelectrolyte distribution in mouse diaphragm muscle. I. The pattern of nonelectrolyte distribution and reversal of the insulin effect. *Biochim Biophys Acta, 339*, 71–84.

Neville, M. C. (1979). The extracellular compartments of frog skeletal muscle. *J Physiol, 288*, 45–70.

Neville, M. C., & White, S. (1979). Extracellular space of frog skeletal muscle in vivo and in vitro: relation to proton magnetic resonance relaxation times. *J Physiol, 288*, 71–83.

Palmer, L. G., & Civan, M. M. (1977). Distribution of Na^+, K^+, and Cl^- between nucleus and cytoplasm in Chironomus salivary gland cells. *J Membr Biol, 33*, 41–61.

Palmer, L. G., Century, T. J., & Civan, M. M. (1978). Activity coefficients of intracellular Na^+ and K^+ during development of frog oocytes. *J Membr Biol, 40*, 25–38.

Pauling, L. (1960). *The Nature of the Chemical Bond and the Structure of Molecules and Crystals; an Introduction to Modern Structural Chemistry* (3rd ed.). Ithaca, NY: Cornell University Press.

Robinson, R. A., & Stokes, R. H. (1959). *Electrolyte Solutions* (2nd ed.). London: Butterworths.

Scatchard, G., Coleman, J. S., & Shen, A. L. (1957). Physical chemistry of protein solutions. VII. The binding of some small anions to serum albumin. *J Am Chem Soc, 79*, 12–20.

Schwan, H. P., & Foster, K. R. (1977). Microwave dielectric properties of tissue. Some comments on the rotational mobility of tissue water. *Biophys J, 17*, 193–197.

Silver, B. L. (1985). *The Physical Chemistry of Membranes*. Boston: Allen and Unwin.

Tanford, C. (1961). *Physical Chemistry of Macromolecules*. New York: Wiley.

Tsien, R. Y. (1988). Fluorescence measurement and photochemical manipulation of cytosolic free calcium. *Trends Neurosci, 11*, 419–424.

Weiss, T. F. (1996). *Cellular Biophysics, Vol. 1: Transport, Vol. 2: Electrical Properties*. Cambridge, MA: The MIT Press.

Chapter 2

Physiological Structure and Function of Proteins

Matthew R. Pincus

Chapter Outline

I. SUMMARY

We see in this chapter that the three-dimensional structures of proteins are dictated by their linear sequences of amino acids. A protein's structure is the one of lowest free energy for the given polypeptide chain, the detailed conformation of which is determined by the dihedral angles of the backbone and side chains. Proteins are structured in such a way that their polar amino acids tend to be directed towards the aqueous solvent while the non-polar or hydrophobic residues tend to point towards the interior of the protein. The three-dimensional structures of proteins can be determined by a variety of techniques, which include circular dichroism (for regular structure), x-ray crystallography, two-dimensional nuclear magnetic resonance spectroscopy (NMR) and theoretical techniques.

The three-dimensional structures of proteins determine bulk properties of these proteins, such as their behavior towards titration with acids or bases, their isoionic points and their migration in electric fields, as in electrophoresis. The ionization of charged groups on the surfaces of proteins can be treated, and thus their titration curves can be predicted using ligand-binding theory combined with electrostatic

Cell Physiology Sourcebook. DOI: 10.1016/B978-0-12-387738-3.00002-0

field theory (using the Debye-Hückel formulation) or using more explicit models based on the actual three-dimensional structure of the protein surrounded by water dipoles.

The structure of a protein and its functioning have a well-defined relationship. Membrane proteins, for example, tend to fold into α-helices. This structure is of critical importance to the functioning of leader peptides that allow for proteins to be secreted both within the cell and outside of the cell. The ability of melittin to intercalate into cell membranes and to cause cell lysis depends on its ability to adopt an α-helical conformation and to change the angle of these helices. Membrane active peptides, like PNC-27, fold into membrane-active helix-loop-helix amphipathic structures and bind to unique protein targets in the membranes of cancer cells allowing them to kill the cancer cells but not affect normal cells making them potentially effective anti-cancer agents.

Certain large proteins, like *neu*/HER-2, contain major transmembrane domains which can adopt several different conformations, some of which allow them to dimerize and thus initiate cellular signal transduction. This process is especially critical for oncogene-encoded proteins that are involved in mitogenic signal transduction to the nucleus, causing cell division. We have begun to understand the structural basis for this process using conformational analysis as described in this chapter. In this regard, conformational analysis has now been extended to the identification of the regions of oncogenic proteins involved in activation of downstream target proteins and has opened new possibilities in the field of drug design. Voltage-dependent conformational changes in the transmembrane domains of ion channel proteins are vital to their regulated functioning. The basic functioning of cells is therefore controlled by the proper folding and functioning of cellular proteins, making vital the understanding of protein structure.

II. MOLECULAR STRUCTURE OF PROTEINS

Proteins are biopolymers that are essential for all plant and animal life. All antibodies, enzymes and cell receptors are proteins. The basis for all connective tissue is the fibrous proteins, such as elastin and collagen. The entire genetic apparatus of every cell, regardless of how simple or complex its functions, is dedicated to the synthesis of proteins. The building blocks for proteins are α-amino acids that are linked to one another by peptide (or amide) bonds. The twenty naturally occurring amino acids (Fig. 2.1) all have the same *backbone* structure, the $N{-}C^{\alpha}{-}C{=}O$ unit, but differ from one another in that they have different side chains attached to the α-carbon, as shown in Fig. 2.1. Also, all of these amino acids are chiral – optically active and in the L-configuration – except for the simplest amino acid, glycine, which has two H atoms attached to the α-carbon. Note that cysteine has a sulfhydryl group, giving it the capacity to form disulfide bonds (Fig. 2.1). Disulfide bonds are important in stabilizing the three-dimensional structures of proteins, as discussed in Section IIC.

Topographically, proteins are divided into the *fibrous proteins*, which are long repeating helical proteins and the *globular proteins*, which tend to fold up into spherical or ellipsoidal shapes. As we will show, how proteins fold is governed uniquely by their linear sequences of amino acids.

IIA. Primary Amino Acid Structure

All proteins are composed of linear sequences of amino acids that are unique to each protein and are covalently bound to one another by peptide bonds (Fig. 2.2). This peptide bond is almost always arranged so that the C^{α} atoms of two successive residues are *trans* to one another and the atoms attached to the C′ and N of the peptide all lie in the same plane since the C′–N bond has double-bond character, namely, the *trans*-planar peptide bond described long ago by Linus Pauling. The linear sequence of amino acids is called the *primary structure*.

Note that the amino acids in Fig. 2.1 are classified as *polar, non-polar* and *neutral* depending on the nature of the side chain. Thus, for example, leucine and valine are non-polar amino acids with aliphatic side chains that are hydrophobic, or non-miscible with water and other polar solvents. Amino acids like lysine and glutamic acid, on the other hand, contain charged side chains that are highly soluble in water and are completely miscible in polar solvents. Amino acids such as glycine and alanine do not contain groups that predispose them to be classified as either polar or non-polar, so they are referred to as neutral.

IIB. Regular or Secondary Structure in Proteins

The three-dimensional structures of over 300 proteins have been determined by x-ray crystallography. One striking feature in all of these proteins is the presence of recurrent regular structures, in particular, α-helices, β-sheets and reverse turns (Fig. 2.3). The existence of the first two of these structural types was predicted by Linus Pauling in the early 1950s on the basis of x-ray diffraction patterns of model poly-α-amino acids.

Note that in the α-helix in Fig. 2.3A, the residues form a spiral such that at every 3.6 residues, the spiral or helix makes one complete turn. The repeat distance of this helix is 5.4 Å. This structural motif is observed in virtually all proteins and, some proteins like myoglobin, are virtually completely α-helical. One very important interaction for stabilizing helices is the *i*-to-*i*+4 hydrogen-bonding

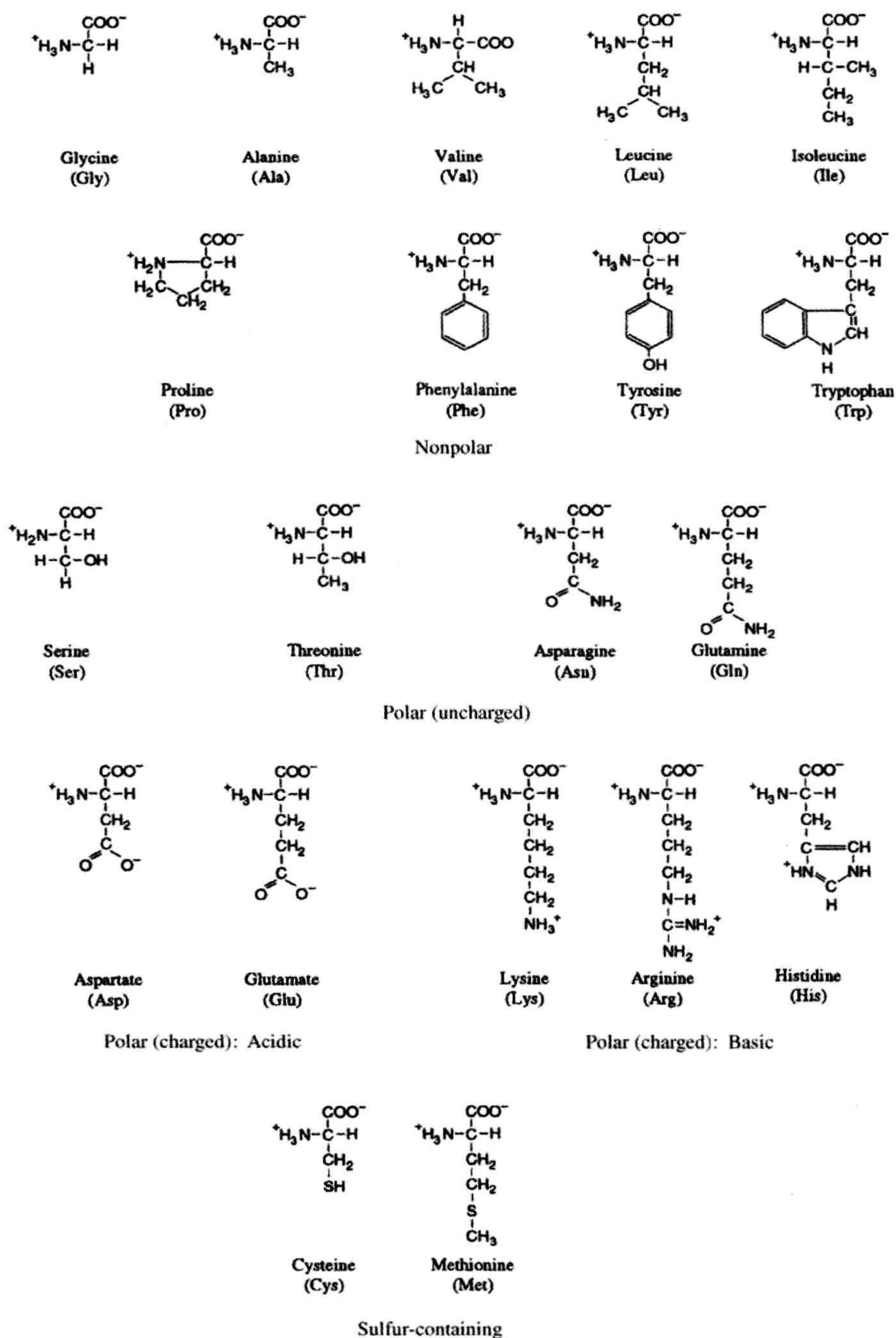


FIGURE 2.1 The 20 naturally occurring amino acids grouped by type. Note that Cys residues can form disulfide bonds in the following reaction: R—SH + R—SH → R—S—S—R, where R is the backbone atoms of Cys + the side chain CH_2 group.

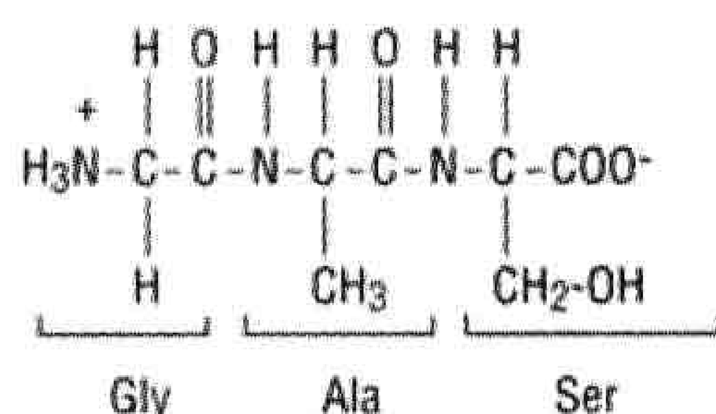


FIGURE 2.2 A typical tripeptide, Gly-Ala-Ser, showing the CO—NH peptide bond linkage.

scheme shown in Fig. 2.3A. The C=O of the ith residue accepts a hydrogen bond from the N—H of the i+4th residue. The hydrogen bond can provide up to 3 kcal/mol in stabilization energy. For an amino acid residue in the middle of an α-helix, two hydrogen bonds form to its N—H and C=O groups. This occurrence tends to cause helices to propagate because the more such double hydrogen bonds form, the greater the stabilization energy provided. Two other long-range factors stabilize α-helices. The first is the presence of negatively charged amino acid residues on the amino terminal end of a helix and positively charged amino acids on the carboxyl terminal end of the helix. This stabilization results from the backbone dipole moment of an α-helix, where the center of positive charge is on the amino terminus of the helix and the center of negative charge is on the carboxyl terminus of the helix. The presence of the oppositely charged amino acids stabilizes the helical dipole.

The second stabilizing factor is *amphipathicity*. This refers to the i-to-i+4 side chain—side chain interactions such that non-polar or hydrophobic amino acids contact one another on one face of the helix while other polar i-to-i+4 interactions occur on the opposite side of the helix. This segregation of polar and non-polar faces allows for hydrophobic clustering to occur on one face and hydrogen bonding and charge neutralization to occur on the opposite face. This motif is vital in stabilizing α-helices in membrane proteins such as ion channel proteins.

α-Helices are extremely important in membrane proteins, in the transmembrane domains of cellular receptors and in ion channel proteins, as we discuss in Section V.

In contrast, the β-sheet is composed of alternating residues of amino acids that are "flipped" 180° with respect to their nearest neighbors, as shown in Fig. 2.3B. We may regard the structure of single strands in these sheets as a flat helix whose repeat is every two residues. Note that within each strand of a β-sheet are minimal interactions between the backbone atoms of different amino acid residues. The hydrogen-bonding stabilization comes from other strands that lie in proximity to one another. As shown in Fig. 2.3B, the arrangement of the strands is either *parallel* or *antiparallel*. Regardless of the arrangement of the two interacting strands, it should be noted from Fig. 2.3B that two hydrogen bonds between the backbone atoms form for *alternate* residues; every other residue forms no hydrogen bond to the neighboring strand. Thus there is twice the number of hydrogen bonds in long α-helices as in long β-sheets. Evidently, other interactions are important in stabilizing β-sheets besides backbone—backbone hydrogen bonding.

Another type of regular structure is the *reverse turn*, the prototype of which is shown in Fig. 2.3C. In this structure, the polypeptide chain reverses its direction. A minimum of two amino acids is needed to form a reverse or hairpin turn, which is also called a β-bend. Usually, three amino acids are involved, however, because the C=O of the first residue can form an i-to-i+3 hydrogen bond with the N—H of the i+3rd residue, as shown in Fig. 2.3.

Of the three regular structures described, α-helices tend to propagate most strongly due to the double hydrogen bonding of the NH and C=O groups of central residues in the helix discussed above and illustrated in Fig. 2.3D. This type of "medium-range" interaction is not present for the two other types of regular structures.

The specific sequences of amino acids in proteins will adopt specific structures such as the three basic regular structures just described. Thus the amino acid sequences of proteins determine their respective three-dimensional structures. This conclusion has been verified as we now describe.

IIC. Tertiary or Three-Dimensional Structure of Proteins

IIC1. The Amino Acid Sequences of Proteins Determine their Three-Dimensional Structures

In a classic series of experiments, Christian Anfinsen and his coworkers at the National Institutes of Health showed in the early 1960s that the primary structure (linear sequence of amino acids) of a protein determines its unique three-dimensional structure (Anfinsen et al., 1961). These investigators took the protein ribonuclease A, which hydrolyzes RNA and whose amino acid sequence had just been determined and was known to contain four disulfide bonds, and denatured it in the denaturing agent 6 M guanidine hydrochloride. This agent and 8 M urea are both known to disrupt the hydrogen bonds in proteins and destroy their three-dimensional structures. In addition, using β-mercaptoethanol, they reduced the four disulfides to eight sulfhydryl (SH) groups, thereby destroying all of the major determinants of the three-dimensional structure. The denatured protein was completely inactive towards RNA hydrolysis and possessed spectral properties that differed greatly from those of the native protein. They then allowed the sulfhydryl groups to reoxidize to disulfides and dialyzed the 6 M guanidine hydrochloride. Within 2 hours, virtually all of the native enzymatic activity returned and the spectral properties of the refolded protein were identical to those of the undenatured protein. In addition, all of the disulfides were paired exactly as they were in the native protein.

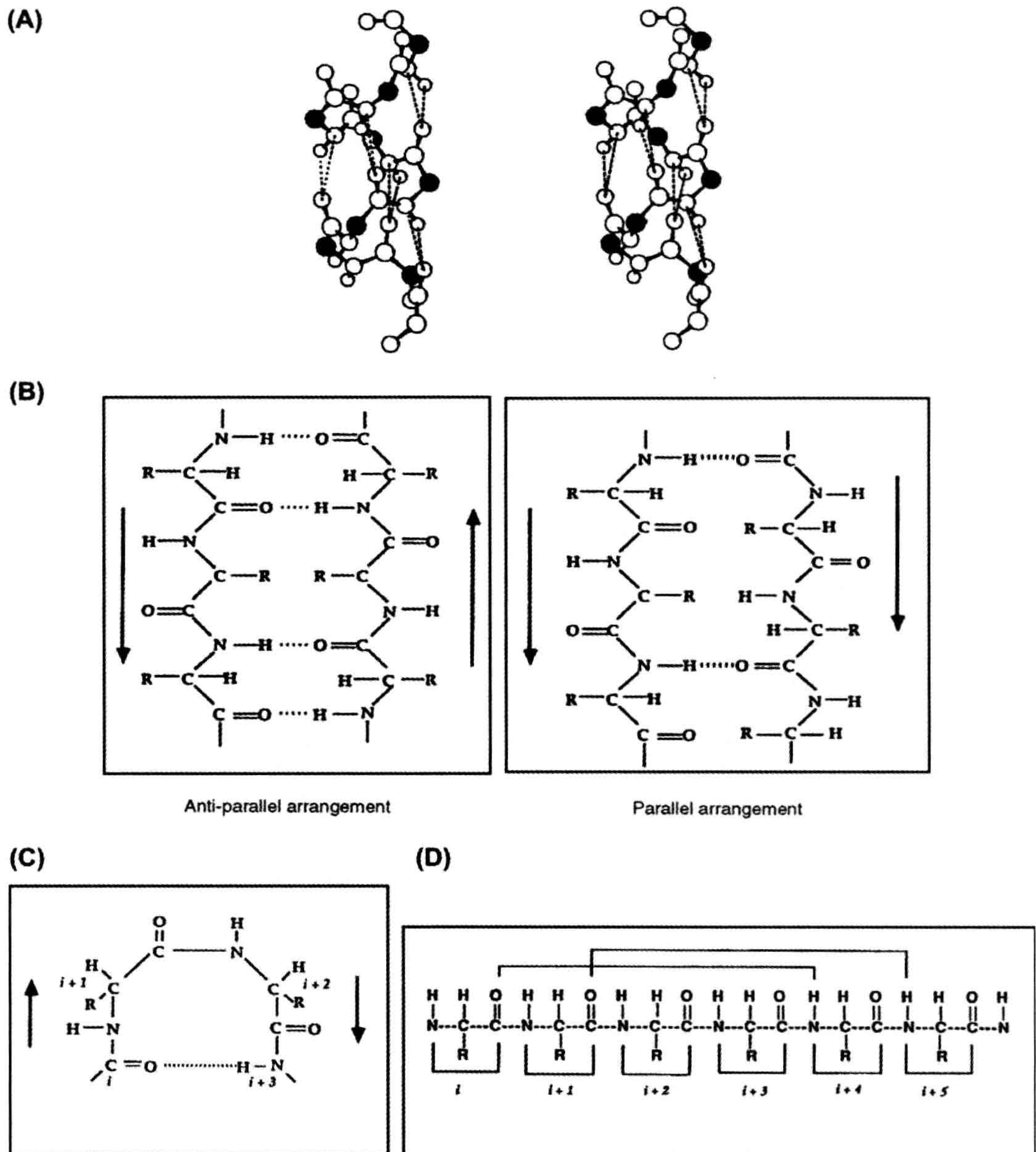


FIGURE 2.3 Three types of regular (secondary) structure. (A) Stereo view of an α-helix for a polypeptide backbone showing the *i*-to-*i*+4 hydrogen bond. The filled circles are α-carbons; double dashed lines are drawn from C=O to NH (shorter dashed line) and from C=O to N (longer dashed line). (B) Two types of β-sheets. The left side shows the antiparallel arrangement while the right side shows the parallel arrangement, as indicated by the arrows in both figures. (C) The arrangement of backbone atoms in a β-bend showing how an *i*-to-*i*+3 hydrogen bond stabilizes the reverse turn structure. (D) Illustration of an extended α-helical chain showing how internal residues have both their NH and CO groups involved in hydrogen bonds. Residue *i*+4 would have its NH and C=O both hydrogen-bonded if 2 more residues were added to the carboxyl terminal end.

This experiment illustrated that the primary sequence of amino acids in a protein determines its three-dimensional structure. Further, it demonstrated that the interactions that govern the correct folding of a protein must be highly specific and strong because, of the vast number of possible structures that the polypeptide could have adopted, only one such structure actually ultimately formed. This conclusion is reinforced by the following consideration. Once the protein is reduced to the eight-sulfhydryl state, there are many ways in which these eight sulfhydryls can pair to give four disulfides. In particular, there are seven ways in which the first disulfide can form, five for the second, three for the third and one for the fourth, or $7 \times 5 \times 3 \times 1 = 105$ possible ways. Of this total, only one pairing scheme, the native pairing, ultimately was found to form in this experiment.

Similar results have been obtained for a number of different proteins. In every case, the native structure is regenerated. Such dramatic results imply that, given the amino acid sequence, it should be possible to infer the three-dimensional structure of the protein.

Indeed, methods have been and are continuing to be developed that allow us to predict the three-dimensional structure of a polypeptide or a protein from its amino acid sequence. At present, it is possible to compute the three-dimensional structures of polypeptides from their amino acid sequences for polypeptides and proteins containing more than 100 amino acid residues. As might be imagined, the field of structure prediction is a burgeoning one that is developing rapidly. All of the methods used to predict protein structure are based on the physicochemical principle that the observed structure of a molecule is the one with the lowest free energy. If we can compute the energies for the possible conformations of a protein, we can pick out the structure of lowest energy, which is the structure that the protein is most likely to adopt. In order to perform this task, we must understand the types of energetic interactions within a polypeptide chain that must be optimized for the protein to fold correctly.

IID. Possible Interactions Between Amino Acids in a Protein Chain

As might be expected from the differing nature of the side chains of the naturally occurring amino acids, a vast number of possible interactions between different side chains and backbone are possible for given amino acid sequences. These types of interactions include *electrostatic interactions* (given by the Coulombic potential q_1q_2/DR_{12}, where the *qs* are the charges on two different interacting atoms, *R* is the distance between them, and *D* is the dielectric constant of the medium) between positive and negative charges of oppositely charged side chains, such as the $-COO^-$ group of glutamic acid and the $-NH_3^+$ group of lysine as well as the interactions between the partial charges on all of the atoms of the protein; *non-bonded* interactions between the individual atoms, explained below; *hydrogen-bonding interactions* between polar atoms with H atoms and other polar atoms; and a *solvation energy* for most proteins.

This solvation energy is such that the non-polar side chains of non-polar amino acids tend to avoid water and therefore "bury" themselves in the core of the protein, while the side chains of polar amino acids tend to interact strongly with water and become solvated. This favorable solvation energy is due to water dipole interactions with charged residues such that the charges on the side-chain atoms are reduced by favorable interactions with the water dipoles. It is also due to hydrogen bonding between water molecules and the polar atoms of the exposed polar side chains.

IID1. Specific Interactions: Hydrogen-Bonding, Non-Bonded and Hydrophobic Interactions

In the preceding paragraph, we noted that hydrogen-bonding interactions between polar atoms in a protein can greatly stabilize the structure of a protein. These interactions are due to the sharing of a hydrogen atom between the donor atom to which the H atom is covalently linked and the receptor polar atom as in Fig. 2.4. This interaction stabilizes the distribution of charges over the three atoms involved in the hydrogen bonding system (Fig. 2.4). For a given protein sequence, hydrogen bonding patterns can be arranged in many possible ways. However, in every protein whose three-dimensional structure is known, only one or a few hydrogen-bonding schemes are observed, many of these occurring between backbone atoms (NH—O=C) and others occurring between the polar atoms of side chains.

In addition to the hydrogen-bonding interactions between the atoms of a protein, all pairs of atoms in a protein interact with one another so as to attract each other weakly until they become sufficiently close that their electron clouds repel one another. The weak attractive interactions between a pair of atoms are due to the polarization of charges in each atom between the negatively charged electrons and the positively charged nucleus that is induced by the other interacting atom. This induced-dipole—induced-dipole interaction is attractive because the positive end of

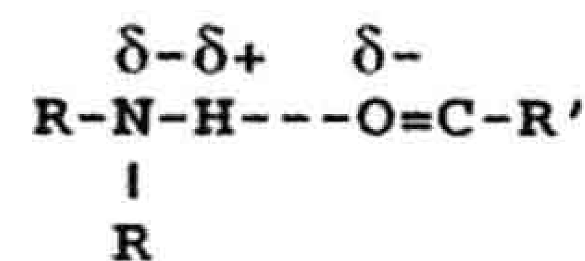


FIGURE 2.4 Illustration of how hydrogen bonds are stabilized by partial sharing of a polar H atom between two polar heavy atoms (N and O in this case).

the dipole of the first atom interacts attractively with the negative end of the dipole of the other atom of the pair and vice versa. The overall attractive energy for this interaction can be simply expressed as $-B_{ij}/R_{ij}^6$, where B_{ij} represents a constant that characterizes the magnitude of the attractive energy between any two interacting atoms and R_{ij} is the distance between the two interacting atoms. As shown in Fig. 2.5, as two interacting atoms approach one another, the attractive energy becomes progressively stronger until the electrons in the outer shells repel one another. This repulsive energy increases rapidly as the internuclear distance between the atoms decreases.

Most proteins fold in an aqueous environment. Changing the solvent, such as by adding non-polar solvents to water, is known to denature proteins so that they cannot function properly. Evidently, water provides important interactions with proteins, such that they fold correctly to their native conformations.

The three-dimensional structures of over 300 proteins have been determined mostly by the technique of x-ray crystallography (see Section III.B). In all of these proteins, the non-polar amino acid residues tend to "pack" in the interior of the protein, while the polar residues tend to interact with water on the surface of the protein. Avoidance of interaction of the non-polar residues with water is due to the *hydrophobic (water-avoiding) effect*. This behavior is caused predominantly by an entropy effect. Water molecules tend to become highly ordered around the side chains of non-polar or hydrophobic amino acid residues. On the other hand, water molecules can interact in a large number of low-energy complexes with polar side chains and so are less constricted structurally. This ordering of water molecules by non-polar residues causes the latter to "pack" into the interior of the protein, allowing the water to be more disordered on the outside of the protein.

If one measures the free energy of transfer, ΔG, of non-polar compounds (such as benzene or n-hexane) from non-polar to polar solvents, it is found that the enthalpy of transfer, ΔH, is small whereas the entropy of transfer, ΔS, is a large negative value. From the Gibbs free energy expression,

$$\Delta G = \Delta H - T\Delta S \tag{2.1}$$

it can be seen that a large negative entropy makes the overall process unfavorable; in other words ΔG becomes more positive. This effect can be attributed to the water structure effect (see Scheraga, 1984).

All of the above interactions have been taken into account in a variety of computer programs that generate the conformations of polypeptides and proteins and calculate their conformational energies. One such program is ECEPP (Empirical Conformational Energies of Peptides Program) developed in the laboratory of Professor Harold A. Scheraga of Cornell University. The energy parameters, such as the constants for the non-bonded interaction energies, have been determined experimentally. This program has been used to compute the structures of many polypeptides and proteins with excellent agreement between predicted and experimentally determined structures (Scheraga, 1984). We give examples below of how these methods have been used to predict protein structure and provide insight into the relationship between the structure of a protein and its function. First, we describe the properties of the structures of proteins.

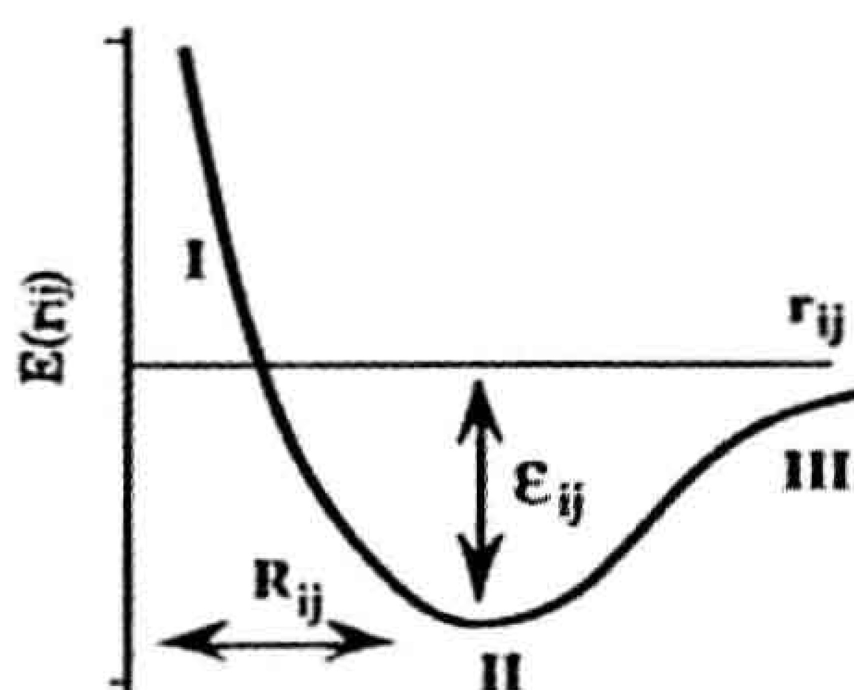


FIGURE 2.5 Interatomic van der Waals energy as a function of distance. Notice that two atoms can approach one another with decreasing energy (regions II and III) until the energy reaches a minimum (ε_{ij}) at a distance of R_{ij}. If the atoms become closer, they then repel one another so that the energy rises steeply (region I).

IIE. Properties of the Structures of Proteins

IIE1. Geometry and Dihedral Angles

Among the many protein structures that have been determined by crystallography, each of the amino acid residues that compose the protein have geometries that are remarkably constant throughout the protein and when compared between any two proteins. Remarkably, this geometry is essentially the same as that found in single crystals of the individual amino acids. Geometry refers to the bond lengths and bond angles of the individual amino acid. An example of the geometry of an amino acid is illustrated for glycine in Fig. 2.6. The basic variables that allow for changes in chain conformation are the dihedral angles, defined as the angle made between two overlapping planes. For example, in Fig. 2.7, the angle between the planes determined by the N−Cα−C′ atom and the Cα−C′−N atoms of the two amino acid residues shown is a dihedral angle. These angles are generated by rotation around single bonds. As shown in Fig. 2.7, for the backbone of a single amino acid residue, three dihedral angles exist:Φ, ψ and ω.

The dihedral angle Φ is determined by the angle between the planes of C′−N−Cα and N−Cα−C′, whereas the dihedral angle ψ is determined by the angle between the planes of N−Cα−C′ and Cα−C′−N. To determine Φ, one merely has to look down the N−Cα axis using the C′-N

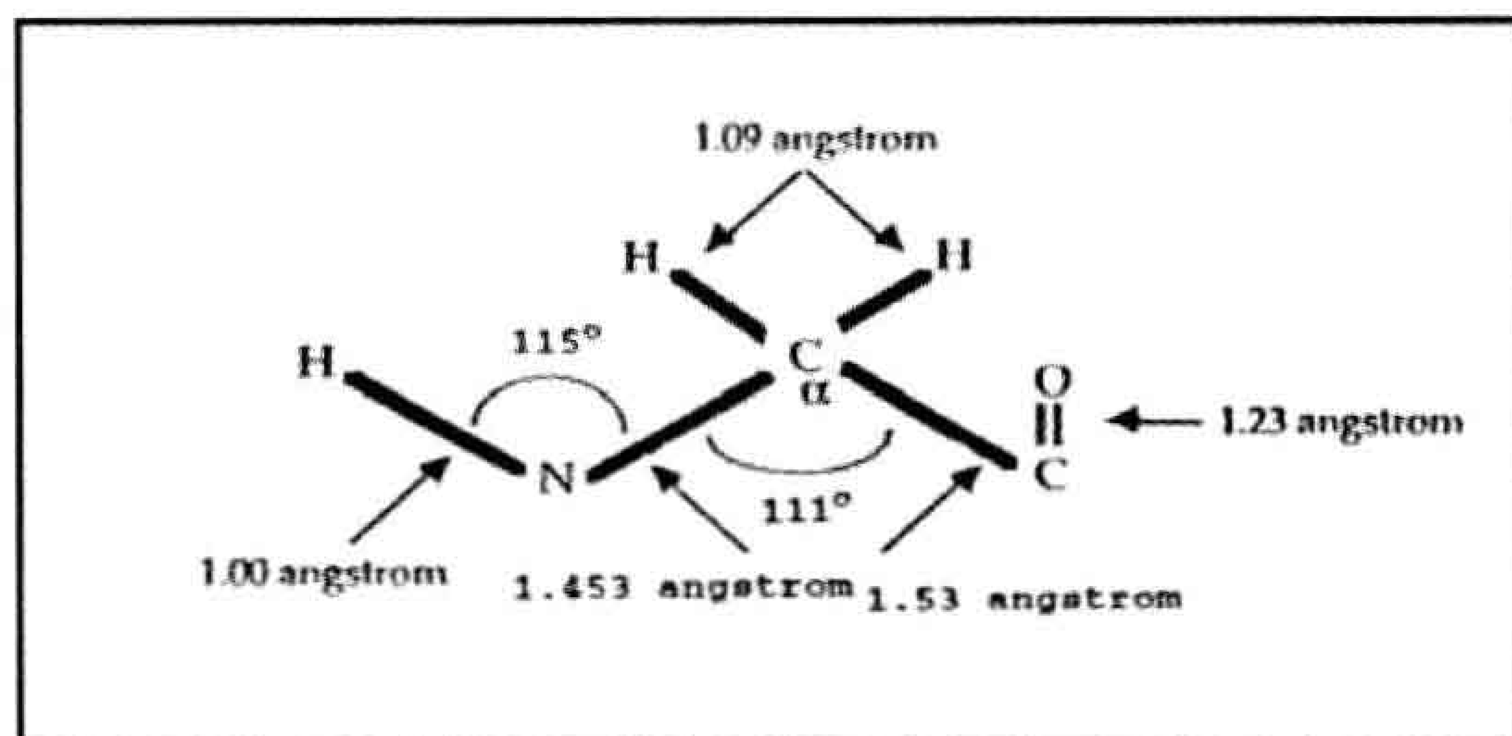


FIGURE 2.6 The geometry of a glycine residue showing typical bond lengths and bond angles.

bond as a reference and determine the angle made between the C′—N bond and the Cα—C′ bond as shown in Fig. 2.7. To determine ψ, one uses the N—Cα bond as a reference and measures its angle with the C′—N bond. The dihedral angle ω is the interpeptide dihedral angle, which is determined by rotation around the C′—N bond shown in Fig. 2.7. It can be measured by determining the angle made between the Cα—C′ bond and the N—Cα bond when sighting down the C′—N bond. This angle is almost always close to 180°, the trans-planar peptide conformation.

Given the geometry and a complete set of dihedral angles for a given sequence of amino acids in a polypeptide, a unique three-dimensional structure can be generated, called the conformation of the protein. All regular structures described above have repeating values for Φ and ψ from residue to residue. All α-helices have values for Φ and ψ that are close to −60° while, for the individual extended chains of β-sheets, the values for both of these dihedral angles lie close to 180°.

In fact, the α-helical or A and extended or E conformations are minimum-energy conformations for all of the

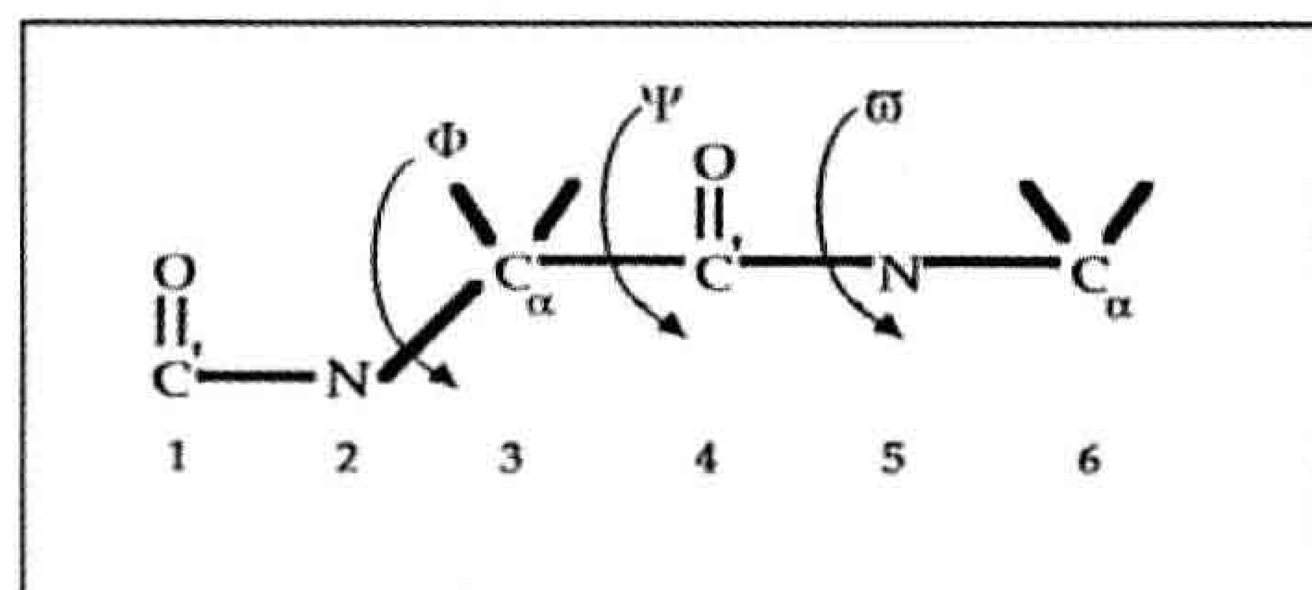


FIGURE 2.7 Dihedral angles, Φ, ψ and ω, for the backbone of an amino acid. Φ is determined by atoms 1, 2, 3, and 4. Clockwise rotations of the 3–4 bond relative to the 1–2 bond are considered positive while counterclockwise rotations are considered negative. 0° is the conformation in which the 3–4 bond is eclipsed relative to the 1–2 bond, while 180° is the conformation in which the two bonds are *trans* relative to one another. Ψ is determined by the 4–5 bond relative to the 2–3 bond. The same considerations apply to this dihedral angle as to those for Φ. ω is determined by the angle between the 5–6 bond and the 3–4 bond. This dihedral angle is almost always very close to 180° (i.e. the 5–6 bond is *trans* to the 3–4 bond).

naturally occurring amino acids. Using conformational energy calculations based on ECEPP, all of the low-energy minimum conformations for the 20 naturally occurring amino acids have been computed as a function of the dihedral angles Φ and ψ. In Fig. 2.8, these energies are plotted as isoenergetic contours in the same way that different elevations are plotted on contour maps. All of the amino acids have at least seven basic low-energy minima as indicated by the dots in Fig. 2.8.

Note in this figure that large regions of the map are energetically forbidden and that the allowed (low-energy) regions of the map are relatively restricted (see Fig. 2.8). Analysis of the conformations of the individual amino acids in proteins whose three-dimensional structures are known reveals that virtually all of these amino acids adopt one of these eight basic conformational states, consistent with the results of the energy calculations.

IIE2. Computation of the Structures of Polypeptides and Proteins

Using programs such as ECEPP, systematic methods, reviewed extensively in Vasquez et al. (1994), have been developed that generate representative sets of the low-energy structures for a given polypeptide chain. These methods include the chain build-up procedure (Pincus, 1988), molecular dynamics (Karplus and McCammon, 1986), Monte Carlo procedures, and more specialized methods that allow for "jumping" potential energy barriers

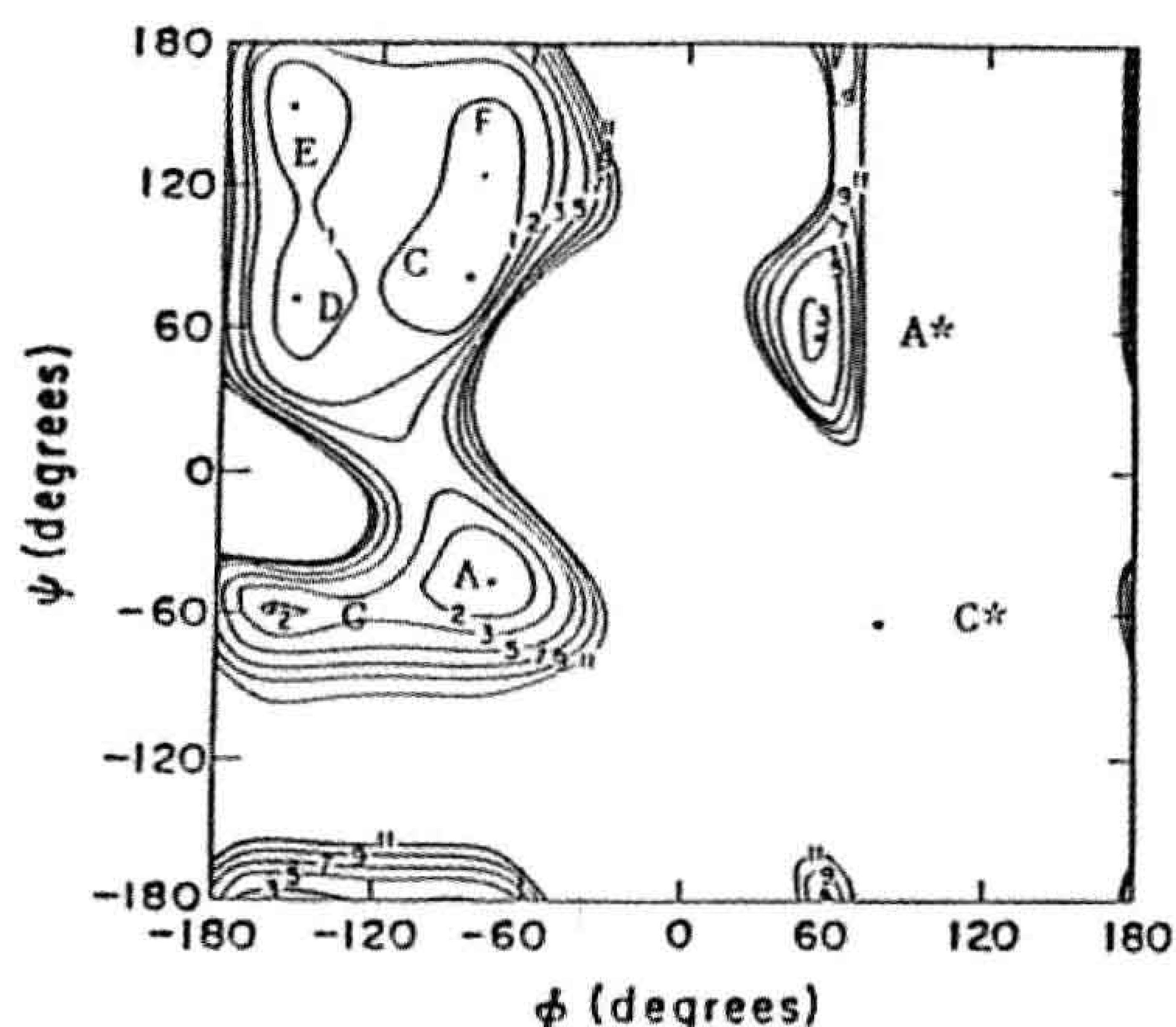


FIGURE 2.8 Contour map for Φ and ψ for N-acetyl-alanine-N′-methyl amide as computed by ECEPP (Scheraga, 1984). Note that the actual energy minima are denoted by dots on the energy contour map. Seven low-energy minima are shown: A (α-helical), C, D (both of which are seen in bends), G, E, and F (which are seen in β-sheets), A* (left-handed α-helix), and C*, which is energetically forbidden for all L-amino acids except glycine. Note also that some of these regions are "split" (i.e. more than one minimum can exist for a given conformational region).

between different conformations of the given polypeptide chain (Scheraga, 1989). All of these methods take advantage of the energy map shown in Fig. 2.8, since the backbone of each amino acid is constricted to adopting one of the low-energy states shown in this figure. Once the low-energy conformations for a given polypeptide are generated and their energies computed, the lowest energy structure is selected and this structure is the one that should be observed experimentally.

Successful ECEPP computations of the three-dimensional structures of a number of polypeptides and proteins have been performed. Examples are shown in Fig. 2.9 for the cyclic decapeptide gramicidin A, collagen and melittin (Pincus and Scheraga, 1985). There is close agreement between these computed structures and the experimentally determined ones. Excellent agreement between theory and experiment has also been achieved for other proteins, such as avian pancreatic polypeptide and bovine pancreatic trypsin inhibitor (Scheraga, 1989) and a 100-residue segment of human leukocyte interferon (Gibson et al., 1986). The experimental structures of these polypeptides and proteins have been determined by specific methods, namely, x-ray crystallography, two-dimensional NMR, or circular dichroism.

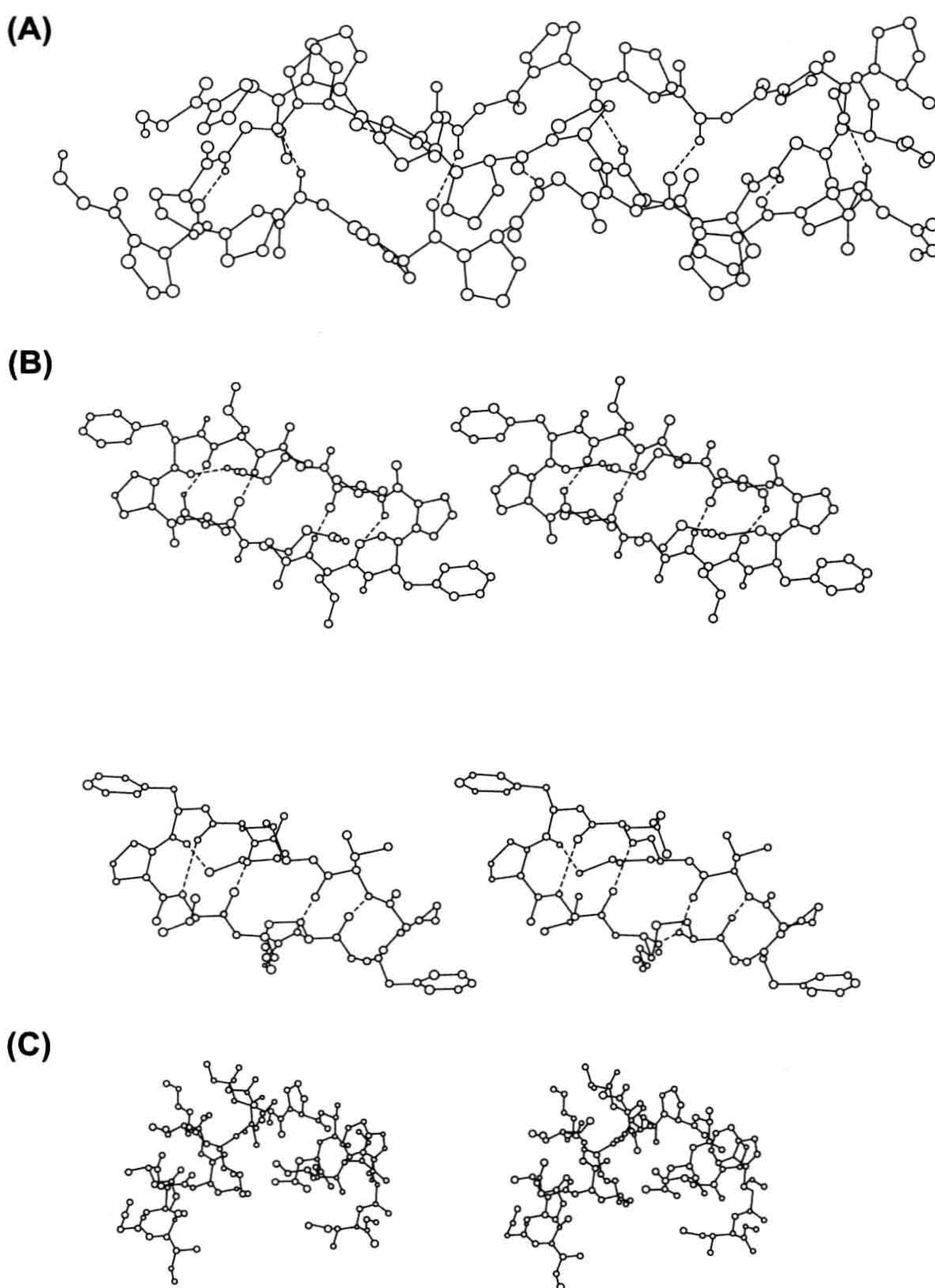


FIGURE 2.9 Views of computed structures. (A) The structure of a section of collagen model polypeptide, $(\text{Gly-Pro-Pro})_{20}$, (Miller and Scheraga, 1976), which was directly confirmed by single-crystal x-ray crystallographic studies subsequent to the computations of the structure of this molecule. (B) The computed structure for the cyclic decapeptide gramicidin A (upper part) and the x-ray structure of the same polypeptide (lower part) show the close agreement between the predicted structure and the x-ray crystal structure (Dygert et al., 1975). (C) The computed structure for the membrane-active protein melittin, which consists of two α-helical rods, separated by a bend in the middle of the chain (Pincus et al., 1982). These features have been described in the x-ray crystal structure of this protein. Each polypeptide represents a type of structure seen in many proteins, viz., the collagen helix (A) in fibrous proteins, β-sheets with reverse turns (B) and α-helices (C). (See Pincus and Scheraga, 1985, for a further description of these structures.)

More recently, methods have been developed that allow for the computation of the lowest energy structures of larger proteins. In one of these, called UNRES (Scheraga et al., 2004), a virtual protein chain represents a given sequence. This chain consists of Cα atoms attached to centroids inside ellipsoids representing side chains of the individual amino acids. Peptide centroids along each Cα-Cα bond are inserted. These centroids represent the backbone peptide (amide) groups. The conformational energies are then computed as the sum of backbone centroid–backbone centroid, side-chain–side chain, backbone centroid–side chain and torsion terms for rotations around the virtual bonds and the side-chain centroids. This simplified polypeptide chain greatly reduces the complexity of the calculation of conformational energies.

Search procedures for low energy conformations are then carried out on this virtual chain. These include molecular dynamics, genetic algorithms and a technique called the electrostatically-driven-Monte Carlo method (EDMC) technique. In this latter approach, the electric field for a given energy minimum structure is searched for the backbone dipole moment(s) that is (are) the least optimally aligned with the field. The backbone dihedral angles are changed such that the alignment is optimized. The resulting structure is then subjected to energy minimization and the process is repeated.

If the same energy minima are repeated frequently in the search, the chain is randomly perturbed via the Monte Carlo procedure and the new chain is subjected to energy minimization and then the procedure described above. Once low energy conformations are computed, they are classified into different structure types. Then for each structure, the full atom representation of the chain is generated and the search is repeated for each of these structures. The lowest energy structures from this search are then determined. This approach has been used to compute the low energy structures for proteins of 140 amino acids or more using supercomputers that can perform the computations in a little over an hour. The lowest energy structures are in good agreement with the experimentally determined ones. A good case in point is the agreement between the computed structure for the first 75 residues of bovine calbindin and the x-ray crystal structure of this protein, the root-mean square deviation being 3.9 Å (Scheraga, 2004).

III. TECHNIQUES FOR THE DETERMINATION OF THE STRUCTURES OF PROTEINS

IIIA. Regular (Secondary) Structure: Circular Dichroism

One of the most widely used techniques for determining regular structure is circular dichroism, which is based on the principle that molecules with asymmetric structures absorb light asymmetrically. Light is electromagnetic radiation which can be plane-polarized to the right or to the left. Normally light consists of both types of plane-polarized waves. When a molecule with an asymmetric structure absorbs light, it preferentially absorbs either the left- or right-polarized light wave. The amount of light absorbed, A, is equal to E×C, where E is the molar extinction coefficient and C is the concentration of the molecules. For molecules with asymmetric structures, the E values for left- and right-plane-polarized light differ. The difference EL−ER depends on the wavelength of the incident light. A plot of EL−ER (called the molar ellipticity) versus wavelength is referred to as the circular dichroism or CD spectrum. Regular structures in proteins are asymmetric both because the amino acids in these structures are themselves asymmetric and because these structures have a handedness or a twist-sense as in the case of the α-helix, which is right-handed (see van Holde, 1985, for a complete treatment of circular dichroism). Since the peptide bond has strong absorption in the far-UV wavelengths from 230 nm down to about 190 nm, CD spectra for each different type of regular structure should be unique in this range of wavelengths. The patterns in the CD spectra found for each structure type are shown in Fig. 2.10. In this figure, the term random coil is a misnomer: the term refers collectively to all structures that are not α-helices or β-sheets, but these other structures are unique, not random.

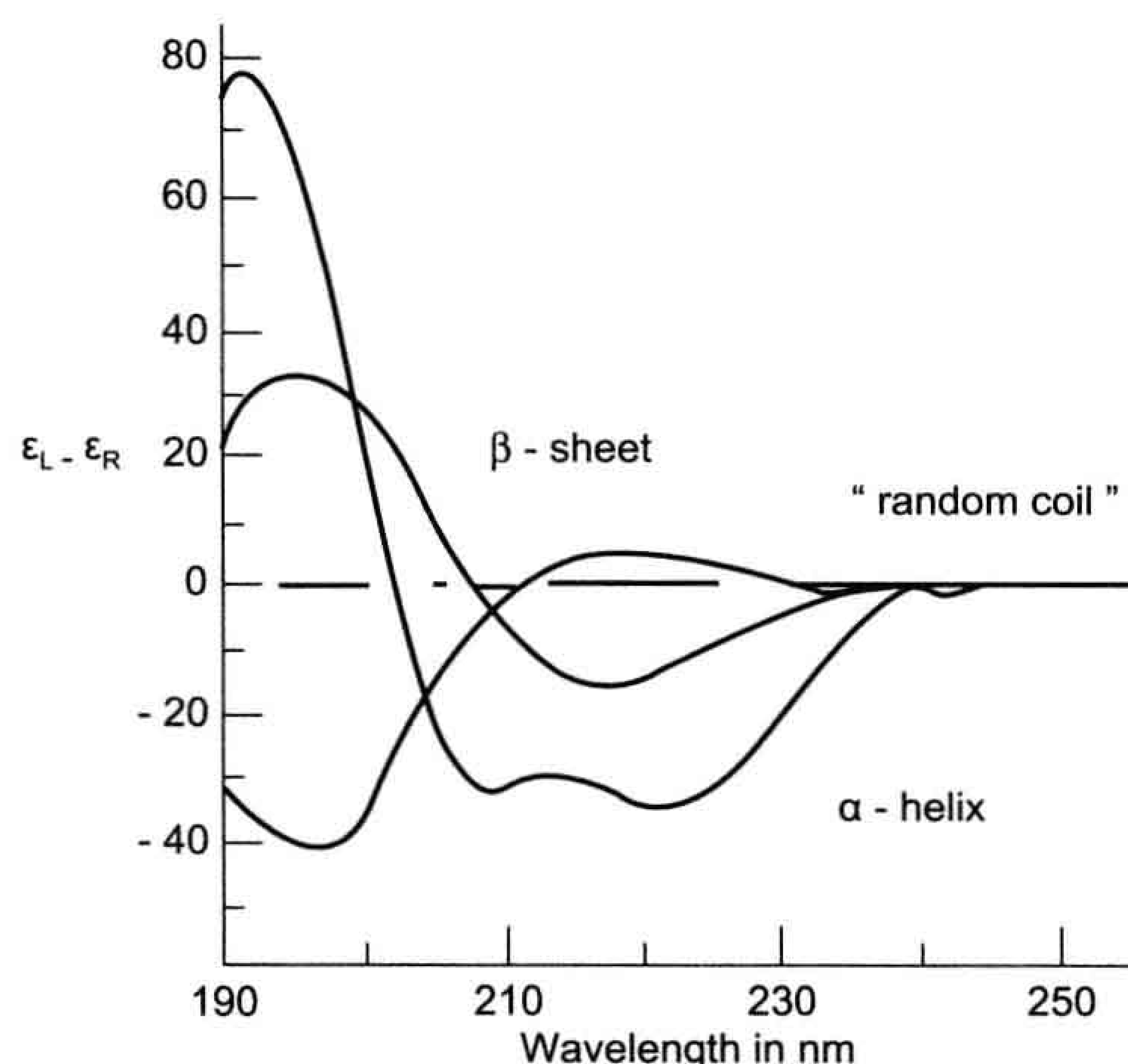


FIGURE 2.10 CD spectra for regular structures: α-helix, β-sheet, and so-called random coil. Note that α-helices have a characteristic "dip" in the region around 210 nm. For a given protein, one can compute the amount of each such structure from its CD spectrum by curve-fitting, using different amounts of each structure type and assuming that the resulting spectrum is the sum of the individual spectra for each structure type.

For proteins of unknown three-dimensional structures, a knowledge of the contents of regular structures (α-helices and β-pleated sheets) can be obtained by taking their CD spectra. Since patterns for α-helix, β-sheet and random coil structures are known, these patterns may be combined to reproduce the observed CD spectrum of a particular protein by curve-fitting. The combination of regular structure that best fits the observed CD curve is the one most likely to exist in the protein. This methodology has been tested on proteins of known three-dimensional structures (so that the percentage of regular structures can be determined) and found to reproduce the regular structure quite satisfactorily.

IIIB. Three-Dimensional Structure of Proteins: X-Ray Crystallography

This technique is based on the principle that the electron clouds around atoms diffract incident light in a predictable way. If the atoms are parts of an oriented molecule, in other words, the protein molecules are all oriented in a crystal, the same atoms of different molecules diffract the light in the same way. The closer two atoms are in the molecule, the farther apart the diffraction pattern will be. Conversely, the farther away two atoms are in the molecule, the closer the diffraction patterns from each atom will be. Thus, the diffraction pattern is the reciprocal of the atomic pattern. The diffraction pattern can be analyzed with respect to the amplitude of diffraction and the relative positions of the scattering pattern. The light diffracted must be x-rays because the wavelength of light used must be of the order of single bond lengths, around 1.5–2.0 Å. Only x-rays have this range of wavelengths.

Once a diffraction pattern has been obtained, the problem is to relate the positions of the atoms to one another from the diffraction pattern. The relative positions of two atoms can be computed from their (diffraction) amplitudes and a phase factor that is related to the angular displacement of one atom relative to the other. This phase factor cannot be determined from the diffraction pattern. Since the position of at least one atom is required, in the x-ray diffraction of proteins, a heavy atom bound to the protein is used in the so-called heavy atom replacement method. Once the phase factor is determined, the individual atomic positions can be computed from the diffraction pattern as a Fourier transform that converts from reciprocal (diffraction) space to real (three-dimensional) space.

IIIC. Two-Dimensional High-Resolution NMR

In one of the most exciting developments in protein chemistry, this technique is being applied to solving the structure of proteins in solution without requiring them to be oriented in a crystal. NMR is based on the principle that most nuclei of atoms have spins. If a magnetic field is applied to the atom, the nuclei tend to align their spins with the field. The energy difference between the spins in the absence and the presence of the field is proportional to the magnetic field strength and is given as:

$$\Delta E = hv = g\beta H \tag{2.2}$$

where ΔE is the energy difference, h is the Planck constant, v is the resonance frequency corresponding to the energy absorbed by the spinning nuclei, gβ is a constant and H is the magnetic field strength. Nuclei like hydrogen exist in a protein in different environments so that some are more shielded by electrons than others, thereby requiring higher v values or field strengths to excite them. The frequencies corresponding to the transitions of the spins of individual nuclei to align themselves with the field is in the radio-frequency range. Because different H atoms absorb at different field strengths or values, one can obtain an absorption spectrum for a given compound or protein, where, for a given field strength, H, different radio frequencies excite the nuclei to change their spins to orient with the field. When two H atoms from different parts of a protein approach one another, their spins either add to or subtract from one another and affect the intensity of each other's absorption in a phenomenon known as the nuclear Overhauser effect or NOE. This change in intensity is inversely proportional to the sixth power of the distance between the two H atoms. If the individual resonant frequencies for the two interacting H atoms are known, the distance between them can be calculated.

The specific H atoms that give rise to different NOE values in a protein can be identified by an elegant technique called two-dimensional NMR (2D-NMR) (Wuthrich, 1986). By irradiating the nuclei at two different frequencies, it is possible to construct a correlation map between the different interacting atoms. A large number of inter-H distances allows us to fit well-defined structures that have these distances so that a class of structures can be directly determined for the given polypeptide or protein.

Once a protein has adopted its final folded form, it possesses a unique size and shape that confer on it certain bulk properties, among the most important of which are electrical properties, which we now discuss.

IV. BULK PROPERTIES OF PROTEINS: PROTEINS AS POLYELECTROLYTES

Folded proteins will, in general, have different shapes and sizes depending on their specific sequences of amino acids. Virtually all folded proteins have their non-polar groups buried in the interior of the protein as a result of hydrophobic interactions and their polar and charged groups on the surface of the protein interacting with the

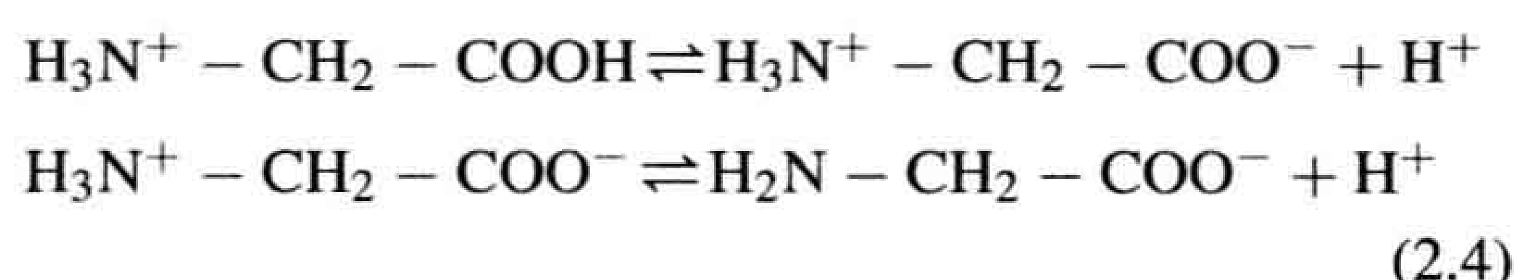
solvent. This distribution of charged groups on the surfaces of proteins strongly affects the manner in which these proteins will be oriented and migrate in electric fields that are either applied in electrophoresis experiments or that result from the transmembrane potential in cells. Proteins with net charges also contribute to the fixed charge inside cells. How proteins migrate in electric fields gives much information about their sizes, shapes and molecular masses. We must therefore consider the properties of proteins as polyelectrolytes dissolved in solution.

IVA. Acid–Base Properties of Amino Acids

All amino acids have free α-amino (NH_2) groups and carboxyl (COOH) groups. Amino groups are *basic*, i.e. *take up* hydrogen ions (H^+), while carboxyl groups are *acidic*, i.e. *give up* hydrogen ions. Using glycine as an example, at neutral pH (7.0), the only form to exist is the dipolar, or zwitterionic, form, $^+H_3N{-}CH_2{-}COO^-$. Figure 2.11 shows a prototypical titration curve for a dibasic acid such as glycine over the pH range of 1–10. In this figure, note that there are two regions of the titration curve where the change in pH is minimal for added base: at pH of around 2.0 and 9.0, the pK_a values for the COOH and NH_2 groups, respectively. At pH 2.0, the buffering capacity of the COOH group is maximal, while at pH 9.0, the buffering of the NH_2 is maximal. The buffering capacity is governed by the Henderson–Hasselbalch equation:

$$pH = pK_a + \log\frac{[\text{conjugate base form}]}{[\text{acid form}]} \qquad (2.3)$$

where the pK_a is the negative logarithm of the proton dissociation constant for the acid. For the acid segment of the titration curve in Fig. 2.11, these two forms are $H_3N^+{-}CH_2{-}COO^-$ and $H_3N^+{-}CH_2{-}COOH$, respectively; for the high-pH portion of the curve, these forms are $H_2N{-}CH_2{-}COO^-$ and $H_3N^+{-}CH_2{-}COO^-$, respectively. Note also that the following equilibria exist over this range:



$$H_3N^+ - CH_2 - COOH \rightleftharpoons H_3N^+ - CH_2 - COO^- + H^+$$
$$H_3N^+ - CH_2 - COO^- \rightleftharpoons H_2N - CH_2 - COO^- + H^+ \qquad (2.4)$$

We can write two separate sets of equilibrium conditions for the two reactions in Equation 2.4 as follows:

$$K_1 = \frac{[H_3N^+ - CH_2 - COO^-]\ [H^+]}{[H_3N^+ - CH_2 - COOH]}$$

$$K_2 = \frac{[H_2N - CH_2 - COO^-]\ [H^+]}{[H_3N^+ - CH_2 - COO^-]} \qquad (2.5)$$

Solving both of these equations for the common zwitterionic species, $H_3N^+{-}CH_2{-}COO^-$, we obtain the expression:

$$K_1K_2 = \frac{[H_3N^+ - CH_2 - COOH]}{[H_2N - CH_2 - COO^-]} \times [H^+]^2 \qquad (2.6)$$

Taking the negative logarithms of both sides of Equation. 2.6, we obtain the expression:

$$pH = \frac{pK_1 + pK_2}{2} + \frac{1}{2}\log\frac{[H_2N - CH_2 - COO^-]}{[H_3N^+ - CH_2 - COOH]} \qquad (2.7)$$

where pK_1 and pK_2 are the negative logarithms of K_1 and K_2. This equation is the same as the Henderson–Hasselbalch equation for any acid–base equilibrium except, in this case, it is written for two equilibria. The *isoelectric point*, pI, is defined as the pH at which the total negative charge of the molecule is equal to its total positive charge (i.e. where only the zwitterionic species exists). In terms of Equation 2.7, this condition is met if the numerator and denominator are equal. In this case:

$$pH = \frac{pK_1 + pK_2}{2} \qquad (2.8)$$

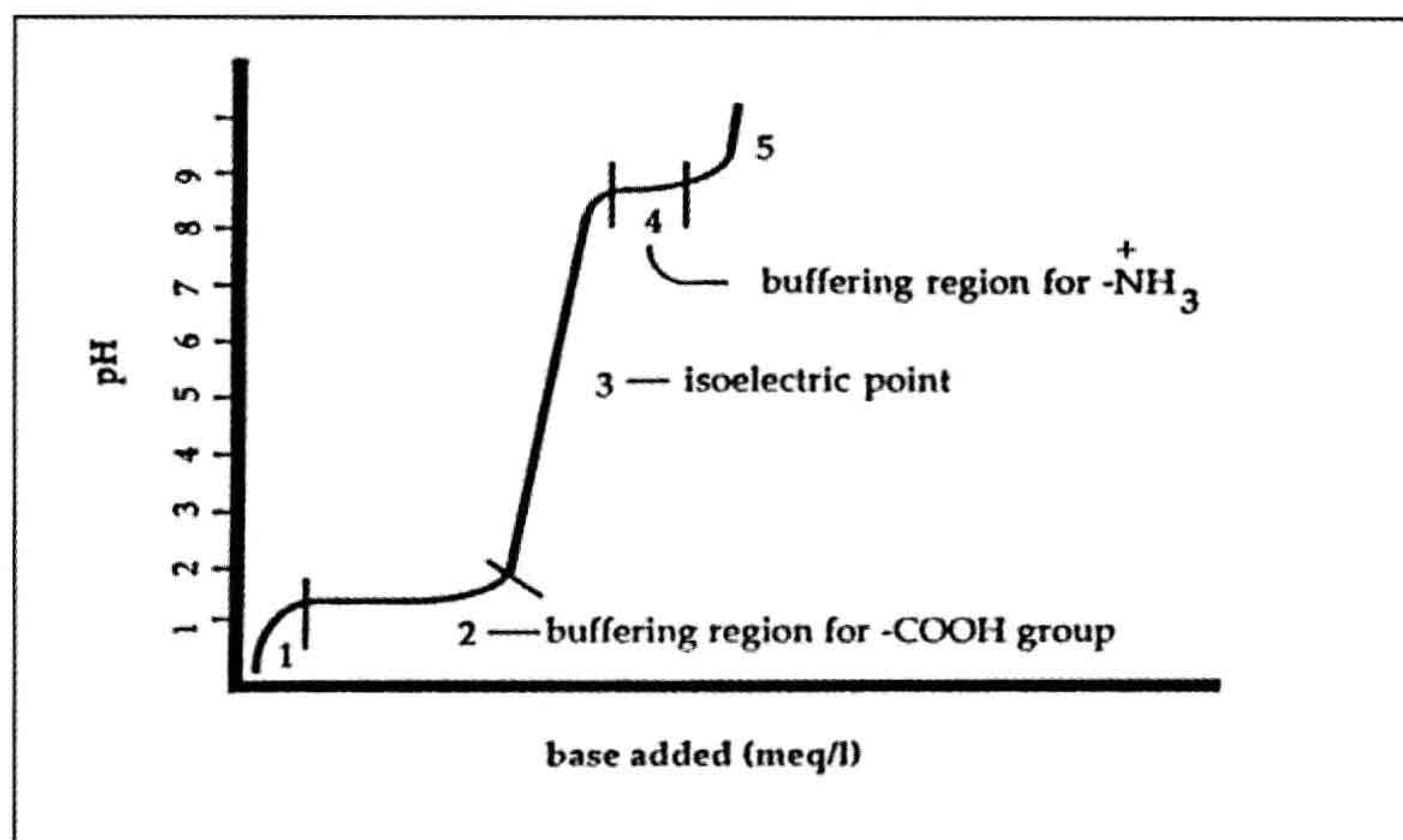
For amino acids with charged side chains, the isoelectric point is easily shown to be that pH equal to $(pK_1 + pK_2 + pK_3)/3$. In general, for multiple prototropic dissociations for a whole protein, the isoelectric point of the protein is simply that point on the titration curve for the whole protein where:

$$pH = \sum pK_i/N \qquad (2.9)$$

where the sum is taken over all proton-dissociating groups, and N is the number of these groups in the protein.

IVB. Protein Charge and Solubility

Since all proteins are charged because of charged side chains and the α-NH_3^+ group and the $-COO^-$ carboxyl terminal group, there is generally a *net* charge on the protein. These net charges tend to be solvated and interact with counterions in solution. The solvation of these charges makes the protein soluble in H_2O. However, interactions of the charged side chains of the protein with surrounding ions and aqueous solvent become minimal at the isoelectric point, where the charges on the protein exactly balance one another. At its isoelectric point, the solubility of the protein in water is minimal and it will tend to precipitate from solution. Different proteins have different sequences and different charges and isoelectric points so that their tendencies to precipitate will differ from one another and



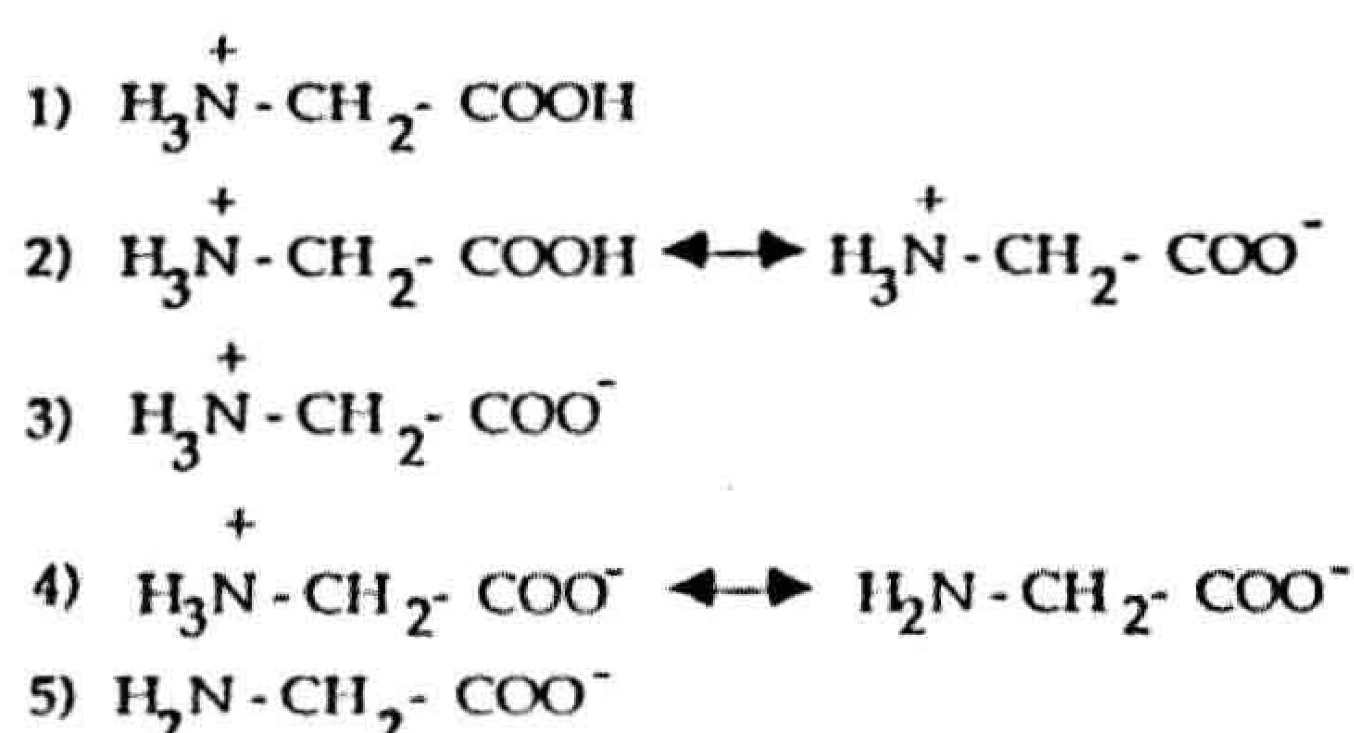


FIGURE 2.11 Titration curve for a dibasic acid like glycine to show the two buffering regions for the $COOH^-$ and NH_3^+ groups and the isoelectric point that can be computed as $(pK_{a1} + pK_{a2})/2$. A protein has multiple buffering regions, characteristic of each residue type that is involved in a prototropic dissociation.

depend on the pH of the solution. Thus, by changing the pH of protein solutions, it is possible to effect differential precipitation of these proteins. A more sophisticated version of isolation of proteins based on their isoelectric points is *isoelectric focusing*, an electrophoretic method discussed in Section IVD.

IVB1. Isoionic Point

This term is used when proteins are dissolved in aqueous solutions where the only counterions are H^+ and OH^-; in other words, the counterion for the anionic groups is H^+, and the counterion for the cationic groups is OH^-. Since the total number of positive charges for the system must equal the total number of negative charges for the system:

$$(H^+) + (\text{total positive charges on protein}) = (OH^-) + (\text{total negative charges on protein}) \tag{2.10}$$

From Equation 2.10, if the isoionic point of a protein is at pH 7 (i.e. $H^+ = OH^-$), *the isoelectric point is the same as the isoionic point* since from Equation 2.10, if $H^+ = OH^-$, then total positive charges on the protein equal total negative charges on the protein.

IVC. Titration of Proteins

Because of their large number of exposed acidic and basic groups, proteins behave as buffers. Generally, the pH of the buffering region will depend on the relative numbers of acidic and basic groups on the protein surface. Binding of protons to proteins may be considered to be formally the same as the binding of ligands (small molecules) to proteins. To understand the behavior of proteins as buffers, it is important to understand ligand-binding theory.

IVC1. Ligand-Binding Theory

Suppose a protein has n equivalent sites for binding to a ligand and each site is completely independent of any other site. The equilibrium for the binding of a ligand, A, to any one site of the protein can be written as:



$$A + P \rightleftharpoons AP \tag{2.11}$$

where A is the free ligand, P is the unbound protein and AP is the ligand bound to protein. The equilibrium association constant, K, for this process is:

$$K = \frac{[AP]}{[A][P]} \tag{2.12}$$

where [A] is the free ligand concentration, [P] is the concentration of unbound protein and [AP] is the concentration of ligand bound to protein. If there are n equivalent binding sites per protein molecule, then the total concentration of sites is $n[\mathrm{P}]_o$, where $[\mathrm{P}]_o$ is the concentration of total protein and is equal to the sum of the concentrations of free and bound protein:

$$[\mathrm{P}]_o = [\mathrm{P}] + [\mathrm{AP}] \tag{2.13}$$

Combining Equations 2.12 and 2.13, we find that:

$$[\mathrm{P}]_o = [\mathrm{P}] + K[\mathrm{A}][\mathrm{P}] \tag{2.14}$$

Solving for [P], we obtain:

$$[\mathrm{P}] = \frac{[\mathrm{P}]_o}{1 + K[\mathrm{A}]} \tag{2.15}$$

Since from Equation 2.12, $[\mathrm{AP}] = K[\mathrm{A}][\mathrm{P}]$, the ratio of bound protein to total protein is:

$$\frac{[\mathrm{AP}]}{[\mathrm{P}]_o} = \frac{K[\mathrm{A}]}{1 + K[\mathrm{A}]} \tag{2.16}$$

If there are n equivalent binding sites per protein molecule, the fraction of sites bound from Equation 2.15 is:

$$\frac{[\mathrm{AP}]}{n[\mathrm{P}]_o} = \frac{K[\mathrm{A}]}{1 + K[\mathrm{A}]} \tag{2.17}$$

This equation can be linearized. Defining $R = [\mathrm{AP}]/[\mathrm{P}]_o$:

$$R/[\mathrm{A}] = nK - KR \tag{2.18}$$

Plots of $R/[\mathrm{A}]$ versus R (called *Scatchard plots*) should give a straight line whose slope is K and whose intercept is nK. Thus both K and n are readily determined.

For n equivalent proton binding sites on a protein, we can write Equation 2.16 as:

$$R = \frac{K[\mathrm{H}^+]}{1 + K[\mathrm{H}^+]} \tag{2.19}$$

In this case, $R = [\mathrm{PH}^+]/n\,[\mathrm{P}]_o$. If we use the dissociation constant $K' = 1/K$, Equation 2.19 may be recast as:

$$[\mathrm{PH}^+]\,K' = (n\,[\mathrm{P}]_o - [\mathrm{PH}^+])\,[\mathrm{H}^+] \tag{2.20}$$

Rearranging and taking logs of both sides of Equation 2.20, we obtain the equation:

$$\mathrm{pH} = \mathrm{p}K_a + \log\frac{n[\mathrm{P}]_o - [\mathrm{PH}^+]}{[\mathrm{PH}^+]} \tag{2.21}$$

where $\mathrm{p}K_a$ is $-\log\,(K')$. Note that Equation 2.21 is the Henderson–Hasselbalch equation for multiple dissociations. The denominator in the logarithmic term in Equation 2.21 represents the concentration of H^+-bound protein while the numerator represents non-proton-bound protein. This equation is useful for titration of proteins provided that the $\mathrm{p}K_a$ of each group is independent of that of any other group for a given set of groups, such as the carboxyl groups of Glu and Asp.

For proteins, it is not generally correct to assume that the above condition holds because, as each carboxyl group dissociates from a protein, the protein becomes progressively negatively charged, so that it becomes progressively difficult for the next proton to dissociate. In fact, the protein behaves as a polyelectrolyte wherein proton dissociations are strongly dependent on the electric field of the protein.

IVC2. The Electrostatic Field Effect (Bull, 1943)

To account for the electrostatic field effect of the charged protein on the dissociation process, we note that the free energy of dissociation per mole of acid group, ΔG, can be written as:

$$\Delta G = \Delta G_i + \Delta G_e \tag{2.22}$$

where ΔG_i is the intrinsic dissociation free energy for the group and ΔG_e is the electrostatic free energy for dissociating a proton from the acid group in the presence of the field of the protein. From electrostatic theory:

$$\Delta G_e = eU \tag{2.23}$$

where $e = 1$ electrostatic charge unit and U is the electrical potential from the protein. Since the standard free change for dissociation, ΔG, equals $-2.303 \times RT \log K$ and ΔG_i equals $-2.303 \times RT \log K_i$ (where R is the gas constant and T is the temperature in K), from Equation 2.22, we obtain the relation:

$$\mathrm{p}K = \mathrm{p}K_i + eU/2.303RT \tag{2.24}$$

From Equation 2.21, we have:

$$\mathrm{pH} - \log\frac{n[\mathrm{P}]_o - [\mathrm{PH}^+]}{[\mathrm{PH}^+]} = \mathrm{p}K_i + eU/2.303RT \tag{2.25}$$

It is of obvious importance to obtain an explicit expression for U since it strongly influences the dissociation of protons from proteins.

IVC3. Computation of the Electrical Potential

To compute the electrical potential U, it is necessary to use a model for the interaction of protein charges with those of small ions. The simplest model is to assume that the protein is a charged sphere and that the counterions surrounding it, like protons, form a spherical shell around

the central charged protein sphere as represented in Fig. 2.12. The overall arrangement is that of two concentric spheres of radii R_1 and R_2, the first term being the distance from the center of the protein to its surface, and the second term being the distance from the center of the protein to the center of mass of the ions surrounding the protein. It is clear from this figure that the interactions of protons, and/or any ions, with the central, charged protein molecule depend on the distance of the centers of these ions from the center of the protein ion. The distribution of ions around the central charged protein ion is given by the Boltzmann distribution:

$$\psi = \sum en_iZ_i \exp - (en_iZ_iU/RT) \quad (2.26)$$

where Z_i is the valence of the ith ion. We can expand the exponential term in a Taylor series as follows:

$$\psi = \sum n_iZ_ie - \sum n_iZ_ie(eZ_iU/RT) + (\sum n_iZ_ie/2)(Z_ieU/RT)^2 + \cdots \quad (2.27)$$

We make the assumption that the eZU term is much less in value than RT, and that electrical neutrality must be preserved (i.e. the first sum on the right of Equation 2.27 is 0). Then:

$$\psi \approx - \sum n_iZ_i^2e^2U/RT \quad (2.28)$$

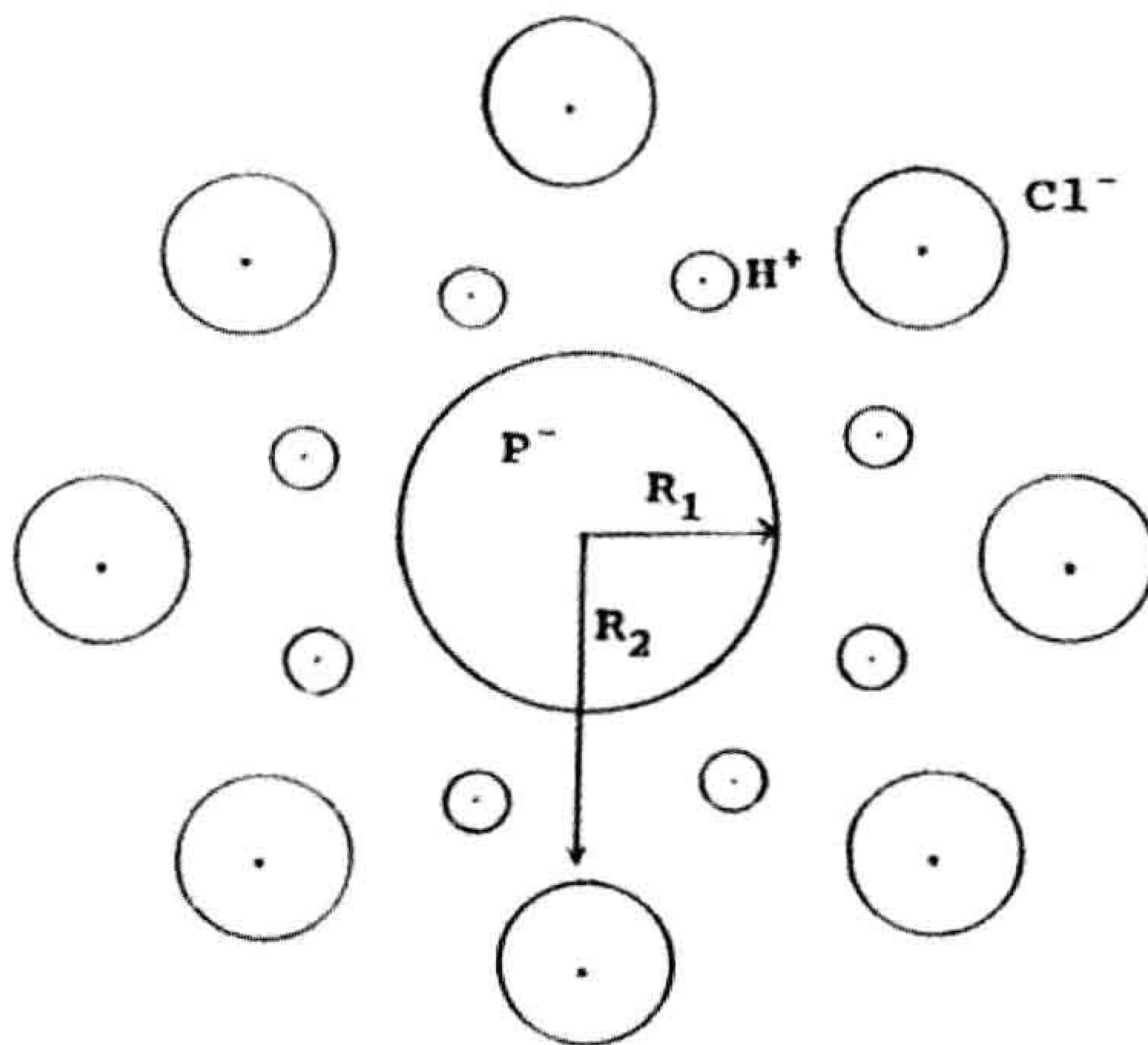


FIGURE 2.12 The model for the effect of the charge on a protein (p⁻) on the dissociation of protons from groups on the protein involved in prototropic dissociations. R_1 is the radius of the protein, assuming that it has a spherical shape. R_2 is the distance from the center of the protein sphere to the mean center of the ions surrounding the protein. In this figure, H^+ ions are shown as the positive ions and Cl^- as the negative ions. Their distributions around the protein will depend upon the charge on the protein and the Boltzmann factors for each surrounding ion type. R_2 is therefore a mean distance from the center of the protein to the mean center of the surrounding ions.

This charge distribution must satisfy the Poisson charge distribution equation:

$$\nabla^2U = -4\pi\psi/D \quad (2.29)$$

where ∇^2U is the second derivative of the potential with respect to the sum of the coordinates of the system, ψ is the charge distribution and D is the dielectric constant of the medium, water. Combining Equations 2.28 and 2.29, we obtain:

$$\nabla^2U = (4\pi e^2)/(DRT) \times \sum n_iZ_i^2U \quad (2.30)$$

Solution of this equation for U as a function of the coordinates of the system constitutes the Debye-Hückel theory and it depends on the assumed configuration of small ions around the central large protein ion, assumed here to be spherical in shape as in Fig. 2.12.

Solution of Equation 2.30 for this circumstance at R_1 gives:

$$U = Ze(R_2 - R_1)/DR_1R_2$$

where $Z = \sum n_iZ_i$. Letting $1/\chi = R_2 - R_1$,

$$U = \frac{Ze}{DR_1(\chi R_1 + 1)} \quad (2.31)$$

Combining Equations 2.24 and 2.31, we obtain:

$$pK = pK_i + \frac{Ze^2}{2.303RTD} \times \frac{1}{R_1(\chi R_1 + 1)} \quad (2.32)$$

Setting:

$$W = \frac{e^2}{2.303RTD} \times \frac{1}{R_1(\chi R_1 + 1)} \quad (2.33)$$

Equation 2.25 may now be written as:

$$pH - \log\frac{n[P]_o - [PH^+]}{[PH^+]} = pK_i + 0.868\ WZ \quad (2.34)$$

This equation now takes into account the field effect of protein and surrounding ion charges provided that the system conforms to the assumptions made for this model: that $U << RT$, that the protein is spherical in shape and that the ions around the protein form a spherical shell around it. Plots of the left side of Equation 2.34 versus Z, the overall protein charge, should yield a straight line whose slope is $0.868W$. This term may be regarded as a structure term that depends on the radius of the protein and the position of the center of mass of the surrounding ion cloud.

IVC4. More Explicit Models Based on Protein Structures

The above theoretical expression is based on several critical assumptions that do not always apply to proteins, namely, that the charge distribution around the protein is uniform

and spherical and that its electrical potential is such that the ZU term <<RT. We know from the many x-ray crystallographically determined protein structures that protein surfaces are far from spherical and that the charge distributions are not uniform. Thus, to understand the effects of protein charge and the effect of the medium on proton dissociations from the protein, more explicit and detailed models are needed. One treatment is based on conformational energy calculations on proteins surrounded explicitly by solvent molecules. These calculations have thus far been aimed at determination of the intrinsic pK_as of specific groups on protein surfaces.

In this approach (Russell and Warshel, 1985), the energy of dissociation of a particular acid group, AH, is computed for the whole protein surrounded by water molecules placed on a grid around the protein. The energy of interaction of the atoms of the protein with one another is computed using energy functions similar to those discussed in Section IID. Included in this energy is the effect of the permanent dipoles of the atoms of the protein that induce dipoles on the other atoms of the protein. The magnitude of this energy depends on the polarizability of the interacting atoms. Further account is taken of the effect of the interaction of the dipoles of the atoms of the protein with water molecules which themselves are represented as dipoles. The calculations are then applied to the dissociation of a proton from a particular group, e.g. Asp 3 and Glu 7 in bovine pancreatic trypsin inhibitor (BPTI) whose structure has been determined at high resolution by x-ray crystallography (see Section IIIB).

In this procedure, a thermodynamic cycle is employed in which the free energy difference of the system is computed for the acid group in the AH form in the protein and for the AH group dissolved in water (process 1). The group is then allowed to dissociate in water at a given pH (process 2). The free energy difference between AH and A^- in water is known (for Asp residues, this would be the free energy of the dissociation of acetic acid in water at a given pH) and is equal to $2.303RT(pK_a - pH)$. Finally, the free energy difference between solvated A^- in water and A^- in the protein (process 3) is computed. The overall free energy for dissociation is then computed as the difference between the free energy for process 1 and the free energy for process 3 plus a constant (free energy for dissociation of AH in water).

These calculations have been carried out on a supercomputer using molecular dynamics and iterative procedures (for the polarization energies) and have reproduced ionization constants satisfactorily. The method, which is computer intensive, includes the effects of both solvent and the atoms of the whole protein on the ionization process. Thus the approach appears to be a fruitful one in the investigation of prototropic dissociations in proteins.

IVD. Protein Charge and Electrophoresis

Different proteins have different net charges as discussed above. If these proteins are placed in an electric field, positively charged proteins migrate towards the negatively charged pole, the cathode, while negatively charged proteins migrate to the positively charged pole, the anode. If a protein is present at a pH equal to its isoelectric point, it will generally not move toward either pole. The electrostatic force on a protein present in an electric field is equal to ZeU, where U is the electric field, e is the charge of an electron (or a proton), and Z is the number of charges present. There is a drag force on the proteins that is proportional to the velocity at which they move towards either pole, fv, where v is the velocity of the protein moving in the electric field and f is a proportionality constant. This force balances the electrostatic force so that:

$$ZeU = fv \tag{2.35}$$

and

$$v = ZeU/f \tag{2.36}$$

The value of f generally increases with increasing size and molecular weight so that, for proteins of similar charge but different molecular weights, the higher molecular weight proteins move more slowly than the lower molecular weight proteins.

There are several types of electrophoresis, all of which are extremely effective not only in separating proteins but in directly determining their molecular weights.

IVD1. Slab Gel Electrophoresis

Proteins are separated on gels made up of such polymers as starch, polyacrylamide and agarose. The separation is based mainly on charge, and, to an extent, on size.

IVD2. Sodium Dodecylsulfate (SDS) Electrophoresis

SDS is a detergent that contains a long aliphatic chain and a sulfate group. This detergent interacts with denatured proteins to form a strongly negatively charged complex (the negative charge arising from the SO_4^{2-} groups of SDS). The proteins are first denatured by heat and then the SDS is added in large excess. The SDS–protein complexes all contain about the same negative charge because the SDS swamps out all of the protein charges. Since the charges are all the same, the proteins all separate from one another strictly on the basis of their sizes. From Equation 2.36, the larger polypeptide chains of higher molecular weight migrate the most slowly while the lower molecular weight proteins migrate more rapidly towards the anode. Proteins of known molecular weight can be subjected to this procedure and used as "markers". A plot of the molecular weights versus the log of the distance traveled from the

point of application yields a straight line. The log of the distance of migration of a protein of unknown molecular weight can then be plotted on this line and the molecular weight directly determined.

IVD3. Isoelectric Focusing

In this elegant technique, a polymer is used in which acidic and basic groups change in density from one end of the polymer to the other. When this polymer is placed in solution, a continuous pH gradient is established along the polymer. A mixture of proteins is then applied to the polymer in a weak buffer. When the proteins migrate in the electric field, they experience local differences in pH on the polymer and eventually reach a local pH equal to their individual pIs. At the pI, the protein no longer migrates in the electric field. This method of separation depends only on the presence of proteins with different pI values.

IVD4. Two-Dimensional Gel Electrophoresis

Proteins can be separated from one another in one lane as described in the preceding three sections; however, these approaches may not meet the conditions for separating all of the proteins. For example, on agarose gel electrophoresis, two proteins may not separate well at the pH of the buffer used. A buffer of different pH may then be added and the electrophoresis carried out at right angles to the original direction of migration to allow further separation of the proteins.

IVD5. Western Blots (Immunoblots)

All proteins are antigens and can provoke the production of antibodies against them when injected into animals. The antibodies are immunoglobulins which are proteins that bind very specifically to and with high affinity for specific antigens. Antibodies and, in fact, all proteins can be conjugated covalently to fluorescent dyes or to enzymes. If we wish to identify a particular protein on an electrophoretogram, we can use a "tagged" antibody to the protein and reveal its presence on the electrophoretic gel. The antibody is "tagged" with a covalently labeled enzyme that catalyzes a reaction that produces a chromophoric (colored) reaction product. For example, alkaline phosphatase catalyzes the hydrolysis of *p*-nitrophenol phosphate, which is colorless, to *p*-nitrophenol (more accurately, *p*-nitrophenoxide anion), which is bright yellow. Since antibody cannot be added directly to the gel from electrophoresis, the gel itself is blotted onto nitrocellulose or another suitable membrane that contains all of the separated bands of proteins as they were on the original electrophoretic gel. This nitrocellulose strip is then incubated in a solution containing the antibody. The antibody itself may be conjugated to an enzyme like alkaline phosphatase, and the band can be identified, or antibodies to the primary antibodies, such as goat anti-rabbit IgG, are conjugated to the enzyme and the blot is incubated with these secondary antibodies after being treated with the primary antibody. The secondary antibodies are then markers for the desired protein band.

V. RELATIONSHIP OF PROTEIN STRUCTURE TO FUNCTION

In this section, we discuss some of the relationships of the conformations of proteins to their functions. This is a vast field and so we concentrate on one aspect of fundamental importance to cell physiology, membrane polypeptides and proteins.

VA. Membrane Polypeptides and Proteins

Membrane proteins have exceptional physiological importance in a number of different ways. Virtually all extracellular receptors have a transmembrane domain that is essential to the functioning of the receptor protein. Other membrane polypeptides are vital in the transport of secreted proteins across cell membranes. Still other membrane proteins, such as the components of the complement system, are involved in intercalating into the cell membrane, causing cell lysis. Yet other membrane proteins form ion channels which allow for selective entry or exit of specific ions to and from the cell. In this section, we discuss the relationship of the structures of some of these membrane proteins to their functions. It should be emphasized that this entire field of structure–function relationships of membrane proteins is quite new. Most of our knowledge in this field comes from experimental cell biological data on specific proteins and from the results of computations on membrane and membrane-associated protein structure.

VA1. Structure and Function of Leader Peptides

Each protein, after it is synthesized on the ribosome, must be transported across the rough endoplasmic reticulum (RER) membranes. If the protein is to be secreted from the cell, or to intercalate into the cell membrane, it must undergo transport across and/or into the cell membrane. For virtually every protein that is synthesized in the cell, there is a polypeptide segment beginning at the N-terminal methionine residue that consists of about 20–30 amino acid residues. Typically, these sequences consist of several hydrophilic amino acids followed by a long stretch of hydrophobic amino acids. When the protein is secreted across the RER membrane, this *leader sequence* is cleaved off, presumably by intracellular proteases. Absence of these leader sequences results in the inability of the protein to traverse the RER membrane, resulting in ultimate intracellular degradation of the protein. Thus, these leader sequences are of vital importance to cellular protein function in general.

The regulation of transmembrane transport of newly-synthesized proteins is delicate. It has been shown in in vitro systems that newly synthesized proteins that are secreted across reticulocyte membranes do not undergo leader sequence cleavage. These proteins are non-functional because they do not fold correctly. Thus, leader sequences must be attached to the polypeptide chain to enable protein secretion, but must be cleaved off to allow correct protein folding.

To explain how proteins are secreted across membranes, Engelman and Steitz (1981) proposed the so-called *helical hairpin hypothesis* in which the leader sequence adopts an α-helical conformation. At the end of this segment there is a hairpin turn followed by another α-helix involving 30–40 residues of the protein itself. Both the amino terminal end of the leader sequence and the carboxyl terminal end of the growing polypeptide chain lie on the same side of the membrane while the hairpin turn lies on the opposite side of the membrane. Because the leader sequence helix and the succeeding helical sequence are both independently stable, they interact minimally with one another so that the growing polypeptide chain can slide past the hydrophobic leader sequence in the membrane. As the nascent polypeptide chain pushes through the membrane, anchored by the leader sequence, it begins to fold in the aqueous environment of the cytoplasm on the opposite side of the RER membrane. The leader sequence, however, remains in the membrane because of its hydrophobic character. The hairpin connection between the two helices is a signal for intracellular proteases that ultimately results in cleavage of the leader sequence.

Pincus and Klausner (1982), using ECEPP, have computed the low energy structures for the leader sequence of the κ-light chain immunoglobulin. This sequence, which contains 16 amino acids, is Asp-Thr-Glu-Thr-Leu-Leu-Leu-Trp-Val-Leu-Leu-Leu-Trp-Val-Pro-Gly. These investigators found that the first four polar residues tend to adopt an extended conformation followed by a long α-helix that ends in a hairpin turn at the carboxyl terminal Val-Pro-Gly sequence. This structure was lower in energy than any other competing structure by at least 10 kcal/mol. Thus, these calculations support the essential features of the Engelman–Steitz hypothesis and have been further corroborated experimentally. For example, the CD spectrum of synthetically prepared leader sequences shows high α-helical content when the sequence is dissolved in hexafluoroisopropanol, a non-polar solvent that simulates the low dielectric medium of the membrane (Rosenblatt et al., 1980).

In site-specific mutagenesis experiments, Thomas Silhavy and his coworkers, then at the National Cancer Institute, have placed proline residues in the middle of the hydrophobic transmembrane domain of a bacterial leader sequence (Emr and Silhavy, 1982). Proline residues tend to disrupt α-helices. These investigators found that if they introduced two proline residues close together in the sequence, the protein to which the leader sequence was attached was no longer secreted. This result strongly corroborates the conclusion that leader sequences must adopt α-helices in the membrane.

In a series of elegant experiments, Blobel and his coworkers (1979) have shown that specific sequences in proteins will insert into membranes but will not lead to cleavage of the inserted sequence from the rest of the protein. These specific sequences contain what are referred to as "stop signals" that do not permit cleavage. Because the transmembrane domain is hydrophobic, it remains inserted in the membrane and there is no impetus for it to move through the membrane, resulting in secretion. This mechanism is extremely important for the function of receptor proteins, as will be discussed in Section VA3.

VA2. Membrane-Active Peptides: Melittin and Magainin

These are peptides that insert into cell membranes and induce lysis of these membranes, by forming pores.

Melittin

Melittin is one of the smallest proteins known to fold spontaneously. Unlike most proteins, it folds in non-polar media and is denatured in aqueous solutions and consists of 26 amino acids, i.e. $^{+}$H-Gly-Ile-Gly-Ala-Val-Leu-Lys-Val-Leu-Thr-Thr-Gly-Leu-Pro-Ala-Leu-Ile-Ser-Trp-Ile-Lys-Arg-Lys-Arg-Gln-Gln-NH_2. As the major component by mass of bee venom, it specifically induces lysis of red blood cell membranes. Note that this peptide contains six positive charges and *no* negative charges. Also note that most of the positively charged residues occur at the carboxyl terminal end of the molecule. As discussed in Section IIB above, α-helices are stabilized by the presence of positively charged residues on their carboxyl terminal ends as is present in this sequence.

As noted in Section IIE above, the structure of melittin has been computed (see Fig. 2.9) and determined by x-ray crystallography (Terwiliger, 1982). Overall, the structure of this protein may be thought of as a bent α-helical rod with α-helices from Gly 1 to Thr 10, a reverse turn at Thr 11 to Gly 12, followed by another α-helix from Pro 14 to Gln 26. Leu 13 can adopt an energetically favorable conformation, a D state (see Fig. 2.8) that results in a compact structure for the monomeric state. In the x-ray structure of tetrameric melittin, this residue adopts an energetically less favorable α-helical conformation, causing it to adopt a more open, "straight" structure. In both structures, melittin forms an amphipathic helix in which the non-polar groups contact one another on the inside of the structure while the polar groups protrude out towards the solvent.

Inspection of the structure for the tetrameric protein reveals that packing between the monomeric units is such that the positive charges of each lie as far away from one another as possible while the hydrophobic cores pack as tightly as possible with one another. This can be accomplished if the monomeric units become slightly less compact by allowing Leu 13 to adopt the α-helical conformation. The sacrifice in conformational energy is about 3 kcal/mol (Kempf et al., 1982).

Magainin

This 23-residue peptide intercalates into the cell membranes of bacteria and some fungi and induces lysis of these membranes, but has low activity in lysing red blood cell membranes. The sequence of magainin is H-Gly-Ile-Gly-Lys-Phe-Leu-His-Ser-Ala-Lys-Lys-Phe-Gly-Lys-Ala-Phe-Val-Gly-Glu-Ile-Met-Asn-Ser-OH. As with melittin, this sequence contains a preponderance of positive charges (6 Lys, 1 His [positive at pHs below 7] and one amino terminal positive charge vs two negative charges, one Glu and carboxyl terminal carboxylate). Unlike melittin, magainin has the positively charged residues closer to the amino terminal domain of the peptide. This peptide has been found to adopt an α-helical structure.

Multiple theories about the mechanism by which melittin and magainin cause cell lysis have been proposed. Most recently, studies with artificial membranes using 1,2-dioleoyl-*sn*-glycero-3-phosphatidylcholine (DOPC) and 1,2-dioleoyl-*sn*-glycero-3-phosphatidylglycerol (DOPG) indicate that melittin interacts strongly with DOPG which is negatively charged in two ways: flat, i.e. in the plane of the membrane and perpendicular to the plane of the membrane. In the latter manner, melittin can form channels that disrupt the membrane while molecules in the former mode of binding block channel formation (Bogaart et al., 2008). Deductions about the arrangement of melittin molecules in artificial membranes using fluorescence quenching of the Trp 19 and use of Raman spectroscopy suggest that melittin forms terameric pores through the membrane (Vogel and Jahnig, 1986). These pores would allow extrusion of the intracellular contents resulting in cell death.

The structure of magainin in artificial membranes has been determined using neutron diffraction of magainin in membranes containing 1,2-dimyristoyl-sn-glycero-3-phosphatidylcholine (DMPC) and 1,2-dimyristoyl-sn-glycero-3-phosphatidylglycerol (DMPG). It appears to form hexagonal pores that are stacked across the membrane that can explain membrane lysis (Yang et al., 2000). The pores appear to have variable sizes over time that are also dependent on the concentration of magainin (Tamba et al., 2010). Thus far it is not clear what causes the selectivity of each peptide for specific cell membranes, i.e. melittin for red blood cell membranes and magainin for bacterial and fungal membranes.

Other theories include the possibility that melittin and magainin have detergent actions because they are both amphipathic, containing both polar positively charged groups and hydrophobic groups, which allows them to interact favorably with water and the hydrophobic membrane lipid bilayer, respectively, resulting in solubilization of the membrane causing its breakdown. This theory does not account for the fact that virtually all biological membranes contain lysolecithins and like fatty acid derivatives that contain non-polar and positively charged headgroups that actually stabilize membrane structure.

A third theory (Kempf et al., 1982), based on evidence that formation of melittin channels depends on the transmembrane potential, proposes that melittin undergoes a conformational change in the presence of a transmembrane electric field such that it adopts a less compact structure and becomes a more rigid rod-like structure that spans the whole membrane and disrupts the lipids in the lipid bilayer. In this theory, monomeric melittin would form pores or channels. Evidence for this theory comes from experimental work in which melittin was added to artificial bilayers. Proteolytic enzymes (pronase) were added to the aqueous phase under the bilayer. If the transmembrane potential was 0 or such that the outside was negative relative to the inside of the bilayer, no proteolysis of melittin occurred. However, if the inside of the membrane was made negative with respect to the outside such that the transmembrane potential was −60 mV or less, proteolysis of melittin occurred. A potential of −60 mV, found in most resting cells, corresponds to an energy of 2−3 kcal/mol, sufficient to convert compact monomeric melittin to a straightened structure that then spans the membrane and encounters the proteolytic enzymes. This example illustrates the great biological relevance of the relationship of charges on the protein surface to their interactions with electric fields, as in electrophoresis, and to the effects of an electric field on the conformations of proteins. This relationship is vital in understanding the functioning of ion channel proteins as described in Section VA4.

New Membrane-Active Anti-Cancer Peptides Kill Cancer Cells (Yazdi et al., 2010)

Recently, peptides derived from the p53 protein have been developed that kill cancer cells but not normal cells. p53 is an anti-oncogenic protein that slows down or blocks cell division and induces apoptosis of cancer cells. Its lifetime is shortened when it binds to another important protein in the cell, the double-minute-binding protein of human (H) or mouse (M) origin, and called H(M)DM-2 (called HDM-2 in this section). HDM-2 induces the addition of a 76 amino acid protein, called ubiquitin, onto p53, targeting p53 for proteolysis. p53 binds to HDM-2 using its amino terminal amino acid residues 12−26 in the human sequence.

Originally, this p53 peptide was to be introduced into cancer cells to block the binding of p53 to ubiquitin, resulting in increasing the half-life of p53. In order to get the p53 12–26 peptide into cancer cells, it had to be attached to a transmembrane carrier. There is a group of peptides, called penetratins, that are highly positively charged and include the TAT sequence of HIV, that cause the transport of proteins across cell membranes, much in the same manner as leader sequences, discussed in Section VA1 above. Since the structure of the HDM-2-binding domain of p53 is largely α-helical when bound to HDM-2 (Kussie et al., 1996), the positively charged transmembrane-penetrating sequence (or membrane residency peptide or MRP) was added to the carboxyl terminal end of the p53 12–26 peptide using the principal that α-helices are stabilized by positive charges on their carboxyl terminal ends. When the p53 12–26-MRP, called PNC-27, was incubated with cancer cells, it killed them within 1 hour. Surprisingly, it killed p53-defective cells just as rapidly. On the other hand, it had no effect on the growth or viability of normal cells. Electron micrographs of cancer cells killed by PNC-27 and a shorter analog consisting of p53 residues 17–26-MRP, called PNC-28, showed that transmembrane pores formed. The two-dimensional NMR structure of PNC-27 showed that it had the classical α-helix-loop-α-helix structure as shown in Fig. 2.13 (Rosale et al., 2004). This structure was highly amphipathic. Thus PNC-27 and PNC-28 kill cancer cells selectively by forming pores in their membranes as membrane-active peptides.

The question, as with melittin and magainin, was why these peptides were selective for one cell type, in this case, cancer cells. Recent work has shown that cancer cells express HDM-2 in their cell membranes while normal cells do not. The reason is thought to be that HDM-2 in the cell membrane binds to cadherin, a cell-to-cell adhesion protein. When it binds to cadherin, it targets its catabolism so that the cells do not stick together and therefore undergo contact-inhibited cell growth. Thus PNC-27 and PNC-28, which adopt a membrane-active amphipathic helix-loop-helix structure, bind to and are held by HDM-2 in the cell membrane. In this conformation, they form transmembrane pores, resulting in cell lysis. Thus it is possible that membrane-active peptides can become effective agents in the treatment of cancer.

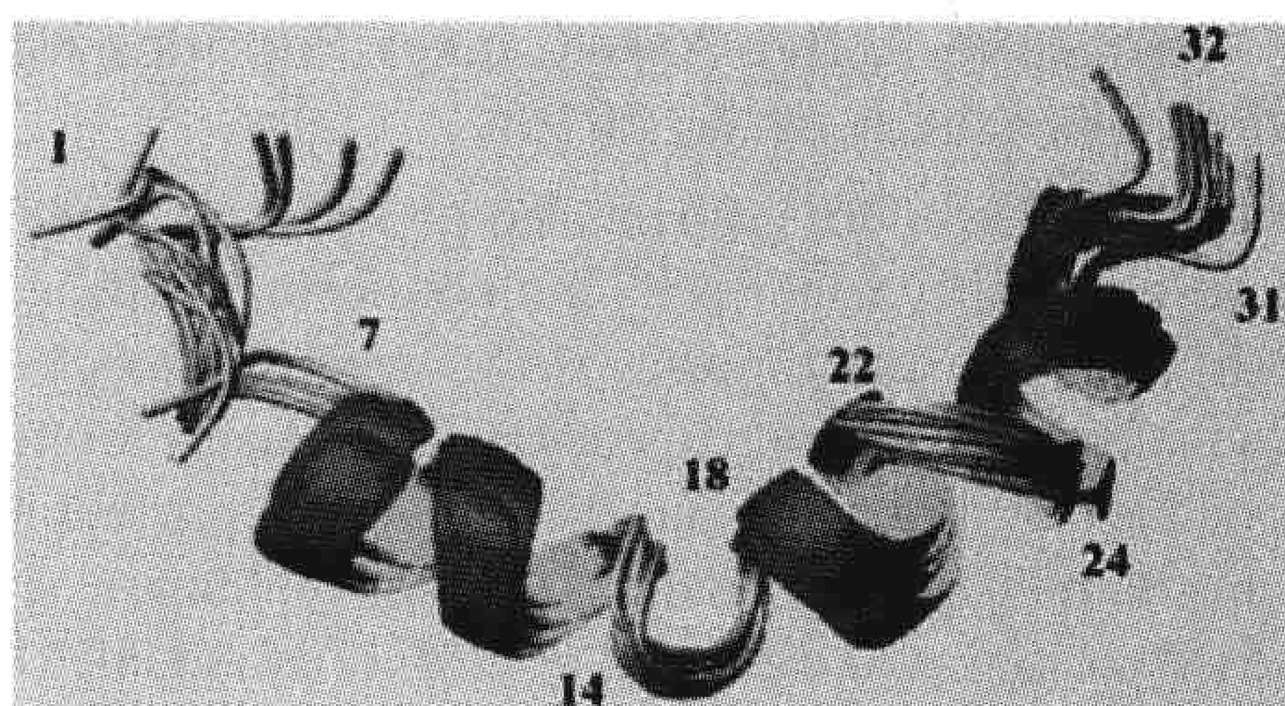


FIGURE 2.13 Ribbon structure for PNC-27, an anti-cancer, amphipathic, helix-loop-helix peptide structure that binds to membrane-bound HDM-2 that holds it in the membrane allowing it to form transmembrane pores. The two α-helical domains are shown as the spiral ribbons.

VA3. The Function of Transmembrane Proteins

Currently, there appear to be three classes of transmembrane proteins: intercellular adhesion molecules, receptor proteins and ion channel proteins. Studies on the first category of these proteins are incipient whereas the second and third categories of proteins have been better studied. Generally, receptor proteins contain three specific domains: an extracellular domain (ECD), an intramembrane domain and an intracytoplasmic domain which often contains a tyrosine kinase. This motif has been found to exist for several growth factor receptors and for the T-cell receptor. The x-ray crystal structures of several growth factor receptors (mostly their extracellular domains) have been determined (see, for example, Cho et al., 2003). Mutagenesis experiments and these x-ray structures have elucidated critical features concerning their functioning. A seemingly constant feature of growth factor receptor proteins is that, when the growth factor, which is often a polypeptide, binds to its transmembrane receptor, the receptor dimerizes. This dimerization induces the activation of the intracellular tyrosine kinase that results in activation of critical cellular processes in a so-called signal transduction pathway.

One of the critical growth factor receptors involved in mitogenic signaling is the epidermal growth factor receptor (EGFR). The x-ray crystal structure of the ECD of EGFR has been determined. In its unbound state, the ECD is folded such that it cannot dimerize spontaneously. When EGF binds to the ECD, however, the internal interactions in the native state are disrupted such that the dimerization domains are exposed and able to interact with one another (Ferguson et al., 2003). Thus binding of the growth factor EGF to EGFR ECD results in critical changes in the structure of EGFR allowing for dimerization and activation of this protein.

As another example, the sequence for the growth factor receptor called *neu* or *her-2*, which is a protein of molecular weight 185 kDa, or p185, is known (Padhy et al., 1982). This growth factor receptor is extremely important in the control of mitogenesis in epithelial cells (Padhy et al., 1982). Defects in this receptor protein can result in unregulated cell division and have been found to be highly associated with breast cancer (King et al., 1985; Slamon et al., 1987). It is known that activation of this protein requires that its growth factor bind simultaneously to two receptors (Ben-Levy et al., 1992), thus cross-linking them.

As a result of this cross-linking process, tyrosine kinases become activated, as noted above, resulting in phosphorylation of critical target proteins in a mitogenic signal transduction pathway (Bargmann and Weinberg, 1988).

It is known that substitution of single amino acids within the transmembrane domain of this protein activates the protein, presumably by facilitating dimerization in the membrane (Bargmann and Weinberg, 1988). The essential segment of the transmembrane domain contains the sequence (residues 650–683) -Glu-Gln-Arg-Ala-Ser-Pro-Val-Thr-Phe-Ile-Ile-Ala-Thr-Val-XXX-Gly-Val-Leu-Leu-Phe-Leu-Ile-Leu-Val-Val-Val-Val-Gly-Ile-Leu-Ile-Lys-Arg-Arg-. The XXX amino acid residue can be Val, His, Tyr, Lys or Gly for normal proteins and Gln or Glu for transforming proteins.

Calculations (Brandt-Rauf et al., 1989) on the structure of the transmembrane domain of the *neu* protein indicate that the entire transmembrane domain, most of which is hydrophobic, can exist in two states, as shown schematically in Fig. 2.14. The normal non-mutated transmembrane domain is a bent α-helix in which two helices are separated by a β-turn at residues 664–665. (These conformations are defined in Section II above.) In the "off" state for the normal protein, not bound to ligand, the α-helices are bent and are not favorably disposed to interact with one another. Amino acid substitutions at critical positions around where the bend occurs that obliterate the bend between the helices result in the formation of two regular α-helices that can easily associate with one another.

A complete analysis (Brandt-Rauf et al., 1990) of the Boltzmann distribution of the low-energy conformations of the p185 protein shows that 90% of the protein is in the bent helical state while 10% is in the all-helical state for all normal proteins. For the transforming proteins with Gln or Glu at position 664, this distribution reverses so that 90% of the protein is in the all-helical conformation while 10% is in the bent-helical conformation. These results predict therefore that if the normal protein is overexpressed by about a factor of 10, then sufficient all-helical forms would be present in the cell to cause cell transformation. This computed result has been confirmed in experiments where overexpression of the normal protein by factors of 1–4 causes no effect on the cell (Hudziac et al., 1987) while 10-fold overexpression of the normal protein has been found to cause cell transformation (DiFiore et al., 1987). They have been further directly confirmed in ligand-binding experiments using Scatchard plots (see Section IVC1) (Ben-Levy et al., 1992), in which it was found that, for the normal cellular protein with Val at position 664, 90% of the protein was in a low-affinity state for the cross-linking ligand and only about 10% of the protein was in a high-affinity state. However, with Glu at position 664, a transforming substitution, the reverse was found: over 90% of the receptors were in the high-affinity state, or readily cross-linked.

Thus a change in conformation from a bent to a straight helix may cause major changes in the functioning of a transmembrane protein, much like the proposed change in structure of melittin in the presence of an electric field. It is clear from the above examples that to understand cell function it is necessary to understand the conformational properties of proteins, the basis of which have been presented in this chapter.

VA4. Ion Channels (Caterall, 1995)

As discussed in the preceding section on melittin and as explained in detail in several later chapters of this textbook, cell membranes are polarized, resulting in a voltage change across them as a result of the fact that the inside of the cell is negative with respect to the outside. Furthermore, in the resting state of most cells, the extracellular sodium ion concentration is much higher than the intracellular sodium, while the reverse is true for potassium ions. During action potentials in electrically excitable cells, such as neurons and myocytes, the membrane becomes depolarized. During this period, there is a large influx of sodium ions, followed during repolarization by an almost equivalent efflux of potassium ions. These fluxes are then rapidly reversed, during which time the cell becomes refractory to further excitation.

The change in the permeability of the cell to sodium and potassium ions is caused by changes in voltage across the cell membrane. Thus the motion of these ions across the membrane is said to be *voltage dependent*. During action potentials, there is a voltage-dependent increase in the conductance of the membrane to sodium, followed by a rapid and then a slower inactivation of sodium conductance.

All of these changes in conductance and permeability-selectivity of the membrane are mediated by sodium, potassium and calcium channel proteins, all of which have been cloned, purified and expressed in different cell lines and in artificial lipid bilayers (Caterall, 1995). More recently, x-ray crystallographic structures of the potassium channel protein have been determined (see, for example, Long et al., 2005). All of these channel proteins have remarkably similar linear amino acid sequences with differences that cause each to bind selectively to different ions.

All of the channel proteins are composed of an α-subunit of molecular mass between 240–250 kDa that is heavily glycosylated. Sequencing of the gene for this protein reveals four domains that contain six repeating sequences (called S1–S6). These repeats are characterized by regular spacing in the sequence between hydrophobic amino acid residues and positively charged residues. As with leader sequences, melittin and the transmembrane domain of the *neu/her-2* protein, the six repeat sequences are highly hydrophobic. Therefore, they are thought to be transmembrane domains and have been

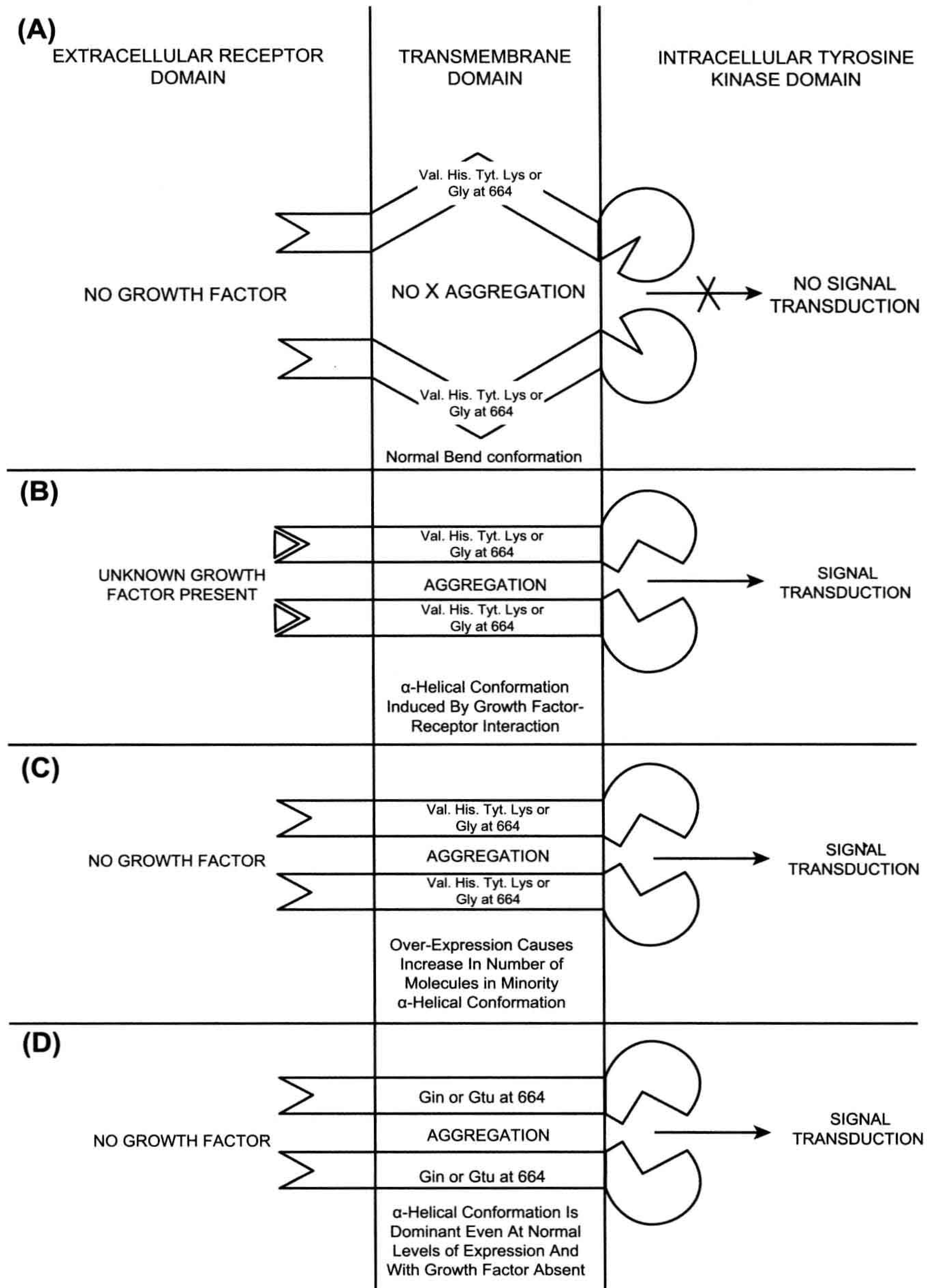


FIGURE 2.14 The effects of transmembrane domain structure of transmembrane proteins on their function. The *neu*-oncogene-encoded p185 protein is a transmembrane protein that has three distinct domains: an extracellular ligand-binding domain (left), a transmembrane domain (middle) and an intracellular signaling domain (right). To get signal transduction of a mitogenic signal to the nucleus, two p185 molecules must associate by the binding of their transmembrane domains to one another. This can be accomplished in a variety of ways as shown in this figure. (Modified from Brandt-Rauf et al., 1990.) (A) The normal protein has Val, His, Tyr, Lys, or Gly at position 664 in the amino acid sequence for the normal protein. The structure of the transmembrane domain is a bent α-helix, preventing the two domains from associating with one another. (B) When a growth factor binds to the extracellular domain of the protein, the bend is removed from the middle of the helix, allowing two straight helices to associate. This dimerization allows for activation of mitogenic signaling elements via the intracellular domain in the pathway ending in the nucleus. (C) From the calculations of the

postulated to be α-helical. The basic arrangement of the four domains is shown schematically in Fig. 2.15. In three dimensions, these four domains would be arranged in a cylindrical fashion and would surround a pore. The α subunit in the sodium channel protein is non-covalently linked to a heavily glycosylated β-1 subunit of molecular mass 36 kDa and by a disulfide link to a β-2 subunit.

Voltage Activation

The actual voltage at which activation of the sodium channel occurs has recently been shown to depend on positively-charged and hydrophobic amino acid residues in the S4 amphipathic helical segment of each transmembrane domain. As shown schematically in Fig. 2.16, seven critical positively-charged Arg and Lys residues are interspersed among many hydrophobic residues. Each of these positive charges must interact with a negative charge from an Asp or Glu residue from another subunit.

In site-specific mutagenesis experiments, each of the positively-charged residues has been replaced with neutral amino acid residues. Neutralization of positively-charged residues 1, 3, 5 and 7 results in shifting the activation transmembrane potential to more positive values so that the influx of sodium ions begins to occur at more depolarized states. Neutralization of charged residues 2 and 4 produces the opposite effect. Thus residues 1, 3, 5 and 7 are involved with activation of sodium influx while residues 2 and 4 are involved with pore closing and inactivation of sodium influx.

To explain how the S4 segment causes activation of sodium influx, it has been hypothesized that at a certain level of depolarization, the S4 helix rotates such that positive charges on the helix change negatively charged partners in an upward spiral from the inner to the outer membrane, resulting in effective transfer of a positive charge to the outside of the membrane. Since, as indicated in the above discussion, not all positive charges perform the same function, this hypothesis may be oversimplified.

Another explanation for charge transfer across the membrane is that, at a critical transmembrane voltage, the S4 helix unfolds into a fully extended conformation, allowing for the shifting of positive charges towards the outer membrane surface. One problem with this explanation is that the energy required to convert an all-helical protein into an all-extended form requires the disruption of a large number of hydrogen bonds, each about 1–2 kcal/mol in energy. Unless the fully extended form can make hydrogen bonds with other segments in a β-pleated sheet arrangement, the energy barriers for this conformational transition would be very high.

Nonetheless, it is clear that the change in the transmembrane potential causes a change in the conformation of the S4 helix, resulting in the opening or closing of the sodium channel. This effect is strongly analogous to the proposed effect of the transmembrane potential on the conformation and function of melittin discussed above. Pore formation is clearly influenced by transmembrane voltage and results from a conformational change in the transmembrane protein.

Permeability-Selectivity

Neural toxins, such as from snake venom, have long been known to bind with high affinity for and selectivity to specific ion channels. The toxin tetrodotoxin is known to bind to the sodium channel pore at its outermost surface. Localization of the tetrodotoxin (and sodium channel pore) binding site has recently been accomplished. Between the S5 and S6 helical segments are two short segments, named short segments 1 and 2 (SS1 and SS2), shown in Fig. 2.15. In SS2, neutralization of Glu 387 by site-specific mutagenesis results in a 10 000-fold decrease in the binding of tetrodotoxin to the mutated sodium channel. In similar experiments, it has further been found that additional residues are vital to perm-selectivity of the sodium ion channel. These include negatively charged residues in domains 1 and 2, a positively-charged amino acid residue in domain 3, and a neutral amino acid in domain 4.

Position 385 is also a vital amino acid residue in SS2. In brain and skeletal muscle sodium channels, this residue is Phe or Tyr; in cardiac muscle, it contains the non-conservative substitution, Cys. The cardiac muscle sodium channel has a several hundred-fold lower affinity for tetrodotoxin than does brain or skeletal muscle channel protein. If the Cys residue of cardiac muscle channel protein is changed to Tyr or Phe, the high affinity for tetrodotoxin is restored. Thus Tyr/Phe 385 appears to be vital in tetrodotoxin binding and ion selectivity.

Sodium and calcium channel structure are similar to one another. However, calcium ions bind with only about one-tenth the affinity to the sodium channel protein as that for sodium ions. However, mutation of Lys 1422 and Ala 1714 to Glu residues completely reverses the order of affinity of these two ions to the mutated sodium channel protein. These two residues are therefore implicated as being present at the mouth of the pore of the sodium channel.

distribution of conformations for the normal transmembrane domain (Brandt-Rauf et al., 1990) of p185, 90% of the molecules exist in the bent helix state, while 10% are straight helices. Overexpression of the normal protein by a factor of 10 was therefore predicted to produce sufficient straight helices to cause mitogenic cell signaling, leading to cell transformation. (D) Finally, substitution of Glu or Gln at position 664 reverses the distribution of bent and straight helices directly so that 90% of the molecules are straight helices while only 10% are bent helices. This results in significant levels of dimerization, resulting in permanent mitogenic cell signaling and oncogenic transformation of the cells.

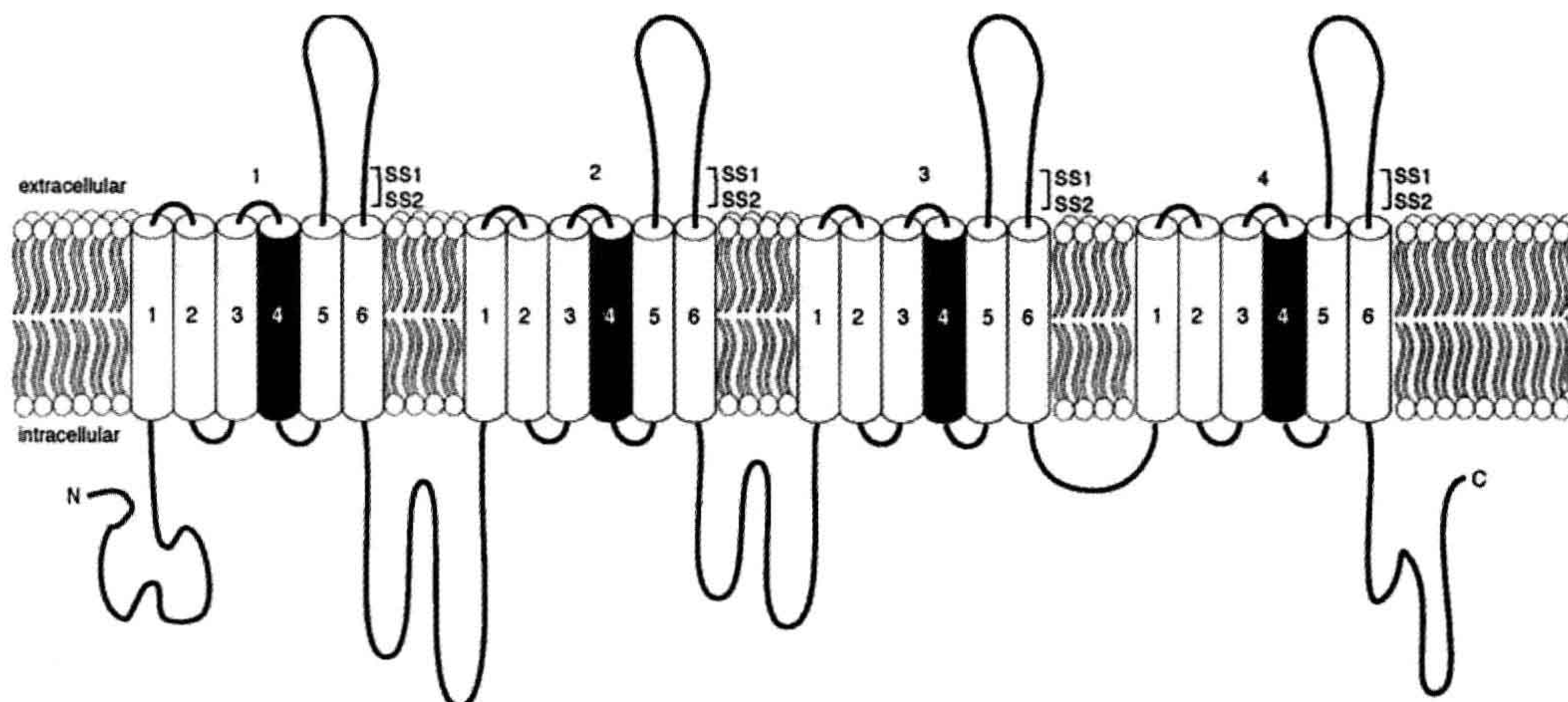


FIGURE 2.15 Model for the arrangement of the domains in the α-subunit of the sodium ion channel protein. The four domains are labeled 1–4. Each domain is shown to contain six transmembrane helical segments labeled 1–6. Subdomain 4 is highlighted in each domain because it contains the critical residues for voltage-dependent gating. The short segments 1 and 2 that are critical for ion selectivity are labeled SS1 and SS2, respectively. This region contains the critical residues Glu 387 and Phe/Tyr or Cys 385. *(This model is modified from Hall, 1992, p. 109.)*

Inactivation

Normally, after the voltage-gated increase in sodium ion permeability, there is a rapid inactivation of the sodium conductance. This inactivation process can be blocked by treatment of the intracellular domain of the sodium channel protein with proteases and by a monoclonal antibody directed against a segment of the protein connecting domains 3 and 4. Further studies involving site-specific mutagenesis have identified three critical amino acid residues as being vital to the inactivation process: residues 1488–1490, the sequence of which is Ile-Phe-Met, all hydrophobic amino acid residues. Mutation of Phe 1489 to Gln completely blocks inactivation of sodium channel conductance.

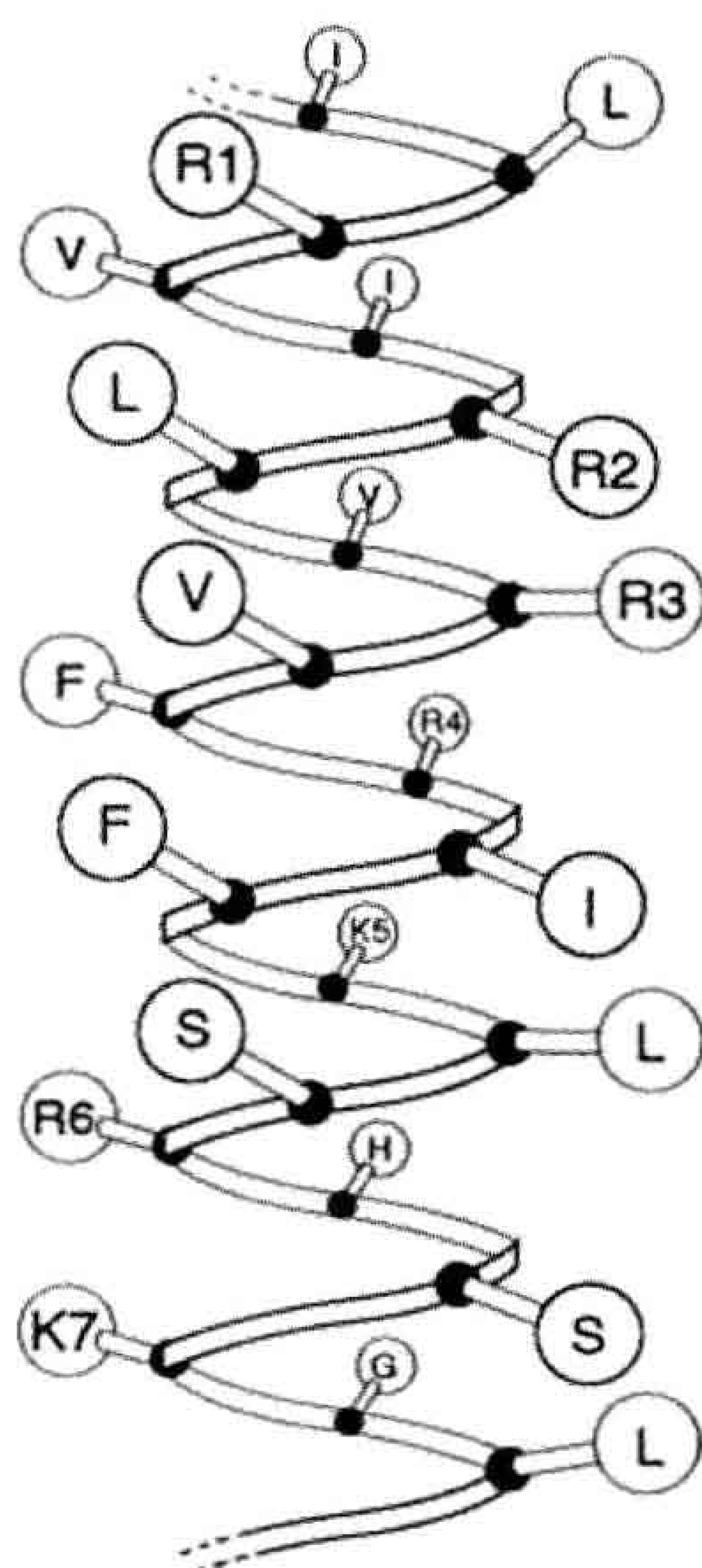


FIGURE 2.16 Helical model for the critical segment of the S4 subdomain of the sodium channel. The critical positively charged residues are labeled in numerical order. *(Modified from Caterall, 1995, Fig. 3, p. 515.)*

To explain the inactivation process, the three-residue segment has been proposed to constitute a "hinged lid" which moves to form a block in the sodium conductance channel after the conformational changes occur that increase sodium ion conductance. Phe 1489 would bind to another as yet unidentified pocket in the protein, blocking further movement of sodium ions.

Similar experiments on the potassium channel protein have identified a completely different segment of this protein involved in the inactivation of potassium conductance. This constitutes the amino terminal domain consisting of hydrophobic (especially Leu 7) and hydrophilic amino acid residues.

The model for inactivation for the potassium channel protein is the "ball and chain" model in which the amino terminal arm of the protein swings into the pore, blocking further potassium conductance. Convincing evidence for this model has been provided by experiments in which native amino terminal peptides hybridized with mutant potassium channel proteins, which do not inactivate potassium ion conductance, completely restore their abilities to inactivate

potassium ion conductance. These results compared with those for the sodium channel suggest that inactivation of sodium channels occurs on the intracellular surface whereas that for the potassium channels occurs on the extracellular surface.

Our knowledge of the functioning of ion channels is incipient but has been greatly advanced by the cloning of the sodium, potassium and calcium channel proteins and the site-specific mutagenesis work. The x-ray structures of the potassium channel are also providing more insights. These studies all suggest that the functioning of all of these proteins is based on the principles discussed earlier in this chapter. Selective binding of ions is caused by specific ionic (electrostatic) interactions; changes in conductance of the channel proteins is caused by changes in the three-dimensional structure of the proteins induced by changes in the electric field across the cell membrane as proposed for the simpler melittin protein. The basic structure of the channel protein consists of a series of amphipathic α-helices containing large numbers of hydrophobic amino acid residues. As found for the transmembrane domain of the *neu/her*-2 receptor protein, the interaction of the helices with one another is responsible for the functioning of the channel protein.

VA5. Effects of Amino Acid Substitutions on the ras-p21 Protein

One of the most striking discoveries over the past three decades has been the finding that a single base change at codon 12 in the human *ras* gene, which encodes a protein of Mr 21 kDa called the p21 protein (with 189 amino acids in its sequence), results in the malignant transformation of quiescent (NIH 3T3) cells in culture. The encoded p21 protein contains a Val in place of the normally occurring Gly at position 12 in its amino acid sequence. Transfection of the oncogene, but not its normal counterpart proto-oncogene, into NIH 3T3 cells in culture results in their malignant transformation (Barbacid, 1987).

Microinjection of cloned, purified oncogene-encoded (Val 12-containing) p21 protein, but not its normal counterpart protein, into NIH 3T3 cells also causes these cells to undergo cell transformation. Thus the transforming agent is the *ras*-gene-encoded p21 protein itself. Similarly, oncogenic but not normal p21 induces maturation (meiotic division) of frog *(Xenopus laevis)* oocytes. The biochemical changes induced by oncogenic p21 in all of these cells are very similar, suggesting that *ras*-p21 induces stereotypical events in each cell line. Incredibly, oncogenic *ras* genes have been identified overall in about one out of three common human cancers, in over 90% of human pancreatic and 70% of human colon cancers (Almoguerra et al., 1988). Oncogenic p21 protein has also been found to occur at elevated concentrations in the sera of patients with specific types of malignant neoplasms (Pincus et al., 2006).

There are other critical positions in the polypeptide chain of p21, such as at Gly 13, Ala 59 and Gln 61, where single amino acid substitutions result in a transforming protein. By far the most common site for oncogenic substitution is Gly 12. Since 18 out of 20 amino acids that occur at position 12 cause the protein to become oncogenic, it seems reasonable to conclude that these substitutions induce changes in the three-dimensional structure of the protein, resulting in its being permanently activated.

Activation of *ras*-p21 (Pincus et al., 2000)

ras-p21 is a *G protein* that becomes activated when GDP, bound to the protein in its inactive state, is exchanged for GTP. This process of activation is set in motion when a specific growth factor, such as epidermal growth factor (EGF), itself a polypeptide, binds to its receptor. As discussed under the *neu/her*-2 growth factor receptor section (Section VA3), the transmembrane receptor contains an extracellular growth factor binding domain, a transmembrane domain and an intracytoplasmic domain which, for *neu* and EGF receptors, contains a tyrosine kinase domain. This kinase becomes activated when the growth factor receptor dimerizes as a consequence of the binding of the growth factor to it.

As a result, the intracytoplasmic domain binds to an "adapter" molecule, called *grb*-2, which simultaneously binds to a protein called SOS that, in turn, binds to p21, promoting the exchange of GDP for GTP. Modulating the effect of GTP on activation of p21 is the GTPase activating protein (GAP), which binds to activated p21 and induces the hydrolysis of GTP to GDP, thereby resulting in the inactivation of *ras*-p21.

All of these events occur in or near the inner cell membrane. *ras*-p21 is attached to the inner cell membrane by a covalent link at Cys 186 (Willumsen et al., 1984) in which its sulfur atom is in thioether link to the farnesyl moiety, a lipophilic hydrocarbon that intercalates in the lipid medium of the cell membrane. Thus, like melittin, *ras*-p21 is active as a membrane-associated protein.

Thioether synthesis is catalyzed by the enzyme farnesyl transferase. In site-specific mutagenesis experiments, if Cys 186 is replaced by a Ser residue, *ras*-p21 not only is inactive, even if it contains oncogenic amino acid substitutions, but it competes with its cell-membrane associated counterpart protein so as to *inhibit* mitogenesis. The double inactive mutant of p21 with the Val-for-Gly 12 and Ser-for-Cys 186 substitutions, is therefore called a dominant negative mutant of *ras*-p21. A number of farnesyl transferase inhibitors have been synthesized that block insertion of p21 into the membrane and allow the cytosolic p21 to compete with its membrane-bound counterpart protein, resulting in the slowing down or halting of mitogenesis in *ras*-induced cancers (James et al., 1993; Downward, 2003).

Signal transduction induced by G proteins is a generalized phenomenon that explains the action of many hormones and external stimuli. For example, polypeptide hormones, such as ACTH, growth hormone, calcitonin, cholecystokinin and insulin, all activate G proteins that stimulate phosphorylation cascades. Light induces electrical signals on the retina; conversion of light to electrical signals traveling to the brain is performed by the G protein transducin in the retina. Much pharmacotherapy is currently aimed at interfering with the signal transduction events that occur after the hormone has bound to its receptor.

Function of *ras*-p21

A natural question that arises from the foregoing discussion is that, if *ras*-p21 is membrane bound, what is the mechanism by which it induces mitosis, when the latter process occurs in the nucleus? The answer to this question appears to be that activated *ras*-p21 induces a number of phosphorylation cascades in the cytosol in which successive proteins become activated until one or more of these proteins directly activates nuclear proteins that are intimately involved in DNA synthesis. These successive activation cascades are referred to as signal transduction pathways.

Activated *ras*-p21 binds directly to a protein called *raf*-p74 (Mr, 74 kDa). When activated by *ras* or other intracellular proteins, *raf* binds to and phosphorylates an extracellular *mitogen-stimulated kinase* called MEK which, in turn, binds to and phosphorylates a vital protein, MAP kinase (mitogen-activated protein kinase) or ERK. This protein is critical in catalyzing cytoskeletal rearrangements in mitosis and in activating the highly important nuclear transcriptional activating factor, *fos*. To be active, *fos* forms a heterodimeric complex with another protein, *jun*. Together, these two activated proteins bind to promoter regions of the genome and induce the transcription of mRNA for a number of mitogenesis-promoting proteins such as the cyclins. The factor *jun* is activated by another pathway in which it is activated by the critical kinase, *jun* kinase (JNK). Further, oncogenic (Val 12-containing) *ras*-p21 interacts preferentially with both JNK and *jun* proteins, providing a "short circuit" pathway for activating direct nuclear transcription.

Remarkably, the above-described cascades occur in a wide variety of different cells with differing effects depending on the cell type. Thus, for example, in frog oocytes, oncogenic *ras*-p21 induces meiosis and cell *maturation*, not malignant transformation. In cardiac muscle that has suffered injury, infarction or hypertrophy, the above cascades also become activated.

Relationship of Structure to Function of *ras*-p21

The fact that arbitrary amino acid substitutions at critical positions in the polypeptide chain cause the *ras*-p21 protein to become oncogenic suggests that critical changes in its three-dimensional structure occur in response to these substitutions. Another point of view is that these substitutions affect the ability of GAP to induce an increase in the GTPase activity of p21. There is an excellent correlation of the abilities of some oncogenic p21 proteins to induce cell transformation with their diminished levels of GAP-induced GTPase activities and with their binding affinities to GAP. On the other hand, there are striking exceptions to this correlation. For example, a Glu-for-Asp 38—substituted p21 protein binds tightly to GAP and has low GTPase activity but does *not* transform cells. Some substituted proteins efficiently hydrolyze GTP to GDP but transform cells. Also there are triply substituted forms of p21 that do not bind at all to any nucleotide but are permanently activated and strongly induce cell transformation. Thus it appears that for many substituted oncogenic p21 proteins, permanent activation is related to structural changes induced by the oncogenic amino acid substitutions themselves.

The x-ray structures of wild-type and oncogenic forms of p21 bound to GDP and GTP and of wild-type p21 bound to the *ras*-binding domain of *raf*, to SOS and to GAP proteins have all been determined. Comparison of oncogenic and normal unbound p21 structures reveals some conformational changes in an effector loop from residues Tyr 32-Asp 47, which is involved in the binding of p21 to GAP, *raf* and SOS. Because the protein occurs in a crystal lattice, wherein interactions between protein molecules limit conformational flexibility, the x-ray structures may not identify other regions that undergo conformational changes.

Use of Conformational Energy Calculations to Identify Effector Domains of p21

To identify other regions of the protein that may change conformation when the oncogenic form is compared with that of the wild-type protein, calculations of the low-energy conformations of these proteins have been carried out. These calculations are based on the principle, discussed in Section IIE1, that the observed structure of a protein is the one of lowest energy; there may be a group of lowest energy structures for a protein that have the same overall chain fold but which differ from one another in the conformation of local regions.

In these calculations, using sampling methods such as molecular dynamics (discussed in Section IIE1), the x-ray crystal structure is subjected to energy minimization and then allowed to move so that all of the low-energy structures that lie close to this structure, but which may differ from it regionally, are sampled. The average structure is the average of these low-energy structures. If oncogenic amino acid substitutions induce permanent, regional conformational changes in the three-dimensional structure

of the protein, these will be reflected in differences in the average structures for the oncogenic proteins compared with that of the normal (wild-type) protein. We might expect that synthetic segments of p21 corresponding to these regions may inhibit the functioning of the oncogenic protein.

Results of these calculations on the wild-type protein bound to GDP and GTP and of the Val 12- and Leu 61-substituted proteins bound to GTP (Monaco et al., 1995; Pincus et al., 2007) show that the overall fold of the proteins is virtually identical, but local regions differ in conformation between oncogenic and the inactive (GDP-bound) protein. There are six such regions: residues 4–20, 35–47, 55–71, 81–93, 96–110 and 115–126. Peptides corresponding to each of these regions have been synthesized and tested for their abilities to alter the ability of *ras*-p21 to induce mitogenesis.

Test Cell System for Identification of Functional Domains of *ras*-p21

As it happens, a very convenient cell system for measuring the abilities of agents to inhibit *ras*-p21 is oocytes. Oocyte maturation induced by a particular agent, such as oncogenic *ras*-p21, is easy to evaluate because of the large structural changes, like disappearance of the brown-colored animal pole, that each matured oocyte undergoes. Maturation of all oocytes in a given experiment occurs in a relatively short time, within 1–2 days after injection or treatment of the oocytes with a maturation-promoting agent. Finally, oocytes contain an abundance of insulin receptors; insulin is a growth factor that induces oocyte maturation by activating normal cellular *ras*-p21.

Proof that insulin acts through *ras*-p21 was provided by the finding that if oocytes are first injected with an inactivating antibody against *ras*-p21 and then incubated in insulin, they do not undergo maturation. Prior injection of other, unrelated antibodies has no effect; insulin induces maturation in these oocytes. Thus oocytes are ideal for studying the specificity of anti-*ras*-p21 agents to study whether they have a preferential effect on the oncogenic form versus the normal form of p21 by either co-injecting the agent with oncogenic p21 or by injecting the agent into oocytes that are then incubated with insulin.

Effects of p21 Peptides from Effector Domains Identified by Conformational Analysis (Pincus et al., 2000, 2007)

Microinjection into oocytes of each of the synthesized peptides from the *ras*-p21 domains identified from the conformational energy calculations mentioned above, either together with oncogenic *ras*-p21 or into oocytes subsequently incubated with insulin, has been performed. Three peptides, 35–47 (PNC-7) from the previously identified effector domain, 96–110 (PNC-2), and 115–126 (PNC-1), all strongly block the ability of oncogenic p21 to induce oocyte maturation. Significantly, these peptides, especially peptides corresponding to residues 96–110 and 115–126, only minimally affected the ability of insulin, hence activated normal p21, to induce maturation. This finding suggests that oncogenic and normal p21 induce mitogenesis by differing signal transduction pathways. As it happens, the latter two peptides have been found to interfere in the interaction of oncogenic p21 with JNK and *jun* proteins; their abilities to inhibit oncogenic p21-induced oocyte maturation strongly correlate with their abilities to inhibit this interaction.

The above results suggest that activated normal and oncogenic *ras*-p21 stimulate different pathways; the oncogenic form can preferentially activate JNK and *jun* directly, leading to unregulated nuclear transcriptional processes. By breaking this "short circuit" with effector peptides, selective inhibition of oncogenic *ras*-p21 can be achieved. This result has important implications for the design of new selective chemotherapeutic agents.

The Two *ras* Peptides, PNC-2 and PNC-7, Block Cancer Cell but not Normal Cell Growth (Pincus et al., 2007)

Two *ras*-p21 peptides, PNC-2 and PNC-7, attached to the transmembrane-penetrating sequence discussed above, were used to treat ras-transformed cancer cells. It was found that a ras-transformed rodent pancreatic cancer cell line called TUC-3, when incubated with either peptide but not a control peptide, are induced to revert to the untransformed phenotype. These cells, unlike their untreated or control peptide-treated cancer cells, do not grow when transplanted into nude mice. Neither PNC-2 nor PNC-7 has any effect on the growth of normal cells such as the untransformed counterpart cells to TUC-3, called BMRPA1. Both peptides likewise exert the same effect on ras-transformed HT1080 human fibrosarcoma cells and have cytotoxic effects on other cancer cell lines. It seems, therefore, that these *ras*-p21 peptides have potential for treating cancers.

Thus, use of the methods of conformational analysis based on the principles of protein structure described in this chapter has resulted in our being able to identify critical residues of an oncogenic protein that are vital to their function, to design peptides that selectively inhibit oncogenic *ras*-p21, and to detect differences in signal transduction pathways induced by oncogenic and normal p21 protein.

BIBLIOGRAPHY

Almoguerra, C., Shibata, D., Forrester, K., Martin, J., Arnheim, M., & Perucho, M. (1988). Most human carcinomas of the endocrine pancreas contain mutant c-K-*ras* genes. *Cell, 53*, 813–815.

Anfinsen, C. B., Haber, E., Sela, M., & White, F. H., Jr. (1961). The kinetics of formation of native ribonuclease during oxidation of the reduced polypeptide chain. *Proc Natl Acad Sci USA, 47*, 1309–1314.

Barbacid, M. (1987). ras genes. *Ann Rev Biochem, 56*, 779–827.

Bargmann, C. I., & Weinberg, R. A. (1988). Oncogenic activation of the neu-encoded receptor protein by point mutation and deletion. *EMBO J, 7*, 2043–2052.

Ben-Levy, R., Peles, E., Goldman-Michael, R., & Yarden, Y. (1992). An oncogenic point mutation confers high affinity ligand binding to the neu receptor. *J Biol Chem, 267*, 17304–17313.

Blobel, G., Walter, P., Chang, C. N., Goldman, B. M., Erickson, A. H., & Lingappa, R. (1979). Translocation of proteins across membranes: the signal hypothesis and beyond. *Symp Soc Exp Biol, 33*, 9–37.

Bogaart, G. V. D., Guzman, J. V., Mica, J. T., & Poolman, B. (2008). On the mechanism of pore formation by melittin. *J Biol Chem, 283*, 33854–33857.

Brandt-Rauf, P. W., Pincus, M. R., & Chen, J. M. (1989). Conformational changes induced by the transforming amino acid substitution in the transmembrane domain of the neu-oncogene-encoded p185 protein. *J Protein Chem, 8*, 749–755.

Brandt-Rauf, P. W., Rackovsky, S., & Pincus, M. R. (1990). Correlation of the transmembrane domain of the neu-oncogene-encoded p185 protein with its function. *Proc Natl Acad Sci USA, 87*, 8660–8664.

Bull, H. B. (1943). *Physical Biochemistry*. London: John Wiley and Sons.

Caterall, W. A. (1995). Structure and function of voltage-gated ion channels. *Annu Rev Biochem, 64*, 493–531.

Cho, H. S., Mason, K., Ramyar, K. X., et al. (2003). Structure of the extracellular region of HER2 alone and in complex with the Herceptin Fab. *Nature, 421*, 756–760.

Di Fiore, P. P., Pierce, J. H., Kraus, M. H., Segatto, O. S., King, R., & Aaronson, S. A. (1987). erbB-2 is a potent oncogene when overexpressed in NIH/3T3 cells. *Science, 237*, 178–182.

Downward, J. (2003). Targeting the Ras signalling pathway in cancer therapy. *Nat Rev Cancer, 3*, 11–22.

Dygert, M., Go, N., & Scheraga, H. A. (1975). Use of a symmetry condition to compute the conformation of gramicidin S. *Macromolecules, 8*, 750–761.

Emr, S. D., & Silhavy, T. J. (1982). Molecular components of the signal sequence that function in the initiation of protein export. *J Cell Biol, 95*, 689–696.

Engelman, A. M., & Steitz, T. A. (1981). The spontaneous insertion of proteins into and across membranes: the helical hairpin hypothesis. *Cell, 23*, 411–422.

Ferguson, K. M., Berger, M. B., Mendrola, J. M., Cho, H., Leahy, D. J., & Lemmon, M. A. (2003). EGF activates its receptor by removing interactions that autoinhibit ectodomain dimerization. *Mol Cell, 11*, 507–517.

Gibson, K., Chin, S., Pincus, M. R., Clementi, E., & Scheraga, H. A. (1986). Parallelism in conformational energy calculations on proteins: partial structure of interferon. In M. Dupuis (Ed.), *Montreal Symposium on Supercomputer Simulation in Chemistry. Lecture Notes in Chemistry, Vol. 44* (pp. 198–213).

Hall, Z. W. (1992). Ion channels. In Z. W. Hall (Ed.), *An Introduction to Molecular Neurobiology* (pp. 81–118). Sunderland: Sinauer Associates, Inc.

Hudziak, R. M., Schlessinger, J., & Ullrich, A. (1987). Increased expression of the putative growth factor reception $p185^{HER2}$ causes transformation and tumorigenesis of NIH/3T3 cells. *Proc Natl Acad Sci USA, 84*, 7159–7163.

James, G. L., Goldstein, G. L., Brown, M. S., et al. (1993). Benzodiazepine peptidomimetics: potent inhibitors of ras farnesylation in animal cells. *Science, 260*, 1937–1942.

King, C. F., Kraus, M. H., & Aaronson, S. A. (1985). Amplification of a novel v-erbB-related gene in a human mammary carcinoma. *Science, 229*, 974–976.

Karplus, M., & McCammon. (1986). The dynamics of proteins. *Sci Am, 254*, 42–52.

Kempf, C., Klausner, R. D., Weinstein, J. N., van Renswoude, J., Pincus, M. R., & Blumenthal, R. (1982). Voltage-dependent trans-bilayer orientation of melittin. *J Biol Chem, 257*, 2469–2475.

Kussie, P. H., Gorina, S., Marechal, V., et al. (1996). Structure of the MDM2 oncoprotein bound to the p53 tumor suppressor trans-activation domain. *Science, 274*, 921–922.

Long, S. B., Campbell, E. B., & MacKinnon, R. (2005). Crystal structure of a mammalian voltage-dependent shaker family K^+ channel. *Science, 309*, 897–903.

Miller, M. H., & Scheraga, H. A. (1976). Calculation of the structure of collagen models. Role of interchain interactions in determining the triple helical coiled coil conformation. *J Polymer Sci, 54*, 171–200.

Monaco, R., Chen, J. M., Friedman, F. K., Brandt-Rauf, P. W., & Pincus, M. R. (1995). Structural effects of the binding of GTP to the wild-type and oncogenic forms of the ras-gene-encoded p21 proteins. *J Protein Chem, 14*, 721–730.

Padhy, L. C., Shih, C., Cowing, D., Finkelstein, R., & Weinberg, R. A. (1982). Identification of a phosphoprotein specifically induced by the transforming DNA of rat neuroblastomas. *Cell, 28*, 865–871.

Pincus, M. R. (1988). The chain build-up procedure in computing the structures of biologically active polypeptides and proteins. *Int J Quant Chem: Quant Biol Symp, 15*, 209–220.

Pincus, M. R., & Klausner, R. D. (1982). Prediction of the three-dimensional structure of the leader sequence of murine pre-kappa light chain, a hexadecapeptide. *Proc Natl Acad Sci, USA, 79*, 3413–3417.

Pincus, M. R., & Scheraga, H. A. (1985). Conformational analysis of biologically active polypeptides, with application to oncogenesis. *Accnt Chem Res, 18*, 372–379.

Pincus, M. R., Klausner, R. D., & Scheraga, H. A. (1982). Calculation of the three-dimensional structure of the membrane-bound portion of melittin from its amino acid sequence. *Proc Natl Acad Sci, USA, 79*, 5107–5110.

Pincus, M. R., Brandt-Rauf, P. W., Michl, J., & Friedman, F. K. (2000). ras-p21-induced cell transformation: unique signal transduction pathways and implications for the design of new chemotherapeutic agents. *Cancer Invest, 18*, 39–50.

Pincus, M. R., Brandt-Rauf, P. W., & Bluth, M. (2006). Oncoproteins and early tumor detection. In R. McPherson, & M. R. Pincus (Eds.), *Henry's Clinical Diagnosis and Management by Laboratory Methods* (21st ed.). (pp. 1367–1380) Philadelphia: Elsevier.

Pincus, M. R., Michl, J., Bowne, W., & Zenilman, M. (2007). Anti-cancer peptides from the ras-p21 and p53 proteins. In R. M. Mohan (Ed.), *Research Advances in Cancer* (pp. 65–90). Kerala, India: Global Research Network Publishers.

Rosale, R., Pincus, M. R., Brandt-Rauf, P. W., Fine, R. L., Michl, J., & Wang, H. (2004). NMR solution structure of a peptide from the mdm-2 binding domain of the p53 protein that is selectively cytotoxic to cancer cells. *Biochemistry, 43*, 1754–1861.

Rosenblatt, M., Beaudette, N. V., & Fasman, G. D. (1980). Conformational studies of the synthetic precursor-specific region of pre-proparathyroid hormone. *Proc Natl Acad Sci USA, 77*, 3983–3987.

Russell, S. T., & Warshel, A. (1985). Calculations of electrostatic energies in proteins. The energetics of ionized groups in bovine pancreatic trypsin inhibitor. *J Mol Biol, 185*, 389–404.

Sarafraz-Yazdi, E., Bowne, W. B., Adler, V., et al. (2010). Anticancer peptide PNC-27 adopts an HDM-2-binding conformation and kills cancer cells by binding to HDM-2 in their membranes. *Proc Natl Acad Sci USA, 107*, 1918–1923.

Scheraga, H. A. (1984). Protein structure and function, from a colloidal to a molecular point of view. *Carlsberg Res Commun, 49*, 1–55.

Scheraga, H. A. (1989). Calculations of stable conformations of polypeptides, proteins, and protein complexes. *Chim Scripta, 29A*, 3–13.

Scheraga, H. A., Liwo, A., Oldziej, S., et al. (2004). The protein folding problem:global optimization of force fields. *Front Biosci, 9*, 3296–3323.

Slamon, D. J., Clark, G. M., Wong, S. G., Levin, W. J., Ullrich, A., & McGuire, W. L. (1987). Human breast cancer: correlation of relapse and survival with amplification of the her-2/neu oncogene. *Science, 235*, 177–182.

Tamba, Y., Arivama, H., Levadny, V., & Yamazaki, M. (2010). Kinetic pathway of antimicrobial peptide magainin 2-induced pore formation in lipid membranes. *J Phys Chem B, 114*, 2018–2026.

Terwilliger, T. C., Weissman, L., & Eisenberg, D. (1982). The structure of melittin in the form I crystals and its implication for melittin's lytic and surface activities. *Biophys J, 37*, 353–361.

van Holde, K. E. (1985). *Physical Biochemistry.* Englewood Cliffs: Prentice Hall, Inc.

Vasquez, M., Nemethy, G., & Scheraga, H. A. (1994). Conformational energy calculations on polypeptides and proteins. *Chem Rev, 94*, 2183–2239.

Vogel, H., & Jahnig, F. (1986). *The structure of melittin in membranes Biophys J, 50*, 573–582.

Willumsen, B. M., Christensen, A., Humbert, N. L., Papageorge, A. G., & Lowy, D. R. (1984). The p21 ras C-terminus is required for transformation and membrane association. *Nature, 310*, 583–586.

Wuthrich, K. (1986). *NMR of Proteins and Nucleic Acids.* New York: John Wiley and Sons.

Yang, L., Weiss, T. M., Lehrer, R. I., & Huang, H. W. (2000). Crystallization of antimicrobial pores in membranes: magainin and protegrin. *Biophys J, 79*, 2002–2009.

Chapter 3

Cell Membranes

Jeffrey C. Freedman

Chapter Outline

I. SUMMARY

This chapter reviews some basic biochemical properties of membrane lipids and describes the experimental evidence for models of the structure of cell membranes, starting with the Gorter and Grendel bimolecular phospholipid leaflet and proceeding through the Davson–Danielli paucimolecular model and the Singer–Nicholson fluid mosaic model. Extensions of the fluid mosaic model include heterogeneous lipid phases, lateral domains of cholesterol-poor and cholesterol-rich pools, annular lipids whose properties differ from bulk lipids, phospholipid asymmetry and membrane microdomains known as rafts. The much-studied red blood cell membrane is considered throughout this chapter as a paradigm applicable to other plasma membranes.

II. THE BIMOLECULAR LIPID MEMBRANE

The term *plasma membrane* derives from the German *Plasmamembran,* a word coined by Karl Wilhelm Nägeli (1817–1891) to describe the firm film that forms when the proteinaceous sap of an injured cell comes into contact with water. The physiologist L.V. Heilbrunn referred to this and similar phenomena as the "surface precipitation reaction", as described in his book *The Dynamics of Living Protoplasm* (1956). "Protoplasm" was the old term for the substance inside cells and was in general use before the techniques of electron microscopy and differential centrifugation helped to elucidate the detailed structures and specific functions of discrete cell organelles. The involvement of what we know today as the cell membrane and the biochemistry of the formation of a surface film in response to cell injury have not subsequently been explained. The original usage of the term "plasma membrane," therefore, has an obscure relationship to its current meaning.

Much knowledge concerning membrane structure and function derives from studies of red blood cells, as depicted in the scanning electron photomicrograph in Fig. 3.1. Red cells are highly differentiated and are specialized for the transport of oxygen and carbon dioxide in the blood. They consist essentially of a plasma membrane surrounding a concentrated solution of hemoglobin and lack a nucleus, mitochondria, endoplasmic reticulum, ribosomes, Golgi apparatus and lysosomes. Over 100 years ago, extensive osmotic and permeability studies of red cells by Hamburger,

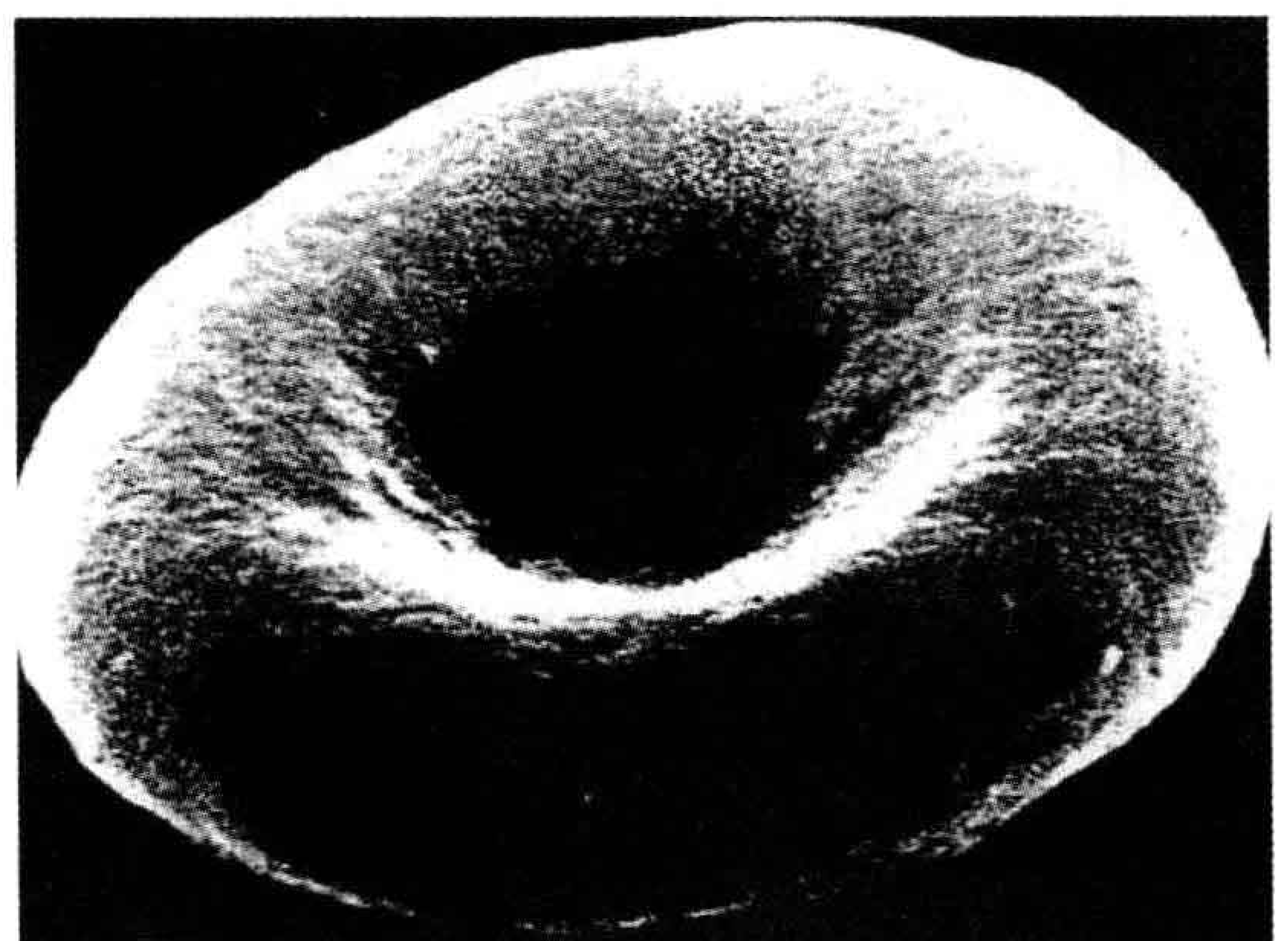


FIGURE 3.1 Scanning electron photomicrograph of human red blood cells. The biconcave discoid cells are 8 μm in diameter and 2.4 μm thick at the rim and 1.0 μm thick at the center. *(From Bessis, M. 1974. Corpuscles. Atlas of Red Blood Cell Shapes. Springer-Verlag, New York, Fig. 1, with permission.)*

Cell Physiology Sourcebook. DOI: 10.1016/B978-0-12-387738-3.00003-2

of plant cells by de Vries and of many living cells by Overton provided evidence that a lipoid membrane surrounds cells. Fat-soluble substances that are lipophilic and easily dissolve in lipids enter cells easily, whereas water-soluble substances enter cells more slowly, if at all. Overton recognized a correlation between the oil—water partition coefficient and membrane permeability; nevertheless, in none of these early studies was a membrane postulated as a distinct structural entity to explain the findings (see Jacobs, 1962).

In 1925, Gorter and Grendel used acetone to extract lipids from a known quantity of red blood cells and, after evaporating the solvent, measured the area that the extracted lipids occupied as a monomolecular film at an air—water interface using a Langmuir trough. From the area of the film of extracted lipids and from the surface area of the red cells as estimated by light microscopy, they concluded that: "It is clear that all our results fit in well with the supposition that the chromocytes are covered by a layer of fatty substances that is two molecules thick" (Gorter and Grendel, 1925, p. 443). Some 40 years later, however, it was pointed out that the red blood cell surface area is actually 50% greater; also, the acetone extraction had left about 30% of the lipid remaining in the ghosts. Fortunately, these two errors tended to offset each other (Bar et al., 1966), showing that on infrequent occasions in science, you can be right for the wrong reasons. The bimolecular lipid leaflet, 75—100 Å thick, first proposed by Gorter and Grendel as a model for the cell membrane (Fig. 3.2), still forms the basis for contemporary thinking about the structure of cell membranes. The essence of this model is that membrane phospholipids are arranged in parallel sheets forming two hemileaflets with their polar head-groups facing the aqueous intracellular and extracellular solutions and their non-polar fatty acid chains interacting laterally within the hydrophobic core of the membrane.

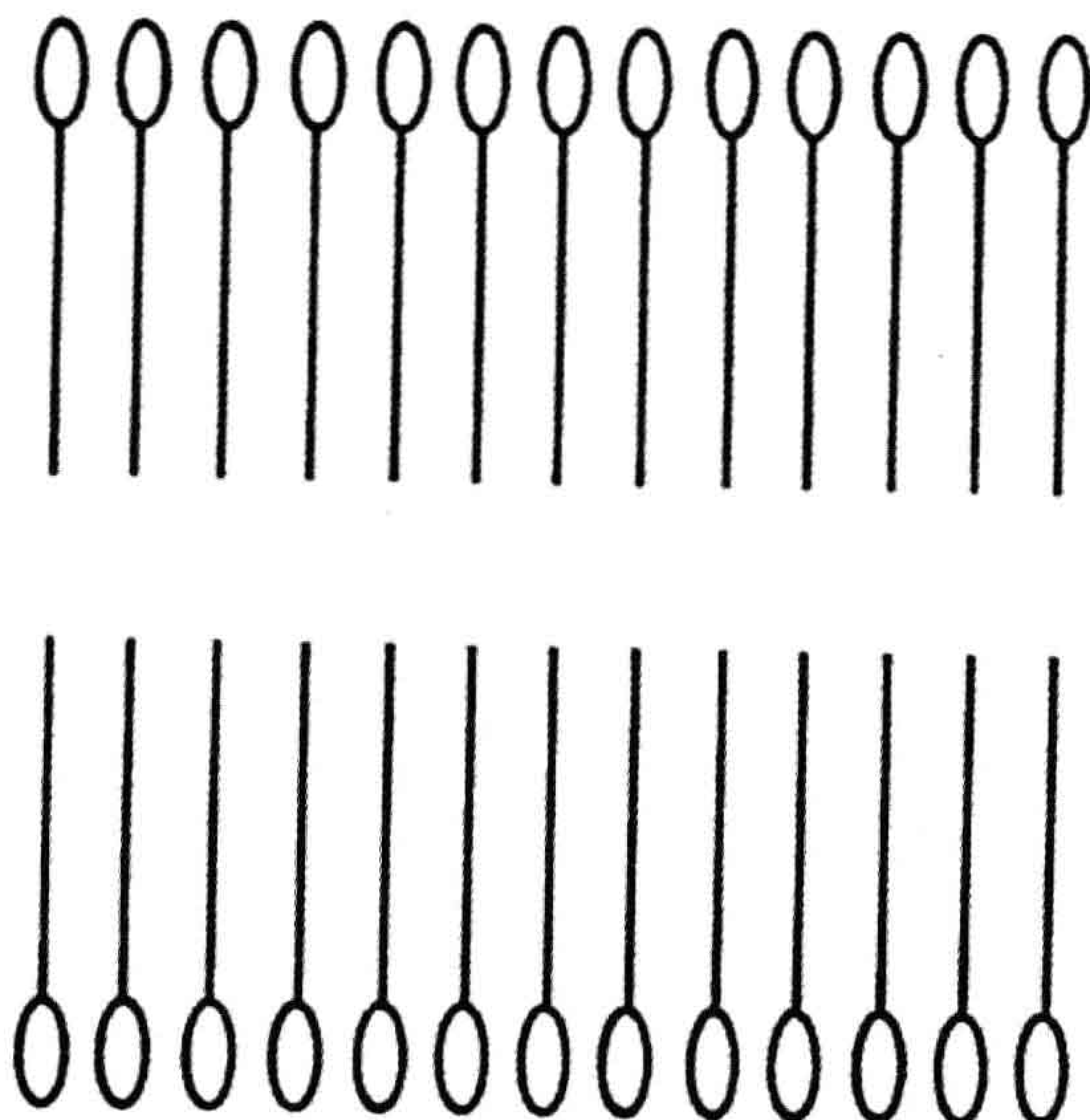


FIGURE 3.2 Model of bimolecular phospholipid membrane as proposed by Gorter and Grendel (1925).

For pure lipids, the expected *surface tension*, as measured in a Langmuir trough, is about 9 dyn/cm, but the surface tension of marine eggs and other types of cells is about 50—100 times less at only 0.1—0.2 dyn/cm. The surface tension can be visualized as the force necessary to close a slit in the surface of the membrane. Danielli and Harvey found that egg protein can lower the surface tension of an oil—water interface to about 0.6 dyn/cm, leading Davson and Danielli (1943) to postulate the presence of two films of protein associated with the polar head groups at each side of the bimolecular lipid leaflet, a model that became known as the *Davson—Danielli paucimolecular membrane* (Fig. 3.3). Presumably, the protein functioned to strengthen and stabilize the thin lipid film. *Paucimolecular* means that this model included just a few molecules: a bimolecular lipid leaflet with adhering protein films on the inner and outer surfaces.

Using electrophysiological techniques, the electrical resistance of cell membranes was measured and found to be very high, a finding that was also consistent with the proposal of an insulating lipid membrane surrounding cells. In other studies of membranes their *birefringence* was determined. Birefringence is an optical property of certain oriented materials that can be determined by placing a specimen between two crossed Polaroids on a microscope stage. A Polaroid film only passes light that has its electric vector parallel with the axis of the Polaroid film; two Polaroid films, crossed at right angles and held up to a light, appear black. But, if a crystal, or some other substance in which the molecules themselves are oriented, is placed between the crossed Polaroids, the transmitted light is circularly polarized, and the specimen looks brilliantly bright. A specimen that appears bright when placed between crossed Polaroids is said to be birefringent. *Intrinsic birefringence* is due to the oriented nature of individual molecules, such as filamentous proteins, whereas *form birefringence* is due to the oriented arrangement of molecules in an array, such as occurs with the parallel packing of actin and myosin filaments in muscle sarcomeres. When red cell membranes were viewed with a polarization microscope, the lipids contributed to birefringence, as did the underlying cytoskeleton, in a fashion consistent with the paucimolecular model of membrane structure.

High-resolution electron micrographs of the *unit membrane* also supported the Davson—Danielli paucimolecular model. The term *unit membrane* refers to the ubiquitous trilaminar structure, 75—100 Å thick, seen in

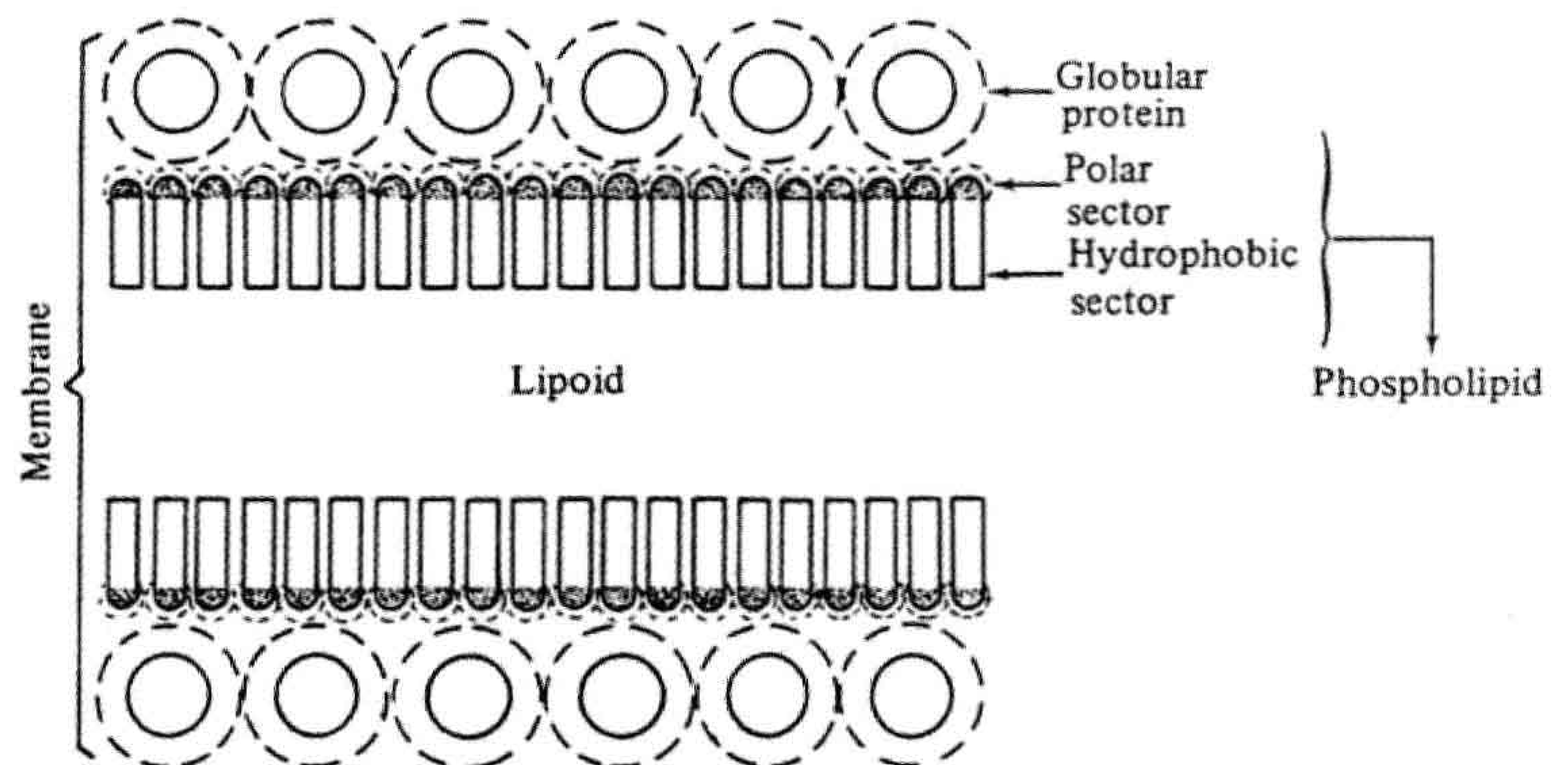


FIGURE 3.3 Paucimolecular model of membrane structure. *(From Danielli, J.F. and Davson, H.A. (1935). A contribution to the theory of permeability of thin films. J Cell Comp Physiol. 5, 495–508, p. 498, reprinted by permission of Wiley-Liss, Inc., a subsidiary of John Wiley and Sons, Inc.)*

electron micrographs of thin sections of cells and organelles. The image appears as two dark lines, each about 25–30 Å thick, sandwiching a lighter zone, and is especially well-resolved in samples fixed with potassium permanganate. A thin section electron micrograph of the human red blood cell plasma membrane is shown in Fig. 3.4. Virtually the same trilaminar structure was seen not only at the surface of red cells but also in muscle cells, nerve cells, epithelial cells, plant cells, bacterial cells and in just about every membranous cell organelle that was examined. In situations where two cells were tightly apposed, two trilaminar structures constituted a *double membrane*. In the myelin sheath that surrounds nerve cells, a series of trilaminar structures was seen in a spiral arrangement, consistent with the envelopment of nerve axons by the membrane of Schwann cells, as shown in Fig. 3.5A. Since the detailed chemical reactions of potassium permanganate with tissue are not entirely understood, some uncertainty remained concerning the basis of the image that was observed in thin sections. The universal occurrence of the unit membrane, however, was taken as strong evidence in support of the Davson–Danielli paucimolecular model. Further studies of the multilamellar myelin sheath of nerve axons by x-ray diffraction of centrifuged unfixed and unstained membranes yielded electron density profiles that were also consistent with the Davson–Danielli paucimolecular model (Worthington and McIntosh, 1973). As seen in Fig. 3.5B, the electron density is low in the hydrophobic core of the membrane and high in the polar regions of the phosphate groups. Moreover, the thickness of the membrane, as determined from these computed electron density profiles of unstained myelin sheath, quantitatively agrees with that seen as the unit membrane in thin sections fixed with potassium permanganate – an observation constituting compelling evidence supporting the proposal of a bimolecular phospholipid leaflet as the backbone structure of cell membranes. Thus, the evidence for the paucimolecular membrane model consisted of studies of permeability, electrical resistance and microscopic observations of birefringence with the light microscope, as well as high-resolution images of both stained and unstained cells with the electron microscope. These convincing arguments were summarized in the classic monograph entitled *The Permeability of Natural Membranes* written by Davson and Danielli (1943), a book that greatly influenced subsequent development of cellular and membrane physiology.

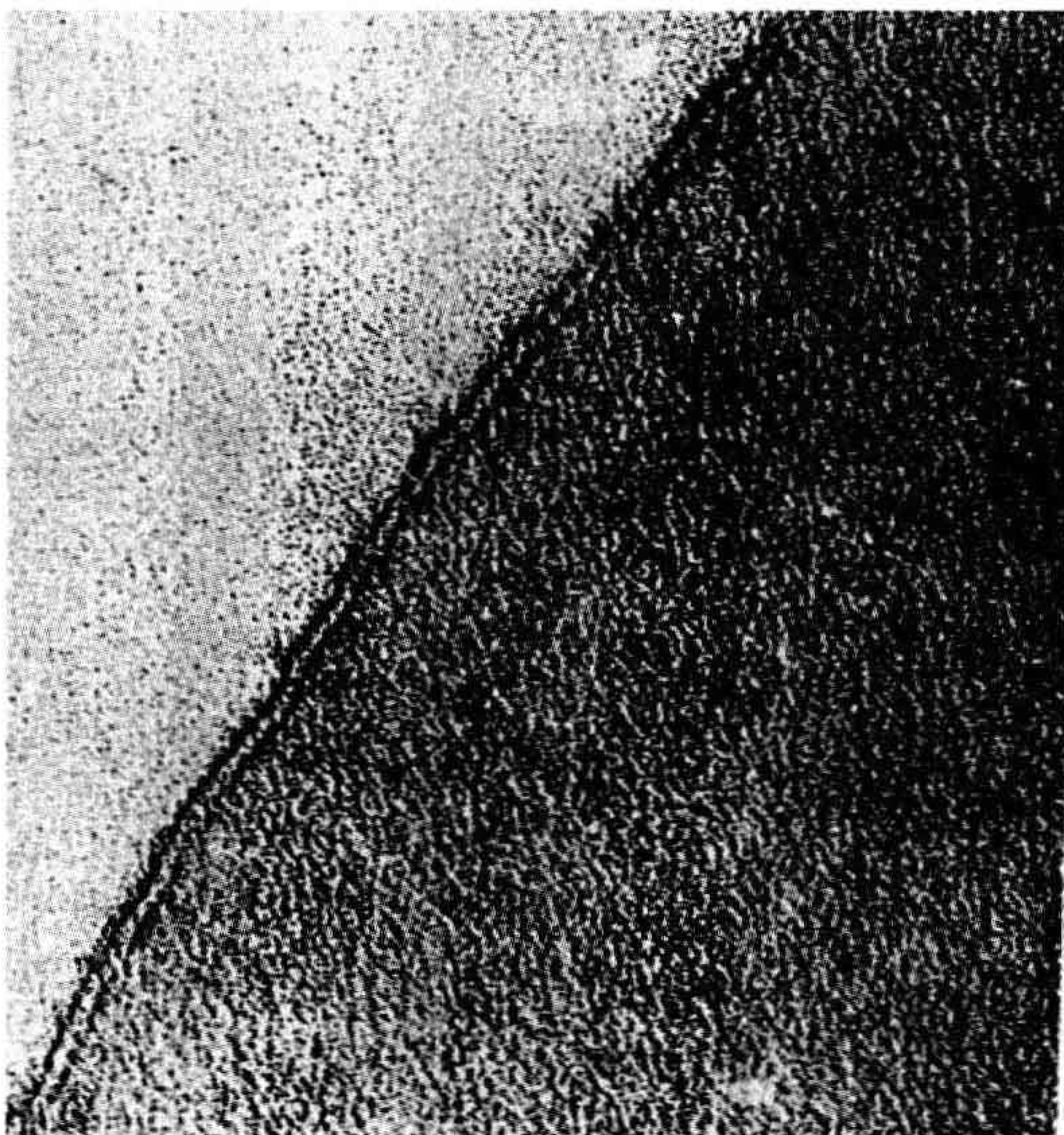
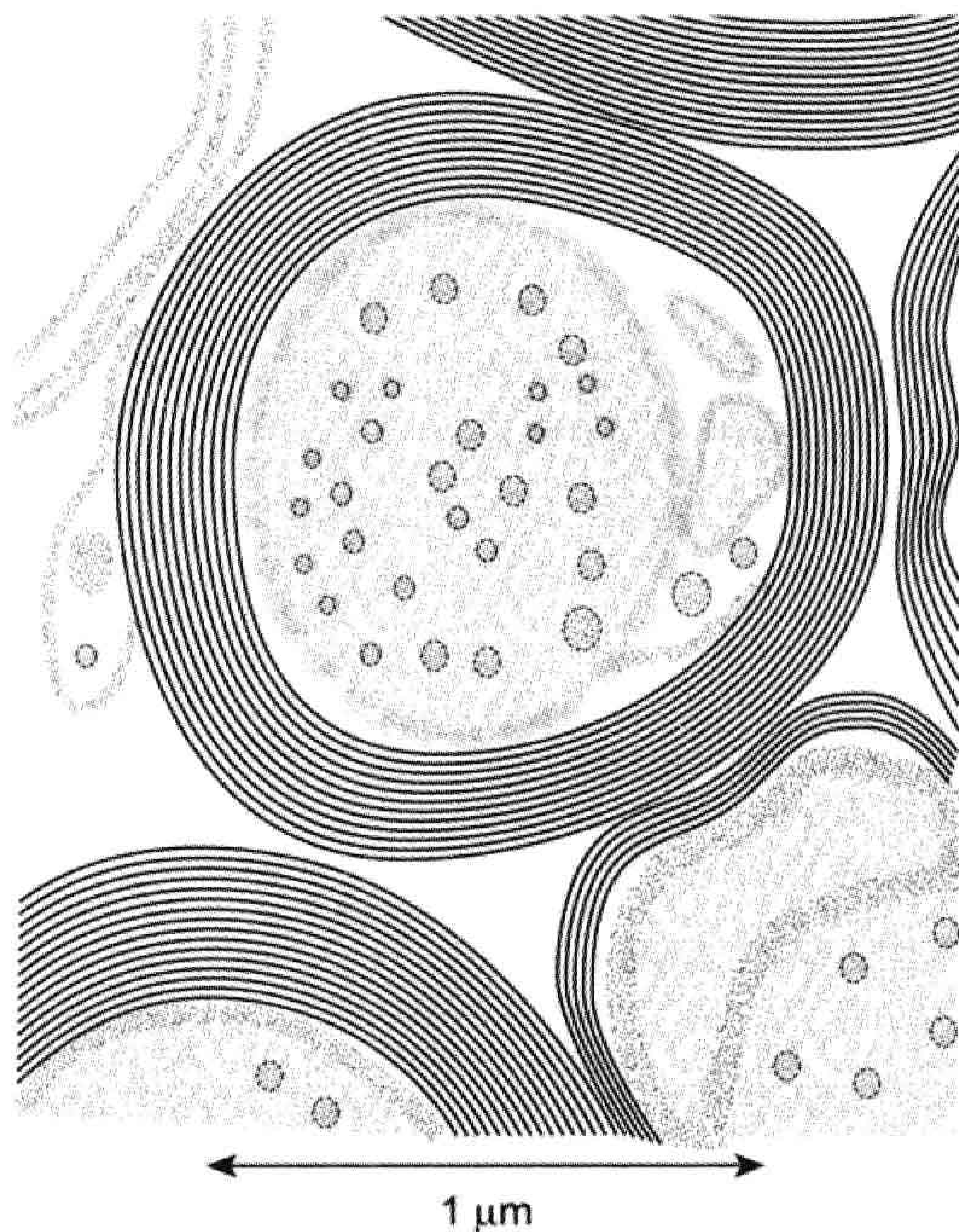


FIGURE 3.4 Thin-section electron micrograph of the unit membrane of a red blood cell. *(Photomicrograph by J.D. Robertson from Dyson, R.D. (1974). Cell Biology. A Molecular Approach. Allyn and Bacon, Boston, with permission.)*



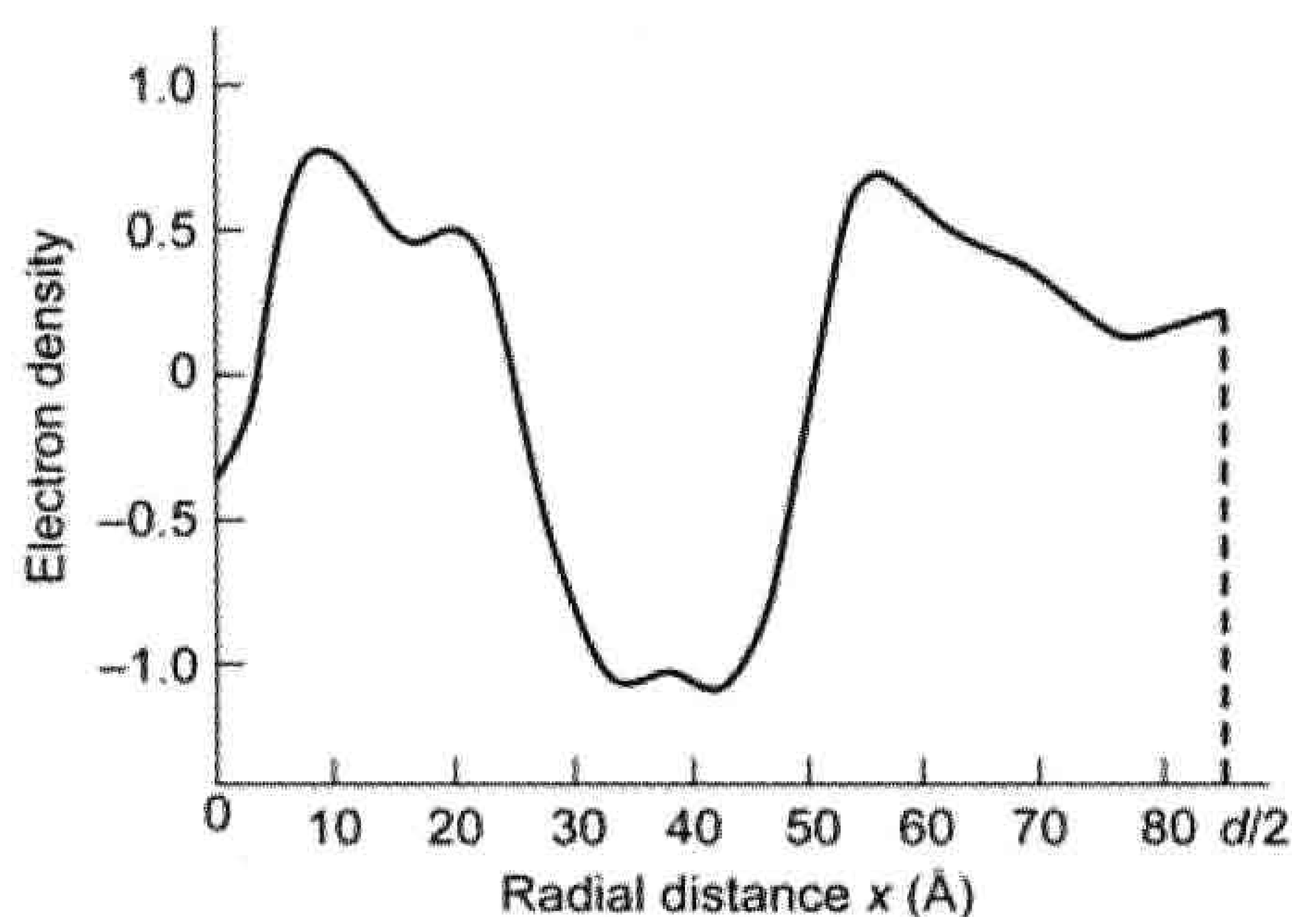


FIGURE 3.5 (A) Myelin sheath of spinal cord axon (courtesy of Dr Cedric Raine.) (B) Electron density profile of frog sciatic nerve. *(From Worthington, C.R. and McIntosh, T.J. (1973). Direct determination of the electron density profile of nerve myelin. Nature-New Biology. 245, 97–99, p. 99. Reprinted by permission from* Nature *copyright 1973 Macmillan Magazines Ltd.)*

III. MEMBRANE LIPIDS AND PROTEINS

The ability to separate intact red blood cell membranes from the rest of the cell by hypotonic hemolysis (Dodge et al., 1963) was further evidence for the existence of a distinct membrane and enabled detailed studies of the chemical composition of cell membranes. After centrifugation of red blood cells, followed by resuspension in distilled water, the water enters the cells by *osmosis* and then the cells swell and hemolyze. Following centrifugation and washing of the pellet by further resuspension and centrifugation at the optimal pH and ionic strength to remove adherent hemoglobin, the resultant pellet is pure white. When these isolated washed membranes are examined by the technique of negative staining with an electron microscope (a negative stain is excluded from biological structures in contrast with positive stains, which bind more or less specifically to various structures), the image resembles an empty bag, as seen in Fig. 3.6. In red cell physiology, the isolated membranes are known as *ghosts*, which can be either pink or white depending on the extent and conditions of washing. Red blood cell membranes were the first to be isolated and remain the best characterized.

The mass ratio of protein to lipid ranges from about 1:4 to 4:1 in various membranes. Myelin, which electrically insulates nerve axons from the extracellular solution, has only 18% protein by mass. In contrast, the energy-transducing inner membranes of mitochondria and chloroplasts, where ATP is synthesized by oxidative or photo phosphorylation, respectively, are densely packed with

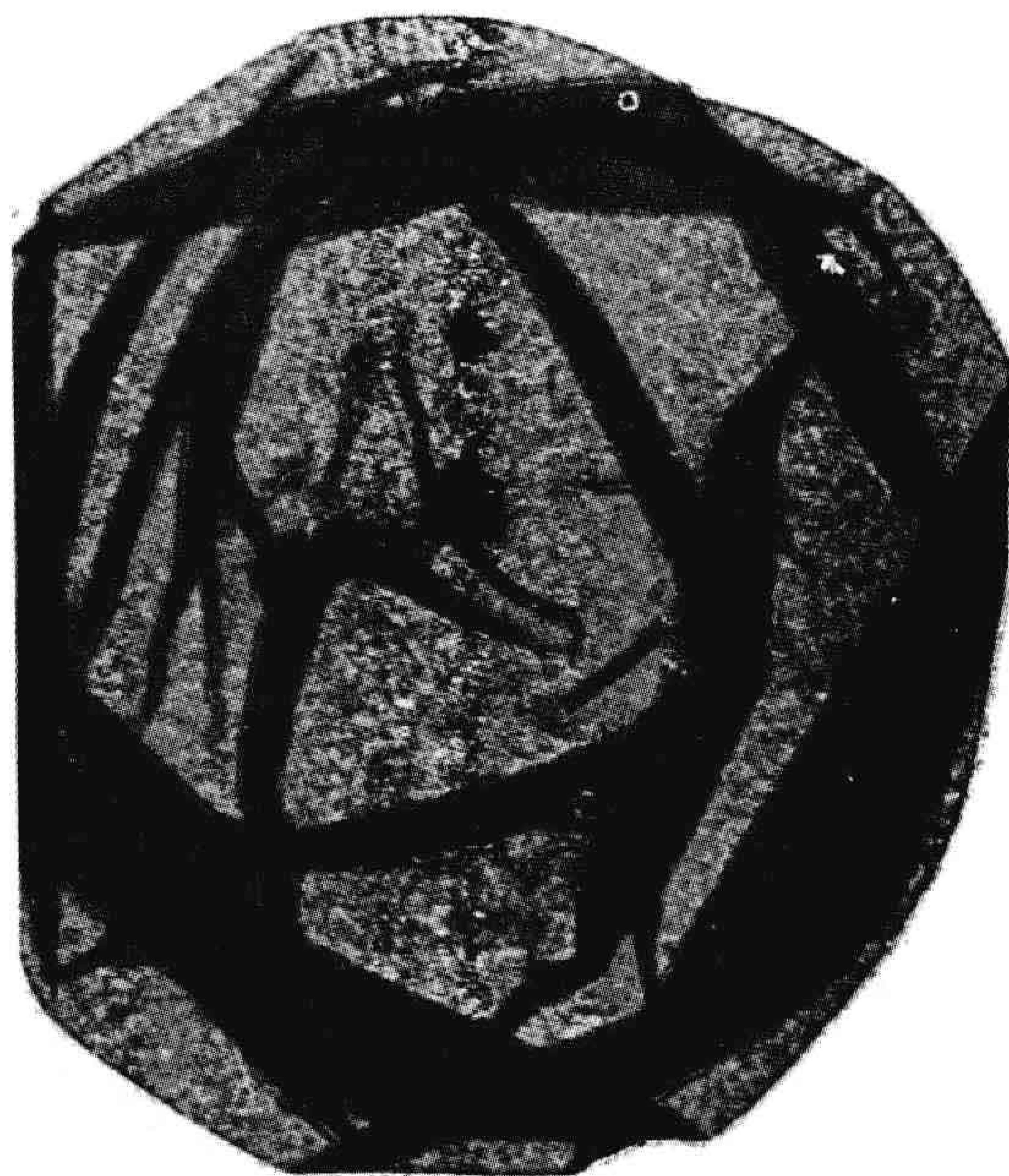
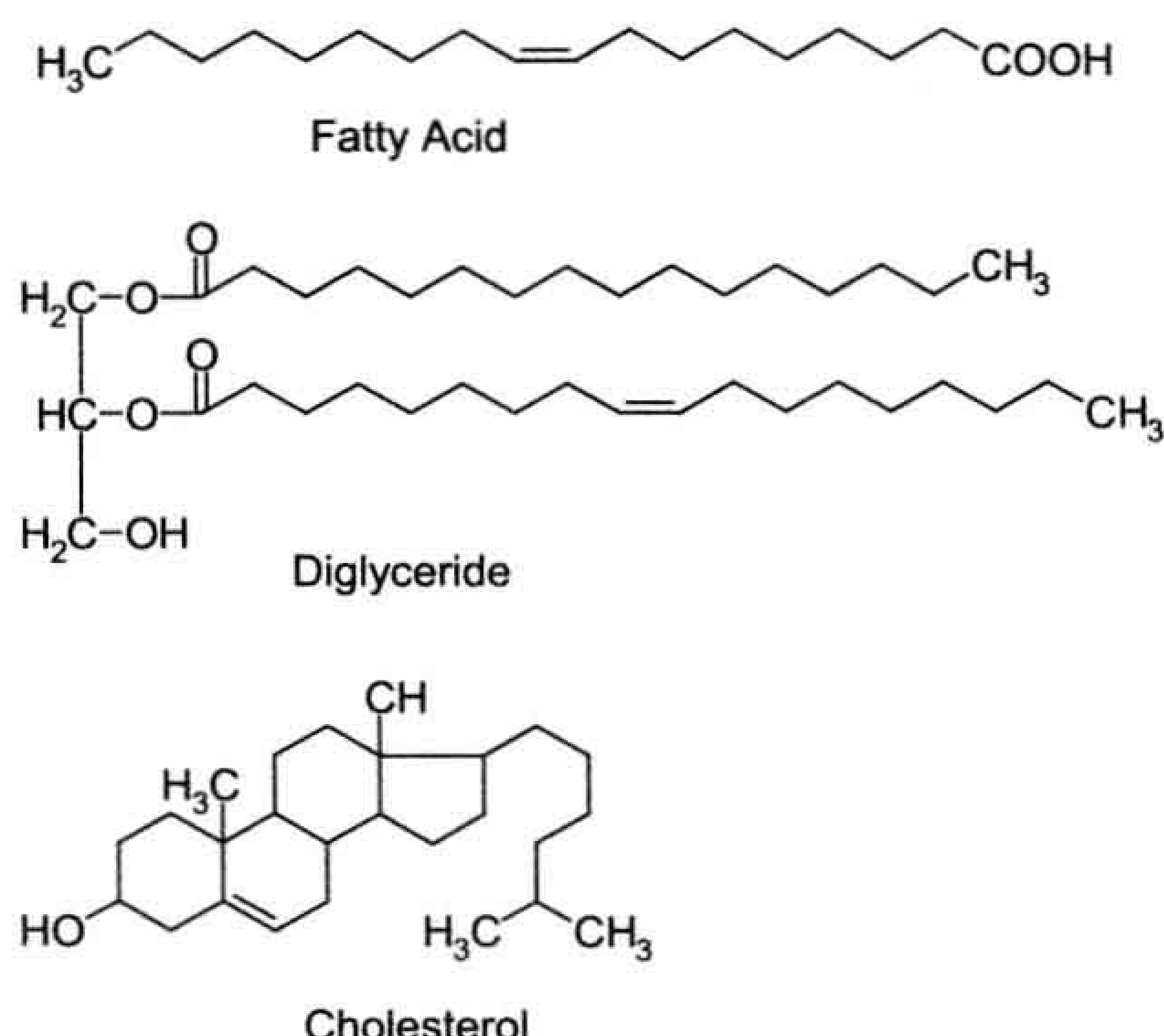


FIGURE 3.6 Isolated red cell membrane negatively stained with phosphotungstic acid. *(From McMillan, P.N. and Luftig, R.B. (1973). Preservation of erythrocyte ghost ultrastructure achieved by various fixatives. Proc Natl Acad Sci USA. 70, 3060–3064, p. 3061, with permission.)*

TABLE 3.1 Composition of Red Blood Cell Ghosts

Substance	Mass Percent
Protein	49
Phospholipid	33
Cholesterol	11
Lipid (total)	44
Carbohydrate (total)	7

Adapted from Rosenberg, S.A. and Guidotti, G.J. (1968). The protein of human erythrocyte membranes. I. Preparation, solubilization, & partial characterization. J Biol Chem. 243, 1985–1992.



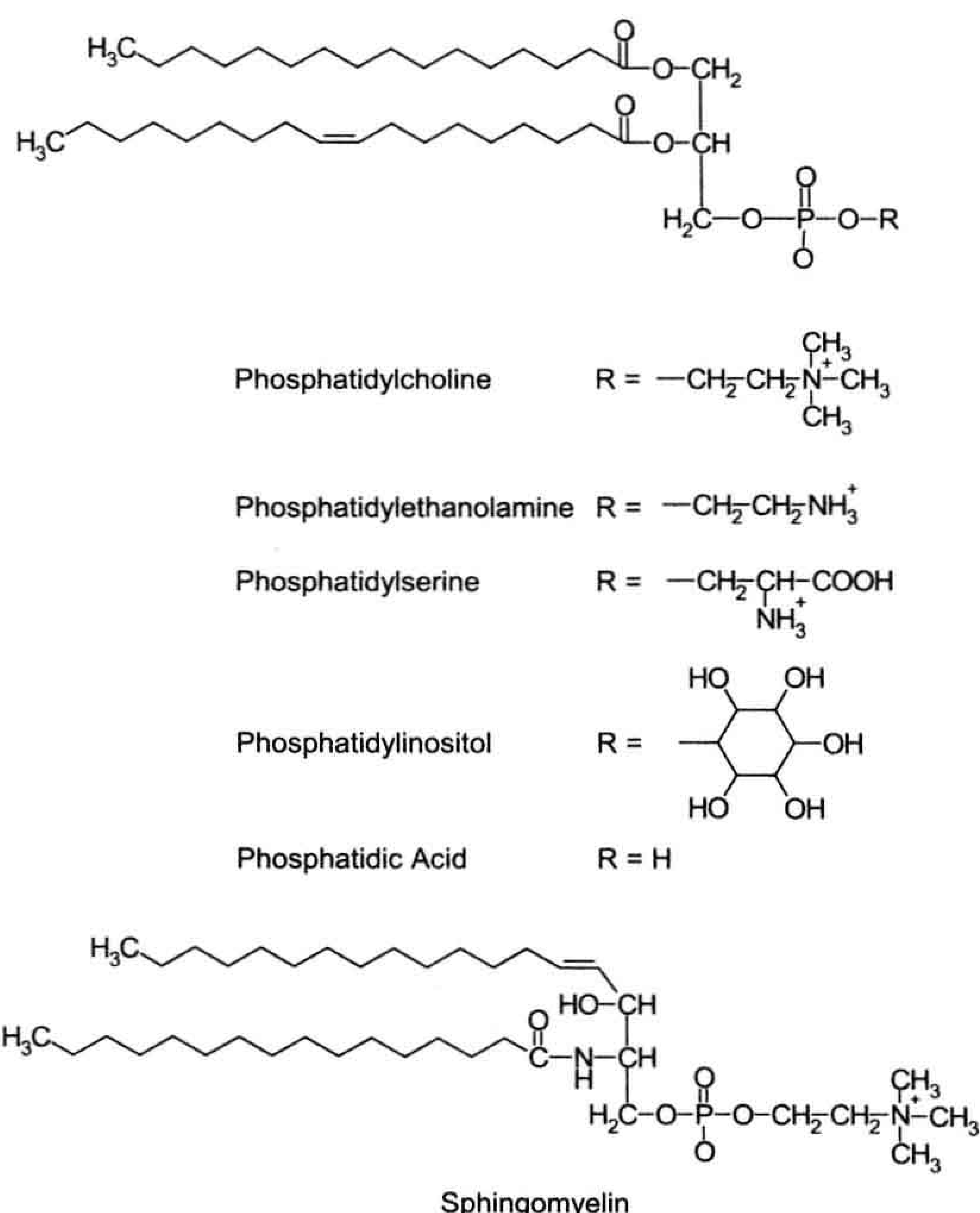


FIGURE 3.7 (A) Chemical structure of fatty acid, cholesterol, diglyceride. (B) Structures of phospholipids. *(Structures drawn by T.B. Freedman.)*

75% protein. The chemical composition of isolated red cell membranes is summarized in Table 3.1, which indicates that these membranes, like many other membranes, are about half protein and half lipid by mass, with an additional fraction of carbohydrate. The carbohydrate exists as sugars on glycoproteins, glycolipids and on sialic acid; the sugars always protrude from the outer membrane surface. Due to sialic acids on *glycophorin*, an integral membrane glycoprotein, the external surface of red cells is negatively charged. The external surface of the red cell membrane is also coated with adsorbed albumin and also with some plasma globulins.

The three major classes of membrane lipids are phospholipids, glycolipids and cholesterol. *Phospholipids* are derived either from glycerol, a 3-carbon alcohol, or from sphingosine, a more complex amino alcohol with a long unsaturated carbon chain. Phosphoric acid esterified to diacylglycerol forms phosphatidate, from which the major glycero-phospholipids are formed. The chemical structures of a fatty acid, cholesterol and a diglyceride are shown in Fig. 3.7A, along with the structures of some phospholipids in Fig. 3.7B. Membrane lipids are *amphipathic* molecules comprised of a polar (hydrophilic) headgroup, an interfacial region and a non-polar (hydrophobic) tail. Phospholipids can be neutral (e.g. phosphatidylcholine, PC, also known as lecithin; phosphatidylethanolamine, PE; sphingomyelin, SM) or carry a net negative charge (e.g. phosphatidylserine, PS; phosphatidylinositol, PI). *Diacylphospholipids* are the major components of the plasma membrane of mammalian cells and usually occur as mixed-chain lipids such that two different fatty acids are linked to the glycerol backbone. The two esterified fatty acids have a different even number of carbon atoms ranging from 14 to 24. The sn-1 acyl chain esterified at the end carbon position is often saturated and assumes the all-*trans* conformation, whereas the sn-2 acyl chain esterified at the middle carbon position is predominantly unsaturated. The conformation of double bonds in unsaturated fatty acids is nearly always *cis*, which produces a bend along the chain where the double bond occurs. POPC, or 1-palmitoyl-2-oleoyl-phosphatidylcholine, is one of the most abundant

membrane lipids found in animal cell membranes. PE is often the principal phospholipid of microorganisms and is also abundant in rod outer segments of photoreceptor cells. PI typically comprises 2–8% of the phospholipid in animal cells and can be phosphorylated to participate in intracellular signaling pathways. Diphosphatidylglycerol, or cardiolipin, is abundant in mitochondrial membranes. PS is an important constituent of brain cell membranes and it activates protein kinase C in signaling pathways. Over one thousand distinct species of phospholipids exist in eukaryotic membranes.

The space-filling model of C(14):C(14) PC obtained by x-ray diffraction of single crystals shown in Fig. 3.8 agrees closely with the conformation calculated by minimizing the free energy of the structure. Even-numbered saturated fatty acids have a bend at the second carbon of the sn-2 chain, known as the h-shaped geometry, resulting in effectively uneven lengths of the two chains. These uneven lengths of the two acyl chains can interact across the bilayer to further stabilize the bimolecular phospholipid membrane.

Since the mole ratio of phospholipid to cholesterol is 0.8 in red cells, the paucimolecular model needed modification to include cholesterols interspersed among the phospholipid fatty acyl chains in parallel with the phospholipids. The plasma membranes of eukaryotic cells are rich in cholesterol, whereas organelle membranes have less of this neutral lipid.

The proportions of phospholipids found in human red blood cell membranes are shown in Table 3.2. The fatty acyl chains in the phospholipids usually contain an even number of carbons between 14 and 24; the 16- and 18-carbon fatty acids are the most common. In red cells, the major fatty acids are palmitic (16:0), oleic (18:1), linoleic (18:2), stearic (18:0) and arachidonic (20:4) (Table 3.3), which together account for some 92% of the total fatty acid content. Different membranes differ in their *lipid signature*, a term that refers to the characteristic pattern of phospholipids, cholesterol and fatty acids that comprise the plasma membranes of different cells and of specific organelles. Lipid composition and content are usually measured by chromatographic methods and have been measured and cataloged for many different membranes (Ansell et al., 1973). The functional significance, however, of the different lipid signatures that occur in various specialized cells and organelles is largely not understood.

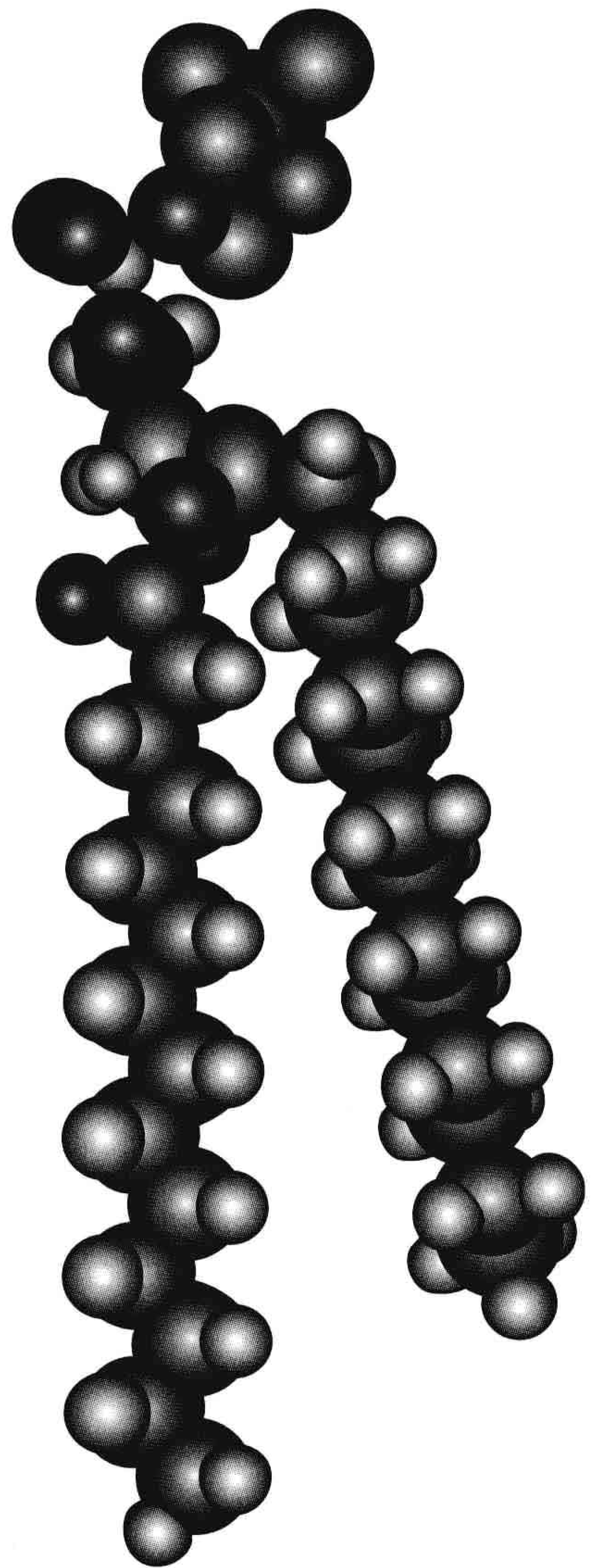


FIGURE 3.8 The x-ray single crystal structure of C(14):C14) PC shown as a space-filling model. *(Adapted from Huang, C.-H. (1998). Membrane lipid structure and organization. In Cell Physiology Sourcebook, 2nd edn, Chapter 3, p. 44, Academic Press, New York.)*

With two hydrophobic acyl chains, individual phospholipids have very low solubility in water, but form micelles at a critical micelle concentration of about 10^{-10} M. A *micelle* is a globular structure, usually less than 200 Å in diameter, with the polar head groups on the outside and the hydrophobic fatty acyl chains buried in the interior. Salts of fatty acids readily form micelles, whereas phospholipids tend to form bilayers. The *self-association* of phospholipids to form a bimolecular leaflet depends on the *hydrophobic effect*: the release of structured water molecules from around the hydrocarbon tails of the fatty acids results in an overall gain of entropy that serves as the driving force for self-assembly of phospholipids into bimolecular membranes. The membrane is further

TABLE 3.2 Approximate Proportions of Phospholipids in Human Red Blood Cells

Phospholipid	Abbreviation	Mass Percent
Phosphatidylcholine (lecithin)	PC	35
Lysolecithin	Lyso-PC	2
Sphingomyelin	SM	23
Phosphatidylethanolamine	PE	30
Phosphatidylserine + phosphatidylinositol	PS + PI	10

Adapted from van Deenen, L.L.M. and de Gier, J. (1964). Chemical composition and metabolism of lipids in red blood cells of various animal species. In (C. Bishop and D.M. Surgenor, eds), The Red Blood Cell, a Comprehensive Treatise, p. 266. Academic Press, New York.

stabilized by lateral van der Waals attractive forces between the fatty acyl chains, by electrostatic forces and by hydrogen bonding between adjacent polar headgroups. Depending on the method of preparation, membranes can form as planar bilayers, multilamellar vesicles (MLVs) and as small (200−500 Å) or large (0.1−1 μm) unilamellar vesicles (SUVs and LUVs), as illustrated in Fig. 3.9. In each structure, the polar, or hydrophilic, headgroups have an affinity for water whereas the non-polar, or hydrophobic, fatty acyl chains avoid water.

TABLE 3.3 Fatty Acids in the Membrane Phospholipids of Human Red Blood Cells

Fatty Acid	X:Y[a]	Mass Percent
Lauric	12:0	0.3
Myristic	14:0	1.0
	15:0	0.3
Palmitic	16:0	27.1
	16:1	3.4
	17:0	0.6
Stearic	18:0	9.4
Oleic	18:1	19.5
Linoleic	18:2	16.5
	18:3	0.5
	20:0	0.2
	20:3	1.4
Arachidonic	20:4	19.5

[a]*In X:Y,X refers to the number of C atoms in the acyl chain and Y refers to the number of double bonds.*
Data from de Gier, J., van Deenen, L.L.M., Verloop, M.C. & van Gastel, C. (1964). Phospholipid and fatty acic characteristics of erythrocytes in some cases of anaemia. Brit J Haematol. 10, 251.

When isolated red cell membranes are solubilized in the detergent sodium dodecyl sulfate (SDS), then subjected to electrophoresis on polyacrylamide gels containing SDS, followed by staining with the dye Coomassie blue, seven major bands are found (Fig. 3.10 and Table 3.4). In addition, stains for carbohydrate reveal glycophorin and other glycoproteins. Actually, more than 10 bands can be counted and many more spots are seen when two-dimensional chromatography is employed. Specific proteins mediate the distinctive functions of membranes; e.g. membrane proteins serve as ion channels, pumps, receptors, energy transducers and enzymes. Membranes with different functions show different banding patterns of proteins on SDS gels. Whereas the membrane lipids form a permeability barrier to most polar molecules and also form closed compartments around and within cells, specific proteins mediate most other membrane functions.

When a cell membrane, such as the human red blood cell, is rapidly frozen in liquid nitrogen and then fractured with the sudden impact of a microtome blade, the cleavage plane can pass along the outer surface of the cell, then slice through the hydrophobic core of the membrane and then continue along the inner surface of the membrane. *Freeze-fracture electron micrographs* provide a view of the unfixed interior of the membrane. After shadowing with carbon and platinum, a replica of the membrane interior is obtained. A variation of this technique is *freeze-etching*, in which some of the ice is sublimed away before the shadowing. With this technique, globular intramembranous particles (75 Å) are seen to lie in the plane of the membrane (Fig. 3.11). In red cells, the surface density of these particles (10^6 per cell) approximately corresponds to the number of copies of the major membrane protein variously known as band 3, capnophorin, or AE1, the anion exchange protein. In contrast, freeze-etch images of myelin are relatively poor in intramembranous particles and images of pure lipid membranes are devoid of such particles.

IV. THE FLUID MOSAIC MODEL OF CELL MEMBRANES

Spectroscopic studies provided evidence that lipids and proteins have some degree of rotational and translational mobility in the plane of the membrane. Subsequently, the review article entitled "The fluid mosaic model of the structure of cell membranes" (Singer and Nicholson, 1972) popularized the view that the overall structure of the membrane is a two-dimensional solution of globular proteins embedded in a fluid lipid matrix, as shown in Fig. 3.12. *Integral proteins* span the membrane and can be extracted only with detergents or organic solvents;

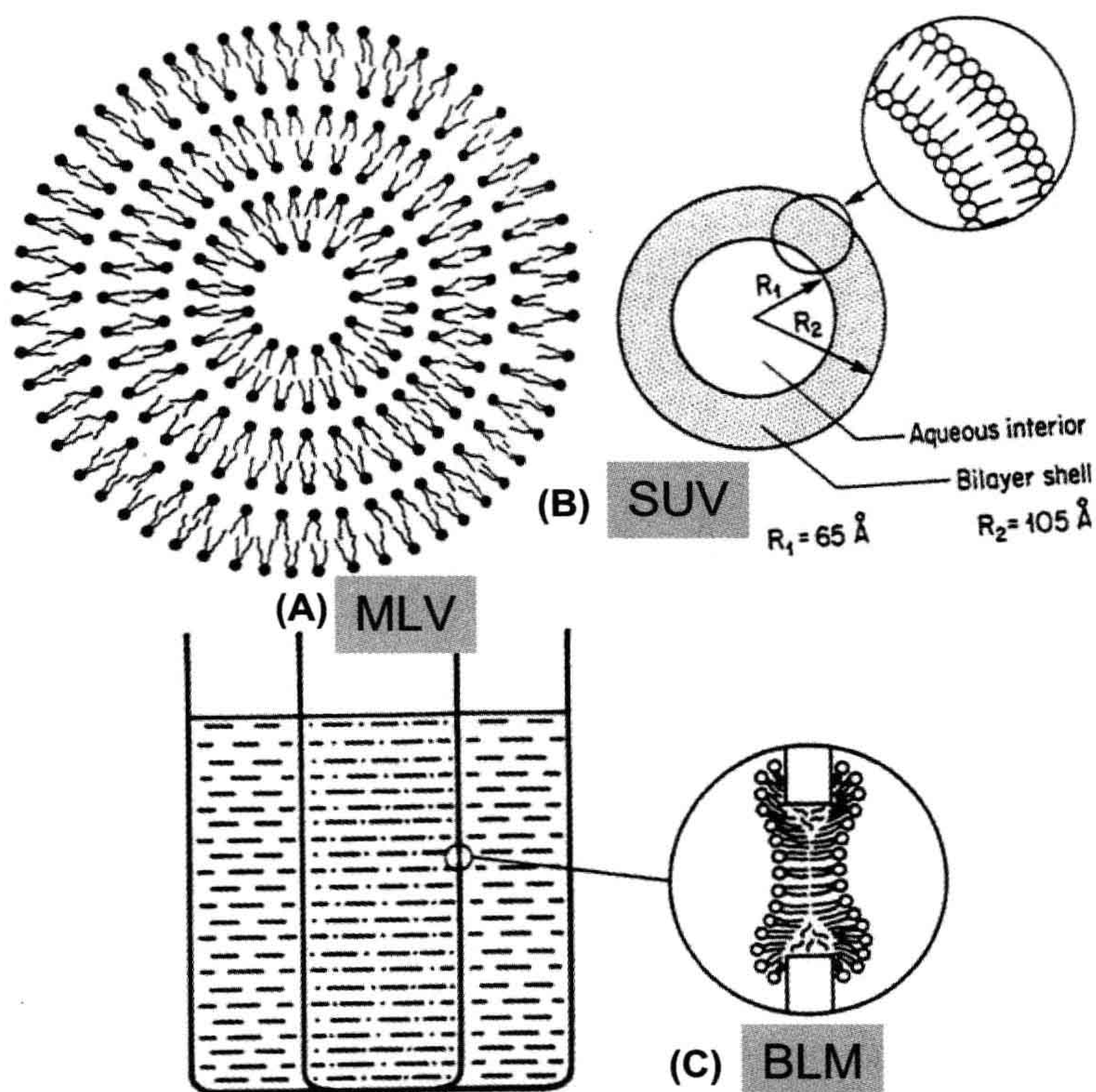


FIGURE 3.9 Model membranes: (A) liposomes; (B) vesicles; (C) planar bilayers. *(From Yeagle, P.L. (1993). The Membranes of Cells, 2nd edn, pp. 48, 52, and 54, Academic Press, New York, with permission.)*

peripheral proteins are attached more loosely to the surface of the membrane and are more easily extracted by more mild chemical treatments, such as by changing the pH or by exposure to high ionic strength solutions (e.g. 1 M NaCl). Peripheral proteins interact with the membrane by electrostatic or hydrogen-bonding interactions; integral proteins have transmembrane hydrophobic domains that interact extensively with the hydrophobic core of the membrane. The *fluid mosaic model* constituted an important extension of the Davson–Danielli paucimolecular model, especially with regard to the fluid state of the lipids and the location of integral membrane proteins. Further refinement of the fluid mosaic model incorporates lipid heterogeneities, such as annular phospholipid microdomains around integral membrane proteins, transbilayer phospholipid asymmetry, lipid phase separations and lateral microdomains of cholesterol-rich and cholesterol-poor pools.

Lipid molecules and some proteins diffuse rapidly in the plane of the membrane, but rarely flip across the membrane from one hemileaflet to the other. The diffusion coefficient of lipids in a variety of membranes is about 10^{-8} cm^2/s, corresponding to a distance traveled of about 2 μm in 1 s. From the diffusion coefficient it is estimated that the viscosity of the membrane lipids is about 100 times that of water, similar to olive oil. Cell fusion experiments first demonstrated that fluorescent labeled antibodies attached to human and mouse cell surface proteins could diffuse a distance of several microns in approximately 1 min (Frye and Edidin, 1970). Another way of measuring the lateral translational mobility of membrane lipids and proteins is the technique of fluorescence recovery after photobleaching (FRAP). In human red blood cells, FRAP studies showed that a portion of band 3 protein is slowly mobile, whereas another fraction is immobile due to attachments to the cytoskeletal protein matrix adjacent to the inner surface of the membrane. Proteins in different cells, and different proteins in a single cell, vary markedly in their *lateral mobility*, Bloom and Webb (1983).

Attachments between integral membrane proteins and the cytoskeleton represent another refinement of the fluid mosaic model of membrane structure. In red cells, the

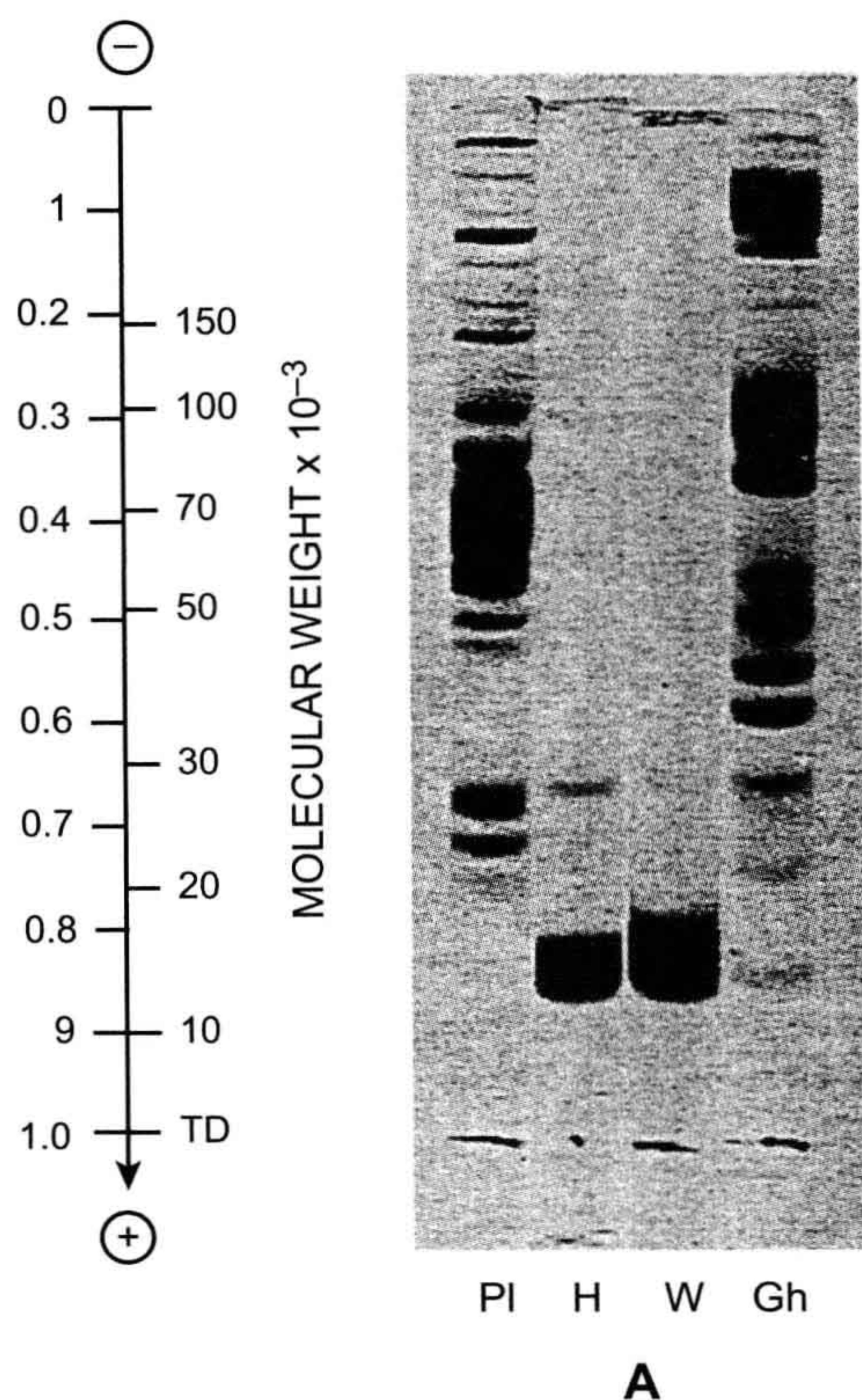


FIGURE 3.10 SDS gel of red blood cell membrane proteins. *(From Steck, P.L. and Yu, J. (1973). Selective solubilization of proteins from red blood cell membranes by protein perturbants. J Supramolec Struct. 1, 220–232, p. 223, Copyright © 1973. Reprinted by permission of Wiley-Liss, Inc., a subsidiary of John Wiley & Sons, Inc.)*

cytoskeleton is an organized polygonal fibrous network, about 60 nm thick containing spectrin and actin. Sides of the regular five- or six-sided polygons are formed by *spectrin*, a flexible filamentous protein 200 nm in length. Vertices of the polygons are formed by *β-actin* protofilaments 30–40 nm in length consisting of 12–14 actin monomers; both grooves of the actin filaments contain *tropomyosin*, which binds to *tropomodulin* at junctional complexes. At the mid-region of the spectrin filaments, a junctional ternary complex formed by *ankyrin* and band 4.2 protein links spectrin to the membrane-spanning integral band 3 protein. At the ends of the spectrin filaments, an additional linkage site to band 3 and to *glycophorin C* may be provided by protein 4.1. Spectrin–actin junctional complexes also contain the actin-bundling protein *dematin* (band 4.9) and the calmodulin-binding protein *adducin*, which functions to cap and to regulate the length of the actin filaments and which may be involved in Ca^{2+}-dependent alterations in cytoskeletal structure. A small amount of *myosin* is also found in the red-cell cytoskeleton, but whether active tension is generated or regulated in mature red cells is not known. Presumably, the cytoskeleton is actively involved during *enucleation* in developing red cells and during *diapedesis*, or egress of red cells from the bone marrow to the peripheral circulation.

Rotational molecular motions in membranes may be studied by the technique of *fluorescence polarization*, also called *fluorescence anisotropy*. A hydrophobic fluorescent probe, such as diphenylhexatriene (DPH), is first added to the membrane. The fluorescence is excited by light that is polarized, say in the vertical direction. Vertical exciting light only excites those probe molecules that are oriented in the same direction as the polarized excitation beam, a phenomenon known as *selective excitation*. If the probe molecule is immobilized during the time interval between excitation and emission, all of the emitted light would remain polarized in the vertical direction. However, if the probe molecule can rotate before light is emitted, then the emitted light will no longer be vertically polarized, but instead will contain a mixture of light that is polarized in all directions. By detecting and measuring the intensity of the emitted light that is polarized in the vertical and horizontal planes, one obtains a measure of the rotational mobility of the probe. By using the equations of motion, one further obtains a measure of the *microviscosity* of the fluid membrane. The inverse of microviscosity is termed *fluidity* and many studies have been performed to attempt to elucidate the determinants of membrane fluidity. Lipid composition, the length and degree of unsaturation of fatty acyl chains, the cholesterol content and the temperature all have profound effects on membrane lipid fluidity.

Deeper insight into the structure of pure lipid membranes has been obtained using the technique of *differential scanning calorimetry* (DSC). When liposomes are enclosed in a calorimeter and the temperature is slowly and continuously raised, the membranes absorb heat at particular temperatures corresponding to the occurrence of structural rearrangements, or *phase transitions*. In a plot of excess heat capacity versus temperature, the peaks in the DSC scans occur at the phase transition temperature, Tm, and the area under the peak corresponds to the transition enthalpy. The main transition is often called the gel-to-liquid crystalline phase transition. Below Tm the lipid is a gel with the fatty acyl chains in an ordered rigid state. Above Tm the lipid melts into a more disordered fluid-like liquid crystalline phase. A liquid crystal is a substance that flows like a liquid but has more short range order than a typical liquid. In the rigid gel state, the C-C bonds of the fatty acyl chains are all in the *trans* conformation. In the more disordered fluid state, some have rotated

TABLE 3.4 Protein Composition of Human Red Blood Cell Membrane

Band	MW	%	Position[a]	Name
Band 1	240 000	15	P	Dimeric spectrin
Band 2	215 000	15	P	Monomeric spectrin, myosin
Band 3	101 700	24	I	Capnophorin, Na^+,K^+-ATPase
Band 4.1	78 000	4.2	P	Junctional protein
Band 4.2	72 000	5.0	P	Junctional protein
Band 4.9	50 000			Dematin (actin-bundling protein)
Band 5	43 000	4.5	P	Actin
Band 6	35 000	5.5	P	Glyceraldehyde-3-phosphate dehydrogenase
Band 7	29 000	3.4		

[a]*P refers to a peripheral, and I to an integral, membrane protein.*
Data from Stack, T.L. (1974). The organization of proteins in the human red blood cell membrane. A review. J Cell Biol. 62, 1–19, Table 1, p. 4.

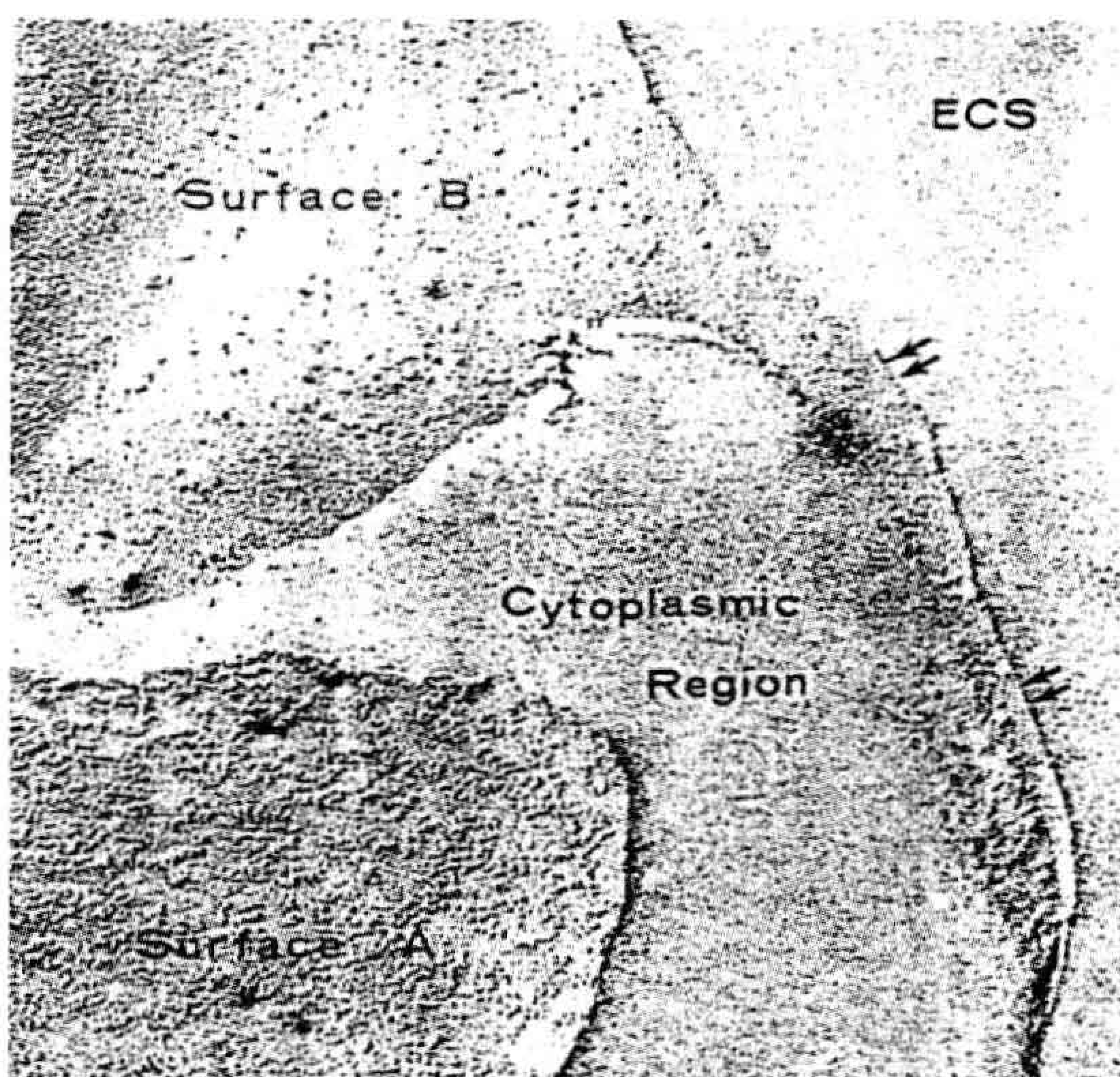


FIGURE 3.11 Freeze-etch image of red cell membrane showing intramembranous particles. *(From Weinstein, R.S. (1969). Electron microscopy of surfaces of red cell membranes. In (G.A. Jamieson and T.J. Greenwalt, eds), Red Cell Membrane. Structure and Function, p. 54. J.B. Lippincott Company, Philadelphia, with permission.)*

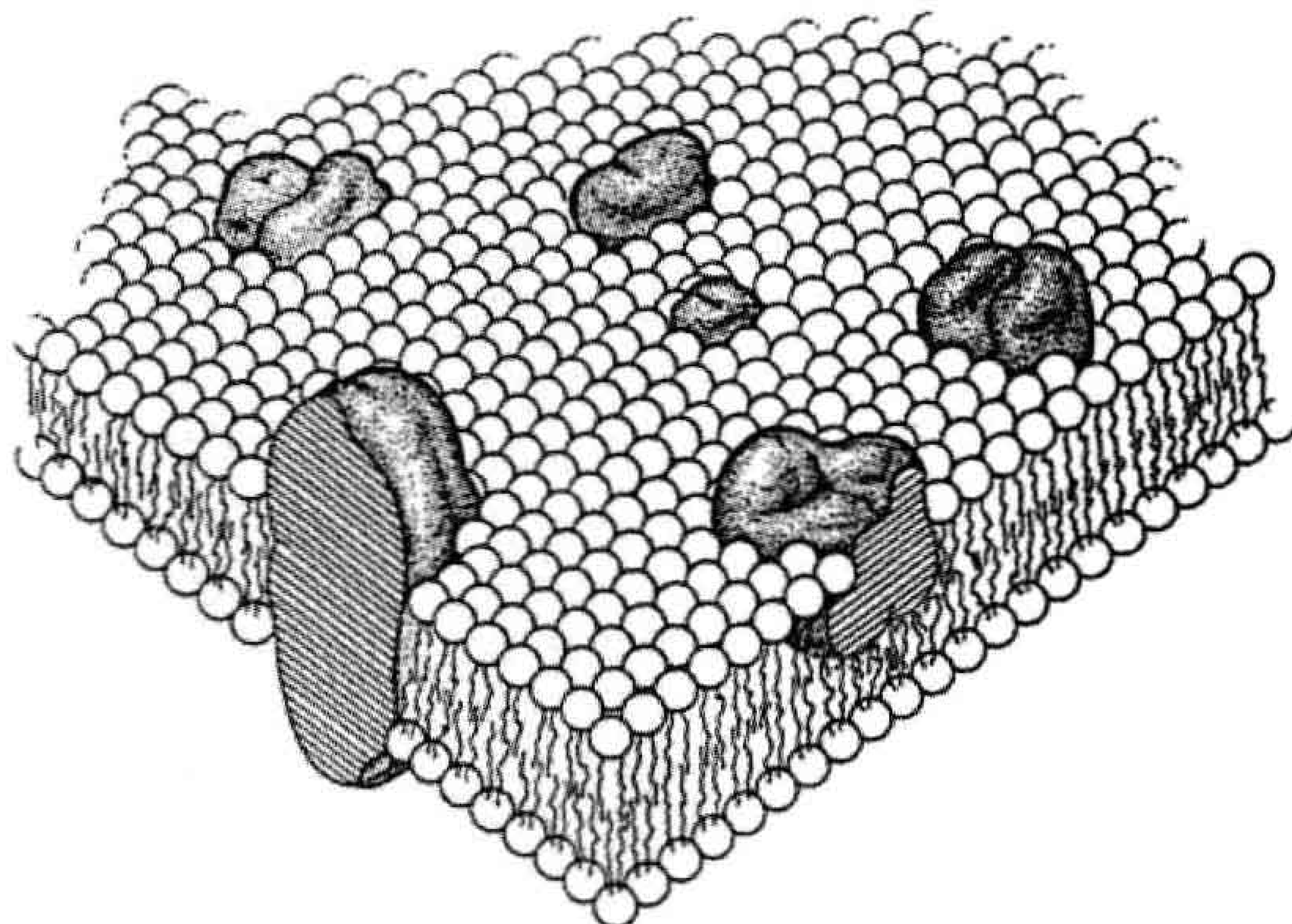


FIGURE 3.12 Fluid mosaic model of the structure of cell membranes.

120° clockwise or counterclockwise about the C-C bonds into the gauche conformation. Tm depends on the length of the fatty acyl chains and on their degree of unsaturation. Saturated fatty acids promote the gel state, whereas the presence of double bonds produces a bend in the carbon chain that disorders the lipid and lowers Tm. Longer carbon chains have higher melting points due to the stronger lateral interactions with neighboring chains.

Cholesterol is heterogeneously distributed in the membrane, with some regions being cholesterol-poor and other regions cholesterol-rich. In cholesterol-rich lateral domains, known as cholesterol pools, cholesterol located between phospholipids prevents crystallization, thereby abolishing phase transitions; it also sterically interferes with large motions of fatty acyl chains and thereby promotes order and reduces membrane fluidity. In cholesterol-poor regions, cholesterol is randomly distributed in a highly fluid phospholipid domain.

In mixtures of lipids, Tm may be experimentally determined by DSC as a function of systematic variation of the mole fraction of the components of the mixture. At elevated temperature, both lipids are melted in the liquid state, whereas at low temperature both lipids are solidified in the gel state. At intermediate temperatures and depending on the composition of the mixture, the lipid with the lower Tm is in the liquid state in equilibrium with the gelled lipid that has the higher Tm. Thus, depending on the temperature, different lipid phases may coexist in a cell membrane, thereby extending the concept of the fluid mosaic model of cell membranes, which assumed that membrane lipid is a homogeneous fluid. More recently, membrane microdomains enriched in sphingolipids and cholesterol, denoted as *rafts* in the ordered liquid phase, have been associated with various cellular functions including protein sorting, signal transduction, calcium

homeostasis, endocytosis, internalization of toxins, bacteria and viruses and cholesterol transport.

The lipids that directly surround integral membrane proteins differ in conformation and mobility from the bulk membrane lipids due to interactions with the protein. The *annular lipid* may either be more ordered or more disordered. In the case of the Ca-ATPase, which spans the bilayer, 15 annular phospholipid molecules in each of the two hemileaflets are in contact with the protein. If less than 30 molecules of lipid are associated with the protein, then activity is lost, showing that the annulus lipid is essential for the function of this particular protein. In a mixture of membrane lipids, the Ca-ATPase specifically attracts to itself and segregates into its annulus those particular lipids that optimize its activity.

In contrast to the rapid movement of lipids in the plane of the membrane, their spontaneous movement from one hemileaflet to the other, known as *flip-flop*, is slow. A typical phospholipid molecule flip-flops once every several hours, as measured by electron spin resonance spectroscopy. Thus, it takes about 10^9 times as long to flip-flop across the membrane as it does to diffuse along the equivalent distance of 50 Å in the plane of the membrane. Flip-flop of membrane proteins has not been detected and is unlikely because of the energetic barrier against moving the polar protein surface through the hydrophobic core of the membrane. The phospholipids in the red cell membrane and in many other cells as well are asymmetrically distributed, with the electrically neutral PC and SM preferentially located in the outer hemileaflet and the negatively-charged PS and PI preferentially located in the inner hemileaflet along with the neutral PE. Experiments with phospholipases added to the inside or outside of cells have experimentally established this phospholipid asymmetry. Cholesterol is located in both hemileaflets of the plasma membrane. The phospholipid asymmetry is maintained in part by the action of an aminophospholipid translocase, or "flippase", which catalyzes the inward translocation of PS or PE. This enzyme utilizes ATP, is stereospecific in the transport of L isomers and is inhibited by intracellular calcium or by sulfhydryl reagents.

BIBLIOGRAPHY

Ansell, G. B., Hawthorne, J. N., & Dawson, R. M. C. (1973). *Form and Function of Phospholipids*. New York: Elsevier Scientific Publishing Company.

Bar, R. S., Deamer, D. W., & Cornwell, D. G. (1966). Surface area of human erythrocyte lipids: reinvestigation of experiments on plasma membrane. *Science, 153*, 1010–1012.

Bloom, J. A., & Webb, W. E. (1983). Lipid diffusibility in the intact erythrocyte membrane. *Biophys J, 42*, 295–305.

Davson, H., & Danielli, J. F. (1943). *The Permeability of Natural Membranes*. Darien, CT: Hafner Publishing Company.

Dodge, J. T., Mitchell, C., & Hanahan, D. J. (1963). The preparation and chemical characteristics of hemoglobin-free ghosts of human erythrocytes. *Arch Biochem Biophys, 100*, 119–130.

Frye, C. D., & Edidin, M. (1970). The rapid intermixing of cell surface antigens after formation of mouse-human heterokaryons. *J Cell Sci, 7*, 319–335.

Gorter, E., & Grendel, F. (1925). On bimolecular layers of lipoids on the chromocytes of the blood. *J Exp Med, 41*, 439–443.

Heilbrunn, L. V. (1956). *The Dynamics of Living Protoplasm*. New York: Academic Press.

Jacobs, M. H. (1962). Early osmotic history of the plasma membrane. In Symposium on the Plasma Membrane, New York Heart Association, Inc. *Circulation, 26*, 1013–1021.

Luckey, M. (2008). *Membrane Structural Biology: with Biochemical and Biophysical Foundations*. New York: Cambridge University Press.

McMillan, P. N., & Luftig, R. B. (1973). Preservation of erythrocyte ghost ultrastructure achieved by various fixatives. *Proc Natl Acad Sci USA, 70*, 3060–3064.

Singer, S. J., & Nicholson, G. L. (1972). The fluid mosaic model of the structure of cell membranes. *Science, 175*, 720–731.

Weinstein, R. S. (1969). Electron microscopy of surfaces of red cell membranes. In G. A. Jamieson, & T. J. Greenwalt (Eds.), *Red Cell Membrane. Structure and Function*. Philadelphia: J. B. Lippincott Company.

Worthington, C. R., & McIntosh, T. J. (1973). Direct determination of the electron density profile of nerve myelin. *Nat New Biol, 245*, 97–99.

Yeagle, P. L. (2005). *The Structure of Biological Membranes* (2nd ed.). Boca Raton: CRC Press.

Chapter 4

Ionophores in Planar Lipid Bilayers

Jeffrey C. Freedman

Chapter Outline

I. SUMMARY

Planar lipid bilayers made from synthetic lipids and incorporating ionophores such as valinomycin or gramicidin, provide a useful tool for the study of membrane transport. Fusion of vesicles from native cell membranes into planar lipid bilayers provides information concerning ion channels that complements what is available from patch-clamp studies. Selective ion channels in planar lipid bilayers display high transport rates and low temperature coefficients, characteristics that distinguish ion channels from other modes of mediated transport. Finally, the features of cation transport by gramicidin in planar lipid bilayers are summarized. Detailed kinetic studies have shown that transport of cations and water through gramicidin occurs by means of single-file diffusion in which the ions and the waters cannot pass each other in the narrow part of the pore. The cation binds at a site near either end of the pore and then is driven over an energy barrier in the pore by the electrochemical gradient. The rate-limiting step, however, is the dissociation of the ion from the channel.

II. IONOPHORES

Ionophores are a class of compounds that form complexes with specific ions and facilitate their transport across cell membranes. An ionophore typically has a hydrophilic pocket (or hole) that forms a binding site specific for a particular ion. The exterior surface of an ionophore is hydrophobic, allowing the complexed ion in its pocket to cross the hydrophobic membrane. A list of ionophores showing the ion specificity of each is given in Table 4.1. Ionophores are useful tools in cell physiology experiments. *Nystatin* forms a channel in membranes for monovalent cations and anions and has proven useful for altering the cation composition of cells. *Gramicidin* forms dimeric channels specific to monovalent cations. *Valinomycin* carries K^+ across membranes with a high selectivity and has been used extensively to impose a high K^+ permeability on cell membranes. *Monensin* is a carrier with specificity for Na^+. *Hemisodium* is a synthetic Na^+ ionophore with an even greater degree of selectivity for Na^+. The *Ca^{2+} ionophore A23187* has been used extensively to permit entry of Ca^{2+} into cells, which normally have a low native permeability to Ca^{2+}, and thereby to activate a variety of cellular processes that are regulated by Ca^{2+}. *Nigericin* exchanges K^+ for protons and has been used in many studies of mitochondrial bioenergetics to alter electrical and chemical gradients for

TABLE 4.1 Ionophores and their Ion Selectivities

Conductive Carriers	
Valinomycin	K^+
Hemisodium	Na^+
FCCP, CCCP	H^+
Electroneutral Exchangers	
A23187	Ca^{2+}/Mg^{2+}; $Ca^{2+}/2H^+$
Nigericin	K^+/H^+
Channels	
Gramicidin	$H^+ > Cs^+ \approx Rb^+ > K^+ > Na^+ > Li^+$
Nystatin	Monovalent cations and anions

Cell Physiology Sourcebook. DOI: 10.1016/B978-0-12-387738-3.00004-4

protons. Ionophores such as *FCCP* and *CCCP* are specific for protons. Study of the mechanism of membrane transport mediated by ionophores has provided important conceptual insights relevant to the understanding of ion transport mediated by native transport proteins.

III. PLANAR LIPID BILAYERS

Planar lipid bilayers, also called *black lipid membranes* (BLMs), were first described in 1963 by Mueller and colleagues using the painting technique. A small aperture of about 1 mm diameter in a Teflon or polyethylene septum separating two aqueous salt solutions is coated by means of a beveled Teflon rod with a solution of pure lipids that are usually dissolved in decane. The thick lipid film covering the aperture then spontaneously thins to a bimolecular lipid leaflet surrounded by a thicker annular torus (Fig. 4.1A). The bimolecular portion of the film appears black because light reflected from the front surface undergoes a phase shift of 180° and destructively interferes with light reflected from the back surface. The film thickness of about 100 Å is small compared to the wavelength of visible light (3800–7600 Å). The lipids used to make the film are usually commercially purchased phospholipids – phosphatidylethanolamine (PE), phosphatidylcholine (PC), phosphatidylserine (PS), cardiolipin – and are sometimes supplemented with cholesterol for added stability. The proportions of the various lipids in the bilayer are set by dissolving the pure lipids in chloroform/methanol, mixing in desired proportions, evaporating the solvent with a stream of nitrogen and then re-dissolving the mixed lipids in decane.

The first attempts at reconstituting native ion channels into planar lipid bilayers were made by adding cell membrane extracts or partially purified membrane proteins into the aqueous solutions. Increases in electrical conductance were noted, often followed by breakage of the membrane; these effects were often due to adsorption of protein onto the bilayer and a generalized non-specific disruption of the membrane associated with increased leakage of current. Some success was achieved by adding membranes, membrane proteins or membrane extracts directly to the lipid-forming solution. Subsequently, techniques were developed for fusing vesicles, either native vesicles isolated from cell membranes or, alternatively, vesicles reconstituted with specific ion channels, into the planar lipid bilayer (see Miller, 1986, 1987). Tip-dipping is an alternative technique involving dipping the tip of a micropipette into a pure lipid film twice to form a bilayer covering the tip of the pipette so as to form a tight electrical seal, with a resistance of 1–5 GΩ (1 GΩ = 10^{15} Ω). Tip-dipping improves the time resolution and reduces noise due to the smaller area of membrane that is being examined; this technique allows the study of asymmetric bilayers and does not require solvents if the monolayers are formed from dried lipids (Coronado and Latorre, 1983).

The planar lipid bilayer technique is an excellent method for studying the transport kinetics of lipid-soluble ionophores. With planar lipid bilayers, one can easily vary the membrane lipid composition and also change the solutions or add reagents on either side of the membrane. Purified membrane channels may be studied apart from the regulatory mechanisms of intact cells and the resultant information should complement that obtained from

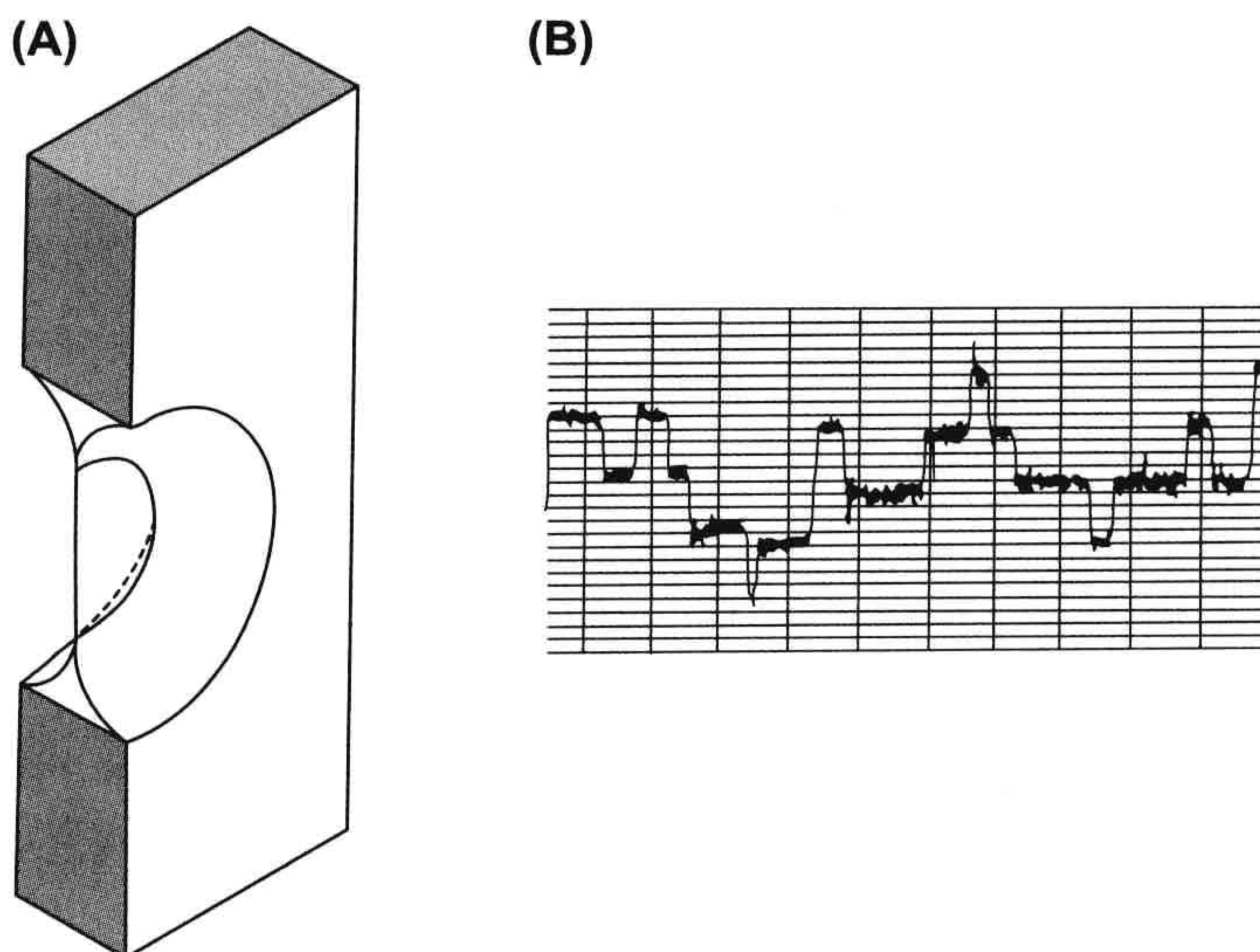


FIGURE 4.1 (A) Septum with planar lipid bilayer. (B) Traces showing currents through four dimeric gramicidin channels associating and dissociating in a black lipid membrane, as determined in the author's laboratory.

patch-clamp studies of intact cells. Planar lipid bilayers can also be used as an assay for channel purification. The planar lipid bilayer technique has several disadvantages. One is that the membranes tend to break. Once observed, the channels may disappear during the period of observation by diffusing into the thick annulus around the bilayer. The organic solvent, when present, may alter the properties of ion channels. The increases in conductance that are detected may not necessarily be physiologically relevant because the conductance properties may change during isolation of the vesicles or during purification of the channels and the conductances themselves may originate from small amounts of impurities or from contaminating cells. Some channels incorporate into bilayers more easily than others, so there may be long periods of time when nothing happens and the channel ultimately studied may not be the channel that was desired to be studied.

IV. ION CHANNEL PROPERTIES IN PLANAR LIPID BILAYERS

Studies of ion transport through channels in planar lipid bilayers revealed that ion channels are characterized by high transport rates and low temperature coefficients. Observations of single ion channels show that the current passing through a channel is on the order of picoamps (10^{-12} A). In order to convert 1 pA to the flux J in ions/s, note that the flux through a channel can be estimated from the single channel current i (C/s), using Avogadro's number N_A (ions/mol), the Faraday constant F (C/eq) and the ionic valence z (eq/mole).

$$J = \frac{iN_A}{Fz}$$

So for 1 pA of current carried by a univalent ion, we have:

$$J(ions/s) = \frac{(10^{-12}\text{C/s})(6 \times 10^{23}\ \text{ions/mol})}{(9.6 \times 10^4\ \text{C/eq})(1\ \text{eq/mol})}$$
$$= 6 \times 10^6\ \text{ions/s}$$

or 6 million ions/s. By comparison, enzymes and membrane transporters that are not ion channels have turnover rates that are less than 10^5/s. For example, the Na^+,K^+-ATPase pumps at a maximal rate of about 100 ions/s. The fastest non-channel transporter is the Cl^--HCO^{3-} exchanger of red blood cells, which has an exchange rate of 10^4 ions/s at 25°C. The enzymes carbonic anhydrase and acetylcholinesterase have turnover rates of about 10^5/s. Thus, ion channels typically show high transport rates, one to several orders of magnitude faster than the fastest enzymes or non-channel transporters.

Ion channels were also found to have low temperature coefficients. Q_{10} is defined to be the change in the rate of a reaction when the temperature is increased by 10°C. Hodgkin and Huxley found that Q_{10} for Na^+ and K^+ currents in squid axon is 1.2—1.4, which is comparable to that for unrestricted diffusion of ions in free solution, a finding consistent with these ions moving through ion channels in nerve membranes. From thermodynamics, the Q_{10} is related to the enthalpy of activation for the reaction. The Q_{10} for Na^+ and K^+ currents in squid axon corresponds to an enthalpy of activation of only 5 kcal/mol. Enzymes and non-channel transporters have a Q_{10} of 3—4 or higher, corresponding to higher enthalpies of activation.

V. GRAMICIDIN

One of the best-studied ion channels in planar lipid bilayers is gramicidin, an antibiotic synthesized by *Bacillus brevis* against Gram-positive bacteria (hence the name). Gramicidin is commercially used as a topical bacteriostatic agent. The primary sequence of gramicidin A is a linear pentadecapeptide consisting of 15 alternating D- and L-amino acids. Natural sequence variations occur at position 11 with substitution of Trp with Phe (gramicidin B) or Tyr (gramicidin C). The natural mixture is termed gramicidin D and contains about 80% gramicidin A. All of the amino acids in gramicidin are hydrophobic with no free charges. Gramicidin is thus virtually insoluble in water. Both end groups are blocked: the N-terminal valine (the head) is blocked by a formyl group; the C-terminal tryptophan (the tail) is blocked by an ethanolamine. In membranes, the peptide chain is wound in a β-helix with a pore right down the central core of the molecule (Fig. 4.2). Carbonyl and imino



FIGURE 4.2 Space-filling model of gramicidin. *(From Urry, D.W. (1972) A molecular theory of ion-conducting channels: a field-dependent transition between conducting and nonconducting conformations. Proc Natl Acad Sci USA, 69, 1610-1614, with permission.)*

groups of the peptide bonds line the pore. All amino acid side chains extend away from the pore into the membrane lipid. The β-helix is stabilized by −NH ··· O− hydrogen bonds extending parallel to the pore axis. The aqueous pore is about 25 Å long and 4 Å in diameter. Gramicidin assumes different conformations in organic solvents; the double helical structure deduced from spectroscopic studies does not pertain to the channel conformation in membranes. The conducting pore is formed by a head-to-head dimer linked transiently by six hydrogen bonds. Evidence for a head-to-head dimer is that chemical modifications at the N-terminus (the head) drastically affect channel formation, whereas similar modifications at the C-terminus (the tail) do not. With fluorescent analogs of gramicidin, it was possible to measure simultaneously the conductance and the concentration of gramicidin in the membrane. The conductance was proportional to the square of the gramicidin concentration, and the equilibrium constant for dimerization was determined (Veatch et al., 1975). Since gramicidin is synthesized non-ribosomally in vivo and contains D-amino acids that are not normally genetically coded, site-directed mutagenesis using recombinant DNA methods is not possible. Chemical synthesis has permitted alterations of the primary sequence for studies relating chemical structure to ion transport function.

Hladky and Haydon (1972) first observed single-channel conductances with gramicidin in planar lipid bilayers (see Fig. 4.1B for an example). The channel lifetimes are on the order of a second (compared to ms for Na^+ channels). With symmetrical 0.1 M NaCl, the single-channel current is 1.0 pA at 200 mV, corresponding to a single-channel conductance of 5 pS and a flux of 6.3×10^6 ions/s. The high flux is consistent with a channel mechanism. The highest conductance so far reported is 107 pS at 23°C with 3 M RbCl solutions in a neutral membrane made from glycerylmonooleate-hexadecane mixtures. The mean single-channel lifetime depends on lipid dynamics. For example, channels in thicker membranes, where pinching of the membrane may be required for dimer formation, have shorter lifetimes. Greater interfacial tension shortens channel lifetime.

Despite the absence of fixed negative charges in the pore, the gramicidin channels are cation selective (Myers and Haydon, 1972). The permeability ratios are determined from bi-ionic potentials, whereas the conductance ratios are determined in symmetrical salt solutions. The channels are ideally selective to cations. With a gradient of monovalent chloride salt, the reversal potential equals the Nernst potential for the cation, implying that the permeability to Cl^- is negligible. The channel is also impermeant to divalent cations. The selectivity order corresponds to Eisenman's sequence I, indicative of a weak field strength interaction between the pore and the ions.

The selectivity for K^+:Na^+ is only about 4:1 – much less than that of the delayed rectifier K^+ channel (20:1 to 100:1), which is primarily responsible for resetting the resting potential of nerve and muscle following activation, and very much less than that of the carrier valinomycin (more than 1000:1).

The gramicidin channel is blocked by divalent cations (e.g. Ca^{2+}, Ba^{2+} and, to a lesser extent, Mg^{2+} and Zn^{2+}). These ions probably block by binding near the channel mouth and occluding entrance into the channel. Flicker block may be observed with iminium ions; this transient block is thought to result from transient association of these ions with the channel wall during permeation.

Passage of ions or water through gramicidin is by means of *single-file transport*. The high proton conductance, and the known geometrical dimensions of the pore, suggest that the pore is filled with a continuous column of hydrogen-bonded water molecules (2.8 Å). The diffusive water permeability through gramicidin in bilayers has been measured with tracers and is about 10^8 water molecules per second at low ionic strength. Water permeation is probably by means of a Grotthus, or "hopping" mechanism (see Chapter 1). The pore diameter is too small to permit passage of urea (5 Å diameter) or larger non-electrolytes. Consequently, a *streaming potential* develops when non-electrolyte is added to the salt solution on one side of the bilayer to make an osmotic gradient. In another type of study, an *electro-osmotic* volume flow occurs when an ionic current is passed across the membrane. For single file transport, the number N of water molecules in the channel is obtained by dividing the water flux ϕ_w (molecules/s) by the ion flux J (ions/s):

$$N = \frac{\phi_w}{J}$$

For gramicidin channels, the number N of water molecules in the pore is 5–6. Quantitative analysis of streaming potentials and electro-osmosis indicates that an ion passing through a gramicidin channel drags with it a column of about six water molecules in single file.

The channel is too narrow for water molecules to slip past each other; nor can ions and water molecules pass each other in the single-file part of the channel. However, sodium ion occupancy does not depress water permeability. The water permeability of a channel at high $[Na^+]$, when the channel always contains a sodium ion, is essentially the same as that of a channel at low $[Na^+]$, when the channel never contains a sodium ion. Thus, water can pass the sodium ion somewhere in the channel, presumably near an ion-binding site at the end of the channel.

The single-channel conductance for sodium increases as a function of Na^+ concentration, but then saturates at around 1 M NaCl. Half-maximal conductance is reached at 0.31 M NaCl, at which concentration half the channels have

one Na^+ ion and half are empty. The curve of conductance g versus $[Na^+]$ fits a single-ion occupancy model, given by:

$$g_{Na} = \frac{g_{max}[Na^+]}{C_{1/2} + [Na^+]}$$

where $C_{1/2}$ is the concentration of Na^+ that gives half-maximal conductance. The single-ion occupancy model indicates that an ion-binding site, or energy well, exists near the end of the channel. Since the dimeric structure is symmetrical, there must be two binding sites, one at each end, but only one at a time is occupied by sodium. Additional compelling evidence for single-ion occupancy for sodium is that the flux ratio equation is satisfied at all sodium concentrations ranging from 0.1 to 5 M. Given that single-file transport occurs, a net flux in one direction would inhibit the unidirectional flux in the opposite direction, thus producing deviations from the flux ratio equation if the two Na^+ binding sites were simultaneously occupied. Consequently, double occupancy must not occur for Na^+. These two lines of evidence imply that there is never more than one sodium ion at a time in the gramicidin channel (Sandblom et al., 1977).

The dehydration energy for ions is of the order of 100 kcal/mol; the selectivity sequence indicating a weak field strength interaction with the pore suggests that ions do not dehydrate during passage through the gramicidin pore. The hydration shell of water around the permeating ions is partially replaced by hydrophilic groups lining the channel wall. The dielectric constant is lower in the middle of the pore than near the ends of the pore. Thus, the electrostatic energy of the ion in the middle of the pore is greater than at either end of the pore. The actual flux of Na^+ at high $[Na^+]$ is within a factor of 5 of the maximal possible flux of Na^+, given the water permeability of an ion-free channel. This means that there is no significant electrostatic energy barrier to Na^+ movement through the channel. The rate of Na^+ transport is largely determined by the necessity for six water molecules to be moved along with the ion. Thus, two energy wells near the ends of the channel are separated by a low-energy barrier (or a series of small barriers) in the middle of the channel. Strict single filing of water and ions occurs between the two wells, whereas water can pass a sodium ion sitting in either well. The kinetic equations describing single-file transport are complex and beyond the scope of this text (see Finkelstein and Anderson, 1981).

Cation transport through gramicidin also involves channel motions, subconductance states and channel flickering. The gramicidin channel is not rigid but, instead, motion of the peptide appears to be essential to its function. Solid-state nuclear magnetic resonance (NMR) measurements of ^{15}N-labeled Ala 3 and Leu 4 indicate rocking motions of $\pm 8°$ and $\pm 15°$, respectively, for these sites in the absence of ions. Molecular dynamics simulations confirm local distortions in gramicidin structure during ion transport. Peptide rotation is not necessary for function since the channel is active in gel-phase lipid. Subconductance states, or "mini-channels", are frequently observed as an intermediate in the opening and closing of normal channels. These may constitute from 5 to 40% of the channel events in a single-channel recording, with lifetimes similar to those of normal gramicidin channels. The low-conductance state may correspond to less common side-chain conformations with altered coordinating ability in the conducting pore. Channel flickering to a low-conductance state with lifetimes ranging from 20 μs to about 1 ms is also observed. Rapid flickering may correspond to a state in which the dimer is partially dissociated. An increase in membrane thickness increases the frequency of these low-conductance states. This rather detailed analysis of ion channel permeation through gramicidin channels in planar lipid bilayers provides some basis for understanding ion permeation through native ion channel proteins in cell membranes.

BIBLIOGRAPHY

Coronado, R., & Latorre, R. (1983). Phospholipid bilayers made from monolayers on patch-clamp pipettes. *Biophys J, 43*, 231–236.

Ehrlich, B. (1992). Planar lipid bilayers on patch pipettes: bilayer formation and ion channel incorporation. *Meth Enzymol, 207*, 463–470.

Finkelstein, A. (1974). Bilayers: formation, measurements, and incorporation of components. *Meth Enzymol, 32B*, 489–501.

Finkelstein, A., & Andersen, O. S. (1981). The gramicidin A channel: a review of its permeability characteristics with special reference to the single-file aspect of transport. *J Memb Biol., 59*, 155–171.

Hille, B. (2001). *Ion Channels of Excitable Membranes* (3rd ed.). Sunderland, MA: Sinauer Associates Inc.

Hladky, S. B., & Haydon, D. A. (1972). Ion transfer across lipid membranes in the presence of gramicidin A. I. Studies of the unit conductance channel. *Biochim Biophys Acta, 274*, 294–312.

Labarca, P., & Latorre, R. (1992). Insertion of ion channels into planar lipid bilayers by vesicle fusion. *Meth Enzymol, 207*, 447–463.

Miller, C. (1986). *Ion Channel Reconstitution*. New York: Plenum Press.

Miller, C. (1987). How ion channel proteins work. In L. K. Kaczmarek, & I. B. Levitan (Eds.), *Neuromodulation. The Biochemical Control of Neuronal Excitability* (pp. 39–63). New York: Oxford University Press.

Montal, M., & Mueller, P. (1972). Formation of bimolecular membranes from lipid monolayers and a study of their electrical properties. *Proc Natl Acad Sci USA, 69*, 3561–3566.

Mueller, P., Rudin, D. O., Ti Tien, H., & Wescott, W. C. (1963). Methods for the formation of single bimolecular lipid membranes in aqueous solution. *J Phys Chem, 67*, 534–535.

Myers, V. B., & Haydon, D. A. (1972). Ion transfer across lipid membranes in the presence of gramicidin A. II. The ion selectivity. *Biochim Biophys Acta, 274*, 313–322.

Sandblom, J., Eisenman, G., & Neher, E. (1977). Ionic selectivity, saturation and block in gramicidin A channels: I. Theory for the

electrical properties of ion selective channels having two pairs of binding sites and multiple conductance states. *J Memb Biol, 31*, 383–417.

Veatch, W. R., Mathies, R., Eisenberg, M., & Stryer, L. (1975). Simultaneous fluorescence and conductance studies of planar bilayer membranes containing a highly active and fluorescent analog of Gramicidin A. *J Mol Biol, 99*, 75–92.

Woodbury, D. J., & Hall, J. E. (1988). Role of channels in the fusion of vesicles with a planar bilayer. *Biophys J, 54*, 1053–1063.

Woodbury, D. J., & Miller, C. (1990). Nystatin-induced liposome fusion. A versatile approach to ion channel reconstitution into planar bilayers. *Biophys J, 58*, 833–839.

Wooley, G. A., & Wallace, B. A. (1992). Model ion channels: gramicidin and alamethicin. *J Memb Biol, 129*, 109–136.

Chapter 5

Cell Structure

Michael S. Forbes

Chapter Outline

I. INTRODUCTION

Vertebrate cells (and to a degree, cells of any type) are variations on basic themes, namely the classes of substructures of which the cells are composed. While certain disciplines of biomedicine can be engaged in without recourse to cell structure, others such as pathology are vitally dependent upon this knowledge. Though this chapter, formerly entitled "Ultrastructure of Cells", has appeared in several versions of this book, the editor and publishers have made their wishes clear, that the book is now – rather than being a "Sourcebook" – intended rather to serve as a *textbook.* Because of this, I have broadened the title to "Cell Structure" so as to provide a more useful context. Cell structure cannot be considered in practical terms without considering the various techniques that belong to *microscopy.* Since the student involved in biomedical study and practice is far more likely to have access to the so-called light (as opposed to electron) microscopes and, since the electron microscope – in addition to its cost, availability and difficulty of operation – has some severe limitations, I have included pictures of cells obtained from both sources. Since examples of many of the different cell components are present in pictures throughout the chapter (see, e.g. Fig. 5.7), only a minimal attempt has been made to make a close correlation of plates of figures with the individual sections on Nucleus, Mitochondria, etc.

II. TECHNIQUES

What follows is intended to acquaint the reader with just how structure can be documented. The potential investigator will benefit wherever possible by availing him/herself of the opportunity of actually observing and, when possible, performing the procedures described below, in order to understand the process, all the better to interpret the results.

First some basic facts: light microscopes depend on a beam of light, passing through a specimen, to form an image. Depending on the source of light and other mechanical features, light microscopes include instruments known variously as "bright-field", fluorescent, differential-interference-contrast (a.k.a. "Nomarski") and confocal scanning microscopes, among others. Since the beam of light contains a range of wavelengths, different stains interact with the light to generate images that have different colors which correspond to different cell types and intracellular structures. Transmission-type electron microscopes use a beam of electrons that pass through the specimen, which is kept in a vacuum, to generate what amounts to a "shadowgram", since more dense regions deflect the electrons and less dense ones allow the electrons to pass through. This results in a grayscale image, since by and large the beam of electrons has a limited wavelength and thus does not generate colors (micrographs – which is the

Cell Physiology Sourcebook. DOI: 10.1016/B978-0-12-387738-3.00005-6

term for pictures made with a microscope – from electron microscopes that appear in color in some magazines have been artificially colored). Those with some experience with microscopes will note that I have ignored the so-called "dissecting" microscope which, although it uses light as illumination only shows the surface of, say, an insect or an isolated organ; so too I have not spoken of the scanning electron microscope, or SEM, which produces much the same sort of picture as the dissecting light microscope (albeit, again, in shades of black and gray), since it either bounces electrons off a surface or, more commonly, generates secondary electrons just below the surface to form an image.

All that established, let us compare only microscopes that use a transmitted beam (i.e. one that passes through a specimen). It turns out that the preparation techniques for light microscopes (LMs) and transmission electron microscopes (TEMs) have a great deal in common. Though in science there are always exceptions (a phrase you commonly hear is "*It's not that simple, though*"), *in general*, to view something in a microscope one has to: (1) *preserve it* (the term "fix" is usually used, implying immobilization by techniques such as freezing, immersing in chemicals, or even heat-inactivating ["cooking" for lack of a better term]); (2) *dehydrate it* so as to make it compatible with anhydrous materials such as paraffin or plastic; and (3) *infiltrate it* ("embed") with those media. This last step is to stabilize the specimen (for our purposes, let us say a piece of brain, liver or kidney) so that it can be cut ("sectioned") into thin slices ("sections"). Such sections range from one micrometer (abbreviated as "μm" and equivalent to roughly four one hundred-thousandths of an inch) in thickness up to 50 μm or so for LM examination, and generally in the range of 0.05–0.1 μm (known as *ultrathin* sections) for the TEM. Obviously, the μm to inch conversion is unwieldy; one can readily estimate sizes in microscopic images by using a couple of rules of thumb: (1) in the LM, the practical limit of resolution (meaning essentially what one can clearly distinguish as a separate structure) is about 1 μm; (2) mitochondria, when they can be resolved, are usually on the order of 1–2 μm in size (see Figs. 5.2, 5.4A, 5.5A, 5.6C, 5.7, 5.9, 5.12); also, the contractile units ("sarcomeres": see Figs. 5.6C, 5.10) in skeletal and cardiac muscle are around 2 μm in length.

The purpose of having sections is...? ...Simply to have the specimen thin enough so that the imaging beam can pass through it! This necessity leads to a basic limitation of microscopy: only a sample, a mere slice of a specimen is being examined, which can lead to erroneous conclusions about three-dimensional relationships. Also, while on the subject, interpretation of microscopic images should be recognized as an exercise in "making dynamic conclusions from static entities". In any event, for LM specimens, paraffin – similar to the stuff some of our grandmothers and great-grandmothers may have used to seal their jars of home-made jam and jelly – is used. Specimens embedded in paraffin can be readily sectioned with a razorblade, though usually dedicated "knives" are used, designed to fit into a cutting machine – a "microtome" – that can be adjusted to cut sections of consistent thickness. These sections are floated onto glass microscope slides, usually about 1"×3" (2.54×7.62 cm) in size. To process the sections further, however, the paraffin in them must be removed with some organic solvent such as xylene, and then gradually *rehydrated* – brought back to water – to stain them. This deparaffinization and rehydration serves two purposes: it removes the paraffin, which would interfere with the passage of the LM's light beam, and it renders the sectioned material – the liver, heart, kidney, whatever – compatible with a wide variety of stains (including immunohistochemical reagents), which are prepared as aqueous solutions and would not react with the material if it were still in paraffin.

TEM specimens also are cut into extremely thin slices with some sort of sharp blade, but in order to have a hard enough embedment, some sort of plastic is used to infiltrate the specimen. Most often this is an epoxy-type plastic, somewhat similar to the two-component glue (resin and catalyst) that one uses in "civilian" life. Here there is seen a substantial difference between LM and TEM preparation, though: for the TEM, the embedding plastic is *not* removed from the specimen, since the section – which is cut either with a knife edge made of glass or diamond, and affixed onto a 3-mm circular piece of metallic mesh known as a *grid* – has to withstand imaging within a vacuum chamber, through which there passes an electron beam of perhaps 100 000 volts in penetrating/imaging power. The "ultrathin" sections on their grids, rather than being stained with colored dyes, instead are contrasted with heavy metals (including osmium, uranium and lead), which enhance details of the shadowgram spoken of earlier, in particular their unit membranes (see below). The electrons are deflected or let pass at various angles, depending on the density of the parts of the section, and expose an image either on a piece of film in the microscope or, more commonly these days, the electron pattern is converted into a digital image (as also is now routinely the case with the LM).

So as a result of these processes, we can visualize either *structure* as seen through the LM on a glass slide, or *ultrastructure* (meaning literally "beyond structure"; an unfortunate term, but one that has nevertheless become firmly embedded in the literature) in the TEM, on a specimen grid. Structure and ultrastructure remain compatible, though, with limitations at both ends of the spectrum: the images in Fig. 5.1 are of the same type of structure (rat kidney glomerulus) and the specialized nature and specific appearance of the various cells can be appreciated in one

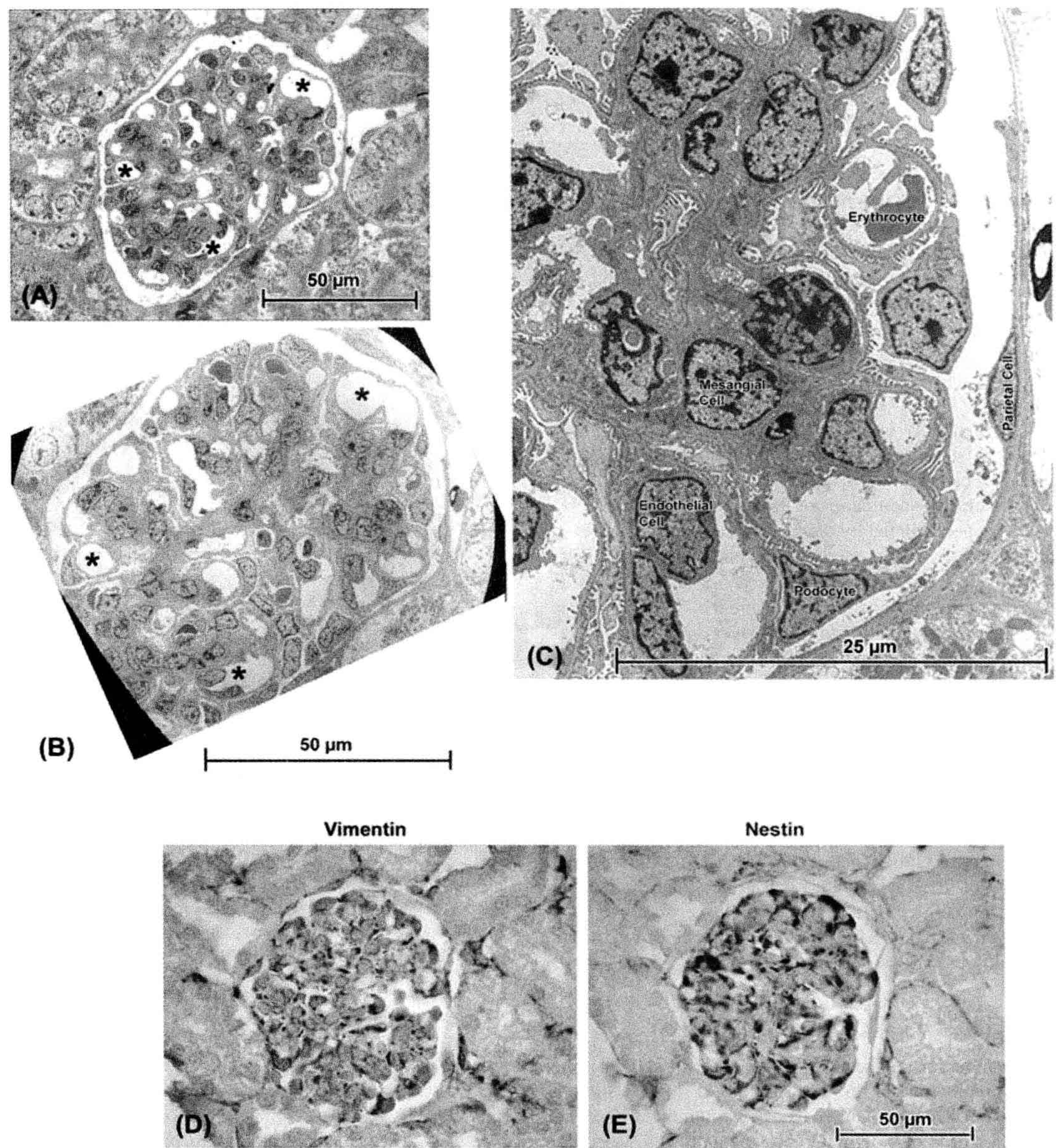


FIGURE 5.1 (A) and (B) are consecutive serial sections, taken with a diamond knife on an ultramicrotome, of a glomerulus in rat kidney. The semithin section ((A): ca. 0.25 µm thick) was cut immediately before the ultrathin section ((B): ca. 900 Å, i.e. 0.09 µm thick) and there is close correlation between such features as the pattern of capillaries (* in both micrographs). An enlarged view of the electron micrograph (C) identifies examples of the various cell types found in glomeruli. For most purposes, the ultrathin section – which required considerably more effort to document than the semithin – does not provide any special advantage to the investigator unless high-resolution details such as podocyte processes, endothelial fenestrations, cytoskeletal filaments or intercellular junctions are specific subjects of interest. (D) and (E) are serial consecutive paraffin sections in which immunohistochemical staining is readily accomplished: here the podocytes show reactivity (dark staining) for both vimentin, a structural protein, and nestin, a protein which under normal conditions is restricted to these cells.

way or another in each micrograph, regardless of its origin. By combining the techniques (plastic embedding and serial sectioning with a diamond-edge for both LM and TEM: Figs. 5.1A and B, respectively) bring the two microscopic images into even closer correlation. An important thing to note is that, at the enlargements (magnifications) shown, which are low for a TEM but high for an LM, the LM gives just about as much general information as the TEM! Kidney structure, which I have been studying for the past couple of decades, can be fantastically complicated when viewed in a TEM, since the various cylindrical structures, including epithelial tubules and blood vessels that make up the majority of the organ, weave in and out of section, and particularly so in ultrathin sections (Fig. 5.2). I have found that so-called "semithin" plastic sections – on the order of a quarter of a micrometer in thickness – bridge the gap between the LM and TEM nicely (Fig. 5.1). It is somewhat ironic, however, to remember that many kidney ailments depend absolutely on the TEM and thin sections for their diagnosis, since structures such as immune deposits are best appreciated there. Certainly, one must choose one's goals carefully when choosing to do electron microscopy, but this is necessitated by the presence of many features of cells that are either poorly resolved or are practically invisible with light microscopy (Fig. 5.8 demonstrates an example of the former situation, where the TEM is required to make positive identification of autophagic bodies).

Even though I have described microscopy largely in terms of slices of tissue, it has been necessary to diverge from this in several figures (Figs. 5.4B, 5.4C, 5.5B, and 5.11B,C) to illustrate an important concept of unit membrane structure by means of the procedure known as "freeze-fracture", in which a cutting action is retained in terms of breaking a specimen at low temperature and under vacuum, with subsequent deposition of a carbon and metal film to make a replica that demonstrates the different sides ("faces") of these membranes that in large part define and limit many cell components (including the plasmalemma, nuclear membrane, Golgi and endoplasmic reticulum, mitochondria and lysosomes).

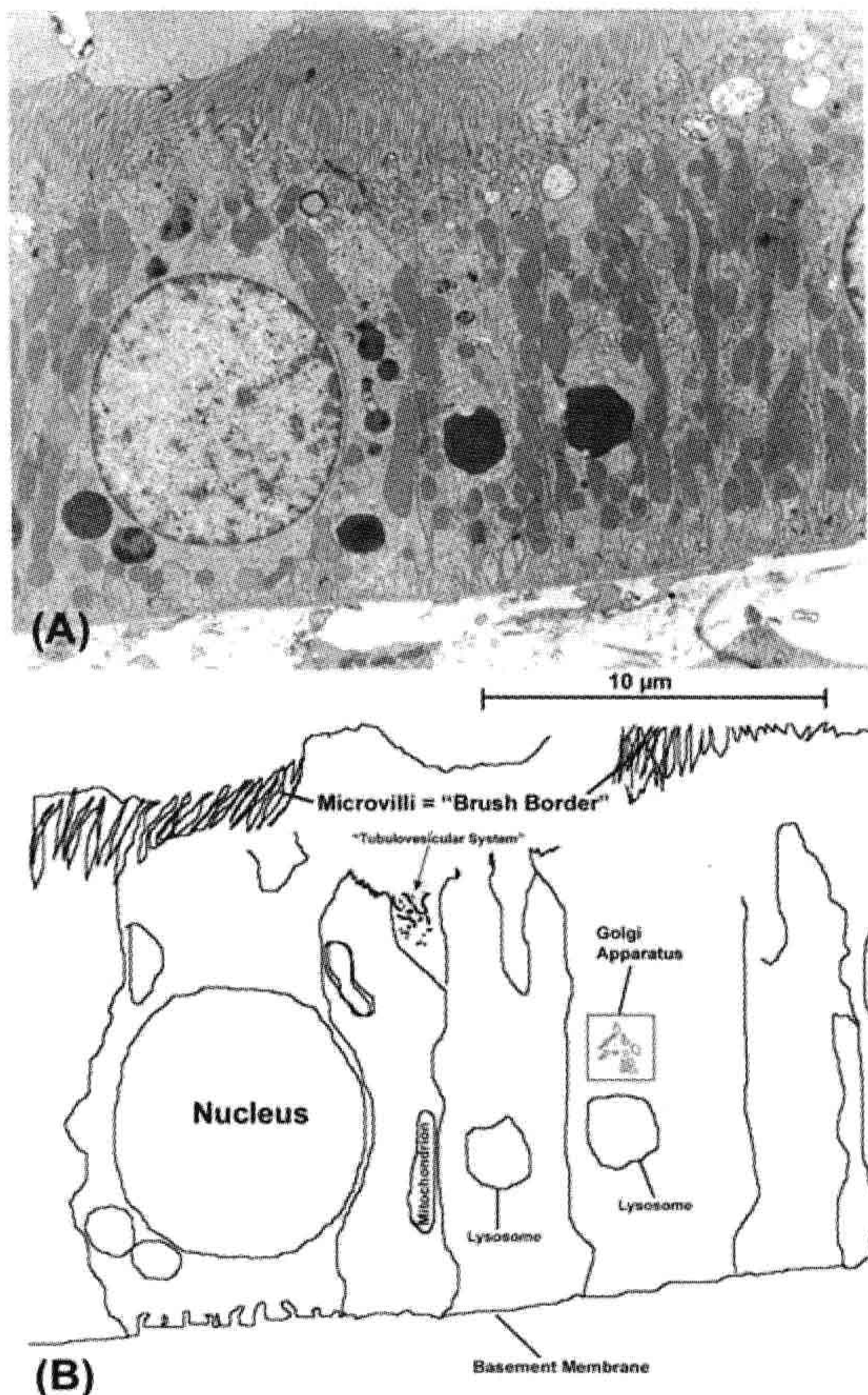


FIGURE 5.2 (A) Though a "typical" cell exists only in idealized diagrams, one type that is often used to illustrate general structural features is the epithelial cell of kidney tubules (here shown in a rat proximal tubule). In (B), a tracing of some of the cells and their organelles is shown. These cells exhibit the "polarity" that is a consistent feature of epithelial cell layers, with apical specializations ("brush border", consisting of tightly-packed thin cell-membrane extensions known as microvilli) that provide the cell tip with a greatly enlarged surface area for absorption and release and a basal reinforcing layer of extracellular material on which the cells sit ("basement membrane").

III. CELL THEORY

The appreciation of the very existence of individual cells did not come about in the form of a linear, smooth progression. Despite Robert Hooke's often-cited observations (ca. 1665) of individual units (actually cell walls; the living cells were long gone) in thin sheets of cork, aided by one of the earliest microscopes (he likened the units to cubicles [L. "cellula: small rooms"] occupied by monks or other sorts of prisoners, thence the term "cells"), centuries later the cellular nature of some tissues was still questioned. Though in the late 1830s Matthias Schleiden and Theodor Schwann had proposed that most tissues were composed of individual cells, toward the end of the 19th century the *reticular theory* of Joseph von Gerlach and Camillo Golgi came to stand as an exception. This posited that nervous tissue was a *syncytium*, i.e. a system possessing multiple nuclei but having its cell substance continuous through its entire network. Opposed to reticular theory was the *neuronal theory* of Santiago Ramon y Cahal, whose exquisite staining techniques and careful microscopic renderings demonstrated neurons to be individual entities (the accuracy of his drawings has in fact been confirmed in modern times, by examination of his original preparations

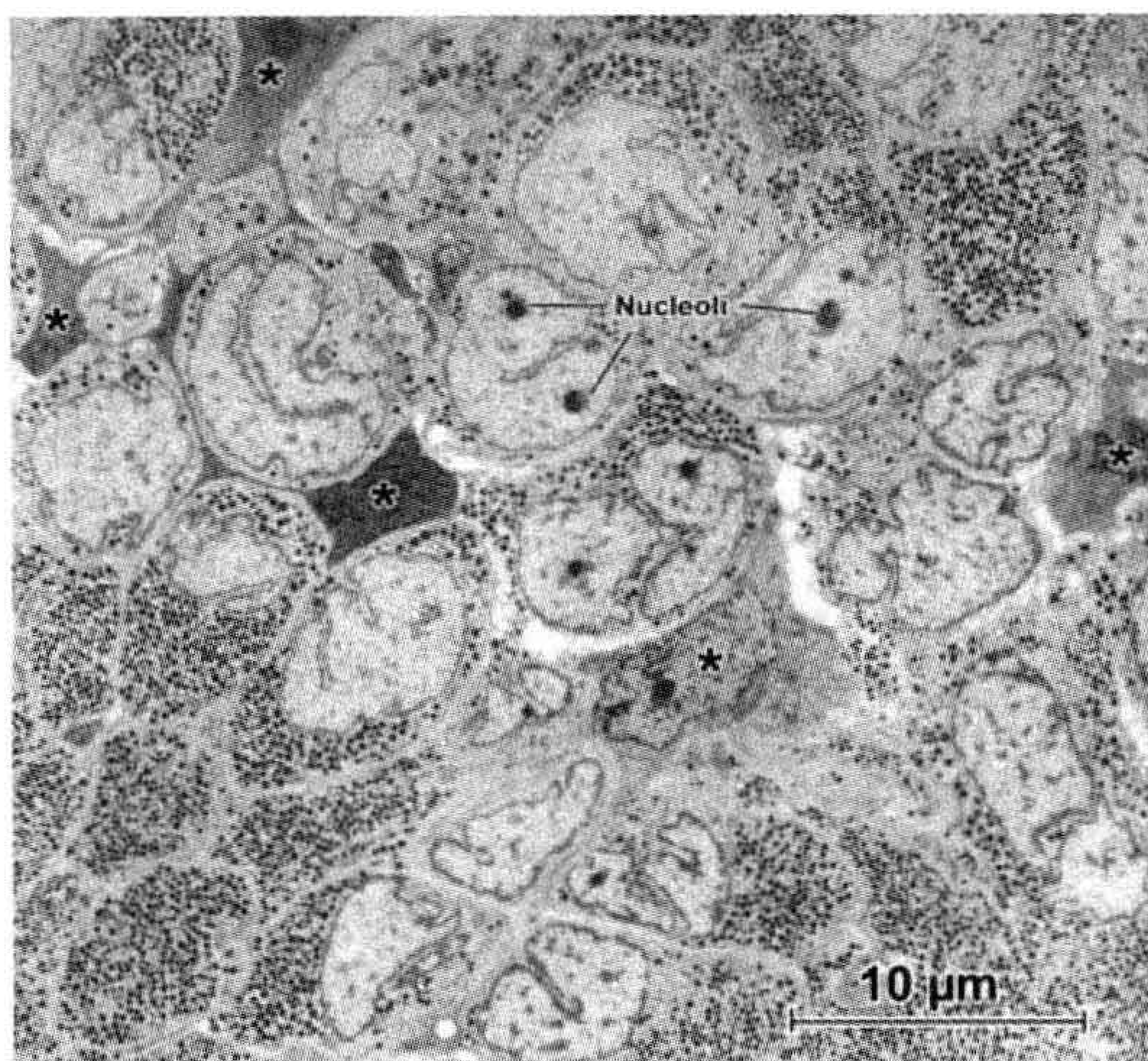


FIGURE 5.3 Pituitary gland. Low magnification ("survey") transmission electron micrograph shows the dense concentrations of granules that contain the hormones produced by the secretory cells. Note the elaborate profiles of the nuclei (several nucleoli are indicated by Nuc). A supporting framework of "stellate" cells (examples at *) is recognizable because of their extended cell processes. It is instructive to point out what this picture does not show. Though the glial-like stellate cells are evident because of their opaque cytoplasm and lack of secretory granules, on the basis of their ultrastructure, the granulated cells themselves cannot be identified as to their specific hormonal content; for this, additional coordinated approaches are needed, including additional characterization and measurements of the granules at higher magnification, correlation of precise location of these cells within the whole gland and histo- and immunocytochemical staining both at the LM and TEM levels, in addition to biochemical analysis to confirm the presence of the hormones in question.

and three-dimensional reconstruction from them by the confocal scanning light microscope).

While the battle over nerve structure was carried out in Europe, an international controversy developed in the case of the heart, with cellular theory being espoused by the camp of Zimmerman in Germany (among others) and the contrasting view – namely that heart muscle was a true syncytium – being defended by Harvey Ernest Jordan in America (Jordan, incidentally, was the first dean of the University of Virginia School of Medicine, where this review is being written). In truth, both nervous tissue and cardiac muscle *behave* as if they were true syncytia, with impulses being passed from cell to cell; in the case of nerve this most often happens through the intercellular contacts known as *synapses* (see Fig. 5.12C), whereas in heart, the muscle cells are held together via elaborate arrays of intercellular connections known collectively as *intercalated disks*, components of which are the basis of cell-to-cell transmission (see Fig. 5.11D).

Ultimately refinements to microscopic equipment – in particular the invention of electron microscopes – carried the day for the establishment of cell theory as valid for both brain and heart, since the actual separations between adjacent cells could finally be visualized. This did not happen until the 1950s, however, and even in the face of definitive electron microscopic evidence, some clung to the syncytial theory of heart organization into the following decade (for further review of this, see Forbes and Sperelakis, 1985).

IV. THE PLASMA MEMBRANE AS THE BASIS OF CELLULARITY

To understand the fundamental mechanisms that constitute the normal activities of any organism, it is essential to consider the structural correlates that underlie these activities. Once cell theory was established, there arose another important question which revolved around the nature of the barriers that separate cells from one another and from the surrounding environment. A major breakthrough in resolving this question was made independently by Gorter and Grendel in the 1920s and Davson and Danielli in the 1930s. The latter authors examined the behavior of phospholipids in aqueous environments and determined that the most favorable energetic configuration was a bilayer having the hydrophilic polar headgroups located at the water interface and the hydrophobic non-polar tails apposed to each other. Such a cell membrane ("plasmalemma"), formed by a phospholipid bilayer, would be impermeable to fluids and charged species, such as ions. Thus it would isolate the cell contents from the extracellular environment. It should be understood that those cell contents, specifically organelles including the Golgi complex, mitochondria and endoplasmic reticulum, are themselves composed in large part of similarly-constructed unit membranes.

Proteins were recognized as being closely associated with the phospholipid bilayer and early models proposed that they form a layer on either side of the membrane (i.e. a protein–lipid sandwich). This model remained hypothetical until the introduction and refinement of the transmission electron microscope (TEM) in the 1930s and 1940s; in the TEM, resolution was so much improved that, in properly-prepared "ultrathin" sections, all cells were bounded by a trilaminar membrane, 70 Å (=7 nm) thick that to some observers resembled a "railroad track" consisting of two darker lines separated by a relatively clear inner region (Fig. 5.4A). This structure was termed the unit membrane by J.D. Robertson in the early 1950s. It had already been recognized by Davson and Danielli that many of the proteins associated with the cell membrane were tightly attached, since they were not extracted by changing the ionic strength of the bathing solutions or even by mild detergent treatment. Thus, the notion of a phospholipid bilayer with a coating of protein had evolved, by the 1960s, into a "fluid mosaic" model proposed by Singer and Nicholson. In this model, there were both peripheral

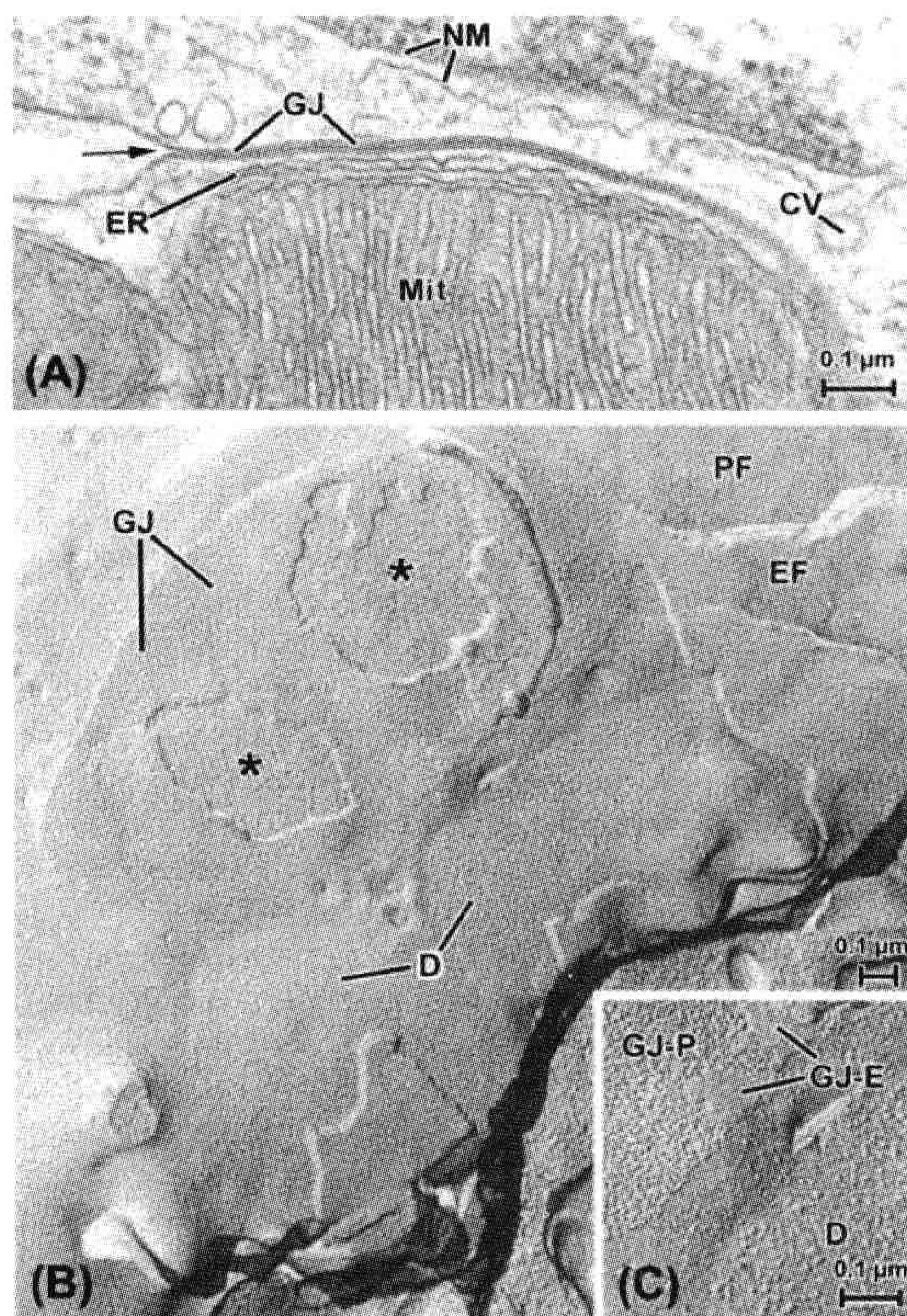


FIGURE 5.4 Unit membranes of cells. (A) Cell border formed by two cardiac muscle cells. Unit membranes are the basis of most of the structures shown here, including the double membrane of the nucleus (NM), the outer envelope and inner membrane shelves (cristae) of a mitochondrion (Mit) and several vesicular bodies, including a coated vesicle at the right of the picture (CV). The membrane-based, multilayered structure that dominates this view is a specialized adhesion known as a gap junction (GJ), formed between the two cells where the outer faces of the two cells' plasmalemmata come into close apposition. At the arrow, the relatively unspecialized cell surface membranes are clearly continuous with the membranes that form the gap junction. Note the membrane-based tubule of endoplasmic reticulum (ER) sandwiched between the mitochondrion and the gap junction. (B) and (C) show cardiac cell membranes as revealed by the technique of freeze-fracture, in which tissue is quickly frozen and broken and a thin (ca. 2–3 nm) coating of metal is evaporated onto the specimen and stabilized with a thicker carbon film (similar techniques were used to produce the replicas depicted in Figs. 5.5B, 5.11B,C). The tissue is then digested away, leaving only the metal–carbon replica of the fractured surfaces. The fracturing process specifically cleaves unit membranes to expose their inner "faces", thus showing the intramembranous particles (IMPs) that correspond to a variety of functionally important proteins. This also demonstrates the characteristic asymmetry inherent within a unit membrane; typically there is a greater density of larger particles on the P face, the face adjacent to the protoplasm (cytoplasm), whereas the E face (that closest to the "ectoplasm", i.e. the extracellular space) is characteristically smoother. Compare, for example, the regions labeled PF and EF at the upper right corner of (B). This region shows the relatively unspecialized plasmalemmas of two apposed cells (cf. the cell surface membranes in (A)). The large oval body is a gap junction between the two muscle cells, broken away in two regions (*) to expose underlying intracellular structures, probably mitochondria (a similar association is shown in the thin section in (A)). The detail shown in panel (C) shows that though this gap junction replica consists mainly of large P-face particles (GJ–P), in some areas, small regions of the junction's E face (labeled GJ–E) have adhered, which are characterized by a finer topography of pit-like depressions, into which the P-face particles fit in the intact gap junction. In (B), two smaller ovoid membrane regions (D) appear which correspond to another type of intercellular junction, the desmosome (see also Fig. 5.11). The P-face particles belonging to desmosomes (also shown at higher magnification in (C)) are larger and more coarse-appearing than those of either the gap junction or the unspecialized plasmalemma.

(or extrinsic) and integral (or intrinsic) membrane proteins. Peripheral proteins are associated with the inner and outer surfaces of the membrane, but are not anchored in it. Integral membrane proteins are actually embedded in at least one leaflet of the phospholipid bilayer (Figs. 5.4B,C) and some traverse the entire thickness of the membrane.

The fluid mosaic model was more consistent with functional studies, which clearly demonstrated that cell membranes were not totally impermeable, but rather were semipermeable. The integral membrane proteins included ion channels that acted as low-resistance pores, as well as energy-dependent pumps. This model better accounted for the establishment of ionic gradients and the influx or efflux of ions under various conditions.

As mentioned, the extrinsic proteins are membrane-associated rather than actually embedded in the lipid bilayer. The extracellular matrix exists on the outer cell surface as a layer of varying thickness, known as the basement membrane or *basal lamina*, depending on the cell type (see Figs. 5.2 and 5.7). Historically, this coating was considered to be an inert structural framework composed of collagen and elastic fibrils. Not only can the extracellular matrix act as a filtration device but, in addition, recent evidence points to a more dynamic role, with proteins such as fibronectin and laminin active in stimulating a number of cellular activities. These functions are likely mediated through interactions with intrinsic membrane proteins which, in turn, are connected to and exert influences on the extrinsic membrane proteins that form subplasmalemmal networks on the inner (cytoplasmic) surface of the cell membrane. Ultimately, signals from outside the cell may be communicated deep within the cell via the interior membrane systems and elements of the cytoskeleton and may even influence gene activity in the nucleus. In this sense, the unit membranes can be considered to represent the "nervous system" of the cell.

The contents of the cell enclosed by the plasmalemma are collectively known as the cytoplasm. The cytoplasm is not an amorphous soup, but in fact contains a number of distinct structural elements known as organelles

(by analogy to the different organs of the body). Figure 5.2A is an electron micrograph of kidney tubule epithelial cells, often considered to be a characteristic type of animal cell, with a diagrammatic representation of the same micrograph in Fig. 5.2B, where some of the organelles are shown; these serve to compartmentalize different activities of the cell, just as the organs perform different functions within the body.

V. NUCLEUS

The most prominent organelle within the cell is readily visible in the light microscope and, since it is most often located at the cell center, it came to be called the *nucleus*. The nucleus contains most of the cell's DNA and its genetic apparatus as well. Because it is the locus of the genetic programming that directs cytoplasmic synthetic activity, as well as the site at which cell division is initiated, the nucleus can be considered as the organelle that corresponds in the cell in part to the reproductive system of the body.

In most cells, the nucleus is an ovoid body, but it can assume a variety of shapes and sizes (see Figs. 5.1, 5.2, 5.3 and 5.5). Multiple nuclei are characteristic of certain cell types (e.g. skeletal myocytes). Early EM observations discovered the nucleus to be bounded by the *nuclear envelope*, essentially a double unit membrane (see Fig. 5.4A) and noted as well a dense intranuclear body, the *nucleolus* (see Figs 5.3, 5.5). The nucleus was characterized in addition by darker material (*heterochromatin*), found interspersed with the lighter euchromatin (see Fig. 5.2). Beyond these initial descriptions, the regional specializations of the nucleoplasm remain rather poorly understood. Recent studies with antibody localization of nuclear-specific proteins demonstrate the presence of domains within the nucleoplasm; these are not readily apparent even with ultrastructural inspection, but appear to be organized through attachment to the filamentous proteins of the nuclear matrix. On the basis of compartmentation of DNA polymerases and RNA splicing factors, it has been suggested that discrete domains are involved in different processes, such as transcription and translation of the genetic material.

As noted earlier, the nuclear envelope is a double bilayer. The outer membrane, often decorated with spherical RNA-containing particles called *ribosomes*, is often continuous in places with a network of cytoplasmic membranes known collectively as the endoplasmic reticulum (ER) (e.g. Fig. 5.6B). The nuclear envelope has a proteinaceous lamina at its inner surface, which is composed of cytoskeletal proteins called lamins; the major portion of the envelope is the prominent double membrane itself (see Fig. 5.4A), which is interrupted at periodic intervals by circular discontinuities, the *nuclear pore complexes* (see Fig. 5.5B,C). Detailed studies have

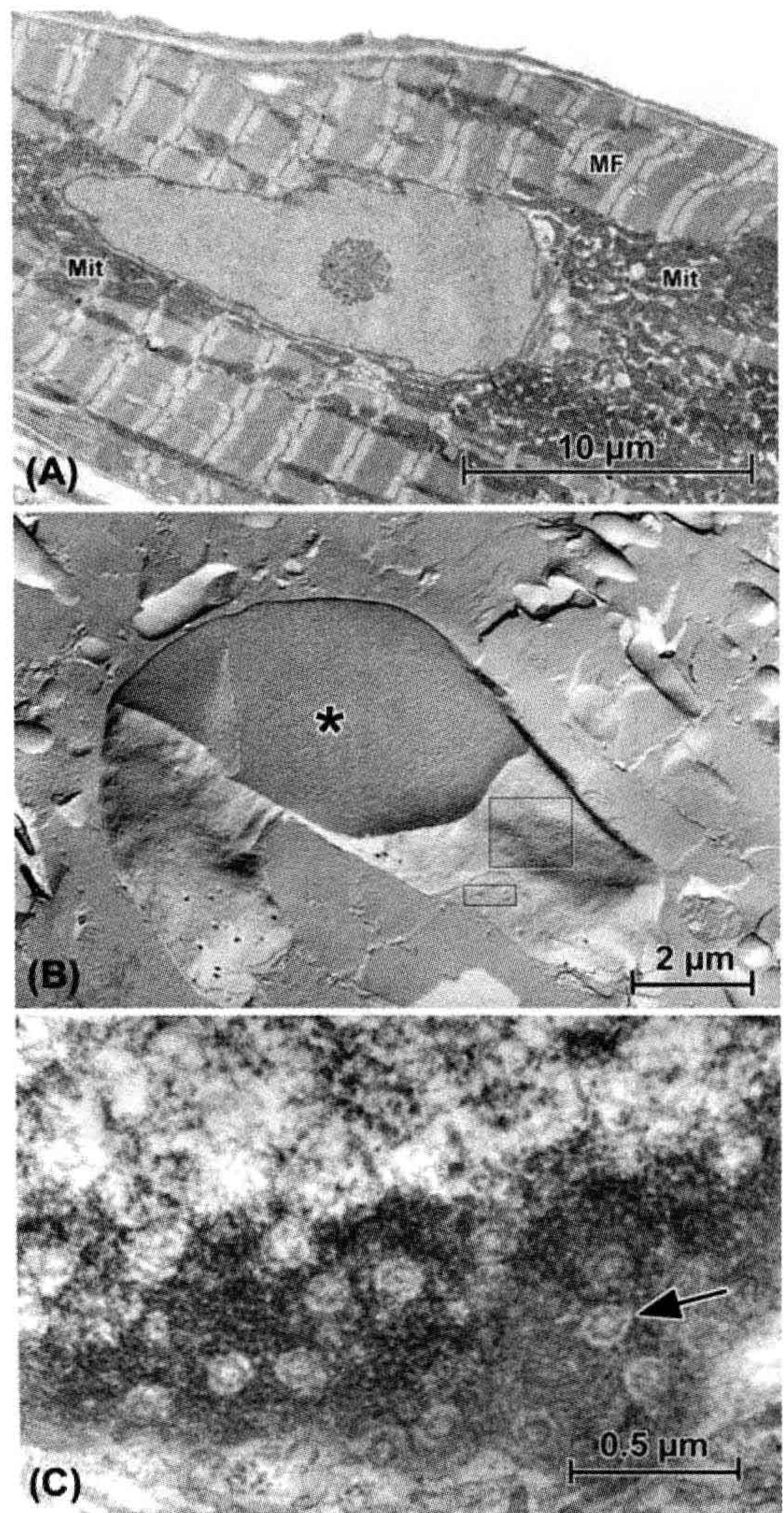


FIGURE 5.5 Aspects of nuclear structure as seen in cardiac muscle cells ("cardiomyocytes"). (A) The nucleolus is prominent within this nuclear profile. Additional characteristics of the cardiomyocyte are the interspersed arrays of myofibrils (MF) and mitochondria (Mit). (B) Freeze-fracture replica of a nucleus. The plane of fracture reveals cytoplasmic myofibrils and mitochondria (see panel (A)) and breaks through the nucleus to show the homogeneous nucleoplasm (*), then passes into the outer nuclear membrane leaflet (larger rectangle) to show nuclear pores as depressions, then into the inner nuclear membrane (small rectangle), where the pores appear as corresponding protuberances. (C) Grazing thin section of nucleus, passing through the peripheral dark heterochromatin to reveal the complex nuclear pores' substructure (arrow).

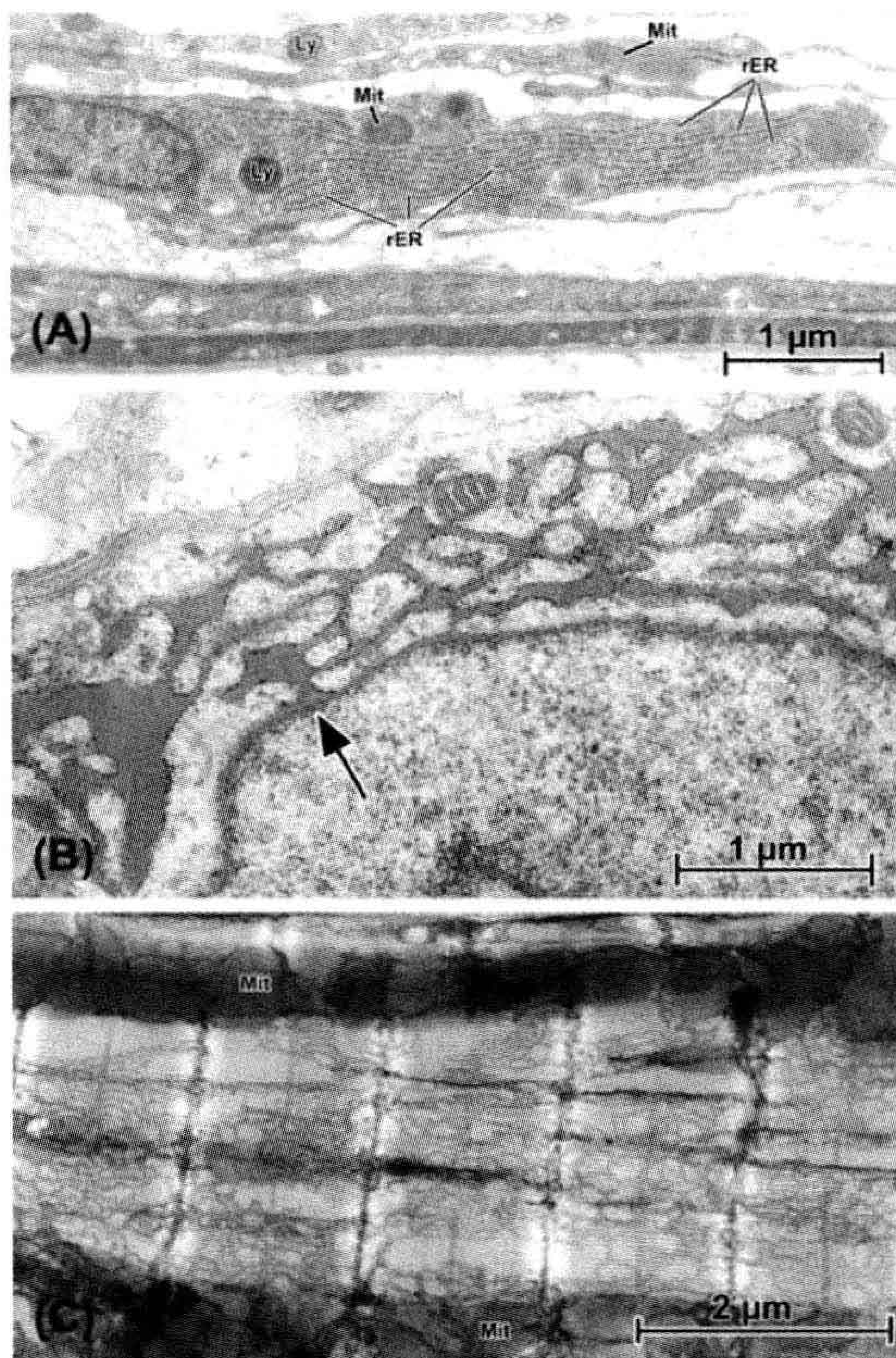


FIGURE 5.6 The variable appearances of endoplasmic reticulum ("ER"). (A) Fibroblastic cells that form the capsule layer of kidney. Each of these elongated cells is characterized by a corresponding flattened nucleus, along with limited numbers of lysosomes (Ly) and mitochondria (Mit). Filling the cytoplasm of these collagen-producing cells are parallel arrays of rough ER (rER). (B) Pituitary cell (thyrotroph) in which synthetic activity has been stimulated by removal of the thyroid gland. This induces a dramatic increase in production of thyroid-stimulating hormone (TSH) and, instead of generating storage granules (see Fig. 5.3), the rough ER expands into interconnected networks of dilated tubules and cisternae filled with freshly-synthesized hormone. Note (at arrow) the connection between the nuclear envelope and rER. (C) Atrial tissue from mouse in which the smooth endoplasmic reticulum (known as "SR" in muscle, is specifically stained by an osmium impregnation technique related to those used by Golgi and Cajal (see Cell Theory section) to contrast neurons. In this application, only the SR is darkened; by cutting relatively thick (ca. 2 μm) plastic sections for the TEM, the extent, distribution and elaborate patterning of the SR where it enwraps the banded myofibrils can be appreciated. Linear masses of mitochondria (Mit) are seen running between some myofibrils.

demonstrated that the nuclear pore complexes are complicated structures indeed, incorporating an eight-subunit annular structure centered around an aqueous channel that allows passive diffusion of small molecules and ions. The nuclear envelope is not a complete barrier, because it is necessary for RNA, proteins and ions to pass in and out of the nucleus; the system of nuclear pores regulates the trafficking of these substances.

VI. ENDOPLASMIC RETICULUM

The ER was originally described by light microscopists in the late 1800s, who used special preparative procedures that selectively infiltrated this organelle system with a variety of staining moieties (see Fig. 5.6C). Understanding of the structure of the ER was greatly advanced in the late 1940s and early 1950s by the elegant EM work of Porter and Palade, who demonstrated that the ER was an extensive network of interconnecting tubules and cisterns.

Ribosomes are compact rounded particles, approximately 300 nm in diameter, that dissociate in the presence of low Mg^{2+} into two smaller units. They consist in large part of ribosomal RNA but, in eukaryotes, as much as 50% of the ribosomal mass can be composed of associated proteins. Ribosomes are often found organized into strands or rosettes called polyribosomes or simply "polysomes" (Fig. 5.7). These are aggregations of ribosomes active in the messenger RNA-directed linkage of amino acids to form peptide chains. Protein synthesis is initiated on ribosomes, which may be free in the cytoplasm or bound to the ER to form a complex known as rough endoplasmic reticulum

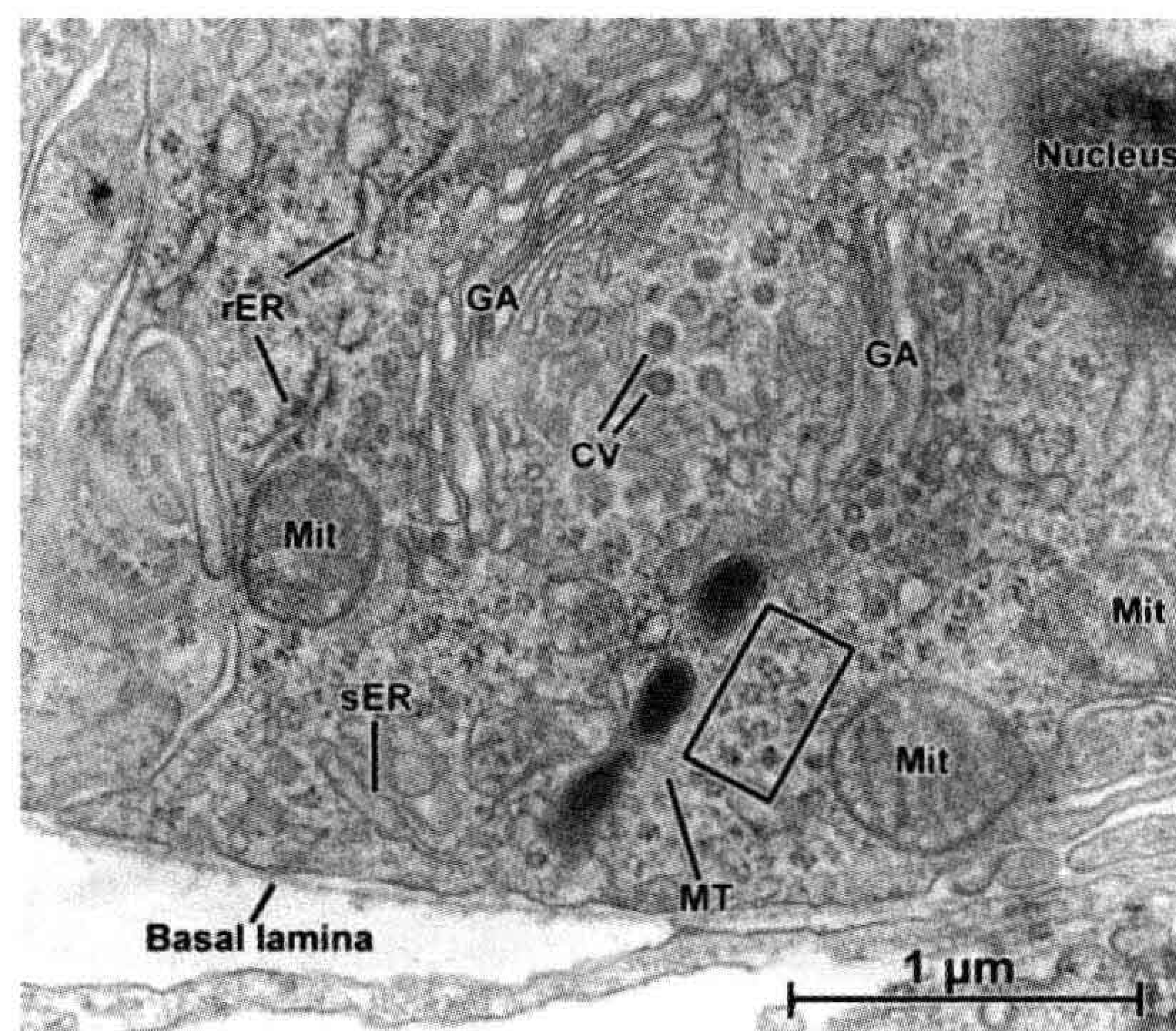


FIGURE 5.7 Transmission electron micrograph of a "juxtaglomerular cell" in kidney blood vessel. In this limited area, examples of many of the organelles described in this chapter are seen in close proximity to one another. In particular, the saccules, cisternae and vesicles that make up the Golgi system (GA) are clearly defined. In this cell, which is the source of the vasoactive hormone renin, polyribosomes are abundant (examples within the rectangle), along with smooth ER (sER), rough ER (rER), mitochondria (Mit), and a microtubule (MT).

(see Figs. 5.6A,B, 5.7). The rough ER is presumed to be involved virtually exclusively in protein synthesis. In contrast, ER that does not have attached ribosomes is known as smooth endoplasmic reticulum (see Figs. 5.6C, 5.7) and has been implicated in a number of different functions depending on the particular cell type. In steroid hormone-secreting cells, for example, smooth ER is associated with the production of secretory products. In liver cells, the smooth ER has been shown to be active in glycogen metabolism. In cardiac, skeletal and smooth muscle, the smooth ER is better known as the *sarcoplasmic reticulum* (SR) (see Fig. 5.6C); SR membrane proteins are responsible for the uptake, sequestration, and release of Ca^{2+} during the cycles of excitation–contraction coupling and relaxation. ER in non-muscle cells may also be involved in Ca^{2+} metabolism.

VII. GOLGI APPARATUS

Synthesis of membrane proteins and secretory products is completed in another organelle, which is at least functionally connected with the ER and is called the *Golgi apparatus* (see Fig. 5.7). This organelle was named for Camillo Golgi, a 19th-century microscopist-histologist who developed numerous staining techniques and described many of the light-microscopic features of cells. In the electron microscope, this organelle was found to be composed of flattened disk- or saucer-shaped membranous elements known as cisternae. In each Golgi apparatus, numbers of these cisternae are organized into stacks, with individual cisternae interconnected through tubular channels. As secretory products pass through the Golgi apparatus, they undergo chemical modifications such as glycosylation, proteolytic cleavage, phosphorylation and sulfation. Other functions performed by the Golgi apparatus include carbohydrate metabolism, targeting of plasmalemmal proteins (pumps, channels and receptors) and the condensation of secretory materials into opaque "secretory granules" (see Fig. 5.3).

Although a variety of terminologies has been used to identify different regions of the Golgi apparatus, four morphological subsections are generally recognized. The cisternae are slightly dished in conformation, which confers both concave and convex faces to the Golgi complexes. The convex or *cis* face is also known as the forming or immature face, since it is at this level that newly synthesized proteins enter the Golgi. The medial or intermediate region comprises the varying numbers of cisternae in the middle of the stack. The concave or *trans* face is also called the mature or secretory face, since it is the site from which large secretory vesicles bud off after their contents have been modified for export. The trans-Golgi network is a reticulum of tubules emanating from the *trans* face and is thought to be associated with the lysosomal system.

This general scheme is applicable to all Golgi complexes and transport within the Golgi is generally vectorial, going from the *cis* to the *trans* face. However, more recent evidence suggests that maturation and pinching off is not totally restricted to the *trans* face. There is likely much more intra-Golgi shuttling back and forth of material than was originally believed. The numerous vesicles of various shapes and sizes in the immediate vicinity of the Golgi complex (see Fig. 5.7) may be transporting proteins along the pathway during maturation and processing. There is also evidence for some retrograde transport from the Golgi apparatus to the ER.

VIII. LYSOSOMES

In addition to packaging and modifying secretory products, the Golgi apparatus plays a role in the formation of another important cellular organelle, the *lysosome* (see Figs. 5.2, 5.6A, 5.8A,B). In fact, the functional continuity of the ER, the Golgi apparatus and the lysosomes has led to the

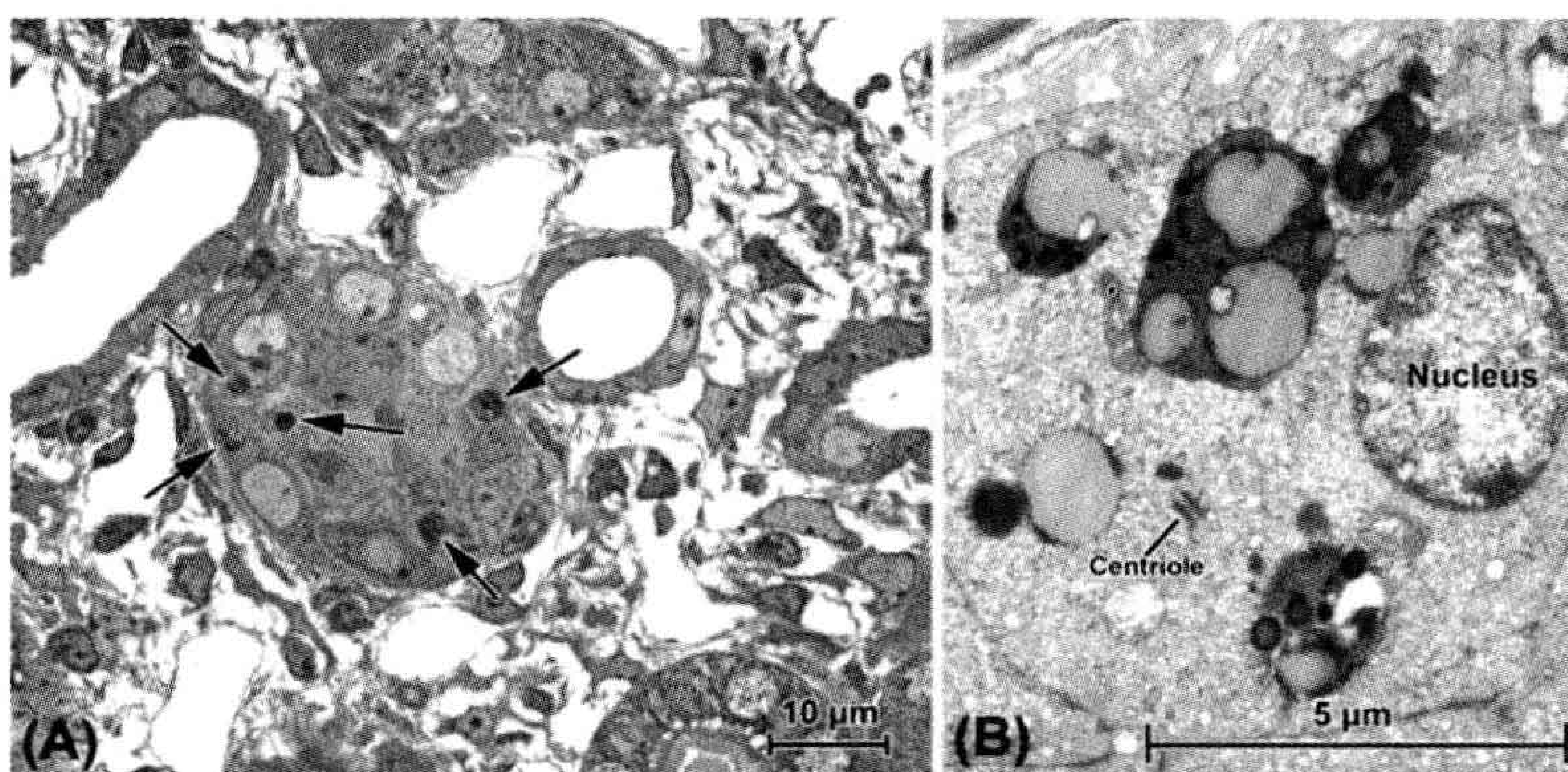


FIGURE 5.8 Autophagy in kidney proximal tubules following obstruction of the ureter. (A) "Semithin" (ca. 0.25 μm) section of tissue embedded in plastic. Use of such sections allows survey viewing in the light microscope for selection of areas to be more closely examined in the TEM, as seen in (B). In this case, the structures of interest are the dark bodies indicated in (A) by arrows; for all practical purposes, their substructure is below the resolution of the light microscope and it is only in the TEM that they are revealed to be autolysosomes, the complex products of a multistep process (described in text) that isolates defunct or excess cell contents for digestion. Nuclei in cells undergoing autophagy often appear normal; a centriole is also present in one cell.

concept of the GERL (Golgi–endoplasmic reticulum–lysosome) system. Lysosomes are a heterogeneous population of membrane-limited vesicles, differing in size and density, that were identified and characterized by De Duve in the mid-1950s. Lysosomes contain hydrolytic enzymes that can break down virtually every form of biological material and thus these organelles act, in part, as the cell's digestive system. Many of the lysosomal enzymes are more effective at low pH and the lumen of the lysosome accordingly is more acidic than the cytoplasm. The lysosome acts to break down and recycle intracellular components such as cytoskeletal proteins and defunct organelles, such as mitochondria (by a process known as *autophagy*), as well as to digest extracellular material that has been trapped in phagocytic vesicles formed by internalized plasmalemma (heterophagy). Viewed in the electron microscope, newly formed "primary" lysosomes are more uniform in size, with an amorphous electron-opaque content. After fusing with phagocytic vesicles or other cell contents, they form "secondary" lysosomes, whose size and internal density is more variable (Fig. 5.8). Lysosomes containing indigestible material often remain in the cytoplasm as residual bodies, also variously known as aging pigment or *lipofuscin*.

Cell death mechanisms are now of particular interest. *necrosis*, in which the semipermeable properties of the plasmalemma are compromised, has been well known for many decades and the term *apoptosis* (a.k.a. "type I programmed cell death") was coined in the 1970s (apoptosis is discussed further in the section on Mitochondria). More recently, however, autophagy has attracted special interest. Though lysosomes were well-established as fundamental cellular organelles, their role in autophagy (literally "self-eating"; also known as type II programmed cell death) is only now being detailed. The sequestration of cellular materials into lysosomes to form secondary lysosomes has now been found, largely on the basis of electron microscopic studies, to be more complex. Autophagy is now considered to be initiated by the formation of a double-membrane structure, the "isolation membrane" (likely derived from the ER, but this is still not completely clear), which develops into a body known as an *autophagosome* (or autophagic vacuole), which is the entity that envelops the target organelle or substance. The autophagosome with its contents then joins ("docks and fuses") with the lysosome proper, forming the secondary lysosome, now known as the *autolysosome*. Autophagy is not entirely an ineluctable path to cell death, however, and in some cases – such as starvation – promotes cell survival.

Peroxisomes, while similar in overall appearance to lysosomes, are considered to be a separate class of organelle. These bodies are abundant in liver, kidney and heart (among others) and contain both peroxidase and catalase, through the action of which fatty acids are broken down and the resulting, potentially harmful hydrogen peroxidase is dissociated into water and oxygen. Endogenous peroxidatic activity is of technical interest when one is performing immunohistochemistry; peroxisomes and erythrocytes (which also have peroxidatic activity) require "quenching" with hydrogen peroxidase to neutralize endogenous peroxidase, since certain steps of standard immunohistochemical procedures utilize exogenous peroxidase in generating the colored compounds (chromogens) that mark the sites of antigens (see Fig. 5.1D,E).

IX. MITOCHONDRIA

Aside from the nucleus, the most obvious feature of the majority of cells is the collection of organelles called mitochondria (Fig. 5.9). The term "mitochondrion" (literally "thread-grain") was introduced at the turn of the 20th century based on the appearance of these bodies, under the light microscope, as elongated granules. In the TEM, each mitochondrion is seen to be bounded by a double bilayer membrane (see Fig. 5.4A). The outer bilayer is smooth in contour and forms the boundary around the entire mitochondrion. The inner membrane has a variable number of infoldings, called *cristae*, which increase the internal surface area substantially (see Figs. 5.4A, 5.9).

It is now clear that the mitochondria are sites of cellular respiration and thus are the center of energy production in the cell. The inner mitochondrial membrane contains abundant transport proteins responsible for establishing a proton gradient between the intermembrane space and the matrix. The proton motive force created by this gradient is essential for driving many of the reactions of oxidative phosphorylation, a fundamental metabolic process occurring within the inner compartment of the mitochondrion. Oxidative phosphorylation generates much of the cell's adenosine triphosphate (ATP), the high-energy compound that is the source of energy for most cellular activities. The enzymes responsible for the tricarboxylic acid cycle, one component of oxidative phosphorylation, are located in the mitochondrial matrix and the enzymes involved in electron transport, another major function of the oxidative phosphorylation process, are associated with the inner mitochondrial membrane.

As would be expected, mitochondria concentrate at sites within the cell that require high energy utilization, as well as being more abundant in cells that exhibit a high degree of metabolic activity. For example, heart muscle tissue has one of the higher measured metabolic rates; accordingly, in myocardial cells, mitochondria constitute up to 40% of the total cell volume, and are sandwiched in between the collections of contractile proteins (myofibrils) (see Figs. 5.5A, 5.6C).

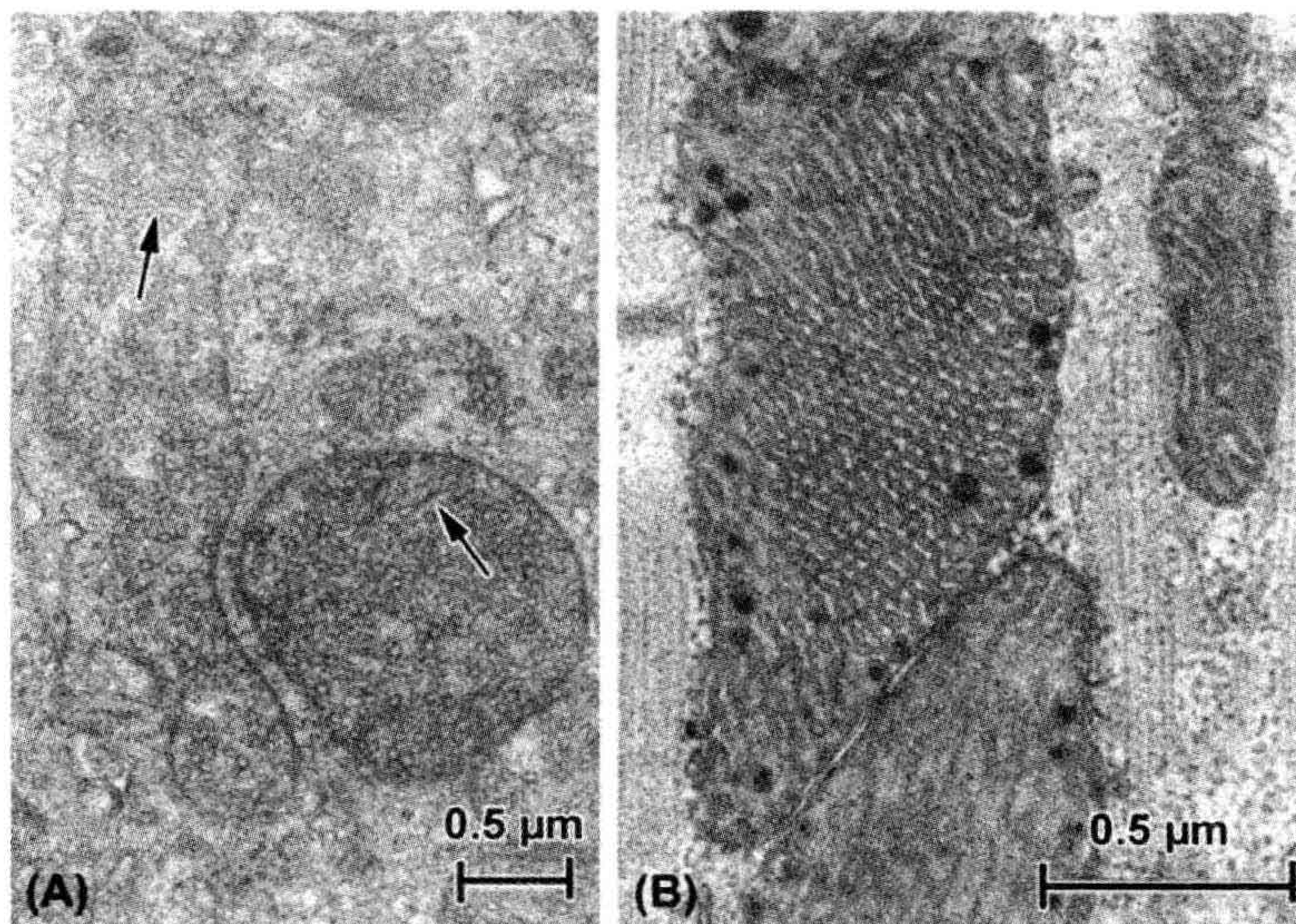


FIGURE 5.9 Mitochondria. (A) Mitochondria in cell from adrenal cortex. Steroid-secreting cells often are characterized by spheroidal or elongate mitochondria packed with internal membranes (cristae) that take the form of fine tubules (arrows) or chains of tiny vesicles. (B) Mitochondria in cardiac muscle. In addition to being tightly sandwiched between the myofibrils (collections of contractile filaments; see also Figs 5.6C, 5.10A), cardiac mitochondria are often densely populated with elaborate pleated shelves of internal cristae. Opaque granules often are present within the mitochondrial matrix.

Apoptosis, as mentioned earlier, is a mechanism of "programmed cell death". Morphologically, it is most clearly evident in changes in nuclear appearance (condensed chromatin, nuclear fragmentation). However, the impetus for the apoptotic process is found in the mitochondrion where, under certain circumstances, there is a change in its membrane permeability and thence its electrical potential. "Apoptogenic factors" such as cytochrome c and proteases are then released from the mitochondria and lead to the so-called "caspase cascade" and eventually to the nuclear alterations that are obvious in the microscope. Like autophagy, however, apoptosis can serve beneficial purposes. Apoptosis is a necessary process, particularly in development; e.g. it is thought to bring about the establishment of microvessel lumina in kidney glomeruli (Fierlbeck et al., 2003).

X. CYTOSKELETON

The cytoplasm is not just a watery bag in which organelles move about at will. In fact, cell contents are to one degree or another compartmentalized, with certain cytoplasmic regions specialized to subserve particular functions. Underlying this compartmentalization is the framework of fibrillar structures that make up the cytoskeleton of each cell. Normally, 20–35% of the total protein of a cell is tied up in the cytoskeleton, although this proportion can vary, being considerably greater in muscle, where cytoskeletal proteins also form part of the extensive contractile apparatus. In all cells, cytoskeletal elements are involved in intracellular motility (such as migration of chromosomes during mitosis, translocation of organelles and cytoplasmic streaming), cell locomotion, and maintenance of cell shape. More specialized functions, such as muscle contraction and ciliary/flagellar movement, also are supported by cytoskeletal elements.

XA. Filaments

Filaments are composed of backbones of single proteins, polymerized to form long, slender fibrillar structures. Such filaments are both helical and polar and frequently interact with one another. There are three general filament categories in cells: *microfilaments*, often called "thin filaments", which are primarily composed of the protein actin and ranging from 6 to 8 nm in diameter; *thick filaments*, consisting mainly of myosin and 12–15 nm in average diameter; and *intermediate filaments*, so called because their customary 10 nm average diameter is intermediate between that of thin and thick filaments (thus also known as 100 Å or 10 nm filaments). Intermediate filaments may be composed of a variety of related proteins, depending on cell type.

XA1. Microfilaments

As noted above, the backbone of microfilaments is composed of the cytoskeletal protein actin; in most cell types, however, additional regulatory proteins (e.g. troponin) and structural proteins (e.g. tropomyosin) are intimately associated with the actin filaments. G (globular)-actin polymerizes to form filaments and in this form is

known as F (filamentous)-actin. A number of associated proteins may regulate initiation and growth of a filament, as well as its final length. Tropomyosin, for example, stabilizes thin filaments of muscle cells.

In different cells, and in different tissues, thin filaments are associated with a variety of recognizable intracellular formations. Bundles of filaments, all having the same polarity, form the cores of microvilli in epithelial cells; actin filaments are also evident in smooth muscle and striated muscle cells as intrinsic parts of the contractile apparatus (Fig. 5.10). Bundles of thin filaments having opposite polarities are also found, located on opposing sides of the Z disks in skeletal and cardiac muscle, across from one another at dense bodies in smooth muscle, and within the stress fibers of non-muscle cells. Three-dimensional networks of filaments are found in subplasmalemmal (cortical) arrays in many cells.

XA2. Thick Filaments

The most detailed structural information regarding myosin-containing filaments comes from the study of striated muscle thick filaments (see Fig. 5.10A,B). Smooth muscle cells clearly contain thick filaments (see Fig. 5.10C), but the exact organization of the molecules within the filaments is still controversial. It is likely that non-muscle cells also contain thick filaments, but that they are shorter and less ultrastructurally obvious.

It is generally accepted that thick filaments are required for movement and motility, which are carried out through interactions with actin-containing thin filaments.

XA3. Intermediate Filaments

Intermediate filaments (IFs) actually comprise a related family of proteins found in virtually all cell types; lamins are IF proteins that form the internal lamina of cell nuclei, for example. However, there are also tissue-specific IF proteins. Vimentin is found in mesenchymal tissue (connective tissue, bone, blood, cartilage); desmin is localized in muscle; neurofilament protein, or neurofilamin (NF), is found in neurons; GFAP (for "glial fibrillar acidic protein") is found in glial cells of the nervous system. Finally, keratins are IF proteins that are abundant in epithelial cells. Additional IF proteins do not form filaments (e.g. nestin: see Fig. 5.1E), but help to stabilize the filamentous forms.

IFs are often observed as loose three-dimensional networks, intermixed with other cellular components (see Fig. 5.10C), but in astrocytes and other cells can form dense skeins that consist primarily of 10 nm filaments. As pointed out above, IFs form the framework of the inner nuclear membrane, the nuclear lamina. IFs are also associated with subplasmalemmal plaques adjacent to the plasma membrane at specialized cell–cell contacts (desmosomes)

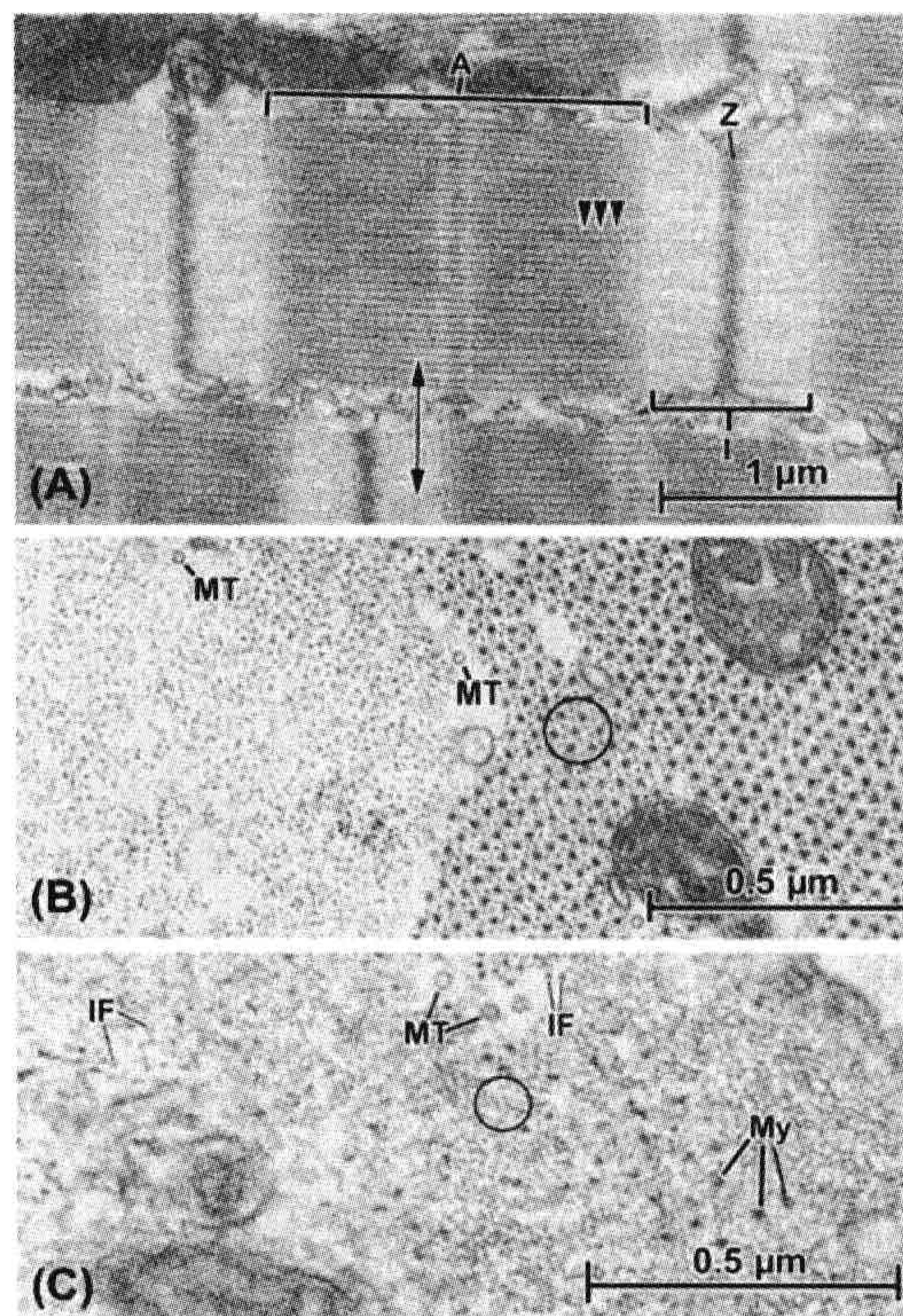


FIGURE 5.10 Fibrillar elements in muscle cells. (A) Longitudinal section through a cardiac muscle cell, showing the characteristic banded pattern of the ordered masses of contractile filaments known as myofibrils. Between myofibrils, other cell organelles, such as mitochondria and endoplasmic (sarcoplasmic) reticulum, are sandwiched. The units of the banding pattern are known as sarcomeres and the major filament categories that contribute to their formation are thin (actin) filaments and thick (myosin) filaments. The so-called A band (A) is a composite of interdigitated actin and myosin and the subtle cross-hatching pattern derives from portions of the myosin filaments that form cross-bridges (several shown by arrowheads) with the adjacent actin filaments. The I band (I) is occupied only by thin filaments, which insert into the dense material of the Z bands (Z), which are primarily composed of the protein α-actinin. Adjacent Z bands define a sarcomere unit, each of which covers a distance of ca. 2.2 μm in heart. Note in this panel that adjacent myofibrils are not always aligned with one another in terms of the levels of their sarcomere patterns. (B) A transverse section through two cardiac myofibrils, its plane of sectioning corresponding to the double-headed arrow in (A). At the left of the picture, the section passes through the I-band region and therefore reveals only actin filaments, whereas at the right the A band is cut, showing the characteristic hexagonally arrayed myosin filaments, each surrounded by actin filaments, usually in the "six-around-one" pattern circled. Mitochondria are enmeshed by the filaments in one myofibril, and additional fibrillar components, namely microtubules (MT), appear in the same orientation as the muscle filaments. (C) Cross-section through a vascular smooth muscle cell in the wall of a coronary artery. Like the cardiac muscle shown in the other panels, the smooth muscle contains examples of actin (circled) and myosin (My), but a geometric arrangement similar to that of cardiac or skeletal muscle is not evident. Cytoskeletal fibrils, including microtubules (MT) and intermediate filaments (IF), also are present in the same orientation as the contractile actin and myosin.

(see Fig. 5.11D, F) and are disposed in muscle in transverse meshworks that link and align myofibrils to one another, to the sarcolemma, and perhaps also to the nucleus. Thus, IFs are an internal scaffolding that can form networks to link peripheral and central components of the cell as a mechanically integrated complex.

XB. Microtubules

Microtubules are elongate, hollow cylinders of notably larger diameter (ca. 25 nm) than other cytoskeletal fibrils (see Figs. 5.7, 5.10B,C) and are composed of the protein tubulin. The walls of the microtubules are formed from protofilaments aligned parallel to the long axis of the microtubule. The number of protofilaments that make up the microtubule cross-section varies, but 13 is the most common complement. The protofilaments are polar structures and are assembled so that they confer polarity to the microtubule.

There are several different microtubule-associated proteins (MAPs), including MAPI, MAP2 and tau (aberrant formations composed of tau are responsible for the formation of "tangles" within neurons in Alzheimer's disease). The MAPs serve to stabilize the microtubules and are the targets of regulatory signals. One of the most functionally important MAPs is dynein, which forms side arms on the microtubules found in the cores of cilia and flagella. These side arms enable microtubules to slide past one another, allowing bending of the whole structure and accounting for their basic motility. In addition to being the fibrillar component of cilia and flagella, microtubules are the basis of the so-called MTOCs (microtubule-organizing centers). Microtubules are involved in movement of chromosomes during cell division and perform a role in translocation of organelles within the cytoplasm. In some cases, microtubules also can form the framework on which some of the cell compartments are organized and it has even been shown that the orientation of IFs depends, in some instances, upon the integrity of the microtubules in the same cell.

XI. CELL JUNCTIONS

Where they are located in tissues and organs, cells do not exist in isolation, but rather exert multiple influences on one another. When they reside in different parts of the organism, the influences are usually realized through an intermediary milieu such as the bloodstream, but where neighboring cells come into contact with one another, specialized structures known as *intermembranous junctions* connect them. The electron microscope has proven a particularly apt tool for detecting such connections, since they usually incorporate some form of modification of the apposed cell plasmalemmas that is best visualized in the TEM.

Four types of intercellular junctions are commonly encountered in vertebrate tissue: (1) tight junctions; (2) gap junctions; (3) intermediate or adherens junctions; and (4) desmosomes. Epithelial layers such as seen in small intestine display a rather stylized "junctional complex" that consists of the four junctional types arranged in a sequence from the luminal surface down to the basal surface; in order, the complex goes tight junction/adherens junction/desmosome/gap junction.

Because of the extreme thinness of sections used in the electron microscope, the views of cells and their constituents are essentially two-dimensional; in such views, the casual observer can easily fail to appreciate the true shape and extent of any particular profile. This is certainly the case for specialized intercellular junctions. More stringent observations, including examination of multiple sections of cells in various orientations, as well as use of serial sections, has shown, in epithelium as well as other tissues, that some categories of junctions occupy continuous bands of plasmalemma (zonulae) that form rings about the lateral cell surface. Other junctions are more strictly delimited, in three dimensions occupying round, ovoid, or sometimes irregular patches of plasmalemma in each of the joined cells (see Fig. 5.4B).

Tight junctions, viewed in thin sections, are identified, as the name would imply, by plasmalemmal appositions that come into such close contact as to obliterate the intercellular space between cells. Often multiple points of leaflet fusion are visible along short stretches of apposed membranes (Fig. 5.11A). Replication of membrane surfaces by freeze-fracture techniques (Figs. 5.11B,C) has revealed that tight junctions actually are composed of intramembranous particles arranged to form networks of "tongue-and-groove" interdigitations, which provide a barrier largely impenetrable to most particles and fluids. Tight junctional arrays prevent direct diffusion of various products through the extracellular fluid space, thus forcing their passage "through proper channels," so to speak, namely via mechanisms such as vesicular transport through the cytoplasm. Tight junctions are also found in abundance in pancreatic acini, as well as between endothelial cells in certain segments of blood vessels. To some degree, tight junctions are likely responsible for maintenance of the blood−brain barrier.

Gap junctions, also known as nexuses or *maculae communicantes*, were in early studies mistaken for tight junctions, but it was realized, through the use of special staining procedures and particle tracer techniques, that these complexes were different in their overall thickness and, furthermore, allowed particles below a certain size to penetrate the extracellular space at their level. Gap junctions appear in thin EM sections to be composed of seven layers (see Figs. 5.4A, 5.11D), the middle one appearing as a 2−4 nm "gap", explaining the common name for this type

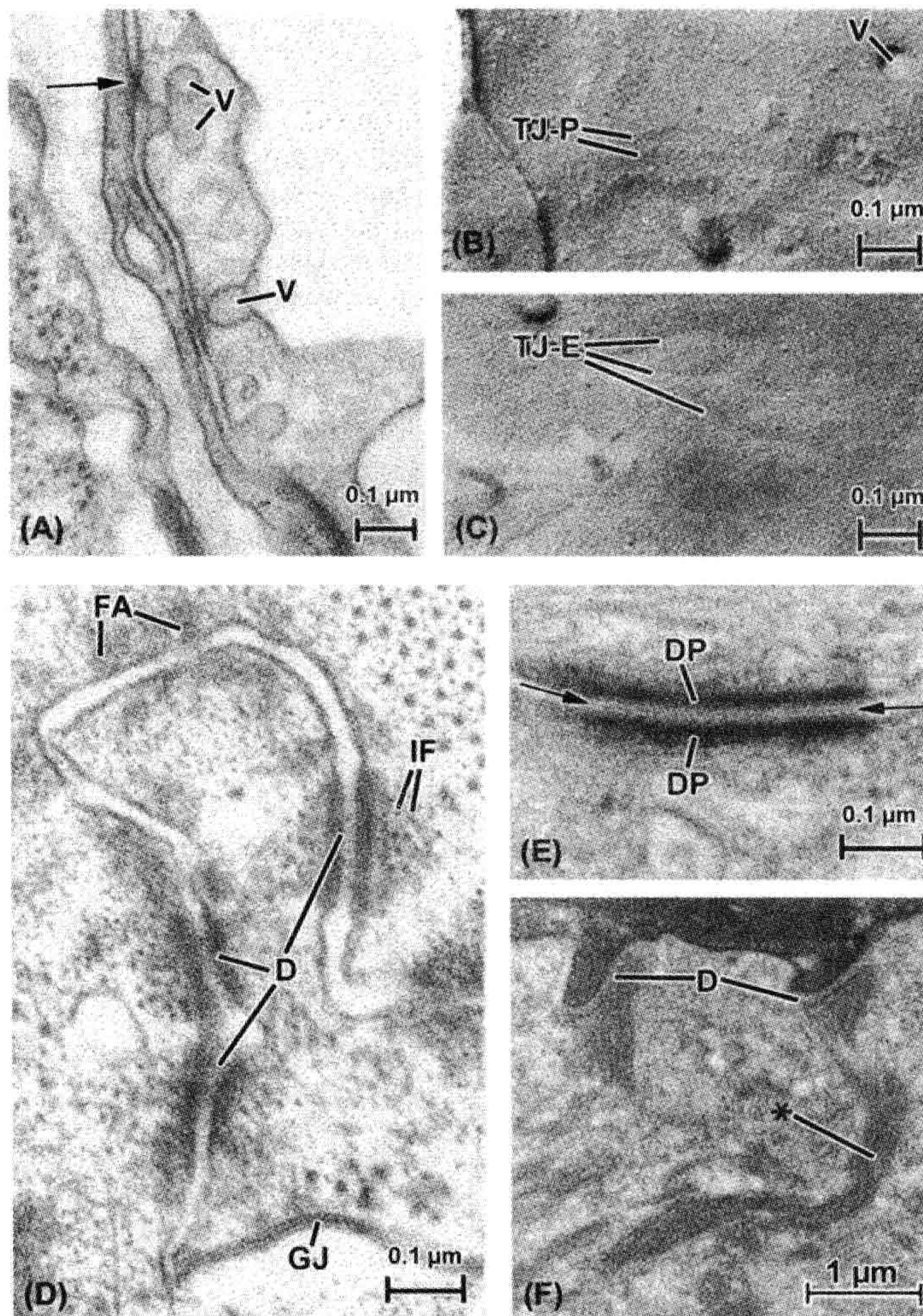


FIGURE 5.11 Cell-to-cell appositions, also called intercellular junctions. (A), (B) and (C) show endocardium (the endothelial lining of the heart) both in thin section (A) and freeze-fracture replicas (B) and (C). (A) The plane of section passes vertically through two overlapping endocardial cells, whose plasmalemmas bear cytoplasmic vesicles (V) that support transport of materials in and out of these cells. The plasma membranes of the two endocardial cells come into close proximity at several points, at one appearing to touch or fuse (arrow). Such junctions are known generally as "tight junctions" and form barriers to the penetration of certain materials past them in the intercellular spaces. (B) A freeze-fracture replica of the endocardial membrane's P face (see Fig. 5.4B) shows vesicular openings (V) as well as linear arrays of particles that correspond to the tight junction (TJ-P). (C) These correspond in replicas of the E face to linear indentations (TJ—E) into which the corresponding P-face particles fit to form an interlocking junctional barrier. (D) and (E) show junctions from the myocardial cell-to-cell junctional complex (the "intercalated disk"), which consists of interdigitated muscle cell tips that bear a variety of interspersed types of junctions, including gap junctions (GJ, see also Fig. 5.4). (D) At the top of the micrograph there appears a zone of fascia adherens (FA), the points at which thin actin filaments of the myofibrils insert into the intercalated disk. The adherens-type junctions are characterized primarily by accumulations of intracellular dense material that face one another across the intercellular space, but which incorporate no particular extracellular specializations. In contrast, the adhesive junctions known as desmosomes (three of which appear in this picture, D) not only bear intensely opaque intracellular densities closely associated with intermediate filaments (IF), but also contain a distinct component located in the extracellular space (see also (E)). (E) A desmosome is shown at high magnification. The intracellular material is concentrated into desmosomal "plaques" (DP) which, together with the associated plasmalemmal unit membranes, are arranged in a striking parallel array. The extracellular material, known as a "central lamella" (between arrows), is likely responsible for maintaining the register of the apposed membranes, having toothed projections from a center linear component that anchor in the adjacent plasma membrane leaflets. (F) Keratinocytes in the epithelium of skin. Here the major filament type is keratin, considered to be one of the family of intermediate filaments. Keratin is concentrated into fibrous cords (*) that insert onto the intracellular plaque material of the numerous desmosomes (D) that connect the cells of this layer of the skin.

of junction. Closer examination has revealed that the gap junction is an assemblage of hexagonally packed "connexons" (as their individual intramembranous particles are called; see Fig. 5.4B,C), each of which contains a tiny pore at its center. It is thought that such pores are aligned to form thin channels, allowing intracytoplasmic passage of ions (e.g. Ca^{2+}) and other substances (such as ATP and amino acids) directly from the cytoplasm of one cell into the interior of the other, a distance calculated to be only about 2.5 nm. In this way, it is postulated, neighboring cells can be "coupled" both electrically and metabolically.

Adherens junctions, though often descriptively linked with desmosomes, can be distinguished from them structurally on the basis of the adherens junctions being more diffuse-appearing and more widely distributed than desmosomes (see Fig. 5.11D). In addition to this morphological disparity are fundamental differences in the species of proteins associated with and composing the two types of junctions.

Adherens junctions are frequently associated with microfilaments, whereas desmosomes instead are accompanied by intermediate filaments. A well-described example of this dichotomy is found in cardiac muscle in the intercalated disks, the zones of extensive junctional attachment between adjacent cardiac muscle cells (see Fig. 5.11D,E). Here at the cell tips, the actin filaments of the myofibrils terminate in the amorphous dense zones of the fascia adherens portion of the disk. In contrast, myofibrils do not come into contact with desmosomes. Furthermore, desmosomes exhibit a far more distinct and layered ultrastructure (see Fig. 5.11E), including a central lamella lying in the extracellular space between cells and intensely opaque intracellular, subplasmalemmal plaques, within whose substance profiles of intermediate filaments can often be detected. In epithelial cells, both desmosomes and hemidesmosomes – which are essentially "half" desmosomes confined to the cells' basal regions – contain subplasmalemmal plaques that are the insertion points for cords of keratin-type intermediate filaments (see Fig. 5.11F). As mentioned, distinctly different types of proteins are specific to each type of junction, and so, according to the philosophy of form following function, their structural resemblance to one another is related largely to their similar adhesive roles in cells.

XII. SPECIAL TISSUES, SPECIALIZED ULTRASTRUCTURE

Although a chapter such as this one necessarily deals in generalities, in reality few researchers work on generic "cells". Instead, certain types of cells, for one or many reasons, are of special interest to individual investigators. It is therefore useful to view cell ultrastructure as it is specifically arranged to form a cell type that is particularly appealing to physiologists: the nerve cell or neuron. This cell type not only generates and transfers electrochemical signals, it is also heavily devoted to synthetic activity. Though neurons vary considerably in size and shape in their various locations in the central, peripheral and enteric nervous systems, as a group they are characterized by their ability to exercise their functions at points far removed from the central cell region that contains the nucleus. This action-at-a-distance ability can be directly correlated with ultrastructural features of neurons. The cell body or *soma*, which contains a single prominent nucleus, also houses the bulk of the synthetic machinery of the cell (Fig. 5.12A), including extensive, often multiple Golgi apparatus and groupings of rough endoplasmic reticulum cisternal profiles, known collectively as "Nissl substance", because of the staining properties of their ribonucleoprotein. "Free" ribosomes (i.e. not attached to membranes) and polysomes abound as well within the neuronal soma.

It is the cytoplasmic processes of neurons, their dendrites and axons, that most effectively attest to their specialized functions. While dendrites, which generally bring signals toward the cell body, are usually limited to no more than several micrometers in length, the points at which the axons terminate may be located several millimeters away (or even farther, depending upon such factors as the size of the animal, type of neuron and its particular location in the body). Both dendrites and axons, as would be expected, are well endowed with cytoskeletal elements, oriented preferentially along the processes in a configuration that best supports their attenuated shapes. Electron microscopic observation demonstrates that microtubules and intermediate filaments are the most prominent constituents of axons (see Fig. 5.12B).

As pointed out, neurons, though organized along certain unified architectural lines, can vary markedly in their ultrastructure. Nowhere is this more pronounced than at their most distal portions, the tips of the axons, or axon terminals. These termini may have as their target other neurons, or may abut contractile cells, such as smooth muscle (both in viscera and blood vessels), cardiac muscle cells or skeletal myocytes. Axon terminals are usually characterized by concentrations of vesicles of one type or another. Where these axon terminals occur, they may lack any specialized structure that attaches them to the target cell. Often, though, where neurons terminate on one another, a distinct appositional complex known as the synapse is found.

The axon terminal (also known as a "bouton") constitutes the presynaptic element, and may terminate on a neuronal soma or another axon but, in the central nervous system (CNS), more often is found in contact with a dendrite (see Fig. 5.12C). In addition to the neurosecretory vesicles that fill the axonal bouton, there is a prominent synaptic density whose function appears similar to that of an adherens or desmosomal type of adhesive junction. The

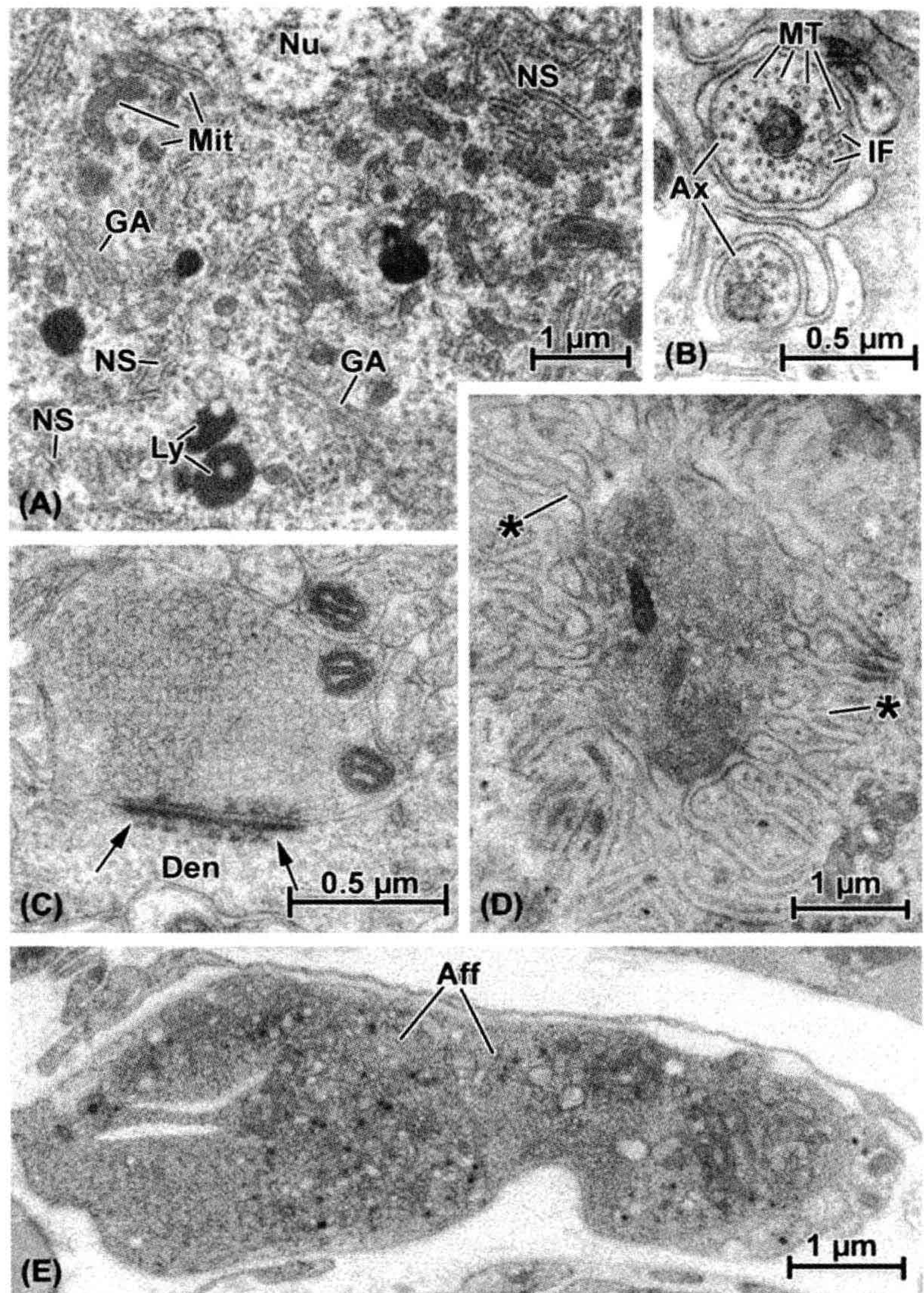


FIGURE 5.12 Electron micrographs illustrating specialized ultrastructure of neurons. (A) A portion of the cell body, or soma, that contains the nucleus (Nu). The cytoplasm in this region is filled with membrane-based synthetic organelles, including multiple profiles of the Golgi apparatus (GA) and cytoplasmic islands of rough endoplasmic reticulum and polyribosomes (known collectively as "Nissl substance," NS). Numerous small mitochondria are scattered throughout the soma and other examples of typical cell organelles such as lysosomes (Ly) are represented as well. (B) High-magnification view of axons (Ax), the elongated cytoplasmic processes of neurons. These are cut transversely and contain individual mitochondria (Mi) and numerous cross-sectioned cytoskeletal elements, including both microtubules (MT) and intermediate filaments (IF). (C) Axodendritic synapse (i.e. a nerve-to-nerve contact made by an axon with a dendrite, Den). The presynaptic axon terminal is packed with neurosecretory vesicles and also contains mitochondria. The hallmark of this complex is the synaptic density (arrows) which both attaches the two apposed nerve elements and delineates the region in which transfer of neurotransmitter will occur. (D) Motor endplate, a contact made by an axon terminal of the peripheral nervous system with a skeletal muscle fiber. Although much larger than the CNS terminal (see scale bars in (B), (C), (D) and (E)), like it, the end-plate terminal is filled with vesicles; instead of a dense plaque at the point of contact, however, there is a deep depression in the skeletal muscle into which the terminal nestles, together with elaborate secondary folds formed by the muscle cell membrane (*). (E) An afferent or sensory nerve terminal (Aff) in heart. This axon termination is considerably larger than most efferent terminals (see (C) and (D)) and contains a variety of inclusions such as mitochondria, clear and dense vesicles and other structures.

synapse functions through a process of vesicle fusion with the presynaptic membrane, with subsequent exocytosis of the transmitter chemical substance (which can be either excitatory or inhibitory) into the synaptic cleft, where it acts on the postsynaptic membrane side of the complex (i.e. the dendritic membrane in Fig. 5.12C), changing its electrical potential and thus generating a signal (thence the term "chemoelectric" for such an event). Where no synapse is formed, as for example in axon terminations near blood vessel walls, diffusion of neurotransmitter is sufficient to modulate the contractile activity of the vascular smooth muscle cells there.

In the case of vertebrate motor neuron axons, which terminate on skeletal muscle fibers, considerable specialization characterizes both the axon terminal and the adjacent muscle cell. This sort of "synapse" is better known as a *motor end-plate* (see Fig. 5.12D). The axon tip here is considerably larger than the typical boutons

found in the CNS and, accordingly, contains a considerably greater number of neurosecretory vesicles. The underlying muscle cell plasmalemma ("sarcolemma"), furthermore, has itself become specialized, containing concentrations of membrane-associated receptors (usually for acetylcholine) and forming both a large depression into which the axon fits (the synaptic "gutter") and numerous secondary infoldings that increase the amount of excitable muscle membrane available to the released neurotransmitter.

The terminal axons discussed thus far are efferent, i.e. they convey outbound signals from the nerve cell body to its distant target. Also found are afferent, or sensory, terminals, which function to send stimuli such as pressure or pain back to the soma. The contents of such terminals usually greatly vary, including not only vesicles of different shapes and sizes, but also numerous mitochondria, granules, and whorled membranous bodies (see Fig. 5.12E).

ACKNOWLEDGMENTS

Over a 40-year career in microscopy, I have been privileged to have trained by and collaborated with many excellent scientists, among them Professors James Norman Dent, W. Gerald Robison, Nick Sperelakis and Lennart Heimer. During this time, my research projects were greatly aided by Ms Jan Redick, Miss Barbara Ann Plantholt, Ms Susan Purdy-Ramos, Mr Lawrence A. Hawkey, Ms Ellen van Niel and Ms Barbara Thornhill and many others too numerous to list. Special thanks goes to Dr Robert L. Chevalier, in whose laboratory I have worked for the past decade, and in which this latest version of the present chapter was prepared.

BIBLIOGRAPHY

Andre, J. (1994). Mitochondria. *Biol Cell, 80*, 103–106.

Bershadsky, A. D., & Vasiliev, J. M. (1988). *Cytoskeleton*. New York: Plenum Press.

Clermont, Y., Rambourg, A., & Hermo, L. (1995). Trans-Golgi network (TGN) of different cell types: three-dimensional structural characteristics and variability. *Anat Rec, 24*, 289–301.

Davis, L. I. (1995). The nuclear pore complex. *Annu Rev Biochem, 64*, 865–896.

Dessev, G. N. (1992). Nuclear envelope structure. *Curr Opin Cell Biol, 4*, 430–435.

Di Fiore, M. S. H. (1974). *Atlas of Normal Histology* (6th ed.). Philadelphia: Lea and Febiger.

Fawcett, D. W. (1981). *The Cell* (2nd ed.). Philadelphia: W.B. Saunders.

Fawcett, D. W. (1997). *Bloom and Fawcett: A Textbook of Histology* (12th ed.). New York: Hodder Arnold.

Fierlbeck, W., Liu, A., Coyle, R., & Ballermann, B. J. (2003). Endothelial cell apoptosis during glomerular capillary lumen formation in vivo. *J Am Soc Nephrol, 14*, 1349–1354.

Forbes, M. S., & Sperelakis, N. (1985). Intercalated discs of mammalian heart: a review of structure and function. *Tissue Cell, 17*, 605–648.

Gerace, L. (1992). Molecular trafficking across the nuclear pore complex. *Curr Opin Cell Biol, 4*, 637–645.

Gonatas, N. K. (1994). Contributions to the physiology and pathology of the Golgi apparatus. *Am J Pathol, 145*, 751–761.

Hayat, M. A. (1989). *Principles and Techniques of Electron Microscopy* (3rd ed.). Boca Raton: CRC Press.

Hotchkiss, R. S., Strasser, A., McDunn, J. E., & Swanson, P. E. (2009). Cell death. *New Engl J Med, 361*, 1570–1583.

Lodish, H., Berk, A., Kaiser, C. A., et al. (2007). *Molecular Cell Biology* (6th ed.). New York: W.H. Freeman.

Novikoff, A. B. (1976). The endoplasmic reticulum: a cytochemist's view. *Proc Natl Acad Sci USA, 73*, 2781–2786.

Nunnari, J., & Walter, P. (1992). Protein targeting to and translocation across the membrane of the endoplasmic reticulum. *Curr Opin Cell Biol, 4*, 573–580.

Palade, G. E. (1956). The endoplasmic reticulum. *J Biophys Biochem Cytol, 2*, 85–98.

Pante, N., & Aebi, U. (1996). Molecular dissection of the nuclear pore complex. *Crit Rev Biochem Mol Biol, 31*, 153–199.

Peters, A., Palay, S. L., & Webster, H.deF. (1991). *The Fine Structure of the Nervous System. Neurons and their Supporting Cells* (3rd ed.). New York: Oxford University Press.

Porter, K. R., & Bonneville, M. A. (1973). *Fine Structure of Cells and Tissue*. Philadelphia: Lea and Febiger.

Rhodin, J. A. G. (1974). *Histology. A Text and Atlas*. New York: Oxford University Press.

Shay, J. W. (1986). *Cell and Molecular Biology of the Cytoskeleton*. New York: Plenum Press.

Chapter 6

Signal Transduction and Second Messengers

Aldebaran M. Hofer

Chapter Outline

I. WHAT IS SIGNAL TRANSDUCTION?

Primeval unicellular organisms undoubtedly possessed rudimentary detection systems to sense nutrient and temperature gradients, to react to variations in light and to avoid noxious stimuli in their extracellular environments. With the advent of multicellularity, eukaryotic organisms required progressively more sophisticated means to respond to an ever larger array of external cues and to coordinate activities between different cells. Increasingly complex signal transduction networks evolved in higher organisms to control intricate physiological processes such as cellular differentiation, embryonic development, memory and learning.

Classically defined, signal transduction is usually regarded as a process of information transfer mediated by soluble extracellular chemical stimuli (e.g. hormones, neurotransmitters, cytokines) that bind to transmembrane receptors at the cell surface. This initiates intracellular signaling events (e.g. phosphorylation by a kinase) that culminate in a change in a physiological process. Second messengers refer to small molecule chemical mediators, such as calcium ions, cAMP, cGMP, diacylglycerol (DAG) or inositol trisphosphate ($InsP_3$), the concentration of which is rapidly and transiently increased inside the cell following receptor activation.

In recent years, additional modes of intracellular communication have begun to be recognized. Signal transduction has therefore become more broadly defined to encompass any type of signaling circuit used by cells to monitor external and internal states in order to effect a change in cellular activity. Most of these pathways do not require the generation of soluble second messenger molecules and they do not even necessarily involve the detection of a soluble extracellular ligand. Moreover, many

Cell Physiology Sourcebook. DOI: 10.1016/B978-0-12-387738-3.00006-8

seemingly specialized signaling pathways, e.g. those formerly of interest principally to developmental biologists such as Wnt, Hedgehog and Notch pathways, are now receiving attention from physiologists as well, as these highly conserved signaling mechanisms continue to exert homeostatic effects on the organism throughout its lifetime. Knowledge about the details of signaling circuits and their elaborate interrelationships is continually evolving. In this chapter, we will survey this complex topic in order to provide a general framework for understanding signaling as it relates to the study of physiology.

II. GENERAL PRINCIPLES

The human genome consists of about 23–25 000 protein-coding genes, but there are actually far more biological processes than unique proteins (including splice variants), indicating that many proteins are "recycled" for multiple purposes. Proteins dedicated to signal transduction are highly represented in the human genome. It has been estimated that there are 1543 genes for receptors, 518 protein kinases and 150 different protein phosphatases. Signals are used to control rapidly cellular functions such as ion channel activity, secretion or motility, but most signaling cascades ultimately converge on transcription factors (of which there are at least 1850) to execute programs of gene expression that result in long-term changes in cellular and organismal physiology (Papin et al., 2005). Differentiated cells (of which there are about 200 different types in humans) express a particular repertoire of signaling components (this has sometimes been referred to as the "signalsome") that allow them to respond appropriately to some types of stimuli while ignoring others.

A number of factors contribute to the enormous diversification that is a hallmark of signaling circuits. First, nearly all types of signaling proteins exist as a multiplicity of distinct *isoforms*. For example, there are 10 isoforms of the adenylyl cyclases, the enzymes that catalyze the production of cAMP, and 12 protein kinase C (PKC) family members. While at first glance this may seem redundant, the presence of specific isoforms for receptors, effectors (the proteins mediating the signal) and final target proteins that have varying affinities for their ligands actually permits further "tuning" of responses, as it allows the pathway to discriminate between small- and large-amplitude stimulus strength. Moreover, individual isoforms of signaling proteins receive *customized inputs* from other signaling circuits of the signalsome to regulate differentially their activity.

Second, while there is great diversity in the individual constituents of signaling cascades, there is also some degree of *redundancy* coming from the fact that multiple signaling pathways frequently converge on the same target to give a similar physiological outcome. An example of this is in transcription factors, which are generally the target of multiple parallel signaling inputs.

A third factor that generates both diversity and specificity among signaling circuits is their *spatial organization*. Scaffolding molecules increase the efficiency of the process by helping to assemble *signaling platforms*. These large multiprotein complexes provide physically coupled activation–deactivation cycles of kinases, their phosphatases, upstream activators and downstream effectors. It is important to remember that the enzymatic reactions taking place in these large immobilized aggregates may not necessarily obey simple models of enzymes kinetics. Messages can also be *temporally encoded*, i.e. some effectors are tuned to respond to short-lived signals, while other processes require sustained signaling to exert an effect. Thus the "*spatiotemporal*" features of a message, even highly diffusible second messengers like Ca^{2+} and cAMP, can dictate the physiological response to that signal.

Subtle *remodeling* of signaling properties takes place throughout the lifetime of a cell due to changes in expression levels of elements within a cascade. This can give rise to a certain degree of heterogeneity even among cells of the same type. Remodeling has been considered to be a key feature in the progression of certain disease states (e.g. cancer, cardiovascular disease).

Finally, there is an incredible degree of *interconnectivity* among the various signaling pathways, which are also subject to complex feedback and feed-forward regulation. The signalsome of any given cell would therefore be more realistically represented as a *non-linear network of interacting circuits*, although generally depicted (as they are in this chapter) as simplified linear sequences of biochemical events.

III. GENERAL TYPES OF SIGNAL TRANSDUCTION CASCADES AND THEIR COMPONENTS

Sir Michael Berridge has categorized the major intracellular signal transduction cascades into ≈19 different groups (Berridge, 2009). Most of these pathways (Fig. 6.1) are highly conserved across animal and even plant species and many are initiated following engagement of two general types of cell surface receptors: G-protein coupled receptors (GPCRs) or receptor tyrosine kinases (RTKs). Signals are often transduced and amplified through cycles of reversible covalent modification of target proteins, catalyzed by an activator and deactivator. For example, protein kinases phosphorylate protein targets and their activity is terminated through the action of phosphatases. Another general class of transducer is the small GTP-binding proteins, whose action is accelerated by guanine-nucleotide exchange factors (GEFs) and terminated by GTPase-activating proteins (GAPs).

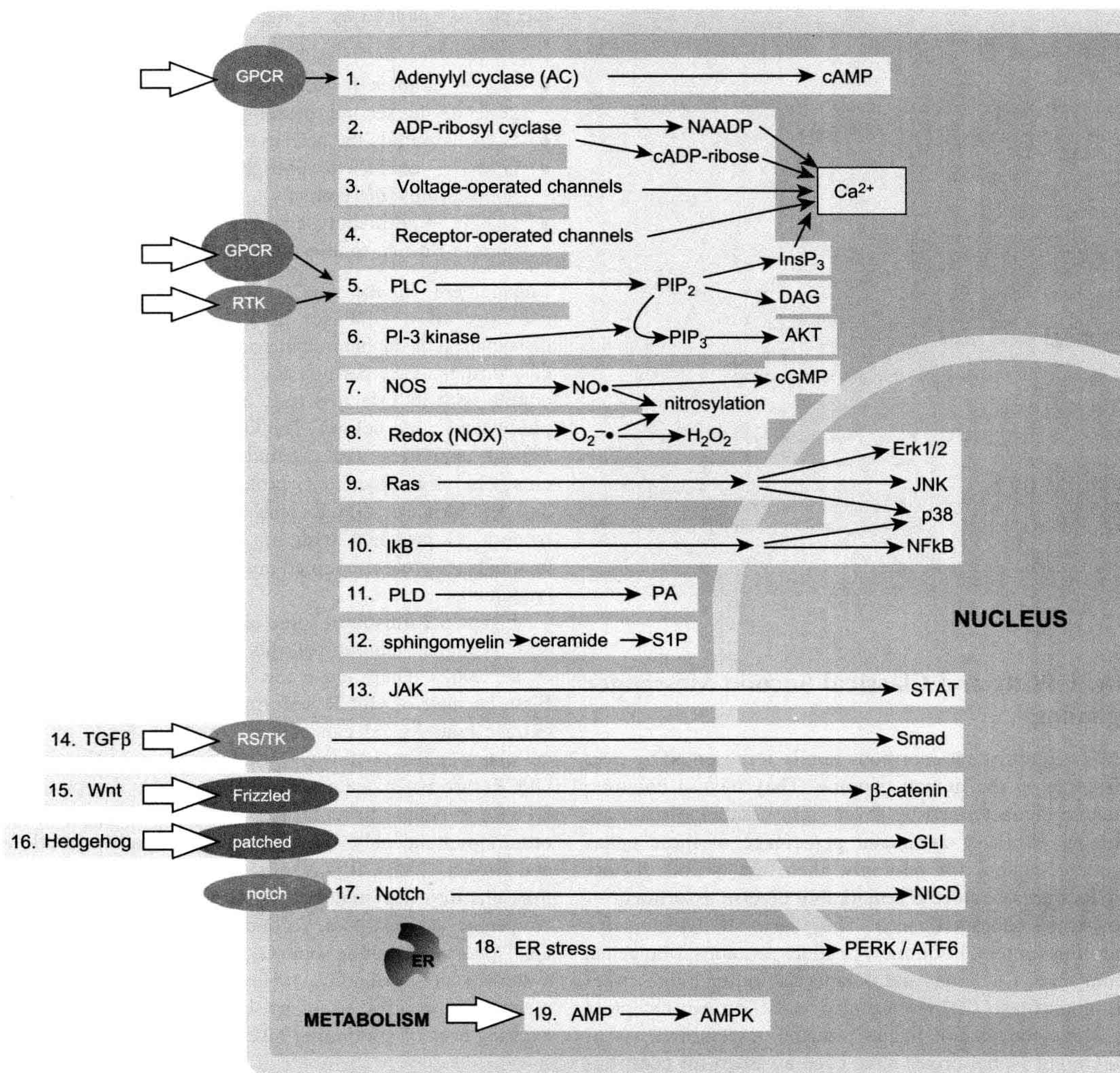


FIGURE 6.1 Inventory of major intracellular signaling pathways. 1. Cyclic AMP signaling pathway; 2. cyclic ADP-ribose and nicotinic acid-adenine dinucleotide phosphate (NAADP); 3. voltage-operated channels (VOCs); 4. receptor-operated channels (ROCs); 5. phospholipase C-dependent hydrolysis of PtdIns4,5P_2 (PIP_2); 6. PtdIns 3-kinase signaling (phosphorylation of PIP_2 to form PIP_3); 7. nitric oxide (NO)/cyclic GMP signaling pathway; 8. redox signaling: NADPH oxidase (NOX)→ reactive oxygen species (ROS); 9. mitogen-activated protein kinase (MAPK) signaling; 10. nuclear factor κB (NF-κB) signaling pathway; 11. phospholipase D pathway: phosphatidylcholine→phosphatidic acid (PA); 12. sphingomyelin signaling pathway: formation of ceramide and sphingosine 1-phosphate (S1P); 13. Janus kinase (JAK)/signal transducer and activator of transcription (STATs); 14. Smad signaling pathway: TGFβ→ Smad transcription factors; 15. Wnt signaling pathway; 16. hedgehog signaling: generation of the transcription factor GLI; 17. Notch signaling: generation of the transcription factor NICD (Notch intracellular domain); 18. endoplasmic reticulum stress signaling: information transfer from the ER to the nucleus; 19. AMP signaling: metabolic sensor. *(Adapted from Berridge (2009). See http://www.cellsignallingbiology.org for further details.)*

Transcription factors are frequently the ultimate target for many of these inputs (Brivanlou and Darnell, 2002). These can be resident in the nucleus, shuttle between nucleus and cytosol or require activation in the cytosol in order to gain access to the nucleus (Table 6.1). We will begin our discussion by briefly introducing some of the common players in signal transduction and then address each pathway separately.

TABLE 6.1 Examples of Signal-Dependent Transcription Factors

Most transcription factors are regulated by multiple signaling inputs; a classic example is CREB (cAMP response element binding), which is phosphorylated by both PKA and Ca^{2+}/calmodulin-dependent kinase IV (CaMKIV).
Nuclear receptors (e.g. steroid hormone receptors) GR, ER, PR, TR, RARs, RXRs, PPARs
Regulated by internal states (e.g. ER stress, DNA damage, hypoxia) SREBP, ATF6, p53, HIF
Regulated by signals generated at the cell surface:
Resident in nucleus CREB, E2F1, ETS, ATMs, SRF, FOS-JUN, MEF2, Myc, MeCP2 Shuttle between nucleus and cytosol DREAM, FOXO Become activated in the cytosol, translocate to nucleus STATs, SMADs, NFκB, β-catenin, NFAT, Tubby, GLI, MITF
From Brivanlou and Darnell, 2002.

IIIA. GPCRs and Classical Second Messenger Signaling

GPCRs comprise an enormous family represented by over 800 genes in the human genome. They have a common structure characterized by seven transmembrane-spanning domains. While a significant percentage of these genes encode receptors for odorants, there are ≈200 distinct GPCRs that recognize a remarkably diverse assortment of known non-odorant ligands. They serve as detectors for neurotransmitters, hormones, peptides, photons, bile acids, amino acids, Ca^{2+} ions and tastants (including bitter, sweet and umami taste). There are also ≈150 orphan receptors for which the natural ligand remains unidentified. As of 2009, eight Nobel prizes have been awarded for contributions in the field of signal transduction via G proteins and second messengers. GPCRs are also targets (directly or indirectly) for at least 30% of all currently prescribed drugs, further attesting to the physiological and medical importance of this class of proteins (Pierce et al., 2002).

G-protein coupled receptors are so-named because they interact with a class of proteins known as *heterotrimeric G-proteins* (Oldham and Hamm, 2008), consisting of a G_α subunit (represented by 16 genes) and fused G_β and G_γ subunits (six and 12 genes, respectively). *Lipid modifications* (e.g. palmitoylation, prenylation) keep the various subunits anchored to the plasma membrane where they interact with GPCRs.

Most of the specificity of the signal derives from the G_α subunit, which is allowed to couple to an effector when the receptor is engaged by its ligand. The major types of Gα subunits are:

- $G_{\alpha s}$ – couples to adenylyl cyclases (AC1–AC9) to generate the second messenger, cAMP
- $G_{\alpha i/o}$ – inhibits the activity of most adenylyl cyclases
- $G_{\alpha q/11}$ – couples to phospholipase C and the Ca^{2+}-phopshoinositide pathway
- $G_{\alpha 12/13}$ – ultimately engages the small GTP-binding protein Rho A, to alter the cytoskeleton.

Engagement of the GPCR with its ligand results in exchange of a GDP for GTP on the G_α subunit and dissociation of the heterotrimeric complex into free G_α and $G_{\beta\gamma}$ dimers. This permits the GTP-bound G_α subunit to couple with its effectors (e.g. adenylyl cyclases or phospholipase C; see below). The $G_{\beta\gamma}$ subunits also have biological activities that include interactions with ion channels, monomeric G-proteins (e.g. Rac, Cdc42) and PI 3-kinase. GPCRs can also interact (via heterotrimeric G proteins) with ion channels, e.g. the GIRK channels (G protein-coupled inwardly rectifying potassium channels).

Figure 6.2 illustrates some of the more common stimuli and biological outputs of this signaling system (Neves et al., 2002). There are a few things worth pointing out. First, because of GPCR isoform diversity, a single type of extracellular ligand can activate multiple kinds of intracellular signaling pathways. It is also the case that certain GPCRs are promiscuous, i.e. it is possible for particular GPCRs to couple to more than one type of G_α subunit in order simultaneously to activate multiple pathways (Hofer and Brown, 2003). It is also noteworthy that communication via the vast majority of GPCR ligands ultimately converges on just two second messenger systems: the Ca^{2+}/phosphoinositide (via $G_{\alpha q/11}$) and cAMP signaling systems (via $G_{\alpha s}$ and $G_{\alpha i/o}$). How these simple messengers manage to control so many biological functions is an exciting area of continuing investigation.

IIIB. Receptor Tyrosine Kinases and Receptor Serine/Threonine Kinases

Numerous growth factors, survival factors and hormones, such as insulin, exert their actions through receptor tyrosine kinases (RTKs). These are single-membrane spanning proteins that are represented by ≈20 different subfamilies. They generally form *dimers* upon engagement with their ligand (an exception is the insulin receptor, which is already in a dimeric configuration in the absence of insulin), causing tyrosine residues in a cytoplasmic domain of the receptor to become autophosphorylated. The RTK then assumes an active conformation that permits it to interface with several types of downstream signaling transducers. RTKs are also linked to scaffolding proteins

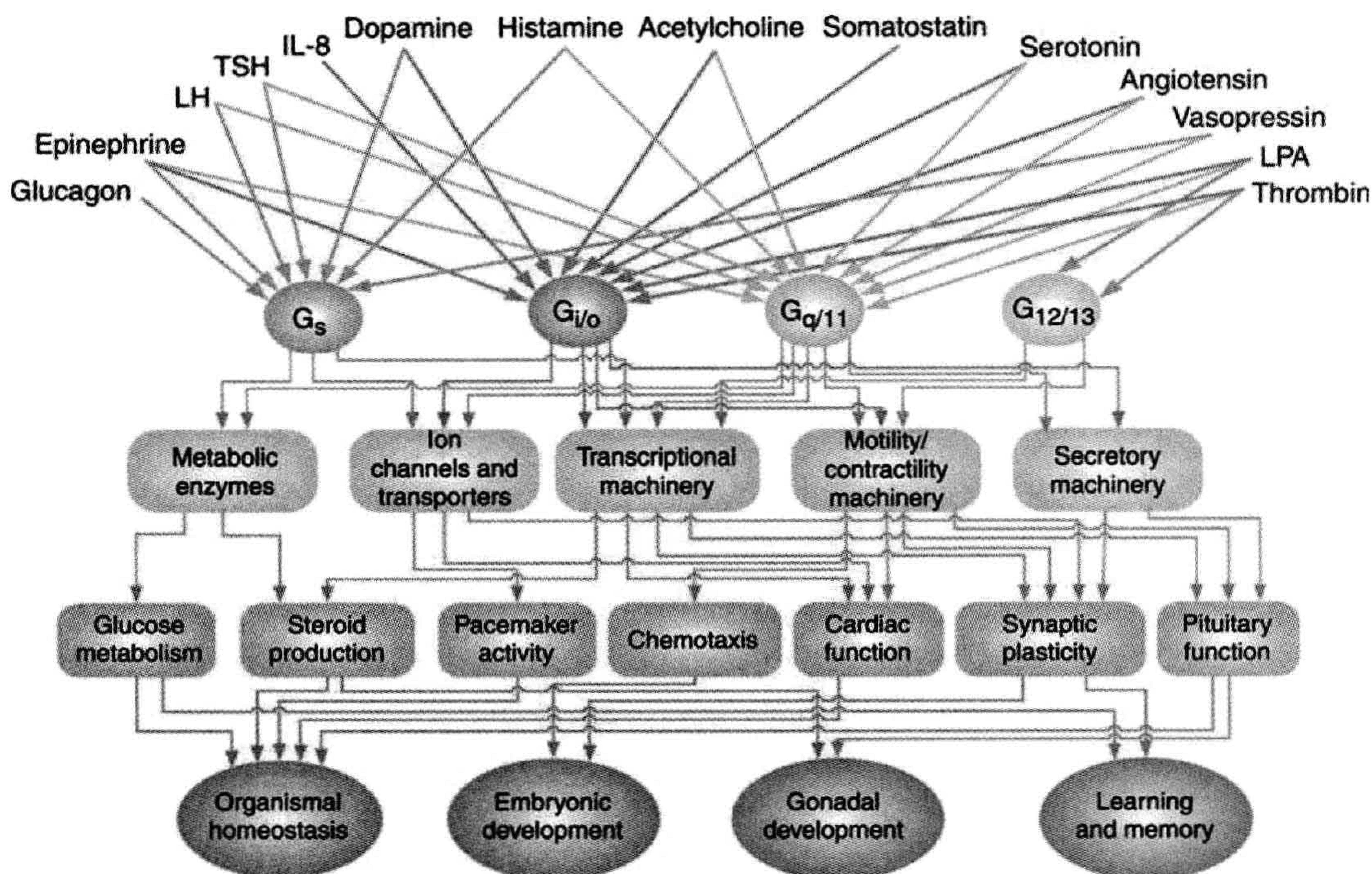


FIGURE 6.2 Regulation of biological functions through heterotrimeric G-protein pathways. Examples of regulatory networks that control functions via the four major classes of heterotrimeric G proteins are depicted. See text for further details. *(Taken from Neves et al. (2002). Science. 296, 1636–1639, AAAS Publishers.)*

that facilitate these processes. Major intracellular pathways that are turned on by RTK stimulation include:

1. Ras – the activated RTK is linked via adaptors proteins (Grb2 and SOS) to the small G protein ras which, in turn, activates another monomeric G protein known as raf. Raf is important in turning on the MAP kinase cascade (e.g. ERK1/2; see below)
2. PLCγ – activation of phospholipase Cγ generates $InsP_3/Ca^{2+}$ and DAG (see Ca^{2+}-phosphoinositide pathway below)
3. PI-3kinase – generates the lipid PIP_3 to activate Akt (protein kinase B; see below)
4. Src family kinases – these are part of a large family of non-receptor tyrosine kinases. They work by both helping to assemble signaling complexes and to phosphorylate tyrosine residues on targets within the complex.

The receptor serine/threonine kinases (RS/TKs) of the transforming growth factor β (TGFβ) superfamily are also single-membrane spanning receptors. RS/TKs are detectors for certain growth stimuli, including bone morphogenetic protein (BMP) and TGFβ (Moustakas et al., 2001). These receptors generally form *tetramers* and couple to the Smad signaling pathway (discussed below).

IIIC. Small GTP-Binding Proteins

As the name suggests, these are small monomeric proteins that bind GTP, which results in the G protein assuming an "on" state. This reaction is generally catalyzed by a large assortment of guanine nucleotide exchange factors (GEFs). When GTP is hydrolyzed to GDP, the G proteins are in the "off" state. GTPase activating proteins (GAPs) accelerate this process (Bos et al., 2007).

Monomeric G proteins (≈150 different ones) are important intermediaries in numerous types of signal transduction systems and can be subdivided into five general families: Ras, Rho, Rab, Ran and Arf. Ras proteins (36 genes) are control points for multiple types of signaling pathways (e.g. MAP kinase and PI-3 kinase pathways; see below). Many of the other G proteins (e.g. Rho family members) have key roles in the control of the cytoskeleton, while others (e.g. Rab, Arf) are involved in membrane trafficking. Ran is involved in nuclear transport.

IV. PHOSPHORYLATION BY KINASES AND OTHER POST-TRANSLATIONAL MODIFICATIONS

The most common motif for altering the activity of a target is through reversible *phosphorylation* of specific amino acid residues by a protein kinase (Pearce et al., 2010). These are usually serine or threonine residues or, in the case of tyrosine kinase family members, a tyrosine residue. Protein kinases have regulatory roles in all aspects of eukaryotic cell function and provide tremendous *signal amplification*. The domains of some of the more common kinases with similarity to the classical protein kinases A, C and G (PKA, PKC, PKG) are illustrated in Fig. 6.3. *Phosphatases* accelerate the removal of phosphate groups on phosphorylated proteins to terminate the signal.

Other types of reversible modifications to amino acid residues are also used (albeit less commonly than

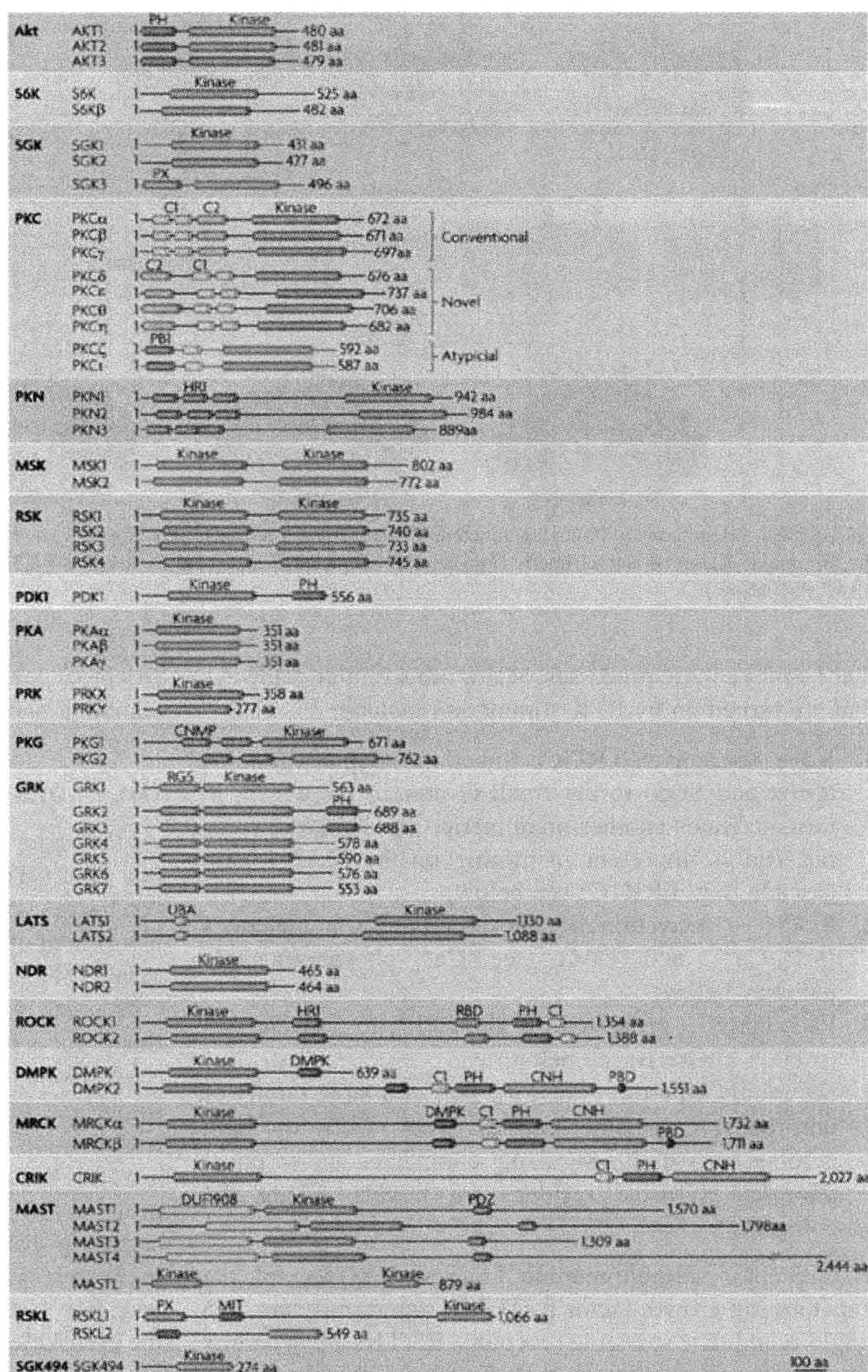


FIGURE 6.3 Examples of kinases with structural similarities to protein kinase A (PKA), protein kinase G (PKG) and protein kinase C (PKC). *(From Pearce, L.R., Komander, D. & Alessi, D.R. (2010). The nuts and bolts of AGC protein kinases. Nat Rev Mol Cell Biol, 11, 9–22.)*

phosphorylation) to control the activity of intermediates and final targets in signaling cascades. These include:

- oxidation of cysteine residues by the redox signaling pathway (see NADPH oxidase pathway below)
- nitrosylation (from nitric oxide pathway; see below)
- sumoylation
- acetylation
- protein methylation
- ubiquitination.

V. INTRACELLULAR SIGNAL TRANSDUCTION PATHWAYS

VA. Cyclic AMP Pathway

The foundations of the second messenger concept were established nearly half a century ago when Sutherland and Rall identified a small heat stable factor that mediated the intracellular actions of the hormones glucagon and epinephrine on glycogen metabolism in the liver. The mysterious factor turned out to be cAMP, a discovery that earned Sutherland the 1971 Nobel Prize in Physiology or Medicine (Rehmann et al, 2007).

This small highly diffusible second messenger is produced mostly through the activation of GPCRs that are coupled via $G_{\alpha s}$ to adenylyl cyclases (ACs; Fig. 6.4). The conventional ACs are a family of nine membrane spanning proteins (AC1−AC9) that are regulated differentially by other signaling pathways (e.g. Ca^{2+}). A given cell type may express several different isoforms of AC. Apart from the conventional ACs, there is also another route to cAMP production via a so-called "soluble" adenylyl cyclase (sAC or AC10). This AC is not a transmembrane protein, but it can nevertheless be localized to discrete regions of the cell (e.g. organelles) to provide localized cAMP signals. Because sAC is activated mainly by HCO_3^-/CO_2 (it is also regulated by Ca^{2+}) it has been considered to function as a metabolic sensor.

Once cAMP is generated, it can bind to and alter the activity of three general types of effector proteins:

- protein kinase A (PKA)
- cyclic nucleotide-gated channels (see Chapter 35)
- epac (exchange protein activated by cAMP; see below).

PKA is without question the most important target of the cAMP signal. At rest, PKA exists as a four-protein complex known as a heterotetramer because it consists of two catalytic subunits and two regulatory subunits. When cAMP binds the regulatory subunits, it releases the catalytic subunits, which are then free to phosphorylate other proteins within the cell. Important PKA targets include ion channels (e.g. CFTR, AMPA receptors), metabolic enzymes (e.g. lipase) and cAMP-dependent transcription factors such as the prototypical CREB (cAMP response element binding) protein. Inputs from other signaling cascades, including Ca^{2+} and MAP kinase pathways, also converge on CREB to regulate its function.

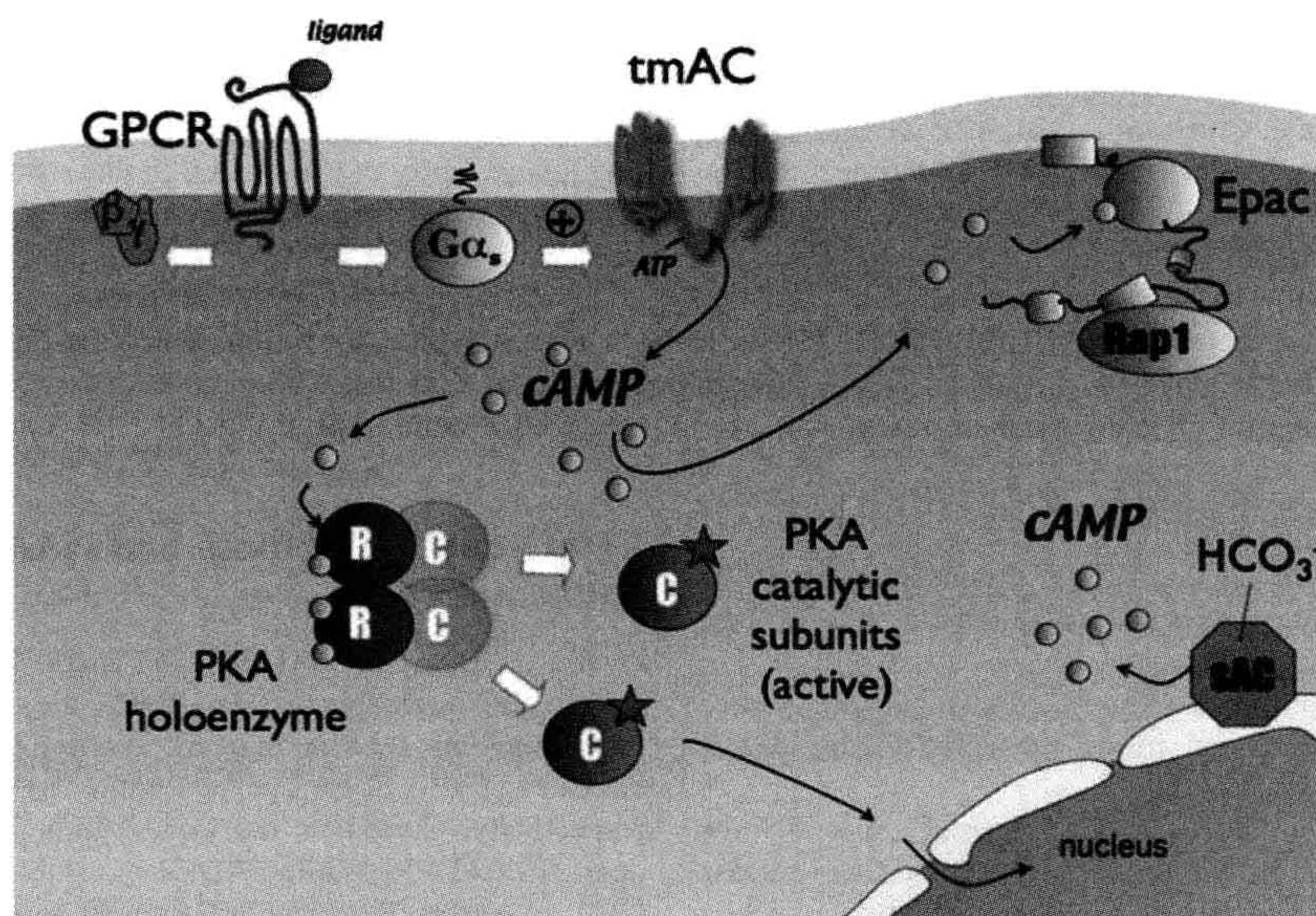


FIGURE 6.4 Basic features of the cyclic AMP signaling cascade.

Epac (exchange protein activated by cAMP) is a more recently identified effector of the cAMP signal for which there are two isoforms, Epac1 and Epac2. The best understood action of Epac is to enhance the GTP-ase activity of the small G proteins of the Ras superfamily, Rap1 and Rap2.

The cAMP signal is terminated by phosphodiesterases (PDEs), a complex family of enzymes with more than 20 members. Some of these isoforms of PDE also preferentially metabolize cyclic GMP (see below). PDEs are of major interest for drug development. Because the various isoforms can have tissue-specific distributions (e.g. in airway and cardiovascular systems), they may provide an avenue for controlling particular tissue functions using isoform-selective drugs.

VB. Calcium Signaling Pathway: VOCs, ROCs, SMOCs, SOCs and Store Release

Calcium is a major second messenger used by virtually all cells. It is at the same time the simplest messenger, since no enzymes are needed to create or destroy this ubiquitous signal, and one of the most versatile, since it can convey information in many different compartments within the cell (e.g. local events within cytosol, mitochondria, ER lumen and extracellular space) (Hofer and Brown, 2003; Berridge et al., 2003). Moreover, signaling targets can respond differentially to specific types of signals. For example, many Ca^{2+} signals are oscillatory in nature and this pattern may preferentially activate one kind of target (e.g. an ion channel) while a sustained elevation in Ca^{2+} may ultimately activate another (e.g. a transcriptional cascade). As details of this system are covered in several other chapters in this volume (e.g. Chapters 13, 14, 42), we will present only a general overview of the Ca^{2+} signaling pathway here.

Ca^{2+} is normally maintained at very low levels in the cytosol ($\approx 50\,nM$ – this is very low if you consider that distilled water contains about $5-10\,\mu M$ free Ca^{2+}!) but it can rapidly become elevated as much as 10–20-fold through any number of different mechanisms:

1. VOCs: voltage-operated Ca^{2+} entry pathways (in excitable cells; see Chapter 21)
2. ROCs: receptor operated Ca^{2+} channels, activated by extracellular ligands such as glutamate or ATP (see Chapter 36)
3. SMOCs: second messenger-gated channels are opened by ligands generated inside the cell (cAMP, cGMP, DAG, arachidonic acid)
4. release from intracellular Ca^{2+} stores, especially the ER, following activation of intracellular Ca^{2+} release channels. These are Ca^{2+} selective channels typically located on the ER or SR membrane, and include $InsP_3R$, release channels activated via cADPR, and RyR (see Chapter 42). These pathways are discussed below.
5. SOCs: store-operated Ca^{2+} entry channels are activated when the free concentration of Ca^{2+} in the ER lumen is reduced, for example following agonist/$InsP_3$-induced release described in the next section.

VC. The Ca^{2+}-Phosphoinositide Pathway

GPCRs and RTKs elicit Ca^{2+} signals via the Ca^{2+}-phosphoinositide pathway, a ubiquitous mechanism found in nearly all cell types (including excitable cells). Receptor engagement results in increased turnover by phospholipases (PLCβ for GPCRS and PLCγ for RTKs) that hydrolyze the plasma membrane lipid PIP_2 to produce DAG (which remains associated with the bilayer) and a small diffusible hydrophilic molecule, $InsP_3$. While DAG works to stimulate certain PKC isoforms, $InsP_3$ is able to bind to a Ca^{2+} release channel on the ER membrane known as the $InsP_3$ receptor. The ER continually sequesters Ca^{2+} via a pump known as the SERCA (sarcoendoplasmic Ca^{2+}-ATPase; see Chapter 13) so that the free resting $[Ca^{2+}]$ is $\approx 500\,\mu M$ in the ER lumen. Once the $InsP_3$ receptor is opened, the cation floods out of the ER into the cytoplasm, generating a spike in cytosolic Ca^{2+} that subsides as the stores become emptied.

There is then a second and very interesting phase of the signal. The reduction in free $[Ca^{2+}]$ within the ER lumen is sensed by the luminal domain of a recently identified ER transmembrane protein known as STIM1. The decreased $[Ca^{2+}]$ causes STIM1 to aggregate in discrete zones of ER just under the plasma membrane and this leads to the activation of Ca^{2+} selective channels (mostly of the family of channels known as Orai channels) in the plasma membrane. Entry of Ca^{2+} through these channels typically generates a sustained phase of the Ca^{2+} signal that serves both as a source of Ca^{2+} for refilling the ER stores and as a signal for cellular targets that require a more persistent elevation for their activation. When the initiating stimulus is removed and $InsP_3$ production ceases, the stores refill through the action of the SERCAs.

VD. Cyclic ADP-Ribose and NAADP Pathways

Cyclic ADP-ribose (cADPR) and nicotinic acid-adenine dinucleotide phosphate (NAADP) are related Ca^{2+}-mobilizing messengers that are synthesized by a single enzyme (ADP ribosyl cyclase) from NAD^+ and NADP, respectively. Curiously, the same synthetic enzyme also degrades cADPR. While cADPR is established to release Ca^{2+} from the ER, the physiological role of cADPR as a messenger has been somewhat controversial. The stimuli

leading up to its production and the precise mechanisms by which it releases Ca^{2+} are, however, an active area of investigation.

NAADP is an extremely potent releaser of intracellular Ca^{2+} stores. The "two-pore channels" (TPC1 and TPC2) that reside in acidic endolysosomal compartments, were recently identified as *bona fide* targets of NAADP (Zhu et al., 2010). Since other intracellular Ca^{2+} release channels on the ER/SR ($InsP_3R$ and RyR) increase their open probability with increasing levels of cytosolic $[Ca^{2+}]$, a small spurt of Ca^{2+} from these acidic compartments may serve to "prime" the $InsP_3R$ and/or RyR, resulting in the generation of global Ca^{2+} signals.

VE. PtdIns 3-Kinase Signaling

The membrane lipid constituent PIP_2 has many biological functions that include regulation of ion channels and exocytosis. It is also an important precursor for other biologically active lipids (Wymann and Schneiter, 2008). As noted above, stimulation of GPCRs and RTKs can lead to activation of phospholipases (PLCβ or PLCγ, respectively) that metabolize PIP_2 into $InsP_3$ and DAG. Following receptor engagement, another parallel arm of these reactions can also be set in motion that involves phosphorylation of PIP_2 by the enzyme phosphatidyl inositol 3-kinase (PI3-kinase). A major target of the newly generated lipid species, PIP_3, is another kinase, protein kinase B (PKB), more commonly known as AKT.

AKT is in effect recruited to the inner leaflet of the plasma membrane by the freshly generated PIP_3 because it contains a domain known as the Pleckstrin Homology (PH) domain, a common lipid-binding motif found in many lipid-dependent signaling proteins. Another player in this cascade, that also has a PH-domain, is PDK1 (phosphoinositide-dependent protein kinase 1). When AKT and PDK1 are both recruited to the plasma membrane at the same time, PDK1 can phosphorylate and turn on AKT. Once activated, AKT phosphorylates or interacts with a wide range of targets (e.g. the kinase mTOR) to govern processes such as growth, protein, lipid and glycogen synthesis and apoptosis and proliferation.

PI3K/AKT signaling is arrested when PIP_3 in the membrane becomes metabolized. This occurs through a specific enzyme known as PTEN. PTEN is a phosphoinositide phosphatase, i.e. an enzyme capable of removing phosphate groups from PIP_3. The timely termination of the signal by PTEN is crucial. For example, during growth factor stimulation, the absence of PTEN leads to overstimulation of this pathway and inappropriate entry into the cell cycle even after the initiating stimulus has been removed. In fact, PTEN is defined as a tumor suppressor gene and PTEN mutations and deficiencies are prevalent in many types of human cancers. PTEN and other elements of the PI3K pathway are actively being investigated as targets for anticancer drugs.

VF. Nitric Oxide (NO)/Cyclic GMP Signaling Pathway

Nitric oxide (NO) is a highly reactive, membrane permeable gaseous transmitter that is produced from the amino acid L-arginine by three different nitric oxide synthase (NOS) enzymes: eNOS (endothelial NOS), nNOS (neuronal NOS) and iNOS (inducible NOS) (Pacher et al., 2007). The nNOS and eNOS isoforms were named for the tissues in which they were originally identified and iNOS was so named because its expression could be induced in macrophages during inflammation, however, all three enzymes are actually widely distributed across different cell types.

NO is generated by eNOS and nNOS following an elevation in intracellular Ca^{2+}. The iNOS enzyme, on the other hand, appears to be constitutively active (although regulated by other signaling molecules, particularly calmodulin) and can produce large amounts of NO for prolonged periods.

Once synthesized, the NO molecule has two major jobs. The first is to activate the so-called "soluble" guanylyl cyclase (sGC), which catalyzes the formation of cGMP (Rehmann et al., 2007) (which is more stable than NO) from GTP. Cyclic GMP in turn activates a cGMP-dependent protein kinase (PKG) that can phosphorylate numerous downstream targets. The cyclic nucleotide can also activate channels in the plasma membrane (see Chapter 35).

Note that there is also a nitric oxide-*independent* route to cGMP production that occurs when certain peptide hormones, such as atrial natriuretic factor (ANP) and guanylin, bind to the transmembrane receptor known as particulate guanylyl cyclase (pGC). In addition to stimulating the formation of cGMP, the other major action of NO is to cause S-nitrosylation of the thiol-side chains of cysteine residues within protein targets, thereby altering their activity.

Ferid Murad, Louis Ignarro, and Robert Furchgott were awarded the 1998 Nobel prize for their discovery of NO, underscoring the physiological and clinical importance of this messenger. NO (originally known as EDRF or endothelial-derived relaxing factor) regulates smooth muscle relaxation and hence controls vasodilatation, bladder function, penile erection and gastrointestinal motility, to name but a few of its functions. Nitric oxide is also used by fireflies to elicit flashes of light and by plants to evade pathogens. Other endogenous "gasotransmitters" have recently been described, including carbon monoxide (CO) and hydrogen sulfide (H_2S) gas.

VG. Redox Signaling through NADPH Oxidase (NOX)

It has long been appreciated that immune cells, such as neutrophils, take advantage of the regulated production of reactive oxygen species (ROS) via NADPH oxidases (Nox) in order to neutralize invading pathogens. It is now known that nearly all cell types utilize Nox (of which there are five isoforms, Nox1−Nox5) and the related dual-oxidase enzymes, Duox (represented by two isoforms, Duox1 and Duox2), to generate reactive oxygen species and peroxide (H_2O_2) metabolites that, in effect, serve as short-lived second messengers to regulate a wide variety of cell functions.

One route to the activation of NADPH oxidases occurs at the plasma membrane after stimulation of receptors for hormones, growth factors or cytokines linked to PI3-K. This enzyme converts PIP_2 into PIP_3 (see above) and the resulting PIP_3 stimulates Nox, producing superoxides that can inactivate many protein targets (e.g. transcription factors, tyrosine phosphatases, PTEN) in the localized microdomain surrounding the Nox complex. It should be noted that substantial amounts of ROS can also be generated as a by-product of mitochondrial respiration.

VH. Mitogen-Activated Protein Kinase (MAPK) Signaling

The MAPK pathway is a major multikinase signaling circuit that is often thought of in the context of growth factor stimulation (e.g. gene expression leading to growth and proliferation). In fact, it controls a multitude of cellular functions including metabolism, motility, apoptosis and long-term memory, to name a few. It receives inputs from multiple signaling systems, including GPCRs, RTKs, Toll receptors and integrins, and can also transduce the effects of environmental stresses (e.g. osmotic stress, UV radiation).

There are three major types of MAPK cascades named after their major transducers:

1. extracellular-signal-related kinase (ERK)
2. c-Jun N-terminal kinase (JNK)
3. p38.

As shown in Fig. 6.5, the general scheme of this pathway involves the initial activation of a MAPKKK, which phosphorylates a MAPKK which, in turn, phosphorylates ERK, JNK or p38 (the MAPK). Although counterintuitive, it is thought that this arrangement of having three kinases in a row may actually conduct the signal faster than systems employing fewer numbers of kinases. Once phosphorylated, ERK, JNK and p38 frequently translocate to the nucleus to regulate gene expression.

VI. Nuclear Factor κB (NF-κB) Signaling Pathway

The NF-κB/Rel family (NF-κB1, NF-κB2, NF-κB3, RelB, and cRel) consists of a group of master transcription factors that remain latent in the cytoplasm until activated (Hayden et al., 2006; Perkins, 2007). It is commonly regarded as

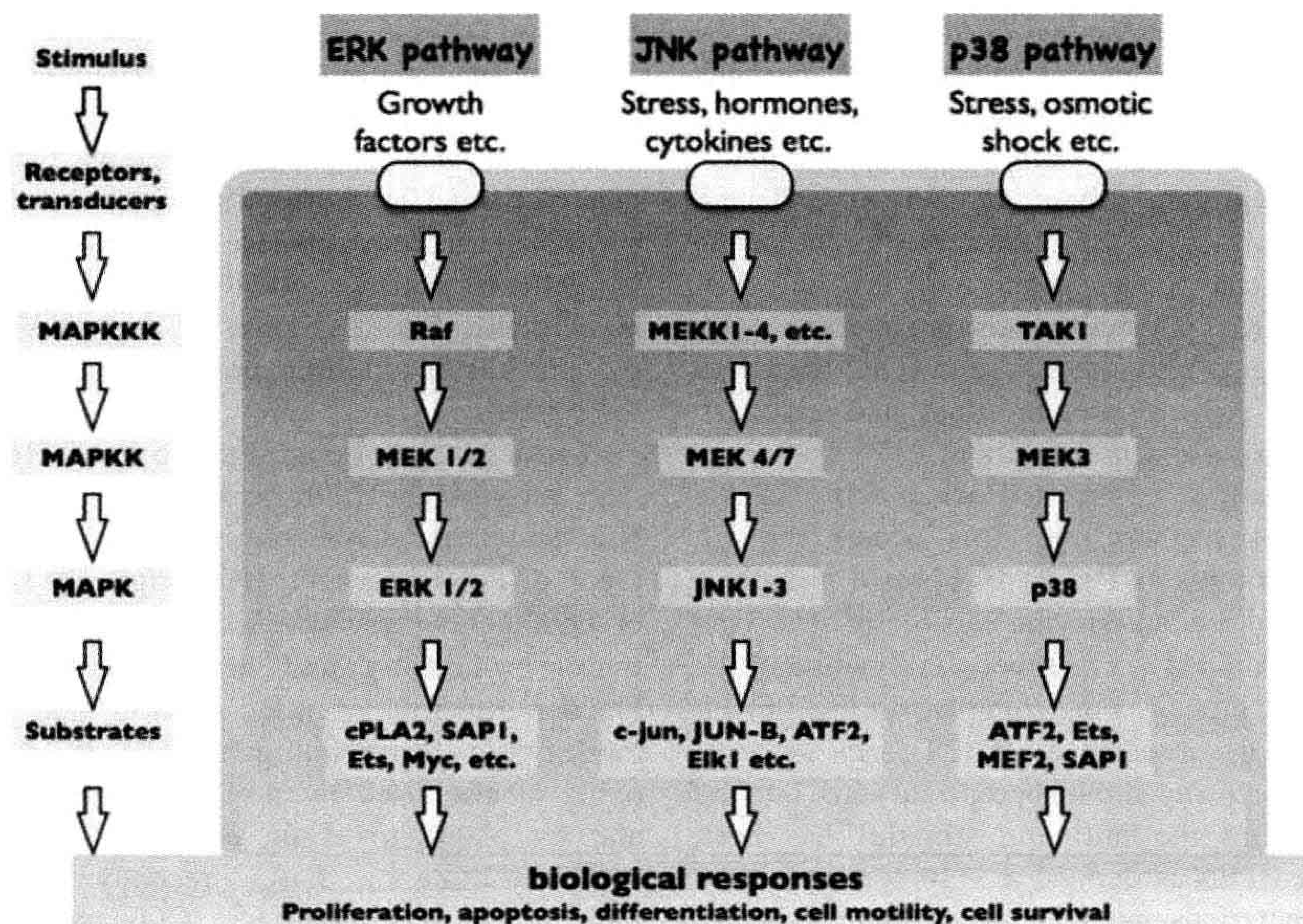


FIGURE 6.5 MAP kinase cascades.

a "first responder" to a large, diverse, panel of stress-induced stimuli that include cytokines (e.g. tumor necrosis factor, TNFα), lymphokines, mitogens, hormones, carcinogens, inflammatory agents, tumor promoters, drugs, UV light, oxidative stress and certain growth factors. There are at least 150 types of extracellular stimuli known to activate this signaling system, which is present in nearly all cells. It also is involved in the control of osteoclastogenesis through the RANKL receptor and activation of receptors, known as Toll-like receptors, whose job it is to recognize pathogens and inflammatory cytokines. Each of these types of inputs requires a complex cast of players (not detailed here) that ultimately converge on the NF-κB pathway according to the following general scheme.

At rest, NF-κB is retained in the cytoplasm (and is therefore kept inactive) by "IκB" (inhibitor of NF-κB). IκB is a cytosolic resident that belongs to a family of six proteins responsible for masking the nuclear localization signal of NF-κB. However, in response to diverse stimuli, a kinase known as "IKK" (inhibitor of NF-κB kinase) becomes activated. There are three forms of IKK (IKKα, IKKβ and "NEMO", a regulatory protein also known as IKKγ), which phosphorylate IκB, thereby tagging it for degradation by the proteasome. Liberated from IκB, NF-κB is now free to enter the nucleus, where it can bind to DNA and turn on expression of large gene sets, e.g. those involved in innate immune and stress responses. The NF-κB pathway also receives inputs from numerous other signaling systems to modulate its activity and is an important object of drug discovery efforts.

VJ. Phospholipase D Pathway

There are more than 1000 types of biological lipids. Phospholipase D enzymes (two isoforms: PLD1 and PLD2) hydrolyze phoshatidylcholine, a ubiquitous lipid constituent of the bilayer, to generate the bioactive lipid, phosphatidic acid (PA). PLD1 is located principally on intracellular membranes (the ER, Golgi and endosomal membranes) and in caveolae of the plasma membrane. PLD1 becomes activated by elements downstream of GPCR or RTK stimulation (e.g. via PKC). PLD2 appears to *not* be activated by these stimuli and is mainly localized to the plasma membrane. Once synthesized, PA acts as a second messenger to regulate a number of enzymes, including protein phosphatases, mTOR and other targets that control budding and fusion, secretion, changes in cytoskeleton and proliferation (Cazzolli et al., 2006).

VK. Sphingomyelin/Ceramide Signaling Pathway

Ceramides are bioactive lipids that can be generated enzymatically in response to stressful stimuli that include TNFα, radiation, chemotherapy drugs and through the activation of "death receptors" by a transmembrane protein known as Fas ligand on a neighboring cell. There are two routes to its formation: (1) from the breakdown of sphingomyelin (a constituent of the lipid bilayer, particularly the plasma membrane); or (2) through de novo synthesis (Hannun and Obeid, 2008).

Ceramide has several protein targets, including the protease cathepsin D, a particular isoform of PKC (PKCξ) and ceramide-activated phosphatases. However, its action does not stop there. Ceramide is further converted to the lipid messenger sphingosine, which activates certain kinases. Like ceramide, sphingosine can drive apoptosis (programmed cell death) and cell cycle arrest.

This cascade continues even further, however, since sphingosine is the precursor for another potent bioactive lipid, sphingosine 1-phosphate (S1P). S1P is generated when sphingosine kinase becomes activated by diverse stimuli that include growth factors (PDGF, IGF, VEGF), cytokines (IL-1, TNF), hypoxia and oxidized LDL to name a few (Wymann and Schneiter, 2008). S1P can act as a local extracellular messenger to stimulate GPCRs of the "EDG" family (specifically EDG1, 3, 5, 6 and 8) on the same cell or on neighboring cells. EDG receptors are coupled to the Ca^{2+}-phosphoinositide signaling pathways.

VL. Janus Kinase (JAK)/Signal Transducer and Activator of Transcription (STATs)

This relatively simple pathway mediates the actions of more than 30 different hormones and cytokines, including numerous interleukins (e.g. IL-2), interferons, growth hormone, erythropoietin and prolactin. It is frequently referred to as a "fast-track" for signaling because there are so few components between the initial activation of the receptor (RTK, GPCR, cytokine receptor etc.) and the translocation of activated STATs to the nucleus, where they bind the promoter region of responsive genes. There are four JAK family members (JAK1–JAK3 and TYK1) and seven STATs.

Typically, JAKs "prime" the ligand-bound cytokine receptor for its interaction with the STATs by phosphorylating specific tyrosine residues on the dimerized receptor. STATs dock onto the phosphorylated receptor and then themselves become phosphorylated by JAKs (which remain associated with the receptor). At this point the activated STATs disengage from the receptor and form dimers, rendering them competent to enter into the nucleus to complete their work as transcription factors.

VM. Smad Signaling Pathway

Instructions from the TGF-β super-family of growth factors, including bone morphogenetic proteins (BMPs),

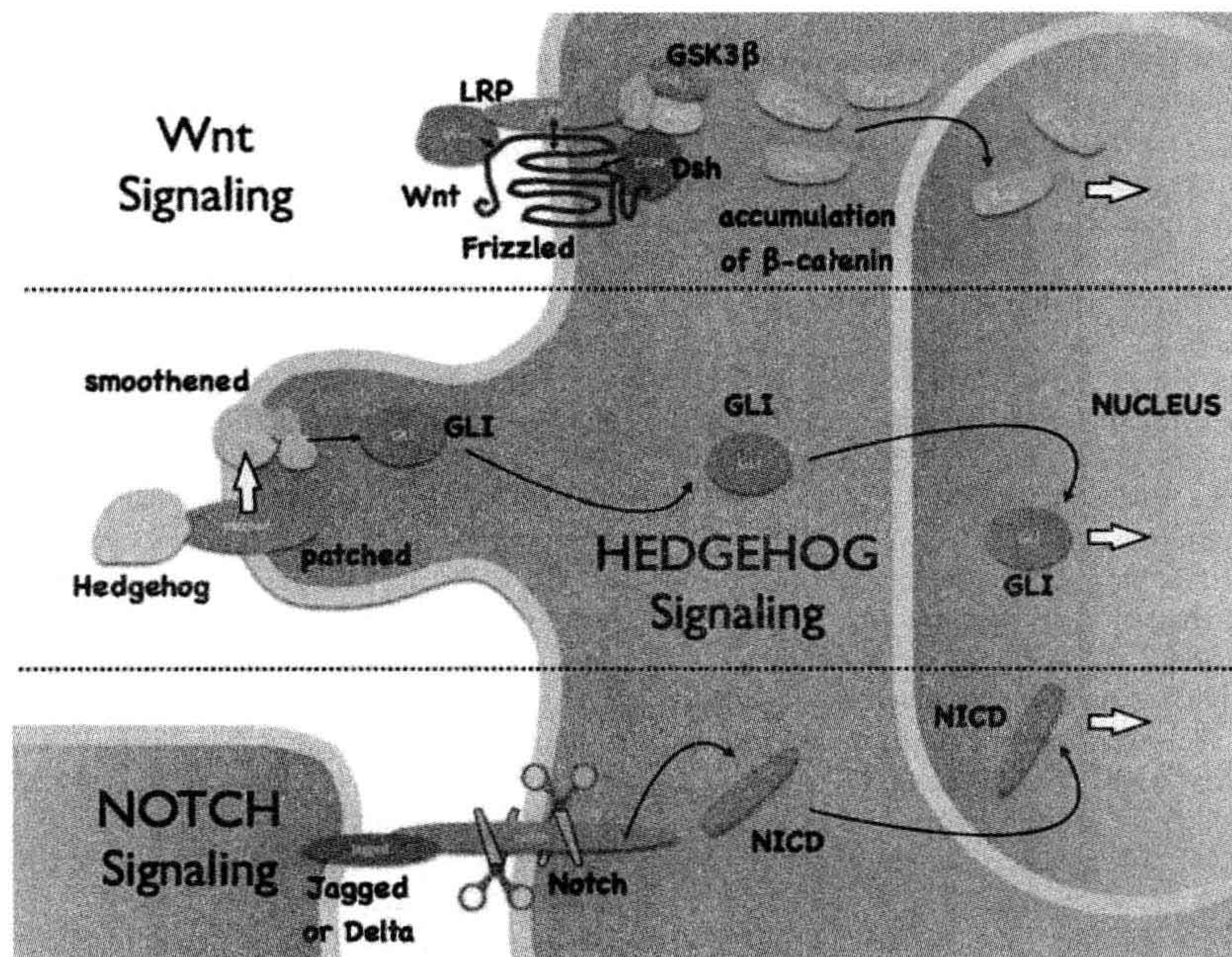


FIGURE 6.6 Wnt, Hedgehog and Notch pathways.

are funneled via their serine-threonine kinase receptors on the cell surface into an intracellular system of transcription factors and regulators known as Smads (Moustakas et al., 2001). Smads exist as three different types: R-Smads, co-Smad and I-Smads. The R-Smads are receptor-regulated and become directly phosphorylated when TGF-β binds its receptor (through a multistep process), activating the R-Smads, Smad2 or Smad3. Alternatively, agonists of the BMP-type bind to their cognate receptors to activate Smad1, Smad5, or Smad8. Smad4 is known as a co-Smad, which serves to facilitate signaling by forming dimers with R-Smads that then translocate to the nucleus to elicit expression of target genes. I-Smads (Smad6, 7) compete with Smad4 to inhibit this process.

In addition to controlling developmental processes, these systems maintain important physiological functions in the adult. For example, BMP is involved in skeletal remodeling and controlling proliferation of cells within the intestinal stem cell niche. TGF-β also directs differentiation of maturing cells within the intestinal villus, a structure characterized by extremely rapid cell turnover.

VN. Wnt Signaling Pathway

Wnt, Notch and Hedgehog (along with the TGF-β and receptor tyrosine kinase systems described above) are the major signaling pathways controlling early development throughout the animal kingdom. These pathways (Fig. 6.6) also exert important homeostatic and remodeling functions in adult organisms and are being increasingly indicted in the genesis of disease states, including tumorigenesis.

Wnts are extracellular lipoprotein growth factors that are encoded by 19 different genes in humans (Gordon and Nusse, 2006). Wnt binds to a receptor known as "Frizzled" (of which there are 10 types) that resembles the seven membrane-spanning receptors of the GPCR family. In the "canonical" (i.e. orthodox) Wnt/β-catenin pathway, Wnt also binds to a co-receptor of the LRP family and these proteins then form a complex with an intracellular protein known as disheveled. The Wnt pathway is somewhat unusual in that ligand binding leads to downstream steps that turn off constitutive degradation of the transcription factor β-catenin by a destruction complex formed by Axin, adenomatous polyposis coli (APC) protein and glycogen synthase kinase 3β (GSK-3). This allows β-catenin to accumulate to high levels and act as a transcription factor in the nucleus. There also exist β-catenin-independent modes of Wnt/Frizzled signaling. Among its many functions, the Wnt pathway is known to turn on proliferation of intestinal stem cells. It is noteworthy that mutations in members of this pathway are frequently observed in colon cancer cells.

VO. Hedgehog Signaling

The hedgehog gene was so named following the discovery of a *Drosophila* mutant possessing anterior-posterior patterning defects. This animal also presented a spiky hedgehog-like appearance due to the condensed solid lawn of denticles (cuticular extensions) on the body surface. The hedgehog protein (of which there are three in vertebrates, Indian hedgehog, desert hedgehog and sonic hedgehog) is a secreted morphogen that has recently emerged as an important target for anticancer drugs, with several compounds in clinical trials. This pathway is active in adult hematopoietic stem cells and hair follicles, where it signals the transition to the growth phase. Components of this pathway are frequently mutated in skin cancer cells.

Hedgehog (often abbreviated Hh) is secreted from cells by an unusual pathway (Chen et al., 2007). The cytosolic protein first acquires certain unique lipid modifications that allow it to be recognized and exported from the cell by a transmembrane enzyme known as dispatched. Carrier proteins in the extracellular milieu facilitate the delivery of Hh to target cells, where it binds a receptor called patched. At rest, the function of patched is to repress another transmembrane protein, smoothened. The job of smoothened is to keep transcription factors of the GLI family (three in mammals: GLI1–GLI3) in a dormant state. Binding of Hh to patched therefore effectively allows for the activation of GLI. An interesting feature of the preceding steps is that they take place almost entirely on the primary cilium of the target cell, a specialized surface projection present in virtually every vertebrate cell type. Once GLI is generated, it translocates to the nucleus where it controls transcription of genes involved in proliferation.

VP. Notch Signaling

Notch is a cell surface receptor that is an integral component of a relatively simple signaling pathway used extensively throughout the animal kingdom for controlling development (Bray, 2006). It takes its name from a notched wing phenotype in *Drosophila* first identified in genetic studies performed nearly a century ago. Flies with the notch mutation have increased numbers of neurons but less epidermal tissue.

There are four human Notch receptors (Notch1–4). Notch is unusual because most of its ligands are transmembrane proteins, therefore it becomes activated only when there is contact between receptor and ligand on a neighboring cell. This pathway is also very straightforward in that it signals without any amplification. The cascade starts when the Notch receptor encounters a transmembrane ligand on the communicating cell. One such ligand is known as Jagged and another is known as Delta. This interaction initiates two proteolytic cleavage events (not detailed here) that ultimately liberate an intracellular fragment of the Notch receptor called NICD (Notch intracellular domain). NICD works as a transcription factor that then translocates to the nucleus to alter gene expression. The signal is terminated via proteolytic degradation of NICD.

It is possible to envision how this arrangement permits one cell to influence gene expression in another and thereby allow an organism to assemble complex multicellular structures with similar or dissimilar phenotypes. In adult organisms, Notch signaling is involved in structural homeostasis, response to injury and repair. For example, this can take the form of influencing of the fate of intestinal cells destined for either secretory or absorptive lineages, and during angiogenesis.

VQ. Endoplasmic Reticulum Stress Signaling

This pathway provides a route for transmitting information from the ER to the nucleus (Ron and Walter, 2007). The ER stress response starts when polypeptides that are being processed in the ER lumen lose their tertiary structure or there is an overload of ER proteins. This can occur physiologically, e.g. if there is a sudden upregulation of protein production so that the protein-folding machinery in the ER becomes overwhelmed, and during viral infections. It also occurs when there is a persistent loss of Ca^{2+} from the ER lumen, causing Ca^{2+}-dependent chaperones to allow unfolding of the proteins they are escorting (note that this underscores the overall importance of reliable ER Ca^{2+} homeostasis, apart from its signaling function).

The presence of unfolded polypeptides in the lumen is sensed by several different systems (Lai et al., 2007). For example, this condition elicits processing and release of an ER-resident transcription factor ATF6, which ultimately travels to the nucleus, where it induces the expression of more chaperone proteins. Another attempt to correct the problem is mediated by the ER kinase PERK, which ultimately turns off protein synthesis. Persistent unfolded protein responses result in apoptosis through other ER stress sensors.

VR. AMPK Signaling: Metabolic Sensors

Cells need a way to communicate and adapt to changes in energetic status. When ATP levels are low, AMP is increased and this is detected by a fuel-sensing kinase, AMPK (AMP-activated protein kinase) (Steinberg and Kemp, 2009). AMPK directs processes that allow the cell to correct its energy deficit by turning on ATP-generating processes (glycolysis, fatty acid oxidation and

mitochondrial biogenesis) while inhibiting activities that use up ATP (gluconeogenesis, glycogen, fatty acid and protein synthesis). It also directly influences appetite-regulation in the hypothalamus.

AMPK is interesting in that it not only senses local AMP concentrations, but it also integrates the actions of hormones involved in energy balance such as leptin, ghrelin, adiponectin, glucocorticoids, insulin, as well as cannabinoids. It has generated recent excitement due to its apparent role in mediating the longevity-producing effects of calorie restriction.

VI. CONCLUSIONS

The preceding provides a brief and highly simplified snapshot of the major signaling pathways involved in the control of physiological processes. It highlights their beautiful diversity but also hints at their overwhelming intricacy. For the physiologist, the interconnected nature of these signaling networks means that perturbation of any one component may result in unforeseen alterations in other aspects of a cell's function. Systems biology approaches and new methods for monitoring signaling molecules with high spatiotemporal resolution (e.g. fluorescence- and GFP-based sensors) are among the tools that are currently being used to help unravel this complexity. The good news for those of us studying the regulation of physiological function is that each cell type and organ system will present us with diverse and exciting challenges for a long time to come.

BIBLIOGRAPHY

Berridge, M. (2009). Cell Signalling Pathways. In www.cellsignallingbiology.org ed.). Portland Press Limited.

Berridge, M. J., Bootman, M. D., & Roderick, H. L. (2003). Calcium signalling: dynamics, homeostasis and remodelling. *Nat Rev Mol Cell Biol, 4*, 517–529.

Bos, J. L., Rehmann, H., & Wittinghofer, A. (2007). GEFs and GAPs: critical elements in the control of small G proteins. *Cell, 129*, 865–877.

Bray, S. J. (2006). Notch signalling: a simple pathway becomes complex. *Nat Rev Mol Cell Biol, 7*, 678–689.

Brivanlou, A. H., & Darnell, J. E., Jr. (2002). Signal transduction and the control of gene expression. *Science, 295*, 813–818.

Cazzolli, R., Shemon, A. N., Fang, M. Q., & Hughes, W. E. (2006). Phospholipid signalling through phospholipase D and phosphatidic acid. *IUBMB Life, 58*, 457–461.

Chen, M. H., Wilson, C. W., & Chuang, P. T. (2007). SnapShot: hedgehog signaling pathway. *Cell, 130*, 386.

Gordon, M. D., & Nusse, R. (2006). Wnt signaling: multiple pathways, multiple receptors, and multiple transcription factors. *J Biol Chem, 281*, 22429–22433.

Hannun, Y. A., & Obeid, L. M. (2008). Principles of bioactive lipid signalling: lessons from sphingolipids. *Nat Rev Mol Cell Biol, 9*, 139–150.

Hayden, M. S., West, A. P., & Ghosh, S. (2006). SnapShot: NF-kappaB signaling pathways. *Cell, 127*, 1286–1287.

Hofer, A. M., & Brown, E. M. (2003). Extracellular calcium sensing and signalling. *Nat Rev Mol Cell Biol, 4*, 530–538.

Lai, E., Teodoro, T., & Volchuk, A. (2007). Endoplasmic reticulum stress: signaling the unfolded protein response. *Physiology (Bethesda), 22*, 193–201.

Moustakas, A., Souchelnytskyi, S., & Heldin, C. H. (2001). Smad regulation in TGF-beta signal transduction. *J Cell Sci, 114*, 4359–4369.

Neves, S. R., Ram, P. T., & Iyengar, R. (2002). G protein pathways. *Science, 296*, 1636–1639.

Oldham, W. M., & Hamm, H. E. (2008). Heterotrimeric G protein activation by G-protein-coupled receptors. *Nat Rev Mol Cell Biol, 9*, 60–71.

Pacher, P., Beckman, J. S., & Liaudet, L. (2007). Nitric oxide and peroxynitrite in health and disease. *Physiol Rev, 87*, 315–424.

Papin, J. A., Hunter, T., Palsson, B. O., & Subramaniam, S. (2005). Reconstruction of cellular signalling networks and analysis of their properties. *Nat Rev Mol Cell Biol, 6*, 99–111.

Pearce, L. R., Komander, D., & Alessi, D. R. (2010). The nuts and bolts of AGC protein kinases. *Nat Rev Mol Cell Biol, 11*, 9–22.

Perkins, N. D. (2007). Integrating cell-signalling pathways with NF-kappaB and IKK function. *Nat Rev Mol Cell Biol, 8*, 49–62.

Pierce, K. L., Premont, R. T., & Lefkowitz, R. J. (2002). Seven-transmembrane receptors. *Nat Rev Mol Cell Biol, 3*, 639–650.

Rehmann, H., Wittinghofer, A., & Bos, J. L. (2007). Capturing cyclic nucleotides in action: snapshots from crystallographic studies. *Nat Rev Mol Cell Biol, 8*, 63–73.

Ron, D., & Walter, P. (2007). Signal integration in the endoplasmic reticulum unfolded protein response. *Nat Rev Mol Cell Biol, 8*, 519–529.

Steinberg, G. R., & Kemp, B. E. (2009). AMPK in health and disease. *Physiol Rev, 89*, 1025–1078.

Wymann, M. P., & Schneiter, R. (2008). Lipid signalling in disease. *Nat Rev Mol Cell Biol, 9*, 162–176.

Zhu, M. X., Ma, J., Parrington, J., Galione, A., & Evans, A. M. (2010). TPCs: Endolysosomal channels for Ca2+ mobilization from acidic organelles triggered by NAADP. *FEBS Lett, 584*, 1966–1974.

Calcium as an Intracellular Second Messenger: Mediation by Calcium-Binding Proteins

John R. Dedman and Marcia A. Kaetzel

Chapter Outline

I. INTRODUCTION

Sidney Ringer provided the first report relating tissue and cellular function with Ca^{2+} in 1883. He demonstrated that Ca^{2+} was necessary for normal regular contractions of the isolated frog heart. Following this landmark study, Ca^{2+} became an essential component of physiological saline solutions. There have been numerous studies relating Ca^{2+} and cell functions including fertilization, development, differentiation, adhesion, growth, division, movement, contraction and secretion. This evidence demonstrates a primary regulatory role for ionized Ca^{2+} in biological systems. Ca^{2+} has also been associated with a number of diseases, particularly those of the muscular and nervous systems, in which this ion plays an important role in contraction and neurotransmitter release.

Understanding the mechanism of Ca^{2+} action has required approaches and expertise from distinct fields. Ca^{2+} is unique compared with other second messengers, which are formed as metabolic intermediates, such as cyclic nucleotides, inositol phosphates and diacylglycerol. Ca^{2+} is a divalent elemental metal and is not converted to any other form as a part of its cellular regulatory properties. Ca^{2+} is unlike other metal ions, such as K^+ and Na^+, which are involved in membrane potentials and excitability, or Mg^{2+} and Zn^{2+}, which act as enzyme cofactors involved in the catalysis of metabolic intermediates. The fact that Ca^{2+} has been associated with a wide variety of cellular functions brings attention to the fact that the blocking of one Ca^{2+}-regulated function could very likely affect interdependent secondary and tertiary functions.

II. DETERMINATION OF CA^{2+} INVOLVEMENT IN PHYSIOLOGICAL PROCESSES

The most direct approach to understanding the involvement of Ca^{2+} in a given physiological activity has been to follow the tradition of Ringer, i.e. through the reduction of extracellular Ca^{2+}. For example, the reduction of $[Ca^{2+}]_o$ from 1 to 0.1 mM markedly alters cell growth, adhesion, secretion and motility. A second approach has been to use various pharmacological agents. As discussed in other chapters, Ca^{2+} channel modulators have also proven useful in probing cellular systems. These distinct chemicals act by binding to the membrane Ca^{2+} channel, thereby blocking (Ca^{2+} channel agonist) the influx of extracellular Ca^{2+}. The

Cell Physiology Sourcebook. DOI: 10.1016/B978-0-12-387738-3.00007-X

antibiotic A23187 has been shown to cage divalent metal ions such as Ca^{2+} and thereby to act as an ionophore to facilitate their movement across biological membranes (Fig. 7.1). The A23187 ionophore binds Ca^{2+}, Mn^{2+} and Mg^{2+} with respective affinities of 210:2:1. Under specified conditions, A23187 can provide evidence for a role for Ca^{2+} in a given biological response. The ionophore elevates intracellular Ca^{2+} and, for example, can induce the activation of lymphocytes, platelets and sea urchin egg development.

III. CA^{2+} AS AN INTRACELLULAR SIGNAL

The total intracellular Ca^{2+} concentration has been estimated to be approximately 1 mM, a value similar to extracellular Ca^{2+} values. Early studies used model systems such as the skinned muscle fiber, in which the sarcolemma was physically removed. In such a system, the Ca^{2+} ion concentration can be regulated in the bathing solution, while contraction and glycogenolysis are monitored. This approach demonstrated that Ca^{2+} was active at micromolar levels, and that it was rapidly sequestered from the cytosol. Conclusions drawn from such studies indicated that contraction and metabolism are regulated at micromolecular Ca^{2+} levels. It was suspected that Ca^{2+} acted by moving from one cellular compartment to another, that is, into and out of the cytosol. Ca^{2+} channels and pumps were identified using isolated intact vesicles through which the uptake of $^{45}Ca^{2+}$ was monitored. Convincing evidence for the movement of Ca^{2+} into and out of cellular compartments using isotopic methods in intact tissues proved difficult, since the ion was in a dynamic state of flux between the various intracellular organelles, the cytoplasm, and the extracellular fluids.

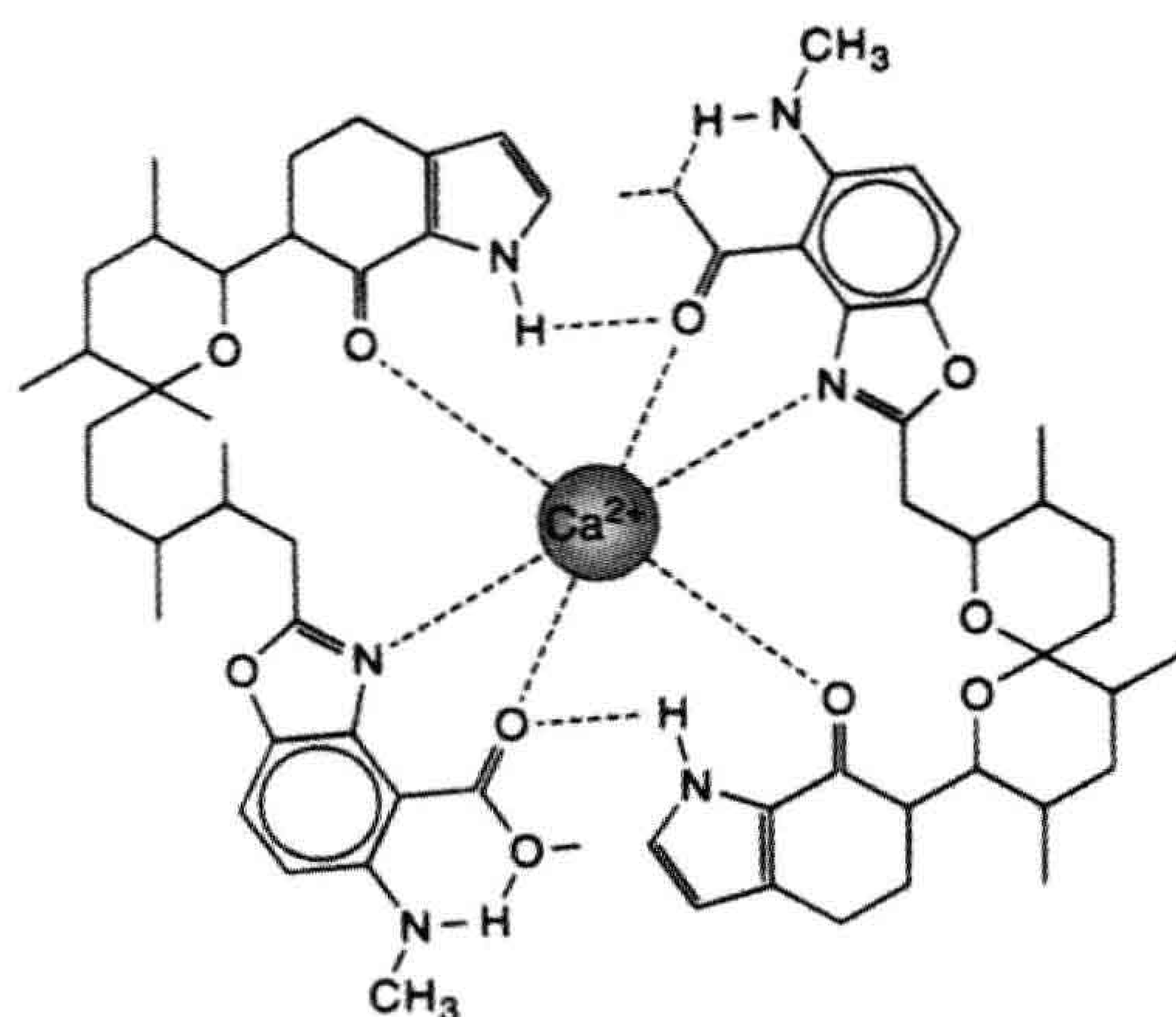


FIGURE 7.1 Molecular structure of A23187. The charged Ca^{2+} ions are extremely impermeable to the plasma membrane. Two molecules of ionophore A23187 form a molecular cage around the charged Ca^{2+} ion. The complex is membrane soluble and dissociates in the cytosol. Intracellular Ca^{2+} is then elevated.

During the past 20 years, however, several generations of Ca^{2+} indicators have been developed. Many coelenterates have the ability to glow by using Ca^{2+}-activated luminescent proteins. Aequorin was the first photoprotein to be used to measure intracellular free Ca^{2+}. Photoproteins can be used to measure free Ca^{2+} levels within the range of 0.1–10 μM. The use of aequorin, however, is limited since it is a relatively large molecule, with a molecular weight of approximately 20 000, and hence must be injected into cells. Early studies with aequorin required the use of large cells for microinjections. For example, the permeability of gap junctions to Ca^{2+} ions into large dipteran salivary glands was determined using aequorin luminescence with image intensification techniques. Under these conditions, nanograms of aequorin can be injected into a cell, which gives the cytosol the capacity to produce 10^4 to 10^8 photons per second. At these levels, the blue light luminescent output is readily measurable with sensitive photomultipliers.

More recently, a series of fluorescent indicator dyes that bind Ca^{2+} with high affinity and selectivity has been developed. The most commonly used is Fura-2. Since the free acids of these fluorescent indicators are not membrane permeable, the carboxyl acid groups are esterified during their chemical synthesis to make them permeable to the plasma membrane. Intact cells are loaded with the permeable form of the dye and the ester groups are then hydrolyzed in the cytoplasm by cellular esterases, thereby trapping the fluorescent probe within the cells. Fura-2 has been used in many biological systems. The use of Fura-2, in combination with high-resolution fluorescence video microscopy and computer-assisted image analysis systems, has provided valuable insight into understanding the intracellular Ca^{2+} signal (Berridge, 1990):

1. the resting intracellular ionized Ca^{2+} level is approximately 0.1 μM. Ca^{2+} ions not complexed to counterions or proteins are frequently referred to as being *free*. Cell stimulation by a variety of agents causes a transient rise in intracellular free Ca^{2+}; the increase is variable, lasting for a fraction of one second to minutes. The amplitude of the Ca^{2+} spike also varies from tissue to tissue
2. the elevation in Ca^{2+} may be uniform throughout a cell or group of cells or highly localized to specific regions of individual cells
3. in many cellular systems, the Ca^{2+} signal occurs as a wave, beginning at a discrete initiation site and then moving across the cell. Fertilization is a cellular process that displays this Ca^{2+} wave phenomenon. The Ca^{2+} influx is initiated at the point of sperm–egg contact,

from where it spreads as a propagated wave toward the opposite pole. This Ca^{2+} signal initiates cellular reactions to prevent polyspermy (penetration of the ovum by more than one sperm)

4. in many cell systems, the intracellular level of Ca^{2+} oscillates. The frequency depends on several factors, including the cell type and cellular effectors such as hormones, neurotransmitters, growth factors and cytokines. Most oscillations occur at a periodicity of 20–60 s when the cell is at "rest". When the cell is stimulated with a hormonal agonist, the frequency can increase to less than 5 s or result in a sustained elevation of up to 100 s. The oscillation frequency in Ca^{2+} may represent a periodic code, which can distinguish extracellular effector type and concentration.

IV. CREATION OF THE CA^{2+} SIGNAL

Cells are able to maintain a resting level of Ca^{2+} of less than 0.1 μM in an environment where the extracellular Ca^{2+} is 1 mM or greater. This gradient is achieved because the plasma membrane is relatively impermeable to Ca^{2+} and also contains ATP-driven Ca^{2+} pumps and Na^{+}-Ca^{2+} exchangers. In addition, the endoplasmic reticulum sequesters cytosolic Ca^{2+}, also by ATP-driven pumps. When $[Ca^{2+}]_i$ increases to above 1 μM, mitochondria will internalize Ca^{2+}. Mitochondria that are heavily loaded with Ca^{2+} reflect a distressed cellular state: under such conditions, the mitochondria develop dense granules containing complexed Ca^{2+}. Collectively, these pump and exchanger systems maintain a resting $[Ca^{2+}]_i$ of less than 0.1 μM.

Initiation of the calcium signal is achieved from two primary sources, the extracellular fluid and sequestered internal stores. The plasma membrane can contain multiple species of Ca^{2+}-specific channels as determined by electrophysiological or pharmacological methods. In general, there are three channel types: voltage-dependent, ligand-gated and mechanical (i.e. stretch-activated). The opening of these channels allows a rush of Ca^{2+} to enter the cytoplasm, producing a localized increase in intracellular Ca^{2+}. The mechanism of Ca^{2+} release from intracellular stores evaded elucidation for many decades. It was shown that inositol 1,4,5-trisphosphate (IP_3) causes Ca^{2+} mobilization from internal vesicular stores, primarily the endoplasmic reticulum (Berridge, 1993). IP_3 is a phospholipase C (PLC) hydrolysis product of phosphatidylinositol 4,5-bisphosphate (PIP_2), which is induced during cell stimulation. Recent evidence indicates that not all of the endoplasmic reticulum-sequestered Ca^{2+} is IP_3 sensitive and release is prompted by cyclic ADP-ribose (Lee, 1993). A second product of PLC hydrolysis of PIP_2 is diacylglycerol (DAG).

Stimulation of the membrane phospholipase C is through receptor binding by agonists and is G-protein regulated. $GTP_{\gamma}S$, a non-metabolizable analog of GTP, can artificially activate PLC production of IP_3 and DAG. G proteins also appear to regulate several processes, including the exchange of Ca^{2+} from IP_3-insensitive to IP_3-sensitive pools, the gating properties of plasma membrane Ca^{2+} channels, and the generation of cyclic AMP. The microinjection of $GTP_{\gamma}S$ causes a marked increase in Ca^{2+} oscillation frequency and amplitude and stimulation of many cellular processes.

V. MEDIATION OF THE CA^{2+} SIGNAL

Intracellular Ca^{2+}, like cyclic AMP, acts as a second messenger. Cyclic AMP is mediated by a limited number of receptor proteins, leading to the activation of specific protein kinases. There are, however, numerous intracellular Ca^{2+}-binding proteins; therefore, the intracellular Ca^{2+} signal has many possible bifurcations of action. A simple example is found in skeletal muscle, where elevated Ca^{2+} binds to troponin C to cause myofibrillar contraction at the expense of ATP. An independent, simultaneous Ca^{2+} pathway is mediated by a second Ca^{2+} receptor protein, calmodulin, which activates phosphorylase kinase. This activation initiates glycogenolysis, which leads to the regeneration of expended ATP (Fig. 7.2).

The most completely described family of intracellular Ca^{2+}-binding proteins to date is characterized by a protein structure known as the EF hand. The binding site is achieved through side-chain coordination of Ca^{2+} within a helix-loop-helix composed of precisely spaced amino acids (Fig. 7.3). This EF hand is found in a number of proteins as determined from the primary amino acid sequence and, in a few cases, has been confirmed by direct Ca^{2+} binding. The sequence data for the Ca^{2+}-dependent protease calpain suggest that it may have resulted from the fusion of a gene encoding four EF hand domains with a thiol protease gene (Ohno et al., 1984). Likewise, α-actinin may have resulted from the fusion of a gene encoding an actin-binding protein with a gene for a single EF hand domain (Noegel et al., 1987). In many cases, the EF hand is non-functional. For example, the Ca^{2+} insensitivity of the muscle form of α-actinin is due to the imprecise positioning of the amino acids shown in Fig. 7.3. The identification of a number of putative Ca^{2+}-binding proteins is based on sequence similarity to members of the troponin C/calmodulin superfamily. For example, cell cycle yeast mutants which carry the temperature-sensitive allele of *CDC31* are blocked in spindle-pole body duplication (Baum et al., 1986). This gene has 42% sequence similarity with human calmodulin and may contain functional EF hands. A second cell division cycle gene, *CDC24*, is required for bud formation. Sequence analysis of *CDC24* indicates two potential Ca^{2+}-binding EF hands (Miyamoto et al., 1987).

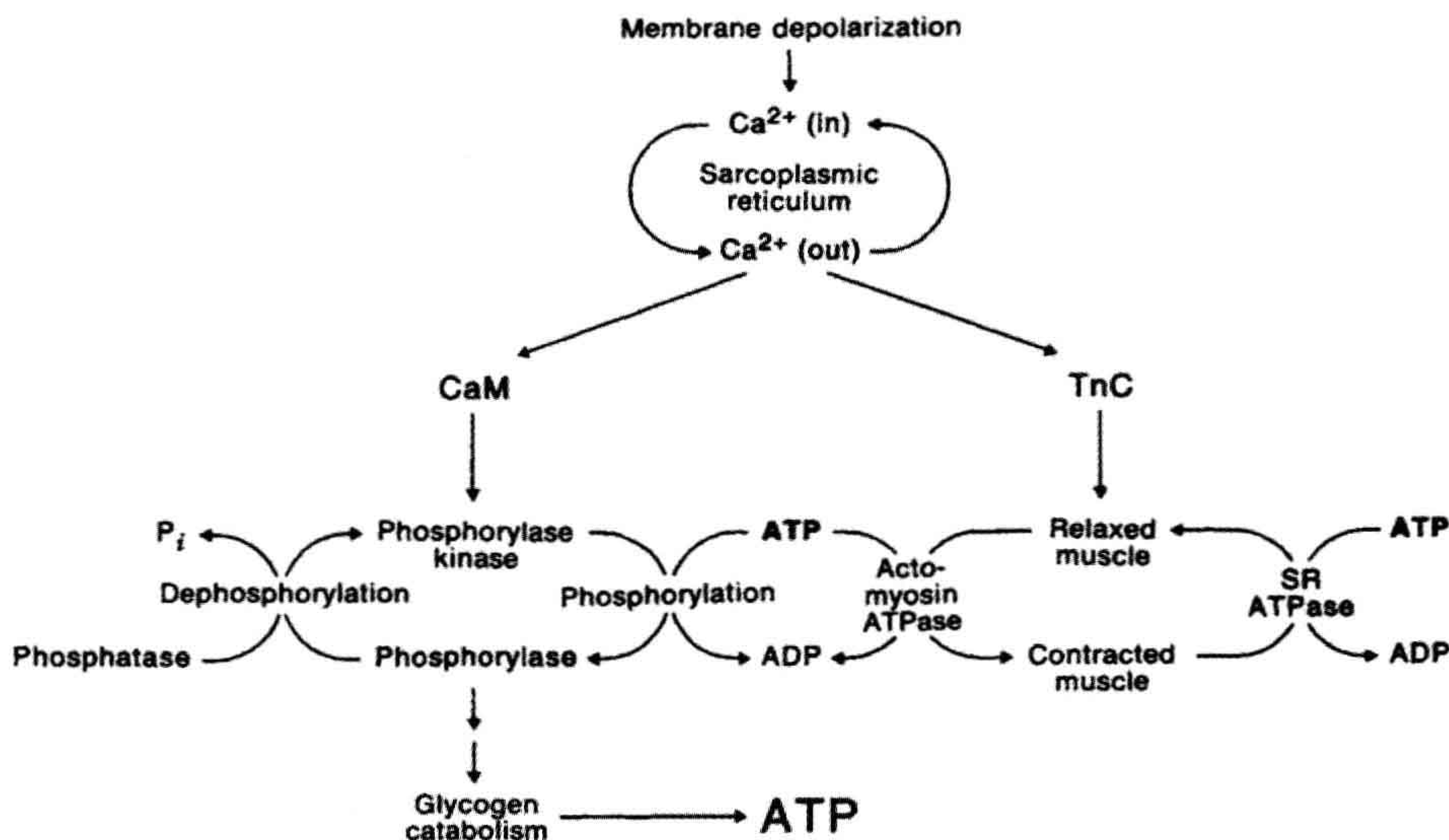


FIGURE 7.2 Independent pathways of Ca^{2+} regulation in skeletal muscle. Depolarization of the sarcolemma causes release of Ca^{2+} stored in the sarcoplasmic reticulum. This elevated Ca^{2+} level triggers contraction, an ATP-consuming process. The same signal Ca^{2+} also binds calmodulin (CaM), which initiates glycogenolysis, an ATP-producing process. This parallelism allows for metabolic coordination.

Troponin C is present only in skeletal and cardiac muscle; calmodulin is present in all cells. The binding of four Ca^{2+} ions causes conformational changes with the formation of an active state. Ca^{2+}-bound calmodulin has very high affinity for its target proteins, which act as additional steps in mediating the original Ca^{2+} signal. The calmodulin target proteins include protein kinases, protein phosphatases, hydrolases, nitric oxide synthetase and ion channels.

Sequence analysis and site-directed mutagenesis studies have provided a general model for calmodulin regulation of its target proteins (Fig. 7.4). The target protein contains a pseudosubstrate attached to a flexible region of the polypeptide chain. This sequence acts as an endogenous inhibitor of the enzyme. Ca^{2+}-activated calmodulin clamps around an adjacent target site and physically displaces the pseudosubstrate from the active site, causing a derepression or activation of the enzyme. This process is reversed by the reduction of intracellular Ca^{2+} levels, which reduces the affinity of calmodulin for the target site and autoinhibition of the enzyme occurs. A smooth muscle contraction is a paradigm for calmodulin mediation of the Ca^{2+} signal (Fig. 7.5).

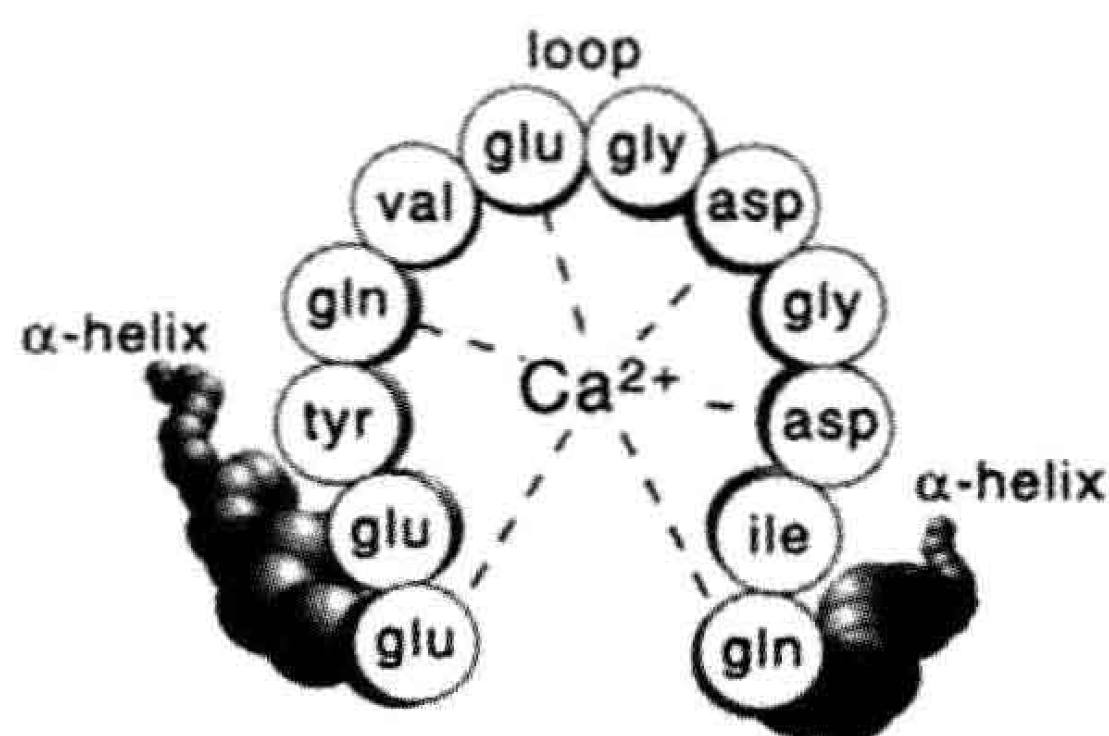


FIGURE 7.3 The EF hand Ca^{2+} binding pocket. Many intracellular Ca^{2+}-receptor proteins contain precisely positioned amino acids in a loop between highly structured α-helical coil. The Ca^{2+} ion is coordinated in this loop, which alters the overall structure of the protein and, in turn, its cellular activity.

One approach to understanding the cellular role of a protein is to correlate subcellular localization with function. This information can be effectively obtained through the use of antibodies that are monospecific for the targeted protein. As shown in Fig. 7.6, when affinity-purified antibodies were used to localize calmodulin during mitosis, the spindle poles were stained most brightly. This result suggested that calmodulin is involved in mitotic function. Indeed, microtubules depolymerize in the presence of Ca^{2+}-bound calmodulin both in vitro and in microinjected cells (Dedman et al., 1982). Many other cellular functions have been assigned to calmodulin through a combination of localization, biochemical and genetic approaches (Davis, 1992).

VI. CA^{2+}-CALMODULIN DEPENDENT PROTEIN KINASE II

Many of the calmodulin-regulated kinases, including phosphorylase kinase (see Fig. 7.2) and myosin light chain

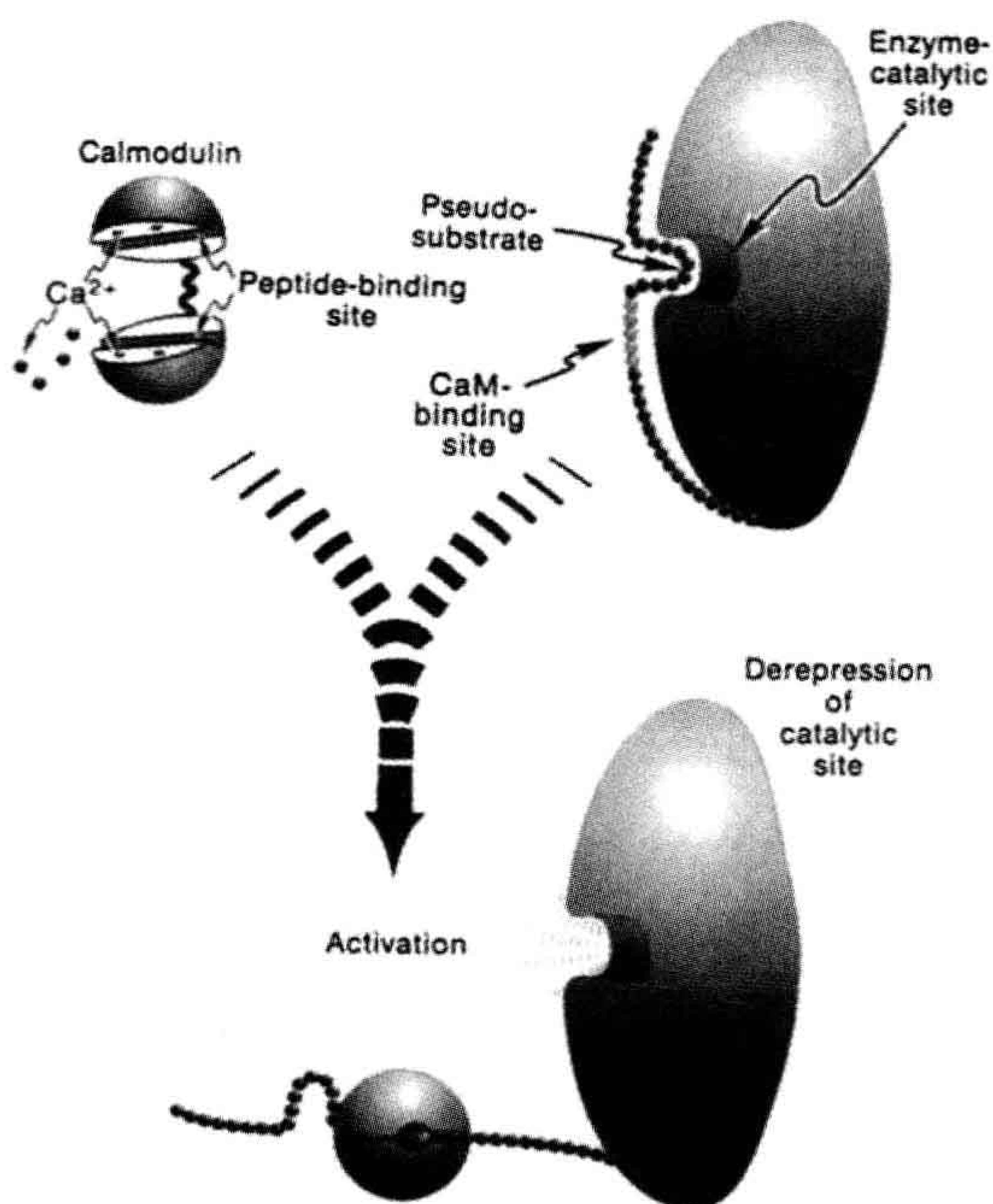


FIGURE 7.4 Mechanism of action of calmodulin regulation of target proteins. Calmodulin is molecularly structured as two opposing lobes containing Ca^{2+}-binding sites connected by a flexible peptide hinge. Ca^{2+} binding causes the formation of complementary grooves on each, which then allows binding to specific regulatory sites on target proteins. Ca^{2+}-dependent binding causes derepression of the enzyme active site by displacing an endogenous inhibitory pseudosubstrate.

kinase (see Fig. 7.5), directly reflect the changes in free cytosolic Ca^{2+} through the phosphorylation of their respective specific protein substrates. Ca^{2+}-calmodulin dependent protein kinase II (CaM kinase II) is distinct in that it is multifunctional, having numerous substrates, and can develop many active states including Ca^{2+}-CaM autonomy (Braun and Schulman, 1999). The individual subunits of CaM kinase II assemble through their association domains to form a flower-like structure of 8–12 "petals" (Fig. 7.7). In low cytosolic free Ca^{2+}, the naive enzyme is inactive. When levels are elevated, free intracellular Ca^{2+} binds CaM which, in turn, binds to the regulatory domain of the CaM kinase II subunits and derepresses the active site. "Autophosphorylation" of adjacent CaM-bound subunits occurs at threonine-286 (pT286) during this activation period. Autophosphorylation renders the individual catalytic sites constitutively active and independent from Ca^{2+}-CaM regulation. A second "wave" of elevated Ca^{2+} allows additional sites to be activated by Ca^{2+}-CaM and provides a further opportunity for transphosphorylation of adjacent pT286. After a series of Ca^{2+} waves, the enzyme complex becomes increasingly autonomous from Ca^{2+}-CaM regulation. In addition, pT286 phosphorylation produces a 1000-fold increase in affinity for CaM and effectively "traps" CaM, making the Ca^{2+} mediator protein temporally unavailable for other target proteins. When Ca^{2+} levels are reduced and calmodulin is released, the regulatory domain may be "capped" by phosphorylation of T305 and/or T306 in the CaM binding domain. Rebinding of CaM in the event of subsequent Ca^{2+} increases is prevented until pT305 and pT306 are dephosphorylated; pT286 autonomy is not affected. Autonomy and capping are reversed by protein phosphatases that are regulated by cAMP. The subunits are

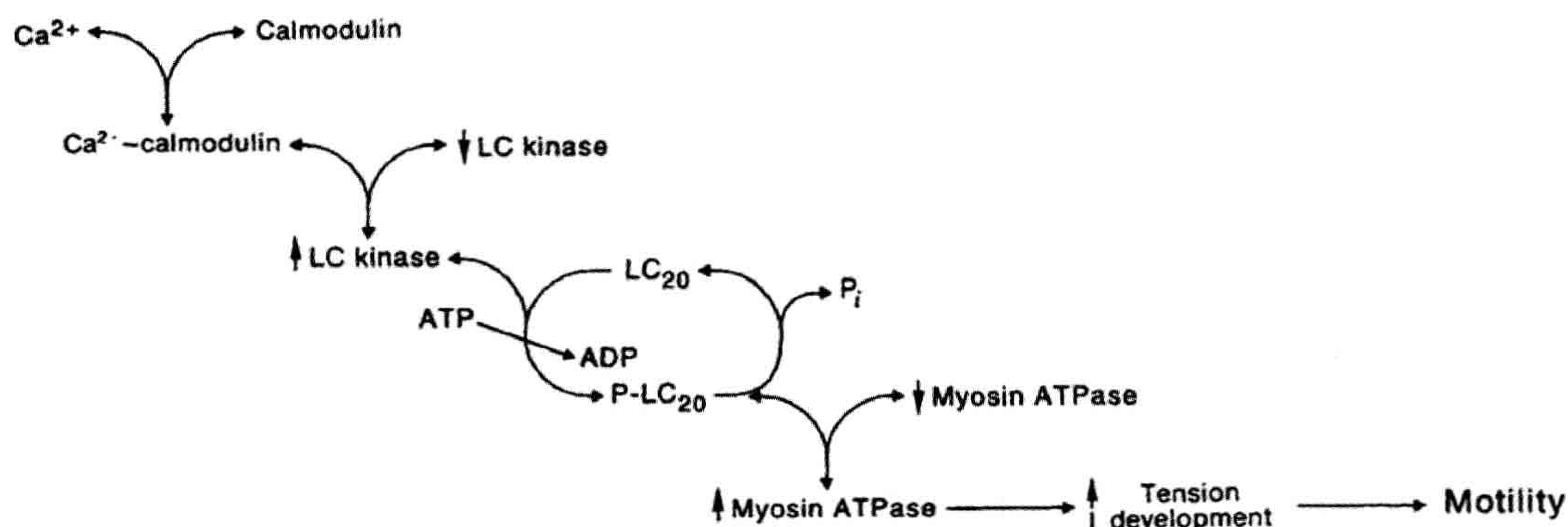
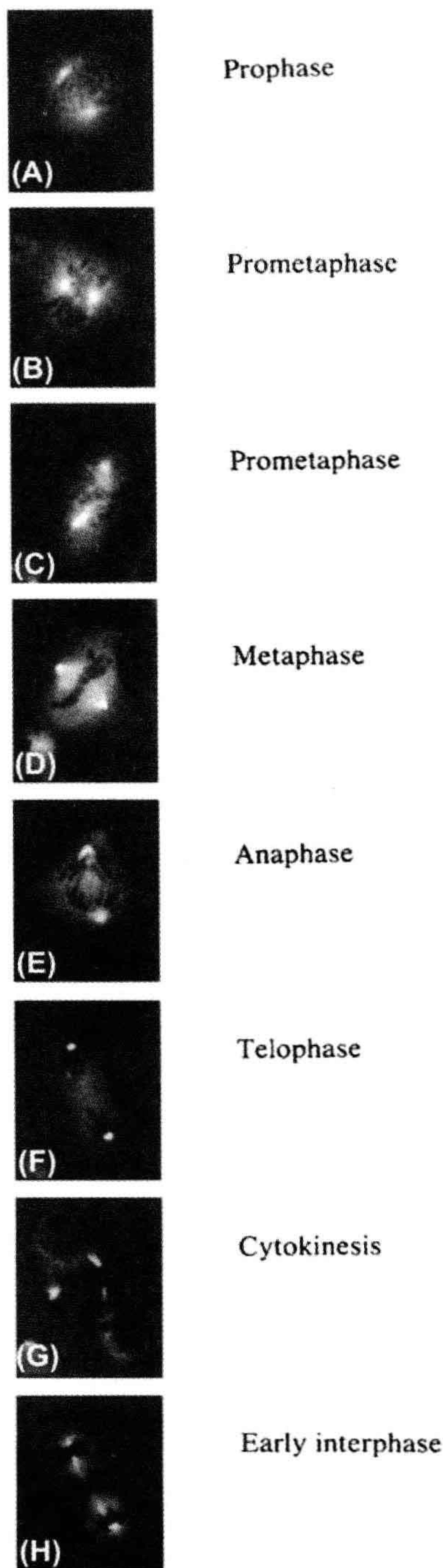


FIGURE 7.5 Calmodulin regulation of non-striated muscle contraction. An increase in intracellular Ca^{2+} binds to calmodulin, causing its increased affinity for the target protein myosin light chain kinase (LC kinase). The activated kinase specifically phosphorylates one of the myosin light chains which, in turn, increases the activity of myosin and its affinity for actin. Cross-bridge formation develops contraction. This process is reversed after cytosolic reduction in Ca^{2+}.



resensitized to Ca^{2+}-CaM following dephosphorylation of T305 and T306.

The metabolic sculpturing of CaM KII reflects the changes in free Ca^{2+} levels, the availability of CaM, autophosphorylation and protein phosphatase activities. These events allow CaM KII to develop numerous active states reflecting the physiologic state of the cell. Dynamic changes in second messenger levels, amplitude and frequency of Ca^{2+} oscillations and cAMP levels are decoded by CaM KII which, in turn, phosphorylates and modifies the activity of numerous enzymes including Ca^{2+}-channels, Ca^{2+}-pumps, synaptic proteins and components of the nuclear envelope. In summary, CaM KII is a molecular microprocessor that integrates and stores cellular signals.

VII. ANNEXINS: CALCIUM-DEPENDENT PHOSPHOLIPID-BINDING PROTEINS

A number of laboratories with distinct experimental goals have identified a family of Ca^{2+}-dependent phospholipid-binding proteins. These proteins have the common property of binding (annexing) membranes (Crumpton and Dedman, 1990). Sequence data indicate that there are 10 unique mammalian annexins. Annexins are also present in the slime mold *Dictyostelium*, in the sponge, in the coelenterate *Hydra*, in the insect *Drosophila* and in the mollusk *Aplysia*, as well as in higher plants.

The sequence organization of the family is highly conserved (Fig. 7.8). All except annexin VI are composed of a core of four repeated domains: annexin VI is composed of eight domains. Each domain is approximately 70 amino acids in length. The sequence conservation for each ranges between 40 and 60% when individual annexins are compared. The amino terminus of each protein is unique, suggesting that this region may confer functional differences to the proteins. This property has been confirmed with annexin II, in that the amino terminus binds a subunit, p11, and forms an actin-binding heterotetramer. Calcium-dependent phospholipid binding is a property of the four-domain core of each protein. In vitro functions of annexins — which include membrane binding and fusion, ion channel activity, modulation of ion channel activity, inhibition of phospholipase A_2 and inhibition of blood coagulation — all require this property. The core does not contain the classic EF hand calcium-binding motif. Coordination of Ca^{2+} is accomplished through a unique, discontinuous binding loop. Chemical cross-linking data indicate that monomeric annexin in solution self-associates into trimers, which then

FIGURE 7.6 Subcellular localization of calmodulin in mitotic cells. Monospecific antibody and immunofluorescence identifies calmodulin to be concentrated at the poles of the spindle apparatus.

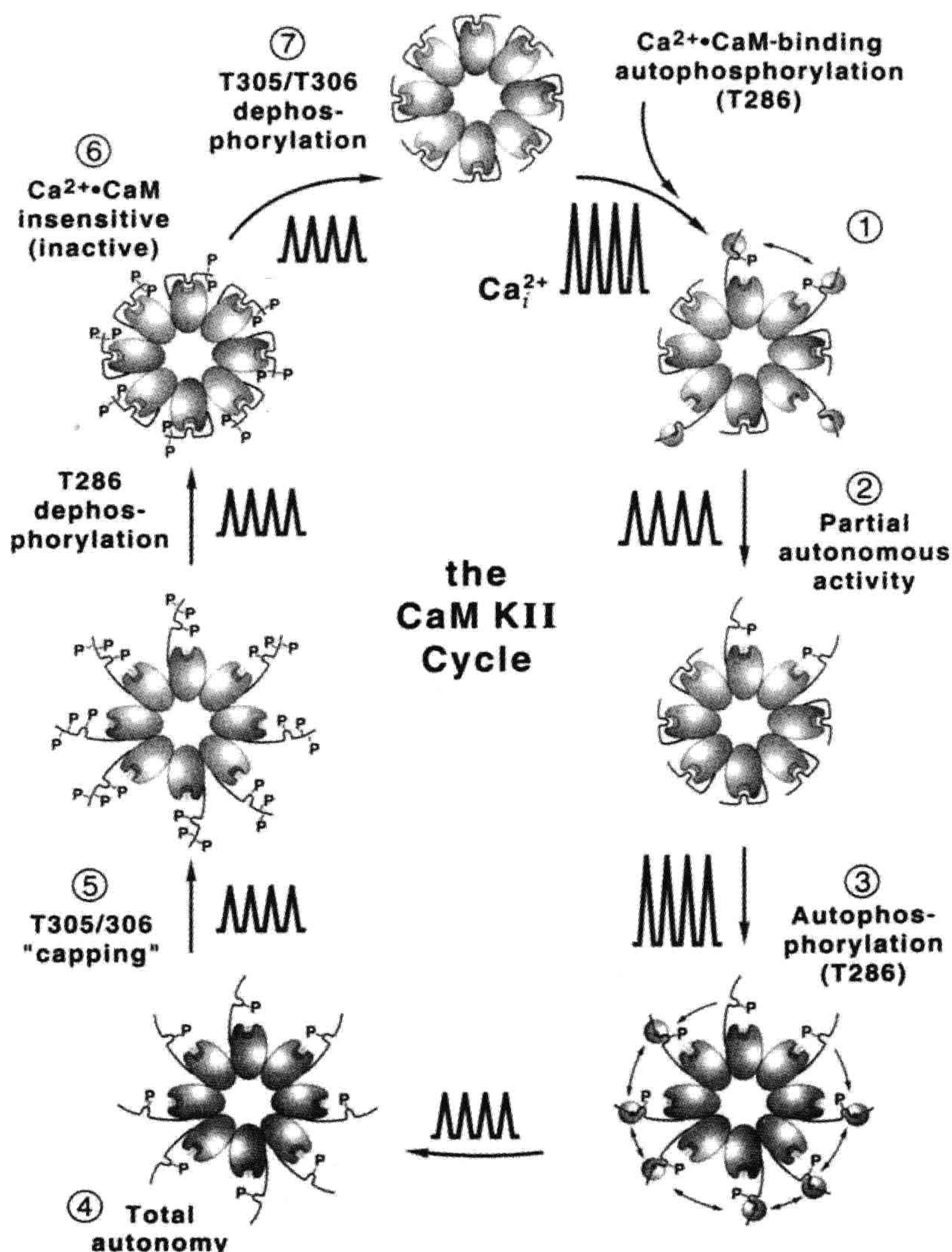


FIGURE 7.7 Ca^{2+}-CaM-dependent kinase II. (1) The active site of each subunit is repressed by an autoregulatory domain. (2–5) Ca^{2+}-CaM binds to this domain and adjacent subunits are transphosphorylated at threonine-286 (T286). These autophosphorylated subunits are active and autonomous from Ca^{2+}-CaM regulation. (6) The regulatory domain can be further phosphorylated at threonine-305 and/or 306 (T305/T306), modifications which inhibit CaM binding. (7) Dephosphorylation of T286 renders the enzyme inactive and insensitive to Ca^{2+}-CaM. (1) Dephosphorylation of T305 and T306 returns the enzyme to its Ca^{2+}-CaM-dependent state.

form higher aggregates when bound to phospholipid vesicles. This observation is consistent with the diffraction pattern obtained from two-dimensional crystals.

Collectively, protein structural data, biophysical reconstitution studies and subcellular localization results allowed development of the following model to describe the cellular function of the annexins. In the resting cell when free Ca^{2+} concentrations are low, the annexin exists as a soluble monomer. During cell stimulation, free Ca^{2+} concentrations subjacent to the cell membrane rise to micromolar levels (Llinas et al., 1992). The annexin would bind to target proteins associated with a phospholipid surface, then organize into trimers, hexamers and higher aggregates, ultimately forming an extended hexagonal

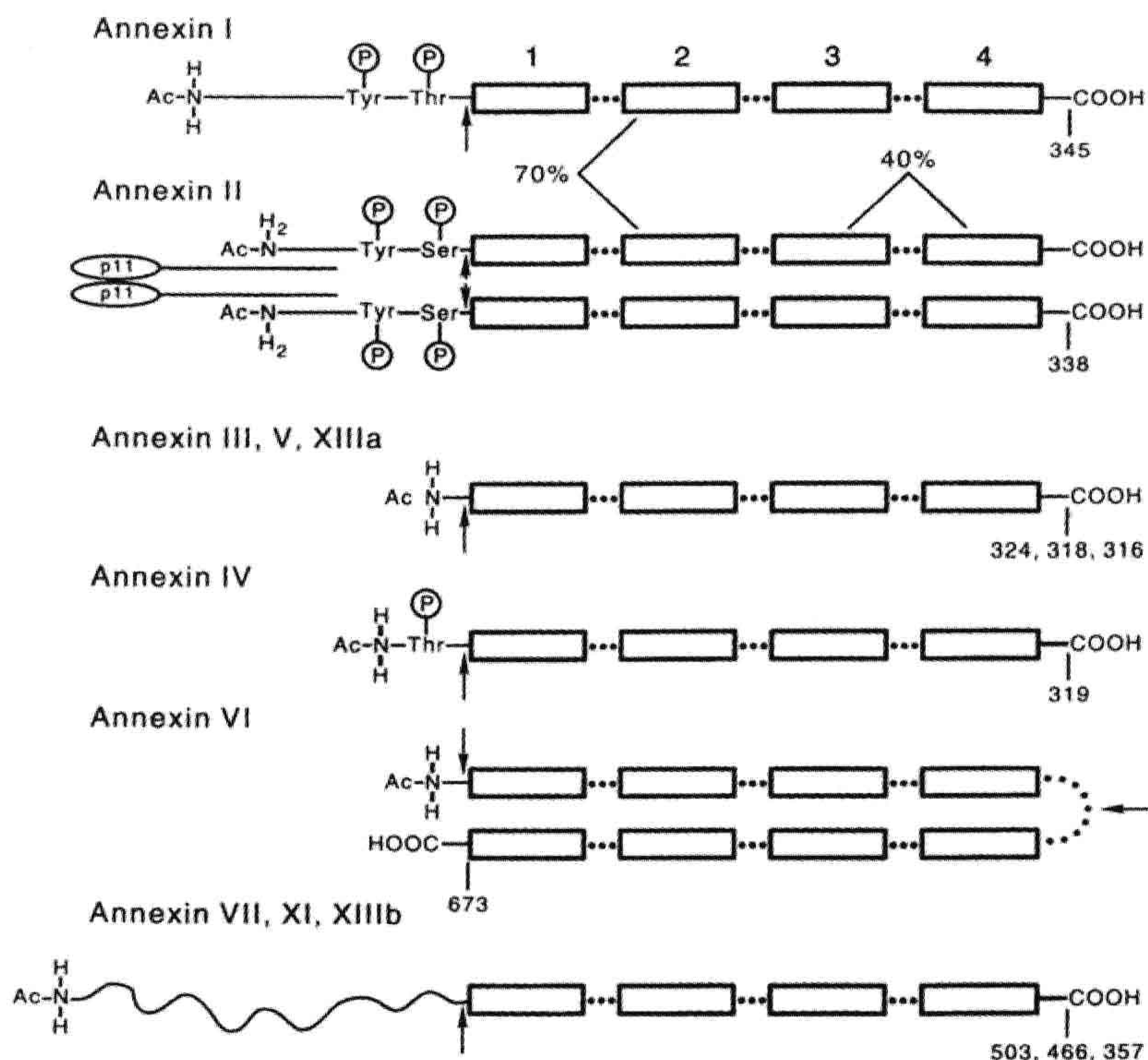


FIGURE 7.8 Structural similarities among the annexins. The boxed regions represent the ordered 70-amino-acid repeat domains. The numbers indicate the relative sequence similarities between repeat domains. The arrows indicate highly sensitive sites of proteolysis. The repeat regions form a highly structured, protease resistant, Ca^{2+}-phospholipid binding core. The amino terminal "tails" are highly variable in length, sequence, and structure and provide individually to each annexin family member.

array around the target protein (Andree et al., 1992; Concha et al., 1992). The immunofluorescent localization studies of annexins support this model. A sheet of annexin multimers lining the inner membrane leaflet would locally alter membrane properties, such as fluidity and sequestration of specific phospholipids. Changes in membrane properties have been shown to modify specific membrane protein function (Bennett, 1985; Sweet and Schroeder, 1988). Such a submembranous scaffolding maintains and stabilizes the membrane. For example, dystrophin is localized to the inner surface of the sarcolemma in normal skeletal muscle. When absent, as in Duchenne muscular dystrophy, the plasma membrane is unstable and the fibers rapidly turn over (Koenig et al., 1988). In addition, the Ca^{2+}-dependent lining of the membrane would sterically block the translocation of phospholipid-binding proteins, such as protein kinase C and cellular phospholipases. The Ca^{2+}-dependent self-association on membrane surfaces represents a novel mechanism of second-messenger coupled cell regulation. This may be the regulatory mechanism by which annexins modify the gating activity of the channels.

Immunolocalization studies have proved valuable in providing insight into evaluating cellular function of the annexins. The individual annexins are associated with secretory granules, the endoplasmic/sarcoplasmic reticulum, actin bundles and the plasma membrane. Annexin IV, for example, is expressed in many epithelia and is concentrated along the apical membrane, subjacent to the lumen of the organ (Fig. 7.9) (Kaetzel et al., 1994). This region is the cellular site of fluid secretion into the lumen. Recent studies indicate that this annexin regulates chloride-ion efflux, which produces an electrochemical gradient to draw sodium ions transcellularly across the epithelium. This salt causes water to follow because of hyperosmotic pressure. The luminal fluid is required for normal tissue function. Abnormal fluid secretion is involved in the pathologies of cholera and cystic fibrosis.

VIII. PROTEIN KINASE C

The protein kinase C family is a third mediation pathway of intracellular Ca^{2+} action. One class of protein kinase C

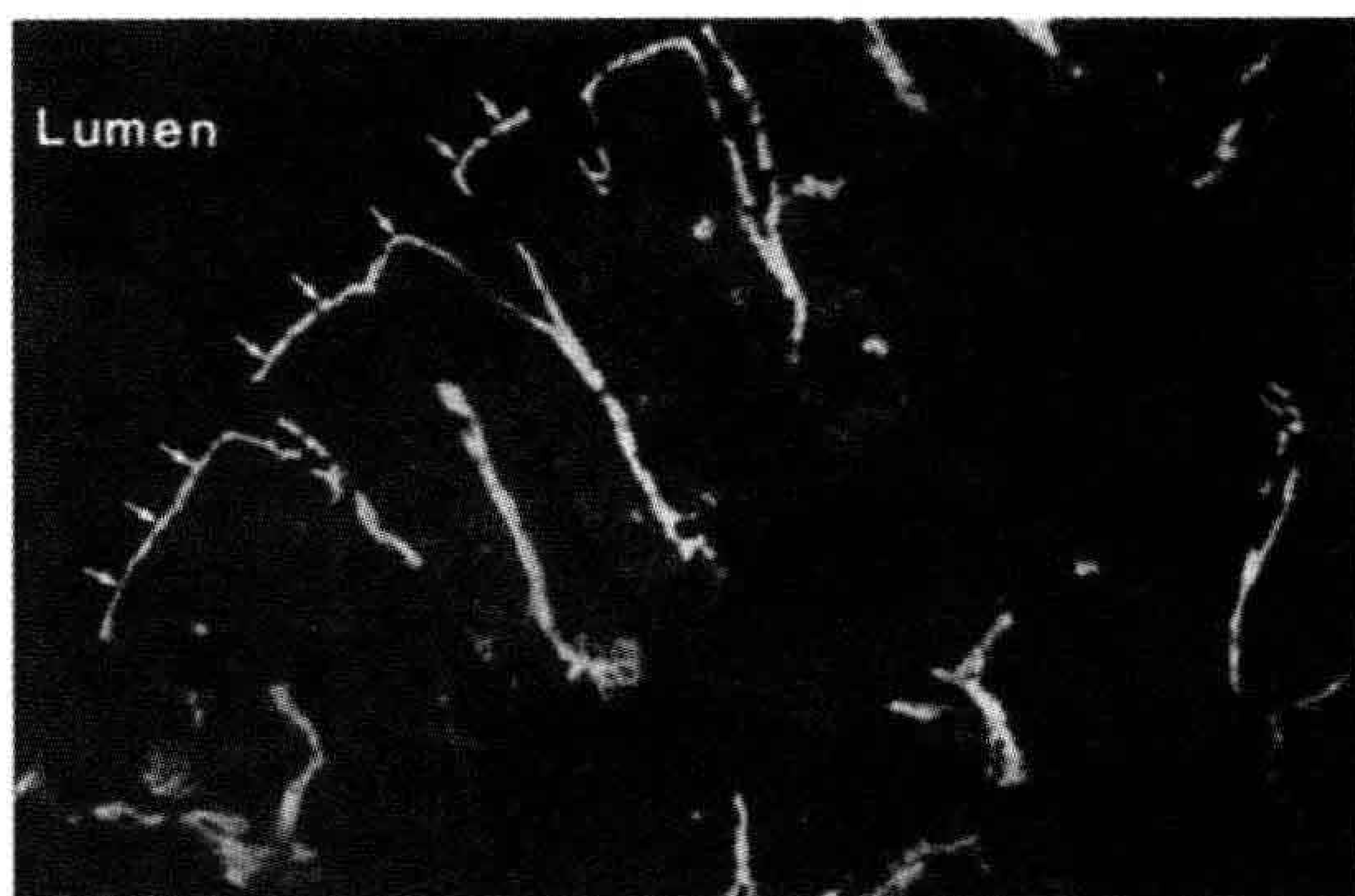


FIGURE 7.9 Localization of annexin IV in the rat fallopian tube. Monospecific antibody identifies annexin IV as concentrated along the membrane bordering the lumen of the oviduct of the ciliated, columnar epithelia (arrows). This region is the cellular site of fluid secretion.

isozymes is activated by Ca^{2+}, which increases the affinity of the enzyme for phosphatidylserine. This ligand binding targets the translocation of protein kinase C to the plasma membrane. Once bound to the membrane surface, the enzyme can be further stimulated by DAG (Fig. 7.10). This latter metabolite is a product of G-protein-activated phospholipase C hydrolysis of membrane PIP_2. Protein kinase C stimulates DNA synthesis and is the cellular mechanism by which many tumor promoters act (Nishizuka, 1992). A major widely distributed cellular substrate for protein kinase C is MARCKS, myristoylated alanine-rich C-kinase substrate (Aderem, 1992). This protein binds to the plasma membrane, calmodulin and actin and has been associated with secretion, motility, vesicle trafficking and transformation through the rearrangement of the actin cytoskeleton. Actin filament bundling by MARCKS is regulated by Ca^{2+}-dependent calmodulin binding which is, in turn, regulated by protein kinase C phosphorylation. The kinase has numerous protein substrates in the cell; however, the precise mechanism of cellular regulation is not fully understood.

There are additional distinct intracellular Ca^{2+} -binding proteins that have been well characterized in biochemical terms (see Smith et al., 1990). Ca^{2+} has the responsibility of regulating a large number of unrelated cellular activities such as cell growth, secretion, motility and transport. The ubiquitous Ca^{2+} signal is discriminated through the individual Ca^{2+}-mediator proteins (Fig. 7.11).

IX. CURRENT PERSPECTIVES

Scientific progress is not restricted by effort, but is dependent on insight and advances in technology. Technical progress in protein chemistry in the late 1960s and early 1970s led to the identification and characterization of

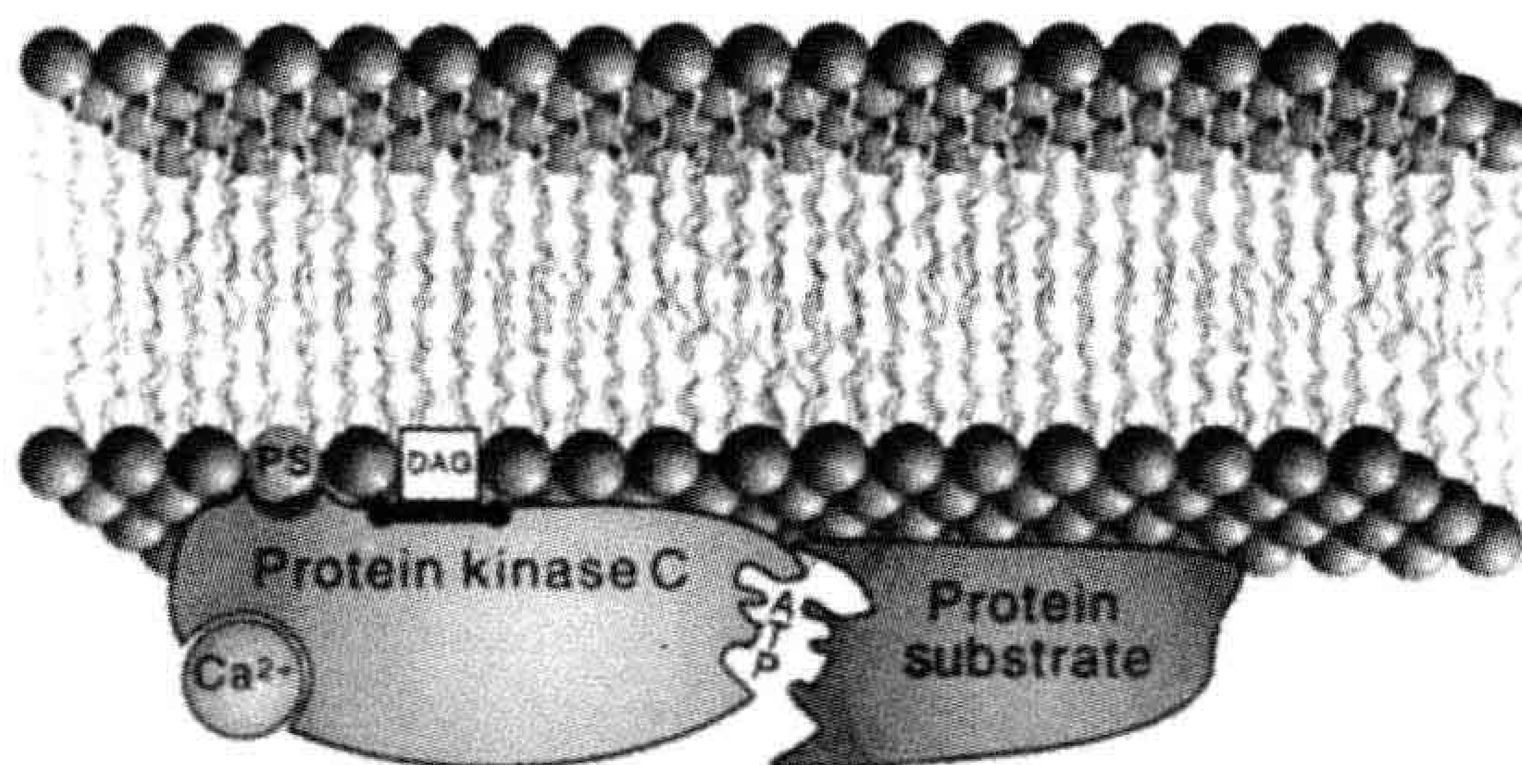


FIGURE 7.10 Regulation of protein kinase C. Elevations in intracellular Ca^{2+} cause translocation of PKC to the plasma membrane where phosphatidylserine (PS) and diacylglycerol (DAG) further activate the enzyme.

the Ca^{2+} receptors, troponin C and calmodulin. Development of recombinant DNA technology in the mid-1970s provided precise knowledge of the molecular evolution and structural conservation of these proteins. In the early 1980s, Ca^{2+}-sensitive dyes and computer-assisted image processing allowed visualization of transient spatial changes in intracellular Ca^{2+}. Detailed information is being obtained on the cellular components that are essential for maintaining these levels, including Ca^{2+} channels, Na^+-Ca^{2+} exchangers and Ca^{2+}-ATPases. The original observations of Hokin and Hokin (1953) concerning the turnover of

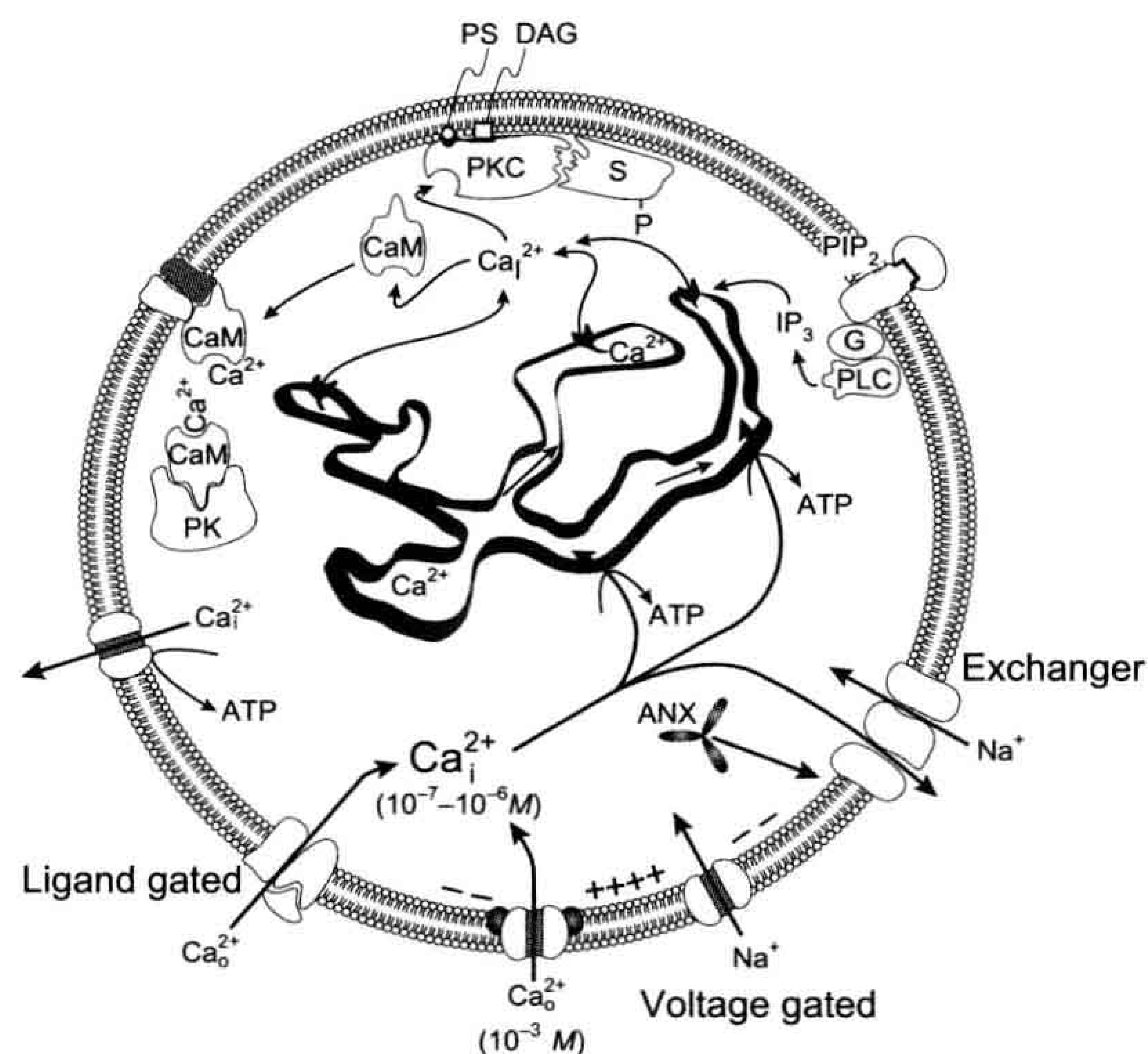


FIGURE 7.11 Interplay of cellular components involved in creating and mediating the intracellular Ca^{2+} signal. Low intracellular Ca^{2+} levels are the result of pumps and ion exchangers. Ca^{2+} transients develop from influx through voltage and ligand-gated channels on the plasmalemma and from IP_3-gated channels located in the endoplasmic/sarcoplasmic reticulum. IP_3 is generated from extracellular stimuli through a G protein (G)-regulated phospholipase C (PLC). The intracellular Ca^{2+} signal is mediated by three primary pathways: calmodulin (CaM), annexins (ANX), and protein kinase C (PKC).

membrane phosphatidylinositols were finally appreciated some 20 years later. New insights in second-messenger action revealed that the hydrolysis of PIP_2 to form IP_3 and DAG could coordinate, respectively, the release of intracellular Ca^{2+} from the endoplasmic reticulum and the activation of protein kinase C. Although the mechanisms involved in maintaining intracellular Ca^{2+} homeostasis are being defined, understanding the events that couple stimuli to specific cellular responses has resisted biochemical definition. The elucidation of physiological regulation by Ca^{2+} through specific Ca^{2+} mediator proteins is not a trivial undertaking. Initial implications of function can be explored by cellular microinjection of inhibitor peptides, antibodies and anti-sense RNA or by in vitro reconstitution. Information obtained from these inhibition experiments, however, is limited because it does not fully reflect the intact organism. For example, although our knowledge of the molecular aspects and regulatory properties of calmodulin in vitro is impressive, little is known of the functional role of calmodulin in the living cell or the whole animal, other than by inference. An attractive approach to obtaining this information is genetic manipulation. Fungi, such as yeast, are powerful models for the introduction and study of site-directed and temperature-sensitive mutations and fundamental questions regarding the regulatory role Ca^{2+} in growth, division and secretion have been addressed (see Davis, 1992). The usefulness of such haploid systems, however, is limited to genes that are expressed in these organisms and to non-lethal mutations in these genes.

The cellular function of the diverse Ca^{2+}-binding proteins that are expressed in highly differentiated cells remains elusive. The respective pathways can be manipulated at many levels. Synthetic genes can be introduced into cultured cells and the resulting phenotypic changes monitored. In addition, specific genes can be deleted or "knocked out" in whole animals using homologous recombination of genes in mouse embryonic stem cells (see Frohmen and Martin, 1989).

Interpretation of targeted gene "knockout" studies is, however, complicated by the fact that the animal lacks the gene in its genome throughout its development. Phenotypic consequences within individual cell types resulting from gene disruptions may be due to defects that occur during embryonic development or inadequate communication with other defective cell types.

An alternative approach to understanding the precise role of proteins associated with the intracellular Ca^{2+} signal is to design and construct dominant-negative genes that, when expressed, neutralize the function of specific proteins. For example, peptides consisting of the calmodulin-binding site on target proteins (see Fig. 7.4) are extremely potent inhibitors of calmodulin. Wang et al. (1995, 1996) constructed a synthetic gene that produced a string of these calmodulin-binding peptides. This peptide inhibitor was targeted to the nucleus of mouse-lung epithelial cells. By neutralizing the activity of nuclear calmodulin, it was shown that the cells did not synthesize DNA and the embryonic lung did not develop. Dominant-positive genes can also be designed to elucidate Ca^{2+}-regulated cellular systems. The amino acid sequence of the pseudosubstrate domain on calmodulin target proteins (see Fig. 7.4) can be altered to abolish inhibition of the catalytic site. This mutated enzyme becomes autonomous from Ca^{2+}-calmodulin regulation and remains active even during periods of low intracellular Ca^{2+}. Mayford et al. (1996) have shown, for example, that expression of an autonomously active CaM kinase II in mouse brain causes deficits in memory.

The understanding of Ca^{2+}-coupled stimulus responses has advanced through direct visualization of Ca^{2+} transients, the identification of Ca^{2+}-binding proteins, determination of their subcellular localization and their biochemical role through reconstitution of a cellular function, and genetic manipulation of intact cells. Although many candidates for Ca^{2+} mediator proteins are currently under investigation, it is anticipated that more Ca^{2+}-binding proteins will be identified as further research continues to solve the stimulus—response coupling puzzle.

X. SUMMARY

Ca^{2+} is a ubiquitous intracellular regulator of cellular function. Levels of Ca^{2+} are controlled by a variety of channels, exchangers and pumps found in the plasmalemma and internal membranes. Cell stimulation causes the intracellular Ca^{2+} to increase transiently. This second-messenger signal is then mediated by Ca^{2+}-binding proteins. There are three primary molecular mechanisms of transmitting the signal: calmodulin, annexins and protein kinase C. Each of these pathways intersects and can be cross-regulatory. Ca^{2+}-calmodulin binds to specific sites on target proteins and activates enzymes by derepressing the active site. In the presence of Ca^{2+}, the annexins have a strong affinity for phospholipids. Annexins can form an interlocking network along membrane surfaces and alter membrane fluidity. Annexins are important in regulating membrane ion conductances. Protein kinase C is regulated by Ca^{2+}, phospholipid and diacylglycerol. Cellular studies using specific activators and inhibitors of protein kinase C have shown this Ca^{2+} pathway to be involved in cell growth, differentiation and development of tumors. Physiological, cellular and molecular techniques are being used in combination to define the precise cellular roles of Ca^{2+}-binding proteins.

BIBLIOGRAPHY

Aderem, A. (1992). The MARCKS brothers: a family of protein kinase C substrates. *Cell, 71*, 713–716.

Andree, H. A. M., Stuart, M. C. A., Hermens, W. T., et al. (1992). Clustering of lipid-bound annexin V may explain its anticoagulant effect. *J Biol Chem, 267*, 17907–17912.

Baum, P., Furlong, C., & Byers, B. (1986). Yeast gene required for spindle pole body duplication: homology of its product with Ca^{2+}-binding proteins. *Proc Natl Acad Sci, USA, 83*, 5512–5516.

Bennett, V. (1985). The membrane skeleton of human erythrocytes and its implications for more complex cells. *Annu Rev Biochem, 54*, 273–304.

Berridge, M. J. (1990). Calcium oscillations. *J Biol Chem, 264*, 9583–9586.

Berridge, M. J. (1993). Inositol trisphosphate and calcium signaling. *Nature, 361*, 315–361.

Braun, A. P., & Schulman, H. (1999). Structural examination of autoregulation of multifunctional calcium/calmodulin-dependent protein kinase II. *J Biol Chem, 274*, 26199–26208.

Concha, N. O., Head, J. F., Kaetzel, M. A., Dedman, J. R., & Seaton, B. A. (1992). Annexin V forms calcium-dependent trimeric units on phospholipid vesicles. *FEBS Lett, 314*, 159–162.

Crumpton, M. J., & Dedman, J. R. (1990). Protein terminology tangle. *Nature, 345*, 212.

Davis, T. N. (1992). What's new with calcium? *Cell, 71*, 557–564.

Dedman, J. R., Welsh, M. J., Kaetzel, M. A., Pardue, R. L., & Brinkley, B. R. (1982). Localization of calmodulin in tissue culture cells. In W. Y. Cheung (Ed.), *Calcium and Cell Function, Vol. 3*. New York: Academic Press.

Frohman, M. A., & Martin, G. R. (1989). Cut, paste, and save: new approaches to altering specific genes in mice. *Cell, 56*, 145–147.

Heizmann, C. W., & Hunziker, W. (1991). Intracellular calcium-binding proteins: more sites than insights. *Trends Biochem Sci, 16*, 98–103.

Hodgkin, A. L., & Keynes, R. D. (1957). Movements of labeled calcium in squid giant axons. *J Physiol, 138*, 253–281.

Hokin, M. R., & Hokin, L. E. (1953). Enzyme secretion and the incorporation of ^{32}P into phospholipids of pancreas slices. *J Biol Chem, 203*, 967–977.

Kaetzel, M. A., Cahn, H. C., Dubinsky, W. P., Dedman, J. R., & Nelson, D. J. (1994). A role for annexin IV in epithelial cell function: Inhibition of calcium-activated chloride conductance. *J Biol Chem, 269*, 5297–5302.

Kaetzel, M. A., Hazarika, P., & Dedman, J. R. (1989). Differential tissue expression of three 35–kDa annexin calcium-dependent phospholipid-binding proteins. *J Biol Chem, 264*, 14463–14470.

Koenig, M., Monaco, A. P., & Kunkel, L. M. (1988). The complete sequence of dystrophin predicts a rod-shaped cytoskeletal protein. *Cell, 53*, 219–228.

Lee, H. C. (1993). Potential of calcium- and caffeine-induced calcium release by cyclic ADP-ribrose. *J Biol Chem, 268*, 293–299.

Llinas, R., Sugimori, M., & Silver, R. B. (1992). Microdomains of high calcium concentration in a presynaptic terminal. *Science, 256*, 677–679.

Mayford, M., Bach, M. E., Huang, Y. Y., Wang, L., Hawkins, R. D., & Kandel, E. R. (1996). Control of memory formation through related expression of a CaMKII transgene. *Science, 274*, 1678–1683.

Meers, P., Daleke, D., Hong, K., & Papahadjopoulos, D. (1991). Interactions of annexins with membrane phospholipids. *Biochemistry, 30*, 2903–2908.

Miyamoto, S., Ohya, Y., Ohsumi, Y., & Anraku, Y. (1987). Nucleotide sequence of the CLS4 (CDC24) gene of *Saccharomyces cerevisiae*. *Gene, 54*, 125–132.

Nishizuka, Y. (1992). Intracellular signaling by hydrolysis of phospholipids and activation of protein kinase C. *Science, 258*, 607–614.

Noegel, A., Witke, W., & Schleicher, M. (1987). Calcium-sensitive nonmuscle α-actinin contains EF-hand structures and highly conserved regions. *FEBS Lett, 221*, 391–396.

Ohno, S., Emori, Y., Imajoh, S., Kawaskai, H., Kisaragi, M., & Suzuki, K. (1984). Evolutionary origin of a calcium-dependent protease by fusion of genes for a thiol protease and a calcium-binding. *Nature, 312*, 566–570.

Ringer, S. (1883). A further contribution regarding the influence of the different constituents of the blood of the contraction of the heart. *J Physiol, 4*, 29–43.

Smith, V. L., Kaetzel, M. A., & Dedman, J. R. (1990). Stimulus-response coupling: the search for intracellular calcium mediator proteins. *Cell Regul, 1*, 165–172.

Sweet, W. D., & Schroeder, F. (1988). *Lipid Domains and the Relationship to Membrane Function*. New York: R. Liss. p. 1742.

Wang, J., Campos, B., Jamieson, A., Kaetzel, M., & Dedman, J. (1995). Functional elimination of calmodulin with the nucleus by targeted expression of an inhibitor peptide. *J Biol Chem, 270*, 30245–30248.

Wang, J., Moreira, K., Campos, B., Kaetzel, M., & Dedman, J. (1996). Targeted neutralization of calmodulin in the nucleus blocks DNA synthesis and cell cycle progression. *Biochim Biophys Acta, 1313*, 223–228.

Section II

Membrane Potential, Transport Physiology, Pumps, and Exchangers

Chapter 8

Diffusion and Permeability

Nicholas Sperelakis and Jeffrey C. Freedman

Chapter Outline

I. SUMMARY

This chapter describes diffusion of uncharged particles and charged ions across membranes with and without partitioning and provides the relevant equations that govern such diffusion. The relationship between the diffusion coefficient (D) and the permeability coefficient (P) is presented, as well as the factors that determine these coefficients. The dependence of P on the mobility of an ion through the membrane under a voltage gradient is also described. Electrochemical potential is defined and the interconversion between flux and current is presented. Finally, the Ussing flux ratio equation is presented and examples of its significance are given. Relating to this, the concept of potential energy wells and barriers is presented, describing the movement of an ion through an ion channel.

II. INTRODUCTION

In order to understand the fundamentals of membrane transport, as well as the mechanisms for development of the electrical resting potential (RP) of cells, it is first necessary to consider the basic processes of *diffusion* and membrane *permeability*. Therefore, this chapter discusses fundamental principles that are utilized in subsequent chapters in this book.

Molecules of gases and liquids and dissolved solutes are continuously in motion. The velocities of individual molecules vary tremendously, as do their kinetic energies (in accordance with the Maxwell–Boltzmann distribution). Diffusion is the process whereby particles in a gas or liquid tend to intermingle due to their spontaneous motion caused by thermal agitation. Any diffusing substance tends to move from *regions of higher concentration* to *regions of lower concentration*, until the substance is uniformly distributed at *equilibrium*. The molecules continue to move at equilibrium, but the *net movement* is zero. In the absence of *convection*, which refers to bulk flow of solvent, such as that caused by stirring, the movement of the molecules is by diffusion only. Diffusion occurs because of the *random thermal motions* of the molecules. Particles flow from a region of high concentration to one of low concentration. If a solution of high solute concentration is adjacent to one of low concentration, but separated by an imaginary plane, it is probable that more molecules per unit of time will be crossing the plane from the side of higher concentration to the side of lower concentration than in the opposite direction. There are *fluxes* (movements of molecules) in both directions (the *unidirectional fluxes*), but the *net flux* is from the side of higher concentration to the side of lower concentration.

Now, if the imaginary plane were replaced with a thin membrane permeable to the molecules, then the same situation would apply; the particles would diffuse from the side of higher concentration to the side of lower concentration across the membrane. In a living cell, it is usually assumed that the bulk solutions are relatively well mixed and diffusion of most substances through the cell membrane is much slower than that through a free solution. Therefore, diffusion through the membrane is the *rate-limiting* step. For simplicity, we assume that the solutions on either side are well stirred (although there may actually

Cell Physiology Sourcebook. DOI: 10.1016/B978-0-12-387738-3.00008-1

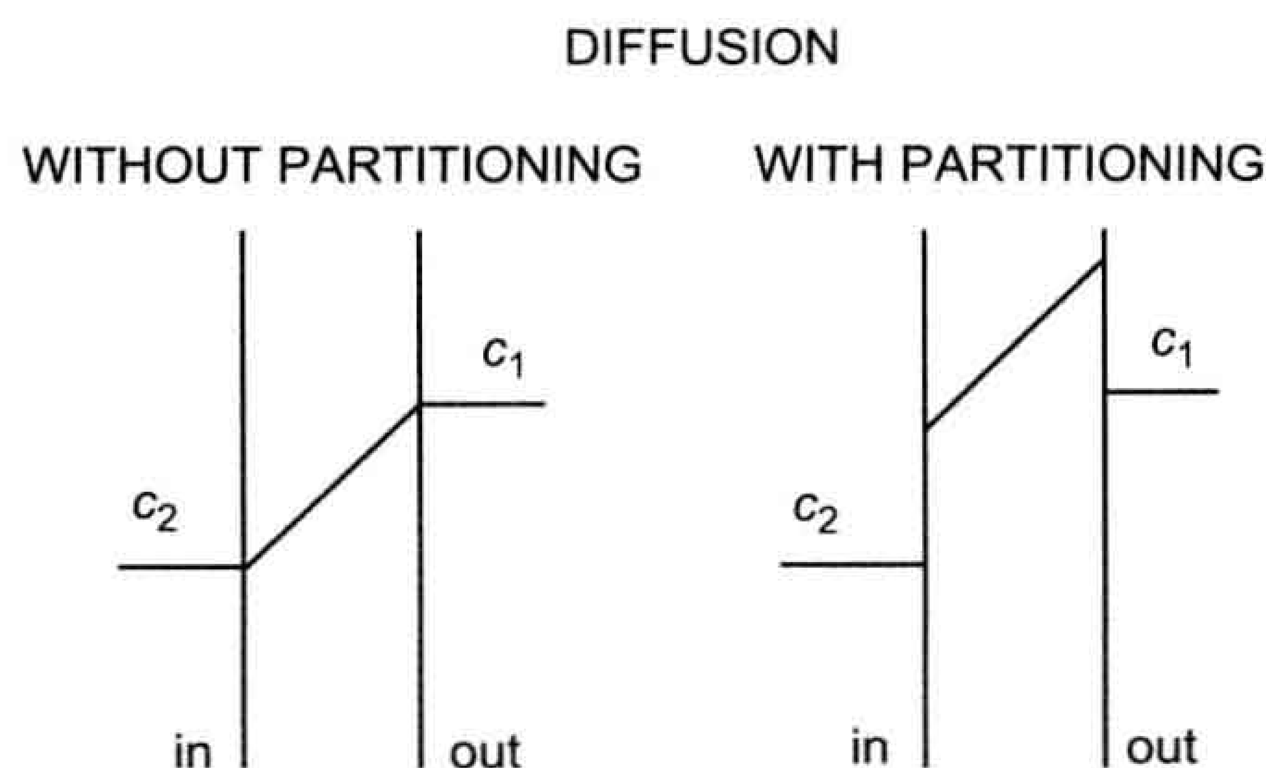


FIGURE 8.1 Concentration gradients across the membrane during diffusion without partitioning (left) and with partitioning (right).

be unstirred layers near the membrane). We confine ourselves here to the diffusion of small molecules or ions across the cell membrane.

For thin membranes, we first consider the case of diffusion without partitioning, as illustrated in Fig. 8.1 (left), in which the diffusing molecule can freely enter the membrane. We will then introduce the effect of partitioning into the membrane, a process that involves a change of chemical potential upon entrance into the membrane phase, as illustrated in Fig. 8.1 (right). We disregard possible structural obstacles that may be a series of *potential energy barriers* within the membrane (Danielli, 1943).

III. FICK'S LAW OF DIFFUSION

The fundamental law describing diffusion was enunciated by Adolph E. Fick in 1855, who noted a similarity between diffusion of solutes and Fourier's law describing the flow of heat in solids. *Fick's law of diffusion* was deduced theoretically in 1860 by James C. Maxwell from the kinetic theory of gases. The derivation of Fick's law includes the following assumptions: (1) statistical laws apply; (2) the average duration of a collision is short compared to the average time between collisions, a condition pertaining to dilute solutions; (3) the particles move independently; (4) classical mechanics can be used to describe molecular collisions; (5) energy, momentum and mass are conserved in every collision; and (6) the diffusing solute particles are much larger than the solvent molecules of the liquid.

IV. DIFFUSION COEFFICIENT

Consider two compartments, separated by a membrane of thickness Δx, in which a substance diffuses from inside a cell (denoted as compartment i with high concentration c_i) across the cell membrane into the outside medium (denoted as compartment o with low concentration c_o). It is assumed that the temperature and pressure are the same in both compartments. For such a system, *Fick's first law of diffusion* states that the *flux density* (J, mol/s-cm^2) is directly proportional to the concentration gradient dc/dx (mol/cm^3/cm) across the membrane.

$$J = \frac{dN}{Adt} = -D\frac{dc}{dx} \tag{8.1}$$

where dN/Adt (mol/(cm^2·s) is the number (dN) of moles that diffuse across a unit area (A, cm^2) of the membrane during an interval of time (dt, s). The diffusion coefficient D (cm^2/s).indicates how much flux will occur for a given concentration gradient.

The concentration gradient in the steady state is equal to the difference in the concentration ($\Delta c = c_o - c_i$) of the solute on both sides of the membrane divided by the thickness of the membrane (Δx), so that:

$$J = -D\frac{\Delta c}{\Delta x} \tag{8.2}$$

$$\frac{mol}{\sec \cdot cm^2} = \frac{cm^2}{\sec}\frac{mol/cm^3}{cm}$$

It is assumed that the concentration gradient through the thin membrane is linear over its thickness (Δx).

The time required for diffusion to become 50, 63 or 90% complete varies directly with the square of the distance and inversely with the diffusion coefficient. Thus, diffusion is extremely fast over short distances (e.g. 10–1000 nm), but is exceedingly slow over long distances (e.g. 1 cm). For a small particle like K^+ or acetylcholine (ACh^+), with a D value of about 1×10^{-5} cm^2/s, the time required for 90% equilibration to be reached over a distance of 1 μm is about 1 ms. Table 8.1 shows how the time required changes as a function of distance. The chef knows that the time

TABLE 8.1 Calculations of Time Required for Diffusion to Become 90% Complete

Distance *d*	Time *t*
100 Å	0.1 μs
0.1 μm	0.01 ms
1 μm	1 ms
10 μm	100 ms
100 μm	10 s
1 mm	16.7 min
1 cm	28 h

Diffusion time varies inversely with square of diffusion distance. These approximate values are for a substance having a diffusion coefficient (*D*) of about 1×10^{-5} cm^2/s in free solution. Einstein's approximation equation is $d = \sqrt{Dt}$, where *d* is the mean displacement.

TABLE 8.2 Physicochemical Properties of Selected Ions

Ion	Limiting Equivalent Conductivity (cm^2/S·eq)	Activity Coefficient[a]	Crystallographic Radius (Å)	Singly-hydrated Radius[b] (Å)	Hydrated Volume[c] (Å ^{3})	Heat of Hydration (kcal/g ion)	Number of Water Molecules[c]
Na^+	50.10	0.778	0.96	3.67	150	−115	(4−6)
K^+	73.50	0.770	1.33	4.05	(150)	−90	(3−6)
Cl^-	76.35	−	1.81	3.92	90	−59	(0−6)
Mg^{2+}	53.05	0.528	0.65	3.60	360	−501	12
Ca^{2+}	59.50	0.518	0.99	3.70	310	−428	10
Sr^{2+}	59.45	0.515	1.13	3.85	310	−381	10
Ba^{2+}	63.63	0.508	1.35	4.08	290	−347	9−10

[a]*Activity coefficient for each cation given for the Cl^- salt at 0.1 M and at 25°C.*
[b]*Singly-hydrated radius equals crystallographic radius plus 2.72 Å (diameter of water molecule) for cations having crystal radii between 0.9 and 1.7 Å, and crystal radius plus 2.23 Å for anions. Values for singly-hydrated radii taken from Mullins (1961).*
[c]*Values in parentheses are estimated.*
Values taken from R.A. Robinson and R.H. Stokes, *Electrolyte Solutions*, London, Butterworth & Co. (Publishers), Ltd., 1959 and from J.O.M. Bockris and B.E. Conway, *Modern Aspects of Electrochemistry*, London, Butterworth & Co. (Publishers), Ltd., 1954.

required for a meat roast to cook in the middle is dependent on the thickness of the roast and the physiologist knows that there is a critical thickness (e.g. 0.5−1.0 mm) of a muscle bundle in an incubation bath that allows adequate diffusion of oxygen to the core of the strip, no matter how vigorously the bath is oxygenated.

The *diffusion coefficient (D)* is a constant for a given substance and membrane under a given set of conditions. The diffusion coefficient of substances in free solution is dependent upon molecular size (and shape, for large molecules). For ions, the smaller the *crystal (unhydrated) radius*, the greater the *charge density*, which means that more water molecules are held in the *hydration shells*, thus giving a larger *hydrated radius*. The larger water shell causes diffusion to be slower. The hydrated and unhydrated radii of some relevant ions are given in Table 8.2. Thus, although Na^+ has a lower atomic weight than K^+, Na^+ attracts and holds a larger hydration shell because of its greater charge density (same charge as K^+, but smaller unhydrated ion size) and, therefore, Na^+ diffuses in water considerably slower than does K^+ (ratio of about 1: 2).

The diffusion coefficient is inversely related to the resistance to free diffusion and, therefore, is very much lower in water than in a gas. *Graham's law* states that the diffusion coefficient of a gas is inversely proportional to the square root of the molecular weight:

$$DM^{1/2} = \text{constant} \tag{8.3}$$

Graham's law was originally discovered by experiment and was later derived theoretically by Maxwell. The *random molecular motions* due to *thermal energy* are opposed by *intermolecular attractive forces* but, in dilute gases, these attractive forces are small because the molecules are relatively far apart.

The *Einstein−Stokes equation* applies to diffusion in liquids when spherical solute molecules are much larger than the solvent molecules, e.g. of colloidal size. The diffusion coefficient of the solute is related to the viscosity (η) of the solvent and the radius (r) of the solute particle:

$$D = \frac{RT}{6\pi\eta r N_A} \tag{8.4}$$

where R is the *gas constant*, T is the absolute temperature and N_A is Avogadro's number.

Temperature also affects the rate of diffusion. The relative increase in the diffusion coefficient when the temperature (T) is raised by 10°C is known as Q_{10}. For dilute solutions, the Q_{10} value should be the same for all molecules and is 1.03 (between 25 and 35°C). A Q_{10} value of 2 or 3 indicates that some process other than diffusion is probably responsible for transport.

In liquids, the solute and solvent molecules are close together. Hence, for any solute particle to move, it must first break away from its surrounding solvent molecules. Diffusion in liquids consequently occurs in a discontinuous manner. A solute molecule is able to move only when it has acquired sufficient energy by collision to break away from its solvent neighbors. Thus, the molecule diffuses in a series of jumps, each jump requiring a critical *activation energy*.

When the attractive forces between solvent molecules are weak, diffusion is more rapid.

The Q_{10} for diffusion of a substance in water depends on the activation energy necessary for a jump. If a large amount of energy is required (high Q_{10}), only a few molecules have the necessary energy to diffuse at any moment. Raising the temperature increases the number of molecules with the required energy and thereby appreciably speeds up the rate of diffusion. If only a small activation energy is required (low Q_{10}), a greater fraction of the molecules possesses this minimal energy at any moment and so raising the temperature has less of an effect. The Q_{10} for diffusion of Na^+ or K^+ in water is only about 1.22.

The cell membrane constitutes a barrier to diffusion. In penetrating through the lipid bilayer matrix, a non-charged small solute molecule must move as follows: (1) detach itself from its surrounding solvent molecules and jump into the membrane phase; (2) move through the thickness of the membrane, perhaps by a series of small jumps over energy barriers; and (3) detach itself from the membrane and jump into the solvent phase on the opposite side of the membrane. The permeability of the membrane to the solute depends greatly on the activation energy required for the molecule to jump into and out of the membrane. If the activation energy is high, the Q_{10} is high and the permeability is low; if the activation energy is low, then the Q_{10} is low and the permeability is high.

V. DIFFUSION ACROSS A MEMBRANE WITH PARTITIONING

When a solute partitions into the membrane, the concentration gradient across the membrane itself differs from that calculated from the internal and external concentrations in the bulk solutions. For example, if a solute is at 10 mM in the internal solution and at 1 mM in the external solution, the concentration gradient would be $c_i - c_o = 10 - 1 = 9$ mM. Now suppose that the solute dissolves into the membrane phase such that the concentration just within the membrane at the internal boundary is 10-fold greater than in the internal solution and the same 10-fold partitioning occurs at the external boundary. With such partitioning, the concentrations in the membrane would be 100 mM at the internal boundary and 10 mM at the external boundary, constituting a gradient of $100 - 10 = 90$ mM, or a 10-fold higher concentration gradient within the membrane. The *partition coefficient* (β) relates the concentration just within the membrane at the boundary to the external or internal concentrations. β is assumed to be equal at the internal and external boundaries of the cell membrane.

The diffusion coefficient across cell membranes for various substances is generally greater when the molecular size of the substance is small and when the lipid solubility is high; i.e. small molecules of high lipid solubility (i.e. less polar and non-polar molecules) penetrate most quickly through the membrane.

The above paragraphs present the basis for Overton's classical rule that the rate of diffusion of many substances across cell membranes correlates with the *oil/water partition coefficient*. The rate of permeation of a water-soluble substance is primarily determined by how easily the substance passes from water to lipid; its oil/water partition coefficient is a measure of this ease. The more a substance dissolves in the membrane, the greater its concentration gradient within the membrane and the faster the rate of diffusion across the membrane. The data for permeation of non-electrolytes, including alcohols, into cells are an example of this mechanism.

VI. PERMEABILITY COEFFICIENT

The *permeability coefficient* (P, cm/s) is the product of the partition coefficient (β) and the diffusion coefficient (D) divided by the thickness (Δx), of the membrane:

$$P = \frac{\beta D}{\Delta x} \quad \text{cm/s} = \text{cm}^2/\text{s/cm} \tag{8.5}$$

Note that permeability coefficients apply only to membranes, whereas diffusion coefficients apply to both membranes and solutions. Equation 8.5 indicates that, the higher the diffusion coefficient for movement of a substance across a membrane, the higher the permeability coefficient.

The flux density (J) across the membrane is given by:

$$J = -P(c_O - c_I) \tag{8.6}$$

$$\frac{mol}{sec \cdot cm^2} = \frac{cm}{sec}\frac{mol}{cm^3}$$

Hence the net flux density of a non-electrolyte across a membrane is equal to the permeability coefficient (P) times the difference in concentration across the membrane. The permeability coefficient for K^+ (P_K) across resting skeletal muscle membrane is about 1×10^{-6} cm/s. Some values for P_K (in cm/s) are given in Table 8.3 for some cardiac tissues. The *unidirectional influx* (J_i) and *efflux* (J_o) are defined by:

$$J_i = -Pc_O \tag{8.7a}$$

$$J_o = -Pc_I \tag{8.7b}$$

The *net flux* is defined as the difference between the efflux and influx. Thus,

$$J = J_o - J_i = -P(c_O - c_I) \tag{8.8}$$

TABLE 8.3 Summary of Internal K^+ and Na^+ Concentrations and Permeabilities for Some Selected Heart Tissues

Preparation	Resting Potential (mV)	P_K (cm/s×10^{-7})	P_{Na}(cm/s×10^{-7})	P_{Na}/P_K	$[K^+]_i$(mM)	$[Na^+]_i$(mM)	Reference
Chick embryo 19 days old	—	3.10	0.053	0.017	122	15	Carmeliet et al. (1976)
Rabbit papillary muscle	−77.5	—	—	—	135	32.7	Lee and Fozzard (1975)
					82.6[a]	5.7[a]	
Rabbit papillary muscle	−86	—	—	—	119[b]	—	Akiyama and Fozzard (1975)
Rabbit ventricle	−76	—	—	—	83.1[a]	—	Fozzard and Lee (1976)
Cow Purkinje	−75	1.66	—	—	—	—	Carmeliet and Verdonck (1977)
Sheep Purkinje	—	—	—	—	160	—	Carmeliet and Bosteels (1969)

Unless otherwise specified, all ion concentrations are based on total tissue analyses, and all permeability coefficients are for tissues bathed in normal Ringer's solution.
[a]*Measured with ion-selective microelectrodes.*
[b]*Calculated from the internal K^+ concentration and activity coefficient.*

which is the same as Equation 8.6. Equations 8.7a and 8.7b show that the influx of a substance is equal to its permeability coefficient times the external concentration (c_O), whereas the efflux (or outflux) is equal to the permeability coefficient times the internal concentration (c_I). Algebraic manipulation shows that the permeability coefficient is equal to the ratio of flux to concentration (influx to c_O and efflux to c_i).

The electrical current (i, in amp) carried by Na^+ is equal to the flux (J' in mol/s) times zF *(coul/mol or coul/equiv, if univalent)*, or

$$i = J' zF \tag{8.9a}$$

Converting to current density:

$$I = JzF \tag{8.9b}$$

$$\frac{\text{amp}}{\text{cm}^2} = \frac{\text{mol}}{\text{sec}\cdot\text{cm}^2}\frac{\text{coul}}{\text{mol}}$$

where I is the current density in amp/cm^2, and J is the flux density in mol/cm^{2-}s.

VII. ELECTRODIFFUSION

Fick's law of diffusion (Equation 8.1) applies only to uncharged molecules. If there is a net charge on the molecule, then the unidirectional fluxes are also determined by any electrical field that may exist across the membrane. The equation for the net flux is then:

$$J = Pf(E_m)(c_1 - c_2 e^{E_m F/RT}) \tag{8.10}$$

where $f(E_m)$ is some function of the *electrical potential difference* (p.d.) across the membrane and F, R and T are the Faraday constant, gas constant and absolute temperature, respectively. Note the similarity of Equation 8.10 to Equations 8.6 and 8.8, except for the membrane potential terms. The electrical p.d. across the membrane (E_m) equals $\psi_I - \psi_O$, where ψ_I is the inside potential and ψ_O is the outside potential. When $f(E_m)$ is equal to E_mF/RT, this term is dimensionless (E_mF is the electrical energy, whereas RT is the thermal energy); $RT/F = 0.026$ V at 25°C. Similarly, the term $e^{E_mF/RT}$ is dimensionless; therefore, the units for flux are the same as those given in Equation 8.6.

For a monovalent cation, *Einstein's law of diffusion* states that:

$$D = U\,kT = U\frac{RT}{F} \tag{8.11}$$

where U is the *electrophoretic mobility* of the ion through the membrane and has units of a velocity per unit driving voltage gradient (cm/s per V/cm) and k is the Boltzmann constant (R/F).

Substituting Equation 8.11 into the definition of the permeability coefficient (Equation 8.5) gives:

$$P = U\frac{\beta}{\Delta x}\frac{RT}{F} \quad (8.12)$$

$$\frac{\text{cm}}{\text{sec}} = \frac{\text{cm/sec}}{\text{V/cm}}\frac{1}{\text{cm}}\frac{\text{V}}{1}$$

where β is the partition coefficient (dimensionless) for the ion between the bulk solution and the edge of the membrane and Δx is the membrane thickness (cm). Equation 8.12 indicates that the permeability coefficient of an ion is directly related to the electrophoretic mobility of the ion through the membrane.

The *Nernst–Planck equation* states that the total flux density, J_i (mol/cm^2·s), of an ion species (i) across the membrane is the sum of the flux density due to diffusion and the flux density due to the electrical potential:

$$J_i = J_{i(\text{diff})} + J_{i(\text{elec})} \quad (8.13)$$

The net outward flux due to diffusion, given by *Fick's law*, is proportional to the concentration gradient, dc_i/dx:

$$J_{O(\text{diff})} = -D_i\frac{dc_i}{dx} \quad (8.14)$$

where D_i (cm^2/s) is the diffusion coefficient of the *ion* species.

The flux of an ion is proportional to the gradient of *electrochemical potential* ($\overline{\mu}$) for that ion. The net flux is from the side of greater electrochemical potential to the side of lesser electrochemical potential. $\overline{\mu}$ is a measure of the useful energy and its units are in joules/mole (just as voltage is in joules/coulomb). Electrochemical potential is composed of a chemical part (μ_c) and an electrical part (μ_e), that is,

$$\overline{\mu} = \mu_c + \mu_e \quad (8.15)$$

The chemical part (μ_c) is given by:

$$\mu_c = \mu_c^0 + RT\ln a \quad (8.16a)$$

where μ_c^0 is the chemical potential at standard temperature and pressure and a is the activity (activity coefficient, γ, times the concentration). The electrical part (μ_e) is given by

$$\mu_e = zF\psi \quad (8.16b)$$

The difference in electrochemical potential for Na^+, for example, between inside and outside ($\Delta\overline{\mu} = \overline{\mu}_2 - \overline{\mu}_1$) is:

$$\Delta\overline{\mu}_{\text{Na}} = RT\ \ln\frac{[\text{Na}^+]_2}{[\text{Na}^+]_1} + zF\Delta\psi \quad (8.17)$$

where $\Delta\psi = \psi_2 - \psi_1$ and is the same as E_m. The activity coefficients cancel out, assuming $\gamma_2 = \gamma_1$.

VIII. SPECIAL TRANSPORT PROCESSES

Most non-polar molecules pass directly through the lipid bilayer matrix of the membrane, i.e. not through special sites (e.g. water-filled pores or channels). Small charged ions (e.g. Na^+, K^+, Cl^-, Ca^{2+}) pass through water-filled channels, some of which have a voltage-dependent gating mechanism. These channels can exhibit a high degree of selectivity for specific ions, with the selectivity orders not being based solely on the hydrated or unhydrated sizes of the ions. One type of ionophore, valinomycin, forms a hydrophobic cage around K^+. This K^+-ionophore complex is lipid soluble and passes rapidly through the lipid bilayer matrix.

Special *transport proteins* are normally present in the cell membrane for net uptake of nutrients, such as glucose and amino acids. Some of these are for *downhill transport* only, i.e. down the electrochemical gradient. One type of protein-mediated transport in cells (e.g. for glucose) is known as *facilitated diffusion*, a type of transport that contrasts with *simple diffusion* across the cell membrane. Another type of mediated transport is known as *exchange diffusion*, in which one molecule of substance (or ion) inside the cell is exchanged for one molecule outside the cell, in which case there is no net movement. In either type of mediated transport, the *rate of downhill movement* of the substance across the membrane is enhanced by the transport protein.

Mediated transport systems differ from simple diffusion in that they exhibit *saturation kinetics*. That is, the rate of transport increases with an increase in the substrate concentration up to a maximum, after which the rate levels off due to a finite number of available transport sites. Other characteristics of mediated transport systems include *competitive inhibition*, in which an inhibitor substance competes at the same site for binding to the transporter. In *non-competitive inhibition*, the *inhibitor* (non-transported) substance binds to the transporter at a site different from the transport site, but still alters or prevents binding of the usual substrate. Mediated transport exhibits greater *specificity* than simple diffusion; e.g. the rate of mediated transport of D-glucose is greater than for L-glucose. Because mediated transport resembles an enzymatic process involving protein conformational changes, the temperature coefficient (Q_{10}) is also higher than for simple diffusion.

IX. USSING FLUX RATIO EQUATION

As pointed out in Equations 8.7a and 8.7b, the unidirectional fluxes are determined also by the permeability coefficient. Ussing (1949) developed the so-called *flux ratio equation*, in which the *ratio of influx to efflux* is used

(permeability cancels out). Specifically, for the ratio of Na^+ fluxes (by simple electrodiffusion), the following applies:

$$\frac{J_i^{Na}}{J_o^{Na}} = \frac{[Na^+]o}{[Na^+]i} e^{-E_m F/RT} \quad (8.18)$$

Thus, the ratio of influx:efflux (or outflux) (passive) in a resting membrane (assuming a RP of −80 mV) is

$$\frac{J_i^{Na}}{J_o^{Na}} = \frac{150 \text{ mM}}{15 \text{ mM}} e^{+80\text{mV}/26\text{mV}} = (10)e^{3.08} = 217 \quad (8.19a)$$

Thus, the passive influx of Na^+ should be 217 times greater than the passive efflux, because of the large electrochemical gradient directed inward.

The flux ratio for K^+ would be

$$\frac{J_i^{K}}{J_o^{K}} = \frac{4 \text{ mM}}{150 \text{ mM}} e^{+80 \text{ mV}/26 \text{ mV}} = (1/37.5)e^{3.07} = 0.574 \quad (8.19b)$$

Thus, the passive influx should be 0.574 times the passive efflux. The K^+ equilibrium potential (E_K) is only slightly greater (more negative by about 14 mV) than the RP and so the passive flux ratio should be close to one.

A modified form of Equation 8.18 can be obtained by substituting the ratio of ions with $e^{E_i F/RT}$ (derived from the Nernst equation), giving

$$\frac{J_i^i}{J_o^i} = e^{-(E_m - E_i)F/RT} \quad (8.20a)$$

where E_i is the ***equilibrium potential*** for the cation in question, and J_i^i and J_o^i are the inward and outward fluxes, respectively, for ion i. The sign convention refers inside solution to outside solution. Thus, for Na^+ we have

$$\frac{J_i^{Na}}{J_o^{Na}} = e^{-[-80 \text{ mV} - (+60 \text{ mV})]/26 \text{ mV}} = 217 \quad (8.20b)$$

This value of 217 obtained for the flux ratio is identical to that obtained from Equation 8.19a. One advantage of Equation 8.20a is that it is obvious at a glance that when $E_i = E_m$, the flux ratio is exactly 1.0, because $e^0 = 1$, where e is the base (2.717) for the natural logarithm. Thus, if Cl^- is passively distributed so that $E_{Cl} = E_m$, its flux ratio should be 1.0; i.e. influx equals efflux, so there is no net flux. The larger the difference between E_i and E_m, i.e. the farther the ion is from equilibrium, the greater the flux ratio.

Sometimes Equations 8.20a and 8.20b do not fit the experimental facts. The data are better fitted if the exponential term contains another factor (n), which is an empirical factor:

$$\frac{J_i^i}{J_o^i} = e^{-n(E_m - E_i)F/RT} \quad (8.21)$$

The best fit of the data is when n has a value of 2.5 to 4.0, depending on the membrane under investigation. One interpretation given to n is that if the length of the water-filled pore that the ion must traverse to cross the membrane is much longer than the ion diameter, as is likely, then for so-called *single-file diffusion*, n hits on the same side are required for the ion to complete its journey across the membrane. One could consider, for example, that there are three potential energy wells, or a chain of reactive sites, along the length of the pore, and the only way for the ion to escape the well is to receive a kinetic bump from an adjacent ion in the file. Complete permeation of an ion through the pore is more likely to happen if the ion is moving in the same direction as the majority of ions, i.e. down the electrochemical gradient. Therefore, this factor (Equation 8.21) makes the flux ratio much greater than would otherwise be predicted.

BIBLIOGRAPHY

Akiyama, T., & Fozzard, H. A. (1975). Influence of potassium ions and osmolality on the resting membrane potential of rabbit ventricular papillary muscle with estimation of activity and the activity coefficient of internal potassium. *Circ Res, 37*, 621–629.

Bockris, J. O'M., & Conway, B. E. (1954). *Modern Aspects of Electrochemistry*. London: Butterworths.

Carmeliet, E., & Bosteels, S. (1969). Coupling between Cl flux and Na or K flux in cardiac Purkinje fibers: influence of pH. Arch Int Physio. *Biochim, 77*, 57–72.

Carmeliet, E., & Verdonck, F. (1977). Reduction of potassium permeability by chloride substitution in cardiac cells. *J Physiol (London), 265*, 193–206.

Carmeliet, E. E., Horres, C. R., Lieberman, M., & Vereecke, J. S. (1976). Developmental aspects of potassium flux and permeability of the embryonic chick heart. *J Physiol (London), 254*, 673–692.

Crank, J. (1956). *Mathematics of Diffusion*. New York: Oxford University Press.

Danielli, J. (1943). The theory of penetration of a thin membrane: Appendix. In D. F. Danielli (Ed.), *The Permeability of Natural Membranes*. London: Cambridge University Press.

Einstein, A., & A.D. Cowper, Transl. (1926). Investigations on the Theory of Brownian Movement. In R. Furth (Ed.), *Methuen*. London: reprinted by Dover Publications, Inc. 1956.

Fozzard, H. A., & Lee, C. O. (1976). Influence of changes in external potassium and chloride ions on membrane potential and intracellular potassium ion activity in rabbit ventricular muscle. *J Physiol (London), 256*, 663–689.

Hodgkin, A. L., & Huxley, A. F. (1952). Currents carried by sodium and potassium ions through the membrane of the giant axon of Loligo. *J Physiol (London), 116*, 449–472.

Jacobs, M. H. (1967). *Diffusion Processes*. New York: Springer-Verlag.

Jost, W. (1960). *Diffusion in Solids, Liquids, Gases*. New York: Academic Press.

Lee, C. O., & Fozzard, H. A. (1975). Activities of potassium and sodium ions in rabbit heart muscle. *J Gen Physiol, 65*, 695–708.

Mullins, L. J. (1961). The macromolecular properties of excitable membranes. *Ann NY Acad Sci, 94*, 390–404.

Robinson, R. A., & Stokes, R. H. (1959). *Electrolyte Solutions*. London: Butterworths.

Ussing, H. H. (1949). Distinction by means of tracers between active transport and diffusion. The transfer of iodide across isolated frog skin. *Acta Physiol Scand, 19*, 43–56.

Chapter 9

Origin of Resting Membrane Potentials

Nicholas Sperelakis

Chapter Outline

I. SUMMARY

Most of the factors that determine or influence the resting E_m of cells are discussed in this chapter. The structural and chemical composition of the cell membrane is briefly examined and correlated with the resistive and capacitative properties of the membrane. The factors that determine the intracellular ion concentrations in cells are examined. These factors include the *Na^+-K^+-coupled pump*, the *Ca^{2+}-Na^+ exchange* reaction and the sarcolemmal *Ca^{2+} pump*. The Na^+-K^+ pump enzyme, Na^+,K^+-ATPase, requires both Na^+ and K^+ for activity and transports three Na^+ ions outward and usually two K^+ ions inward per ATP hydrolyzed. Cardiac glycosides are specific blockers of this transport ATPase. The Na^+-K^+ pump, if electroneutral, is not directly related to excitability, but only indirectly related by its role in maintaining the Na^+ and K^+ concentration gradients.

The carrier-mediated Ca^{2+}-Na^+ exchange reaction is driven by the Na^+ electrochemical gradient; i.e. the energy for transporting out internal Ca^{2+} by this mechanism comes from the Na^+,K^+-ATPase. The Ca^{2+}-Na^+ exchange reaction exchanges one internal Ca^{2+} ion for three external Na^+ ions when working in the *forward mode* in cells at rest. In myocardial cells, during the action potential (AP) plateau depolarization, the energetics cause the Ca^{2+}-Na^+ exchanger to operate in *reverse mode*, allowing Ca^{2+} influx.

The mechanism whereby the *ionic distributions* give rise to diffusion potentials is discussed, as are the factors that determine the magnitude and polarity of each ionic *equilibrium potential*. The equilibrium potential for any ion and the transmembrane potential determine the total *electrochemical driving force* for that ion and the product of this driving force and membrane conductance for that ion

Cell Physiology Sourcebook. DOI: 10.1016/B978-0-12-387738-3.00009-3

determines the net ionic current. The direction of the net ionic movement, inward or outward, depends on the direction of the electrochemical gradient.

The key factor that determines the resting E_m is the *relative permeability* of the various ions, particularly of K^+ and Na^+, i.e. the P_{Na}/P_K ratio (or g_{Na}/g_K ratio), as calculated from the constant-field equation. The major physiologic ions that have some effect on the resting E_m or on the APs are K^+, Na^+, Ca^{2+} and Cl^-. The Ca^{2+} electrochemical gradient has only a small direct effect on the resting E_m, although low external Ca^{2+} can affect the permeabilities and conductances for the other ions, such as Na^+ and K^+. Elevation of internal Ca^{2+} can increase the permeability to K^+ by activating Ca^{2+}-operated K^+-selective $I_{K(Ca)}$ channels.

Cl^- is usually *passively distributed* according to the membrane potential, i.e. not actively transported. However, there is some evidence indicating that, in some smooth muscle cells, $[Cl^-]_i$ may be about twice as high as that predicted from E_m. If so, this would give an E_{Cl} value about 18 mV less negative than the resting E_m. Before one can conclude that there is a Cl^- pump directed inward, however, the calculated E_{Cl} must be significantly more positive than the mean resting E_m averaged over time; i.e. any spontaneous APs must be taken into account. If Cl^- is passively distributed, it cannot determine the resting E_m. However, transient net movements of Cl^- ions, e.g. during the AP, do affect the E_m, particularly when g_{Cl} is high.

Elevation of $[K^+]_o$ to more than the normal concentration of about 4.5 mM decreases the K^+ equilibrium potential (E_K), as predicted from the Nernst equation ($[K^+]_i$ constant) and depolarization is produced.

Not only is the resting E_m the *potential energy storehouse* that is drawn upon for production and propagation of the APs but, because the membrane voltage-dependent cationic channels are inactivated with sustained depolarization, the rate of rise of the AP, and hence propagation velocity, is critically dependent on the level of the resting E_m. For example, a relatively small elevation of K^+ concentration in the blood has dire consequences for functioning of the heart.

The contribution of the Na^+-K^+ pump to the resting E_m depends on: (1) the coupling ratio of Na^+ pumped out to K^+ pumped in; (2) the turnover rate of the pump; (3) the number of pumps; and (4) the magnitude of the membrane resistance. The *electrogenic pump potential* is in parallel to the net ionic diffusion potential (E_{diff}), determined by the ionic equilibrium potentials and relative permeabilities. The contribution of the electrogenic pump potential to the measured resting E_m of cells varies from 2 to 16 mV, depending on the type of cell. The immediate depolarization produced by complete Na^+-K^+ pump stoppage with cardiac glycosides is only a few millivolts in cells like myocardial cells. Of course, long-term pump inhibition produces a larger and larger depolarization as the ionic gradients are dissipated. The rate of Na^+-K^+ pumping, and hence the magnitude of the electrogenic pump contribution to E_m, is controlled primarily by $[Na^+]_i$ and by $[K^+]_o$. The electrogenic pump potential might be physiologically important to various tissues, particularly the heart, under certain conditions that tend to depolarize the cells, such as transient ischemia or hypoxia. In such cases, the actual depolarization produced may be less because of a relatively constant pump potential in parallel with a diminishing E_{diff}. The electrogenic pump potential may also affect *automaticity* of the nodal cells of the heart, as well as other cells that exhibit automaticity.

II. INTRODUCTION

The cell membrane exerts tight control over the electrical activity and the contractile machinery during the process of excitation–contraction (electromechanical) coupling. Some drugs and toxins exert primary or secondary effects on the electrical properties of the cell membrane and thereby exert effects, for example, on automaticity, arrhythmias and force of contraction of the heart. Therefore, for an understanding of the mode of action of therapeutic drugs, toxic agents, neurotransmitters, hormones and plasma electrolytes on the electrical activity of nerve and muscle, it is necessary to understand the electrical properties and behavior of the cell membrane at rest and during excitation. The first step in gaining such an understanding is to examine the electrical properties of nerve and muscle cells at rest, including the origin of the resting membrane potential (E_m). The resting E_m and action potential result from properties of the cell membrane and the ion distributions across it.

III. PASSIVE ELECTRICAL PROPERTIES

IIIA. Membrane Structure and Composition

As discussed in previous chapters, the cell membrane is composed of a bimolecular leaflet of phospholipid molecules with protein molecules floating in the lipid bilayer. The non-polar hydrophobic ends of the phospholipid molecules project toward the middle of the membrane and the polar hydrophilic ends project toward the edges of the membrane bordering on the water phases (Fig. 9.1). This orientation is thermodynamically favorable. The lipid bilayer membrane is about 50–70 Å thick and the phospholipid molecules are about the right length (30–40 Å) to stretch across half of the membrane thickness. *Cholesterol* molecules are in high concentration in the cell membrane (of animal cells) and are inserted between the phospholipid molecules, giving a phospholipid/cholesterol ratio of about 1.0. Some of the large protein molecules, called *integral membrane proteins*, protrude through the entire membrane thickness; e.g. the Na^+, K^+-ATPase, Ca^{2+}-ATPase and the

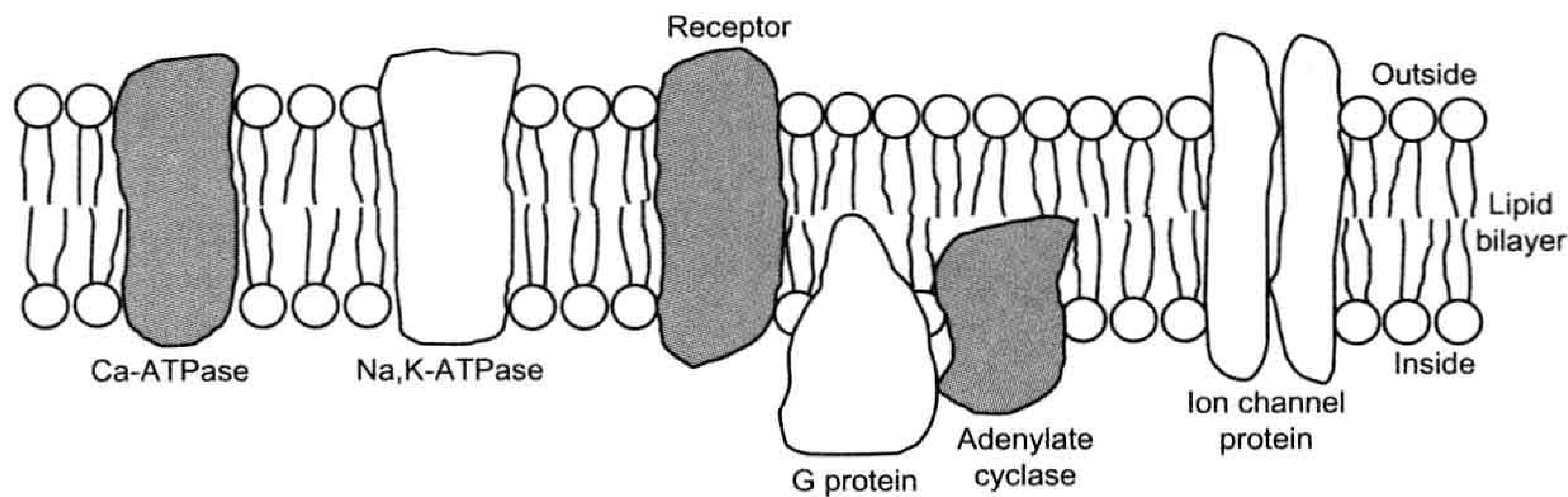


FIGURE 9.1 Diagrammatic illustration of cell membrane substructure showing the lipid bilayer. Non-polar hydrophobic tail ends of the phospholipid molecules project toward the middle of the membrane and polar hydrophilic heads border on the water phase at each side of the membrane. Lipid bilayer is about 50–70 Å thick. For simplicity, the cholesterol molecules are not shown. Large protein molecules protrude through entire membrane thickness or are inserted into one leaflet only, as depicted. These proteins include various enzymes associated with the cell membrane as well as membrane ionic channels. Membrane has fluidity so that the protein and lipid molecules can move around in the plane of the membrane.

various ion channel proteins (i.e., protrude through both leaflets), whereas other proteins are inserted into one leaflet (inner or outer) only. These proteins "float" in the lipid bilayer matrix and the membrane has *fluidity* (reciprocal of microviscosity), such that the protein molecules can move around laterally in the plane of the membrane. Some ion channels, e.g. fast Na^+ channels of the node of Ranvier of myelinated neurons, are tethered in place to the cytoskeleton by *anchoring proteins*, such as ankyrin.

The outer surface of the cell membrane is lined with strands of mucopolysaccharides (the *cell coat* or glycocalyx) that endow the cell with immunochemical properties. The cell coat is highly charged negatively and therefore can bind cations, such as Ca^{2+}. Treatment with neuraminidase to remove sialic acid residues destroys the cell coat.

IIIB. Membrane Capacitance and Resistivity

Lipid bilayer membranes made artificially have a specific *membrane capacitance* (C_m) of 0.4–1.0 μF/cm², which is close to the value for biological membranes. The capacitance of biological cell membranes is due to this *lipid bilayer matrix*. A capacitor consists of two parallel plate conductors separated by a *dielectric material* of high resistance (e.g. oil). The factors that determine the value of the capacitance of a membrane are given in the equation:

$$C_m = \frac{\in A_m}{\delta}\frac{1}{4\pi k} \tag{9.1}$$

where A_m is the membrane area (in cm²) and k is a constant (9.0×10^{11} cm/F). Calculation of membrane thickness (δ) from Equation 9.1, assuming a measured membrane capacitance (C_m) of 0.7 μF/cm² and a dieletric constant (ε) of 5, gives 63 Å. Most oils have dielectric constants of 3–5. The more dipolar the material, the greater the dielectric constant. For example, water, which is very dipolar, has a value of 81, compared with a value of 1.000 for a vacuum (air is nearly equal to that of vacuum).

The artificial lipid bilayer membrane, on the other hand, has an exceedingly high specific resistance (R_m) of 10^6–10^9 Ω·cm², which is several orders of magnitude higher than that of the biological cell membrane (about 10^3 Ω·cm²). R_m is greatly lowered, however, when the bilayer is doped with certain proteins or substances, such as macrocyclic polypeptide antibiotics (ionophores). The added ionophores may be of the ion-carrier type, such as valinomycin, or of the channel-former type, such as gramicidin. Therefore, the presence of proteins that span across the thickness of the cell membrane must account for the relatively low resistance (high conductance) of the cell membrane. These proteins include those constituting the voltage-dependent gated ion channels of the cell membrane. In summary, the capacitance is due to the lipid bilayer matrix and the conductance is due to proteins inserted in the lipid bilayer.

The dielectric property of the cell membrane is very good. For a resting E_m of −80 mV and a thickness of 60 Å, the voltage gradient sustained across the membrane is 133 000 V/cm. Thus, the cell membrane tolerates an enormous voltage gradient.

IIIC. Membrane Fluidity

The electrical properties and the ion transport properties of the cell membrane are determined by the molecular composition of the membrane. The lipid bilayer matrix even influences the function of the membrane proteins; e.g. the Na^+, K^+-ATPase activity is affected by the surrounding lipid. A high cholesterol content lowers the fluidity of the membrane. The polar portion of cholesterol lodges in the hydrophilic part of the membrane and the non-polar part of the planar cholesterol molecule is wedged between the fatty acid tails, thus restricting their motion and lowering fluidity. A high degree of unsaturation and branching of the tails of the phospholipid molecules raises the fluidity; phospholipids with unsaturated and branched-chain fatty acids cannot be packed tightly because of steric

hindrance. Chain length of the lipids also affects fluidity. Low temperature decreases membrane fluidity, as expected. Ca^{2+} and Mg^{2+} may diminish the charge repulsion between the phospholipid headgroups; this allows the bilayer molecules to pack together more closely, thereby constraining the motion of the tails and reducing fluidity. Each phospholipid tail occupies about 20–30 $Å^2$ and each headgroup about 60 $Å^2$ (Jain, 1972). Membrane fluidity changes occur in muscle development and in certain disease states, such as cancer, muscular dystrophy (Duchenne type) and myotonic dystrophy.

The hydrophobic portion of local anesthetic molecules may interpose between the lipid molecules. This separates the acyl chain tails of the phospholipid molecules further, reducing the van der Waals forces of interaction between adjacent tails and thus increasing the membrane fluidity. Local anesthetics depress the resting conductance of the membrane and the voltage-dependent changes in gNa, gK and gCa. That is, the local anesthetics produce a non-selective depression of all ionic conductances of the membrane. At the concentration of a local anesthetic required to completely block excitability, its estimated concentration in the lipid bilayer is more than 100 000/μm^2. This should be compared with a density of fast Na^+ channels of about 20–100/μm^2, and even less for K^+ channels and Ca^{2+} channels. Local anesthetics depress Na^+,K^+-ATPase activity also. Additional information on fluidity is given in several preceding chapters.

IIID. Potential Profile across Membrane

The cell membrane has fixed negative charges on its outer and inner surfaces. The charges are presumably due to acidic phospholipids in the bilayer and to protein molecules either embedded in the membrane (islands floating in the lipid bilayer matrix) or tightly adsorbed to the surface of the membrane. Most proteins have an acid isoelectric point, so at a pH near 7.0 they possess a net negative charge. The charge at the outer surface of the cell membrane, with respect to the solution bathing the cell, is known as the *zeta potential*. This charge is responsible for the electrophoresis of cells in an electric field, the cells moving toward the anode (positive electrode) because unlike charges attract. This surface charge affects the true potential difference (PD) across the membrane, as shown in Fig. 9.2A. At each surface, the fixed charge produces an electric field that extends a short distance into the solution and causes each surface of the membrane to be slightly more negative (by a few millivolts) than the extracellular and intracellular solutions. The potential theoretically recorded by an ideal tiny electrode, as the electrode is driven through the solution perpendicular to the membrane surface, should become negative as the electrode approaches within a few angstroms of the surface. The potential difference between the membrane surface and the solution declines exponentially as a function of distance from the surface. Its length constant is a function of the ionic strength (or resistivity) of the solution: the lower the ionic strength, the greater the length constant. The magnitude of the PD depends on the density of the charge sites (number of chemical groups per unit of membrane area). The number of ionized charge groups is affected by the pH and ionic strength.

The membrane potential (E_m) measured by an intracellular microelectrode is the potential of the inner solution (ψ_i) minus the potential of the outer solution (ψ_o); i.e.:

$$E_m = \psi_i - \psi_o \tag{9.2}$$

The true PD across the membrane (E'_m), however, is really that PD directly across the membrane, as shown in Fig. 9.2A. If the *surface charges* at each surface of the membrane are equal, then $E'_m = E_m$. If the outer surface charge is decreased to zero by extra binding of protons or cations (such as Ca^{2+}), then the membrane becomes slightly hyperpolarized ($E'_m > E_m$), although this is not measurable by the intracellular microelectrode (see Fig. 9.2B). Conversely, if the inner surface charge were neutralized and the outer surface charge restored, then the membrane would become slightly depolarized ($E'_m < E_m$). Again, this change is not measurable by the microelectrode, which can only measure the PD between the two solutions.

Because the membrane ionic conductances are controlled by the PD directly across the membrane (i.e. by E'_m and not by E_m), changes in the surface charges (e.g. by drugs, ionic strength or pH) can lead to apparent shifts in the electrical threshold potential, mechanical threshold potential (the E_m value at which contraction of muscle just begins), activation curve and inactivation curve (discussed in subsequent chapters). For example, elevation of extracellular Ca^{2+} concentration ($[Ca^{2+}]_o$) is known to raise the threshold potential (i.e. the critical depolarization required to reach electrical threshold), as expected from the small increase in E'_m that occurs.

IV. MAINTENANCE OF ION DISTRIBUTIONS

IVA. Resting Potentials and Ion Distributions

The transmembrane potential in resting nerve and muscle cells varies with the type of cell. In myocardial cells, it is about −80 mV (Table 9.1). The resting E_m or maximum diastolic potential in cardiac Purkinje fibers is somewhat greater (about −90 mV), whereas that in the nodal cells of the heart is lower (about −60 mV). In nerve cells, the RP is about −70 mV, whereas in mammalian skeletal muscle fibers the value is close to −80 mV. In most smooth muscle cells, the resting E_m is about −55 mV.

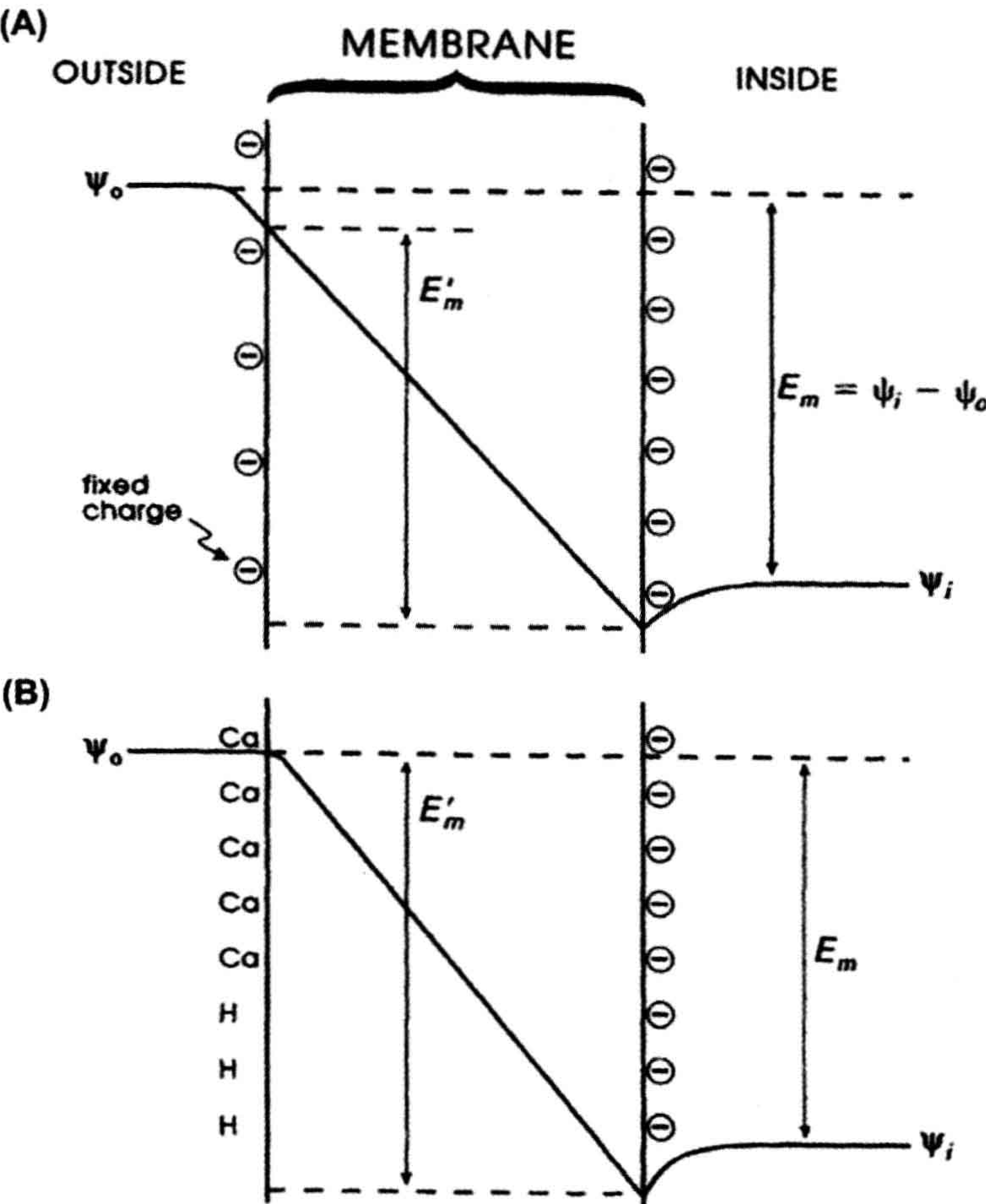


FIGURE 9.2 Potential profile across the cell membrane. (A) Because of fixed negative charges (at pH 7.4) at outer and inner surfaces of the membrane, there is a negative potential that extends from the edge of the membrane into the solutions on both sides. This surface potential falls off exponentially with distance into the solution. Magnitude of the surface potential is a function of the charge density. ψ_o is the electrical potential of the outside solution, ψ_i. is that of the inside solution and membrane potential (E_m) is the difference ($\psi_i - \psi_o$). E_m is determined by the equilibrium potentials and relative conductances. Profile of the potential through the membrane is shown as linear (the constant-field assumption), although this need not be true for the present purpose. If the outer surface potential is exactly equal to that in the inner surface, then the true transmembrane potential (E'_m) is exactly equal to the (microelectrode) measured membrane potential (E_m). (B) If the outer surface potential is different from the inner potential, e.g. by increasing the extracellular Ca^{2+} concentration or decreasing the pH to bind Ca^{2+} or H^+ to more of the negative charges, then the E'_m is greater than the measured E_m. Diminution of the inner surface charge decreases E'_m. The membrane ion channels are controlled by E'_m.

TABLE 9.1 Comparison of the Resting Potentials in Different Types of Cells

Cell Type	Resting Potential (mV)
Neuron	−70
Skeletal muscle (mammalian)	−80
Skeletal muscle (frog)	−90
Cardiac muscle (atrial and ventricular)	−80
Cardiac Purkinje fiber	−90
Atrioventricular nodal cell	−65
Sinoatrial nodal cell	−55
Smooth muscle cell	−55

The ionic composition of the extracellular fluid bathing the muscle cells is similar to that of the blood. It is high in Na^+ (about 145 mM) and Cl^- (about 100 mM), but low in K^+ (about 4.5 mM). The Ca^{2+} concentration is about 2 mM, but about half is bound to serum proteins. In contrast, the intracellular fluid has a low concentration of Na^+ (about 15 mM or less) and Cl^- (about 6–8 mM), but a high concentration of K^+ (about 150–170 mM). These ion distributions are listed in Table 9.2. The free intracellular Ca^{2+} concentration $[Ca^{2+}]_i$ is about 10^{-7} M or less, but during contraction it may rise as high as 10^{-5} M. The total intracellular Ca^{2+} is much higher (about 2 mM/kg), but most of this is bound to molecules, such as proteins, or is sequestered into compartments, such as mitochondria and the sarcoplasmic reticulum (SR). Most of the intracellular K^+ is free and it has a diffusion coefficient only

TABLE 9.2 Summary of the Ion Distributions in Most Types of Cells and the Equilibrium Potentials Calculated from the Nernst Equation

Ion	Extracellular Distribution (mM)	Intracellular Distribution (mM)	Equilibrium Potential (mV)
Na^+	145	15	+60
Cl^-	100	5[a]	−80
K^+	4.5	150	−94
Ca^{2+}	1.8	0.0001	+130
H^+	0.0001	0.0002	−18

[a]*Assuming Cl^- is passively distributed and resting E_m is −80 mV. The extracellular H^+ concentration is given for pH 7; it would be 40 nM at pH 7.4.*

slightly less than that of K^+ in free solution. Thus, under normal conditions, the cell maintains an internal ion concentration markedly different from that in the medium bathing the cells and it is these ion concentration differences that underlie the RP and excitability. The existence of the RP enables APs to be produced in those types of cells that have excitability. The ion distributions and related pumps and exchange reactions are depicted in Fig. 9.3.

Inhibition of the Na^+-K^+ pump (e.g. by cardiac glycosides such as digitalis) causes the ion concentration gradients gradually to run down or dissipate. The cells lose K^+ and gain Na^+, Cl^- and water. Therefore, the K^+ and Na^+ equilibrium potentials (E_K and E_{Na}) become smaller and the cells become depolarized. The depolarization causes the cells to gain Cl^-, and therefore also to gain water because of the resultant gain in osmotic strength, causing the cells to swell.

Although the topic of Na^+,K^+-ATPase and the Na^+-K^+ pump is discussed in detail in a subsequent chapter, a brief description is given here.

IVB. Na^+ and K^+ Distribution and the Na^+-K^+ Pump

The intracellular ion concentrations are maintained differently from those in the extracellular fluid by active ion transport mechanisms that expend metabolic energy to transport specific ions against their concentration (or electrochemical) gradients. These ion pumps are located in the cell membrane at the cell surface and probably also in

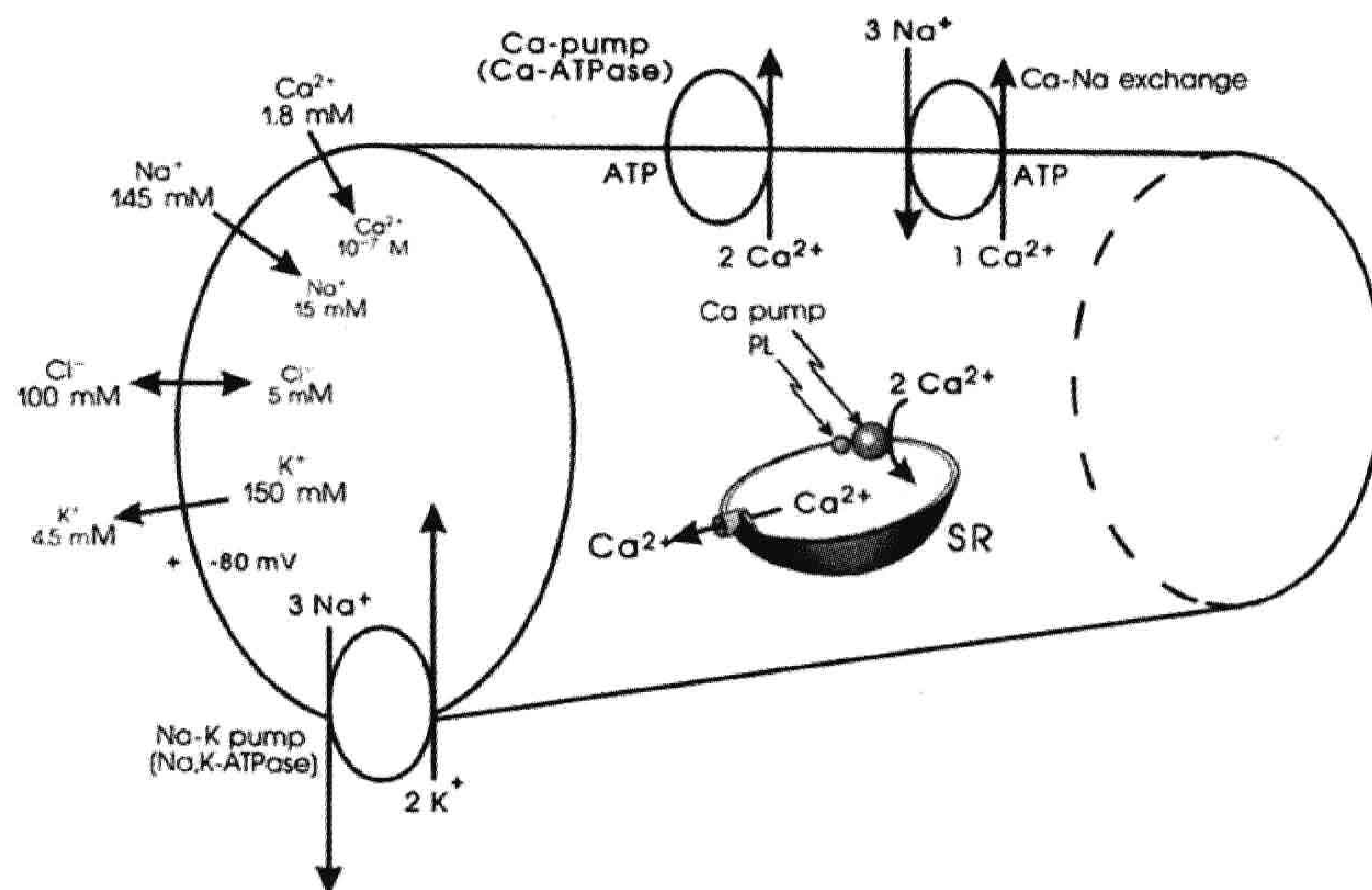


FIGURE 9.3 Intracellular and extracellular ion distributions in a skeletal muscle fiber. Also given are polarity and magnitude of the RP. Arrows give direction of the net electrochemical gradient. Na^+-K^+ pump is located in the cell surface and the T-tubule membranes. A Ca^{2+}-ATPase/Ca^{2+} pump, similar to that in the SR, is located in the cell membrane. A Ca^{2+}-Na^+ exchange carrier is located in the cell membrane.

the transverse tubular membrane of striated muscle cells. The major ion pump is the Na^+-K^+-linked pump, which pumps Na^+ out of the cell against its electrochemical gradient, while simultaneously pumping K^+ in against its electrochemical gradient (see Fig. 9.3). The coupling between Na^+ and K^+ pumping is obligatory, since in zero $[K^+]_o$, the Na^+ can no longer be pumped out. That is, a *coupling ratio* of three Na^+:0 K^+ is not possible. The coupling ratio of Na^+ pumped out to K^+ pumped in is generally 3:2. The Na^+-K^+ pump is half-inhibited (K_i value) when $[K^+]_o$ is lowered to about 2 mM.

If the ratio were 3:3, the pump would be electrically neutral or non-electrogenic. A PD across the membrane would not be produced directly, because the pump would pull in three positive charges (K^+) for every three positive charges (Na^+) it pushed out. When the ratio is 3:2, the pump is electrogenic and directly produces a PD that causes E_m to be greater (more negative) than it would be otherwise, based solely on the ion concentration gradients and relative permeabilities or *net diffusion potential* (E_{diff}). A coupling ratio of 3 Na^+:1 K^+ would produce a greater electrogenic pump potential (V_p). Under normal steady-state conditions, the contribution of the Na^+-K^+ electrogenic pump potential to E_m (ΔV_p) is only a few millivolts in myocardial cells; the contribution is greater in smooth muscle cells (6–8 mV) and mammalian skeletal muscle fibers (12–16 mV).

The driving mechanism for the Na^+-K^+ pump is a membrane ATPase, the *Na^+,K^+-ATPase*, which spans the membrane and requires both Na^+ and K^+ ions for activation. This enzyme requires Mg^{2+} for activity. ATP, Mg^{2+} and Na^+ are required at the inner surface of the membrane and K^+ is required at the outer surface. A *phosphorylated intermediate* of the Na^+,K^+-ATPase occurs in the transport cycle, its phosphorylation being Na^+-dependent and its dephosphorylation being K^+-dependent (for references, see Sperelakis, 1979). The pump enzyme usually drives three Na^+ ions out and two K^+ ions in for each ATP molecule hydrolyzed. The Na^+,K^+-ATPase is specifically inhibited by the *cardiac glycosides* (digitalis drugs) acting on the outer surface. The pump enzyme is also inhibited by vanadate ion and by sulfhydryl (SH) reagents (such as N-ethylmaleimide [NEM], mercurial diuretics and ethacrynic acid), thus indicating that the SH groups are crucial for activity.

Blockade of the Na^+-K^+ pump produces only a small immediate effect on the resting E_m: a small depolarization of about 2–16 mV, depending on cell type, representing the contribution of V_p to E_m (ΔV_p). Because excitability and generation of APs are almost unaffected at short times, excitability is independent of active ion transport. However, over many minutes, depending on the *ratio of surface area to volume* of the cell, the resting E_m slowly declines because of gradual dissipation of the ionic gradients. The progressive depolarization depresses the rate of rise of the AP, and hence the propagation velocity and eventually all excitability is lost. Thus, a large RP and excitability, although not immediately dependent on the Na^+-K^+ pump, are ultimately dependent on it.

The rate of Na^+-K^+ pumping in excitable cells must change with the amount of electrical activity to maintain relatively constant intracellular ion concentrations. A higher frequency of APs results in a greater overall movement of ions down their electrochemical gradients and these ions must be repumped to maintain the ion distributions. For example, the cells tend to gain Na^+, Cl^- and Ca^{2+} and to lose K^+. The factors that control the rate of Na^+-K^+ pumping include $[Na^+]_i$ and $[K^+]_o$. In cells that have a large surface area to volume ratio (such as small-diameter non-myelinated axons), $[Na^+]_i$ may increase by a relatively large percentage during a train of APs and this would stimulate the pumping rate. Likewise, an accumulation of K^+ externally occurs and this also stimulates the pump. The K_m value for K^+, i.e. the concentration for half-maximal rate, is about 2 mM. It has been shown that $[K^+]_o$ is significantly increased during the long AP plateau in cardiac muscle.

IVC. Cl^- Distribution

In many nerve and muscle cells, Cl^- ion does not appear to be actively transported; i.e. there is no Cl^- ion pump. In such cases, *Cl^- distributes itself passively* (no energy used) in accordance with E_m. Consequently, E_{Cl} is equal to E_m in a resting cell. For example, in mammalian myocardial cells, Cl^- seems to be close to passive distribution, because $[Cl^-]_i$. is at, or only slightly above, the value predicted by the Nernst equation from the resting E_m (for references, see Sperelakis, 1979). When passively distributed, $[Cl^-]_i$ is low because the negative potential inside the cell (the RP) pushes out the negatively-charged Cl ion (*like charges repel*) until the Cl^- distribution is at equilibrium with the resting E_m. Hence, for a resting E_m of −80 mV and taking $[Cl^-]_o$ to be 100 mM, $[Cl^-]_i$ calculated from the Nernst equation would be 4.9 mM.

$$
\begin{aligned}
E_{Cl} &= E_m \\
E_m &= +61\ \text{mV} \log \frac{[Cl^-]_i}{[Cl^-]_o} \\
&= -61\ \text{mV} \log \frac{[Cl^-]_0}{[Cl^-]_i} \\
\frac{-80\ \text{mV}}{-61\ \text{mV}} &= \log \frac{100\ \text{mM}}{[Cl^-]_i} \\
\frac{100\ \text{mM}}{[Cl^-]_i} &= \text{antilog} \frac{-80\ \text{mV}}{-61\ \text{mV}} = \text{antilog}\ 1.31 = 20.5 \\
[Cl^-]_i &= \frac{100\ \text{mM}}{20.5} = 4.88\ \text{mM}
\end{aligned}
\tag{9.3}
$$

During the AP, the inside of the cell goes in a positive direction and a net Cl^- influx (outward Cl^- current, I_{Cl}) will occur and thus increase $[Cl^-]_i$. The magnitude of the Cl^- influx depends on the Cl^- conductance (g_{Cl}) of the membrane:

$$I_{Cl} = g_{Cl}(E_m - E_{Cl}) \quad (9.4)$$

The average level of $[Cl^-]_i$ in excitable cells should depend on the frequency and duration of the AP, i.e. the mean E_m averaged over many AP cycles.

In some smooth muscles, $[Cl^-]_i$ is much higher (e.g. 30 mM) than the value of 12.5 mM predicted from passive distribution:

$$E_{Cl} = E_m = -55\,\text{mV}$$

$$[Cl^-]_i = \frac{[Cl^-]_o}{\text{antilog}\dfrac{E_m}{-61\text{ mV}}} = \frac{100\text{ mM}}{\text{antilog}\dfrac{-55\text{ mV}}{-61\text{ mV}}} = \frac{100}{7.973} = 12.5\text{ mM}$$

The elevated $[Cl^-]_i$ in smooth muscle could be due to an exchange carrier (e.g. Cl^-—HCO_3^- exchange) or to a co-transporter (e.g. Na^+-K^+-Cl^- transport).

IVD. Ca^{2+} Distribution

IVD1. Need for Calcium Pumps

For the positively-charged Ca^{2+} ion, there must be some mechanism for removing it from the cytoplasm. Otherwise, the cell would continue to gain Ca^{2+} until there was no electrochemical gradient for net influx of Ca^{2+}. Ca^{2+} loading would occur until the free $[Ca^{2+}]_i$ in the cytoplasm was even greater than that outside (ca. 2 mM) because of the negative potential inside the cell. Therefore, there must be one or more Ca^{2+} pumps in operation. The SR (or ER) membrane contains a *Ca^{2+}-activated ATPase* (which requires Mg^{2+} for activity) that actively pumps two Ca^{2+} ions from the cytoplasm into the SR lumen at the expense of one ATP. This pump ATPase is capable of pumping down the Ca^{2+} to less than 10^{-7} M. The Ca^{2+}-ATPase of the SR is regulated by an associated low-molecular-weight protein, *phospholamban*. Phospholamban is phosphorylated by *cyclic-AMP-dependent protein kinase* and, when phosphorylated, stimulates the Ca^{2+}-ATPase and Ca^{2+} pumping (by a derepression process). The sequestration of Ca^{2+} by the SR is essential for muscle relaxation. The mitochondria also can actively take up Ca^{2+} almost to the same degree as the SR, but this Ca^{2+} pool probably does not play an important role in normal excitation—contraction coupling.

The resting Ca^{2+} influx and the extra Ca^{2+} influx that enters with each AP must be returned to the interstitial fluid. Two mechanisms have been proposed for this: (1) a Ca^{2+}-ATPase, similar to that in the SR, is present in the sarcolemma; and (2) a *Ca^{2+}-Na^+ exchange* occurs across the cell membrane. It has been reported that there is a Ca^{2+}-ATPase in the sarcolemma of myocardial cells (Dhalla et al., 1977; Jones et al., 1980) and smooth muscle (Daniel et al., 1977) that actively transports two Ca^{2+} outward against an electrochemical gradient, using one ATP in the process.

IVD2. Ca_i - Na_o Exchange Reaction

The Ca_i - Na_o exchange reaction exchanges one internal Ca^{2+} ion for three external Na^+ ions via a membrane carrier molecule (see Fig. 9.3). This reaction is facilitated by ATP, but ATP is not hydrolyzed (consumed) in this reaction. Instead, the energy for the transport of Ca^{2+} against its large electrochemical gradient comes from the Na^+ electrochemical gradient. That is, the uphill transport of Ca^{2+} is coupled to the downhill movement of Na^+. Effectively, the energy required for this Ca^{2+} movement is derived from the Na^+,K^+-ATPase. Thus, the Na^+- K^+ pump, which uses ATP to maintain the Na^+ electrochemical gradient, indirectly helps to maintain the Ca^{2+} electrochemical gradient. Hence, the inward Na^+ leak is greater than it would be otherwise. A complete discussion of Ca^{2+}-Na^+ exchange is given in a subsequent chapter.

The *energy cost* (ΔG_{Ca}, in joules/mole) for pumping out Ca^{2+} ion is directly proportional to its electrochemical gradient. These energetic equations are as follows (where ΔG is the change in free energy, z is the valence, and F is the Faraday constant):

$$\Delta G_{Ca} = zF(E_m - E_{Ca}) \quad (9.5)$$

The energy available from the Na^+ distribution is directly proportional to its electrochemical gradient.

$$\Delta G_{Na} = zF(E_m - E_{Na}) \quad (9.6)$$

Depending on the exact values of $[Na^+]_i$ and $[Ca^{2+}]_i$ in a muscle cell at rest, the energetics would be about adequate for an exchange ratio of 3 Na^+:1 Ca^{2+}. An exchange ratio of 3:1 would produce a small depolarization due to a net inward flow of current (3 Na^+ in to 1 Ca^{2+} out) via this electrogenic Ca_i^{2+}-Na_o^+ exchanger. That is, there is a net positive charge moving inward for every cycle of the exchanger. This *net exchanger current* can be measured in whole-cell voltage-clamp studies when all ionic currents and Na^+-K^+ pump currents are blocked.

The exchange reaction depends on relative concentrations of Ca^{2+} and Na^+ on each side of the membrane and on

relative affinities of the binding sites to Ca^{2+} and Na^+. Because of this exchange reaction, whenever the cell gains Na^+, it will also gain Ca^{2+}, because the Na^+ electrochemical gradient is reduced and the exchange reaction becomes slowed. The Ca_i^{2+}- Na_o^+ exchange process has been proposed as the mechanism of the *positive inotropic action* (i.e. more forceful contraction) in the heart resulting from cardiac glycoside inhibition of the Na^+-K^+ pump.

In addition, when the myocardial cell membrane is depolarized during the AP plateau, the exchange carriers will exchange the ions in reverse, namely, internal Na^+ for external Ca^{2+} and thus increase Ca^{2+} influx. The net effect of this mechanism is to elevate $[Ca^{2+}]_i$. Such *reversed* Ca_o^{2+}-Na_i^+ *exchange* appears to be a significant source of Ca^{2+} for contraction in cardiac muscle of some species.

V. EQUILIBRIUM POTENTIALS

VA. Equivalent Electrical Circuit

The electrical equivalent circuit of the cell membrane at rest is depicted in Fig. 9.4. In Fig. 9.4A, the membrane is indicated as a parallel resistance (R_m) and capacitance (C_m). The capacitance results from the lipid bilayer matrix of the membrane and the resistance or conductance (G_m) results from the protein ion channels floating in the lipid bilayer and spanning across it. The RP is depicted as a battery in series with R_m, with the negative pole facing inside the cell.

In Fig. 9.4B, the equivalent circuit for the resting membrane is shown further expanded, by breaking up the membrane conductance (G_m) into its four component parts, one for each ion of major importance electrophysiologically, namely K^+, Cl^-, Na^+ and Ca^{2+}. The respective conductances are g_K, g_{Cl}, g_{Na}, and g_{Ca}. The equilibrium potential (E) for each ion is placed in series with the conductance pathway for that ion, as depicted. The polarity of each battery is as shown; namely, the pole facing inwards is negative for K^+ and Cl^- and positive for Na^+ and Ca^{2+}. These polarities are based on the directions of the concentration gradients and charge on the ions.

VB. Nernst Equation

For each ionic species distributed unequally across the cell membrane, an equilibrium potential (E_i) or battery can be calculated for that ion from the Nernst equation (for 37°C),

$$E_i = \frac{-RT}{zF} \ln \frac{C_i}{C_o} \tag{9.7a}$$

$$E_i = \frac{-2.303\ RT}{zF} \log \frac{C_i}{C_o} \tag{9.7b}$$

$$E_i = \frac{-61\ \text{mV}}{z} \log \frac{C_i}{C_o} \tag{9.7c}$$

where C_i is the internal concentration of the ion, C_o is the extracellular concentration, R is the gas constant (8.3 J/mol/K), T is the absolute temperature in Kelvins (K = 273+°C), F is the Faraday constant (96 500 Coul/eq), and z is the valence (with sign). Thus, zF = Coul/mol. Taking the RT/F constants and the factor of 2.303 for conversion of natural log (ln), or log to the base of e (2.717), to log to the base of 10 ($\log_{10}$) gives:

$$\frac{-RT}{F} \ln N = \frac{-2.303\ RT}{F} \log N = -61\ \text{mV} \log N \tag{9.7d}$$

Therefore, the Nernst equation (Equation 9.7a) becomes

$$E_i = \frac{-2.303\ RT}{zF} \log \frac{C_i}{C_o} \tag{9.7e}$$

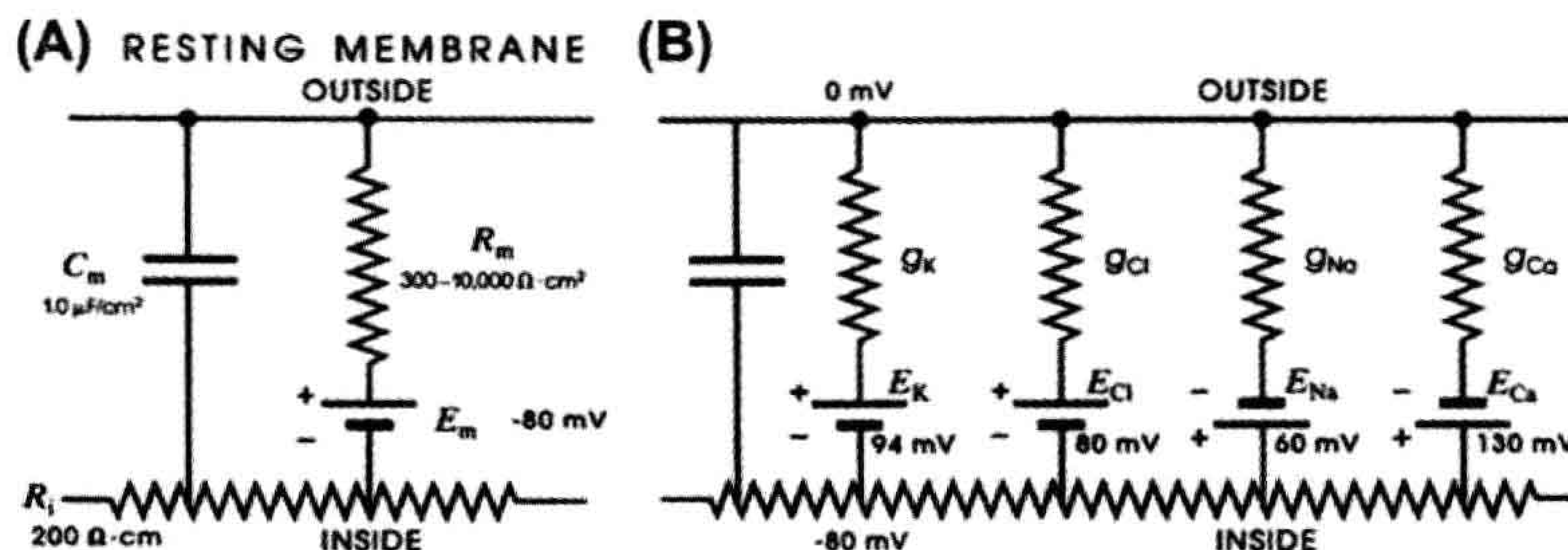


FIGURE 9.4 Electrical equivalent circuits for a cell membrane at rest. (A) Membrane as a parallel resistance-capacitance circuit, the membrane resistance (R_m) being in parallel with the membrane capacitance (C_m). Resting E_m is represented by a −80 mV battery in series with the membrane resistance, the negative pole facing inward. (B) Membrane resistance is divided into its four component parts, one for each of the four major ions of importance: K^+, Cl^-, Na^+ and Ca^{2+}. Resistances for these ions (R_K, R_{Cl}, R_{Na} and R_{Ca}) are parallel to one another and represent totally separate and independent pathways for permeation of each ion through the resting membrane. These ion resistances are depicted as their reciprocals, namely, ion conductances (g_K, g_{Cl}, g_{Na}, g_{Ca}). Equilibrium potential for each ion (e.g. E_K), determined solely by the ion distribution in the steady state and calculated from the Nernst equation, is shown in series with the conductance path for that ion. RP of −80 mV is determined by the equilibrium potentials and by the relative conductances.

$$E_i = \frac{-61\ \text{mV}}{z} \log \frac{C_i}{C_o} \quad (9.7\text{f})$$

The −61 mV constant (2.303 *RT/F*) becomes −59mV at 22°C. A derivation of the Nernst equation is given in the Appendix to this chapter. The Nernst equation gives the *potential difference (PD) (electrical force) that would exactly oppose the concentration gradient (diffusion force).*

Only very small charge separation (Q, in coulombs) is required to build a very large PD.

$$E_m = \frac{Q}{C_\text{m}} \quad (9.8)$$

where C_m is the membrane capacitance. This is further discussed in the next section.

For the ion distributions given previously (see Table 9.2), the approximate equilibrium potentials are:

$E_{\text{Na}} = +60\ \text{mV}$
$E_{\text{Ca}} = +130\ \text{mV}$
$E_{\text{K}} = -93\ \text{mV}$
$E_{\text{Cl}} = -80\ \text{mV}$

The sign of the equilibrium potential represents the inside of the cell with reference to the outside (see Fig. 9.4). Because Na^+ is higher outside (ca. 145 mM) than inside (ca. 15 mM), the positive pole of the Na^+ battery (E_{Na}) is inside the cell. The concentration gradient for Ca^{2+} is in the same direction as for Na^+ (1.8 mM $[Ca^{2+}]_o$ and about 1×10^{-7} M $[Ca^{2+}]_i$,) and so the positive pole of E_{Ca} is inside. K^+ is higher inside (ca. 150 mM) than outside (ca. 4.5 mM) and so the negative pole is inside. Because Cl^- is higher outside (ca. 100 mM) than inside (ca. 5 mM), the negative pole is inside. Voltages are, by convention, given for the inside with respect to the outside.

VC. Concentration Cell

In a concentration cell (essentially a two-compartment system separated by a membrane), the *side of higher concentration becomes negative for cations* (positive ions) and *positive for anions* (negative ions). Any ion whose equilibrium potential is different from the RP (e.g. −80 mV for a myocardial cell or skeletal muscle fiber) is off equilibrium and therefore must effectively be pumped at the expense of energy. In many cell types, only Cl^- ion appears to be at or near equilibrium, whereas Na^+, Ca^{2+} and K^+ are actively transported. Even H^+ ion is off equilibrium, E_H being closer to zero potential (see Table 9.2). If H^+ were passively distributed, the negative intracellular potential would pull in more H^+ ions, causing $[H^+]_i$ to increase, making the cell interior more acidic.

The mechanism for development of the *equilibrium potential* is depicted in Fig. 9.5. To show the development of an equilibrium potential, we can use an artificial membrane (e.g. one made of celloidin) to separate two solutions, i.e. to form a concentration cell. This membrane contains negatively-charged pores, which therefore allows cations (like K^+) to pass through, but prevents anions (like Cl^-) from passing. This is because like charges repel one another and unlike charges attract one another. Therefore, in this particular membrane, K^+ is permeant and Cl^- is impermeant. If one side (side 1) contains a salt like KCl at a concentration higher (e.g. 0.10 M) than that in the other side (side 2) (e.g. 0.01 M), then a steady PD is very quickly built up across the membrane. As calculated from the Nernst equation, for a 10-fold difference in concentration of the permeant monovalent cation (K^+), the PD would be −61 mV at 37°C (or −59 mV at a room temperature of 22°C).

This PD is between the two solutions and expressed across the membrane. Side 1 (side of highest K^+ concentration) becomes negative with respect to side 2. The PD is developed because of the tendency for diffusion (diffusion force) from high concentration to low concentration. This is based on the *random thermal motion* of the ions (particles), somewhat related to *Brownian motion* of larger particles. That is, the side of higher concentration has a *greater probability* of K^+ ions moving from side 1 to side 2 than in the reverse direction, based on the greater number of particles, all moving in random directions. Therefore, there will be a loss of positive charges (K^+ ions) from side 1 and a gain of positive charges in side 2.

Because negative charges (Cl^- ion) cannot accompany the positive charges, as the membrane was made impermeable to anions, a *charge separation* is built up across the membrane. It can now be readily understood why side 1, the side of higher cation concentration, becomes negatively charged (due to loss of positive charges) and why side 2, the side of lower cation concentration, becomes positively charged (due to gain of positive charges). The charge separation is very tiny and they stay plastered very close to the membrane. That is, for the example depicted in Fig. 9.5, side 1 will have the small excess of Cl^- ions held very close to the membrane and side 2 will have the small excess of K^+ ions held very close to the membrane. The force holding them there is called the electrostatic or Coulombic force, based on the attraction between unlike charges. This is related to Coulomb's law and the nature of capacitors.

In the two bulk solutions, the *law of electroneutrality* is upheld; i.e. for every cation (K^+) there is a nearby anion (Cl^-). Thus, the *charge separation* occurs only directly across the membrane and is very tiny with respect to the total number of charges in the two solutions. In fact, after equilibrium is reached (within a few seconds), the most sensitive chemical analyses would fail to detect the very slight decrease in K^+ in side 1 or gain of K^+ on side 2.

Thus, the system comes to equilibrium quickly and with very little charge (K^+ and Cl^-) separation. That is, K^+ does

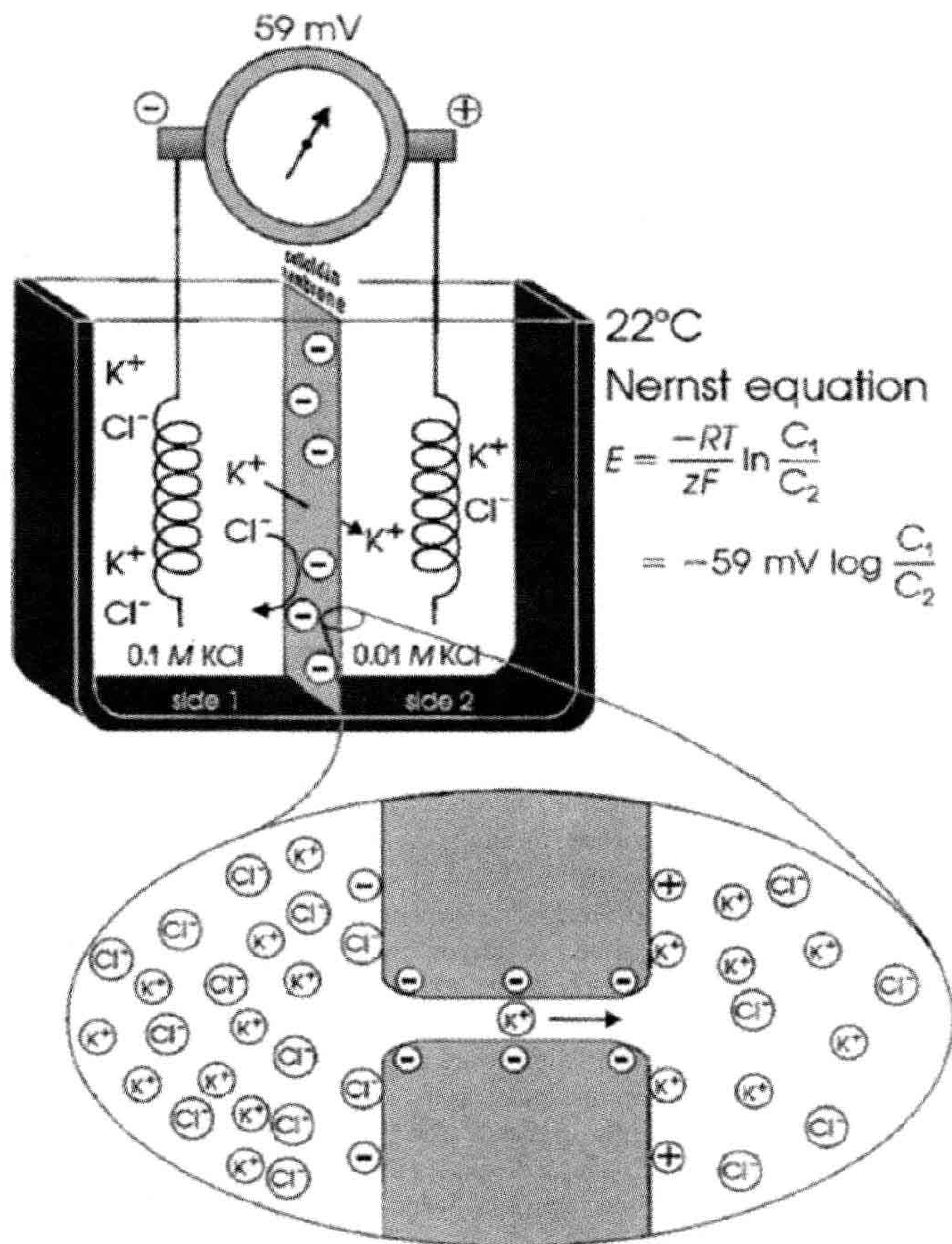


FIGURE 9.5 Upper diagram: concentration cell diffusion potential developed across artificial membrane containing negatively-charged pores. The membrane is impermeable to Cl^- ions, but permeable to cations such as K^+. Concentration gradient for K^+ causes a potential to be generated, the side of higher K^+ concentration becoming negative. Lower diagram: expanded diagram of water-filled pore in the membrane, showing the permeability to K^+ ions, but lack of penetration of Cl^- ions. Potential difference is generated by charge separation, a slight excess of K^+ ions being held close to the right-hand surface of the membrane; a slight excess of Cl^- ions is aggregated close to the left surface.

not continue to have a net movement from side 1 to side 2 until the concentrations become equal. Why not? The answer is that the *small charge separation produces a large PD* across the membrane and this PD is in such a polarity that it antagonizes further net movement of K^+ from side 1 to side 2. That is, the positive voltage that is developing on side 2 repels the positively-charged K^+ ions because like charges repel. At equilibrium, these two forces become equal and opposite and there is no further net movement of ions. Unidirectional fluxes of K^+ ions would still occur (because of their random thermal motion), but these would be equal and opposite and so no further *net flux* would occur.

In the example selected, KCl was used. However, any salt, such as NaCl, $CaCl_2$ or Na_2SO_4, could have been illustrated. If a divalent cation like Ca^{2+} were used, then from the Nernst equation, the same 10-fold concentration gradient would develop a potential of only half, namely 30.5 mV (37°C) or 29.5 mV (22°C). The reason that this factor is half, rather than double as one might guess from the fact that the charge is double, is that the Nernst equation gives the PD that exactly opposes the diffusion force due to the concentration gradient, as stated in the paragraph above. Therefore, because the charge is double, only half the voltage is necessary to oppose effectively the concentration force. If the cation in question were trivalent, such as La^{3+}, then the 2.303 RT/zF factor would be one-third of 61 mV, or about 20.3 mV. It is for this reason that it is convenient to give the Nernst equation in the form shown in Equation 9.7c, namely with the factor (at 37°C) being -61 mV/z. This allows easy calculation of the equilibrium potential for an ion of any charge and sign (polarity).

That is, the sign and charge should be used, for example, $+1$ for K^+ or Na^+, $+2$ for Ca^{2+} and -1 for Cl^-. When the ion in question is an anion like Cl^-, then $-1/-1$ gives a plus (+). Because $[Cl^-]_o > [Cl^-]_i$, this concentration ratio can be

inverted by changing the sign of the 2.30 *RT/zF* factor back to negative (−). That is, changing the sign of the factor in front of a log ratio simply inverts the ratio.

Finally, if the concentration cell depicted in Fig. 9.5 were made with a membrane that had positively-charged pores, then everything would be reversed. The membrane would be permeable to Cl^- and impermeable to K^+ and E_{Cl} would be +59 mV (at 22°C) and +61 mV (at 37°C). Again, the voltage is given for side 1 with respect to side 2. Thus, in dealing with an anion, the side of higher concentration becomes positive (due to a small loss of Cl^-) and the side of lower concentration becomes negative (due to a small gain of Cl^-). The separated charges again are plastered very close to the membrane: K^+ ions on side 1 and Cl^- ions on side 2.

VD. Activity Coefficient

Thus, an equilibrium potential can be calculated for any species of ion that is distributed unequally across a membrane. All that one needs to know are the concentrations in the two solutions and the charge (and temperature). Actually, we should use the *activity* (a) of the ion in question in the two solutions, instead of concentration. Thus, the Nernst equation given in Equation 9.7c becomes (for K^+, for example):

$$E_K = \frac{-61\text{ mV}}{+1}\log\frac{a_K^i}{a_K^o}$$

The activity of an ion (in molar) can be obtained by multiplying the concentration of the ion (in molar) by the activity coefficient (γ) for the ion:

$$a = c \cdot \gamma \tag{9.9}$$

In the biological case, the activity coefficients are relatively close to 1.0 (e.g. 0.7–0.9) for Na^+, K^+ and Cl^- in *both* the extracellular and intracellular solutions. Therefore, in these cases, using the concentrations gives a good approximation. However, in the case of Ca^{2+}, the activity coefficient in the intracellular solution especially is substantially lower and so this would affect the calculated value of E_{Ca}.

VE. Nernst–Planck Equation

The basic Nernst equation has been modified in several ways for special situations. For example, in the concentration cell depicted in Fig. 9.5, a cell in which a single salt (both ions of same valence) is distributed across the membrane at two different concentrations, the PD developed across the membrane (E_m) can be calculated from the equation:

$$E_m = \frac{U_c - U_a}{U_c + U_a}\,\frac{-61\text{ mV}}{z}\log\frac{[\text{salt}]_1}{[\text{salt}]_2} \tag{9.10}$$

where $[\text{salt}]_1$ and $[\text{salt}]_2$ are the concentrations of the salt on side 1 and side 2 and U_c and U_a are the *mobilities* of the cations and anions, respectively, through the membrane. Thus, when the mobilities (or permeabilities) of the cation and anion are equal ($U_c = U_a$), E_m is zero, regardless of the equilibrium potentials. When the anion is impermeable ($U_a = 0$), the mobility fraction in Equation 9.10 becomes 1.0 and the equation reduces to the simple Nernst equation. When the cation is impermeable ($U_c = 0$), the fraction becomes −1.0 and the same numerical value of E_m is produced, but of opposite sign. Equation 9.10 can be used to calculate E_m for any combination of U_a and U_c. For example, if $U_a = 0.5\ U_c$, then for the problem illustrated in Fig. 9.5, E_m would be about −20 mV (side 1 negative). Thus, the membrane potential is related to the relative mobilities.

VF. Energy Wells

Ions do not just "fall" through a water-filled pore in the membrane (protein ion channel) down an electrochemical gradient. Instead, an ion may bind to several charged sites on its journey through the channel pore. The K^+ ion depicted in the bottom of Fig. 9.5, for example, is shown as binding to three negatively-charged sites within the pore. These may be considered energy wells and the ion must gain kinetic energy to become dislodged from this energy well to pass over the next *energy barrier* and into the next energy well. This energy comes from the ion being hit by another ion just entering the pore, producing a billiard-ball effect. Some evidence for this model was presented in Chapter 8, which discusses the Ussing flux ratio equation.

From the measured value of the conductance of single ion channels (e.g. 20 pS, range of 10–300 pS), how many ions that pass through a single channel per second can be estimated. This number is about 6 000 000 ions/s. Therefore, the average transit time for a single ion to cross the membrane (50–70 Å thick) is about 0.17 μs.

VI. ELECTROCHEMICAL DRIVING FORCES AND MEMBRANE IONIC CURRENTS

VIA. Electrochemical Driving Forces

The electrochemical driving force for each species of ion is the algebraic difference between its equilibrium potential, E_i, and the membrane potential, E_m. The total driving force is the sum of two forces: an electrical force (the negative potential in a cell at rest tends to pull in positively-charged ions, because unlike charges attract) and a diffusion force (based on the concentration gradient) (Fig. 9.6); i.e.:

$$\text{driving force} = E_m - E_i \tag{9.11a}$$

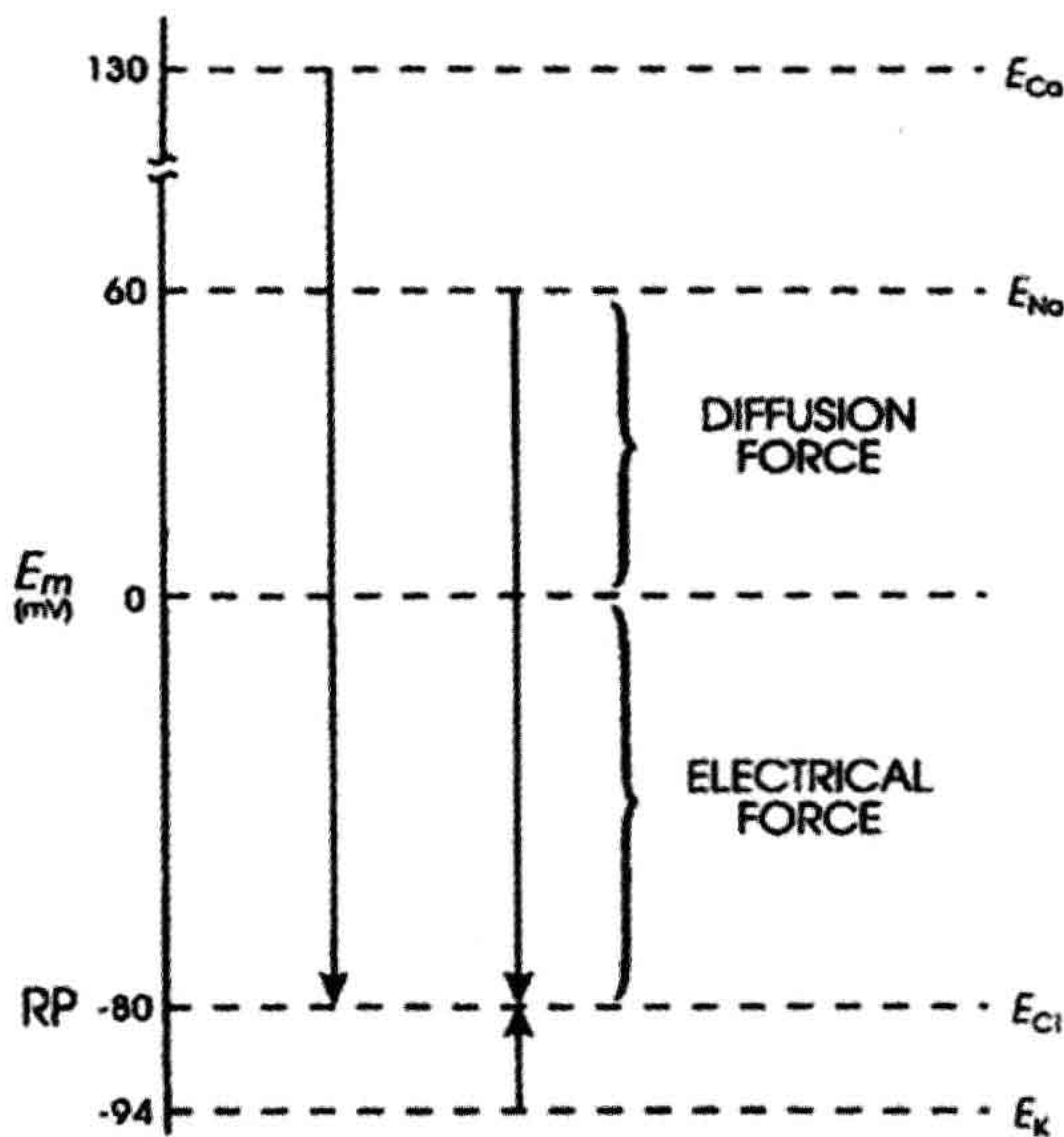


FIGURE 9.6 Representation of the electrochemical driving forces for Na^+, Ca^{2+}, K^+, and Cl^-. Equilibrium potentials for each ion (e.g. E_{Na}) (calculated from the Nernst equation for their extracellular and intracellular concentrations) are positioned vertically according to their magnitude and sign. Measured RP is assumed to be −80 mV. Electrochemical driving force for an ion is the difference between its equilibrium potential (E_i) and the membrane potential (E_m), i.e. ($E_m - E_i$). Thus, at rest, the driving force for Na^+ is the difference between E_{Na} and the resting E_m. If E_{Na} is +60 mV and resting E_m is −80 mV, the driving force is 140 mV. That is, the driving force is the algebraic sum of the diffusion force and the electrical force and is represented by the length of the arrows in the diagram. Driving force for Ca^{2+} (about 210 mV) is even greater than that for Na^+, whereas that for K^+ is much less (about 14 mV). Direction of the arrows indicates the direction of the net electrochemical driving force, namely, the direction for K^+ is outward, whereas that for Na^+ and Ca^{2+} is inward. If Cl^- is passively distributed, then its distribution across the cell membrane is determined by the net membrane potential. For a cell sitting a long time at rest, $E_{Cl} = E_m$ and there is no net driving force.

Thus, in a resting cell, the driving force for Na^+ is:

$$(E - E_{Na}) = -80 \text{ mV} - (+60 \text{ mV}) = -140 \text{ mV} \quad (9.11b)$$

The negative sign means that the driving force is directed to bring about net movement of Na^+ inward. The driving force for Ca^{2+} is very large and is directed inward:

$$(E_m - E_{Ca}) = -80 \text{ mV} - \ +129 \text{ mV}) = -209 \text{ mV} \quad (9.11c)$$

The driving force for K^+ is:

$$(E_m - E_K) = -80 \text{ mV} - (-94 \text{ mV}) = +14 \text{ mV} \quad (9.11d)$$

Hence, the driving force for K^+ is small and directed outward. The driving force for Cl^- is nearly zero for a cell at rest in which Cl^- is passively distributed (e.g. neuron, myocardial cell, skeletal muscle fiber); i.e.:

$$(E_m - E_{Cl}) = -80 \, mV - (-80 \text{ mV}) = 0 \quad (9.12)$$

However, during the AP, when E_m is changing, the driving force for Cl^- becomes large and there is a net driving force for inward Cl^- movement (Cl^- influx is an outward Cl^- current). Similarly, the driving force for K^+ outward movement increases during the AP, whereas those for Na^+ and Ca^{2+} decrease.

VIB. Membrane Ionic Currents

The net current for each ionic species (I_i) is equal to its *driving force* times its *conductance* (g_i, reciprocal of the resistance) through the membrane. This is essentially Ohm's law:

$$I = \frac{V}{R} = g \cdot V \quad (9.13)$$

Ohm's law must be modified to reflect the fact that, in an electrolytic system, the total force tending to drive net movement of a charged particle must take into account both the electrical force and the concentration (or chemical) force. Thus, for the four ions, the net current can be expressed as:

$$I_{Na} = g_{Na}(E_m - E_{Na}) \quad (9.14)$$

$$I_{Ca} = g_{Ca}(E_m - E_{Ca}) \quad (9.15)$$

$$I_K = g_K(E_m - E_K) \quad (9.16)$$

$$I_{Cl} = g_{Cl}(E_m - E_{Cl}) \quad (9.17)$$

In a resting cell, Cl^- and Ca^{2+} can be neglected and the Na^+ current (inward) must be equal and opposite to the K^+ current (outward) to maintain a steady resting potential:

$$I_K = -I_{Na} \quad (9.18a)$$

$$g_K(E_m - E_K) = -g_{Na}(E_m - E_{Na}) \quad (9.18b)$$

Thus, although in the resting membrane the driving force for Na^+ is much greater than that for K^+, g_K is much larger than g_{Na}, so the currents are equal. Hence, there is a continuous leakage of Na^+ inward and K^+ outward, even in a resting cell, and the system would run down if active pumping were blocked. Because the ratio of the Na^+ to K^+ driving forces (−140 mV/−14 mV) is 10, the ratio of conductances (g_{Na}/g_K) will be about 1:10. The fact that g_K is much greater than g_{Na} accounts for the RP being close to E_K and far from E_{Na}.

VII. DETERMINATION OF RESTING POTENTIAL AND NET DIFFUSION POTENTIAL (E_{diff})

VIIA. Determining Factors

For given ion distributions, which normally remain nearly constant under usual steady-state conditions, the resting potential (RP) is determined by the *relative membrane conductances (g)* or *permeabilities (P)* for Na^+ and K^+ ions. That is, the RP (of about −80 mV in cardiac muscle or skeletal muscle) is close to E_K (about −94 mV) because $g_K >> g_{Na}$ or $P_K >> P_{Na}$. There is a direct proportionality between P and g at constant E_m and concentrations. From simple circuit analysis (using Ohm's law and Kirchhoff's laws), one can prove that the membrane potential will always be closer to the battery (equilibrium potential) having the lowest resistance (highest conductance) in series with it (see Figs. 9.4 and 9.6). In the resting membrane, this battery is E_K, whereas in the excited membrane it will be E_{Na} (or E_{Ca}), because there is a large increase in g_{Na} and/or g_{Ca} during the AP.

Any ion that is passively distributed cannot determine the RP; instead, the RP determines the distribution of that ion. Therefore, Cl^- is not considered for myocardial cells, skeletal muscle fibers and neurons because it seems to be passively distributed. However, transient net movements of Cl^- across the membrane do influence E_m; e.g. washout of Cl^- (in Cl^--free solution) produces a transient depolarization and reintroduction of Cl^- produces a transient hyperpolarization. Cl^- movement is also involved in the production of inhibitory postsynaptic potentials (IPSPs) (see chapter on synaptic transmission).

Because of its relatively low concentration, coupled with its relatively low resting conductance, the Ca^{2+} distribution has only a relatively small effect on the resting E_m and can be ignored.

VIIB. Constant-Field Equation

A simplified, but most useful, version of the Goldman–Hodgkin–Katz constant-field equation can be given (for 37°C):

$$E_m = -61\ \text{mV} \log \frac{[K^+]_i + \frac{P_{Na}}{P_K}[Na^+]_i}{[K^+]_o + \frac{P_{Na}}{P_K}[Na^+]_o} \quad (9.19)$$

This equation shows that for a given ion distribution, the resting E_m is determined by the P_{Na}/P_K ratio, the *relative permeability* of the membrane to Na^+ and K^+. For myocardial cells and skeletal muscle fibers, the P_{Na}/P_K ratio is about 0.04, whereas for nodal cells of the heart and smooth muscle cells, this ratio is closer to 0.10 or 0.20.

Inspection of the constant-field equation shows that the numerator of the log term will be dominated by the $[K^+]$ term [since the (P_{Na}/P_K) $[Na^+]_i$ term will be very small], whereas the denominator will be affected by both the $[K^+]_o$ and (P_{Na}/P_K) $[Na^+]_o$ terms. This relationship thus accounts for the deviation of the E_m versus log $[K^+]_o$ curve from a straight line (having a slope of 61 mV/decade) in normal Ringer solution (Fig. 9.7). When $[K^+]_o$ is elevated ($[Na^+]_o$ being reduced by an equimolar amount), the denominator becomes more and more dominated by the $[K^+]_o$ term and less and less by the (P_{Na}/P_K) $[Na^+]_o$ term. Therefore, in bathing solution containing high K^+, the constant-field equation approaches the simple Nernst equation for K^+ and E_m approaches E_K. As $[K^+]_o$ is raised stepwise, E_K becomes correspondingly reduced, because $[K^+]_i$ stays relatively constant; therefore, the membrane becomes more and more depolarized (see Fig. 9.7). Sometimes, however, some hyperpolarization is produced at a $[K^+]_o$ level between 5 and 9 mM. In addition, lowering $[K^+]_o$ to 0.1 mM often produces a prominent depolarization. These effects are usually explained on the basis that: (1) P_K is reduced in low $[K^+]_o$; and (2) an electrogenic Na^+-K^+ pump potential is inhibited at a low $[K^+]_o$ (K_m of about 2 mM).

A more detailed discussion of the constant-field equation is given in the Appendix to this chapter.

When $[K^+]_o$ is elevated (e.g. to 8 mM) in some types of cells, a hyperpolarization of up to about 10 mV may be produced. Such behavior is often observed in cells with a high P_{Na}/P_K ratio (due to low P_K) and therefore a low resting E_m, such as in young embryonic chick hearts. This hyperpolarization could be explained by several factors: (1) stimulation of the electrogenic Na^+ pump current (I_p); (2) an increase in P_K (and therefore g_K) due to $[K^+]_o$ effect on P_K; and (3) an increase in g_K (but not P_K) due to the concentration effect. A similar explanation may apply to the fall-over in the E_m versus log $[K^+]_o$ curve when $[K_o]$ is lowered to 1 mM and less, hence depolarizing the cells. This effect is prominent in rat skeletal muscle, for example (see Fig. 7 of chapter on skeletal muscle excitability).

VIIC. Chord Conductance Equation

An alternative method of approximating the membrane resting potential (E_m) is the chord conductance equation. The word *chord* means a straight line connecting two points on a curve, and here specifically refers to the *average slope* of a non-linear steady-state voltage–current curve, i.e. a straight line from any point on the curve through the origin (zero applied current). (In contrast, slope conductance is the tangent at any point on the curve.) Thus:

$$E_m = \frac{g_K}{\sum g} E_K + \frac{g_{Na}}{\sum g} E_{Na} + \frac{g_{Cl}}{\sum g} E_{Cl} + \frac{g_{Ca}}{\sum g} E_{Ca} \quad (9.20a)$$

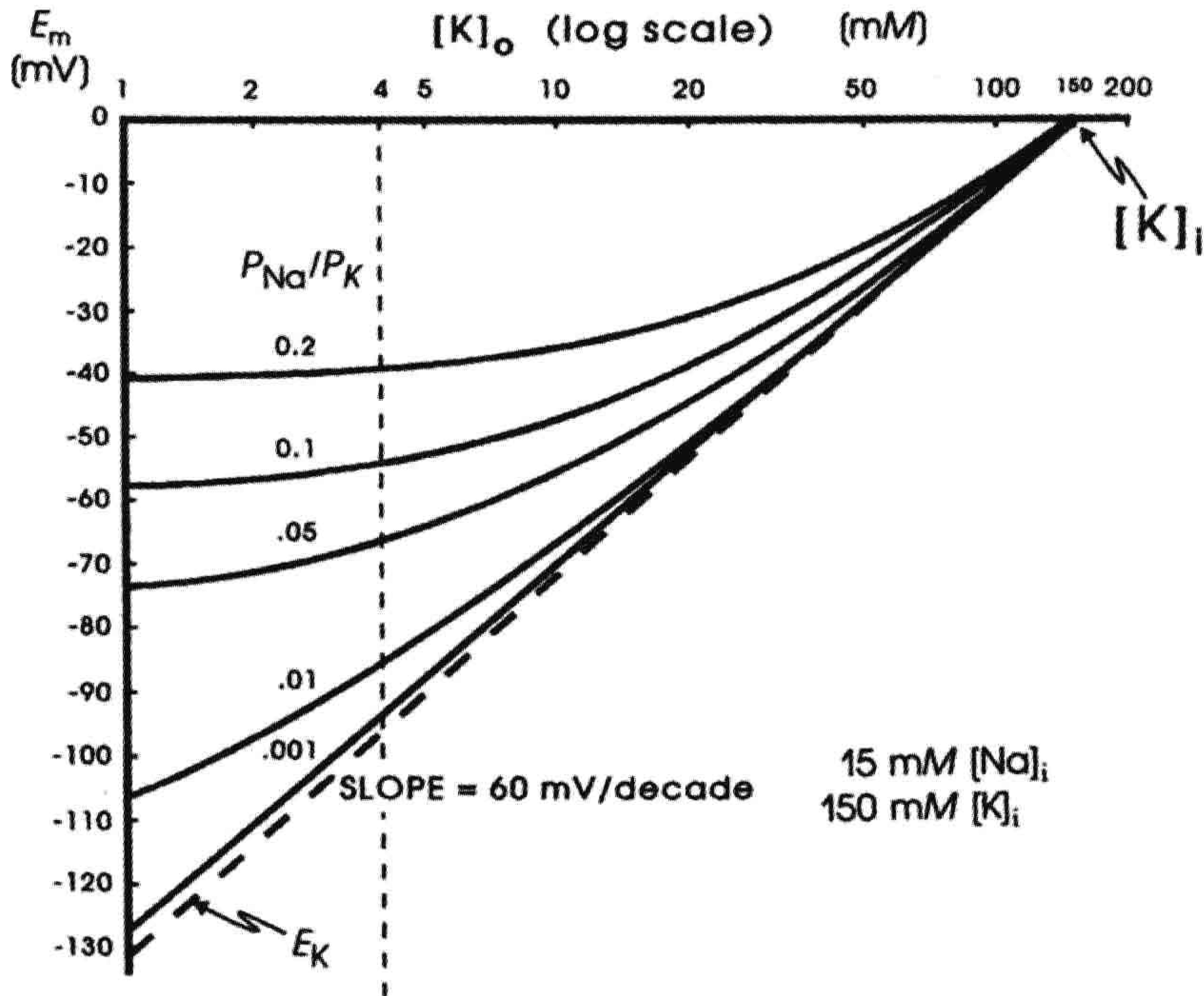


FIGURE 9.7 Theoretical curves calculated from the Goldman constant-field equation for RP (E_m) as a function of $[K^+]_o$. Family of curves is given for various P_{Na}/P_K ratios (0.001, 0.01, 0.05, 0.1 and 0.2). K^+ equilibrium potential (E_K) calculated from the Nernst equation (broken straight line). Curves calculated for a $[K^+]_i$ of 150 mM and a $[Na^+]_i$ of 15 mM. Calculations made holding $[K^+]_o + [Na^+]_o$ constant at 154 mM; i.e. as $[K^+]_o$ was elevated, $[Na^+]_o$ was lowered by an equimolar amount. Possible change in P_K as a function of $[K^+]_o$ was ignored. Point at which E_m is zero gives $[K^+]_i$. The potential reverses in sign when $[K^+]_o$ exceeds $[K^+]_i$.

where g_K, g_{Na}, g_{Cl}, and g_{Ca} are the membrane conductances for K^+, Na^+, Cl^-, and Ca^{2+}, respectively, and Σg is the total conductance (sum of all ionic partial conductances). The ratio of $g_K/\Sigma g$, for example, is the *relative* or *fractional conductance* for K^+.

The chord conductance equation can conveniently take into account all ions, including divalent cations, that are distributed unequally across the membrane. The ions important to membrane potentials (including APs, postsynaptic potentials and receptor potentials) are K^+, Na^+, Cl^- and Ca^{2+}. As discussed previously, Cl^- cannot help in determining the RP if it is passively distributed. Thus, Equation 9.20a can be rewritten, omitting the Cl^- term, as:

$$E_m = \frac{g_K}{\sum g} E_K + \frac{g_{Na}}{\sum g} E_{Na} + \frac{g_{Ca}}{\sum g} E_{Ca} \qquad (9.20b)$$

For simplicity, we can ignore the Ca^{2+} term also, giving:

$$E_m = \frac{g_K}{g_K + g_{Na}} E_K + \frac{g_{Na}}{g_K + g_{Na}} E_{Na} \qquad (9.20c)$$

where Σg is now equal to $g_K + g_{Na}$.

The chord conductance equation can be derived simply from Ohm's law and from circuit analysis for the condition when net current is zero ($I_{Na} + I_K = 0$). (See the Appendix to this chapter for the derivation.) The equation holds true whenever the net current across the membrane is zero, as for the RP.

The chord conductance equation is useful for giving the membrane potential when the ion conductances and distributions are known. For example, at the neuromuscular junction, the neurotransmitter acetylcholine opens the gates of many ionic channels that allow both Na^+ and K^+ to pass through equally well (i.e. $g_{Na} = g_K$). Hence, the potential that the postsynaptic membrane tends to seek when maximally activated (i.e. the equilibrium potential or so-called *reversal potential* for the end-plate potential, EPP) is:

$$\begin{aligned} E_{EPP} &= \frac{1}{2}(-94\,\text{mV}) + \frac{1}{2}(+60\,\text{mV}) \\ &= -17\,\text{mV} \end{aligned} \qquad (9.20d)$$

A disadvantage of the chord conductance equation is that it gives nearly a straight line for the E_m versus log

$[K^+]_o$ plot (actually a slight bend in the opposite direction at low $[K^+]_o$). In contrast, the constant-field equation gives the complete bending of the curves (for different P_{Na}/P_K ratios).

The chord conductance equation again illustrates the important fact that the g_K/g_{Na} ratio determines the RP. When $g_K \gg g_{Na}$, then E_m is close to E_K; conversely, when $g_{Na} \gg g_K$ (as during the spike part of the AP), E_m shifts to close to E_{Na} or to E_{Ca} (in the case of smooth muscle cells).

The chord conductance equation can be rewritten using resistances instead of conductances and may then be called the *chord resistance equation*:

$$E_m = \frac{R_K}{R_K + R_{Na}} E_{Na} + \frac{R_{Na}}{R_K + R_{Na}} E_K \quad (9.20e)$$

where R_K and R_{Na} are the K^+ and Na^+ resistances, which are the reciprocals of the conductances. Note that, in this equation, the positions of the two batteries are interchanged. This equation can be derived by simply substituting the two reciprocals into the chord conductance equation. It can also be derived by circuit analysis, as discussed in the Appendix to this chapter. This Appendix section also shows how circuit analysis can be used to determine what the RP should be, without using either the Goldman constant-field equation or the chord conductance equation.

VIID. Net Diffusion Potential, E_{diff}

In the presence of ouabain (short-term exposure only) to inhibit the Na^+-K^+ pump and V_p, the RP that remains reflects the net diffusion potential, E_{diff}. E_{diff} is determined by the ion concentration gradients for K^+ and Na^+ and by the relative permeability for K^+ and Na^+. When the Na^+-K^+ pump is operating, there is normally a small additional contribution of V_p to the resting E_m of about 2–16 mV, depending on cell type (discussed in the following section).

Inhibition of the Na^+-K^+ pump for long periods will gradually run down the ion concentration gradients. The cells lose K^+ and gain Na^+ and therefore E_K and E_{Na} become smaller. The cells thus become depolarized (even if the relative permeabilities were unaffected), which causes them to gain Cl^- (because $[Cl]_i$ was held low by the large resting potential), and therefore, to also gain water (cells swell).

VIII. ELECTROGENIC SODIUM PUMP POTENTIALS

A brief summary of the previous principles is as follows: the Na^+–K^+ pump is responsible for maintaining the cation concentration gradients. The equilibrium potentials for K^+ (E_K) and Na^+ (E_{Na}) are about −94 mV and +60 mV, respectively. The RP value is usually near E_K, because the K^+ permeability (P_K) is much greater than P_{Na} in a resting membrane. The exact resting membrane potential (E_m) depends on the P_{Na}/P_K ratio, myocardial cells and skeletal muscle fibers having P_{Na}/P_K ratios of 0.01–0.05, whereas smooth muscle or nodal cells of the heart have a ratio closer to 0.10–0.15. In the various types of cells, the resting E_m has a smaller magnitude (i.e. is less negative) than E_K by 10–40 mV. If there were no *electrogenic pump potential* contribution to the RP (i.e. as though the Na^+-K^+ pump was only indirectly responsible for the RP by its role in producing the ionic gradients), E_m would equal E_{diff}.

However, a direct contribution of the pump to the resting E_m can be demonstrated. For example, if the Na^+-K^+ pump is blocked by the addition of ouabain, there usually is an immediate depolarization of 2–16 mV, depending on the type of cell. Thus, the direct contribution of the electrogenic Na^+-K^+ pump to the measured resting E_m is small under physiologic conditions (but very important).

However, under conditions in which the pump is stimulated to pump at a high rate (e.g. when $[Na^+]_i$ or $[K^+]_o$ is abnormally high), the direct electrogenic contribution of the pump to the RP can be much greater and E_m can actually exceed E_K by as much as 20 mV or more. For example, if the ionic concentration gradients are allowed to run down (e.g. by storing the tissues in zero $[K^+]_o$ and at low temperatures for several hours), then after the tissues are allowed to restart pumping, the measured E_m can exceed the calculated E_K (e.g. by 10–20 mV) for a time (Fig. 9.8). The Na^+ loading of the cells is facilitated by placing them in cold low or zero $[K^+]_o$ solutions, because external K^+ is necessary for the Na^+-K^+-linked pump to operate; K_m of the Na^+,K^+-ATPase for K^+ is about 2 mM. After several hours in such a solution, the internal concentrations of Na^+, K^+ and Cl^- approach the concentrations in the bathing Ringer solution and the RP is very low (<−30 mV).

The cells are then transferred to a pumping solution, which is the appropriate Ringer solution containing normal K^+ and at normal temperature. Under such conditions, the pump turns over at a maximal rate, because the major control over pump rate is $[Na^+]_i$ and $[K^+]_o$. The low initial E_m also stimulates the pump rate, because the energy required to pump out Na^+ is less. The measured E_m of such Na^+ preloaded cells increases rapidly and more rapidly than E_K, as shown in Fig. 9.8. After this transient phase, however, a crossover of the two curves occurs, so that E_K again exceeds E_m, as in the physiologic condition. Cardiac glycosides prevent or reverse the transient hyperpolarization beyond E_K. The possibility that ionic conductance changes (e.g. an increase in g_K or a decrease in g_{Na}) can account for the observed hyperpolarization, can be ruled out whenever E_m exceeds (is more negative than) E_K.

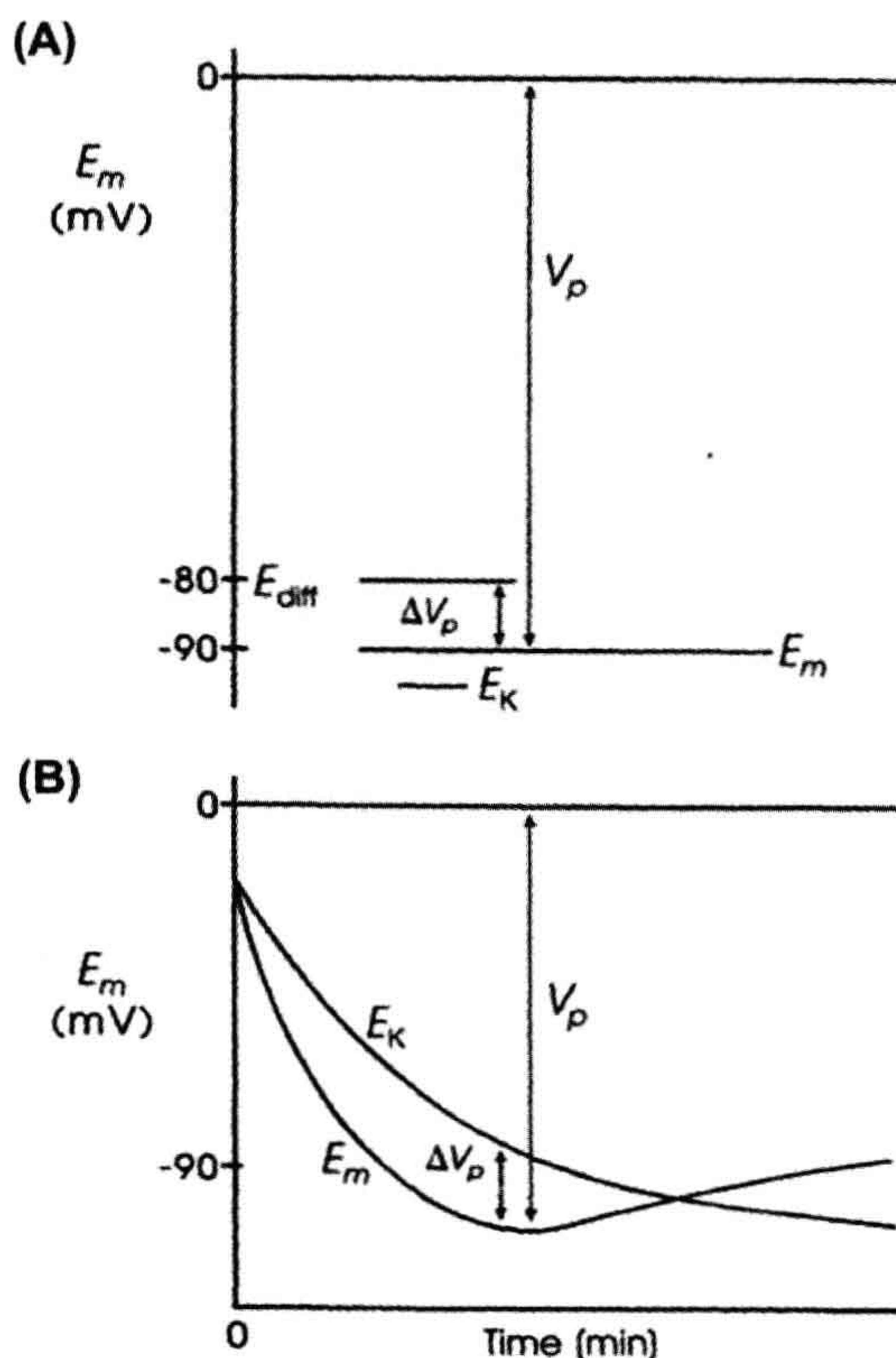


FIGURE 9.8 Diagrammatic representation of an electrogenic sodium pump potential. (A) Muscle fiber in which the net ionic diffusion potential (E_{diff}, function of ion equilibrium potentials and relative conductances) is -80 mV, yet exhibits a measured RP (E_m) that is greater. Difference between E_m and E_{diff} represents the contribution of the electrogenic pump to the RP. The electrogenic pump potential must be equal to V_p. The contribution of the electrogenic pump potential to the RP ($E_m - E_{diff}$) is equal to ΔV_p. (B) Fiber that was run down (Na^+ loaded, K^+ depleted) over several hours by inhibition of Na^+-K^+ pumping, resulting in a low RP. Returning the fiber to a pumping solution allows the resting E_m to rebuild as a function of time. Buildup in E_m occurs faster than buildup in E_K, as illustrated.

Rewarming cells previously cooled leads to the rapid restoration of the normal RP (within 10 min), whereas recovery of the intracellular Na^+ and K^+ concentrations is slower. During prolonged hypoxia, the RP of cardiac muscle decreases much less than E_K decreases (a difference of about 25 mV). This is because the electrogenic pump attempts to hold the RP constant, despite dissipating ionic gradients.

Another method used to demonstrate that the pump is electrogenic is to inject Na^+ ions into the cell through a micropipette. This procedure rapidly produces a small transient hyperpolarization, which is prevented by ouabain. The *pump current* and the rate of Na^+ extrusion increase in proportion to the amount of Na^+ injected. To prove that the pump is electrogenic, it must be demonstrated that the hyperpolarization produced in an intact muscle is not the result of enhanced pumping of an electroneutral pump. This could cause depletion of external K^+ in a restricted diffusion space just outside the cell membrane, leading to a larger E_K and thereby to hyperpolarization. Depletion could occur if the Na^+-K^+ pump pumped in K^+ faster than it could be replenished by diffusion from the bulk interstitial fluid.

The electrogenic Na^+ pump is influenced by the membrane potential. From energetic considerations, depolarization should enhance the electrogenic Na^+ pumping, whereas hyperpolarization should inhibit it. This is because depolarization reduces the electrochemical gradient (and hence the energy requirements) against which Na^+ must be extruded, whereas hyperpolarization increases the gradient. Thus, there should be a distinct potential, more negative than E_K, at which Na^+ pumping is prevented (e.g. a *pump equilibrium potential*). A value close to -140 mV was reported for cardiac cells and rat skeletal muscle fibers.

Any method used to increase membrane resistance increases the contribution of the pump to the RP (Fig. 9.9). That is, the electrogenic Na^+ pump contribution is augmented under conditions that increase membrane resistance. The contribution of the pump potential to the measured E_m is the difference in E_m when the pump is operating versus that immediately after the pump has been stopped by the addition of ouabain or zero $[K^+]_o$. Consequently, it appears as though the contribution from the electrogenic pump potential (ΔV_p) is in series with the net cationic diffusion potential (E_{diff}):

$$E_m = E_{diff} + R_m I_p = E_{diff} + \Delta V_p \qquad (9.21)$$

where I_p is the electrogenic component of the pump current and E_{diff} is the E_m that would exist solely on the basis of the ionic gradients and relative permeabilities in the absence of an electrogenic pump potential. Equation 9.21 states that E_m is the sum of E_{diff} and a voltage (IR) drop produced by the electrogenic pump current across R_m. The electrogenic pump potential (V_p) can be considered to be in parallel with E_{diff} (see Fig. 9.9). Because the *density of pump sites* is more than a 1000-fold greater than that of Na^+ and K^+ channels in resting membrane, there is no relation between the pump pathway (the active flux path) and R_m (the passive flux paths); i.e. the pump path and the passive conductance paths are in parallel. The pump potential should be considered the full potential between zero and the maximum negative pump potential (V_p) while the pump is pumping (see Fig. 9.8).

One possible equivalent circuit for an electrogenic Na^+ pump that takes into account some of the known facts is

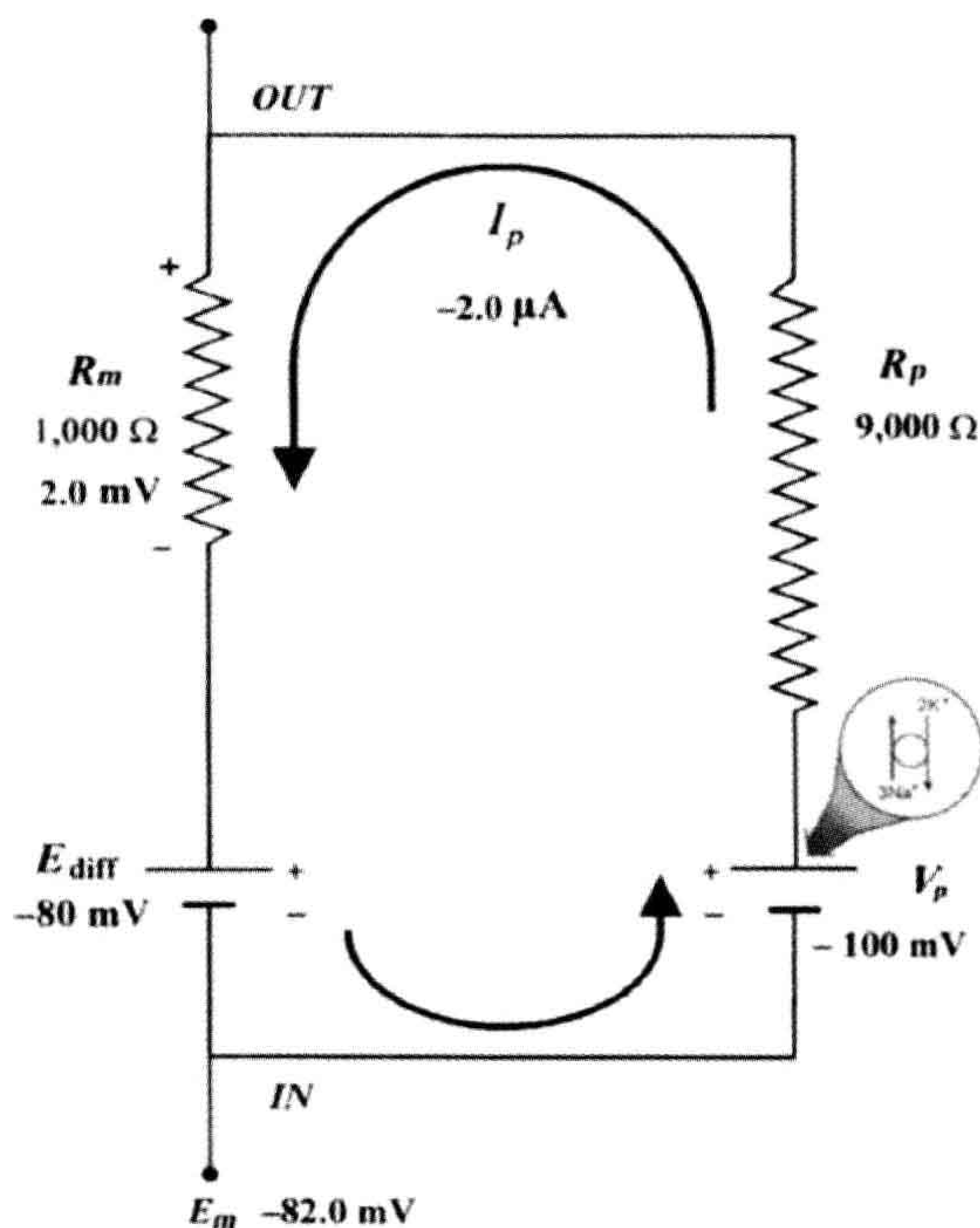


FIGURE 9.9 Hypothetical electrical equivalent circuit for electrogenic sodium pump. Model consists of a pump pathway in parallel with the membrane resistance (R_m) pathway. This model fits the evidence that the pump proteins and channel proteins are embedded in the lipid bilayer as parallel elements. Net diffusion potential (E_{diff}, determined by the ion equilibrium potentials and relative permeabilities) of −80 mV is depicted in series with R_m. Pump leg is assumed to consist of a battery in series with a fixed resistor (pump resistance, R_p) that does not change with changes in R_m and whose value is about ninefold higher than R_m. Pump battery is charged up to some voltage (e.g. V_p of −100 mV) by a pump current generator. Net electrogenic pump current is developed by the pumping in of only two K^+ ions for every three Na^+ ions pumped out. For the values given in the figure (namely, R_m of 1000 Ω, E_{diff} of −80 mV, R_p of 9000 Ω, and V_p of −100 mV), circuit analysis shows that the measured membrane potential (E_m) is −82.0 mV: i.e. the direct electrogenic pump potential contribution to the RP is −2.0 mV. The calculated pump current (I_p) is −2.0 µA.

given in Fig. 9.9. The pump pathway is in parallel with the resistance pathways. The pump resistance (R_p) is estimated to be about ninefold higher than R_m. If so, the pump resistance acts to minimize a short-circuit path to E_{diff} when the pump potential is low or zero (pump inhibited). The pump potential contribution to E_m (ΔV_p) is a function of membrane resistance (R_m); the higher the R_m (R_p constant), the more nearly E_m approaches V_p. The pump battery is charged to some voltage by a pump current generator. If the pump is stopped by ouabain, V_p goes to zero. Using circuit analysis for the values of the parameters given in Fig. 9.9, E_m would be −82.0 mV, moderately close to E_{diff} (−80 mV) (Table 9.3). If R_m is raised twofold (to 2000 Ω), E_m would be −83.6 mV. Thus, this circuit clearly gives a pump potential contribution to E_m that is dependent on R_m. The higher R_m is relative to R_p, the more E_m reflects V_p. If E_{diff} is made smaller (e.g. in smooth muscle cells having a higher P_{Na}/P_K ratio), then the relative contribution of the pump potential to E_m becomes greater (see Table 9.3).

In general, Cl^- ions are known to have a "short-circuiting" effect on the electrogenic Na^+ pump potential. For example, if the external Cl^- is replaced by less permeant anions, the magnitude of the hyperpolarization produced by the electrogenic Na^+ pump is substantially increased. This Cl^- effect could be caused by the lowering of membrane resistance in the presence of Cl^-. The greater the R_m, the greater the contribution of the electrogenic pump potential to resting E_m (see Fig. 9.9 and Table 9.3).

The density of Na^+-K^+ pump sites, estimated by specific binding of [^{3}H]ouabain, is usually about 700–1000/µm^2. The turnover rate of the pump is generally estimated to be 20–100/s. The *pump current* (I_p) has been estimated as:

$$I_p = \frac{\Delta V_p}{R_m} \quad (9.22)$$

where ΔV_p is the pump potential contribution. Values of about 20 pmol/(cm^2/s) were obtained. A density of 1000 sites/µm^2 (10^{11} sites/cm^2) times a turnover rate of 40/s gives 4×10^{12} turnovers/(cm^2/s). If three Na^+ are pumped with each turnover, this gives 12×10^{12} Na^+ ions/(cm^2/s); dividing by Avogadro's number (6.02×10^{23} ions/mol) yields 20×10^{-12} mol/(cm^2/s), which is the same value as the 20 pmol/(cm^2/s) measured. The net pump current would be less, depending on the amount of K^+ pumped in the opposite direction, i.e. depending on the coupling ratio (e.g. 3 Na^+:2 K^+). Whenever the Na^+-K^+ pump is stimulated to turn over faster, e.g. by increasing $[Na^+]_i$ or $[K^+]_o$, the electrogenic pump current is increased.

Ion flux (J) can be converted to current (I) by the relationship:

$$I = J \cdot zF$$
$$\frac{\text{A}}{\text{cm}^2} = \frac{\text{mol}}{\text{s}\cdot\text{cm}^2}\,\frac{\text{C}}{\text{mol}} \quad (9.23)$$

Thus, a flux of 20 pmol/(cm^2/s) is equal to approximately 2 µA/cm^2 (20×10^{-12} mol/(s/cm^2)$\times0.965\times10^5$ coul/mol). Since $\Delta V_p = I_p \times R_m$, if R_m were 1000 Ω/cm^2 and I_p were 2 µA/cm^2, the electrogenic pump contribution to E_m would be 2 mV ($E_m = E_{diff} + I_pR_m$).

Two K^+ ions are usually carried in for every three Na^+ ions moved out. Because the pump is electrogenic, i.e. produces a net current (and hence potential) across the membrane, then the amount of K^+ pumped in must be less

TABLE 9.3 Summary of Calculations of Resting Potential (E_m) for a Model Having an Electrogenic Pump Potential (V_p) in Parallel with Net Diffusion Potential (E_{diff}), as Depicted in Figure 9.9

E_{diff} mV	R_m Ω	V_p mV	I_p μA	V_{rev} mV	ΔV_p mV	RP mV
−80	1000	−100	−2.0	+18	−2.0	−82
−80	2000	−100	−1.82	−16.4	−3.64	−83.6
−80	1000	0	+8.0	−72	+8.0	−72
−50	1000	−100	−5.0	+45	−5.0	−55
−50	2000	−100	−4.55	+40.9	−9.1	−59.1
−50	1000	0	+5.0	−45	+5.0	−45

Pump resistance, R_p, was assumed to have constant value of 9000 Ω. R_m, membrane resistance; ΔV_p contribution of V_p to the measured E_m. E_m was calculated from the equation $E_m = \left(\frac{R_m}{R_m + R_p}\right)V_p + \left(\frac{R_p}{R_m + R_p}\right)E_{diff}$.

than the amount of Na^+ pumped out; e.g. the Na^+/K^+ coupling ratio must be 3:2 (or 3:1). The coupling ratio cannot be 3:0, because of the well-known fact that external K^+ must be present for the pump to operate. The coupling ratio might be increased under some conditions, e.g. when $[Na^+]_i$ is elevated. If the coupling ratio were to increase (e.g. to 3:1), the pump potential contribution would become larger, for a constant pumping rate.

The pump current may be stimulated by increasing the *turnover rate* of each pump site or by increasing the *number of pump sites*. In skeletal muscle, insulin has been reported to increase the number of Na^+-K^+ pump sites in the sarcolemma by increasing the rate of translocation from an internal pool, thereby increasing the pump current. β-Adrenergic agonists, like isoproterenol, stimulate the pump current by cyclic AMP/protein kinase-A phosphorylation of the pump.

The electrogenic pump potential has *physiologic importance* in cells. Although small, the electrogenic pump potential contribution to the RP could have significant effects on the level of inactivation of the fast Na^+ channels and hence on propagation velocity. Further, an electrogenic pump potential could act to delay depolarization under adverse conditions (e.g. ischemia and hypoxia) and would act to speed repolarization of the normal RP during recovery from the adverse conditions. It is crucial that the excitable cell maintain its normal RP as much as possible, because of the effect of small depolarizations on the AP rate of rise and conduction velocity and the complete loss of excitability with larger depolarizations. For example, the rate of firing of pacemaker nodal cells of the heart is affected significantly by very small potential changes.

In cells in which there are lower RPs (e.g. smooth muscle cells and cardiac nodal cells), the electrogenic pump potential contribution can be larger (see Table 9.3). *Sinusoidal oscillations in the Na^+-K^+ pumping rate* could produce oscillations in E_m, which could exert important control over the spontaneous firing of the cell. The period of enhanced pumping hyperpolarizes the cell and suppresses automaticity, whereas slowing of the pump leads to depolarization and consequently to triggering of APs. Oscillation of the pump rate would be brought about by oscillating changes in $[Na^+]_i$. For example, the firing of several APs should raise $[Na^+]_i$ (these cells have a small volume to surface area ratio) and stimulate the electrogenic pump. The increased pumping rate, in turn, hyperpolarizes and suppresses firing, thus allowing $[Na^+]_i$ to decrease again and removing the stimulation of the pump; the latter condition depolarizes and triggers spikes and the cycle is repeated. In rabbit sinoatrial nodal cells, it was concluded that the electrogenic Na^+ pump is one factor that modulates the heart rate under physiologic conditions. When stimulated at a high rate, cardiac Purkinje fibers and nodal cells undergo a transient period of inhibition of automaticity after cessation of the stimulation, known as *overdrive suppression of automaticity*. Stimulation of the electrogenic pump due to elevation in $[Na^+]_i$ is the major cause of this phenomenon.

APPENDIX

AI. MORE DETAILS ON Ca^{2+}-Na^+ EXCHANGER

The ratio of free energy changes for Na^+ to Ca^{2+} was calculated for a coupling ratio of 3 Na^+:1 Ca^{2+} (3 $\Delta G_{Na}/\Delta G_{Ca}$) and a $[Na^+]_i$ of 15 mM, and plotted as a function of membrane potential, for different $[Ca^{2+}]_i$ levels

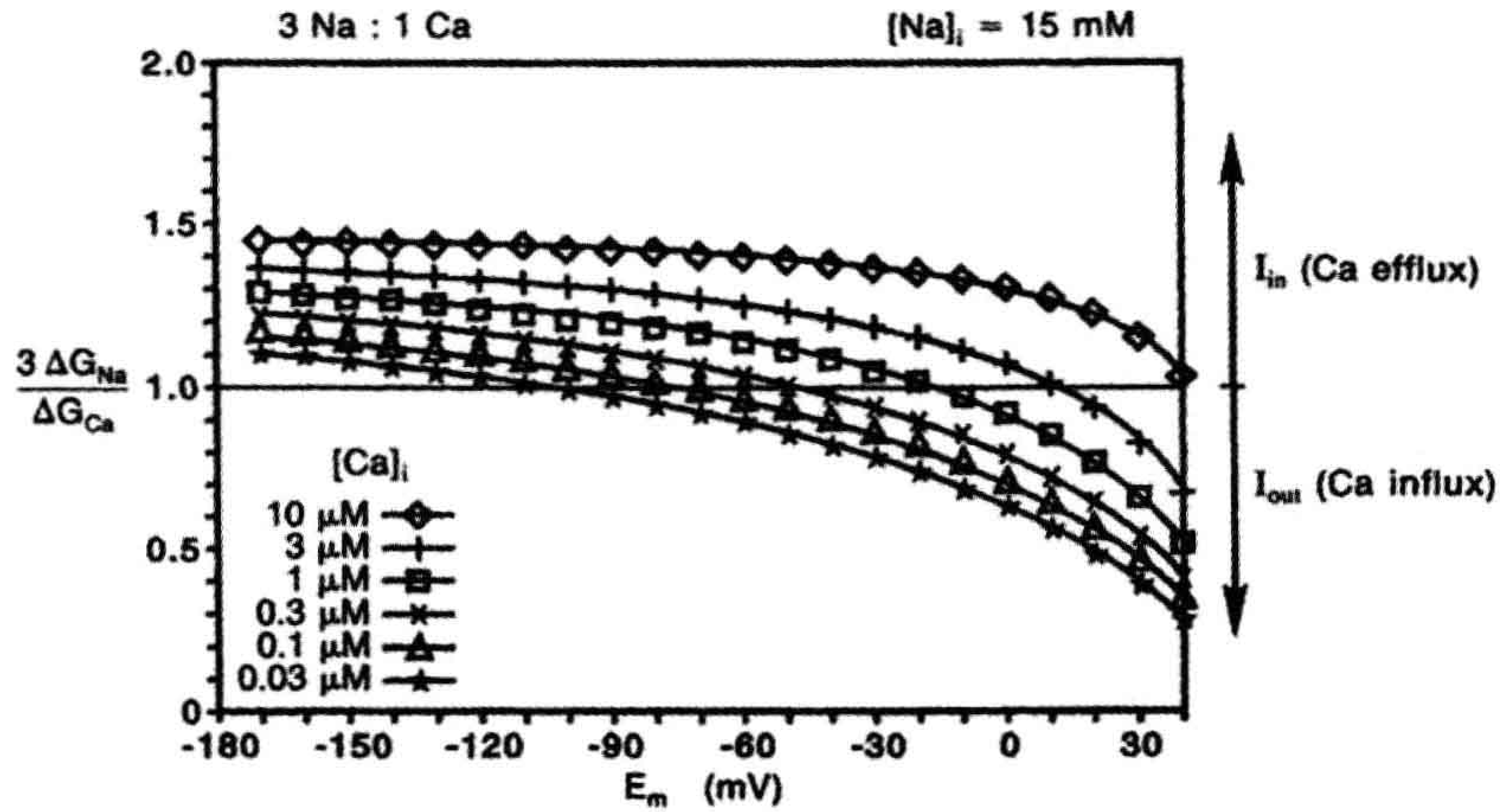


FIGURE 9A.1 Electrogenic Na^+-Ca^{2+} exchange for $[Na^+]_i$ of 15 mM for a coupling ratio of 3 Na^+:1 Ca^{2+}. Calculated ratio of the free energies for Na^+ versus Ca^{2+} (3 $\Delta G_{Na}/\Delta G_{Ca}$) plotted as a function of membrane potentials (E_m) for six different intracellular Ca^{2+} concentrations ($[Ca^{2+}]_i$). At a ratio of 1.0, 3 $\Delta G_{Na} = -\Delta G_{Na}$ and the sum equals zero: 3 $\Delta G_{Na}+\Delta G_{Ca} = 0$. Therefore, the exchange would be at equilibrium at the E_m value at which each curve crosses the ratio of 1.0 line; i.e. this gives the value of the exchanger equilibrium potential, $E_{Na\text{-}Ca}$. At ΔG ratios >1.0, there is a net inward current carried by Na^+ ion, coupled with net Ca^{2+} efflux from the cell. This represents the forward mode of operation of the exchanger. At ΔG ratios <1.0, there is a net outward current carried by Na^+ ion, coupled with net Ca^{2+} influx into the cell. This reflects the reverse mode of operation of the exchanger.

(Fig. 9A.1). This plot allows an assessment of how the directionality of the exchanger is affected by E_m, i.e. *forward mode* versus *reverse mode* of operation, and how the reversal potential of the exchanger is shifted by $[Ca^{2+}]_i$. When the ratio is 1.0, $3\Delta G_{Na} = -\Delta G_{Ca}$ and the sum equals zero: 3 $\Delta G_{Na}+-\Delta G_{Ca} = 0$. Therefore, the exchanger would be at equilibrium. For ΔG ratios >1.0, there is a net inward current carried by Na^+ ion, coupled with net Ca^{2+} efflux from the cell. This represents forward mode of operation of the exchanger. For ΔG ratios <1.0, there is a net outward current carried by Na^+ ion, coupled to a net Ca^{2+} influx into the cell. This represents reverse mode of operation of the exchanger.

The *equilibrium potential* or *reversal potential* for the Ca^{2+}-Na^+ exchanger ($E_{Na\text{-}Ca}$), for an exchange ratio of 3 Na^+:1 Ca^{2+} is:

$$E_{Na-Ca} = 3E_{Na} - 2E_{Ca} \quad (9A.1)$$

where E_{Na} and E_{Ca} are the equilibrium potentials for Na^+ and Ca^{2+}, respectively, as calculated from the Nernst equation. Thus, the $E_{Na\text{-}Ca}$ varies during changes in the $[Ca^{2+}]_i$ level that occurs with contraction.

Therefore, when a myocardial cell changes from the RP (ca. −80 mV) to the AP plateau (ca. +20 mV), simultaneous with $[Ca^{2+}]_i$ being elevated from about 0.1 to 3 μM, the exchanger switches to reverse mode of operation, with Ca^{2+} influx. As stated previously, this Ca^{2+} influx can be a significant source of the total Ca^{2+} influx during excitation–contraction coupling.

AII. DERIVATION OF NERNST EQUATION

The Nernst equation may be derived from the general equation for the free energy change (ΔG_c) resulting from both osmotic work and electrical work for transporting 1 mole of cation (c^+) across a membrane. Thus:

$$\Delta G_c = RT \ln \frac{[c^+]_i}{[c^+]_o} + zFE_m \quad (9A.2)$$

where R is the gas constant (8.3 joule/mole-°K); T is absolute temperature (°K = 273+°C); $[c^+]_i$ and $[c^+]_o$ are the internal and external c^+ concentrations, respectively; z is the valence (equiv/mol); F is the Faraday constant (96 500 coul/equiv); and E_m is membrane potential. The first term on the right side of this equation, $RT \ln ([c+]_i/[c+]_o)$, gives the osmotic work for transporting one mole of particles across the membrane against a concentration gradient. The second term, zFE_m, gives the electrical work for transporting one mole of charged particles across the membrane against an electrical gradient. The sum of these two terms then gives the total work required. At equilibrium, the change in free energy for moving one or only a few particles across the membrane must be zero ($\Delta G = 0$). Therefore:

$$0 = RT \ln \frac{[c^+]_i}{[c^+]_o} + zFE_m \quad (9A.3a)$$

and

$$zFE_m = -RT \ln \frac{[c^+]_i}{[c^+]_o} \quad (9A.3b)$$

or

$$E_m = \left(\frac{-RT}{zF}\right) \ln \frac{[c^+]_i}{[c^+]_o} \qquad (9A.3c)$$

which is the Nernst equation.

Since the Faraday constant (F) is equal to the charge on an electron (e, in coulombs) times Avogadro's number (N_A, number of ions per mole), then:

$$\frac{RT}{F} = \frac{RT}{N_A Q_e} = \frac{kT}{Q_e} \qquad (9A.4)$$

where k (the Boltzmann constant) is equal to the gas constant (R) divided by Avogadro's number (N_A), i.e. the energy (in joules) of an ion per °kelvin; and Q_e is the charge (in coulombs) on an electron (namely, 1.6×10^{-19} coul/e^-).

AIII. HALF-CELL POTENTIALS

In measuring biological potentials, care must be taken not to introduce artifacts, such as half-cell potentials. This section will give a brief description of electrode half-cell potentials. For example, if two beakers containing NaCl at 0.1 and 0.01 M were joined by a salt bridge (agar-NaCl) and if an Ag-AgCl half-cell electrode were placed in each beaker, then a PD of 59 mV would be recorded between the two electrodes, because the potential of each half-cell, reversible to Cl^- ions, would be different (Fig. 9A.2). In this example, the beaker containing the higher Cl^- concentration would be negative and the one with the lower Cl^- concentration would be positive. The AgCl coat of the electrode immersed in the lower Cl^- concentration would have the greater tendency to solubilize and ionize, leaving this electrode positive. Conversely, the AgCl coat of the electrode immersed in the higher Cl^- concentration would have the lower tendency to solubilize and actually would tend to deposit more AgCl, stealing a positive charge from the wire and thus leaving that electrode negatively charged. A positive potential is applied to electroplate the Ag wires with AgCl by electrophoresing Cl^- to the Ag wire, as shown in Fig. 9.A2.

Note that the RP recorded in biological cells by an intracellular microelectrode is not a function of the half-cell potentials (i.e. an artifact), because the solutions bathing the half-cells (e.g. Ag-AgCl wires or calomel half-cells) remain constant; i.e. the half-cell potentials stay the same whether the microelectrode is inside or outside the cell. The two half-cell potentials are nearly equal in magnitude and so cancel each other. Any small amount of difference between the two half-cell potentials (e.g. a few millivolts) when the two electrodes are in the same Ringer's solution is arbitrarily called the zero potential. (In practice, with the microelectrode in position, any small microelectrode tip potential, e.g. up to 5 mV, would be included in the zeroing procedure.) The RP of the cell is added in series with the half-cell potential, and thus the recording system gives the true transmembrane RP.

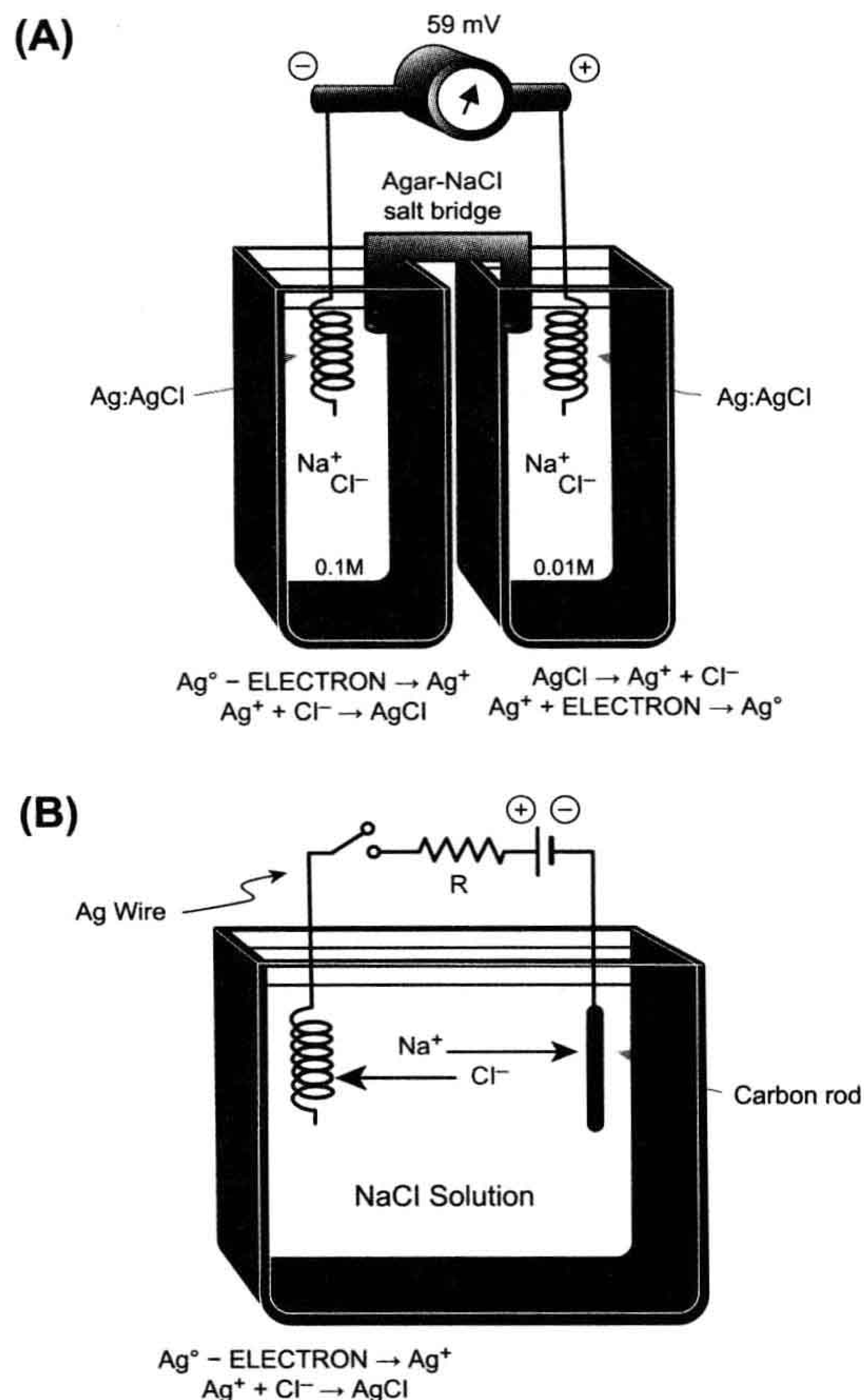


FIGURE 9A.2 Reversible half-cell electrode potentials. (A) Two Ag-AgCl half-cell electrodes are bathed in two different solutions containing Cl^- ion at different concentrations (0.1 and 0.01 M). The Ag-AgCl half-cells are reversible to Cl^- and therefore the half-cell potential depends on the Cl^- concentration in which the electrode is bathed. Therefore, the two half-cell potentials are not equal to one another and their potentials do not cancel out, as is normally true. There is a net PD produced by the two unequal half-cell potentials, the electrode in the higher Cl^- concentration being negative and the electrode in the lower Cl^- concentration being positive. The two solutions are connected by an agar salt bridge to complete the circuit. (B) For electroplating a silver wire electrode with AgCl, the silver wire must be made positive so that Cl^- ions can be electrophoresed through the solution to react with silver atoms to plate AgCl.

AIV. CONSTANT-FIELD EQUATION DETAILS

An important modification of the Nernst equation in common use for calculating the membrane potential, or for

determining the P_{Na}/P_K ratio, is the Goldman–Hodgkin–Katz constant-field equation (Goldman, 1943; Hodgkin and Katz, 1949):

$$E_m = \frac{-RT}{F} \ln \frac{P_K[K^+]_i + P_{Na}[Na^+]_i + P_{Cl}[Cl^-]_o}{P_K[K^+]_o + P_{Na}[Na^+]_o + P_{Cl}[Cl^+]_i} \quad (9A.5a)$$

where P_K, P_{Na} and P_{Cl} are the membrane permeabilities for K^+, Na^+ and Cl^-, respectively. The P_K $[K^+]_i$ product, for example, is given in the units of a flux (mol/s per cm^2), but the entire right-hand term (fraction) is dimensionless. Plugging in the numerical values for the constants and converting from natural logarithm (ln) to logarithm to the base 10 (log): ln N=2.303 log N gives:

$$E_m = -61 \text{ mV} \log \frac{P_K[K^+]_i + P_{Na}[Na^+]_i + P_{Cl}[Cl^-]_o}{P_K[K^+]_o + P_{Na}[Na^+]_o + P_{Cl}[Cl^+]_i} \quad (9A.5b)$$

and E_m is expressed in mV. Dividing the right-hand term by P_K gives:

$$E_m = -61 \text{ mV} \log \frac{[K^+]_i + \frac{P_{Na}}{P_K}[Na^+]_i + \frac{P_{Cl}}{P_K}[Cl^-]_o}{[K^+]_o + \frac{P_{Na}}{P_K}[Na^+]_o + \frac{P_{Cl}}{P_K}[Cl^-]_i} \quad (9A.6)$$

Again, the right-hand term (fraction) is dimensionless. Any ion that is passively distributed, i.e. not actively pumped, however, cannot determine the RP, because the distribution of that ion must follow the RP. Therefore, when Cl^- is passively distributed, it is not considered because RP cannot be determined by Cl^-. As a result, Equation 9A.6 can be reduced to:

$$E_m = -61 \text{ mV} \log \frac{[K^+]_i + \frac{P_{Na}}{P_K}[Na^+]_i}{[K^+]_o + \frac{P_{Na}}{P_K}[Na^+]_o} \quad (9A.7)$$

Equation 9A.7 is one of the most useful forms of the constant-field equation, because if E_m is measured and if the internal and external ion concentrations are known, the P_{Na}/P_K ratio can be calculated. Thus, for given ionic gradients, the RP is determined by the P_{Na}/P_K ratio (i.e. the relative permeabilities of the cell membrane to Na^+ and K^+) and not by the absolute permeabilities. For simplicity, Ca^{2+} is ignored here as a factor contributing to the RP. The relationship between the permeability coefficient for an ion (P_i) and the membrane conductance for that ion (g_i) is complex, involving several terms including membrane potential.

Figure 9.8 gives the expected RP as a function of the P_{Na}/P_K ratio for a muscle fiber (having a $[K^+]_i$ of 150 mM) bathed in normal Ringer's solution ($[K^+]_o$ of 4.5 mM, $[Na^+]_o$ of 150 mM), assuming an $[Na^+]_i$ value of 15 mM. As can be seen, a P_{Na}/P_K ratio of 0.1 gives a RP close to −60 mV, whereas a ratio of 0.01 gives a potential close to −85 mV. Some muscle cells (e.g. smooth muscle and young embryonic chick myocardial cells) have a low RP of about −55 mV, because of a high P_{Na}/P_K ratio of about 0.15 (rather than smaller ionic gradients). The P_{Na}/P_K ratio can be high because of either a high P_{Na} or a low P_K, or both; in most cases the main reason is a low P_K.

One advantage the constant-field equation has over the chord-conductance equation is that it nicely accounts for the bend at low $[K^+]_o$ in the E_m versus log $[K^+]_o$ curves (see Fig. 9.8). As can be seen in Fig. 9.8, which presents theoretical curves calculated from Equation 9A.7, the higher the P_{Na}/P_K ratio, the greater the deviation from a straight line as $[K^+]_o$ is lowered. As mentioned previously, from this equation one can deduce that as $[K^+]_o$ is lowered and $[Na^+]_o$ is concomitantly elevated, the denominator of the right-hand term becomes more and more dominated by the Na^+ term, for any given P_{Na}/P_K ratio. Because the numerator is relatively fixed, E_m is more influenced by E_{Na} as $[K^+]_o$ is lowered more and more. Thus, this relationship accounts for the deviation from the straight line for E_K.

Although the $P_{Na}/P_K = 0.05$ curve is almost linear at high $[K^+]_o$ with a slope of 60 mV/decade, the membrane does not become "purely K^+-selective" as is often stated in textbooks because, for these theoretical calculations, the P_{Na}/P_K ratio was held constant over the entire $[K^+]_o$ range. There is some evidence, however, that P_K itself increases as $[K^+]_o$ increases, but this effect was not taken into consideration in Fig. 9.8. g_K is a function of $[K^+]_o$, namely, $g_K \propto P_K [K^+]_o$. Finally, the increased bending for the higher P_{Na}/P_K ratios can again be seen from Equation 9A.7; at a given $[K^+]_o$ (e.g. 4 mM), the denominator is more and more dominated by the Na^+ term as the P_{Na}/P_K ratio is increased more and more.

The order of selectivity of the resting membrane for the alkali metal ions generally is in the following sequence, from the highest permeability to the lowest: $K^+ > Rb^+ > Cs^+ > Na^+ > Li^+$. For example, the relative permeabilities (assigning $P_K = 1$) in squid giant axon (Baker et al., 1968) are:

$$\begin{array}{ccccccccc} P_K & > & P_{Rb} & > & P_{Cs} & > & P_{Na} & > & P_{Li} \\ 1.0 & & 0.69 & & 0.19 & & 0.17 & & 0.12 \end{array} \quad (9A.8)$$

In frog sartorius (Mullins, 1961) the values are:

$$\begin{array}{ccccccc} P_K & > & P_{Rb} & > & P_{Cs} & > & P_{Na} \\ 1.0 & & 0.54 & & 0.11 & & 0.04 \end{array} \quad (9A.9)$$

So far in our discussion, Ca^{2+} has been ignored. It can be demonstrated that Ca^{2+} has only a negligible effect on the RP, regardless of its P value. This is because of the relatively low extracellular and intracellular concentration of free Ca^{2+} ion compared with K^+ and Na^+ ions.

A modified version of the Goldman constant-field equation, which includes a Ca^{2+} term, is:

$$E_m = -60\,\text{mV} \log \frac{(B-A)+\sqrt{y}}{2(A-4P_{Ca}[Ca^{2+}]_i)} \quad (9A.10)$$

(This equation was kindly provided by Professor D.E. Goldman.)

where

$$A = P_K[K^+]_i + P_{Na}[Na^+]_i$$

$$B = P_K[K^+]_o + P_{Na}[Na^+]_o$$

$$y = (B-A)^2 + 4\,(A + 4P_{Ca}[Ca^{2+}]_i)(B + 4P_{Ca}[Ca^{2+}]_o)$$

For simplification, the analogous Cl^- terms in the definition of A and B have been omitted, assuming Cl^- to be passively distributed.

Calculations made from Equation 9A.10 demonstrate some interesting points: (1) for the same permeabilities ($P_{Ca} = P_{Na}$), Ca^{2+} has much less effect on E_m than does Na^+, because of the lower Ca^{2+} concentrations and because of the square root function for the Ca^{2+} concentrations. For example, the depolarization produced by taking into account the Ca^{2+} ion is only +0.4 mV for a P_{Na}/P_K ratio of 0.1. (2) Even when P_{Ca} is set to 10 times P_{Na}, the effect of Ca^{2+} on the RP is still relatively small (e.g.+3.5 mV for a P_{Na}/P_K ratio of 0.01 and +8.0 mV for a P_{Na}/P_K ratio of 0.1). (3) The effect of Ca^{2+} is somewhat greater when the P_{Na}/P_K ratio is higher (as in cardiac nodal cells or smooth muscle). (4) The effect of Ca^{2+} is considerably less at high $[K^+]_o$ values.

Thus, these calculations indicate that Ca^{2+} can be virtually ignored in discussion of the ionic basis of the RP. This agrees with the well-known fact that variation in $[Ca^{2+}]$ throughout a relatively wide range has a negligible effect on the RP (see Sperelakis, 1972). Further, these facts have implications about the relative importance of Na^+ versus Ca^{2+} background currents (inward) during genesis of the pacemaker potential (concomitant with the decrease in g_K and I_K). Finally, it should be emphasized that, for example, if $P_{Ca} = P_K$, then g_{Ca} does not equal g_K, because of the concentration differences. To calculate g_K from a given P_K, one must use the appropriate equation that takes into account the concentrations and membrane potential.

AV. DERIVATION OF CHORD CONDUCTANCE EQUATION

Ohm's law states that the current (I) is equal to the voltage (E) either divided by the resistance (R) or multiplied by the conductance (g = $1/R$):

$$I = \frac{E}{R} = gE \quad (9A.11)$$

When dealing with solutions, the voltage or driving force must take into account both the concentration force and the electrical force. In this case, the ionic current (I_i) is a product of the conductance for a given ion times the total driving force on that ion ($E_m - E_i$) and so may be expressed as:

$$I_i = g_i(E_m - E_i) \quad (9A.12)$$

In a resting cell membrane (stable RP), the total ionic current must be zero; otherwise, the membrane potential would change. Therefore, the K^+ current in the outward direction (I_K) must be equal and opposite to the Na^+ current (I_{Na}) entering the cell (neglecting Ca^{2+}, Cl^- and minor ions) expressed as:

$$I_K = -I_{Na} \quad (9A.13a)$$

Therefore,

$$I_K + I_{Na} = 0 \quad (9A.13b)$$

Substituting the equations for ionic currents from Equation 9A.12,

$$g_K(E_m - E_K) + g_{Na}(E_m - E_{Na}) = 0 \quad (9A.14)$$

Algebraic manipulations give:

$$0 = g_K E_m - g_K E_K + g_{Na} E_m - g_{Na} E_{Na}$$

$$g_K E_m + g_{Na} E_m = g_K E_K - g_{Na} E_{Na} \quad (9A.15)$$

$$E_m(g_K + g_{Na}) = g_K E_K + g_{Na} E_{Na}$$

Rearrangement gives

$$E_m = \frac{g_K}{g_K + g_{Na}} E_K + \frac{g_{Na}}{g_K + g_{Na}} E_{Na} \quad (9A.16)$$

Equation 9A.16 is the chord conductance equation. The ratios $g_K/(g_K+g_{Na})$ and $g_{Na}/(g_K+g_{Na})$ are the *fractional conductances* (relative) and are dimensionless.

If Cl^- were to be included, one would get:

$$E_m = \frac{g_K}{\sum g} E_K + \frac{g_{Na}}{\sum g} E_{Na} + \frac{g_{Cl}}{\sum g} E_{Cl} \quad (9A.17)$$

where $\Sigma g = g_K + g_{Na} + g_{Cl}$. However, if Cl^- is passively distributed (in equilibrium at the resting E_m), then Cl^- cannot be involved in determining the RP. (However, transient movements of Cl^- do affect the membrane potential when Cl^- is shifted off equilibrium during an AP or postsynaptic potential.)

On the other hand, the Ca^{2+} ion is actively transported and is off equilibrium, so its conductance influences the RP. The chord conductance equation containing the Ca^{2+} term is:

$$E_m = \frac{g_K}{\sum g} E_K + \frac{g_{Na}}{\sum g} E_{Na} + \frac{g_{Ca}}{\sum g} E_{Ca} \quad (9A.18)$$

where $\sum g = g_K + g_{Na} + g_{Ca}$

The chord conductance equation, of course, can be written using resistances rather than conductances. For Equation 9A.16 using only K^+ and Na^+ terms, substitution of $R = 1/g$ in the equation and algebraic manipulation gives the equation:

$$E_m = \frac{R_K}{R_K + R_{Na}} E_{Na} + \frac{R_{Na}}{R_K + R_{Na}} E_K \quad (9A.19)$$

Note that the E_{Na} and E_K terms are interchanged from the chord conductance equation. This form of the equation is the *chord resistance equation.*

The chord conductance equation applies only to those situations in which the net ionic current is zero, such as when the membrane is at rest. This equation is derived simply from Ohm's law and one advantage it has over the constant-field equation is that it can more easily include divalent cations such as Ca^{2+}.

AVI. CIRCUIT ANALYSIS APPLICABLE TO CELL MEMBRANE

Using Ohm's and Kirchhoff's laws and logic, it is possible to see why in the nerve or muscle cell, the K^+ battery dominates the RP, whereas the Na^+ or Ca^{2+} batteries dominate the peak of the AP. The circuit in Fig. 9A.3 will be used to show that the battery having the lowest resistance in series with it is the battery that is the most expressed across the network. Before analyzing the circuit rigorously, we can consider three conditions and make some qualitative judgments: (1) If the left resistor (R_1) equals the right resistor (R_2) (regardless of their absolute values), the PD across the network is +150 V (upper terminal positive with respect to the lower terminal), i.e. halfway between both batteries because both should be equally expressed. (2) If R_2 is made infinite (e.g. open circuit in branch 2) and R_1 is finite, then the PD is exactly +100 V, since the right battery (E_2) cannot be expressed at all. (3) If R_1 is much less than R_2, then the PD approaches +100 V, because E_1 is dominant.

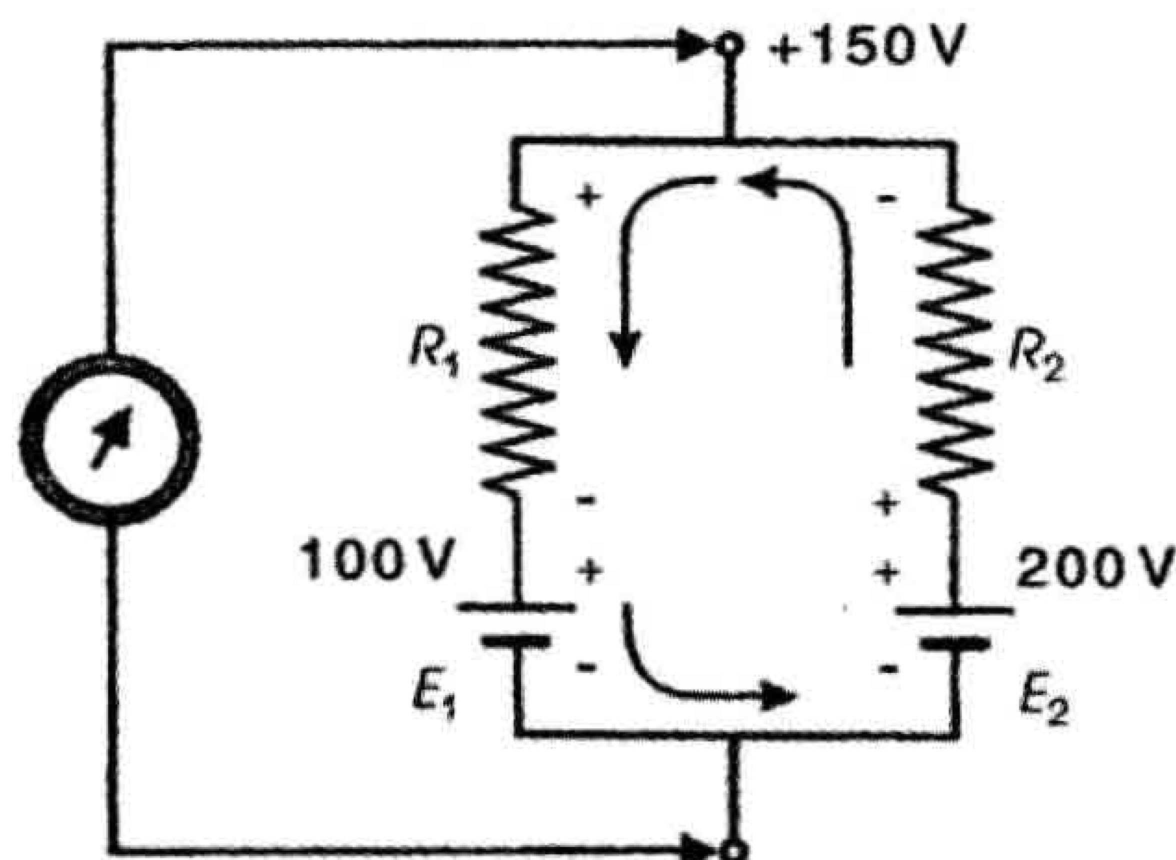


FIGURE 9A.3 Circuit diagram of the circuit analysis applicable to the cell membrane, showing why the RP of a cell is determined by the relative permeabilities (or conductances). Battery having the lowest resistance in series with it is the battery most expressed across such a network.

The circuit in Fig. 9A.3 can also be analyzed quantitatively. For example, if $R_1 = 10\,\Omega$ and $R_2 = 990\,\Omega$, the exact PD may be obtained from the following analysis. The current (I) has one magnitude; i.e. it is constant throughout this closed circuit, but the current flows upward in branch 2 and downward in branch 1. This occurs because the right battery (E_2) is larger than E_1, and so the net driving force for the net current is in the direction as indicated in Fig. 9A.3. Therefore, the voltage drops produced across R_1 and R_2 are in opposite polarities, as shown. The voltage drop across R_1 adds to E_1 to make a greater PD across branch 1, like two batteries in series (+ −, + −). In contrast, the voltage drop across R_2 subtracts from E_2 to make a smaller PD, like two batteries back to back (− +, + −). Therefore, the following two equations can be written for the PD across branch 1 (PD_1) and across branch 2 (PD_2):

$$(PD)_1 = E_1 - IR_1 \quad (9A.20)$$

$$(PD)_2 = E_2 - IR_2 \quad (9A.21)$$

To solve these equations, we must first calculate the current (I). The net driving force for I is equal to $E_2 - E_1$; hence from Ohm's law, the net current is equal to $(E_2 - E_1)$ divided by the total resistance ($R_1 + R_2$):

$$I = \frac{E_2 - E_1}{R_2 + R_1}$$

$$I = \frac{200\text{ V} - 100\text{ V}}{990\,\Omega + 10\,\Omega} \quad (9A.22)$$

$$= \frac{100\text{ V}}{1000\,\Omega} = 0.1\text{ A}$$

Now we can enter this value for I into Equation 9A.20

$$\begin{aligned}(PD)_1 &= E_1 - IR_1 \\ &= 100\text{ V} - (-0.1\text{ A})(10\,\Omega) \\ &= 100\text{ V} - (-1\text{ V}) \\ &= 100\text{ V} + 1\text{ V} \\ &= 101\text{ V}\end{aligned}$$

The negative sign in the current is because the current in branch 1 produces a voltage drop that adds to E_1. Because

the two branches are connected by zero resistances, they are effectively the same point and:

$$(PD)_1 = (PD)_2 \quad (9A.23)$$

Therefore, we can also calculate the PD by substituting into Equation 9A.21.

$$\begin{aligned}(PD)_2 &= E_2 - IR_2\\ &= 200\text{ V} - (+0.1\text{A})(990\,\Omega)\\ &= 200\text{ V} - (99\text{ V})\\ &= 101\text{ V}\end{aligned}$$

Thus, the two methods check.

To summarize, it has been quantitatively demonstrated that the battery with the lowest series resistance is the battery most expressed across this network. This analysis holds true regardless of the absolute values of the resistances or batteries or the polarity of each battery. Other methods of circuit analysis can be used to calculate the PD across such a network, but this method is one of the simplest.

The following chord resistance equation can also be used to calculate the PD across the network:

$$\begin{aligned}PD &= \frac{R_1}{R_1+R_2}E_2 + \frac{R_2}{R_1+R_2}E_1\\ &= \frac{10\,\Omega}{10\,\Omega+990\,\Omega}200\text{ V} + \frac{990\,\Omega}{10\,\Omega+990\,\Omega}100\text{ V}\\ &= \frac{10}{1000}200\text{ V} + \frac{990}{1000}100\text{ V}\\ &= 2\text{ V} + 99\text{ V}\\ &= 101\text{ V}\end{aligned} \quad (9A.24)$$

This equation again emphasizes the point that it is the relative resistances that determine which battery is most expressed.

BIBLIOGRAPHY

Baker, P. F. (1968). Nervous conduction: some properties of the ion selective channels which appear during the action potential. *Br Med Bull, 24*, 179–182.

Daniel, E. E., Kwan, C. Y., Matlib, M. A., Crankshaw, D., & Kidwai, A. (1977). Characterization and Ca^{2+}-accumulation by membrane fractions from myometrium and artery. In R. Casteels, T. Godfraind, & J. C. Ruegg (Eds.), *Excitation-Contraction Coupling in Smooth Muscle* (pp. 181–188). Amsterdam: Elsevier-North-Holland.

Dhalla, N. S., Ziegelhoffer, A., & Hazzow, J. A. (1977). Regulatory role of membrane systems in heart function. *Can J Physiol Pharmacol. 55*, 1211–1234.

Goldman, D. E. (1943). Potential, impedance, and rectification in membranes. *J Gen Physiol, 27*, 37–60.

Hodgkin, A. L., & Katz, B. (1949). The effect on sodium ions in electrical activity of the giant axon of the squid. *J Physiol (London), 108*, 37–77.

Jain, M. K. (1972). *The Bimolecular Lipid Membrane: a System.* New York: Van Nostrand.

Jones, I. R., Maddock, S. W., & Besch, H. R., Jr. (1980). Unmasking effect of alamethicin on the (Na^+, K^+)-ATPase, beta-adrenergic receptor-coupled adenylate cyclase, and cAMP-dependent protein kinase activities of cardiac sarcolemmal vesicles. *J Biol Chem, 255*, 9971–9980.

Mullins, L. J. (1961). The macromolecular properties of excitable membranes. *Ann NY Acad Sci, 94*, 390–404.

Sperelakis, N. (1972). (Na^+, K^+)-ATPase activity of embryonic chick heart and skeletal muscles as a function of age. *Biochim Biophys Acta, 266*, 230–237.

Sperelakis, N. (1979). Origin of the cardiac resting potential. In R. M. Berne, & N. Sperelakis (Eds.), *Handbook of Physiology, Vol. 1, the Cardiovascular System* (pp. 187–267). Bethesda, MD: American Physiological Society.

Chapter 10

Gibbs–Donnan Equilibrium Potentials

Nicholas Sperelakis

Chapter Outline

I. SUMMARY

A Gibbs–Donnan (G-D) equilibrium becomes established and a G-D potential is developed across the cell membrane of cells under conditions in which metabolism and energy production have been inhibited or the Na^+-K^+ pump has been inhibited by digitalis. The G-D equilibrium occurs because of the large impermeant charged macromolecules, such as proteins, inside the cell. The G-D equilibrium does not require energy for its establishment, i.e. it is passive. This contrasts with the normal resting potential (RP) of the cell, which requires active ion transport and use of metabolic energy to establish large ionic electrochemical gradients.

The G-D potential is usually less than −20 mV, whereas the RP is considerably greater. In the G-D equilibrium, all permeable ions are in equilibrium across the membrane, whereas this is not true for the normal RP. The equilibrium potentials for all permeant ions (e.g. E_K, E_{Cl}) are of equal magnitude and polarity. The G-D potential is developed even if the cell membrane had equal permeability or conductance for all small ions, whereas the normal RP requires different permeabilities for Na^+ and K^+, namely a low P_{Na}/P_K ratio. In the G-D equilibrium, the osmolarity of the cell becomes higher than the interstitial fluid bathing the cell and so the cell tends to gain water and swell (unless prevented from doing so by a rigid cell wall, such as in plant cells).

When equilibrium is established, the product of the concentrations of the permeant ions inside the cell is equal to that outside the cell. The gains in cations and anions inside the cell also must be equal to each other. From these required conditions, an equation can be solved to give the final concentrations at equilibrium and, from this, the calculated potential difference across the membrane.

II. INTRODUCTION

Because intracellular cytoplasm contains many colloids, including large non-diffusible polyvalent electrolytes, a *Donnan equilibrium* can be established across the cell membrane with an accompanying transmembrane *Gibbs–Donnan (G-D) potential*. The resting potential (RP) of most cells in the body, including nerve and muscle cells, however, is not due to a Donnan equilibrium and the normal RP is not a Gibbs–Donnan potential, as is erroneously stated in some textbooks (Sperelakis, 1995; Sperelakis, 2001). In the true Donnan equilibrium, all diffusible ions are in equilibrium across the membrane. But many ions, like Na^+, K^+, Ca^{2+} and H^+, in nerve and muscle cells are not in equilibrium; i.e.

$$E_{Na} \neq E_m$$
$$E_K \neq E_m$$
$$E_{Ca} \neq E_m$$

and

$$E_H \neq E_m$$

On the other hand, Cl^- is at equilibrium (i.e. passively distributed) in many vertebrate cells; namely,

$$E_{Cl} = E_m$$

In addition, a large internal pressure and concomitant swelling of animal cells would occur if a Donnan

Cell Physiology Sourcebook. DOI: 10.1016/B978-0-12-387738-3.00010-X

equilibrium were allowed to become established. The action of two types of cation pumps keeps the Donnan osmotic pressure from developing and keeps certain cations out of equilibrium. Thus, a second important function of the Na^+-K^+ pump is the *regulation of cell volume*. The Na^+-K^+ pump actively pumps three Na^+ ions out (to two K^+ ions pumped in) with each cycle. The pump action decreases the osmotic pressure of the cytoplasm and prevents cell swelling. Inhibition of active ion transport by any means leads to osmotic swelling because of the establishment of the Donnan equilibrium. Under such conditions, the cells gain Na^+, Cl^-, Ca^{2+} and H_2O and they lose K^+.

Thus, the G-D potential is *passive*; i.e. energy is not necessary to its establishment. In contrast, the RP is actively generated (indirectly or directly) by the action of the Na^+-K^+ pump. The G-D potential is usually less than -20 mV, whereas the RP is -40 to -100 mV, depending on the cell type (and its ratio of P_{Na} to P_K).

III. MECHANISM FOR DEVELOPMENT OF THE GIBBS–DONNAN POTENTIAL

In the Gibbs–Donnan equilibrium, a small membrane potential is established even though the biological membrane involved, or the artificial membrane used in a laboratory experiment, may be equally permeable to the small diffusible ions used. For the example illustrated in Fig. 10.1, where aqueous solutions of 0.1 M $(Na^+)_n$-proteinate^{n-} (side 1) and 0.1 M NaCl (side 2) are initially placed on the two sides of a two-compartment chamber separated by a membrane and, if $g_{Na} = g_{Cl}$ in this membrane then, at equilibrium, $E_{Na} = E_{Cl} = -18$ mV. The side containing the protein anion becomes negative with respect to the other side. Thus, because both diffusion potentials have the same polarity (as well as magnitude), a potential difference (PD) occurs across the membrane, even though conductances for Na^+ and Cl^- across the membrane may be equal. The osmotic pressure of the

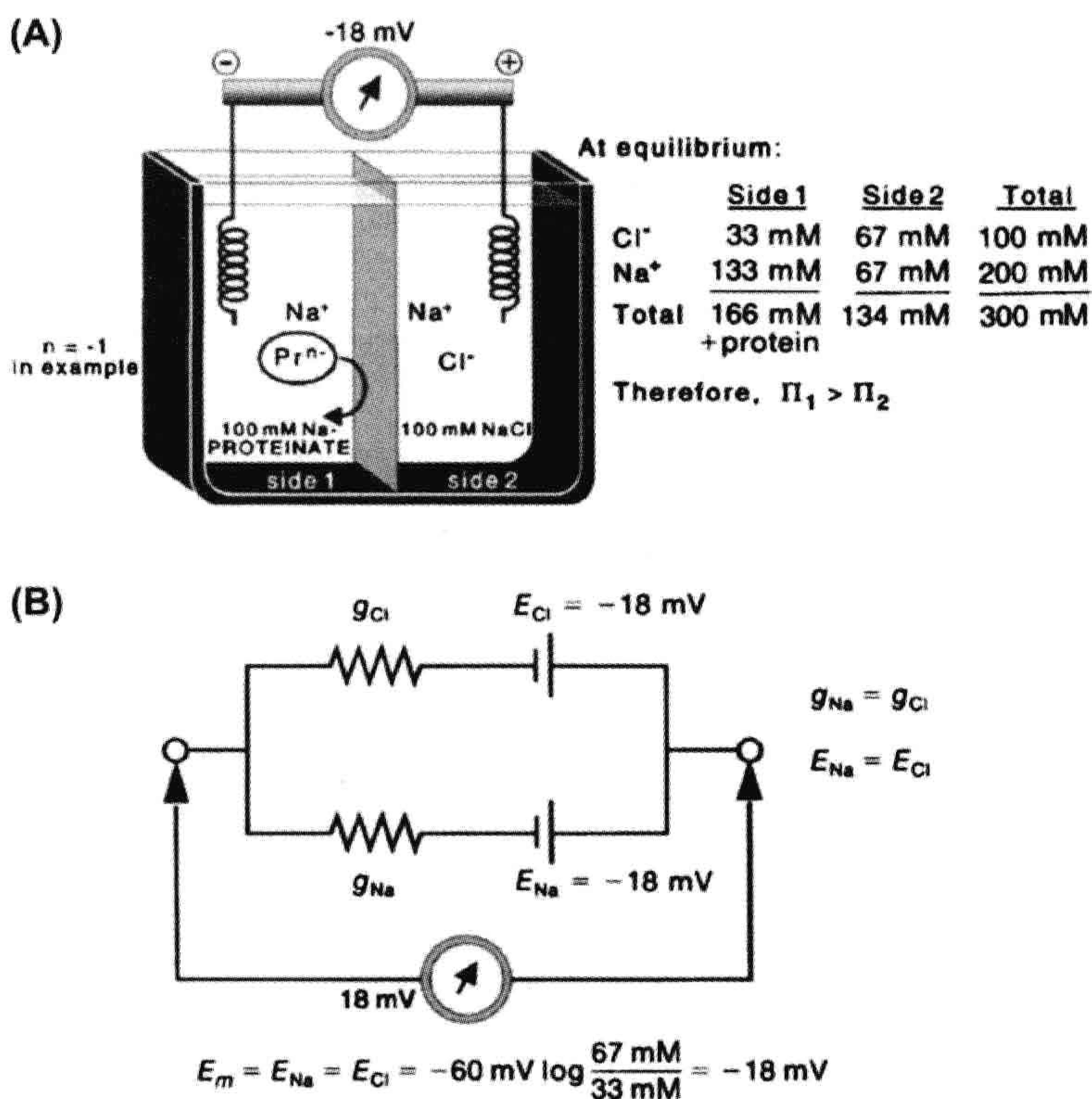


FIGURE 10.1 Gibbs–Donnan potential. (A) Gibbs–Donnan experiment. Diagram depicts the experimental arrangement for obtaining G-D potential. A membrane freely permeable to all small ions, but impermeable to the large protein molecules, is used to separate two solutions, only one of which (side 1) contains protein. Side containing the protein becomes negative, with respect to the other side, by a small voltage (-18 mV in example). This membrane potential (E_m) does not depend on active ion transport or on selective permeability properties of the membrane, as normal cell RP does. The diffusible ions (Na^+ and Cl^- in example), however, become unequally distributed across the membrane and it is their diffusion potentials ($E_{Na} = E_{Cl}$) that produce the G-D potential. (B) Equivalent circuit for experiment depicted in panel A, demonstrating that $E_m = E_{Na} = E_{Cl}$. The Na^+ and Cl^- batteries are of equal magnitude and of the same sign. Therefore, the relative conductances of the membrane to Na^+ and Cl^-, whether equal or not, are irrelevant to the potential (g_{Cl} and g_{Na} are conductances for Cl^- and Na^+, respectively).

solution on side 1 containing the non-permeant protein is greater than that on side 2. In the G-D equilibrium, all permeant ions are in electrochemical equilibrium across the membrane, i.e. they are passively distributed and there is no net electrochemical driving force:

$$(E_m - E_{Na}) = 0$$

$$(E_m - E_{Cl}) = 0$$

A more complete explanation for the development of the G-D potential follows. The G-D potential (which is an equilibrium PD) does not depend on metabolic energy. Therefore, this discussion applies to a cell that either has no ATP for pumping ions against electrochemical gradients or has had its Na^+-K^+ pump completely blocked by either ouabain or another agent. The G-D potential is passively produced by the concentration gradients for diffusible electrolytes (e.g. Na^+ and Cl^-) across a membrane. These ion gradients are caused by the presence of one or more large non-diffusible (with respect to the membrane) polyvalent electrolytes (e.g. *negatively-charged proteins*) on one side of the membrane, as is present in all biological cells. In essence, the negatively-charged protein molecules (at pH 7) inside the cell attract cations (e.g. Na^+ or K^+) and repel anions (e.g. Cl^-). Therefore, in the G-D situation, the inside of the cell has a higher concentration of Na^+ (or K^+) and a lower concentration of Cl^- than has the solution bathing the cell. The equilibrium potentials for Na^+ (E_{Na}) and for Cl^- (E_{Cl}) are equal in magnitude and are of the same sign, thereby producing a PD across the membrane. The PD is negative on the inside (side containing the protein) and usually is about −20 mV or less.

IV. GIBBS–DONNAN EQUILIBRIUM

To quantitate the ion distributions produced at equilibrium and the PD developed, let us examine the artificial system shown in Fig. 10.1A. In this system, a chamber is separated into two compartments by a collodion membrane, which has small uncharged pores that allow Na^+ and Cl^- ions, but not large protein molecules, to diffuse through. A 100 mM solution of Na^+ proteinate is added to one side (compartment 1) and a 100 mM solution of NaCl to the other side (compartment 2). An electrode is positioned on each side so that the PD across the membrane can be recorded (37°C). Let us assume that the Na^+ proteinate is completely ionized and, for simplicity, that the protein has a net negative charge of only one.

Thus, there is, at the first instant, no diffusion force for Na^+, but there is diffusion force for Cl^-, because Cl^- is 100 mM in compartment 2 and 0 mM in compartment 1. Na^+ must accompany the diffusion of Cl^- from side 2 to side 1, because the *principle of electroneutrality* in the bulk solution cannot be violated (i.e. there must be an equal number of cations and anions). So one relation that must be true when the system comes to equilibrium is that:

$$[Na^+]_2 = [Cl^-]_2 \tag{10.1}$$

In actuality, there is a small charge separation directly across the membrane to account for the PD; i.e. side 2 of the membrane has a small excess of Na^+ ions and side 1 has a small excess of Cl^- ions. Such a charge separation is very small, but is necessary to develop a PD across the membrane ($V = Q/C$) and is discussed in the preceding chapter on the RP generation.

The principle of electroneutrality also requires that the increase in Na^+ on side 1 must be exactly equal to the increase in Cl^- on side 1. Thus, the concentration difference of Na^+ that is built up at equilibrium must be exactly equal to the final concentration difference for Cl^-. This is because the large initial gradient for Cl^- is what drives the Na^+ to make its gradient. Therefore, it must also be true that:

$$\frac{[Na^+]_1}{[Na^+]_2} = \frac{[Cl^-]_2}{[Cl^-]_1} \tag{10.2}$$

Cross-multiplying gives:

$$[Na^+]_1[Cl^-]_1 = [Na^+]_2[Cl^-]_2 \tag{10.3}$$

Another way of considering this is that E_{Na} must equal E_{Cl} and, therefore, using the respective Nernst equations (see Chapter 9), we can write:

$$E_{Na} = E_{Cl} \tag{10.4}$$

$$\frac{-61\text{ mV}}{+1}\log\frac{[Na^+]_1}{[Na^+]_2} = \frac{-61\text{ mV}}{-1}\log\frac{[Cl^-]_1}{[Cl^-]_2} = \frac{-61\text{ mV}}{+1}\log\frac{[Cl^-]_2}{[Cl^-]_1} \tag{10.5}$$

Dividing both sides by −61 mV and removing the log gives Equation 10.2:

$$\frac{[Na^+]_1}{[Na^+]_2} = \frac{[Cl^-]_2}{[Cl^-]_1}$$

Equation 10.3 indicates that, at equilibrium, the product of the diffusible ions on side 1 must be equal to the product of the diffusible ions on side 2. From the Nernst equation, the relationships

$$E_{Na} = \frac{-RT}{zF}\ln\frac{[Na^+]_1}{[Na^+]_2} \tag{10.6}$$

$$= \frac{-61\text{ mV}}{+1}\log\frac{[Na^+]_1}{[Na^+]_2} \tag{10.7}$$

and

$$E_{Cl} = \frac{-61\text{ mV}}{-1}\log\frac{[Cl^-]_1}{[Cl^-]_2} \tag{10.8}$$

can be given because Cl^- is negative ($z = -1$), whereas Na^+ is positive ($z = +1$). Equation 10.8 is the same as (note that a negative sign in front of a log inverts the ratio)

$$E_{Cl} = -61 \text{ mV} \log \frac{[Cl^-]_2}{[Cl^-]_1} \quad (10.9)$$

because $[Na^+]_1/[Na^+]_2 = [Cl^-]_2/[Cl^-]_1$, as Equation 10.2 indicates and, from Equations 10.7 and 10.9, one obtains Equation 10.4: $E_{Na} = E_{Cl}$.

V. QUANTITATION OF THE GIBBS–DONNAN POTENTIAL

For quantitation, let us use x to indicate the amount (in mM) of Cl^- or Na^+ that shifted from side 2 to side 1 at equilibrium. Then the amount of Na^+ on side 2 is (100 mM$-x$) (the original amount minus the amount lost); Cl^- on side 2 is also (100 mM$-x$), because $[Na^+]_2 = [Cl^-]_2$. The Na^+ on side 1 at equilibrium is (100 mM$+x$) (the original amount plus the amount gained) and the Cl^- on side 1 is simply x. These parameters may be listed as follows:

$$[Na^+]_2 = 100 \text{ mM} - x$$
$$[Cl^-]_2 = 100 \text{ mM} - x$$
$$[Na^+]_1 = 100 \text{ mM} + x$$
$$[Cl^-]_1 = x$$

The value for x can be obtained by substituting these values into Equation 10.3:

$$[Na^+]_1 [Cl^-]_1 = [Na^+]_2 [Cl^-]_2 \quad (10.3)$$

$$(100 + x)x = (100 - x)(100 - x)$$

$$100x + x^2 = 10\,000 - 200x + x^2$$

$$300x = 10\,000$$

$$x = 33.3$$

Thus, at equilibrium

$$[Cl^-]_1 = 33 \text{ mM}$$
$$[Na^+]_1 = (100 + 33) = 133 \text{ mM}$$
$$[Cl^-]_2 = (100 - 33) = 67 \text{ mM}$$
$$[Na^+]_2 = (100 - 33) = 67 \text{ mM}$$

These values are also given in Fig. 10.1A. Note that all the equations and conditions are obeyed. The G-D potential produced then may be calculated by substituting into Equations 10.7 and 10.8:

$$E_{Na} = \frac{-61 \text{ mV}}{+1} \log \frac{133 \text{ mM}}{67 \text{ mM}} = -18 \text{ mV} \quad (10.10)$$

and

$$E_{Cl} = -\frac{-61 \text{ mV}}{-1} \log \frac{33 \text{ mM}}{67 \text{ mM}} = -18 \text{ mV} \quad (10.11)$$

Hence, $E_{Na} = E_{Cl}$ (Equation 10.4). That is, the two diffusion potentials are equal in magnitude and of the same sign. The PD across the membrane is -18 mV; side 1 containing the protein is negative. Therefore, relative permeability of the membrane to Na^+ and Cl^- is irrelevant. The equivalent circuit for this example at equilibrium is given in Fig. 10.1B.

VI. OSMOTIC CONSIDERATIONS

We should note that, at equilibrium, the sum of Na^+ and Cl^- on side 1 (166 mM) is greater than that on side 2 (134 mM). In addition, there is 100 mM protein on side 1. Thus, the total osmotic concentration on side 1 is 266 mOsm (milliosmolar), compared to 134 mOsm on side 2. Therefore, there is a large osmotic gradient between the two sides. Water moves from side 2 to side 1 (i.e. water accompanies the net movement of Na^+ and Cl^-) until the hydrostatic pressure head buildup is sufficient to oppose further net movement of water. As expected, the biological cell swells when a G-D equilibrium is allowed to develop following a blockade of active ion transport for long periods.

The total osmotic concentration, [osm], on each side, at equilibrium, may be summarized as follows:

$$[osm]_1 = [Na^+]_1 + [Cl^-]_1 + [protein]_1 \quad (10.12)$$

$$[osm]_2 = [Na^+]_2 + [Cl^-]_2 \quad (10.13)$$

Substitution gives:

$$[osm]_1 = 133 \text{ mM} + 33 \text{ mM} + 100 \text{ mM} = 266 \text{ mM}$$

$$[osm]_2 = 67 \text{ mM} + 67 \text{ mM} = 134 \text{ mM}$$

The osmotic pressure (Π, in atm) of each solution is equal to the osmotic concentration in osmol/L (C) times the osmotic coefficient (i) times the gas constant (R, 0.082 L·atm/mol·K) times the absolute temperature (T, in °K)

$$\Pi = iCRT \quad (10.14)$$

where C is the number of osmoles per liter of solution. In the example depicted in Fig. 10.1, a hydrostatic pressure of 3.17 atm would need to be applied to side 1 to prevent this compartment from gaining water from side 2 (at 20°C and assuming $i = 1.0$)

$$
\begin{aligned}
\Pi &= i\Delta CRT \\
&= (1.0)(266\ \text{mM} - 134\ \text{mM})\left(0.082\frac{\text{L}\cdot\text{atm}}{\text{mol}\cdot\text{K}}\right) \\
&\quad \times (273+20)\ \text{K} \\
&= \left(0.132\frac{\text{mol}}{\text{L}}\right)\left(0.082\frac{\text{L}\cdot\text{atm}}{\text{mol}\cdot\text{K}}\right)(293\ \text{K}) \\
&= 3.17\ \text{atm}
\end{aligned}
\tag{10.15}
$$

The situation illustrated in Fig. 10.1 is actually more complex because the net water movement into side 1 acts to dilute the ion concentrations building up there and, therefore, a true G-D equilibrium can become established only if the net water movement is stopped, i.e. by allowing an osmotic pressure gradient to develop by making side 1 a closed, or rigid, system. Otherwise, theoretically all of the water and NaCl eventually would move out of side 2.

The example of a G-D equilibrium in Fig. 10.1 could have been illustrated using another salt, such as KCl, instead of NaCl, or two or more salts.

The extra osmotic pressure in side 1 (or inside a cell) produced by the presence of the negatively-charged proteins and other impermeant large charged molecules is known as the *colloid osmotic pressure* (COP). The COP is also important for water movement across the capillary wall, which separates the blood plasma (containing impermeant proteins) and the interstitial fluid (ISF). At the arterial end of the capillary, the intracapillary hydrostatic blood pressure exceeds the COP, so water moves out of the capillary into ISF space. At the venous end, the COP exceeds the capillary hydrostatic pressure, so water moves into the capillary. In the mid-region of the capillary, the two pressures are about equal and there is no net water flow. Thus, there is a circulation of fluid distributed along the length of the capillary and this idea is generally known as the *Starling hypothesis* (Davson, 1964; Sperelakis, 2001).

BIBLIOGRAPHY

Davson, H. (1964). *A Textbook of General Physiology* (3rd ed.). Boston: Little, Brown.

Sperelakis, N. (1995). *Electrogenesis of Biopotentials*. New York: Kluwer Publishing Co.

Sperelakis, N. (2001). Gibbs–Donnan equilibrium potentials. In *Cell Physiology Sourcebook* (3rd ed.). San Diego: Chapt 15. Academic Press.

Chapter 11

Mechanisms of Carrier-Mediated Transport: Facilitated Diffusion, Cotransport and Countertransport

Steven M. Grassl

Chapter Outline

I. SUMMARY

This chapter describes the functional properties of carrier-mediated transport mechanisms present in the cellular plasma membrane. The functional properties defining facilitated diffusion, cotransport and countertransport are considered with regard to the thermodynamic constraints imposed by primary and secondary active transport as well as passive transport. A stepwise kinetic model is described for each mechanism illustrating the substrate concentration dependence of the rate of transport and differences in the rate limiting steps accounting for transport. The functional properties of facilitated diffusion, cotransport and countertransport are further considered with regard to competitive and non-competitive inhibition, stoichiometric coupling and electrogenic transport. The structure–function relationship of prototypical membrane proteins mediating facilitated diffusion, cotransport and countertransport is briefly considered.

II. INTRODUCTION

The selective and regulated passage of ions and non-electrolytes across the cell membrane is an essential component of cellular homeostasis. The maintenance of cell pH and volume and the accumulation of nutrients for protein synthesis and cell metabolism are physiological processes that depend on membrane transport for cells to thrive. Cell membranes are composed of phospholipids organized as a bilayer (5 nm) of two closely opposed leaflets separating the intracellular from the extracellular space. The hydrophobic properties of phospholipids make the cell membrane an impermeable barrier excluding the transfer of hydrophilic solutes that are either charged (anions and cations) or uncharged (non-electrolytes). The selective passage of hydrophilic solutes across the hydrophobic barrier, a physiological property known as *membrane permeability*, is mediated by the presence of membrane transport proteins that span the phospholipid bilayer. Transport proteins may be functionally subdivided into channels, pumps and carriers according to differences in the mechanism mediating ion and non-electrolyte transport. This chapter describes the mechanisms of *carrier-mediated transport*, which include *facilitated diffusion*, *cotransport* and *countertransport*.

III. ELECTROCHEMICAL POTENTIAL

Transport mechanisms may be distinguished thermodynamically according to their ability to mediate active or passive transport. *Active transport* is defined as movement of a solute from a region of low electrochemical potential on one side of the cell membrane to a region of higher electrochemical potential on the opposite side. *Passive*

Cell Physiology Sourcebook. DOI: 10.1016/B978-0-12-387738-3.00011-1

transport is defined as movement of a solute from a region of high electrochemical potential on one side of the cell membrane to a region of lower electrochemical potential on the opposite side. The *electrochemical potential* of a solute is the partial molar free energy of the solute or the potential to do work when a difference in electrochemical potential exists across the cell membrane. The electrochemical potential of a solute on either side of the cell membrane is a function of the solute activity (or concentration in dilute solution), the solute charge and valence and the electrical potential. The difference in electrochemical potential, therefore, reflects the magnitude of the difference in transmembrane solute concentration and the difference in transmembrane voltage factored by the charge and valence of the solute. Notably, for solutes without charge, such as non-electrolytes, solute free energy is neither increased nor decreased by electrical potential and only the chemical potential of the solute is considered. Thus, the electrochemical or chemical potential difference of a solute across the cell membrane may be considered a driving force acting on solute transport. In the absence of an electrochemical potential difference or a driving force for solute transport, transport mechanisms that are passive mediate equal solute transport in the forward and reverse direction across the membrane resulting in no net transport. For anions and cations, this would occur when the chemical and electrical driving forces acting on solute transport are equal and opposite in direction across the membrane such that the net driving force is zero. For non-electrolytes, this would occur in the absence of a solute concentration gradient where transmembrane solute concentrations are equal. In both instances where no net transport occurs, the ion and non-electrolyte are at electrochemical equilibrium with the driving forces acting on the transported solutes. Where an electrochemical potential difference for a solute exists across the cell membrane, the direction of net solute transport by a passive transport mechanism will depend on the direction and magnitude of the chemical and/or electrical driving forces acting on the solute. The chemical and electrical potential difference of a charged solute or ion may occur as opposing driving forces of unequal magnitude, with the direction of net solute transport determined by the direction of the larger driving force. In no instance would a passive transport mechanism mediate net transport of a charged solute in a direction across the cell membrane that opposed both the chemical and electrical driving forces acting on the ion. The same limitation holds for net transport of non-electrolytes in a direction that opposes the chemical driving force acting on the solute.

Active transport mechanisms may be distinguished from passive transport mechanisms by the ability to generate and maintain an electrochemical or chemical potential difference for ions and non-electrolytes across the cell membrane. This requires net transfer of ions or non-electrolytes across the membrane in a direction that is opposed by the prevailing electrical gradient and/or chemical concentration gradients as driving forces acting on the transported solutes. To perform the work of moving solutes "uphill" against an electrical gradient and/or a chemical concentration gradient, active transport mechanisms require energy. The source of energy driving active transport is the hydrolysis of ATP. The direct or indirect coupling of active transport to ATP hydrolysis distinguishes *primary* active transport from *secondary* active transport. Primary active transport mechanisms, such as the ion translocating ATPases or pumps, are directly coupled to ATP hydrolysis and thermodynamically transduce the energy released upon ATP hydrolysis to the energy stored in the formation of an ion electrochemical potential difference. Secondary active transport mechanisms, such as *cotransporters* and *countertransporters*, are indirectly coupled to ATP hydrolysis and thermodynamically transduce the energy from one solute electrochemical potential difference to the energy stored in the formation of a second solute electrochemical potential difference. The indirect coupling of secondary active transport to ATP hydrolysis arises from the intermediate formation and ATP dependence of the solute electrochemical potential difference that drives secondary active transport.

IV. CARRIER-MEDIATED TRANSPORT MECHANISMS

IVA. Facilitated Diffusion

Facilitated diffusion or *uniport* is the simplest form of carrier-mediated transport and results in the transfer of large hydrophilic molecules (sugars, amino acids, nucleotides and organic acids and bases) across the cell membrane. Transport by facilitated diffusion is passive and reversible, with the direction of net transport into or out of the cell determined by the direction of the electrochemical potential difference of the transported solute. Net transport by facilitated diffusion may continue in either direction until the solute is at equilibrium with the electrical and/or chemical driving forces acting on the solute. At equilibrium, facilitated diffusion of a solute occurs equally in both directions resulting in no net transport. The transport mechanism mediating facilitated diffusion may be modeled as shown in Fig. 11.1. The two main features of the transport mechanism are an association and dissociation of the transported solute with the transport protein and a change in the conformation of the transport protein which makes the occupied or unoccupied site of solute interaction accessible from either side of the membrane (Fig. 11.1A). The transport mechanism may be considered in greater detail as a four-step process (Fig. 11.1B). First, solute S associates with the transport protein C facing side

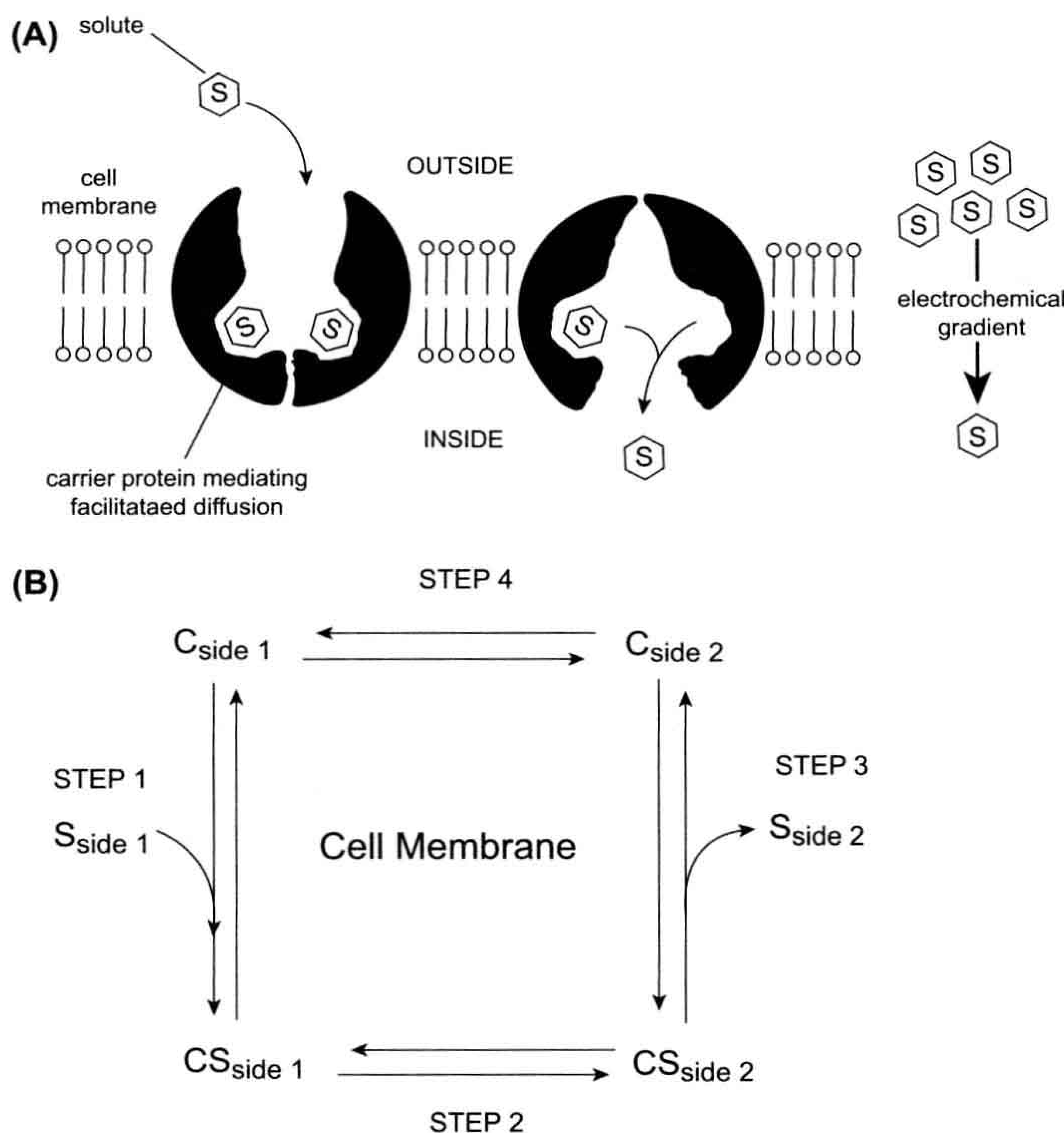


FIGURE 11.1 Conceptual and kinetic model of facilitated diffusion.

1 (labeled "outside" in the figure) to form a solute–carrier complex SC. Second, the solute–carrier complex undergoes a conformational change that reorients the solute–carrier complex to face side 2 (labeled "inside" in the figure). Third, the solute dissociates with the transport protein on side 2. Fourth, the unoccupied carrier undergoes a second conformational change to reorient the solute association site to face side 1. Net solute transport from side 1 to side 2 occurs when an unoccupied solute association site is reoriented from side 2 to side 1. However, as the solute concentration on side 2 increases, net solute transport from side 1 to side 2 decreases because a greater proportion of the unoccupied carrier becomes associated with solute on side 2 and undergoes reorientation moving solute to side 1. When the solute concentrations on side 1 and side 2 are equal, no net solute transport will occur because the occupancy and reorientation of the carrier will be equal at both sides of the membrane. A principal feature of facilitated diffusion illustrated by the model is the interaction with solutes exclusively at one side of the membrane or the other but never at both sides simultaneously. This functional property of facilitated diffusion invokes the need for a conformational change in the protein, alternately orienting the solute association site from side to side across the membrane. Each step in the process is reversible and is linked to the preceding and succeeding step by rate constants defining the rate of solute association and dissociation on either side of the membrane and the rate of conformational change for transporter reorientation in either direction when associated with or without solute. In general, the rate of solute association and dissociation with the transporter occurs more rapidly than the rates of conformational change. Furthermore, the conformational change reorienting the sidedness of the transporter occurs at a faster rate for the solute-occupied transporter than for the solute-unoccupied transporter. The relative slowness of the rate constant for the conformational change reorienting the solute-unoccupied transporter (step 4) makes it the rate-limiting step in the process of facilitated diffusion.

The *unidirectional rate* of solute transport across the cell membrane mediated by facilitated diffusion is dependent on the solute concentration at the side where transport originates. This is analogous to the substrate concentration

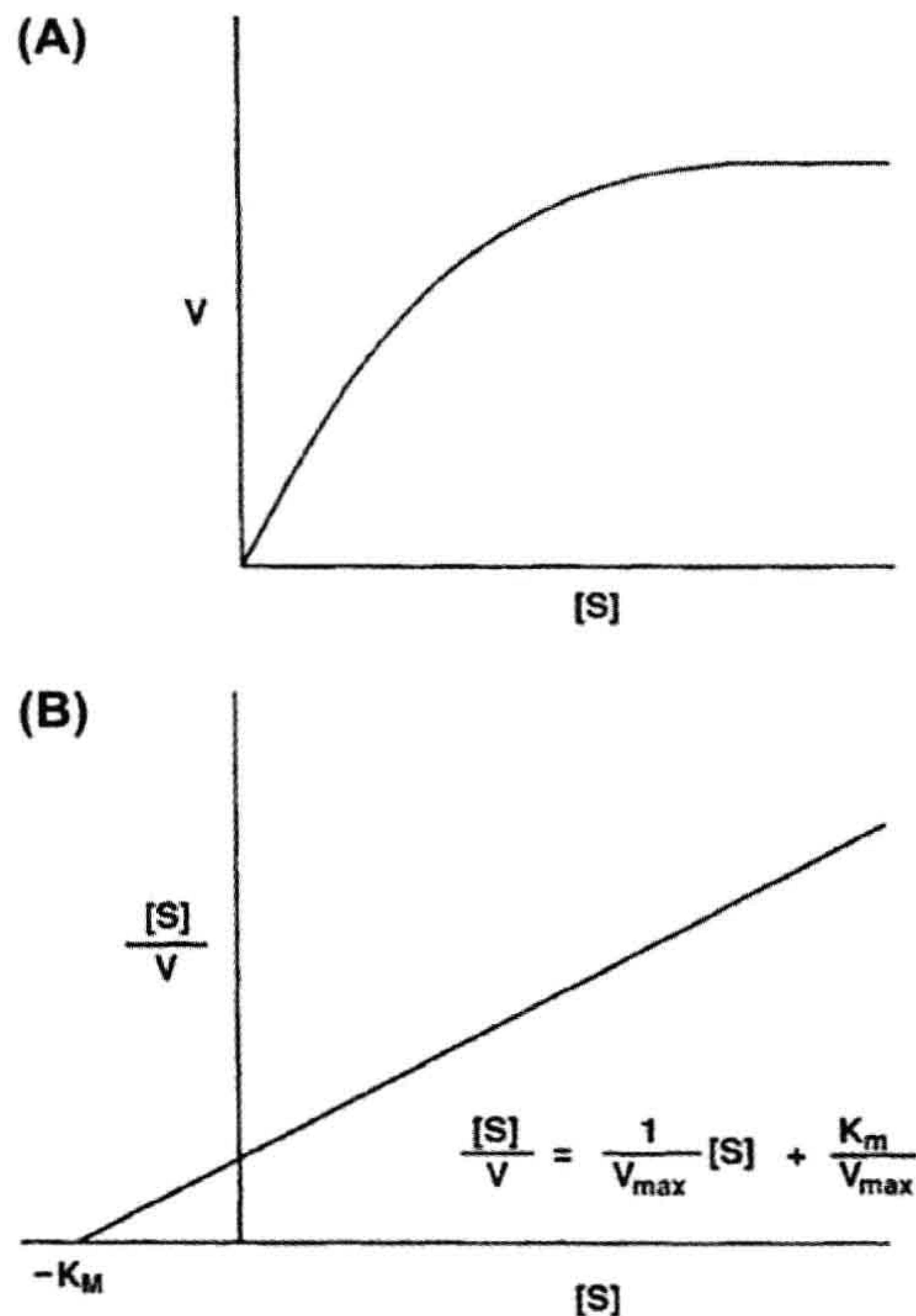


FIGURE 11.2 Relationship of solute transport rate (V) to solute concentration [S].

dependence of the rate of product formation mediated by an enzyme. As shown in Fig. 11.2, at low solute concentrations the rate of solute transport increases linearly with solute concentration and, as solute concentration increases further, the rate of solute transport increases less and less as it approaches a maximum value at high solute concentrations (Fig. 11.2A). The relationship of the unidirectional solute transport rate to solute concentration shown in Fig. 11.2 is described mathematically by an equation analogous to the Michaelis–Menten equation from enzyme kinetics:

$$V = \frac{[S]V_{max}}{K_m + [S]} \tag{11.1}$$

where V is determined experimentally as the initial rate of solute transport, [S] is the solute concentration, V_{max} is the maximal rate of solute transport and K_m is a constant described by the solute concentration where V is one-half the V_{max}. The validity of using the Michaelis–Menten equation in a kinetic analysis of facilitated diffusion requires experimental conditions in which the rate of solute transport reflects solute transport only in one direction. Accordingly, initial rates of solute transport across the cell membrane are measured in the absence of a significant solute concentration on one side of the membrane. The Michaelis–Menten equation may be rearranged to obtain a linear relation as shown in Fig. 11.2B, where the kinetic parameters K_m and V_{max} are the x-intercept and 1/slope, respectively. The kinetic parameters of solute transport are functional properties that characterize different facilitated diffusion mechanisms as well as transport of different solutes by the same facilitated diffusion mechanism. The K_m value characterizes the affinity of solute association–dissociation with the transporter such that a lower or higher K_m value reflects a greater or lesser affinity, respectively. The accuracy of the K_m value as a measure of solute affinity is further dependent on initial rate determinations performed at solute concentrations both above and below the K_m value. The V_{max} value is a measure of the number of transporters present in the membrane and the time required for a transporter to undergo one complete transport cycle or turnover. The maximum velocity of transport occurs when solute association and dissociation with the transporter are not rate-limiting steps in the transport process or when the transporter is saturated. Under these conditions, the maximal velocity of solute transport is only as fast as the rate-limiting step in the transport process, which is the conformational change of the solute dissociated transporter.

The facilitated diffusion of a solute may be inhibited in the presence of other solutes that interact with, but are not necessarily transported by, the same transporter. The nature of interaction of the inhibitor with the transporter may be assessed by observing the effect of the inhibitor on the kinetic parameters characterizing the transport mechanism. An effect of the inhibitor to decrease the maximal velocity of solute transport, without an effect on the K_m value of the solute, characterizes non-competitive inhibition. Non-competitive inhibition is not reversed by increasing the concentration of the transported solute and therefore results from an interaction of the inhibitor with both the solute-associated and -dissociated transporter at a second site that does not interact with the transported solute. An effect of the inhibitor to increase the apparent K_m value of the solute, without an effect on the maximal velocity of transport, characterizes competitive inhibition. Competitive inhibition is reversed by increasing the concentration of the transported solute and, therefore, results from an interaction of the inhibitor with only the solute-dissociated transporter at the same site that interacts with the transported solute.

The same facilitated diffusion mechanism may mediate the transport of multiple solutes that share common chemical and physical determinants, such as negatively-charged carboxyl groups or positively-charged amino groups. The nature of these chemical determinants and their spatial position in the solute molecule permits recognition

and interaction with the solute association site of the transport protein. The solute specificity of a facilitated diffusion mechanism is a functional property of the transporter characterized by solute-specific differences in the kinetic parameters of solute transport. A rank order of the relative affinity of the transporter for different solutes may be compiled by determination of the K_m values for multiple solutes transported by the same mechanism. The transporter is more highly specific for solutes with the lowest K_m values and less specific for solutes with the highest K_m values. However, solutes with higher affinity for the transporter do not necessarily have a greater maximal velocity of transport than solutes with a lower affinity. A comparison of the relative affinities and maximal velocities of solute transport determined experimentally further suggests which solutes are most likely to be transported in a physiological setting where multiple solutes are present at different concentrations.

The kinetic parameters characterizing solute transport by facilitated diffusion may differ depending on the direction of unidirectional solute transport. The K_m value as a measure of solute affinity for transport may be larger or smaller for solute transport mediated in one direction across the cell membrane when compared to the K_m value for solute transport in the reverse direction. However, the kinetic asymmetry of facilitated diffusion is subject to a thermodynamic limitation which requires the product of all the rate constants associated with the stepwise transport in the inward and outward direction be equal. Accordingly, a directional asymmetry in the K_m value of solute transport must be matched by a corresponding asymmetry in the maximal velocity of transport such that the ratio of V_{max} to K_m for transport in either direction is equal. Thus, a kinetic asymmetry of solute transport results from an increase or decrease of both kinetic parameters where an increased or decreased affinity for solute is matched by a corresponding decrease or increase in maximal velocity of transport, respectively.

In contrast to non-electrolytes, the facilitated diffusion of charged solutes, such as organic anions and cations, is *electrogenic* and results in the net transfer of charge in the direction of net solute transport across the membrane. As a consequence of mediating net charge transfer across the membrane, the facilitated diffusion of charged solutes will increase or decrease the electrical potential difference across the membrane depending on the sign and magnitude of the solute charge and on the direction of net transport. As a further consequence of mediating net charge transfer, the rate and direction of electrogenic solute transport by facilitated diffusion is sensitive to membrane potential, which must be considered as an additional driving force acting on electrogenic solute transport. This results from the voltage sensitivity of at least one step in the transport process mediating the facilitated diffusion of charged solutes. A voltage-dependent increase or decrease in the kinetic parameters of electrogenic solute transport may indicate an effect of voltage on the affinity of the transporter for the charged solute (K_m) and/or on the conformational change reorienting the solute-associated or -dissociated transporter (V_{max}).

Facilitated diffusion mechanisms are present in the membranes of all cells and many different mechanisms exist in the same membrane of a single cell. The common features of these different facilitated diffusion mechanisms include: (1) their presence as integral membrane proteins spanning the lipid bilayer; (2) a broad or narrow range of substrate specificity; (3) inhibition by physiological and non-physiological solute analogs; (4) solute saturation conforming to Michaelis–Menten kinetics; and (5) evidence of an alternate side-to-side reorientation of the solute association site. Whereas solute transport via channels and facilitated diffusion are both mediated and passive, sharing the common functional properties of inhibition and saturation, other functional criteria distinguish these two forms of transport. In contrast to solute transport by facilitated diffusion, most channels mediate transport of inorganic anions or cations and have a solute specificity limited by the physical size of the ion. Channels are accessible for solute association from both sides of the membrane simultaneously and mediate transport at a rate orders of magnitude faster than facilitated diffusion, which is rate limited by the relatively slow conformational changes reorienting the sidedness of the carrier. In further contrast to solute transport mediated by facilitated diffusion, the rate-limiting step in ion transport mediated by channels is the association and dissociation of an ion with the channel, not the actual ion translocation through the channel.

The functional properties of solute transport mediated by facilitated diffusion have been characterized in detail for many different cell- and solute-specific transport mechanisms. A major question remaining in the study of facilitated diffusion is the structure–function relationship of the transport protein. This requires the identification of individual membrane proteins as the structural correlates of transport activities of different facilitated diffusion mechanisms present in the cell membrane. A limited number of transport proteins have been identified by a difficult biochemical process involving detergent solubilization of the cell membrane, affinity purification of the protein and functional reconstitution of transport activity to prove its identity. The identification of many more transport proteins has been recently achieved using the techniques of molecular biology to clone the genes coding for these membrane proteins. The molecular cloning of a transporter gene begins with the preparation of mRNA from a tissue rich in a functionally well-characterized transporter activity. A high transporter activity suggests an abundance of transporter protein as well as transporter mRNA from

which the protein is translated. The total mRNA is reverse transcribed to complementary DNA and individual cDNA molecules are inserted into plasmids or minichromosomes used to transform *Escherichia coli* bacterial cells. The transformed *E. coli* are grown to form a library of thousands of colonies or clones each reproducing a different cDNA plasmid. The library serves to renew and amplify a continuous source of cDNA plasmids which may be screened for possible hybridization with short DNA sequences thought to code for various regions of the transporter gene. To assess the function of the putative transporter gene, mRNA may be reverse transcribed from the plasmid cDNA of positively identified clones and injected into frog oocytes for translation or expression of the corresponding protein. The identity of the transporter gene is proven by the mRNA-dependent expression of a transport activity with functional properties similar to those characterizing transport activity in the tissue of origin. The transporter gene may also be identified without prescreening the library for hybridization by systematically preparing mRNA from the entire cDNA library and assessing functional expression of transport activity. The cDNA plasmid coding for the transporter gene may be sequenced to obtain the deduced amino acid sequence, or primary structure, and molecular weight of the transport protein. The deduced amino acid sequence of the transport protein may be further analyzed for the presence and concentration of hydrophobic amino acids at multiple sites along the peptide chain. Typically, 10–12 regions of relative hydrophobicity may be identified in the transporter amino acid sequence and are thought to represent the putative transmembrane domains of the transport protein. The location of the transmembrane domains further suggests the size and topological location of intracellular and extracellular peptide loops between the transmembrane domains as well as the amino and carboxy termini of the transport protein. A topological model depicting the putative secondary protein structure of a mammalian facilitated diffusion transporter for glucose is shown in Fig. 11.3. Further analysis of the amino acid sequence for the presence of asparagine in the extracellular peptide loops may suggest potential sites for N-linked glycosylation of the transport protein. Likewise, the presence of serine, threonine and tyrosine in consensus phosphorylation sites in intracellular peptide loops suggests that the phosphorylation state of the transporter may regulate its activity.

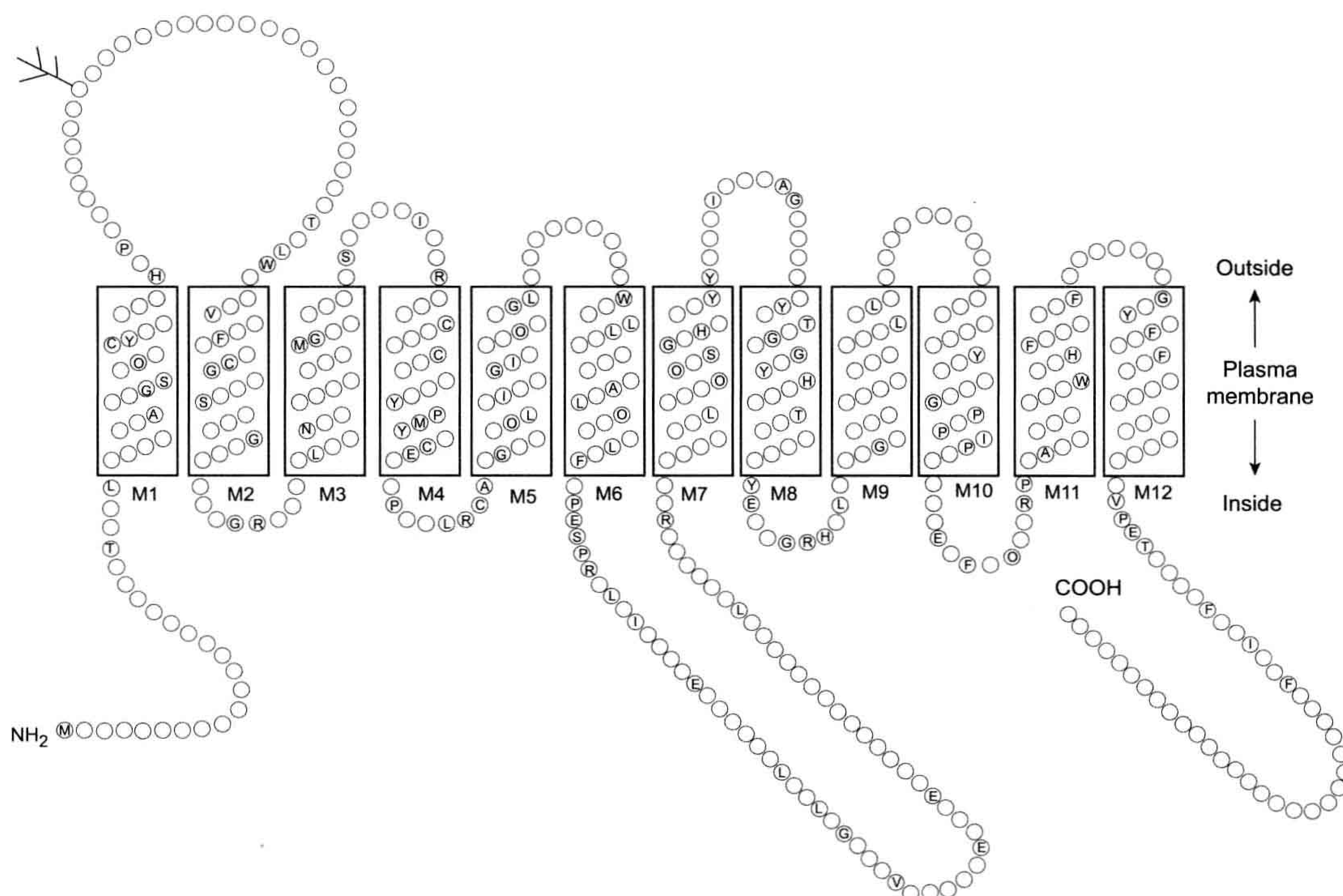


FIGURE 11.3 Consensus structure of the mammalian D-glucose carriers. *(Reprinted with permission from Bell, G.I. (1991). Molecular defects in diabetes mellitus. Diabetes. 40, 413–422. Copyright © 1991 American Diabetes Association.)*

The structure–function relationship of the protein mediating facilitated diffusion may be investigated upon identification of the primary structure or amino acid sequence of the protein. Mutant transport proteins may be engineered with single or multiple amino acid deletions, or with substitutions in the transmembrane domains, the intra- and extracellular peptide loops between transmembrane domains and in the amino and carboxy termini. The functional properties of the engineered transport proteins may be assessed by heterologous expression in frog oocytes or cell cultures and compared to the native protein. Thus, the individual amino acids or amino acid sequences important for solute recognition by, and interaction with, the transport protein may be identified as well as those involved in the conformational change reorienting the solute-associated and -dissociated transporter. The mutational analysis of transporter function is limited by null mutations which result in the expression of non-functional transport proteins or in the absence of expression.

The information obtained from identifying and cloning the gene coding for a facilitated diffusion mechanism may be used to survey the distribution of the same or related transport proteins in different tissues and in different cells within the same tissue. Oligonucleotide probes may be made from short sequences of the transporter gene and used to detect the presence of complementary transporter sequences in cDNA from tissue libraries, in mRNA prepared from multiple tissues, or by in situ hybridization of mRNA in thin tissue slices. The positively identified mRNA or cDNA may be isolated and sequenced for comparison with the deduced amino acid sequences present in different tissues. Such a comparison will indicate either complete sequence identity, suggesting the presence of the same transport protein in different tissues, or will indicate minor tissue-specific differences in sequence, suggesting that different isoforms of the same protein exist in different tissues. Thus, the facilitated diffusion of glucose in different tissues is mediated by at least five different isoforms of the same transport protein as shown in Table 11.1. The high degree of sequence conservation among different isoforms of the same transport protein is consistent with a common solute specificity and mechanism of solute translocation across the membrane. The minor tissue-specific differences in sequence distinguishing isoforms of the same protein presumably reflect a unique variation in the functional properties and/or regulation of the transporter serving the specialized physiology of the tissue.

TABLE 11.1 D–glucose Carrier Isoforms

Designation	Function
GLUT1	Basal uptake in placenta, brain, kidney, colon
GLUT2	Primarily found in transport in liver cells
GLUT3	Basal uptake in the brain
GLUT4	Insulin-stimulated uptake in the skeletal muscle, cardiac muscle and adipose tissue
GLUT5	Absorption in small intestines

IVB. Cotransport

Cotransport, or *symport*, is a form of secondary active transport that mediates net transfer of a solute across the cell membrane from a place of low solute electrochemical potential to a place of higher solute electrochemical potential. The source of energy driving secondary active transport of a solute against its electrochemical potential difference arises from a coupling to the transport of a second solute from a place of higher electrochemical potential to a place of lower electrochemical potential. The coupling of the driving solute to the driven solute results in the cotransport of both solutes in the same direction across the cell membrane. Cotransport mechanisms are reversible and will mediate net transport either into or out of the cell until the opposing electrochemical potential differences of the driven solute and the driving solute become equal across the cell membrane. The direction of net transport mediated by a cotransport mechanism may be determined by either solute, depending on which solute has the larger driving force and by the direction of the larger driving force across the membrane. The mechanism mediating cotransport may be modeled as a six-step process as shown in Fig. 11.4: (1) an association of solutes S and (2) A with the carrier facing side 1 to form the SCA solute-carrier complex; (3) a conformational change reorienting the SCA carrier complex to face side 2; (4) dissociation of A and (5) S with the carrier facing side 2; and (6) a second conformational change reorienting the solute-free carrier to face side 1. The cotransport mechanism may be further modeled in three different variations depending on the solute interaction with the carrier. Solute interaction with the carrier may be *random*, with either solute associating and dissociating first with the carrier, or solute association–dissociation may be *ordered*, in which either one of the solutes must associate or dissociate first with the carrier before the second solute may associate or dissociate. Note, as shown in Fig. 11.4 for an ordered interaction of solute with the carrier, the second solute associating with the carrier at one side of the membrane is the first solute to dissociate with the carrier at the opposite side. Neither form of the partially associated carrier SC or AC may undergo a conformational change reorienting the sidedness of the partially associated carrier and therefore the cotransport mechanism mediates only the coupled transport of both solutes but does not mediate the uncoupled transport of

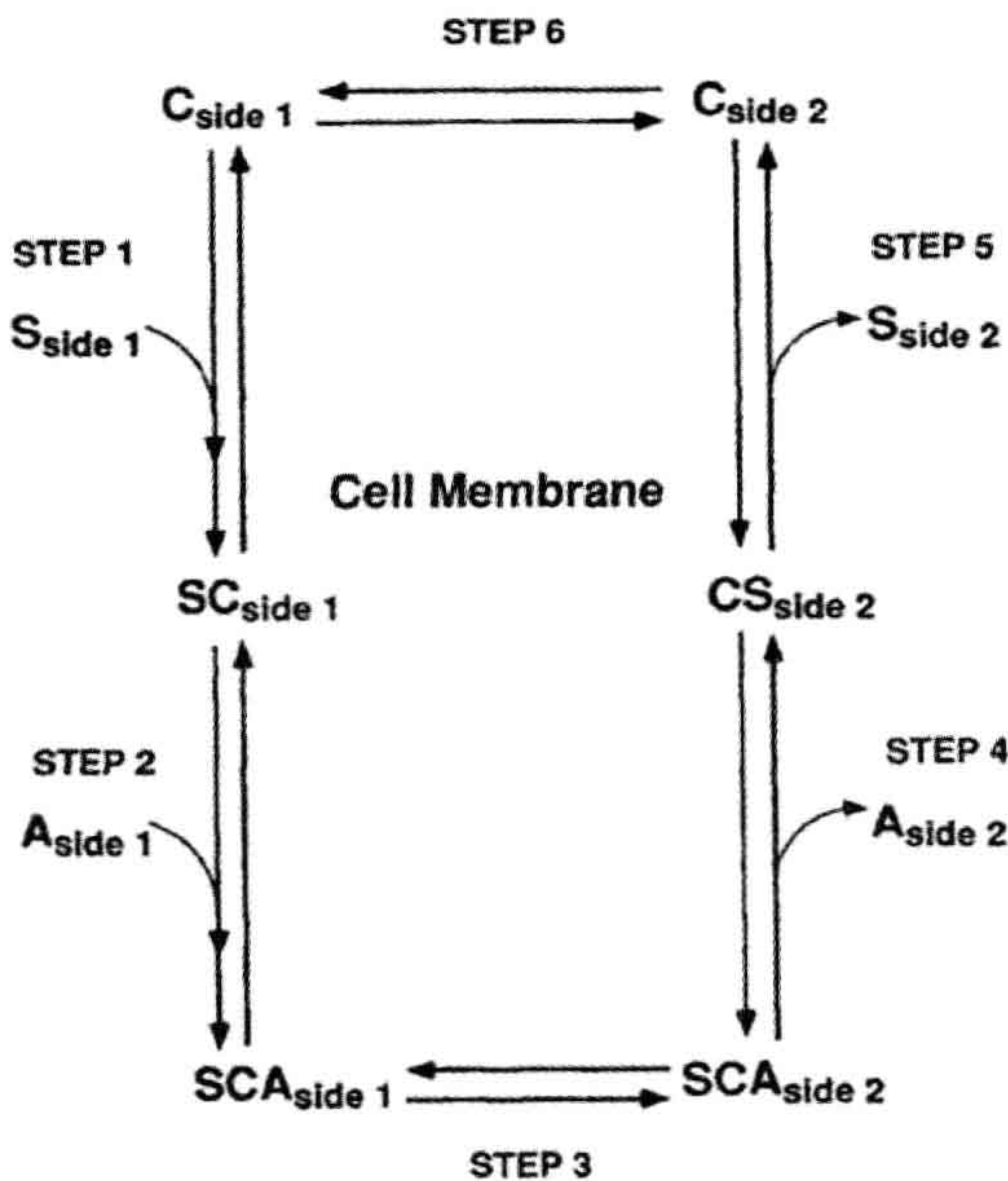


FIGURE 11.4 Kinetic model of cotransport.

either solute. Each step in the cotransport process is reversible and is linked to the preceding and succeeding step by rate constants defining the rate of solute association and dissociation on either side of the membrane and by the rate of conformational change for carrier reorientation in either direction when associated with or without both solutes. Similar to facilitated diffusion, solute association–dissociation with the carrier occurs faster than the conformational change reorienting the sidedness of the carrier and the rate-limiting step in the cotransport process is the conformational change reorienting the solute-dissociated carrier.

The unidirectional rate of solute transport across the cell membrane mediated by a cotransporter is dependent on the concentration of both solutes at the side where cotransport originates. When either solute concentration is constant, the cotransport rate of the second solute will approach a maximum value with increasing solute concentration and the saturation kinetics of the cotransport process may be analyzed using the Michaelis–Menten equation to describe the kinetic parameters K_m and V_{max} for each solute. The random or ordered association of cotransported solutes with the transporter may be determined from the mutual dependence of kinetic parameters on cotransported solute concentrations. As shown in Fig. 11.4, where the association of solutes S and A with the cotransporter at side 1 is ordered and S associates first, solute A will have the same maximal rate of transport (V_{max}) when determined at different concentrations of solute S. However, the K_m value for solute A will decrease when determined at increasing concentrations of solute S, indicating the initial association of S with the cotransporter effectively increases its affinity for association with solute A. In contrast, the V_{max} and K_m values characterizing transport of solute S, the first solute to associate with the cotransporter, will both vary when determined at different solute A concentrations. An increase in solute A concentration will increase the maximal rate of solute S through the cotransport mechanism and will also effectively increase its affinity for solute S as reflected by a decreased K_m value. The effect of solute A on the maximal rate of solute S transport arises from its ordered association, as the second solute, to form the SCA solute–carrier complex, which may then transfer both solutes across the membrane. Thus, where a mutual solute concentration dependence of the kinetic parameters characterizing the transport of both solutes is determined for a cotransport mechanism, an ordered association–dissociation of solutes with the cotransporter may be indicated and a random association–dissociation of solutes may be excluded.

The cotransport of a solute may be inhibited by the presence of other solutes that interact with, but are not necessarily transported by, the same cotransport mechanism. Similar to facilitated diffusion, the competitive or non-competitive nature of inhibitor interaction with the co-transport mechanism may be assessed by determining the effect of the inhibitor on the kinetic parameters characterizing transport of both solutes by the cotransport mechanism.

The same cotransport mechanism may mediate transport of multiple solutes that share common chemical and physical determinants. Similar to facilitated diffusion, the solute specificity of a cotransport mechanism may be characterized by determining the kinetic parameters of different solutes transported by the same cotransport mechanism. A comparison of the relative affinities and maximal velocities of solute transport determined experimentally will suggest the relative magnitudes of solute transport mediated by the cotransporter in vivo.

The cotransport mechanism modeled in Fig. 11.4 will be at a steady state and mediate equal transport of S and A in both directions across the membrane when the driving forces acting on the cotransported solutes are equal and opposite. This would occur when the transmembrane concentration difference or gradient of S in one direction is equal to the transmembrane concentration difference or gradient of A in the opposition direction. At the steady state, where no net solute transport occurs, the solute driving forces will be in thermodynamic equilibrium with each other and the transmembrane concentration ratios of S and A may be described by:

$$\frac{S_1}{S_2} = \frac{A_2}{A_1} \tag{11.2}$$

Thus, in the presence of a 10-fold concentration gradient of S, a cotransport mechanism coupling the transport of S and A across the membrane may generate up to, but not exceeding, a 10-fold concentration gradient of A. Because the cotransport mechanism effectively transduces the energy stored in the concentration gradient of S to the energy stored in the concentration gradient of A, it would be thermodynamically impossible for the cotransport mechanism to generate more than a 10-fold concentration gradient of A.

The cotransport process modeled in Fig. 11.4 describes the coupled transport of one molecule of S together with one molecule of A, or an S to A *coupling ratio* of 1:1. However, the stoichiometric coupling of solutes mediated by a cotransport mechanism may exceed unity, resulting in cotransport of unequal amounts of solute. This may be modeled kinetically as an extension of Fig. 11.4 to include an extra step of solute association on side 1 prior to carrier reorientation to face side 2 and an extra step of solute dissociation on side 2 prior to carrier reorientation to face side 1. The kinetic parameter (K_m) characterizing the solute affinity of a cotransport mechanism must account for each additional solute association or dissociation at mutually exclusive sites in the cotransport protein. The thermodynamic equilibrium of solute driving forces defining the steady state, where no net solute transport occurs, is profoundly affected by the stoichiometric coupling of solutes by the cotransport mechanism. Where the stoichiometric coupling is other than 1:1, the solute driving forces will be in thermodynamic equilibrium at transmembrane solute concentration ratios raised to the power of their respective coupling coefficient as shown.

$$\left(\frac{S_1}{S_2}\right)^s = \left(\frac{A_2}{A_1}\right)^a \qquad (11.3)$$

The coupling coefficients s and a are the number of S and A molecules that must associate with the carrier before a conformational change may occur reorienting the sidedness of the solute–carrier complex. The stoichiometric coupling of solutes by a cotransport mechanism is significant because, in the presence of a 10-fold concentration gradient of S, a cotransport mechanism coupling the transport of two molecules of S to one molecule of A may generate a 100-fold concentration gradient of A.

Similar to the facilitated diffusion of charged solutes, cotransport mechanisms may also be electrogenic and mediate net charge transfer across the membrane in the direction of net solute transport. In general, the electrogenicity of cotransport mechanisms arises from the transport of the inorganic cation sodium coupled to the transport of organic and inorganic anions and cations, such as negatively-charged amino acids, mono- and dicarboxylic acids, sulfate and phosphate or positively-charged amino acids and amines as well as non-electrolytes, such as sugars. In most instances, the coupled transport of charged or uncharged solutes with the transport of sodium results in the net transfer of positive charge in the direction of net solute transport into the cell. The positive electrogenicity of solute transport mediated by a sodium-coupled cotransport mechanism will tend to depolarize the cell membrane potential difference and results from at least one voltage-sensitive step in the process accounting for electrogenic cotransport. A voltage-dependent increase or decrease in the kinetic parameters characterizing an electrogenic cotransport mechanism may indicate an effect of voltage on the affinity of the cotransporter for either or both solutes (K_m) and/or on the conformational change reorienting the solute-associated or -dissociated transporter (V_{max}). However, because the rate-limiting step in the process accounting for cotransport is the conformational change reorienting the solute-dissociated transporter, a voltage-dependent increase in the rate of cotransport must result from the voltage sensitivity and acceleration of at least this step in the cotransport process. The voltage sensitivity of an electrogenic cotransport mechanism makes the voltage difference across the cell membrane a driving force acting on solute cotransport. Thus, the rate, magnitude and direction of solute transport mediated by an electrogenic sodium cotransport mechanism is determined by two driving forces including the transmembrane voltage difference as well as the transmembrane sodium and solute concentration gradients. An electrogenic cotransport mechanism will be at steady state and mediate equal solute transport in both directions across the membrane when the electrical and chemical forces driving cotransport are at equilibrium across the membrane. For an uncharged solute S, and a charged solute A, the driving forces may be related by:

$$RT \ln\left(\frac{S_1}{S_2}\right) = -RT \ln\left(\frac{A_2}{A_1}\right) + zF(\psi_2 - \psi_1) \qquad (11.4)$$

where R is the universal gas constant, T is absolute temperature, z is the valence of A, F is the Faraday constant, and $(\psi_2 - \psi_1)$ is the transmembrane voltage difference. Thus, in the presence of a 10-fold sodium concentration gradient and a transmembrane voltage difference of 60 mV, a cotransport mechanism mediating 1:1 Na-to-solute transport may generate a 100-fold uncharged solute gradient.

The functional properties of solute transport mediated by sodium-dependent cotransport mechanisms have been characterized in detail for many different cell- and solute-specific cotransporters. Like facilitated diffusion, a major question remaining in the study of sodium-dependent cotransport mechanisms is the structure–function relationship of the cotransport protein. Several sodium-dependent

cotransport proteins been identified using a molecular biological approach to clone the genes coding for these membrane proteins. The primary structure of sodium-dependent cotransport proteins suggests topological features similar to membrane proteins mediating facilitated diffusion. These include the presence of 10–12 putative transmembrane domains, the location of extracellular N-linked glycosylation sites and the location of intracellular phosphorylation sites. The structure–function relationship of the sodium–glucose cotransport protein SGLT1 has been investigated in mutagenesis studies of the cotransport protein. Intestinal glucose–galactose malabsorption is a genetic disorder resulting from multiple mutations localized in two putative transmembrane domains of SGLT1. Individual functional analysis of the different mutant SGLT1 proteins suggested the identity and location of specific amino acids that participate in the association of glucose and the inhibitor phloridzin with the cotransport protein as well as the amino acids involved in the conformational changes reorienting the solute-dissociated cotransporter. In addition to identifying the amino acids affecting the functional properties of the cotransport protein, mutagenesis studies of SGLT1 further suggest the identity and location of amino acids that participate in the membrane trafficking of cotransport proteins from its site of synthesis in the cell interior to the cell surface.

Three isoforms of the sodium–glucose cotransporter have been identified (SGLT1, SGLT2, SGLT3) and are distinguished by a high (SGLT1) or low (SGLT2, SGLT3) affinity for glucose, by differences in substrate specificity and by tissue distribution in small intestine (SGLT1) and/or renal proximal tubule (SGLT1, SGLT2). The structural basis for isoform-specific differences in function may be assessed by functional studies of *chimeric proteins* composed of different peptide sequence combinations from different isoforms. Thus, the chimera composed of the amino terminus including the initial seven transmembrane domains of SGLT3 and the final five transmembrane domains including the carboxy terminus of SGLT1 is observed to have the substrate specificity of the SGLT1 isoform. Accordingly, this finding indicates that the topological location of the glucose association site in the sodium–glucose cotransport protein is in a region of the peptide sequence extending from the eighth transmembrane domain to the carboxy terminus.

IVC. Countertransport

Countertransport, or *antiport*, is a form of secondary active transport which, like cotransport, may also mediate net transfer of a solute across the cell membrane in a direction against the electrochemical potential gradient of the solute. The energy driving countertransport of a solute against its electrochemical potential difference arises from a coupling to the transport of a second solute moving across the cell membrane from a place of higher electrochemical potential to a place of lower electrochemical potential. In contrast to cotransport, the coupling of the driving solute to the driven solute in countertransport results in transport of solutes in the opposite direction across the cell membrane. Thus, countertransporters mediate the exchange of intracellular and extracellular solutes across the cell membrane. Countertransport mechanisms are reversible and will mediate net transport either into or out of the cell until the opposing electrochemical potential differences of the driven solute and the driving solute become equal across the cell membrane. The direction of net transport mediated by a countertransport mechanism may be determined by either solute, depending on which solute has the larger driving force and the direction of the larger driving force across the membrane. The mechanism mediating countertransport may be modeled as a six-step process as shown in Fig. 11.5. The principal features of the countertransport mechanism are (1, 4) a mutually exclusive association of either solute S or A with the carrier facing side 1 or side 2 to form the SC or AC carrier complex, (2, 5) a conformational change reorienting the sidedness of the solute–carrier complex and (3, 6) a dissociation of solute with carrier on the opposite side of the membrane. In contrast to the process of facilitated diffusion or cotransport, the solute-free carrier does not undergo a conformational change in countertransport and only the SC or AC carrier complex may undergo

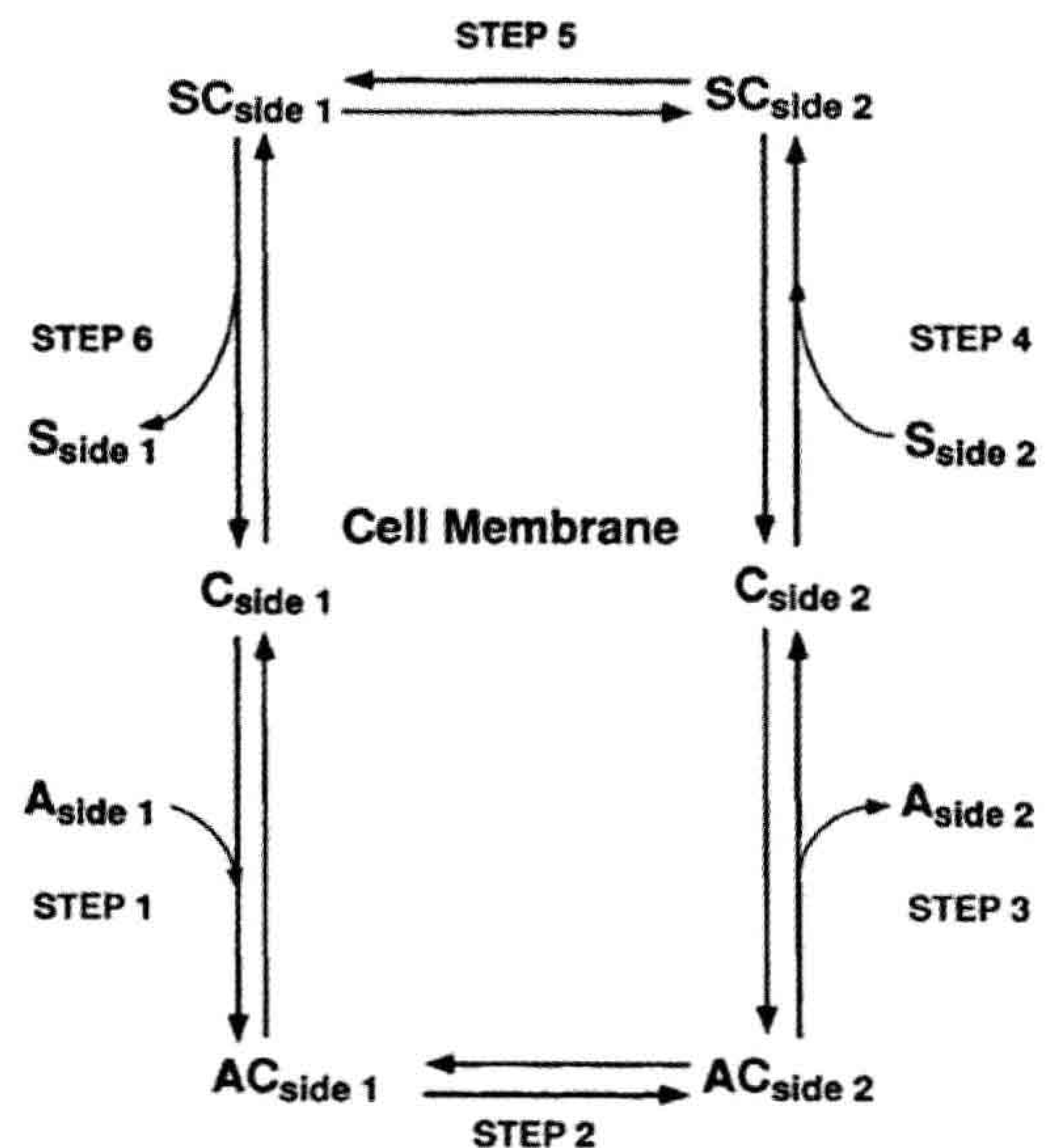


FIGURE 11.5 Kinetic model of countertransport.

a conformational change reorienting the sided access of carrier to solute. It is the absence of a conformational change reorienting the sidedness of the solute-free carrier that explicitly distinguishes countertransport from facilitated diffusion and confers the ability to mediate net solute transport against an electrochemical potential difference. Countertransport mechanisms may mediate the exchange of the same solutes (*homoexchange*) or different solutes (*heteroexchange*) and will mediate net solute transport only when exchanging different solutes. Each step describing the process of countertransport is reversible and is linked to the preceding and succeeding step by rate constants defining the rate of solute association and dissociation on either side of the membrane and by the rate of conformational change reorienting the sidedness of the solute-associated carrier. The conformational change reorienting the sidedness of the solute-associated carrier occurs more slowly than solute association–dissociation with the carrier and is considered the rate-limiting step in the countertransport process.

The unidirectional rate of solute transport across the cell membrane mediated by a countertransport mechanism depends on the concentration of both solutes at opposite sides of the membrane. When either solute concentration is constant, the countertransport rate of the second solute will approach a maximum value with increasing solute concentration and the saturation kinetics of the countertransport process may be analyzed using the Michaelis–Menten equation to obtain the kinetic parameters K_m and V_{max} for each of the exchanged solutes. The solute concentration dependence of the rate of solute transport by countertransport may be different for transport occurring into or out of the cell. A kinetic asymmetry of solute transport mediated by countertransport results from a difference in the apparent affinity (K_m) for solute at either side of the membrane and not from a difference in the maximal rate of transport (V_{max}). This limitation in kinetic asymmetry is a unique property of countertransport arising from the inability of the solute-dissociated carrier to reorient across the membrane. While kinetic asymmetry is not a property of all countertransport mechanisms, the asymmetry in solute transport mediated by a countertransporter is observed to occur for all possible combinations of solutes exchanged by the countertransport mechanism.

The countertransport of a solute may be inhibited by the presence of other solutes that interact with, but are not necessarily transported by, the same countertransport mechanism. The competitive or non-competitive nature of interaction of the inhibitor with the countertransport mechanism may be assessed by determining the effect of the inhibitor on the kinetic parameters characterizing transport of exchanged solutes by the countertransport mechanism. The same countertransport mechanism may mediate the exchange of multiple pairs of solutes that share common chemical and physical determinants. Countertransport mechanisms may be broadly categorized as either anion or cation exchange mechanisms, such as the chloride–bicarbonate countertransporter present in kidney, intestine and red blood cells or the ubiquitous pH-regulating sodium–proton countertransporter. The solute specificity of a countertransport mechanism may be characterized by determining the kinetic parameters of different solutes proven to be countertransported by the same mechanism. A comparison of the relative affinities and maximal velocities of solute transport determined experimentally will suggest the relative magnitudes of solute transport mediated by the countertransporter in vivo.

The countertransport mechanism modeled in Fig. 11.5 will be at a steady state and mediate equal transport of S and A from side 1 to side 2 and from side 2 to side 1, when the driving forces acting on solutes S and A are equal. For countertransport, this will occur when the transmembrane concentration differences of S and A are equal and in the same direction across the cell membrane. At the steady state, where no net solute transport occurs, the solute driving forces will be in thermodynamic equilibrium with each other and the transmembrane concentration ratios of S and A resulting from countertransport may be described by:

$$\frac{S_1}{S_2} = \frac{A_1}{A_2} \tag{11.5}$$

Thus, in the presence of a 10-fold concentration gradient of S, a countertransport mechanism coupling exchange of S for A may generate up to, but not exceeding, a 10-fold concentration gradient of A. Because the countertransport mechanism effectively transduces the energy stored in a 10-fold concentration gradient of S to the energy stored in a concentration gradient of A, it would be thermodynamically impossible for the countertransport mechanism to generate more than a 10-fold concentration gradient of A. The important difference distinguishing cotransport and countertransport at the steady state is the sidedness or direction of solute concentration gradients across the membrane. Cotransport is at steady state when solute concentration gradients are of equal magnitude but in opposite direction across the membrane, whereas countertransport is at steady state when solute concentration gradients are of equal magnitude and in the same direction across the membrane.

The countertransport process modeled in Fig. 11.5 describes the coupled exchange of one molecule of S for one molecule of A, or an S-to-A coupling ratio of 1:1. Whereas most countertransport mechanisms mediate the coupled exchange of single solutes, the stoichiometric coupling of solutes may exceed unity, resulting in unequal amounts of solute transported to opposite sides of the membrane. This may be modeled kinetically as an extension of Fig. 11.5 to include an extra step of solute

association on side 1 prior to carrier reorientation to face side 2 and by an extra step of solute dissociation on side 2. The kinetic parameter (K_m) characterizing the solute affinity of a countertransport mechanism must account for each additional solute association–dissociation at mutually exclusive sites in the countertransport protein. Similar to cotransport, the thermodynamic equilibrium of solute driving forces coupled by the countertransport mechanism and defining the steady state is profoundly affected by the stoichiometric coupling of solutes. Where the stoichiometric coupling of solutes by a countertransport mechanism is other than 1:1, the solute driving force will be in thermodynamic equilibrium at transmembrane solute concentration ratios raised to the power of their respective coupling coefficient as shown.

$$\left(\frac{S_1}{S_2}\right)^s = \left(\frac{A_1}{A_2}\right)^a \tag{11.6}$$

Thus, in the presence of a 10-fold concentration gradient of S, a countertransport mechanism coupling the exchange of two molecules of S for one molecule of A may generate a 100-fold concentration gradient of A in the same direction across the membrane.

Most countertransport mechanisms mediate the coupled exchange of single solutes with the same positive or negative charge and same valence and are therefore electroneutral and do not mediate net charge transfer across the membrane. However, when countertransport mechanisms mediate the coupled exchange of solutes of the same charge but different valence or mediate an unequal stoichiometric coupling of solutes of the same charge, a net charge transfer will occur across the cell membrane. Thus, the countertransport mechanism mediating sodium–calcium exchange across the cell membrane couples the influx of three sodium ions to the efflux of one calcium ion, resulting in a net transfer of positive charge into the cell. The positive electrogenicity of the sodium–calcium countertransport mechanism will tend to depolarize the cell membrane potential and results from the voltage sensitivity of at least one step in the process describing a complete sodium–calcium countertransport cycle. A voltage-dependent increase or decrease in the kinetic parameters characterizing an electrogenic countertransport mechanism would suggest an effect of membrane potential on the solute affinities of the countertransporter (K_m) and/or on the conformational change reorienting the sidedness of the solute-associated countertransporter (V_{max}). Because the conformational change reorienting the countertransporter is the rate-limiting step in the process accounting for electrogenic countertransport, a voltage-dependent increase in the rate of countertransport must result from an acceleration of at least this step. The voltage sensitivity of an electrogenic countertransport mechanism makes the cell membrane potential difference a driving force acting on solute countertransport. Thus, the rate, magnitude and direction of electrogenic countertransport of solutes across the membrane is determined by the transmembrane voltage difference in addition to the transmembrane differences in solute concentration for both solutes coupled by the countertransport mechanism. An electrogenic countertransport mechanism will be at steady state and mediate equal solute transport in both directions across the membrane when the electrical and chemical forces driving countertransport are at equilibrium. For the 1:1 exchange of charged solutes S and A with valences z_S and z_A, respectively, the driving forces may be related by:

$$RT\ln\left(\frac{S_1}{S_2}\right) = -RT\ln\left(\frac{A_1}{A_2}\right) + (z_S - z_A)F(\psi_2 - \psi_1) \tag{11.7}$$

The electrogenicity of a countertransport mechanism may arise from the exchange of solutes with the same charge and valence but with an unequal stoichiometric coupling. In this instance the driving forces acting on electrogenic countertransport must be factored by the stoichiometric coupling coefficients s and a for solutes S and A, respectively, and may be related by:

$$RT\ln\left(\frac{S_1}{S_2}\right)^s = -RT\ln\left(\frac{A_1}{A_2}\right)^a + (sz_S - sz_A)F(\psi_2 - \psi_1) \tag{11.8}$$

Thus, in the presence of a 10-fold sodium concentration gradient and a transmembrane voltage difference of 60 mV, an electrogenic countertransport mechanism mediating the 3:1 exchange of sodium and calcium ions, respectively, may generate a maximum calcium concentration gradient of 10 000-fold across the cell membrane.

The functional properties of solute transport mediated by countertransport mechanisms have been characterized in detail for many different cell- and solute-specific countertransporters. Like facilitated diffusion and cotransport, the structure–function relation of membrane proteins mediating countertransport continues to be an important question under study. The techniques of modern molecular biology have resulted in the cloning of several genes coding for countertransport proteins. Analysis of the deduced amino acid sequences of countertransport proteins suggests topological features similar to membrane proteins mediating facilitated diffusion and cotransport, including the presence of 10–12 putative transmembrane domains, the location of extracellular N-linked glycosylation sites and the location of intracellular phosphorylation sites. Low-resolution electron density maps of the red blood cell chloride–bicarbonate exchange protein have been obtained from two-dimensional crystals of the countertransport protein studied by electron microscopy. The membrane

domain of the countertransport protein exists as a dimeric structure with three electron-dense regions in each monomer. Within each monomer, the configuration of electron densities suggests two closely apposed peptide structures which are spatially separated from a third structure by a peptide domain existing in two different conformations.

The structure–function relationship of the anion exchange protein AE1 has been investigated in mutagenesis studies of the countertransport protein. The functional significance of single amino acids or domains of multiple amino acids on the interaction with transport inhibitors at the extracellular side of AE1 has been studied to determine the nature and topological location of amino acids involved in substrate interaction and translocation. These mutagenesis studies involving both the deletion and substitution of amino acids indicate several positively charged lysines at the surface of AE1 influence, and are necessary for, substrate recognition by the countertransport protein. The genes coding for three anion exchange proteins (AE1, AE2, AE3) have been identified and their gene products may be functionally distinguished by differences in inhibitor sensitivity and by the intracellular pH dependence of anion exchange activity. Multiple species-specific isoforms of the AE1 gene have been identified and the predominant sites of expression are the erythropoietic tissues and the acid-secreting cells of the renal cortical collecting duct. In contrast, AE2 gene expression occurs more widely in epithelial and non-epithelial tissues and AE3 gene expression is predominant in brain and heart. The putative transmembrane amino acid sequences of AE1, AE2 and AE3 are approximately 70% identical. The aligning portion of the N-terminal cytoplasmic domains of AE1 and AE2 are only 30% identical, with little or no corresponding sequence identity among AE1, AE2 or AE3 at the N-terminus. The observed amino acid sequence identity in the putative transmembrane domains of AE1, AE2 and AE3 is consistent with the common functional properties of the three anion exchange proteins. The divergent amino acid sequences noted in the N-terminal regions suggest possible cell- and tissue-specific differences in the regulation of anion exchange activity and/or in the intracellular sorting and membrane targeting of anion exchange proteins. Mutations in the human AE1 gene in the form of nucleotide deletions, insertions and substitutions result in inheritable diseases of the red blood cell which manifest multiple clinical phenotypes ranging from mild to severe. The single amino acid substitution characterizing mutant AE1 in Band 3 Memphis has essentially no effect on red blood cell anion exchange activity. However, the nine-amino-acid deletion characterizing AE1 in Southeast Asian ovalocytosis (SAO) results in a heterozygous genetic disorder of red blood cells with only half the normal complement of functional anion exchangers. Interestingly, the red blood cell membrane of SAO patients is more resistant to plasmodial invasion, a property that may confer a selective survival advantage against malarial infection and thereby perpetuate this genetic disorder.

BIBLIOGRAPHY

Alper, S. L. (1994). The band 3-related AE anion exchanger gene family. *Cell Physiol Biochem, 4*, 265–281.

Aronson, P. S. (1981). Identifying secondary active solute transport in epithelia. *Am J Physiol, 240*, F1–F11.

Heinz, E. (1978). *Mechanics and Energetics of Biological Transport.* New York: Springer-Verlag.

Heinz, E. (1981). *Electrical Potentials in Biological Membrane Transport.* New York: Springer-Verlag.

Naftalin, R. J. (2010). Reassessment of models of facilitated transport and cotransport. *J Membrane Biol, 234*, 75–112.

Neame, K. D., & Richards, T. G. (1972). *Elementary Kinetics of Membrane Carrier Transport.* Oxford: Blackwell Scientific.

Steel, A., & Hediger, M. (1998). The molecular physiology of sodium- and proton-coupled solute transporters. *News Physiol Sci, 13*, 123–131.

Stein, W. D. (1990). *Channels, Carriers and Pumps.* New York: Academic Press.

Chapter 12

Active Ion Transport by ATP-Driven Ion Pumps

Robert A. Farley

Chapter Outline

I. SUMMARY

P-type ATPases are the largest and most diverse of the ATP-dependent ion transporters in biology. They transport many different ions, metals and other substrates and are characterized by a similar structure and transport mechanism. Specific inhibitors of certain P-type ATPases are of clinical importance and the activity of the P-type ATPases is regulated at different levels by hormones and other physiologically important ligands and proteins. The crystal structures of several P-type ATPases have been determined and provide insight into many of the biochemical and pharmacological properties of this important class of transport proteins.

II. INTRODUCTION

Living cells are separated from their surroundings by lipid bilayers that limit the passive diffusion of water-soluble solutes and ions between the cytoplasm and the extracellular environment. In most instances, the concentrations of the solutes and ions are different inside and outside the cell and these concentration differences serve as thermodynamic driving forces that encourage movement of the solutes and ions across the lipid plasma membrane toward equilibrium distributions. Movement of the water-soluble solutes and ions across the impermeable lipid barrier is facilitated by membrane transport proteins that are embedded in the lipid membrane and which provide an aqueous pathway for these molecules to cross the barrier. It is often necessary for cells to maintain or establish concentration differences of ions or solutes across the cell membranes in order to sustain cellular life and this process necessarily involves moving the solutes or ions against the thermodynamic driving forces that favor equilibrium distributions. Movement of matter across cell membranes against electrochemical driving forces is called active transport and is facilitated by specialized membrane proteins that couple the thermodynamically unfavorable movement of the solute or ion to a chemical reaction that releases energy that can be captured by the transport protein. As long as the net change in free energy of the coupled reactions is negative, the active transport protein is able to catalyze the movement of the solutes and ions against their thermodynamic driving forces.

There are two broad classes of active transport proteins: primary active transport proteins and secondary active transport proteins. Primary active transport proteins are distinguished from secondary active transport proteins by the utilization of primary energy sources, such as light or chemical reactions, to drive solute or ion movement across cell membranes. The primary active transporters use energy from these sources by incorporating catalytic mechanisms driven by these energy sources into their structures.

Cell Physiology Sourcebook. DOI: 10.1016/B978-0-12-387738-3.00012-3

Secondary active transporters do not derive energy for transport from these primary energy sources but instead rely on energy stored in ion gradients established by primary active transporters to translocate solutes and ions. Most primary active transport proteins have been found to transport ions rather than water-soluble solutes and, therefore, these proteins are often called ion pumps. Although several different energy sources for ion pumps have been identified in the plant and animal kingdoms (Läuger, 1991), the most abundant and most diverse class of ion pumps utilize energy derived from the hydrolysis of ATP. This chapter is concerned with these ATP-driven ion pumps. Since these proteins derive energy for ion transport from ATP hydrolysis, they are also called ion-transporting ATPases.

III. CLASSES OF ATP-DRIVEN ION PUMPS

There are three main types of ATP-driven ion pumps: the F-type, the V-type and the P-type. The prototypical F-type ion pump is the mitochondrial F_0-F_1-ATP synthase. These proteins are multisubunit complexes containing an F_0 part, which serves as a proton transporter, and an F_1 part, which is associated with ATP hydrolysis or synthesis (Abrahams et al., 1994; Stock et al., 1999). In addition to being located in the inner mitochondrial membrane, F-type ion pumps are found in chloroplasts and bacteria. In mitochondria and chloroplasts, these proteins seem to function exclusively to synthesize ATP from ADP and P_i, with the energy for bond formation being provided by the dissipation of an H^+ gradient across the membrane through the F_0 part of the complex. Bacterial F-type ion pumps, however, can also operate in the reverse direction in which the hydrolysis of ATP releases energy that is utilized by the protein to create a proton gradient. V-type ATPases are found primarily in the membranes of intracellular vacuoles, but are also located in the plasma membranes of certain mammalian cells such as the osteoclasts and intercalated cells of the renal tubules. V-type ion pumps are structurally similar but not identical to the F-type pumps and they also actively transport protons using energy derived from ATP hydrolysis (Toei et al., 2010). The mechanism of both F-type and V-type ATPases is a rotary catalytic mechanism in which the F_0 part of the complex rotates with respect to the F_1 part, thereby coupling H^+ transport to ATP hydrolysis or synthesis. This mechanism has been the subject of several excellent reviews (Boyer, 1997; Nakamoto et al., 2008). The P-type ATPases differ from the F-type and the V-type in both structure and catalytic mechanism (Morth et al., 2011). P-type ATPases derive their names from the fact that during the catalytic cycle the γ phosphate from ATP is transferred to a conserved aspartate residue on the proteins to form a phosphoenzyme intermediate. P-type pumps are also structurally much less complex than the F-type or the V-type ATPases in that most of them are composed of a single polypeptide subunit. Two members of the P-type ATPase family, the Na^+,K^+-ATPase and the H^+,K^+-ATPase, however, also contain a second glycoprotein subunit. As shown in Fig. 12.1, the P-type ATPases are widely distributed throughout the plant and animal kingdoms, in both plasma membranes and intracellular membranes, and they catalyze the transport of many different monovalent or divalent cations, heavy metals, or phospholipids (Axelsen and Palmgren, 1998). Because of their critical importance in maintaining cell viability, the rest of this chapter will focus on P-type ion pump structures and transport mechanisms.

IV. THE ALBERS–POST MECHANISM OF ION TRANSPORT BY P-TYPE ION PUMPS

The Na^+,K^+-ATPase was the first P-type ATPase to be sufficiently well-characterized that a complete catalytic mechanism could be proposed. Although ATP hydrolysis was known for many years to be required for sodium transport out of mammalian cells, Jens Christian Skou was the first person to recognize that both of these activities were located on the same enzyme. For this and for his early contributions to characterize the mechanism of ATP-coupled ion transport by this enzyme, he shared the Nobel Prize in Chemistry in 1997 (Skou, 1998). Many investigators contributed to the elucidation of the mechanism of Na,K-ATPase (Glynn and Karlish, 1975) and the catalytic cycle that represents this mechanism is called the Albers–Post scheme in recognition of the important contributions of R. Wayne Albers and Robert Post. The Albers–Post scheme for Na^+,K^+-ATPase is shown in Fig. 12.2. A detailed account of the kinetic mechanism of the Na^+,K^+-ATPase has been published by Cantley (1981). Except for the identity of the transported ions, the Albers–Post scheme for Na,K-ATPase is generally accepted to represent the mechanism of ATP-coupled ion transport by all P-type ATPases.

In the Albers–Post scheme, the enzyme exists in two major conformations, E1 and E2. In the E1 conformation, the ion and ATP binding sites are accessible from the cytoplasmic side of the cell membrane and, in the E2 conformation, the ion binding sites are accessible from the non-cytoplasmic side of the membrane. Vectorial transport occurs as the ion binding sites are alternately exposed to the different sides of the membrane (alternating access mechanism) as the transporter undergoes conformational changes. ATP binds with high affinity ($K_d \approx 0.1-2\ \mu M$) to the E1 conformation. Cytoplasmic Na^+ also binds to the E1 conformation and activates ATP-dependent phosphorylation of the Na^+,K^+-ATPase hyperbolically with a K_M of approximately 8 mM. Phosphoenzyme formation from ATP in the presence of Na^+ also requires cytoplasmic Mg^{2+}. Na^+ is released to the outside of the cell from the E2

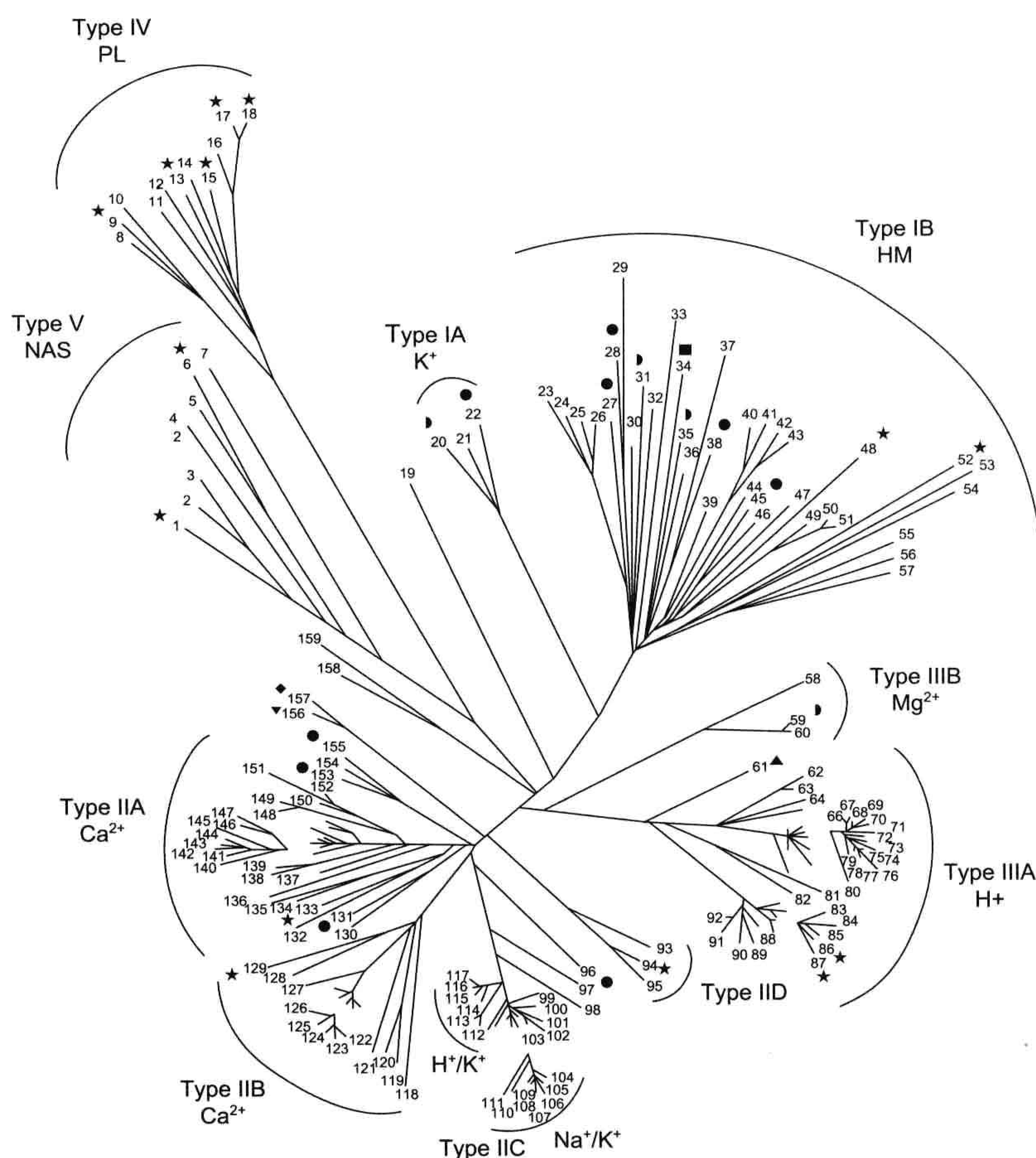


FIGURE 12.1 Phylogenetic tree for P-type ATPases. Based on 159 core amino acid sequences of P-type ATPases, the different transporters are grouped according to the substrates that are transported: *HM*, heavy metal substrates; *PL*, phospholipid substrates; *NAS*, no substrate yet determined. Type IIA and Type IIB Ca^{2+}-ATPases are PMCA and SERCA/SPCA types (see text for details). Numbers refer to the sequences used to construct the tree (Axelsen and Palmgren, 1998). *(Reproduced from Axelsen and Palmgren, 1998, with permission.)*

conformation, which has a low affinity for Na^+. Extracellular potassium binds with high affinity ($K_M \approx 0.1$ mM in the absence of sodium) to the same sites on E2 from which sodium was released and is released into the cytoplasm from the E1 conformation, which binds K^+ with low affinity. The ion binding sites on E1 are very specific for Na^+ and only Li^+ will substitute for Na^+ to catalyze some enzymatic reactions, whereas the ion binding sites on E2 will bind a number of monovalent cations in addition to K^+, including Rb^+, NH_4^+ and Cs^+, in a catalytically competent manner.

Transport of the different ions is sequential, with Na^+ being transported out of the cell before K^+ is transported into the cell. One molecule of ATP is hydrolyzed during a single turnover of the catalytic cycle and is coupled to the transport of three Na^+ ions out of the cell and two K^+ ions into the cell. This difference in charge transport stoichiometry generates an electrical potential difference across the cell membrane as three positive charges are moved to the outside of the cell and two positive charges are moved to the cytoplasm (De Weer et al., 1988). Measurement of ionic current carried by the Na^+,K^+-ATPase under different experimental conditions showed that current is associated with the movement of Na^+, but that transport of K^+ is electroneutral. This observation suggests that there is the equivalent of two negative charges in the ion binding sites of Na^+,K^+-ATPase and that these charges are neutralized by the binding of two monovalent cations.

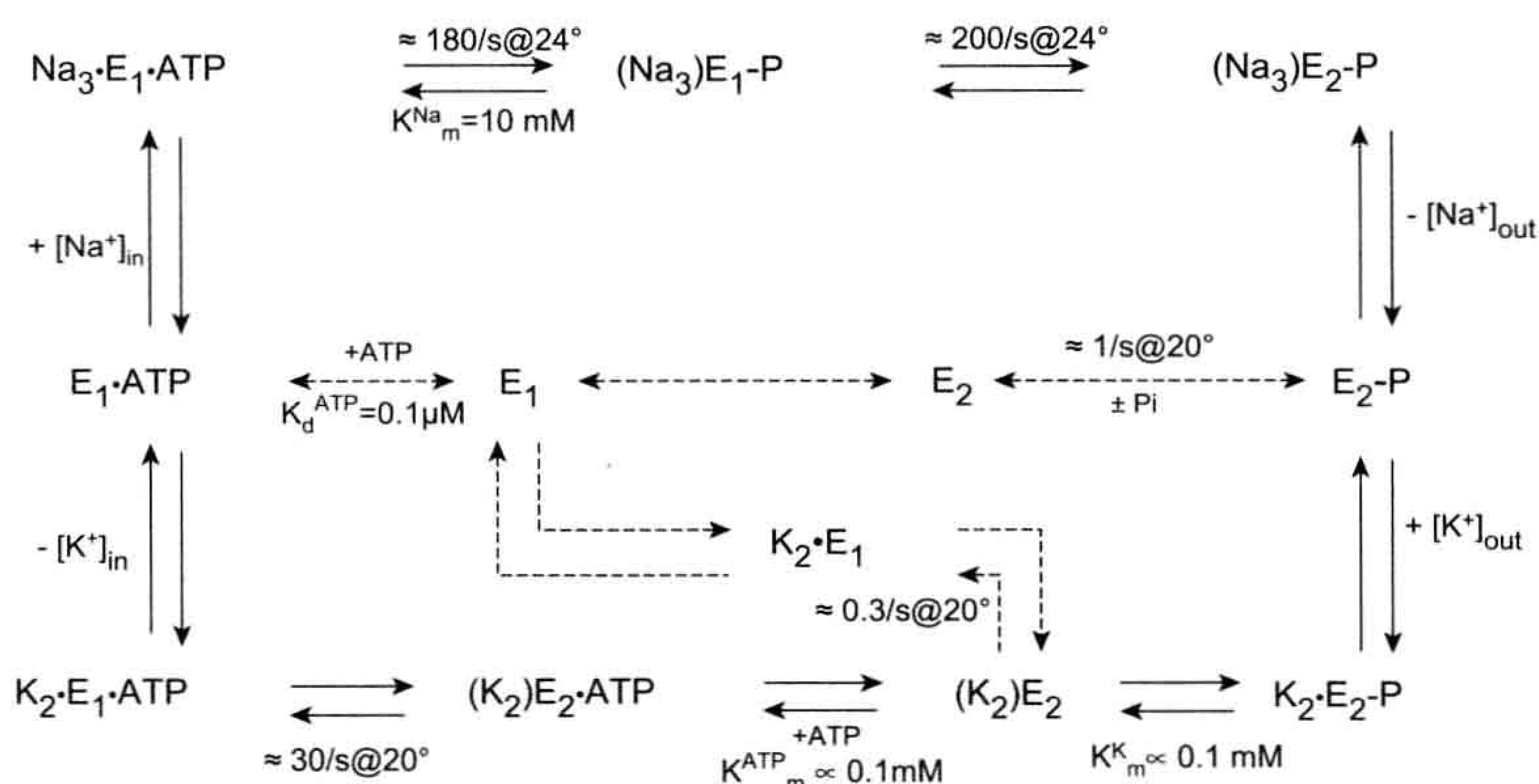


FIGURE 12.2 The Albers–Post scheme for ATP-dependent ion transport by the Na^+,K^+-ATPase. Solid arrows represent forward and reverse transitions between states of the enzyme that are populated under physiological conditions of turnover. Dashed arrows represent transitions between states that are not present under normal physiological conditions but which can be shown to exist under defined experimental conditions. Rate constants and K_d or K_m values are from Cantley (1981). Positive (+) and negative (−) signs correspond to binding and dissociation of ions from the protein. See text for a discussion of the mechanism.

During the transition between the E1 and the E2 conformational states, the transported ions are occluded within the structure of the protein. In the occluded state, the bound ions are not exchangeable with similar ions in either the cytoplasmic or non-cytoplasmic solutions. Occluded transported cations in P-type ATPases, representing an intermediate step during the transition between E1 and E2 states, were first suggested by Glynn and Hoffman, and by Robert Post and his coworkers, and were experimentally measured in Na^+,K^+-ATPase by Ian Glynn and Luis Beauge (Glynn and Karlish, (1990). Recently, crystal structures for several solute transporters have confirmed the existence of occluded states in all types of alternating access transport proteins (Shimamura et al., 2010; Weyand et al., 2010).

When cytoplasmic ATP, Mg^{2+} and Na^+ are bound, the γ phosphate of ATP is transferred from the bound nucleotide to an aspartate residue on the Na^+,K^+-ATPase, forming a covalent phosphoenzyme intermediate, and ADP is released into the cytoplasm. This aspartate residue is conserved in all P-type ATPases. The binding of K^+ to the E2 form of the enzyme catalyzes the hydrolysis of the phosphoenzyme intermediate, with the concurrent release of P_i and Mg^{2+} to the cytoplasm. Upon hydrolysis of the phosphoenzyme, potassium ions become occluded and the enzyme conformation changes from E2 to E1. This transition is very slow in the absence of cytoplasmic ATP ($k \approx 0.2–0.3\ s^{-1}$), but is accelerated more than a 100-fold by the binding of ATP with low affinity to the E2 conformation of the protein ($K_M > 1$ mM). Since normal cytoplasmic ATP concentrations are 2–5 mM, this transition is usually fast under physiological conditions.

In P-type ATPases other than Na^+,K^+-ATPase, the identity of the transported cations is different, but the essential catalytic mechanism is the same. For Ca^{2+}-ATPases, the transport stoichiometry is different for the different subfamilies (see below), with one or two Ca^{2+} ions transported out of the cytoplasm in exchange for one or two protons. In Ca^{2+} pumps where it has been measured, the transport stoichiometry is electrogenic and generates a voltage difference across the membrane. In the gastric H^+,K^+-ATPase, one proton is transported from the cytoplasm of the parietal cell and one K^+ is transported into the cell. In this protein, net transport is electroneutral.

Measurements of individual reaction steps in the Albers–Post cycle have been made under conditions that prevent progression of the pumps through the complete cycle. These partial reactions of the pumps have been very useful for the characterization of individual rates of the reaction steps and the interaction of different ions and ligands with the pumps. In vitro measurements like these have shown that every step in the mechanism is reversible, however, under physiological conditions of ion and ligand concentrations and pH, the pumps progress around the cycle shown in Fig. 12.2 in a clockwise direction. The thermodynamic basis for this directionality was provided by Pickart and Jencks (1984) for the sarcoplasmic reticulum Ca^{2+}-ATPase. After measuring all but one of the microscopic equilibrium constants in the Albers–Post scheme for the Ca^{2+}-pump, these investigators used the equilibrium constants to construct free energy diagrams for the Ca^{2+} transport cycle under standard conditions of 1 M reactant concentrations and under physiological conditions. Under physiological conditions in which active Ca^{2+} transport takes place, the Gibbs free energy changes (ΔG) are favorable for calcium binding from the cytoplasm and dissociation into the lumen of the sarcloplasmic reticulum, while ΔG for the other steps in the cycle are either balanced or slightly negative as the enzyme progresses in a clockwise direction through the cycle shown in Fig. 12.2.

V. STRUCTURES OF P-TYPE ION PUMPS

The nucleotide sequences of complete cDNA clones of both the sarcoplasmic Ca^{2+}-ATPase and the Na^+,K^+-ATPase were published in 1985 by the laboratories of Numa, MacLennan, and Lingrel. Soon thereafter, cDNA sequences of several P-type pumps from different organisms were published. Considerable effort prior to these accomplishments was made by many investigators using protein chemical methods and chemical modification of the proteins to identify amino acids that are important to the catalytic or transport functions of the different pumps, or are located in functionally important sites of the proteins. Photochemical, immunological and biochemical approaches were also used to determine the folding of the pump polypeptides through the cell membrane. After the amino acid sequences of the proteins were deduced from the cDNA sequences, these results could be mapped on the complete sequences of the different pumps and it was found that all P-type pumps contain several highly conserved amino acid sequences that are located in functionally important sites. Particularly highly conserved amino acids are found in the ATP binding sites of these proteins (Aravind et al., 1998) and, perhaps surprisingly given that different pumps transport different cations, many of the same amino acids are found at the ion binding sites in the different proteins (Morth et al., 2011). Extensive site-directed mutagenesis of Ca^{2+}-ATPase and Na^+,K^+-ATPase, together with heterologous expression of the mutant pumps in Xenopus oocytes, yeast or mammalian cells, confirmed the importance of many amino acids previously identified using protein chemical methods and identified additional amino acids that are important for ATP-coupled ion transport by these proteins. Amino acids that are important for specific functions of the pumps, such as ATP binding or hydrolysis, are often found in widely separated sequences of the polypeptides, indicating that the folding of the polypeptides is complex, bringing together these widely separated amino acids into specific functional sites.

The structural basis for active ion transport by the P-type ATPases was elevated to a new level in 2000 when the laboratory of Chikashi Toyoshima published the first atomic resolution structure of the sarcoplasmic reticulum Ca^{2+}-ATPase (Toyoshima et al., 2000). Since that time, crystal structures of the Ca^{2+}-ATPase in conformations that correspond to most of the catalytic intermediates in the Albers–Post cycle have been determined by several investigators. These structures provide an unprecedented opportunity to look into the structural basis for the activity of this ion pump (Moller et al., 2010). The Na^+,K^+-ATPase has also been crystallized and the overall three-dimensional structure of the catalytic α subunit of Na^+,K^+-ATPase is almost identical to that of the Ca^{2+}-ATPase, consistent with the expectation that all P-type ion pumps are composed of a similarly folded catalytic polypeptide (Morth et al., 2007; Shinoda et al., 2009). The structures of the Ca^{2+}-ATPase in the E1 conformation with bound Ca^{2+} ions and the Na^+,K^+-ATPase with bound K^+ ions are shown in Fig. 12.3.

The catalytic polypeptides of the P-type pumps are folded into both a membrane-embedded domain and three separate structural domains that are located in the cytoplasm of the cell. The N domain binds ATP, the P domain contains the conserved aspartate residue that is phosphorylated by ATP and the A domain contains a conserved TGES sequence that is involved in dephosphorylation of the phosphoenzyme. During ATP-coupled ion transport by the P-type ATPases, large rigid body movements of the N, P and A domains occur as ATP bound to the N domain is brought into position for transfer of the γ-phosphate to the aspartate residue in the P domain and the phosphoenzyme is subsequently hydrolyzed in a reaction that requires the TGES residues in the A domain. The movements of the cytoplasmic domains are transmitted to the transmembrane domain and shift the affinity of the ion binding sites located there between high affinity and low affinity to favor ion binding or release. Only a small amount of protein mass of the catalytic subunits is located on the non-cytoplasmic side of the membrane. In contrast, most of the mass of the β subunit of the Na^+,K^+-ATPase and H^+,K^+-ATPase is located on the extracellular side of the plasma membrane of cells in which these proteins are found. The transmembrane domains of the P-type pumps that have been crystallized consists of a bundle of 10 α–helices that are connected to the cytoplasmic domains of the proteins primarily through two long transmembrane α–helices that merge into the cytoplasmic domains. These connections between the membrane-embedded domain and the cytoplasmic domains provide the basis for the mechanical coupling of ATP hydrolysis to changes in the affinity of the ion binding sites for the transported cations. Amino acid sequence comparisons suggest that some members of the P-type ATPase family may contain fewer than 10 transmembrane helices. The structure of the Ca^{2+}-ATPase, shown in Fig. 12.3A, contains two Ca^{2+} ions bound near the middle of the transmembrane domain. In the crystal structure of Na^+,K^+-ATPase, shown in Fig. 12.3B, two bound K^+ ions are bound in the analogous location on the α subunit. The two K^+ ions presumably bind to the same sites where three Na^+ ions bind during sodium transport by the Na^+,K^+-ATPase, but the location of the third Na^+ site remains ambiguous. In both Ca^{2+}-ATPase and Na^+,K^+-ATPase, the bound cations are coordinated by both main chain carbonyl oxygen atoms and by amino acid side chains that contain oxygen atoms. Despite differences in the identity and charge of the bound cations, several of the amino acid side chains that coordinate the cations are identical in both Ca^{2+}-ATPase

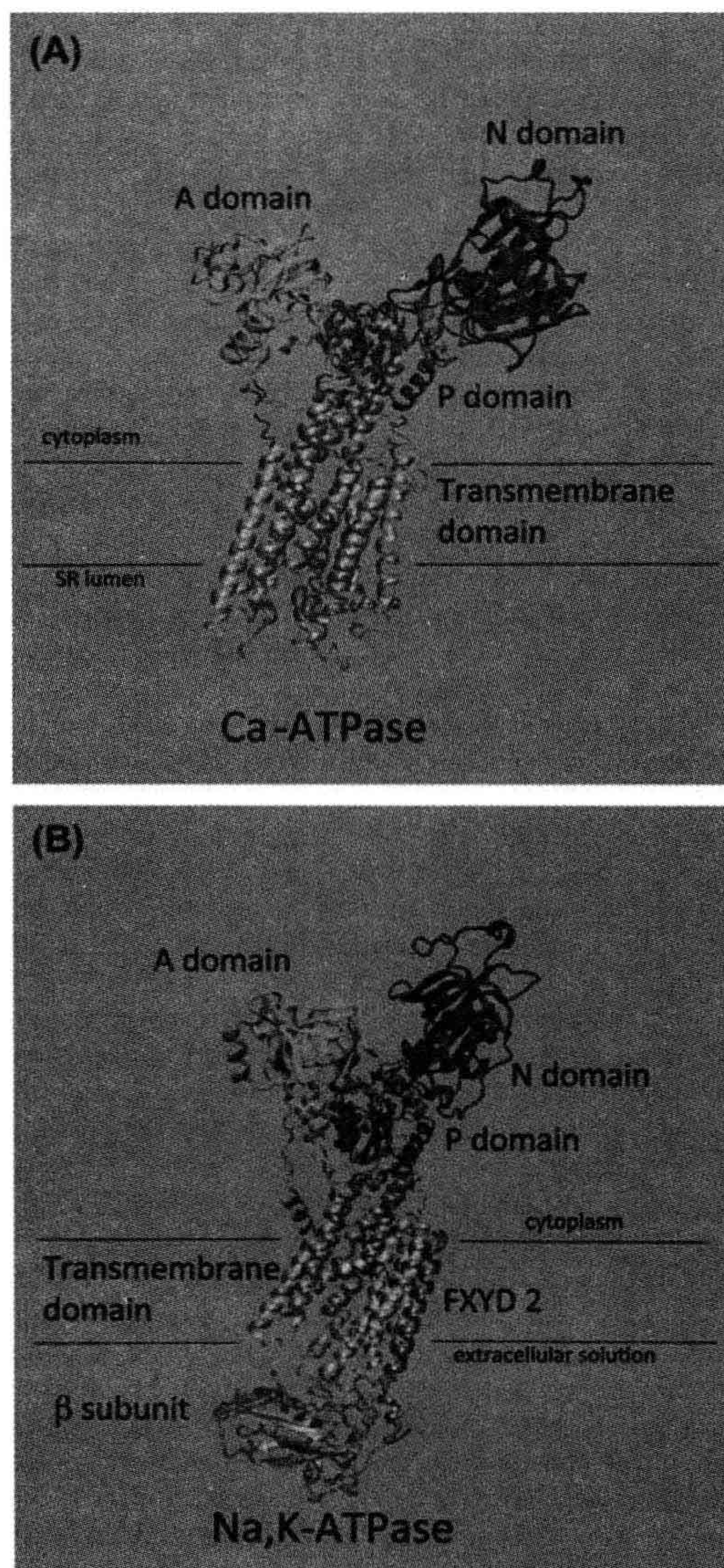


FIGURE 12.3 Molecular structures for sarcoplasmic reticulum Ca^{2+}-ATPase (A) and Na^+,K^+-ATPase (B). In both structures, the approximate locations of the cytoplasmic and non-cytoplasmic membrane surfaces are indicated by black lines. The N domain, the P domain and the A domain of each structure are located on the cytoplasmic side of the membrane, which is at the top of each panel. The transmembrane domain, consisting of 10 transmembrane helices, is colored cyan in both structures. In (A), two Ca^{2+} ions bound within the transmembrane domain are shown as magenta spheres and in (B), two K^+ ions in similar locations in Na^+,K^+-ATPase are also shown. In each structure, the aspartate residue in the P domain that is phosphorylated by ATP is shown in space-filling representation. In (B), the β subunit of Na^+,K^+-ATPase is shown in orange and the FXYD2 protein is shown in gold. Most of the mass of the β subunit is exposed to the non-cytoplasmic side of the membrane at the bottom of the panel. Protein Data Bank files are 1SU4 for panel A and 2ZXE for panel B. Structures were drawn using VMD.

and Na^+,K^+-ATPase. In several of the crystal structures, no clear water-filled access pathway to the ion binding sites from either the cytoplasm or the non-cytoplasmic side of the membrane is obvious, suggesting that some of these structures contain occluded cations.

VI. BETA SUBUNITS

Only the Na^+,K^+-ATPase and the H^+,K^+-ATPase are known to require a second (β) subunit for their activity (McDonough et al., 1990). A requirement for the β subunit was demonstrated for Na^+,K^+-ATPase by showing that yeast cells, which are one of the few eukaryotic cells that do not contain an endogenous Na^+,K^+-ATPase, would express functional Na^+,K^+-ATPase pumps only when cDNA for both α and β subunits was transfected into the cells (Horowitz et al., 1990). Transfection of cDNA for either the α subunit or the β subunit alone did not result in any functional Na^+,K^+-ATPase pumps. As shown in Fig. 12.3B, the β subunits of P-type pumps are integral membrane proteins with a single transmembrane α helix. Most of the mass of these polypeptides is located on the non-cytoplasmic side of the membrane and only a small N-terminal region is found in the cytoplasm. The extracellular domain of the β subunits contains several N-linked oligosaccharide chains, the number of which is different for the different β subunits. Since all of the functionally important amino acids of the P-type pumps are associated with the α subunit, the role of the β subunit in the activity of these pumps was unclear for many years. Early data indicated that the β subunit assembled with the α subunit early in the process of protein synthesis and maturation and it was found that in the absence of the β subunit, the α subunit was not delivered to the plasma membrane and was rapidly degraded. Association of the β subunit with the α subunit facilitates the correct folding of the α subunit (Geering, 1990). Chimeric constructs in which the extracellular domains of the Na^+,K^+-ATPase and gastric or colon H^+,K^+-ATPase β subunits were exchanged onto the other protein's transmembrane domain and proteolytic cleaveage of the β subunits, showed that the structure of the β subunit extracellular domain also influenced the affinity of the α subunits for extracellular K^+ ions. The structural basis for these observations was revealed in the crystal structure of the Na^+,K^+-ATPase (see Fig. 12.3B) where the extracellular domain of β is seen to interact with the α subunit near the site where extracellular K^+ binds to

the protein (Shinoda et al., 2009). Although it is now apparent that the β subunits of Na^+,K^+-ATPase and H^+,K^+-ATPase influence both protein folding and assembly and the interaction of K^+ with the pumps, it is not known why only these two members of the P-type ATPase family require the β subunit. It is also unknown how, in cells that contain both of these ion pumps, such as gastric parietal cells, the correct β subunit assembles with each α subunit, since it has been shown in heterologous expression systems that either α subunit will assemble with the β subunit of the other pump. In colon and kidney, there is immunological evidence that the H^+,K^+-ATPase α subunits assemble into functional pumps with the Na^+,K^+-ATPase β1 subunit.

VII. ISOFORMS OF PUMP SUBUNITS AND SUBFAMILIES OF P-TYPE PUMPS

Multiple isoforms of both α subunits and β subunits of Na^+,K^+-ATPase have been identified (Lingrel, 1992; Woo et al., 1999). These isoforms are encoded by different genes, have >80% identical amino acid sequences and may be located in different cells throughout the organism in which they are found. Four isoforms of the α subunit (α1–α4) of Na^+,K^+-ATPase, for example, and three isoforms of the β subunit (β1–β3) of this pump are present in humans. α1 is widely distributed in many tissues of the body and is usually the isoform found in cells that contain only one isoform of the Na^+,K^+-ATPase. α2 and α3 are found primarily in muscle and neuronal cells and α4 is restricted to testis. More than one isoform of the α subunit may be present in a single cell. The different isoforms of the α subunit have slightly different affinities for Na^+ and K^+ that appear to enable different cells to transport these ions optimally under different conditions. In some cells, such as rat mesenteric artery myocytes and cortical astrocytes, the α2 or α3 subunit of Na^+,K^+-ATPase is confined to microdomains of the plasma membrane located close to the sites of Ca^{2+} release from the sarcoplasmic/endoplasmic reticulum and to the plasma membrane Na^+/Ca^{2+} exchanger. This juxtaposition of the Na^+,K^+-ATPase and proteins involved in calcium homeostasis provides an explanation for how cardiac glycosides, which bind only to Na^+,K^+-ATPase, can influence local $[Ca^{2+}]_{in}$ and cellular processes that depend on mobilization of Ca^{2+} from intracellular stores (Golovina et al., 2003).

Based on cellular location, sensitivity to inhibitors and amino acid sequence, the Ca^{2+}-ATPases can be divided into three subfamilies: those that are located in the plasma membrane of cells (PMCA); those that are located in the sarcoplasmic reticulum of muscle or the endoplasmic reticulum (SERCA); and those that are located in organelles of the secretory pathway (SPCA), such as the Golgi (although these may have a post-Golgi distribution in some cells). Although there are some biochemical differences in the kinetics of these different types of Ca^{2+} pumps, the primary functional difference is that the Ca^{2+} pumps that are located in the plasma membranes are regulated by interaction with the Ca^{2+}-binding protein calmodulin and the pumps located in intracellular membranes do not interact with calmodulin. Plasma membrane Ca^{2+} pumps are autoinhibitory and, when intracellular Ca^{2+} levels rise, Ca^{2+}-calmodulin binds to these pumps, releases the inhibition, and increases Ca^{2+} efflux from the cell. Although these different forms of the Ca^{2+}-ATPases represent different subfamilies of this pump that actively transport Ca^{2+} using the Albers–Post mechanism, within each subfamily different isoforms have been identified (Brini and Carafoli, 2009). There are three isoforms for the SERCA pumps, four isoforms for the PMCA pumps and two isoforms for the SPCA pumps in mammals. For the H^+,K^+-ATPases, there are two subfamilies of pumps, the gastric type and the non-gastric type (Shin et al., 2009; Gumz et al., 2010). Gastric type H^+,K^+-ATPase is found only in the gastric parietal cells and in the renal collecting duct, whereas the non-gastric type has a much wider tissue distribution that includes kidney, prostate, uterus, placenta, skin, brain and colon. In the stomach, the gastric H^+,K^+-ATPase is responsible for the secretion of acid and the inhibition of this enzyme is an effective treatment for symptoms of peptic ulcer. The physiological role of the non-gastric H^+,K^+-ATPases seems to be primarily as a mechanism for the conservation of potassium during states of potassium deprivation.

VIII. FXYD PROTEINS

In some preparations of Na^+,K^+-ATPase, a small polypeptide is found to be associated with the pump in addition to the α and β subunits. It was initially suggested by some investigators that this polypeptide was a third (γ) subunit of the pump, however, it was subsequently shown that sodium pumps do not require the γ polypeptide for their function and so this is not a true subunit of the enzyme. Nevertheless, measurement of the ion dependence of Na^+,K^+-ATPase activity in cells either containing this polypeptide or not, demonstrated that the $K_{½}$ values for activation of pump activity by Na^+ or K^+ were different in the presence of the γ polypeptide and in its absence. The magnitude of the differences is small, but is possibly significant for ionic homeostasis in different tissues. It is now known that there is a small family of proteins containing the conserved amino acid sequence FXYD that modulate the activity of Na^+,K^+-ATPase in different cells (Sweadner and Rael, 2000). These different proteins are listed in Table 12.1.

TABLE 12.1 FXYD Protein Tissue Expression and Functional Effects on Na^+,K^+-ATPase

Family Designation	Common Name	Tissue Expression	Functional Effects on Na^+,K^+-ATPase
FXYD 1	Phospholemman	Heart, liver, skeletal muscle	↑ $K_{½}$ K^+ ↑ $K_{½}$ Na^+
FXYD 2	γ-subunit	Kidney, heart, stomach	↑ $K_{½}$ Na^+
FXYD 3	MAT-8	Colon, stomach, uterus	↑ $K_{½}$ K^+ ↑ $K_{½}$ Na^+
FXYD 4	CHIF	Distal colon, kidney collecting duct	↑ $K_{½}$ K^+ ↓ $K_{½}$ Na^+
FXYD 5	RIC	Heart, brain, spleen, lung, skeletal muscle, kidney, testis	Not determined
FXYD 6	-	Brain, kidney	Not determined
FXYD 7	-	Brain	↑ $K_{½}$ K^+

FXYD proteins have a single transmembrane helix and are expressed in a tissue-specific pattern. The crystal structure of Na^+,K^+-ATPase shows that the FXYD proteins bind to transmembrane helices of the α subunit and also interact with the α subunit and the β subunit near the extracellular surface of the membrane (see Fig. 12.3B) (Shinoda et al., 2009). Based on the crystal structure, it has been suggested that the FXYD proteins exert their effects on ion binding to the α subunit through contacts between amino acids located in the transmembrane helices of each polypeptide. Alterations in either the expression or the function of different FXYD proteins have been implicated in several disease states including acute cardiac ischemia, renal hypomagnesemia, malignancies and ventricular remodeling following myocardial infarction, but the mechanism whereby these changes in FXYD expression or function are involved is not known. One FXYD protein, phospholemman, is a substrate for protein kinase A and protein kinase C in the heart and is involved in the regulation of cardiac contractility (Bers and Despa, 2009). There is some evidence that phospholemman interacts with the cardiac Na^+/Ca^{2+} exchanger in addition to the Na^+,K^+-ATPase and may exert its regulatory effect through interactions with the exchanger.

IX. REGULATION OF P-TYPE ATPase ACTIVITY

In order to survive under different environmental conditions, cells need to increase or decrease their transport of ions and solutes appropriately as the need to take up or excrete these substances changes. The transport capacity of cells for any transported solute can be changed either by increasing or decreasing the abundance of functional transport proteins in the cell membranes or by changing the intrinsic transport activity of the individual transporters. Changes in the number of functional transport proteins in cell membranes can be accomplished by changes in translational and transcriptional rates of transporter genes or by inserting or removing transporters from the cell membranes. Changes in the intrinsic activity of transport proteins can accompany post-transcriptional modification of the transport proteins, changes in the concentration of transported substrates and ions and interaction of the transporters with regulatory proteins or small molecule regulators. All of these mechanisms are known to occur for the regulation of different P-type ATPases and, in several instances, multiple types of regulation are observed. For the Na^+,K^+-ATPase, for example, aldosterone markedly increases transepithelial sodium absorption in the distal nephron by increasing apical Na^+ influx. The increase in $[Na^+]_{in}$ increases Na^+,K^+-ATPase activity because maximal pump activity is achieved at $[Na^+]_{in}$ levels considerably above those found in resting cells (see below). Prolonged aldosterone secretion, however, also induces increases in mRNA levels for both α and β subunits of the sodium pump and an increase in the abundance of the pump protein in the cell membrane. Thyroid hormone also increases mRNA levels for Na^+,K^+-ATPase subunits, leading to an increase in the number of active sodium pumps in the cell membrane. The increase in energy consumption associated with increased sodium pump activity plays an important role in the calorigenic action of thyroid hormone.

Insulin has been shown to increase the number of functional sodium pumps in the plasma membrane of insulin-sensitive cells, such as skeletal muscle, by increasing the movement of intracellular vesicles

containing the pump to the plasma membrane, just as insulin increases GLUT 4 transporter abundance in the plasma membrane and increases glucose uptake in these tissues (Benziane and Chibalin, 2008). The intracellular vesicles containing GLUT4 are different, however, from the vesicles that contain the Na^+,K^+-ATPase. In the stomach, gastric parietal cells are stimulated by histamine that is released from enterochromaffin-like cells after a meal, in response to vagal stimulation and the release of acetylcholine and gastrin. Histamine binds to H2 receptors on the parietal cell and results in an increase in cAMP in the cell. Several targets of cAMP-dependent kinase that bind actin have been identified and, through a mechanisms that is not completely understood, a cytoskeletal rearrangement occurs in the parietal cells that facilitates fusion of intracellular tubulovesicles containing the gastric H^+,K^+-ATPase with the plasma membrane of the cell at the secretory canaliculus (Forte and Zhu, 2010). Delivery of the H^+,K^+-ATPase to the plasma membrane increase the capacity of the cell to secrete acid as it increases the surface area of the canalicular membrane of the cell 50–100-fold. When the stimulus is withdrawn, the H^+,K^+-ATPase is withdrawn and the tubulovesicles are reformed.

The K_M for intracellular Na^+ activation of the sodium pump is near the intracellular concentration of Na^+ for most mammalian cells (5–10 mM) and even small changes in $[Na^+]_{in}$ will have significant effects on pump activity due to the sigmoid relationship between $[Na^+]_{in}$ and pump activity. The dependence of sodium pump activity on $[Na^+]_{in}$ is the primary mechanism for the minute-to-minute regulation of cytoplasmic Na^+ concentrations. Under physiological conditions, the concentration of extracellular potassium is generally close to the saturation concentration for stimulation of Na^+,K^+-ATPase activity and changes in extracellular K^+ do not normally have significant effects on sodium pump activity.

Several hormones and neurotransmitters that bind to receptors at the extracellular surface of the cell membrane activate cascades of protein kinases and protein phosphatases and there are many reports of either activation or inhibition of P-type ATPase activity by these signaling molecules. Although it is possible to recover phosphoryated P-type pump polypeptides from in vitro assays that contain protein kinase A or protein kinase C, it has been difficult to demonstrate a direct relationship between pump phosphorylation and changes in activity in vivo. At this time, there is no conclusive evidence for sodium pump activity being affected by direct phosphorylation of the α or β subunits by protein kinases, despite many reports that the α subunit can be phosphorylated by these enzymes in vitro. One of the best examples of regulation of P-type ATPase activity by direct protein kinase phosphorylation is the response of the fungal plasma membrane H^+-ATPase activity in carbon-starved yeast cells to the addition of glucose (Lecchi et al., 2007). In the yeast Pma1 H^+-ATPase, there are two adjacent serine and threonine amino acids in the cytoplasmic carboxy-terminal tail of the protein that are phosphorylated. T912 is constitutively phosphorylated and is the major site of phosphorylation on the protein in cells that have been starved for carbon and in which the H^+-ATPase activity is low. Addition of glucose to these cells leads to a threefold reduction of phosphorylation at T912, an 11-fold increase in phosphorylation at S911 and a 5–10-fold increase in ATPase activity in the cells. The increase in ATPase activity is due to a several-fold increase in the affinity of the proton pump for ATP that occurs when the phosphorylation status of these two amino acids changes in response to glucose addition.

Regulation of P-type ATPase activity by interaction with other regulatory proteins has been shown for Na^+,K^+-ATPase and the FXYD proteins, as discussed above, and for the SERCA pumps and phospholamban. Phospholamban is an endogenous inhibitor of the SERCA pumps that binds to the pumps and reduces their affinity for Ca^{2+} without affecting the maximum transport rate, especially at low $[Ca^{2+}]$. In response to adrenergic stimulation in the heart, phospholamban is phosphorylated by protein kinase A on a serine residue, and dissociates from the ATPase. Without associated phospholamban, the SERCA pumps have higher affinity for Ca^{2+} and pump activity is increased. Recent data indicate that the FXYD protein phospholemman affects Na^+,K^+-ATPase activity in the same way (Bers and Despa, 2009). Unphosphorylated phospholemman binds to the pump and reduces the affinity of the pump for cytoplasmic Na^+, but when phospholemman is phosphorylated, the affinity of the sodium pump for sodium increases.

X. PHARMACOLOGICAL INHIBITORS OF P-TYPE ATPases

Much of the information that has been obtained for some of the P-type ATPases is a result of the unique inhibition of those pumps by small molecules, several of which are of clinical or physiological importance. The most well-known example is the inhibition of Na^+,K^+-ATPase by cardiac glycosides, such as digoxin, digitalis and ouabain, whose only known receptor is the Na^+,K^+-ATPase. Cardiac glycosides have been used for many years to treat patients with congestive heart failure and these drugs exert their effects on the heart through a mechanism that couples inhibition of a fraction of the total cardiomyocyte sodium pump activity to activation of the Na^+/Ca^{2+} exchanger. Increases in $[Na^+]_{in}$ localized near the exchanger lead to a reduced influx of extracellular Na^+ and efflux of cytoplasmic Ca^{2+}. This results in an increase in sarcoplasmic reticulum Ca^{2+} levels that are available for release when

the cardiomyocyte is stimulated. Increased release of Ca^{2+} from the SR leads to an increase in the force of contraction. Although cardiac glycosides are found abundantly in certain plants, it has been shown recently that an endogenous ouabain is found in many mammals (Schoner and Scheiner-Bobis, 2007). Endogenous ouabain at concentrations significantly lower than those that inhibit the Na^+,K^+-ATPase catalytic activity binds to the sodium pump and activates several signaling pathways in cells that affect protein kinase activity, $[Ca^{2+}]_{in}$ and gene expression. Na^+,K^+-ATPase is also inhibited by very low concentrations of the marine toxin palytoxin. Palytoxin is made by marine corals of the genus *Palythoa* and is one of the most potent animal toxins known, with an LD_{50} of approximately 0.15 μg/kg in mice. When palytoxin binds to animal cells, it causes a non-specific leak of cations across the plasma membrane. Palytoxin-induced K^+ efflux from cells can be antagonized by ouabain, indicating that Na^+,K^+-ATPase is involved in the mechanism of palytoxin toxicity. Expression of mammalian Na^+,K^+-ATPase in yeast showed that palytoxin binds directly to the Na^+,K^+-ATPase and converts the active ion pump into an ion channel (Scheiner-Bobis et al., 1994).

A clinically relevant inhibitor of the gastric H^+,K^+-ATPase is omeprazole. Omeprazole is a benzimidazole that, in its activated form, reacts with sulfhydryl groups on proteins. As such is not specific for the gastric H^+,K^+-ATPase, but because it must be activated by acidic conditions, such as those found in the stomach, it is inactive in most tissues of the body. When activated by the low pH found in the stomach, omeprazole reacts with a specific cysteine residue in the gastric H^+,K^+-ATPase and inhibits gastric acid secretion (Sachs and Wallmark, 1989). The drug is effective for the treatment of the symptoms of hyperacidity and peptic ulcers and is one of the best selling drugs in the world. Because of the clinical and financial benefits of treating these symptoms, much effort has been made to find additional specific gastric H^+,K^+-ATPase inhibitors and several, including the imidazopyridines such as SCH28080, have been identified that inhibit the pump by different mechanisms.

SERCA pumps are uniquely inhibited by thapsigargin, a sesquiterpene lactone from the plant *Thapsia garganica*. Thapsigargin is a component of a root extract from this plant that was used in ancient times for the treatment of muscle and joint inflammations, but which caused skin irritation. This irritation is now known to be due to the effects of thapsigargin on intracellular Ca^{2+} pools and the release of histamine. Thapsigargin inhibits SERCA pumps at subnanomolar concentrations in what appears to be a stoichiometric interaction with the pumps by binding to the SERCA pumps in the transmembrane domain and locking the enzyme in the E2 conformation (Inesi and Sagara, 1992). This interferes with the conformational changes that are needed for the active pumping of Ca^{2+} (Toyoshima and Nomura, 2002).

BIBLIOGRAPHY

Abrahams, J. P., Leslie, A. G. W., Lutter, R., & Walker, J. E. (1994). Structure at 2.8Å resolution of F1-ATPase from bovine heart mitochondria. *Nature, 370*, 621–628.

Aravind, L., Galperin, M. Y., & Koonin, E. V. (1998). The catalytic domain of the P-type ATPase has the haloacid dehalogenase fold. *Trends Biochem Sci, 23*, 127–129.

Axelsen, K. B., & Palmgren, M. G. (1998). Evolution of substrate specificities in the P-type ATPase superfamily. *J Mol Evol, 46*, 84–101.

Benziane, B., & Chibalin, A. V. (2008). Frontiers: skeletal muscle sodium pump regulation: a translocation paradigm. *Am J Endocrinol Metab, 295*, E553–E558.

Bers, D. M., & Despa, S. (2009). Na/K-ATPase – an integral player in the adrenergic fight-of-flight response. *Trends Cardiovasc Med, 19*, 111–118.

Boyer, P. D. (1997). The ATP synthase – a splendid molecular machine. *Annu Rev Biochem, 66*, 717–749.

Brini, M., & Carafoli, E. (2009). Calcium pumps in health and disease. *Physiol Rev, 89*, 1341–1378.

Cantley, L. C. (1981). Structure and mechanism of the (Na, K)-ATPase. *Curr Topics Bioenerget, 11*, 201–237.

De Weer, P., Gadsby, D. C., & Rakowski, R. F. (1988). *Ann Rev Physiol, 50*, 225–241.

Forte, J. G., & Zhu, L. (2010). Apical recycling of the gastric parietal cell H, K-ATPase. *Ann Rev Physiol, 72*, 273–296.

Geering, K. (1990). Subunit assembly and functional maturation of Na, K-ATPase. *J Membr Biol, 115*, 109–121.

Glynn, I. M., & Karlish, S. J. D. (1975). The sodium pump. *Ann Rev Physiol, 37*, 13–55.

Glynn, I. M., & Karlish, S. J. D. (1990). Occluded cations in active transport. *Ann Rev Biochem, 59*, 171–205.

Golovina, V. A., Song, H., James, P. F., Lingrel, J. B., & Blaustein, M. P. (2003). Na^+ pump α2-subunit expression modulates Ca^{2+} signaling. *Am J Physiol Cell Physiol, 284*, C475–C486.

Gumz, M. L., Lynch, I. J., Greenlee, M. M., Cain, B. D., & Wingo, C. S. (2010). The renal H^+, K^+-ATPases: physiology, regulation, and structure. *Am J Physiol Renal Physiol, 298*, F12–F21.

Horowitz, B., Eakle, K. A., Scheiner-Bobis, G., et al. (1990). Synthesis and assembly of functional mammalian Na, K-ATPase in yeast. *J Biol Chem, 265*, 4189–4192.

Inesi, G., & Sagara, Y. (1992). Thapsigargin, a high affinity and global inhibitor of intracellular Ca^{2+} transport ATPases. *Arch Biochem Biophys, 298*, 313–317.

Läuger, P. (1991). *Electrogenic Ion Pumps*. Sunderland, MA: Sinauer Associates, Inc.

Lecchi, S., Nelson, C. J., Allen, K. E., et al. (2007). Tandem phosphorylation of Ser-911 and Thr-912 at the C terminus of yeast plasma membrane H^+-ATPase leads to glucose-dependent activation. *J Biol Chem, 282*, 35471–35381.

Lingrel, J. B. (1992). Na, K-ATPase: isoform structure, function, and expression. *J Bioenerg Biomembr, 24*, 263–270.

McDonough, A. A., Geering, K., & Farley, R. A. (1990). The sodium pump needs its β subunit. *FASEB J, 4*, 1598–1605.

Moller, J. V., Olesen, C., Winther, A. M., & Nissen, P. (2010). The sarcoplasmic Ca^{2+}-ATPase: design of a perfect chemi-osmotic pump. *Q Rev Biophys, 43*, 501–566.

Morth, J. P., Pedersen, B. P., Buch-Pedersen, M. J., et al. (2011). A structural overview of the plasma membrane Na^+, K^+-ATPase and H^+-ATPase ion pumps. *Nat Rev Mol Cell Biol, 12*, 60–70.

Morth, J. P., Pedersen, B. P., Toustrup-Jensen, M. S., et al. (2007). Crystal structure of the sodium-potassium pump. *Nature, 450*, 1043–1050.

Nakamoto, R. K., Baylis Scanlon, J. A., & Al-Shawi, M. K. (2008). The rotary mechanism of the ATP synthase. *Arch Biochem Biophys, 476*, 43–50.

Pickart, C. M., & Jencks, W. P. (1984). Energetics of the calcium-transporting ATPase. *J Biol Chem, 259*, 1629–1643.

Sachs, G., & Wallmark, B. (1989). Biological basis of omeprazole therapy. *J Gastroenterol Hepatol, 4*(Suppl 2), 7–18.

Scheiner-Bobis, G., Zu Heringdorf, D. M., Christ, M., & Habermann, E. (1994). Palytoxin induces K^+ efflux from yeast cells expressing the mammalian sodium pump. *Mol Pharmacol, 45*, 1132–1136.

Schoner, W., & Scheiner-Bobis, G. (2007). Endogenous and exogenous cardiac glycosides: their roles in hypertension, salt metabolism, and cell growth. *Am J Cell Physiol, 293*, C509–C536.

Shimamura, T., Weyand, S., Beckstein, O., et al. (2010). Molecular basis of alternating access membrane transport by the sodium-hydantoin transporter Mhp1. *Science, 328*, 470–473.

Shin, J. M., Munson, K., Vagin, O., & Sachs, G. (2009). The gastric HK-ATPase: structure, function, and inhibition. *Pflügers Arch Eur J Physiol, 457*, 609–622.

Shinoda, T., Ogawa, H., Cornelius, F., & Toyoshima, C. (2009). Crystal structure of the sodium-potassium pump at 2.4Å resolution. *Nature, 459*, 446–451.

Skou, J. C. (1998). Nobel lecture: identification of the sodium pump. *Biosci Rep, 18*, 155–169.

Stock, D., Leslie, A. G. W., & Walker, J. E. (1999). Molecular architecture of the rotary motor in ATP synthase. *Science, 286*, 1700–1705.

Sweadner, K. J., & Rael, E. (2000). The FXYD gene family of small ion transport regulators or channels: cDNA sequence, protein signature sequence, and expression. *Genomics, 68*, 41–56.

Toei, M., Saum, R., & Forgac, M. (2010). Regulation and isoform function of the V-ATPases. *Biochemistry, 49*, 4715–4723.

Toyoshima, C., & Nomura, H. (2002). Structural changes in the calcium pump accompanying the dissociation of calcium. *Nature, 418*, 605–611.

Toyoshima, C., Nakasako, M., Nomura, H., & Ogawa, H. (2000). Crystal structure of the calcium pump of sarcoplasmic reticulum at 2.6Å resolution. *Nature, 405*, 647–655.

Weyand, S., Shimamura, T., Yajima, S., et al. (2010). Structure and molecular mechanism of a nucleobase-cation-symport-1 family transporter. *Science, 322*, 709–713.

Woo, A. L., James, P. F., & Lingrel, J. B. (1999). Characterization of the fourth alpha isoform of the Na, K-ATPase. *J Membr Biol, 169*, 39–44.

Chapter 13

Ca^{2+}-ATPases

Tracy J. Pritchard, Istvan Edes and Evangelia G. Kranias

Chapter Outline

I. INTRODUCTION

During the cardiac action potential, Ca^{2+} enters the cell via Ca^{2+} channels, which also act as dihydropyridine receptors (Fig. 13.1). This Ca^{2+} can either activate the myofilaments directly or produce the release of additional Ca^{2+} from the sarcoplasmic reticulum (SR). The SR Ca^{2+}-release channel in cardiac and skeletal muscle also acts as a ryanodine receptor and spans the gap between the transverse tubule and the SR ("foot" protein). Furthermore, it has been shown that the outer cell membrane Ca^{2+} channel is located close to the SR Ca^{2+} channel. Thus, the excitation–contraction coupling apparently involves the sarcolemmal Ca^{2+} channel and the SR Ca^{2+}-release channel with the Ca^{2+} current through the sarcolemmal channel being responsible for the initiation of Ca^{2+} release from the SR (Fig. 13.1). In skeletal muscle, the sarcolemmal membrane depolarization itself apparently is responsible for the induction of SR Ca^{2+} release. The relative importance of release from the SR in activation of the cardiac muscle contraction varies from preparation to preparation but, in the heart of mammals, it usually accounts for 40–70% of the Ca^{2+} required (Bers, 2008).

The rising cytosolic Ca^{2+} concentration induces contraction through binding to troponin C, which activates a chain of conformational changes, allowing the thin and thick filaments to interact. Subsequently, Ca^{2+} is dissociated from troponin C and is rapidly removed from the cytosol by various systems, resulting in relaxation. At least three processes are responsible for the removal of Ca^{2+} to end contraction (see Fig. 13.1): (1) the SR Ca^{2+} pump, which actively translocates Ca^{2+} at the cost of ATP into the SR system – this is thought to be the most important process in mediating relaxation; (2) the Na^{+}-Ca^{2+} exchanger, which transports Ca^{2+} out of the cell during diastole; and (3) the sarcolemmal Ca^{2+}-ATPase, which also extrudes Ca^{2+} from the cell.

The SR is a tubular network which serves as a sink for Ca^{2+} ions during relaxation and as a Ca^{2+} source during contraction. In cardiac muscle, about 60–70% of the intracellular Ca^{2+} released during systole is taken up by the SR (Bers, 2008) and the remaining amount is extruded from the cell by the Na^{+}-Ca^{2+} exchanger and the sarcolemmal Ca^{2+}-ATPase. The SR in both skeletal and cardiac muscles contains an acidic protein, calsequestrin (see Fig.13.1),

Cell Physiology Sourcebook. DOI: 10.1016/B978-0-12-387738-3.00013-5

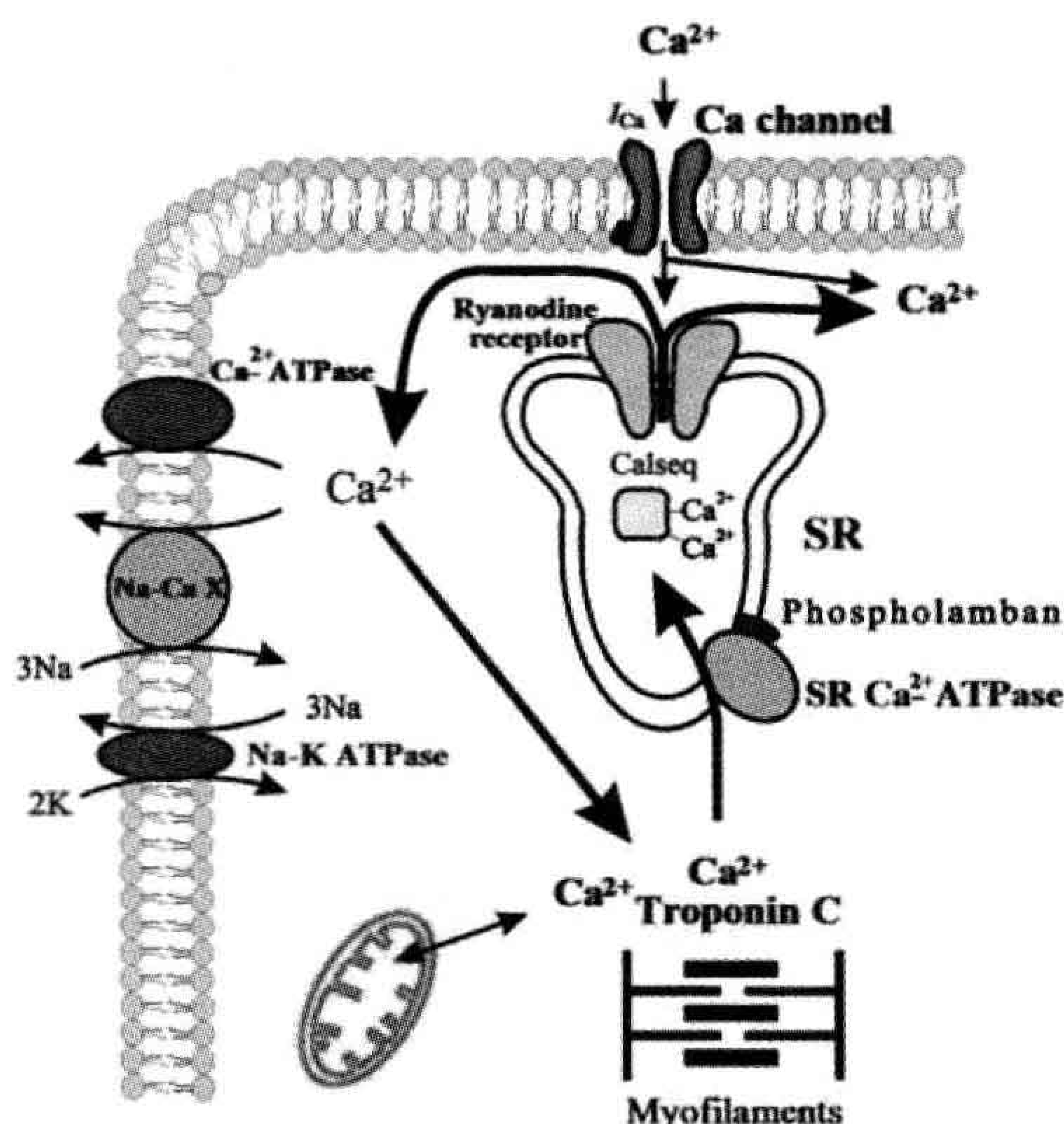


FIGURE 13.1 Schematic diagram of Ca^{2+} fluxes in the cardiac cell. Na-CaX, Na^+-Ca^{2+} exchanger; Calseq., calsequestrin; I_{Ca}, slow inward Ca^{2+} current; SR, sarcoplasmic reticulum.

which binds 40−50 mol of Ca^{2+} per mol of protein (MacLennan et al., 2002). The binding and release of Ca^{2+} by calsequestrin is believed to be an integral step of excitation−contraction coupling, but the details of this process are still not fully understood. Mitochondria can also accumulate large amounts of Ca^{2+} under pathological conditions (ischemia, Ca^{2+} overload, etc.) (Bers, 2008).

II. SARCOPLASMIC RETICULAR (SR) Ca^{2+}-ATPase

IIA. Properties of SR Ca^{2+}-ATPase

The major protein in the SR membrane is the Ca^{2+}-ATPase (M_r 100 000), representing about 40% of the total protein in cardiac SR. The cardiac SR Ca^{2+}-ATPase can create intraluminal Ca^{2+} concentrations of 5−10 mM. The SR or endoplasmic reticulum (ER) Ca^{2+}-ATPase family (SERCA) is the product of at least three alternatively spliced genes, producing a minimum of 11 different proteins (Dally et al., 2010) (Table 13.1). SERCA1 is expressed in fast skeletal muscle and alternative splicing of the 3′ end of the primary transcript gives rise to two mRNA forms (SERCA1a and SERCA1b), which are expressed at different stages of development (Brini and Carafoli, 2009). Alternatively, spliced forms of SERCA2 have been detected in cardiac muscle and slow skeletal muscle (SERCA2a) and in adult smooth muscle and non-muscle tissues (SERCA2b). A third isoform of SERCA2 (SERCA2c) is found in cardiac muscle as well as non-muscle tissue including epithelial, mesenchymal and hematopoietic cells (Gianni et al., 2005). SERCA3 is expressed in a selective manner, with the highest mRNA levels in intestine, spleen, lung, uterus and brain. The human SERCA2 gene is localized on chromosome 12 and maps to position 12q23-q24.1. SERCA2 is about 85% identical to SERCAl, whereas SERCA3 is about 75% identical to either SERCA1 or SERCA2. The SERCA isoforms have different rates of transport, affinities for Ca^{2+} and subcellular compartmentalization.

TABLE 13.1 Structure and Distribution of the Sarcoplasmic Reticular Ca^{2+}-ATPase (SERCA) Isoforms

Gene	Splice	Tissue
SERCA1[a]	a[b]	Adult fast skeletal muscle
SERCA1	b	Neonatal fast skeletal muscle
SERCA2	a	Cardiac/slow skeletal muscle
SERCA2	b	Smooth muscle/non-muscle
SERCA2	c	Cardiac/non-muscle
SERCA3	a–f	Various tissues

[a]The SERCA numbers identify different gene products.
[b]The letters a and b indicate spliced isoforms.

The proposed general model of the enzyme has three cytoplasmic domains joined to a set of 10 transmembrane helices by a narrow extramembrane pentahelical stalk (MacLennan et al., 2002). The cytoplasmic region includes a nucleotide-binding site, or a domain to which the MgATP substrate binds, and a phosphorylation domain (Fig. 13.2). The third cytoplasmic domain is the actuator domain, which may be involved in conformational changes. In skeletal muscle, 2 mol of Ca^{2+} is transported per mole of ATP hydrolyzed. In cardiac muscle, a similar stoichiometry is expected, but this ratio has been generally found to be lower (0.4−1.0 mol Ca^{2+}/mol ATP). Ca^{2+} has been shown to bind to a region involving several of the membrane-spanning α-helices (M4, M5, M6 and M8) on the cytoplasmic side (MacLennan et al., 2002). During the Ca^{2+} transport cycle, the enzyme undergoes a transition from a high-affinity state to a low-affinity state for Ca^{2+} and the ions are translocated from the binding sites into the lumen of the SR (Fig. 13.2). This reaction pathway is characterized by the covalent phosphorylated Ca^{2+}-ATPase form (E_1~P), when the energy of ATP is transferred to an acylphosphoprotein intermediate (Fig. 13.3). E_1~P rapidly becomes E_2−P when the energy contained originally in the acylphosphoprotein is transduced into the translocation of bound Ca^{2+} into the SR ("marionette" model, see Fig. 13.2)

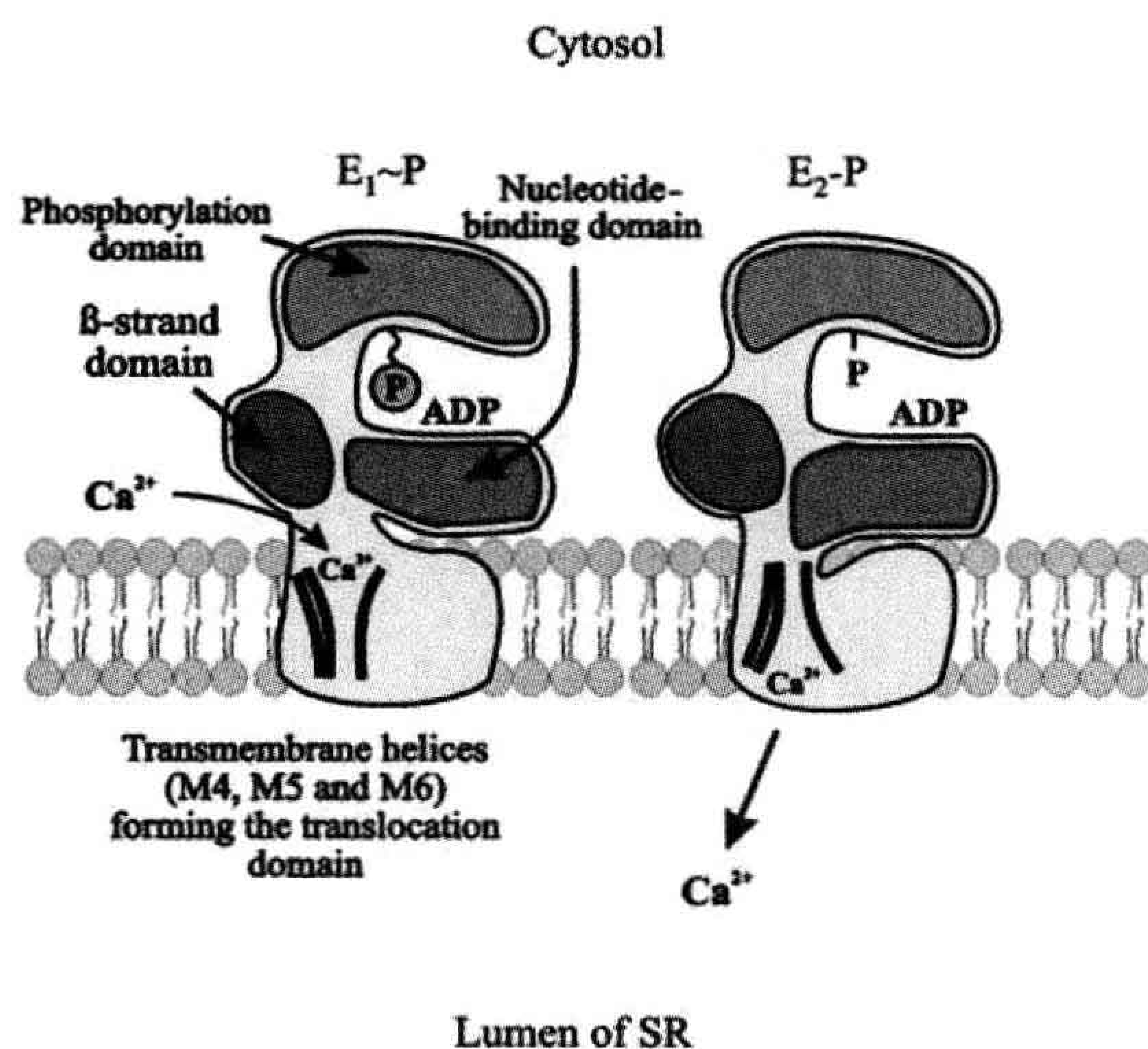


FIGURE 13.2 Model illustrating Ca^{2+} translocation by SERCA-type Ca^{2+} pumps. In E_1~P conformation, Ca^{2+} binds to the high-affinity binding sites in the cytosol. The energy of the hydrolyzed ATP triggers a series of conformational changes and transforms the E_1~P intermediate to the E_2−P intermediate. These conformational changes are directly coupled to alterations in the orientation of the transmembrane regions, leading to Ca^{2+} release into the lumen of the sarcoplasmic reticulum.

in exchange for two to three protons from the lumen of the SR to the cytosol. Subsequently, the acid-labile intermediate (E_2−P) decomposes to enzyme (E_2) and inorganic phosphate (Møller et al., 2005).

The Ca^{2+}-free form of the enzyme exists in two different conformational states: one with low affinity for

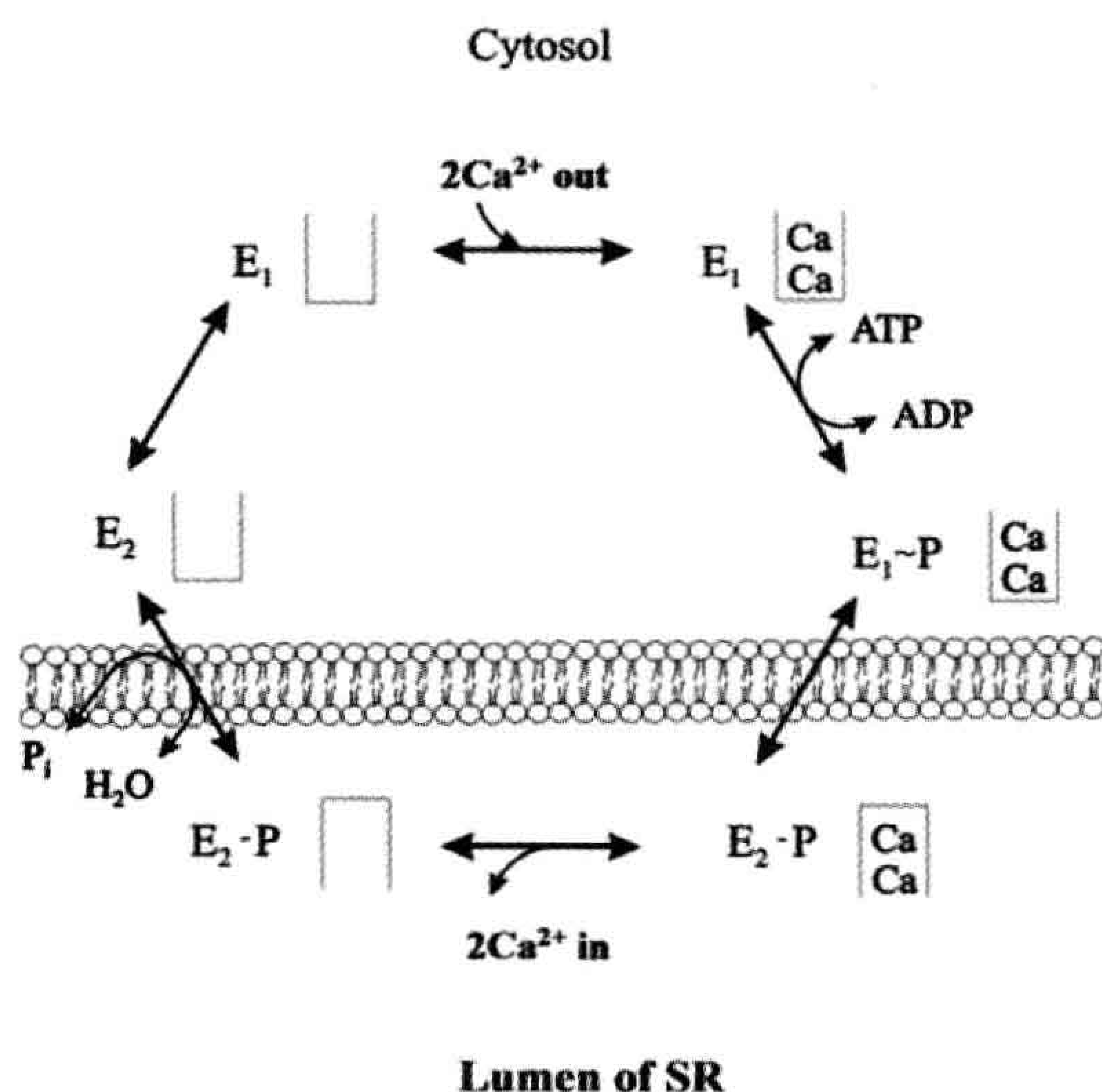


FIGURE 13.3 Reaction scheme of sarcoplasmic reticular Ca^{2+}-ATPase.

Ca^{2+} (E_2) and one with high affinity for Ca^{2+} (E_1) (see Fig. 13.3). The conversion of E_2 to E_1 is proposed to be the rate-limiting step in the cycle. Thapsigargin (a plant sesquiterpene lactone) has been shown to interact specifically with the M3 transmembrane segment of the E_2 form of all members of the SR Ca^{2+}-ATPase family and to inhibit enzyme activity even at subnanomolar concentrations (Brini and Carafoli, 2009). It has been shown that the cardiac SR Ca^{2+}-ATPase (SERCA2) can be phosphorylated by the Ca^{2+}/CAM-dependent protein kinase at Ser 38 (Toyofuku et al., 1994). However, the physiological role of this phosphorylation is still not fully understood.

IIB. Genetic Models to Elucidate SERCA Function In Vivo

Human mutations in both SERCA1 and SERCA2 genes have been identified and linked to disease. Brody myopathy, an autosomal recessive disorder, can be caused by mutations in SERCA1 and results in defective muscle relaxation contributing to cramping and stiffness with exercise (Odermatt et al., 1996). Another genetic disease presenting as a skin disorder, Darier disease, is caused by a mutation in the SERCA2 gene (Sakuntabhai et al., 1999) and results in decreased SERCA2 protein expression.

SERCA isoform gene-targeted mouse models have also been designed to elucidate further the function of the Ca^{2+}-ATPase in physiological and pathophysiological conditions. Ablation of the SERCA1 gene was not embryonically lethal in mice. However, these mice had respiratory malfunction, likely due to reduced Ca^{2+} uptake by the diaphragm, resulting in death soon after birth (Pan et al., 2003). Consistent with Brody myopathy, the SERCA1 knockout mice had impaired limb movement and cramping (Pan et al., 2003). In the case of SERCA2, mice lacking one copy of the SERCA2 gene had decreased myocyte contractility and SR Ca^{2+} load, compared to wild-type (WT) mice (Ji et al., 2000). Moreover, mean arterial blood pressure and cardiac function was depressed in vivo in SERCA2 heterozygous mice (Periasamy et al., 1999). Interestingly, these mice did not develop heart failure spontaneously, but exhibited reduced function and increased susceptibility to heart failure development upon aortic constriction (Schultz et al., 2003). Similar to Darier disease in humans, which is associated with SERCA2 mutations, mice lacking one copy of SERCA2 have defects in keratinocytes and develop squamous cell tumors (Liu et al., 2001). To determine further the function of the major cardiac isoform of SERCA2, SERCA2a, another model was generated with SERCA2a ablation. There were cardiac malformations observed in this mouse and SERCA2b was upregulated. SERCA2a null mice developed cardiac hypertrophy and had decreased cardiac contractility and impaired relaxation (Ver Heyen et al., 2001). Gene ablation of SERCA3 in mice did not result in any gross phenotypes or

lethality. Ca^{2+} handling in endothelial cells and endothelium-dependent smooth muscle relaxation was impaired in SERCA3 null mice (Liu et al., 1997). Conversely, overexpression of SERCA1a or SERCA2a in the heart in transgenic mice increased Ca^{2+} transport by the pump. This translated to improved cardiac function with increases in cardiac contraction and relaxation (Baker et al., 1998; Loukianov et al., 1998). Together these studies indicate SERCA is important in maintaining proper Ca^{2+} cycling in the cell. Loss of SERCA impairs calcium uptake which can result in altered tissue function and disease phenotypes while overexpression of SERCA1a or 2a improves cardiac function.

IIC. Regulation of SR Ca^{2+}-ATPase by Phospholamban

IIC1. Structure of Phospholamban

In cardiac muscle, slow-twitch skeletal muscle and smooth muscle, SERCA2a can be regulated by a low-molecular-weight protein, phospholamban, which can be phosphorylated by various protein kinases. In the dephosphorylated form, a substantial fraction of phospholamban monomers (20%) exists and this has been proposed to be the active species of phospholamban that binds SERCA2 and inhibits it. Upon phosphorylation, phospholamban appears to form mainly pentamers, which is due to changes in the isoelectric point (from 10 to 6.7) of the protein (Simmerman and Jones, 1998).

The complete amino acid sequence of phospholamban has been determined for various tissues and species. There is currently no evidence for the existence of any isoforms for this protein and the phospholamban gene has been mapped to human chromosome 6 (Fujii et al., 1991). The calculated molecular weight of phospholamban is 6080 Da and the protein has been proposed to contain two major domains (Fig. 13.4): a hydrophilic domain (domain I) with three unique phosphorylatable sites (Ser 10, Ser 16 and Thr 17), and a hydrophobic C-terminal domain (domain II) anchored into the SR membrane. The hydrophilic domain (amino acids 1–30) has been further divided into two subdomains: domain Ia (amino acids 1–20) and Ib (amino acids 21–30). Domain Ia has a net positive charge in the dephosphorylated form and consists of an α-helix followed by a Pro residue at position 21 (stalk region). Domain Ib has been suggested to be relatively unstructured (MacLennan et al., 1998, 2002). The hydrophobic domain (amino acids 31–52) forms an α-helix in the SR membrane (Fig. 13.4).

Phospholamban migrates as a 24- to 28-kDa pentamer on sodium dodecyl sulfate (SDS) gels and dissociates into dimers and monomers upon boiling in SDS before electrophoresis. Spontaneous aggregation of phospholamban into pentamers was also observed upon expression of this protein in bacteria or in mammalian cells. Site-specific

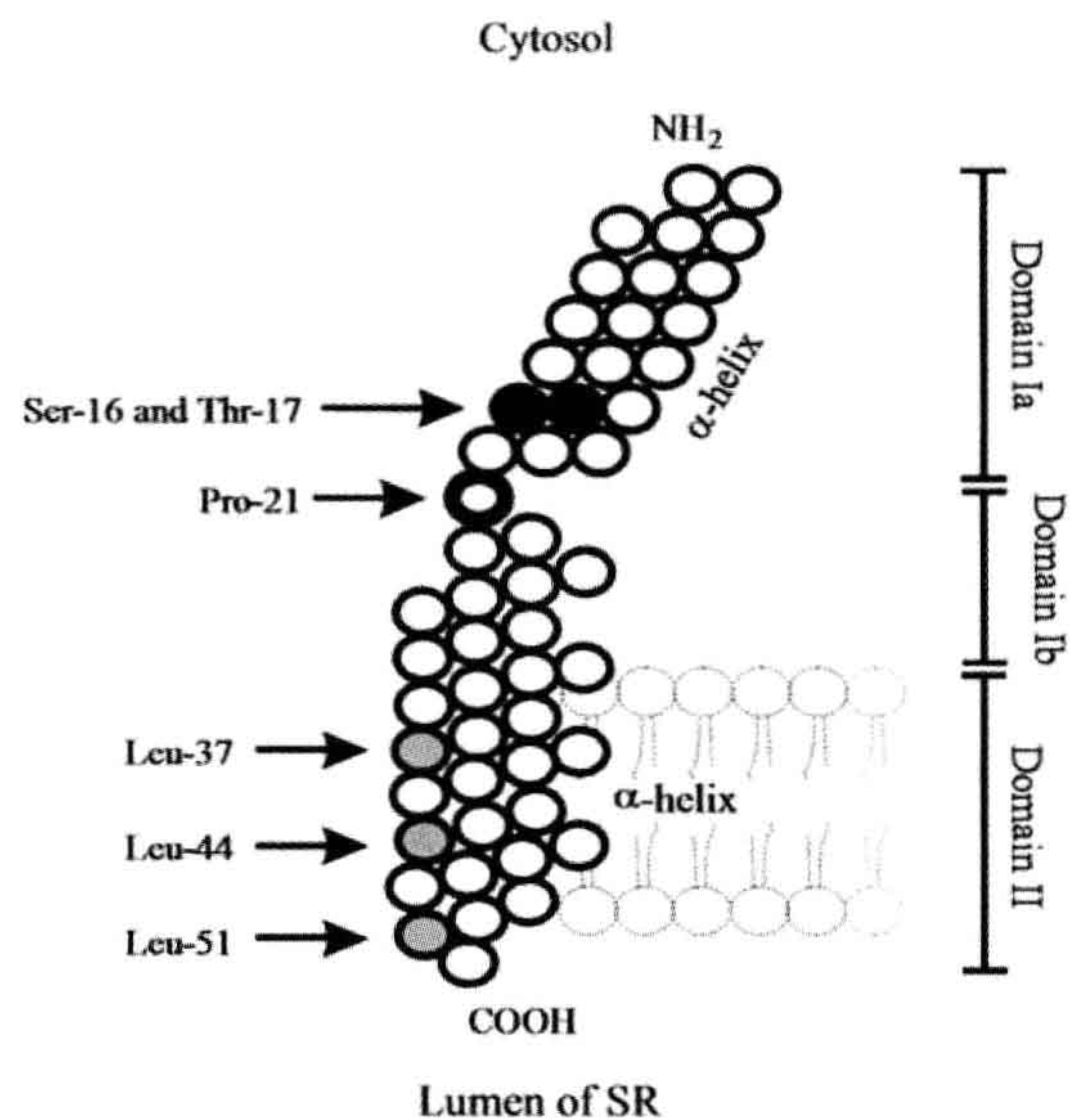


FIGURE 13.4 Molecular model of the structure of phospholamban. The cytoplasmic α-helix (domain Ia, residues 8–20) is interrupted by Pro 21 (heavy circle). Residues 22–32 (domain Ib) are relatively unstructured and may interconvert between transient conformations; residues 33–52 constitute the transmembrane domain II (α-helix). Ser 16 and Thr 17 (black circles) are the adjacent phosphorylation sites. The shaded circles indicate the leucines (Leu 37, Leu 44 and Leu 51), which are important for the phospholamban subunit interactions (pentamer formation).

mutagenesis experiments identified Cys (Cys 36, Cys 41 and Cys 46), Leu (Leu 37, Leu 44 and Leu 51), and Ile (Ile 40 and Ile 47) residues in the hydrophobic transmembrane domain as essential amino acids for phospholamban pentamer formation (reviewed in MacLennan et al., 1998). The leucine and isoleucine amino acids are suggested to form five zippers in the membrane that stabilize the pentameric form of the protein with a central pore (Fig. 13.5), defined by the surface of the hydrophobic amino acids (Simmerman and Jones, 1998).

Monoclonal antibodies raised against phospholamban stimulate SR Ca^{2+} uptake in vitro (Morris et al., 1991). Furthermore, removal of phospholamban from the SR or uncoupling phospholamban from the Ca^{2+}-ATPase (using detergents, high-ionic-strength solutions or polyanions such as heparin sulfate) markedly increases the affinity of the SR Ca^{2+} pump for Ca^{2+}. These findings suggest that the dephosphorylated form of phospholamban is an inhibitor of the SR Ca^{2+}-ATPase. This "depression hypothesis" has been confirmed by studies using purified Ca^{2+}-ATPase and purified or recombinant phospholamban in reconstituted systems. Inclusion of phospholamban resulted in inhibition of the SR Ca^{2+}-ATPase activity in reconstituted vesicles or cells (Kim et al., 1990; Reddy et al., 1996). Cyclic AMP

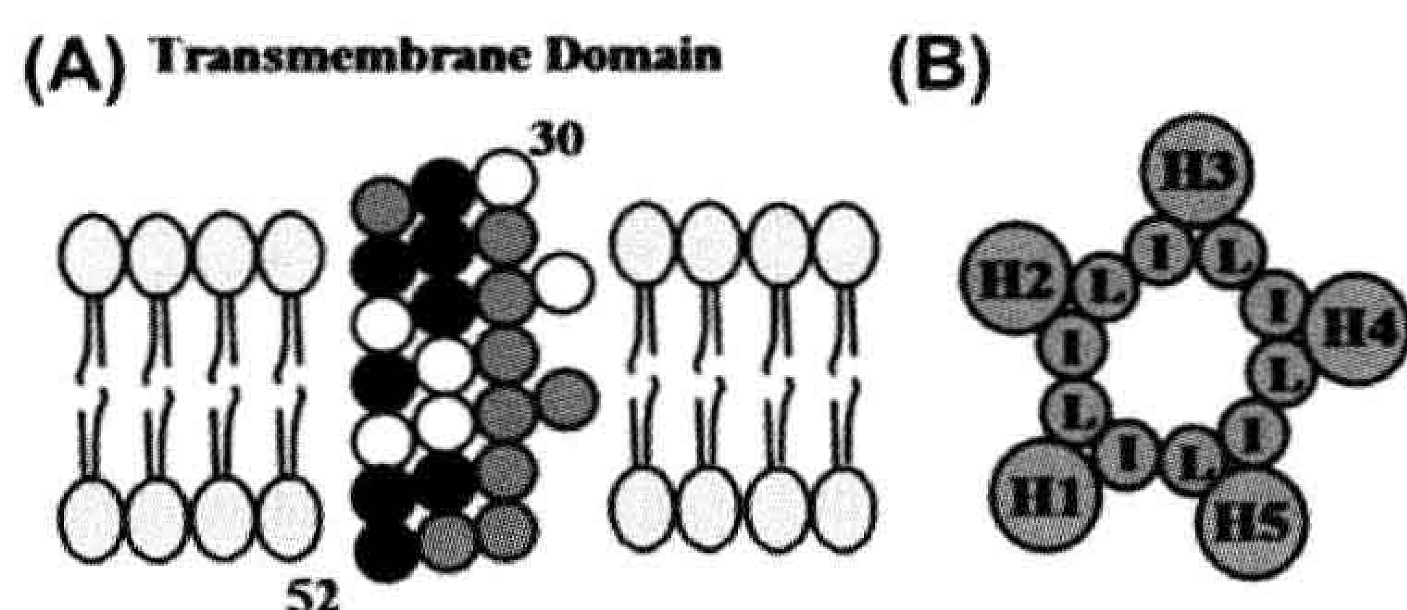


FIGURE 13.5 Model of the transmembrane domain of phospholamban monomer (A) and pentamer (B). (A) Residues 31–52 of monomeric phospholamban are configured as a 3.5 residues/360° turn helix. Darkly shaded circles represent mutations that enhance the inhibitory function of phospholamban by enhanced monomer formation (destabilization of pentamer structure). Lightly shaded circles represent mutations that reduce inhibitory function. (B) The phospholamban pentamer model shows the interaction between the monomer transmembrane domains (H1–H5) at Leu (L) and Ile (I) residues constituting zippers.

phosphorylation of phospholamban reversed its inhibitory effect on the Ca^{2+} pump. The inhibitory role of phospholamban on SR and cardiac function has been directly confirmed using transgenic animal models. Overexpression of the protein (phospholamban-overexpressing mice) was associated with inhibition of SR Ca^{2+} transport, Ca^{2+} transient and depression of basal left ventricular function (Kadambi et al., 1996). On the other hand, partial (phospholamban-heterozygous mice) or complete ablation of the protein (phospholamban-deficient mice) in mouse models was associated with increases in SR Ca^{2+} transport and cardiac function (Luo et al., 1994, 1996; Hoit et al., 1995). Actually, a close linear correlation between the levels of phospholamban and cardiac contractile parameters was observed (Lorenz and Kranias, 1997), indicating that phospholamban is a prominent regulator of myocardial contractility. These findings suggest that changes in the level of this protein will result in parallel changes in SR function and cardiac contractility.

The region of phospholamban interacting with the Ca^{2+}-ATPase may involve amino acids 2–18 (reviewed in MacLennan et al., 1998). Based on these reports, the simplest model for the interaction between the phospholamban cytoplasmic domain and the SR Ca^{2+}-ATPase is one in which the highly positively-charged region of phospholamban (residues 7–16) interacts directly with a negatively-charged region on the surface of the Ca^{2+}-ATPase (Lys-Asp-Asp-Lys-Pro-Val 402) to modulate the inhibitory interactions between the two proteins (Fig. 13.6) (reviewed in MacLennan et al., 1998). This association is disrupted by phosphorylation of Ser 10, Ser 16 or Thr 17 (phosphorylated by protein kinase C, cAMP-dependent and Ca^{2+}-calmodulin dependent protein kinase, respectively) in phospholamban, because the positive charges of the phospholamban cytosolic domain are partially neutralized by the phosphate moiety in this vicinity. Phosphorylation of phospholamban by the cAMP-dependent protein kinase at Ser 16 is associated with local unwinding of the α-helix at position 12–16 resulting in conformational changes in the recognition unit of the protein (Mortishire-Smith et al., 1995).

Interestingly, phospholamban peptides, corresponding to the hydrophobic membrane-spanning domain, also affect Ca^{2+}-ATPase activity by lowering its affinity for Ca^{2+} (reviewed in MacLennan et al., 1998). The importance of the membrane-spanning region of phospholamban in inhibiting SR Ca^{2+}-ATPase activity was demonstrated through mutagenesis studies (reviewed in MacLennan et al., 1998). It was shown that substitution of the pentamer-stabilizing residues (Leu 37, Leu 44, Leu 51, Ile 40 and Ile 47) in the membrane-spanning region (domain II) by Ala resulted in monomeric mutants, which were more effective inhibitors of the SR Ca^{2+}-ATPase activity than wild-type phospholamban. These phospholamban monomeric mutants were called "supershifters" because they decreased the apparent affinity of SR Ca^{2+}-ATPase more

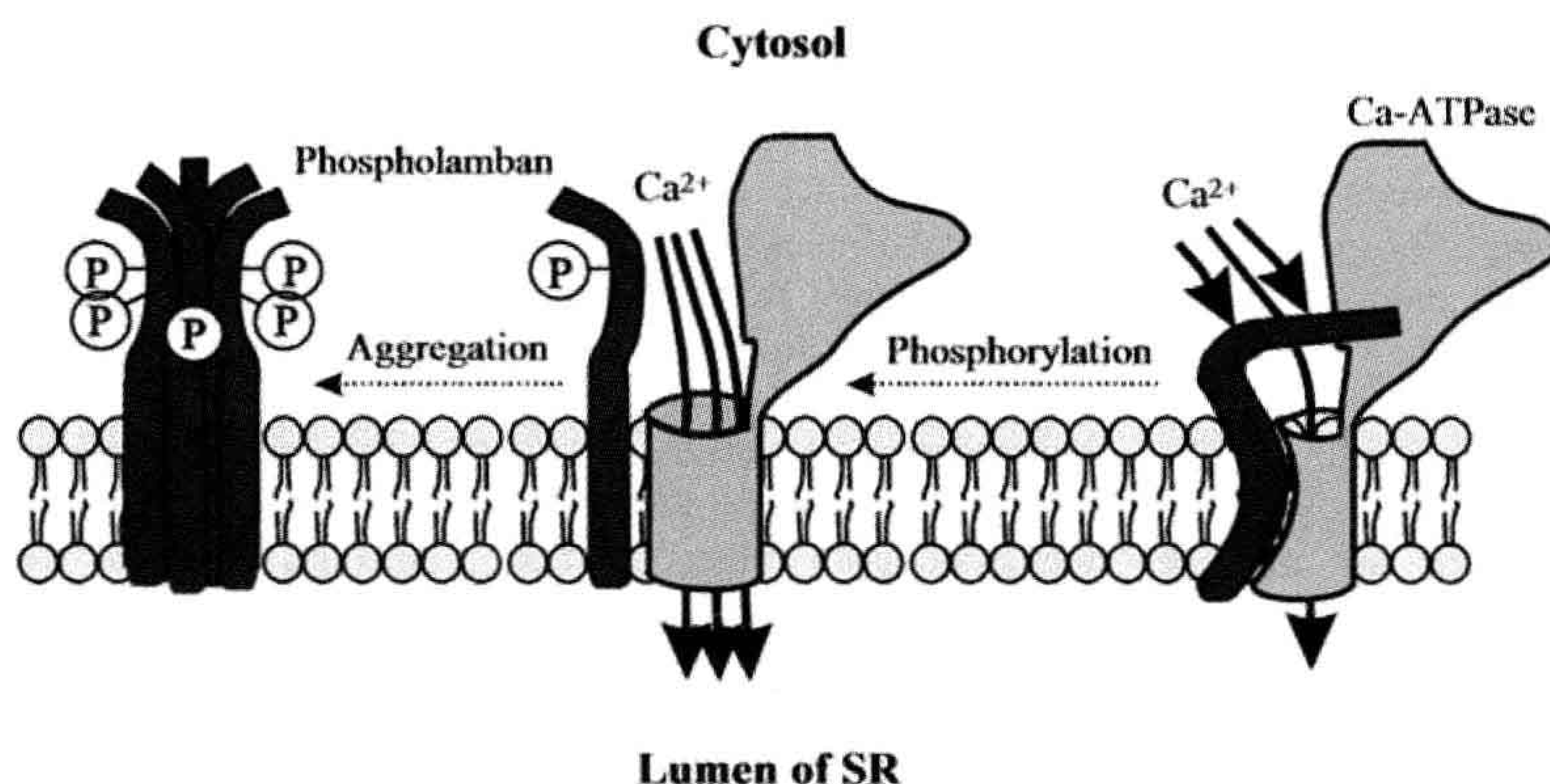


FIGURE 13.6 Model for regulation of SR Ca^{2+}-ATPase by phosphorylated and non-phosphorylated phospholamban. Phosphorylation of phospholamban disrupts the interaction between the two proteins so that the inhibition of the Ca^{2+}-ATPase is relieved. Note that both the cytosolic domain and the membrane-spanning region of phospholamban are involved in the phosphorylation-mediated conformational change to relieve the inhibition. Phosphorylation of phospholamban monomers promotes association into inactive phosphorylated pentamers.

effectively than wild-type phospholamban. Thus, it was proposed that monomeric phospholamban is the active form, which is involved in the interaction with SR Ca^{2+}-ATPase. Furthermore, scanning alanine-mutagenesis studies have identified the amino acid residues in the transmembrane domain of phospholamban (Leu 31, Asn 34, Phe 35, Ile 38, Leu 42, Ile 48, Val 49 and Leu 52), which are associated with loss of function (reviewed in MacLennan et al., 1998). These amino acids are located on the exterior face of each helix in the pentameric assembly of phospholamban (opposite from the pentamer-stabilizing face) (see Fig. 13.5). The importance of these transmembrane domain residues of phospholamban to SR Ca^{2+}-ATPase function has been demonstrated in vivo using several transgenic models. N27A phospholamban can act as a superinhibitor, where hearts have depressed Ca^{2+}-ATPase activity and cardiac function, that cannot be recovered completely by β-adrenergic stimulation and progressed to heart failure (Zhai et al., 2000; Schmidt et al., 2002). Mice expressing the V49G variant in the phospholamban transmembrane domain exhibited diminished cardiac function and hypertrophy which progressed to dilated cardiomyopathy (Haghighi et al., 2001). Moreover, L37A and I40A phospholamban transgenic mice showed similar decreased function and pathology (Zvaritch et al., 2000).

A schematic representation of interaction of phospholamban with SR Ca^{2+}-ATPase is shown in Fig. 13.6. It has been proposed that the phospholamban monomer is the active species for interaction with the SR Ca^{2+}-ATPase and the pentamers are regarded as functionally inactive forms of phospholamban (MacLennan et al., 1998). Phosphorylation of phospholamban monomers promotes association into inactive pentamers. Thus, two important steps for SR Ca^{2+}-ATPase inhibition have been suggested: (1) dissociation of monomeric phospholamban from dephosphorylated pentamers (K_{d1}); and (2) binding of phospholamban monomers to the SR Ca^{2+}-ATPase (K_{d2}). These dissociation constants (K_{d1} and K_{d2}) will control both the concentration of phospholamban monomers and the concentration of units in which monomers are associated with the SR Ca^{2+}-ATPase (MacLennan et al., 1998). There are at least two interaction sites between phospholamban and the SR Ca^{2+}-ATPase (see Fig. 13.6): one in the cytoplasmic domains of the two proteins and another one within the transmembrane sequences. The interaction between the hydrophobic membrane-spanning regions is associated with inhibition of the apparent affinity of SR Ca^{2+}-ATPase for Ca^{2+} (K_{Ca}). The interaction between the cytosolic phospholamban domain Ia and the SR Ca^{2+}-ATPase modulates the inhibitory interaction in the transmembrane region (domain II) through long-range coupling. Disruption of the cytosolic interactions (domain Ia) by phosphorylation of phospholamban or binding of a phospholamban antibody results in disruption of the inhibitory intramembrane interactions. However, resolution of the exact molecular mechanism by which phospholamban inhibits the SR Ca^{2+}-ATPase Ca^{2+} affinity and the concomitant regulation of SR Ca^{2+} transport will have to await the development of a new methodology that allows detection of protein–protein interactions in a membrane environment.

IIC2. In Vitro Studies on Regulation of SR Ca^{2+}-ATPase

In the early 1970s, it was suggested that the effects of various catecholamines on cardiac function may be partly attributed to phosphorylation of the SR by cAMP-dependent protein kinase(s). It soon became clear that the substrate for the protein kinase (PK) was not the SR Ca^{2+}-ATPase but phospholamban. Various other high- and low-molecular-weight SR proteins were also identified as minor substrates for cAMP-dependent PK, but only the changes in the phosphorylation of phospholamban were associated with functional alterations of the cardiac SR.

cAMP-dependent and Ca^{2+}-CaM-dependent PKs have been shown to phosphorylate phospholamban independently of each other (reviewed in Mattiazzi et al., 2005). Phosphorylation by cAMP-dependent PK occurred on Ser 16, whereas Ca^{2+}-CaM-dependent PK catalyzed exclusively the phosphorylation of Thr 17 (reviewed in Mattiazzi et al., 2005). Phosphorylation by either kinase was shown to result in stimulation of the SR Ca^{2+}-ATPase activity and the initial rates of SR Ca^{2+} transport. Stimulation was associated with an increase in the apparent affinity of the SR Ca^{2+}-ATPase for Ca^{2+} (K_{Ca}).

In vitro, phospholamban is phosphorylated by two additional PKs: PK-C and a cGMP-dependent PK. Protein kinase C (Ca^{2+}/phospholipids-dependent PK) phosphorylated the protein at a site distinct (Ser 10) from those phosphorylated by either cAMP-dependent PK or Ca^{2+}-CaM-dependent PK (reviewed in Mattiazzi et al., 2005). Phosphorylation stimulated the SR Ca^{2+}-ATPase activity and it was postulated that this activity played a role in the action of agents known to stimulate phosphoinositide (PI) hydrolysis, since one product of PI hydrolysis, diacylglycerol, is an activator of PK-C. Cyclic GMP-dependent PK was shown to phosphorylate phospholamban on the same residue (Ser 16) as that phosphorylated by cAMP-dependent PK (reviewed in Mattiazzi et al., 2005). This phosphorylation stimulated cardiac SR Ca^{2+} transport, similar to the effects of cAMP-dependent PK. Furthermore, the stimulatory effects on Ca^{2+} transport, mediated by cGMP-dependent phosphorylation of phospholamban, were also observed in smooth muscle and this may be of particular interest because some vasodilators act by increasing cGMP levels in vascular smooth muscle.

IIC3. In Vivo Studies on Regulation of SR Ca^{2+}-ATPase

The phosphorylation of SR proteins and their regulatory effects on the SR Ca^{2+}-ATPase activity have been studied in perfused hearts from various animal species whose ATP pool was labeled with [^{32}P]orthophosphate. Microsomal fractions enriched in SR were prepared from hearts freeze-clamped during stimulation with different agonists (catecholamines, forskolin, phosphodiesterase inhibitors, phorbol esters) and analyzed by gel electrophoresis and autoradiography for ^{32}P incorporation. β-Adrenergic agonist (isoproterenol) stimulation of the perfused hearts produced an increase in ^{32}P incorporation into phospholamban (Kranias and Solaro, 1982; Lindemann et al., 1983). The stimulation of ^{32}P incorporation into phospholamban was associated with an increased rate of Ca^{2+} uptake into SR membrane vesicles and an increased SR Ca^{2+}-ATPase activity (Lindemann et al., 1983; Kranias et al., 1985).

These biochemical changes were associated with increases in left ventricular functional parameters (contractility and relaxation). The in vivo phosphorylation of phospholamban was specific only for inotropic agents that increased the cAMP content of the myocardium (β-adrenergic agonists, forskolin and phosphodiesterase inhibitors). On the other hand, positive inotropic interventions, which increased the intracellular Ca^{2+} level by cAMP-independent mechanisms (α-adrenergic agonists, ouabain and elevated [Ca^{2+}]), failed to stimulate phospholamban phosphorylation and relaxation. Calmodulin inhibitors (fluphenazine) attenuated the isoproterenol-induced phosphorylation of phospholamban (Lindemann and Watanabe, 1985a) and it was shown that at steady-state isoproterenol exposure, phospholamban contains equimolar amounts of phosphoserine (pSer 16) and phosphothreonine (pThr 17). Phosphorylation of Ser 16, however, correlated most closely with changes in cardiac function in beating hearts (Talosi et al., 1993). Based on these results and findings in transgenic animals (Luo et al., 1998), it is proposed that: (1) prevention of Ser 16 phosphorylation (Ser 16 → Ala mutation) results in attenuation of the β-adrenergic response in mammalian hearts; and (2) that phosphorylation of Ser 16 is a prerequisite for Thr 17 phosphorylation. Indeed, in mice containing an alanine substitution for Ser 16, there were diminished responses to the β-adrenergic stimulation. Also, in these animals there was no phosphorylation at Thr 17 (Luo et al., 1998). Conversely, substituting alanine for Thr 17 did not interfere with phosphorylation of Ser 16, and hearts were responsive to β-adrenergic stimulation (Chu et al., 2000). Moreover, overexpression of a non-phosphorylatable form of phospholamban (both Ser 16 and Thr 17 sites mutated to Ala) resulted in maximum inhibition of the SR Ca^{2+}-ATPase calcium affinity (Brittsan et al., 2000). It should be noted that, in some conditions, Thr 17 has been shown to be phosphorylated independently of Ser 16, such as increased frequency stimulation of the heart, elevated intracellular Ca^{2+}, ischemia-reperfusion injury and acidosis (Zhao et al., 2004; Mattiazzi et al., 2005).

The muscarinic agonist acetylcholine attenuated the increases in cAMP levels, phosphorylation of phospholamban and the SR Ca^{2+}-ATPase activity produced either by β-adrenergic stimulation or by phosphodiesterase inhibition (using isobutylmethylxanthine) (Lindemann and Watanabe, 1985b). Protein kinase C and cGMP-dependent PK, which have been shown to phosphorylate phospholamban in vitro, failed to demonstrate similar effects in beating guinea pig hearts in response to stimuli that activate PK-C or elevate the cGMP levels (Huggins et al., 1989; Edes and Kranias, 1990). Thus, the physiological relevance of PK-C and PK-G in beating hearts is not clear at present.

The functional alterations in the SR Ca^{2+}-ATPase activity may explain, at least partly, the activating and relaxing effects of β-adrenergic agents in cardiac muscle (Figs. 13.7 and 13.8). The cAMP-dependent phosphorylation of phospholamban under either in vitro or in vivo conditions increases the rate of SR Ca^{2+} transport and SR Ca^{2+}-ATPase activity. Such an increase in Ca^{2+} transport is expected to contribute primarily to the relaxing effects of

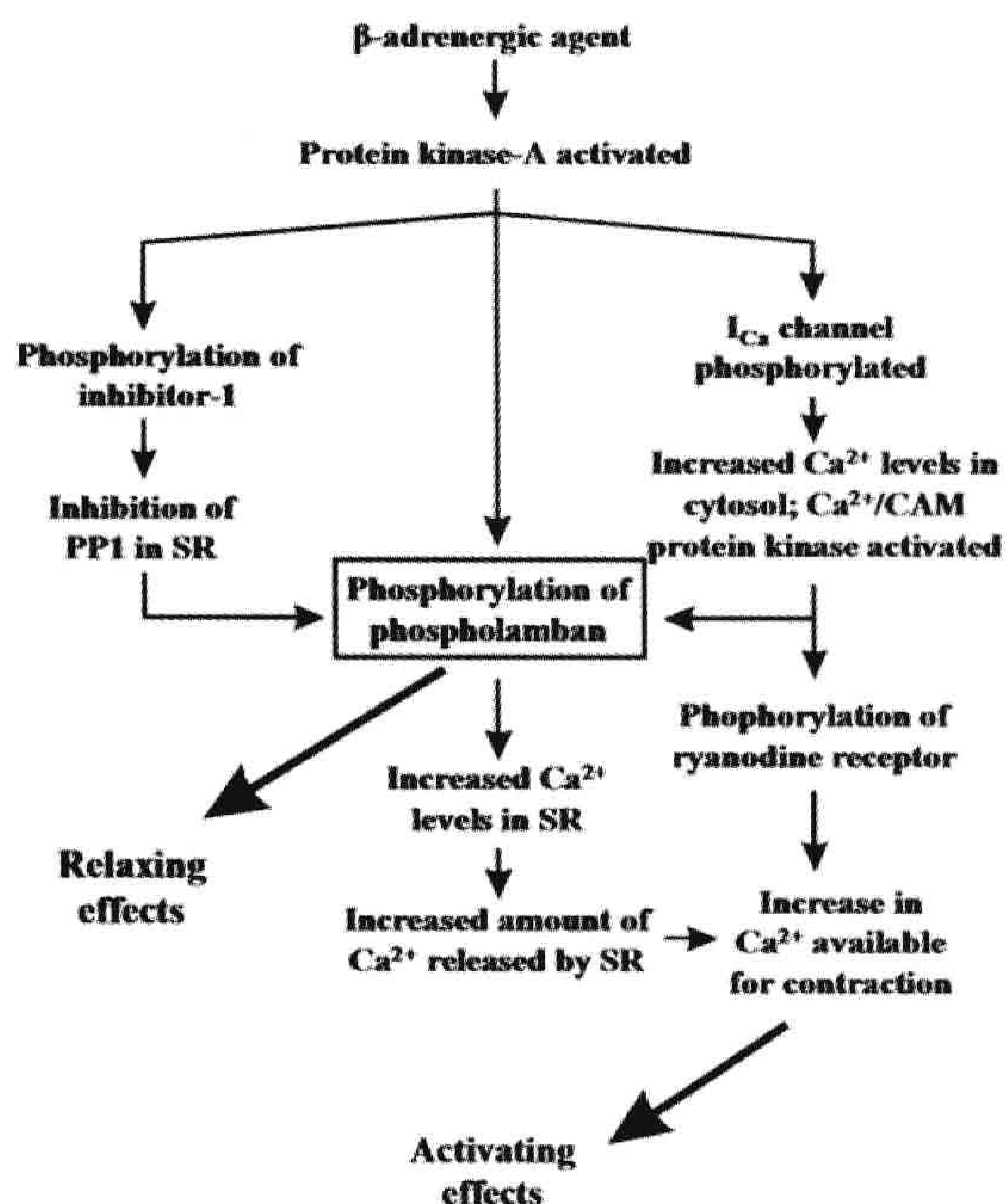


FIGURE 13.7 Schematic diagram of possible relaxing and activating effects of β-adrenergic agents in the heart. PP1, protein phosphatase 1.

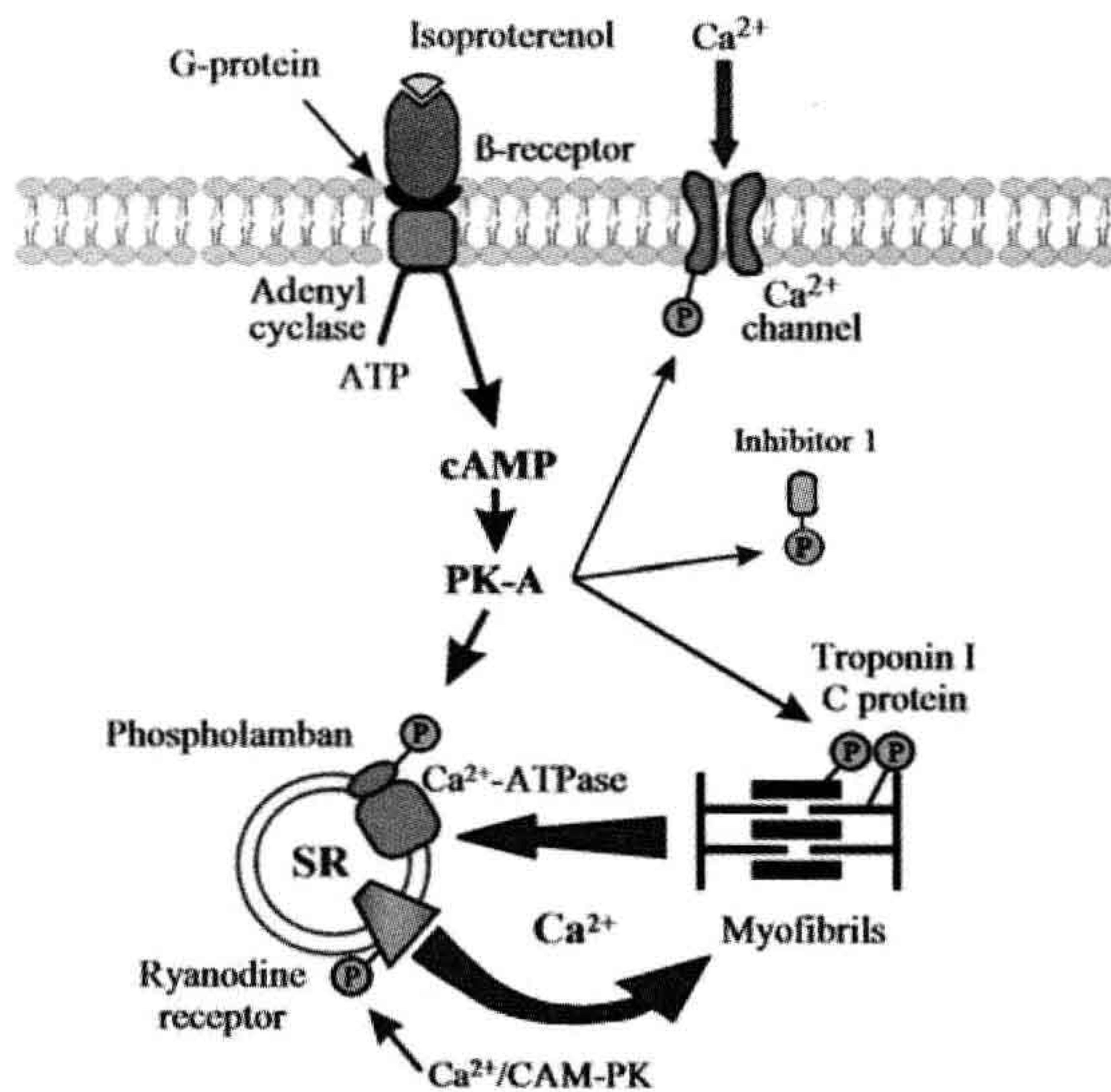


FIGURE 13.8 Effects of β-adrenergic agents on protein phosphorylation in cardiac cells. Increased intracellular cAMP levels activate the cAMP-dependent protein kinase(s), which phosphorylates various proteins (phospholamban, inhibitor-1, Ca^{2+}-channel and myofibrillar proteins) and increases the rates of SR Ca^{2+} uptake and release.

catecholamines (Fig. 13.7). An additional mechanism which contributes to the increased phosphorylation of phospholamban upon β-adrenergic stimulation is the phosphorylation of the phosphatase inhibitor protein by the stimulated cAMP-dependent kinase. This phosphorylation results in inactivation of protein phosphatase 1 and, thus, inhibition of dephosphorylation of phospholamban during the action of catecholamines (Fig. 13.7). The increased phosphorylation of phospholamban and the increased Ca^{2+} levels accumulated by the SR would lead to the availability of higher levels of Ca^{2+} to be subsequently released for binding to the contractile proteins (Fig. 13.7). The critical and prominent role of phospholamban in the mediation of β-adrenergic functional responses was also confirmed in transgenic animal studies. Cardiac myocytes or work-performing heart preparations from phospholamban-deficient mice exhibited largely attenuated responses to β-adrenergic agonist stimulation (Luo et al., 1996; Wolska et al., 1996), indicating that phospholamban is a key phosphoprotein in the heart's responses to β-adrenergic agonists.

Phosphorylation of other myocardial phosphoproteins has also been suggested to be involved in the mediation of positive inotropic and lusitropic effects of β-adrenergic agonists. Cyclic AMP-dependent protein kinase-mediated phosphorylation of the α_1 subunit of the Ca^{2+} channel (see Fig. 13.8) is associated with an increase in the voltage-dependent Ca^{2+} current (I_{Ca}), which enhances the Ca^{2+} levels available in the cytosol during β-adrenergic agonist stimulation. Phosphorylation of troponin I has been shown to decrease the sensitivity of myofilaments for Ca^{2+} both in intact myocardium and skinned fibers (Kranias et al., 1985). The desensitization of myofibrils is accompanied by an increased off-rate of Ca^{2+} from troponin C, which could contribute to faster relaxation (see Fig. 13.8). In addition, phosphorylation of the SR Ca^{2+}-release channel (ryanodine receptor) by Ca^{2+}-CaM-dependent protein kinase may stimulate Ca^{2+} release from the SR vesicles and contribute to the elevation of intracellular Ca^{2+} levels during systole. Thus, the enhanced Ca^{2+} influx across the sarcolemma, together with the increased Ca^{2+} levels to be released from the SR, may result in an elevation of the Ca^{2+} available for the contractile machinery, leading to an increase in the amplitude of contraction (see Fig. 13.8).

In recent years, several human mutations in the phospholamban gene have been identified and additional insights into phospholamban regulation of SERCA2 have been obtained. The first mutation discovered encoded Arg 9 Cys, which is included in the PKA phosphorylation consensus sequence of phospholamban. This mutation reduced the phosphorylation of phospholamban in vitro and in vivo using a gene-targeted mouse model (Schmitt et al., 2003). Two human mutations, Leu 39 stop and Arg 14 del, in phospholamban interfered with targeting of the protein to the endoplasmic reticulum. The Leu 39 stop mutation produces a truncated phospholamban protein that, when introduced in HEK 293 cells, resulted in an unstable protein that was misrouted to other membranes. Cardiac explants from human carriers of Leu 39 stop had no detectable phospholamban in the endoplasmic reticulum (Haghighi et al., 2003). Deletion of Arg 14 also interfered with targeting of phospholamban to the endoplasmic reticulum (Sharma et al., 2010). Mice expressing the Arg 14 del mutation had ventricular dilation and fibrosis accompanied by increased mortality with death as early as two weeks (Haghighi et al., 2006). These naturally occurring mutations in phospholamban have revealed the importance of the balance of phosphorylated and unphosphorylated phospholamban and its localization in the heart.

IID. Other Regulators of the SR Ca^{2+}-ATPase

While phospholamban is the primary regulator of SR Ca^{2+}-ATPase activity, several other proteins have been identified that modulate the SR Ca^{2+} pump (Fig. 13.9). For example, sarcolipin, a homolog of phospholamban, has been shown to inhibit SERCA1a and SERCA2a; however, sarcolipin is expressed more abundantly in atria unlike phospholamban which is predominantly in the ventricle of the heart (Bhupathy et al., 2007). Overexpression of sarcolipin in mice resulted in reduced Ca^{2+} affinity of SERCA2a as well as decreased cardiac function which was improved by

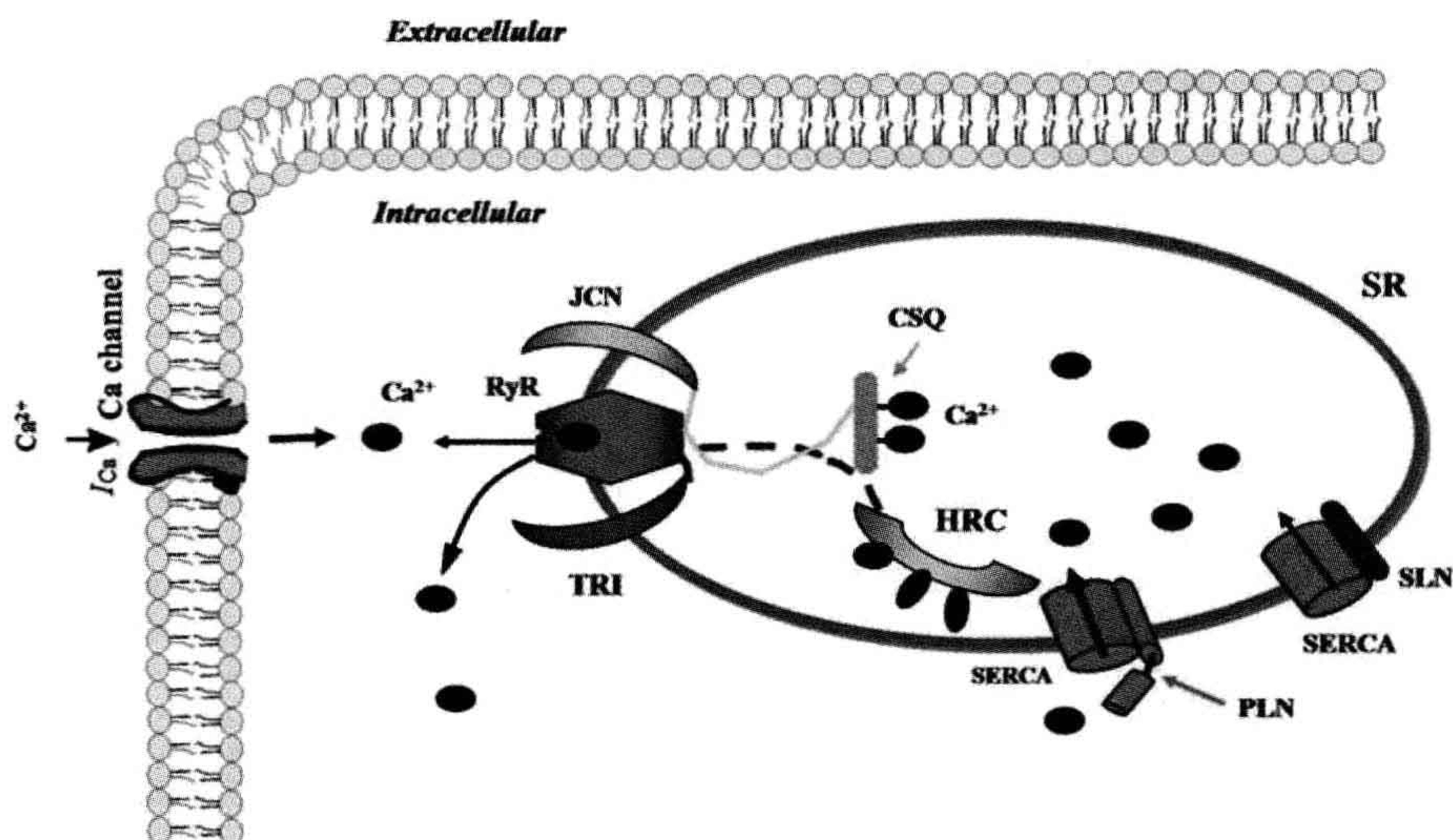


FIGURE 13.9 Schematic of regulators of SR Ca^{2+}-ATPase (SERCA) function. Phospholamban (PLN) is the primary regulator of the SR Ca^{2+} pump. Sarcolipin (SLN), a homolog of PLN, can also modulate SERCA activity and may be important to Ca^{2+} cycling in the atria where it is abundant. Histidine-rich Ca^{2+}-binding protein (HRC) is an SR lumen protein that binds Ca^{2+} and has been shown to interact with SERCA and affect Ca uptake. HRC also interacts with triadin, a protein that is part of the Ca^{2+} release quaternary complex including the ryanodine receptor (RyR) and junctin (JCN).

β-adrenergic stimulation in vivo (Bhupathy et al., 2007). Conversely, ablation of sarcolipin in mice resulted in elevated SR Ca^{2+} uptake and faster relaxation of the atria (Babu et al., 2007). The histidine-rich calcium binding protein (HRC), located in the SR, was shown to interact with SERCA2a in vitro in a Ca^{2+} sensitive manner with maximal binding occurring at low Ca^{2+} concentrations (Arvanitis et al., 2007). HRC also interacts with triadin, a protein that is part of the Ca^{2+} release quaternary complex; therefore, HRC can regulate both Ca^{2+} release uptake and release making it an interesting new molecule in SR Ca^{2+} handling. Indeed, acute overexpression of HRC decreased Ca^{2+} release and contractility in vitro while chronic overexpression reduced SR Ca^{2+} uptake and contractility in vivo (Fan et al., 2004; Gregory et al., 2006). Moreover, HRC transgenic mice exhibited cardiac remodeling with aging (Gregory et al., 2006).

IIE. SR Ca^{2+}-ATPase in Cardiac Diseases

The complex regulation of the SR function clearly indicates that even small disturbances in SR Ca^{2+} handling may result in profound changes and deterioration of normal myocardial function. The fast removal of Ca^{2+} by the SR Ca^{2+}-ATPase during diastole and the subsequent rapid release through the SR Ca^{2+} channel (ryanodine receptor) at the beginning of contraction are prerequisites for normal diastolic and systolic function. We briefly outline in the next section the alterations in the SR Ca^{2+}-ATPase in the major cardiac diseases.

IIE1. SR Ca^{2+}-ATPase in Hyperthyroidism and Hypothyroidism

Thyroid hormones are important regulators of myocardial contractility and relaxation. Chronic increases in thyroid hormone levels lead to cardiac hypertrophy, with increases in the heart rate and cardiac output as well as left ventricular contractility and velocity of relaxation. On the other hand, opposite effects are associated with a hypothyroid condition. The mechanisms underlying these changes have been the subject of numerous investigations. It is assumed that in hypo- and hyperthyroid hearts the altered gene expression of the cardiac SR proteins and, hence, the changes in the intracellular Ca^{2+} transients, is the most important determinant of the altered myocardial function. It was shown that the velocity of ATP-dependent Ca^{2+} transport and the Ca^{2+}-ATPase activity are specifically increased in SR vesicle preparations from hyperthyroid compared with euthyroid hearts (Beekman et al., 1989). Opposite changes were noted for hypothyroid animals compared with euthyroid ones (Beekman et al., 1989).

Examination of the steady-state mRNA levels of the cardiac SR Ca^{2+}-ATPase and the ryanodine receptor revealed a significant increase (140–190%) in hyperthyroid and a marked decline (40–50%) in hypothyroid

animals (Arai et al., 1991). The changes in mRNA levels for the Ca^{2+}-ATPase in hypothyroid and hyperthyroid conditions also reflected changes in the protein amounts of the enzyme in these hearts (Kiss et al., 1994, 1998). Interestingly, in the case of phospholamban, the regulator of the Ca^{2+}-ATPase, and calsequestrin, there was no coordinated regulation with respect to the Ca^{2+}-ATPase. In fact, both the relative mRNA level and the protein content of phospholamban were reported to decrease in hyperthyroid animals, whereas there was no change noted in the calsequestrin mRNA level upon L-thyroxine treatment. In hypothyroid hearts, an opposite trend was noted since the protein amount of phospholamban was found to be increased as compared to the euthyroid or hyperthyroid animals (Kiss et al., 1994, 1998). Consequently, the phospholamban-Ca^{2+}-ATPase protein ratio was highest in the hypothyroid animals, followed by euthyroid and hyperthyroid animals. These changes in the phospholamban-Ca^{2+}-ATPase ratio were associated with coordinate alterations in the SR Ca^{2+} uptake, affinity of the SERCA2 for Ca^{2+} and myocardial function (Kiss et al., 1994; Kimura et al., 1994).

These changes indicate that the SR proteins responsible for Ca^{2+} uptake and release (Ca^{2+}-ATPase and ryanodine receptor) are coordinately regulated in hypothyroid and hyperthyroid hearts and provide a simple explanation for the altered Ca^{2+} release and reuptake capacity and hence the myocardial function under these conditions.

IIE2. SR Ca^{2+}-ATPase in Cardiomyopathies

Dilated cardiomyopathy is a frequent form of cardiac muscle disease and is characterized by an impaired systolic function and dilatation of both ventricles (systolic pump failure). In various animal models of primary and secondary dilated cardiomyopathy, it was shown that both SR Ca^{2+} binding capacity and uptake were depressed because of the decreased activity and protein level of the SR Ca^{2+}-ATPase (Edes et al., 1991). In some studies of human idiopathic dilated cardiomyopathy, decreases were noted for both SR Ca^{2+} uptake rates and Ca^{2+}-ATPase activity (Limas et al., 1987; Unverferth et al., 1988) as well as myocardial Ca^{2+} handling (Gwathmey et al., 1987; Beuckelmann et al., 1992). Examination of the mRNA levels in left ventricular biopsies from patients with dilated cardiomyopathy revealed a significant decrease in mRNA content for the SR Ca^{2+}-ATPase relative to other mRNA forms (Mercadier et al., 1990; Arai et al., 1993). In contrast, other authors were unable to detect a decrease in SR Ca^{2+} uptake activity (Movsesian et al., 1989) or the immunodetectable levels of the SR Ca^{2+}-ATPase protein (Schwinger et al., 1995) in the left ventricular myocardium from patients with idiopathic dilated cardiomyopathy. Furthermore, the gating mechanism of the SR Ca^{2+}-release channel was reported to be abnormal in dilated cardiomyopathy (D'Agnolo et al., 1992; Sen et al., 2000), and it was suggested that defective excitation–contraction coupling is involved in the pathogenesis of this disease.

Another type of cardiomyopathy, hypertrophic cardiomyopathy, has only been recognized in clinical practice for the last four decades. The characteristics of this disease are asymmetric interventricular septal hypertrophy and narrowing of the left ventricular outflow tract, with or without outflow obstruction (outflow tract pressure gradient). In the familial form of hypertrophic cardiomyopathy, which accounts for about 45–70% of all cases, mutations in myofibrillar protein genes (β-myosin heavy chain, troponin T, troponin I, α-tropomyosin and C protein among others) are associated with the disease (Ho, 2010). Additionally, prolongation of the Ca^{2+} transient, abnormal Ca^{2+} handling and a decline in SR Ca^{2+}-ATPase mRNA levels are reported to be characteristic for human hypertrophic cardiomyopathy (Lipskaia et al., 2009), which may explain the diastolic function impairment in this disease.

In chronic heart failure due to hemodynamic overload, irrespective of the specific etiology (valvular heart disease, cardiomyopathy, chronic ischemic heart disease or hypertension), a reduction was observed in both the number and the activity of the SR Ca^{2+} pump (Limas et al., 1987; Unverferth et al., 1988). Furthermore, a close correlation was obtained between the SR Ca^{2+}-ATPase mRNA or protein levels and the myocardial function (Gregory and Kranias, 2006). In addition, total phospholamban protein levels are unchanged in heart failure, but phosphorylated phospholamban levels are decreased further compounding reduced SR Ca^{2+}-ATPase activity (Gregory and Kranias, 2006). Interestingly, the Na^{+}-Ca^{2+} exchanger gene expression is increased in failing human hearts and it is hypothesized that the upregulation of this protein may compensate for the depressed SR function (Bers and Despa, 2006).

IIE3. SR Ca^{2+}-ATPase in Ischemia

A brief period of ischemia (10–20 min) induces reversible tissue damage in cardiac muscle, resulting in a "stunned" myocardium. This condition is characterized by regional contractile abnormalities (declines in both systolic and diastolic function) that persist for several hours despite the absence of necrosis. These hemodynamic changes are associated with a reduction in SR Ca^{2+} transport (Krause et al., 1989; Limbruno et al., 1989). The maximal activity of the SR Ca^{2+}-ATPase was found to be depressed and the Ca^{2+} sensitivity of this enzyme was decreased (Krause et al., 1989). Furthermore, a decrease in the coupling ratio (mol Ca^{2+}/mol ATP) was observed in the SR membranes isolated from the stunned

myocardium, which was suggested to be the result of an increase in the Ca^{2+} permeability of the SR membrane. The SR Ca^{2+}-release process was also found to be impaired in the stunned myocardium due to a reduction of the number of ryanodine receptors (Zucchi et al., 1994). These data suggest that complex modifications of the SR function occur in the stunned myocardium, which are at least partly responsible for the contractile impairment found in this condition.

In long-lasting myocardial ischemia, gradual declines in both SR Ca^{2+}-ATPase activity and Ca^{2+} uptake were found, which may be due to decreased SR Ca^{2+}-ATPase protein (Talukder et al., 2009). Increasing SERCA2a via gene transfer or transgenic overexpression is cardioprotective against ischemia/reperfusion injury. Ischemia was also shown to result in variable changes in the phosphorylation of phospholamban (Talukder et al., 2009). Thus, the role of phospholamban regulation of sarcoplasmic reticulum Ca^{2+}-ATPase in ischemia is not resolved. A combination of various pathogenic factors has been suggested to be responsible for the reduced SR function and the final tissue necrosis in the ischemic myocardium. These pathological factors include pH reduction (acidosis), activation of intracellular proteolytic enzymes, and increased generation of free radicals.

IIE4. SR Ca^{2+}-ATPase as a Target for Heart Failure Treatment

Given the central importance of the SR Ca^{2+}-ATPase to proper SR Ca^{2+} cycling, excitation–contraction coupling and thus cardiac function, SERCA2 has been a focus of potential gene-targeted therapy for heart failure, especially since pump activity is depressed in failing hearts. SERCA2a gene transfer in animal models and human failing cardiomyocytes has shown beneficial effects, including improved contractility and energetics as well as prevention of arrhythmias and hypertrophy. For example, adenoviral delivery of SERCA2a to human failing cardiomyocytes rescued the depressed contractility and Ca^{2+} transients (reviewed in Lipskaia et al., 2010). Adenovirus-mediated gene transfer also improved function and survival in rat failing hearts. Additionally, SERCA2a delivery suppressed arrhythmias as well as infarct size in a rat model of ischemia/reperfusion injury (reviewed in Lipskaia et al., 2010). These beneficial effects in heart failure have also been demonstrated in large animals (reviewed in Lipskaia et al., 2010).

III. OTHER ATPases

The Ca^{2+} regulation in eukaryotic cells involves a complex mechanism that maintains a low background Ca^{2+} concentration (usually 0.1–0.2 μM) in the cell interior. Eukaryotic cells generally satisfy their Ca^{2+} demands by extracting Ca^{2+} from their own internal stores, but it is also evident that the long-term regulation of the Ca^{2+} gradient across the plasma membrane is a result of the concerted operation of the importing (Ca^{2+} channel) and exporting (SR Ca^{2+} pump; Na^{+}-Ca^{2+}exchanger and Ca^{2+} pump of the surface membrane) Ca^{2+} systems. The plasma membrane Ca^{2+}-ATPase is a low-capacity system possessing a very high Ca^{2+} affinity, which enables the enzyme to interact with Ca^{2+} at low intracellular concentrations. Consequently, its function is continuous and presumably satisfies the fine tuning of Ca^{2+} homeostasis.

IIIA. General Properties of Plasma Membrane Ca^{2+}-ATPase(s)

The plasma membrane Ca^{2+}-ATPase (molecular mass of 140 kDa) general kinetic mechanism follows the pattern of the SR Ca^{2+}-ATPase. ATP phosphorylates an Asp residue to yield an acid-stable phosphorylated intermediate. The elementary steps of the cycle are probably similar in both SR and plasma membrane Ca^{2+}-ATPases (Schatzmann, 1989). The stoichiometry between transported Ca^{2+} and hydrolyzed ATP is only 1.0 for the plasma membrane Ca^{2+} pump. The administration of La^{3+} under various experimental conditions has been associated with an increase in the steady-state phosphoenzyme level of the plasma membrane Ca^{2+}-ATPase and this increase possibly results from stabilization of the aspartyl phosphate (inhibition of hydrolysis of the phosphate group). The other classic inhibitor of Ca^{2+} pumps, vanadate, has been found to be a potent inhibitor of the plasma membrane Ca^{2+}-ATPase (Brini and Carafoli, 2009).

Calmodulin stimulates the plasma membrane Ca^{2+}-ATPase by direct interaction with the enzyme. It has been shown that the stimulation results from a combined effect on the affinity for Ca^{2+} (K_m) and the maximal transport rate (V_{max}) (Brini and Carafoli, 2009). The calmodulin-binding domain of the Ca^{2+} pump has been suggested to function as a repressor of the enzymatic activity (autoinhibitory function) and calmodulin may relieve this inhibition (Brini and Carafoli, 2009). A common mechanism in the autoinhibition of plasma membrane Ca^{2+}-ATPase and phospholamban inhibition of SR Ca^{2+}-ATPase has been suggested. In both proteins, the interacting sites are amphiphilic and located in the cytoplasmic region. The interaction occurs with homologous regions in the SR and plasma membrane Ca^{2+}-ATPases close to the phosphorylation sites. In the absence of calmodulin, the plasma membrane Ca^{2+} pump can be activated by several other compounds. Polyunsaturated fatty acids and acidic phospholipids (phosphatidylinositol, phosphatidylinositol 4-phosphate and phosphatidylinositol 4,5-diphosphate) have been reported to be good activators

and, since they are present in the plasma membrane, they may be important regulators of the Ca^{2+}-ATPase under in vivo conditions (Brini and Carafoli, 2009). Phosphorylation of the enzyme by cAMP-dependent PK or PK-C has also been reported to stimulate plasma membrane Ca^{2+}-ATPase activity. The cAMP-dependent phosphorylation occurs C-terminally to the calmodulin-binding domain and the phosphorylation-mediated activation may likewise be significant in vivo. The PK-C phosphorylation occurs in the calmodulin-binding domain, inhibiting the binding of calmodulin to the plasma membrane Ca^{2+}-ATPase and lowering the autoinhibitory potential of this domain (Brini and Carafoli, 2009). Cyclic GMP–dependent PK has also been reported to stimulate the plasma membrane Ca^{2+} pump in vascular smooth muscle, but the Ca^{2+}-ATPase enzyme was not found to be the substrate for this kinase.

IIIB. Primary Structure and Topography of Plasma Membrane Ca^{2+}-ATPase(s)

The complete amino acid sequence of the plasma membrane Ca^{2+} pump has been deduced from rat and human cells (Shull and Greeb, 1988; Verma et al., 1988). It appears that four plasma membrane Ca^{2+}-ATPase (PMCA 1–4) isoforms are encoded by a multigene family and additional variability is produced by alternative RNA splicing of each gene transcript (Table 13.2). The regions important for the catalytic function and the transmembrane domains are highly conserved, with no observed diversity. The isoform diversity seems to alter primarily the regulatory characteristics of the enzyme and it can be regarded as an adaptation to tissue specificity.

The secondary structure of the plasma membrane Ca^{2+}-ATPase is similar to that of the SR Ca^{2+}-ATPase (Shull and Greeb, 1988). The enzyme contains 10 putative transmembrane helices, which are connected on the outside of the plasma membrane by short loops. Three primary domains (about 80% of the pump protein) protrude into the cytoplasm. The first domain corresponds to the transducing unit, which couples ATP hydrolysis to Ca^{2+} translocation. The second protruding domain contains the aspartyl phosphate site (phosphorylation domain). The C-terminal portion of this domain can also be labeled by ATP analogs and contains a "hinge" region that permits the movement of aspartyl phosphate and the ATP-binding site. The third C-terminal protruding domain contains the calmodulin-binding sequence and the phosphorylation sites for protein kinase C and cAMP-dependent protein kinase. The latter is not present in all isoforms. As in the SR Ca^{2+}-ATPase, selective mutations in the M4 and M6 transmembrane segments in the plasma membrane Ca^{2+}-ATPase have been associated with loss of its ability to form the ATP- and Ca^{2+}-dependent phosphorylated intermediate and to transport Ca^{2+} (Guerini et al., 1998).

IIIC. Isoform-Specific Function of the Plasma Membrane Ca^{2+}-ATPase

While there is no specific inhibitor of the plasma membrane Ca^{2+}-ATPase (PMCA), the use of gene-altered mouse models has provided insights into the function of specific isoforms of the pump. Ablation of the PMCA1 gene in mice is lethal, suggesting its importance in a housekeeping function (Okunade et al., 2004). However, ablation of PMCA2 does not result in lethality, but mice have a reduction in spinal cord motor neurons, hearing loss and abnormalities in balance control. The deafness in PMCA2 null mice is related to a loss of otoconia and pathology of the auditory system. The PMCA2 isoform is also involved in lactation as PMCA2 null mice had a decrease in the Ca^{2+} levels in the milk (reviewed in Brini and Carafoli, 2009). PMCA4 homozygous null mice are also viable, but male mice are infertile due to reduced sperm motility (Okunade et al., 2004). No mouse model of PMCA3 ablation has been generated yet, thus the functional importance of this isoform is not currently clear. These studies indicate that the plasma membrane Ca^{2+}-ATPase is essential for maintaining various processes in a variety of cell types and there are different functional roles for the various isoforms.

TABLE 13.2 Distribution of the Human Plasma Membrane Ca^{2+}-ATPase (PMCA) Isoforms

Gene	Tissue Distribution	Level of Expression	Inhibition by Calmodulin
PMCA1[a]	Ubiquitous	High	Medium sensitive
PMCA2	Restricted (brain high)	High	Highly sensitive
PMCA3	Restricted (brain low)	Low	N/A[b]
PMCA4	Ubiquitous	Medium	Medium sensitive

[a]*PMCA numbers identify different gene products.*
[b]*N/A = data not available.*

IV. OVERVIEW

The Ca^{2+} levels in muscle are primarily regulated by the sarcoplasmic reticulum (SR) network, which serves as a sink for Ca^{2+} ions during relaxation and as a Ca^{2+} source during contraction. In cardiac muscle, most of the intracellular Ca^{2+} released during systole is taken up by the SR through its Ca^{2+}-ATPase. This translocation of Ca^{2+} from the cytosol into the SR lumen uses ATP as the energy source, and is characterized by the formation of a phosphorylated intermediate (E_1~P) for the Ca^{2+}-ATPase.

In cardiac muscle, slow-twitch skeletal muscle and smooth muscle, the Ca^{2+}-ATPase is regulated by a low-molecular-weight phosphoprotein called phospholamban. In its dephosphorylated form, phospholamban is an inhibitor of the Ca^{2+}-ATPase and phosphorylation relieves this inhibition. Phosphorylation of phospholamban occurs by cAMP-dependent, cGMP-dependent, Ca^{2+}-calmodulin-dependent, and Ca^{2+}-phospholipid-dependent protein kinases in vitro. However, in vivo studies have indicated that phospholamban is phosphorylated only by cAMP-dependent and Ca^{2+}-calmodulin-dependent protein kinases in intact beating hearts. A phospholamban phosphatase activity has been reported to be present in SR membranes, which can dephosphorylate this regulatory protein and reverse its stimulatory effects on the Ca^{2+}-ATPase.

Alterations in the SR Ca^{2+}-ATPase activity and its regulation by phospholamban have been shown to occur in cardiac diseases such as hypothyroidism, hyperthyroidism, hypertrophy, heart failure and ischemia. In most instances, alterations in Ca^{2+}-ATPase activity correlated with alterations in its mRNA levels and ventricular function. Recent studies have supported the targeting of the SR Ca^{2+}-ATPase as a therapeutic modality in cardiomyopathy and heart failure.

Another Ca^{2+}-ATPase, which is also important for maintaining Ca^{2+} homeostasis in muscle, is the plasma membrane Ca^{2+}-ATPase. This enzyme transports Ca^{2+} to the extracellular space and uses ATP as its energy source, similar to the SR Ca^{2+}-ATPase. The plasmalemmal Ca^{2+}-ATPase may be distinguished from the SR Ca^{2+}-ATPase primarily by its distinct sensitivity to La^{3+}, vanadate and calmodulin.

The primary structure of the various Ca^{2+} pumps has been elucidated and efforts are underway to further understanding the structural–functional relationships of these enzymes under pathological conditions. Furthermore, there is a growing interest in uncovering the mechanisms underlying regulation of the Ca^{2+}-ATPases by key endogenous proteins.

ACKNOWLEDGMENTS

The authors' research discussed in this chapter was supported by National Institutes of Health Grants HL-26057, HL-64018 and HL007382 training grant. This article was published in *Cell Physiology Sourcebook* 3rd edn, I. Edes and E.G. Kranias, eds (2001), Ch. 18, Ca^{2+}-ATPases, pp. 271-282. Copyright Elsevier, Inc.

BIBLIOGRAPHY

Arai, M., Alpert, N. R., MacLennan, D. H., Barton, P., & Periasamy, M. (1993). Alterations in sarcoplasmic reticulum gene expression in human heart failure. A possible mechanism for alterations in systolic and diastolic properties of the failing myocardium. *Circ Res, 72*, 463–469.

Arai, M., Otsu, K., MacLennan, D. H., Alpert, N. R., & Periasamy, M. (1991). Effect of thyroid hormone on the expression of mRNA encoding sarcoplasmic reticular proteins. *Circ Res, 69*, 266–276.

Arvanitis, D. A., Vafiadaki, E., Fan, G. C., et al. (2007). Histidine-rich Ca-binding protein interacts with sarcoplasmic reticulum Ca-ATPase. *Am J Physiol Heart Circ Physiol, 293*, H1581–H1589.

Babu, G. J., Bhupathy, P., Timofeyev, V., et al. (2007). Ablation of sarcolipin enhances sarcoplasmic reticulum calcium transport and atrial contractility. *Proc Natl Acad Sci USA, 104*, 17867–17872.

Baker, D. L., Hashimoto, K., Grupp, I. L., et al. (1998). Targeted overexpression of the sarcoplasmic reticulum Ca^{2+}-ATPase increases cardiac contractility in transgenic mouse hearts. *Circ Res, 83*, 1205–1214.

Beekman, R. E., van Hardeveld, C., & Simonides, W. S. (1989). On the mechanism of the reduction by thyroid hormone of β-adrenergic relaxation rate stimulation in rat heart. *Biochem J, 259*, 229–236.

Bers, D. M. (2008). Calcium cycling and signaling in cardiac myocytes. *Annu Rev Physiol, 70*, 23–49.

Bers, D. M., & Despa, S. (2006). Cardiac myocytes Ca^{2+} and Na^{+} regulation in normal and failing hearts. *J Pharmacol Sci, 100*, 315–322.

Beuckelmann, D. J., Nabauer, M., & Erdmann, E. (1992). Intracellular calcium handling in isolated ventricular myocytes from patients with terminal heart failure. *Circulation, 85*, 1046–1055.

Bhupathy, P., Babu, G. J., & Periasamy, M. (2007). Sarcolipin and phospholamban as regulators of cardiac sarcoplasmic reticulum Ca^{2+} ATPase. *J Mol Cell Cardiol, 42*, 903–911.

Brini, M., & Carafoli, E. (2009). Calcium pumps in health and disease. *Physiol Rev, 89*, 1341–1378.

Brittsan, A. G., Carr, A. N., Schmidt, A. G., & Kranias, E. G. (2000). Maximal inhibition of SERCA2 Ca^{2+} affinity by phospholamban in transgenic hearts overexpressing a non-phosphorylatable form of phospholamban. *J Biol Chem, 275*, 12129–12135.

Chu, G., Lester, J. W., Young, K. B., Luo, W., Zhai, J., & Kranias, E. G. (2000). A single site (Ser^{16}) phosphorylation in phospholamban is sufficient in mediating its maximal cardiac responses to β-agonists. *J Biol Chem, 275*, 38938–38943.

D'Agnolo, A., Luciani, G. B., Mazzucco, A., Gallucci, V., & Salviati, G. (1992). Contractile properties and Ca^{2+} release activity of the sarcoplasmic reticulum in dilated cardiomyopathy. *Circulation, 85*, 518–525.

Dally, S., Corvazier, E., Bredoux, R., Bobe, R., & Enouf, J. (2010). Multiple and diverse coexpression, location, and regulation of additional SERCA2 and SERCA3 isoforms in nonfailing and failing human heart. *J Mol Cell Cardiol, 48*, 633–644.

Edes, I., & Kranias, E. G. (1990). Phospholamban and troponin I are substrates for protein kinase C in vitro but not in intact beating guinea pig hearts. *Circ Res, 67*, 394–400.

Edes, I., Talosi, L., & Kranias, E. (1991). Sarcoplasmic reticulum function in normal heart and in cardiac disease. *Heart Failure, 6*, 221–237.

Fan, G. C., Gregory, K. N., Zhao, W., Park, W. J., & Kranias, E. G. (2004). Regulation of myocardial function by histidine-rich, calcium-binding protein. *Am J Physiol Heart Circ Physiol, 287*, H1705–H1711.

Fujii, J., Zarain-Herzberg, A., Willard, H. F., Tada, M., & MacLennan, D. H. (1991). Structure of the rabbit phospholamban gene, cloning of the human cDNA, and assignment of the gene to human chromosome 6. *J Biol Chem, 266*, 11669–11675.

Gianni, D., Chan, J., Gwathmey, J. K., del Monte, F., & Hajjar, R. J. (2005). SERCA2a in heart failure: role and therapeutic prospects. *J Bioenerg Biomembr, 37*, 375–380.

Gregory, K. N., & Kranias, E. G. (2006). Targeting sarcoplasmic reticulum calcium handling proteins as therapy for cardiac disease. *Hellenic J Cardiol, 47*, 132–143.

Gregory, K. N., Ginsburg, K. S., Bodi, I., et al. (2006). Histidine-rich Ca binding protein: a regulator of sarcoplasmic reticulum calcium sequestration and cardiac function. *J Mol Cell Cardiol, 40*, 653–665.

Guerini, D., Garcia-Martin, E., Zecca, A., Guidi, F., & Carafoli, E. (1998). The calcium pump of the plasma membrane: membrane targeting, calcium binding sites, tissue-specific isoform expression. *Acta Physiol Scand Suppl, 643*, 265–273.

Gwathmey, J. K., Copelas, L., MacKinnon, R., et al. (1987). Abnormal intracellular calcium handling in myocardium from patients with end-stage heart failure. *Circ Res, 61*, 70–76.

Haghighi, K., Kolokathis, F., Gramolini, A. O., et al. (2006). A mutation in the human phospholamban gene, deleting arginine 14, results in lethal, hereditary cardiomyopathy. *Proc Natl Acad Sci USA, 103*, 1388–1393.

Haghighi, K., Kolokathis, F., Pater, L., et al. (2003). Human phospholamban null results in lethal dilated cardiomyopathy revealing a critical difference between mouse and human. *J Clin Invest, 111*, 869–876.

Haghighi, K., Schmidt, A. G., Hoit, B. D., et al. (2001). Superinhibition of sarcoplasmic reticulum function by phospholamban induces cardiac contractile failure. *J Biol Chem, 276*, 24145–24152.

Ho, C. Y. (2010). Hypertrophic cardiomyopathy. *Heart Fail Clin, 6*, 141–159.

Hoit, B. D., Khoury, S. F., Kranias, E. G., Ball, N., & Walsh, R. A. (1995). In vivo echocardiographic detection of enhanced left ventricular function in gene-targeted mice with phospholamban deficiency. *Circ Res, 77*, 632–637.

Huggins, J. P., Cook, E. A., Piggott, J. R., Mattinsley, T. J., & England, P. J. (1989). Phospholamban is a good substrate for cyclic GMP-dependent protein kinase in vitro, but not in intact cardiac or smooth muscle. *Biochem J, 260*, 829–835.

Ji, Y., Lalli, M. J., Babu, G. J., et al. (2000). Disruption of a single copy of the SERCA2 gene results in altered Ca^{2+} homeostasis and cardiomyocyte function. *J Biol Chem, 275*, 38073–38080.

Kadambi, V. J., Ponniah, S., Harrer, J. M., et al. (1996). Cardiac-specific overexpression of phospholamban alters calcium kinetics and resultant cardiomyocyte mechanics in transgenic mice. *J Clin Invest, 97*, 533–539.

Kim, H. W., Steenaart, N. A., Ferguson, D. G., & Kranias, E. G. (1990). Functional reconstitution of the cardiac sarcoplasmic reticulum Ca^{2+}-ATPase with phospholamban in phospholipid vesicles. *J Biol Chem, 265*, 1702–1709.

Kimura, Y., Otsu, K., Nishida, K., Kuzuya, T., & Tada, M. (1994). Thyroid hormone enhances Ca^{2+} pumping activity of the cardiac sarcoplasmic reticulum by increasing Ca^{2+} ATPase and decreasing phospholamban expression. *J Mol Cell Cardiol, 26*, 1145–1154.

Kiss, E., Brittsan, A. G., Edes, I., Grupp, I. L., & Kranias, E. G. (1998). Thyroid hormone-induced alterations in phospholamban-deficient mouse hearts. *Circ Res, 83*, 608–613.

Kiss, E., Jakab, G., Kranias, E. G., & Edes, I. (1994). Thyroid hormone-induced alterations in phospholamban protein expression. regulatory effects on sarcoplasmic reticulum Ca^{2+} transport and myocardial relaxation. *Circ Res, 75*, 245–251.

Kranias, E. G., & Solaro, R. J. (1982). Phosphorylation of troponin I and phospholamban during catecholamine stimulation of rabbit heart. *Nature, 298*, 182–184.

Kranias, E. G., Garvey, J. L., Srivastava, R. D., & Solaro, R. J. (1985). Phosphorylation and functional modifications of sarcoplasmic reticulum and myofibrils in isolated rabbit hearts stimulated with isoprenaline. *Biochem J, 226*, 113–121.

Krause, S. M., Jacobus, W. E., & Becker, L. C. (1989). Alterations in cardiac sarcoplasmic reticulum calcium transport in the postischemic "stunned" myocardium. *Circ Res, 65*, 526–530.

Limas, C. J., Olivari, M. T., Goldenberg, I. F., Levine, T. B., Benditt, D. G., & Simon, A. (1987). Calcium uptake by cardiac sarcoplasmic reticulum in human dilated cardiomyopathy. *Cardiovasc Res, 21*, 601–605.

Limbruno, U., Zucchi, R., Ronca-Testoni, S., Galbani, P., Ronca, G., & Mariani, M. (1989). Sarcoplasmic reticulum function in the "stunned" myocardium. *J Mol Cell Cardiol, 21*, 1063–1072.

Lindemann, J. P., & Watanabe, A. M. (1985). Muscarinic cholinergic inhibition of β-adrenergic stimulation of phospholamban phosphorylation and Ca^{2+} transport in guinea pig ventricles. *J Biol Chem, 260*, 122–133.

Lindemann, J. P., & Watanabe, A. M. (1985). Phosphorylation of phospholamban in intact myocardium. Role of Ca^{2+}-calmodulin-dependent mechanisms. *J Biol Chem, 260*, 4516–4525.

Lindemann, J. P., Jones, L. R., Hathaway, D. R., Henry, B. G., & Watanabe, A. M. (1983). β-adrenergic stimulation of phospholamban phosphorylation and Ca^{2+}-ATPase activity in guinea pig ventricles. *J Biol Chem, 258*, 464–471.

Lipskaia, L., Chemaly, E. R., Hadri, L., Lompre, A., & Hajjar, R. J. (2010). Sarcoplasmic reticulum Ca^{2+} ATPase as a therapeutic target for heart failure. *Expert Opin Biol Ther, 10*, 29–41.

Lipskaia, L., Hulot, J. S., & Lompre, A. M. (2009). Role of sarco/endoplasmic reticulum calcium content and calcium ATPase activity in the control of cell growth and proliferation. *Pflugers Arch, 457*, 673–685.

Liu, L. H., Boivin, G. P., Prasad, V., Prasad, V., Periasamy, M., & Shull, G. E. (2001). Squamous cell tumors in mice heterozygous for a null allele of Atp2a2, encoding the sarco(endo)plasmic reticulum Ca^{2+}-ATPase isoform 2 Ca^{2+} pump. *J Biol Chem, 276*, 26737–26740.

Liu, L. H., Paul, R. J., Sutliff, R. L., et al. (1997). Defective endothelium-dependent relaxation of vascular smooth muscle and endothelial cell Ca^{2+} signaling in mice lacking sarco(endo)plasmic reticulum Ca^{2+}-ATPase isoform 3. *J Biol Chem, 272*, 30538–30545.

Lorenz, J. N., & Kranias, E. G. (1997). Regulatory effects of phospholamban on cardiac function in intact mice. *Am J Physiol, 273*, H2826–H2831.

Loukianov, E., Ji, Y., Grupp, I. L., et al. (1998). Enhanced myocardial contractility and increased Ca^{2+} transport function in transgenic hearts expressing the fast-twitch skeletal muscle sarcoplasmic reticulum Ca^{2+}-ATPase. *Circ Res, 83*, 889–897.

Luo, W., Chu, G., Sato, Y., Zhou, Z., Kadambi, V. J., & Kranias, E. G. (1998). Transgenic approaches to define the functional role of dual site phospholamban phosphorylation. *J Biol Chem, 273*, 4734–4739.

Luo, W., Grupp, I. L., Harrer, J., et al. (1994). Targeted ablation of the phospholamban gene is associated with markedly enhanced myocardial contractility and loss of β-agonist stimulation. *Circ Res, 75*, 401–409.

Luo, W., Wolska, B. M., Grupp, I. L., et al. (1996). Phospholamban gene dosage effects in the mammalian heart. *Circ Res, 78*, 839–847.

MacLennan, D. H., Abu-Abed, M., & Kang, C. (2002). Structure–function relationships in Ca^{2+} cycling proteins. *J Mol Cell Cardiol, 34*, 897–918.

MacLennan, D. H., Kimura, Y., & Toyofuku, T. (1998). Sites of regulatory interaction between calcium ATPases and phospholamban. *Ann NY Acad Sci, 853*, 31–42.

Mattiazzi, A., Mundina-Weilenmann, C., Guoxiang, C., Vittone, L., & Kranias, E. G. (2005). Role of phospholamban phosphorylation on Thr17 in cardiac physiological and pathological conditions. *Cardiovasc Res, 68*, 366–375.

Mercadier, J. J., Lompre, A. M., Duc, P., et al. (1990). Altered sarcoplasmic reticulum Ca^{2+}-ATPase gene expression in the human ventricle during end-stage heart failure. *J Clin Invest, 85*, 305–309.

Møller, J. V., Nissen, P., Sorensen, T. L., & le Maire, M. (2005). Transport mechanism of the sarcoplasmic reticulum Ca^{2+} -ATPase pump. *Curr Opin Struct Biol, 15*, 387–393.

Morris, G. L., Cheng, H. C., Colyer, J., & Wang, J. H. (1991). Phospholamban regulation of cardiac sarcoplasmic reticulum (Ca^{2+}-Mg^{2+})-ATPase. Mechanism of regulation and site of monoclonal antibody interaction. *J Biol Chem, 266*, 11270–11275.

Mortishire-Smith, R. J., Pitzenberger, S. M., Burke, C. J., Middaugh, C. R., Garsky, V. M., & Johnson, R. G. (1995). Solution structure of the cytoplasmic domain of phopholamban: phosphorylation leads to a local perturbation in secondary structure. *Biochemistry, 34*, 7603–7613.

Movsesian, M. A., Bristow, M. R., & Krall, J. (1989). Ca^{2+} uptake by cardiac sarcoplasmic reticulum from patients with idiopathic dilated cardiomyopathy. *Circ Res, 65*, 1141–1144.

Odermatt, A., Taschner, P. E., Khanna, V. K., et al. (1996). Mutations in the gene-encoding SERCA1, the fast-twitch skeletal muscle sarcoplasmic reticulum Ca^{2+} ATPase, are associated with Brody disease. *Nat Genet, 14*, 191–194.

Okunade, G. W., Miller, M. L., Pyne, G. J., et al. (2004). Targeted ablation of plasma membrane Ca^{2+}-ATPase (PMCA) 1 and 4 indicates a major housekeeping function for PMCA1 and a critical role in hyperactivated sperm motility and male fertility for PMCA4. *J Biol Chem, 279*, 33742–33750.

Pan, Y., Zvaritch, E., Tupling, A. R., et al. (2003). Targeted disruption of the ATP2A1 gene encoding the sarco(endo)plasmic reticulum Ca^{2+} ATPase isoform 1 (SERCA1) impairs diaphragm function and is lethal in neonatal mice. *J Biol Chem, 278*, 13367–13375.

Periasamy, M., Reed, T. D., Liu, L. H., et al. (1999). Impaired cardiac performance in heterozygous mice with a null mutation in the sarco(endo)plasmic reticulum Ca^{2+}-ATPase isoform 2 (SERCA2) gene. *J Biol Chem, 274*, 2556–2562.

Reddy, L. G., Jones, L. R., Pace, R. C., & Stokes, D. L. (1996). Purified, reconstituted cardiac Ca^{2+}-ATPase is regulated by phospholamban but not by direct phosphorylation with Ca^{2+}/calmodulin-dependent protein kinase. *J Biol Chem, 271*, 14964–14970.

Sakuntabhai, A., Ruiz-Perez, V., Carter, S., et al. (1999). Mutations in ATP2A2, encoding a Ca^{2+} pump, cause Darier disease. *Nat Genet, 21*, 271–277.

Schatzmann, H. J. (1989). The calcium pump of the surface membrane and of the sarcoplasmic reticulum. *Annu Rev Physiol, 51*, 473–485.

Schmidt, A. G., Zhai, J., Carr, A. N., et al. (2002). Structural and functional implications of the phospholamban hinge domain: impaired SR Ca^{2+} uptake as a primary cause of heart failure. *Cardiovasc Res, 56*, 248–259.

Schmitt, J. P., Kamisago, M., Asahi, M., et al. (2003). Dilated cardiomyopathy and heart failure caused by a mutation in phospholamban. *Science, 299*, 1410–1413.

Schultz, Jel. J., Glascock, B. J., Witt, S. A., et al. (2003). Accelerated onset of heart failure in mice during pressure overload with chronically decreased SERCA2 calcium pump activity. *Am J Physiol Heart Circ Physiol, 286*, H1146–H1153.

Schwinger, R. H., Bohm, M., Schmidt, U., et al. (1995). Unchanged protein levels of SERCA II and phospholamban but reduced Ca^{2+} uptake and Ca^{2+}-ATPase activity of cardiac sarcoplasmic reticulum from dilated cardiomyopathy patients compared with patients with nonfailing hearts. *Circulation, 92*, 3220–3228.

Sen, L., Cui, G., Fonarow, G. C., & Laks, H. (2000). Differences in mechanisms of SR dysfunction in ischemic vs. idiopathic dilated cardiomyopathy. *Am J Physiol Heart Circ Physiol, 279*, H709–H718.

Sharma, P., Ignatchenko, V., Grace, K., Ursprung, C., Kislinger, T., & Gramolini, A. O. (2010). Endoplasmic reticulum protein targeting of phospholamban: a common role for an N-terminal di-arginine motif in ER retention? *PLoS One, 5*, e11496.

Shull, G. E., & Greeb, J. (1988). Molecular cloning of two isoforms of the plasma membrane Ca^{2+}-transporting ATPase from rat brain. Structural and functional domains exhibit similarity to Na^+, K^+- and other cation transport ATPases. *J Biol Chem, 263*, 8646–8657.

Simmerman, H. K., & Jones, L. R. (1998). Phospholamban: protein structure, mechanism of action, and role in cardiac function. *Physiol Rev, 78*, 921–947.

Talosi, L., Edes, I., & Kranias, E. G. (1993). Intracellular mechanisms mediating reversal of β-adrenergic stimulation in intact beating hearts. *Am J Physiol, 264*, H791–H797.

Talukder, M. A., Zweier, J. L., & Periasamy, M. (2009). Targeting calcium transport in ischaemic heart disease. *Cardiovasc Res, 84*, 345–352.

Toyofuku, T., Curotto Kurzydlowski, K., Narayanan, N., & MacLennan, D. H. (1994). Identification of Ser^{38} as the site in cardiac sarcoplasmic reticulum Ca^{2+}-ATPase that is phosphorylated by Ca^{2+}/calmodulin-dependent protein kinase. *J Biol Chem, 269*, 26492–26496.

Unverferth, D. V., Lee, S. W., & Wallick, E. T. (1988). Human myocardial adenosine triphosphatase activities in health and heart failure. *Am Heart J, 115*, 139–146.

Ver Heyen, M., Heymans, S., Antoons, G., et al. (2001). Replacement of the muscle-specific sarcoplasmic reticulum Ca^{2+}-ATPase isoform SERCA2a by the nonmuscle SERCA2b homologue causes mild concentric hypertrophy and impairs contraction–relaxation of the heart. *Circ Res, 89*, 838–846.

Verma, A. K., Filoteo, A. G., Stanford, D. R., et al. (1988). Complete primary structure of a human plasma membrane Ca^{2+} pump. *J Biol Chem, 263*, 14152–14159.

Wolska, B. M., Stojanovic, M. O., Luo, W., Kranias, E. G., & Solaro, R. J. (1996). Effect of ablation of phospholamban on dynamics of cardiac myocyte contraction and intracellular Ca^{2+}. *Am J Physiol, 271*, C391–C397.

Zhai, J., Schmidt, A. G., Hoit, B. D., Kimura, Y., MacLennan, D. H., & Kranias, E. G. (2000). Cardiac-specific overexpression of a super-inhibitory pentameric phospholamban mutant enhances inhibition of cardiac function in vivo. *J Biol Chem, 275*, 10538–10544.

Zhao, W., Uehara, Y., Chu, G., et al. (2004). Threonine-17 phosphorylation of phospholamban: a key determinant of frequency-dependent increase of cardiac contractility. *J Mol Cell Cardiol, 37*, 607–612.

Zucchi, R., Ronca-Testoni, S., Yu, G., Galbani, P., Ronca, G., & Mariani, M. (1994). Effect of ischemia and reperfusion on cardiac ryanodine receptors—sarcoplasmic reticulum Ca^{2+} channels. *Circ Res, 74*, 271–280.

Zvaritch, E., Backx, P. H., Jirik, F., et al. (2000). The transgenic expression of highly inhibitory monomeric forms of phospholamban in mouse heart impairs cardiac contractility. *J Biol Chem, 275*, 14985–14991.

Chapter 14

Na^+-Ca^{2+} Exchange Currents

John H.B. Bridge, Natalia S. Torres and Michela Ottolia

Chapter Outline

I. SUMMARY

At first, study of the Na^+-Ca^{2+} exchange current was impeded because multicellular preparations did not permit adequate control of the driving forces producing exchange. However, methods for isolating single cells, together with the patch-clamp technique, made it possible to isolate exchange current and to provide reliable measurements of its properties. Now that the exchange molecule has been cloned, it is possible to express the mammalian exchanger in other cell types including frog oocytes. Currents may now be measured in these cell types with the giant patch technique or with the whole-cell patch-clamp method. These preparations and methods introduce the possibility of studying mutated forms of the exchanger with a view to understanding the relationship between structure and function.

Studies with isolated giant patches have resulted in significant advances in our understanding of both the regulation and mechanism of exchange activity. The phenomenon of Na^+-dependent inactivation of exchange was first identified in isolated patches and our understanding of secondary Ca^{2+} regulation, as well as regulation by phosphatidylinositol-4,5-bisphosphate (PIP_2) and phosphorylation, have been significantly advanced by this technique. Advances in the molecular biology of the Na^+-Ca^{2+} exchanger – which include the elucidation of the primary structure of the exchange molecule together with the development of recombinant DNAs coding for the Na^+-Ca^{2+} exchanger, their expression in systems suitable for current measurement and, finally, the production of various mutations – have already resulted in extensive studies of the relationship between structure and function which we have discussed in this chapter.

Measurements of both whole-cell currents as well as currents in giant patches have produced evidence in favor of the idea that a consecutive mechanism can explain exchange activity. Moreover, at least two laboratories have claimed to have isolated currents associated with partial reactions of the exchanger consistent with the idea that a consecutive (ping-pong) reaction scheme is operative. Preliminary results seem to suggest that much of the voltage dependence of the exchange resides in rate-limiting steps associated with Na^+ translocation in NCX1, although not with NCX-SQ1, in which voltage dependence appears to be associated with Ca^{2+} translocation. With the availability of the techniques of modern molecular biology, it

Cell Physiology Sourcebook. DOI: 10.1016/B978-0-12-387738-3.00014-7

seems likely that we may expect further progress in the study of the relationship between the structure and function of the exchange molecule. Elegant measurements of whole-cell currents have resulted in a plausible model of the behavior of the Na^+-Ca^{2+} exchange during the cardiac cycle. The way that the Na^+-Ca^{2+} exchange contributes to excitation coupling is not completely understood but is an active area of research. The advent of peptide inhibitors like XIP, together with methods for rapidly changing extracellular solutions, suggest that we may soon gain more insight into the contribution of both inward and outward exchange currents to the events of excitation–contraction coupling.

II. INTRODUCTION

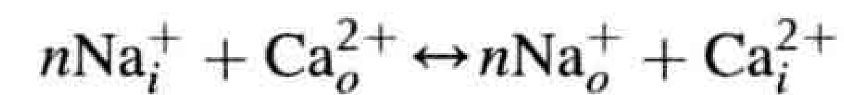
The existence of Na^+-Ca^{2+} exchange was first postulated in 1964 by both Repke (1964) and Langer (1964) as a consequence of their studies on the contractility of heart muscle. Three years later, Baker and his colleagues (Baker et al., 1967) provided the first report documenting Na^+-Ca^{2+} exchange in giant squid axons. Shortly after this, Reuter and Seitz (1968) presented the first complete study describing Na^+-Ca^{2+} countertransport in heart. Based on studies of isotopic fluxes, these authors proposed that two Na^+ ions were coupled to the extrusion of a single Ca^{2+} ion in a modified exchange diffusion process. Blaustein and Hodgkin (1969) then published the results of their studies on squid axons. They recognized that the distribution of free Ca^{2+} could not be predicted on simple electrochemical principles. However, cyanide (which was expected to block metabolic processes) failed to prevent the efflux of ^{45}Ca, so that it seemed unlikely that a metabolic pump was involved in Ca^{2+} extrusion. However, this efflux of Ca^{2+} was (among other things) dependent upon external Na^+. Blaustein and Hodgkin therefore concluded that, in unpoisoned axons, some or possibly all of the energy for extruding Ca^{2+} ions came from the inward movement of Na^+ down its electrochemical gradient.

These early studies were seminal and provided impetus for an enormous number of subsequent investigations that have led not only to a study of Na^+-Ca^{2+} exchange currents, but to the molecular cloning and elucidation of the structure of the exchanger molecule itself. This, in turn, introduced the possibility of studying the relationship between molecular structure and function.

This chapter provides a brief description of current knowledge of Na^+-Ca^{2+} exchange currents. The ease with which heart cells can be patch-clamped, together with the presence of a vigorous exchange activity, doubtless explains the fact that most of our information on exchange current comes from this tissue. Na^+-Ca^{2+} exchange currents have been measured in other cell types including the squid giant axon (Matsuoka et al., 1997). Although measurements of exchange current are difficult in many tissues, it is now possible to express Na^+-Ca^{2+} exchangers in other cell types, for example frog oocytes. This, together with the development of giant excised patches that can be voltage-clamped, has made studies of the relationship between structure of the exchanger and function much easier.

III. ENERGETICS OF Na^+-Ca^{2+} EXCHANGE

Reuter and Seitz in their classic study (Reuter and Seitz, 1968) proposed that two Na^+ ions exchanged for a single Ca^{2+} ion in a modified exchange diffusion process. Based upon this proposal, one would not expect steady-state exchange activity to produce a measurable electric current. However, the existence of exchange currents is a well-established fact and one that can be appreciated by consideration of the energetic and stoichiometric properties of the exchange as they are currently understood. It is convenient (but not necessarily correct) to represent the transmembranous exchange reaction as a sequential (simultaneous) process:



$$n\mathrm{Na}_i^+ + \mathrm{Ca}_o^{2+} \leftrightarrow n\mathrm{Na}_o^+ + \mathrm{Ca}_i^{2+}$$

where n is the stoichiometric coefficient of the exchange reaction. If the forward and reverse reaction rates are equal, the exchange reaction is at equilibrium. Even if n is greater than 2, there can be no net charge movement and, hence, no electric current generated at equilibrium. An electric current can only be measured when the exchange is displaced from equilibrium. While the net reaction rate at equilibrium is zero, the unidirectional rates might be substantial (Axelsen and Bridge, 1985). As soon as the forward and reverse exchange rates differ from one another, net ion translocation takes place; provided that the stoichiometric coefficient is appropriate (i.e. n greater than 2) and no ions of opposite charge are co-transported, one can expect to measure an electric current as a consequence of exchange.

If electrochemical forces solely determine net movement of ions through the Na^+-Ca^{2+} exchanger, classical thermodynamics may be used to calculate both the direction of exchange and the conditions under which we may expect equilibrium to occur. Having the capacity to do this is of enormous value when designing experiments to measure exchange currents. The electrochemical potential difference or driving force ($n\Delta\tilde{\mu}$) producing exchange is the difference between n times the electrochemical potential difference or force producing sodium movement ($n\Delta\tilde{\mu}_{Na}$) and calcium movement ($\Delta\tilde{\mu}_{Ca}$). Driving force can be expressed in terms of membrane potential (Em), Na^+ equilibrium potential (ENa) and Ca^{2+} equilibrium potential (ECa). Thus, we may write:

$$\Delta\tilde{\mu} = n\Delta\tilde{\mu}_{Na} - \Delta\tilde{\mu}_{Ca} \tag{14.1}$$

At equilibrium, $\Delta\tilde{\mu} = 0$, so that:

$$n\Delta\tilde{\mu}_{Na} - \Delta\tilde{\mu}_{Ca} = 0 \quad (14.2)$$

$$\Delta\tilde{\mu}_{Na}(mV) = \frac{RT}{F}\ln\frac{[Na^{+}]_o}{[Na^{+}]_i} + E_m = E_{Na} + E_m \quad (14.3)$$

$$\Delta\tilde{\mu}_{Ca}(mV) = \frac{RT}{F}\ln\frac{[Ca^{2+}]_o}{[Ca^{2+}]_i} + 2E_m = 2E_{Ca} + 2E_m \quad (14.4)$$

Substitution yields:

$$nE_{Na} - 2E_{Ca} - (n-2)E_m = 0 \quad (14.5)$$

The exponential form of Equation 14.5 is:

$$\frac{[Ca^{2+}]_o}{[Ca^{2+}]_i} = \left(\frac{[Na^{+}]_o}{[Na^{+}]_i}\right)^n \exp\left(-(n-2)\frac{E_m F}{RT}\right) \quad (14.6)$$

The driving force $\Delta\tilde{\mu}$ on exchange is given as:

$$\Delta\tilde{\mu} = 3ENa - 2ECa - Em \quad (14.7)$$

These are the equations that can be used to predict the equilibrium conditions of the exchanger. Before doing so, one needs to know the stoichiometric coefficient (n) of the exchanger. This issue has been the subject of a lengthy debate and numerous investigations. However, there now appears to be broad agreement that three Na^{+} ions are exchanged for a single Ca^{2+} ion in most mammalian systems studied (Bridge and Bassingthwaighte, 1983; Reeves and Hale, 1984; Kimura et al., 1987; Bridge et al., 1990; Crespo et al., 1990). There is also good evidence that exchange stoichiometry is 3:1 in barnacle fibers (Rasgado-Flores and Blaustein, 1987).

Besides predicting equilibrium conditions we can, with sufficient information, predict the direction of exchange. Consider a heart cell at rest (or during diastole). If we assume the internal Na^{+} concentration is 5 mM and Ca^{2+} is at 100 nM while external Ca^{2+} is 2 mM and Na^{+} is 140 mM and, finally, the membrane potential is −80 mV, we can use Equation 14.7 to predict the direction of exchange if we assume n to be three (Fig. 14.1A). Thus the driving force on exchange is 18 mV which produces a net extrusion of Ca^{2+}. The exchange is said to be operating in its forward mode and there is net inward charge movement or a net inward current. If the cell is depolarized to +50 mV, the quantity $\Delta\tilde{\mu}$ becomes −112 mV and there is net Ca^{2+} influx through the exchange (see Fig. 14.1C). The exchange is then said to be operating in reverse mode and there is net outward current. Finally, equilibrium will occur at −62 mV for these ionic concentrations (see Fig. 14.1B). It should be noted that, in a cell like a heart cell, which has a small surface to volume ratio, ion movements through the exchange may alter the intracellular concentrations so that the quantities that we have just calculated will change. For a description of the way that the exchange changes during the phases of a cardiac action potential, we refer the reader to Bers (2001).

An elegant (though somewhat indirect) demonstration of exchange stoichiometry was provided by Reeves and Hale (Reeves and Hale, 1984). This demonstration employed the foregoing principles and equations. Their study not only produced a value for the exchange stoichiometry, but provided an excellent example of the way that the foregoing energetic principles may guide experimental design. These authors took advantage of the fact that exchange equilibrium can be achieved simply by appropriate adjustment of the Na^{+} and Ca^{2+} electrochemical gradients. Bovine sarcolemmal vesicles containing Na^{+}-Ca^{2+} exchanger were equilibrated with solutions of both Na^{+} and ^{45}Ca. Under these circumstances, the equilibrium may be described by Equation 14.5. After treating the membrane with valinomycin in the presence of KCl, known membrane potentials were established that caused disequilibrium of the exchanger and either Ca^{2+} entry or exit. By adjusting the Na^{+} gradient, it was possible to null precisely the tendency of membrane potential to produce Ca^{2+} movement. Thus, if any of the quantities E_m, E_{Na}, and E_{Ca} are held constant, the relationship between the other two may be found. The point at which Ca^{2+} movement was nulled by Na^{+} gradient is given by:

$$E_{rev} = 3E_{Na} - 2E_{Ca} = -50 \text{ mV} \quad (14.8)$$

By nulling Ca^{2+} movement over a range of membrane potentials, the value for n that these authors obtained was 2.97 ± 0.03, which is close to the currently accepted value of 3.0.

IV. METHODS AND PROBLEMS ASSOCIATED WITH THE MEASUREMENT OF Na^{+}-Ca^{2+} EXCHANGE CURRENT

Several recent techniques have greatly facilitated the isolation of exchange current. First, the *whole-cell ruptured patch voltage clamp* in conjunction with intracellular dialysis (Hamill et al., 1981) has probably contributed most to the initial isolation of exchange currents. To record whole-cell current with the ruptured patch technique, a microelectrode or patch pipette is pressed onto the cell membrane and suction is applied, usually with a syringe or directly by the experimentalist. This often results in a high-resistance seal that forms between the pipette and the cell membrane. The resistance of this seal is ideally $>10^{10}$ ohms and it is therefore referred to as a gigaseal. This is usually accompanied by the formation of an Ω structure as the membrane is pulled into the pipette (see Chapter 20). Continued suction ruptures the Ω, and this creates continuity between the cell interior and the pipette solution. By

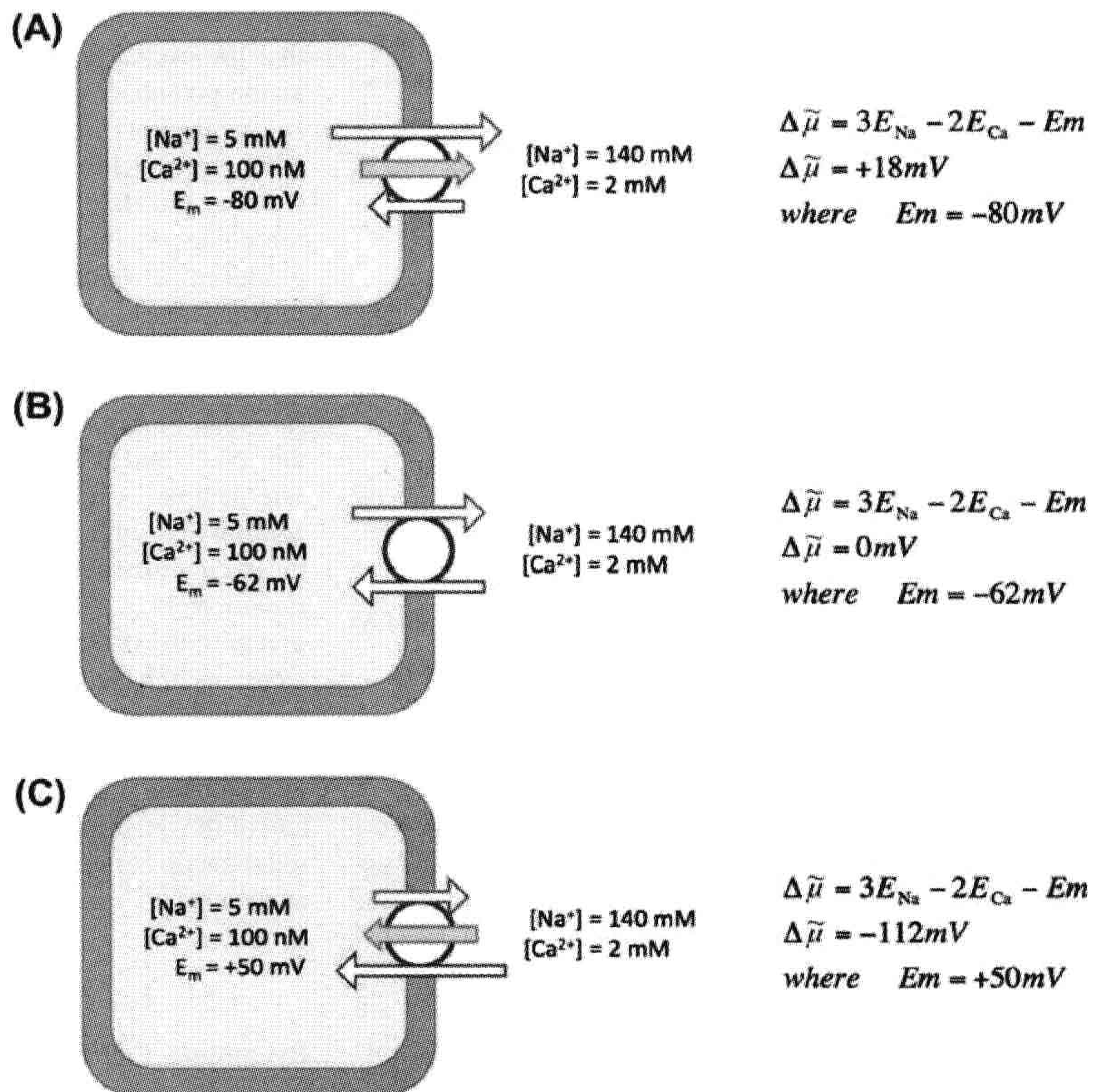


FIGURE 14.1 (A) The red arrow represents the rate of the forward exchange reaction which exceeds the rate of the reverse reaction represented by the blue arrow (see the reaction described in section II). This results in net extrusion of Ca^{2+} and a net inward current (light blue arrow). This is usually referred to as the forward mode of the exchange. The calculations to the right of all figures simply indicate the magnitude and direction of the driving force producing net exchange. (B) The red and blue arrows have the same significance as in (A). In this case, the forward and reverse reactions occur at the same rate so that there is no net reaction and therefore no net current. The exchange is at equilibrium, as the calculation to the right indicates, i.e. there is not net driving force on the exchange. (C) Again red and blue arrows retain their significance. However, the rate of the reverse reaction exceeds the rate of the forward reaction. This results in net influx of Ca^{2+} accompanied by an outward current. The calculation to the right indicates both the magnitude and direction of the driving force.

pulling the sealed pipette from the cell one may isolate an outside-out patch. It is also possible with the methods illustrated in Chapter 20 to create an inside-out patch. Hilgemann has refined this technique so that very large membrane patches can be isolated from appropriately treated cell membranes (Hilgemann, 1989).

A simplified arrangement for voltage-clamping heart cells and recording exchange current through a ruptured patch is depicted in Fig. 14.2. Essentially the same arrangement applies to the voltage-clamping of an isolated patch. The micropipette attached to the cell is connected via a (non-polarizable) electrode to the front end of a high-gain amplifier known as a current-to-voltage converter. The most significant feature of this high amplifier is the feedback loop R_f and its branch point (the summing junction). In operational amplifiers (of which this current-to-voltage converter is an example), this branch point has special significance. Negative feedback through the feedback loop tends to cancel the input signal at S. A command potential V_c is applied to the non-inverting input (+). A property of this amplifier is that, as a result of negative feedback through R_f, current always flows so that the voltage at the summing junction is identical to the voltage V_c (the command potential). The potential difference between the summing junction and ground is therefore ideally equal to V_c. This potential difference therefore falls across the electrode resistance (and any other resistances in series with the membrane resistance R_m). Provided that the product of this series resistance (R_s) and the exchange current $I_{Na\text{-}Ca}$ ($R_s I_{Na\text{-}Ca}$) is small, most of the potential difference V_c occurs across the membrane. Feedback through R_f always compensates varying input at the summing junction, thus ensuring that the voltage across the membrane is held constant (i.e. is clamped). Exchange current $I_{Na\text{-}Ca}$ passing across the membrane produces a potential difference across the membrane. As this potential difference causes the membrane potential to depart from V_c, current (equal in magnitude to the exchange current) flows into the summing junction. In reality, additional circuitry is required to reduce noise in the recording system while increasing its fidelity. This is dealt with in greater detail in Chapter 20.

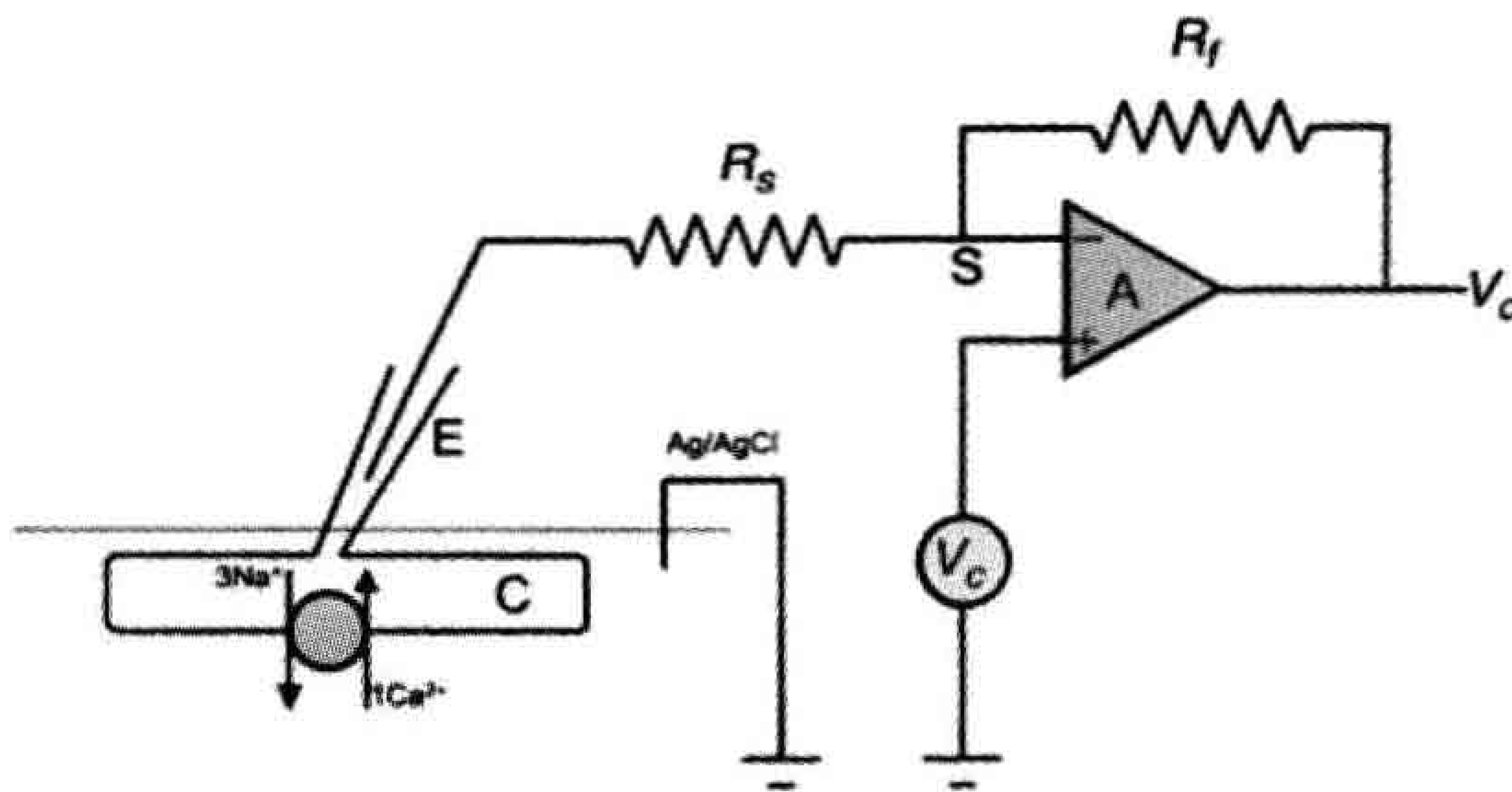


FIGURE 14.2 An arrangement suitable for measuring Na^+-Ca^{2+} exchange current in a ventricular heart cell. Under these circumstances, the exchanger is producing a net outward current across the cell membrane by exchanging three internal Na^+ ions with a single external Ca^{2+} ion. This produces outward movement of one net charge. The voltage-clamp circuit consists of a high-gain amplifier A. Any deviations from the command potential V_c produced by the exchanger are compensated by feedback from the output through the feedback resistor R_f. The amplifier is connected to the cell through the electrode E, which is sealed to a ruptured patch. The output of this amplifier is proportional to the current flowing through the feedback resistor R_f and hence the cell C. The success of this method depends upon minimizing voltage drops across the series resistance R_s. The bath in which the cell is maintained is grounded by an Ag/AgCl electrode connected to a salt bridge (not shown).

The current flowing through a heart cell membrane, I_m, consists of two components: a capacity current and an ionic current I_i. The capacity current $I_C = CdV/dt$ and the membrane current is denoted I_m. Therefore:

$$I_m = C\frac{dV}{dt} + I_i + I_{Na-Ca} \qquad (14.9)$$

The ionic current consists of ions flowing through ion channels as well as those translocated by ion exchange mechanisms (principally the Na^+-Ca^{2+} exchange and the Na^+ pump). For purposes of illustration, the exchange current has been separated from the ionic current in Equation 14.9. Under voltage-clamp $dV/dt = 0$,

$$I_m = I_i + I_{Na-Ca} \qquad (14.10)$$

If one can remove or minimize I_i (which includes the Na^+ pump current and all contaminating channel currents) without affecting exchange current $I_{Na\text{-}Ca}$, one may measure a membrane current that is comprised mainly of $I_{Na\text{-}Ca}$.

How will the activity of an electrogenic Na^+-Ca^{2+} exchange affect membrane potential? A convenient equivalent circuit to explain this is depicted in Fig. 14.3. This simplified equivalent resting membrane circuit consists of a membrane capacitance that is in parallel with a battery E_m, which is largely responsible for producing the membrane potential. The membrane resistance R_m is modeled as the internal resistance of this battery. Under resting conditions, the reversal potential for the Na^+-Ca^{2+} exchange in heart is approximately -40 mV. At -80 mV

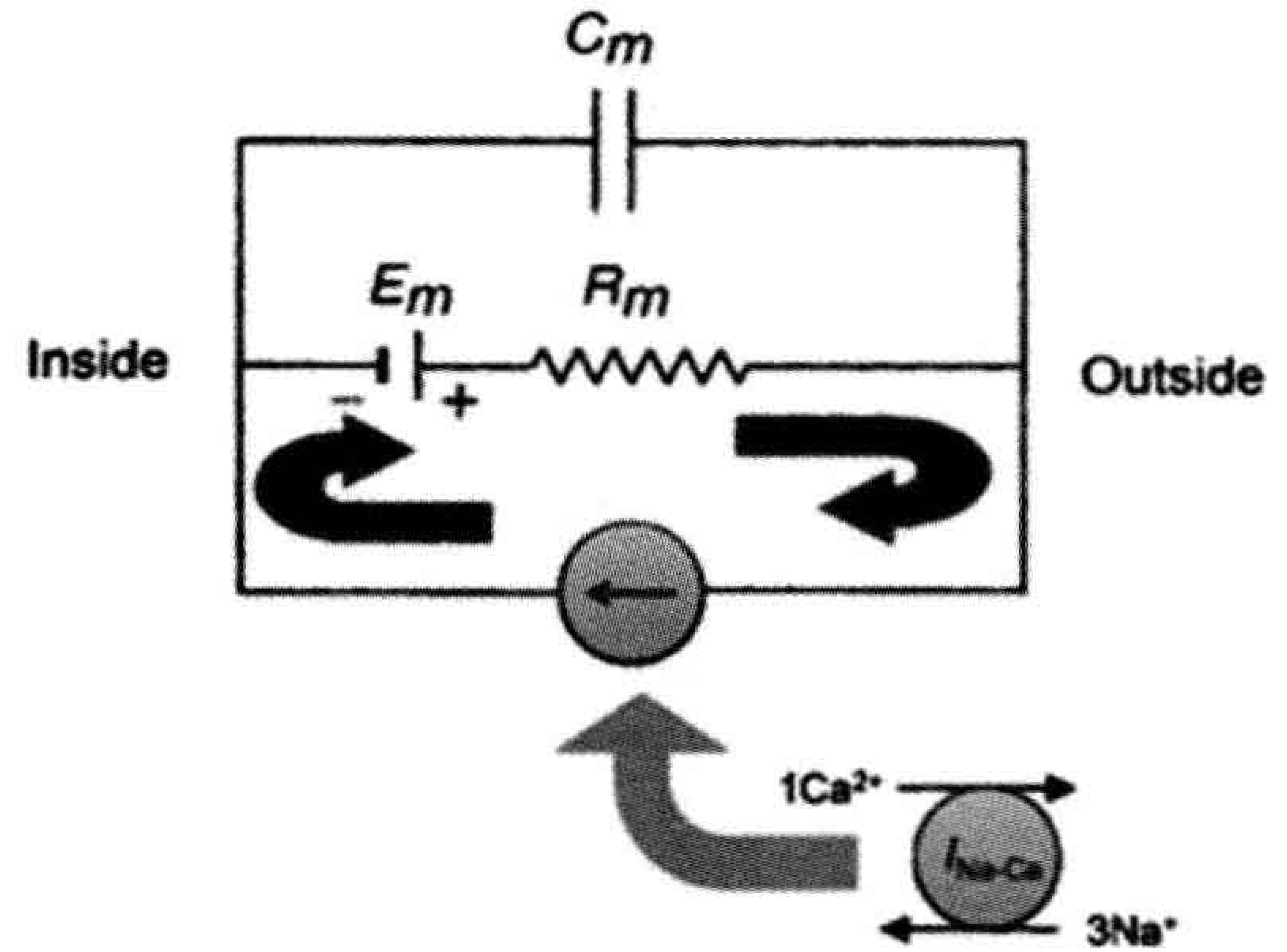


FIGURE 14.3 A simple equivalent circuit for a resting heart cell. The resting membrane potential E_m is typically about -80 mV. This resting membrane potential is modeled as a battery in series with an internal resistance of about 50 MΩ. The membrane capacitance is in series with the battery. The Na^+-Ca^{2+} exchanger may be considered to be a current generator in parallel with the battery and membrane resistance (symbolized by an open circle containing an arrow). At rest, with the exchanger steadily extruding Ca^{2+}, a small depolarizing current $I_{Na\text{-}Ca}$ causes a small voltage drop across the membrane resistance R_m. The solid arrows indicate the direction of current. The circle containing an arrow indicates a current generator (the Na^+-Ca^{2+} exchange). Thus, for each cycle of the exchanger a single net charge is conveyed from the cell exterior to its interior.

the exchange will produce a net inward current, which can be modeled as a current generator that is in parallel with the membrane battery and capacitance (Fig. 14.3). At the steady state, when the resting membrane potential is not changing, $C\,dV/dt = 0$. Thus, the net membrane potential is composed of contributions from ionic currents (mainly through K^+ channels), exchange currents and the Na^+ pump current (Equation 14.10). The exchange will produce an IR drop across the membrane resistance so that the contribution of Na^+-Ca^{2+} current to the membrane potential ($V_{Na\text{-}Ca}$) at rest is given by:

$$V_{Na-Ca} = R_m\, I_{Na-Ca} \qquad (14.11)$$

A large inward exchange current produced by elevated intracellular $[Ca^{2+}]$ may be of the order 200 pA. If we assume that the resting exchange current is one-tenth of this value and given a resting R_m of 50 mΩ, the exchange will contribute about 1 mV to the resting membrane potential. In reality, the value is likely to be less than this but cannot be specified with certainty because reliable measurements of resting current are not available.

The first observations of exchange current were not published until nearly 20 years after Reuter and Seitz originally reported Na^+-Ca^{2+} exchange activity in heart tissue. It is worth considering some of the problems associated with the measurement of exchange current that might account for this lengthy hiatus.

To stimulate exchange so that it can be measured, one can either change electrochemical gradients (and hence the exchange driving forces) by using a voltage-clamp step or one can abruptly change external ion composition with a rapid switching device. In the case of the voltage-clamp step, the experimentalist must have a complete understanding of what interfering currents will be activated, as well as some means of inhibiting them. If exchange is to be activated by changing ionic gradients, then these changes must be sufficiently rapid that they are not immediately dissipated by the exchange activity. It is difficult rapidly to change or control extracellular ionic composition in multicellular preparations because diffusion distances are large and diffusion may be hindered by a surface structure. In multicellular preparations, voltage-clamp is usually established with small microelectrodes, which are unsuitable for cell dialysis. It is, therefore, very difficult to control the intracellular ionic composition. This doubtless contributed to the difficulty of isolating exchange currents in multicellular preparations. Despite these difficulties, a measurement of exchange currents has been reported in multicellular preparations (Horackova and Vassort, 1979).

Recently, it has proved feasible to use the patch-clamp technique in conjunction with wide-tipped microelectrodes (10-μm diameter) to obtain an isolated patch whose surface area is approximately 75 μm^2 (see Fig. 14.2). A conventional isolated patch is of the order 2–3 μm^2. These *giant patches* are sufficiently large to permit the detection of exchange currents (Hilgemann, 1989). Their great virtue is that they permit relatively easy access to either side of the membrane. Thus, solution adjacent to the external surface of the sarcolemma can be changed by changing the pipette solution. The internal surface of the sarcolemma can be changed rapidly by changing the bathing solution. Clearly, this method of voltage-clamp allows the experimentalist considerable control over the forces that drive exchange.

Several other techniques have recently become available that improve exchange current isolation. For example, forward exchange current in intact cells can be activated by abruptly elevating intracellular Ca^{2+}, which is then transported to the cell exterior. This has been accomplished in an elegant fashion by Niggli and Lederer (Niggli and Lederer, 1991). These workers used the compound DM-dinitrophen that is commonly referred to as *caged* Ca^{2+}. This can be introduced into the cell interior through a patch pipette. Upon appropriate irradiation with UV light, Ca^{2+} is released from the caged Ca^{2+} with extremely rapid kinetics. This abruptly elevates cytosolic Ca^{2+} and transiently stimulates forward Na^+-Ca^{2+} exchange as the released Ca^{2+} is pumped to the cell exterior.

As we have indicated, to activate exchange it is desirable to change external ionic composition (and the electrochemical gradients driving exchange) extremely rapidly in comparison with the time required for the exchange to dissipate these changes. It is now possible to change external solutions surrounding heart cells or isolated patches with a half-time of about 20 ms (this includes exchange of the unstirred layer). One method consists of placing a cell with attached microelectrodes in one of two adjacent microstreams of solution (Spitzer and Bridge, 1989). The boundary separating these streams is abruptly moved across the cell so that it is placed in the adjacent stream. This rapid switching method has proved valuable in stimulating both inward and outward exchange currents (Chin et al., 1993).

V. ISOLATION OF Na^+-Ca^{2+} EXCHANGE CURRENT

VA. Whole-Cell Patch-Clamp Studies

The first clear evidence that an electric current was generated by Na^+-Ca^{2+} exchange was provided simultaneously by Kimura and coworkers (Kimura et al., 1986) and by Mechmann and Pott (Mechmann and Pott, 1986). Given the probable stoichiometry of the exchange, electrophysiologists expected to be able to measure a current generated by the exchange. By using the whole-cell patch-clamp technique together with intracellular dialysis, Junko Kimura and her associates were able to isolate the Na^+-Ca^{2+} exchange current. These investigators voltage-clamped guinea pig ventricular myocytes with single microelectrodes. The pipette contained a dialyzing solution completely deficient in Na^+ and in which Ca^{2+} was buffered to a value of 73 nM with EGTA. The superfusing external solution contained no Ca^{2+}. Under these circumstances, no exchange could take place. Very little change in current was observed when external Ca^{2+} was reapplied and subsequently removed. However, an outward current was generated after changing the pipette solution for one containing 30 mM Na^+ and then applying 1.0 mM external Ca^{2+}. Under these circumstances, Ca^{2+} entered the cell in exchange for internal Na^+, which was extruded. This current (Fig. 14.4) is clearly attributable to the operation of electrogenic Na^+-Ca^{2+} exchange. This conclusion was strengthened by several additional observations. Upon removal of external Ca^{2+}, the current was turned off. The current was reduced when lower concentrations of dialyzing Na^+ were used and enlarged by increasing external Ca^{2+}. Thus, the current exhibited the expected dependency on both Na^+ and Ca^{2+}. The current was blocked by La^{3+}, which is known to block Na^+-Ca^{2+} exchange. The current also exhibited *voltage dependence* (see Section XI). One might have expected sustained current under these circumstances, but this was not observed (see Fig. 14.4) and the current exhibited a tendency to decay. One plausible explanation for this is that excessive Ca^{2+} entry displaces protons when it is

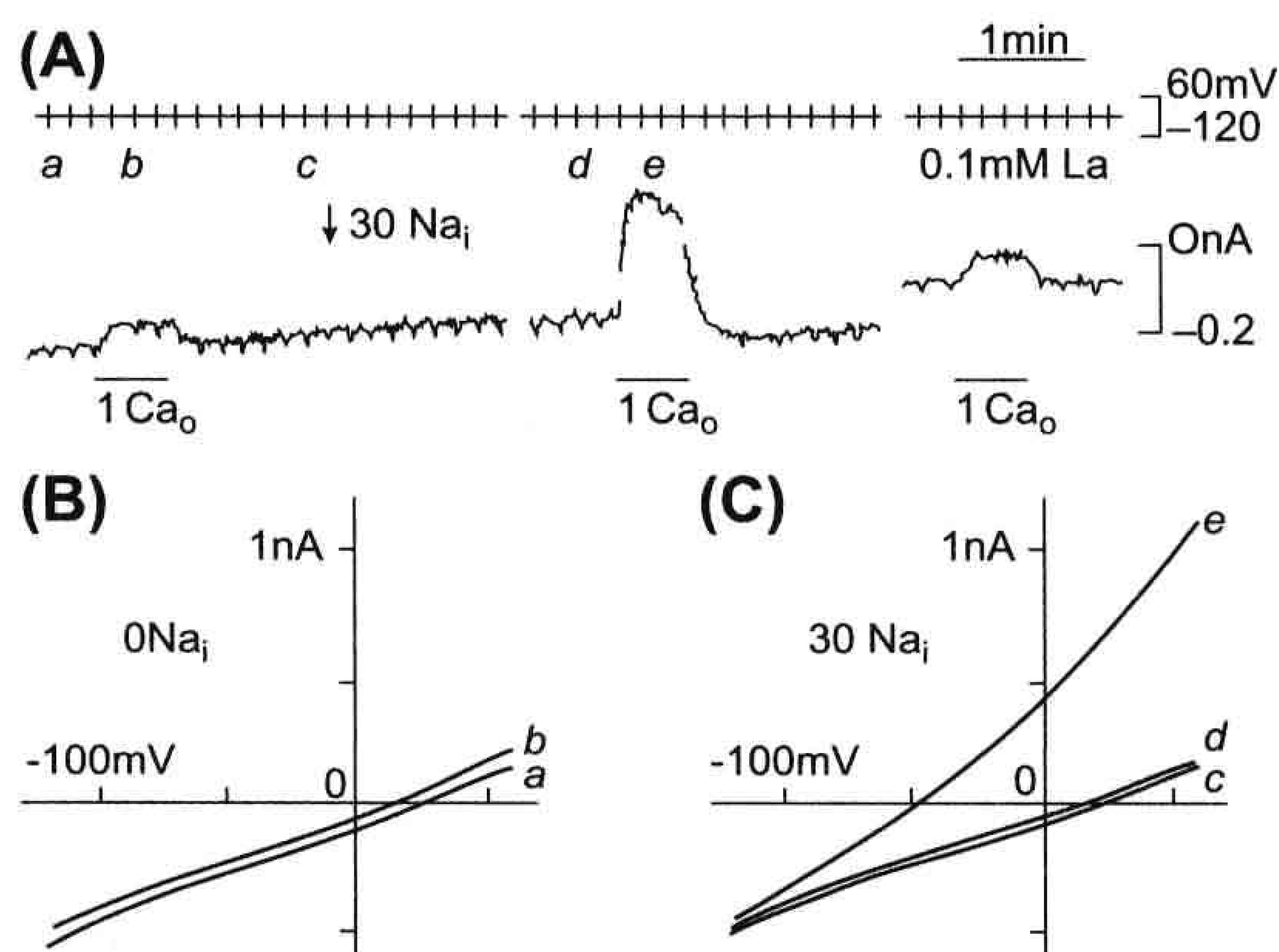


FIGURE 14.4 (A) Voltage-clamp record from a single myocyte showing voltage (upper trace) and current (lower trace). A ramp pulse from +60 mV to −120 mV was given from a holding potential of −30 mV every 10 s at a ramp speed of about 0.2 V/s. Current–voltage relationships were then constructed. An application of 1 mM Ca^{2+} in the absence of intracellular Na^+ (zero pipette Na^+) produced a small outward current. To exchange the pipette solution, a piece of tapered polyethylene tube was inserted into the pipette. The arrow indicates when the solution change was started. The holding current shifted outward slightly on loading Na^+. The middle current record shows 1 mM Ca^{2+} superfusion in the presence of 30 mM pipette Na^+. The Ca^{2+}-induced outward current appears to decay after reaching a peak. Current undershoot is seen after washing off Ca^{2+}. These phenomena may be due to Ca^{2+} accumulation immediately below the membrane of acid induced by binding of Ca^{2+} to EGTA. (B) I-*V* relations measured before (a) and during (b) 1 mM Ca^{2+} superfusion in the absence of Na_i^+. (C) I-V curves before (c) and after (d) loading Na_i^+ and during subsequent 1 mM Ca_o^{2+} application (e). *(Reprinted from Kimura et al. (1986) with kind permission of the authors and* Journal of Physiology.*)*

buffered by the dialyzing EGTA. The resulting acidification in the vicinity of the exchanger should inhibit exchange activity. An alternative possibility is that EGTA fails to buffer incoming Ca^{2+}, which accumulates in the vicinity of the exchanger. The resulting collapse of the Ca^{2+} gradient would also slow exchange.

Kimura and colleagues reported the measurement of an outward current corresponding to the entry of Ca^{2+} and extrusion of Na^+ from the cell. Mechmann and Pott demonstrated the existence of an inward exchange current corresponding to Ca^{2+} extrusion and Na^+ entry into a cardiac cell (Mechmann and Pott, 1986). In one experiment, these authors voltage-clamped spherical atrial cells from an adult guinea pig. Transient inward current occurred spontaneously in this preparation. These transient inward currents seemed to depend on intracellular Ca^{2+} because they were abolished if the cell was dialyzed with 1.0 mM EGTA. Moreover, they could not be elicited in the presence of caffeine, which depletes the SR of Ca^{2+}. Presumably, the transient release of SR Ca^{2+} activated these currents. The currents also showed a dependence on extracellular Na^+ and voltage as expected of a Na^+-Ca^{2+} exchange current. The more negative the voltage, the larger the inward current. This is reasonable and simply indicates that, at more negative potentials, the exchange rate is greater so that Ca^{2+} released from the SR is removed rapidly from the cell.

Shortly after these early demonstrations of exchange current, Hume and Uehara were able to demonstrate Na^+-Ca^{2+} exchange currents in isolated frog atrial cells by using the whole-cell patch-clamp technique in combination with intracellular dialysis (Hume and Uehara, 1986a,b). It is fair to say that since this time measurement of exchange current has become both reliable and routine. An example of an inward exchange current measured in a ventricular cell is displayed in Fig. 14.5.

The development of the giant patch technique has also facilitated measurement of the exchange current produced by the squid exchanger NCX–SQ1 (He et al., 1998).

VB. Na^+-Ca^{2+} Exchange Current Reversal Potential

It is desirable when studying any ionic current to be able to demonstrate a *reversal potential* for that current. The existence of reversal potentials is a thermodynamic necessity and provides one of the least ambiguous ways of identifying an ionic current. However, it is not always a straightforward matter to demonstrate reversal potentials. For example, if exchange current were extremely small

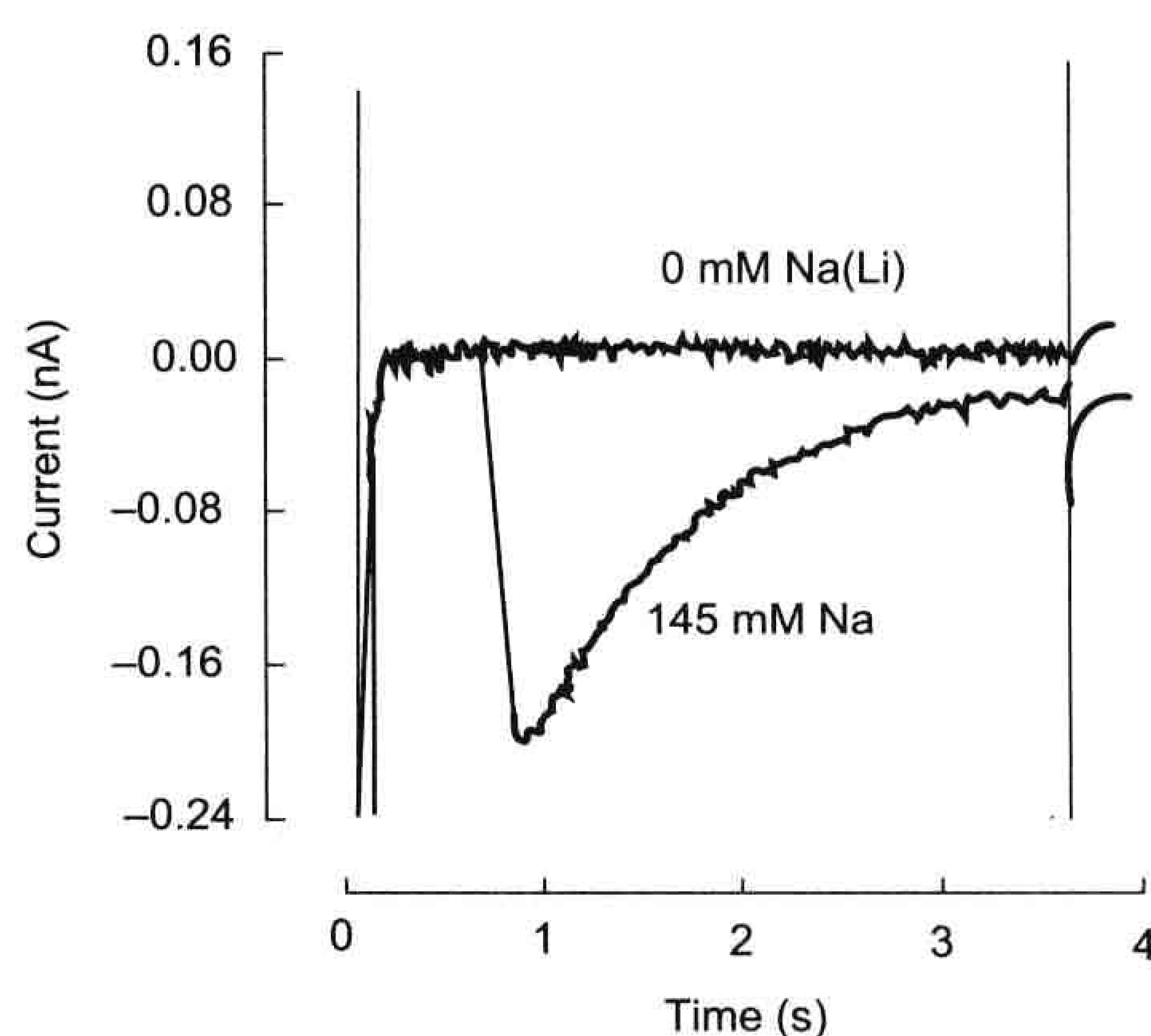


FIGURE 14.5 Transient inward Na^+-Ca^{2+} exchange. To activate this current, a guinea pig ventricular cell was tetanized with voltage-clamp pulses in the presence of ryanodine and in the absence of external Na^+. This resulted in an elevation of cytosolic Ca^{2+} and a sustained contraction (not shown). Abrupt application of 145 mM extracellular Na^+ while the cell was held at −40 mV produced mechanical relaxation and activated a transient inward Na^+-Ca^{2+} exchange current. As intracellular Ca^{2+} declined, the current decayed.

over a large voltage range in the vicinity of the reversal potential, then the precise potential at which zero current occurred could be extremely difficult to specify. Moreover, subsarcolemmal spaces from which diffusion is restricted can produce changes in ionic concentration that confound measurement of the exchange reversal potential. For the Na^+-Ca^{2+} exchange in heart, the reversal potential is given by Equation 14.8. For the conditions of their experiment, Kimura and coworkers (see Fig. 14.4) calculated that the reversal potential of exchange ought to be −131 mV (Kimura et al., 1986). Their results indicate that exchange current becomes zero at a potential close to this value. Ehara and colleagues extended studies of the exchange reversal potential (Ehara et al., 1989). With the fairly specific exchange inhibitor Ni^{2+}, these authors were able to show that, over a wide range of external Na^+ values, the measured exchange reversal potential conformed to theoretical expectation. Moreover, in view of the wide range over which the reversal potential remains constant, the stoichiometry is unlikely to vary.

VI. IONIC DEPENDENCIES OF Na^+-Ca^{2+} EXCHANGE CURRENT

It is of considerable physiological significance that the Na^+-Ca^{2+} exchange current is extremely sensitive to internal Na^+. There are two aspects of this sensitivity to consider, one purely thermodynamic and the other kinetic. If we assume that a resting heart cell contains 100 nM free cytosolic Ca^{2+} and is bathed in 2.0 mM Ca^{2+} and 140 mM Na^+, we can use Equation 14.8 to calculate the way the exchange reversal potential varies with internal Na^+. The results are displayed in Fig. 14.6.

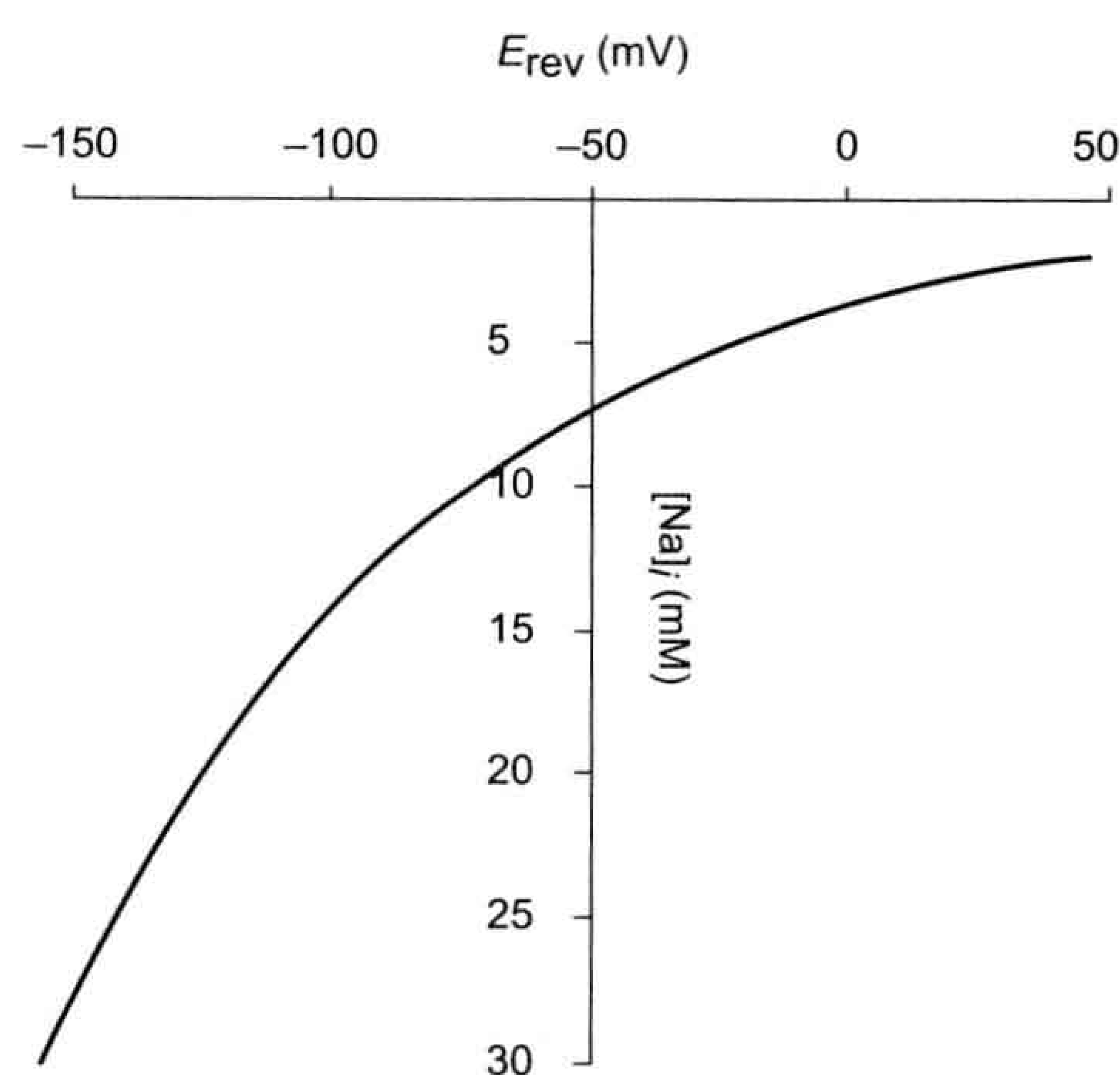


FIGURE 14.6 Calculated variation of exchange reversal potential with intracellular Na^+. Intracellular Ca^{2+} was set at 100 nM and extracellular Ca^{2+} was 2.0 mM. Extracellular Na^+ was 140 mM.

It is apparent that with 7 mM intracellular Na^+, 140 mM extracellular Na^+, and 100 nM intracellular free Ca^{2+}, the reversal potential for exchange is approximately −50 mV. Since the resting membrane potential is at least 30 mV negative to this, at rest the exchanger will extrude Ca^{2+}. However, a modest increase in intracellular Na^+ to 12 mM would change the reversal potential by 14 mV to −64 mV. Were the Na^+ to accumulate to 15 mM, then the reversal potential would be −80 mV. Since the resting potential is likely to be close to this value, the exchange would be close to, or at equilibrium and would be incapable of extruding intracellular Ca^{2+}. Further Na^+ accumulation would cause the exchange to reverse and transmit Ca^{2+} into the cell. Na^+ accumulation will tend to bring the exchange closer to its equilibrium potential and, therefore, increase the likelihood of Ca^{2+} entry via the exchanger upon membrane depolarization. Cardiac glycosides which, depending on dose, partially or completely block the sodium pump, tend to produce an accumulation of intracellular Na^+ (Sheu and Fozzard, 1982). Part of the basis of their inotropic effect resides in their shifting the reversal potential of the Na^+-Ca^{2+} exchange to more negative values. In extreme cases, this will prevent Ca^{2+} extrusion which, in the face of continued Ca^{2+} leak, will lead to Ca^{2+} accumulation.

The Na^+-Ca^{2+} exchange current also exhibits a physiologically important kinetic dependence upon internal Na^+. This issue has been investigated directly by Miura and Kimura, who studied outward exchange current in guinea pig ventricular cells under voltage-clamp (Miura and Kimura, 1989). Intracellular Ca^{2+} was buffered to 100 nM and intracellular Na^+ was varied by varying the pipette Na^+ concentration. External Na^+ was reduced to zero and a unidirectional exchange reaction was activated by applying 0.2 mM Ca^{2+} as rapidly as possible to the cell exterior. The results demonstrate that exchange current density exhibits a steep and somewhat sigmoid dependence on internal Na^+. The K_m for this dependency is approximately 20 mM and Hill plots reveal a Hill coefficient of 1.9. It is notable that an application of rate theory revealed that the voltage dependence of the exchange did not depend on intracellular Na^+ (see Section XI). It is clear from these results that at least Ca^{2+} influx on the exchange will be extremely sensitive to fluctuations in intracellular Na^+ produced, for example, by increases in stimulation rate or cardiac glycosides. It is unfortunate that we have no information on the intracellular Na^+ dependence of inward exchange current which corresponds to Ca^{2+} efflux. However, studies with isotopic fluxes reveal that Na^+ and Ca^{2+} compete for transport on the exchanger. For example, Na^+ on the same side of the cardiac sarcolemmal membrane as Ca^{2+} inhibits Ca^{2+} flux through the exchanger with a K_i of about 15 mM (Reeves and Sutko, 1983). Finally, the net inward exchange current

does depend on external Na^+. This has been investigated by Kimura and coworkers, who showed that inward current exhibited a sigmoidal dependence on external Na^+ with a $K_{1/2}$ of 87.5 mM and a Hill coefficient of 2.9 (Kimura et al., 1986).

Net inward exchange current (i.e. Ca^{2+} extrusion in exchange for Na^+ entry) is also dependent on intracellular Ca^{2+}. The relationship between Ca^{2+} concentration and current has been measured in two different ways. Miura and Kimura used whole-cell patch-clamp on guinea pig myocytes to determine K_m (Ca^{2+}) (Miura and Kimura, 1989). They controlled intracellular Ca^{2+} by dialyzing the cell with various EGTA-buffered solutions and determined a K_m (Ca^{2+}) to be 0.6 μM. With a different approach, Barcenas-Ruiz and colleagues used guinea pig ventricular myocytes to measure exchange current and intracellular Ca^{2+} simultaneously (Barcenas-Ruiz et al., 1987). Intracellular Ca^{2+} was measured with the Ca^{2+}-sensitive indicator Fura−2, introduced through the dialyzing pipette used to voltage-clamp the cells. Heart cells can be tetanized or caused to go into contracture in the presence of ryanodine. Various clamp pulses up to 120 mV in amplitude (holding potential of −80 mV) produced slow and sustained increases in Ca^{2+}. This Ca^{2+} declined upon repolarization and the decline was accompanied by a Na^+-Ca^{2+} exchange current tail. Plots of current against $[Ca^{2+}]_i$ revealed a linear relationship and no sign of saturation (Fig. 14.7). It is not possible to extract a K_m value from these data since the relationship between Ca^{2+} and current does not saturate. However, it is reasonable to conclude that the K_m value is well above the 0.6 μM obtained by Kimura and colleagues. Discrepancies of this nature are not easy to resolve. It is, however, worth noting that EGTA has the rather curious effect of increasing the affinity of the exchanger for Ca^{2+} (Trosper and Philipson, 1984).

VII. REGULATION OF Na^+-Ca^{2+} EXCHANGE CURRENT

The regulation of Na^+-Ca^{2+} exchange current has largely been studied in NCX1. We will consider five types of regulation. First, intracellular Ca^{2+} regulates the exchange current. The exchange current also exhibits a regulatory phenomenon known as Na^+-dependent inactivation. Thus, the exchanger not only transports Na^+ and Ca^{2+}, but these ions are capable of regulating its function as well. Exchange current is also known to be regulated by phosphatidylinositol-4,5-bisphosphate (PIP_2), phosphorylation and, finally, the XIP region of the exchanger in the cytosolic loop appears to be involved in the regulation of the NCX (see Section VIII). In addition, a great deal has been learned about regulatory function and its relationship to the structure of the exchanger.

VIIA. Regulation by Na^+ and Ca^{2+}

There are two Ca^{2+}-binding sites on the cytoplasmic loop of NCX (see Section VIII). It is now apparent that Ca^{2+} influx in exchange for internal Na^+ cannot occur if intracellular Ca^{2+} is reduced below a certain critical level. Dipolo provided the first evidence that Ca^{2+} was required to activate NCX (DiPolo and Beauge, 1987b). However, in

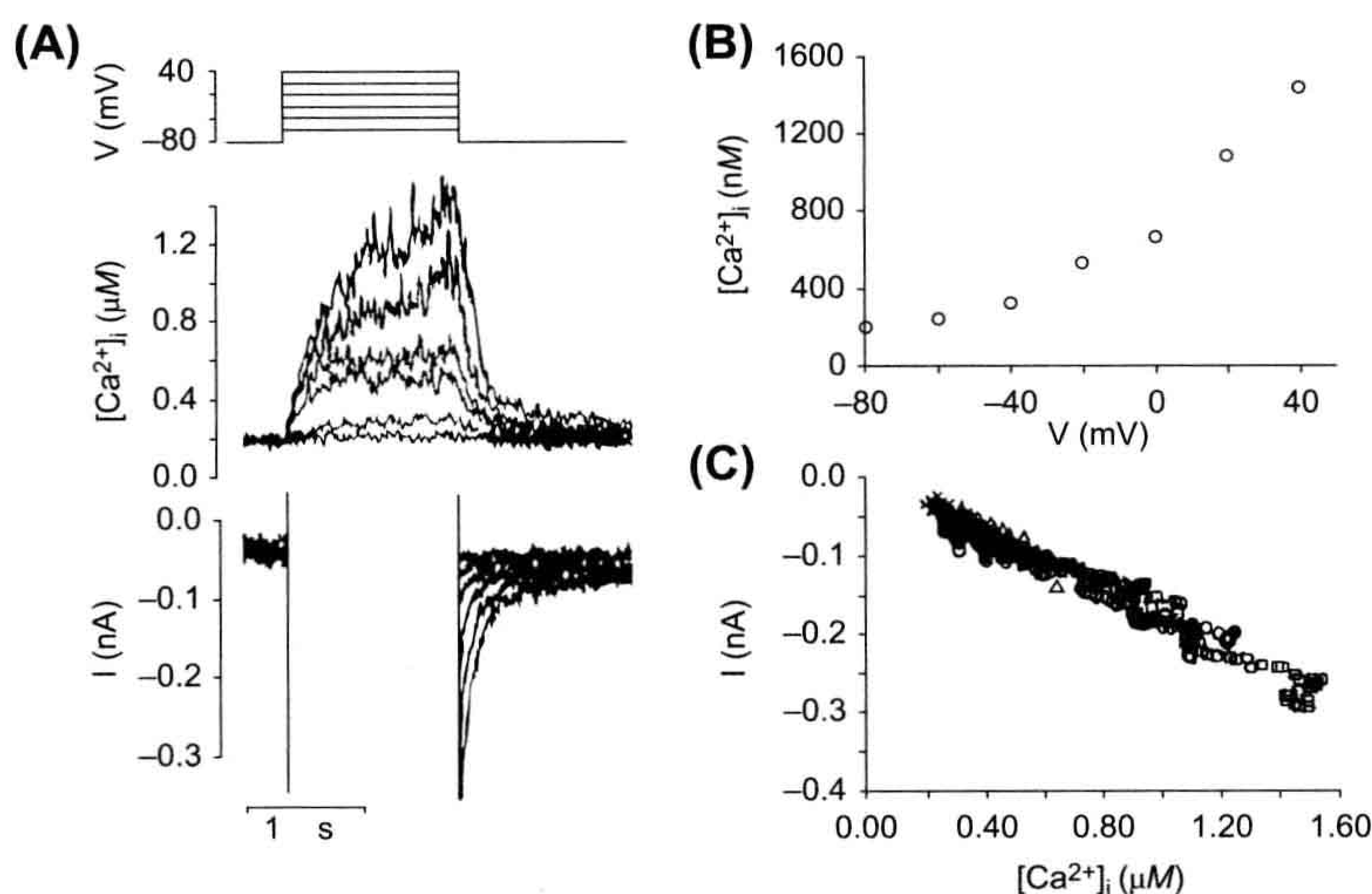


FIGURE 14.7 Changes in $[Ca^{2+}]_i$ and membrane current attributed to Na^+-Ca^{2+} exchange in a single guinea pig ventricular myocyte under voltage-clamp. Micropipette $[Na^+]$ was 7.5 mM. (A) Simultaneous recordings of $[Ca^{2+}]_i$ and membrane current. The holding potential was −80 mV, and depolarizing pulses lasting for 1.5 s were given from −60 mV to +40 mV. Outward currents during the depolarizing pulse are off-scale. (B) Voltage dependence of the change in $[Ca^{2+}]_i$. Values plotted are average $[Ca^{2+}]_i$ over the last 200 ms of the depolarizing pulse. (C) The relationship between $[Ca^{2+}]_i$ and membrane current after repolarization. The current, I, has been plotted as a function of $[Ca^{2+}]_i$ at 2 ms intervals during the first second after repolarization from +40 mV (circles), 0 mV (triangles), −20 mV (diamonds), and −40 mV (crosses). *(Reprinted with permission from Barcenas-Ruiz, L., Beuckelmann, D.J. and Wier, W.G. (1987). Sodium-calcium exchange in heart: membrane currents and changes in $(Ca^{2+})_i$. Science. 238, 1720–1722. Copyright 1987 American Association for the Advancement of Science).*

isolated patches from cardiac cells, the K_D appears to be from 0.1 to 0.3 μM (Hilgemann et al., 1992b; Matsuoka et al., 1995). This is reasonable because Ca^{2+} in junctional regions is thought to rise by as much as 15 μM (Acsai et al., 2011). The possible physiological significance of Ca^{2+} regulation will be discussed in a later section. Moreover, regions of the NCX molecule involved in Ca^{2+} regulation are now understood (see section VIII). Na^+-dependent inactivation of exchange current is a rather curious regulatory phenomenon first described by Hilgemann and coworkers (Hilgemann et al., 1992b). Outward Na^+-Ca^{2+} exchange currents were activated in giant sarcolemmal patches by increasing Na^+ on the cytoplasmic side of the patch. Ca^{2+} was then transported from the pipette to the cytoplasmic side of the patch in exchange for Na^+. This outward current declined with a time constant of approximately 1 s. This decay rate is far too low to represent an initial turnover of exchangers and it appears to be a true regulatory phenomenon. An example of this sort of behavior is displayed in Fig. 14.8. Here, application of 100 mM Na^+ to the cytoplasmic surface activated a transient outward current. It is believed that the XIP region of the exchange molecule (see Section VII) is involved in this process.

VIIB. PIP_2

Hilgemann has been able to show that outward exchange current in isolated giant sarcolemmal patches is stimulated by MgATP (Hilgemann, 1990). With this preparation, it is possible to control MgATP on the cytoplasmic side of the cell membrane. This stimulation by MgATP appears to be a different process than that described in squid axon. For example, it does not appear to involve a protein-dependent kinase (Collins et al., 1992). Hilgemann has also shown that brief treatment of membrane patches with chymotrypsin abolished modulation of exchange current by MgATP. However, recent evidence has been obtained for a mechanism that seems likely to explain regulation by ATP (Hilgemann and Ball, 1996). It now appears that phosphatidylinositol-4,5-bisphosphate (PIP_2) can strongly activate the cardiac Na^+-Ca^{2+} exchanger. Apparently ATP generates PIP_2 from phosphatidylinositol (PI). A number of observations suggest that the generation of PIP_2 can explain the regulation of Na^+-Ca^{2+} exchange by ATP: (1) PI-specific phospholipase C can abolish the action of ATP which can, in turn, be restored by the addition of exogenous PI. (2) The effect of ATP can be reversed by a PIP_2-specific phospholipase C. However, the stimulatory effect of ATP can be mimicked by exogenous PIP_2. (3) Aluminum, which binds with high affinity to PIP_2, reverses the effect of ATP on the exchanger. It therefore appears that the generation of PIP_2 is an important regulator of Na^+-Ca^{2+} exchange activity in heart. A possible mechanism for this is explained in Section VIII.

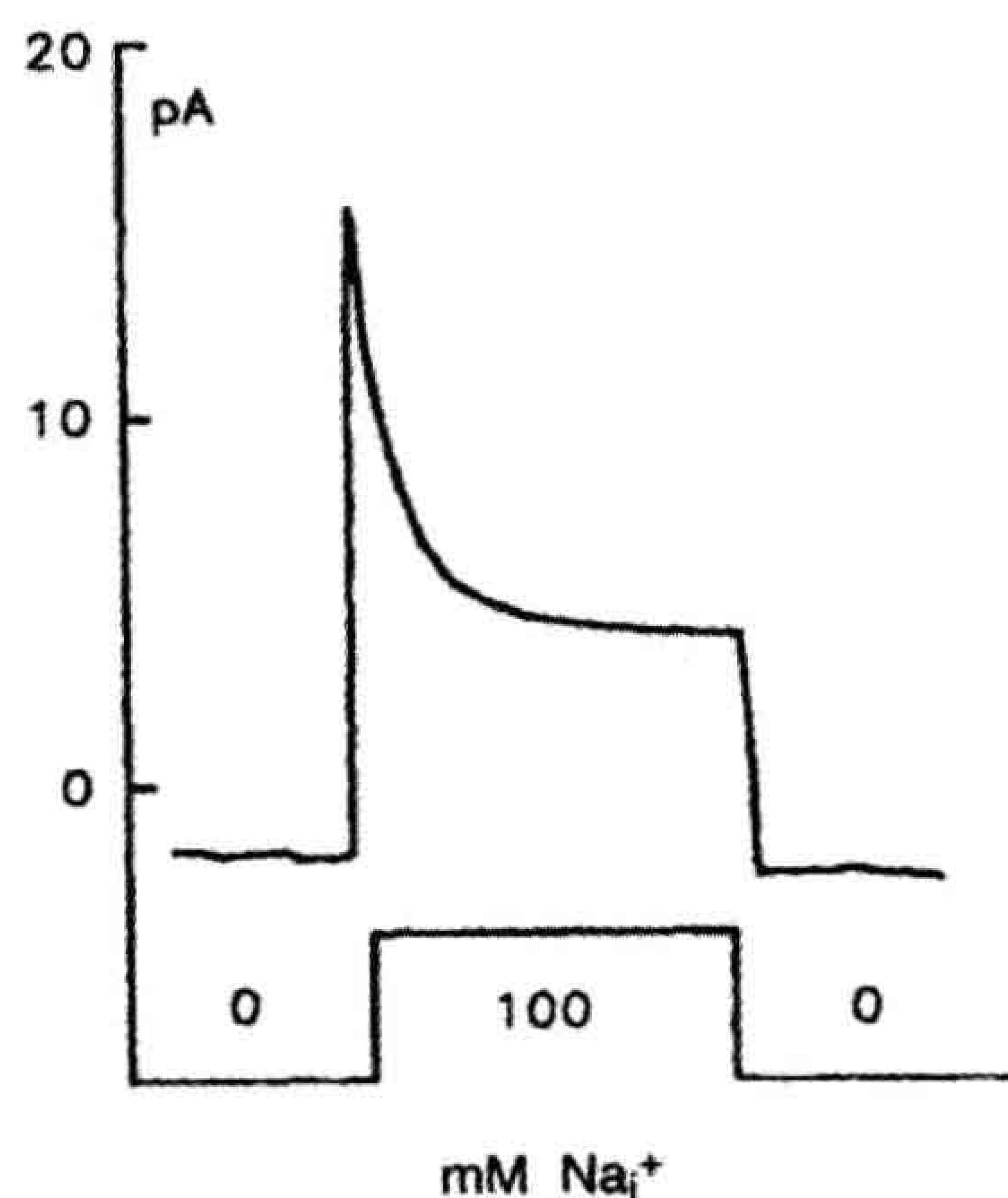


FIGURE 14.8 Secondary modulation of outward Na^+-Ca^{2+} exchange current in giant excised inside-out patches (37°C, 0 mV). Current transients activated with 100 mM Na^+ (substituted for 100 mM Cs^+). *(This figure was kindly provided by Dr Donald Hilgemann.)*

VIIC. Phosphorylation

It has been known for some time that exchange activity in squid giant axons could be regulated by ATP. The main effect of ATP is to increase the affinity of the exchanger for its substrates Na^+ and Ca^{2+}. Moreover, recent evidence suggests the involvement of a Ca^{2+}-dependent protein kinase. It appears that, at least in the squid, Na^+-Ca^{2+} exchange that is stimulated by ATP requires intracellular Ca^{2+} and can be mimicked by hydrolyzable ATP analogs (DiPolo and Beauge, 1987a,b).

It has been difficult to demonstrate regulatory effects of ATP in cardiac tissues. The whole-cell isolated patch technique does not lend itself to studies of this nature because it is extremely difficult, if not impossible, to control intracellular ATP concentrations. However, recent evidence suggests that the molecule may be phosphorylated and regulated by two mechanisms. One which remains controversial is that phophorylation can take place by β-adrenergic/PKA activation. There appears to be stronger evidence that PKC mediated signaling can regulate NCX phosphorylation. We refer the interested reader to the review by Zhang and Hancox (Zhang and Hancox, 2009).

VIID. Regulation by the XIP region of the exchanger

The XIP region of the exchanger refers to a stretch of amino acid (Li et al., 1991; Matsuoka et al., 1997) modeled at the N-terminus of the large cytoplasmic loop. This domain,

which is well conserved among the exchangers, is autoinhibitory and involved in Na^+-dependent inactivation and PIP_2 regulation. The mechanisms of action of XIP are unknown. A possible model is that the autoinhibition is accomplished when the site interacts with some other undisclosed region of the exchanger molecule: Na^+-dependent inactivation could be explained if high concentrations of Na^+ promoted this interaction (Reeves and Condrescu, 2008). PIP_2, instead, could exert its effect by interacting with the XIP sequence preventing it to block the exchanger (He et al., 2000). The properties of the XIP region are further discussed in the next section.

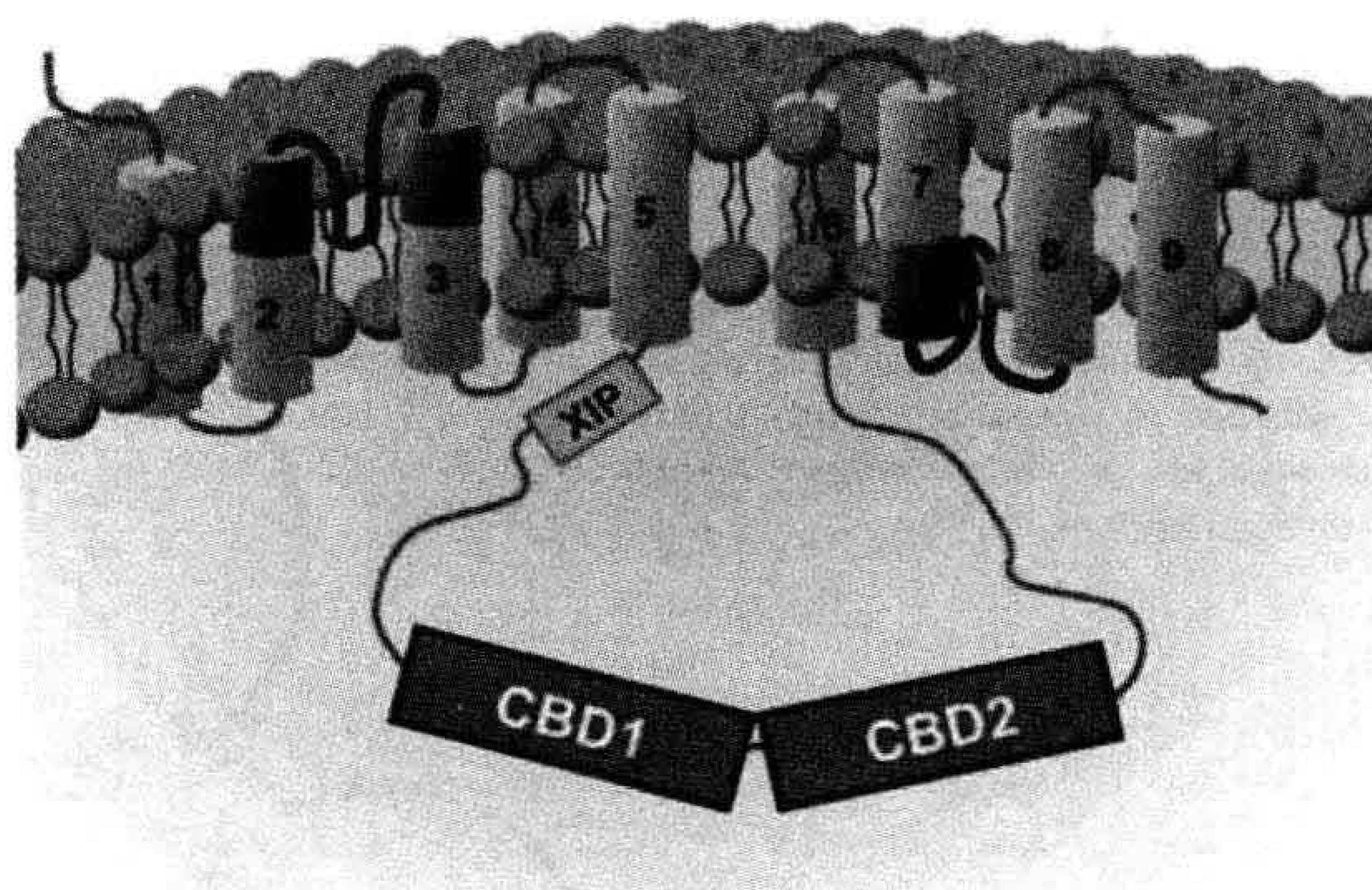


FIGURE 14.9 Secondary structure of the cardiac Na^+-Ca^{2+} exchanger. The exchanger is organized into nine transmembrane segments and a large intracellular loop between TMS5 and 6. The α repeats, which are involved in ion translocation, are indicated in black. The large intracellular loop is involved in NCX regulation. The XIP region, shown in green, is a stretch of residues that controls the Na^+-dependent inactivation and the modulation of NCX by lipids. CBD1 and CBD2 are the Ca^{2+}-binding domains. Calcium bound to these sites is not transported but activates the exchanger and rescues it from the Na^+-dependent inactivation.

VIII. STRUCTURE OF NCX AND ITS RELATIONSHIP TO FUNCTION

The cardiac Na-Ca exchanger (NCX1) has been cloned and isolated (Philipson et al., 1988; Nicoll et al., 1990). Besides revealing its primary structure, this has lead to considerable understanding of its regulation and the relationship between its structure and function. These issues will be the focus of this section.

Our current knowledge of the exchanger's structure principally arises from cysteine accessibility mutagenesis (Nicoll et al., 1999; Iwamoto et al., 2000), epitope mapping (Porzig et al., 1993) and cross-linking studies (Philipson et al., 2002). Although these studies were conducted using the cardiac exchanger isoform, their results are likely to be true for all other isoforms of the exchanger.

The 938 amino acids comprising the primary structure of the exchanger are organized into three regions. The N-terminal region, composed of five transmembrane segments (TMS), a large cytoplasmic loop and a C-terminal group of four TMSs. A schematic drawing of NCX1 is displayed in Fig. 14.9.

At present, there are no structural data on the exchanger TMSs organization. Nevertheless, extensive disulfide cross-linking studies (Qiu et al., 2001; Ren et al., 2006, 2008, 2010) have provided information on the exchanger TMS packing arrangement. This has enabled Ren and her colleagues to generate a model describing the exchanger TMSs organization (Fig. 14.10).

TMSs 2, 3, 7 and 8 (Qiu et al., 2001) are in close proximity and this is of considerable interest. Within these TMSs are found the α repeats (see Fig. 14.9). These are two stretches of about 40 amino acids each with a similar sequence which are highly conserved among the exchanger family (Schwarz and Benzer, 1997). The α repeats are modeled as spanning TMSs 2 and 3 (α1 repeat) and parts of TMS 7 and the following cytoplasmic loop (α2 repeat). The hydrophilic portions of the α repeats appear to form re-entrant loops (Iwamoto et al., 1999; Nicoll et al., 1999; Shigekawa et al., 2002), similar to P-loops found in ion channels (Hille et al., 1999). This suggests that they are involved in ion translocation. This suggestion has been supported by studying mutations at these sites, which have been shown to affect ion transport (Nicoll et al., 1996; Iwamoto et al., 2000; Ottolia et al., 2005). This provides the first information on regions of NCX that may be crucial for ion translocation. For example, several residues within the hydrophilic region of the α repeats set the sensitivity of NCX for extracellular Ca^{2+}, while two residues within TMS3 (Ala^{140} and Ile^{147}) of the α1 repeat influence the cytoplasmic affinity of NCX for the transported Na^+. To date, the residues that directly coordinate the binding of transported Na^+ or Ca^{2+} have not been found, so that additional studies in this area are required.

Our understanding of the modes of operation of the exchanger has been clouded by new evidence indicating that this secondary transporter exists as a dimer in the plasma membrane. First, cross-linking studies showed that cysteines at position 122 (TMS2) in adjacent exchangers form disulfide bonds (Ren et al., 2008). Similar results were obtained for cysteines introduced at position 40 of TMS1, indicating that NCX exists as oligomers in the plasma membrane. This was then confirmed by fluorescence resonance energy transfer (FRET) studies, which demonstrated the dimeric organization of NCX (John et al., 2011). We will provide a short explanation of this technique shortly. However, how dimerization of NCX affects either its transport or regulatory properties is still unknown.

While transport functions are associated with the transmembrane segments of NCX, the large cytoplasmic loop between TMS 5 and 6 is involved in regulatory

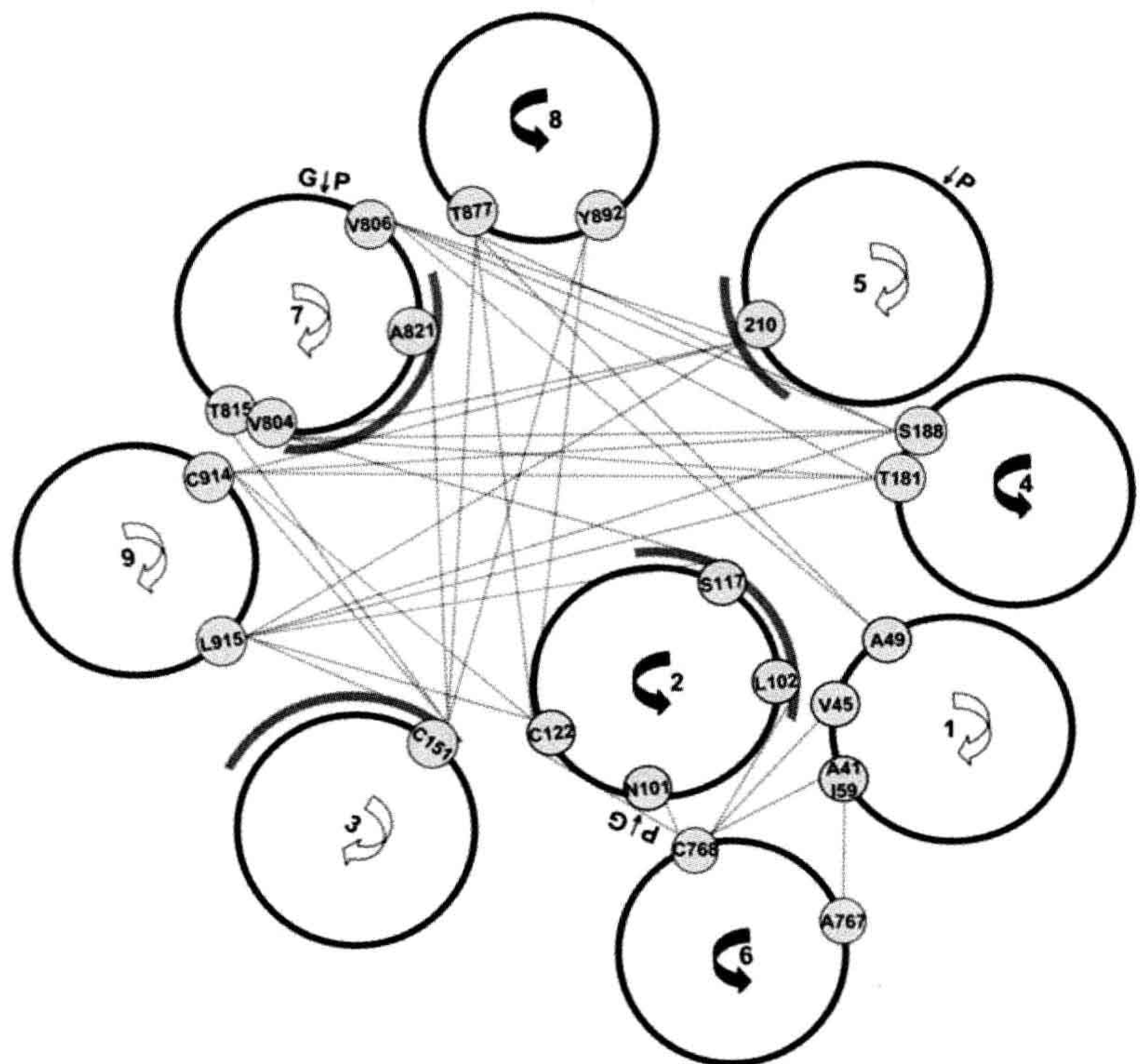


FIGURE 14.10 Computer-generated model of NCX1 helix packing. Pairs of residues that demonstrated cross-linking are indicated with lines. The faces of TMSs that contain residues that have altered activity upon mutagenensis are indicated with gray arcs. *(Reprinted from Ren et al. with kind permission of the authors and* Biochemistry.*)*

mechanisms. This is confirmed by the fact that a mutant lacking this loop still transport Na^+ and Ca^{2+} (Matsuoka et al., 1993). Within this portion of NCX there are several regions of interest. For example, the XIP region is found at the N-terminal side of the loop. This is a stretch of hydrophobic and positive residues (amino acids 219–238) named after a synthetic peptide (exchanger inhibitory peptide) with an identical sequence which potently blocks NCX transport activity (Hilgemann et al., 1991a). This site is mainly known to regulate the Na^+-dependent inactivation (see Section VI; Matsuoka et al., 1997) since mutations within it either eliminate this secondary regulation or alter its properties. Also exogenous regulators such as lipids interact with this region to modulate exchanger activity by affecting the Na^+-dependent inactivation (He et al., 2000; Riedel et al., 2006).

Two Ca^{2+}-binding domains are downstream of the XIP region (see Figs 14.9 and 14.11). These are indicated as Ca^{2+}-binding domains 1 and 2 (CBD1 and CBD2). In the cardiac exchanger isoform NCX1, CBD1 encompasses residues 371 to 501, CBD2 consists of residues 501–689. Cytoplasmic Ca^{2+} that binds to these sites is not transported (thereby indicated as regulatory Ca^{2+}) but activates the exchanger and rescues it from Na^+-dependent inactivation (Hilgemann et al., 1992a,b).

Both CBD1 and CBD2 are organized into seven-stranded antiparallel β-sandwiches with Ca^{2+} ions bound at

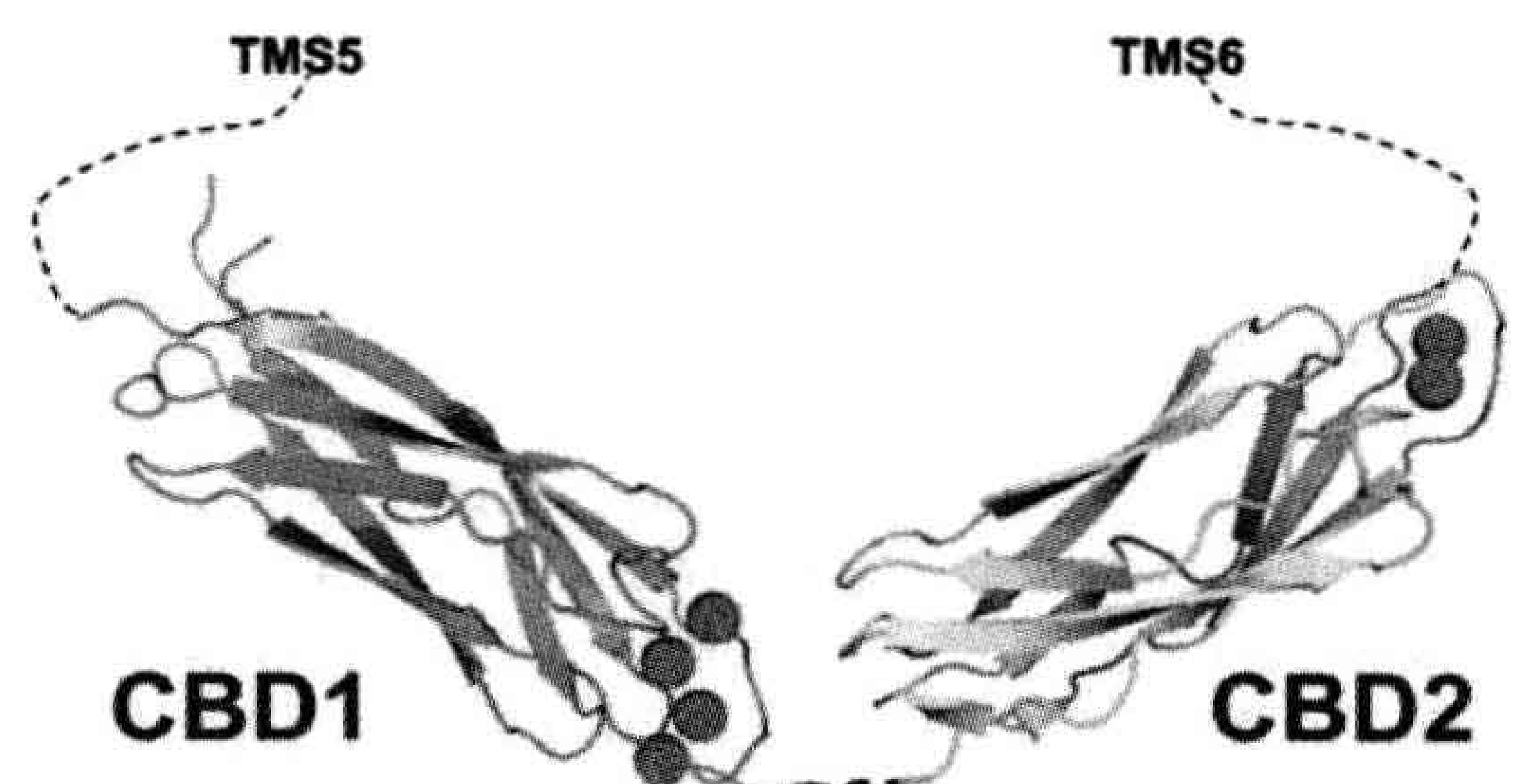


FIGURE 14.11 Structure of the cardiac Na^+-Ca^{2+} exchanger Ca^{2+}-binding domains. Shown is the crystal structure of the first and second Ca^{2+}-binding domains (CBD1 and CBD2). The orientation between the two domains is arbitrary since there is no information about their structure as conjunct domains. CBD1 spans residues 371 to 501, while CBD2 consists of residues 501 to 689 (cardiac isoform, NCX1.1). Calcium ions are shown as green spheres.

one end of the β-barrel (Hilge et al., 2006, 2009; Besserer et al., 2007; Johnson et al., 2008; Chaptal et al., 2009; Wu et al., 2009a,b). The structure of the conjunct CBDs is currently unknown. CBD1 binds four Ca^{2+} ions, however, mutagenesis studies indicate that only the occupancy of sites 3 and 4 is important for Ca^{2+} regulation (Ottolia et al., 2009). CBD2 coordinates two Ca^{2+} ions and removal of the primary Ca^{2+} completely abolishes the sensitivity of NCX to cytoplasmic Ca^{2+} (Besserer et al., 2007).

While CBD1 does not drastically vary among the exchanger isoforms, CBD2 contains a region of diversity that is the result of alternative exon splicing. Six exons exist within CBD2 which are indicated A to F. While A and B are mutually exclusive, the remaining can mix in different combinations. As a result, CBD2s of different lengths and Ca^{2+}-binding properties are created providing unique biophysical properties to the various NCX products. Generally, exon A-containing exchangers (such as the cardiac NCX) can alleviate the Na^+-dependent inactivation at high Ca^{2+} concentrations while exchangers with exon B (such as NCX1.3, kidney) lack this capability (Dyck et al., 1999; Hilge et al., 2009).

The molecular mechanisms underlying Ca^{2+} regulation of the exchanger are unexplained. It is reasonable to speculate that the Ca^{2+}-binding domains undergo conformational changes upon Ca^{2+} binding. This is based on isolated individual and conjoined CBD studies which show the loss of structure of CBD1 in absence of Ca^{2+} (Hilge et al., 2006). In addition, FRET studies show Ca^{2+}-dependent movements within the isolated CBDs (Ottolia et al., 2004; Xie et al., 2008; John et al., 2011) and the full length exchanger (John et al., 2011).

It has also been proposed that electrostatic interactions occur between CBD1 and CBD2 and that these interactions are disrupted by Ca^{2+} binding to CBD1 thereby reorienting CBD in respect to CBD2 (Hilge et al., 2009). This model is supported by recent evidence showing that either the orientation or the proximity of CBD1 and CBD2 is important for NCX Ca^{2+} regulation as is demonstrated by inserting seven alanines between the two CBDs and showing that the resulting ionic currents were less sensitive to cytoplasmic Ca^{2+} (Ottolia et al., 2010). Subsequently, the kinetic properties of a peptide consisting of the conjunct CBD1 and CBD2 were found profoundly altered by the insertion of the seven alanines (Giladi et al., 2010), consistent with the electrophysiological data.

These results suggest that the two Ca^{2+}-binding domains do not act as separate entities but somehow act synergistically to regulate exchanger activity. Indeed, the apparent affinity of the conjunct Ca^{2+}-binding domains for cytoplasmic Ca^{2+} (John et al., 2011) and its kinetics (Giladi et al., 2010) are different from those of CBD1 or CBD2. Although synergism between the CBDs has been demonstrated, two puzzles remain. How do the two CBDs interact mechanistically with each other upon Ca^{2+} binding/unbinding; and, how does this combined entity of CBD1 and CBD2 transmit its information to the remainder of NCX?

Since FRET studies have been useful in detecting movements of these subunits, it is perhaps worth providing a brief description of this technique. Fluorescence resonance energy transfer is the non-radiative transfer of energy from a fluorescent donor to another excitable moiety which can be attached to, for example, different regions of the same molecule (in this case NCX) or to two closely apposed molecules. In FRET, a donor fluorophore in an excited electronic state can transfer its excitation energy to an acceptor chromophore. Although the process does not involve photon emission, usually the donor and the acceptor molecules are fluorescent. Energy transfer quenches donor fluorescence and there is an increase in acceptor fluorescence emission. The efficiency of energy transfer varies in proportion to the inverse sixth power of the distance separating donor and acceptor molecules. Donor and acceptor molecules can be on the same molecules, e.g. NCX, or different molecules. There are two requirements for FRET to occur: first, the emission spectrum of the donor has to overlap the excitation spectrum of the acceptor and, second, the two moieties have to be in close proximity (10 nm). Since the efficiency of energy transfer is strongly dependent on this distance, FRET therefore is a powerful technique to measure the proximity of molecules or their changes in conformation. Labeling the protein, e.g. NCX, can be achieved either chemically, by attaching a fluorophore to the protein, such as maleimide fluorophores dyes, or by molecular biology techniques. Examples of the latter are the cyan (CFP) and yellow (YFP) variants of the green fluorescent protein (GFP), which are popular FRET pairs.

The methods for measuring FRET are several; however, the ratiometric and photobleaching approaches are the mostly widely used. The ratiometric method involves the recording of both acceptor and donor emissions either sequentially or simultaneously. This is because, when FRET occurs, excitation of the donor causes acceptor emission at the expense of donor emission. Hence, the acceptor/donor fluorescence intensity ratio is an estimate of the amount of energy transfer. FRET recording in this manner has the advantage that it can monitor changes in real time. To measure FRET efficiency, which can give estimates of actual distance between fluorescent moieties, the alternative method acceptor photobleaching approach is used. This method relies on the concept that when FRET occurs part of the energy of excited donor is transferred to the acceptor resulting in decreased donor emission. This energy transfer is eliminated by bleaching of YFP and leads to an increase in CFP emission. A cartoon describing the

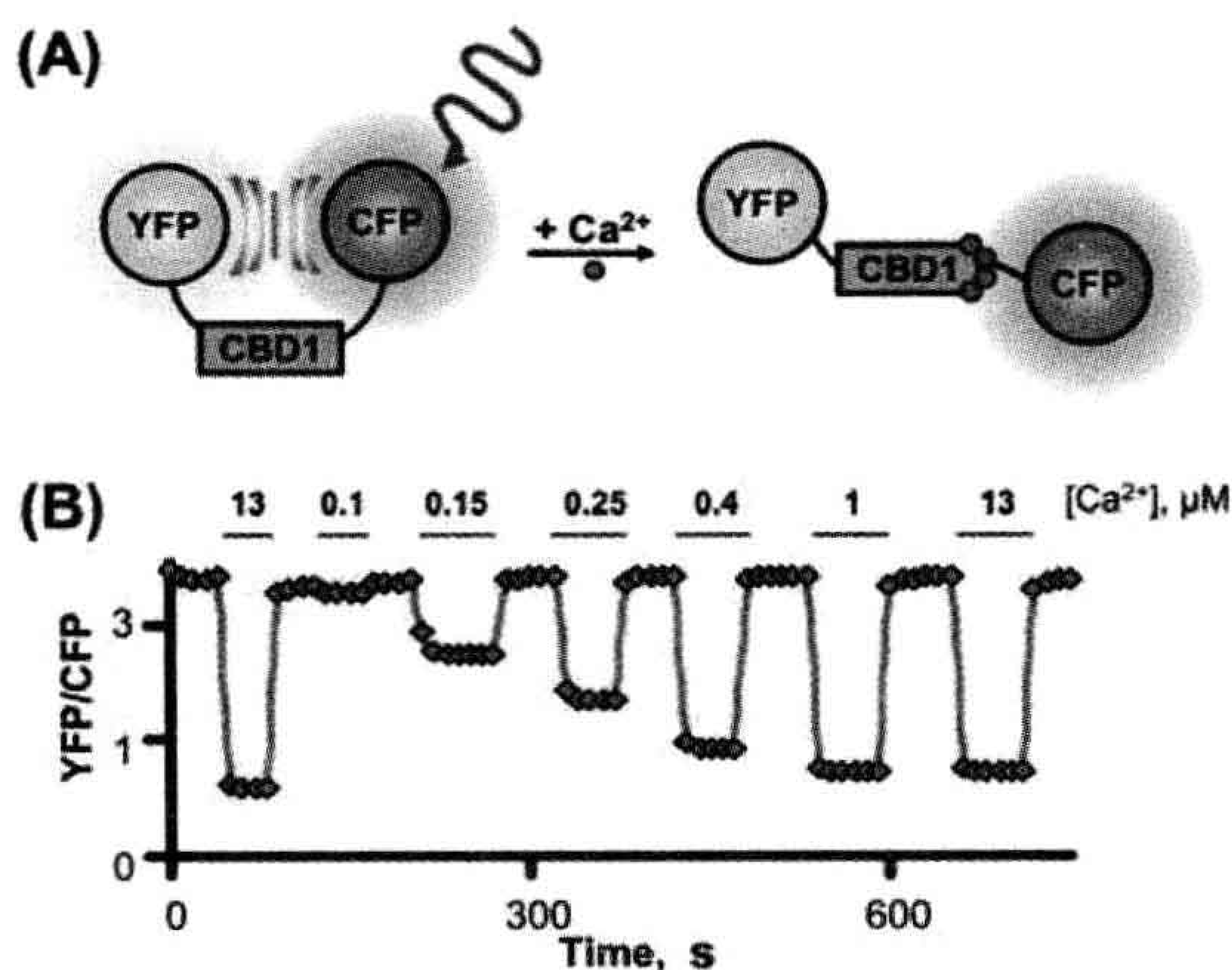


FIGURE 14.12 Example of FRET between CFP and YFP. The yellow and cyan variants of the green fluorescent protein were fused to the N and C termini of the first Ca^{2+}-binding domain (CBD1) of the cardiac Na^+-Ca^{2+} exchanger (A). In absence of cytoplasmic Ca^{2+}, excitation of the CFP caused YFP emission since the two fluorophores are in close proximity. However, as shown in plot (B), addition of cytoplasmic Ca^{2+} moved the fluorophores apart causing a decrease in FRET (measured as YFP/CFP ratio). For this experiment, the fluorescent CBD1 was anchored to the plasma membrane by fusing to its C terminus a short plasma membrane targeting sequence. The construct was then expressed into *Xenopus laevis* oocytes to isolated portion of its plasma membrane onto coverslip. This technique allows accessibility to the cytoplasmic surface of the membrane which now are perfused with different Ca^{2+} concentrations, indicated above the trace. *(Reprinted from John et al. with kind permission of the authors and* PNAS*).*

way that this technique can be use to detect the CBD movements is displayed in Fig. 14.12.

IX. THE PHYLOGENY OF THE Na^+-Ca^{2+} EXCHANGER

The number of proteins belonging to the exchanger family is increasing. These proteins are defined by the presence of the signature sequence α repeats (see previous sections) and a membrane topology of two clusters of transmembrane segments separated by a cytoplasmic loop of different length. Recent analysis indicates five families of exchangers, which constitute a "superfamily". This is explained in some detail in the review by Lytton (Lytton, 2007). Among them is the *NCX family.* These are all mammalian exchangers and include NCX1, the first exchanger to be isolated, as well as NCX2 and NCX3. These exchangers are ubiquitous with NCX1 found in the heart, brain and kidney, NCX2 in the brain and NCX3 in the brain and skeletal muscle. NCX1 is particularly abundant in the heart and it has been the subject of intensive investigations. It is on NCX1 that most studies of currents that are generated by exchange have been performed.

Other exchangers in the NCX family are found, for example, in the nematode *C. elegans* and also in the fruit fly *Drosophila.* The NCX family is found in a wide variety of mammalian species including human, dog, rabbit, cow, rat and guinea pig as well as in various non-mammalian species.

The other four members of the Ca^{2+}/cation antiporter gene superfamily are: bacterial exchangers, Ca^{2+}/anion exchanger, Ca^{2+}/cation exchanger and the NCKX family. Discussion of the first three families of exchangers is outside the scope of this chapter. Here we will briefly described the NCKX family.

NCKX are plasma membrane proteins that, at difference from NCX, require K^+ for transport exchanging four Na^+ for one Ca^{2+} and one K^+ during each cycle. The first member of this family, NCKX1, was cloned from retinal tissue. Here, NCKX1 is associated to the cGMP-gated channel which opens in the dark allowing Ca^{2+} to enter the cell. As Ca^{2+} extrusion mechanism, NCKX counterbalance this Ca^{2+} influx maintaining resting levels of intracellular Ca^{2+}. The physiological impact of the remaining NCKX is less understood but evidence suggests an important role of NCKX2, 3 and 4 in neuronal Ca^{2+} signaling. The fifth member of this family NCKX 5 is, instead, found in skin and retinal epithelia but its function has yet to be explained. Excellent reviews are available to the reader (Cuomo et al., 2007; Lytton, 2007).

X. ISOFORMS OF THE Na^+-Ca^{2+} EXCHANGER

The large intracellular loop of NCX1 can be spliced in different ways to produce a variety of splice variants. The region of alternative splicing is found in the second Ca^{2+}-binding domains (CBD2) (see Section VIII). Six small exons are used in different combinations to produce CBD2 with different properties (Hilge et al., 2006, 2009; Besserer et al., 2007). The resulting exchanger isoforms are tissue-specific (Quednau et al., 1997; Hryshko, 2002) and have different properties such as the ability to overcome Na^+-dependent inactivation (Dyck et al., 1999), altered stimulatory effects of Ca^{2+} (Hilge et al., 2009) and, in the case of the *Drosophila* NCX (CalX), negative regulation by cytoplasmic Ca^{2+} (Hryshko et al., 1996). Still, the physiological significance of tissue-specific isoforms is unclear. Presumably they evolved to perform functions required only by those tissues in which they are found.

XI. CURRENT—VOLTAGE RELATIONSHIPS AND VOLTAGE DEPENDENCE OF Na^+-Ca^{2+} EXCHANGE CURRENT

The origin of the voltage dependence of Na^+-Ca^{2+} exchange has yet to be explained. However, current—voltage

relationships obtained under a variety of ionic conditions can provide a great deal of information that forms a basis for discussing possible mechanisms of voltage dependence. Here we will try to show what can and cannot be concluded about voltage-dependent mechanisms from available current–voltage data. Before interpreting current–voltage relationships, the experimentalist should be confident that he or she is dealing with a pure current. Thus, considerable care in eliminating contaminating currents with appropriate inhibitors and an understanding of which currents (besides exchange current) are activated over the voltage range of interest is essential.

Most Na^+-Ca^{2+} exchange current–voltage relationships that have been measured so far do not show a region of negative slope. This is consistent with the idea that only a single rate-limiting charge translocation step exists in the reaction pathway. Were a second voltage-dependent step to exist in which charge moved in the opposite direction, then one might expect a region of slight negative slope. This is because the increasing voltages that stimulated forward exchange would necessarily begin to retard the movement of exchange in the opposite direction, with resulting decline in net transport and hence current. However, conditions under which a region of negative slope in an exchange current–voltage relationship have been detected. Using the giant patch technique, Hilgemann and coworkers have measured outward exchange current–voltage relationships as a function of extracellular Ca^{2+} (Fig. 14.13) (Hilgemann et al., 1991b). When extracellular Ca^{2+} is 0.1 mM, voltage dependence is diminished and, at extreme depolarization, the slope of the current–voltage relationship becomes discernibly negative. It is currently believed that most of the exchange voltage dependence is associated with Na^+ translocation. Hilgemann has suggested that the negative slope could be explained if Ca^{2+} passes through a small fraction of the membrane field before binding to the carrier. This would constitute a second voltage-dependent step associated with Ca^{2+} translocation in the transport pathway.

A second property expected of current–voltage relationships for electrogenic exchange reactions is that they should saturate at extreme voltages. This is because reaction steps whose rate increases with voltage should become sufficiently rapid that they cease to be rate limiting for the entire reaction sequence. The reaction may then be rate limited by a voltage-independent step, at which point reaction rate will cease to be responsive to voltage. Many current–voltage relationships do show clear evidence of saturation. For example, the measurements of outward current depicted in Fig. 14.13 clearly exhibit saturation. Though not so obvious, measurements of inward current by Bridge and colleagues and by Miura and Kimura also show signs of saturation at extremely negative voltages (Miura and Kimura, 1989; Bridge et al., 1991). In contrast,

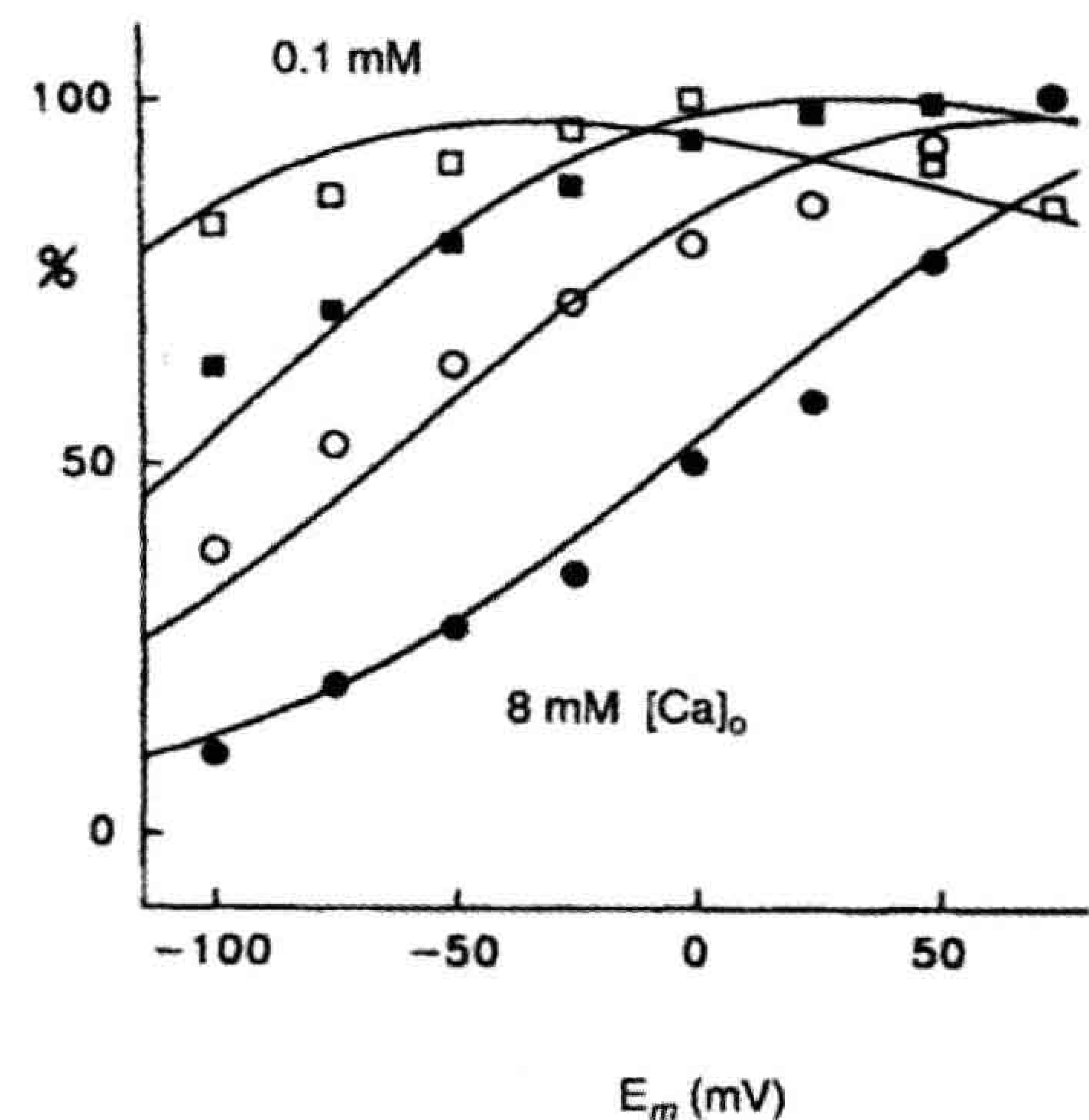


FIGURE 14.13 Ion and voltage dependencies of cardiac Na^+-Ca^{2+} exchange current conform to consecutive exchange model with voltage dependencies at extracellular Na^+ release and binding. Flattening and saturation of outward $I_{Na\text{-}Ca}$-voltage relations as extracellular $[Ca^{2+}]$ is lowered from 8 mM (closed circles) to 2 mM (open circles) to 0.4 mM (closed squares) to 0.1 mM (open squares). All results are normalized to the largest current occurring in the current–voltage relation. Note the negative slope with strong depolarization at 0.1 mM. *(Reprinted with kind permission of the author and* Nature.*)*

results (from giant patches) under zero *trans* conditions suggest little saturation of inward exchange current at very negative potentials (Matsuoka and Hilgemann, 1992). The origin of these discrepancies is not clear, but may be related to whether or not net or unidirectional exchange is producing the inward current. Moreover, current–voltage relationships obtained in whole cells may be complicated by other partial reactions (e.g. Ca^{2+} dissociation from intracellular buffers) not present in the giant patch experiments.

The way that exchange current–voltage relationships depend on ionic conditions can also yield information about voltage-dependent steps in the reaction sequence that leads to exchange. With voltage-clamped giant patches under zero *trans* conditions – i.e. Ca^{2+} in the pipette (extracellular) side and Na^+ in the bath solution – that superfuse the cytoplasmic surface, outward current-voltage relationships showed a striking dependence on pipette (extracellular) Ca^{2+} (see Fig. 14.13). However, when the extracellular (pipette) Ca^{2+} is reduced to very low values, voltage dependence tends to disappear. An attractive explanation for this result is that as extracellular Ca^{2+} is reduced, a voltage-independent step or a step with very modest voltage dependence (presumably associated with Ca^{2+} translocation) starts to become rate limiting, with the result that exchange loses its voltage dependence. However,

Ca^{2+} translocation is not independent of voltage in all species. In the squid Na^+-Ca^{2+} exchanger NCX-SQ1, charge movement accompanies Ca^{2+} translocation rather than Na^+ translocation, as has been shown rather elegantly by He and coworkers (He et al., 1998). These authors examined giant patches from oocytes expressing either NCX1 or NCX1-SQ1. Na^+ and Ca^{2+} were respectively inside the pipette. This forced Na^+- and Ca^{2+}-binding sites to the intracellular surface. Rapid application of Na^+ or Ca^{2+} to the intracellular (outside) surface of the patch produces a transient half-reaction which, in turn, was expected to produce a transient charge movement if the half-reaction is electrogenic. It appears that, in NCX1, transient current is produced by application of Na^+ but, in the case of NCX1-SQ1, application of Ca^{2+} produces an electrogenic half-reaction. Thus, it seems that, in the squid, Ca^{2+} translocation is electrogenic (Fig. 14.14).

The dependence of outward current–voltage relationships on Na^+ is also interesting. Hilgemann and colleagues, using the giant patch technique, have measured outward current–voltage relationships when extracellular Na^+ was 100 and 400 mM (Fig. 14.15). At 400 mM, there was a pronounced flattening of the current–voltage relationship (Hilgemann et al., 1991b). There are two possible (and not necessarily unrelated) explanations for this. If we assume that some step in the Na^+ translocation pathway is both rate limiting and voltage dependent, it is possible that, as extracellular Na^+ increases, this step ceases to be rate limiting because it is accelerated. Were some other voltage-independent step to become rate limiting, one would expect a flattening of the current–voltage relationship as it became dominated by the voltage-independent step, as is in fact observed. Alternatively, if Na^+ binding to some external site were voltage dependent, one would expect voltage dependence of this binding to be lost as the site becomes saturated (Lagnado and McNaughton, 1990).

These results seem to suggest that, somewhere in the Na^+ translocation pathway, a voltage-dependent (charge translocation) step may be involved. In this regard, the data obtained with giant patches, where ideal zero *trans* conditions are most likely to be achieved, are particularly compelling.

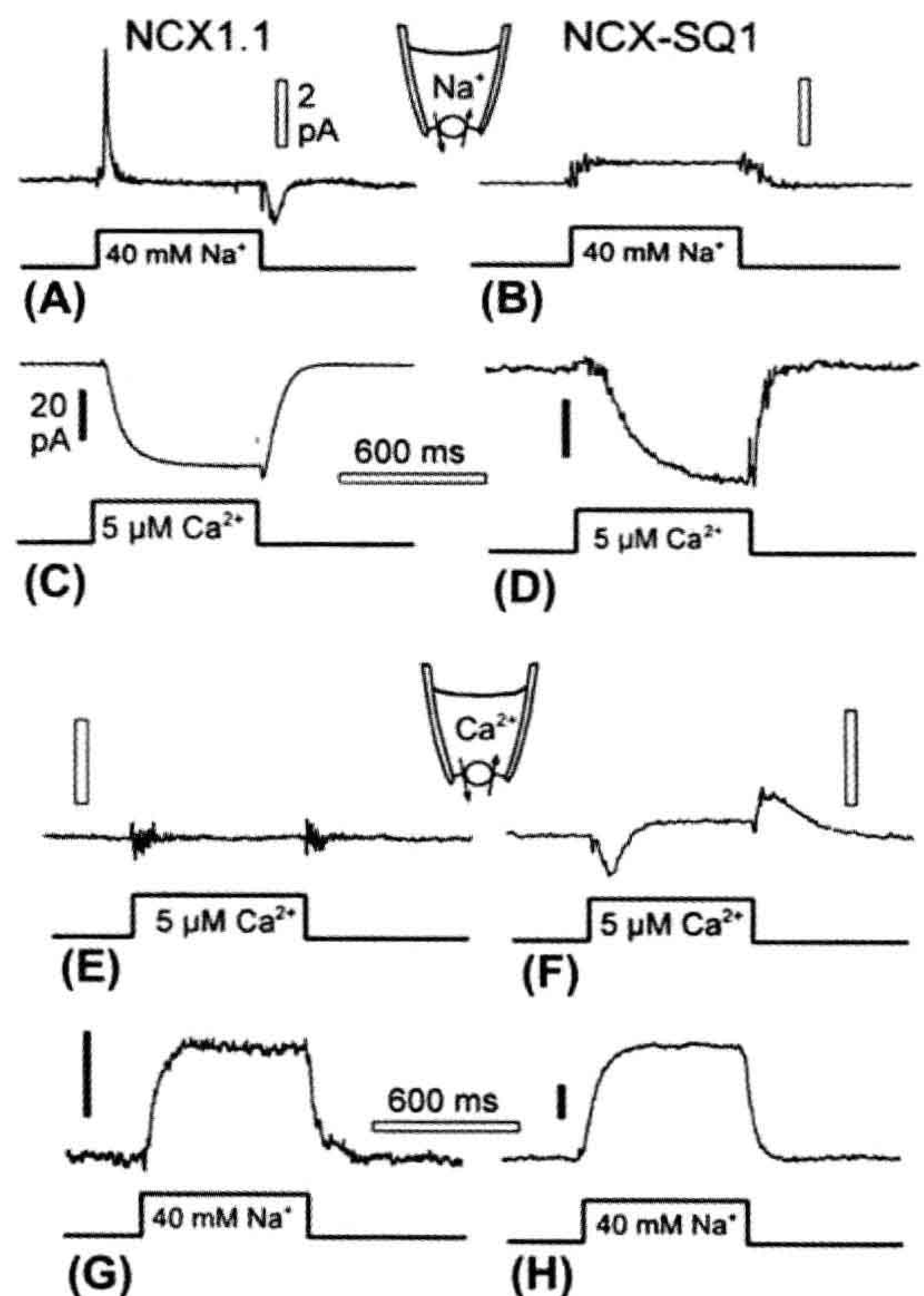


FIGURE 14.14 Identification of electrogenic reactions of NCX1 and NCX-SQ1 using concentration jumps. (A) Current transients recorded from NCX1-expressing patch when 40 mM cytoplasmic Na^+ is applied and removed in the presence of 20 mM extracellular Na^+. (B) Typical lack of current transients recorded from NCX-SQ1-expressing patch when 40 mM cytoplasmic Na^+ is applied and removed in the presence of 20 mM extracellular Na^+. (C) Inward NCX1 current activated when a solution with 5 μM free Ca^{2+} is applied as in (A). (D) Inward NCX-SQ1 current activated when a solution with 5 μM free Ca^{2+} is applied as in (B). (E) Typical lack of current transients for a Ca^{2+} jump to 5 μM free Ca^{2+} in NCX1- expressing patch; 50 μM extracellular Ca^{2+}. (F) Current transients recorded from NCX-SQ1-expressing patch when a solution with 5 μM free Ca^{2+} is applied and removed in the presence of 50 μM extracellular Ca^{2+}. (G) Outward current activated by applying 40 mM Na^+ to an NCX1 patch with 50 μM extracellular Ca^{2+}. (H) Outward current activated by applying 40 mM Na^+ to an NCX1 patch with 50 μM extracellular Ca^{2+}. *(Reprinted from He et al. (1998) with kind permission from the* Journal of General Physiology.*)*

XII. MECHANISM OF Na^+-Ca^{2+} EXCHANGE

A discussion of the evidence for and against various kinetic schemes to account for Na^+-Ca^{2+} exchange is beyond the scope of this chapter. The interested reader is referred to Khananshvili (Khananshvili, 1991). Here we will simply show the way in which measurement of exchange current can be used to infer mechanism. It should, however, be clearly understood that the measurement of isotopic fluxes and rapid mixing techniques provide indispensable tools to investigate mechanism but will not be discussed here.

For the Na^+-Ca^{2+} exchange, two different basic mechanisms for ion translocation can be considered: the *ping-pong* or *consecutive mechanism* and the *sequential* or *simultaneous mechanism*. Although it has been difficult to distinguish between these mechanisms, recent data using the patch-clamp technique provide strong evidence in favor

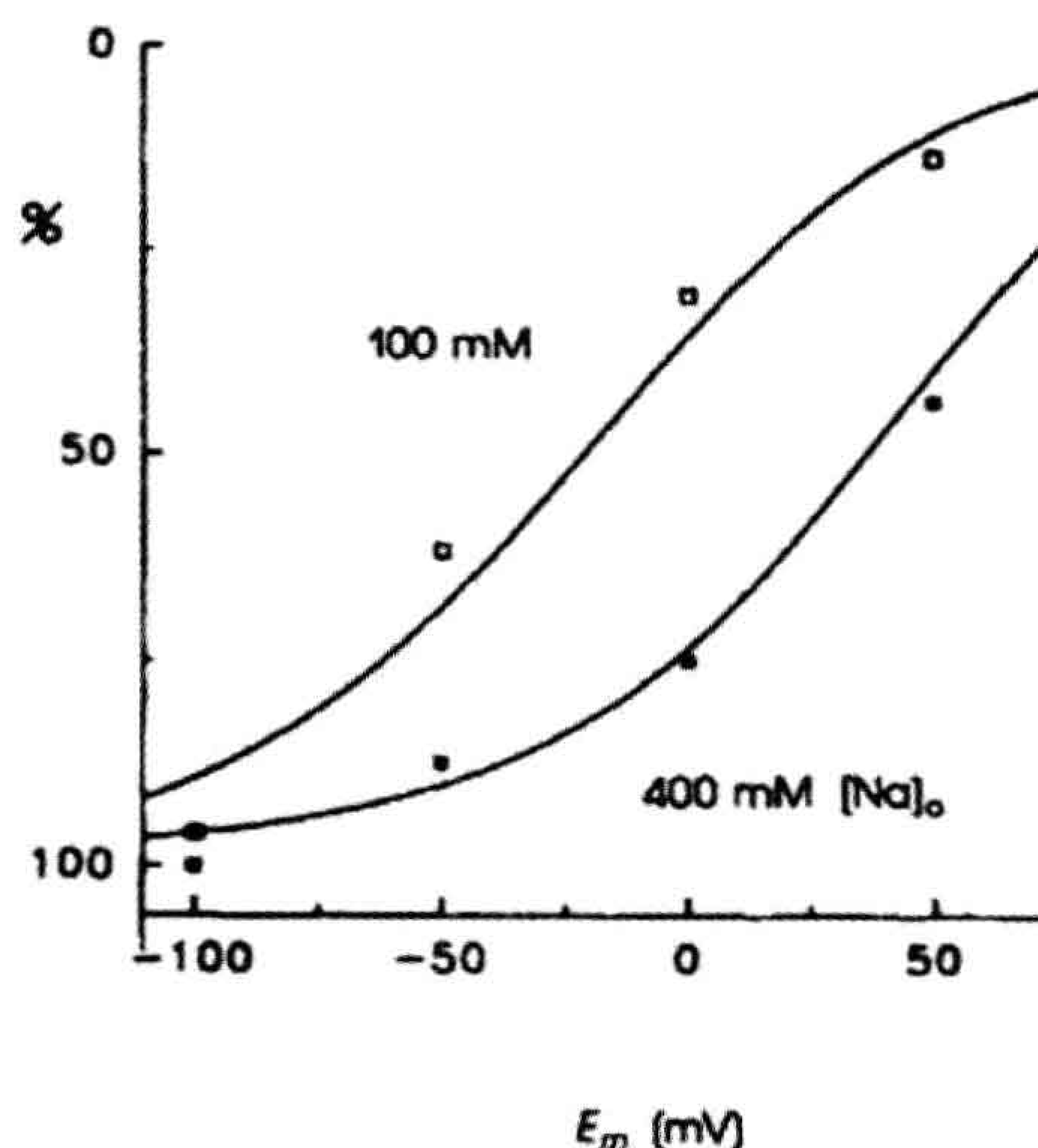


FIGURE 14.15 Flattening and saturation of inward $I_{Na\text{-}Ca}$-voltage relationships when extracellular [Na^+] is increased from 100 mM to 400 mM. Na^+-MES was replaced by Ca^{2+}-MES in the pipette, as osmolarity for all extracellular solutions was equal. 20 μM free [Ca^{2+}] on the cytoplasmic side. $I_{Na\text{-}Ca}$ magnitudes in each current–voltage relationship were normalized to values at −100 mV. *(Reprinted from Hilgemann et al. (1991) with kind permission from the* Journal of General Physiology.*)*

of the ping-pong mechanism, diagrammed in its simplest form in Fig. 14.16. There is only one set of binding sites that binds either Ca^{2+} or Na^+ and the translocation of Na^+ and Ca^{2+} are separate events. For example, Ca^{2+} binds to the carrier E′ at the inner (cytoplasmic) surface and is translocated to the exterior, where it is released. The carrier E″ then can either bind Na^+ or Ca^{2+} at the external face, which is then transported to the internal surface where it is in turn released. A basic property of the ping-pong mechanism is that Na^+-Na^+ and Ca^{2+}-Ca^{2+} exchange are

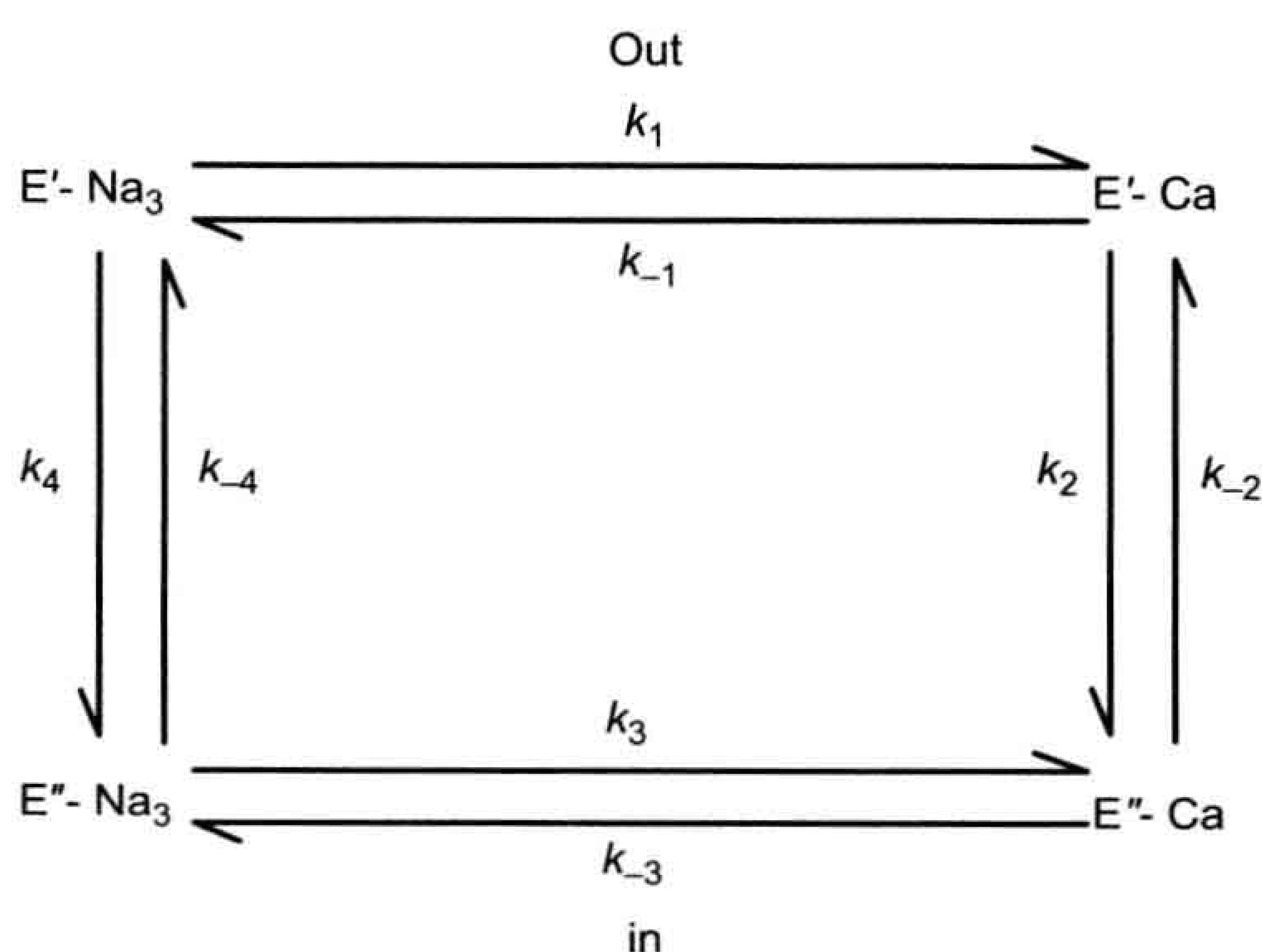


FIGURE 14.16 Diagram of the ping-pong mechanism of ion translocation.

reversible partial reactions of the exchange. As such, it should be possible to isolate them (see Fig. 14.14). These partial reactions do not exist as elementary steps in the simultaneous mechanism.

Partial reactions of the exchanger have been observed (Hilgemann, 1991a). Using giant sarcolemmal patches, rapid application of Na^+ to the intracellular surface caused binding and translocation of intracellular Na^+ to the pipette side. This produced a transient current which could be blocked by exchange blockers including the exchanger inhibitory peptide (XIP) (Li et al., 1991). Similar currents were measured in giant oocyte patches in which the cloned exchanger had been expressed. Control oocytes did not exhibit this current. It appears that charge translocation is associated with Na^+ translocation and that the Na^+ translocation step can be isolated, consistent with the idea that a ping-pong mechanism is operative.

Further support for a consecutive model of exchange comes from work by Niggli and Lederer. These authors measured very small transient Ca^{2+} currents induced by the photo release of caged Ca^{2+} DM-dinitrophen (Niggli and Lederer, 1991). Insofar as these currents could be inhibited by known blockers of the Na^+-Ca^{2+} exchange, they appear to be associated with exchange. Since they are unaffected by Na^+, they are presumably associated with a partial reaction of the exchange. These authors have speculated that this current represents a charge movement associated with Ca^{2+} binding and the associated conformational change of the exchange molecule. This suggests that (as we have already seen) a voltage-dependent step might be associated in some way with the partial reactions leading to Ca^{2+} translocation. It is becoming clear that we as yet do not know exactly how many charge-translocating steps are actually in the exchange pathway. However, evidence is accruing that the mechanism is consecutive in nature.

Two additional pieces of evidence suggest that a consecutive mechanism could account for Na^+-Ca^{2+} exchange. First, Hilgemann and colleagues have demonstrated that the apparent affinity of one ion for the exchanger is a function of the concentration of the other (Hilgemann et al., 1991a). This is a requirement of a sequential reaction scheme. Moreover, Kimura has employed classic enzyme kinetics to outward exchange currents under assumed zero *trans* conditions. Her results suggest that while it is difficult to discriminate between a simultaneous and consecutive reaction, the available evidence favors a consecutive reaction (Li and Kimura, 1991).

XIII. Na^+-Ca^{2+} EXCHANGE CURRENTS DURING THE CARDIAC ACTION POTENTIAL

During every action potential, a Ca^{2+} current is activated and a modest quantity of Ca^{2+} enters the cell. As we shall discuss, it now seems likely that reverse exchange takes

place, which also causes some Ca^{2+} entry. During a steady-state train of action potentials, this continual Ca^{2+} entry must in some way be compensated. It is therefore likely that forward exchange during the repolarizing phase of the action potential extrudes the Ca^{2+} entering during the initial phase of the action potential and thus maintains a beat-to-beat homeostasis. Direct evidence that Ca^{2+} entering the cell through Ca^{2+} channels can be extruded by the Na^+-Ca^{2+} exchange has been obtained by Bridge et al. (Bridge et al., 1990). Guinea pig ventricular cells treated with caffeine can be tetanized in the absence of extracellular Na^+ with a voltage-clamp pulse from −40 mV to +10 mV. During this clamp, an inward Ca^{2+} current can be measured (Fig. 14.17). Although the SR is depleted by caffeine, the enlarged Ca^{2+} current can apparently produce sufficient Ca^{2+} entry to cause contractures. It should be

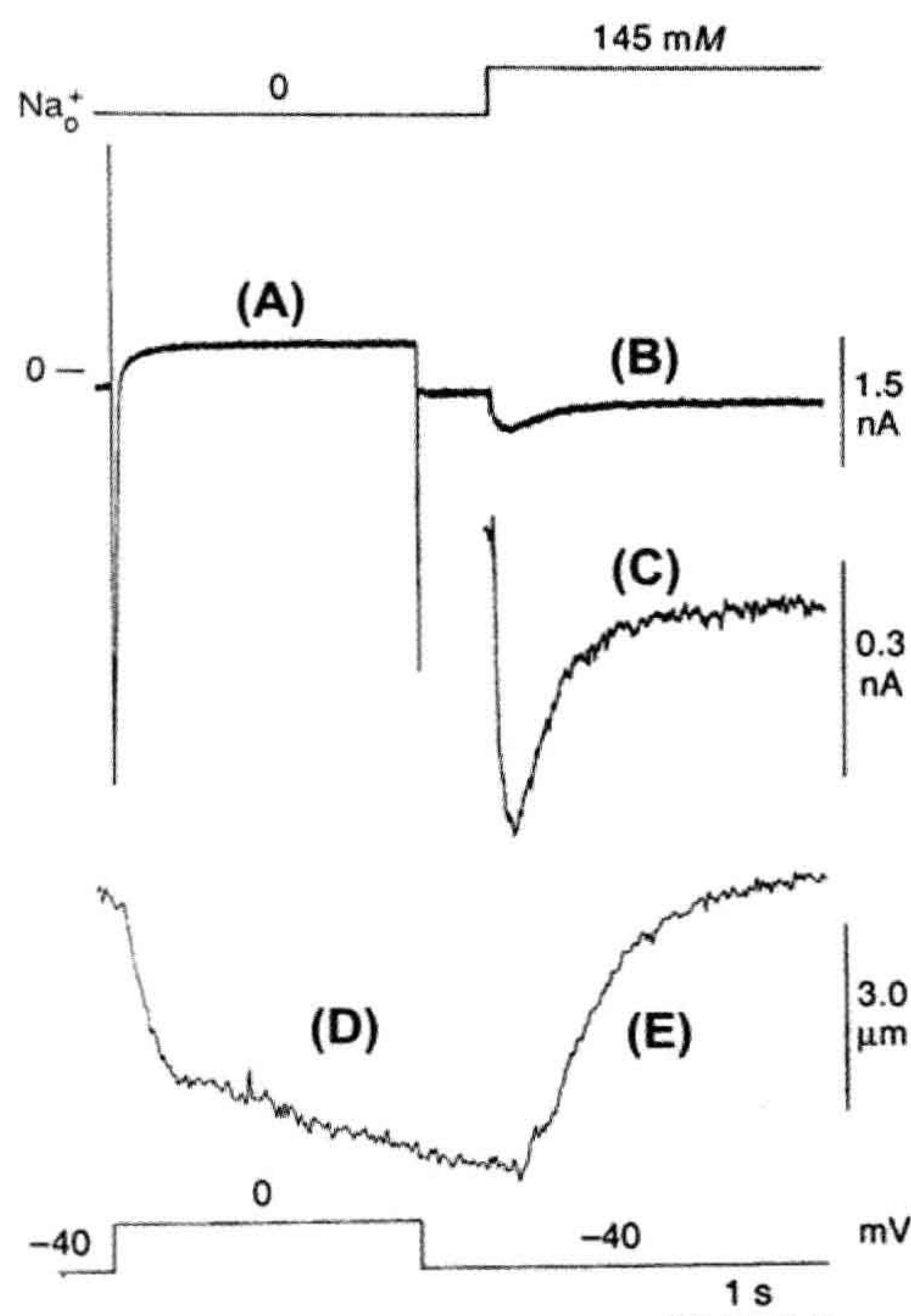


FIGURE 14.17 Two-second voltage-clamp pulses in the absence of Na^+_o and presence of 10.0 mM caffeine cause contraction. Rapid application of Na^+_o 500 ms after repolarization causes relaxation. (A) I_{Ca} elicited by membrane depolarization. (B) The application of Na^+ produces putative transient inward $I_{Na\text{-}Ca}$. (C) This current is displayed on an expanded scale. (D) Contraction (cell shortening) activated by I_{Ca} recorded in (A). (E) After repolarization to −40 mV, relaxation does not occur until 500 ms after the clamp pulse when Na^+ is suddenly applied. *(Reprinted with permission from Bridge, J.H.B., Smolley, J.R. and Spitzer, K.W. (1990). The relationship between charge movements associated with/Ca and INa-Cain cardiac myocytes.* Science. *248, 376-378. Copyright 1990 American Association for the Advancement of Science.)*

emphasized that in these experiments the pipette contained no Na^+ so that in the absence of extracellular Na^+, Ca^{2+} entry by reverse exchange was unlikely. At the peak of the contracture, rapid application of extracellular Na^+ produced prompt mechanical relaxation and activated an inward transient current. This current was most likely due to forward Na^+-Ca^{2+} exchange because it could not be activated when intracellular Ca^{2+} was buffered with EGTA. If the Na^+-Ca^{2+} exchange current extruded all the entering Ca^{2+} and, if we further assume that three Na^+ ions exchange with a single Ca^{2+} ion, it follows that the integral of the exchange current is one-half that of the Ca^{2+} current. The relationship between the integrals of exchange current and Na^+-Ca^{2+} exchange current was best explained by assuming that three Na^+ ions exchange with a single Ca^{2+} ion and that the exchange extruded all the entering Ca^{2+}. It seems therefore that the Na^+-Ca^{2+} exchange does have the capacity to extrude all Ca^{2+} entering during the duty cycle.

It now seems likely that the activity of Na^+-Ca^{2+} exchange is profoundly modified by the cardiac action potential. It is also likely that the exchange current in part determines the duration of the cardiac action potential. The first comprehensive discussion of this topic was made by Mullins (Mullins, 1979). We will consider the behavior of the Na^+-Ca^{2+} exchange during the ventricular action potential. The guinea pig ventricular action potential is approximately 300 ms in duration. During the initial part of this action potential Ca^{2+} is released from the sarcoplasmic reticulum and this causes a rise of Ca^{2+} in the cytosol. Peak values for cytosolic free Ca^{2+} are probably 1−2 µM. The Ca^{2+} transient rises to a peak in approximately 50 ms, whereas the peak of the upstroke of the action potential occurs in approximately 2 ms. After the upstroke of the action potential, but before intracellular Ca^{2+} has risen appreciably, the membrane potential becomes positive to the exchange reversal potential, which is about −50 mV. Therefore, an outward exchange current is generated and this will be accompanied by Ca^{2+} entry and Na^+ exit. This current has been implicated in the "triggering" of SR Ca^{2+} release (Leblanc and Hume, 1990). As the Ca^{2+} released from the SR begins to rise and the membrane begins to repolarize, the membrane potential will become negative to the reversal potential, the exchange current will reverse its direction and Ca^{2+} will be extruded in exchange for Na^+. As the intracellular Ca^{2+} begins to decline, inward exchange current will also decline to resting values. The same principles presumably govern the behavior of the atrial cell. Earm and Noble have modeled the time course of Ca^{2+} current, Na^+-Ca^{2+} exchange current, and the Ca^{2+} transient during the rabbit atrial action potential (Fig. 14.18) (Earm and Noble, 1990). Other more recent models seek to explain the way exchange current behaves during action potencials (Luo and Rudy, 1994; Iyer et al., 2004). The Na^+-Ca^{2+} exchange current is the main

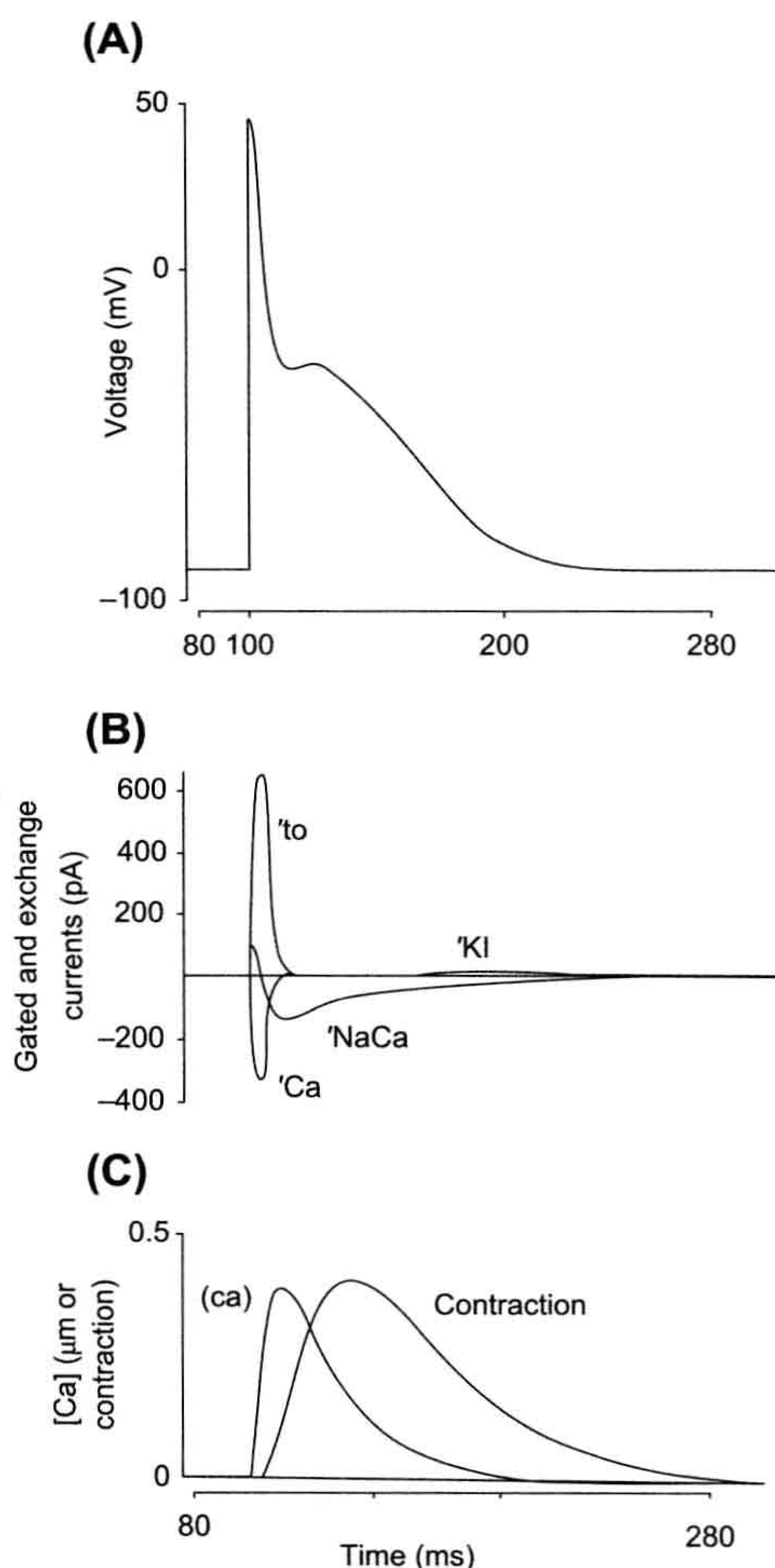


FIGURE 14.18 The Earm–Noble model of the single rabbit atrial cell, based on the multicellular model of Hilgemann and Noble (1987). (A) Computed action potential. (B) Computed currents. (C) $[Ca^{2+}]_i$ and contraction (Earm and Noble, 1990). *(Reprinted with kind permission of the author and the Royal Society.)*

depolarizing current during the plateau. Moreover, the exchange activity required to maintain the late plateau is precisely sufficient to balance Ca^{2+} influx (Ca^{2+} current + Na^+-Ca^{2+} exchange) during the early part of the action potential. It should be appreciated that, regardless of the value of intracellular Ca^{2+}, membrane repolarization will tend to stimulate inward exchange current. On the other hand, the decline of the Ca^{2+} transient will tend to reduce exchange current. Therefore, the relationship between the Ca^{2+} transient and membrane repolarization will largely determine the time course of inward exchange current and therefore the pattern of Ca^{2+} extrusion.

XIV. Na^+-Ca^{2+} EXCHANGE CURRENTS AND EXCITATION–CONTRACTION COUPLING

Contractions occur in heart cells when Ca^{2+} released from intracellular stores known as the sarcoplasmic reticulum (SR) activates the contractile elements (for a more detailed account of excitation–contraction the reader is referred to Bers (2001)). This release is coupled to electrical excitation at the surface membrane and the whole process is often referred to as *excitation–contraction coupling*. The pioneering studies on skinned fibers by Alexander Fabiato led to at least two fundamental findings (for a discussion of these see Stern and Lakatta, 1992). The first was that Ca^{2+} can be released from the SR when the concentration of Ca^{2+} in the vicinity of the SR is abruptly increased. This small increase in the concentration of Ca^{2+} leads to a much larger release of SR Ca^{2+}, so the system is one of inherently high gain. This process is usually referred to as *Ca^{2+}-induced Ca^{2+} release* or CICR. A second and important property of CICR is that, under voltage clamp, the release is graded with the size of the Ca^{2+} increase that induces the release. A priori such a system might be expected to be regenerative since the Ca^{2+} that is released from the SR ought to stimulate further release. A discussion of why SR Ca^{2+} release in heart is not normally regenerative is beyond the scope of this chapter. Nevertheless, will discuss some of the evidence that suggests that Na^+-Ca^{2+} exchange currents are involved in CICR.

It is now known that large tetrameric Ca^{2+}-release channels (usually referred to as ryanodine receptors) are embedded in the sarcoplasmic reticulum (Saito et al., 1988). These apparently respond to elevations of Ca^{2+} in their vicinity by gating the release of Ca^{2+} from the SR (Stern and Lakatta, 1992). Therefore, a molecular basis for the early observations by Fabiato has been established. A central question for those studying excitation–contraction in heart is, what in intact cells produces the rise in intracellular Ca^{2+} that gates the SR release channel and triggers SR Ca^{2+} release?

It is now well established that the L-type Ca^{2+} current is principally involved in triggering SR Ca^{2+} release in mammalian ventricular cells (London and Krueger, 1986; Beuckelmann and Wier, 1988; Cheng et al., 1993; Lopez-Lopez et al., 1994). Because Fabiato showed SR Ca^{2+} release is graded with the size of the increase in Ca^{2+} concentration that induces the release, it follows that if L-type Ca^{2+} channels trigger or induce the release of Ca^{2+}, the extent of SR Ca^{2+} release also should be graded with the size of the L-type Ca^{2+} current. Since the size of the Ca^{2+} current has a bell-shaped dependence on voltage, the finding that the rate or extent of SR Ca^{2+} release (or the magnitude of triggered contractions) is (under appropriate conditions) also bell-shaped lends strong support to

the idea that the Ca^{2+} current is a trigger for SR Ca^{2+} release. For example, a detailed study by Beuckelmann and Wier has clearly established the bell-shaped relationship between triggered Ca^{2+} transients and voltage (Beuckelmann and Wier, 1988).

However, a number of studies in ventricular cells have revealed that, under certain circumstances, a more complex relationship between the voltage dependence of triggered contractions and Ca^{2+} current (Nuss and Houser, 1992; Vornanen et al., 1994; Litwin et al., 1998). In particular, tension measurements did not follow a simple bell-shaped relationship with voltage but rather showed a sigmoid relationship. At positive potentials, shortening did not decline steeply with voltage. The studies by Litwin et al. on guinea pig cells under voltage-clamp and dialyzed with various Na^+ solutions indicate that while the shape of the Ca^{2+} current/voltage relationship was independent of pipette Na^+, the triggered shortening-voltage relationship showed a striking dependence on pipette Na^+ (Fig. 14.19) (Litwin et al., 1998). At positive potentials the shortening-voltage relationship departed from a simple bell shape and the extent of this departure depended on the concentration of dialyzing Na^+.

If L-type Ca^{2+} current is blocked extremely rapidly, triggered contractions are reduced but not abolished (Levi et al., 1996). Thus, if Ca^{2+} currents are elicited under voltage-clamp, it is possible to record what could be a triggered contraction or a triggered Ca^{2+} transient. It therefore seems likely that another process besides the Ca^{2+} current is involved, triggering the release of SR Ca^{2+}. The most likely process is in fact the Na^+-Ca^{2+} exchange. Grantham and Cannell used voltage-clamp pulses shaped like an action potential to infer the

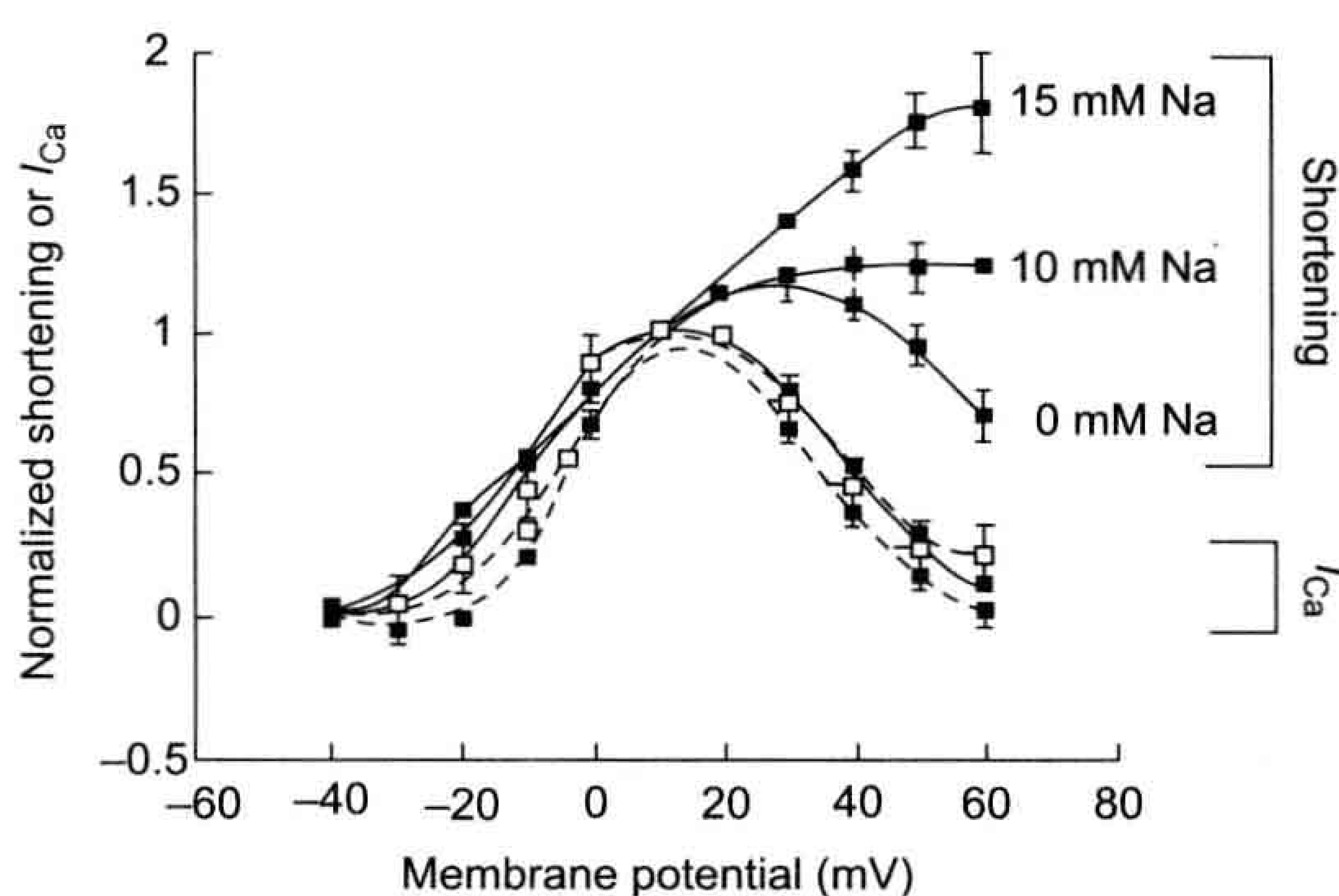


FIGURE 14.19 The relationship between voltage and I_{Ca} is bell-shaped regardless of dialyzing Na^+ concentration. However, the relationship between triggered shortening and voltage depends upon the concentration of dialyzing Na^+. When dialyzing Na^+ is nominally zero mM, the relationship between voltage and the extent of shortening approaches a bell shape. *(Reprinted with permission of the* Proceeding of the New York Academy of Sciences.*)*

magnitude and trajectory of Na^+-Ca^{2+} exchange currents during the initial part of an action potential. They found that the magnitude of the exchange current was somewhat less than 30% of the magnitude of the Ca^{2+} current that occurred during the initial part of the action potential (Fig. 14.20) (Grantham and Cannell, 1996). As the authors point out, this is not a negligible current and is consistent with the idea that at least some of the triggered SR Ca^{2+} release could be due to the activity of the Na^+-Ca^{2+} exchange. It is worth mentioning that if the Na^+-Ca^{2+} exchange is capable of contributing part of the trigger for SR Ca^{2+} release, then this component of the trigger will be extremely sensitive to intracellular Na^+. In this regard, it has been proposed that the initial Na^+ current might provide enough Na^+ accumulation (provided the accumulation takes place in a restricted space) in the vicinity of the Na^+-Ca^{2+} exchangers to enhance triggering by reverse Na^+-Ca^{2+} exchange current (Leblanc and Hume, 1990; Lipp and Niggli, 1994). A difficulty with the idea that exchange can under physiological circumstances trigger significant Ca^{2+} release is that it is extremely small (Sipido et al., 1997).

Litwin et al. have suggested, for example, that the exchange may sum its effects with the Ca^{2+} current in a highly non-linear way to augment triggering by Ca^{2+} current (Litwin et al., 1998). It is possible that one function of the exchange is to increase the probability with which a Ca^{2+} current triggers exchange in a highly non-linear system. It is therefore not yet clear what contribution Na^+-Ca^{2+} exchange currents make to triggering SR Ca^{2+} release under physiological circumstances. However, since the exchanger is regulated by intracellular Na^+, Ca^{2+} and voltage, it seems likely that its contribution to triggering (either direct or indirect) will be both complex and variable. Recently, the idea that NCX is involved in CICR has been significantly strengthened (Sobie et al., 2008). In both mouse and rabbit cells (Larbig et al., 2010; Torres et al., 2010), inactivation of Na^+ currents while applying action potential shaped voltage clamps abolished a significant fraction of the SR Ca release. Between 27 and 34% of the release was eliminated in rabbits and as much as 50% in mice. When this experiment was repeated in mice lacking NCX (mouse NCX knockout), inactivation of the Na^+ current had no effect on SR Ca^{2+} release, which provides additional strong support for the idea that the effect of Na^+ current on triggering is mediated by NCX.

A report by Maier et al. indicated that a brain or neuronal type Na^+ channel is involved in excitation contraction coupling in heart (Maier et al., 2002). Both neuronal (brain) and skeletal muscle Na^+ channels are thought to exist in heart (Sills et al., 1989; Dhar Malhotra et al., 2001; Huang et al., 2001; Maier et al., 2002; Pereon et al., 2003; Haufe et al., 2005a,b; Marionneau et al., 2005; Gershome et al., 2011). These channels are sensitive to

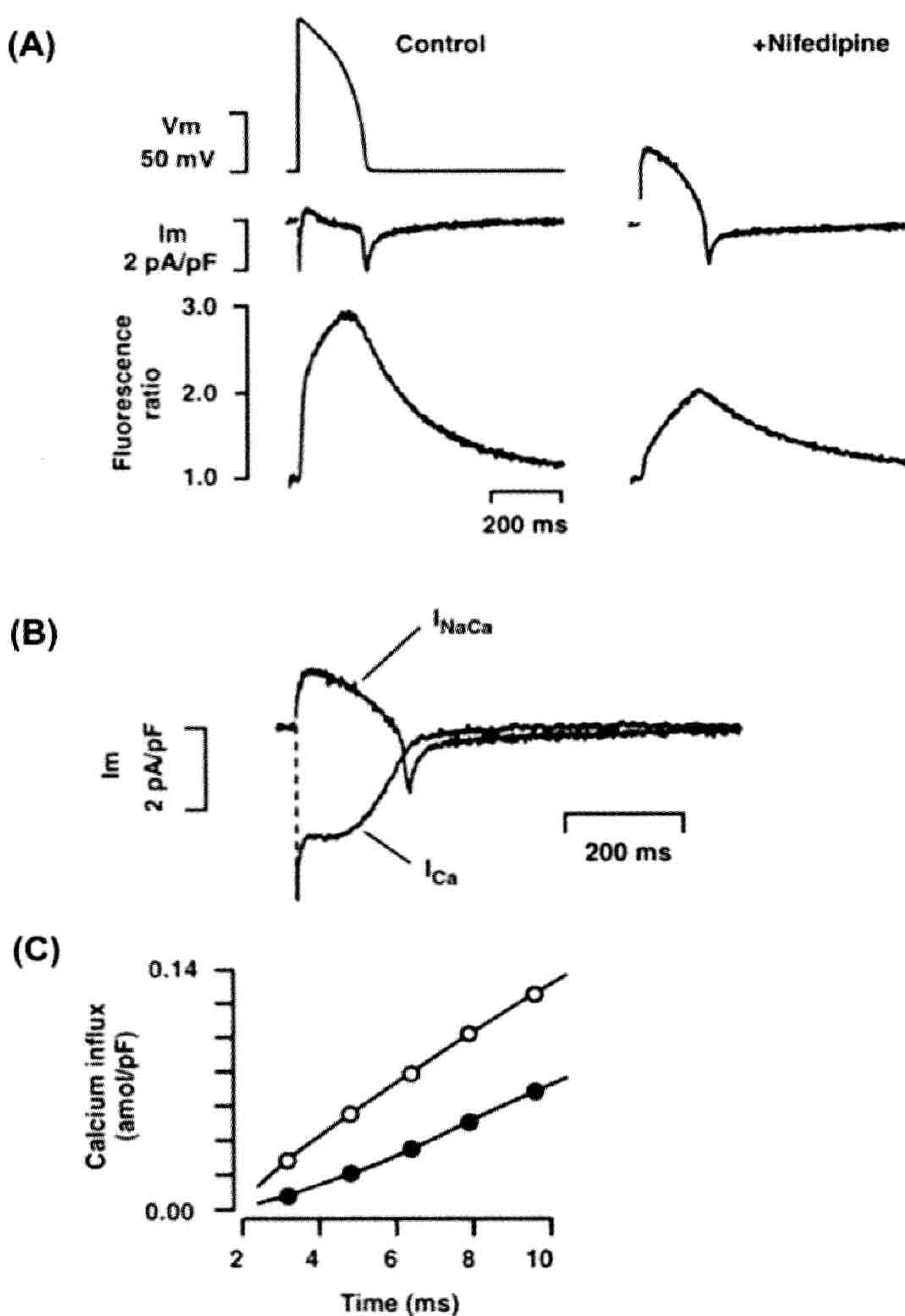


FIGURE 14.20 Membrane currents and Ca^{2+} influx in a myocyte with intact Na^+-Ca^{2+} exchange and SR release in response to an action potential (AP). The myocyte was at steady state, having been stimulated continuously at 0.2 Hz with a train of at least 20 APs. (A) Top, AP command; middle, membrane current; and bottom, $[Ca^{2+}]$ transient time course in the absence of nifedipine or, on the right, immediately after blockade of I_{Ca} by 10 µmol/L nifedipine. (B) Time course of AP-evoked nifedipine-sensitive current (I_{Ca}) and calculated $I_{Na\text{-}Ca}$. (C) Cumulative Ca^{2+} influx via I_{Ca} (open circles) and the calculated $I_{Na\text{-}Ca}$ (closed circles) at the beginning of the AP. Cell capacitance, 150 pF. Similar results were obtained in at least four other cells. *(Reprinted with permission of* Circulation Research *from Grantham and Cannell, 1996.)*

TTX, i.e. they are blocked by relative low doses of TTX (100 nM TTX), whereas the cardiac Na^+ channel Nav 1.5 is blocked by much higher concentrations of this drug (in the order of micromolar). Torres et al. obtained clear evidence that very low doses of TTX (100 nM) eliminated as much as 27% of the release flux (Torres et al., 2010). This is similar to the effect of voltage dependent inactivation of the Na^+ current. It is therefore possible that a rapidly activating TTX-sensitive Na^+ current could significantly increase Na^+ concentration in junctional regions between the sarcolemma and the sarcoplasmic reticular membranes. This, in turn, could cause the reverse of exchange prior to activation of Ca^{2+} currents and prime the junction with Ca^{2+}, although the process might not in itself produce much triggering. However, with a primed junction, Ca^{2+} currents might trigger SR Ca^{2+} release much more efficiently since they would not first have to fill the junctional regions with Ca^{2+}. In the absence of intracellular Na^+, the efficiency of release is extremely low at positive potential (when one would expect it to be high). A process of the type that we have just described might increase triggering efficiently when it is most needed and, in effect, set the efficiency of EC coupling. Such a process is likely to be inherently non-linear and account for the non-linear summation of NCX and Ca currents proposed by Litwin et al. (Litwin et al., 1998).

BIBLIOGRAPHY

Acsai, K., Antoons, G., Livshitz, L., Rudy, Y., & Sipido, K. R. (2011). Microdomain [Ca2+] near ryanodine receptors as reported by L-type Ca2+ and Na+/Ca2+ exchange currents. *J Physiol, 589*, 2569–2583.

Axelsen, P. H., & Bridge, J. H. B. (1985). Electrochemical ion gradients and the Na/Ca exchange stoichiometry. Measurements of these gradients are thermodynamically consistent with a stoichiometric coefficient >3. *J Gen Physiol, 85*, 471–478.

Baker, P. F., Blaustein, M. P., Hodgkin, A. L., & Steinhardt, R. A. (1967). Effect of sodium concentration on calcium movements in giant axons of loligo forbesi. *J Physiol (Lond), 192*, 43–44.

Barcenas-Ruiz, L., Beuckelmann, D. J., & Wier, W. G. (1987). Sodium-calcium exchange in heart: membrane currents and changes in $(Ca2+)_i$. *Science, 238*, 1720–1722.

Bers, D. M. (2001). *Excitation-contraction Coupling and Cardiac Contractile Force*. Dordrecht: Kluwer Academic Publishers.

Besserer, G. M., Ottolia, M., Nicoll, D. A., et al. (2007). The second Ca2+-binding domain of the Na+ Ca2+ exchanger is essential for regulation: crystal structures and mutational analysis. *Proc Natl Acad Sci USA, 104*, 18467–18472.

Beuckelmann, D. J., & Wier, W. G. (1988). Mechanism of release of calcium from sarcoplasmic reticulum of guinea- pig cardiac cells. *J Physiol (Lond), 405*, 233–255.

Blaustein, M. P., & Hodgkin, A. L. (1969). The effect of cyanide on the efflux of calcium from squid axons. *J Physiol, 200*, 497–527.

Bridge, J. H. B., & Bassingthwaighte, J. B. (1983). Uphill sodium transport driven by an inward calcium gradient in heart muscle. *Science, 219*, 178–180.

Bridge, J. H. B., Smolley, J., Spitzer, K. W., & Chin, T. K. (1991). Voltage dependence of sodium-calcium exchange and the control of Ca extrusion in the heart. *Ann NY Acad Sci, 639*, 34–47.

Bridge, J. H. B., Smolley, J. R., & Spitzer, K. W. (1990). The relationship between charge movements associated with I_{Ca} and $I_{Na\text{-}Ca}$ in cardiac myocytes. *Science, 248*, 376–378.

Chaptal, V., Ottolia, M., Mercado-Besserer, G., Nicoll, D. A., Philipson, K. D., & Abramson, J. (2009). Structure and functional analysis of a Ca2+ sensor mutant of the Na+/Ca2+ exchanger. *J Biol Chem, 284*, 14688–14692.

Cheng, H., Lederer, W. J., & Cannell, M. B. (1993). Calcium sparks: elementary events underlying excitation-contraction coupling in heart muscle. *Science, 262*, 740–744.

Chin, T. K., Spitzer, K. W., Philipson, K. D., & Bridge, J. H. B. (1993). The effect of exchanger inhibitory peptide (XIP) on sodium-calcium exchange current in guinea pig ventricular cells. *Circ Res, 72*, 497–503.

Collins, A., Somlyo, A. V., & Hilgemann, D. W. (1992). The giant cardiac membrane patch method: stimulation of outward Na^+-Ca^{2+} exchange current by MgATP. *J Physiol, 454*, 27–57.

Crespo, L. M., Grantham, C. J., & Cannell, M. B. (1990). Kenetics, stoichiometry and role of the Na-Ca exchange mechanism in isoleted cardiac myocytes. *Nature, 345*, 618–621.

Cuomo, O., Pignataro, G., Gala, R., et al. (2007). Involvement of the potassium-dependent sodium/calcium exchanger gene product NCKX2 in the brain insult induced by permanent focal cerebral ischemia. *Ann NY Acad Sci, 1099*, 486–489.

Dhar Malhotra, J., Chen, C., Rivolta, I., et al. (2001). Characterization of sodium channel alpha- and beta-subunits in rat and mouse cardiac myocytes. *Circulation, 103*, 1303–1310.

DiPolo, R., & Beauge, L. (1987a). Characterization of the reverse Na/Ca exchange in squid axons and its modulation by Cai and ATP. Cai-dependent Nai/Cao and Nai/Nao exchange modes. *J Gen Physiol, 90*, 505–525.

DiPolo, R., & Beauge, L. (1987b). In squid axons ATP modulates Na+-Ca2+ exchange by a Ca2+i dependent phosphorylation. *Biochim Biophys Acta, 897*, 347–354.

Dyck, C., Omelchenko, A., Elias, C. L., et al. (1999). Ionic regulatory properties of brain and kidney splice variants of the NCX1 Na(+)-Ca(2+) exchanger. *J Gen Physiol, 114*, 701–711.

Earm, Y. E., & Noble, D. (1990). A model of the single atrial cell: relation between calcium current and calcium release. *Proc R Soc Lond B, 240*, 83–96.

Ehara, T., Matsuoka, S., & Noma, A. (1989). Measurement of reversal potential of Na^+-Ca^{2+} exchange current in single guinea-pig ventricular cells. *J Physiol, 410*, 227–249.

Gershome, C., Lin, E., Kashihara, H., Hove-Madsen, L., & Tibbits, G. F. (2011). Colocalization of voltage-gated Na+ channels with the Na+/Ca2+ exchanger in rabbit cardiomyocytes during development. *Am J Physiol Heart Circ Physiol, 300*, H300–311.

Giladi, M., Boyman, L., Mikhasenko, H., Hiller, R., & Khananshvili, D. (2010). Essential role of the CBD1-CBD2 linker in slow dissociation of Ca2+ from the regulatory two-domain tandem of NCX1. *J Biol Chem, 285*, 28117–28125.

Grantham, C. J., & Cannell, M. B. (1996). Ca2+ influx during the cardiac action potential in guinea pig ventricular myocytes. *Circ Res, 79*, 194–200.

Hamill, O. P., Marty, E., Neher, E., Sakmann, B., & Sigworth, F. (1981). Improved patch-clamp techniques for high resolution current recording from cells and cell-free membrane patches. *Pflügers Arch, 391*, 85–100.

Haufe, V., Camacho, J. A., Dumaine, R., et al. (2005a). Expression pattern of neuronal and skeletal muscle voltage-gated Na+ channels in the developing mouse heart. *J Physiol, 564*, 683–696.

Haufe, V., Cordeiro, J. M., Zimmer, T., et al. (2005b). Contribution of neuronal sodium channels to the cardiac fast sodium current INa is greater in dog heart Purkinje fibers than in ventricles. *Cardiovasc Res, 65*, 117–127.

He, Z., Feng, S., Tong, Q., Hilgemann, D. W., & Philipson, K. D. (2000). Interaction of PIP(2) with the XIP region of the cardiac Na/Ca exchanger. *Am J Physiol Cell Physiol, 278*, C661–666.

He, Z., Tong, Q., Quednau, B. D., Philipson, K. D., & Hilgemann, D. W. (1998). Cloning, expression, and characterization of the squid Na+-Ca2+ exchanger (NCX-SQ1). *J Gen Physiol, 111*, 857–873.

Hilge, M., Aelen, J., Foarce, A., Perrakis, A., & Vuister, G. W. (2009). Ca2+ regulation in the Na+/Ca2+ exchanger features a dual electrostatic switch mechanism. *Proc Natl Acad Sci USA, 106*, 14333–14338.

Hilge, M., Aelen, J., & Vuister, G. W. (2006). Ca2+ regulation in the Na+/Ca2+ exchanger involves two markedly different Ca2+ sensors. *Mol Cell, 22*, 15–25.

Hilgemann, D. W. (1989). Giant excised cardiac sarcolemmal membrane patches: Sodium and sodium-calcium exchange currents. *Pflügers Arch, 415*, 1–3.

Hilgemann, D. W. (1990). Regulation and deregulation of cardiac Na^+-Ca^{2+} exchange in giant excised sarcolemmal membrane patches. *Nature, 344*, 242–245.

Hilgemann, D. W., & Ball, R. (1996). Regulation of cardiac Na+-Ca2+ exchange and K_{ATP} potassium channels by PIP_2. *Science, 273*, 956–959.

Hilgemann, D. W., Collins, A., Cash, D. P., & Nagel, G. A. (1991a). Cardiac Na^{+}-Ca^{2+} exchange system in giant membrane patches. *Ann NY Acad Sci, 639*, 126–139.

Hilgemann, D. W., Collins, A., & Matsuoka, S. (1992a). Steady-state and dynamic properties of cardiac sodium-calcium exchange. Secondary modulation by cytoplasmic calcium and ATP. *J Gen Physiol, 100*, 933–961.

Hilgemann, D. W., Matsuoka, S., Nagel, G. A., & Collins, A. (1992b). Steady-state and dynamic properties of cardiac sodium-calcium exchange. Sodium-dependent inactivation. *J Gen Physiol, 100*, 905–932.

Hilgemann, D. W., Nicoll, D. A., & Philipson, K. D. (1991b). Charge movement during Na^{+} translocation by native and cloned cardiac Na^{+}/Ca^{2+} exchanger. *Nature, 352*, 715–718.

Hille, B., Armstrong, C. M., & MacKinnon, R. (1999). Ion channels: from idea to reality. *Nat Med, 5*, 1105–1109.

Horackova, M., & Vassort, G. (1979). Sodium-Calcium exchange in regulation of cardiac contractility. Evidence for an electrogenic, voltage-dependent mechanism. *J Gen Physiol, 73*, 403–424.

Hryshko, L. V. (2002). Tissue-specific modes of Na/Ca exchanger regulation. *Ann NY Acad Sci, 976*, 166–175.

Hryshko, L. V., Matsuoka, S., Nicoll, D. A., et al. (1996). Anomalous regulation of the Drosophila Na(+)-Ca2+ exchanger by Ca2+. *J Gen Physiol, 108*, 67–74.

Huang, B., El-Sherif, T., Gidh-Jain, M., Qin, D., & El-Sherif, N. (2001). Alterations of sodium channel kinetics and gene expression in the postinfarction remodeled myocardium. *J Cardiovasc Electrophysiol, 12*, 218–225.

Hume, J. R., & Uehara, A. (1986a). "Creep currents" in single frog atrial cells may be generated by electrogenic Na-Ca exchange. *J Gen Physiol, 87*, 857–884.

Hume, J. R., & Uehara, A. (1986b). Properties of "creep currents" in single frog atrial cells. *J Gen Physiol, 87*, 833–855.

Iwamoto, T., Nakamura, T. Y., Pan, Y., Uehara, A., Imanaga, I., & Shigekawa, M. (1999). Unique topology of the internal repeats in the cardiac Na+/Ca2+ exchanger. *Febs Lett, 446*, 264–268.

Iwamoto, T., Uehara, A., Imanaga, I., & Shigekawa, M. (2000). The Na+/Ca2+ exchanger NCX1 has oppositely oriented reentrant loop domains that contain conserved aspartic acids whose mutation alters its apparent Ca2+ affinity. *J Biol Chem, 275*, 38571–38580.

Iyer, V., Mazhari, R., & Winslow, R. L. (2004). A computational model of the human left-ventricular epicardial myocyte. *Biophys J, 87*, 1507–1525.

John, S. A., Ribalet, B., Weiss, J. N., Philipson, K. D., & Ottolia, M. (2011). Ca2+-dependent structural rearrangements within Na+-Ca2+ exchanger dimers. *Proc Natl Acad Sci, USA*.

Johnson, E., Bruschweiler-Li, L., Showalter, S. A., Vuister, G. W., Zhang, F., & Bruschweiler, R. (2008). Structure and dynamics of Ca2+-binding domain 1 of the Na+/Ca2+ exchanger in the presence and in the absence of Ca2+. *J Mol Biol, 377*, 945–955.

Khananshvili, D. (1991). Mechanism of partial reactions in the cardiac Na-Ca exchange system. *Ann NY Acad Sci., 639*, 85–95.

Kimura, J., Miyamae, S., & Noma, A. (1987). Identification of sodium-calcium exchange currents in single ventricular cells of guinea-pig. *J Physiol, 384*, 199–222.

Kimura, J., Noma, A., & Irisawa, H. (1986). Na-Ca exchange current in mammalian heart cells. *Nature, 319*, 596–599.

Lagnado, L., & McNaughton, P. A. (1990). Electrogenic properties of the Na: Ca exchange. *J Memb Biol, 113*, 177–191.

Langer, G. A. (1964). Kinetic studies of calcium distribution in ventricular muscle of the dog. *Circ Res, 15*, 393–405.

Larbig, R., Torres, N., Bridge, J. H., Goldhaber, J. I., & Philipson, K. D. (2010). Activation of reverse Na+-Ca2+ exchange by the Na+ current augments the cardiac Ca2+ transient: evidence from NCX knockout mice. *J Physiol, 588*, 3267–3276.

Leblanc, N., & Hume, J. R. (1990). Sodium current-induced release of calcium from cardiac sarcoplasmic reticulum. *Science, 248*, 372–376.

Levi, A. J., Li, J., Spitzer, K. W., & Bridge, J. H. B. (1996). Effect on the Indo-1 transient of applying Ca2+ channel blocker for a single beat in voltage-clamped guinea-pig cardiac myocytes. *J Physiol (Lond), 494.3*, 653–673.

Li, J. M., & Kimura, J. (1991). Translocation mechanism of cardiac Na-Ca exchange. *Ann NY Acad Sci, 639*, 48–60.

Li, Z., Nicoll, D. A., Collins, A., et al. (1991). Identification of a peptide inhibitor of the cardiac sarcolemmal Na(+)-Ca2+ exchanger. *J Biol Chem, 266*, 1014–1020.

Lipp, P., & Niggli, E. (1994). Modulation of Ca^{2+} release in cultured neonatal rat cardiac myocytes: insight from subcellular release patterns revealed by confocal microscopy. *Circ Res, 74*, 979–990.

Litwin, S. E., Li, J., & Bridge, J. H. (1998). Na-Ca exchange and the trigger for sarcoplasmic reticulum Ca release: studies in adult rabbit ventricular myocytes. *Biophys J, 75*, 359–371.

London, B., & Krueger, J. W. (1986). Contraction in voltage-clamped, internally perfused single heart cells. *J Gen Physiol, 88*, 475–505.

Lopez-Lopez, J. R., Shacklock, P. S., Balke, C. W., & Wier, W. G. (1994). Local, stochastic release of Ca2+ in voltage-clamped rat heart cells: visualization with confocal microscopy. *J Physiol (Lond), 480*, 21–29.

Luo, C. H., & Rudy, Y. (1994). A dynamic model of the cardiac ventricular action potential. I. Simulations of ionic currents and concentration changes. *Circ Res, 74*, 1071–1096.

Lytton, J. (2007). Na+/Ca2+ exchangers: three mammalian gene families control Ca2+ transport. *Biochem J, 406*, 365–382.

Maier, S. K., Westenbroek, R. E., Schenkman, K. A., Feigl, E. O., Scheuer, T., & Catterall, W. A. (2002). An unexpected role for brain-type sodium channels in coupling of cell surface depolarization to contraction in the heart. *Proc Natl Acad Sci USA, 99*, 4073–4078.

Marionneau, C., Couette, B., Liu, J., et al. (2005). Specific pattern of ionic channel gene expression associated with pacemaker activity in the mouse heart. *J Physiol, 562*, 223–234.

Matsuoka, S., & Hilgemann, D. W. (1992). Steady-state and dynamic properties of cardiac sodium-calcium exchange. Ion and voltage dependencies of the transport cycle. *J Gen Physiol, 100*, 963–1001.

Matsuoka, S., Nicoll, D. A., He, Z., & Philipson, K. D. (1997). Regulation of cardiac Na(+)-Ca2+ exchanger by the endogenous XIP region. *J Gen Physiol, 109*, 273–286.

Matsuoka, S., Nicoll, D. A., Hryshko, L. V., Levitsky, D. O., Weiss, J. N., & Philipson, K. D. (1995). Regulation of the cardiac Na(+)-Ca2+ exchanger by Ca2+. Mutational analysis of the Ca(2+)-binding domain. *J Gen Physiol, 105*, 403–420.

Matsuoka, S., Nicoll, D. A., Reilly, R. F., Hilgemann, D. W., & Philipson, K. D. (1993). Initial localization of regulatory regions of the cardiac sarcolemmal Na(+)-Ca2+ exchanger. *Proc Natl Acad Sci, USA, 90*, 3870–3874.

Mechmann, S., & Pott, L. (1986). Indentification of Na-Ca exchange current in single cardiac myocytes. *Nature, 319*, 597–599.

Miura, Y., & Kimura, J. (1989). Sodium-calcium exchange current. *J Gen Physiol, 93*, 1129–1145.

Mullins, L. J. (1979). The generation of electric currents in cardiac fibers by Na/Ca exchange. *Am J Physiol, 236*, C103–C110.

Nicoll, D. A., Hryshko, L. V., Matsuoka, S., Frank, J. S., & Philipson, K. D. (1996). Mutation of amino acid residues in the putative transmembrane segments of the cardiac sarcolemmal Na+-Ca2+ exchanger. *J Biol Chem, 271*, 13385–13391.

Nicoll, D. A., Longoni, S., & Philipson, K. D. (1990). Molecular cloning and functional expression of the cardiac sarcolemmal Na(+)-Ca2+ exchanger. *Science, 250*, 562–565.

Nicoll, D. A., Ottolia, M., Lu, L., Lu, Y., & Philipson, K. D. (1999). A new topological model of the cardiac sarcolemmal Na+-Ca2+ exchanger. *J Biol Chem, 274*, 910–917.

Niggli, E., & Lederer, W. J. (1991). Photorelease of Ca2+ produces Na-Ca exchange currents and Na-Ca exchange "gating" currents. *Ann NY Acad Sci, 639*, 61–70.

Nuss, H. B., & Houser, S. R. (1992). Sodium-calcium exchange-mediated contractions in feline ventricular myocytes. *Am J Physiol Heart Circ Physiol, 263*, H1161–H1169.

Ottolia, M., Nicoll, D. A., John, S., & Philipson, K. D. (2010). Interactions between Ca(2+) binding domains of the Na(+)-Ca(2+) exchanger and secondary regulation. *Channels (Austin)* 4.

Ottolia, M., Nicoll, D. A., & Philipson, K. D. (2005). Mutational analysis of the alpha-1 repeat of the cardiac Na(+)-Ca2+ exchanger. *J Biol Chem, 280*, 1061–1069.

Ottolia, M., Nicoll, D. A., & Philipson, K. D. (2009). Roles of two Ca2+-binding domains in regulation of the cardiac Na+-Ca2+ exchanger. *J Biol Chem.*

Ottolia, M., Philipson, K. D., & John, S. (2004). Conformational changes of the Ca(2+) regulatory site of the Na(+)-Ca(2+) exchanger detected by FRET. *Biophys J, 87*, 899–906.

Pereon, Y., Lande, G., Demolombe, S., et al. (2003). Paramyotonia congenita with an SCN4A mutation affecting cardiac repolarization. *Neurology, 60*, 340–342.

Philipson, K. D., Longoni, S., & Ward, R. (1988). Purification of the cardiac Na+-Ca2+ exchange protein. *Biochim Biophys Acta, 945*, 298–306.

Philipson, K. D., Nicoll, D. A., Ottolia, M., et al. (2002). The Na+/Ca2+ exchange molecule: an overview. *Ann NY Acad Sci, 976*, 1–10.

Porzig, H., Li, Z., Nicoll, D. A., & Philipson, K. D. (1993). Mapping of the cardiac sodium-calcium exchanger with monoclonal antibodies. *Am J Physiol, 265*, C748–756.

Qiu, Z., Nicoll, D. A., & Philipson, K. D. (2001). Helix packing of functionally important regions of the cardiac Na(+)-Ca(2+) exchanger. *J Biol Chem, 276*, 194–199.

Quednau, B. D., Nicoll, D. A., & Philipson, K. D. (1997). Tissue specificity and alternative splicing of the Na+/Ca2+ exchanger isoforms NCX1, NCX2, and NCX3 in rat. *Am J Physiol, 272*, C1250–1261.

Rasgado-Flores, H., & Blaustei, M. P. (1987). Na/Ca exchange in barnacle muscle cells has a stoichiometry of 3 Na+/1 Ca+. *Am J Physiol Cell Physiol, 252*, C499–C504.

Reeves, J. P., & Condrescu, M. (2008). Ionic regulation of the cardiac sodium-calcium exchanger. *Channels (Austin), 2*, 322–328.

Reeves, J. P., & Hale, C. C. (1984). The stoichiometry of the cardiac sodium-calcium exchange system. *J Biol Chem, 259*, 7733–7739.

Reeves, J. P., & Sutko, J. L. (1983). Competitive interactions of sodium and calcium with the sodium-calcium exchange system of cardiac sarcolemmal vesicles. *J Biol Chem, 258*, 3178–3182.

Ren, X., Nicoll, D. A., Galang, G., & Philipson, K. D. (2008). Intermolecular cross-linking of Na+-Ca2+ exchanger proteins: evidence for dimer formation. *Biochemistry, 47*, 6081–6087.

Ren, X., Nicoll, D. A., & Philipson, K. D. (2006). Helix packing of the cardiac Na+-Ca2+ exchanger: proximity of transmembrane segments 1, 2, and 6. *J Biol Chem, 281*, 22808–22814.

Ren, X., Nicoll, D. A., Xu, L., Qu, Z., & Philipson, K. D. (2010). Transmembrane segment packing of the Na(+)/Ca(2+) exchanger investigated with chemical cross-linkers. *Biochemistry.*

Repke, K. (1964). Ubersichten uber den biochemischen wirkungsmodus von digitalis [On the Biochemical Mode of Action of Digitalis]. *Klin Wochenschr, 42*, 157–165.

Reuter, H., & Seitz, N. (1968). The dependence of calcium efflux from cardiac muscle on temperature and external ion composition. *J Physiol, 195*, 451–470.

Riedel, M. J., Baczko, I., Searle, G. J., et al. (2006). Metabolic regulation of sodium-calcium exchange by intracellular acyl CoAs. *EMBO J, 25*, 4605–4614.

Saito, A., Inui, M., Radermacher, M., Frank, J., & Fleischer, S. (1988). Ultrastructure of the calcium release channel of sarcoplasmic reticulum. *J Cell Biol, 107*, 211–219.

Schwarz, E. M., & Benzer, S. (1997). Calx, a Na-Ca exchanger gene of Drosophila melanogaster. *Proc Natl Acad Sci, USA, 94*, 10249–10254.

Sheu, S. S., & Fozzard, H. A. (1982). Transmembrane Na+ and Ca2+ electrochemical gradients in cardiac muscle and their relationship to force development. *J Gen Physiol, 80*, 325–351.

Shigekawa, M., Iwamoto, T., Uehara, A., & Kita, S. (2002). Probing ion binding sites in the Na+/Ca2+ exchanger. *Ann NY Acad Sci, 976*, 19–30.

Sills, M. N., Xu, Y. C., Baracchini, E., et al. (1989). Expression of diverse Na+ channel messenger RNAs in rat myocardium. Evidence for a cardiac-specific Na+ channel. *J Clin Invest, 84*, 331–336.

Sipido, K. R., Maes, M., & Van de Werf, F. (1997). Low efficiency of Ca2+ entry through the Na(+)-Ca2+ exchanger as trigger for Ca2+ release from the sarcoplasmic reticulum. A comparison between L-type Ca2+ current and reverse-mode Na(+)-Ca2+ exchange. *Circ Res, 81*, 1034–1044.

Sobie, E. A., Cannell, M. B., & Bridge, J. H. (2008). Allosteric activation of Na+-Ca2+ exchange by L-type Ca2+ current augments the trigger flux for SR Ca2+ release in ventricular myocytes. *Biophys J, 94*, L54–56.

Spitzer, K. W., & Bridge, J. H. B. (1989). A simple device for rapidly exchanging solution surrounding a single cardiac cell. *Am J Physiol Cell Physiol, 256*, C441–C447.

Stern, M. D., & Lakatta, E. G. (1992). Excitation-contraction coupling in the heart: the state of the question. *FASEB J, 6*, 3092–3100.

Torres, N. S., Larbig, R., Rock, A., Goldhaber, J. I., & Bridge, J. H. (2010). Na+ currents are required for efficient excitation-contraction coupling in rabbit ventricular myocytes: a possible contribution of neuronal Na+ channels. *J Physiol, 588*, 4249–4260.

Trosper, T. L., & Philipson, K. D. (1984). Stimulatory effect of calcium chelators on Na-Ca exchange in cardiac sarcolemmal vessicles. *Cell Calcium, 5*, 211–222.

Vornanen, M., Shepherd, N., & Isenberg, G. (1994). Tension-voltage relations of single myocytes reflect Ca release triggered by Na/Ca

exchange at 35 degrees C but not 23 degrees C. *Am J Physiol, 267*, C623–632.

Wu, M., Le, H. D., Wang, M., et al. (2009a). Crystal structures of progressive Ca2+ binding states of the Ca2+ sensor Ca2+ binding domain 1 (CBD1) from the CALX Na+/Ca2+ exchanger reveal incremental conformational transitions. *J Biol Chem, 285*, 2554–2561.

Wu, M., Wang, M., Nix, J., Hryshko, L. V., & Zheng, L. (2009b). Crystal structure of CBD2 from the Drosophila Na(+)/Ca(2+) exchanger: diversity of Ca(2+) regulation and its alternative splicing modification. *J Mol Biol, 387*, 104–112.

Xie, Y., Ottolia, M., John, S. A., Chen, J. N., & Philipson, K. D. (2008). Conformational changes of a Ca2+-binding domain of the Na+/Ca2+ exchanger monitored by FRET in transgenic zebrafish heart. *Am J Physiol Cell Physiol, 295*, C388–393.

Zhang, Y. H., & Hancox, J. C. (2009). Regulation of cardiac Na+-Ca2+ exchanger activity by protein kinase phosphorylation – -still a paradox? *Cell Calcium, 45*, 1–10.

Chapter 15

Intracellular Chloride Regulation

Francisco J. Alvarez-Leefmans

Chapter Outline

I. INTRODUCTION

The importance of chloride ions in cell physiology has not been fully recognized until relatively recently. This is in spite of the fact that chloride (Cl^-), together with bicarbonate (HCO_3^-), is the most abundant free anion in living animal cells and, as will be seen in this chapter, it performs or determines fundamental biological functions in virtually all tissues. For decades it was thought that Cl^- moved through plasma membranes by a purely electrodiffusive mechanism, i.e. a passive mechanism in which membrane permeation of a given ion is driven by both its electrical and concentration gradients. According to this view, Cl^- was distributed passively across the plasma membrane, in thermodynamic equilibrium as defined by Equation 15.2 (see Section III, below), and from a functional perspective it was necessary just to maintain electroneutrality of intra- and extracellular fluids and for keeping the cell osmotic balance. The notion that Cl^- was passively distributed implied that it was not actively transported, nor could it provide energy for transport of other substances. Moreover, if passively distributed, Cl^- was unlikely to play any role in cell signaling functions. Research carried out during the last two decades has led to a revolutionary change in this simplistic view. It is now well established that Cl^- plays vital roles in cell physiology and that most animal cell types exhibit a non-equilibrium distribution of Cl^- across their plasma membranes (Alvarez-Leefmans and Delpire, 2009b; Hartzell, 2009). Far from being passively distributed across the plasma membrane in accordance with the membrane potential (E_m), we now know that Cl^- is actively transported and tightly regulated. Some cells actively extrude Cl^-, others actively accumulate it, but few cells ignore it. The intracellular Cl^- concentration, $[Cl^-]_i$, is determined by the relative contribution of various anion

Cell Physiology Sourcebook. DOI: 10.1016/B978-0-12-387738-3.00015-9

transporting proteins expressed in cell membranes. These transport proteins include several types of Cl^- channels as well as numerous transporters that work mostly as cotransporters (symporters) or as exchangers (antiporters). During the last two decades, the molecular structure and function of these specialized Cl^- transport proteins have been elucidated. The three-dimensional crystal structure of some prokaryotic homologous and, more recently, that of eukaryotes is beginning to emerge, providing insights into the working mechanisms of these proteins at the atomic and molecular levels (Warmuth et al., 2009; Feng et al., 2010).

By virtue of being distributed out of electrochemical equilibrium, Cl^- serves as a key player in a variety of cellular functions, such as pH_i regulation, cell volume regulation, transepithelial salt and water transport and membrane potential stabilization. In addition to these functions, in the nervous system, Cl^- gradients are fundamental in synaptic signaling mediated by the neurotransmitters GABA (γ-aminobutyric acid) and glycine. This signaling results from ionic currents flowing through ligand-gated anion channels primarily permeable to Cl^-. The signals can be in the depolarizing and hyperpolarizing directions thereby determining mechanisms such as presynaptic and postsynaptic inhibition, or the GABA-mediated depolarizing excitation observed in immature neurons. In some cell types, the "ligand" that opens Cl^- channels, instead of being a neurotransmitter, is ionized calcium (Ca^{2+}). Cl^- gradients also play key roles in neuronal growth and development, cell migration, extracellular K^+ scavenging, neurotransmitter reuptake and vesicular storage, and sensory transduction including olfaction and nociception (Alvarez-Leefmans and Delpire, 2009a). In this chapter, some examples are presented to illustrate how Cl^- is regulated and involved in some of these processes.

II. ORIGIN OF THE PASSIVE Cl^- DISTRIBUTION ASSUMPTION

The notion that Cl^- is non-passively distributed and actively transported across cell membranes may sound obvious nowadays. However, it took decades to eradicate the generalization of the passive Cl^- distribution assumption and its implications. When dealing with the Goldman–Hodgkin–Katz equation for resting membrane potential, Cl^- is still often omitted. One of the usual arguments for this omission is that any ion that is passively distributed cannot determine the resting membrane potential (E_m); instead, E_m determines the distribution of that ion across the membrane. Another argument is that P_{Cl}, the membrane permeability to Cl^-, is negligible. However, neither of these arguments is applicable to all cell types. The question arises as to how and why basic facts such as the non-equilbrium distribution of Cl^- across the plasma membranes, the transport mechanisms that make it possible and its functional significance were missed, neglected and even denied for decades. The passive Cl^- distribution assumption exemplifies how scientific knowledge often advances by learning from our mistakes.

The notion that Cl^- was passively distributed in all cells emerged from three key experimental observations made in squid axons, skeletal muscle cells and red blood cells between the 1940s and the 1960s. First, in the early 1940s an influential paper reported that in freshly dissected squid axons, still one of the best animal cell models to study ion transport, the average $[Cl^-]_i$ was 36 mmol/kg axoplasm (Steinbach, 1941). Taking the water content of squid axoplasm as 880 g/kg, this corresponded to 41 mM, a value close to what would be expected if Cl^- was in electrochemical equilibrium across the axolemma of this seawater animal. However, in 1963, the British physiologist Richard Keynes (1919–2010) published a landmark paper entitled "chloride in squid giant axons" in which he reanalyzed the chloride content of extruded axoplasm from *Loligo forbesi*, and Steinbach's low values for $[Cl^-]_i$ could not be confirmed (Keynes, 1963). The average $[Cl^-]_i$ measured by Keynes in squid axoplasm was 108 ± 2 mM, a concentration "...well over twice that expected for a simple passive distribution..." Thus, E_{Cl}, the Nernst equilibrium potential for Cl^- as defined by Equation 15.1 (see below, Section III), was less than −40 mV, which was different to the resting E_m of −60 to −70 mV typically measured in squid axons. Based on these findings and measurements of Cl^- fluxes, Keynes suggested that Cl^- was "...being transported inwards against the electrochemical gradient by some form of active transport mechanism..." The nature of the transport mechanism in squid axons was elucidated nearly 20 years later by the biophysicist John M. Russell. The active Cl^- uptake mechanism turned out to be an electroneutral Na^+-K^+-Cl^- cotransporter (Russell, 2000) similar to that described in 1980 by P. Geck, E. Heinz and coworkers in Ehrlich cells, a mammalian cell line (Geck et al., 1980; Geck and Heinz, 1986). The difference between the squid and the mammalian Na^+-K^+-Cl^- is in the stoichiometry which is $2Na^+{:}1K^+{:}3Cl^-$ in the squid and $1Na^+{:}1K^+{:}2Cl^-$ in most mammalian cells, probably reflecting some hitherto unknown differences in the protein structure.

The second set of observations that gave rise to the "passive distribution assumption" came from work on frog skeletal muscle done in the late 1950s and early 1960s, that showed that the resting membrane Cl^- conductance was twice as large as that for K^+ (Hodgkin and Horowicz, 1959; Hutter and Noble, 1960). Further, measured $[Cl^-]_i$ was consistent with a distribution of Cl^- determined by a purely passive mechanism (Adrian, 1961). Thus, E_{Cl} was found to be close or equal to E_m. Direct, real-time measurements of $[Cl^-]_i$ and E_m in skeletal muscle by means of Cl^--sensitive microelectrodes demonstrated that, indeed, in skeletal

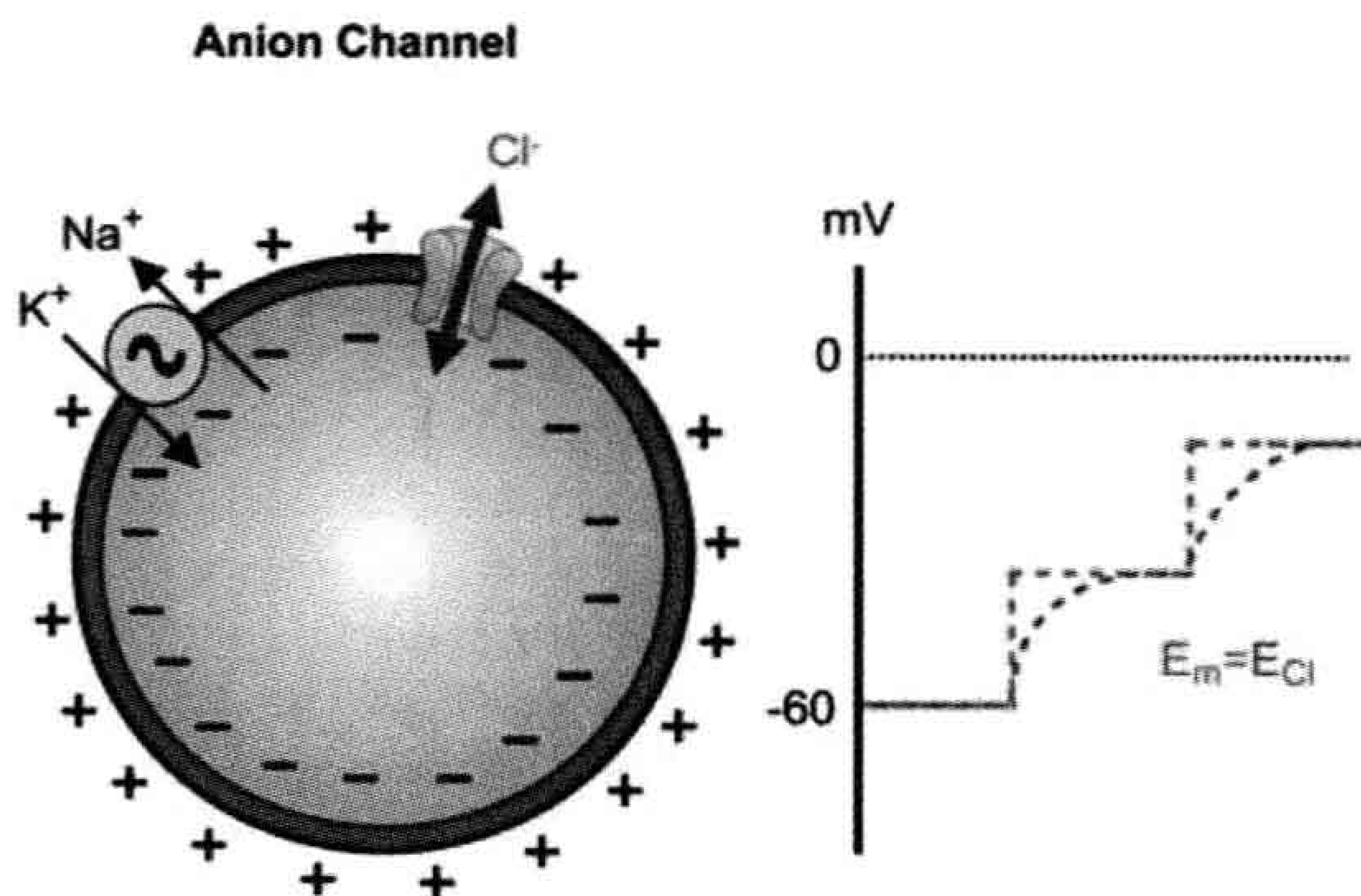


FIGURE 15.1 Passive Cl^- distribution across the cell membrane of an idealized cell having only Cl^- channels and a Na^+/K^+ ATPase (left). The resting membrane potential (E_m) is -60 mV. Right: E_m is changed in steps of ≈ 20 mV, from the initial resting membrane potential. Chloride redistributes passively, following E_m. At each steady state $E_m = E_{Cl}$. *(Reproduced with permission from Alvarez-Leefmans and Delpire, 2009b.)*

muscle, E_{Cl} closely follows E_m (Vaughan-Jones, 1982). This is due to the relatively high P_{Cl} characteristic of the sarcolemma, as illustrated schematically in Fig. 15.1. We now know that this exceptionally high resting P_{Cl} of skeletal muscle fibers is due to the expression of CLC-1 chloride channels. CLC-1 is a member of the CLC family of chloride channels and transporter proteins (Jentsch, 2008). The functional significance of this high P_{Cl} is that it stabilizes the membrane potential of skeletal muscle fibers. Thus, for all practical purposes, Cl^- appears passively distributed across the sarcolemma. Nevertheless, the fact that $E_m = E_{Cl}$ does not preclude the existence of carrier-mediated active transport of Cl^- in skeletal muscle cells or in any cell type. In fact, there is compelling evidence for an inward active transport of Cl^- in skeletal muscle (Aickin, 1990). This inward transport of Cl^- is mediated primarily by one of the two isoforms of the Na^+-K^+-$2Cl^-$ cotransporters, NKCC1, a member of the electroneutral cation-coupled chloride cotransporter protein family encoded by the *SLC12* gene family (Wong et al., 2001; Gosmanov et al., 2003; Jurkat-Rott et al., 2006; Kristensen and Juel, 2010). However, as shown in Fig. 15.2, the relatively high P_{Cl} mediated by CLC-1 masks any effects that the operation of this inward transport system may have on $[Cl^-]_i$. Accordingly, reducing P_{Cl} by pharmacological blockage of CLC-1 with 9-anthracene carboxylic acid (9-AC) unmasks the active Cl^- uptake mediated by NKCC1.

The third set of observations that led to the generalization of the "passive distribution assumption" came from red blood cells in which $[Cl^-]_i$ was also found to be close to that predicted for electrochemical equilibrium. Several Cl^- transport studies in red blood cells were consistent with the

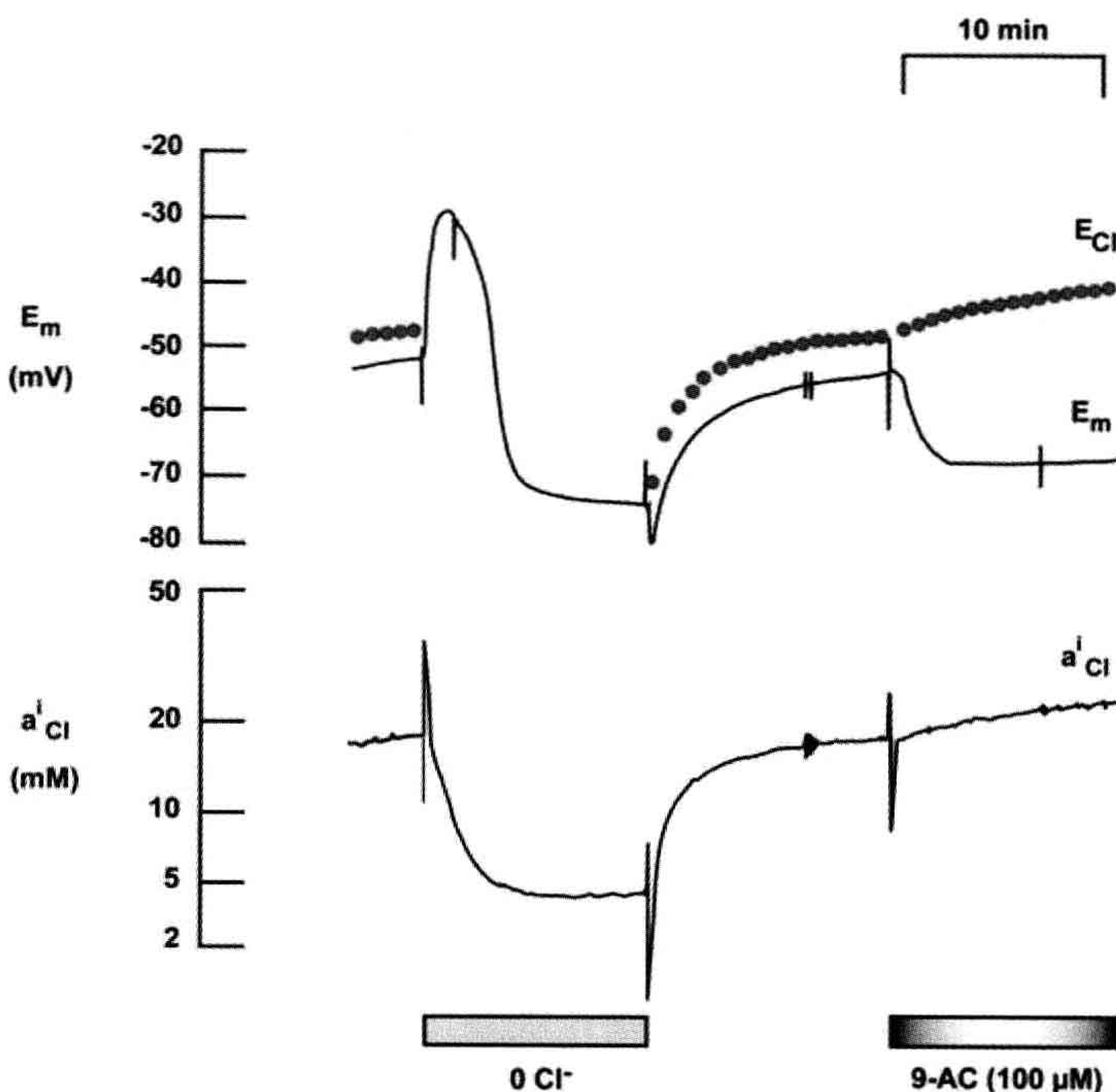


FIGURE 15.2 Active accumulation of Cl^- in rat skeletal muscle unmasked by reducing the resting Cl^- conductance mediated by Cl^- channels. Membrane potential (E_m) and the intracellular Cl^- activity (a^i_{Cl}) were measured simultaneously in a rat lumbrical muscle during the removal and readdition of external Cl^- and the inhibition of the resting Cl^- conductance by application of 9-anthracene carboxylic acid (9-AC). The Cl^- equilibrium potential (E_{Cl}), calculated from the recorded a^i_{Cl} and a^o_{Cl}, using Equation 15.1 has been plotted as red filled circles above the recording of E_m. Note that E_{Cl} was slightly positive with respect to E_m, indicating that a^i_{Cl} was maintained just above equilibrium. Upon reduction of the Cl^- conductance a^i_{Cl} began to increase, and the difference between E_m and E_{Cl} became significantly larger. The recording was made with a double-barreled microelectrode, one barrel sensing E_m and the other the a^i_{Cl}. The preparation was maintained in the nominal absence of CO_2 in solutions equilibrated with 100% O_2. The mechanism responsible for the uphill accumulation of Cl^- is a Na^+-K^+-Cl^- cotransporter. *(Modified from Aickin, 1990.)*

view that the Cl^- transmembrane distribution was thermodynamically passive and, in addition, showed that Cl^- crossed the membrane extremely rapidly. This latter finding, erroneously interpreted for a long time as being only the result of high passive P_{Cl}, made it quite likely that Cl^- could remain at thermodynamic equilibrium. In fact, it was later found that the high P_{Cl} of erythrocytes was primarily due to expression of an anion exchanger transport protein, the Cl^-/HCO_3^- exchanger originally identified as "Band 3" because of its relative migration position in SDS-PAGE (Sodium dodecyl sulfate polyacrylamide gel electrophoresis) gels. "Band 3" is now known as "anion exchanger 1" (AE1) and it is one of 10 members of the SLC4 gene and protein family of anion transporters (Alper, 2009).

The three sets of experimental observations that we have considered above were generalized so that virtually all cells were thought to have a very high P_{Cl} and a thermodynamically passive Cl^- transmembrane distribution, implying that Cl^- was not actively transported. Moreover, to make things worse for the case of Cl^-, cations claimed center stage during this period with attention focused on the Na^+ and Ca^{2+} action potentials, the K^+ channels and the Na^+/K^+ pump. Thus, the belief that Cl^- played no major role in membrane physiology and the attention directed to the study of cations combined to cause research on Cl^- transport to be largely neglected for many years.

III. PASSIVE AND NON-PASSIVE Cl^- DISTRIBUTION ACROSS THE PLASMA MEMBRANE

The Cl^- equilibrium potential, E_{Cl}, is defined by the Nernst equation:

$$E_{Cl} = \frac{RT}{zF}\ln\frac{[Cl^-]_i}{[Cl^-]_o} \tag{15.1}$$

where $[Cl^-]_i$ and $[Cl^-]_o$ are the intracellular and extracellular Cl^- concentrations, R is the gas constant, T is absolute temperature, F is the Faraday's constant and z the valence (=−1). If Cl^- is passively distributed, E_m will have the same value as E_{Cl} and therefore:

$$E_m = \frac{RT}{zF}\ln\frac{[Cl^-]_i}{[Cl^-]_o} \tag{15.2}$$

From Equation 15.2, the predicted $[Cl^-]_i$ at electrochemical equilibrium, $[Cl^-]_i^{eq}$, is given by:

$$[Cl^-]_i^{eq} = [Cl^-]_o e^{E_m F/RT} \tag{15.3}$$

Thus, Equation 15.3 predicts the value that $[Cl^-]_i$ will reach when Cl^- is passively distributed across the plasma membrane. Evidently, this value will change with E_m, as illustrated in Fig. 15.1. For example, if $[Cl^-]_o$ is 113 mM and E_m is constant at −60 mV, *RT/F* at 37°C will be 26.73 mV and $[Cl^-]_i^{eq} \approx 12$ mM. Clearly, both E_m and E_{Cl} are −60 mV. If the cell is depolarized, say by 20 mV, to −40 mV, Cl^- redistributes across the membrane until reaching equilibrium which, for the example considered, will occur when $[Cl^-]_i^{eq} = 25.3$ mM, and thus $E_{Cl} = -40$ mV.

Another way of arriving at Equation 15.2 and grasping its meaning is to consider once more the idealized cell shown in Fig. 15.1 that has only anion channels and Na^+ pumps, but no active (uphill) Cl^- transporters. In this cell, Cl^- distributes passively following E_m. The Cl^- flux through the anion channel is driven by the electrochemical potential gradient for Cl^-, $\Delta\mu_{Cl}$, which is the sum of a chemical and an electrical component. This is formally defined by Equation 15.4:

$$\Delta\mu_{Cl} = RT\ln\frac{[Cl^-]_i}{[Cl^-]_o} + zFE_m \tag{15.4}$$

Since the cell is negative inside with respect to the outside (in the model shown $E_m = -60$ mV and z, the Cl^- valence is −1), the electrical potential gradient will tend to drive Cl^- out of the cell. However, the chemical potential gradient is inward; $[Cl^-]_o$ is higher than $[Cl^-]_i$. Consequently, the chemical gradient will drive Cl^- towards the cell interior. When the two forces cancel each other (they are equal and opposite), the system reaches equilibrium. At that point $\Delta\mu_{Cl} = 0$. When this condition is met, we can readily derive Equation 15.2 from Equation 15.4. That is, when Cl^- is passively distributed, E_m will have the same value as E_{Cl}.

If Cl^- is non-passively distributed it means that it is actively transported and this implies energy consumption. Active Cl^- transport (i.e. transport against Cl^- electrochemical equilibrium or "uphill" transport) requires demonstrating that $[Cl^-]_i$ is maintained at a level different from that predicted by Equation 15.3 and this implies that E_{Cl} and E_m will have different values. In most cells, $[Cl^-]_i$ is maintained at a value different from that predicted from Equation 15.3. However, as mentioned above, *equal values of E_m and E_{Cl} do not preclude the presence of carrier-mediated active Cl^- transport*. A clear example illustrating this notion is the case of skeletal muscle cells which, as mentioned above (Section II) and shown in Fig. 15.2, have a substantial channel-mediated (electrodiffusional) Cl^- permeability that masks the effects of an inwardly directed active Cl^- transport mechanism (Harris and Betz, 1987; Aickin, 1990).

In most cell types of both vertebrates and invertebrates, in which Cl^- is not in electrochemical equilibrium, the $[Cl^-]_i$ is maintained at a higher value than that predicted for a passive distribution across the plasma membrane, i.e. E_{Cl} has a more depolarized (less negative) value than E_m. This implies the presence of transport mechanisms that actively accumulate Cl^- often referred to as "Cl^- loaders". Examples of mammalian cells in which $[Cl^-]_i$ is maintained

above equilibrium include primary sensory neurons, sympathetic ganglion cells, immature central nervous system neurons, epithelial cells, leukocytes and both smooth and cardiac muscle cells (Fig. 15.3). In contrast, in some cells, mature cortical neurons in particular, $[Cl^-]_i$ is maintained at a value lower than that predicted for a passive Cl^- distribution across the plasma membrane due to the presence of active Cl^- extrusion mechanisms (i.e. Cl^- extruders). In this case, E_{Cl} has a more hyperpolarized (more negative) value than E_m. This lower than passive Cl^- distribution in adult neurons in the CNS constitutes the basis for hyperpolarizing synaptic inhibition mediated by neurotransmitters such as GABA and glycine. A prototypical case is the hyperpolarizing inhibition produced by GABA acting via $GABA_A$ receptors thereby opening Cl^- channels with consequent hyperpolarizing Cl^- influx that results in an increase in neuronal firing threshold (i.e. decreased excitability). By controlling neuronal excitability, Cl^--mediated postsynaptic inhibition shapes the firing pattern of individual neurons and entire neuronal networks and thus this mechanism plays a key role in the processing of information in the nervous system. The carrier protein that actively extrudes Cl^- in mature CNS neurons, making possible hyperpolarizing inhibition, is one of four isoforms of the K^+-Cl^- cotransporters, KCC2, a member of the electroneutral cation-coupled chloride cotransporter protein family encoded by the SLC12A gene family, as discussed below (see Section VI).

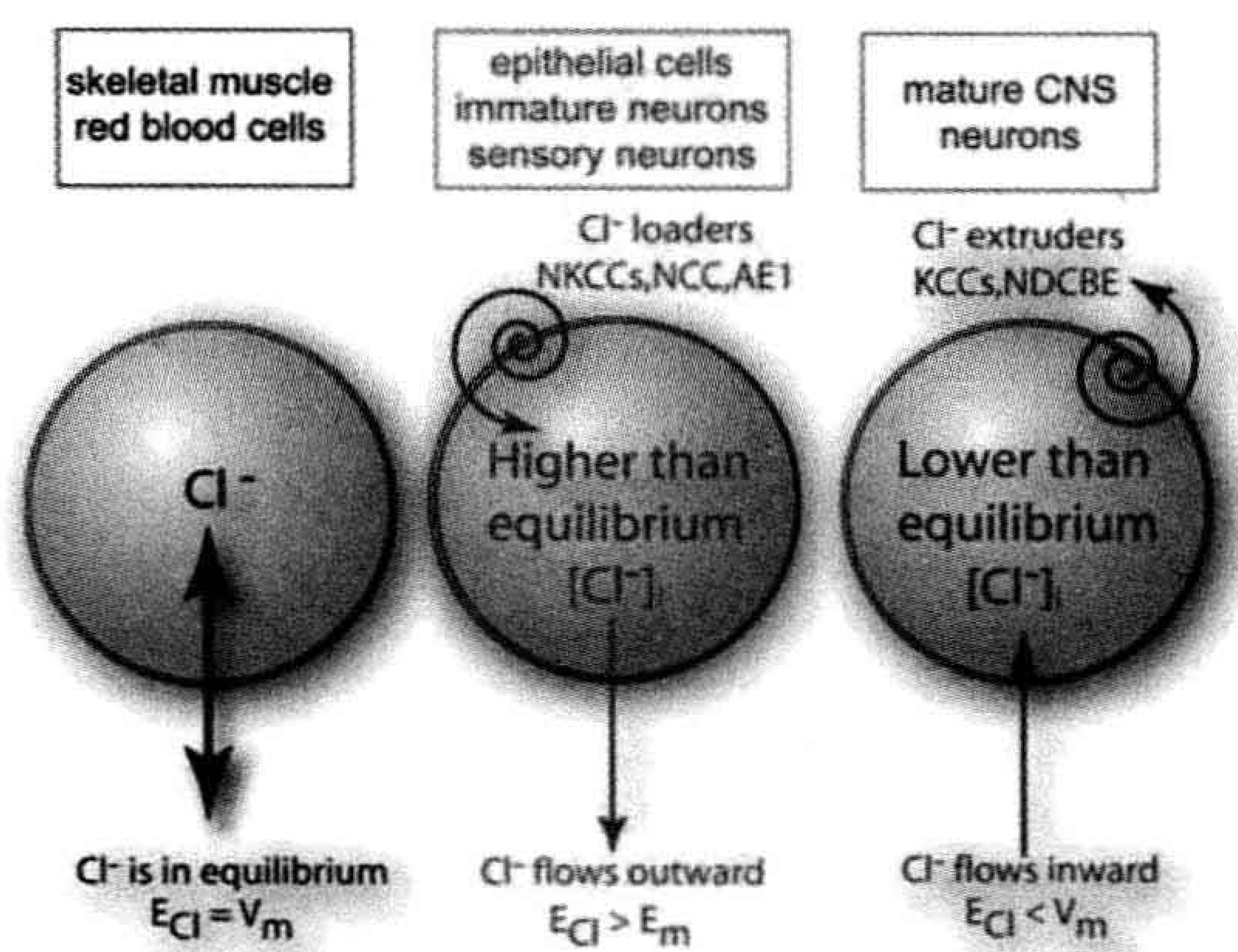


FIGURE 15.3 Control of cytosolic Cl^- in different cell types. In skeletal muscle and erythrocytes, Cl^- appears to be in electrochemical equilibrium because there is a large resting Cl^- conductance that masks active Cl^- transport. In epithelial cells, immature neurons and adult sensory neurons, Cl^- loaders establish a higher than electrochemical equilibrium intracellular Cl^- concentration. In mature neurons, Cl^- extruders establish a lower than electrochemical equilibrium intracellular Cl^- concentration. Examples of Cl^- loaders are: the Na^+, K^+, $2Cl^-$ cotransporters (NKCCs), the Na^+-Cl^- cotransporter (NCC), and the anion exchanger 1(AE1). Examples of Cl^- extruders are some K^+-Cl^- cotransporters (KCCs) and the Na^+-driven Cl^-/HCO_3 exchanger (NDCBE). *(Modified from Hartzell, 2009.)*

IV. ACTIVE TRANSPORT MECHANISMS FOR Cl^-

Intracellular Cl^- levels are determined by the relative contributions of the various Cl^- transport mechanisms expressed in the plasma membrane of a given cell type. A variety of mechanisms capable of transporting Cl^- across the plasma membrane have been identified in vertebrate and invertebrate cells. They include various types of Cl^- channels that behave as *passive leak pathways*, and a series of specialized *carriers that mediate "active" Cl^- transport*. All Cl^- carrier proteins known in animal cells are secondary active transport mechanisms and all of them are encoded by members of the solute carrier (SLC) gene superfamily (see http://ghr.nlm.nih.gov/geneFamily/slc). As we will see, secondary active transport does not directly utilize ATP hydrolysis to drive "uphill" solute transport. In animal cells, there is no firm evidence for the existence of an active Cl^- pump, i.e. a primary active transport mechanism *directly* energized by ATP. Chloride channels are the subject of other chapters of this book and therefore they will only be briefly mentioned here. The carrier protein molecules that actively transport Cl^- include but are not limited to (1) *anion exchangers* (AEs) and (2) the *electroneutral cation-chloride cotransporters*. The latter are the main focus of this chapter. *Neurotransmitter transporters* encoded by the SLC6 gene family (Na^+- and Cl^--dependent neurotransmitter transporter family) cotransport Cl^-. An example is the GABA transporter GAT1 (SLC6A1). The ion-substrate stoichiometry of GABA transporters has been determined to be $2Na^+:1Cl^-:1GABA$. The role of Cl^- in the transport process is not understood and it is unclear whether this Cl^- cotransport impacts $[Cl^-]_i$ or Cl^- is merely used as a cofactor (Wu et al., 2007). For this reason, neurotransmitter transport proteins are not considered further in the present chapter.

IVA. Anion Exchangers

Anion exchangers are encoded by two evolutionarily unrelated mammalian gene families, SLC4 and SLC26 (Alper, 2009; Romero et al., 2009). Plasmalemmal Cl^-/HCO_3^- exchangers are ubiquitously expressed in various cell types. Their primary function is the regulation of intracellular pH, but they also play key roles in the regulation of $[Cl^-]_i$ and cell volume. The Cl^-/HCO_3^- exchangers of polarized epithelial cells contribute to transepithelial secretion and reabsorption of acid–base equivalents and Cl^-. The mammalian SLC4 gene and protein family includes three Na^+-independent Cl^-/HCO_3^- exchangers (AE1, AE2 and AE3) that couple the electroneutral movement of 1 Cl^- in exchange for 1 HCO_3^- across plasma membranes. Under physiological conditions, most AEs of the SLC4 family behave as cell Cl^- loaders; they couple the

inward movement of 1 Cl^- with the outward movement of 1 HCO_3^-. However, *reversibility is a key thermodynamic feature of carrier-mediated transport* proteins and thus solutes can be transported in either inward or outward direction under physiological conditions; these proteins use the chemical gradient of either one of the transported ions to move the other. The transport process of AE1, AE2 and AE3 is *electroneutral*. This means that the transport process occurs without net charge transfer across the membrane and without being affected by the membrane potential (see below). This is in contrast with *electrogenic* transport, in which the driving force for the transport process is the sum of the chemical and electrical gradients of the transported ions and thus the transport process is affected by the membrane potential and it generates a current across the membrane, i.e. it transfers net charge across the membrane. An example of carrier electrogenicity and reversibility is the Cl^-/HCO_3^- exchanger SLC26A6. This carrier protein mediates the coupled exchange of Cl^- and HCO_3^- with a transport stoichiometry of $1Cl^-:2HCO_3^-$ (Fig. 15.4).

One of the best examples of transport reversibility of an electroneutral transporter under physiological conditions is the erythroid Cl^-/HCO_3^- exchanger (AE1), a carrier that is essential for removing CO_2 produced by tissue metabolism and transporting it to the lungs where the gas can be expelled from the body. AE1 operates near equilibrium (see below) so that a relatively small variation in the chemical gradients of Cl^- or HCO_3^- across the plasma membrane of red blood cells (RBCs) alters the direction of transport. This feature permits HCO_3^- formed from CO_2 in the systemic capillaries by the intracellular enzyme carbonic anhydrase (CA) to leave the RBCs in exchange for Cl^-, thus effectively storing CO_2 in the blood in the form of plasma HCO_3^-, greatly increasing the CO_2 carrying capacity of the blood. In the lungs, the process is reversed to regenerate CO_2 that is then exhaled. In other words, the relatively high external concentration of CO_2 generated by metabolism in tissues drives CO_2 entry into RBCs. CO_2 is then hydrated inside RBCs, a forward reaction catalyzed by the enzyme CA ($CO_2 + H_2O \rightarrow H_2CO_3 \rightarrow H^+ + HCO_3^-$). The resulting increase in $[HCO_3^-]_i$ drives the Cl^-/HCO_3^- exchanger to operate in the bicarbonate-out-chloride-in mode. In the alveolar capillaries, the CO_2 concentration gradient is reversed because of the relatively low CO_2 concentration in the alveolar space, thereby driving CO_2 from the RBCs into the alveolus. This process is possible because the reactions catalyzed by CA are also reversible, so CA now catalyzes the net dehydration of H_2CO_3 ($H^+ + HCO_3^- \rightarrow H_2CO_3 \rightarrow H_2O + CO_2$). The consequent decrease in $[HCO_3^-]_i$ drives the Cl^-/HCO_3^- exchanger to operate in the bicarbonate-in-chloride-out mode.

Heart muscle cells are an interesting example in which $[Cl^-]_i$ is determined by the presence of electrogenic anion exchangers working in parallel with the electroneutral Cl^- loader NKCC1. Early studies using intracellular ion-selective microelectrodes demonstrated that $[Cl^-]_i$ is maintained at a *higher* value than that predicted for a passive distribution across the sarcolemma of cardiac muscle cells (Vaughan-Jones, 1982). It is now known that a variety of sarcolemmal AEs, in conjunction with the Na^+-K^+-$2Cl^-$ cotransporter NKCC1, serve as uphill Cl^- accumulating mechanisms in cardiac cells. The anion exchangers predominantly expressed in adult heart muscle are AE3 (SLC4A3), SLC26A3 and particularly SLC26A6, all of which play a central role in the regulation of pH_i in cardiomyocytes (Alvarez et al., 2004). Both SLC26A3 and SLC26A6 function as dual Cl^-/OH^- and Cl^-/HCO_3^- exchangers. The transport stoichiometry of SLC26A6 is $2HCO_3^-:1Cl^-$, whereas that of SLC26A3 is $1HCO_3^-:2Cl^-$ (Shcheynikov et al., 2006). These stoichiometries mean that both these SLC26 transporters are *electrogenic*; on each cycle they transport net charge across the plasma

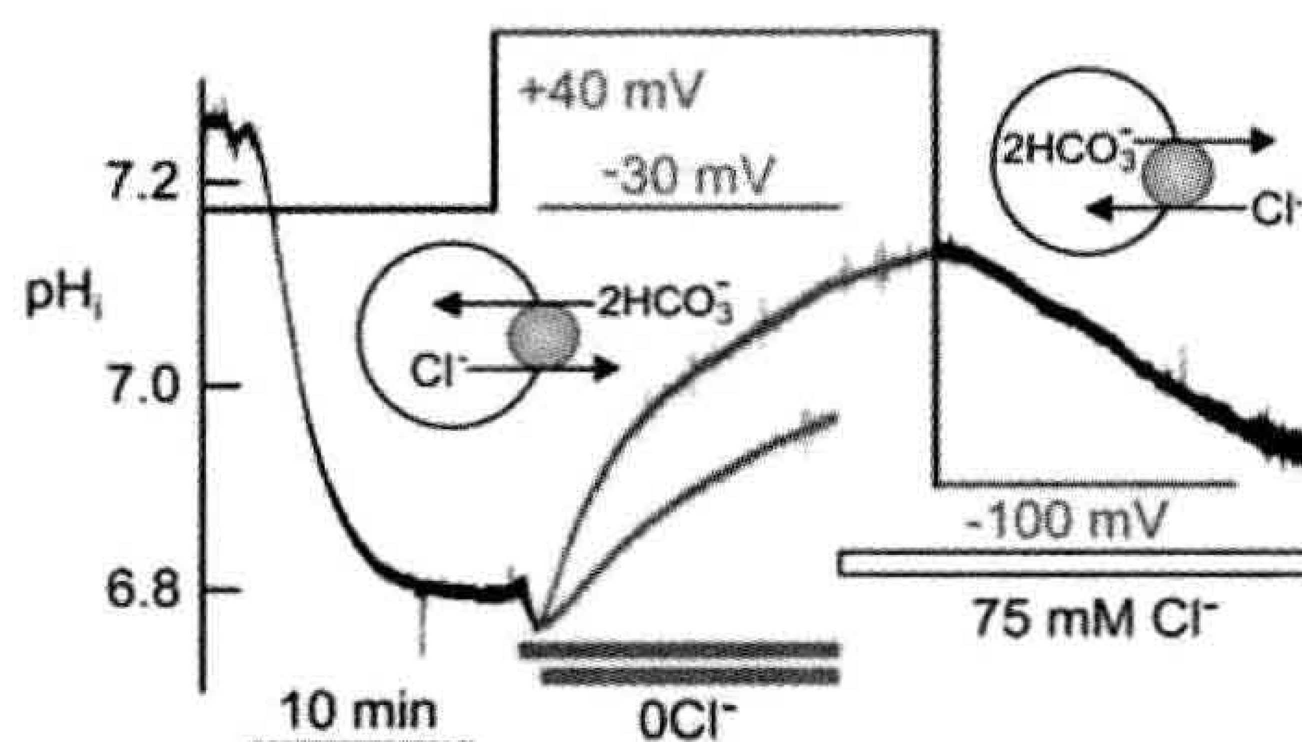


FIGURE 15.4 Electrogenicity and flux reversibility of the Cl^-/HCO_3^- exchanger SLC26A6 heterologously expressed in *Xenopus* oocytes. The membrane potential of transfected *Xenopus* oocytes was controlled by voltage clamp as indicated. Intracellular pH (pH_i) changes were measured with pH_i-sensitive microelectrodes. Changes in $[Cl^-]_i$ were also measured (not shown) using Cl^--sensitive microelectrodes. The experiment shows the effect of membrane potential and external $[Cl^-]$ on HCO_3^- transport by SLC26A6. The HCO_3^- fluxes are inferred from the pH_i changes reflecting net H^+ fluxes. Accordingly, when HCO_3^- enters the cell in exchange for Cl^-, the cell interior is alkalinized (green and red traces) and when HCO_3^- exits the cell in exchange for Cl^-, the cell is acidified (black trace following green trace). The reversibility and direction of transport occurring during the experiment are illustrated in the inset diagrams. In this experiment, the *Xenopus* oocyte expressing SLC26A6 was bathed in HCO_3^-- buffered media. After the stabilization of pH_i, the membrane potential was clamped at −30 mV (red pH_i trace) or +40 mV (green pH_i trace) before exposing the oocyte to Cl^--free medium (0 Cl^-). Note the effect of membrane potential on HCO_3^- influx upon removal of eternal Cl^- (green trace at +40 mV and red trace at −30 mV). At the time indicated by the white bar, external $[Cl^-]$ (75 mM) was restored and, after an additional period of 5 min, the membrane potential was switched from +40 mV to −100 mV. This resulted in intracellular acidification (black trace) due to HCO_3^- efflux. SLC26A6 mediates the coupled exchange of Cl^- and HCO_3^- with a transport stoichiometry of $1Cl^-/2HCO_3^-$. Accordingly, holding the membrane potential at +40 (green pH_i trace) and −100 mV (black trace) accelerated and inhibited, respectively, Cl^--mediated HCO_3^- influx and holding the membrane potential at −100 mV increased HCO_3^--mediated Cl^- influx. *(Modified from Shcheynikov et al., 2006.)*

membrane thereby producing a change in membrane potential (Romero et al., 2009). Thus, their operation is also affected by the membrane potential (see Fig. 15.4). The "opposite" stoichiometry of SLC26A6 and SLC26A3 transporters means that their relative transport activity will vary with the membrane potential; SLC26A6 will operate to cause efflux of HCO_3^- at resting membrane potential (≈ -80 mV), while SLC26A3 will become active in the HCO_3^- efflux mode as the cell moves to more positive potential during the cardiac action potential.

All these AEs (SLC4A3, SLC26A3 and SLC26A6) play key roles in the regulation of pH_i in cardiac myocytes. Further, the outward Cl^- gradient of cardiac myocytes that is generated and maintained by the above mentioned AEs in conjunction with the operation of NKCC1 is of high functional significance, as revealed by studies using double knockout mice in which both AE3 (SLC4A3) and NKCC1 (SLC12A2) are genetically deleted resulting in impaired cardiac contractility (Prasad et al., 2008). Numerous Cl^- channels are expressed in cardiac muscle (Duan, 2009). Their activation produces significant effects on cardiac action potential characteristics and pacemaker activity. The repertoire of cardiac Cl^- channels include the cystic fibrosis transmembrane conductance regulator (CFTR), which is a member of the ATP-binding cassette (ABC) transporter superfamily and may be responsible for the Cl^- currents activated by protein kinase A (PKA), ClC-2, ClC-3 and the Ca^{2+}activated Cl^- channel TMEM16A. The resting E_m of cardiac myocytes is -80 to -90 mV and during an action potential the overshoot and plateau phases can be several millivolts positive. Given that E_{Cl} remains fairly constant, E_m can be either more positive or more negative than E_{Cl} during the normal cardiac action potential cycle. Thus, cardiac Cl^- channels can generate both outward and inward currents and cause both depolarization and repolarization during the action potential.

Anion exchangers, in parallel with NKCC1, also appear to play a role in intracellular Cl^- homeostasis in developing neurons in some CNS areas. For instance, in developing rat auditory brainstem neurons (Becker et al., 2003) and in embryonic chick motoneurons (Gonzalez-Islas et al., 2009), AEs contribute to the maintenance of $[Cl^-]_i$ at *higher* values than predicted for a passive distribution across the plasma membrane. The resulting outward Cl^- gradient underlies the *depolarizing* action of glycine and GABA, which is important in these and other central neurons in promoting neurogenesis, migration and differentiation (Reynolds et al., 2008; Wang and Kriegstein, 2009).

How much Cl^- can a cell accumulate through electroneutral anion exchangers like AE1, AE2 or AE3? It depends on *thermodynamic equilibrium conditions of the AEs*, on kinetic constraints dictated by mechanisms regulating ion translocation, as well as on the presence of other transporters and channels expressed in the same cell. For understanding the $[Cl^-]_i$ that would be reached when an anion exchanger attains thermodynamic equilibrium consider the cell model shown in Fig. 15.5. Let us assume that the cell expresses only an electroneutral Cl^-/HCO_3^- exchanger with a stoichiometry of $1Cl^-:1HCO_3^-$ per cycle, that there are no kinetic constraints and that the only passive leak pathway is a GABA-gated Cl^- channel. Since AEs are secondary active transporters, the driving force for anion transport will be determined by the overall net free energy (ΔG) of the system, which in this case is the sum of the *chemical* potential gradients of the anions involved. Because the anions are transported in opposite directions, the combined chemical gradient ($\Delta\mu_{Cl/HCO_3}$) is given by the *difference* of the Cl^- and HCO_3^- chemical potential gradients $\Delta\mu_{Cl}$ and $\Delta\mu_{HCO_3}$, respectively:

$$\Delta G = \Delta\mu_{Cl/HCO_3} = \Delta\mu_{Cl} - \Delta\mu_{HCO_3} \quad (15.5)$$

Hence,

$$\Delta G = \Delta\mu_{Cl/HCO_3} = RT \ln \frac{[Cl^-]_i}{[Cl^-]_o} - RT \ln \frac{[HCO_3^-]_i}{[HCO_3^-]_o} \quad (15.6)$$

The transport process reaches thermodynamic equilibrium when $\Delta G = \Delta\mu_{Cl/HCO_3} = 0$, and Equation 15.6 becomes:

$$\frac{[Cl^-]_i}{[Cl^-]_o} = \frac{[HCO_3^-]_i}{[HCO_3^-]_o} \quad (15.7)$$

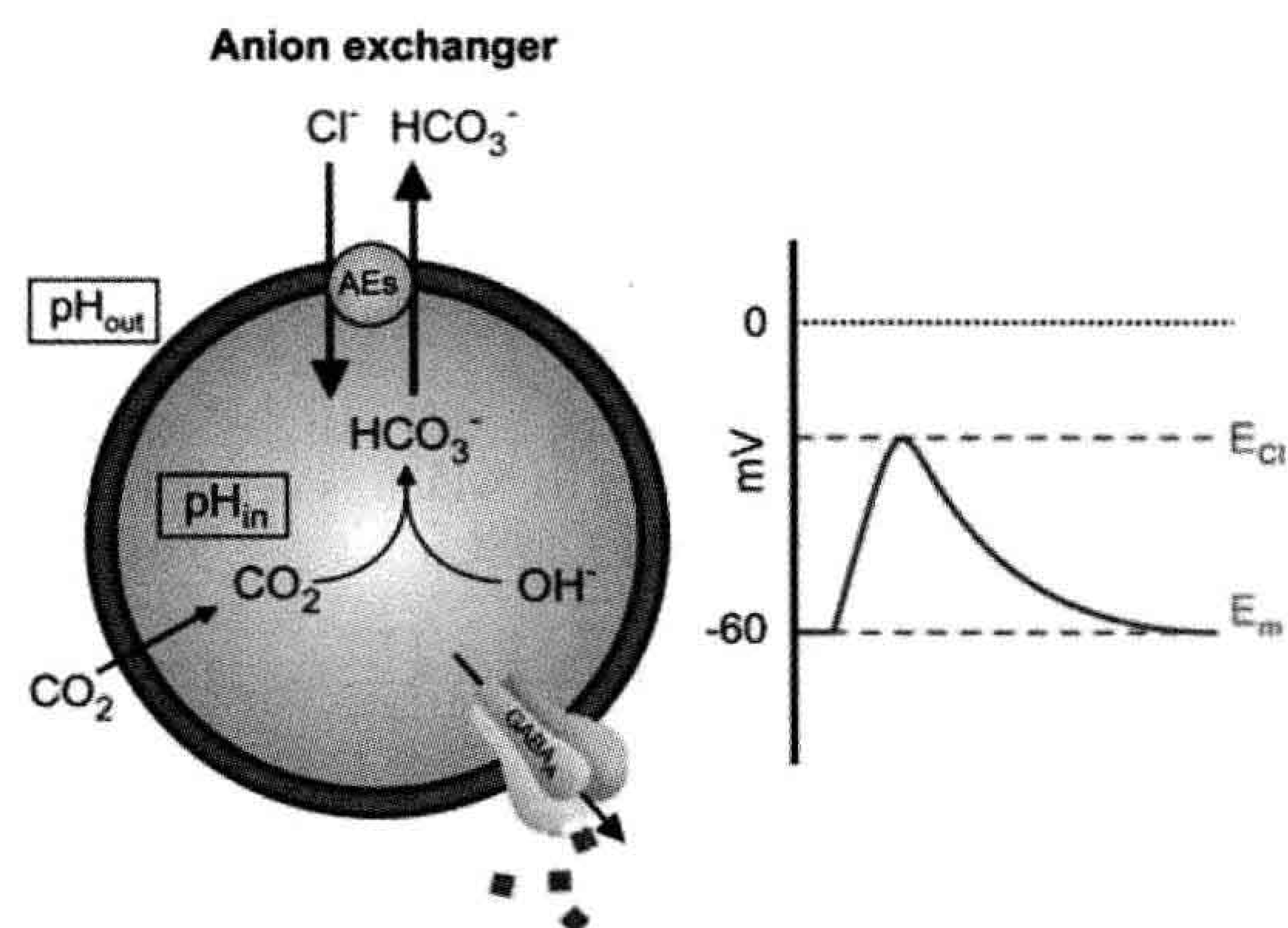


FIGURE 15.5 Model of a cell (e.g. a neuron) expressing only anion exchangers (AEs), Na^+/K^+ ATPase (not shown) and a ligand-gated anion channels ($GABA_A$ receptor-channels). The ΔpH across the plasma membrane ($pH_{in}-pH_{out}$) is constant. Resting $E_m = -60$ mV. The AEs mediate active accumulation of Cl^- in exchange for HCO_3^-. Intracellular $[Cl^-]$ is maintained at higher than passive levels. Consequently, E_{Cl} is more positive than E_m. Opening GABA-gated anion channels produces a depolarization mediated by electrodiffusional Cl^- efflux. The red squares represent GABA molecules acting on the $GABA_A$ receptor-channel. *(Reproduced from Alvarez-Leefmans and Delpire, 2009b.)*

Equation 15.7 relates the intracellular and extracellular Cl^- and HCO_3^- concentrations when the Cl^-/HCO_3^- exchange mechanism has reached equilibrium, i.e. when no further net movement of Cl^- and HCO_3^- can occur across the membrane. For the model shown in Fig. 15.5, $pH_o=7.3$ and $pH_i=7.1$ (i.e. $\Delta pH=0.2$) and $[HCO_3^-]_o$ is taken as 22 mM, the concentration measured in mammalian arterial plasma. In the presence of a CO_2/HCO_3^--buffered solution, the distribution of Cl^- will be determined by the distribution of HCO_3^- across the membrane. This is because CO_2 is freely permeable through the membrane and, at constant PCO_2 ($[CO_2]_i=[CO_2]_o$), the ratio of intracellular and extracellular $[HCO_3^-]$ is determined by ΔpH. Under these conditions E_H, the equilibrium potential for H^+, is equal to $E_{HCO_3^-}$, the equilibrium potential for bicarbonate (Bevensee and Boron, 1998). In the model considered here, the cell possesses only an anion exchanger (see Fig. 15.5). Thus, the $[Cl^-]_i$ when the anion exchanger reaches equilibrium can be predicted by knowing the $[Cl^-]_o$ and the ΔpH. Since we know ΔpH we can calculate E_H, which is given by the Nernst equation:

$$E_H = \frac{RT}{F}\ln(pH_i - pH_o) \quad (15.8)$$

At 37°C, and taking $pH_o = 7.3$ and $pH_i = 7.1$, $E_H = -12.3$ mV. Since $E_H = E_{HCO_3}$, we can now calculate the $[HCO_3^-]_i$ at equilibrium using the following expression:

$$[HCO_3^-]_i = [HCO_3^-]_o \exp\left(\frac{E_{HCO_3}F}{RT}\right) \quad (15.9a)$$

Hence,

$$[HCO_3^-]_i = 22\text{ mM}\exp\left(\frac{-12.3\text{ mV}F}{RT}\right) = 13.9\text{ mM} \quad (15.9b)$$

We can now calculate $[Cl^-]_i$ when the Cl^-/HCO_3^- reaches equilibrium, using Equation 15.10, which is derived from Equation 15.7. For $[Cl^-]_o=113$ mM,

$$[Cl^-]_i = \frac{[HCO_3^-]_i\,[Cl^-]_o}{[HCO_3^-]_o} = \frac{13.9\times 113}{22} = 71.4\text{ mM} \quad (15.10)$$

Thus, the maximal possible $[Cl^-]_i$ due to the AE under the conditions considered here would be 71.4 mM. Obviously, in a cell endowed with AEs, activation of $GABA_A$ receptors would produce a depolarizing Cl^- efflux (see Fig. 15.5). For thermodynamic equilibrium conditions of other anion exchangers the interested reader should consult the excellent review by Romero and colleagues (Romero et al., 2009). It is important to mention that AEs may be kinetically inhibited at different set points for $[Cl^-]_i$ and thus these "kinetic brakes" may prevent the exchanger from reaching thermodynamic equilibrium under physiological conditions (Alper et al., 2002; Kurschat et al., 2006). A key kinetic brake is pH itself (Alper et al., 2002; Alper, 2009). However, the discussion of regulatory mechanisms of AEs is beyond the scope of the present chapter.

AE1, AE2 and AE3 are often referred to as "Na^+-independent SLC4 anion exchangers" to distinguish them from the *Na^+-driven Cl^-/HCO_3^- exchanger NDCBE*, also an electroneutral transporter of the SLC4 family (SLC4A8) that, under physiological conditions, mediates the uptake of $1Na^+$ and $2HCO_3^-$ in exchange for $1Cl^-$. Thus, NDCBE normally behaves as a Cl^- extruder and, because of its capacity to transport HCO_3^- inwardly, it is a major acid extruder. Although NDCBE mediates a large Cl^- efflux that can potentially affect $[Cl^-]_i$, its role in intracellular Cl^- regulation is little known (see below); instead, NDCBE appears to be a major pH_i regulator in several types of CNS neurons (Chen et al., 2008). In fact, NDCBE was the first transporter shown to be involved in pH_i regulation, a discovery made in the mid-1970s in squid giant axons by Walter Boron, Paul De Weer and John Russell, and by Roger C. Thomas working independently in snail neurons (for references see Thomas, 1984; Romero et al., 2004). Human NDCBE was cloned by Boron's group (Grichtchenko et al., 2001). The possible role of NDCBE in the regulation of $[Cl^-]_i$ has been recently addressed in certain type of mammalian neurons, the cartwheel cells of the dorsal cochlear nucleus. These neurons exhibit activity-dependent intracellular acidification that is offset by activation of NDCBE with a consequent hyperpolarizing shift in E_{Cl} due to a decrease in $[Cl^-]_i$ mediated by NDCBE (Kim and Trussell, 2009). More recently, work on neurons of the nematode *Caenorhabditis elegans* shows that NDCBEs function with KCCs in generating the neuronal inward Cl^- gradient necessary for the hyperpolarizing action of GABA, and suggests a mechanism for the close tie between pH and excitability in the brain (Bellemer et al., 2011).

IVB. The Electroneutral Cation-Chloride Cotransporter Family

The electroneutral cation-chloride cotransporter family (SLC12A), which is the main focus of this chapter, comprises the major proteins responsible for intracellular Cl^- regulation (Gamba, 2005; Di Fulvio and Alvarez-Leefmans, 2009; Garbarini and Delpire, 2009; Payne, 2009). The SLC12A gene/protein family encompasses nine members: SLC12A3 (the thiazide-sensitive Na^+-Cl^- cotransporter NCC), SLC12A2 (the Na^+-K^+-$2Cl^-$ cotransporter NKCC1), SLC12A1 (the Na^+-K^+-$2Cl^-$ cotransporter NKCC2) and four Na^+-independent K^+-Cl^- cotransporters, namely SCLC12A4 (KCC1), SCLC12A5 (KCC2), SLC12A6 (KCC3), SLC12A7 (KCC4) and two orphan members named SLC12A9 (CIP) and SLC12A8 (CCC9) that do not

appear to transport ions and whose function is little understood. Thus only seven of the nine members of the SCL12A family have been established to function as cation-coupled Cl^- cotransporters. NKCC1, NKCC2 and NCC normally work as active Cl^- loaders, whereas the four KCCs (1–4) normally work as Cl^- extruders (see Fig. 15.3).

As mentioned above, all of these cation-coupled Cl^- cotransporters, as well as the Cl^-/HCO_3^- exchangers, are secondary active transport mechanisms. In this kind of transport, the translocation of the substrate is coupled to the translocation of another substrate that uses the same carrier, whether in the opposite direction (countertransport, antiport or exchanger) or in the same direction (cotransport or symport). The energy consumed in this type of transport process comes secondarily or indirectly from ATP. In other words, in these transporters, the flow of the substrate that is being translocated up its electrochemical gradient is coupled to the flow of a second substrate down its electrochemical gradient; the gradient of this second substrate is maintained by a primary active transport mechanism, i.e. one that consumes metabolic energy directly derived from the hydrolysis of ATP. In the case of cation-coupled Cl^- cotransporters, the primary active transport mechanism that generates and maintains the Na^+ and K^+ gradients is the Na^+/K^+ pump, also known as the Na^+/K^+ATPase. For example, let us consider the Na^+-Cl^- cotransporter (NCC). The uphill movement of Cl^- carried out by this electroneutral cotransporter system is driven primarily by the energy stored in the Na^+ chemical potential gradient which, in turn, is maintained by the ATP-requiring Na^+/K^+ pump. The Na^+ that enters the cell is pumped back out by the Na^+/K^+ pump. Hence there is no net gain of intracellular Na^+. In essence, energy is directly invested into a primary active transport mechanism (the Na^+/K^+ pump) that is responsible for extruding Na^+ from the cell (in exchange for K^+) and thereby maintaining a low and constant intracellular Na^+ concentration that results in a steep Na^+ inward gradient. The Na^+-Cl^- cotransport mechanism can then convey the uphill movement of Cl^- energized by the downhill flow of Na^+.

V. ELECTRONEUTRAL Na^+-K^+-Cl^- COTRANSPORTERS

VA. Isoforms and Splice Variants: An Overview of their Functional Roles

The Na^+-K^+-Cl^- cotransporters (NKCCs) are a class of membrane proteins that mediate the coupled, electrically neutral movement of Na^+, K^+ and Cl^- ions across the membrane of many animal cells, in most cases with a stoichiometry of $1Na^+$:$1K^+$:$2Cl^-$ (Russell, 2000). Under normal physiological conditions, NKCCs work as active ("uphill") transport mechanisms for accumulating Cl^- in cells. NKCCs maintain $[Cl^-]_i$ at levels above the predicted electrochemical equilibrium, generating an outward Cl^- gradient across the plasma membranes of many cell types. The higher than equilibrium $[Cl^-]_i$ is used in multifarious functions, depending on the cell type in which NKCCs are expressed. Some examples of these functions are given below and in Section VE.

Two distinct but highly homologous isoforms of the Na^+-K^+-Cl^- cotransporter proteins (NKCC1 and NKCC2) have been identified by cDNA cloning and functional expression (Delpire et al., 1994; Gamba et al., 1994; Payne and Forbush, 1994, 1995; Xu et al., 1994). The two genes encoding Na^+-K^+-Cl^- cotransporter are members of the SLC12A family and are known as SLC12A1 and SLC12A2. The SLC12A1 gene encodes NKCC2, often referred to as "the renal Na^+-K^+-Cl^- cotransporter" because it is predominantly expressed in the apical membrane of the epithelial cells that form the thick ascending limb of Henle's loop (TALH) and the macula densa. The SLC12A2 gene encodes the ubiquitously expressed NKCC1, a cotransporter that is found in nearly all cell types, whether epithelial or not. In the vast majority of secretory epithelial cells, NKCC1 expression is restricted to the basolateral membrane, together with the Na^+/K^+-ATPase (Haas and Forbush, 2000), as shown in Fig. 15.14A. So far the definitive exception is the choroid plexus epithelium where both NKCC1 and the Na^+/K^+ ATPase reside in the apical membrane (Wu et al., 1998), as depicted in Fig. 15.17. A similar case appears to be that of the retinal pigment epithelium, where the Na^+/K^+-ATPase is also located in the apical membrane (Gundersen et al., 1991) together with a Na^+, K^+, $2Cl^-$ mechanism that most likely is NKCC1 (Strauss, 2005). However, the evidence comes from functional studies and the molecular identity and exact location of this NKCC have not been established.

The high $[Cl^-]_i$ maintained by NKCC1 is used in polarized epithelial cells to promote net salt and water transport (Haas and Forbush, 2000). For instance, in salivary glands, NKCC1 is the major Cl^- uptake mechanism across the basolateral membrane of acinar cells and is critical for driving saliva secretion in vivo. Mice with targeted disruption of the *Slc12a2* gene encoding NKCC1 exhibit a dramatic reduction (>60%) in the volume of saliva secreted in response to a muscarinic agonist, the primary in situ salivation signal (Evans et al., 2000).

Besides epithelial cells, NKCC1 is expressed in many non-polarized cells, such as neurons. By virtue of the outward Cl^- gradient that NKCC1 generates and maintains, it makes possible the depolarizing action of neurotransmitters that open Cl^- channels, such as GABA and glycine, or second messengers such as Ca^{2+}, that open Ca^{2+}-activated Cl^- channels. For instance, the GABA-induced depolarizations made possible by NKCC1 in the

intraspinal terminals of primary sensory neurons constitute the basis for the phenomenon of presynaptic inhibition in the spinal cord (Alvarez-Leefmans et al., 1998; Alvarez-Leefmans, 2009), as illustrated in Fig. 15.15 and discussed below in more detail (Section VE). This GABAergic presynaptic control is a crucial mechanism in the gating of afferent flow of information of various sensory modalities, including proprioception and pain, into the spinal cord (Rudomin and Schmidt, 1999; Willis, 1999, 2006). NKCC1 is also involved in sensory transduction. Two well documented examples that are discussed below (Section VE) are the inner ear and the olfactory sensory neurons.

NKCCs play key roles in cell volume regulation and maintenance. There is evidence that in some cell types NKCCs function to offset osmotically induced cell shrinkage by mediating the net influx of ions and water (Russell, 2009). In addition, recent evidence demonstrates that NKCC1 serves to maintain cell volume under euvolemic conditions (Rocha-Gonzalez et al., 2008) and that, in addition to ions, it cotransports water (Hamann et al., 2010). NKCC1 function is also important in cell cycle and cell division (Russell, 2009). Overexpression of the NKCC1 cotransporter gene has been shown to induce cell proliferation and phenotypic transformation in mouse fibroblasts (Panet et al., 2000). NKCC1 also functions as a K^+ uptake mechanism, thereby contributing to the maintenance of $[K^+]_i$ at constant levels. It has also been proposed that NKCC1 works as an extracellular K^+ buffer, keeping $[K^+]_o$ constant, thereby preventing K^+ accumulation in the extracellular space (Walz, 1992; Wu et al., 1998; Alvarez-Leefmans et al., 2001; Lytle, 2003; Kristensen and Juel, 2010).

The introduction of knockout mice models in biomedical research has greatly advanced our understanding of the function of cation-chloride-cotransporters and many other proteins. Knockout mice are transgenic animals that contain a modification in a specific gene that makes the gene product (i.e. the protein) non-functional. The functional roles of various members of the SLC12A gene/protein family have been studied using knockout mice models (Garbarini and Delpire, 2009) or animals or humans with mutations in specific SLC12A genes. NKCC1 knockout mice exhibit several abnormalities. The most salient are: deafness, imbalance, hypotension, increased nociceptive threshold suggesting NKCC1 involvement in pain perception, severe salivation impairment and male infertility (Delpire et al., 1999; Flagella et al., 1999; Evans et al., 2000). So far there are no known human phenotypes of NKCC1 gene abnormalities.

The SLC12A1 gene encodes NKCC2 which, as mentioned above, is predominantly expressed in kidney, specifically in the apical membrane and in subapical vesicles of the epithelial cells of both the thick ascending limb of the loop of Henle (TALH) and the macula densa (Nielsen et al., 1998). NKCC2-dependent salt transport constitutes the major apical entry pathway for transepithelial salt reabsorption in the TALH; 80% of the NaCl uptake across the apical membrane of TALH cells is mediated by NKCC2 (Castrop and Schnermann, 2008). To achieve net salt absorption, electroneutral cotransport of Na^+, K^+ and $2Cl^-$ via NKCC2 is complemented by recycling of K^+ via apical K^+ channels (the so called ROMK), efflux of Cl^- via basolateral Cl^- channels and basolateral extrusion of Na^+ by the Na^+/K^+-ATPase which, in addition, generates the inward Na^+ gradient necessary to energize the cotransport (see Fig. 15.14B). Pharmacological blockade of NKCC2 by loop diuretics like bumetanide results in marked natriuresis, diuresis and decrease in blood pressure. This is the rationale for using loop diuretics in the treatment of high blood pressure.

Besides effecting transcellular absorption of Na^+ and Cl^- by the medullary and cortical TALH, NKCC2 plays a secondary role in the paracellular transport of Na^+, Ca^{2+} and Mg^{2+} by this nephron segment (Gamba and Friedman, 2009). The TALH also functions in renal acid secretion given that NH_4^+ competes with K^+ at its binding site on the NKCC2 (Good, 1994; Weiner and Verlander, 2011). The NH_4^+ generated by the renal proximal tubule is thus reabsorbed from the tubule lumen in the TALH and excreted from the renal interstitium by more distal nephron segments.

Besides its function in TALH salt retrieval, NKCC2-mediated transport constitutes the first step in the tubulovascular signaling pathway between macula densa cells in the juxtaglomerular region with the afferent arteriole. NKCC2 is located in the apical membrane of macula densa cells, a specialized group of tubular cells situated at the point of apposition of renal tubules with their parent glomeruli. Macula densa cells are modified epithelial cells that sense luminal Na^+ and Cl^- concentrations and generate paracrine chemical signals to the glomerular vascular elements. Thus, these cells control two important physiological processes: tubuloglomerular feedback and tubular regulation of renin release. The tubuloglomerular feedback mechanism plays a crucial role in regulating glomerular filtration rate and blood flow. An increase in luminal Na^+ and Cl^- concentrations at the macula densa decreases glomerular filtration by inducing constriction of the afferent renal arteriole. Increases in luminal Na^+ and Cl^- concentration at the macula densa also inhibit renin release from juxtaglomerular cells in the afferent arteriole. Thus NKCC2 plays a central role in the regulation of body fluid volume and osmolarity (Bell et al., 2009; Peti-Peterdi and Harris, 2010).

Although NKCC2 is encoded by a single gene, differential splicing results in the generation of several alternative transcripts. Specifically, three full length NKCC2 splice variants (NKCC2A, NKCC2B and NKCC2F) and three variants with truncated carboxyl termini have been described. They differ in their location along the TALH and the macula densa, and have different kinetic properties.

Analysis of the molecular and functional properties of individual splice variants is beyond the scope of this chapter. References on this subject can be found in excellent reviews (Gamba, 2005, 2009a; Gamba and Friedman, 2009) and in studies reported by Castrop's group (Oppermann et al., 2006, 2007; Castrop and Schnermann, 2008; Carota et al., 2010).

Inactivating homozygous mutations of the human NKCC2 gene product are the cause of Bartter's disease. The characteristic clinical picture includes a salt-wasting state with hypotension, metabolic alkalosis with hypokalemia, hypercalciuria and secondary aldosteronism. The vital function of NKCC2 proteins is also manifest in various knockout mice models. Targeted disruption of the promoter and the first three exons of mouse NKCC2 gene results in a full NKCC2 knockout with a phenotype sharing many similarities to Bartter's syndrome (Takahashi et al., 2000).

VB. Basic Functional Features of the Na^+-K^+-Cl^- Cotransporters

Four functional features define the NKCCs:

1. Ion translocation by the NKCCs requires the simultaneous presence of all three ions (Na^+, K^+ and Cl^-) on the same side of the membrane
2. The cotransport process is electroneutral; in vertebrate cells the stoichiometry is $1Na^+{:}1K^+{:}2Cl^-$ in nearly all cases (Lytle, 2003)
3. The transporter can work in forward and backward modes, i.e. net transport may occur into or out of the cells, the magnitude and direction of this transport being determined by the sum of the chemical potential gradients of the transported ions (Lytle et al., 1998)
4. Transport is inhibited by the so-called loop diuretics derived from 5-sulfamoyl benzoic acid, which include furosemide, bumetanide, and benzmetanide, as shown in Fig. 15.11 (O'Grady et al., 1987b; Hannaert et al., 2002).

VB1. Absolute Requirement for All Three Ions on the Same Side of the Membrane

NKCC-mediated fluxes of all three ions require the presence of the other two ions on the side of the membrane from which the flux originates (termed the *cis*-side). This property has been definitely proved by measuring individual fluxes of Na^+, K^+ and Cl^- and looking at their interdependence. Perhaps the most stringent test for this coupling of ion fluxes has been carried out in internally dialyzed squid giant axons. This preparation has the unique advantage of permitting the simultaneous control of the composition of the intracellular as well as the extracellular milieu while measuring unidirectional fluxes. Using this preparation Russell and his coworkers have demonstrated the absolute requirement for the *cis*-side presence of all three ions both for unidirectional influx and efflux (Russell, 2000). Each of the three co-ions was systematically removed while measuring the bumetanide-sensitive influx of the other two, using a double-label flux approach. This is illustrated in Fig. 15.6A, which shows the effects on ^{36}Cl (yellow dots) and ^{24}Na (green squares) influx when an axon was sequentially superfused with external solutions without K^+ (0 K^+), with K^+ (10 mM) and, finally, with K^+ (10 mM) plus bumetanide (10 μM). Clearly, the presence of extracellular K^+ increased the influx of both Cl^- (by $\approx 21\ pmol\cdot cm^{-2}\ s^{-1}$) and Na^+ (by $\approx 14\ pmol\cdot cm^{-2}\ s^{-1}$) and these increases were reversed by blocking the cotransporter with bumetanide. Figure 15.6 shows a similar protocol applied to examine the external Na^+ (Fig. 15.6B) and Cl^- (Fig. 15.6C) requirement. Note that in each case, the increase in the influx of the two co-ions caused by supplying the third one is reversed by bumetanide treatment.

The absolute requirement for the *cis*-side presence of Na^+, K^+ and Cl^- for the uphill accumulation of Cl^- mediated by NKCC was first demonstrated in vertebrate cells using different methodologies. Examples include Ehrlich ascites tumor cells (Geck et al., 1980), Madin-Darby canine kidney (MDCK) cell line (McRoberts et al., 1982), duck red cells (Haas et al., 1982), frog and rat dorsal root ganglion (DRG) neurons (Alvarez-Leefmans et al., 1988; Rocha-Gonzalez et al., 2008), immature rat neocortical neurons (Achilles et al., 2007) and other cell types (Russell, 2000). In frog sensory neurons, measurements were made using Cl^--selective intracellular microelectrodes. Measurements of changes in intracellular Cl^- activity (a^i_{Cl}) with intracellular microelectrodes reflect net Cl^- fluxes occurring through the plasma membrane. Figure 15.7 shows an example of one experiment in which the cell body of a single neuron was penetrated with a double-barreled microelectrode (inset), one barrel containing a liquid anion exchanger (the Cl^--sensitive barrel) and the other a reference electrolyte to measure E_m. The advantages of this method are obvious; it is possible to measure simultaneously intracellular a^i_{Cl} and E_m in single cells. Moreover, in contrast with methods that measure total $[Cl^-]_i$, which includes free-plus-bound or sequestered Cl^-, the microelectrodes give a measurement of free Cl^- in the cytosolic space (Alvarez-Leefmans et al., 1990). The dependence on extracellular Na^+ and K^+ of the bumetanide-sensitive active accumulation of Cl^- was explored in these cells. To this end, the effects of Na^+- or K^+-free isosmotic solutions on a^i_{Cl} were studied in the steady state and during the active Cl^- reaccumulation following exposure to Cl^--free solutions. A typical result showing the effects of external Na^+ removal on a^i_{Cl} is shown in Fig. 15.7. The basal a^i_{Cl} (upper trace) and E_m (lower trace) were recorded in the standard frog Ringer's

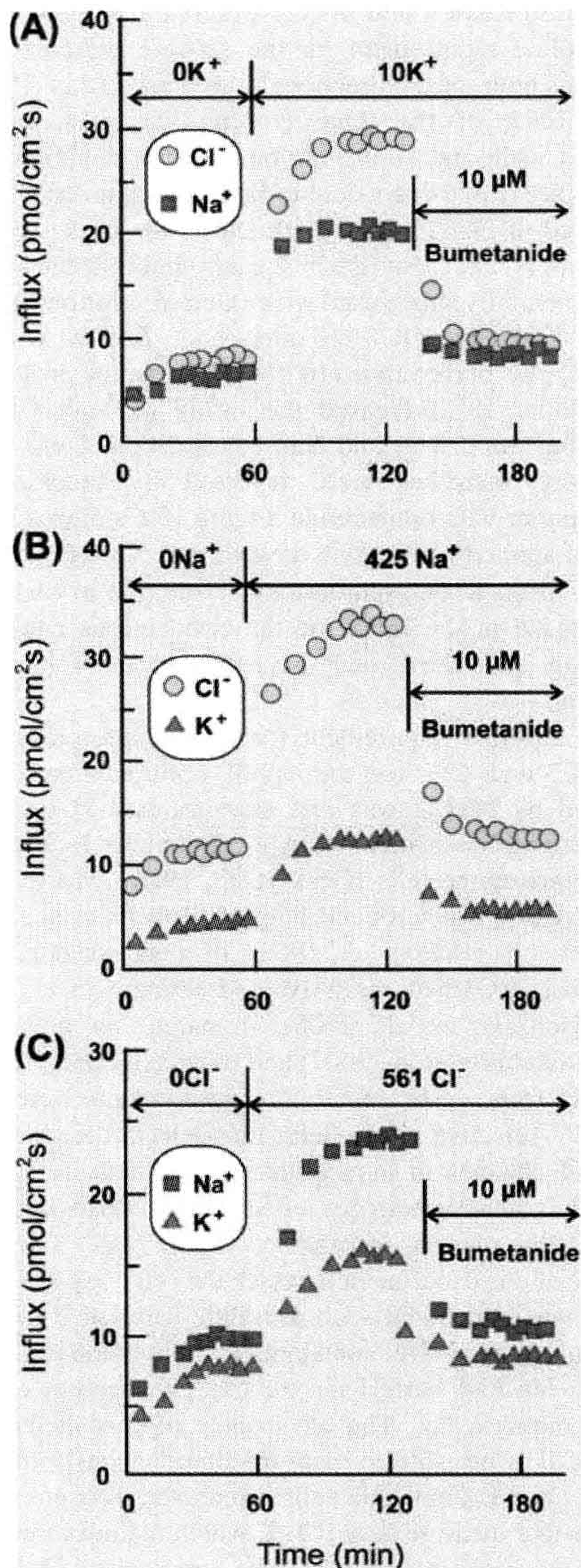


FIGURE 15.6 Dependence of cotransporter influxes of Na^+, K^+ and Cl^- on simultaneous presence of all three ions in external fluid. Experiments were carried out on internally dialyzed squid axons. Internal fluid in all cases contained the following (in mM): 400 K^+, 0 Na^+, 0 Cl^-, 8 Mg^{2+} and 4 ATP. Ouabain and tetrodotoxin were present to block the Na^+/K^+ pump and Na^+ channels, respectively. (A) Effect of external K^+ on $^{24}Na^+$ and $^{36}Cl^-$ influxes. After a control period (0 K^+) in which the external K^+ was replaced with N-methyl-D-glucammonium (NMDG), 10 mM K^+ was applied and influxes of both $^{24}Na^+$ (green squares) and $^{36}Cl^-$ (yellow circles) increased. Finally, bumetanide (10 μM) was added and both influxes decreased to levels similar to those seen in the absence of external K^+. (B) Effect of external Na^+ on $^{42}K^+$ (blue triangles) and $^{36}Cl^-$ (yellow circles) influxes. After a control period in which the external Na^+ was removed and replaced with NMDG (0 Na^+), 425 mM Na^+ was applied, leading to increases in both $^{42}K^+$ and $^{36}Cl^-$ influxes. Subsequent application of bumetanide caused influxes to decrease to values close to those observed in 0 Na^+. (C) Effect of external Cl^- on $^{42}K^+$ (blue triangles) and $^{24}Na^+$ (green squares) influxes. In the control condition (0 Cl^-), gluconate substituted for Cl^-. Note that upon admission of the external solution containing 561 mM Cl^-, both $^{42}K^+$ and $^{24}Na^+$ increased. Subsequent application of bumetanide caused influxes to decrease to levels near those observed in the absence of external Cl^-. *(Adapted from Russell, 2000.)*

solution (FR) for about 3 min after impalement. The initial E_m was ≈ -50 mV and a^i_{Cl} was 25 mM. The latter value was twice the a^i_{Cl} predicted for an equilibrium distribution according to Equation 15.3. It is important to mention that the measured a^i_{Cl} is equivalent to an intracellular [Cl^-] of ≈ 33 mM, considering 0.76 as the intracellular activity coefficient. Then, the cell was exposed for about 3.5 min to a solution in which Na^+ was eliminated (0 Na^+) and replaced mole by mole with the impermeant cation N-methyl-D-glucammonium, keeping a^o_{Cl} at the same level as in the FR solution. This resulted in an immediate decrease in a^i_{Cl} accompanied by a membrane hyperpolarization. The latter was due to suppression of a resting Na^+ conductance. Both E_m and a^i_{Cl} returned to control levels upon readmission of FR solution to the bath. Observations like these indicate that external Na^+ is required to maintain internal Cl^- above electrochemical equilibrium in the resting state.

To explore if external Na^+ is required for the active reaccumulation of Cl^- after intracellular Cl^- depletion, external Cl^- was removed (0 Cl^-) and replaced mole by mole with the impermeant anion gluconate, keeping the other ions as in control FR. This also resulted in a decrease in a^i_{Cl}. The reaccumulation of Cl^- was then observed in the Na^+-free solution containing normal Cl^- (0 Na^+) and, finally, in standard FR. It was found that the rate of Cl^- reaccumulation in the Na^+-free solution was slowed to about 15% of its value in standard FR solution.

These observations indicate that extracellular Na^+ is required for active reaccumulation of Cl^- following cell Cl^- depletion. The concurrent changes in E_m and calculated values for E_{Cl} in the same experiment are shown in Fig. 15.8A, which illustrates more clearly the effects of external Na^+ on the distribution of Cl^- across the cell membrane. External Na^+ removal reduced the basal intracellular accumulation of Cl^-, as reflected by the reduction in the difference between E_m (blue filled circles) and E_{Cl} (red filled circles). In addition, Na^+ removal after Cl^- depletion impeded the reaccumulation of Cl^- even though E_{Cl} was now more negative than E_m, a situation in which the direction of the Cl^- gradient was reversed, favoring Cl^- influx. Therefore, it can be concluded that external Na^+ is required to accumulate Cl^- above equilibrium and for keeping it out of equilibrium in basal conditions.

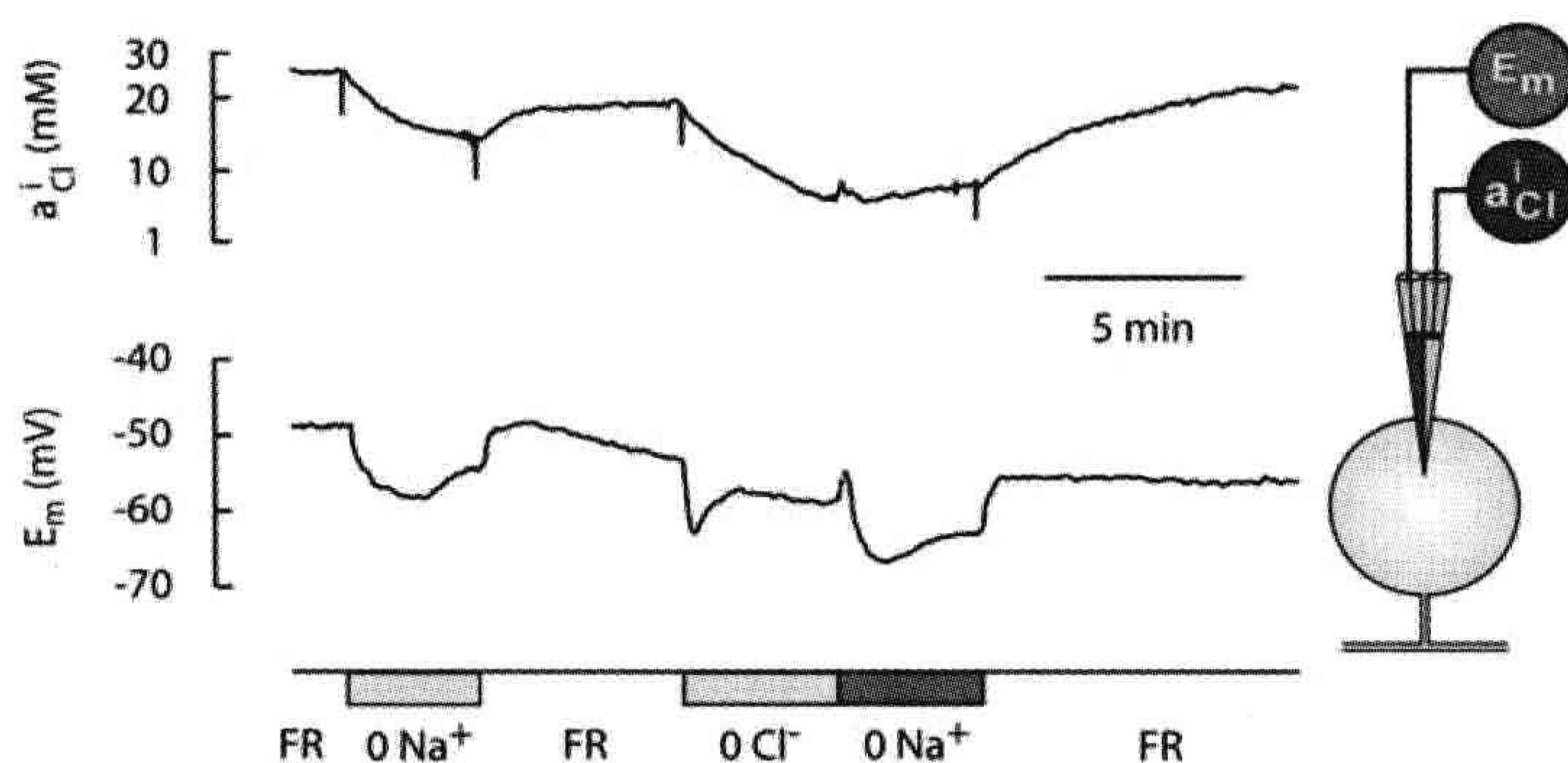


FIGURE 15.7 Effect of external Na^+ removal on intracellular Cl^- activity (a^i_{Cl}) and on membrane potential (E_m) in a frog dorsal root ganglion neuron. The recording was made with a double-barreled microelectrode, one barrel sensing E_m and the other a^i_{Cl}. Inset (right), diagram of a double-barreled electrode where a^i_{Cl} denotes the Cl^--selective barrel filled with a liquid anion exchanger which senses a^i_{Cl}. When the microelectrode is inside the cell, the a^i_{Cl} barrel records the sum of a potential proportional to a^i_{Cl} plus E_m. To obtain a^i_{Cl}, the potential on the E_m barrel is subtracted from that recorded by the Cl^--sensitive barrel giving a differential voltage signal that is proportional to a^i_{Cl} (top trace). During the times indicated by the bottom bars, the bathing solution was changed from frog Ringer (FR) to a Na^+-free solution (0 Na^+), in which external Na^+ was replaced with N-methyl-D-glucammonium, and back to FR. Note that removal of external Na^+ led to a decrease in a^i_{Cl}. The cell was then exposed to Cl^--free solution (0 Cl^-), which also produced a decrease in a^i_{Cl}. Then the reaccumulation of internal Cl^- was monitored in the absence of external Na^+ (0 Na^+) and in FR, i.e. in the presence of external Na^+. Note that in the absence of external Na^+, active Cl^- uptake was inhibited. *(Modified from Alvarez-Leefmans et al., 1988.)*

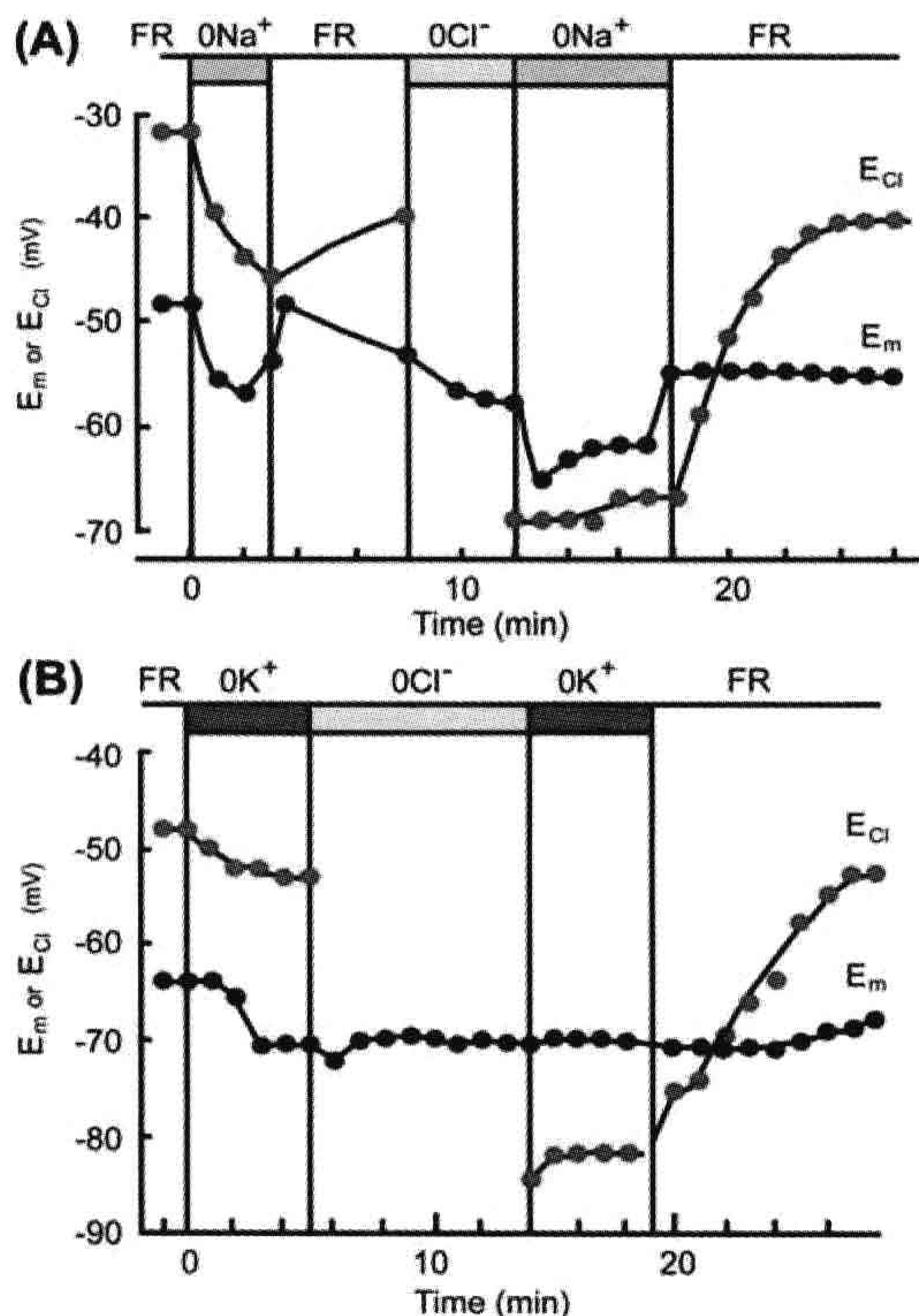


FIGURE 15.8 (A) Effects of external Na^+ on the intracellular accumulation of Cl^-. Membrane potential (E_m, blue dots) and the calculated Cl^- equilibrium potential (E_{Cl}, red dots) from measured a^i_{Cl} and a^o_{Cl} are plotted on the same time scale using data from the experiment illustrated in Fig. 15.7. (B) Effects of external K^+ on the intracellular accumulation of Cl^-. Symbols as in (A). Data were obtained from an experiment similar to that shown in Fig. 15.7 but in which external K^+ was removed instead of external Na^+. *(Modified from Alvarez-Leefmans et al., 1988.)*

The effects of extracellular K^+ on a^i_{Cl} were similar to those observed for Na^+. Figure 15.8B shows a plot of E_m and E_{Cl} from an experiment similar to that shown in Fig. 15.7 but in which external K^+, instead of external Na^+, was removed during the periods indicated. Removal of external K^+ was accompanied by an immediate reduction in a^i_{Cl} revealed in the graph by the changes in E_{Cl} toward more negative values. In the absence of extracellular K^+ the reaccumulation of Cl^- in standard FR solution was impeded. Summarizing, the steady-state a^i_{Cl} levels in DRG cells depend on the simultaneous presence of extracellular Na^+ and K^+. Similarly, the active reaccumulation of Cl^- after intracellular Cl^- depletion requires the simultaneous presence of Na^+ and K^+ in the extracellular medium.

Similar results to those described above for frog sensory neurons have been recently obtained in rat DRG neurons, which are also characteristically endowed with NKCC1. Mammalian neurons are too delicate to stand penetration with microelectrodes and thus a non-invasive procedure to measure changes in $[Cl^-]_i$ is needed. These non-invasive procedures to measure changes in $[Cl^-]_i$ use various types of fluorescent indicators, some of which are genetically engineered (Berglund et al., 2009; Verkman, 2009; Waseem et al., 2010). The strategy used in rat DRG neurons was to study the external ion requirements of native NKCC1 by measuring changes in $[Cl^-]_i$ using the fluorescent dye MQAE (Rocha-Gonzalez et al., 2008).

VB2. Electroneutral Cotransport Process: Stoichiometry of 1Na$^+$:1K$^+$:2Cl$^-$

Geck and coworkers (Geck et al., 1980; Geck and Heinz, 1986), working with Ehrlich ascites tumor cells, provided the first comprehensive evidence for the existence of the electrically neutral cotransport of Na^+, K^+ and Cl^- ions,

with a stoichiometry of $1Na^+:1K^+:2Cl^-$. A solidly documented exception is the squid axon cotransporter which has a stoichiometry of $2Na^+:1K^+:3Cl^-$ (Russell, 2000). This different stoichiometry probably reflects differences in molecular structure with respect to the vertebrate isoforms. Unfortunately, the squid isoform has not yet been cloned, so it is impossible to know what determines the difference. The $1Na^+:1K^+:2Cl^-$ stoichiometry has been found in many vertebrate cells (O'Grady et al., 1987a; Russell, 2000; Hoffmann, 2001; Lytle, 2003; Flatman, 2004; Gamba, 2005). However, some "atypical" stoichiometries have also been described in some vertebrate cells, as recently discussed (Delpire and Gagnon, 2011).

There is general agreement that the NKCC is electrically silent, which means that the overall transport process of Na^+, K^+ and Cl^- via the cotransporter is not driven by the transmembrane voltage, nor does the transport process directly generate a membrane current that may affect the transmembrane voltage. As pointed out by Russell (2000), the electrical silence of the NKCC is now well accepted by workers in the field, yet direct evidence for the assertion is surprisingly sparse. Electrical silence is often inferred from the apparent stoichiometry of the cotransport process, but arriving at this conclusion involves a somewhat circular argument.

Conclusive proof of electrical silence requires direct and simultaneous measurement of transmembrane potential and cotransporter mediated ion fluxes. There are only two reports in the literature fulfilling these requirements, one for the squid axon NKCC cotransporter (Russell, 1984) and one for amphibian dorsal root ganglion neurons (Alvarez-Leefmans et al., 1988). The latter is, so far, the only existing direct evidence for the electroneutrality of Cl^- transport through NKCC in a vertebrate cell. Figure 15.9 shows an example of one of these experiments in which a frog DRG cell was penetrated with a double-barreled microelectrode (inset). At the time indicated by the downward orange arrow, the cell was penetrated with the microelectrode and E_m stabilized at about −55 mV. The deflection in the differential signal (upper trace) at this time corresponded to an *apparent* intracellular Cl^- activity $(a^i_{Cl})_{app}$ of about 40 mM, which, after correction for background intracellular interference produced by other native intracellular anions on microelectrode response (Alvarez-Leefmans, 1990), gave an a^i_{Cl} of 30 mM. If Cl^- were passively distributed, a^i_{Cl} as predicted from Equation 15.3 should be only 10.2 mM. It is worth mentioning here that the ion-selective electrodes measure a^i_{Cl} and not $[Cl^-]_i$. Thus, for an activity coefficient of 0.76, the basal a^i_{Cl} of 30 mM is equivalent to a basal $[Cl^-]_i$ of ≈40 mM. Clearly, *intracellular Cl^- was almost three times the value expected for an equilibrium distribution.* E_{Cl} was −27 mV and the driving force for Cl^-, (E_m-E_{Cl}), was 28 mV. The red filled circles superimposed on the E_m trace (lower record in Fig. 15.9) correspond to the point by point values of E_{Cl} calculated using Equation 15.1. Removal of external Cl^- and its replacement with an impermeant anion (gluconate) led to a rapid decrease in $(a^i_{Cl})_{app}$, reaching a final steady-state level of ≈10 mM in about 10 min. The recovery of intracellular Cl^- started immediately after external Cl^- was restored. Note that the net Cl^- movements occurred without changes in E_m, i.e. they were electroneutral (Fig. 15.9 large gray arrow). The small rapid changes that can be observed in the E_m trace upon removal and readmission of external Cl^- were due to liquid junction potentials at the reference (bath) electrode. Subtraction of this liquid junction potential yielded the

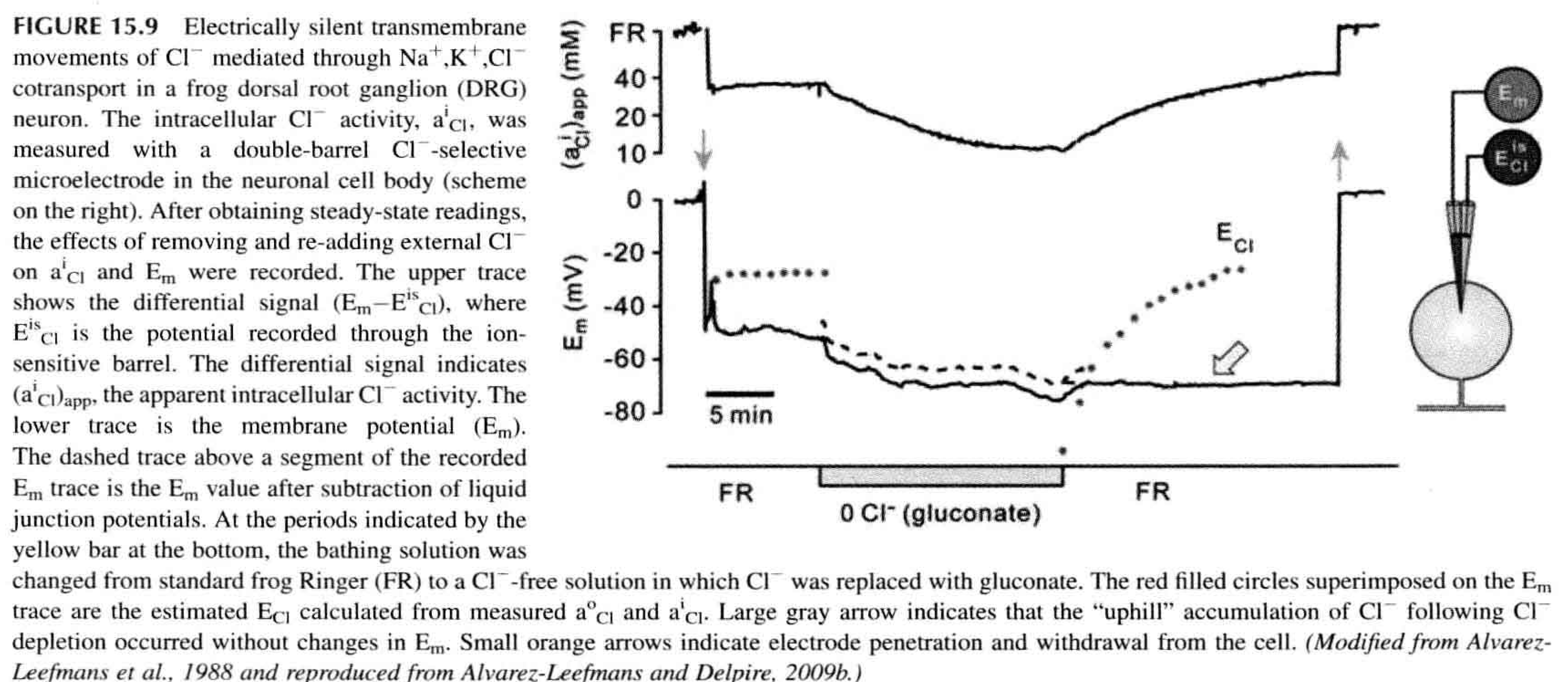


FIGURE 15.9 Electrically silent transmembrane movements of Cl^- mediated through Na^+,K^+,Cl^- cotransport in a frog dorsal root ganglion (DRG) neuron. The intracellular Cl^- activity, a^i_{Cl}, was measured with a double-barrel Cl^--selective microelectrode in the neuronal cell body (scheme on the right). After obtaining steady-state readings, the effects of removing and re-adding external Cl^- on a^i_{Cl} and E_m were recorded. The upper trace shows the differential signal $(E_m-E^{is}_{Cl})$, where E^{is}_{Cl} is the potential recorded through the ion-sensitive barrel. The differential signal indicates $(a^i_{Cl})_{app}$, the apparent intracellular Cl^- activity. The lower trace is the membrane potential (E_m). The dashed trace above a segment of the recorded E_m trace is the E_m value after subtraction of liquid junction potentials. At the periods indicated by the yellow bar at the bottom, the bathing solution was changed from standard frog Ringer (FR) to a Cl^--free solution in which Cl^- was replaced with gluconate. The red filled circles superimposed on the E_m trace are the estimated E_{Cl} calculated from measured a^o_{Cl} and a^i_{Cl}. Large gray arrow indicates that the "uphill" accumulation of Cl^- following Cl^- depletion occurred without changes in E_m. Small orange arrows indicate electrode penetration and withdrawal from the cell. *(Modified from Alvarez-Leefmans et al., 1988 and reproduced from Alvarez-Leefmans and Delpire, 2009b.)*

dashed trace superimposed on the recorded E_m trace. If Cl^- movements had occurred through an electrodiffusional pathway (i.e. channel-mediated) or through an electrogenic "carrier," E_m should have changed both upon Cl^- efflux and upon Cl^- influx. Clearly, that was not the case. Since the cell membrane of DRG neurons has a relatively low resting Cl^- permeability, the movements of Cl^- should have occurred through a non-electrodiffusional pathway, i.e. an electroneutral carrier mechanism. As already mentioned, the red circles superimposed on the E_m trace in Fig. 15.9 correspond to the calculated values of E_{Cl}. Note that on exposure to the Cl^--free Ringer's solution, the cell was depleted of Cl^- and, immediately after restoring the external Cl^-, E_{Cl} was transiently below E_m. However, during the recovery period in Ringer's solution, the movement of Cl^- occurred against its electrochemical potential difference across the cell membrane, i.e. uphill, without changes in E_m. Since the Cl^- fluxes were bumetanide-sensitive and required the simultaneous presence of external Na^+ and K^+, this was direct functional evidence for the presence of an active process for accumulation of Cl^- in DRG cells through an electroneutral membrane transport mechanism, i.e. an Na^+-$1K^+$-$2Cl^-$ cotransporter. The presence of NKCC protein in frog DRG cells was corroborated later on using immunolabeling and Western blot analyses (Alvarez-Leefmans et al., 2001). NKCC was also found in DRG cells of cat, rat and mouse (Plotkin et al., 1997; Sung et al., 2000; Alvarez-Leefmans et al., 2001).

VB3. The Magnitude and Direction of the Cotransport Process are Determined by the Sum of the Chemical Potential Gradients of the Transported Ions

We have seen that the transport process carried out by NKCC is electrically neutral and thus net cotransport neither affects nor is affected by the membrane potential. Consequently, the magnitude and direction of the driving force for net ion movement must be calculated from the *chemical*, rather than the *electrochemical* potential gradients of all the transported ions.

The NKCC is a secondary active transport mechanism and hence it is reversible, i.e. it mediates ion fluxes into or out of the cell, the net direction of cotransport depending on the overall net free energy (ΔG) of the system. If ΔG is negative, it means that the direction of the cotransport will be inward, i.e. favoring uptake. If ΔG is zero, the system is at equilibrium. Since NKCC is electroneutral and has a $1Na^+$:$1K^+$:$2Cl^-$ stoichiometry, ΔG is given by the following equation:

$$\Delta G = \Delta\mu_{Na,K,Cl} = \Delta\mu_{Na} + \Delta\mu_K + 2\Delta\mu_{Cl} \quad (15.11)$$

In other words, the driving force for the electroneutral $1Na^+$,$1K^+$,$2Cl^-$ cotransport ($\Delta\mu_{Na,K,Cl}$) is the sum of the chemical potential differences of Na^+ ($\Delta\mu_{Na}$) and K^+ ($\Delta\mu_K$) plus twice the Cl^- potential difference ($\Delta\mu_{Cl}$), since two Cl^- ions are translocated per cycle. From the definition of chemical potential for each of the ions involved, it follows:

$$\begin{aligned}\Delta G &= \Delta\mu_{Na,K,Cl} \\ &= RT\ln\frac{[Na^+]_i}{[Na^+]_o} + RT\ln\frac{[K^+]_i}{[K^+]_o} + 2RT\ln\frac{[Cl^-]_i}{[Cl^-]_o}\end{aligned} \quad (15.12)$$

Hence,

$$\Delta G = \Delta\mu_{Na,K,Cl} = RT\ln\frac{[Na^+]_i\,[K^+]_i\,[Cl^-]_i^2}{[Na^+]_o[K^+]_o[Cl^-]_o^2} \quad (15.13)$$

In most vertebrate cells, under physiological conditions and for a stoichiometry $1Na^+$:$1K^+$:$2Cl^-$, ΔG is always negative, therefore favoring net ion uptake. Russell has computed ΔG for a variety of vertebrate cells; it ranges from -0.71 KJ/mol in bovine aortic endothelial cells up to -8.86 KJ/mol in rabbit ventricular myocytes (Russell, 2000). ΔG has been estimated to be -1.29 KJ/mol and -2.8 KJ/mol in rat and frog DRG neurons, respectively (Russell, 2000; Rocha-Gonzalez et al., 2008). As pointed out by Lytle (2003), the rare exception may be red blood cells which, as discussed above, have an usually high $[Cl^-]_i$ (75–100 mM) reflecting their high anion permeability mediated by the anion exchanger protein AE1, which has translocation rates and characteristics similar to channels (Alper et al., 2008). The consequence of this high $[Cl^-]_i$ is that $\Delta\mu_{Na,K,Cl}$ is nearly 0. Indeed, in human, duck and ferret red blood cells under physiological conditions, $\Delta\mu_{Na,K,Cl}$ is nearly 0, leaving little if any driving force to run the cotransporter under basal conditions (Lytle, 2003). This means that relatively small variations in the chemical gradients of any of the transported ions can alter the direction of transport in these red blood cells.

The NKCC cotransport mechanism reaches thermodynamic equilibrium when $\Delta G = \Delta\mu_{Na,K,Cl} = 0$, i.e. when the product of the concentrations of Na^+ and K^+ times the square of the Cl^- concentration on one side of the membrane is matched by the product of these ions in the *trans* side:

$$[Na^+]_i\,[K^+]_i\,[Cl^-]_i^2 = [Na^+]_o\,[K^+]_o\,[Cl^-]_o^2 \quad (15.14)$$

Since the cotransporter is electroneutral, thermodynamic equilibrium will not be affected by E_m. Assuming for the sake of argument that Na^+,K^+,Cl^- cotransport is the only Cl^- transport system operating at steady state in a cell, that it has a $1Na^+$:$1K^+$:$2Cl^-$ stoichiometry and that there are no kinetic constraints, the predicted $[Cl^-]_i$ when the

cotransport reaches thermodynamic equilibrium is given by the following equation derived from Equation 15.14:

$$[Cl^-]_i = \sqrt{\frac{[Na^+]_o [K^+]_o [Cl^-]_o^2}{[Na^+]_i [K^+]_i}} \quad (15.15)$$

For example, consider the model cell shown in Fig. 15.10, an idealized neuron in which NKCC is the sole mechanism for active Cl^- transport. The $[Na^+]_i$ and $[K^+]_i$ are maintained at constant levels by the operation of the Na^+/K^+ pump. The cell has a resting E_m of −60 mV and relevant physiological ion concentrations (in mM) are: $[Na^+]_o = 132$; $[K^+]_o = 3$; $[Cl^-]_o = 113$; $[Na^+]_i = 10$ and $[K^+]_i = 120$. Under these conditions, when the cotransporter reaches thermodynamic equilibrium, *without any kinetic constraints* (e.g. phosphorylation or dephosphorylation of the cotransporter), the $[Cl^-]_i$ will be ≈65 mM and this would be the *maximal possible* $[Cl^-]_i$ under these conditions. Thus, we can conclude from the examples considered in Figs. 15.1 and 15.10 that if Cl^- were in electrochemical equilibrium, $[Cl^-]_i$ calculated from Equation 15.3 would be 12 mM, but if we add NKCC to the same cell (Fig. 15.10), assuming that the resting channel-mediated permeability to Cl^- is negligible, the $[Cl^-]_i$ can increase up to about five times above its equilibrium level, and E_{Cl} would now be ≈ −12 mV. Since E_m is kept constant, at −60 mV, opening of Cl^- channels, for example $GABA_A$-receptor-channels in the example considered, will produce an efflux of Cl^-. Since Cl^- is negatively charged, its electro-diffusional efflux produces an inward (depolarizing) current. However, most vertebrate cells endowed with NKCC do not have the high intracellular Cl^- level of the cell considered in this example (i.e. ≈65 mM). Why is that? Are there parallel mechanisms that prevent the NKCC from achieving thermodynamic equilibrium? The answer is yes. The first point to be considered is that, besides NKCC, other Cl^- transport systems, such as Cl^- channels, anion exchangers (Cl^-/HCO_3^-) and KCl cotransporters (KCCs) could and in fact do coexist in the same cell with NKCC. The final $[Cl^-]_i$ will be determined by the coordinated functional interaction between the various transporter systems present in the cell. For instance, in skeletal muscle, active Cl^- uptake via NKCC is "shunted" by a large Cl^- conductance, as shown in Fig. 15.2. In this case, the $[Cl^-]_i$ will be determined by a balance between the net Cl^- influx mediated by NKCC and the net Cl^- efflux occurring through Cl^- channels. Since the Cl^- leak through channels is larger than the net Cl^- influx brought up by NKCC, $[Cl^-]_i$ in skeletal muscle is very low, so low that E_{Cl} is close to E_m as discussed above in Section II. In addition to Cl^- channels, in most cells, NKCC coexists with KCC. Under physiological conditions, KCCs mediate net efflux of K^+ and Cl^- from cells, thus functioning as active Cl^- extruders (see Fig. 15.3). Hence NKCCs and KCCs have opposing roles; the former are Cl^- loaders and the latter are Cl^- extruders. Thus, KCCs may influence the levels of intracellular Cl^- just by counteracting Cl^--uptake mechanisms and vice versa. This interaction between two cotransporters working in opposite directions is ideally suited for achieving tight regulation of an intracellular ion, in this case Cl^- (and K^+). However, the result of these interactions is not just the simple algebraic sum of two fluxes having opposite direction; cotransporters are *kinetically* regulated by several mechanisms, notably by phosphorylation/dephosphorylation via a complex system of kinases, some of which are sensitive to $[Cl^-]$ (Flatman, 2004; Delpire and Gagnon, 2008; Gamba et al., 2009; Kahle et al., 2010).

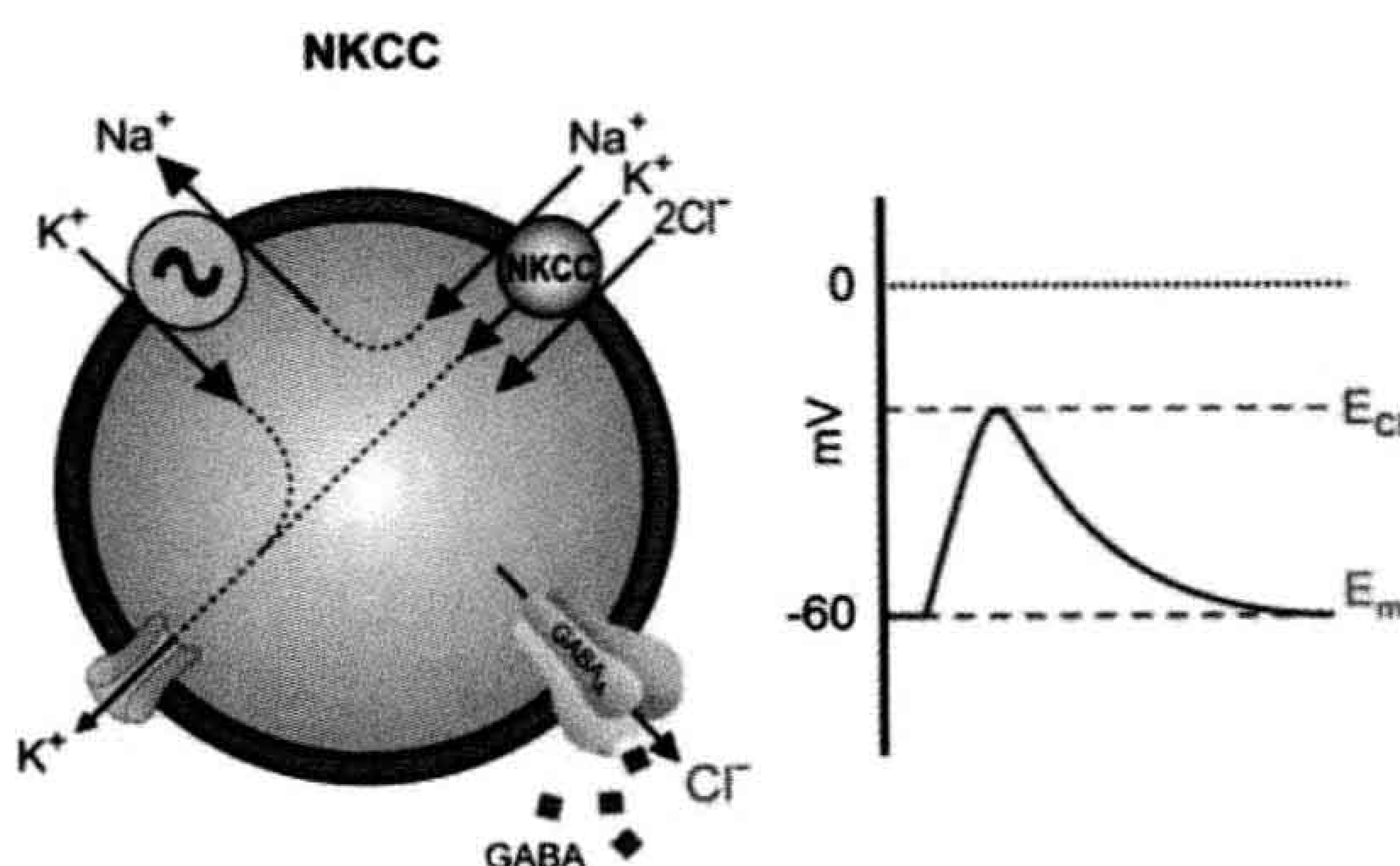


FIGURE 15.10 Model of a cell expressing $Na^+,K^+,2Cl^-$cotransport (NKCC) and a $GABA_A$-gated anion channel. The energy stored mainly in the inward Na^+ chemical gradient maintained by the Na^+/K^+ ATPase is used by NKCC for the active Cl^- uptake process. The Na^+/K^+ ATPase expels the Na^+ entering through NKCC. The K^+ entering through NKCC diffuses out of the cell via K^+ channels. Cl^- is accumulated above electrochemical equilibrium, shifting E_{Cl} to values more positive than E_m. Opening of GABA-gated anion channels produces a membrane depolarization (blue trace) due to Cl^- efflux.

The consequences of functional interactions between KCCs and NKCCs have been experimentally addressed using human embryonic kidney cells (HEK-293), an epithelial cell line in which the ubiquitous isoform of the KCCs, KCC1, was overexpressed by transfection (Gillen and Forbush, 1999). Overexpression of KCC1 not only led to a decrease in $[Cl^-]_i$ but also to a significant increase in endogenous NKCC activity. Indeed, the reduction of $[Cl^-]_i$ produced by KCC1 was responsible for NKCC activation. A steep relationship between cell Cl^- and NKCC activity was found over the physiological ranges supporting a primary role for $[Cl^-]_i$ in activation of NKCC. This means that *NKCC activity is determined not only by the thermodynamic driving force but also by kinetic constraints.* In this case, internal Cl^- acts as a "kinetic brake" on the ion translocating capacity of NKCC. Thus, kinetic constraints can inactivate the cotransporter, even in the presence of a substantial thermodynamic driving force. The experimental results of Gillen and Forbush in transfected HEK-293 cells, are in agreement with previous observations showing that lowering $[Cl^-]_i$ activates NKCC, and increasing $[Cl^-]_i$ inhibits its activity. In other words, intracellular Cl^- acts as

a negative feedback signal controlling the transport activity of NKCC. It was the Danish physiologist Hans Ussing (1911–2000) who first proposed that NKCC might be activated by a fall in $[Cl^-]_i$. Working with frog skin epithelium, Ussing realized that when the cells lose Cl^- NKCC restores it back to its initial higher than equilibrium level, but that the cotransporter "...seems to be virtually dormant unless the cells have lost chloride" (Ussing, 1982). The definitive proof came from studies in the internally dialyzed squid axon preparation, in which it was shown that elevation of $[Cl^-]_i$ inhibits bumetanide-sensitive unidirectional fluxes of all three cotransported ions in both the influx and efflux direction (Russell, 2000, 2009). The negative-feedback system in which intracellular Cl^- regulates its own influx via NKCC has been recently demonstrated for the endogenous NKCC1 protein of a mammalian cell, namely rat DRG neurons (Rocha-Gonzalez et al., 2008). As mentioned above, the mechanisms by which intracellular Cl^- regulate NKCCs involve a complex system of kinases (see below). Regulation of NKCCs and other members of the SLC12A family is an extensive topic that is beyond the scope of the present chapter.

VB4. Loop Diuretics Derived From 5-sulfamoylbenzoic Acid Inhibit NKCCs

Diuretics derived from 5-sulfamoylbenzoic acid are organic anions that reversibly inhibit NKCCs in a variety of preparations by a concentration-dependent mechanism, with a half inhibitory constant (IC_{50}) ranging from ≈ 0.1 μM to 8.7 μM in mammalian cells (Russell, 2000). These compounds are members of the so-called *loop diuretics* because they inhibit Na^+ and Cl^- reabsorption by the thick ascending limb of the loop of Henle (TALH) by blocking the NKCC isoform located in the apical membrane of these epithelial cells, i.e. NKCC2, thereby promoting diuresis (increased formation and excretion of urine). However, 5-sulfamoylbenzoic acid derivatives also block NKCC1. Native NKCC2 is a very active transport mechanism under basal conditions, permanently reabsorbing Na^+ and Cl^-. In contrast, basal activity of native NKCC1 of extra-renal non-epithelial cells is relatively small; the cotransporter is "dormant" which means that *net* ion fluxes in basal conditions are negligible. NKCC1 can be activated by either cell shrinkage produced by exposure to hypertonic solutions ("anisosmotic shrinkage") and or by decreases in $[Cl^-]_i$. For instance, decreases in $[Cl^-]_i$ leading to activation of NKCC1 can be accompanied by "isosmotic shrinkage," like that produced by removal of external Cl^- in isosmotic media. Intracellular $[Cl^-]$ can also decrease by activation of Cl^- conductances, producing relatively small changes in cell volume, e.g. the decrease in $[Cl^-]_i$ produced by secretagogues in several epithelia. When measuring the inhibitory effect of 5-sulfamoylbenzoic acid derivatives like bumetanide, piretanide and furosemide on the native NKCC proteins, *activated* NKCC1 has the same sensitivity to these compounds as *basal* NKCC2 (Hannaert et al., 2002).

The relative efficacy (IC_{50} values) and order of potency for blocking NKCC1 was systematically investigated in the intestinal epithelium of winter flounder (O'Grady et al., 1987b). As shown in Fig. 15.11B, the order of potency of 5-sulfamoylbenzoic acid derivatives to block NKCC1 was: benzmetanide > bumetanide > piretanide > furosemide > amino-piretanide. This order of potency is similar to that determined for NKCC2 in TALH from rabbit kidney (Schlatter et al., 1983) and in other mammalian cells like human fibroblasts and dog trachea that express NKCC1 (O'Grady et al., 1987b).

Bumetanide and furosemide are among the most commonly prescribed drugs worldwide. They are clinically used to treat moderate hypertension and edema associated with congestive heart failure, hepatic and renal disease, including nephrotic syndrome (Shankar and Brater, 2003). Research during the last decade shows that NKCC1 is involved in many more functions and pathologies than previously thought, depending on the tissues in which it is expressed. Thus it is not surprising that NKCC1 has emerged as a potential therapeutic drug target for bumetanide and other loop diuretics in conditions as diverse as inflammatory pain given its analgesic effects (Granados-Soto et al., 2005), neonatal seizures given that it blocks this abnormal brain electrical activity (Kahle and Staley, 2008; Dzhala et al., 2010), idiopathic intracranial hypertension (Dzhala et al., 2010), ischemic brain edema (Kahle et al., 2009) and glioma cell invasion (Haas and Sontheimer, 2010), to mention the most salient.

Besides their clinical importance, loop diuretics, particularly bumetanide, have played a crucial role in the identification of the NKCC proteins and in their subsequent cloning and functional characterization. Bumetanide is by far the most commonly used loop diuretic for research on NKCCs. As mentioned above, bumetanide is not a specific blocker of NKCC1; it also blocks NKCC2 at similar concentrations under physiological conditions in endogenous/native cotransporters. Bumetanide inhibits *basal* NKCC2 activity in medullary TALH tubules isolated from rat kidney with a half inhibitory constant (IC_{50}) of 0.33 μM and, with the same IC_{50}, it inhibits *activated* NKCC1 from either rat erythrocytes or rat thymocytes (Hannaert et al., 2002). In these experiments, NKCC1 was activated by exposing the cells to hypertonic solutions. An increase in NKCC2/NKCC1 selectivity was found when comparing diuretic sensitivity of *basal* NKCC2 versus *basal* NKCC1. For the specific case of bumetanide, the IC_{50} for *basal* NKCC1 goes up from 0.33 μM (activated state) to 2.5 μM in rat erythrocytes and 2.2 μM in rat thymocytes. In other mammalian cells expressing native/endogenous NKCC1, bumetanide inhibits the cotransporter with an IC_{50} ranging from 0.1 μM in human fibroblasts (HSWP) to

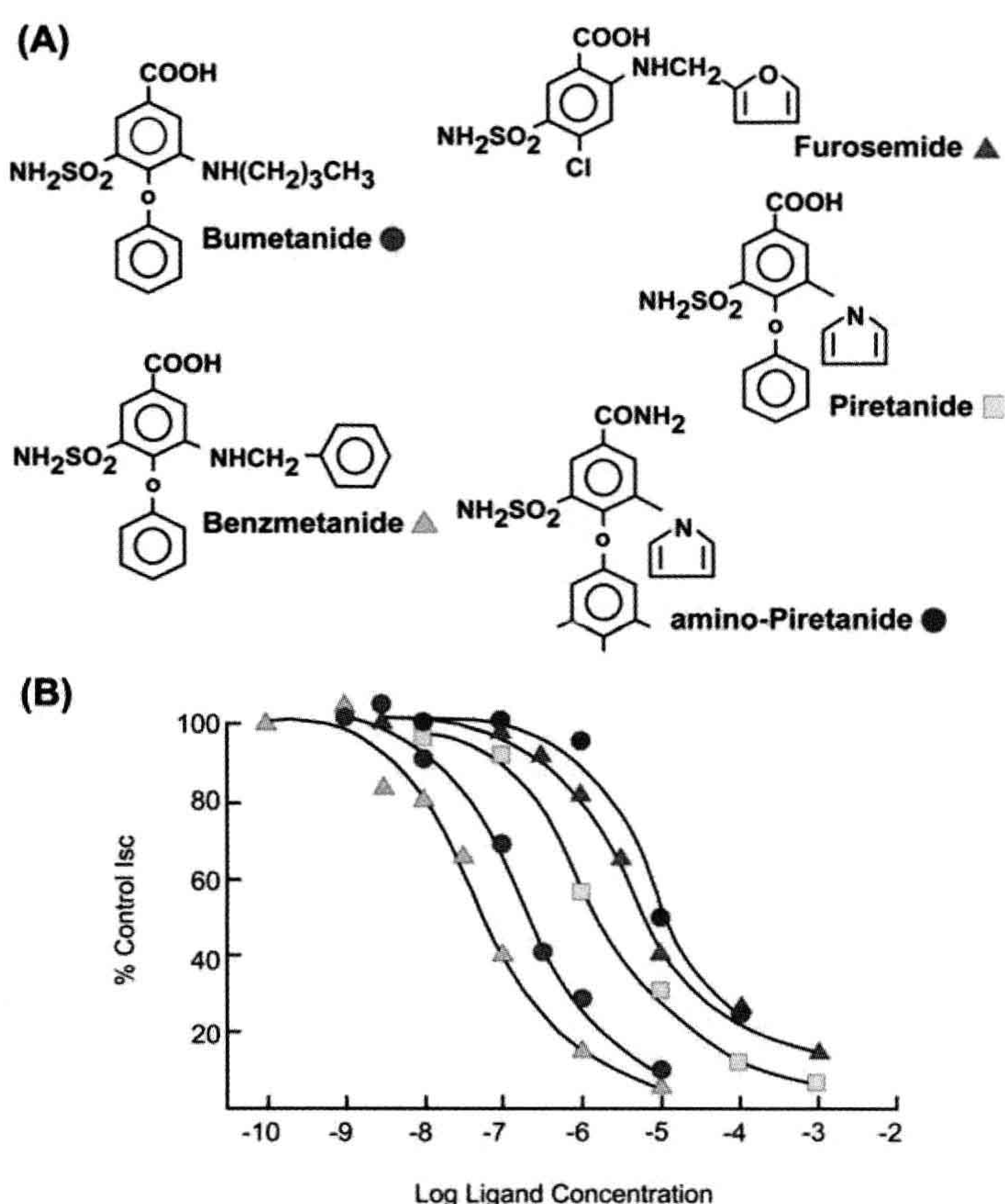


FIGURE 15.11 (A) Structures of several 5-sulfamoyl benzoic acid derivatives that affect NKCC in flounder intestine. (B) Dose–response curves for these derivatives on epithelial short-circuit current (Isc) measured in flounder intestine. Order of potency is benzmetanide (5×10^{-8} M; $n = 4$), bumetanide (3×10^{-7} M; $n = 7$), piretanide (3×10^{-6} M; $n = 4$), furosemide (7×10^{-6} M; $n = 4$), amino-piretanide (1×10^{-5} M; $n = 4$). *(Modified from O'Grady et al., 1987b.)*

8.7 μM in Ehrlich ascites tumor cells, the cells in which NKCC was first discovered (Hoffmann et al., 1986). The bumetanide IC_{50} of *activated* NKCC1 in rat DRG neurons is 5.7 μM, slightly lower than that reported for Ehrlich ascites tumor cells (Rocha-Gonzalez et al., 2008). In DRG neurons, NKCC1 was activated by cell Cl^- depletion, which also led to isosmotic cell shrinkage, and the effect of bumetanide was tested on the Na^+ dependent re-accumulation of Cl^-. Bumetanide sensitivity has also been measured in NKCC1 expressed in HEK-293 cells. Bumetanide inhibits human NKCC1 expressed in HEK-293 cells with an IC_{50} of 0.16 ± 0.03 μM (Payne et al., 1995), whereas it inhibits rat NKCC1 expressed in HEK-293 cells with an IC_{50} of 2.4 ± 0.7 μM. Interestingly, mutating alanine 483 with cysteine (A483C) of rat NKCC1 shifts the bumetanide dose-response curve to the left, i.e. this point mutation renders NKCC1 more sensitive to bumetanide, shifting the IC_{50} from 2.4 ± 0.7 μM (wild-type) to 0.37 ± 0.02 μM for the A483C mutant (Dehaye et al., 2003). Clearly, at least for mammalian NKCC1, bumetanide sensitivity (IC_{50}) varies almost two orders of magnitude; it appears to be dependent on animal species, cell type, activation state of NKCC1 and whether measurements are done in native/endogenous NKCC1 or in heterologous expression systems. *Based on bumetanide sensitivity, it is impossible to discriminate between NKCC1 and NKCC2.* However, in many recent publications, it is often mistakenly stated that bumetanide is a "specific NKCC1 blocker".

The sensitivity to bumetanide of the three full-length spliced variants of NKCC2 has been studied in the *Xenopus* oocyte heterologous expression system. When mouse NKCC2s are expressed in *Xenopus* oocytes, the IC_{50} values for bumetanide are 3.4 μM for NKCC2F, 2.0 μM for NKCC2A, and 0.6 μM for NKCC2B (Plata et al., 2002). The IC_{50} values for bumetanide inhibition of the human NKCC2 full-length splice variants expressed in *Xenopus* oocytes are 0.16 μM for NKCC2F, 0.54 μM for NKCC2A and 0.22 μM for NKCC2B (Carota et al., 2010). Thus,

the human NKCC2A variant is the least sensitive to bumetanide, whereas in mouse, the least sensitive variant is NKCC2F. The reasons for these discrepancies between mouse and human NKCC2 variants remain to be elucidated. However, we can conclude that *it is impossible to discriminate between NKCC2 splice variants based on bumetanide sensitivity.*

The overall conclusion is that sensitivity of NKCCs to bumetanide varies over two orders of magnitude; it depends on whether it is assessed under basal conditions or upon activation of the cotransporters (Hannaert et al., 2002), on degree of glycosylation (Paredes et al., 2006), on animal species, on cell type and on whether these proteins are in their native cell (endogenous) or expressed in heterologous systems like *Xenopus* oocytes or HEK-293 cells. Moreover, used alone and/or in relatively high concentrations (e.g. >50 μM), not even bumetanide can provide positive proof that a given function is mediated by the NKCCs. This is because bumetanide also blocks KCCs, although at significantly higher concentrations than those needed to block NKCCs. As discussed below, bumetanide blocks KCCs with IC_{50} values of ≈60−180 μM for KCC1 (Gillen et al., 1996; Mercado et al., 2000); 55−80 μM for KCC2 (Payne, 1997; Song et al., 2002), although values as high as 655 μM have been reported for KCC2 measuring net fluxes with a new fluorescence-based assay (Delpire et al., 2009); 100 μM for KCC3 (Mount et al., 1999; Race et al., 1999) and 900 μM for KCC4 (Mercado et al., 2000). Clearly, bumetanide is a less effective inhibitor of the KCCs than of the NKCCs. Thus, *bumetanide sensitivity can be used to differentiate between NKCCs and KCCs activity in functional assays.*

Finally, it is necessary to keep in mind that 5-sulfamoylbenzoic acid derivatives can inhibit channels or other carriers, although at considerably higher concentrations than those with which they inhibit NKCCs or KCCs. For instance, bumetanide blocks native CFTR Cl^- channels in sweat ducts with an IC_{50} of 300 μM (Reddy and Quinton, 1999). Furosemide blocks NMDA-induced currents in cultured spinal neurons but with an IC_{50} of 1.2 mM. Likewise, piretanide (5 mM) and bumetanide (2 mM) partially block NMDA-induced currents at millimolar concentrations (Lerma and Martin del Rio, 1992). Bumetanide and furosemide, also at very high concentrations (400 μM and 1 mM, respectively), partially block Ca^{2+}-activated Cl^- channels in rat lacrimal glands (Evans et al., 1986). Bumetanide and furosemide block vesicular glutamate uptake with an IC_{50} of 230 and 250 μM, respectively (Roseth et al., 1995). More recently, it has been suggested that bumetanide reduces aquaporin 4 osmotic water flow at concentrations well above 100 μM (Migliati et al., 2009). However, a possible direct effect of bumetanide on NKCC1 could not be ruled out. This is important because there is strong evidence supporting the notion that NKCC1 cotransports water and ions (Hamann et al., 2005, 2010). These observations are also significant from a "translational research" perspective local (Yan et al., 2003) as well as intravenous administration of bumetanide (O'Donnell et al., 2004) attenuate brain edema associated with transient as well as permanent experimental focal cerebral ischemia. The overall conclusion based on the data discussed above is that bumetanide at or below 20 μM concentrations can be used as a "selective" inhibitor of NKCCs.

Loop diuretics are anionic at physiological pH range, with very high lipid solubility, and hence can cross cell membranes (Alvarez-Leefmans et al., 1990). This raises the question of their site of action. It has long been suggested that bumetanide binds exclusively to the external face of NKCCs (Haas, 1994). Work from Forbush, Isenring and colleagues suggests that the central hydrophobic domain of NKCC1 determines its apparent affinities for Na^+, K^+ and Cl^- as well as for bumetanide, and that the cytosolic N- and C-termini have little effect on these properties and are mainly involved in the regulation of transport activity (Isenring and Forbush, 2001).

VC. Molecular Structure and Distribution of Na^+-K^+-Cl^- Cotransport Proteins

VC1. The Na^+-K^+-$2Cl^-$ Cotransporter 1 (NKCC1)

As already mentioned, two distinct Na^+-K^+-Cl^- cotransporter isoforms encoded by the SLC12A2 and the SLC12A1 genes have been identified by cDNA cloning and expression, NKCC1 and NKCC2 respectively. NKCC1 is still often referred to as BSC2 (bumetanide-sensitive cotransporter 2) or as "the basolateral bumetanide-sensitive Na-K-2Cl cotransporter" or as "the secretory isoform". Fortunately, these confusing and inappropriate nomenclatures are being superseded; NKCC1 is not sensitive to bumetanide only, neither is it exclusively located in the basolateral membrane of epithelial cells, nor is it expressed exclusively in epithelial cells, nor is it always "secretory." Thus, the nomenclature used by the GenBank (National Center for Biotechnology Information) is recommended.

A cDNA encoding NKCC1 was first cloned from the shark rectal gland (Xu et al., 1994), a well-characterized secretory epithelium that has been used as a model to study Cl^- secretion in epithelial cells. More important, shark rectal gland has a high density of Na^+-K^+-Cl^- cotransporters located in the basolateral membrane of the epithelial cells (Silva et al., 1996). Subsequently, cDNAs encoding NKCC1 were cloned from other secretory epithelia, including T84 cells, a human colonic epithelial cell line (Payne et al., 1995) and cultured inner medullary collecting duct cells (mIMCD-3) from mouse kidney (Delpire et al., 1994). Both of these mammalian NKCC1 proteins share a high degree of homology with the shark NKCC1 (71−74%) and even

higher identity with each other (91%). Later on, a cDNA encoding for the bovine aortic endothelial cell NKCC1 was also cloned and it was found that the predicted protein exhibits ≈95% amino acid identity with the T84 cell cotransporter amino acid sequence (Yerby et al., 1997).

There is evidence for the existence in rodents of an NKCC1 splice variant lacking exon 21. This shorter NKCC1 was first detected by partial cloning in mouse brain tissue (Randall et al., 1997). Exon 21 encodes 16 amino acid residues from the carboxyl terminus of the NKCC1 protein (Fig. 15.12). The function of this shorter NKCC1 splice variant is unknown. The absence of exon 21 predicts the loss of a protein kinase A (PKA) consensus site of the cotransporter protein. This suggests that the short NKCC1 could be subjected to different regulation than the full-length NKCC1. The absence of exon 21 does not appear to affect NKCC1 transport function, as suggested from experiments in MDCK (Madin Darby Canine Kidney) epithelial cells transfected with constructs of this short NKCC1 (Carmosino et al., 2008). Further, NKCC1 phosphorylation related to cotransport activation is carried out by the kinases SPAK (STE20/SPS1-related proline/alanine-rich kinase) and OSR1 (oxidative stress-responsive kinase 1) at specific threonine residues located in the N-terminus of the cotransporter (Delpire and Gagnon, 2008; Gamba et al., 2009; Kahle et al., 2010), as discussed below. Little is known about whether PKA phosphorylation plays a direct role in NKCC1 activation. Interestingly, the sequence encoded by exon 21 contains a conserve dileucine motif that appears to be involved in sorting of NKCC1 in polarized epithelial cells (Carmosino et al., 2008).

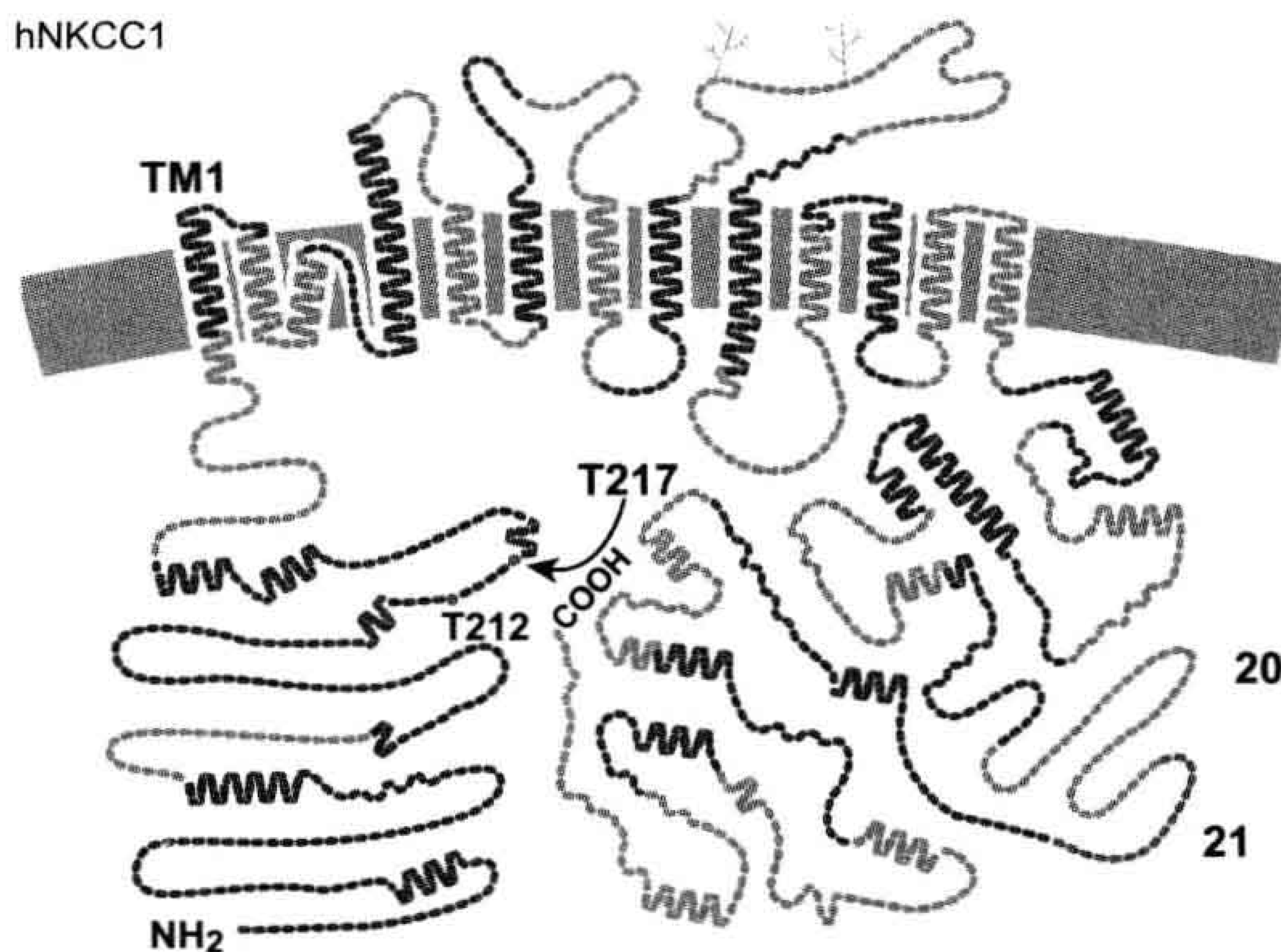


FIGURE 15.12 Hypothetical structural model of the human Na^+-K^+-$2Cl^-$ cotransporter protein NKCC1 (hNKCC1) showing the boundaries betwen amino acid sequences encoded by each exon (highlighted in light and dark blue, except for exon 21 highlighted in red). Each link symbolizes a single amino acid residue. "NH_2" and "COOH" indicate amino- and carboxy-termini, respectively. The branched lines in the long extracellular loop formed between putative transmembrane (TM) segments 7 and 8 indicate potential N-linked glycosylation sites. Biochemically identified phosphorylated threonine (T) residues (positions T212 and T217) are indicated by red dots. The proposed secondary structure of this protein with 12 TM helices and large intracellular amino- and carboxy-terminal domains is shared by other members of the cation-chloride cotransporter family. TM1 indicates the position of transmembrane segment 1. The residues encoded by exons 20 and 21 in the carboxyl terminus are indicated. *(Adapted from Carmosino et al., 2008.)*

Full-length NKCC1 comprises ≈1200 amino acids and has a molecular weight of 130–132 kDa. The predicted two-dimensional topology of NKCC1 from shark rectal gland shows 12 α-helical transmembrane (TM) domains and hydrophilic amino- and carboxyl-terminal regions (NH_2 and COOH) flanking a central hydrophobic domain. Whereas the amino (N) terminus displays considerable variability, the large carboxyl (C) terminus is well conserved among the different NKCC proteins. This predicted two-dimensional topology appears to be preserved in mammals and is similar to that predicted for NKCC2 and NCC (Gamba, 2009a) and the KCCs (see below). So far, NKCC1 is the only member of the SLC12A family for which the proposed topology is supported by experimental data (Gerelsaikhan and Turner, 2000a,b; Gerelsaikhan et al., 2006). Fig. 15.12 shows the predicted two-dimensional topology of human NKCC1.

NKCCs are glycoproteins and therefore possess consensus sites for N-linked glycosylation (*sequons*) within the large hydrophilic (extracellular) loop between TM segments 7 and 8, as shown in Fig. 15.12 (Haas and Forbush, 1998). A *sequon* is a sequence of three consecutive amino acids in a protein that can serve as the attachment site to a polysaccharide (sugar) called an N-linked-glycan. N-linked protein glycosylation occurs at asparagines (N) of the NXS/T *sequon*, where X is any amino acid except proline, S is serine and T threonine (Ben-Dor et al., 2004). There are two conserved extracellular N-glycosylation *sequons* which correspond to asparagines 547 and 556 (N^{547} and N^{556}) in mouse NKCC1 and N^{544} and N^{553} in rat NKCC1 (Gerelsaikhan et al., 2006). Evidence that NKCC1s are N-glycosylated in vivo comes from Western blot analyses of various tissues from animals of various species including shark, frog, duck, rat, cat, rabbit and human. These analyses show proteins with molecular weight higher than predicted for the core protein (≈160 KDa). Upon enzymatic deglycosylation, the molecular weight decreases to ≈130 kDa, the core molecular weight (reviewed in Di Fulvio and Alvarez-Leefmans, 2009). The impact of N-glycosylation on NKCC1 function has not been studied. The protein in its physiological plasma membrane environment is glycosylated. It is believed that glycosylation enhances cell-surface expression of these proteins.

NKCC1 has several potential phosphorylation sites within the predicted amino- and carboxy-terminal domains. As already mentioned, phosphorylation of NKCC1 plays a critical role in regulating its transport activity. Activation of NKCC1 by intracellular Cl^- depletion is associated with

increased phosphorylation of the cotransporter at conserved threonine (T) residues located within the N-terminal domain. The pioneering studies of Lytle and Forbush in the shark rectal gland epithelium yielded the first evidence suggesting that activation of NKCC1 was associated with phosphorylation of a threonine (T) residue (Lytle and Forbush, 1992). Later studies demonstrated that the phosphoacceptor amino acid sites within the cotransporter N-terminal domain corresponded to the threonines located at positions 184, 189 and 202 of shark NKCC1. Of these residues, T189 was found to be absolutely necessary for NKCC1 to be functional. Forbush and colleagues carried out studies in vivo using an antiphospho-NKCC1 antibody raised against a synthetic peptide of the amino terminal domain containing T212 and T217 of human NKCC1, which correspond to T184 and T189 of shark NKCC1 (Darman and Forbush, 2002; Flemmer et al., 2002) and demonstrated that activation of NKCC1 was associated with phosphorylation of these threonines (see Fig. 15.12).

Immunofluorescence studies using anticotransporter antibodies have shown that in secretory epithelia, NKCC1 protein is localized in the basolateral membrane (Lytle et al., 1995; Evans et al., 2000; Shillingford et al., 2002; McDaniel et al., 2005; Nejsum et al., 2005; Chou et al., 2008). As mentioned above, the only exception documented by functional and molecular methods is the choroid plexus (CP) where NKCC1 is located in the apical membrane (Plotkin et al., 1997; Wu et al., 1998). Another possible exception are the cells of the retinal pigment epithelium (RPE); there is abundant functional evidence for the apical location of an NKCC mechanism together with the Na^+/K^+ATPase, but the molecular identity of this NKCC has not been determined. The NKCC1 cotransporters that are localized in the basolateral membrane mediate net salt influx into the cells and, in doing so, act in concert with apical Cl^- channels and basolateral K^+ channels to produce net salt and fluid secretion in these epithelia. The location of NKCC1 in the apical membrane of CP argues against its involvement in ion secretion into cerebrospinal fluid. It has been proposed that the CP cotransporter is constitutively active and that it functions to reabsorb K^+ from cerebrospinal fluid to blood (Wu et al., 1998). The location of NKCC in the paranodal region of the Schwann cells suggests a similar role in K^+ uptake from the peri-axonal space, thereby preventing extracellular K^+ accumulation which could produce abnormal changes in axonal excitability (Alvarez-Leefmans et al., 2001).

VC2. The Na^+-K^+-$2Cl^-$ Cotransporter 2 (NKCC2)

NKCC2 has thus far been identified exclusively in the kidney (Gamba, 2009a; Gamba and Friedman, 2009) where, as already mentioned, it is located in the apical membrane of the TALH epithelial cells. For this reason, NKCC2 is still often referred to as "the apical bumetanide-sensitive Na^+-K^+-$2Cl^-$ cotransporter", as "BSC1" (bumetanide-sensitive cotransporter 1) or as "the absorptive isoform." As with NKCC1, these nomenclatures are not recommended, among other reasons because NKCC1 can also be located in the apical membrane of some epithelial cells, because NKCC2 is sensitive to other loop diuretics besides bumetanide and because the possible expression of NKCC2 in extrarenal locations has not been excluded.

NKCC2 shares only $\approx$60% amino acid sequence identity with NKCC1. In fact, these two proteins are the products of independent genes; SLC12A1 located on human chromosome 15 encodes NKCC2, whereas SLC12A2 located on human chromosome 5 encodes NKCC1 (Gamba and Friedman, 2009). As already mentioned, the gene encoding for NKCC2, gives rise to different NKCC2 transcripts derived from alternative splicing events. These splicing events yield three full-length NKCC2 variants: NKCC2A, NKCC2B and NKKC2F, all of which are differentially distributed in different regions of the TALH, have different transport kinetics characteristics and have been found in different species including humans (Carota et al., 2010). In addition to these three full-length variants, there are shorter variants with truncated carboxyl-terminal ends. The meaning of this differential splicing is that it contributes to the diversity of proteins encoded by a limited number of genes in the genome. Discussion about the possible function of each of these variants is beyond the scope of the present chapter. The interested reader should consult recent reviews by the groups of Gamba, Castrop and Schnermann (Castrop and Schnermann, 2008; Gamba, 2009a; Gamba and Friedman, 2009; Carota et al., 2010).

Full-length NKCC2 proteins are smaller than NKCC1, with a deduced amino acid sequence of $\approx$1095–1099 residues and a core molecular mass of $\approx$110–120 kDa. Like NKCC1, NKCC2 is N-glycosylated at two sites located in the long extracellular loop between TM7 and TM8, which is consistent with the size of $\approx$150–160 kDa of the glycosylated cotransporter. N-glycosylation has been shown to impact NKCC2F function when expressed in oocytes (Gamba, 2005). Protein N-glycosylation is a co- and post-translational modification crucial for folding, trafficking, insertion and function of many proteins (for references see Di Fulvio and Alvarez-Leefmans, 2009). Prevention of N-glycosylation in rat NKCC2F by site directed mutagenesis produces a protein with reduced transport activity and decreased bumetanide sensitivity (Paredes et al., 2006). The predicted topology of NKCC2 is very similar to that of NKCC1 featuring a central hydrophobic domain made up of 12 putative transmembrane (TM) spanning regions. The difference between the two isoforms can be accounted for almost entirely by the additional amino acids at the amino

terminus of NKCC1. In fact, the amino terminus is the most divergent region of the entire protein, both between the two isoforms and when comparing the same isoform between species (Haas and Forbush, 1998).

VD. A Kinetic Model of Na^+-K^+-$2Cl^-$ Cotransport

Normal operation of NKCC requires the binding to the cotransporter of all the ions involved (i.e. $1Na^+$, $1K^+$ and $2Cl^-$) on the same side of the membrane before ion translocation occurs. The order of binding of the cotransported ions does not seem to occur at random. Evidence shows a preferred order of ion binding resulting from an allosteric effect such that the binding of one ion increases the apparent affinity of a binding site for the next ion. The best-tested model to date is still the one based on a systematic study of ion dependencies of self-exchange fluxes mediated by the cotransporter in duck and human red blood cells (Lytle et al., 1998; Lytle, 2003). Two partial reactions of the cotransporter cycle have been revealed: K^+-K^+ exchange in normal high-K^+ cells and Na^+-Na^+ exchange in high-Na^+ cells. The internal and external ion requirements of each mode can be explained by a reaction cycle based on ordered binding and glide symmetry. The latter means that the first ion to bind on one side of the "carrier" will be the first ion to be released on the other.

Figure 15.13 shows the cotransport model based on ordered ion binding and glide symmetry. Net cotransport influx would require that the ions bind to the cotransporter in the order shown. In the initial loading of the empty carrier at the outer face of the membrane, binding of a Na^+ in the pocket (reaction 2) induces formation of a Cl^- site, and binding of that Cl^- (reaction 3) creates a site that can bind K^+, and so forth. All four ions are occluded momentarily in a transitional state (E_4) without access to either side of the membrane. Reaction 5 represents a conformational change of the NKCC such that the binding sites are now accessible from the intracellular compartment, and reactions 6 to 9 represent the ordered release of ions. Reaction 10 leads to a conformational change that involves the reorientation of the totally unloaded cotransporter to an outwardly facing conformation. The model has been quantitatively tested using simulations based on flux data from duck red blood cells, HeLa cells and epithelial cells (Benjamin and Johnson, 1997). Russell (2000) and more recently Delpire and Gagnon (2011) have offered stimulating critiques of this model showing its weaknesses and strengths. Also recently, a mathematical model of NKCC2 has been proposed (Marcano et al., 2009). This model basically adopts the kinetic scheme proposed by

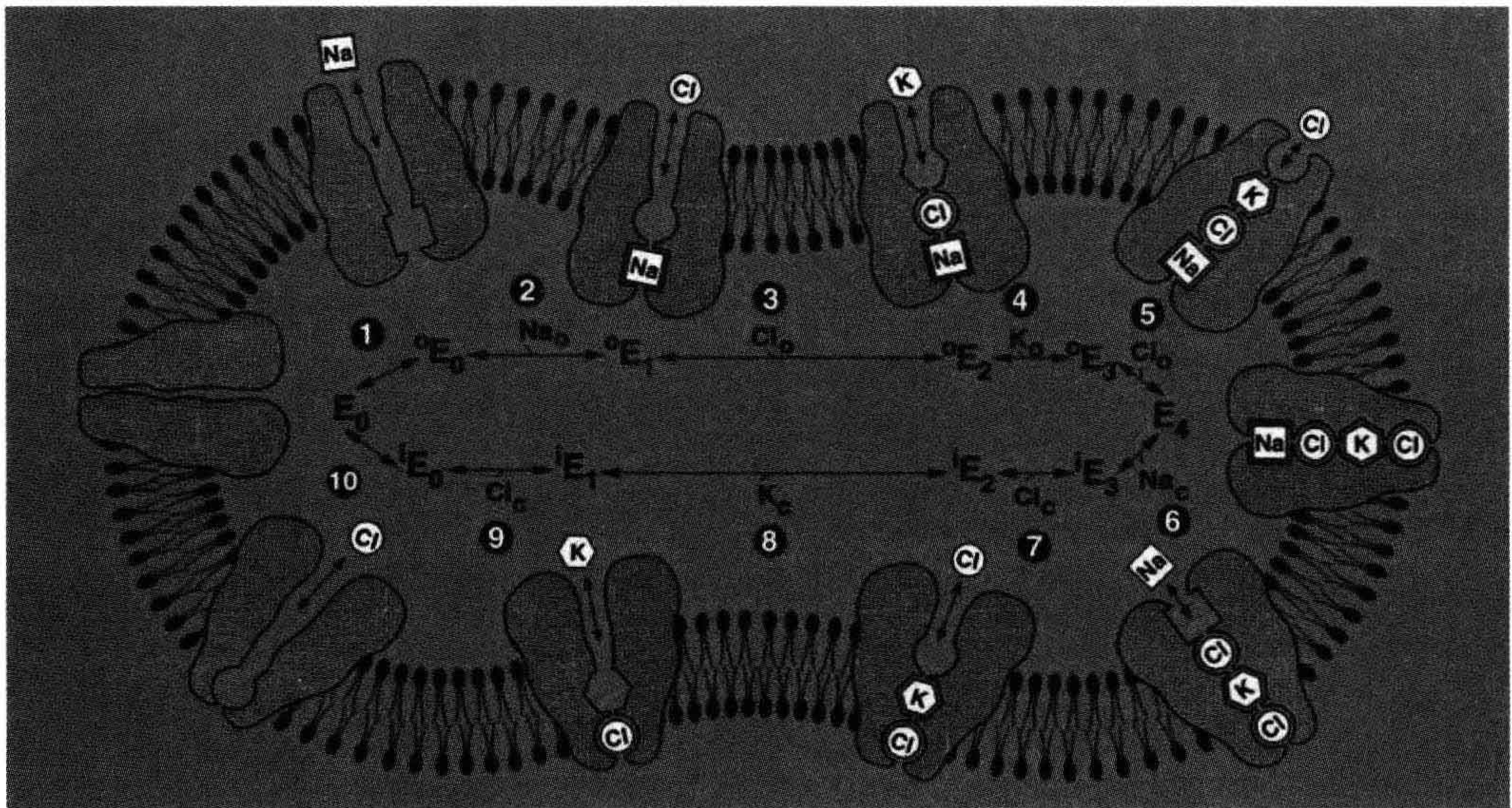


FIGURE 15.13 Hypothetical model of transport cycle of Na^+-K^+-$2Cl^-$ cotransport by ordered ion binding with glide symmetry. Ten intermediate states of the transporter are depicted. The model assumes that cotransport is completely reversible and that only fully loaded (E_4) and completely unloaded (E_0) forms of cotransporter protein are capable of changing orientation from inward- to outward-facing (and vice versa). The idea is that when all sites are occupied (E_4), a major conformational change occurs, allowing bound ions to unload on the opposite side of the membrane in the order they were bound (first on, first off). When the carrier is completely unloaded (E_0), the empty form can also undergo a major conformational change, allowing it to begin reloading ions at the opposite side of the membrane, thus facilitating net cotransport. Numbers refer to order of binding, reorientation and release for one complete influx cycle. *(Modified from Lytle et al., 1998.)*

Lytle and colleagues, but uses kinetic data reported for each splice variant of NKCC2. The authors conclude that the three long splice variants of NKCC2 differ only in ion-binding affinities, a result that is consistent with published mutagenesis analysis and differences in $^{86}Rb^+$ uptake among the A, B and F variants. NKCC2 cotransporter models will facilitate the development of larger scale models of ion transport by TALH cells. One problem in studying the partial reactions of the transport cycle of NKCCs is that they are electroneutral transporters. Thus, it is not possible, as with electrogenic transporters, to measure the partial reactions by electrophysiological means (Garcia-Celma et al., 2010). Future molecular dynamics studies will be potentiated when the crystal structure of NKCCs becomes available.

VE. Functions of Na^+-K^+-2 Cl^- Cotransport

The coupled electroneutral cotransport of Na^+, K^+ and Cl^- mediated by NKCCs serves multiple functions depending on the cell type expressing these proteins. Some examples of NKCCs functions are discussed below in this section. Some of them have been mentioned in Section VA and can be summarized as follows:

1. NKCCs maintain $[Cl^-]_i$ at levels above those predicted for electrochemical equilibrium. The resulting outward Cl^- gradient is used by epithelial cells to promote transepithelial ion and water transport. In neurons, the outward Cl^- gradient generated and maintained by NKCC1 provides the driving force for the depolarizing efflux of Cl^- through ligand-gated Cl^- channels activated by neurotransmitters like GABA or glycine, or second messengers like intracellular Ca^{2+}. The ensuing depolarizations play important roles in central and peripheral neurons
2. Another major function of NKCCs is their participation in cell volume regulation, particularly in cell volume recovery in response to cell shrinkage
3. NKCCs contribute to extracellular K^+ buffering in various cell types
4. NKCCs have been implicated in cell cycle and cell division.

NKCCs are key players in transepithelial Cl^- transport. In most cases, Cl^- transporting epithelia are *secretory* (e.g. exocrine glands such as salivary, pancreatic, eccrine, lacrimal, airway epithelium, intestinal crypts and corneal epithelium) and, in a few instances, they are *absorptive* (e.g. TALH). In cells of Cl^--absorptive and Cl^--secretory epithelia, NKCCs serve as the major Cl^- entry pathway and functions in concert with three other transport proteins, namely Cl^- and K^+ channels and the Na^+/K^+pump, to carry out net transepithelial movements of salt (Fig. 15.14). The impact of the Na^+/K^+ pump in the operation of NKCCs in all cell types, whether epithelial or not, cannot be overstated; it is the primary active transport mechanism that generates and maintains the inward Na^+ gradient that, in turn, provides a substantial part of the driving force that energizes the NKCCs (see Section VB3 above). Thus, the net Cl^- flux in epithelia depends on the Na^+ chemical gradient developed and maintained by primary active transport. In fact, as expected, active transepithelial Cl^- transport is abolished by Na^+ removal or by dissipating the Na^+ gradient between the extracellular fluid and the cell interior (Silva et al., 1977).

In *secretory epithelia* (see Fig. 15.14A), the essential components for active transepithelial Cl^- transport are a Cl^- channel in the apical membrane and a three-component mechanism located in the basolateral membrane causing

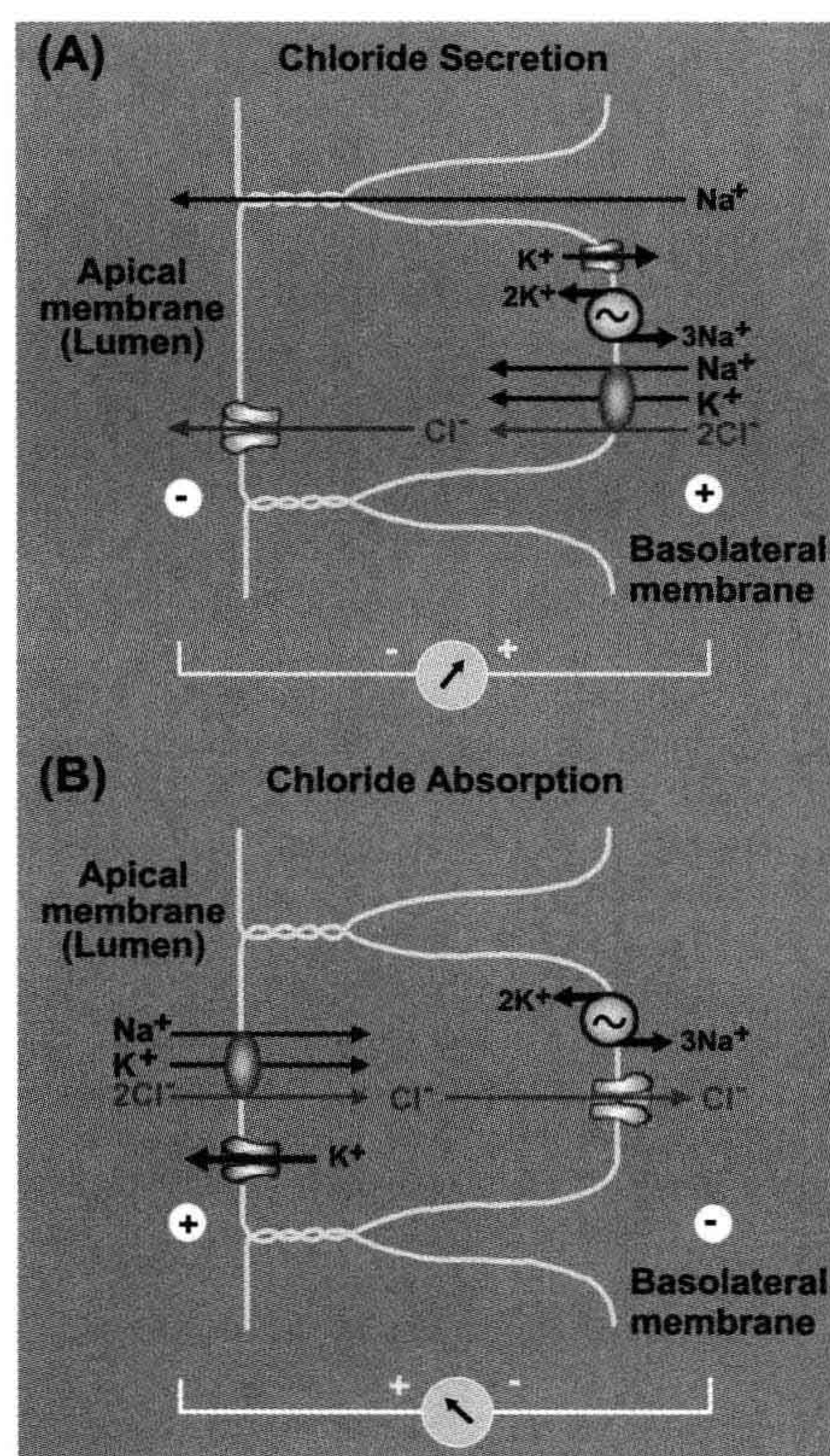


FIGURE 15.14 Mechanisms for active Cl^- absorption and secretion in Cl^- transporting epithelia. (A) Transport model for exocrine gland Cl^--secreting epithelium (e.g. salivary glands or tracheal epithelium). Intracellular $[Cl^-]$ is maintained above electrochemical equilibrium by NKCC1 across the basolateral membrane. Na^+ influx is balanced by efflux via Na^+/K^+-ATPase; K^+ influxes are balanced by efflux via K^+ channels. Transepithelial secretion is induced by activation of apical-membrane Cl^- channels. (B) Model of Cl^- transport in thick ascending limb of Henle's loop, a Cl^--absorptive epithelium. Cl^- entry across the apical membrane is mediated by NKCC2. Most basolateral Na^+ and Cl^- efflux proceeds through the Na^+/K^+-ATPase and Cl^- channels, respectively.

active Cl^- influx across this membrane. The three components that operate in concert to cause net Cl^- uptake across the basolateral membrane are NKCC1, the Na^+/K^+pump and a K^+ channel. NKCC1 maintains $[Cl^-]_i$ above electrochemical equilibrium and transepithelial secretion is produced by activation of apical Cl^- channels. The Na^+ that enters through NKCC1 is balanced by efflux through the Na^+/K^+-pump. The K^+ influx mediated by NKCC and the Na^+/K^+ pump is balanced by efflux via K^+ channels. The end result is that transcellular transport involves only Cl^-; both Na^+ and K^+ recycle across the basolateral membrane via the Na^+/K^+ pump and the K^+ channels, respectively. In Cl^- secretory epithelia, there is an apical negative transepithelial voltage which acts as a driving force for paracellular Na^+ transport towards the lumen. The net result is NaCl secretion which, in turn, results in net fluid secretion. The mechanisms and the pathways of epithelial fluid transport remain unsolved. There is evidence for water being transported through both transcellular (through the cells) and paracellular (intercellular, through tight junctions in series with lateral intercellular spaces) pathways (Reuss, 1997; Tradtrantip et al., 2009; Fischbarg, 2010). Whether fluid transport occurs *purely* by osmotic water flow through aquaporins is also controversial. There is evidence suggesting that cotransporters including NKCC1 and KCCs cotransport water and ions and thus they may contribute to transcellular fluid transport (MacAulay et al., 2009; Hamann et al., 2010; Zeuthen, 2010).

The transport mechanisms in *Cl^--absorptive epithelia*, like the one lining the thick ascending limb of the loop of Henle (TALH), are illustrated in Fig. 15.14B. In this case, the Cl^- channels (ClC-Kb) are located in the basolateral membrane and the NKCC (NKCC2 in TALH) is characteristically located in the apical membrane together with K^+ channels (ROMK2). However, the Na^+/K^+ pump is located at the basolateral membrane, so that Na^+ entering the cell via NKCC2 is not recycled, but instead undergoes transcellular transport. The same occurs with Cl^-; it enters through the apical NKCC2 and exits though basolateral Cl^- channels. Thus, NKCC2 contributes to net Na^+ and Cl^- reabsorption. Most of the K^+ taken up by NKCC2 recycles across the apical membrane via inward rectifier K^+ channels ROMK2. In the TALH, Cl^- absorption is entirely transcellular, whereas Na^+ absorption is partly transcellular and partly paracellular (Gamba and Friedman, 2009). The paracellular Na^+ flux is driven by the transepithelial voltage, which in contrast with Cl^--secreting epithelia is lumen positive.

Primary sensory neurons (PSNs) convey virtually all somatic and visceral information to the spinal cord and brainstem, including nociceptive signals, i.e. incoming signals arising from nociceptors. The latter are sensory receptors capable of transducing and encoding noxious stimuli. NKCC1 maintains $[Cl^-]_i$ of PSNs above electrochemical equilibrium throughout adulthood. In this case, the Na^+ and K^+ entering the cell via NKCC1 recycle through the Na^+/K^+ ATPase and K^+ channels respectively (Fig. 15.15). Thus, $[Na^+]_i$ and $[K^+]_i$ are maintained at a constant level by the Na^+/K^+ ATPase. The outward Cl^- gradient generated by NKCC1 is maintained throughout the entire cell surface, including the soma (located in DRG ganglia) and the central and peripheral processes. This Cl^- gradient is of high functional significance; at the peripheral endings, it is thought to contribute to excitation of nociceptors produced by chemical mediators of pain released upon tissue damage, whereas at the central terminals, it makes possible the GABA-mediated depolarizing Cl^- efflux underlying presynaptic inhibition, a key mechanism in gating the flow of somatosensory information of various sensory modalities to the spinal cord and brainstem (Alvarez-Leefmans, 2009). The mechanisms that make possible presynatic inhibition in the spinal cord are depicted in Fig. 15.15. The prevailing notion is that GABA released from dorsal horn interneurons depolarizes primary afferent fibers via axoaxonic synapses. This primary afferent depolarization (PAD) inactivates Na^+ channels thereby reducing the amplitude of the action potential as it invades the primary afferent terminals, resulting in a reduction in neurotransmitter release from these terminals (Rudomin and Schmidt, 1999; Willis, 2006). The depolarizing inward current results from opening of $GABA_A$-gated Cl^- channels expressed in intraspinal terminals of primary afferent fibers. Opening of these GABA-gated channels results in efflux of Cl^- which transiently drives the transmembrane potential toward the E_{Cl}. This peculiar depolarizing action of a traditionally hyperpolarizing inhibitory transmitter like GABA is possible because the $[Cl^-]$ inside the nerve terminals of primary sensory neurons is maintained at a level higher than predicted from a passive distribution, thereby providing the necessary driving force for electrodiffusional (i.e. channel-mediated) Cl^- efflux. An example of how this mechanism can impact nociceptive signaling is the antihyperalgesic action of diazepam, a $GABA_A$ receptor modulator that enhances PAD by increasing the open probability of Cl^- channels activated by GABA. By potentiating PAD and presynaptic inhibition on nociceptive primary afferents, diazepam has been found to have an antihyperalgesic action against inflammatory hyperalgesia in vivo (Witschi et al., 2011). It is worth remembering here that hyperalgesia is defined as increased pain sensitivity.

NKCC1 is involved in sensory transduction. Two well documented examples are the *inner ear* and the *olfactory sensory neurons.* The mechanisms of acoustic transduction are discussed in detail in Chapter 37 in this book. Here we briefly examine the role of NKCC1 as an important component of the sensory transduction machinery in the inner ear. Hearing critically depends on the ion composition

of the cochlear endolymph, the fluid surrounding the upper surface of mechanosensitive hair cells. These cells carry out mechano-transduction, the conversion of a mechanical stimulus (sound-induced vibration of hair cells cilia) into an electrical response that is then processed by the central nervous system. Endolymph has a high K^+ concentration (157 mM) and low Na^+ (1.3 mM) and Ca^{2+} ($\approx$20 μM) concentrations. Thus, the ion composition of the endolymph resembles intracellular fluid. This ionic composition depends on active transport processes in the stria vascularis, a specialized epithelium at the lateral cochlear wall. NKCC1 is located at the basolateral membrane of the strial marginal cells, together with the Na^+/K^+ ATPase and Cl^- channels (ClC-Ka/barttin and ClC-Kb/barttin), whereas the apical membrane, facing the "lumen" which in this case is the endolymph-filled scala media, expresses outwardly conducting K^+ channels (KCNQ1/KCNE1). Clearly, strial marginal cells form a *K^+-secreting epithelium;* Na^+ and Cl^- entering the cells via NKCC1 recycle though the Na^+/K^+ pump and the Cl^- channels, whereas K^+ entering though NKCC1 and the Na^+/K^+ pump exits though the apical K^+ channels. Thus, transcellular transport in these cells involves only K^+. The unique composition of the endolymph is needed because the apical mechanosensitive channels of sensory hair cells function as K^+ channels (they are in fact mechanosensitive non-selective cation channels). Sound-induced movement of the basilar and tectorial membranes deflects the cilia of sensory hair cells and opens these mechanosensitive channels through which K^+ enters. The resulting K^+ influx depolarizes the hair cells and triggers a complex cascade of events that culminate in exocytosis of synaptic vesicles at their basal pole. K^+ leaves outer hair cells through KCNQ4 K^+ channels and is recycled through a complex mechanism that involves other members of the SLC12A family of cation-coupled cotransporters (Hubner and Rust, 2007; Mistrik and Ashmore, 2009; Zdebik et al., 2009). The important role played by SLC12A members for inner ear ion homeostasis and endolymph secretion may explain the well-known ototoxic effects of loop diuretics (Ikeda et al., 1997) and the deafness exhibited by gene disruption of some members of the SLC12A family in knockout mouse models.

In *olfactory sensory neurons,* the transduction strategy is different from that of inner hair cells in the cochlea, but the mechanism is also critically dependent on NKCC1 function (Frings, 2009). Mammalian olfactory receptor neurons (ORNs) present to the air a tuft of sensory cilia expressing odorant receptors. Upon contact with odorants, these receptors trigger a cascade of events that culminates with the firing of action potentials. The cascade of events begins with the activation of odorant receptors, resulting in a rise of the second messengers cAMP and Ca^{2+} inside the cilia, a process that involves cAMP-gated-Ca^{2+} channels. The resulting Ca^{2+} influx opens Cl^- channels (TMEM16B). ORNs accumulate Cl^- through NKCC1 and maintain a higher than equilibrium $[Cl^-]_i$ thereby setting an outward Cl^- gradient. Thus, opening of Ca^{2+}-activated Cl^- channels (TMEM16B) leads to a depolarizing Cl^- efflux from the cilia, a mechanism that amplifies the receptor potential approximately 10-fold, thus helping to excite the neuron even when stimulation is weak. Accordingly, disruption of the NKCC1 gene, as well as the pharmacologic suppression of Cl^- accumulation or blocking the Cl^- efflux, strongly inhibits the sensory response of ORNs. Experiments with NKCC1 knockout mice have shown that NKCC1 is not the only Cl^- transporter active in ORNs. In fact, NKCC1 knockout mice retain the ability to smell, a finding that suggests the existence of an additional Cl^--uptake mechanism. The latter turned out to be the AE1, i.e. SLC4A1 (Hengl et al., 2010).

The role of NKCCs in *cell volume regulation* has also been mentioned. In many cells, NKCC is involved in regulatory volume increase in response to hypertonic cell shrinkage, by promoting net gain of K^+, Cl^- and osmotically obliged water. For detailed accounts on this subject the reader should consult the reviews by Russell (2000, 2009) and Hoffmann and colleagues (Hoffmann et al., 2009). In the cell bodies of primary sensory neurons (i.e. DRG neurons) known to express NKCC1, it has been possible to measure changes in cell water volume that reflect solute and water fluxes and $[Cl^-]_i$. The results demonstrate a tight link between $Na^+,K^+,2Cl^-$ cotransporter activity, water fluxes, steady-state $[Cl^-]_i$ and cell water volume (Rocha-Gonzalez et al., 2008). Isosmotic removal of external Cl^- results in intracellular Cl^- depletion and immediate cell shrinkage. The extent of cell shrinkage is accounted for in terms of measured Cl^- depletion. Upon readmission of the isosmotic control solution, water influx takes place in *isosmotic* media. This water influx requires the presence of external Na^+ and K^+ and is abolished by 10 μM bumetanide. Thus, net water flux is tightly linked to NKCC1 transport activity. In DRG neurons, NKCC1 determines not only the higher than passive $[Cl^-]_i$ characteristic of these neurons but also the cell volume set point, through a negative feedback system in which intracellular Cl^- regulates water and Cl^- influx, thereby maintaining intracellular Cl^- concentration and cell volume constant (Alvarez-Leefmans, 2009). Moreover, due to their small volume/surface ratio, presynaptic nerve terminals of primary sensory neurons are expected to be partially depleted of solutes (Cl^- and K^+) and water upon repetitive GABA action. It has been proposed that NKCC1 is capable of restoring ionic gradients and osmotic balance altered as a consequence of neurotransmitter action (see Fig. 15.15).

As mentioned above, NKCC exhibits some of the features required for an efficient extracellular K^+ buffer;

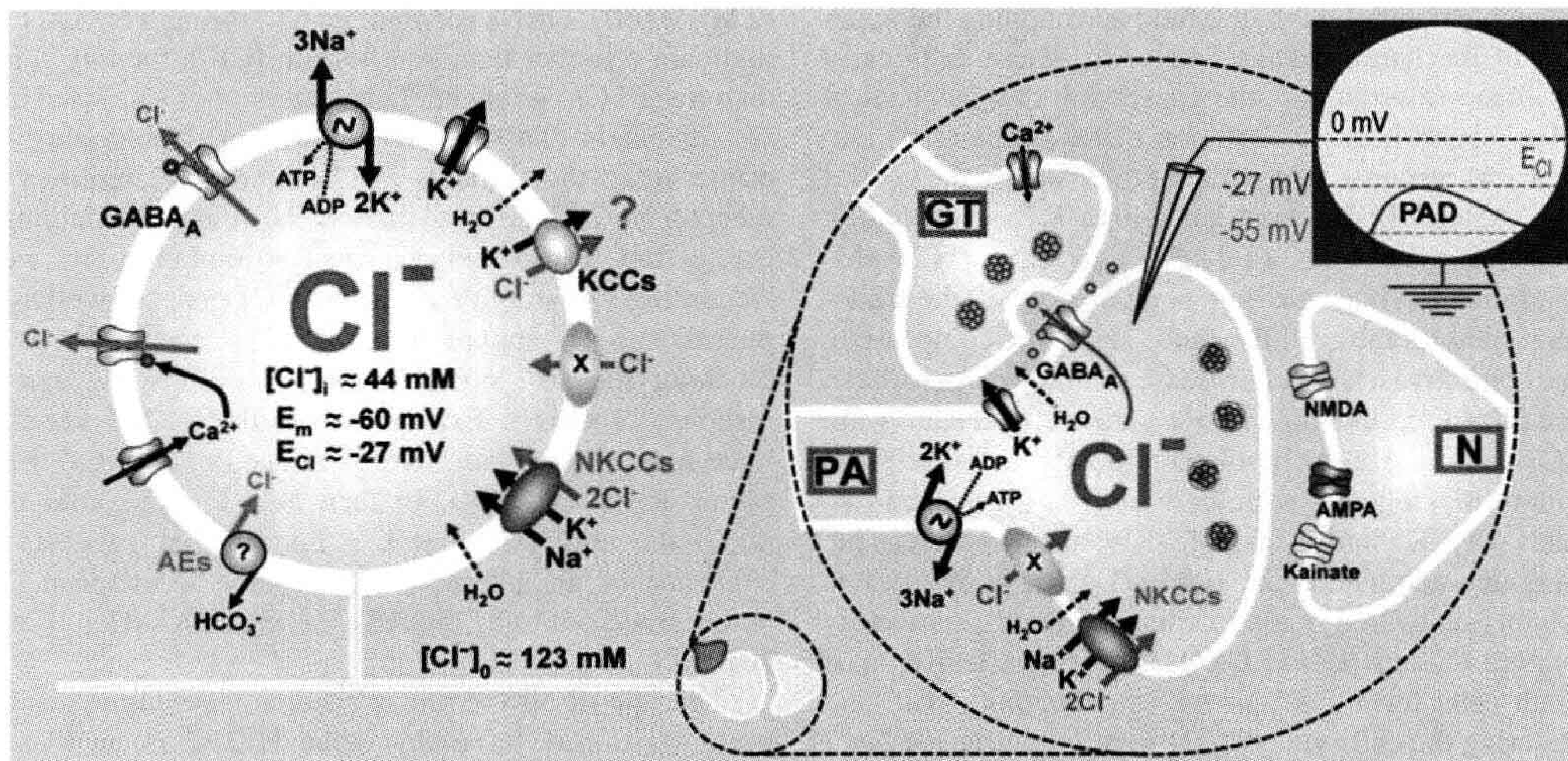


FIGURE 15.15 Schematic diagram depicting the known and hypothetical transporters and channels involved in intracellular Cl^- regulation in primary sensory neurons and proposed mode of generation of primary afferent depolarization (PAD) and presynaptic inhibition in the intraspinal terminals of these neurons. The left circle represents a mammalian DRG neuron showing measured values of intracellular Cl^- concentration, $[Cl^-]_i$; membrane potential (E_m) and Cl^--equilibrium potential, E_{Cl}. The Na^+/K^+ ATPase maintains the Na^+ and K^+ gradients across the membrane. AEs, anion exchangers; NKCCs, $Na^+,K^+,2Cl^-$ cotransporters; KCCs are K^+-Cl^- cotransporters 1,3 or 4. The contribution of KCCs to intracellular Cl^- regulation in these neurons under euvolemic conditions is not clear. KCC2 is not expressed in primary sensory neurons. X represents other yet to be identified active Cl^--uptake transporters. The right diagram encircled by a dashed line represents a magnified intraspinal primary afferent terminal from which an intracellular micropipette connected to an oscilloscope monitors E_m. PA, primary afferent; GT, GABAergic terminal from an interneuron; N, postsynaptic terminal with glutamate receptor-channels. Note that PAD (blue trace in the oscilloscope screen) blocks the release of neurotransmitter from the PA terminal. *(Reproduced from Alvarez-Leefmans, 2009.)*

i.e. it has a strong net inwardly directed driving force and a high affinity for external K^+ (Payne and Forbush, 1995). There is some evidence for its role as a K^+-uptake mechanism that contributes to buffering and regulation of extracellular K^+ in some tissues. For instance, NKCC1 is present in the apical membrane of mammalian choroid plexus and, in concert with other transport systems coexisting in these polarized cells, may play an important role in the reabsorption of K^+ from the cerebrospinal fluid to the blood, thereby contributing to the buffering and regulation of brain interstitial $[K^+]$, as illustrated in Fig. 15.17 (Wu et al., 1998). NKCC is also prominently located in the paranodal region of Schwann cells of myelinated axons, a region prone to extracellular K^+ accumulation resulting from axonal impulse activity. This suggests the possible involvement of NKCC in K^+ uptake from the periaxonal space, thereby regulating the external $[K^+]$ and maintaining the axonal excitability in this critical location (Alvarez-Leefmans, 2009).

VI. ELECTRONEUTRAL K^+-Cl^- COTRANSPORTERS

K^+-Cl^- cotransporters (KCCs) are carrier proteins that mediate the coupled, electroneutral movement of K^+ and Cl^- across the plasma membrane. This coupled transport is obligatory as it absolutely requires the simultaneous presence of both K^+ and Cl^- on the same side of the membrane for net transport to proceed. As other electroneutral secondary active transport mechanisms, the direction of the net movement of K^+ and Cl^- by KCCs is determined solely by the sum of the chemical potential gradients of the two cotransported ions. Under normal physiological conditions, the outwardly directed K^+-chemical potential gradient maintained by the Na^+/K^+ pump drives the uphill movement of Cl^- against its chemical potential gradient. Hence, under normal conditions, KCCs are efflux pathways for K^+ and Cl^-. However, the cotransporters are bidirectional and can mediate net ion efflux or influx, depending upon the prevailing K^+- and Cl^--chemical potential gradients. In neurons, this is crucial because KCC2, the neuronal-specific isoform, might work near its thermodynamic equilibrium and, therefore, it would have the potential to mediate Cl^- fluxes in both directions (Payne, 2009). The stoichiometry of KCCs is $1K^+:1Cl^-$, as determined in rabbit red blood cells (Jennings and Adame, 2001). This means that the transport process involves one-for-one movement of K^+ with Cl^-. Thus, the overall transport process of K^+ and Cl^- via the cotransporter is not driven by the transmembrane voltage, nor does the

transport process directly generate a membrane current that may change the transmembrane voltage (Kaji, 1993).

This transport mechanism has been implicated in regulatory volume decrease in response to hyposmotic cell swelling, by promoting net efflux of K^+ and Cl^- and osmotically obliged water (Hoffmann et al., 2009). All four main isoforms of the cotransporter can be activated by significant hypotonic challenges. However, the fact that they are volume sensitive does not necessarily mean that the physiological function of these cotransporters is to regulate cell volume. As lucidly stated by Payne (2009): "...a transporter should be considered volume regulatory only after it has been demonstrated that the transport rate is a graded function of the stimulus and that the net ion transport is large enough to restore cell volume to normal. In the absence of such measurements, it is best to refer to the transporter as volume sensitive until more extensive experimentation is conducted." Besides its possible function in cell volume regulation, K^+-Cl^- cotransport plays important roles in the vectorial movement of salt and water across some epithelia (Reuss, 1997; Velazquez and Silva, 2003; Gamba, 2005). A crucial function of an isoform of the K^+-Cl^- cotransporters, KCC2, has been clearly demonstrated in neurons, where by effecting active extrusion of Cl^- it keeps E_{Cl} at more negative values than E_m, making possible the hyperpolarizing action of inhibitory neurotransmitters like GABA and glycine in the adult central nervous system (Payne et al., 2003; Payne, 2009). A brief account of what is known about the function and distribution of KCCs is presented below.

VIA. Basic Features of the K^+-Cl^- Cotransporters

The basic functional characteristics of KCCs have been summarized in a recent review (Gibson et al., 2009). A defining feature of KCCs is that the transport process is Na^+ independent. Another key feature of KCCs is that the thiol-alkylating reagent N-ethylmaleimide (NEM) stimulates transport (Lauf and Theg, 1980). The cotransporters can also be activated by osmotic cell swelling (Ellory and Dunham, 1980). Reducing $[Mg^{2+}]_i$ stimulates the cotransporter, presumably via effects on regulatory kinases (Delpire and Lauf, 1991). Likewise, KCC is stimulated by the protein kinase inhibitor staurosporine (Bize and Dunham, 1994). Unlike either the NKCC or the NCC, KCCs can be inhibited by disulfonic acid stilbenes such as DIDS (Delpire and Lauf, 1992). KCCs are also inhibited by loop diuretics but, in general, the sensitivity for furosemide>>bumetanide, as discussed above in Section VB4. They can also be inhibited by dihydroindenyloxyalkanoic acid (DIOA), which is often erroneously used as if it were a "specific" KCC inhibitor. More recently, a new series of KCC2 inhibitors such as *N*-(4-methylthiazol-2-yl)-2-(6-phenylpyridazin-3-ylthio) acetamide has been reported (Delpire et al., 2009). The new inhibitors are more potent than furosemide and DIOA. Another series of KCC2 inhibitors has also been recently described (Pégurier et al., 2010). Future experiments will reveal if these new compounds are specific for KCCs. Activity of all KCCs can be influenced by intracellular pH (pH_i), with KCC1 and KCC3 exhibiting lower activity at pH_i <7.0 or >7.5, KCC2 at <7.5 and KCC4 at >7.5.

VIB. Molecular Structure, Distribution and Functions of K^+-Cl^- Cotransport Proteins

Four distinct isoforms and several splice variants of these members of the cation-coupled Cl^- cotransporter family (SLC12A) have been identified. The isoforms are KCC1, KCC2, KCC3 and KCC4. They are encoded by the genes *SLC12A4, SLC12A5, SLC12A6* and *SLC12A7,* respectively. In vertebrates, all of these genes code for proteins over 1000 amino acids with core molecular weights of 120–128 kDa (Payne, 2009). The four KCCs exhibit alternative exon splicing and the use of alternative promoters and first exons, leading to even greater protein diversity. The four KCC proteins are 69–75% identical when comparing their full length sequences. The most variable segment of these proteins is the N-terminal domain, defined as the portion that extends from the first methionine to the beginning of TM1. Identity of the N-terminal domain sequence among KCCs varies between 38 and 50% (Gamba, 2005). It is important to mention that in the original cloning report of Mount and coworkers (1999), the isoform KCC3 (Hiki et al., 1999) was misleadingly named KCC4 and the latter was named KCC3. This was clarified in subsequent work. In the present chapter, the corrected nomenclature has been followed.

NKCC1, NKCC2, NCC and the four KCCs share a predicted basic membrane topology consisting of a central core of 12 TM domains flanked by hydrophilic amino- and carboxy-terminal domains that have a cytoplasmic orientation. The carboxy-termini of KCCs make up nearly half the size of these proteins (Fig. 15.16). When compared over their entire length, KCC proteins are 25–30% identical to NCC and NKCCs. A major structural difference between the KCCs and the NKCCs is the position of a large glycosylated extracellular loop, predicted to occur between TM5 and TM6 in the KCCs and between TM7 and TM8 in the NKCCs and the NCC (Mount et al., 1999). This can be appreciated by comparing Fig. 15.12 with Fig. 15.16.

KCC1 was the first isoform of the KCCs to be cloned and functionally characterized by heterologous expression in HEK 293 cells (Gillen et al., 1996). The gene for human KCC1 is at chromosomal location 16q22.1. KCC1 has a deglycosylated molecular mass of ≈120 kDa and it is widely expressed in mammalian tissues (brain, kidney, heart, lung, liver, stomach, colon, spleen and placenta). This ubiquitous tissue distribution suggests that KCC1 may

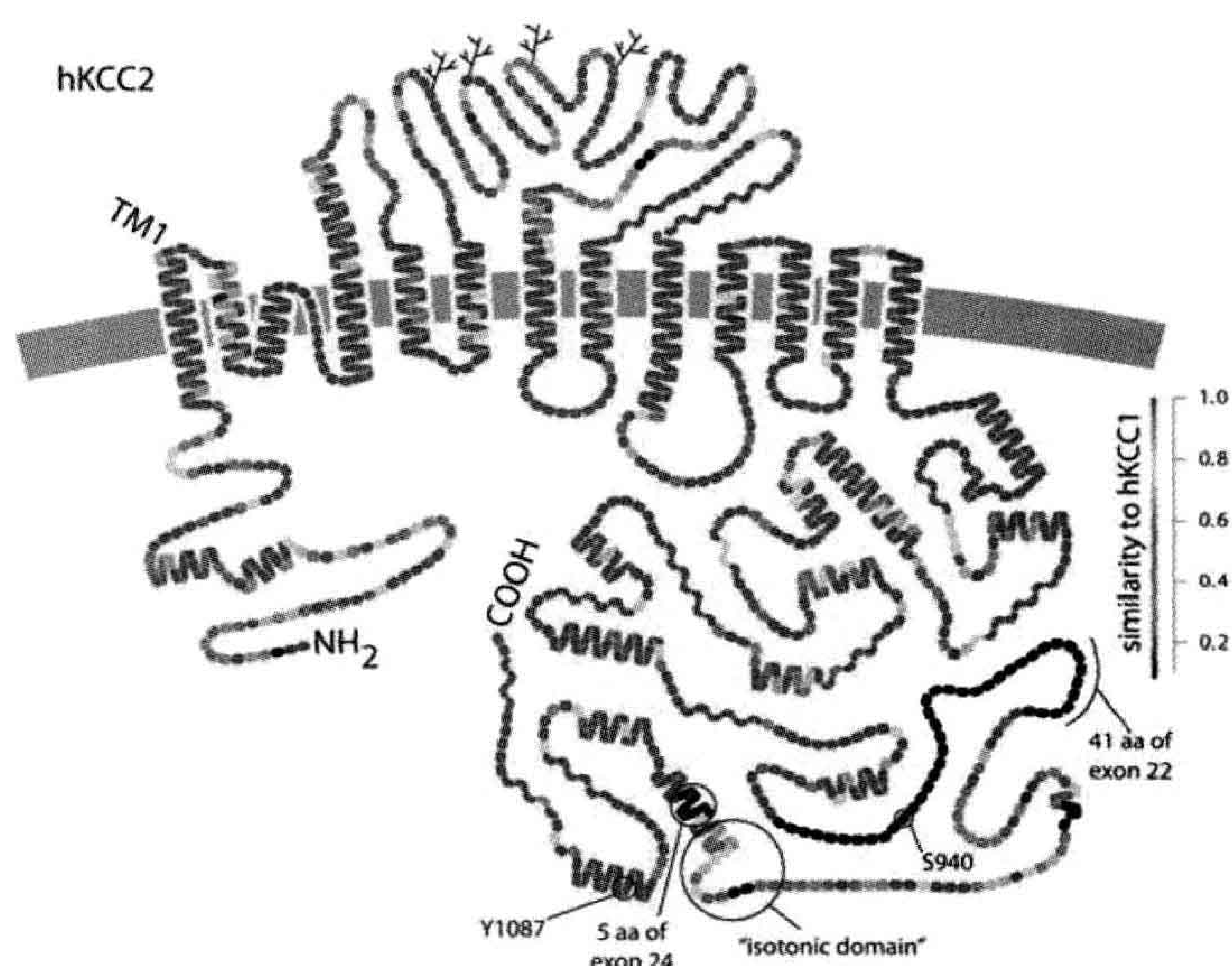


FIGURE 15.16 Hypothetical structural model of the K^+-Cl^- cotransporter. Human KCC2 (hKCC2) and human KCC1 (hKCC1) are compared to one another by colors that indicate the degree of similarity on a per residue basis: red residues are identical and black residues are absent from hKCC1 (alignment performed using CLUSTAL X ver. 1.8). The branched lines in black are potential N-linked glycosylation sites between putative transmembrane segments (TM) 5 and 6. Predicted secondary structural elements are shown as helices for predicted α-helix and wavy lines for predicted β-sheet. A reentrant loop between putative TM segments 2 and 3 has also been predicted for NKCC2 and is shown for KCC2. The 15 amino acid region required for constitutive "isotonic" activity of KCC2 is encircled. Serine-940 (S940) is also encircled. Protein kinase C directly phosphorylates S940 of KCC2. S940 phosphorylation is required for activation of KCC2 by protein kinase C (Payne, 2009). KCC2 has a large region in the carboxy-terminus (COOH), exhibiting little identity with the other KCCs. This unique region of KCC2 is coded by two extra exons (exons 22 and 24) which are apparently absent from the other KCC genes. Exon 22 of KCC2 codes for 41 amino acids and exon 24 of KCC2 codes for five amino acids. Exon 23 of the KCC2 gene is conserved among the KCC genes, however, the identity of the predicted amino acids in exon 23 of KCC2 is low when compared to the other KCCs. A consensus tyrosine protein kinase phosphorylation site is also shown (Y1087). Mutation of this tyrosine residue (Y1087D) inhibits constitutive "isotonic" activity as well as swelling-induced activity in heterologously expressed KCC2 (see Payne, 2009 for references). *(This figure was kindly provided by John Payne and Bliss Forbush. It was generated using DNAPLOT.)*

represent a "housekeeping" isoform responsible for cell volume regulation and maintenance, and for the regulation of $[Cl^-]_i$. However, this "housekeeping" role is difficult to reconcile with the fact that disruption of KCC1 gene does not produce any obvious phenotype even in vertebrate red blood cells where KCC1 was thought to be the key player in cell volume control. In fact, KCC1 knockout are indistinguishable from wild-type animals (Rust et al., 2007). It is now known that red blood cells express KCC1, KCC3 and KCC4, but that the volume-sensitive K^+-Cl^- cotransporter activity in mouse and human red blood cells is mostly mediated by KCC3 (Rust et al., 2007; Pan et al., 2011). Heterologous expression of KCC1 in HEK-293 cells showed that the cotransporter is little active in isosmotic media but that its activity can be stimulated by cell swelling (≈twofold) and N-ethylmaleimide, and inhibited by furosemide (K_i of ≈40 μM) and by bumetanide (K_i of ≈60 μM). When KCC1 is expressed in *Xenopus* oocytes, it also shows minimal transport activity in isosmotic media. However, when exposed to hyposmotic solutions, its activity increases by 20-fold (Mercado et al., 2000). The cotransporter in the *Xenopus* expression system is inhibited by bumetanide and furosemide with a K_i of 180 μM. Clearly, the sensitivity to loop diuretics of KCC1 varies between expression systems but, in all cases, is significantly different than that of NKCCs. The latter are in general more sensitive to bumetanide than furosemide; the K_i for bumetanide is at least an order of magnitude lower. Even though the expression of human KCC1 has been found in every cell and tissue tested so far, its specific physiological function remains unclear. The fact that K^+-Cl^- cotransport activity in red blood cells is undiminished in KCC1 knockout mice suggests that this protein has other hitherto unknown functions.

KCC2 is a neuron-specific isoform of the K^+-Cl^- cotransporters. It was first cloned and characterized by Payne and colleagues (Payne et al., 1996; Payne, 1997). KCC2 is present in the plasma membrane of cell bodies and dendrites of various types of CNS neurons, but appears to be absent in axons and glial cells (Williams et al., 1999; Stil et al., 2009; reviewed in Blaesse et al., 2009; Payne, 2009; Viemari et al., 2011). As originally proposed by Payne and colleagues, KCC2 is the isoform that actively extrudes Cl^- from nerve cells, rendering E_{Cl} more negative than E_m and thus setting an inwardly directed electrochemical gradient for Cl^-, making possible hyperpolarizing inhibition mediated by GABA- or glycine-gated Cl^- channels in mature CNS neurons. The cloning and molecular characterization of KCC2 has been a highly significant discovery in the field of Cl^- transport; although it had long been suspected that the mechanism of active Cl^- extrusion in CNS neurons was a K^+-Cl^- cotransporter (Alvarez-Leefmans, 1990), its

molecular identity and its functional and kinetic features had remained elusive. However, as discussed below, KCC2 might not be the only candidate for such an important function; in some neurons KCC3 appears to have a significant role in setting the inward Cl^- gradient needed for hyperpolarizing inhibition (Boettger et al., 2003). Finally, KCC2 expression in the CNS increases with development and becomes functionally dominant over NKCC1. This explains why GABA and glycine responses, which are depolarizing in embryonic or early postnatal nerve cells, become hyperpolarizing in the adult brain (Rivera et al., 1999).

The mammalian KCC2 gene (SLC12A5) generates two variants of KCC2, named KCC2a and KCC2b, with different N-termini (Uvarov et al., 2007). This N-termini heterogeneity is due to the use of alternative promoters and alternative first exons. Exon 1a encodes 40 N-terminal amino acid residues giving rise to KCC2a, and exon 1b encodes 17 amino acids giving rise to KCC2b, the variant originally described by Payne and coworkers (1996). The function of KCC2a is not known. Both variants are exclusively expressed in CNS neurons, but they differ in timing, level and site of expression. During postnatal development, KCC2b is steeply upregulated whereas KCC2a is not. KCC2b is more abundant in the cortex whereas KCC2a appears more abundant in brainstem and spinal cord. Interestingly, full KCC2 knockout mice die immediately after birth due to respiratory failure and other motor disturbances (Hubner et al., 2001), whereas mice lacking KCC2b retaining normal levels of KCC2a, survive for up to 2 weeks, although they exhibit abnormal posture and gait, and generalized seizures (Woo et al., 2002). So far, there is no KCC2a knockout model. However, the observations mentioned above in available knockout mice suggest that KCC2a may to a certain extent compensate for the lack of KCC2b in brainstem and spinal cord, making possible the survival of these animals for up to postnatal day 17. Expression of either KCC2a or KCC2b in HEK 293 cells demonstrated that both variants exhibit comparable cotransport activity. Further, both variants exhibit constitutive activity in isosmotic media, a functional characteristic that makes KCC2 suitable for the control of $[Cl^-]_i$ (Payne, 2009). Since most published data reflect expression of both KCC2a and KCC2b, "KCC2" will be used here to refer to both splice variants.

Human KCC2 has a predicted core molecular mass of 123.5 kDa (Payne, 2009), close to that predicted for mouse and rat KCC2 (123.6 kDa). Western blots of membranes isolated from rat brain show that the glycosylated molecular mass of KCC2 is $\approx$140 kDa and, upon deglycosylation, the protein migrates to near $\approx$125 kDa, which is close to the predicted molecular mass (Williams et al., 1999). Similarly, human KCC2 has a glycosylated molecular mass of $\approx$140 kDa and, upon deglycosylation, the protein migrates to a broad band centered around 120 kDa (Munoz et al., 2007). KCC2 expressed in HEK 293 is also stimulated by NEM and inhibited by furosemide (K_i of $\approx$25 μM), bumetanide (K_i of $\approx$55 μM), DIDS and DIOA. The main functional difference from other KCC isoforms is that KCC2 is not stimulated by osmotic swelling when expressed in HEK 293 cells. However, when expressed in *Xenopus* oocytes its activity increases 3.5–20-fold by hyposmotic swelling (Gamba, 2005; Payne, 2009). These and other discrepancies (e.g. bumetanide sensitivity in HEK versus *Xenopus*) highlight the limitations of studying transporters in heterologous expression systems. A key feature of KCC2 is that it exhibits significant basal constitutive activity, i.e. it is active in isotonic media, a functional property shared with KCC3a (see below). This constitutive activity makes these KCCs ideal, from the functional perspective, to establish the steady state $[Cl^-]_i$ of adult CNS neurons. The segment of the KCC2 protein conferring constitutive "isotonic" activity, known as the "isotonic domain", comprises 15 amino acids coded by exon 23 (see Fig. 15.16).

Like NKCC1, KCC2 exhibits all the features required for an efficient $[K^+]_o$ buffer: (1) it is reversible and the direction of net transport is sensitive to subtle changes in $[K^+]_o$; (2) the affinity of the cotransporter for external K^+ is compatible with the range of the observed $[K^+]_o$ (3–10 mM), allowing a high rate of cotransport activity. These requirements seem to be a feature of both KCC2 (K_m $\approx$5.2 mM) and KCC3 (K_m $\approx$10 mM). Hence, it has been postulated that KCC2 could also act as a $[K^+]_o$ buffer (Payne, 1997). However, external $[K^+]$ in CNS interstitial fluid is tightly regulated and, under normal physiological conditions, never exceeds 3 mM. Only during extreme seizure activity does $[K^+]_o$ exceed 3 mM and can reach up to 12 mM, the so-called *ceiling* level (Somjen, 2004). Thus, most likely KCC2 normally works in the efflux mode.

KCC3 was first identified by three groups simultaneously (Hiki et al., 1999; Mount et al., 1999; Race et al., 1999). The KCC3 gene (SLC12A6) gives rise to two major splice variants, KCC3a and KCC3b. The KCC3 cDNA cloned by Hiki et al. (1999) predicted a protein of 1099 amino acids, whereas the cDNA cloned by Race et al. (1999) and Mount et al. (1999) predicted a protein of 1150 amino acids. These two KCC3 variants are termed KCC3a (1150 aa) and KCC3b (1099 aa). They are identical except for their N-termini. Both variants come from the same gene which, in humans, is located in chromosome 15 (15q13). KCC3 proteins have deglycosylated molecular mass of $\approx$120 to 128 kDa. Subsequent studies showed that the mammalian KCC3 gene has the potential to produce more than two alternative splice variants giving rise to proteins with considerable N-termini heterogeneity (Mercado et al., 2005). To date, six different KCC3 transcripts coding for

five different KCC3 variants are known to exist. They are termed KCC3a, KCC3a−x2M (KCC3a minus exon 2), KCC3a-S (encodes a protein 60 amino acids shorter than KCC3a), KCC3b and KCC3b−x2M (KCC3b minus exon 2). Exon 2 encodes 15 amino acid residues. When expressed in *Xenopus* oocytes all five variants function as K^+-Cl^- cotransporters (Mercado et al., 2005). It is not clear how the N-termini heterogeneity impacts KCC3 function. When expressed in HEK 293 cells, human KCC3a is not active in isotonic media and is activated by cell swelling, staurosporine and prominently by NEM. However, recent work shows that the activity of KCC3a in isosmotic media depends upon the phosphorylation state of the protein, suggesting that dephosphorylation increases KCC3's intrinsic transport activity (Rinehart et al., 2009). Human KCC3a expressed in HEK cells is inhibited by bumetanide (K_i ≈100 μM), furosemide (K_i ≈103 μM) and DIOA (K_i ≈9.3 μM). Hence, the most potent inhibitor of KCC3a is DIOA (Race et al., 1999). When expressed in HEK 293 cells, human KCC3b is active in isotonic media but its activity does not increase upon hypotonic swelling. KCC3b is inhibited by bumetanide (K_i ≈40 μM) and furosemide (K_i ≈10 μM). Thus, the emerging picture is that KCC3a in neurons may play functions similar to those that are carried out by KCC2.

KCC3s have different distribution patterns; KCC3a is expressed predominantly but not exclusively in various brain regions, in the basolateral membrane of choroid plexus epithelial cells (Fig. 15.17), in heart and skeletal muscle, lung, liver and pancreas (Pearson et al., 2001). A recent study using in situ hybridization and immunohistochemical techniques demonstrated that KCC3a is mainly expressed in neurons and, to a much lesser extent, in some glial cells, whereas KCC3b is not expressed in brain tissue (Shekarabi et al., 2011). In human red blood cells, KCC3a is the functionally dominant isoform (Pan et al., 2011), whereas KCC3b is abundantly expressed in kidney, localized in the basolateral membranes of proximal tubule epithelial cells where it may contribute to proximal tubular cell volume regulation (Lang et al., 2007).

Mutations in the human gene SLC12A6, which encodes KCC3s, lead to a rare neurological illness known as Andermann's syndrome (Howard et al., 2002). This syndrome is characterized by a progressive sensorimotor neuropathy associated with complete or partial absence of corpus callosum, mental retardation, progressive physical disability and an average life expectancy of 33 years. Death is usually caused by respiratory complications (Dupre et al., 2003). Full KCC3 knockout mice models not only display peripheral neuropathy, but reduced seizure threshold and deafness. The latter is due to inner ear defects in K^+ transport in the cochlea, where some of the cells involved in K^+ recirculation slowly degenerate, as do sensory hair cells (Boettger et al., 2003). KCC3 knockout mice also show hypertension of neurogenic origin due to elevated sympathetic tone (Rust et al., 2006). Further, full KCC3 knockout mice exhibit axonal and Schwann cell swelling of sciatic nerves that ultimately results in neurodegeneration (Byun and Delpire, 2007). This suggests that KCC3 may play a role in cell water volume maintenance in sensorimotor axons and that this mechanism is critical for peripheral nerve integrity and function. In sum, KCC3s appear to have significant roles in transepithelial transport and in the regulation of cell volume and $[Cl^-]_i$. While KCC2 may be the key regulator of neuronal $[Cl^-]_i$, data suggest that KCC3a may have a similar role.

KCC4 was first cloned and functionally characterized by Mount and coworkers (1999). The KCC4 gene is located on chromosome 5, at 5p15, and encodes for a protein product of 1083 amino acids that shares high identity (≈75%) with KCC2. However, unlike KCC2 (and KCC3), KCC4 does not mediate constitutive K^+-Cl^- cotransport under isotonic conditions, but cotransport is activated by osmotic cell swelling. Indeed, when expressed in *Xenopus* oocytes, KCC4 does not mediate K^+-Cl^- cotransport activity in isotonic media. However, its activity increases 200-fold when exposed to hypotonic solutions (Mercado et al., 2000). Using this heterologous expression system, it has been possible to establish functional comparisons between KCC1 and KCC4. Although cell swelling activates both cotransporters, KCC4 is one order of magnitude more sensitive to hypotonic activation than KCC1. Another distinctive feature of KCC4 is its relatively poor sensitivity to both furosemide (K_i ≈900 μM) and bumetanide (K_i ≈900 μM), and its sensitivity to barium and high concentrations of thiazides. Among the four KCC isoforms, KCC4 is the least sensitive to furosemide as corroborated using the HEK 293 expression system, in which KCC2 properties were compared with KCC4 (Hartmann et al., 2010). KCC2 was more sensitive to furosemide (K_i ≈185 μM) than KCC4 (K_i ≈550 μM).

KCC4 is prominently expressed in several epithelia including the apical membrane of choroid plexus cells (Karadsheh et al., 2004), the basolateral membrane of α-intercalated cells of the cortical collecting duct in kidney (Boettger et al., 2002) and the apical membrane of gastric parietal cells (Fujii et al., 2009). In the apical membrane of the choroid plexus, KCC4 is thought to be involved in K^+ recycling, working in parallel with the Na^+/K^+ pump and NKCC1 (Karadsheh et al., 2004) and in Cl^- recycling working in parallel with NKCC1. However, given its high volume sensitivity and its lack of constitutive activity, it is conceivable that KCC4 works to regulate cell volume in choroidal epithelial cells. In the basolateral membrane of α-intercalated cells in cortical collecting ducts in kidney, KCC4 is involved in the regulation of acid secretion working in parallel with the basolateral AE1 and the apical

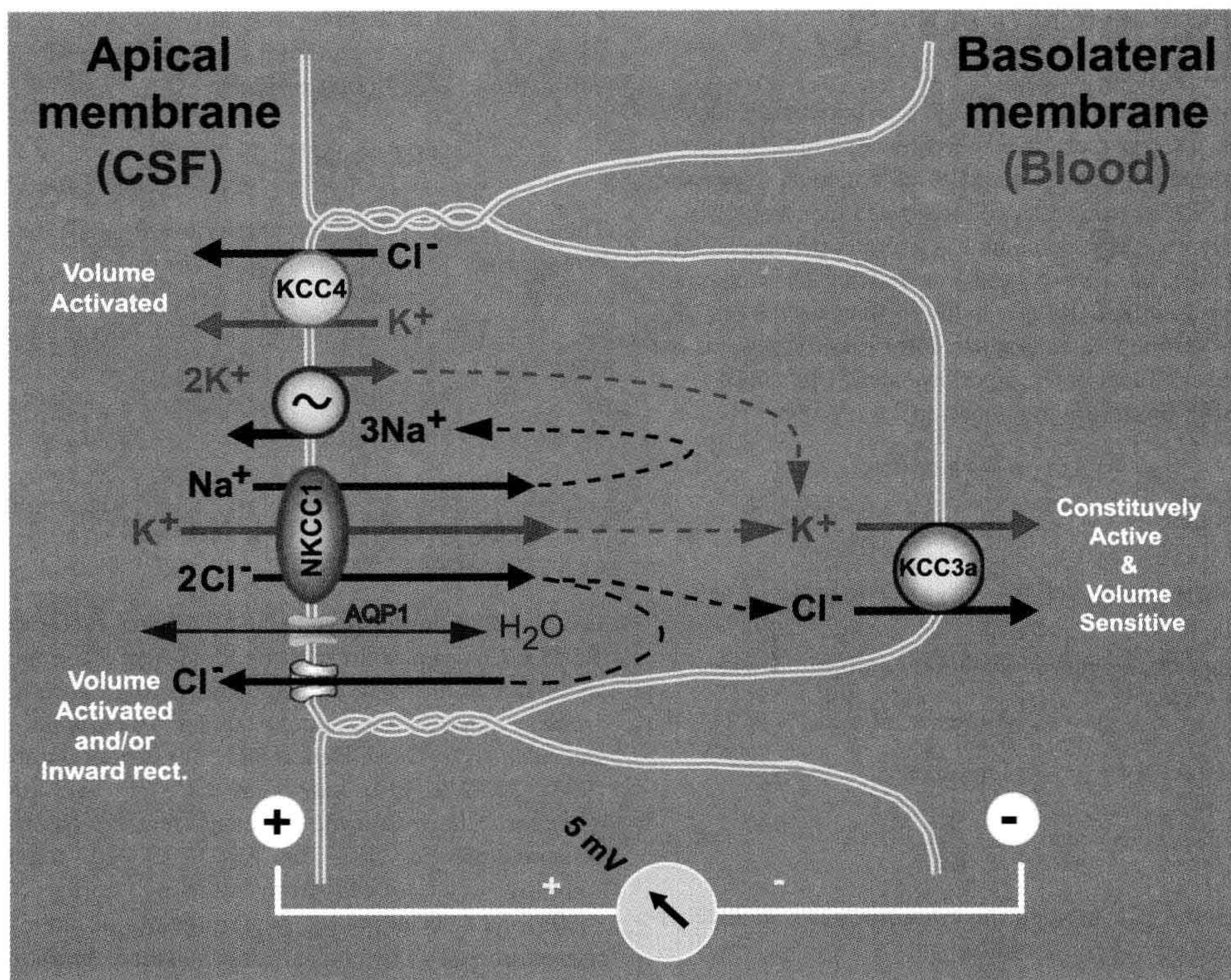


FIGURE 15.17 Model of Na^+-K^+-$2Cl^-$cotransporter function in choroid plexus (CP) epithelial cells. The Na^+-K^+-$2Cl^-$ cotransporter (NKCC1) and the Na^+/K^+-ATPase are localized in the apical membrane facing cerebrospinal fluid (CSF). K^+ is taken up into CP cells via the Na^+-K^+-$2Cl^-$ cotransporter NKCC1 and it exits via K^+-Cl^- cotransporter KCC3 in the basolateral membrane (facing blood). Na^+ is recycled by the apical Na^+/K^+-ATPase. Cl^- is partly recycled via Cl^- channels in the apical membrane. It is proposed that NKCC1 plays a central role in the reabsorption of K^+ from CSF to the blood and in the buffering and regulation of brain interstitial K^+ concentration.

proton pump. The apical proton pump secretes H^+ into the lumen of the collecting duct. At the basolateral membrane, acid equivalents are transported by the AE1. Basolateral HCO_3^- efflux is coupled to Cl^- uptake, which is recycled by KCC4. Interestingly, KCC4 knockout mice exhibit renal tubular acidosis that probably results from an impairment of Cl^- recycling across the basolateral membrane of acid-secreting α-intercalated cells (Boettger et al., 2002). In the apical membrane of gastric parietal cells, the K^+/H^+-ATPase (i.e. the proton pump) working in parallel with KCC4 is the main mechanism for basal HCl secretion in the apical canalicular membrane of parietal cells (Fujii et al., 2009). KCC4 is also expressed in the Deiter's cells of the inner ear where it participates in the K^+ recycling mechanism (Boettger et al., 2002). KCC4 knockout mice are deaf due to hair cell degeneration after the beginning of hearing (Boettger et al., 2002). KCC4 is also expressed in some areas of the nervous system (the suprachiasmatic nucleus of the hypothalamus, cranial nerves, spinal cord and peripheral nerves), but its function in nervous tissue is unknown (Karadsheh et al., 2004; Le Rouzic et al., 2006). KCC4 is also expressed in red blood cells, but its functional role there is also unknown. More exciting is the emerging role of KCC4 in cancer cell invasiveness and tumor metastasis. It has been found that epidermal-growth factor (EGF) and insulin-like growth factor 1 (IGF-1) stimulate the membrane recruitment of KCC4 at lamellipodia through myosin Va-actin trafficking route. KCC4 functions as a membrane scaffold for the assembly of signal complexes via the association with the actin-binding protein ezrin. Further, molecular studies of surgical specimens suggest that the expression of KCC3, KCC4 and their stimulators, EGF or IGF-1, exhibit a close association with the clinical outcome of cancer patients. It has been proposed that KCC4 may be used as a biomarker to predict cancer patient outcome (Chen et al., 2010).

VIC. Thermodynamics of K^+-Cl^- Cotransport

Let us now turn our attention to the thermodynamic aspects of K^+-Cl^- cotransport. Consider the example shown in Fig. 15.18 which depicts a model of a neuron expressing a KCC, a Na^+/K^+ pump, a voltage-gated Cl^- leak channel and a GABA-gated Cl^- channel. Assuming that the K^+-Cl^- cotransport is the sole system transporting Cl^- (channels are closed) and that $[K^+]_i$ is held constant by the Na^+/K^+ pump, the driving force for the cotransport $\Delta\mu_{K,Cl}$ is the sum of the chemical potential differences of K^+ and Cl^-, as expressed in the following equation:

$$\Delta\mu_{K,Cl} = \Delta\mu_K + \Delta\mu_{Cl} \quad (15.16)$$

It follows that

$$\Delta G = \Delta\mu_{K,Cl} = RT\ln\frac{[K^+]_i}{[K^+]_o} + RT\ln\frac{[Cl^-]_i}{[Cl^-]_o} \quad (15.17)$$

This system attains thermodynamic equilibrium when

$$\Delta G = \Delta\mu_{K,Cl} = 0 \quad (15.18)$$

and, therefore, for a 1:1 stoichiometry,

$$\frac{[K^+]_o}{[K^+]_i} = \frac{[Cl^-]_i}{[Cl^-]_o} \quad (15.19)$$

and hence the $[Cl^-]_i$ when the cotransporter reaches thermodynamic equilibrium will be

$$[Cl^-]_i = \frac{[K^+]_o[Cl^-]_o}{[K^+]_i} \quad (15.20)$$

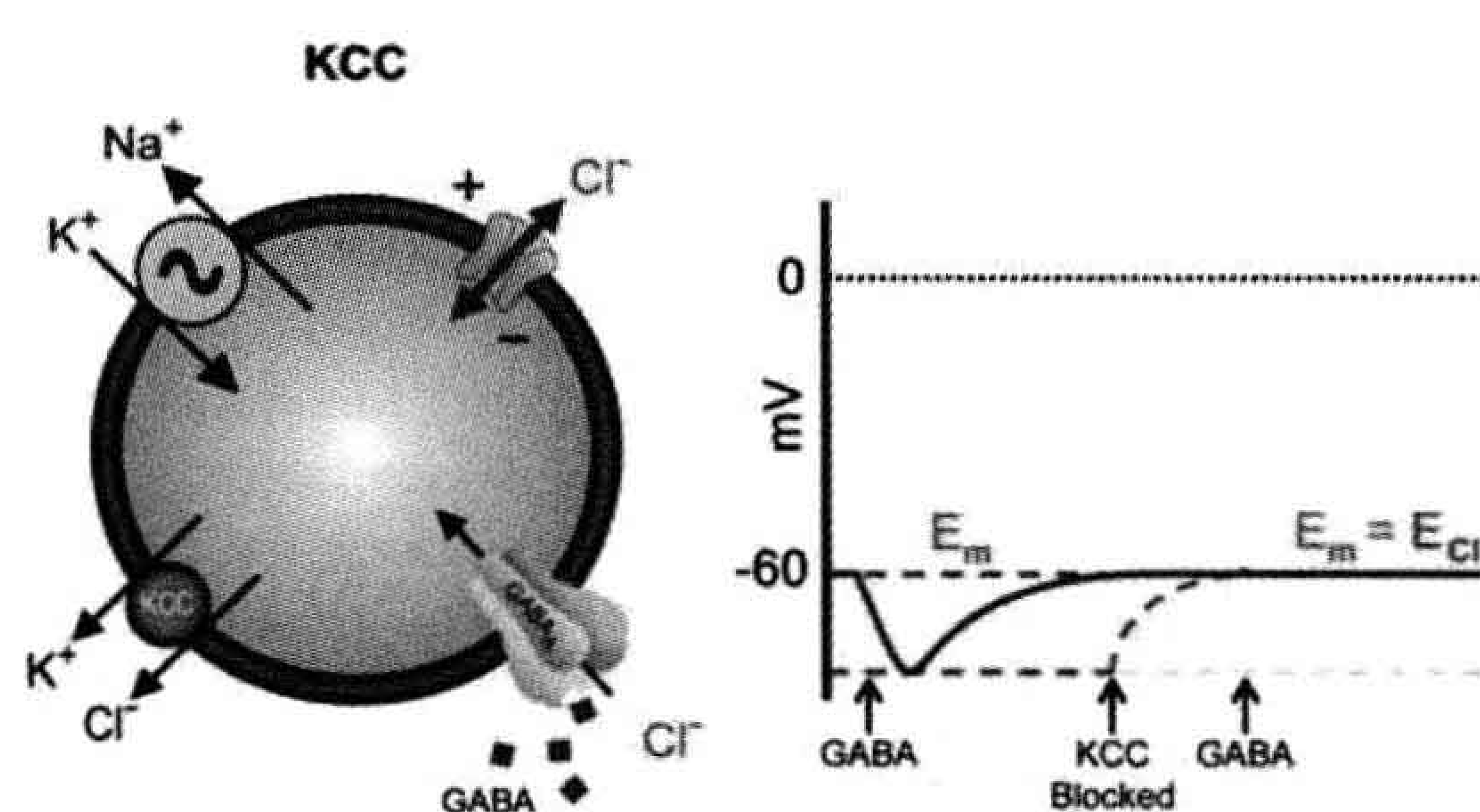


FIGURE 15.18 Model of a neuron expressing only K^+-Cl^- cotransporter, Na^+/K^+ ATPase, voltage-gated anion channels and GABA-gated anion channels. KCC actively extrudes Cl^- from the cell shifting E_{Cl} (red dashed line) to a more negative value than E_m (green dashed line). Right: A puff of GABA produces a hyperpolarizing IPSP (blue trace). When KCC is blocked, $[Cl^-]_i$ raises until reaching passive equilibrium ($E_m = E_{Cl}$). A second GABA application under these conditions does not produce a change in E_m but an increase in membrane conductance which is the basis of "shunting synaptic inhibition". *(Reproduced from Alvarez-Leefmans and Delpire, 2009b.)*

From Equation 15.20 one can readily calculate the $[K^+]_o$ at which the flux reverses from outward to inward or vice versa (flux reversal point or FRP):

$$\text{FRP} = [K^+]_o = \frac{[K^+]_i[Cl^-]_i}{[Cl^-]_o} \quad (15.21)$$

The FRP is an important parameter. At the FRP, the driving force for net K^+-Cl^- cotransport is zero ($\Delta\mu_{K,Cl} = 0$). For instance, in a cortical neuron having typical intracellular K^+ and Cl^- concentrations of 120 mM and 10 mM respectively, and $[Cl^-]_o = 113$ mM, the KCC2 mediated flux will reverse from efflux to influx when $[K^+]_o = 10.6$ mM.

VII. ELECTRONEUTRAL Na^+-Cl^- COTRANSPORTER

The Na^+-Cl^- cotransporter (NCC) was the first member of the SLC12A gene family to be identified at the molecular level. It was initially cloned from epithelial cells of the urinary bladder of the winter flounder (*Pseudopleuronectes americanus*) by Steve Hebert and colleagues (Gamba et al., 1993). NCC is also known as CC3 or TSC (thiazide-sensitive sodium chloride cotransporter), but the preferred nomenclature is NCC or SLC12A3. Its mammalian homolog was isolated from rat renal cortex (Gamba, 2009b). NCC is expressed predominantly in kidney, but is also expressed in osteoblasts and intestine. In mammalian kidney, NCC is located in the apical membrane of the epithelial cells of the distal convoluted tubule (DCT), where it functions as the major salt reabsorption pathway. The DCT mediates reabsorption of 5–15% of glomerular filtrate. The Na^+ gradient that drives transport from the lumen to the interstitium is generated and maintained by the Na^+/K^+ ATPase located in the basolateral membrane of DCT epithelial cells. A distinctive feature of NCC is its sensitivity to thiazides. The natriuretic effect of the thiazide diuretics underlies their therapeutic effect in edema states and hypertension. In addition, luminal thiazide in the DCT has a hypocalciuric effect, implicating NCC in the fine-tuning of Ca^{2+} excretion.

In humans, SLC12A3 is a 55-kb gene containing 26 exons. NCC is a membrane protein of 1002 to 1028 amino acid residues with a predicted topology typical of all the members of the SLC12A family. It exhibits a central hydrophobic domain made up of 12 putative trans-membrane (TM) spanning regions. A hydrophilic loop connects TMs 7 and 8 and contains two glycosylation sites. The hydrophobic domain is flanked by a short amino-terminal domain and a long carboxy-terminal domain that are located inside the cell. Functional expression of this cotransporter in *Xenopus laevis* oocytes demonstrated the known characteristics of the cotransporter in native

tissue: sensitivity to thiazide diuretics (metolazone > cyclothiazide > hydrochlorothiazide > chlorothiazide), insensitivity to amiloride and loop diuretics, K^+ independence, lower affinity for Cl^- than for Na^+ and a $1Na^+$:$1Cl^-$ stoichiometry; hence, it is an electroneutral transporter. The molecular mass of the core (deglycosylated) protein is ≈ 110 kDa. It has ≈ 45% amino acid identity with NKCC1; 45–48% with NKCC2 and ≈ 25% with KCC1 and KCC2 (Gamba, 2005, 2009b).

ACKNOWLEDGMENTS

This chapter is dedicated to the memory of Professor Richard D. Keynes (1919–2010), who revolutionized our thinking about chloride transport across cell membranes. The author thanks Professor Eric Delpire for enriching discussions and for reading the manuscript, Professor Shmuel Muallem for providing the original data used in Fig. 15.4 and Professors John Payne and Bliss Forbush for providing Fig. 15.16. Likewise, the author thanks Ms Jeannine Crum for reading the manuscript. The work done by the author has been supported by The National Institute of Neurological Disorders and Stroke Grant NS29227 and by Wright State University Boonshoft School of Medicine Research Challenge and Seed Grant Programs.

BIBLIOGRAPHY

Achilles, K., Okabe, A., Ikeda, M., et al. (2007). Kinetic properties of Cl uptake mediated by Na^+-dependent K^+-$2Cl^-$ cotransport in immature rat neocortical neurons. *J Neurosci, 27*, 8616–8627.

Adrian, R. H. (1961). Internal chloride concentration and chloride efflux of frog muscle. *J Physiol, 156*, 623–632.

Aickin, C. C. (1990). Chloride transport across the sarcolemma of vertebrate smooth and sketal. In F. J. Alvarez-Leefmans, & J. M. Russell (Eds.), *Chloride Channels and Carriers in Nerve, Muscle, and Glial Cells* (pp. 209–249). New York: Plenum Press.

Alper, S. L. (2009). Molecular physiology and genetics of Na^+-independent SLC4 anion exchangers. *J Exp Biol, 212*, 1672–1683.

Alper, S. L., Chernova, M. N., & Stewart, A. K. (2002). How pH regulates a pH regulator: a regulatory hot spot in the N-terminal cytoplasmic domain of the AE2 anion exchanger. *Cell Biochem Biophys, 36*, 123–136.

Alper, S. L., Vandorpe, D. H., Peters, L. L., & Brugnara, C. (2008). Reduced DIDS-sensitive chloride conductance in Ae1-/- mouse erythrocytes. *Blood Cells Mol Dis, 41*, 22–34.

Alvarez, B. V., Kieller, D. M., Quon, A. L., Markovich, D., & Casey, J. R. (2004). Slc26a6: a cardiac chloride-hydroxyl exchanger and predominant chloride-bicarbonate exchanger of the mouse heart. *J Physiol, 561*, 721–734.

Alvarez-Leefmans, F. J. (1990). Intracellular Cl^- regulation and synaptic inhibition in vertebrate and invertebrate neurons. In F. J. Alvarez-Leefmans, & J. M. Russell (Eds.), *Chloride Channels and Carriers in Nerve, Muscle, and Glial Cells* (pp. 109–158). New York: Plenum Press.

Alvarez-Leefmans, F. J. (2009). Chloride transporters in presynaptic inhibition, pain and neurogenic inflammation. In F. J. Alvarez-Leefmans, & E. Delpire (Eds.), *Physiology and Pathology of Chloride Transporters and Channels in the Nervous System* (pp. 439–470). Amsterdam: Academic Press-Elsevier.

Alvarez-Leefmans, F. J., & Delpire, E. (2009a). *Physiology and Pathology of Chloride Transporters and Channels in the Nervous System: from Molecules to Diseases*. Amsterdam: Academic Press-Elsevier.

Alvarez-Leefmans, F. J., & Delpire, E. (2009b). Thermodynamics and kinetics of chloride transport in neurons: an outline. In F. J. Alvarez-Leefmans, & E. Delpire (Eds.), *Physiology and Pathology of Chloride Transporters and Channels in the Nervous System* (pp. 81–108). Amsterdam: Academic Press-Elsevier.

Alvarez-Leefmans, F. J., Gamino, S. M., Giraldez, F., & Nogueron, I. (1988). Intracellular chloride regulation in amphibian dorsal root ganglion neurones studied with ion-selective microelectrodes. *J Physiol, 406*, 225–246.

Alvarez-Leefmans, F. J., Giraldez, F., & Russell, J. M. (1990). Methods for measuring chloride transport across nerve, muscle, and glial cells. In F. J. Alvarez-Leefmans, & J. M. Russell (Eds.), *Chloride Channels and Carriers in Nerve, Muscle, and Glial Cells* (pp. 3–66). New York: Plenum Press.

Alvarez-Leefmans, F. J., Leon-Olea, M., Mendoza-Sotelo, J., Alvarez, F. J., Anton, B., & Garduno, R. (2001). Immunolocalization of the Na^+-K^+-$2Cl^-$ cotransporter in peripheral nervous tissue of vertebrates. *Neuroscience, 104*, 569–582.

Alvarez-Leefmans, F. J., Nani, A., & Márquez, S. (1998). Chloride transport, osmotic balance, and presynaptic inhibition. In P. Rudomin, R. Romo, & L. M. Mendell (Eds.), *Presynaptic Inhibition and Neural Control* (pp. 50–79). New York: Oxford University Press.

Becker, M., Nothwang, H. G., & Friauf, E. (2003). Differential expression pattern of chloride transporters NCC, NKCC2, KCC1, KCC3, KCC4, and AE3 in the developing rat auditory brainstem. *Cell Tissue Res, 312*, 155–165.

Bell, P. D., Komlosi, P., & Zhang, Z. R. (2009). ATP as a mediator of macula densa cell signalling. *Purinergic Signal, 5*, 461–471.

Bellemer, A., Hirata, T., Romero, M. F., & Koelle, M. R. (2011). Two types of chloride transporters are required for $GABA_A$ receptor-mediated inhibition in C. elegans. *Embo J, 30*, 1852–1863.

Ben-Dor, S., Esterman, N., Rubin, E., & Sharon, N. (2004). Biases and complex patterns in the residues flanking protein N-glycosylation sites. *Glycobiology, 14*, 95–101.

Benjamin, B. A., & Johnson, E. A. (1997). A quantitative description of the Na-K-2Cl cotransporter and its conformity to experimental data. *Am J Physiol, 273*, F473–482.

Berglund, K., Kuner, T., & Augustine, G. J. (2009). Clomeleon, a genetically encoded chloride indicator. In F. J. Alvarez-Leefmans, & E. Delpire (Eds.), *Physiology and Pathology of Chloride Transporters and Channels in the Nervous System* (pp. 125–139). Amsterdam: Academic Press-Elsevier.

Bevensee, M. O., & Boron, W. F. (1998). Thermodynamics and physiology of cellular pH regulation. In K. Kaila, & B. R. Ransom (Eds.), *pH and Brain Function* (pp. 173–194). New York: Wiley-Liss.

Bize, I., & Dunham, P. B. (1994). Staurosporine, a protein kinase inhibitor, activates K-Cl cotransport in LK sheep erythrocytes. *Am J Physiol, 266*, C759–770.

Blaesse, P., Airaksinen, M. S., Rivera, C., & Kaila, K. (2009). Cation-chloride cotransporters and neuronal function. *Neuron, 61*, 820–838.

Boettger, T., Hubner, C. A., Maier, H., Rust, M. B., Beck, F. X., & Jentsch, T. J. (2002). Deafness and renal tubular acidosis in mice lacking the K-Cl cotransporter Kcc4. *Nature, 416*, 874–878.

Boettger, T., Rust, M. B., Maier, H., et al. (2003). Loss of K-Cl cotransporter KCC3 causes deafness, neurodegeneration and reduced seizure threshold. *Embo J, 22*, 5422–5434.

Byun, N., & Delpire, E. (2007). Axonal and periaxonal swelling precede peripheral neurodegeneration in KCC3 knockout mice. *Neurobiol Dis, 28*, 39–51.

Carmosino, M., Gimenez, I., Caplan, M., & Forbush, B. (2008). Exon loss accounts for differential sorting of Na-K-Cl cotransporters in polarized epithelial cells. *Mol Biol Cell, 19*, 4341–4351.

Carota, I., Theilig, F., Oppermann, M., et al. (2010). Localization and functional characterization of the human NKCC2 isoforms. *Acta Physiol (Oxf), 199*, 327–338.

Castrop, H., & Schnermann, J. (2008). Isoforms of renal Na-K-2Cl cotransporter NKCC2: expression and functional significance. *Am J Physiol Renal Physiol, 295*, F859–866.

Chen, L. M., Kelly, M. L., Parker, M. D., et al. (2008). Expression and localization of Na-driven $Cl^{-}HCO_3^{-}$ exchanger (SLC4A8) in rodent CNS. *Neuroscience, 153*, 162–174.

Chen, Y. F., Chou, C. Y., Ellory, J. C., & Shen, M. R. (2010). The emerging role of KCl cotransport in tumor biology. *Am J Transl Res, 2*, 345–355.

Chou, C. L., Yu, M. J., Kassai, E. M., et al. (2008). Roles of basolateral solute uptake via NKCC1 and of myosin II in vasopressin-induced cell swelling in inner medullary collecting duct. *Am J Physiol Renal Physiol, 295*, F192–201.

Darman, R. B., & Forbush, B. (2002). A regulatory locus of phosphorylation in the N terminus of the Na-K-Cl cotransporter, NKCC1. *J Biol Chem, 277*, 37542–37550.

Dehaye, J. P., Nagy, A., Premkumar, A., & Turner, R. J. (2003). Identification of a functionally important conformation-sensitive region of the secretory Na^+-K^+-$2Cl^-$ cotransporter (NKCC1). *J Biol Chem, 278*, 11811–11817.

Delpire, E., & Gagnon, K. B. (2008). SPAK and OSR1: STE20 kinases involved in the regulation of ion homoeostasis and volume control in mammalian cells. *Biochem J, 409*, 321–331.

Delpire, E., & Gagnon, K. B. (2011). Kinetics of hyperosmotically-stimulated Na-K-2Cl cotransporter in Xenopus laevis oocytes. *Am J Physiol Cell Physiol.*

Delpire, E., & Lauf, P. K. (1991). Magnesium and ATP dependence of K-Cl cotransport in low K^+ sheep red blood cells. *J Physiol, 441*, 219–231.

Delpire, E., & Lauf, P. K. (1992). Kinetics of DIDS inhibition of swelling-activated K-Cl cotransport in low K sheep erythrocytes. *J Membr Biol, 126*, 89–96.

Delpire, E., Days, E., Lewis, L. M., et al. (2009). Small-molecule screen identifies inhibitors of the neuronal K-Cl cotransporter KCC2. *Proc Natl Acad Sci, USA, 106*, 5383–5388.

Delpire, E., Lu, J., England, R., Dull, C., & Thorne, T. (1999). Deafness and imbalance associated with inactivation of the secretory Na-K-2Cl cotransporter. *Nat Genet, 22*, 192–195.

Delpire, E., Rauchman, M. I., Beier, D. R., Hebert, S. C., & Gullans, S. R. (1994). Molecular cloning and chromosome localization of a putative basolateral Na^+-K^+-$2Cl^-$ cotransporter from mouse inner medullary collecting duct (mIMCD-3) cells. *J Biol Chem, 269*, 25677–25683.

Di Fulvio, M., & Alvarez-Leefmans, F. J. (2009). The NKCC and NCC genes: an in silico view. In F. J. Alvarez-Leefmans, & E. Delpire (Eds.), *Physiology and Pathology of Chloride Transporters and Channels in the Nervous System: from Molecules to Diseases* (pp. 169–208). Amsterdam: Academic Press-Elsevier.

Duan, D. (2009). Phenomics of cardiac chloride channels: the systematic study of chloride channel function in the heart. *J Physiol, 587*, 2163–2177.

Dupre, N., Howard, H. C., Mathieu, J., et al. (2003). Hereditary motor and sensory neuropathy with agenesis of the corpus callosum. *Ann Neurol, 54*, 9–18.

Dzhala, V. I., Kuchibhotla, K. V., Glykys, J. C., et al. (2010). Progressive NKCC1-dependent neuronal chloride accumulation during neonatal seizures. *J Neurosci, 30*, 11745–11761.

Ellory, J. C., & Dunham, P. B. (1980). Volume-dependent passive potassium transport in LK LK sheep red cells. In U. V. Lassen, H. H. Ussing, & J. O. Wieth (Eds.), *Membrane Transport in Erythrocytes, Alfred Benzon Symposium, Vol. 14* (pp. 409–427). Munksgaard.

Evans, M. G., Marty, A., Tan, Y. P., & Trautmann, A. (1986). Blockage of Ca-activated Cl conductance by furosemide in rat lacrimal glands. *Pflügers Arch, 406*, 65–68.

Evans, R. L., Park, K., Turner, R. J., et al. (2000). Severe impairment of salivation in $Na^+/K^+/2Cl^-$ cotransporter (NKCC1)-deficient mice. *J Biol Chem, 275*, 26720–26726.

Feng, L., Campbell, E. B., Hsiung, Y., & MacKinnon, R. (2010). Structure of a eukaryotic CLC transporter defines an intermediate state in the transport cycle. *Science, 330*, 635–641.

Fischbarg, J. (2010). Fluid transport across leaky epithelia: central role of the tight junction and supporting role of aquaporins. *Physiol Rev, 90*, 1271–1290.

Flagella, M., Clarke, L. L., Miller, M. L., et al. (1999). Mice lacking the basolateral Na-K-2Cl cotransporter have impaired epithelial chloride secretion and are profoundly deaf. *J Biol Chem, 274*, 26946–26955.

Flatman, P. W. (2004). Regulation of Na-K-2Cl cotransport in red cells. *Adv Exp Med Biol, 559*, 77–88.

Flemmer, A. W., Gimenez, I., Dowd, B. F., Darman, R. B., & Forbush, B. (2002). Activation of the Na-K-Cl cotransporter NKCC1 detected with a phospho-specific antibody. *J Biol Chem, 277*, 37551–37558.

Frings, S. (2009). Chloride-based signal amplification in olfactory sensory neurons. In F. J. Alvarez-Leefmans, & E. Delpire (Eds.), *Physiology and Pathology of Chloride Transporters and Channels in the Nervous System* (pp. 413–424). Amsterdam: Academic Press-Elsevier.

Fujii, T., Takahashi, Y., Ikari, A., et al. (2009). Functional association between K^+-Cl^- cotransporter-4 and H^+, K^+-ATPase in the apical canalicular membrane of gastric parietal cells. *J Biol Chem, 284*, 619–629.

Gamba, G. (2005). Molecular physiology and pathophysiology of electroneutral cation-chloride cotransporters. *Physiol Rev, 85*, 423–493.

Gamba, G. (2009a). The sodium-dependent chloride cotransporters. In F. J. Alvarez-Leefmans, & E. Delpire (Eds.), *Physiology and Pathology of Chloride Transporters and Channels in the Nervous System: from Molecules to Diseases* (pp. 307–331). Amsterdam: Academic Press-Elsevier.

Gamba, G. (2009b). The thiazide-sensitive Na^+-Cl^- cotransporter: molecular biology, functional properties, and regulation by WNKs. *Am J Physiol Renal Physiol, 297*, F838–F848.

Gamba, G., & Friedman, P. A. (2009). Thick ascending limb: the Na^+:K^+:$2Cl^-$ cotransporter, NKCC2, and the calcium-sensing receptor, CaSR. *Pflügers Arch, 458*, 61–76.

Gamba, G., Garbarini, N., & Delpire, E. (2009). Regulation of cation-chloride cotransporters. In F. J. Alvarez-Leefmans, & E. Delpire (Eds.), *Physiology and Pathology of Chloride Transporters and Channels in the Nervous System: from Molecules to Diseases* (pp. 357–381). Amsterdam: Academic Press-Elsevier.

Gamba, G., Miyanoshita, A., Lombardi, M., et al. (1994). Molecular cloning, primary structure, and characterization of two members of the mammalian electroneutral sodium-(potassium)-chloride cotransporter family expressed in kidney. *J Biol Chem, 269*, 17713–17722.

Gamba, G., Saltzberg, S. N., Lombardi, M., et al. (1993). Primary structure and functional expression of a cDNA encoding the thiazide-sensitive, electroneutral sodium-chloride cotransporter. *Proc Natl Acad Sci, USA, 90*, 2749–2753.

Garbarini, N., & Delpire, E. (2009). Kockout models of cation-chloride cotransporters. In F. J. Alvarez-Leefmans, & E. Delpire (Eds.), *Physiology and Pathology of Chloride Transporters and Channels in the Nervous System: from Molecules to Diseases* (pp. 159–166). Amsterdam: Academic Press-Elsevier.

Garcia-Celma, J. J., Ploch, J., Smirnova, I., Kaback, H. R., & Fendler, K. (2010). Delineating electrogenic reactions during lactose/H^+ symport. *Biochemistry, 49*, 6115–6121.

Geck, P., & Heinz, E. (1986). The Na-K-2Cl cotransport system. *J Membr Biol, 91*, 97–105.

Geck, P., Pietrzyk, C., Burckhardt, B. C., Pfeiffer, B., & Heinz, E. (1980). Electrically silent cotransport on Na^+, K^+ and Cl^- in Ehrlich cells. *Biochim Biophys Acta, 600*, 432–447.

Gerelsaikhan, T., Parvin, M. N., & Turner, R. J. (2006). Biogenesis and topology of the secretory Na^+-K^+-$2Cl^-$ cotransporter (NKCC1) studied in intact mammalian cells. *Biochemistry, 45*, 12060–12067.

Gerelsaikhan, T., & Turner, R. J. (2000a). Membrane topology and function of the secretory Na^+-K^+-$2Cl^-$ cotransporter (NKCC1). *J Korean Med Sci.*(15 Suppl), S3–S4.

Gerelsaikhan, T., & Turner, R. J. (2000b). Transmembrane topology of the secretory Na^+-K^+-$2Cl^-$ cotransporter NKCC1 studied by in vitro translation. *J Biol Chem, 275*, 40471–40477.

Gibson, J. S., Ellory, J. C., Adragna, N. C., & Lauf, P. K. (2009). Pathophysiology of the K^+-Cl^-cotransporters: paths to discovery and overview. In F. J. Alvarez-Leefmans, & E. Delpire (Eds.), *Physiology and Pathology of Chloride Transporters and Channels in the Nervous System* (pp. 27–42). Amsterdam: Academic Press-Elsevier.

Gillen, C. M., & Forbush, B., 3rd. (1999). Functional interaction of the K-Cl cotransporter (KCC1) with the Na-K-Cl cotransporter in HEK-293 cells. *Am J Physiol, 276*, C328–336.

Gillen, C. M., Brill, S., Payne, J. A., & Forbush, B., 3rd. (1996). Molecular cloning and functional expression of the K-Cl cotransporter from rabbit, rat, and human. A new member of the cation-chloride cotransporter family. *J Biol Chem, 271*, 16237–16244.

Gonzalez-Islas, C., Chub, N., & Wenner, P. (2009). NKCC1 and AE3 appear to accumulate chloride in embryonic motoneurons. *J Neurophysiol, 101*, 507–518.

Good, D. W. (1994). Ammonium transport by the thick ascending limb of Henle's loop. *Annu Rev Physiol, 56*, 623–647.

Gosmanov, A. R., Schneider, E. G., & Thomason, D. B. (2003). NKCC activity restores muscle water during hyperosmotic challenge independent of insulin, ERK, and p38 MAPK. *Am J Physiol Regul Integr Comp Physiol, 284*, R655–665.

Granados-Soto, V., Arguelles, C. F., & Alvarez-Leefmans, F. J. (2005). Peripheral and central antinociceptive action of Na^+-K^+-$2Cl^-$ cotransporter blockers on formalin-induced nociception in rats. *Pain, 114*, 231–238.

Grichtchenko, I. I., Choi, I., Zhong, X., Bray-Ward, P., Russell, J. M., & Boron, W. F. (2001). Cloning, characterization, and chromosomal mapping of a human electroneutral Na^+-driven Cl^--HCO_3 exchanger. *J Biol Chem, 276*, 8358–8363.

Gundersen, D., Orlowski, J., & Rodriguez-Boulan, E. (1991). Apical polarity of Na, K-ATPase in retinal pigment epithelium is linked to a reversal of the ankyrin-fodrin submembrane cytoskeleton. *J Cell Biol, 112*, 863–872.

Haas, B. R., & Sontheimer, H. (2010). Inhibition of the sodium-potassium-chloride cotransporter isoform-1 reduces glioma invasion. *Cancer Res, 70*, 5597–5606.

Haas, M. (1994). The Na-K-Cl cotransporters. *Am J Physiol, 267*, C869–885.

Haas, M., & Forbush, B., 3rd. (1998). The Na-K-Cl cotransporters. *J Bioenerg Biomembr, 30*, 161–172.

Haas, M., & Forbush, B., 3rd. (2000). The Na-K-Cl cotransporter of secretory epithelia. *Annu Rev Physiol, 62*, 515–534.

Haas, M., Schmidt, W. F., 3rd, & McManus, T. J. (1982). Catecholamine-stimulated ion transport in duck red cells. Gradient effects in electrically neutral [Na^+ K^+ $2Cl^-$] Cotransport. *J Gen Physiol, 80*, 125–147.

Hamann, S., Herrera-Perez, J. J., Bundgaard, M., Alvarez-Leefmans, F. J., & Zeuthen, T. (2005). Water permeability of Na^+-K^+-$2Cl^-$ cotransporters in mammalian epithelial cells. *J Physiol, 568*, 123–135.

Hamann, S., Herrera-Perez, J. J., Zeuthen, T., & Alvarez-Leefmans, F. J. (2010). Cotransport of water by the Na^+-K^+-$2Cl^-$ cotransporter NKCC1 in mammalian epithelial cells. *J Physiol, 588*, 4089–4101.

Hannaert, P., Alvarez-Guerra, M., Pirot, D., Nazaret, C., & Garay, R. P. (2002). Rat NKCC2/NKCC1 cotransporter selectivity for loop diuretic drugs. *Naunyn Schmiedebergs Arch Pharmacol, 365*, 193–199.

Harris, G. L., & Betz, W. J. (1987). Evidence for active chloride accumulation in normal and denervated rat lumbrical muscle. *J Gen Physiol, 90*, 127–144.

Hartmann, A. M., Wenz, M., Mercado, A., et al. (2010). Differences in the large extracellular loop between the K^+-Cl^- cotransporters KCC2 and KCC4. *J Biol Chem, 285*, 23994–24002.

Hartzell, H. C. (2009). Chloride channels: an historical perspective. In F. J. Alvarez-Leefmans, & E. Delipre (Eds.), *Physiology and Pathology of Chloride Transporters and Channels in the Nervous System: from Molecules to Diseases* (pp. 3–15). Amsterdam: Academic Press-Elsevier.

Hengl, T., Kaneko, H., Dauner, K., Vocke, K., Frings, S., & Mohrlen, F. (2010). Molecular components of signal amplification in olfactory sensory cilia. *Proc Natl Acad Sci, USA, 107*, 6052–6057.

Hiki, K., D'Andrea, R. J., Furze, J., et al. (1999). Cloning, characterization, and chromosomal location of a novel human K^+-Cl^- cotransporter. *J Biol Chem, 274*, 10661–10667.

Hodgkin, A. L., & Horowicz, P. (1959). The influence of potassium and chloride ions on the membrane potential of single muscle fibres. *J Physiol, 148*, 127–160.

Hoffmann, E. K. (2001). The pump and leak steady-state concept with a variety of regulated leak pathways. *J Membr Biol, 184*, 321–330.

Hoffmann, E. K., Lambert, I. H., & Pedersen, S. F. (2009). Physiology of cell volume regulation in vertebrates. *Physiol Rev, 89*, 193–277.

Hoffmann, E. K., Schiodt, M., & Dunham, P. (1986). The number of chloride-cation cotransport sites on Ehrlich ascites cells measured with [3H]bumetanide. *Am J Physiol, 250*, C688–693.

Howard, H. C., Mount, D. B., Rochefort, D., et al. (2002). The K-Cl cotransporter KCC3 is mutant in a severe peripheral neuropathy

associated with agenesis of the corpus callosum. *Nat Genet, 32*, 384–392.

Hubner, C. A., & Rust, M. B. (2007). Physiology of cation-chloride cotransporters. In M. Pusch (Ed.), *Chloride Movements across Cellular Membranes, Vol. 38* (pp. 241–277). Amsterdam: Elsevier.

Hubner, C. A., Stein, V., Hermans-Borgmeyer, I., Meyer, T., Ballanyi, K., & Jentsch, T. J. (2001). Disruption of KCC2 reveals an essential role of K-Cl cotransport already in early synaptic inhibition. *Neuron, 30*, 515–524.

Hutter, O. F., & Noble, D. (1960). The chloride conductance of frog skeletal muscle. *J Physiol, 151*, 89–102.

Ikeda, K., Oshima, T., Hidaka, H., & Takasaka, T. (1997). Molecular and clinical implications of loop diuretic ototoxicity. *Hear Res, 107*, 1–8.

Isenring, P., & Forbush, B. (2001). Ion transport and ligand binding by the Na-K-Cl cotransporter, structure-function studies. *Comp Biochem Physiol A Mol Integr Physiol, 130*, 487–497.

Jennings, M. L., & Adame, M. F. (2001). Direct estimate of 1:1 stoichiometry of K^+-Cl^- cotransport in rabbit erythrocytes. *Am J Physiol Cell Physiol, 281*, C825–832.

Jentsch, T. J. (2008). CLC chloride channels and transporters: from genes to protein structure, pathology and physiology. *Crit Rev Biochem Mol Biol, 43*, 3–36.

Jurkat-Rott, K., Fauler, M., & Lehmann-Horn, F. (2006). Ion channels and ion transporters of the transverse tubular system of skeletal muscle. *J Muscle Res Cell Motil, 27*, 275–290.

Kahle, K. T., Rinehart, J., & Lifton, R. P. (2010). Phosphoregulation of the Na-K-2Cl and K-Cl cotransporters by the WNK kinases. *Biochim Biophys Acta, 1802*, 1150–1158.

Kahle, K. T., Simard, J. M., Staley, K. J., Nahed, B. V., Jones, P. S., & Sun, D. (2009). Molecular mechanisms of ischemic cerebral edema: role of electroneutral ion transport. *Physiology (Bethesda), 24*, 257–265.

Kahle, K. T., & Staley, K. J. (2008). The bumetanide-sensitive Na-K-2Cl cotransporter NKCC1 as a potential target of a novel mechanism-based treatment strategy for neonatal seizures. *Neurosurg Focus, 25*, E22.

Kaji, D. M. (1993). Effect of membrane potential on K-Cl transport in human erythrocytes. *Am J Physiol, 264*, C376–382.

Karadsheh, M. F., Byun, N., Mount, D. B., & Delpire, E. (2004). Localization of the KCC4 potassium-chloride cotransporter in the nervous system. *Neuroscience, 123*, 381–391.

Keynes, R. D. (1963). Chloride in the squid giant axon. *J Physiol, 169*, 690–705.

Kim, Y., & Trussell, L. O. (2009). Negative shift in the glycine reversal potential mediated by a Ca^{2+}- and pH-dependent mechanism in interneurons. *J Neurosci, 29*, 11495–11510.

Kristensen, M., & Juel, C. (2010). Potassium-transporting proteins in skeletal muscle: cellular location and fibre-type differences. *Acta Physiol (Oxf), 198*, 105–123.

Kurschat, C. E., Shmukler, B. E., Jiang, L., et al. (2006). Alkaline-shifted pHo sensitivity of AE2c1-mediated anion exchange reveals novel regulatory determinants in the AE2 N-terminal cytoplasmic domain. *J Biol Chem, 281*, 1885–1896.

Lang, F., Vallon, V., Knipper, M., & Wangemann, P. (2007). Functional significance of channels and transporters expressed in the inner ear and kidney. *Am J Physiol Cell Physiol, 293*, C1187–1208.

Lauf, P. K., & Theg, B. E. (1980). A chloride dependent K^+ flux induced by N-ethylmaleimide in genetically low K^+ sheep and goat erythrocytes. *Biochem Biophys Res Commun, 92*, 1422–1428.

Le Rouzic, P., Ivanov, T. R., Stanley, P. J., et al. (2006). KCC3 and KCC4 expression in rat adult forebrain. *Brain Res., 1110*, 39–45.

Lerma, J., & Martin del Rio, R. (1992). Chloride transport blockers prevent N-methyl-D-aspartate receptor-channel complex activation. *Mol Pharmacol, 41*, 217–222.

Lytle, C. (2003). Na^+-K^+-$2Cl^-$ cotransport. In I. Bernhardt, & J. C. Ellory (Eds.), *Red Cell Membrane Transport in Health and Disease* (pp. 173–195). Berlin ; New York: Springer.

Lytle, C., & Forbush, B., 3rd. (1992). The Na-K-Cl cotransport protein of shark rectal gland. II. Regulation by direct phosphorylation. *J Biol Chem., 267*, 25438–25443.

Lytle, C., McManus, T. J., & Haas, M. (1998). A model of Na-K-2Cl cotransport based on ordered ion binding and glide symmetry. *Am J Physiol, 274*, C299–309.

Lytle, C., Xu, J. C., Biemesderfer, D., & Forbush, B., 3rd. (1995). Distribution and diversity of Na-K-Cl cotransport proteins: a study with monoclonal antibodies. *Am J Physiol, 269*, C1496–1505.

MacAulay, N., Hamann, S., & Zeuthen, T. (2009). Chloride transporters as water pumps: elements in a new model of epithelial water transport. In F. J. Alvarez-Leefmans, & E. Delpire (Eds.), *Physiology and Pathology of Chloride Transporters and Channels in the Nervous System* (pp. 547–568). Amsterdam: Academic Press-Elsevier.

Marcano, M., Yang, H. M., Nieves-Gonzalez, A., Clausen, C., & Moore, L. C. (2009). Parameter estimation for mathematical models of NKCC2 cotransporter isoforms. *Am J Physiol Renal Physiol, 296*, F369–381.

McDaniel, N., Pace, A. J., Spiegel, S., et al. (2005). Role of Na-K-2Cl cotransporter-1 in gastric secretion of nonacidic fluid and pepsinogen. *Am J Physiol Gastrointest Liver Physiol, 289*, G550–560.

McRoberts, J. A., Erlinger, S., Rindler, M. J., & Saier, M. H., Jr. (1982). Furosemide-sensitive salt transport in the Madin-Darby canine kidney cell line. Evidence for the cotransport of Na^+, K^+, and Cl. *J Biol Chem, 257*, 2260–2266.

Mercado, A., Song, L., Vazquez, N., Mount, D. B., & Gamba, G. (2000). Functional comparison of the K^+-Cl^- cotransporters KCC1 and KCC4. *J Biol Chem, 275*, 30326–30334.

Mercado, A., Vazquez, N., Song, L., et al. (2005). NH2-terminal heterogeneity in the KCC3 K^+-Cl^- cotransporter. *Am J Physiol Renal Physiol, 289*, F1246–1261.

Migliati, E., Meurice, N., DuBois, P., et al. (2009). Inhibition of aquaporin-1 and aquaporin-4 water permeability by a derivative of the loop diuretic bumetanide acting at an internal pore-occluding binding site. *Mol Pharmacol, 76*, 105–112.

Mistrik, P., & Ashmore, J. (2009). The role of potassium recirculation in cochlear amplification. *Curr Opin Otolaryngol Head Neck Surg, 17*, 394–399.

Mount, D. B., Mercado, A., Song, L., et al. (1999). Cloning and characterization of KCC3 and KCC4, new members of the cation-chloride cotransporter gene family. *J Biol Chem, 274*, 16355–16362.

Munoz, A., Mendez, P., DeFelipe, J., & Alvarez-Leefmans, F. J. (2007). Cation-chloride cotransporters and GABA-ergic innervation in the human epileptic hippocampus. *Epilepsia, 48*, 663–673.

Nejsum, L. N., Praetorius, J., & Nielsen, S. (2005). NKCC1 and NHE1 are abundantly expressed in the basolateral plasma membrane of secretory coil cells in rat, mouse, and human sweat glands. *Am J Physiol Cell Physiol, 289*, C333–340.

Nielsen, S., Maunsbach, A. B., Ecelbarger, C. A., & Knepper, M. A. (1998). Ultrastructural localization of Na-K-2Cl cotransporter in thick ascending limb and macula densa of rat kidney. *Am J Physiol, 275*, F885–893.

O'Donnell, M. E., Tran, L., Lam, T. I., Liu, X. B., & Anderson, S. E. (2004). Bumetanide inhibition of the blood-brain barrier Na-K-Cl cotransporter reduces edema formation in the rat middle cerebral artery occlusion model of stroke. *J Cereb Blood Flow Metab, 24*, 1046–1056.

O'Grady, S. M., Palfrey, H. C., & Field, M. (1987a). Characteristics and functions of Na-K-Cl cotransport in epithelial tissues. *Am J Physiol, 253*, C177–192.

O'Grady, S. M., Palfrey, H. C., & Field, M. (1987b). Na-K-2Cl cotransport in winter flounder intestine and bovine kidney outer medulla: [3H] bumetanide binding and effects of furosemide analogues. *J Membr Biol, 96*, 11–18.

Oppermann, M., Mizel, D., Huang, G., et al. (2006). Macula densa control of renin secretion and preglomerular resistance in mice with selective deletion of the B isoform of the Na, K,2Cl cotransporter. *J Am Soc Nephrol, 17*, 2143–2152.

Oppermann, M., Mizel, D., Kim, S. M., et al. (2007). Renal function in mice with targeted disruption of the A isoform of the Na-K-2Cl cotransporter. *J Am Soc Nephrol, 18*, 440–448.

Pan, D., Kalfa, T. A., Wang, D., et al. (2011). KCl cotransporter gene expression during human and murine erythroid differentiation. *J Biol Chem.*

Panet, R., Marcus, M., & Atlan, H. (2000). Overexpression of the $Na^+/K^+/Cl^-$ cotransporter gene induces cell proliferation and phenotypic transformation in mouse fibroblasts. *J Cell Physiol, 182*, 109–118.

Paredes, A., Plata, C., Rivera, M., et al. (2006). Activity of the renal Na^+-K^+-$2Cl^-$ cotransporter is reduced by mutagenesis of N-glycosylation sites: role for protein surface charge in Cl^- transport. *Am J Physiol Renal Physiol, 290*, F1094–1102.

Payne, J. A. (1997). Functional characterization of the neuronal-specific K-Cl cotransporter: implications for $[K^+]_o$ regulation. *Am J Physiol, 273*, C1516–1525.

Payne, J. A. (2009). The potasium-chloride cotransporters: from cloning to structure and function. In F. J. Alvarez-Leefmans, & E. Delpire (Eds.), *Physiology and Pathology of Chloride Transporters and Channels in the Nervous System: from Molecules to Diseases* (pp. 333–356). Amsterdam: Academic Press-Elsevier.

Payne, J. A., & Forbush, B., 3rd. (1994). Alternatively spliced isoforms of the putative renal Na-K-Cl cotransporter are differentially distributed within the rabbit kidney. *Proc Natl Acad Sci USA, 91*, 4544–4548.

Payne, J. A., & Forbush, B., 3rd. (1995). Molecular characterization of the epithelial Na-K-Cl cotransporter isoforms. *Curr Opin Cell Biol, 7*, 493–503.

Payne, J. A., Rivera, C., Voipio, J., & Kaila, K. (2003). Cation-chloride cotransporters in neuronal communication, development and trauma. *Trends Neurosci, 26*, 199–206.

Payne, J. A., Stevenson, T. J., & Donaldson, L. F. (1996). Molecular characterization of a putative K-Cl cotransporter in rat brain. A neuronal-specific isoform. *J Biol Chem, 271*, 16245–16252.

Payne, J. A., Xu, J. C., Haas, M., Lytle, C. Y., Ward, D., & Forbush, B., 3rd. (1995). Primary structure, functional expression, and chromosomal localization of the bumetanide-sensitive Na-K-Cl cotransporter in human colon. *J Biol Chem, 270*, 17977–17985.

Pearson, M. M., Lu, J., Mount, D. B., & Delpire, E. (2001). Localization of the K^+-Cl^- cotransporter, KCC3, in the central and peripheral nervous systems: expression in the choroid plexus, large neurons and white matter tracts. *Neuroscience, 103*, 481–491.

Pégurier, C., Bosman, N., Collart, P., Delporte, M. L., Leclercq, K., Lengelé, S., Kanduluru, A. K., Meunier, S., Pacico, N., Vadali, L. R., Wagner, A., Wolff, C., & Provins, L. (2010). Benzyl prolinate derivatives as novel selective KCC2 blockers. *Bioorg Med Chem Lett, 20*, 2542–2545.

Peti-Peterdi, J., & Harris, R. C. (2010). Macula densa sensing and signaling mechanisms of renin release. *J Am Soc Nephrol, 21*, 1093–1096.

Plata, C., Meade, P., Vazquez, N., Hebert, S. C., & Gamba, G. (2002). Functional properties of the apical Na^+-K^+-$2Cl^-$ cotransporter isoforms. *J Biol Chem, 277*, 11004–11012.

Plotkin, M. D., Kaplan, M. R., Peterson, L. N., Gullans, S. R., Hebert, S. C., & Delpire, E. (1997). Expression of the Na^+-K^+-$2Cl^-$ cotransporter BSC2 in the nervous system. *Am J Physiol, 272*, C173–183.

Prasad, V., Bodi, I., Meyer, J. W., et al. (2008). Impaired cardiac contractility in mice lacking both the AE3 Cl^-/HCO_3^- exchanger and the NKCC1 Na^+-K^+-$2Cl^-$ cotransporter: effects on Ca2+ handling and protein phosphatases. *J Biol Chem, 283*, 31303–31314.

Race, J. E., Makhlouf, F. N., Logue, P. J., Wilson, F. H., Dunham, P. B., & Holtzman, E. J. (1999). Molecular cloning and functional characterization of KCC3, a new K-Cl cotransporter. *Am J Physiol, 277*, C1210–1219.

Randall, J., Thorne, T., & Delpire, E. (1997). Partial cloning and characterization of Slc12a2: the gene encoding the secretory Na^+-K^+-$2Cl^-$ cotransporter. *Am J Physiol, 273*, C1267–1277.

Reddy, M. M., & Quinton, P. M. (1999). Bumetanide blocks CFTR GCl in the native sweat duct. *Am J Physiol, 276*, C231–237.

Reuss, L. (1997). Epithelial transport. In J. P. Hoffman, & J. D. Jamieson (Eds.), *Handbook of Physiology. Section 14: Cell Physiology* (pp. 309–388). New York: Oxford University Press.

Reynolds, A., Brustein, E., Liao, M., et al. (2008). Neurogenic role of the depolarizing chloride gradient revealed by global overexpression of KCC2 from the onset of development. *J Neurosci, 28*, 1588–1597.

Rinehart, J., Maksimova, Y. D., Tanis, J. E., et al. (2009). Sites of regulated phosphorylation that control K-Cl cotransporter activity. *Cell., 138*, 525–536.

Rivera, C., Voipio, J., Payne, J. A., et al. (1999). The K^+/Cl^- cotransporter KCC2 renders GABA hyperpolarizing during neuronal maturation. *Nature, 397*, 251–255.

Rocha-Gonzalez, H. I., Mao, S., & Alvarez-Leefmans, F. J. (2008). Na^+, K^+,$2Cl^-$ cotransport and intracellular chloride regulation in rat primary sensory neurons: thermodynamic and kinetic aspects. *J Neurophysiol, 100*, 169–184.

Romero, M. F., Chang, M.-H., & Mount, D. (2009). From cloning to structure, function, and regulation of chloride-dependent and independent bicarbonate transporters. In F. J. Alvarez-Leefmans, & E. Delipre (Eds.), *Physiology and Pathology of Chloride Transporters and Channels in the Nervous System: from Molecules to Diseases* (pp. 43–79). Amsterdam: Academic Press-Elsevier.

Romero, M. F., Fulton, C. M., & Boron, W. F. (2004). The SLC4 family of HCO_3^- transporters. *Pflügers Arch, 447*, 495–509.

Roseth, S., Fykse, E. M., & Fonnum, F. (1995). Uptake of L-glutamate into rat brain synaptic vesicles: effect of inhibitors that bind specifically to the glutamate transporter. *J Neurochem, 65*, 96–103.

Rudomin, P., & Schmidt, R. F. (1999). Presynaptic inhibition in the vertebrate spinal cord revisited. *Exp Brain Res, 129*, 1–37.

Russell, J. M. (1984). Chloride in the squid giant axon. *Curr Top Membr Transp, 22*, 177–193.

Russell, J. M. (2000). Sodium-potassium-chloride cotransport. *Physiol Rev, 80*, 211–276.

Russell, J. M. (2009). Sodium-coupled chloride cotransporters: discovery and newly emerging concepts. In F. J. Alvarez-Leefmans, & E. Delpire (Eds.), *Physiology and Pathology of Chloride Transporters and Channels in the Nervous System* (pp. 17–26). Amsterdam: Academic Press-Elsevier.

Rust, M. B., Alper, S. L., Rudhard, Y., et al. (2007). Disruption of erythroid K-Cl cotransporters alters erythrocyte volume and partially rescues erythrocyte dehydration in SAD mice. *J Clin Invest, 117*, 1708–1717.

Rust, M. B., Faulhaber, J., Budack, M. K., et al. (2006). Neurogenic mechanisms contribute to hypertension in mice with disruption of the K-Cl cotransporter KCC3. *Circ Res, 98*, 549–556.

Schlatter, E., Greger, R., & Weidtke, C. (1983). Effect of "high ceiling" diuretics on active salt transport in the cortical thick ascending limb of Henle's loop of rabbit kidney. Correlation of chemical structure and inhibitory potency. *Pflügers Arch, 396*, 210–217.

Shankar, S. S., & Brater, D. C. (2003). Loop diuretics: from the Na-K-2Cl transporter to clinical use. *Am J Physiol Renal Physiol, 284*, F11–21.

Shcheynikov, N., Wang, Y., Park, M., et al. (2006). Coupling modes and stoichiometry of Cl^-/HCO_3^- exchange by slc26a3 and slc26a6. *J Gen Physiol, 127*, 511–524.

Shekarabi, M., Salin-Cantegrel, A., Laganiere, J., Gaudet, R., Dion, P., & Rouleau, G. A. (2011). Cellular expression of the K^+-Cl^- cotransporter KCC3 in the central nervous system of mouse. *Brain Res, 1374*, 15–26.

Shillingford, J. M., Miyoshi, K., Flagella, M., Shull, G. E., & Hennighausen, L. (2002). Mouse mammary epithelial cells express the Na-K-Cl cotransporter, NKCC1: characterization, localization, and involvement in ductal development and morphogenesis. *Mol Endocrinol, 16*, 1309–1321.

Silva, P., Solomon, R. J., & Epstein, F. H. (1996). The rectal gland of Squalus acanthias: a model for the transport of chloride. *Kidney Int, 49*, 1552–1556.

Silva, P., Stoff, J., Field, M., Fine, L., Forrest, J. N., & Epstein, F. H. (1977). Mechanism of active chloride secretion by shark rectal gland: role of Na-K-ATPase in chloride transport. *Am J Physiol, 233*, F298–306.

Somjen, G. S. (2004). *Ions in the Brain*. New York: Oxford University Press.

Song, L., Mercado, A., Vazquez, N., et al. (2002). Molecular, functional, and genomic characterization of human KCC2, the neuronal K-Cl cotransporter. *Brain Res Mol Brain Res, 103*, 91–105.

Steinbach, H. B. (1941). Chloride in the giant axons of the squid. *J Cell Comp Physiol, 17*, 57–64.

Stil, A., Liabeuf, S., Jean-Xavier, C., Brocard, C., Viemari, J. C., & Vinay, L. (2009). Developmental up-regulation of the potassium-chloride cotransporter type 2 in the rat lumbar spinal cord. *Neuroscience, 164*, 809–821.

Strauss, O. (2005). The retinal pigment epithelium in visual function. *Physiol Rev, 85*, 845–881.

Sung, K. W., Kirby, M., McDonald, M. P., Lovinger, D. M., & Delpire, E. (2000). Abnormal $GABA_A$ receptor-mediated currents in dorsal root ganglion neurons isolated from Na-K-2Cl cotransporter null mice. *J Neurosci, 20*, 7531–7538.

Takahashi, N., Chernavvsky, D. R., Gomez, R. A., Igarashi, P., Gitelman, H. J., & Smithies, O. (2000). Uncompensated polyuria in a mouse model of Bartter's syndrome. *Proc Natl Acad Sci USA, 97*, 5434–5439.

Thomas, R. C. (1984). Experimental displacement of intracellular pH and the mechanism of its subsequent recovery. *J Physiol, 354*, 3P–22P.

Tradtrantip, L., Tajima, M., Li, L., & Verkman, A. S. (2009). Aquaporin water channels in transepithelial fluid transport. *J Med Invest* (56 Suppl), 179–184.

Ussing, H. H. (1982). Volume regulation of frog skin epithelium. *Acta Physiol Scand, 114*, 363–369.

Uvarov, P., Ludwig, A., Markkanen, M., et al. (2007). A novel N-terminal isoform of the neuron-specific K-Cl cotransporter KCC2. *J Biol Chem, 282*, 30570–30576.

Vaughan-Jones, R. D. (1982). Chloride activity and its control in skeletal and cardiac muscle. *Philos Trans R Soc Lond B Biol Sci., 299*, 537–548.

Velazquez, H., & Silva, T. (2003). Cloning and localization of KCC4 in rabbit kidney: expression in distal convoluted tubule. *Am J Physiol Renal Physiol, 285*, F49–58.

Verkman, A. S. (2009). Chemical and GFP-based fluorescent chloride indicators. In F. J. Alvarez-Leefmans, & E. Delipre (Eds.), *Physiology and Pathology of Chloride Transporters and Channels in the Nervous System: from Molecules to Diseases* (pp. 111–123). Amsterdam: Academic Press-Elsevier.

Viemari, J. C., Bos, R., Boulenguez, P., et al. (2011). Importance of chloride homeostasis in the operation of rhythmic motor networks. *Prog Brain Res, 188*, 3–14.

Walz, W. (1992). Role of Na/K/Cl cotransport in astrocytes. *Can J Physiol Pharmacol*, (70 Suppl), S260–262.

Wang, D. D., & Kriegstein, A. R. (2009). Defining the role of GABA in cortical development. *J Physiol, 587*, 1873–1879.

Warmuth, S., Zimmermann, I., & Dutzler, R. (2009). X-ray structure of the C-terminal domain of a prokaryotic cation-chloride cotransporter. *Structure, 17*, 538–546.

Waseem, T., Mukhtarov, M., Buldakova, S., Medina, I., & Bregestovski, P. (2010). Genetically encoded Cl-sensor as a tool for monitoring of Cl-dependent processes in small neuronal compartments. *J Neurosci Meth, 193*, 14–23.

Weiner, I. D., & Verlander, J. W. (2011). Role of NH_3 and NH_4^+ transporters in renal acid-base transport. *Am J Physiol Renal Physiol, 300*, F11–23.

Williams, J. R., Sharp, J. W., Kumari, V. G., Wilson, M., & Payne, J. A. (1999). The neuron-specific K-Cl cotransporter, KCC2. Antibody development and initial characterization of the protein. *J Biol Chem, 274*, 12656–12664.

Willis, W. D. (2006). John Eccles' studies of spinal cord presynaptic inhibition. *Prog Neurobiol, 78*, 189–214.

Willis, W. D., Jr. (1999). Dorsal root potentials and dorsal root reflexes: a double-edged sword. *Exp Brain Res, 124*, 395–421.

Witschi, R., Punnakkal, P., Paul, J., et al. (2011). Presynaptic alpha2-$GABA_A$ receptors in primary afferent depolarization and spinal pain control. *J Neurosci, 31*, 8134–8142.

Wong, J. A., Gosmanov, A. R., Schneider, E. G., & Thomason, D. B. (2001). Insulin-independent, MAPK-dependent stimulation of NKCC activity in skeletal muscle. *Am J Physiol Regul Integr Comp Physiol, 281*, R561–571.

Woo, N. S., Lu, J., England, R., et al. (2002). Hyperexcitability and epilepsy associated with disruption of the mouse neuronal-specific K-Cl cotransporter gene. *Hippocampus, 12*, 258–268.

Wu, Q., Delpire, E., Hebert, S. C., & Strange, K. (1998). Functional demonstration of Na^{+}-K^{+}-$2Cl^{-}$ cotransporter activity in isolated, polarized choroid plexus cells. *Am J Physiol, 275*, C1565–1572.

Wu, Y., Wang, W., Diez-Sampedro, A., & Richerson, G. B. (2007). Nonvesicular inhibitory neurotransmission via reversal of the GABA transporter GAT-1. *Neuron, 56*, 851–865.

Xu, J. C., Lytle, C., Zhu, T. T., Payne, J. A., Benz, E., Jr., & Forbush, B., 3rd. (1994). Molecular cloning and functional expression of the bumetanide-sensitive Na-K-Cl cotransporter. *Proc Natl Acad Sci USA, 91*, 2201–2205.

Yan, Y., Dempsey, R. J., Flemmer, A., Forbush, B., & Sun, D. (2003). Inhibition of Na^{+}-K^{+}-Cl^{-} cotransporter during focal cerebral ischemia decreases edema and neuronal damage. *Brain Res, 961*, 22–31.

Yerby, T. R., Vibat, C. R., Sun, D., Payne, J. A., & O'Donnell, M. E. (1997). Molecular characterization of the Na-K-Cl cotransporter of bovine aortic endothelial cells. *Am J Physiol, 273*, C188–197.

Zdebik, A. A., Wangemann, P., & Jentsch, T. J. (2009). Potassium ion movement in the inner ear: insights from genetic disease and mouse models. *Physiology (Bethesda), 24*, 307–316.

Zeuthen, T. (2010). Water-transporting proteins. *J Membr Biol, 234*, 57–73.

Chapter 16

Osmosis and Regulation of Cell Volume

Clive M. Baumgarten and Joseph J. Feher

Chapter Outline

I. SUMMARY

The study of mechanisms underlying osmosis and the regulation of cell volume under both isosmotic and anisosmotic conditions has been fruitful. We understand in substantial detail how water and ions cross the membrane. Where do we go from here? Many directions are possible and as many details are missing as are known. For example, the identification and cloning of water channels raise several important questions. What is it about the protein structure that makes this a water

Cell Physiology Sourcebook. DOI: 10.1016/B978-0-12-387738-3.00016-0

channel? How does water interact with the channel? From a theoretical perspective, how is osmotic pressure sensed and how does osmosis occur through a channel structure that is different in important ways from the well-explored hydrodynamic models? From the perspective of regulation of ion transport, much remains to be understood about how cells sense swelling and shrinking and how a cell decides on its optimal volume. There are also unanswered questions concerning the regulation of volume regulatory ion transporters by cellular messengers, metabolic demands and pathological states. In short, we can look forward to many more fruitful years of research on these topics.

II. INTRODUCTION

In whole blood, erythrocytes are biconcave disks about 7 μm in diameter and 2 μm thick. When diluted in a solution of 0.9% NaCl (w/v), erythrocytes retain this shape. When diluted with higher concentrations of salt, the erythrocytes shrink, appearing as spheres with spikes all over their surface. These cells are described as *crenated*. If erythrocytes are diluted with a markedly lower concentration of salt, the cells swell. They first become spherical and then, if the solution is sufficiently low in salt, the cells burst and release their contents. These simple observations give rise to the concept of tonicity. *Tonicity* is operationally defined as the ability of a solution to shrink or swell specified cells. Thus, an *isotonic* solution induces no volume change when placed in contact with the cells. The tonicity of the solution is equal to the tonicity of the cell's contents. *Hypertonic* solutions shrink cells, whereas *hypotonic* solutions increase cell volume. A solution that is isotonic for one type of cell may or may not be isotonic for others.

All animal cells shrink or swell on exposure to *anisotonic* solutions. Figure 16.1 shows the volume response of single isolated heart cells on exposure to hypertonic or hypotonic solutions. In hypotonic solution, myocytes swelled to more than 1.5 times their initial volume. The swelling was complete within 2 min, the new volume was stable and volume returned to normal upon return of the isotonic solution. In hypertonic solution, cell volume decreased to about 0.65 times normal and the original volume was restored upon return of the isotonic solution.

The data in Fig. 16.1 show that volume changes in anisotonic media are very rapid. What is moving when the cells swell or shrink? What routes do these substances take? Are there homeostatic mechanisms that limit swelling and shrinking? If so, how are the compensatory mechanisms engaged? The answers to these questions are not yet complete. The purpose of this chapter is to provide the basis for understanding regulation of cell volume through the exchange of water and solutes across the plasma membrane.

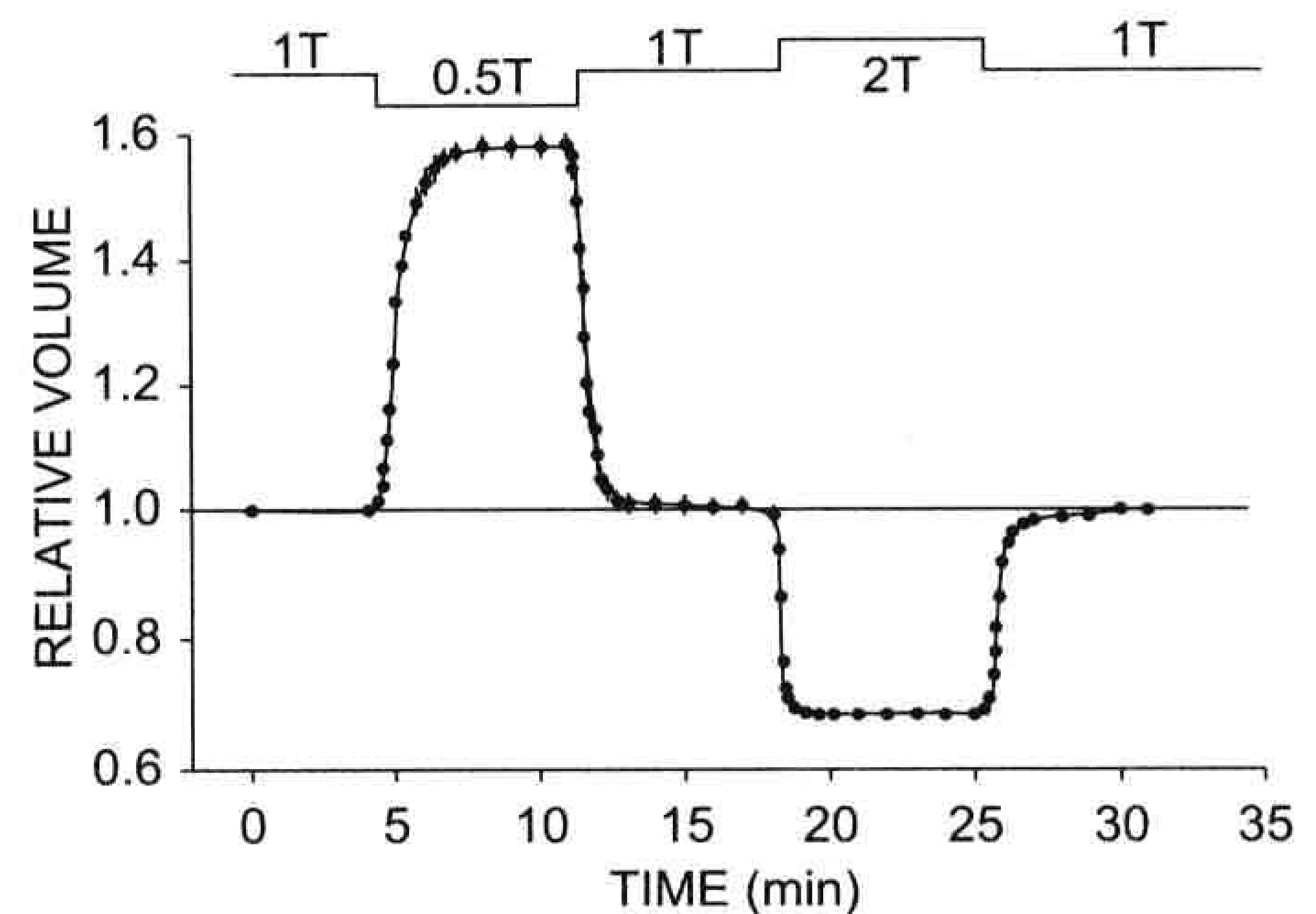


FIGURE 16.1 Response of isolated rabbit ventricular myocytes to osmotic stress. Cell volume was initially measured in isotonic solution (1T). Myocytes rapidly swelled 58% in a hypotonic solution with an osmolarity 0.5 times that of 1T and rapidly shrank 33% in a hypertonic solution with an osmolarity two times that of 1T. Cell volume was stable for the duration of perfusion with either hypotonic or hypertonic media and rapidly returned to its control value when 1T solution was readmitted. Volume was measured by digital video microscopy, and relative volume was calculated as $volume_{test}/volume_{1T}$. Solution osmolarity was adjusted by varying the concentration of mannitol. (From Suleymanian and Baumgarten (1996). *Reproduced from The Journal of General Physiology, 1996, 107, 503–514, by copyright permission of The Rockefeller University Press.)*

III. WATER MOVEMENT ACROSS MODEL MEMBRANES

IIIA. Definition of Osmosis

Osmosis refers to the movement of fluid across a membrane in response to differing concentrations of solutes on the two sides of the membrane. Osmosis has been used since antiquity to preserve foods by dehydration with salt or sugar. The removal of water from a tissue by salt was referred to as imbibition. This description comes from the notion that these solutes attracted water from material they touched. In 1748, J.A. Nollet used an animal bladder to separate chambers containing water and wine. He noted that the volume in the wine chamber increased and, if this chamber was closed, a pressure developed. He named the phenomenon osmosis from the Greek ωσμος, meaning thrust or impulse.

Pfeffer (1877) provided early quantitative observations on osmosis. He made an artificial membrane in the walls of an unglazed porcelain vessel by reacting copper salts with potassium ferrocyanide to form a copper ferrocyanide precipitation membrane on the surface of the vessel. He used this membrane to separate a sucrose solution inside the vessel from water outside and found a volume flow from the water side to the sucrose side. Pfeffer observed that the flow was proportional to the sucrose concentration. Further, a pressure applied inside the vessel produced a filtration flow proportional to the pressure. He found that a closed

vessel containing a sucrose solution would develop a pressure proportional to the concentration of sucrose. He recognized this as an equilibrium state in which the pressure balanced the osmosis caused by the sucrose solution. Pfeffer's original data for the osmotic pressure of sucrose solutions are plotted in Fig. 16.2. He defined *osmotic pressure* as the hydrostatic pressure necessary to stop osmotic flow across a barrier (e.g. a membrane) that is impermeable to the solute. This concept is illustrated in Fig. 16.3. Osmotic pressure is a property intrinsic to the solution and is measured at equilibrium, when the pressure-driven flow exactly balances the osmotic-driven flow. By defining osmotic pressure in this way, we assign a positive value to an apparent reduction in pressure brought about by dissolving the solute. Thus, fluid movement occurs from the solution of low osmotic pressure (water) to the solution of high osmotic pressure, opposite in direction to the hydraulic flow of water from high to low hydrostatic pressure.

An ideal *semipermeable* membrane is required for determining osmotic pressure. These membranes are permeable to water but absolutely impermeable to solute. The concept of osmotic pressure differs from tonicity in that tonicity compares two solutions separated by a specific non-ideal membrane. If the membrane is highly permeable to solute as well as to water, no water flow will occur and, therefore, the externally applied pressure required to stop osmosis is zero. This observation makes it plain that the *effective* osmotic pressure, which is measured with a real membrane, must be due to some interaction of the membrane with the solute because pressure depends on both the specific solute and the specific membrane.

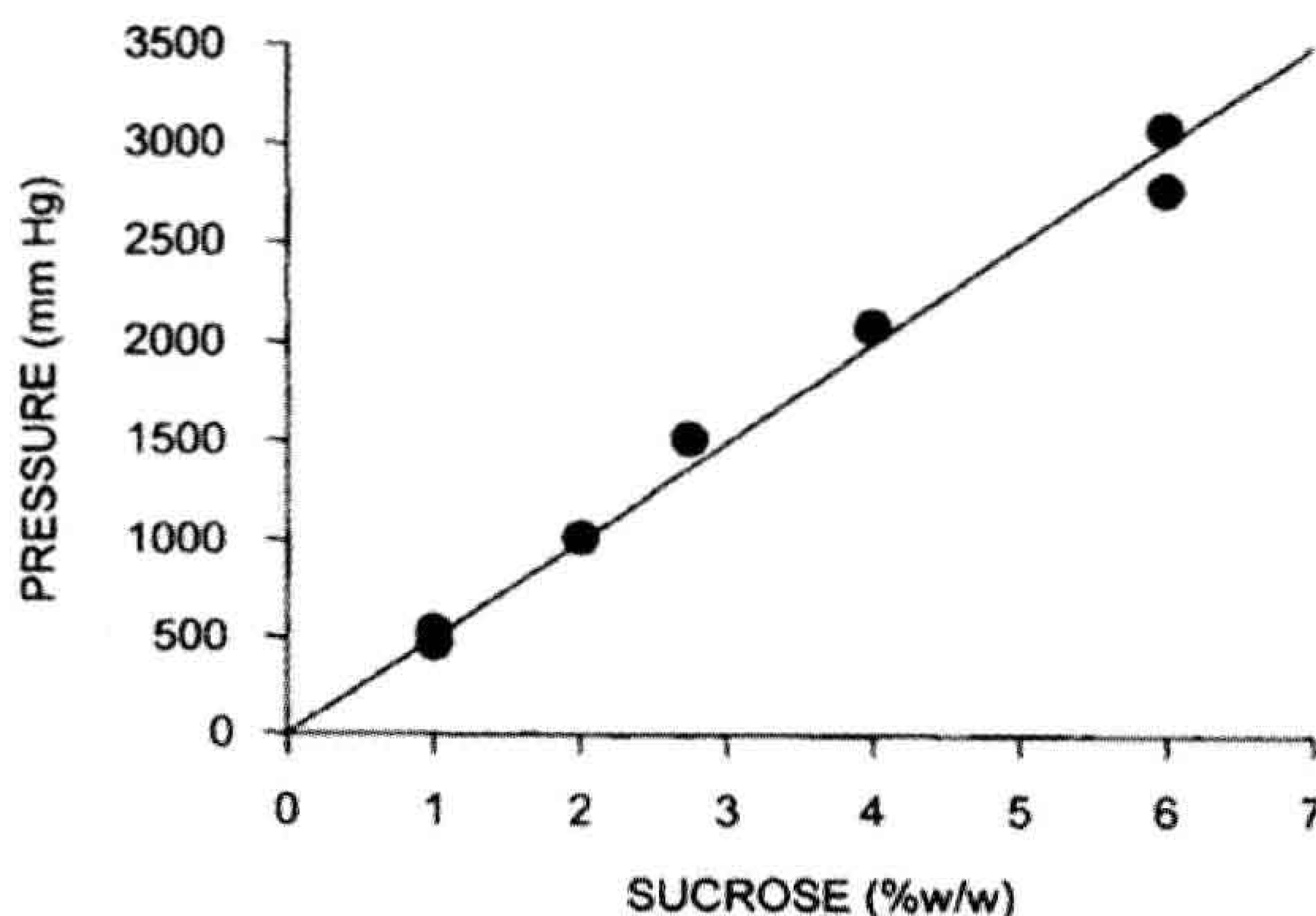


FIGURE 16.2 Plot of data from Pfeffer (1877) for the osmotic pressure of sucrose solutions. A copper ferrocyanide precipitation membrane was formed in the walls of an unglazed porcelain cup. The membrane separated a sucrose solution in the inner chamber from water in the outer chamber. The inner chamber was then attached to a manometer and sealed. The linear relation between the pressure measured with this device and the sucrose concentration were the experimental impetus for deriving van't Hoff's law.

IIIB. van't Hoff's Law

From Pfeffer's data and thought experiments considering gases in equilibrium with water, van't Hoff (1887) argued that the osmotic pressure should be given by:

$$\pi = RT\,\Sigma C_s \qquad (16.1)$$

where π is the usual symbol for osmotic pressure, R is the gas constant, T is the temperature in kelvins, and C_s is the concentration of solute particles in solution. This equation is known as van't Hoff's law. Table 16.1 lists common units for osmotic pressure along with the values and units of R and C_s needed to make the calculation.

The concentration used in van't Hoff's law, ΣC_s, refers to the number of osmotically active particles that are formed upon dissolution of the solute. For example, organic compounds such as glucose ideally yield one particle, whereas strong salts such as NaCl or $CaCl_2$ ideally yield two (Na^+ and Cl^-) or three (Ca^{2+} and two Cl^-) particles. The osmolarity of a solution equals ΣC_s and is expressed in osmol per liter to indicate that we are referring to the number of osmotically active particles, termed osmolytes, rather than the concentration of the solute. An alternative scale, osmolality, defines ΣC_s per kilogram of solvent. Although the osmolal scale better describes the osmotic pressure in van't Hoff's equation, the osmolar scale is more generally used in physiological studies. As we shall see, van't Hoff's law is a limiting law that is true only for dilute solutions. In this limit of dilute solutions, both osmolal and osmolar concentration scales converge to the same results.

To illustrate the magnitude of osmotic pressure, ideal solutions of 10 mM glucose or 5 mM NaCl, which dissociates into two particles, both have an osmolarity of 10 mosmol L^{-1} and an osmotic pressure at 37°C of $0.082\,L \cdot atm \cdot moL^{-1} \cdot K^{-1} \times 310\ K \times 0.01\,mol \cdot L^{-1} =$ 0.254 atm or 193 mmHg. Thus, the osmotic pressure of even dilute solutions are large in comparison to normal hydrostatic pressures in physiological systems.

IIIC. Thermodynamic Derivation of van't Hoff's Law

One of the conclusions of chemistry is that all spontaneous processes are accompanied by a decrease in free energy. The total free energy of a solution can be divided among its components. This parceling out of the Gibbs free energy, G, is embodied in the concept of chemical potential:

$$\mu_i = \left[\frac{\partial G}{\partial n_i}\right]_{T,P,n_k} \qquad (16.2)$$

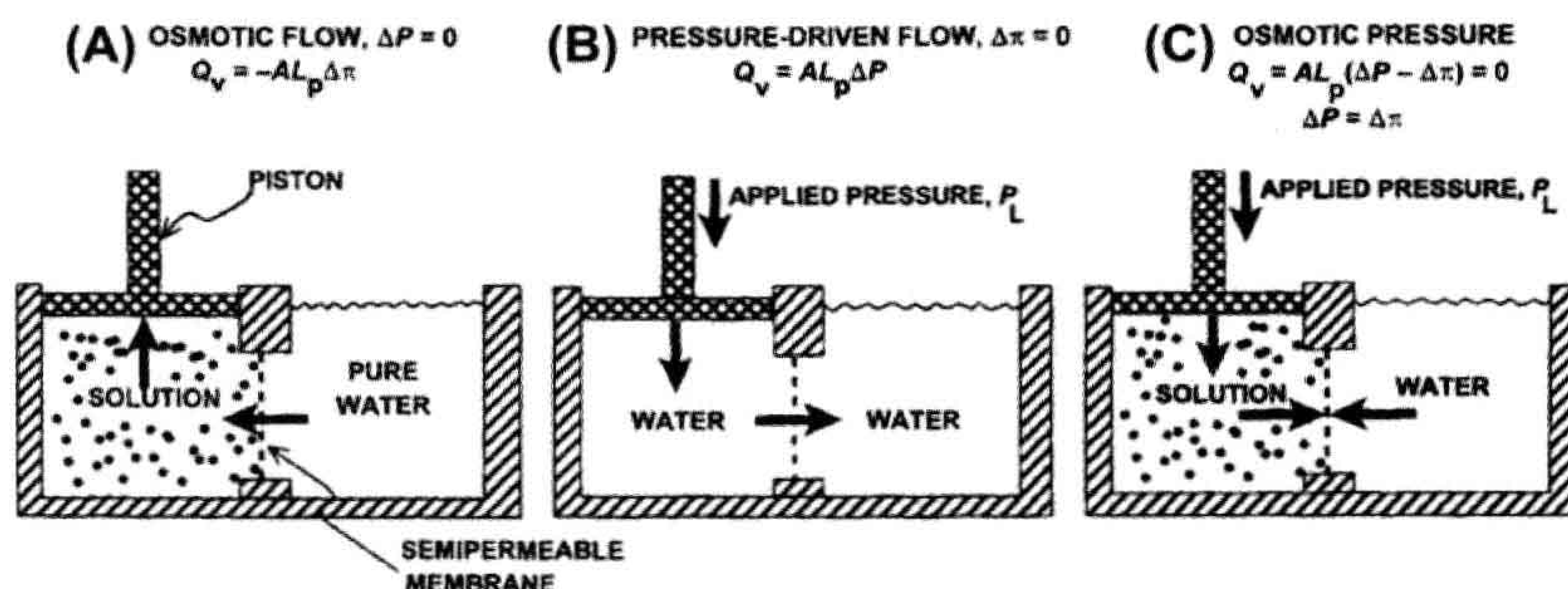


FIGURE 16.3 Equivalence of hydrostatic and osmotic pressures in driving fluid flow across a membrane. (A) An ideal, semipermeable membrane is freely permeable to water, but is impermeable to solute. When the membrane separates pure water on the right from solution on the left, water moves to the solution side. This water flow is *osmosis*. The flow, Q_v, in $cm^3 \cdot s^{-1}$, is linearly related to the difference in osmotic pressure, $\Delta\pi$, by the area of the membrane, A, and the hydraulic conductivity, L_p. Positive Q_v is taken as flow to the right. The flow causes expansion of the left compartment and movement of the piston (which is assumed to be weightless). (B) Application of a pressure, P_L, to the left compartment forces water out of this compartment, across the semipermeable membrane. The flow is linearly related to the pressure difference between the two compartments. (C) Application of a P_L so that $\Delta P = \Delta\pi$ results in no net flow across the membrane. The osmotic pressure of a solution is defined as the pressure necessary to stop water movement when the ideal, semipermeable membrane separates water from the solution.

where μ_i is the chemical potential of component i, n_i is the number of moles of component i and $i \neq k$. The chemical potential of a component of a solution consists of three terms: a standard potential, which refers to the chemical energy involved in the formation of the material from standard states; a compositional term, which depends on the presence of other constituents; and a work term, encompassing other work required (per mole) to bring additional material into the solution. The work term in the chemical potential of water is $\int d(\overline{V}_w P)$, where $\overline{V}_w$ is the volume of water per mole and P is the pressure. The electrochemical potential of ions in solution requires the inclusion of an electrical work term, $\int z_i F \, d\psi$, where z_i is the ion's valence, F is Faraday's constant, and ψ is voltage.

In the case of a solution separated from pure water by an ideal semipermeable membrane, water movement will occur when there is a difference in the chemical potential of water on the two sides of the membrane, such that water movement will result in a decrease in free energy. When the pressure applied to the solution is equal to the osmotic pressure, equilibrium is established and the chemical potential of water is equal on both sides of the membrane; no net water movement occurs. This equality of chemical potential is written as:

$$\mu^0 + \overline{V}_w \ P_L + RT \ \ln \ a_{w,\,L} = \mu^0 + \overline{V}_w P_R + RT \ \ln \ a_{w,\,R} \quad (16.3)$$

where the subscripts L and R refer to the left and right sides of the semipermeable membrane, μ^0 is the chemical potential of liquid water in its standard state (pure water at 1 atm pressure) and a_w is the activity of water. For an ideal solution, the activity of water can be replaced by its *mole fraction*, X_w

$$a_w = X_w = \frac{n_w}{n_w + n_s} \quad (16.4)$$

TABLE 16.1 Units for Calculation of Osmotic Pressure

Pressure Units	1 atm Equivalent	Gas Constant (R)	Solute Osmolyte Concentration, ΣC_s
atm	1	0.082 $L \cdot atm \cdot moL^{-1} \cdot K^{-1}$	$mol \cdot L^{-1}$
mmHg	760	62.36 $L \cdot mm\ Hg \cdot moL^{-1} \cdot K^{-1}$	$mol \cdot L^{-1}$
$Pa = N \cdot m^{-2}$	1.013×10^5	8.314 $N \cdot m \cdot moL^{-1} \cdot K^{-1}$	$Mol \cdot m^{-3} = mol \cdot (1000\ L)^{-1}$
$dyn \cdot cm^{-2}$	1.013×10^6	8.314×10^7 $dyn \cdot cm \cdot moL^{-1} \cdot K^{-1}$	$Mol \cdot cm^{-3}$

Osmolarity ($osmol \cdot L^{-1}$) is defined as the concentration of osmotically active particles, osmolytes, in $mol \cdot L^{-1}$. Therefore, the units osmoles and moles cancel in the calculation of osmotic pressure.

where n_w and n_s are the moles of water and solute, respectively. The balance of the chemical potential can be written as:

$$\mu^0 + \overline{V}_w P_L + RT \ln X_{w,L} = \mu^0 + \overline{V}_w P_R + RT \ln X_{w,R} \quad (16.5)$$

Consider the situation in Fig. 16.3, where pure water is on the right side of the membrane and a solution is on the left. $X_{w,R} = 1.0$ and thus, $\ln X_{w,R} = 0$. Rearranging we find:

$$\overline{V}_w(P_L - P_R) = -RT \ln X_{w,L} \quad (16.6)$$

The mole fractions of water and solute in a solution must sum to 1.0. This is expressed as:

$$\begin{aligned} X_{w,L} + X_{s,L} &= 1 \\ \ln X_{w,L} &= \ln(1 - X_{s,L}) \end{aligned} \quad (16.7)$$

where $X_{s,L}$ is the mole fraction of solute in the solution on the left. In dilute solutions, $X_{s,L} << 1.0$, and thus, $\ln(1 - X_{S,L}) \approx -X_{S,L}$. Substitution of this approximation in Equation 16.6 gives:

$$P_L - P_R = \frac{RT}{\overline{V}_w} X_{s,L} \quad (16.8)$$

The left-hand side of Equation 16.8 is just the osmotic pressure, π, which is equal to the extra pressure that must be applied to the solution on the left side in order to establish equality of the chemical potential of water on the two sides of the membrane. For physiological studies, it is convenient to express π in terms of concentration. From the definition of mole fraction and the assumption of dilute solutions ($n_s << n_w$), we get:

$$\begin{aligned} \pi &= \frac{RT}{\overline{V}_w} X_{s,L} = \frac{RT}{\overline{V}_w} \frac{n_s}{n_s + n_w} \approx \frac{RTn_s}{n_s \overline{V}_w} \\ &= RT\frac{n_s}{V} = RTC_s \end{aligned} \quad (16.9)$$

where $n_w \overline{V}_w \approx V$, is the total volume of solution and C_s is the concentration of impermeable solute on the solution side of the membrane. This last expression is the van't Hoff equation for the osmotic pressure, Equation 16.1. The thermodynamic derivation entails two assumptions: (1) the solution is sufficiently dilute as to approach ideality; and (2) the solution is incompressible so that $\int d(\overline{V}_w P) = \overline{V}_w \Delta P$. It is important to recognize that Equation 16.9 is not exact for physiological solutions. Rather, it is an approximation that is strictly true only for dilute ideal solutions.

The van't Hoff equation is based on thermodynamics and, as such, it tells us nothing about the rate of osmosis or the mechanism by which it occurs. Conceivably, the semipermeable membrane could be like a sieve that allows water to pass freely while blocking solute movement. Alternatively, solvent could dissolve in the membrane, whereas solute is insoluble. Both of these models would exhibit osmotic flow from the region of low osmotic pressure (pure water) to that of high osmotic pressure (impermeant solute solution). The mechanism by which osmosis occurs must be determined by methods of chemical kinetics, and must be determined for every membrane-solvent pair.

IIID. Other Colligative Properties of Solutions

The thermodynamic derivation given previously indicates that osmotic pressure (and osmotic flow) originates in the lowering of the chemical potential of water by the amount $\approx RTX_s$ when solute is dissolved. Several other properties of solutions also are a consequence of the lowered chemical potential of water because of dissolution of solutes. Together, these are called the *colligative* properties (from the Latin, *ligare,* meaning to bind) and include *osmotic pressure, vapor pressure depression, boiling point elevation* and *freezing point depression.* Consider two open compartments enclosed in a chamber. One compartment contains pure water and the other a solution of a non-volatile solute. The vapor pressure above a solution is defined as the partial pressure of water vapor in equilibrium with the solution. Since the vapor pressure of pure water is higher than that of the solution, water vapor above pure water will be at a higher pressure than that above the solution. As a result, water vapor will diffuse from the water side to the solution side. At the surface of the solution, water vapor will condense because the vapor pressure there will be higher than the equilibrium vapor pressure for the solution. Thus, water will move from the pure water to the solution side. In short, "osmosis" would occur through the "semipermeable membrane" represented by the surfaces of the two fluids and the intervening air. This illustrates the strong connection among the colligative properties of solutions. Laboratory osmometers typically use either vapor pressure depression or freezing point depression to determine the total solute concentration in an aqueous solution.

IIIE. Osmotic Pressure of Non-ideal Solutions

As discussed above, the van't Hoff equation is an approximation that adequately describes the osmotic pressure for dilute solutions. Its derivation requires the assumptions that the solutions are dilute and that the solutions are ideal. Here, *ideal* means that Raoult's law (vapor pressure is proportional to mole fraction of solvent) is valid for the solution (Hildebrand, 1955; Kiil, 1989).

Because the behavior of real solutions is not ideal, the van't Hoff equation must be modified to include a correction term, the osmotic coefficient (ϕ_s):

$$\pi = RT \sum \phi_s C_s \tag{16.10}$$

At physiological concentrations, the osmotic coefficients for NaCl and $CaCl_2$ are 0.93 and 0.85, respectively. This means the osmolarity of 150 mM NaCl is $0.93 \times 2 \times 150 = 279$ mosmol L^{-1} and the osmolarity of 150 mM $CaCl_2$ is $0.85 \times 3 \times 150 = 382.5$ mosmol L^{-1}. The osmotic coefficients for electrolytes vary with temperature, concentration and the chemical nature of the electrolyte. For most electrolytes, $\phi < 1.0$ for dilute solutions, due to weak attraction of the ions. At higher concentrations, ϕ increases to exceed 1.0. Values for the osmotic coefficients for electrolytes can be found in Robinson and Stokes (1959) or can be calculated from the parameters tabulated by Pitzer and Mayorga (1973). These osmotic coefficients are corrections to van't Hoff's law due to interactions only for the particular solute. When more than one solute is present, interactions could occur that are not accounted for by the osmotic coefficients. Therefore, calculations of the osmotic pressure of a mixture of solutes, even when osmotic coefficients are used, are only approximations.

Non-electrolytes and polyelectrolytes, especially proteins, also show marked departure from van't Hoff's law with increasing concentration. According to Equation 16.10, the osmotic coefficient for a single solute can be calculated as:

$$\phi_s = \frac{\pi_{\text{observed}}}{\pi_{\text{calculated}}} = \frac{\pi_{\text{observed}}}{RTC_s} \tag{16.11}$$

The osmotic coefficient for sucrose is plotted against sucrose concentration in Fig. 16.4. The osmotic coefficient is nearly 1.0 in dilute solutions, but approaches 3 in saturated sucrose solutions. Thus, the van't Hoff equation successfully describes the osmotic pressure of dilute solutions, but fails at high solute concentrations. The failure of the van't Hoff equation for highly concentrated solutions is due to deviation of reality from the assumptions used to derive the equation, that solutions are dilute and ideal. The osmotic coefficient accounts for these deviations.

For high solute concentrations, we can calculate the osmotic pressure from the mole fraction of water without assuming a dilute solution by identifying $\pi = P_L - P_R$ in Equation 16.6:

$$\pi = -\frac{RT}{\overline{V}_w} \ln X_w \tag{16.12}$$

This equation still requires the assumption of ideal solution behavior: the activity of water is equal to its mole fraction.

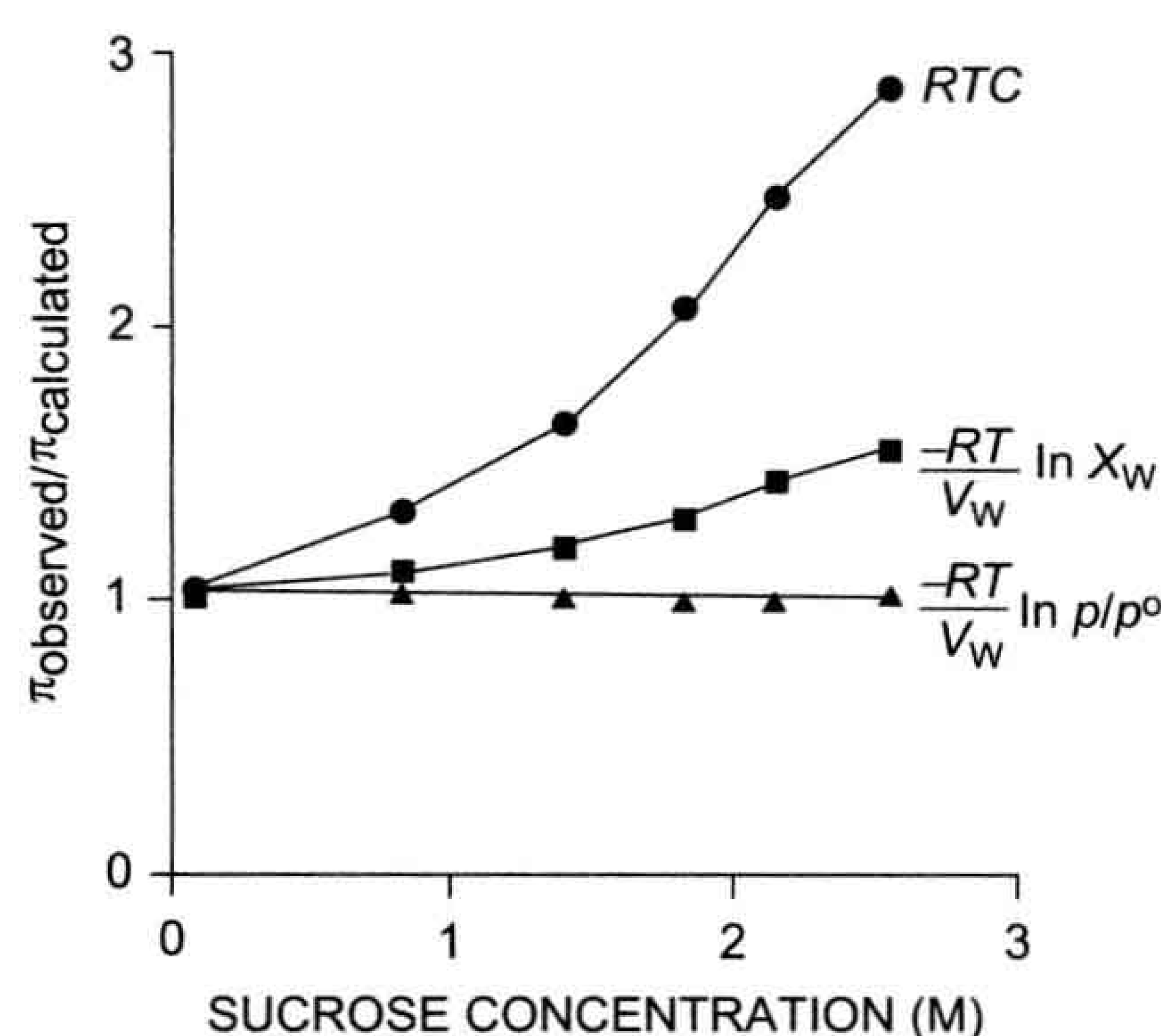


FIGURE 16.4 Osmotic coefficients as a function of sucrose concentration. Plotted are the molar osmotic coefficient, defined as ϕ_s in Equation 16.11 (●), obtained by dividing the observed osmotic pressure by *RTC*; the rational osmotic coefficient, g, defined in Equation 16.15 (■), obtained by dividing the observed osmotic pressure by $(-RT/\overline{V}_w)$ ln X_w; and the observed osmotic pressure divided by that predicted by vapor pressure measurements $(-RT/\overline{V}_w)$ ln p/p^0 according to Equation 16.13 (▲). Deviation of the molar osmotic coefficient from 1.0 means that the van't Hoff law fails to describe adequately the osmotic pressure at high concentrations, but is accurate for dilute solutions. The van't Hoff law requires the assumption of dilute solution and ideal behavior. Deviation of the rational osmotic coefficient from 1.0 means that the solution is not ideal, as the equation requires this assumption. The nearly perfect agreement between the theoretical osmotic pressure predicted from vapor pressure measurements illustrates the connection between these two colligative properties. *Data from Glasstone (1946).*

The expression for osmotic pressure without assuming a dilute solution or ideality is given by:

$$\pi = -\frac{RT}{\overline{V}_w} \ln a_w = -\frac{RT}{\overline{V}_w} \ln \frac{p}{p^0} \tag{16.13}$$

where p and p^0 are the vapor pressures of the solution and pure water, respectively.

The rational osmotic coefficient, *g*, accounts for non-ideal behavior and is defined as:

$$\ln a_w = g \ln X_w \tag{16.14}$$

Then, from Equations 16.12–16.14, we find that:

$$g = \frac{\pi_{\text{observed}}}{\pi_{\text{calculated}}} = \frac{\pi_{\text{observed}}}{-\frac{RT}{\overline{V}_w} \ln X_w} \tag{16.15}$$

The rational osmotic coefficient is closer to 1.0, but still deviates significantly at higher sucrose concentrations where solution behavior is further from ideal (see Fig. 16.4). In contrast, the ratio of the observed osmotic pressure to the theoretical osmotic pressure calculated from vapor pressure measurements, according to Equation 16.13, is very close to 1.0 throughout the entire concentration range. This shows the validity of Equation 16.13 and the

absolute correlation between vapor pressure depression and osmotic pressure as different measures of the same phenomenon, the lowering of the activity of solvent water by the dissolution of solute. Equation 16.12 does not adequately describe the variation of π with C_s because it requires ideal adherence to Raoult's law (vapor pressure is proportional to X_w); van't Hoff's limiting law further deviates from a linear relationship between π and C_s because it requires the additional approximation of dilute solutions. Despite these limitations in the high concentration domain, van't Hoff's law remains a good approximation for electrolyte solutions in the physiological range.

Because of their importance in physiological systems, the non-ideality of the osmotic pressure of protein solutions requires special comment. Adair (1928) found that the observed osmotic pressure increased faster than the concentration in hemoglobin solutions, as shown in Fig. 16.5. Part of the osmotic pressure was due to the unequal distribution of ions across the semipermeable membrane caused by electric charge on the immobile protein molecules. This is the Gibbs–Donnan equilibrium, discussed in more depth later. The contribution of the Gibbs–Donnan distribution to osmotic pressure is small, however, and nearly all of the non-linearity between π and C_s is due to the protein itself. From the data obtained by Adair (1928), $\phi_{\text{Hb}} = 4.03$ at the concentration of hemoglobin within erythrocytes (34.4 g hemoglobin per 100 ml of solution).

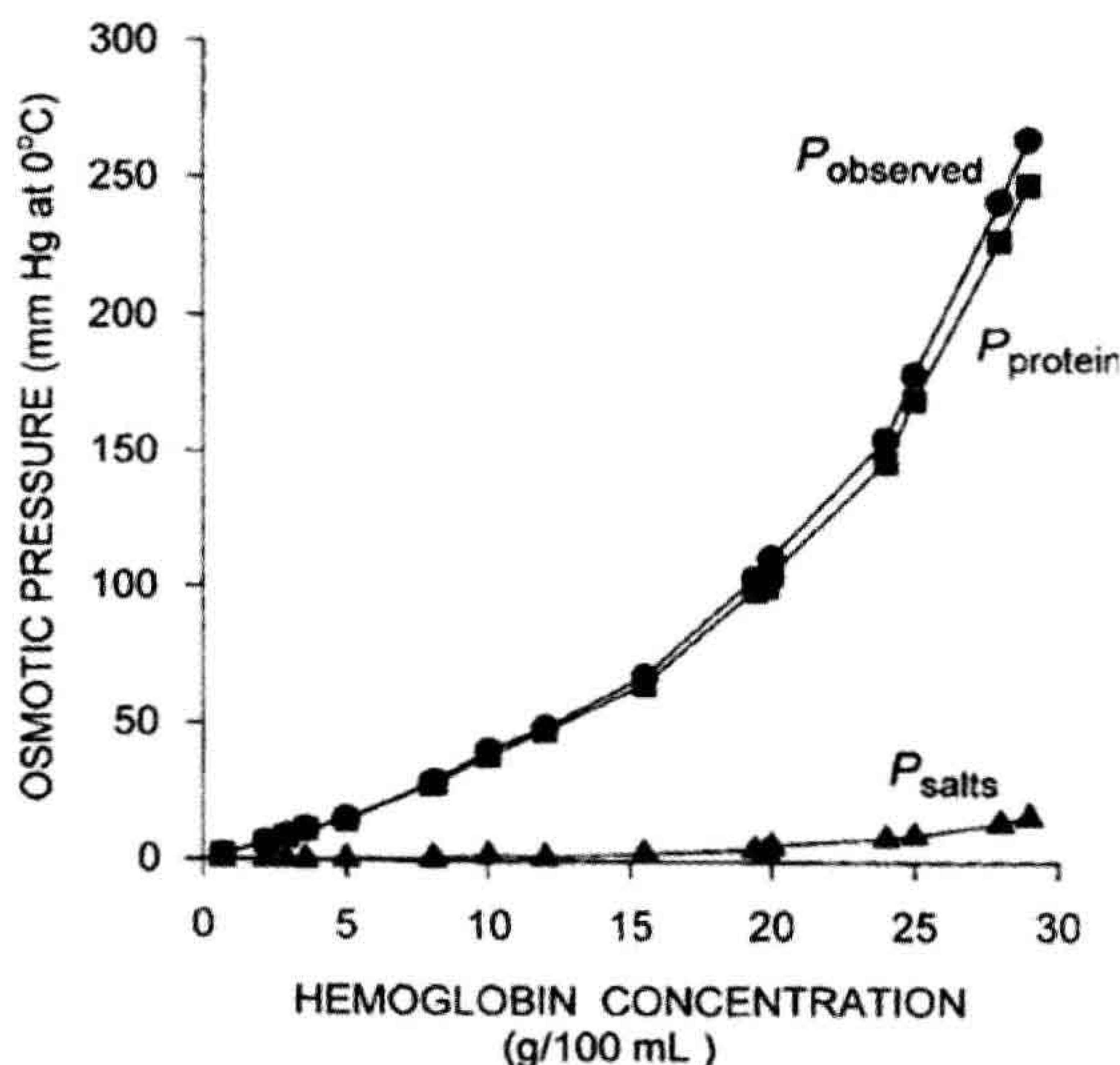


FIGURE 16.5 Dependence of the observed osmotic pressure on hemoglobin concentrations. P_{observed} is the observed osmotic pressure (●). P_{salts} is the contribution of the salts to the osmotic pressure as calculated from the Gibbs–Donnan distribution and the van't Hoff equation (▲). Protein is the contribution of the protein itself to the observed osmotic pressure, calculated as $P_{\text{observed}} - P_{\text{salts}}$ (■). *Data from Adair (1928).*

The observed osmotic pressure of solutions of plasma proteins also increases more rapidly than concentration, but the degree of deviation from linearity is different for different proteins. Thus, serum albumin shows marked deviation, whereas γ-globulins are more nearly linear. The empirical fits to the concentration-dependence of osmotic pressure are given by Landis and Pappenheimer (1963) as:

$$\begin{aligned} \pi_{\text{albumin}} &= 2.8C + 0.18C^2 + 0.012C^3 \\ \pi_{\text{globulins}} &= 1.6C + 0.15C^2 + 0.006C^3 \\ \pi_{\text{plasma proteins}} &= 2.1C + 0.16C^2 + 0.009C^3 \end{aligned} \tag{16.16}$$

In each of these three equations, the first term represents the limiting law of van't Hoff.

The rather large ϕ_s for proteins and polymers is due in part to *excluded volume effects*. That is, proteins and polymers exclude solvent from a larger volume than inorganic ions. The lowering of the free energy of solvent water upon dissolution of solute, which gives rise to osmosis, can be calculated from the increase of entropy on mixing. This entropy of mixing depends on the volume occupied by the solute. From considerations of the excluded volume, it can be shown (Tanford, 1961) that the expected osmotic pressure is given as:

$$\pi = RTC\left(1 + \frac{\overline{V}_s}{\overline{V}_w}C\right) \tag{16.17}$$

IIIF. Equivalence of Osmotic and Hydrostatic Pressure

As mentioned earlier, Pfeffer originally observed a linear relationship between the flow rate and the concentration of solute. This is expressed as:

$$J_v = -L_p(\pi_L - \pi_R) = -L_p\,\Delta\pi \tag{16.18}$$

where J_v is the volume flux in $\text{cm}^3 \cdot \text{s}^{-1}$ per unit area of membrane, L_p is variously called the *filtration coefficient*, *hydraulic conductivity*, or *hydraulic permeability* and $\Delta\pi$ is the osmotic pressure difference. A positive J_v in Equation 16.18 represents flux from the left to the right compartment and this is the order in which the osmotic pressure difference is taken. The minus sign before L_p indicates flux is from the region of low osmotic pressure to the region of high osmotic pressure. In Fig. 16.3A, $\pi_L > \pi_R$, $\Delta\pi > 0$, and J_v is negative. This means that the flux is from the right to the left compartment. The flow across an extent of membrane is just the flux times the area exposed to the driving forces, expressed as:

$$Q_v = -AL_p\,\Delta\pi \tag{16.19}$$

where A is the area of the membrane and Q_v is the flow in units of $\text{cm}^3 \cdot \text{s}^{-1}$.

In the absence of solute, the volume flow across Pfeffer's artificial membrane was also linearly related to the hydrostatic pressure:

$$\begin{aligned} J_v &= L_p(P_L - P_R) = L_p\ \Delta P \\ Q_v &= AL_p\ \Delta P \end{aligned} \tag{16.20}$$

In a study on collodion membranes, Meschia and Setnikar (1958) found that the proportionality constant for hydrostatic pressure-driven filtration was the same as the constant relating flow and osmotic pressure. That means that the L_p in Equation 16.19 is the same as the L_p in Equation 16.20. Thus, not only can the osmotic flow be nulled by opposing osmotic pressure with an equal but opposite hydrostatic pressure, but the equivalent proportionality implies that the mechanism of volume flow is also identical for osmotic and hydraulic flow. The equivalence of osmotic and hydrostatic pressures allows us to write:

$$\begin{aligned} Q_v &= AL_p[(P_L - P_R) - (\pi_L - \pi_R)] \\ &= AL_p(\Delta P - \Delta\pi) \end{aligned} \tag{16.21}$$

This equation describes the net flow that would be observed in the presence of both hydrostatic and osmotic pressure differences across a semipermeable membrane.

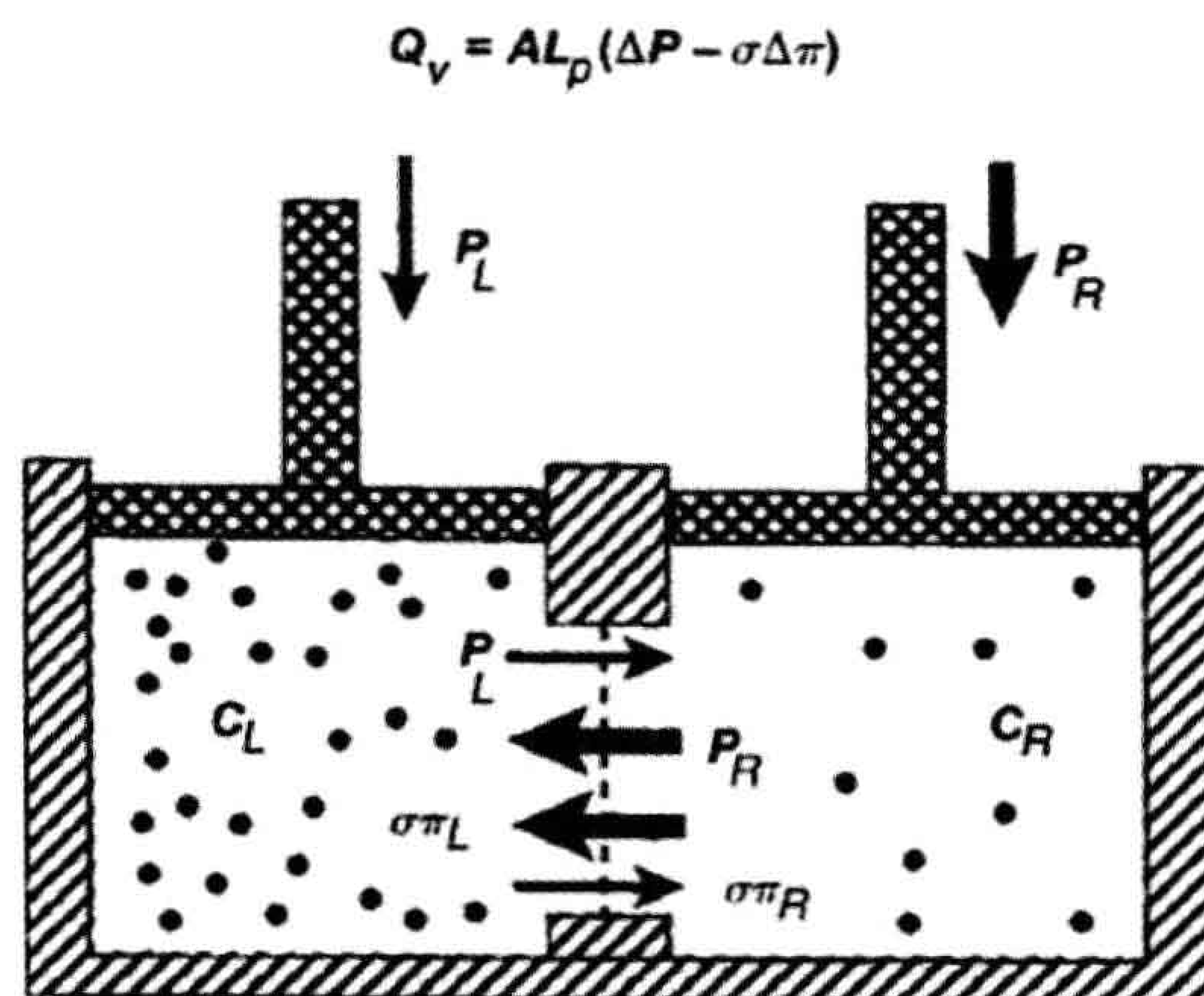


FIGURE 16.6 Net flow in the presence of osmotic and hydrostatic pressures. For a real membrane, the effective osmotic pressure on the left, $\sigma\pi_L$, causes flow toward the left, while the applied hydrostatic pressure, P_L, drives flow to the right. A similar situation occurs on the right. The *net* flow is driven by the balance of the forces, $\Delta P - \sigma\Delta\pi$, and is proportional to the area, A, and the hydraulic conductivity, L_p.

IIIG. Reflection Coefficient

Equation 16.1, van't Hoff's law, describes the relation between osmotic pressure and concentration when a solution is separated from water by an ideal semipermeable membrane. Recall that a semipermeable membrane is defined as absolutely impermeable to the solute. Real membranes may not fit this ideal; they may be somewhat permeable to the solute. When membranes are permeable to the solute, the measured osmotic pressure is actually less than that predicted by van't Hoff s law. This phenomenon has led to a second membrane parameter, σ, the *reflection coefficient* which is defined as:

$$\sigma = \frac{\pi_{\text{observed}}}{\pi_{\text{theoretical}}} = \frac{\pi_{\text{observed}}}{\phi_s\ RTC_s} \tag{16.22}$$

The reflection coefficient derives its name from the idea that all of the collisions of solute with a semipermeable membrane will result in the solute being reflected back into the solution. The reflection coefficient for an ideal membrane is 1.0. For a permeable solute, some fraction of the collisions with the membrane will result in permeation of the membrane, so that $\sigma < 1.0$ and the observed osmotic pressure will be less than that predicted by van't Hoff s law. The value of σ is not simply the fraction of collisions that penetrate the membrane. It involves discrimination by the membrane between solvent and solute. Thus, σ is a parameter that is different for every membrane-solute pair. A vapor pressure osmometer or a freezing-point osmometer would still register the proper osmolarity of the solution, however (for non-volatile solutes). A molecular interpretation of the origin of the reflection coefficient is given later.

Permeation of the solute should reduce osmotic flow along with osmotic pressure. In the presence of both hydrostatic pressure differences and concentration differences across a membrane, the resulting volume flow is given by:

$$Q_v = AL_p\left[(P_L - P_R) - \left(\sum_i \sigma_i\ \pi_{i,L} - \sum_i \sigma_i\ \pi_{i,R}\right)\right] \tag{16.23}$$

where σ_i is the reflection coefficient of solute i, and $\pi_{i,L}$ and $\pi_{i,R}$ are the osmotic pressures of solute i on the left and right sides of the membrane, respectively. The π_i in this equation is that given by van't Hoff's law; its multiplication by the reflection coefficient, σ, gives the effective osmotic pressure. The consequence of a combination of hydrostatic and osmotic pressures on the flow across a membrane is shown in Fig. 16.6.

IV. MECHANISMS OF OSMOSIS

The ultimate cause of osmosis is the reduction of the chemical potential of water in a solution. This thermodynamic statement and equations derived from it tell us nothing about the rate of osmosis or its mechanism. Several

possible mechanisms have been investigated. As will be developed, classes of models can be distinguished by comparing the proportionality between applied force, which is either a pressure or concentration gradient, and water flow.

IVA. Microporous Membranes

IVA1. Osmotic and Pressure-Driven Flow through Porous Membranes

The equivalence of L_p for osmotic and pressure-driven flow suggests a common mechanism. At least three different models have been proposed to explain flow across membranes: (1) hydrodynamic flow through a porous membrane; (2) diffusion through the membrane; and (3) non-hydrodynamic flow through narrow pores. As we shall see, it is likely that biological membranes are not modeled well by any one of these. Despite this, we shall consider these model membranes because investigators have relied heavily on them to clarify their thinking.

First, we consider a porous membrane as a model for understanding osmotic and hydrostatic pressure-driven flow and derive L_p, the proportionality constant relating pressure and flow. We assume the membrane is a flat, thin sheet of thickness δ. We imagine that the membrane is pierced by right-cylindrical pores of radius r, and the number of pores, N, per unit area is $n = N/A$. The membrane separates two compartments of water that are at different hydrostatic pressures. If we assume that the pores are large enough for laminar flow to occur, then the filtration flow will be given by the Poiseuille equation:

$$q_v = \frac{\pi r^4}{8\eta\delta}\Delta P \tag{16.24}$$

where q_v is the flow per pore in $cm^3 \cdot s^{-1}$, η is the viscosity of the fluid, δ is the thickness of the membrane (equal to the length of the pore), and ΔP is the pressure difference across the pore. The π in this equation is the geometric ratio, 3.14..., and should not be confused with the symbol for osmotic pressure. Since the flow through N pores is just Nq_v, the observed macroscopic flux and flow are:

$$\begin{aligned} J_v &= \frac{Nq_v}{A} = nq_v = \frac{n\pi r^4}{8\eta\delta}\Delta P \\ Q_v &= AJ_v = Nq_v = \frac{N\pi r^4}{8\eta\delta}\Delta P \end{aligned} \tag{16.25}$$

Recall here that J_v is the flux, or flow per unit area of membrane and Q_v is the flow in units of volume per unit time.

Equation 16.25 describes the steady-state flow of water across the membrane. Because at steady-state there is no buildup or depletion of water, there is no difference in the flow of water at any two points in the pore. Consequently, pressure changes linearly with distance through the pore, and the gradient of pressure, $\Delta P/\delta$, is constant.

A comparison of Equation 16.25 with Equation 16.20 indicates that the hydraulic conductivity is:

$$L_p = \frac{n\pi r^4}{8\eta\delta} \tag{16.26}$$

Thus, L_p is a parameter determined by the viscosity of the fluid and by membrane characteristics including the number of pores per unit area, n, the pore radius, and the membrane thickness.

IVA2. Diffusional Permeability of Porous Membranes: P_d

In the absence of a pressure gradient, solute and water cross a porous membrane by diffusion through the pores. If we assume that the membrane is impermeable at all other points, the permeability is given by Fick's first and second law of diffusion:

$$\begin{aligned} j_s &= -D\frac{\partial C}{\partial x} \\ \frac{\partial C}{\partial t} &= D\frac{\partial^2 C}{\partial x^2} \end{aligned} \tag{16.27}$$

where j_s is the flux of solute through one pore. The second expression describes the time dependence of the concentration profile over distance, x, within the pore. At steady-state, the concentration profile no longer changes. This means that $\partial C/\partial t = \partial^2 C/\partial x^2 = 0$; the concentration gradient is linear; and $\delta C/\delta x = (C_L - C_R)/(0 - \delta) = -\Delta C/\delta$, where δ is the thickness of the membrane. Total solute flux across the entire membrane, J_s, is:

$$J_s = \frac{n\pi r^2 D}{\delta}\Delta C \tag{16.28}$$

where n is the number of pores per unit area of membrane. According to this equation, the observed macroscopic flux of solute across a porous membrane is linearly related to the concentration difference by a coefficient that includes properties of the solute (diffusion coefficient) and the membrane (thickness, pore density and pore cross-sectional area). The *permeability* of the membrane to solute, p_s, includes several parameters in Equation 16.28 that are difficult to obtain experimentally; p_s relates solute flux, J_s, to the difference in concentration across the membrane:

$$J_s = p_s \, \Delta C \tag{16.29}$$

From Equations 16.28 and 16.29, p_s is defined as:

$$p_s = \frac{n\pi \, r^2 D}{\delta} \tag{16.30}$$

Isotopic water on one side of a porous membrane is distinguishable from ordinary water and may be viewed as a solute. Thus, water itself will obey these equations. This allows us to define the diffusional permeability of water, P_d, for a porous membrane:

$$P_d = \frac{n\pi r^2 D_w}{\delta} \quad (16.31)$$

where D_w is the diffusion coefficient of water. The units of P_d are $cm \cdot s^{-1}$. Note that multiplication of a permeability by a concentration, as in Equation 16.29, gives a flux with units of $mol \cdot cm^{-2}\ s^{-1}$.

IVA3. Evidence for Pores: P_f/P_d Ratio

In the absence of a concentration gradient, pressure-driven water flow gives rise to a second permeability constant termed the *filtration permeability* or *osmotic permeability*, P_f, which has units of $cm \cdot s^{-1}$. Mauro (1957) realized that the proportionality constants relating pressure and concentration-gradient-driven water flow, P_f and P_d, provide evidence for the mechanism of transport. The ratio P_f/P_d should be 1.0 if water crosses by a dissolution-diffusion process. Mauro (1957) recognized that the flux of water in response to a pressure gradient could be partitioned into two components, diffusional and non-diffusional (e.g. bulk flow) and that the diffusional component of water flux, J_w, would obey the Nernst–Planck equation:

$$J_w = -\frac{n\pi r^2 D_w}{RT} C_w \frac{d\mu_w}{dx} \quad (16.32)$$

where C_w is the concentration of water. In the case where only a hydrostatic pressure is applied, $d\mu_w = \overline{V}_w dP$, and $C_w \overline{V}_w = 1$. Assuming steady-state flows and a uniform membrane, $dP/dx = -\Delta P/\delta$, and Equation 16.32 becomes:

$$J_w = -\frac{n\pi r^2 D_w}{RT\delta} \Delta P \quad (16.33)$$

This flow of water is in units of moles of water per second per cm^2 of membrane. It can be converted to units of volume per second per cm^2 (the units of J_v) by multiplying by the volume of water per mole, or $\overline{V}_w$:

$$J_v = \overline{V}_w J_w = \frac{\overline{V}_w n\pi r^2 D_w}{RT\delta} \Delta P \quad (16.34)$$

This equation relates the volume flux to the pressure difference across the membrane.

The total volume flux was earlier given as $J_v = L_p \Delta P$ (see Equation 16.20). If diffusional flux is the only component of volume flux, Equations 16.20 and 16.34 may be combined to give:

$$L_p = \frac{\overline{V}_w n\,\pi\, r^2 D_w}{RT\delta} \quad (16.35)$$

Part of this expression for L_p incorporates P_d. Insertion of Equation 16.31 into Equation 16.35 gives:

$$P_f = \frac{L_p\ RT}{\overline{V}_w} = \frac{n\,\pi\, r^2\, D_w}{\delta} = P_d \quad (16.36)$$

This definition of P_f converts L_p into a parameter having the same units as P_d, thereby allowing direct comparison of filtration and diffusional permeabilities. The equality of P_f and P_d obtained in Equation 16.36 is dependent on the condition that the flow of water in response to a hydrostatic pressure difference is due only to diffusional processes. Thus, for a purely diffusional process, $P_f/P_d = 1$. In contrast, Mauro (1957) found that P_f/P_d was 727 in collodion membranes. That is to say, pressure-driven water movement was much greater than expected from a diffusional process. From this he concluded that pressure-driven and osmotic flow across these membranes was predominately non-diffusional.

IVA4. Physical Origin of Osmotic Pressure

If a porous membrane separates a solution containing only impermeant solutes from pure water, we observe experimentally that water flows through the membrane from the pure water to the solution side. The flow is proportional to the osmotic pressure of the solution times L_p (see Equation 16.20). The question is, what causes this water movement? Because the membrane is impermeable to solute, solute cannot enter the pores and the fluid in the pore is pure water. Consider a water molecule in the middle of the pore. How does the water "know" to move toward the solution side? It appears there are only two possible answers to this question. Either there is a concentration gradient of water within the pore, or there is a pressure gradient within the pore. These two possibilities are not mutually exclusive, but diffusion-driven water flow and pressure-driven water flow are often thought of as separate mechanisms. The dichotomy reflects the notion that water is an incompressible fluid. Water is not absolutely incompressible, however. The coefficient of compressibility is given as:

$$\beta = -\frac{1}{V}\left(\frac{\partial V}{\partial P}\right)_T \quad (16.37)$$

and the value of β for water is $4.53 \times 10^{-5}\ atm^{-1}$. The equation for the volume of water is:

$$V = V^0\ (1 - \beta P) \quad (16.38)$$

where V^0 is the volume at a standard temperature and pressure (1 atm), and P is the pressure in excess of 1 atm. The coefficient of compressibility is virtually constant in the range −500 to +1000 atm. Equation 16.38 indicates that application of a negative pressure of 2.5 atm would expand a pure water solution by 0.01%, which corresponds to a change in the concentration of water of about 5 mM.

Looked at the other way, an expansion of water of only 0.01% would induce a negative pressure of 2.5 atm, equal to the osmotic pressure of a 0.1 molal solution at 37°C.

Dainty (1965) proposed a model in which he considered the density of water immediately within the pore opening on the solution side. As solute molecules cannot enter the pore, Dainty reasoned that the concentration of water within the pore must be higher than in the solution. Because of this difference in concentration, he argued that water would diffuse into the solution side faster than water could diffuse into the pore. The resulting net movement of water toward the solution side would lower the density of water in the pore, thereby creating a reduced pressure. Bulk movement of water down its pressure gradient would follow.

This explanation of the origin of osmotic pressure supposes that the driving force is actually water diffusing down its concentration gradient. The data in Fig. 16.7 show, however, that the concentration of water cannot be the major determinant of the colligative properties of solutions. In Fig. 16.7A, the water concentration in solutions of sucrose and glucose are plotted against the concentration of the solute. The water concentration is indeed decreased by dissolving solute, but sucrose, being almost twice as large as glucose, displaces almost twice as much solvent. As shown in Fig. 16.7B, however, the colligative properties, represented here by the freezing point depression, depend *only* on the concentration of solute. Solutions with equal solute concentrations but different water concentrations have the same freezing point.

An alternative view of the physical origin of the osmotic pressure begins with the notion of pressure as a force divided by an area. The macroscopic concept of pressure relies on the averaging over time of the myriad of collisions that produce the pressure. By Newton's law, force is the time derivative of momentum. An elastic collision of a solvent or solute molecule with the walls of the vessel results in a momentum change of $2mv$, where m is the mass of the molecule and v is its velocity, which contributes to the pressure against the vessel wall. At the entrance to the pore, however, solute molecules cannot transfer their momentum to the interior of the pore because they collide with the rim of the pore and are reflected back into the solution. Thus, the water molecules immediately inside the pore experience a momentum deficit that is equal to the component of pressure contributed by the solute molecules in the bulk phase.

Figure 16.8 shows the one-dimensional concentration profile of solute molecules near a pore opening. Because there is a steep solute gradient, there should be a diffusion of solute toward the pore opening. However, the actual steady-state flux of solute in this direction is zero because of the force exerted on the solute molecules by the membrane. The equation that describes the solute flux, J_s, in units of mol $cm^{-2}s^{-1}$, is:

$$J_s = -D\frac{\partial C(x)}{\partial x} + \frac{D}{RT} f\ C(x) \qquad (16.39)$$

where $C(x)$ is the concentration of solute at position x, D is the solute diffusion coefficient in units of $cm^2 \cdot s^{-1}$, f is the force per solute molecule and R and T have their usual meanings.

Villars and Benedek (1974) derived an equation for the drop in pressure immediately inside the pore on the solution side by setting the flux in Equation 16.39 to zero and analyzing the net force on a plug of volume near the pore. Under steady-state conditions with zero J_s through the pore, Equation 16.39 gives:

$$f\ C(x) = RT\frac{\partial C(x)}{\partial x} \qquad (16.40)$$

where $f\,C(x)$ is the force per molecule times the number of molecules per unit volume, or the force per unit volume. Figure 16.9 shows a volume element near the opening of

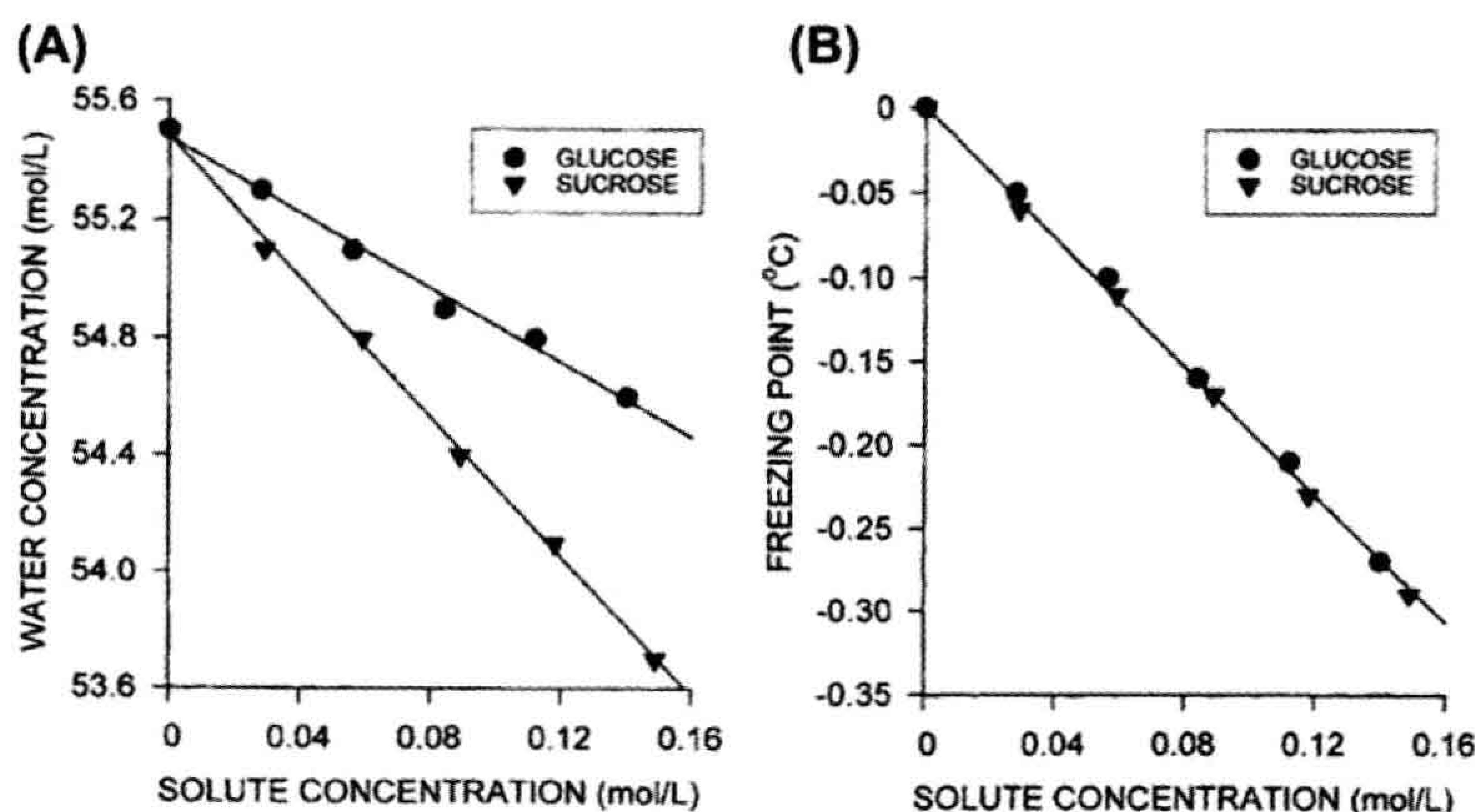


FIGURE 16.7 Effect of solute concentration on water concentration and freezing point depression in glucose and sucrose solutions. (A) Because solute displaces water, the water concentration decreases with increasing solute concentration. Sucrose is nearly twice the size of glucose. Consequently, there is less water in a sucrose solution having the same molarity as a glucose solution. (B) The freezing point depression, however, is dependent only on the solute concentration. It is the *mole fraction* of water that determines the colligative properties of solutions (the osmotic pressure, vapor pressure depression, boiling point elevation, and freezing point depression). *(Data from The Handbook of Chemistry and Physics, Chemical Rubber Company, Cleveland, OH, 1965.)*

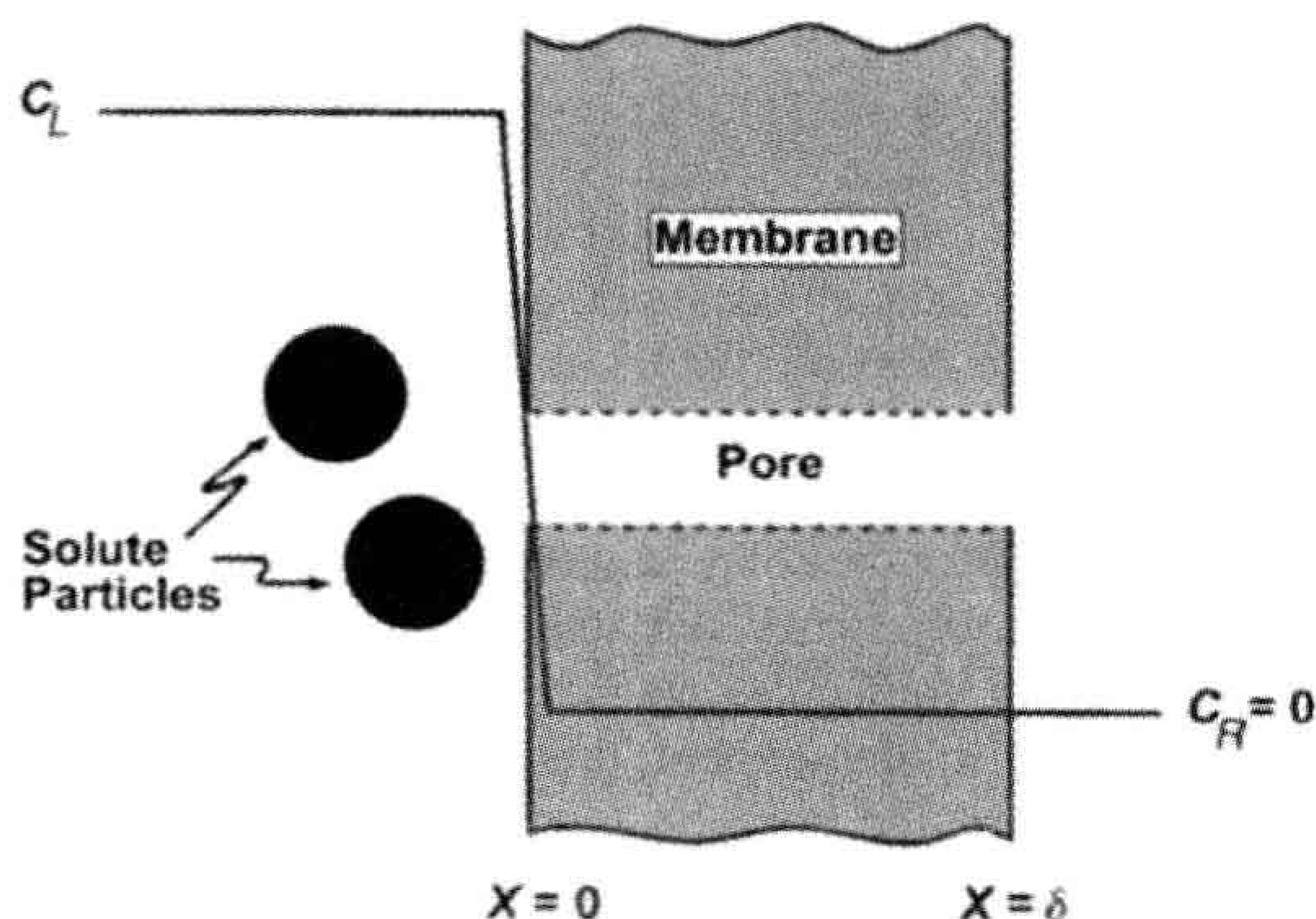


FIGURE 16.8 Concentration profile in the vicinity of a pore in a microporous membrane. The membrane is impermeable at all places except the pores, where water may penetrate but solute particles (solid circles) are too large to enter the pore. The concentration of solute in the bulk solution (C_L) must fall to zero upon entering the pore. The steep concentration gradient is accompanied by diffusion towards the pore that is balanced by reflection of solute by collision with the membrane.

the pore on the solution side. We consider the forces acting on the element of fluid with an area A from a point x well within the bulk solution to a point $x + \Delta x$ just inside the pore. We assume that this element is in mechanical equilibrium; although it may be moving, it is not accelerated or decelerated. The forces acting on the volume are contact

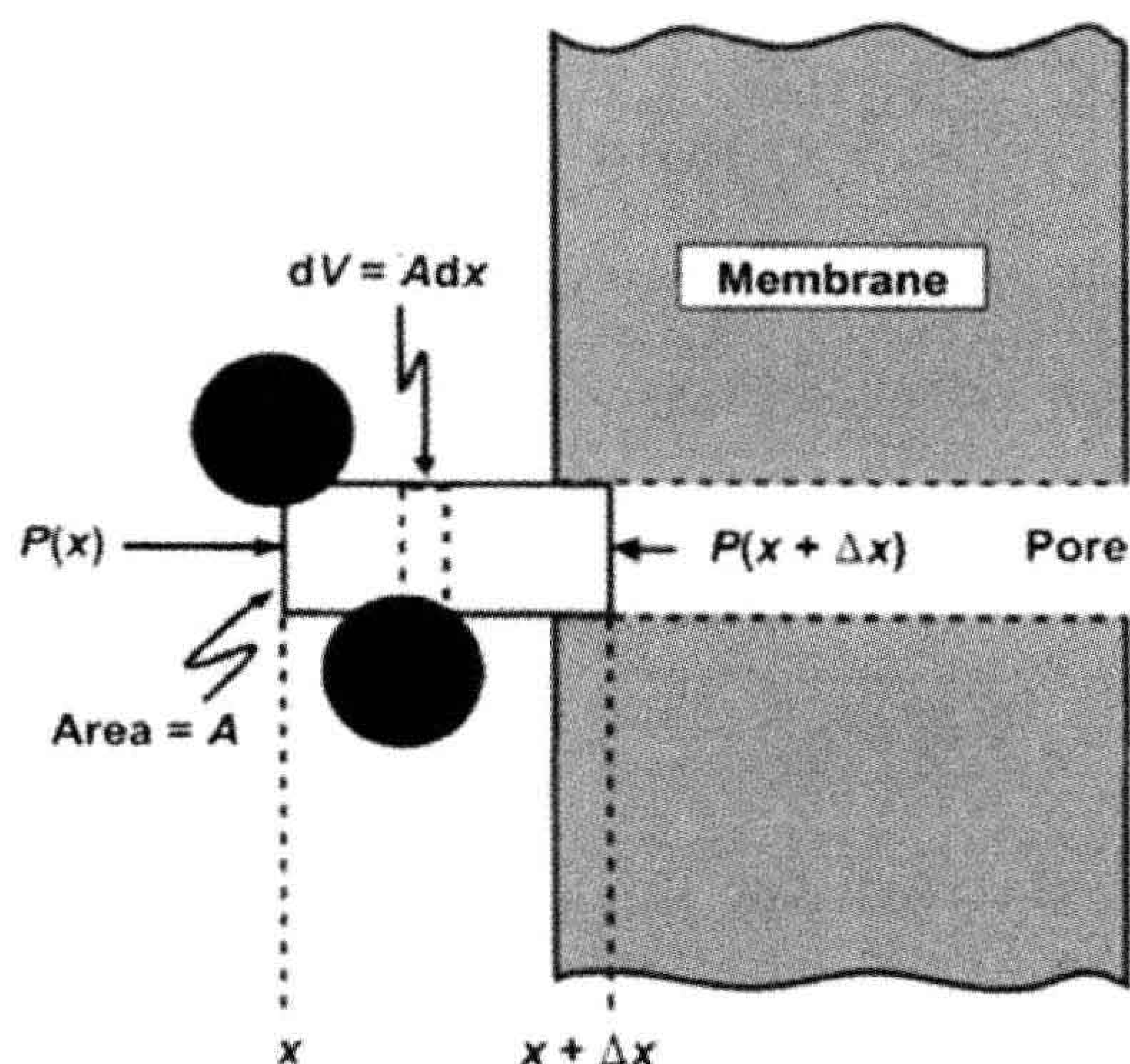


FIGURE 16.9 Forces acting on a volume element immediately adjacent to a pore opening. The ideal, porous, semipermeable membrane separates pure water on the right from solution of impermeant solute on the left. The volume element has an area, A, equal to the cross-sectional area of the pore. The pressure in the bulk phase at position x is $P(x)$. The pressure at position $x + \Delta x$, just within the pore, is $P(x + \Delta x)$. The net force on the element is the sum of the forces at both ends plus the forces acting only on the solute particles (solid circles) within the element.

forces on the edges of the volume and additional forces acting on the solute molecules alone to counteract the diffusive flux. At mechanical equilibrium the sum of the forces must be zero. This is written as:

$$F_s + F_c = 0 \tag{16.41}$$

where F_s is the total force acting on the solutes in the volume and F_c is the net contact force due to the pressure from the adjacent volume elements. The net contact forces are the result of pressure acting over an area:

$$F_c = AP(x) - AP(x + \Delta x) \tag{16.42}$$

The forces acting on the volume due to the solute particles is given by integrating Equation 16.40:

$$F_s = \int_x^{x+\Delta x} f\, C(x)\, dV \tag{16.43}$$

Inserting the volume element $dV = A\ dx$ and $fC(x) = RT\partial C(x)/\partial x$ from Equation 16.40, we obtain:

$$\begin{aligned} F_s &= ART \int_x^{x+\Delta x} \frac{\partial C(x)}{\partial x} dx \\ &= ART\ [C(x + \Delta x) - C(x)] \end{aligned} \tag{16.44}$$

Since $C(x + \Delta x) = 0$ because solute particles are not in the pore, this becomes:

$$F_s = -ART\, C(x) \tag{16.45}$$

where the negative sign indicates that F_s is directed to the left. Inserting Equations 16.42 and 16.45 into Equation 16.41, we have:

$$AP(x) - AP(x + \Delta x) = ART\, C(x) \tag{16.46}$$

or

$$P(x + \Delta x) = P(x) - RTC_L \tag{16.47}$$

This last equation indicates that the pressure experienced by the volume of fluid immediately inside the pore is less than the bulk pressure, $P(x)$, by the amount RTC_L, where C_L is the concentration of impermeant solute in the solution on the left of the membrane. This analysis is consistent with the intuitive idea that water movement from the water side to the solution side of a semipermeable membrane must be due to a real force, which appears in this analysis to be due to the momentum deficit, and thus pressure deficit, within the pore on the solution side.

IVA5. Physical Interpretation of the Reflection Coefficient, σ

The microporous semipermeable membrane presented previously distinguishes between solvent water and solute on the basis of pore and solute size. That is, the solute is too

large to enter the pore and so cannot cross the membrane. If the pores were somewhat larger or the solute molecules smaller, the solute could enter the pore, but with a lower probability than water because of the tight fit. In this case, rather than the solute being absolutely impermeant, the membrane would allow its slow passage. How does this affect the situation? Let us suppose that solute molecules that hit the rim of the pore before entry are reflected back into the bulk solution. This is shown diagrammatically in Fig. 16.10, looking down the axis of the pore perpendicular to the surface of the membrane. The area of the pore that is accessible to solute is:

$$A_s = \pi(r-a)^2 = \pi r^2\left(1-\frac{a}{r}\right)^2 \tag{16.48}$$

where a is the radius of the solute molecule. Assuming that the radius of water molecules (0.75 Å) is negligible compared to the pore's radius, the ratio of areas available to solute and solvent water is:

$$\frac{A_s}{A} = \frac{\pi r^2\left(1-\frac{a}{r}\right)^2}{\pi r^2} = \left(1-\frac{a}{r}\right)^2 \tag{16.49}$$

The fraction of collisions of solute molecules with the pore opening that are reflected back, compared with those of water, is approximated by the ratio of the area of the gray annulus in Fig. 16.10 to the cross-sectional area of the pore. This is identified with the reflection coefficient:

$$\sigma = \frac{A-A_s}{A} = 1-\frac{A_s}{A}$$
$$\sigma = 1-\left(1-\frac{a}{r}\right)^2 \tag{16.50}$$

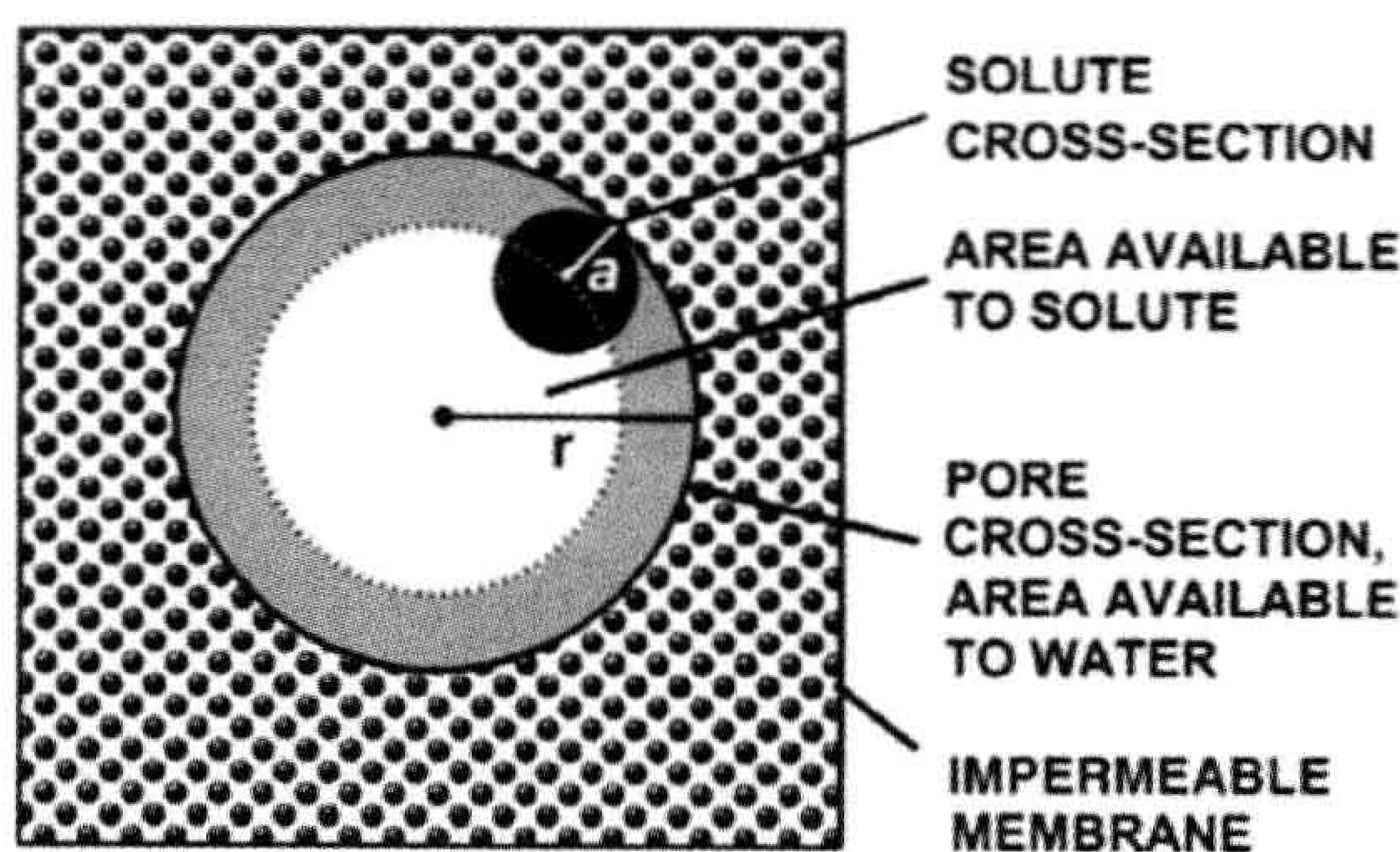


FIGURE 16.10 A physical interpretation of the reflection coefficient, σ, for a solute and a porous membrane. The view is down the pore in a direction perpendicular to the membrane. The pore is modeled as a right circular cylinder of radius r. The model assumes that any contact of the membrane with a solute particle of radius a (solid circle) will result in reflection of the particle back into the solution. The area available to solute is indicated in white. The total area of the pore, white plus gray annulus, is available for water movement.

According to this view, the concentration of solute immediately within the pore would not be zero, as in the case when the solute was impermeant, but instead would be $(1-\sigma)C$ and the excluded concentration would be σC. Thus, the momentum deficit inside the pore would be due only to the excluded solute and would be equal to σRTC, which is equal to $\sigma\pi$.

In addition to entrance effects, the concentration profile within the pore will be influenced by the combination of diffusion through the pore, solvent drag due to movement of fluid in response to pressure gradients and interaction of the solutes with the non-linear velocity profile within the pore. Laminar flow through long pores is characterized by a parabolic velocity profile, with a motionless layer of fluid adjacent to the pore walls and most rapid flow in the center. Large solute molecules will span several layers of velocity, thereby distorting the velocity profile and changing the solute molecule's velocity. Various equations have been derived to relax the assumption of negligible water radius and to relate the effective filtration area of the solute to the geometric radius of the pore (Renkin, 1954; Villars and Benedek, 1974; Hobbie, 1978). Although models assuming hydrodynamic flow through pores have been useful, their applicability to osmotic flow across biological membranes remains an open question.

IVB. Lipid Bilayer Membranes: the Dissolution–Diffusion Model

There are two types of lipid bilayer membranes that are useful models of membranes: the lipid vesicle and the planar bilayer membrane. The lipid vesicle is a small spherical shell of lipid usually produced by sonicating a dispersion of lipid in water. Planar bilayer membranes consist of a thin film of phospholipids formed over a small hole in a partition between two aqueous compartments. The film is formed by "painting" the hole with a non-polar solvent containing the lipids, which then spontaneously form a bilayer to separate fully the two solutions. This arrangement allows measurement of electrical and permeability properties of the bilayer. In the case of the liposome, the inner compartment is exceedingly small and experimentally inaccessible. In both cases, there are no components of the membranes other than the lipid.

IVB1. Osmotic and Pressure-Driven Flow for the Dissolution-Diffusion Model: P_f

One model of water permeation through the lipid bilayer supposes that the water dissolves in the lipid phase and crosses the membrane by simple diffusion. In this model, the solution in contact with the membrane is one phase, while the hydrophobic core of the membrane is a second phase. Equilibrium of water in the solution phase with

water in the membrane phase is described by equating the chemical potential of water in the two phases:

$$\mu^0_{w(\text{solution})} + RT \ln X_{w(\text{solution})} + P\overline{V}_{w(\text{solution})} = \mu^0_{w(\text{membrane})} + RT \ln X_{w(\text{membrane})} + P\overline{V}_{w(\text{membrane})} \quad (16.51)$$

where $X_{w\ (\text{solution})}$ and $X_{w\ (\text{membrane})}$ are the mole fractions of water in the solution in equilibrium with the membrane and in the membrane phase, respectively. The partition coefficient is defined as:

$$K_w = \frac{X_{w(\text{membrane})}}{X_{w(\text{solution})}} = \exp\frac{\mu^0_{w(\text{solution})} - \mu^0_{w(\text{membrane})} + \Delta P\overline{V}_w}{RT} \quad (16.52)$$

Consider the case where only osmotic pressure drives water flow and hydrostatic pressure across the membrane, ΔP, is 0. Since water generally partitions poorly into hydrocarbon solvents, we may assume that the mole fraction of water in the membrane phase is low. That is, the water concentration is dilute, and we may replace the mole fraction of water with its concentration:

$$C_{w(\text{membrane})} \simeq \frac{X_{w(\text{membrane})}}{\overline{V}_{\text{lipid}}} \quad (16.53)$$

where $\overline{V}_{\text{lipid}}$ is the partial molar volume of lipid in the membrane. If the concentration of water immediately inside the membrane is in equilibrium with the solution in contact with the membrane, we combine Equations 16.52 and 16.53 to get:

$$C_{w(\text{membrane})} \simeq K_w \frac{X_{w(\text{solution})}}{\overline{V}_{\text{lipid}}} \quad (16.54)$$

For dilute solutions, this is approximated by:

$$C_{w(\text{membrane})} \simeq K_w \frac{(1 - \overline{V}_w\ C_s)}{\overline{V}_{\text{lipid}}} \quad (16.55)$$

where C_s is the solute concentration. The concentration of water immediately inside the left side of the membrane, $C_{w,L}$, is given by Equation 16.55 where C_s is the concentration of solute in the solution on the left side of the membrane. A similar expression pertains to the concentration of water immediately inside the membrane on the right side ($C_{w,R}$). From the concentrations of water at both faces of the membrane, its diffusion across the membrane is given by Fick's law:

$$J_w = -D^m_w \frac{(C_{w,L} - C_{w,R})}{(0 - \delta)} \quad (16.56)$$

where D^m_w is the diffusion coefficient of water in the membrane phase. Substitution from Equation 16.55 into Equation 16.56 gives:

$$J_w = -\frac{D^m_w\ K_w\ \overline{V}_w(C_{s,L} - C_{s,R})}{\overline{V}_{\text{lipid}}\delta} = -\frac{D^m_w\ K_w\ \overline{V}_w \Delta C_s}{\overline{V}_{\text{lipid}}\delta} \quad (16.57)$$

The flux of water, J_w, is in units of moles of water per second per cm^2 of membrane. It is converted to units of volume flow by multiplying by V_w, as in Equation 16.34, to obtain:

$$J_v = \overline{V}_w J_w = -\frac{D^m_w\ K_w\ \overline{V}^2_w \Delta C_s}{\overline{V}_{\text{lipid}}\delta} = -\frac{D^m_w\ K_w\ \overline{V}^2_w}{\overline{V}_{\text{lipid}} RT\delta} RT\Delta C_s \quad (16.58)$$

The last term on the right is the osmotic pressure difference, $\Delta\pi$. This equation relates the volume flux to the osmotic pressure difference when the mechanism of water flow is dissolution and diffusion. Comparison to the earlier description of osmotic flow by Equation 16.18 allows us to identify L_p as:

$$L_p = \frac{D^m_w\ K_w \overline{V}^2_w}{\overline{V}_{\text{lipid}} RT\delta} \quad (16.59)$$

From the definition, $P_f = L_p RT/\overline{V}_w$, we get the expression for P_f as:

$$P_f = \frac{D^m_w\ K_w \overline{V}_w}{\overline{V}_{\text{lipid}}\delta} \quad (16.60)$$

Equation 16.58 was derived for an osmotic gradient ($\Delta C_s > 0$) in the absence of a hydrostatic gradient ($\Delta P = 0$). The expression relating volume flux and pressure when $\Delta C_s = 0$ can be derived by returning to Equation 16.51 and setting the mole fractions of water on the two sides of the membrane equal, while the pressures differ. The result is that exactly the same L_p is derived for pressure-driven flow as for osmotic flow when the mechanism is by rapid dissolution of water followed by slow diffusion through the lipid membrane phase (Finkelstein, 1987).

IVB2. Diffusional Water Permeability through Lipid Membranes: P_d

The permeability of lipid membranes to a diffusional water flux is expressed as:

$$J_w = P_d\ \Delta C_w \quad (16.61)$$

where P_d is the diffusional permeability and ΔC_w is the difference in water concentration across the

membrane. The overall permeation of the membrane by water is a consequence of three steps: dissolution into the membrane phase at the left interface; diffusion across the membrane phase; and reversal of dissolution at the right interface. If we assume, as we did in the derivation of P_f, that the rate-limiting step is diffusion through the membrane phase, then Equation 16.61 may be written as:

$$J_w = D_w^m \frac{\Delta C_{w(\text{membrane})}}{\delta} \tag{16.62}$$

From Equation 16.54, this is:

$$J_w = \frac{D_w^m \; K_w}{\overline{V}_{\text{lipid}}} \frac{\Delta X_{w(\text{solution})}}{\delta} \tag{16.63}$$

Because $\Delta X_w = \overline{V}_w \Delta C_w$, this becomes:

$$J_w = \frac{D_w^m K_w \overline{V}_w}{\overline{V}_{\text{lipid}}\delta} \Delta C_w \tag{16.64}$$

P_d can be identified by comparing Equations 16.64 and 16.61:

$$P_d = \frac{D_w^m K_w \overline{V}_w}{\overline{V}_{\text{lipid}}\delta} \tag{16.65}$$

IVB3. P_f/P_d Ratio for the Dissolution–Diffusion Model

The expressions for P_f in Equation 16.60 and P_d in Equation 16.65 derived for a lipid membrane under identical assumptions (equilibrium at the interfaces with relatively slow diffusion across the membrane), indicate that the P_f/P_d ratio for diffusive flow of water across lipid membranes should be 1.0. Cass and Finkelstein (1967) measured the osmotic and diffusive permeability of planar lipid bilayers and found that, within experimental uncertainty, the ratio was indeed 1.0. The uncertainty arose mainly in the determination of P_d because of the presence of unstirred layers adjacent to the planar lipid bilayer. These unstirred layers are an additional diffusional barrier that affects the experimental determination of P_d much more than P_f. In the flux equations, permeability appears as a conductance relating a flux (J_w or J_s) to a driving force (ΔC_w or ΔC_s). Thus, the inverse of permeability is like a resistance. For a membrane in series with unstirred layers, the total resistance is the inverse of the observed permeability, which is the sum of the resistances offered by the individual barriers, the membrane and the unstirred layers. We write this as:

$$\frac{1}{P_{d(\text{obs})}} = \frac{1}{P_d} + \frac{1}{P_u} \tag{16.66}$$

From this equation, it is plain that if P_u, the combined permeability of the unstirred layers on both sides of the membrane, is less than infinity, the observed P_d will be less than the actual P_d of the membrane alone. Since diffusion of water through the unstirred layer is given by Fick's law, Equation 16.66 may be rewritten as:

$$\frac{1}{P_{d(\text{obs})}} = \frac{1}{P_d} + \frac{\delta_L + \delta_R}{D_w} \tag{16.67}$$

where δ_L and δ_R are the equivalent unstirred layer thickness on the left and right sides of the membrane.

Unstirred layers also can affect measurement of the coefficients for pressure gradient-driven flow, P_f and L_p, but the error introduced is much less than for concentration gradient-driven flow, P_d (Barry and Diamond, 1984; Finkelstein, 1987), and was safely ignored in evaluating the P_f/P_d ratio (e.g. Cass and Finkelstein, 1967). The osmotic flow sweeps solute toward the membrane on the side with lower osmolarity and away from the membrane on the other side. As long as convection is faster than diffusion, this diminishes the transmembrane osmotic gradient, reducing J_v for the apparent $\Delta\pi$ and causing underestimation of P_f and L_p. The observed P_f, $P_{f\,(\text{obs})}$, is given as:

$$P_{f(\text{obs})} = P_{f(\text{membrane})}\exp(-J_v \; \delta/D_s) \tag{16.68}$$

where $P_{f(\text{membrane})}$ is the true membrane parameter, δ is the unstirred layer thickness, J_v is the volume flux and D_s is the diffusion coefficient of the osmolyte. The error can be minimized by determining P_f with a small $\Delta\pi$ so that J_v is small. Because P_f and L_p are proportional (Equation 16.36), the errors are also proportional.

The value of P_d and P_f varies with the lipid composition of the membrane and ranges from 1×10^{-5} $\text{cm}\cdot\text{s}^{-1}$ to 5×10^{-3} $\text{cm}\cdot\text{s}^{-1}$ (Deamer and Bramhall, 1986). Cholesterol, which generally reduces the fluidity of lipid bilayers, reduces P_d and P_f progressively with increasing cholesterol content (Finkelstein and Cass, 1968). The *unidirectional* flux across a lipid membrane equals $P_d \times C_w$. Using a typical P_d of 1×10^{-3} $\text{cm}\cdot\text{s}^{-1}$ and a C of 55 $\text{mol}\cdot\text{L}^{-1}$, the unidirectional flux across a membrane is 5.5×10^{-5} $\text{mol}\cdot\text{cm}^{-2}\cdot\text{s}^{-1}$. By comparison, the unidirectional flux of water across a distance $\delta = 5$ nm (approximately the thickness of the lipid bilayer) can be calculated as $(D_w \times C_w)/\delta$. Using 3×10^{-5} $\text{cm}^2\cdot\text{s}^{-1}$ for D_w, the unidirectional flux of water in water is 3.3 $\text{mol}\cdot\text{cm}^{-2}\cdot\text{s}^{-1}$. Thus, water flux through the membrane is about 60 000 times slower than that through water. Nevertheless, the water flux is still enormous. Taking 0.7 nm^2 as the average area of a typical phospholipid in the bilayer, the unidirectional water flux corresponds to about 2.2×10^5 water molecules passing each phospholipid molecule each second.

IVC. Flow through Narrow Pores: P_f/P_d Ratio

The equations derived earlier for P_f for a porous membrane required the assumption that the pores were large enough to allow laminar flow as described by the Poiseuille equation. Suppose that the pores are so narrow that water passes through the pores in single file. It is clear that laminar flow cannot occur here and the Poiseuille equation does not apply. As shown in Fig. 16.11, the narrow pore restricts free diffusion in the pore because diffusion of one water molecule from one position in the pore to the next requires its neighbor to move away to provide a vacancy. In this way, diffusion within the restricted geometry of the pore becomes a collective property of all of the molecules in the pore. The likelihood that a tracer molecule will diffuse all the way through the pore will depend on the number of water molecules in the pore, as movement of tracer water (solid circle) through the pore requires the movement of a vacancy (×) all the way through the pore.

Suppose that there are N water molecules in a pore. We may assume that the length of the pore, δ, is proportional to

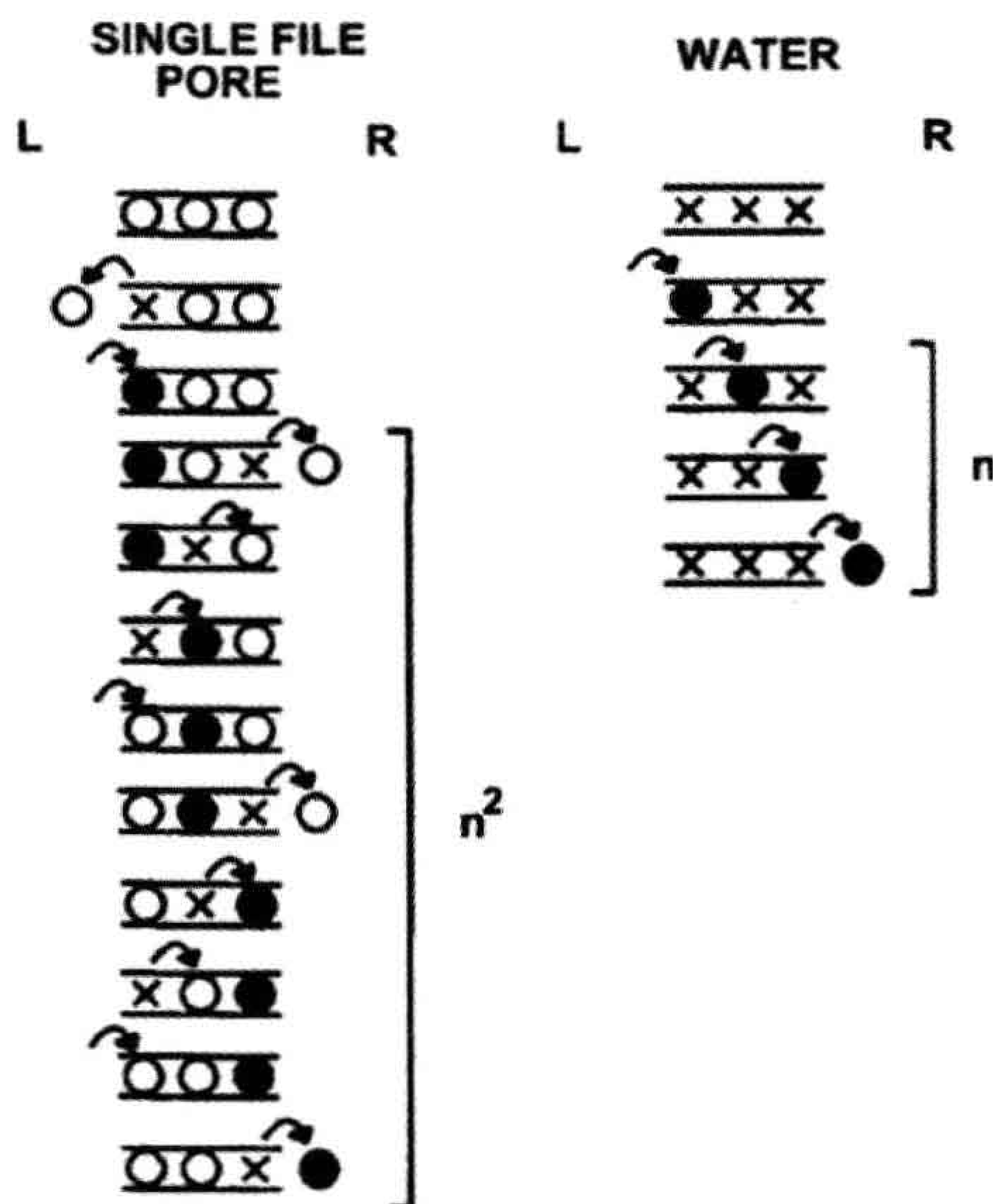


FIGURE 16.11 Jumping model of diffusion of water through a narrow pore. In the model of free water diffusion (right), tracer water (solid circles) makes successive jumps from one vacancy (×) to another. In order to move three places, it must make three jumps. In a narrow pore (left), tracer water cannot move to the next position in the pore unless a vacancy is present because unlabeled water (open circles) cannot move out of the way. Movement of tracer water from one site to the next in the pore requires a vacancy to diffuse all the way through the pore. Since the vacancy requires three steps to diffuse through the pore, tracer water diffusion through three steps in a narrow pore requires nine jumps. The result is that single-file diffusion becomes a collective property of the single file and is slower than free water diffusion.

N, and that the water molecules reside in more or less specific positions separated by δ/N. In the free diffusion of liquid water in the bulk solution, according to Fick's first law of diffusion, the flux of water is proportional to $1/\delta$ or $1/N$. In the case of a single-file diffusion through a narrow pore, the diffusion of a vacancy through the water within the pore looks exactly like the diffusion of water through a series of vacancies in free diffusion. Thus, the flux of the vacancy also is proportional to $1/N$. The movement of tracer from one position to the next in the pore requires the diffusion of a vacancy all the way through the pore, so that the flux of tracer one step is proportional to $1/N$. In order to diffuse all the way through the pore, the tracer must make N such jumps. The unidirectional flux of tracer over N steps of equal flux is given by Stein (1976):

$$J_{0\to N} = \frac{J_{ij}^N}{N\ J_{ij}^{N-1}} = \frac{1}{N} J_{ij} \tag{16.69}$$

where $J_{0\to N}$ is the unidirectional flux of tracer across N steps (all the way through the membrane) and J_{ij} is the unidirectional flux of tracer over one step. Since J_{ij} requires diffusion of a vacancy all the way through the pore, it is proportional to $1/N$. The unidirectional diffusional flux of tracer through a single-file pore is thus proportional to $1/N^2$, rather than $1/N$. Pressure-driven flow, on the other hand, remains inversely proportional to pore length. The theoretical analysis of both pressure-driven flow and diffusive flow through a single-file pore has led to the conclusion that the proportionality constants relating P_f to $1/N$ and P_d to $1/N^2$ are identical. The result, for a single-file pore, is:

$$\frac{P_f}{P_d} = N \tag{16.70}$$

where N is the number of water "binding sites" within the pore (Finkelstein, 1987). A more recent theoretical analysis suggests that this result is true near equilibrium, but the ratio of osmotic to diffusive permeability may exceed N for a membrane far from equilibrium (Hernandez and Fischbarg, 1992).

IVD. Mechanism of Water Transport across Lipid Bilayer Membranes

The previous discussion suggests that water transport across lipid bilayer membranes occurs by rapid dissolution at the membrane interface followed by diffusion across a hydrocarbon-like interior. Three observations strongly support this mechanism: (1) the P_f/P_d ratio, after correction for unstirred layers, appears to be close to 1.0 (Cass and Finkelstein, 1967; Andreoli and Troutman, 1971); (2) insertion of pore-forming antibiotics such as nystatin, amphotericin B or gramicidin A increases the P_f/P_d ratio to small values of N (between 3 and 5) (Holz and

Finkelstein, 1970; Rosenberg and Finkelstein, 1978); and (3) the activation energy for water transport, typically 10–20 kcal·moL^{-1}, is larger than the activation energy for free water diffusion, ≈4 kcal·moL^{-1}, which should apply if water moves through a pore (Solomon, 1972; Fettiplace and Haydon, 1980). However, experimental studies of water permeation across liposomes appear to give a different answer. The P_f of liposomes, measured by turbidimetric methods, is not affected by the chain length of the lipids or the degree of saturation (Carruthers and Melchior, 1983; Jansen and Blume, 1995), whereas water solubility in hydrocarbons is affected by chain length (Schatzberg, 1963). Further, the activation energy of P_f in liposomes is only 3.2 kcal·moL^{-1} (Carruthers and Melchior, 1983), similar to the activation energy for free water diffusion. The P_f of liposomes is discontinuous near phase transitions of the lipid and P_f/P_d ratios from 7 to 23 have been reported (Jansen and Blume, 1995). From these observations, it appears that liposomes do not behave as planar lipid bilayers, perhaps because of membrane defects induced by the marked curvature of the membrane in these small structures. The activation energy has been taken as diagnostic of whether water traverses the membrane through pores or by diffusion through the lipid itself (Finkelstein, 1987; Verkman, 1993). Low activation energies of water transport are associated with a high P_f or L_p in membranes containing water channels or pores, whereas high activation energies are associated with a low P_f or L_p, indicating diffusional water transport in membranes without pores or when pores are blocked by mercurials (Table 16.2).

In the dissolution–diffusion mechanism, water encounters a minimum of three sequential barriers: dissolution on one side of the membrane; transport across the hydrocarbon-like interior; and then removal from the membrane on the opposite side. Assuming rapid equilibration at the interfacial regions is equivalent to assuming that the barriers there are insignificant compared to the barrier of diffusion, but there is no a priori reason to make this assumption. The alternate view proposes that the rate-limiting step is lateral movement of the phospholipid head groups that creates a transient defect required for penetration of water into the interfacial region of the membrane (Trauble, 1971; Haines, 1994). Water transport through the hydrophobic core requires vacancies within the bilayer that form when hydrocarbon chains make *gauche-trans-gauche* kinks caused by the rotation of carbon–carbon bonds in the hydrocarbon tails. Kinks in the hydrocarbon tails propagate rapidly down acyl chains and provide sufficient space for water. Experimental support for this model comes from studies showing addition of cardiolipin to phosphatidylcholine liposomes decreases P_f without changing bilayer fluidity by stabilizing head group interactions (Shibata et al., 1994). These two models make very different assumptions, and the detailed mechanism of water permeation through lipid bilayers remains uncertain.

TABLE 16.2 Hydraulic Conductivity and its Apparent Activation Energy

Tissue	Lp 10^{-10} L·N^{-1}·s^{-1}	E_a kcal·moL^{-1}
	Water channels	
RBC, human	18.0	3.9
RBC, beef	18.2	4.0
RBC, dog	23.0	4.3
Prox. tubule BLM-V, rabbit	21.9	2.5
Liposomes + AQP1	30.8	3.1
	Water channels + mercurials	
RBC, human + PCMBS	1.3	11.6
Prox. tubule BLM-V, rabbit + Hg	4.4	8.2
	Diffusional	
RBC, chicken	0.6	11.4
Intestinal brush border, rat	0.9	9.8
Ventricle, rabbit	1.2	10.5
Liposomes	1.9	16.0
PC bilayer	1.6	13.0
PC/chol bilayer	0.4	12.7
Water self-diffusion	—	4.2

Hydraulic conductivity, L_p, and activation energy, E_a, are characteristic of the mechanism of water transport. High L_p and low E_a are typical of membranes containing functioning water channels, whereas low L_p and high E_a indicate diffusional water transport. Note that 10^{-10} L·N^{-1}·s^{-1} (SI units)=10^{-12}·cm^3·dyn^{-1}·s^{-1} (cgs units). RBC, red blood cell; BLM-V, basolateral membrane vesicles; AQP1, aquaporin-1; PCMBS, *p*-chloromercuribenzene sulfonate; PC, phosphatidylcholine; chol, cholesterol. For references, see Suleymanian and Baumgarten (1996).

V. WATER MOVEMENT ACROSS CELL MEMBRANES

In the prior sections, we considered osmotic- or pressure-driven flow and diffusive flow of water across membranes that were characterized as: (1) porous membranes with pores large enough to allow laminar flow; (2) lipid membranes with no pores, but allowing water permeation by a dissolution–diffusion mechanism; and (3) membranes containing narrow pores. We found expressions for the osmotic permeability, P_f, and the diffusive permeability,

P_d, for each and found that the membranes could be distinguished in principle by the ratio P_f/P_d: large values of P_f/P_d indicate a porous membrane, $P_f/P_d=1$ signifies a diffusive mechanism and small values of $P_f/P_d>1$ are characteristic of narrow pores. What are the permeabilities of real biological membranes, and what do these permeabilities tell us about the routes of water transport through membranes?

VA. Rate of Water Exchange: Experimental Measure of P_d

Paganelli and Solomon (1957) measured the diffusional exchange of water across erythrocyte membranes by rapidly mixing a suspension of the cells with an isotonic buffer with added tracer ^3H_2O. The mixture was forced down a tube and samples of the extracellular water were obtained by filtration at various distances, corresponding to various times of exchange. Paganelli and Solomon found that the half-time for exchange of ^3H_2O was 4.2 ms at room temperature. This means that 90% of all of the water within an erythrocyte is exchanged with extracellular water every 14 ms. This is an extraordinarily rapid rate of exchange. Erythrocytes are sufficiently small that the presence of an unstirred layer within the cells does not appreciably affect the determination of P_d (i.e. $(\delta_L + \delta_R)/D_w << 1/P_d$; see Equation 16.67).

Diffusional exchange of water across erythrocyte membranes also can be measured by nuclear magnetic resonance (NMR) spectroscopy. Relaxation of the nuclear spin states of hydrogen is much slower inside a cell than outside when a relatively impermeant paramagnetic ion like Mn^{2+} is added to the extracellular solution. This allows calculation of P_d because the relaxation of the spin states is then effectively limited by permeation through the membrane. The values of P_d for the erythrocyte determined by isotopic or NMR methods cluster around $4\times10^{-3}\,cm\cdot s^{-1}$ (Solomon, 1989).

VB. Rate of Osmotic Flow: Experimental Measure of P_f and L_p

According to Equation 16.23, the hydraulic conductivity, L_p, can be determined experimentally as:

$$L_p = \left(\frac{-Q_v}{A\sigma\Delta\pi}\right)_{\Delta P=0} \tag{16.71}$$

The osmotic permeability, P_f, can then be calculated as $P_f=L_pRT/\overline{V}_w$ (Equation 16.36). The experimentally determined values reflect the rate of water flow, Q_v, in the presence of a known osmotic pressure difference, $\Delta\pi$, produced by a solution with a known reflection coefficient, $\sigma\approx1.0$, over a known surface area, A.

The rate of water movement into or out of erythrocytes in response to mixing with hypertonic or hypotonic media has been measured by using light scattering as an index of erythrocyte volume. The experiments are similar to those used to determine P_d; a suspension of erythrocytes is mixed with media of defined osmolality and the mixture then flows down a tube passing through an observation cell. Light scattering is monitored at known distances down the tube and cell volume changes are calculated from changes in light scattering. This and other methods give values for L_p that cluster around $1.8\times10^{-11}\,cm^3\cdot dyn^{-1}\cdot s^{-1}$ (Solomon, 1989). Using $R = 8.314\times10^7\,dyn\cdot cm\cdot mol^{-1}\cdot K^{-1}$, $\overline{V}_w = 18\,cm^3\cdot mol^{-1}$ and $T = 298\,K$, this average value of L_p corresponds to a P_f of about $2.5\times10^{-2}\,cm\cdot s^{-1}$.

VC. Water Channels in Biological Membranes

The ratio of P_f/P_d for the erythrocyte membrane described earlier is about 5. Although there is some uncertainty in this ratio, it is clearly in excess of the value of 1.0 predicted for a diffusive mechanism. This suggests that there are pores in the erythrocyte membrane. The actual value of P_f/P_d for the pore alone cannot be obtained from just this information, however, because the erythrocyte membrane is actually a mosaic of lipid bilayer and pores; water moves through both in parallel, so the permeabilities of the components add. Experiments that block the pore suggest that the P_f/P_d ratio for the pore alone is about 10 and that 90% of water flux is via the pore, whereas 10% crosses the lipid bilayer (Macey, 1979; Finkelstein, 1987).

Two distinct means of inhibiting water transport provide additional evidence for proteinaceous pores. Mercurial sulfhydryl reagents, such as $HgCl_2$, *p*-chloromercuribenzoate (PCMB) and *p*-chloromercuribenzene sulfonate (PCMBS), decrease the erythrocyte P_f by a factor of 10 and P_d by less than a factor of 2 and the osmotic and diffusional permeabilities become equal (Macey and Farmer, 1970; Macey et al., 1972). Concurrently, the activation energy for permeation is increased from about $4\,kcal\cdot mol^{-1}$ expected for water-filled pores to $>10\,kcal\cdot mol^{-1}$, a value typical of artificial lipid bilayers (see Table 16.2). Mercurials inhibit water transport primarily by targeting protein SH groups because their effect is fully and rapidly reversed by cysteine. The second inhibitor is radiation. High doses of radiation inhibit water transport in both erythrocytes (van Hoek et al., 1992) and renal brush-border membrane vesicles (van Hoek et al., 1991). The characteristics of radiation inactivation suggest that the target is the size of a 30-kDa protein and are inconsistent with the entire membrane or transient defects serving as the major water pathway.

Although these studies and others, especially in epithelia (e.g. Verkman, 1993), made it clear that water pores or channels must exist, until recently, their identity and characteristics remained mysterious. Are what we call "water channels" simply water moving through open ion channels or through an ion exchanger or ion co-transporter? Are water channels specific, admitting water but excluding ions? These questions have been answered with the cloning and expression of a family of water channels called aquaporins (Agre et al., 1993; King and Agre, 1996; Verkman et al., 1996; Heymann et al., 1998; Nielsen et al., 1999).

VC1. Aquaporins

Water channels are related to the membrane integral protein (MIP) family (20–40% homology). The first water channel identified was cloned from a human bone marrow library by Preston and Agre (1991) based on the sequence of a purified protein of uncertain function. Initially called CHIP28 (channel-forming integral protein, 28 kDa), this protein was later redesignated aquaporin-1 (AQP1) and MIP-1 is referred to as AQP0. Ten mammalian aquaporins are known and more than 100 related proteins have been found in amphibians, *Drosophila*, plants, *Escherichia coli* and yeast, but not all of these conduct water (Heyman et al., 1998; Nielsen et al., 1999; Heymann and Engel, 1999).

The cloned AQP protein exhibits all of the characteristics of a water channel. AQP1 expressed in *Xenopus* oocytes induces up to 30-fold increases in P_f that is blocked by $HgCl_2$ (Preston et al., 1992). Reconstitution of purified AQP1 protein in liposomes verified that AQP1 itself, rather than modulation of an endogenous oocyte membrane protein, was responsible for mercurial-sensitive water permeation (Zeidel et al., 1992). Furthermore, incorporation of AQP1 into liposomes reduced the activation energy of P_f from 16.1 kcal·mol^{-1}, characteristic of permeation through the bilayer, to 3.1 kcal·mol^{-1}, characteristic of water passing through water-filled pores. Moreover, AQP1 appears to be active and highly selective for water without requiring regulatory subunits or cofactors (Preston et al., 1992; Zhang et al., 1993).

There are about 2×10^5 AQP1 molecules per erythrocyte (Zeidel et al., 1992). Taking the erythrocyte's membrane area as 1.35×10^{-6} cm^2 (Solomon, 1989), this corresponds to a density of about 1.5×10^{11} AQP1 cm^{-2} or 1500 AQP1 μm^{-2}. Despite this remarkable density of pores, the water permeability of a human erythrocyte is only ≈ 10 to 50 times greater than that of a phosphatidylcholine/cholesterol bilayer (Fettiplace and Haydon, 1980). Thus, 30–150 aquaporin channels are needed to equal the permeability of 1 μm^2 of bilayer.

AQP1 contains 269 amino acid residues and was postulated to have six membrane-spanning domains based on an analysis of hydrophilicity (Preston and Agre, 1991) and selective proteolysis of protein loops that face the intra- or extracellular side (Preston et al., 1994). The topology for the AQP1 and the other members of the AQP family is shown in Fig. 16.12. Mercurial-inhibition, N-glycosylation and PKA phosphorylation sites have been identified. There is an internal homology between the halves of AQP designated repeat-1 and -2. The greatest homology among AQPs is in the segments surrounding asparagine-proline-alanine (NPA) motifs in loops B and E. These loops are thought to be arranged antiparallel and are postulated to dip back into the membrane to form an hourglass-shaped pore represented in the cartoon in Fig. 16.12 (Jung et al., 1994).

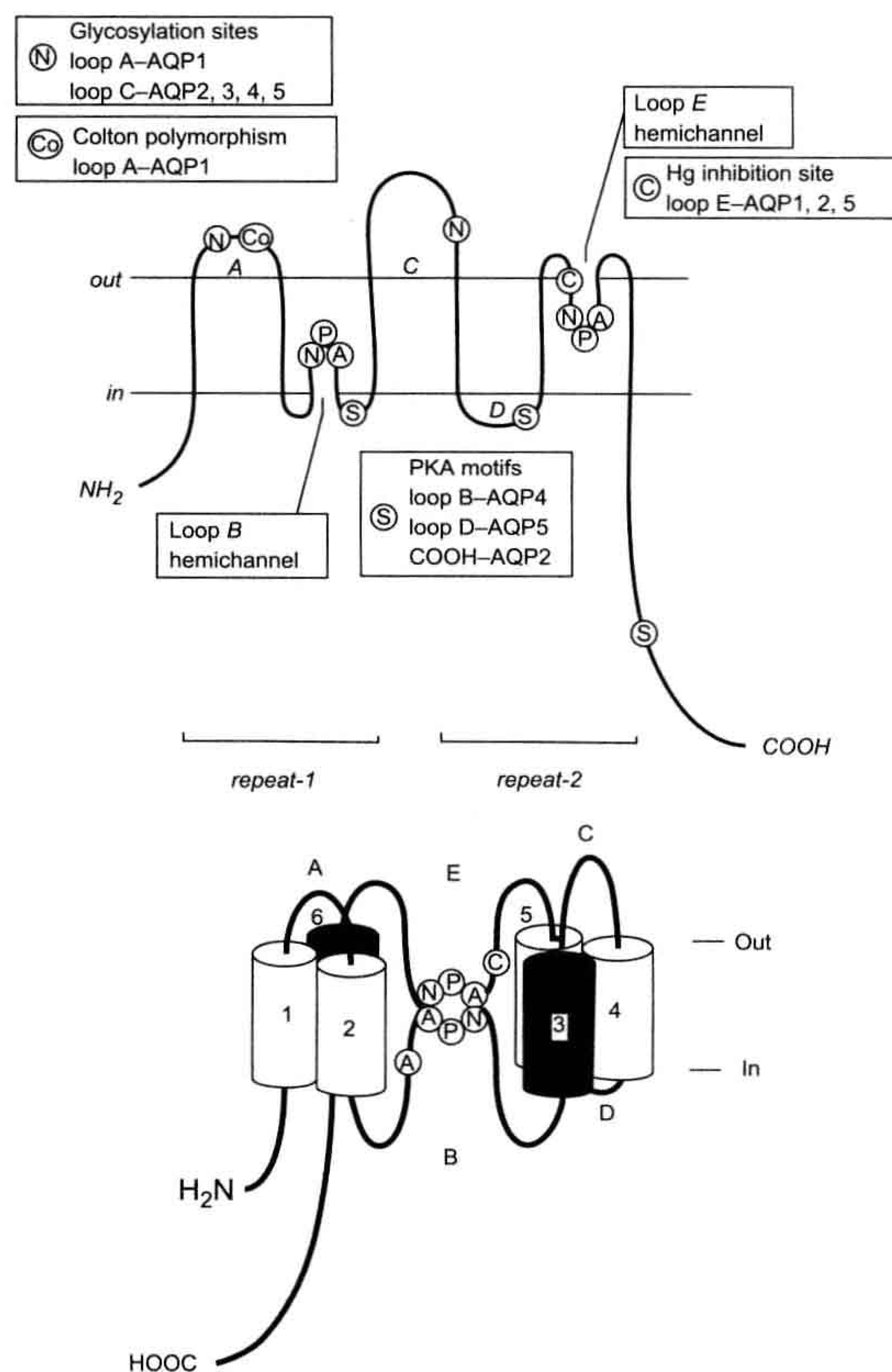


FIGURE 16.12 AQP family portrait. Cartoon illustrating the postulated topology of AQP as a structure with six membrane spanning α-helices (top). Cysteine (C) responsible for inhibition by mercurials and consensus PKA phosphorylation (S) and glycosylation (N) sites are also shown. Loops B and E are envisioned to dip into the membrane with the two NPA motifs forming the narrow neck of an hourglass-shaped, water-filled pore (bottom). Single letter codes are standard amino acid abbreviations. The position of the Colton polymorphic blood group antigen (Co) is noted. *(Reproduced from King and Agre (1996) with permission, from the Annual Review of Physiology, volume 58, © 1996, by Annual Reviews, Inc. and from Jung et al. (1994) with permission.)*

It is hypothesized that four highly conserved polar residues, E17, N76, N192, E142, comprise a critical portion of the water permeation pathway (Heymann et al., 1998).

The biochemical behavior of solubilized erythrocyte AQP1 suggested that it is a non-covalently-linked tetrameric structure and electron microscopy of negatively stained AQP1 confirmed this (Walz et al., 1994). Co-expression of Hg-sensitive and -insensitive recombinant proteins indicates that each AQP monomer forms an independent functioning pore, however (Preston et al., 1993). An exception to the tetrameric design of AQPs is AQP4. AQP4 forms large multimeric square arrays in the end-feet of astrocytes that surround capillaries (Rash et al., 1998). X-ray diffraction patterns at 3.5- and 6-Å resolution have been obtained from two-dimensional crystalline AQP1 arrays (Jap and Li, 1995; Walz et al., 1997). Electron density contour maps confirmed a tetrameric arrangement of monomers and each monomer appeared to have a central low density core, presumably the permeation pathway, surrounded by six tilted high density regions thought to represent membrane-spanning α-helicies.

Immunohistochemistry, Western blot (protein determination) and Northern and in situ hybridization and RNase protection assays (mRNA determinations) have identified broad but only partially overlapping distributions of AQP homologs in regions where water permeability is high (Hasegawa et al., 1993; Nielsen et al., 1993, 1999; Zhang et al., 1993; Umenishi et al., 1996; Ma and Verkman, 1999). For example, AQP1 is located in erythrocytes, renal proximal tubules and the descending thin limb of the loop of Henle (but not in the collecting duct, where water permeability is controlled by vasopressin), the choroid plexus, the iris, ciliary and lens epithelia and corneal endothelium of the eye, lung alveolar capillaries and epithelium, red splenic pulp (with erythrocyte precursors), colonic crypt epithelium and non-fenestrated capillary and lymphatic endothelium in a number of organs including cardiac, skeletal and smooth muscle. The exception with regard to broad distribution is AQP2. AQP2 underlies the vasopressin-regulated water permeation pathway of the renal collecting duct apical membrane that maintains water balance (Nielsen et al., 1995, 1999). Mutation of AQP2 is responsible for inherited nephrogenic diabetes insipidus and targeting and expression defects may cause acquired forms of this disease. On the other hand, AQP2 expression is upregulated in pregnancy and congestive heart failure, states associated with enhanced water retention (Nielsen et al., 1999).

Several cautions are warranted when drawing physiological interpretations from the localization of AQP. For example, AQP1 mRNA is higher in cardiac homogenate than in homogenate from any other organ (Umenishi et al., 1996), but functionally, the story is different. In isolated myocytes, L_p is very low and the activation energy is high, about 10 kcal·mol^{-1} (Suleymanian and Baumgarten, 1996) (see Table 16.2). Thus, AQPs do not significantly contribute to water transport across the myocyte membrane.

Organs comprise cells with diverse functions and often different requirements for water transport. Because of its localization in vascular tissue, AQP detected in homogenates should not be attributed to the principal cells of the organ without confirmation. Even careful immunohistochemistry and in situ hybridization may lead the physiologist astray. The problem is the high density of AQP necessary to significantly affect P_f. If, for example, the density of AQP1 in the erythrocyte membrane was 10 AQP1 μm^{-2} rather than 1500 AQP1 μm^{-2}, AQP1 would still be detected by modern techniques, but it would make a physiologically insignificant contribution to P_f.

VC2. Other Channels and Transporters

The identification of specific water channels does not exclude the possibility that water flux through ion channels or transporters significantly contributes to the water permeability of the membrane. One interesting example is the cystic fibrosis conductance regulator (CFTR). CFTR functions as a cAMP-regulated Cl^- channel. Hasegawa et al. (1992) recently found that CFTR expressed in oocytes also acts as a water channel with an estimated single channel P_f comparable to that of AQP1. Both P_f and Cl^- conductance were increased by cAMP. The effect of the CFTR channel on P_f is large but not unique. Pore-forming antibiotics such as gramicidin, nystatin and amphotericin, are reported to induce a more modest P_f. Transporters also may contribute to P_f. Fischbarg et al. (1990) found that expression of Na^+-independent glucose transporters in oocytes increases water permeability and Solomon et al. (1983) suggested that some of the water permeability of erythrocytes was contributed by the Cl^--HCO^-_3 exchanger. However, water flux mediated by these transporters does not account for the macroscopic properties of water transport.

VI. REGULATION OF CELL VOLUME UNDER ISOSMOTIC CONDITIONS

VIA. Gibbs–Donnan Equilibrium

Because ions exert an effective osmotic pressure, the distribution of ions affects water flow across the cell membrane and thus cell volume. The starting point for understanding these effects is the theoretical ideas of Gibbs that were first demonstrated experimentally by Donnan. The phenomenon is now called *Gibbs–Donnan equilibrium* or simply *Donnan equilibrium*. Macknight and Leaf (1977) elegantly describe the history of how these ideas were applied to cell volume regulation and Overbeek

(1956) provides a detailed derivation and considers non-ideal solution behavior.

In a Donnan system, the membrane permits the movement of small charged solutes (e.g. K^+ and Cl^-) between two compartments but restricts the movement of large charged species, such as proteins, which are usually polyvalent and negatively charged at intracellular pH. It is the inability of one (or more) charged species to distribute freely between the compartments that profoundly influences the distribution of the mobile ions and, consequently, water. For a cell, it is the cell membrane that restricts the movement of large ions. A membrane is not required to establish a Donnan equilibrium, however. All that is needed is a means of restricting one charged species to a single compartment. Donnan equilibria can arise in gels consisting of charged structural components (e.g. an ion-exchange column) because the charges on the gels are fixed in place. Donnan equilibria can also arise in cells after their membranes have been removed, leaving a cytoplasmic "gel" consisting of interconnected cellular proteins. A Donnan system represents a true equilibrium, although as we will see, an equilibrium is not attained under the usual biological conditions.

There are three important characteristics in a Donnan equilibrium system: (1) an unequal distribution of ions; (2) a potential difference between the compartments; and (3) an osmotic pressure. These characteristics can be understood from the application of a basic thermodynamic principle to the system. Species that can cross the membrane, including both mobile ions and water, will distribute themselves so that their electrochemical potential (μ_i) is the same in both compartments.

To understand how a Donnan equilibrium develops, imagine starting an experiment by "filling" the cell and the extracellular space with solutions of concentrations indicated in Fig. 16.13A. Since ions move down their electrochemical gradients, the first question is: what are the electrochemical gradients? Initially, there is no potential difference across the membrane because both internal and external solutions start with an equal number of positive and negative charges. There is no concentration gradient for K^+ because the amount of K^+ is the same on both sides of the membrane. Due to the presence of impermeant anions inside the cell, however, $[Cl^-]_o$ must be greater than $[Cl^-]_i$. Consequently, Cl^- will enter the cell, moving down its electrochemical gradient, which is initially just the concentration gradient. Inward movement of Cl^- makes the inside of the cell negative with respect to the outside. The developing inside negative potential has two consequences. First, it slows the rate of further influx of Cl^-. Second, the electrical gradient causes the accumulation of K^+ inside the cell. As K^+ moves down its

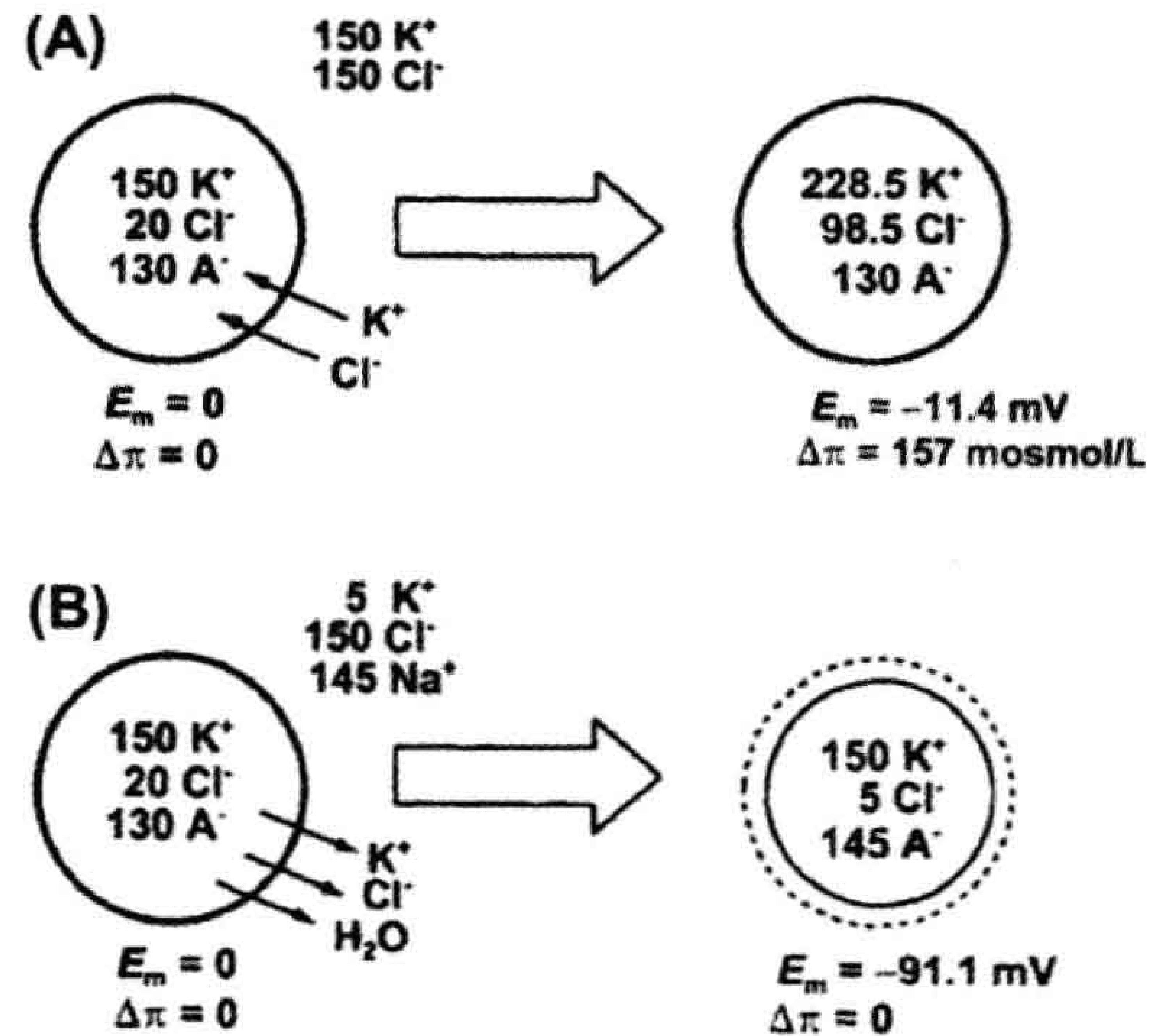


FIGURE 16.13 Development of a Donnan equilibrium. (A) Cell bathed in 150 mM KCl is "filled" with 150 mM K^+, 20 mM Cl^-, and 130 mM A^-. Initially, there is no potential or osmotic gradient (left). K^+ and Cl^- enter the cell until $[K^+]_o \cdot [Cl^-]_o = [K^+]_i \cdot [Cl^-]_i$ and the ionic fluxes establish a potential and osmotic gradient (right). An equilibrium is achieved only if the membrane is rigid and cell volume is constant. With a biological membrane, however, water enters the cell, cell volume increases and $[K^+]_i \cdot [Cl^-]_i$ decreases. This causes further entry of solute and solvent and the cycle repeats until the cell bursts. (B) Double-Donnan system. Part of the extracellular K^+ is replaced by Na^+, which is assumed to be impermeant. With impermeant ions on both sides of a membrane (left), equilibrium is attained (right) without an osmotic pressure gradient. In this case, K^+, Cl^-, and water leave the cell, until at equilibrium $[K^+]_o \cdot [Cl^-]_o = [K^+]_i \cdot [Cl^-]_i$. The amount of A^- in the cell is fixed, and thus, the decrease in cell volume increases $[A^-]_i$.

electrochemical gradient in the direction set by the potential gradient, an opposing concentration gradient is created. Finally, an equilibrium is reached when the electrical and concentration gradients for both K^+ and Cl^- are equal in magnitude and opposite in direction. This satisfies the requirement that μ_K and μ_{Cl}, the electrochemical potential for K^+ and Cl^-, respectively, are the same in both compartments.

During the evolution of the equilibrium, the influx of K^+ and Cl^- are equal on a macroscopic scale and are said to be coupled by the requirement for macroscopic electroneutrality. This is simply a shorthand for the idea that any difference in rates of anion and cation transmembrane flux (a separation of charge) gives rise to a potential that equalizes the fluxes (e.g. if the influx of K^+ was greater than that of Cl^-, an inside positive potential would develop, slowing K^+ influx and accelerating Cl^- influx until the rates matched exactly). In the example in Fig. 16.13A, both $[K^+]_i$ and $[Cl^-]_i$ increased by $\approx$78.5 mM. The total entry of K^+ and Cl^- cannot be precisely equal, however, because establishing a potential

difference implies that a separation of charge, albeit quite small, must have taken place. If this were a spherical cell with a radius of 20 μm, an inequality of the K^+ and Cl^- fluxes of less than 1 ion per 100 000 would cause a potential difference of 100 mV.[1]

The basis for Donnan equilibrium can be expressed in terms of the electrochemical potentials[2] of ions that cross the membrane, here K^+ and Cl^-. For ideal solutions, μ is given by:

$$\begin{aligned}\mu_{Ko} &= \mu^0 + RT \ \ln \ [K^+]_o + z_K \ F\psi_o \\ \mu_{K_i} &= \mu^0 + RT \ \ln \ [K^+]_i + z_K F\psi_i\end{aligned} \qquad (16.72a)$$

and

$$\begin{aligned}\mu_{Clo} &= \mu^0 + RT \ \ln \ [Cl^-]_o + z_{Cl} \ F\psi_o \\ \mu_{Cli} &= \mu^0 + RT \ \ln \ [Cl^-]_i + z_{Cl} \ F\psi_i\end{aligned} \qquad (16.72b)$$

where the subscripts o and i represent the outside and inside of a cell, μ^0 is the chemical potential of the standard state, ψ is the potential of the compartment, z_i is the valence of species i and R, T and F have their usual meanings. At equilibrium, each permeant species distributes so that μ is identical inside and outside the cell. Equating the expressions for μ and simplifying gives:

$$\begin{aligned}RT \ln \ [K^+]_o + z_K \ F\psi_o &= RT \ln \ [K^+]_i + z_K F\psi_i \\ RT \ln \ [Cl^-]_o + z_{Cl} \ F\psi_o &= RT \ln \ [Cl^-]_i + z_{Cl} F\psi_i\end{aligned} \qquad (16.73)$$

Membrane potential, E_m, is measured as $\psi_i - \psi_o$. Rearranging and substituting in for E_m and z gives:

$$\begin{aligned}E_m &= E_K = \frac{RT}{F} \ln \frac{[K^+]_i}{[K^+]_o} \\ E_m &= E_{Cl} = \frac{RT}{F} \ln \frac{[Cl^-]_o}{[Cl^-]_i}\end{aligned} \qquad (16.74)$$

These expressions are the *Nernst equilibrium potentials* for K^+ (E_K) and Cl^- (E_{Cl}). Thus, when the mobile ions attain their equilibrium distribution in a Donnan system, the potential between the compartments, E_m, simultaneously equals both E_K and E_{Cl}. Equating the Nernst potentials and simplifying gives the ratio of intra and extracellular ions predicted by Donnan equilibrium:

$$\frac{[K^+]_i}{[K^+]_o} = \frac{[Cl^-]_o}{[Cl^-]_i} \qquad (16.75)$$

or expressed another way:

$$[K^+]_i \cdot [Cl^-]_i = [K^+]_o \cdot [Cl^-]_o \qquad (16.76)$$

In a Donnan equilibrium, the KCl product inside a cell equals the KCl product outside.

This simple rule implies that increasing extracellular K^+ (e.g. by replacing Na^+) will cause a cell obeying Donnan equilibrium to take up K^+ and Cl^- and swell. Ion movements in a number of tissues appear to follow Donnan equilibrium, at least for some conditions. Boyle and Conway (1941) made careful measurements of $[K^+]_i$, $[Cl^-]_i$ and cell water in frog sartorius muscles while varying extracellular KCl. For $[K^+]_o$ greater than 6 mM, the experimental ratio of the KCl products, $([K^+]_o \cdot [Cl^-]_o)/([K^+]_i \cdot [Cl^-]_i)$, was very nearly 1.0, as predicted by Equation 16.76. The deviation at low $[K^+]_o$ occurs because Na^+ influx causes E_m to deviate from E_K. Accompanying changes in cell water in these experiments and in separate experiments in which K^+ replaced Na^+ also agreed with theory.

The expectations for a Donnan equilibrium are calculated for the system shown in Fig. 16.13A. When the intracellular and extracellular KCl products are equal, $E_m = E_K = E_{Cl} = -11.4$ mV. In addition, because the number of ions inside the cell is much greater than that outside, the

---

[1] The amount of charge, q, necessary to establish a potential difference, E_m, is related to the specific capacitance of the membrane, C_m, and its area, A, by:

$$q = C_m AE_m$$

Assuming a specific membrane capacitance of 1 μF/cm², as is typical of most biological membranes, the amount of charge necessary to develop a potential of 100 mV in a spherical cell with a radius of 20 μm is:

$$q = \left(1 \times 10^{-6} \ \text{F/cm}^2\right)\left[4\pi(20 \times 10^{-4} \ \text{cm})^2\right]\left(0.1 \ \text{V}\right)\left(\frac{C/V}{F}\right)$$

$$q = 5.0 \times 10^{-12} \text{C}$$

This can be converted to a change in the concentration, ΔC, of ions in the cell:

$$\Delta C = (q/F)/\vartheta$$

where F is Faraday's constant, and ϑ is used for the volume of the cell here to distinguish it from voltage. For the same 20-μm-radius cell:

$$\Delta C = \left(5.0 \times 10^{-12} \ C/96\,500 \ C/\text{mol}\right) \Big/ \left[\frac{4}{3}\pi(20 \times 10^{-4}\text{cm})^3\left(\frac{1\text{L}}{1000 \ \text{cm}^3}\right)\right]$$

$$\Delta C = 1.5 \times 10^{-6} \ \text{mol/L}$$

Thus, a potential gradient of 100 mV would develop if ion influx were to increase $[K^+]_i$ by only 1.5 μM more than it increased $[Cl^-]_i$.

[2] Formally, as presented previously in Equation 16.3 for the chemical potential of a neutral species, μ_i should be defined in terms of the mole fraction rather than the concentration of a component and an additional term, $P\overline{V}$, representing the pressure times the partial molar volume, should be added. For dilute solutions, the mole fraction of a solute closely approximates its concentration (see Equations 16.5 and 16.9). The $P\overline{V}$ terms are ignored in the derivation of the ion distribution for a Donnan equilibrium because to simplify we initially assume the membrane is rigid (see Fig. 16.13A) and then we consider a situation without a pressure gradient where the $P\overline{V}$ terms cancel (see Fig. 16.13B). Derivations of Donnan equilibrium retaining the mole fraction and the pressure-volume terms can be found in Overbeek (1956) and Lakshminarayanaiah (1984).

Donnan system has established a significant osmotic gradient. Assuming ideal behavior, the osmolarity inside the cell, $\approx 457\ \text{mosmol}\cdot\text{L}^{-1}$, is about 1.5 times that outside, $300\ \text{mosmol}\cdot\text{L}^{-1}$. The resulting osmotic pressure can be calculated as follows:

$$\begin{aligned}\Delta\pi &= RT\,\Delta C \\ &= (0.082\ \text{L}\cdot\text{atm}\cdot\text{K}^{-1}\cdot\text{mol}^{-1})(310\ \text{K}) \\ &\quad \times (0.457 - 0.300\ \text{mol}\cdot\text{L}^{-1}) \\ &= 3.99\ \text{atm}\end{aligned} \tag{16.77}$$

Because most cells are readily permeable to water, the osmotic pressure generated here would cause water to enter the cell. This influx of water dilutes the intracellular ion content and the product $[K^+]_i\cdot[Cl^-]_i$ must fall below $[K^+]_o\cdot[Cl^-]_o$. As a result, more KCl would enter the cell, followed again by more water, in an endless cycle that would lead to destruction of the cell. That is to say, the simple Donnan system described in Fig. 16.13A fails to reach equilibrium when typical cell membrane properties are assumed.

VIB. Double-Donnan or Pump-Leak Hypothesis

How can we reconcile the failure of the simple Donnan equilibrium model (see Fig. 16.13A) and the experimental studies demonstrating behavior consistent with Donnan equilibrium? The Donnan system can be stabilized in two ways. A hydrostatic pressure could be applied to balance the osmotic pressure and arrest transmembrane water movement. In view of the enormous pressures required, this is not a realistic solution for animal cells. Alternatively, equilibrium can be attained by restricting an ionic species to the extracellular compartment just as one is restricted to the intracellular compartment. This arrangement is referred to as a *double-Donnan* (Leaf, 1959) or *pump-leak system* (Tosteson and Hoffman, 1960) and is illustrated diagrammatically in Fig. 16.13B. Assume that both Na^+ and macromolecular anions, A^-, are restricted to the extracellular and intracellular compartments, respectively. Filling the cell with the same concentrations of K^+, Cl^- and A^- as before, we find now that $[K^+]_i\cdot[Cl^-]_i>[K^+]_o\cdot[Cl^-]_o$ and thus KCl must leave the cell to establish Donnan equilibrium. In the process, water follows the KCl, adjusting cell volume until the KCl, products are equal. A consequence of water flow is that the concentration of the impermeant intracellular ion exactly equals the concentration of the impermeant extracellular ion. At equilibrium, $E_m = E_K = E_{Cl} = -91.1$ mV. In contrast to the simple Donnan system, the osmotic pressure developed by intracellular macromolecules and their counterions (sometimes referred to as *colloid osmotic pressure*) is exactly balanced in the double-Donnan system by the osmotic pressure developed by ions restricted to the extracellular fluid and their counterions. As a consequence, there is no net osmotic pressure across the membrane, and the system is stable.

Another approach for considering the volume change expected in the system in Fig. 16.13B is to calculate the effective osmotic pressure of each compartment. We can suppose that the reflection coefficients, σ, are 1.0 for both A^- and Na^+ because they are impermeant and that the reflection coefficients are 0 for both K^+ and Cl^- because they freely pass the membrane. Extracellular and intracellular osmotic pressures are given by:

$$\begin{aligned}\pi &= \sum_n \sigma_n C_n \\ \pi_o &= 1\cdot[Na^+]_o + 0\cdot[K^+]_o + 0\cdot[Cl^-]_o \\ \pi &= 1\cdot[A^-]_i + 0\cdot[K^+]_i + 0\cdot[Cl^-]_i\end{aligned} \tag{16.78}$$

Because only the impermeant species contribute to osmotic pressure, the only way for the cell to reach osmotic equilibrium, $\pi_o = \pi_i$, is to alter cell volume until $[Na^+]_o = [A^-]_i$. As a result, the ratio of $\text{volume}_{t=\infty}/\text{volume}_{t=0}$ must equal $[A^-]_i/[Na^+]_o$.

It is important to realize that an ion does not need to be impermeant to be *effectively* restricted to the extracellular space and thus counterbalance the osmotic pressure developed by intracellular macromolecules. Na^+ is permeant, but it adequately plays this role anyway. As long as the leak of Na^+ down its electrochemical gradient into the cell is matched by its transport back out, cell volume will remain stable. Consequently, the existence of a pump that actively extruded Na^+ against its concentration gradient was postulated to explain cell volume (Leaf, 1956) and, subsequently, the Na^+, K^+-ATPase, which extrudes three Na^+ while taking up two K^+ at the cost of ATP hydrolysis, was identified. Because energy is consumed to extrude Na^+, the cell is in a *steady state* rather than a true equilibrium.

VIC. Modulation of the Na^+-K^+ Pump

One implication of the double-Donnan or pump-leak model is that the Na^+-K^+ pump is ultimately responsible for cell volume regulation. Perturbations that alter passive Na^+ entry must lead to offsetting changes in the rate of Na^+ extrusion by the Na^+-K^+ pump, or cell volume will change. Because the K_m of the Na^+-K^+ pump, for intracellular Na^+ is close to the physiological $[Na^+]_i$, alterations in Na^+ influx automatically give rise to a compensatory modulation of Na^+ efflux. Nevertheless, metabolic or pharmacologic inhibition of the Na^+-K^+ pump should lead to a net gain of Na^+ and anions coupled by macroscopic electroneutrality and result in a swelling of the cell.

The effect of pump inhibition has been examined extensively (Macknight and Leaf, 1977; Macknight, 1988). The predicted cell swelling has been reported in many tissues, including brain slices, kidney slices, renal tubules, hepatocytes and sheep erythrocytes, when the Na^+-K^+ pump is inhibited by cardiac glycosides (e.g. ouabain) or by depleting ATP. It is equally clear, however, that swelling after pump inhibition in renal cortex, liver slices, various muscle preparations, lymphocytes and human erythrocytes is very slow or even absent, perhaps reflecting a low Na^+ permeability.

Several processes may affect the response of cell volume to Na^+-K^+ pump inhibition and the outcome in some tissues depends on the experimental conditions. Rather than accumulating Cl^- with Na^+, cells might instead lose K^+ to satisfy macroscopic electroneutrality. An equivalent gain of Na^+ and loss of K^+ replaces one osmotically active particle with another, causing no change in cell volume. Closer consideration of this mechanism indicates that it can only be a holding action, however. The loss of intracellular K^+ eventually must lead to a reduction of the K^+ gradient and a less negative E_m. This will lead to accumulation of Cl^- with Na^+ and cell swelling. Nevertheless, a loss of K^+ must slow the swelling that otherwise would have occurred and this would explain the absence of swelling in cells with appropriate Na^+ and K^+ permeabilities over the time course of experiments.

The possibility that a mechanism other than the Na^+-K^+ pump can extrude Na^+ has been considered. Although controversial, a cardiac glycoside-insensitive but metabolically dependent volume regulation mechanism in kidney that does not incorporate the Na^+-K^+ pump has been described (for review, see Macknight and Leaf, 1977). In addition, circulating erythrocytes from a number of carnivores, including dog, cat, bear and ferret, lack a functioning Na^+-K^+ pump and must regulate their volume by a different mechanism (Sarkadi and Parker, 1991). In these cells, Na^+ efflux must depend on the gradient of other ions.

VID. Isosmotic Volume Regulation

Although principles of the pump-leak or double-Donnan model are correct and still relevant to the regulation of cell volume, it has become apparent that neither the leak nor the pump is constant. Not only is the control of these fluxes more complex than originally envisioned, but a myriad of other transport processes also contribute to cell volume regulation. Stated simply, constant cell volume under isosmotic conditions implies an equality of intra- and extracellular osmolarity that is perpetuated by a continuous balance of the efflux and influx of osmolytes. The transport processes involved include, but are not limited to: (1) ion and organic osmolyte channels; (2) the Na^+-K^+ pump; (3) the Na^+-K^+-$2Cl^-$, K^+-Cl^- and Na^+-Cl^- co-transporters, which transport the specified ions in one direction; (4) Na^+-dependent sugar and amino acid co-transport; (5) Na^+-Ca^{2+}; exchange, which exchanges three Na^+ for one Ca^{2+}; and (6) osmotically neutral exchangers that indirectly provide a net solute flux. For example, Na^+-H^+ exchange allows the cell to accumulate Na^+, but the H^+ removed is replaced by dissociation of H^+ from intracellular buffers. Cl^--HCO_3^- and Na^+-H^+ exchange can operate in parallel to mediate a net influx of Na^+ and Cl^- in exchange for H^+ and HCO_3^-, which are converted to CO_2 and H_2O by the action of carbonic anhydrase. It should be noted that CO_2 freely crosses the cell membrane ($\sigma = 0$) and does not directly contribute to solution tonicity. Also, the direct extrusion of water by these two parallel exchangers is negligible compared to the osmotic water gain caused by the accumulation of Na^+ and Cl^-.

Of the number of transporters that participate in volume regulation in any given type of cell, which are most important in regulating cell volume under isosmotic conditions? No simple answer can be offered. The importance of each process to cell volume regulation depends critically upon the tissue and species under consideration as well as the conditions. Moreover, transporters and channels are modulated by multiple signaling pathways and they extensively interact by altering membrane potential or the concentration of the transported species. If the rates of ion transport are not correctly matched, cells will inappropriately shrink or swell. The precise maintenance of cell volume exemplifies the need for sensitive and complex regulatory mechanisms. Attempts to integrate mathematically the fluxes and study their interaction have been made based on the cell's requirement for macroscopic electroneutrality and osmotic equilibrium and the equations governing ion fluxes (Jakobsson, 1980). For erythrocytes, the non-ideal behavior of hemoglobin has been added (Bookchin et al., 1989). Although these simplified models correctly predict a number of observations, they fail to explain others. In short, we remain a long way from a complete quantitative description of the processes underlying cell volume regulation. In the following sections, we will discuss three examples of isosmotic regulation of cell volume that illustrate some of the underlying principles.

VID1. Na^+-K^+-$2Cl^-$ Co-transport in Heart

Recent findings indicate that the Na^+-K^+-$2Cl^-$ co-transporter plays a critical role in regulating cardiac myocyte cell volume under isosmotic conditions. As in other tissues, Na^+-K^+-$2Cl^-$ co-transport conveys osmolytes into cardiac cells under physiological conditions. Because *net* transmembrane fluxes control cell volume, a decreased osmolyte influx is equivalent to increased efflux. Therefore, inhibition of the Na^+-K^+-$2Cl^-$ co-transport by bumetanide, for

example, favors a reduction of cell volume. Consistent with this idea, bumetanide decreases the volume of atrial and ventricular myocytes by about 10% in less than 5 min and myocyte volume is stable at this new level (Drewnowska and Baumgarten, 1991). The Na^+-K^+-$2Cl^-$ co-transporter cannot operate without Na^+ and Cl^- in the extracellular fluid and removing either ion renders bumetanide ineffective. These data imply that ion uptake by Na^+-K^+-$2Cl^-$ co-transport in the heart must be responsible for a significant osmolyte flux under isosmotic conditions and that other transport processes are incapable of fully compensating when this flux is removed. In contrast, myocyte volume was unchanged after inhibiting the Na^+-K^+ pump with 10 μM ouabain (Drewnowska and Baumgarten, 1991) or by cooling to 9°C (Drewnowska et al., 1991) for 20 min. At least in the short term, cardiac cell volume in isosmotic solution is influenced more by Na^+-K^+-$2Cl^-$ co-transport than by the Na^+-K^+ pump.

Modulation of Na^+-K^+-$2Cl^-$ co-transport by intracellular messengers, such as cGMP, may provide a physiological means of modulating cell volume in heart tissue. Figure 16.14 shows the effects of elevating intracellular cGMP in three ways: (1) by adding 8-Br-cGMP, a membrane-permeant analog of cGMP; (2) by adding atrial natriuretic factor (ANF), a natriuretic, diuretic and vasodilatory hormone released by the heart that elevates cGMP by activating guanylate cyclase; and (3) by adding sodium nitroprusside (SNP), a vasodilator, that also activates guanylate cyclase. In each case, cell volume decreased. Furthermore, blocking cGMP-specific phosphodiesterase with zaprinast (M&B22948) augmented the effect of ANF. Based on its sensitivity to bumetanide and the requirement for ions transported by Na^+-K^+-$2Cl^-$ co-transport, cGMP-dependent volume decreases were shown to be due to an inhibition of Na^+-K^+-$2Cl^-$ co-transport by cGMP (Clemo et al., 1992; Clemo and Baumgarten, 1995). Interestingly, *lowering* cGMP levels by inhibiting guanylate cyclase with LY83583 resulted in a small amount of cell swelling. Thus, changing cGMP from its physiological level in either direction altered cell volume. The mechanism and evidence for isosmotic regulation of cell volume in the heart are summarized in Fig. 16.15.

Does the same mechanism regulate cell volume under isosmotic conditions in other tissues? Perhaps it does in some cells, such as vascular endothelium, in which cGMP inhibits Na^+-K^+-$2Cl^-$ co-transport. In other cells, Na^+-K^+-$2Cl^-$ co-transport is stimulated by cAMP, cGMP or a PKC-dependent pathway, and perhaps by a number of other signaling pathways (Palfrey and O'Donnell, 1992; Palfrey, 1994). This diversity in the control of Na^+-K^+-$2Cl^-$ co-transport may be related to the variety of transporter isoforms that have been identified and cloned (Haas, 1994; Kaplan et al., 1996). Although the physiological significance of this diversity in the control of ion transport is not well understood, it must lead to diversity in the regulation of cell volume.

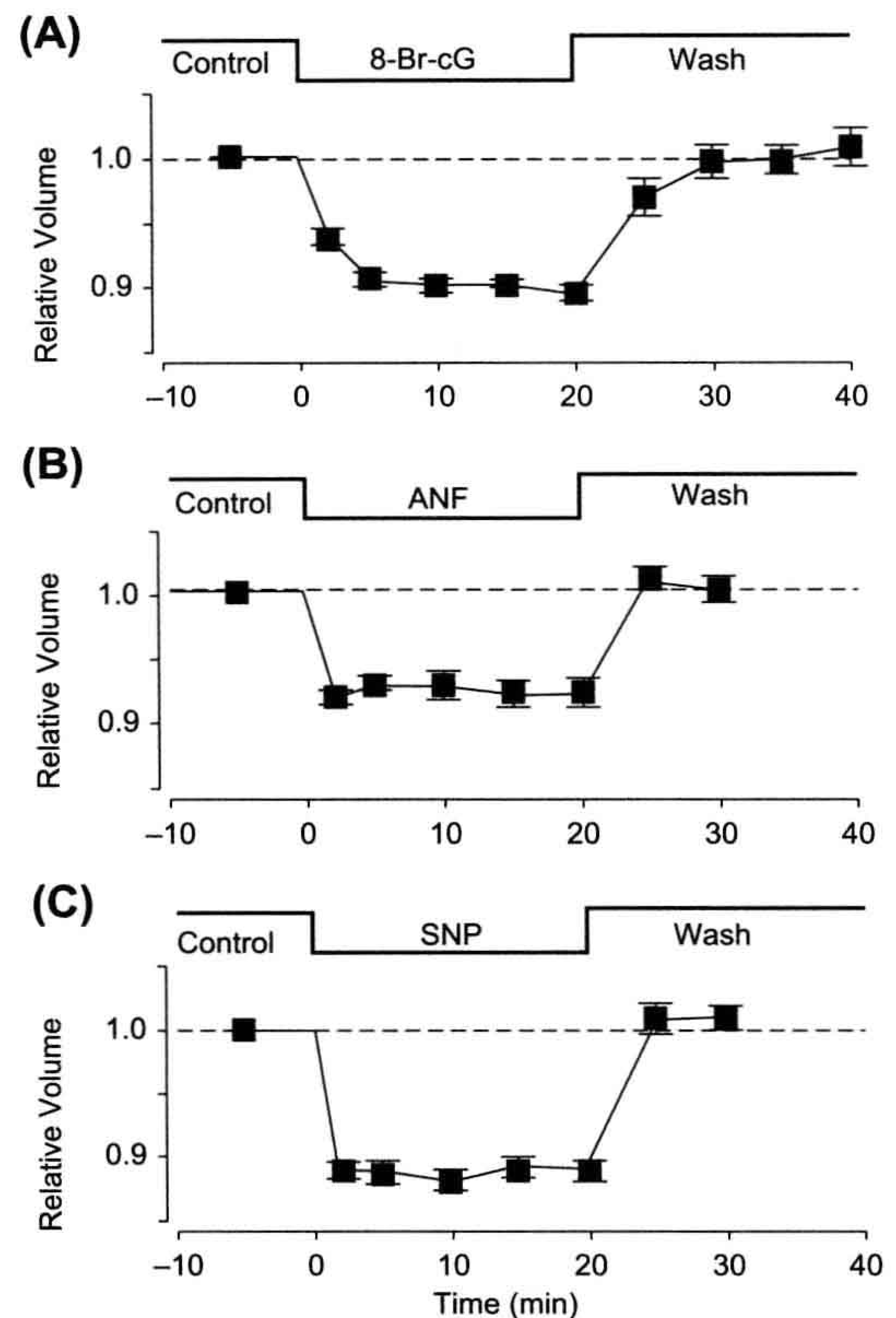


FIGURE 16.14 Changes in the volume of isolated ventricular myocytes during a 20-min exposure to: (A) 10 μM 8-Br-cGMP (8-Br-cG), a permeable cGMP analog; (B) 1 μM atrial natriuretic factor (ANF); and (C) 100 μM sodium nitroprusside (SNP). These agents reversibly decreased cell volume 11%, 8% and 11%, respectively (n=5 for each time point). The decreases in cell volume were caused by inhibition of Na^+-K^+-$2Cl^-$ co-transport by cGMP. Relative cell volume was measured and calculated as described in the legend of Fig. 16.1. *(From Clemo et al. (1992). Reproduced from The Journal of General Physiology, 1992, 100, 89–114, by copyright permission of The Rockefeller University Press.)*

VID2. Hormones and Substrate Transport in Liver

Another interesting example of isosmotic volume regulation is found in hepatocytes. An impressive number of hormones induce either cell swelling or cell shrinkage at physiological concentrations and these actions are related to their control of liver metabolism (Häussinger and Lang, 1991; Häussinger et al., 1994; Agius et al., 1994; Häussinger, 1998). Na^+-H^+ exchange, Na^+-K^+-$2Cl^-$

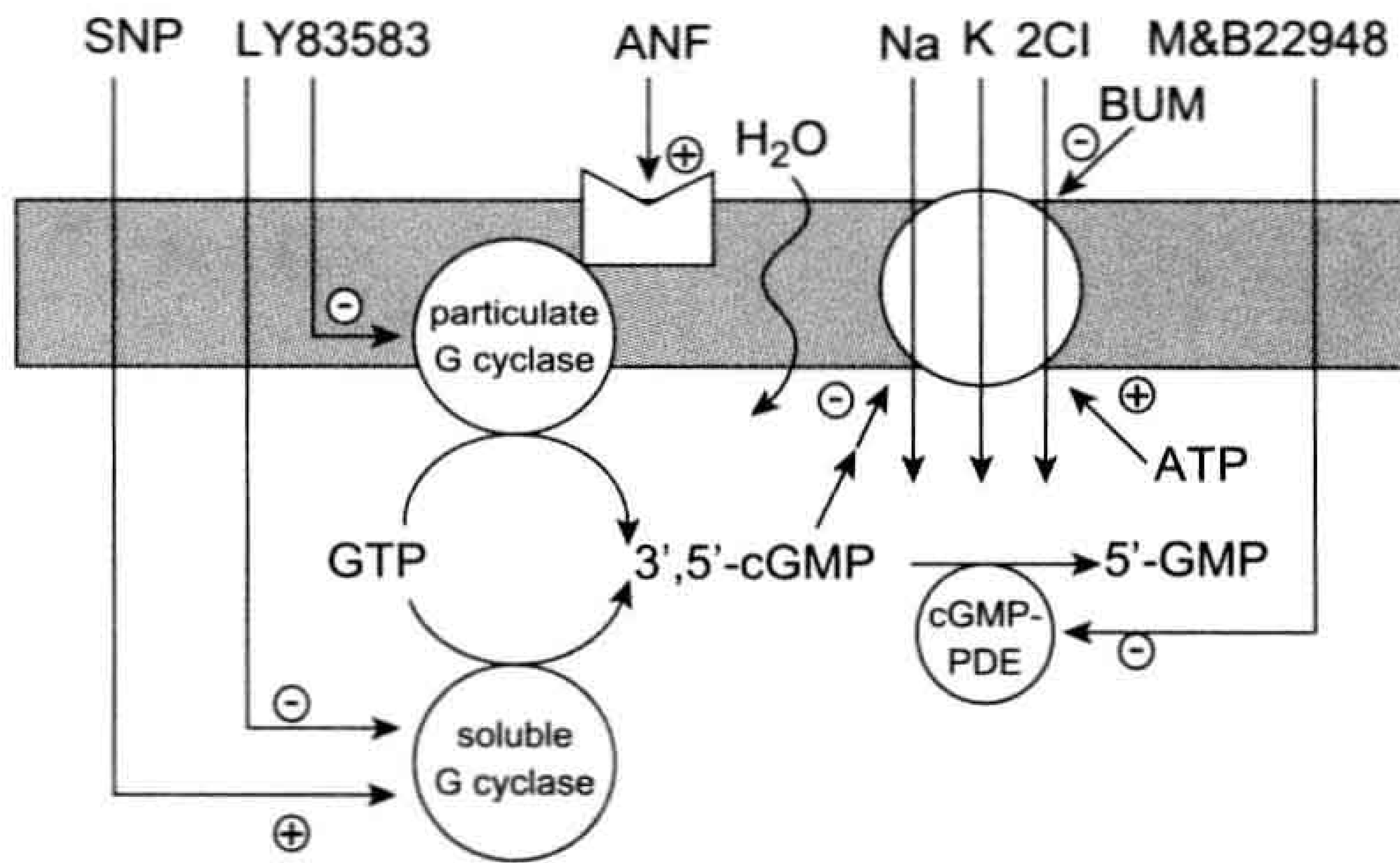


FIGURE 16.15 Schematic diagram of the action of atrial natriuretic factor (ANF) and cGMP on cardiac cell volume. Binding of ANF activates guanylate cyclase and increases intracellular cGMP levels. By one or more steps, cGMP inhibits Na^+-K^+-$2Cl^-$ co-transport. Reducing ion influx by this means is equivalent to increasing *net* ion efflux and cell shrinkage ensues. LY83583 inhibits guanylate cyclase, thereby blocking the effect of ANF and zaprinast (M&B22948) potentiates the effect of ANF by inhibiting cGMP-specific phosphodiesterase (PDE). Sodium nitroprusside (SNP) also increases cGMP levels, and bumetanide (BUM) directly inhibits the co-transporter; both cause cell shrinkage. *(From Clemo et al. (1992) Reproduced from The Journal of General Physiology, 1992, 100, 89–114, by copyright permission of The Rockefeller University Press.)*

co-transport and the Na^+-K^+ pump are stimulated in rat liver cells by insulin. The net effect is that insulin increases $[K^+]_i$, $[Na^+]_i$ and $[Cl^-]_i$ and causes cells to swell by about 12%. This swelling is prevented by bumetanide, a blocker of Na^+-K^+-$2Cl^-$ co-transport, or by amiloride, a blocker of Na^+-H^+ exchange. In contrast, glucagon shrinks hepatocytes by about 14%. Instead of directly opposing the action of insulin, glucagon reduces cell volume by increasing K^+ and Cl^- efflux through ion channels. Other agents that swell hepatocytes include bradykinin and phenylephrine. Shrinking is initiated by adenosine, 5-HT, vasopressin and cAMP.

Hepatocytes also swell as a result of Na^+-dependent amino acid co-transport in isosmotic media (Häussinger and Lang, 1991; Boyer et al., 1992; Häussinger et al., 1994; Häussinger, 1998). Exposure to amino acids that are accumulated with Na^+ (e.g. alanine, glutamine, glycine, hydroxyproline, phenylalanine, proline and serine) causes cell swelling. These effects occur at amino acid levels found physiologically in the portal vein. For example, glutamine provokes up to a 10% swelling with a half-maximal effect at approximately 0.7 mM. Amino acid co-transport gives rise to an inward current and Cl^- enters to maintain macroscopic electroneutrality. Instead of loading the cell, Na^+ is pumped out, mainly by the Na^+-K^+ pump, leaving an accumulation of K^+ and Cl^-. In contrast to these amino acids, substances not accumulated by the liver, such as glucose and leucine, do not affect hepatocyte volume. Cell swelling caused by Na^+-dependent amino acid co-transport has also been observed in intestine and renal proximal tubule.

VID3. Na^+-Ca^{2+} Exchange in Carnivore Erythrocytes

The Na^+-K^+ pump in erythrocytes from dogs, cats, ferrets and bears ceases to function as cells mature. As a result, $[K^+]_i$ and $[Na^+]_i$ are similar to $[K^+]_o$ and $[Na^+]_o$. This poses a special problem for cell volume regulation. How can these cells offset the osmotic pressure generated by impermeant intracellular molecules and avoid swelling without an Na^+-K^+ pump to make Na^+ effectively impermeant? Carnivore erythrocytes solve this dilemma by extruding three Na^+ in exchange for one Ca^{2+} via the Na^+-Ca^{2+} exchanger (Parker, 1973; Sarkadi and Parker, 1991). In most cells, the electrochemical gradients for Na^+ and Ca^{2+} favor the efflux of Ca^{2+}. In these erythrocytes, however, the gradients favor Ca^{2+} entry because the Na^+ gradient is reduced and Na^+-Ca^{2+} exchange operates in what is called the *reverse mode*. To stabilize their volume, carnivore erythrocytes also must have a means of maintaining the Ca^{2+} gradient (i.e. low $[Ca^{2+}]_i$). This is accomplished by an ATP-dependent Ca^{2+} pump in the plasma membrane. Thus, as in other cells, maintaining cell volume in the face of impermeant intracellular colloids requires the expenditure of energy in a pump-leak mechanism. In this case, ATP is expended by a plasma membrane Ca^{2+} pump rather than by the Na^+-K^+ pump.

VII. REGULATION OF CELL VOLUME UNDER ANISOSMOTIC CONDITIONS

VIIA. Osmometric Behavior of Cells

Because the permeability of most cell membranes to water is much greater than that to solutes, cells swell or shrink when placed in an environment that is hyposmotic or hyperosmotic, respectively. Water rapidly flows to equalize its chemical potential, μ_w, inside and outside the cell. The initial volume response is often close to that predicted for an ideal osmometer from van't Hoff's law. An example is shown in Fig. 16.16, which illustrates the response of rabbit ventricular myocytes to solutions with osmolarities ranging from 195 to 825 mosmol/L (0.60 to 2.55 times isotonic). Relative cell volume (V), calculated as $V_{test}/V_{isosmotic}$, is plotted against the inverse of relative osmolality, $\pi_{isosmotic}/\pi_{test}$, and the data are fit to

$$V = (1 - V_b)\,(\pi_{isosmotic}/\pi_{test}) + V_b \qquad (16.79)$$

By definition, relative volume is 1.0 at a relative osmolarity of 1.0. Two conclusions can be reached from the data in Fig. 16.16. First, as expected from van't Hoff's law, the relationship between relative cell volume and the inverse of

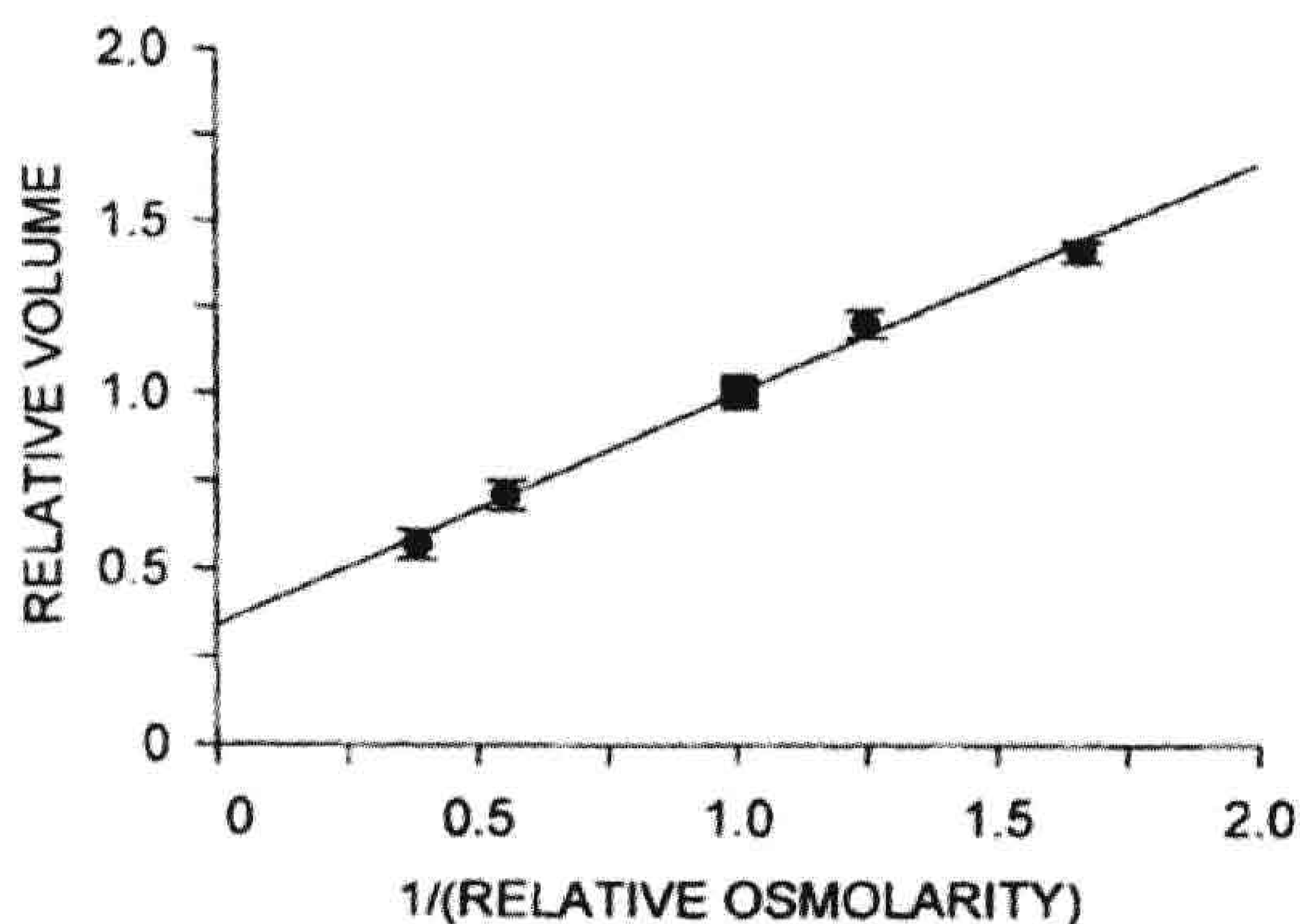


FIGURE 16.16 Relationship between relative cell volume and the inverse of relative osmolarity in cardiac ventricular myocytes. Data from 38 measurements of relative cell volume in anisosmotic solutions (0.6T, 0.8T, 1.8T and 2.6T) were fit to a least squares regression line constrained to pass through (1, 1) (square) because relative cell volume is 1 in isotonic solution by definition. The extrapolated intercept on the relative volume axis, 0.34, represents the fraction of cell volume that is osmotically inactive (see Equation 16.79). Volume measurements, calculation of relative cell volume, and means of adjusting osmolarity are as described for Fig. 16.1. *(Reproduced from Drewnowska and Baumgarten, 1991.)*

relative osmolarity is linear. Second, the intercept of the relationship on the volume axis, V_b, is 0.34, which is significantly different from 0. This is interpreted as meaning that a fraction of cell volume is *osmotically inactive*, i.e. it apparently does not participate in the response to anisosmotic solutions.

Several arguments can be made to justify the observation of an osmotically inactive volume. The expectation from the simplest model is that *cell water* should vary in proportion to osmolarity. However, not all of cell volume is water. The volume of non-aqueous components, such as small solutes and proteins, which represent 25–30% of the cell on a weight/weight basis, is unaffected by water movements. Even measurements of cell water show non-ideal behavior, however (Macknight and Leaf, 1977; Solomon, 1989), so additional explanations are necessary. One suggestion is that a fraction of cell water is intimately associated with cell proteins or membranes and thereby is *bound* or *structured* and unavailable as solvent (e.g. LeNeveu et al., 1976; Hinke, 1980). Although the state of water molecules adjacent to proteins and membranes must be different from that in the bulk phase of the cytoplasm, in light of NMR, intracellular ion activity, and other data, most investigators believe that virtually all water ($\approx$95%) is available as solvent (Shporer and Civan, 1977; Hladky and Rink, 1978). Another possibility is that the behavior of intracellular macromolecules is concentration dependent. For example, the osmotic coefficient and charge on hemoglobin increase with its concentration as red cells shrink and anions are drawn in to maintain electroneutrality. These phenomena are important in explaining water movement in red cells (Freedman and Hoffman, 1979), but their importance in other tissues remains uncertain. A third possibility is that intracellular compartments, such as mitochondria, nuclei, endoplasmic reticulum and sarcoplasmic reticulum of muscle cells, may undergo volume changes that are not proportional to those of the whole cell. Differential responses to an osmotic challenge are expected because the plasmalemma and intracellular membranes possess distinct arrays of transporters and ion channels and each sees a unique environment. Most methods for determining cell water or cell volume fail to distinguish between cytoplasmic and total cell water or volume (for a method that does distinguish these, see Reuss, 1985).

A crucial assumption made in determining osmotically inactive volume also may affect the value obtained for V_b in Equation 16.79. The analysis assumes that only water has moved at the time volume is measured. That is to say, transmembrane ionic fluxes can be ignored. Although the permeability of the cell membrane to water is many times greater than the permeability to ions, the net fluxes of both water and ions start at the instant extracellular osmolarity is changed. If ion fluxes significantly affect intracellular osmolarity at the time of measurement, the extrapolated osmotically inactive volume will be imprecise. If, in addition, the ion fluxes depend on the direction or magnitude of the osmotic gradient, the plot of relative volume versus $\pi_{isosmotic}/\pi_{test}$ can become non-linear (e.g. Grinstein et al., 1984).

VIIB. Compensatory Regulation of Cell Volume

Although an osmotic gradient initiates cell swelling or shrinkage, the initial volume response is not maintained in a wide variety of cells. Cell swelling activates compensatory processes that lead to an efflux of osmolytes and a reduction of cell volume. This is called a *regulatory volume decrease* (RVD). Similarly, cell shrinking activates an influx of osmolytes in some cells, leading to a compensatory swelling referred to as a *regulatory volume increase* (RVI). RVD and RVI nearly restore the original cell volume in some cells, are far less complete in others and are absent in a few types of cells.

Regulatory volume effects are thought to be adaptive and were first identified in nucleated duck erythrocytes (for a review, see Kregenow, 1981). Examples of an RVD and RVI taken from work by Grinstein et al. (1983) are shown in Fig. 16.17. Exposure of human peripheral blood lymphocytes to a solution made hypotonic by 50% dilution with water leads to a rapid, 1.6-fold increase in cell volume (Fig. 16.17B). Then, over about 10 min, an RVD returned cell volume almost completely to its initial value. On

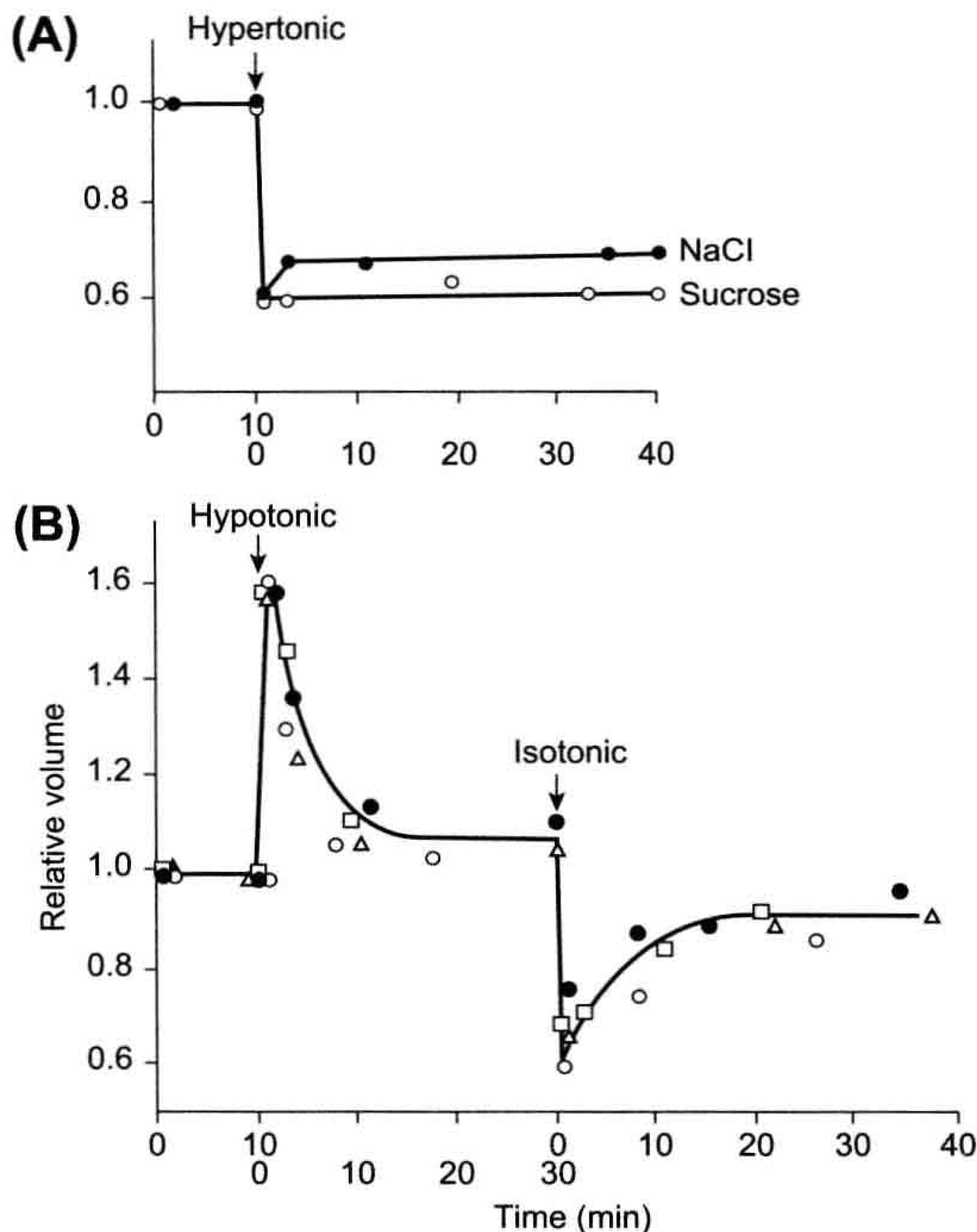


FIGURE 16.17 (A) Effect of hypertonic solution (2T) on relative cell volume of human peripheral blood mononuclear lymphocytes. Solution osmolarity was increased by adding 300 mosmol·L^{-1} of NaCl or sucrose. Cells shrank 40% in hypertonic solution and a small regulatory volume increase (RVI) was observed in the NaCl solution. Points are representative of four experiments. (B) Response to hypotonic solution (0.5T). After swelling by nearly 60%, a regulatory volume decrease (RVD) virtually restored cell volume to its initial value in 10 min. On returning to isotonic solution, cell volume decreased below its control value, and an RVI lead to full recovery. Different symbols represent separate experiments selected from over 40. Cell volume was measured with a Coulter counter that determines volume from the change in electrical resistance of a column of solution as cells pass through an aperture. *(From Grinstein et al. (1983). Reproduced from The Journal of General Physiology, 1983, 82, 619–638, by copyright permission of The Rockefeller University Press.)*

switching back to isotonic solution, cell volume shrank to less than the control value and then was restored by an RVI. RVDs and RVIs may differ in magnitude, however. A much less complete RVI was observed when lymphocytes in isotonic solution were shrunk in media made hyperosmotic by adding of 300 mosmol·L^{-1} of NaCl and the RVI was absent when the lymphocytes were challenged with 300 mosmol·L^{-1} of sucrose instead of NaCl (Fig. 16.17A). The RVD also could be eliminated, for example, by cooling lymphocytes to 4°C (Grinstein et al., 1984). Thus, regulation of cell volume following an osmotic challenge depends on the particulars of the perturbation as well as the cell under study (compare Figs. 16.1 and 16.17).

VIIC. Transport Processes Responsible for RVD and RVI

How do cells gain or lose osmotic equivalents in anisosmotic media? The mechanisms underlying RVDs and RVIs have been extensively characterized in a variety of cell types and exhaustively reviewed (Hoffmann and Simonsen, 1989; Chamberlin and Strange, 1989; Grinstein and Foskett, 1990; Sarkadi and Parker, 1991; Häussinger and Lang, 1991; McCarty and O'Neil, 1992; Strange, 1994; Hoffmann and Dunham, 1995; Lang et al., 1998; O'Neil, 1999). In general, cells undergo RVD or RVI by translocating Na^+, K^+, and Cl^- and a variety of channels, exchangers, co-transporters and pumps can participate. In some cases, organic osmolytes (e.g. taurine, betaine, sorbitol, and urea) are transported instead of, or in addition to, inorganic ions. Table 16.3 lists processes that are activated by altering the volume of various cells and Fig. 16.18 illustrates some of the mechanisms diagrammatically. The compensatory mechanisms invoked vary with the tissue, species and conditions under which osmotic stress is applied.

The primary mechanism of RVD in a number of cell types is activation of conductive pathways and this process will be discussed in more detail. Cell swelling, acting directly or via a messenger, opens ion channels that allow increased efflux of K^+ and Cl^- and H_2O follows. Although the openings of cation and anion channels are independent events, K^+ and Cl^- efflux are tightly coupled by the need to maintain macroscopic electroneutrality. If only the anion or cation channel were to open, the resulting change in E_m would rapidly make ion efflux self-limiting and arrest volume regulation. The effect of this coupling of K^+ and Cl^- fluxes is illustrated in Fig. 16.19A, which shows RVDs in Ehrlich ascites cells (Hoffmann et al., 1986; Hoffmann and Dunham, 1995). At time zero, cells were switched from 300 to 150 mosmol·L^{-1} media. Cells rapidly swelled to about 1.9 times their initial volume and then underwent an RVD that returned relative cell volume to about 1.3 within 5 min. When K^+ conductance was increased by pretreating cells with 0.5 μM gramicidin, a K^+ ionophore, the compensation by the RVD was more rapid and larger in magnitude, returning cell volume to nearly its control level in 2 min. When K^+ channels were blocked with 1 μM quinine, however, only a feeble RVD took place. These data argue that conductive K^+ efflux cannot keep up with Cl^- efflux in control cells and limits the rate of RVD (Hoffmann et al., 1986). Thus, cell swelling must increase Cl^- conductance more than K^+ conductance, leading to greater efflux of Cl^- than of K^+. Consistent with this idea, a depolarization is observed during the RVD. The activation of Cl^- conductance by swelling is only transient, however. The ability of gramicidin to induce RVD decays with time, as shown in Fig. 16.19B. In contrast to the high

TABLE 16.3 Ionic Mechanisms of Regulatory Responses to Anisosmotic Solutions

Transport Mechanism Activated	Cell Types
Cell swelling-induced regulatory volume decrease	
K^+ and Cl^- conductances	Frog urinary bladder
	Chinese hamster ovary cells
	Ehrlich ascites tumor cells
	Frog skin
	HeLa carcinoma cells
	Human platelets
	Human granulocytes
	Human lymphocytes
	Intestinal 407 cells
	Madin-Darby canine kidney (MDCK) cells
	Necturus enterocytes
	Necturus gallbladder
	Rabbit renal proximal convoluted tubule
	Rat hepatocytes
K^+-Cl^- co-transport	Avian, dog, fish, human, rabbit, and low-K^+ sheep erythrocytes
	Ehrlich ascites tumor cells (Ca^{2+} depleted)
	Necturus gallbladder
Coupled K^+-H^+ and Cl^--HCO_3^- exchange	*Amphiuma* erythrocytes
Na^+-Ca^{2+} exchange	Dog and ferret erythrocytes
Organic osmolyte efflux	Crustacean muscle and myocardium
	Ehrlich ascites tumor cells
	Elasmobranch and molluscan erythrocytes
Cell shrinkage-induced regulatory volume increase	
Na^+-K^+-$2Cl^-$ co-transport	Astrocytes
	C6 glioma cells
	Duck, fish, rat, and human erythrocytes
	Ehrlich ascites tumor cells
	Frog skin
	HeLa cells
	Rat kidney medullary thick ascending limb
	3T3 cells
Coupled Na^+-H^+ and Cl^--HCO_3^- exchange	Amphibian gallbladder
	Dog and amphibian erythrocytes
	Human lymphocytes
	Mouse medullary thick ascending limb
	Rabbit renal proximal straight tubule

(Continued)

TABLE 16.3 Ionic Mechanisms of Regulatory Responses to Anisosmotic Solutions—cont'd

Transport Mechanism Activated	Cell Types
	Ehrlich ascites tumor cells
Na^+-Cl^- co-transport	Ehrlich ascites tumor cells
	Necturus gallbladder
K^+ and Cl^- conductances, inhibited	Madin-Darby canine kidney (MDCK) cells
Organic osmolyte influx	Many animal and plant cells, bacteria and fungi

For references, see Yancey et al. (1982), Hoffmann and Simonsen (1989), Chamberlin and Strange (1989), Grinstein and Foskett (1990), Wolff and Balaban (1990), Sarkadi and Parker (1991), Häussinger and Lang (1991), McCarty and O'Neil (1992), Boyer et al. (1992), Strange (1994), Hoffmann and Dunham (1995), Lang et al. (1998) and O'Neil (1999).

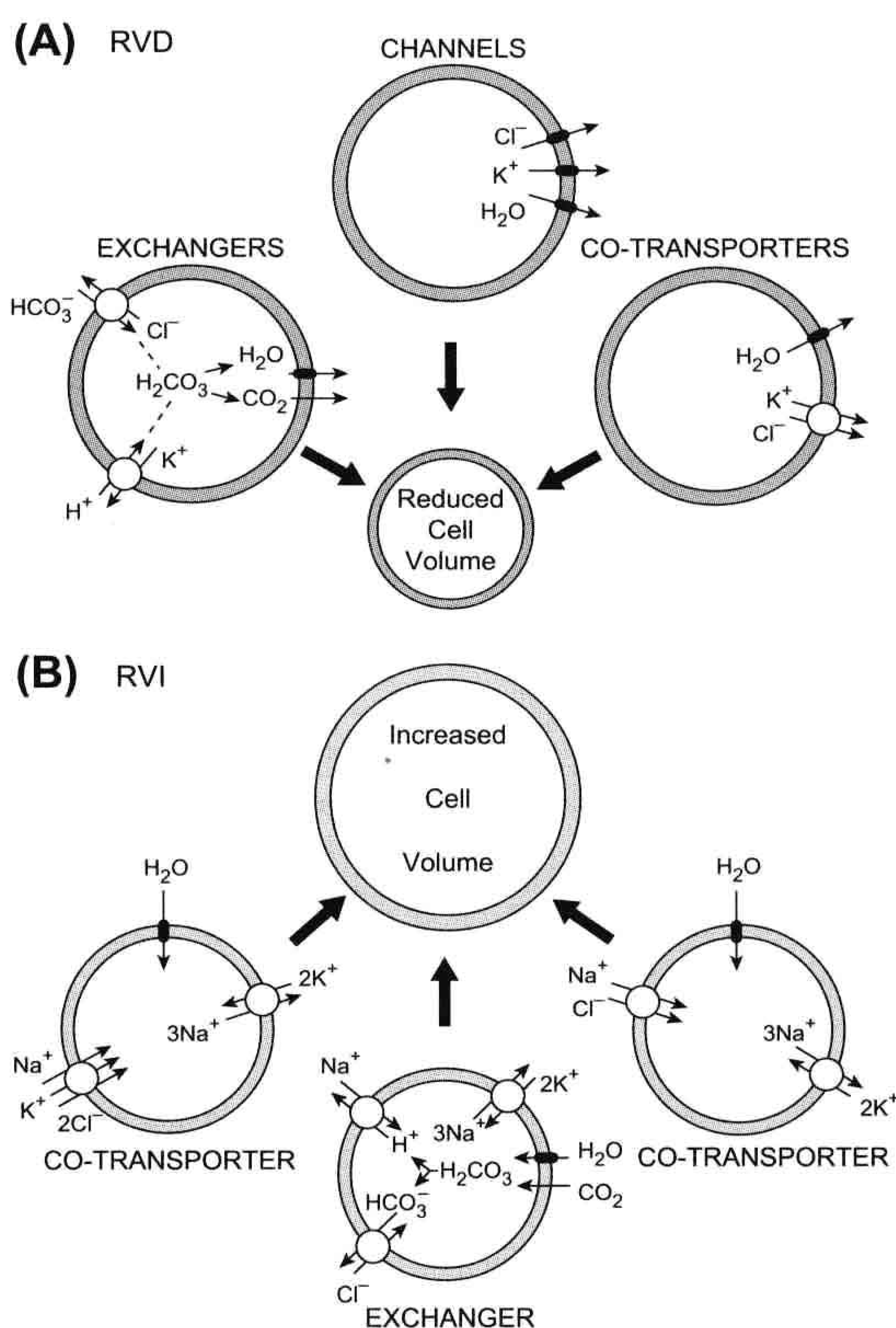


FIGURE 16.18 Schematic diagrams of the transport processes involved in (A) regulatory volume decrease (RVD) and (B) regulatory volume increase (RVI). Following cell swelling, a compensatory reduction in cell volume (RVD) may result from increased K^+ and Cl^- conductance (channels), activation of functionally coupled Cl^--HCO_3^- and K^+-H^+ exchange (exchangers) or activation of K^+-Cl^- co-transport (co-transporters). Following cell shrinking, a compensatory increase in cell volume (RVI) may result from activation of the Na^+-K^+-$2Cl^-$ or Na^+-Cl^- co-transporters (co-transporters) or activation of functionally coupled Cl^--$HCO^-{}_3$) and Na^+-H^+ exchange (exchangers). The Na^+-K^+ pump extrudes the Na^+ that enters during RVI, so that cells gain K^+ and Cl^-.

selectivity of Cl^--dependent co-transporters, RVD is also supported by Br^-, NO_3^- and SCN, suggesting the Cl^- channel responsible for RVD poorly discriminates among these anions. Furthermore, RVD can be suppressed by Cl^- channel blockers such as inacrinone (MK-196) and diphenylamine-2-carboxylate (DPC), but not by the co-transport inhibitors. Taken together, the data in Ehrlich ascites cells provide strong evidence that two independent channels are responsible for RVD instead of, for example, activation of a single K^+-Cl^- co-transporter. Organic osmolytes also permeate a class of swelling-activated Cl^- channels referred to as volume-sensitive organic osmolyte-anion channels (VSOAC) and are released by a number of cells to regulate volume (Jackson et al., 1994). VSOAC have a high permeability to taurine ($P_{taurine}/P_{Cl} = 0.75$) and glutamate ($P_{glutamate}/P_{Cl} = 0.20$) and other amino acids and small organic molecules are permeant (Bandarali and Roy, 1992).

Whereas many types of cells exhibit extensive RVDs, fewer cells exhibit robust RVIs. RVIs are usually due to an accumulation of Na^+, Cl^- and, in some cases, K^+, which occurs over minutes. The primary mechanisms underlying RVIs are acceleration of Na^+-K^+-$2Cl^-$ or Na^+-Cl^- co-transport and coupled Na^+-H^+ and Cl^--HCO_3^- exchange. Volume recovery can be blocked by application of appropriate inhibitors such as bumetanide for Na^+-K^+-$2Cl^-$ co-transport, amiloride for Na^+-H^+ exchange and SITS (4-acetamido-4′-isothiocyano-stilbene-2,2′-disulfonic acid) for Cl^--HCO_3^- exchange. RVI in most cells is readily observed when simple salt solutions bathe the cells, but in renal cortical collecting duct and proximal tubules, butyrate, acetate or other metabolizable fatty acids must be in the perfusate to support RVI. Substrate metabolism may provide H^+ and HCO_3^- to support Na^+-H^+ and Cl^--HCO_3^- exchange in these cells (for a review, see McCarty and O'Neil, 1992).

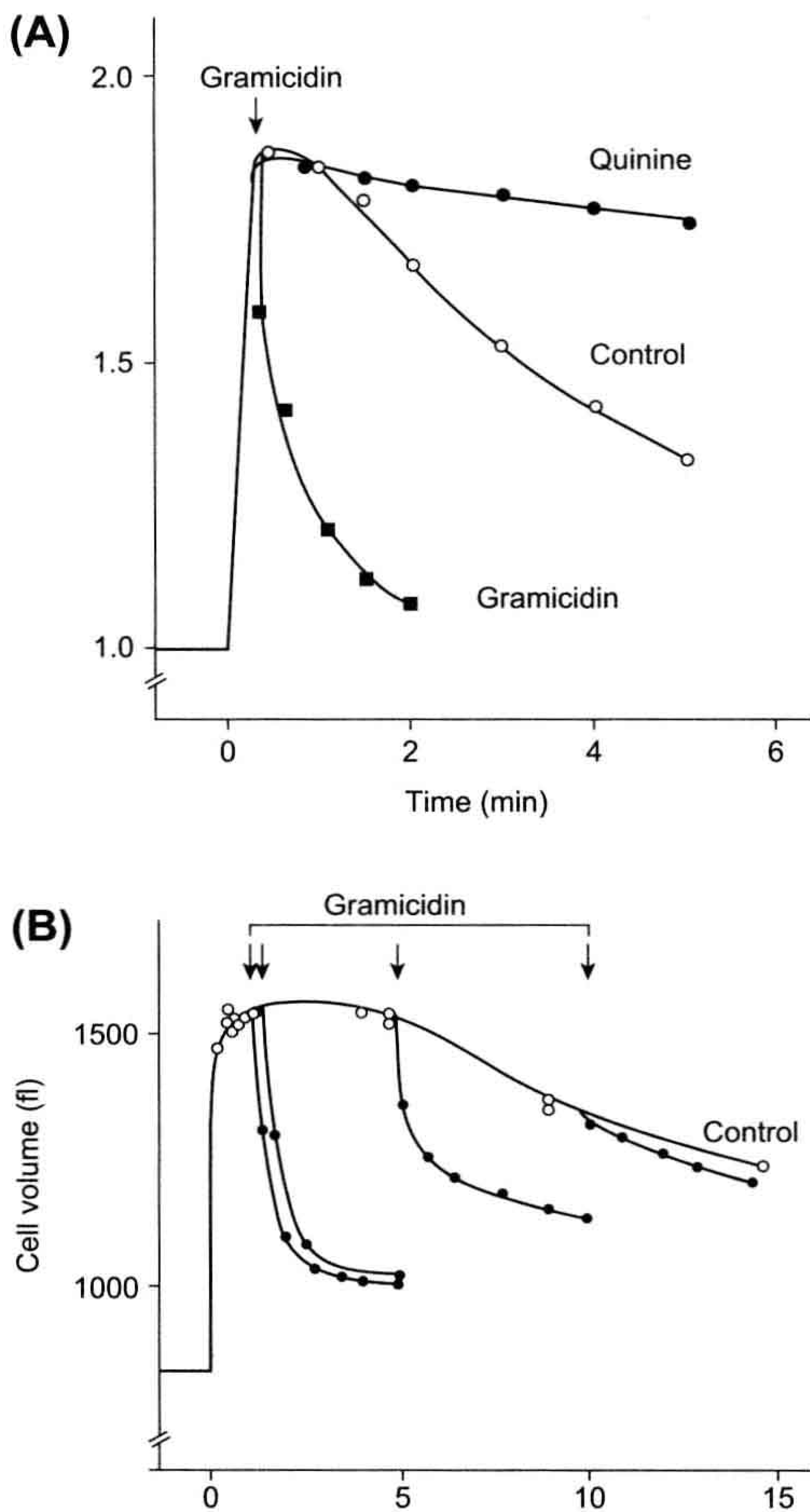


FIGURE 16.19 (A) Effects of quinidine (1 mM) and gramicidin (5 μM) on regulatory volume decrease (RVD) in Ehrlich ascites cells suspended in a Na^+-free choline medium with 1 mM Ca^{2+}. Swelling was induced by diluting the medium to 0.5T. Quinidine blocks Ca^{2+}-activated K^+ channels, and gramicidin increases cation conductance (K^+ conductance in the absence of Na^+). The data indicate that K^+ permeability is rate-limiting during the RVD. (B) The swelling-induced increase in Cl^- conductance is transient. Same protocol as in (A), except that quinidine (1 mM) was added to the hypotonic media to reduce K^+ conductance (control). At selected times, 0.5 μM gramicidin was added to increase cation permeability. The ability of gramicidin to induce an RVD follows the time-course of the swelling-induced Cl^- conductance. Relative cell volumes measured with a Coulter counter, as described for Fig. 16.17. *(Reproduced with permission from Hoffmann et al., 1986.)*

VIID. Organic Osmolytes

Adaptation to hyperosmolarity over a longer term also occurs in some cells and is mediated by an accumulation of organic osmolytes, including amino acids, polyols, and urea (Yancey et al., 1982; Chamberlin and Strange, 1989; Wolff and Balaban, 1990; Garcia and Berg, 1991; Yancey, 1994; Berg, 1995). Three of these organic osmolytes, taurine, betaine, and inositol, are taken up by Na^+-dependent or Na^+- and Cl^--dependent co-transporters. The taurine and betaine transporters have been cloned and belong to the same family as the Na^+- and Cl^--dependent norepinephrine, γ-aminobutyric acid (GABA), dopamine, serotonin and proline transporters (Uchida, 1992). The taurine transporter is found in a variety of cell types. The distribution of mRNA levels is kidney>ileum>brain>liver>heart (Berg, 1995). This sequence for taurine transporter mRNA is surprising because heart has the highest intracellular taurine concentration among these tissues. The mRNA level for the betaine transporter is also highest in the kidney (Yamauchi et al., 1992). A different family of transporters is responsible for Na^+-dependent inositol uptake. The inositol transporter is related to those for glucose and nucleosides and is highly expressed in renal medulla (Kwon et al., 1992). A common feature of all three osmolyte transporters is that gene transcription is upregulated by hypertonic stress. Cells cultured under hypertonic conditions slowly increase their maximum rates of transport and intracellular concentrations rise. For example, betaine transporter mRNA levels in MDCK cells peak about 16 h after the osmotic challenge, and the transport rate peaks at about 24 h (Uchida et al., 1993).

Another mechanism for accumulating organic osmolytes while adapting to hypertonicity and cell shrinkage is to modulate their synthesis. For example, renal medullary cells, which experience osmolarities of more than 1200 $mosmol \cdot L^{-1}$ during antidiuresis, accumulate sorbitol and inositol to regulate their volume (Wolff and Balaban, 1990; Garcia and Berg, 1991; Sands, 1994). Sorbitol levels rise 12–24 h after osmotically challenging cultured renal medullary cells and accumulation depends on the induction of aldose reductase by enhanced transcription. Aldose reductase converts exogenous glucose to sorbitol. Sorbitol is synthesized from stored glycogen in other tissues. This requires coordinated upregulation of glycogen phosphorylase and hexosekinase to produce glucose 6-phosphate, an intermediate for sorbitol production, and the downregulation of phosphofructokinase to prevent consumption of substrates for sorbitol production.

Inhibition of degradation is another mechanism for accumulating organic osmolytes when cells are challenged by hypertonicity. This is the main mechanism by which MDCK and medullary collecting duct accumulate glycerophosphocholine (GPC) (Berg, 1995). In response to hypertonicity or elevated urea, GPC-choline phosphodiesterase is inhibited. Under some conditions, synthesis of GPC by phospholipase also may be enhanced.

The accumulation of organic osmolytes is metabolically expensive, especially considering that many cells dump

organic osmolytes to respond acutely to swelling (Chamberlin and Strange, 1989; Rasmusson et al., 1993; Jackson et al., 1994, Hoffmann and Dunham, 1995). Why does the cell expend extra energy to use organic compounds rather than inorganic ions? Apparently the reason is that accumulation of inorganic ions may perturb protein structure within cells. The Hofmeister series, first described more than 100 years ago, lists inorganic ions according to their ability to alter the solubility and conformation of proteins. Nonspecific effects of inorganic salts include changes in V_{max}, K_m, tertiary structure and subunit assembly of enzymes (Yancey et al., 1982; Somero, 1986; Yancey, 1994). Why are some organic compounds accumulated rather than others? Yancey et al. (1982) categorized osmolytes as non-perturbing (stabilizing) or perturbing (destabilizing). Elevated concentrations of non-perturbing osmolytes are compatible with normal enzyme function, whereas high concentrations of perturbing osmolytes are not. This distinction could be due either to direct interaction of osmolytes with enzymes or substrates or to effects on hydration, solubility or charge interactions of proteins. Organic solutes that are non-perturbing generally are uncharged [e.g. trimethylamine N-oxide (TMAO), glycerol] or zwitterionic (e.g. betaine, taurine), although negatively-charged octopine is used by some cells. In contrast, most perturbing organic osmolytes are positively charged (e.g. arginine, guanidinium). Neutral urea, however, perturbs proteins. Finally, non-perturbing osmolytes can counteract the destabilizing effects of perturbing osmolytes. Several organisms accumulate perturbing osmolytes, such as urea, in fixed ratios with non-perturbing osmolytes.

VIIE. Signaling Pathways Underlying RVD and RVI

How do cells detect alterations in their volume and activate the transport processes underlying compensatory volume regulation? Do the transporters themselves sense cell volume and respond by changing their activity? Alternatively, does water movement simply change the concentration of a critical regulatory substance? Answers to these questions are just beginning to emerge. It appears that the signaling pathways modulated by cell volume are as diverse as the transporters that respond.

VIIE1. Anisosmotic Media

An obvious candidate for signaling a change in cell volume is the composition of the anisosmotic media itself, i.e. the ionic strength or concentrations of ions in the bathing media might initiate a regulatory volume response. Changing concentration or ionic strength must affect various ion transport processes and transmembrane ion fluxes to some degree. Nevertheless, these factors seem relatively unimportant in volume regulation because comparable responses are observed when non-electrolytes, such as mannitol or sucrose, replace a large fraction of the electrolytes in the bathing media. RVDs also are initiated in isosmotic solutions after swelling caused by sugar or amino acid uptake. Thus, it appears that regulation is initiated by the volume change itself rather than the composition of the bathing media.

VIIE2. Membrane Potential

Another possibility is that regulatory volume responses are initiated by dilution or concentration of intracellular K^+ via an effect on E_m. A two-fold change in volume without compensatory K^+ fluxes would alter $[K^+]_i$ and cause an 18 mV change in E_m in a cell that conforms to the Nernst equation. Fluxes through K^+ and Cl^- channels are voltage dependent, reflecting both the electrochemical driving force and the voltage-dependent conductance. For many K^+ channels, the current–voltage relationship is highly non-linear. Furthermore, the Na^+-K^+ pump and Na^+-Ca^{2+} exchange are both voltage dependent because they mediate a net movement of charge across the membrane. Despite this, it is unlikely that changes in E_m are the primary cause of RVDs or RVIs in most cells. Regulatory responses have been observed with changes in cell volume of $<5\%$ (Hoffmann and Simonsen, 1989), which would directly alter E_m by only ≈ 1 mV. This is too small to have a significant effect. Nevertheless, it is clear that E_m can modulate RVDs due to activation of K^+ and Cl^- channels. In most instances, the increase in Cl^- conductance is greater than that for K^+ (Hoffmann and Simonsen, 1989; Grinstein and Foskett, 1990). This leads to a significant depolarization during the RVD due to a greater passive efflux of Cl^- than K^+ and the depolarization equalizes the anion and cation fluxes (due to macroscopic electroneutrality). Depolarization may have additional effects that support the RVD. The sensitivity of certain K^+ channels to intracellular Ca^{2+} (i.e. Ca^{2+}-activated K^+ channels) is increased by depolarization, and other K^+ channels are directly opened by depolarization.

VIIE3. Cytoskeleton

The cytoskeleton consists of three main elements: actin filaments (F-actin), which are microfilaments 5–7 nm in diameter that are double-stranded α-helical polymers of globular actin (G-actin); microtubules, which are hollow tubes 25 nm in diameter that are made from tubulin monomers arranged in 13 threads; and intermediate filaments (IF), which are 10-nm diameter strands composed of tissue-specific proteins, such as keratin in epithelial cells and desmin in muscle cells (Bershadsky and Vasiliev, 1988; Luna and Hitt, 1992; Mills et al., 1994). In non-muscle cells, the majority of actin filaments are associated with the

cell membrane. F-actin is tied together to integral membrane proteins by ankyrin, spectrin, MARKS (myristolated acid-rich C-kinase substrate) and other binding proteins to form a structural unit. This scaffolding undergoes constant reorganization as G-actin polymerizes and depolymerizes in response to various stimuli. The main role of microtubules in mature cells is thought to be the transport of vesicles within the cell using specific microtubule-associated proteins (MAPs) to attach to kinesin and dynein, which act as molecular motors. The functions of IF are not fully understood. Because IF binds to ankyrin and to desmosomal plaques, it is thought that these filaments have a structural role and link organelles to the membrane or cytoskeleton. Intermediate filaments are phosphorylated and dephosphorylated by protein kinases and phosphatases and it is likely that their phosphorylation state regulates function.

Alterations in cell volume lead to deformation or reorganization of the cytoskeleton, and ideas of how these effects may be linked to cell volume regulation have been proposed (Chamberlin and Strange, 1989; Sachs, 1989; Sarkadi and Parker, 1991; Mills et al., 1994; Hoffmann and Dunham, 1995; Henson, 1999). One possibility is that the cytoskeleton might mechanically resist cell swelling, but the evidence for this is inconclusive.[3] Ion channels, exchangers and co-transporters are structurally anchored in the membrane by specific components of the cytoskeleton (Luna and Hitt, 1992) and their interaction may help regulate cell volume. Agents that disrupt the microfilaments, such as the cytochalasins, modify the regulatory responses to both hypotonic and hypertonic stress by inhibiting K^+ and Cl^- channels that promote RVD and stimulating Na^+-K^+-$2Cl^-$ co-transport responsible for RVI (Chamberlin and Strange, 1989; Mills et al., 1994; Hoffmann and Dunham, 1995). In a few cases, cell volume under isosmotic conditions is affected (McCarty and O'Neil, 1992). Microtubules also may be involved in some cell lines. Colchicine, which prevents microtubule polymerization, decreases macrophage volume by 20% (Mills et al., 1994). The shrinkage is inhibited by SITS, suggesting that either Cl^--HCO_3^- exchange or Cl^- channels are involved. Additionally, water and ion channels are inserted reversibly into the membrane in response to volume perturbations in a process that can be blocked by cytochalasin B (Lewis and de Moura, 1982). Furthermore, mechanical deformation of the membrane and supporting structures can modulate biochemical signaling systems such as the cAMP and protein kinase C cascades (Richter et al., 1987; Watson, 1991). Emerging evidence suggests that protein kinases and phosphatases may be specifically localized by cytoskeletal binding proteins to sites adjacent to their target transport proteins. Moreover, the extracellular matrix is coupled to the cytoskeleton by integrins which regulate complex signaling cascades including focal adhesion kinase (FAK) and extracellular signal regulated kinases (ERK/MAPK) (Boudreau and Jones, 1999). These developments are important because it remains obscure how the cytoskeleton exerts its regulatory effect on ion transporters and whether or not constraints imposed by three-dimensional tissues in situ affect cell volume.

Another role for the cytoskeleton involves widely distributed mechanosensitive and volume-sensitive ion channels (Sachs, 1989; Morris, 1990; Hu and Sachs, 1997; Vandenberg et al., 1996; Wright and Rees, 1998). The probability of channel opening is increased by osmotic stretch or mechanical deformation. It has been proposed that mechanical forces detected by a cytoskeletal protein, spectrin, can directly affect cation channel gating, whereas the gating of volume-sensitive anion channels is regulated by their phosphorylation state. Most stretch-activated channels poorly discriminate between permeant species (e.g. the stretch-activated cation channel admits Na^+, K^+, and Ca^{2+}), but some are highly selective for K^+. There are also reports of mechanosensitive channels that are inactivated by stretch (Sachs, 1989; Morris, 1990). Mechanosensitive channels are potentially important in cell volume regulation as both sensors and effectors. The evidence that they are opened by osmotic stretch is convincing and they carry substantial currents, which might directly or indirectly lead to volume regulation. For example, it has been argued that K^+-selective stretch-activated channels in molluscan heart cells pass sufficient current to alter $[K^+]_i$ by 1% in 1 s when the cell is voltage-clamped away from E_K (Brezden et al., 1986) and that poorly selective cation stretch-activated channels in *Necturus* choroid epithelium raise Ca^{2+} sufficiently in 100 s to open Ca^{2+}-activated K^+ channels and initiate an RVD (Christensen, 1987). Such calculations must be regarded as estimates, however,

[3] For eukaryotic cells, it is generally assumed that the osmotic gradient across a membrane is negligible. This view arises because the thin bilayer membrane is too fragile to resist the substantial forces developed by even small differences in osmotic pressure. A tension of $\approx 10\,\text{dyn}\cdot\text{cm}^{-2}$ is sufficient to rupture erythrocyte (Evans et al., 1976), protoplast (Wolfe et al., 1986), or lipid bilayer (Needham and Nunn, 1990) membranes. The relationship between tension on the membrane and transmembrane pressure is given by the law of Laplace. For a thin-walled spherical cell $P = 2T/r$ where P is pressure, T is tension and r is the cell's radius. If we assume a radius of 10 µm, a lytic tension is developed by a pressure of 2×10^4 dyn cm^{-2}, which equals ≈ 15mmHg. This is the osmotic pressure developed by only ≈ 0.0008 osmol L^{-1}. Hence, the membrane cannot support a sufficient hydrostatic pressure to offset an osmotic gradient.

Before accepting this conclusion, it is necessary to consider the effective radius of the cell in view of the geometry of the cytoskeleton (Jacobson, 1983). For example, there are $\approx 10^5$ copies of ankyrin per erythrocyte. If all these attach integral membrane proteins to the cytoskeleton and are evenly distributed, the membrane is strengthened by load-bearing cytoskeletal elements at ≈ 40 nm intervals. Even if we assume an effective radius of 100 nm, lytic tension now requires a pressure of 2×10^6 dyn cm^{-2}, which equals ≈ 1500 mmHg or nearly 2 atm. This is equivalent to the osmotic pressure generated by 0.078 osmol L^{-1}.

because they do not reflect E_m under the relevant conditions. Nevertheless, Ca^{2+} entry via stretch-activated channels has been implicated in volume regulation in several types of cells (Foskett, 1994) and arguments favoring the idea that stretch-activated channels participate in cell volume regulation are accumulating (Sackin, 1994). It has been found that Gd^{3+}, a blocker of non-selective stretch-activated cation channels, reduced swelling of both intact (i.e. unclamped) and voltage-clamped cardiac myocytes in hypoosmotic solutions and that 9-anthracene carboxylic acid (9-AC), a blocker of stretch-activated anion channels, increased swelling in the same solutions (Suleymanian et al., 1995; Clemo and Baumgarten, 1997; Clemo et al., 1998, 1999). Opposite effects of the two blockers are expected because anions and cations travel in opposite directions under these conditions. In contrast, Gd^{3+} and 9-AC have negligible effects on myocyte volume in isosmotic solution when stretch-activated channels are expected to be closed. Interestingly, the same volume-sensitive cation and anion channels became persistently activated and modulated cell volume under isosmotic conditions in a canine model of congestive heart failure (Clemo et al., 1998, 1999).

VIIE4. Calcium

A role for Ca^{2+} in cell volume regulation has been recognized for many years (Pierce and Politis, 1990; McCarty and O'Neil, 1992; Foskett, 1994; Hoffmann and Dunham, 1995). RVD is blocked by removing extracellular Ca^{2+} in *Amphiuma* erythrocytes, *Necturus* gallbladder, proximal convoluted and straight tubule, intestine 407 and osteosarcoma cells. Extracellular Ca^{2+} is not a requirement for RVD in lymphocytes and Ehrlich ascites cells, but RVD is more rapid in Ehrlich ascites cells when Ca^{2+} is present. In some tissues, it appears that the Ca^{2+} involved in RVD enters, at least in part, through dihydropyridine-sensitive, L-type Ca^{2+} channels. Significant Ca^{2+} entry can also occur via non-selective stretch-activated cation channels. Block of RVD by lanthanides and disruption of the cytoskeleton, both of which affect stretch-activated cation channels, is consistent with this possibility. Instead of the entry of extracellular Ca^{2+}, release of Ca^{2+} from intracellular stores is critical for RVD in a variety of cells, including lymphocytes, Ehrlich ascites, intestine 407 and opossum kidney cells. Depletion of internal Ca^{2+} stores eliminates RVD in these cells; it is restored by extracellular Ca^{2+} and the Ca^{2+} ionophore, A23187. $[Ca^{2+}]_i$ has been shown to increase during swelling of *Amphiuma* erythrocytes using arsenazo III as a Ca^{2+} indicator. More recently, fluorescent Ca^{2+} indicators, quin-2 and fura-2, have been used to demonstrate increases in $[Ca^{2+}]_i$ that accompany cell swelling in urinary bladder, osteosarcoma, lymphoma and proximal and straight convoluted tubule cells. On the other hand, $[Ca^{2+}]_i$ remains unchanged during volume changes in some cells, including human lymphocytes. More evidence for elevated Ca^{2+} comes from patch-clamp studies. In a number of tissues, recordings of single channel activity established that Ca^{2+}-activated K^+ channels open more frequently during RVD than under isotonic conditions. This suggests an increase in $[Ca^{2+}]_i$ because the probability that these channels open increases as $[Ca^{2+}]_i$ increases. Although studied in less detail, a decrease in $[Ca^{2+}]_i$ has been implicated in RVI in *Amphiuma* erythrocytes, Ehrlich ascites cells and lymphocytes.

The mechanism by which Ca^{2+} modulates cell volume appears to vary (Table 16.4). Ca^{2+} has direct effects on ion channels, but additional signaling mechanisms may be involved. For example, calmodulin inhibitors can block the increased K^+ conductance in lymphocytes, Ehrlich ascites cells and *Necturus* gallbladder; the increased Cl^- conductance in Ehrlich ascites cells; and increased K^+-H^+ exchange in *Amphiuma* erythrocytes. In other cells, modulation of protein kinase C and leukotriene synthesis by Ca^{2+} have been proposed as signals in volume regulation.

VIIE5. Phosphorylation

The activities of many of the transporters discussed here are modified by phosphorylation (Parker, 1992; McCarty and O'Neil, 1992; Palfrey, 1994; Hoffmann and Dunham, 1995). This raises the possibility that cell volume alterations initiate an RVD or RVI by either increasing or decreasing the fraction of transporters in the phosphorylated state. Until recently, supporting data have been lacking. Over the last few years, however, strong evidence for this idea has come from studies in several tissues. We will discuss some of these data from erythrocytes in detail.

Pewitt et al. (1990) studied RVI in duck erythrocytes and determined that activation of Na^+-K^+-$2Cl^-$ co-transport on shrinking is caused by phosphorylation. Both cAMP-dependent and cAMP-independent protein kinase phosphorylate the Na^+-K^+-$2Cl^-$ co-transporter (or possibly a regulatory protein), but cAMP levels in duck erythrocytes are not affected by osmotic stress. Pewitt et al. (1990) found that the protein kinase inhibitors K252a and H-9 prevent transporter activation on shrinking. Conversely, an inhibitor of serine and threonine protein-phosphatases, okadaic acid, which slows protein dephosphorylation, stimulates Na^+-K^+-$2Cl^-$ co-transport under isotonic conditions. These changes in the activity of the transporter with phosphorylation and with shrinking apparently result largely from a modulation of the number of functioning transporters, as detected by bumetanide binding, rather than from a modulation of their turnover rate. At about the same time, Jennings and

TABLE 16. 4 Intracellular Signaling Pathways for RVD and RVI

Signal	Effector	Cell Type
Ca^{2+}	K^+ conductance	*Necturus* gallbladder Frog urinary bladder Ehrlich ascites cells Human lymphocytes
	Cl^- conductance	Ehrlich ascites cells
	Taurine efflux Na^+-H^+ exchange K^+-H^+ exchange	Elasmobranch and molluscan erythrocytes Human lymphocytes *Amphiuma* erythrocytes
Phosphorylation	Na^+-H^+ exchange Taurine efflux Na^+-K^+-$2Cl^-$ co-transport K^+-Cl^- co-transport	Human lymphocytes Elasmobranch erythrocytes Duck erythrocytes Duck, rabbit, and dog erythrocytes
Leukotrienes	K^+ conductance Cl^- conductance	Ehrlich ascites cells Ehrlich ascites cells
cAMP	Na^+-H^+ exchange Cl^--HCO_3^- exchange Na^+-Cl^- co-transport	Mouse thick ascending limb of Henle (mTALH) cells Mouse thick ascending limb of Henle (mTALH) cells *Necturus* gallbladder
G proteins	Na^+-H^+ exchange	Barnacle skeletal muscle
Voltage	K^+ channels	Human lymphocytes

For references, see Chamberlin and Strange (1989), Sarkadi and Parker (1991), McCarty and O'Neil (1992), Strange (1994), Hoffmann and Dunham (1995), Lang et al. (1998), O'Neil (1999), Häussinger and Schliess (1999).

al-Rohil (1990) and Jennings and Schulz (1991) developed evidence that K^+-Cl^- co-transport in rabbit erythrocytes, which is responsible for RVD, is activated by a dephosphorylation. They discovered that swelling inhibits a protein kinase distinct from protein kinases A and C. An RVD occurred only after a slow dephosphorylation, now identified as due to a type 1 protein phosphatase (PP1) that is blocked by calyculin A (Starke and Jennings, 1993). Parker et al. (1991) obtained similar results in dog erythrocytes.

Parker et al. (1991) also recognized the important reciprocal coordination of K^+-Cl^- co-transport and Na^+-H^+ exchange by phosphorylation and dephosphorylation during both RVDs and RVIs in mammalian erythrocytes. This strategy is illustrated in Fig. 16.20 and can be summarized as follows: (1) shrinking activates and swelling inhibits a protein kinase. (2) On shrinking, activated protein kinase rapidly phosphorylates regulatory sites associated with the K^+-Cl^- co-transporter and the Na^+-H^+ exchanger (or the Na^+-K^+-$2Cl^-$ co-transporter in duck erythrocytes). (3) Phosphorylation inhibits the K^+-Cl^- co-transporter, reducing osmolyte efflux, but stimulates the Na^+-H^+ exchanger or Na^+-K^+-$2Cl^-$ co-transporter, stimulating osmolyte uptake and leading to an RVI. (4) Conversely, slow dephosphorylation on swelling stimulates K^+-Cl^- co-transport and inhibits Na^+-H^+ exchange or Na^+-K^+-$2Cl^-$ co-transport, leading to an RVD. Thus, the transporters underlying ion influx and efflux are regulated reciprocally by the activity of a protein kinase that reflects cell volume.

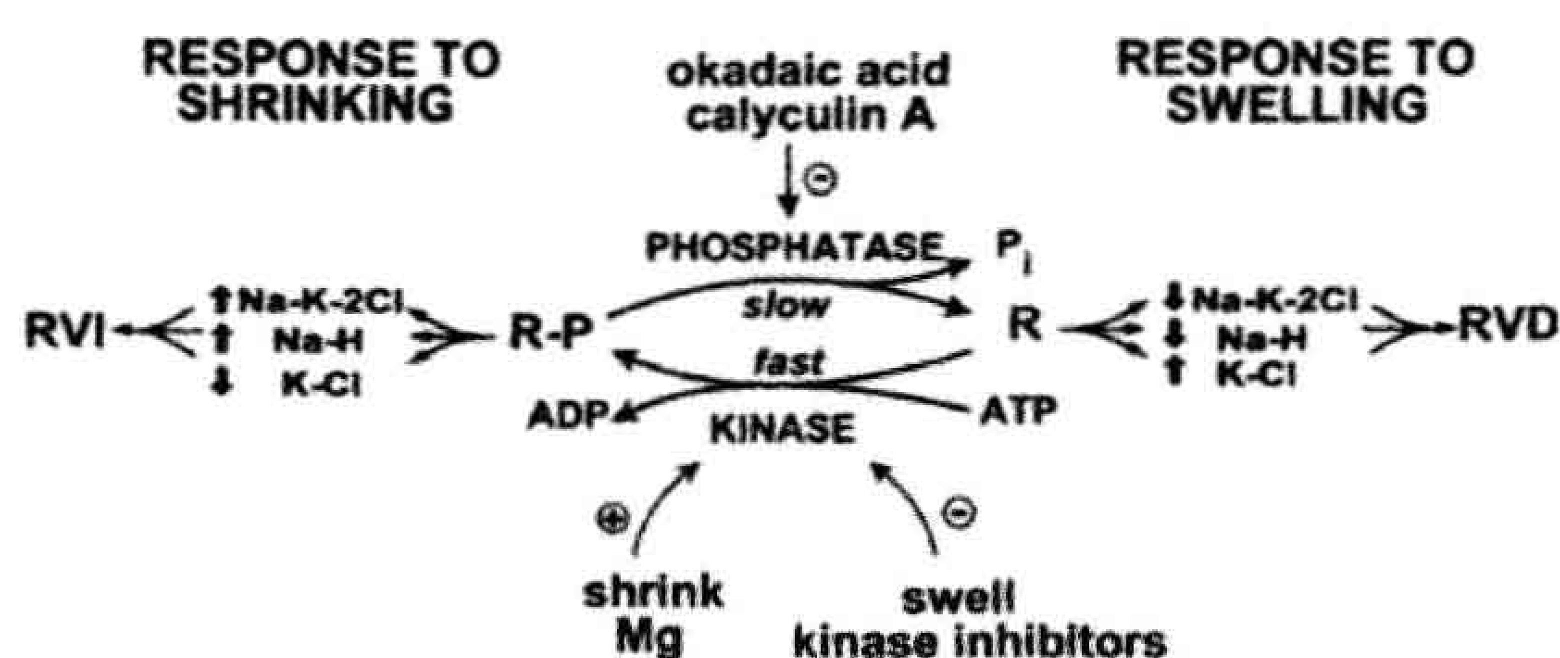


FIGURE 16.20 Schematic diagram of the mechanism of coordination of Na^+-K^+-$2Cl^-$ co-transport and Na^+-H^+ and Na^+-K^+ exchange during cell swelling and shrinking. R-P and R represent phosphorylated and dephosphorylated regulatory sites that modulate the activity of transporters leading to a regulatory volume decrease (RVD) or regulatory volume increase (RVI). Changes in cell volume affect protein kinase activity. Several interventions that inhibit or stimulate the protein kinase and phosphatase are indicated.

How does cell volume govern the activity of a protein kinase? Several possible detectors have been considered: cell shape or cytoskeletal deformation; the concentration of an impermeant intracellular co-factor such as Mg^{2+}; and a concept referred to as macromolecular crowding. The first possibility was already discussed, but experimental evidence suggests cell shape does not regulate phosphorylation of the relevant transport proteins, at least in erythrocytes. The last two possibilities will be considered next.

VIIE6. Mass Action Model

Increasing intracellular Mg^{2+} activates Na^+-H^+ exchange and inhibits K^+-Cl^- co-transport and it has been suggested that Mg^{2+} might act by activating a kinase. Before accepting the idea that Mg^{2+} or another intracellular ion is the volume sensor, it is necessary to explain the steep dependence of ion transport on cell volume. Jennings and Schulz (1990) illustrated one possible answer for K^+-Cl^- co-transport with a theoretical mass action model. They assumed: (1) the volume sensor (e.g. Mg^{2+}) is an impermeant intracellular species; (2) the kinase and phosphatase are soluble enzymes; and (3) the sensor inhibits dephosphorylation. They then described the model in terms of three first-order Michaelis–Menten expressions. Taking into account that the concentrations of sensor, kinase and phosphatase vary inversely with volume, they were able to reproduce the steep volume dependence of experimental K^+ influx data. As the authors emphasized, however, a good fit of the experimental data does not prove that the model is correct. Rather, it illustrates only that a simple dilution mechanism can give rise to a steep volume dependence of transport if dilution has different effects on the activity of enzymes that regulate the transporter (e.g. Fig. 16.20).

VIIE7. Macromolecular Crowding

The concept of *macromolecular crowding* comes from the idea that proteins do not behave ideally in solution at concentrations in the physiological range. We have already mentioned that the osmotic coefficient for hemoglobin and other proteins increases steeply with concentration and that Freedman and Hoffman (1979) used this fact to explain water movement in red cells. Non-ideal behavior is thought to be a more general phenomenon, however. Minton (1983, 1990, 1994) has argued that the kinetics and equilibria of enzymes (macromolecules) are markedly altered by the presence of inert macromolecules that occupy more than a few percent of the total solution volume. Just as one hemoglobin molecule affects another, macromolecules that are neither substrate nor product affect the behavior of their macromolecular neighbors in solution. This results because crowding reduces the solution volume accessible to a macromolecule by excluded-volume effects illustrated in Fig. 16.21. An excluded volume means that solution behavior is non-ideal and the chemical potential, μ_i, and activity, a_i, of a macromolecule is increased by crowding. Consequently, reaction rates are affected. On the other hand, small solutes (e.g. ions) are unaffected by the same concentration of macromolecules. Several examples are worth noting. Minton (1983) showed that the specific activity of glyceraldehyde-3-phosphate dehydrogenase decreased dramatically as the concentration of bovine serum albumin, β-lactoglobulin, polyethylene glycol (PEG) or ribonuclease in the reaction medium was increased. This

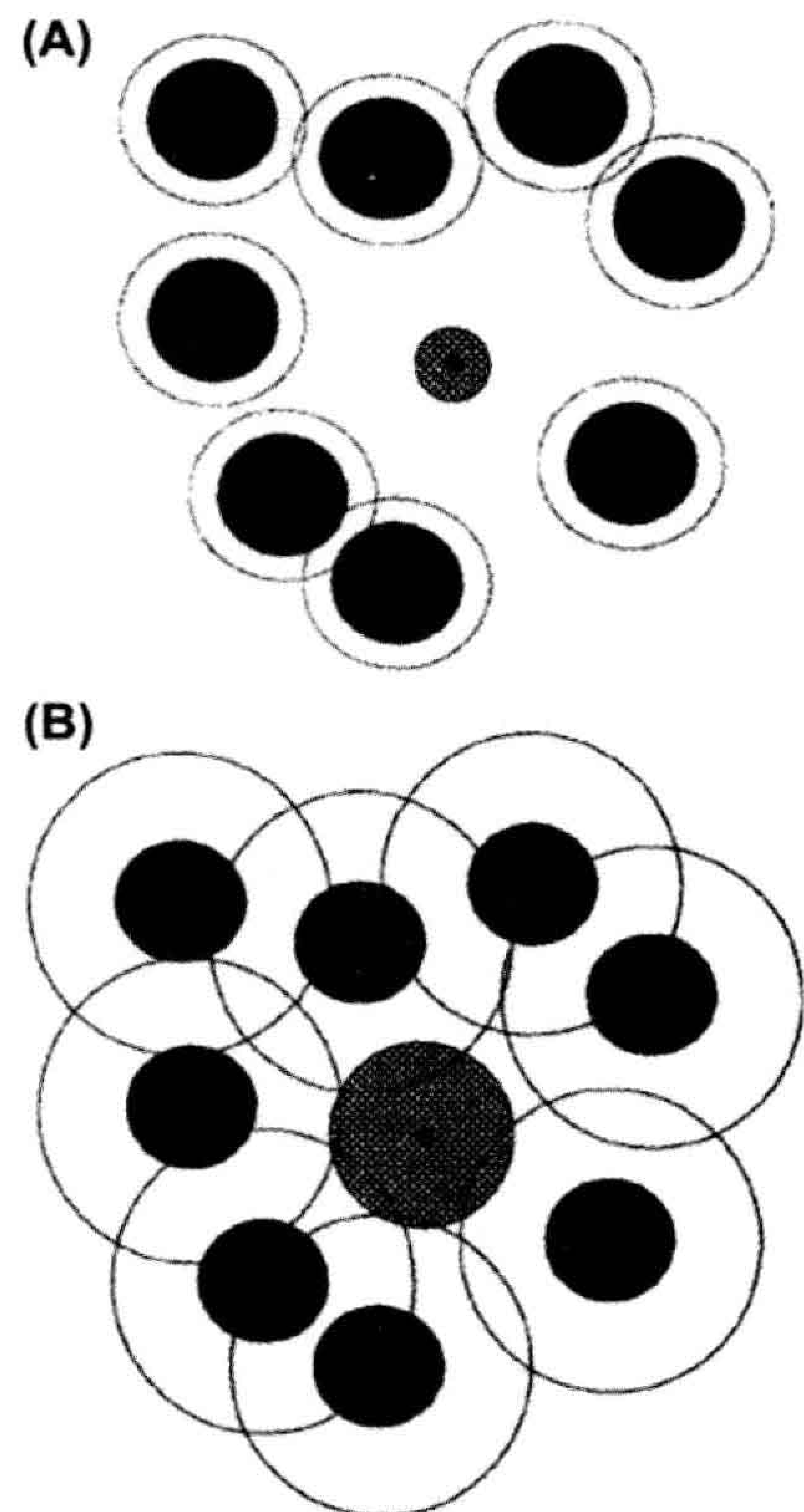


FIGURE 16.21 Diagram of macromolecular crowding. Background macromolecules (solid) in solution differentially affect the behavior of small molecules, such as ions (A) and other macromolecules (B). A test molecule (cross-hatched) cannot enter the excluded volume represented by a circle with a radius equal to the sum of the radii of the test molecule and the background macromolecule. The excluded volume is much greater for a test macromolecule (B) than for a test small molecule (A). Restricting the volume that a test molecule can enter increases its activity, a, and chemical potential, μ. Consequently, both reaction rates and equilibria are altered. *(Reproduced with permission from Minton (1994). Copyright CRC Press, Boca Raton, Florida.)*

was explained by suggesting that crowding favored the formation of tetramers of the enzyme that possess a lower catalytic specific activity than monomers. Similarly, the cohesion of complementary ends of λ DNA can be increased up to 2000-fold by albumin, Ficoll 70 or PEG (Zimmerman and Harrison, 1985) and the activity of T4 polynucleotide kinase is augmented by PEG (Harrison and Zimmerman, 1986). Protein concentrations within cells are sufficient to give significant excluded-volume effects (Zimmerman and Trach, 1991).

How does macromolecular crowding relate to cell volume regulation? Perhaps the activity of the kinase governing the phosphorylation state of transporters decreases as macromolecular crowding is lessened during cell swelling. This would, for example, activate K^+-Cl^- co-transport and inactivate Na^+-H^+ exchange (see Fig. 16.20) and an RVD would ensue. Colclasure and Parker (1991, 1992) provided experimental support for this hypothesis (see also Sarkadi and Parker, 1991; Parker, 1992). They osmotically ruptured dog erythrocytes and then allowed the "ghosts" to reseal in a hypotonic medium. This gave resealed ghosts with about 1/4 normal volume but with a normal protein (hemoglobin or hemoglobin plus albumin) concentration. During osmotic challenge, K^+-Cl^- co-transport and Na^+-H^+ exchange were regulated at about the same protein concentration as in normal erythrocytes even though the volumes of the resealed ghosts were vastly different. This hypothesis is also consistent with studies on the kinetics of volume regulation by Jennings and al-Rohil (1990) who concluded that the swelling-sensitive step was a decrease in the rate of phosphorylation rather than an increase in the rate of dephosphorylation.

The new insight that macromolecular crowding may be a mechanism for volume transduction is an interesting possibility. Minton et al. (1992) have presented a model quantitatively accounting for volume-dependent stimulation of ion fluxes on this basis. It is important to recognize that operation of the scheme depends on the components having appropriate sensitivity. In erythrocytes, for example, the activities of both the kinase and the phosphatase should be reduced by swelling. Consequently, as the rate of protein phosphorylation falls, so does the rate of protein dephosphorylation. Whether this leads to an increase or decrease in the fraction of transporters in the phosphorylated state must depend both on the relative effects of macromolecular crowding and the amount of substrate available for each enzyme. With injudicious choices for the parameters (e.g. pathological interventions), this mechanism might lead to an inappropriate RVI rather than an RVD.

ACKNOWLEDGMENTS

We thank J. Maghirang for preparing numerous figures. Supported by National Institutes of Health grants HL-24847, HL-46764, and NS-19235, and Grants-in-Aid from the American Heart Association and its Mid-Atlantic Affiliate.

BIBLIOGRAPHY

Adair, G. S. (1928). A theory of partial osmotic pressures and membrane equilibrium with special reference to the application of Dalton's law to haemoglobin solutions in the presence of salts. *Proc Roy Soc London, 120A*, 573–603.

Agius, L., Peak, M., Beresford, G., al-Habori, M., & Thomas, T. (1994). The role of ion content and cell volume in insulin action. *Biochem Soc Trans, 22*, 518–522.

Agre, P., Preston, G. M., Smith, B. L., et al. (1993). Aquaporin CHIP: the archetypal molecular water channel. *Am J Physiol, 265*, F463–F476.

Andreoli, T. E., & Troutman, S. L. (1971). An analysis of unstirred layers in series with "tight" and "porous" lipid bilayer membranes. *J Gen Physiol, 57*, 464–478.

Bandarali, U., & Roy, G. (1992). Anion channels for amino acids in MDCK cells. *Am J Physiol, 263*, C1200–C1207.

Barry, P. H., & Diamond, J. M. (1984). Effects of unstirred layers on membrane phenomena. *Physiol Rev, 64*, 763–873.

Berg, M. B. (1995). Molecular basis of osmolyte regulation. *Am J Physiol, 268*, F983–F996.

Bershadsky, A. D., & Vasiliev, J. M. (1988). *Cytoskeleton*. New York: Plenum Press.

Bookchin, R. M., Ortiz, O. E., Freeman, C. J., & Lew, V. L. (1989). Predictions and tests of a new integrated reticulocyte model: implications for dehydration of sickle cells. In *The Red Cell: Seventh Annual Ann Arbor Conference* (pp. 615–625). New York: Alan R. Liss Publishers.

Boudreau, N. J., & Jones, P. L. (1999). Extracellular matrix and integrin signalling: the shape of things to come. *Biochem J, 339*, 481–488.

Boyer, J. L., Graf, J., & Meier, P. J. (1992). Hepatic transport systems regulating pH_i, cell volume, and bile secretion. *Annu Rev Physiol, 54*, 415–438.

Boyle, P. J., & Conway, E. J. (1941). Potassium accumulation in muscle and associated changes. *J Physiol, 100*, 1–63.

Brezden, B. L., Gardner, D. R., & Morris, C. E. (1986). A potassium-selective channel in isolated Lymnaea stagnalis heart muscle cells. *J Exp Biol, 123*, 175–190.

Carruthers, A., & Melchior, D. L. (1983). Studies of the relationship between bilayer water permeability and bilayer physical state. *Biochemistry, 22*, 5797–5807.

Cass, A., & Finkelstein, A. (1967). Water permeability of thin lipid membranes. *J Gen Physiol, 20*, 1765–1784.

Chamberlin, M. E., & Strange, K. (1989). Anisosmotic cell volume regulation: a comparative view. *Am J Physiol, 257*, C159–C173.

Christensen, O. (1987). Mediation of cell volume regulation by Ca^{2+} influx through stretch-activated channels. *Nature, 330*, 66–68.

Clemo, H. F., & Baumgarten, C. M. (1995). cGMP and atrial natriuretic factor regulate cell volume of rabbit atrial myocytes. *Circ Res, 77*, 741–749.

Clemo, H. F., & Baumgarten, C. M. (1997). Swelling-activated Gd^{3+}-sensitive cation current and cell volume regulation in rabbit ventricular myocytes. *J Gen Physiol, 110*, 297–312.

Clemo, H. F., Feher, J. J., & Baumgarten, C. M. (1992). Modulation of rabbit ventricular cell volume and $Na^+/K^+/2Cl^-$ cotransport by cGMP and atrial natriuretic factor. *J Gen Physiol, 100*, 89–114.

Clemo, H. F., Stambler, B. S., & Baumgarten, C. M. (1998). Persistent activation of a swelling-activated cation current in ventricular myocytes from dogs with tachycardia-induced congestive heart failure. *Circ Res, 83*, 147–157.

Clemo, H. F., Stambler, B. S., & Baumgarten, C. M. (1999). Swelling-activated chloride current is persistently activated in ventricular myocytes from dogs with tachycardia-induced congestive heart failure. *Circ Res, 84*, 157–165.

Colclasure, C. G., & Parker, J. C. (1991). Cytosolic protein concentration is the primary volume signal in dog red cells. *J Gen Physiol, 98*, 881–892.

Colclasure, C. G., & Parker, J. C. (1992). Cytosolic protein concentration is the primary volume signal for swelling-induced [KCl] cotransport in dog red cells. *J Gen Physiol, 100*, 1–10.

Dainty, J. (1965). Osmotic flow. *Symp Soc Exptl Biol, 19*, 75–85.

Deamer, D. D., & Bramhall, J. (1986). Permeability of lipid bilayers to water and ionic solutes. *Chem Phys Lipids, 40*, 167–188.

Drewnowska, K., & Baumgarten, C. M. (1991). Regulation of cellular volume in rabbit ventricular myocytes: bumetanide, chlorothiazide, and ouabain. *Am J Physiol, 260*, C122–C131.

Drewnowska, K., Clemo, H. F., & Baumgarten, C. M. (1991). Prevention of myocardial intracellular edema induced by St Thomas' Hospital cardioplegic solution. *J Molec Cell Cardiol, 23*, 1215–1221.

Evans, E., Waugh, R., & Melnik, L. (1976). Elastic area compressibility modulus of red cell membrane. *Biophys J, 16*, 585–595.

Fettiplace, R., & Haydon, D. A. (1980). Water permeability of lipid membranes. *Physiol Rev, 60*, 510–550.

Finkelstein, A. (1987). Water Movement Through Lipid Bilayers, Pores, and Plasma Membranes. *Theory and Reality*. New York: Wiley-Interscience.

Finkelstein, A., & Cass, A. (1968). Permeability and electrical properties of thin lipid membranes. *J Gen Physiol, 52*, 145s–172s.

Fischbarg, J., Kuang, K., Vera, J. C., et al. (1990). Glucose transporters serve as water channels. *Proc Natl Acad Sci USA, 87*, 3244–3247.

Foskett, J. K. (1994). The role of calcium in the control of volume-regulatory pathways. In K. Strange (Ed.), *Cellular and Molecular Physiology of Cell Volume Regulation* (pp. 259–277). Boca Raton: CRC Press.

Freedman, J. C., & Hoffman, J. F. (1979). Ionic and osmotic equilibria of human red blood cells treated with nystatin. *J Gen Physiol, 74*, 157–185.

Garcia, A., & Berg, M. B. (1991). Role of organic osmolytes in adaption of renal cells to high osmolarity. *J Memb Biol, 119*, 1–13.

Glasstone, S. (1946). *Textbook of Physical Chemistry*. Princeton: Van Nostrand.

Grinstein, S., & Foskett, J. K. (1990). Ionic mechanisms of cell volume regulation in leukocytes. *Annu Rev Physiol, 52*, 399–414.

Grinstein, S., Clarke, C. A., & Rothstein, A. (1983). Activation of Na^+/H^+ exchange in lymphocytes by osmotically-induced volume changes and by cytoplasmic acidification. *J Gen Physiol, 82*, 619–638.

Grinstein, S., Rothstein, A., Sarkadi, B., & Gelfand, E. W. (1984). Responses of lymphocytes to anisotonic media: volume-regulating behavior. *Am J Physiol, 246*, C204–C215.

Haas, M. (1994). The Na-KCl cotransporters. *Am J Physiol, 267*, C869–C885.

Haines, T. H. (1994). Water transport across biological membranes. *FEBS Lett, 346*, 115–122.

Harrison, B., & Zimmerman, S. B. (1986). T4 polynucleotide kinase: macromolecular crowding increases the efficiency of reaction at DNA termini. *Anal Biochem, 158*, 307–315.

Hasegawa, H., Skach, W., Baker, W., Calayag, M. C., Lingappa, V., & Verkman, A. S. (1992). A multifunctional aqueous channel formed by CFTR. *Science, 258*, 1477–1479.

Hasegawa, H., Zhang, R., Dohrman, A., & Verkman, A. S. (1993). Tissue-specific expression of mRNA encoding rat kidney water channel CHIP28k by in situ hybridization. *Am J Physiol, 264*, C237–C245.

Häussinger, D. (1998). Osmoregulation of liver cell function: signalling, osmolytes and cell heterogeneity. *Contrib Nephrol, 123*, 185–204.

Häussinger, D., & Lang, F. (1991). Cell volume in the regulation of hepatic function: a mechanism for metabolic control. *Biochim Biophys Acta, 1071*, 331–350.

Häussinger, D., & Schliess, F. (1999). Osmotic induction of signaling cascades: role in regulation of cell function. *Biochem Biophys Res Commun, 255*, 551–555.

Häussinger, D., Lang, F., & Gerok, W. (1994). Regulation of cell function by the cellular hydration state. *Am J Physiol, 267*, E343–E355.

Henson, J. H. (1999). Relationships between the actin cytoskeleton and cell volume regulation. *Microsc Res Tech, 47*, 155–162.

Hernandez, J. A., & Fischbarg, J. (1992). Kinetic analysis of water transport through a single-file pore. *J Gen. Physiol, 99*, 645–662.

Heymann, J. B., & Engel, A. (1999). Aquaporins: phylogeny, structure, and physiology of water channels. *News Physiol Sci, 14*, 187–193.

Heymann, J. B., Agre, P., & Engel, A. (1998). Progress on the structure and function of aquaporin 1. *J Struct Biol, 121*, 191–206.

Hildebrand, J. H. (1955). Osmotic pressure. *Science, 121*, 116–119.

Hinke, J. A. M. (1980). Water and electrolyte content of the myofilament phase in the chemically skinned barnacle fiber. *J Gen Physiol, 75*, 531–551.

Hladky, S. B., & Rink, T. J. (1978). Osmotic behaviour of human red blood cells: an interpretation in terms of negative intracellular fluid pressure. *J Physiol, 274*, 437–446.

Hobbie, R. K. (1978). *Intermediate Physics for Medicine and Biology, pp. 126–132*. New York: John Wiley.

Hoffmann, E. K., & Dunham, P. B. (1995). Membrane mechanisms and intracellular signalling in cell volume regulation. *Int Rev Cytol, 161*, 173–262.

Hoffmann, E. K., & Simonsen, L. O. (1989). Membrane mechanisms in volume and pH regulation in vertebrate cells. *Physiol Rev, 69*, 315–382.

Hoffmann, E. K., Lambert, I. H., & Simonsen, L. O. (1986). Separate, Ca^{2+}-activated K^+ and Cl^- transport pathways in Ehrlich ascites tumor cells. *J Memb Biol, 91*, 227–244.

Holz, R., & Finkelstein, A. (1970). The water and nonelectrolyte permeability induced in thin lipid membranes by the polyene antibiotics nystatin and amphotericin B. *J Gen Physiol, 56*, 125–145.

Hu, H., & Sachs, F. (1997). Stretch-activated ion channels in the heart. *J Mol Cell Cardiol, 29*, 1511–1523.

Jackson, P. S., Morrison, R., & Strange, K. (1994). The volumesensitive organic osmolyte-anion channel VSOAC is regulated by non-hydrolytic ATP binding. *Am J Physiol, 267*, C1203–C1209.

Jacobson, B. S. (1983). Interaction of the plasma membrane with the cytoskeleton: an overview. *Tissue Cell, 15*, 829–852.

Jakobsson, E. (1980). Interactions of cell volume, membrane potential, and membrane transport parameters. *Am J Physiol, 238*, C196–C206.

Jansen, M., & Blume, A. (1995). A comparative study of diffusive and osmotic water permeation across bilayers composed of phospholipids with different head groups and fatty acyl chains. *Biophys J, 68*, 997–1008.

Jap, B. K., & Li, H. (1995). Structure of the osmo-regulated H_2O^- channel, AQP-CHIP, in projection at 3.5 Å resolution. *J Mol Biol, 251*, 413–420.

Jennings, M. L., & al-Rohil, N. (1990). Kinetics of activation and inactivation of swelling-stimulated K^+/Cl^- transport. The volume sensitive parameter is the rate constant for inactivation. *J Gen Physiol, 95*, 1021–1040.

Jennings, M. L., & Schulz, R. K. (1990). Swelling-activated KCl cotransport in rabbit red cells: flux is determined mainly by cell volume rather than shape. *Am. J. Physiol, 259*, C960–C967.

Jennings, M. L., & Schulz, R. K. (1991). Okadaic acid inhibition of KCl cotransport. Evidence that protein dephosphorylation is necessary for activation of transport by either cell swelling or N-ethylmaleimide. *J Gen Physiol, 97*, 799–817.

Jung, J. A., Preston, G. M., Smith, B. L., Guggino, W. B., & Agre, P. (1994). Molecular structure of the water channel through aquaporin CHIP: the hourglass model. *J Biol Chem, 269*, 14648–14654.

Kaplan, M. R., Mount, D. B., & Delpire, E. (1996). Molecular mechanisms of NaCl cotransport. *Annu Rev Physiol, 58*, 649–668.

Kiil, F. (1989). Molecular mechanisms of osmosis. *Am J Physiol, 256*, R801–R808.

King, L. S., & Agre, P. (1996). Pathophysiology of the aquaporin water channels. *Annu Rev Physiol, 58*, 619–648.

Kregenow, F. M. (1981). Osmoregulatory salt transporting mechanisms: control of cell volume in anisotonic media. *Annu Rev Physiol, 43*, 493–505.

Kwon, H. M., Yamauchi, A., Uchida, S., et al. (1992). Cloning of a Na^+/myo-inositol cotransporter, a hypertonicity stress protein. *J Biol Chem, 267*, 6229–6301.

Lakshminarayanaiah, N. (1984). *Equations of Membrane Biophysics, pp. 107–118.* Orlando: Academic Press.

Landis, E. M., & Pappenheimer, J. R. (1963). *Exchange of substances through the capillary walls.* In: *Handbook of Physiology, Vol. 2.* Washington, DC: American Physiological Society. Sec. 2, 961–1034.

Lang, F., Busch, G. L., & Volkl, H. (1998). The diversity of volume regulatory mechanisms. *Cell Physiol Biochem, 8*, 1–45.

Leaf, A. (1956). On the mechanism of fluid exchange of tissues in vitro. *Biochem J, 62*, 241–248.

Leaf, A. (1959). Maintenance of concentration gradients and regulation of cell volume. *Ann NY Acad Sci, 72*, 396–404.

LeNeveu, D. M., Rand, R. P., & Parsegian, V. A. (1976). Measurement of forces between lecithin bilayers. *Nature, 259*, 601–603.

Lewis, S. A., & de Moura, J. L. (1982). Incorporation of cytoplasmic vesicles into apical membrane of mammalian urinary bladder epithelium. *Nature, 297*, 685–688.

Luna, E. J., & Hitt, A. L. (1992). Cytoskeleton-plasma membrane interactions. *Science, 258*, 955–964.

Ma, T., & Verkman, A. S. (1999). Aquaporin water channels in gastrointestinal physiology. *Am J Physiol, 517*, 317–326.

Macknight, A. D. C. (1988). Principles of cell volume regulation. *Renal Physiol Biochem, 3–5*, 114–141.

Macknight, A. D. C., & Leaf, A. (1977). Regulation of cellular volume. *Physiol Rev, 57*, 510–573.

Macey, R. I. (1979). Transport of water and nonelectrolytes across red cell membranes. In G. Giebisch, D. C. Tosteson, & H. H. Ussing (Eds.), *Membrane Transport in Biology, Vol. II Transport Across Single Biological Membranes* (pp. 1–57). Berlin: Springer Verlag.

Macey, R. I., & Farmer, R. E. L. (1970). Inhibition of water and solute permeability in human red cells. *Biochim Biophys Acta, 211*, 104–106.

Macey, R. I., Karan, D. M., & Farmer, R. E. L. (1972). Properties of water channels in human red cells. In F. Kreuzer, & J. F. G. Slegers (Eds.), *Biomembranes, Vol. 3, Passive Permeability of Cell Membranes* (pp. 331–340). New York: Plenum Press.

Mauro, A. (1957). Nature of solvent transfer in osmosis. *Science, 126*, 252–253.

McCarty, N. A., & O'Neil, R. G. (1992). Calcium signaling in cell volume regulation. *Physiol Rev, 72*, 1037–1061.

Meschia, G., & Setnikar, I. (1958). Experimental study of osmosis through a collodion membrane. *J Gen Physiol, 42*, 429–444.

Mills, J. W., Schweibert, E. M., & Stanton, B. A. (1994). The cytoskeleton and cell volume regulation. In K. Strange (Ed.), *Cellular and Molecular Physiology of Cell Volume Regulation* (pp. 241–258). Boca Raton: CRC Press.

Minton, A. P. (1983). The effect of volume occupancy upon the thermodynamic activity of proteins: some biochemical consequences. *Molec Cell Biochem, 55*, 119–140.

Minton, A. P. (1990). In *Holobiochemistry: the effect of local environment upon equilibria and rates of biochemical reactions. Int J Biochem, 22* (pp. 1063–1067).

Minton, A. P. (1994). Influence of macromolecular crowding on intracellular association reactions: possible role in volume regulation. In K. Strange (Ed.), *Cellular and Molecular Physiology of Cell Volume Regulation* (pp. 181–190). New York: Academic Press.

Minton, A. P., Colclasure, G. C., & Parker, J. C. (1992). Model for the role of macromolecular crowding in regulation of cellular volume. *Proc Natl Acad Sci USA, 89*, 10504–10506.

Morris, C. E. (1990). Mechanosensitive ion channels. *J Memb Biol, 113*, 93–107.

Needham, D., & Nunn, R. S. (1990). Elastic deformation and failure of lipid bilayer membranes containing cholesterol. *Biophys J, 58*, 997–1009.

Nielsen, S., Smith, B. L., Christensen, E. I., Knepper, M. A., & Agre, P. (1993). CHIP28 water channels are localized in constitutively wateRPermeable segments of the nephron. *J Cell Biol, 120*, 371–383.

Nielsen, S., Chou, C. L., Marples, D., Christensen, E. I., Kishore, B. K., & Knepper, M. A. (1995). Vasopressin increases water permeability of kidney collecting duct by inducing translocation of aquaporin-CD water channels in rat kidney inner medulla. *Proc Natl Acad Sci USA, 92*, 1013–1017.

Nielsen, S., Kwon, T. H., Christensen, B. M., Pomeneur, D., Frokiaer, J., & Marples, D. (1999). Physiology and pathophysiology of renal aquaporins. *J Am Soc Nephrol, 10*, 647–663.

O'Neil, W. C. (1999). Physiological significance of volume regulatory transporters. *Am J Physiol, 276*, C995–C1011.

Overbeek, J. T. G. (1956). The Donnan equilibrium. *Prog Biophys Biophys Chem, 3*, 57–84.

Paganelli, C. V., & Solomon, A. K. (1957). The rate of exchange of tritiated water across the human red cell membrane. *J Gen Physiol, 41*, 259–277.

Palfrey, H. C. (1994). Protein phosphorylation control in the activity of volume-sensitive transport systems. In K. Strange (Ed.), *Cellular and Molecular Physiology of Cell Volume Regulation* (pp. 201–214). Boca Raton: CRC Press.

Palfrey, H. C., & O'Donnell, M. E. (1992). Characteristics and regulation of the Na/K/2Cl cotransporter. *Cell Physiol Biochem, 2*, 293–307.

Parker, J. C. (1973). Dog red blood cells. Adjustment of density in vitro. *J Gen Physiol, 62*, 147–156.

Parker, J. C. (1992). Volume-activated cation transport in dog red cells: detection and transduction of the volume stimulus. *Comp Biochem Physiol, 102A*, 615–618.

Parker, J. C., Colclasure, G. C., & McManus, T. J. (1991). Coordinated regulation of shrinkage-induced Na/H exchange and swelling-induced [K-Cl] cotransport in dog red cells. Further evidence from activation kinetics and phosphatase inhibition. *J Gen Physiol, 98*, 869–880.

Pewitt, E. B., Hegde, R. S., Haas, M., & Palfrey, H. C. (1990). The regulation of Na/K/2Cl cotransport and bumetanide binding in avian erythrocytes by protein phosphorylation and dephosphorylation: effects of kinase inhibitors and okadaic acid. *J Biol Chem, 265*, 20747–20756.

Pfeffer, W. (1877). *Osmotische Untersuchungen. Studien zur Zellmechanik. Wilhelm Engelmann, Leipzig. [Translated by G.R. Kepner and E.J. Tadelmann (1985). Osmotic investigations. Studies on cell membranes*. New York: Van Nostrand Reinhold.

Pierce, S. K., & Politis, A. D. (1990). Ca^{2+}-activated cell volume recovery mechanisms. *Annu Rev Physiol, 52*, 27–42.

Pitzer, K. S., & Mayorga, G. (1973). Thermodynamics of electrolytes. II. Activity and osmotic coefficients for strong electrolytes with one or both ions univalent. *J Phys Chem, 77*, 2300–2308.

Preston, G. M., & Agre, P. (1991). Isolation of the cDNA for erythrocyte integral membrane protein of 28 kilodaltons member of an ancient channel family. *Proc Natl Acad Sci USA, 88*, 11110–11114.

Preston, G. M., Carroll, T. P., Guggino, W. B., & Agre, P. (1992). Appearance of water channels in Xenopus oocytes expressing red cell CHIP28 protein. *Science, 256*, 385–387.

Preston, G. M., Jung, J. S., Guggino, W. B., & Agre, P. (1993). The mercury-sensitive residue at cysteine-189 in the CHIP28 water channel. *J Biol Chem, 268*, 17–20.

Preston, G. M., Jung, J. S., Guggino, W. B., & Agre, P. (1994). Membrane topology of aquaporin CHIP: analysis of functional epitope scanning mutants by vectorial proteolysis. *J Biol Chem, 269*, 1668–1673.

Rash, J. E., Yasumura, T., Hudson, C. S., Agre, P., & Nielsen, S. (1998). Direct immunogold labeling of aquaporin-4 in square arrays of astrocyte and ependymocyte plasma membranes in rat brain and spinal chord. *Proc Natl Acad Sci USA, 95*, 11981–11986.

Rasmusson, R. L., Davis, D. G., & Lieberman, M. (1993). Amino acid loss during volume regulatory decrease in cultured chick heart cells. *Am J Physiol, 264*, C136–C145.

Renkin, E. M. (1954). Filtration, diffusion, and molecular sieving through porous cellulose membranes. *J Gen Physiol, 38*, 225–243.

Reuss, L. (1985). Changes in cell volume measured with an electrophysiological technique. *Proc Natl Acad Sci USA, 82*, 6014–6018.

Richter, E. A., Cleland, P. J. F., Rattigan, S., & Clark, M. G. (1987). Contraction-associated translocation of protein kinase C. *FEBS Lett, 217*, 232–236.

Robinson, R. A., & Stokes, R. H. (1959). *Electrolyte Solutions, pp. 480–490*. London: Butterworth.

Rosenberg, P. A., & Finkelstein, A. (1978). Water permeability of gramicidin A-treated lipid bilayer membranes. *J Gen Physiol, 72*, 341–350.

Sachs, F. (1989). Ion channels as mechanical transducers. In W. D. Stein, & F. Bronner (Eds.), *Cell Shape: Determinants, Regulation, and Regulatory Role* (pp. 63–92). San Diego: Academic Press.

Sackin, H. (1994). Stretch-activated ion channels. In K. Strange (Ed.), *Cellular and Molecular Physiology of Cell Volume Regulation* (pp. 215–240). Boca Raton: CRC Press.

Sands, J. M. (1994). Regulation of intracellular polyols and sugars in response to osmotic stress. In K. Strange (Ed.), *Cellular and Molecular Physiology of Cell Volume Regulation* (pp. 133–144). Boca Raton: CRC Press.

Sarkadi, B., & Parker, J. C. (1991). Activation of ion transport pathways by changes in cell volume. *Biochim Biophys Acta, 1071*, 407–427.

Schatzberg, P. (1963). Solubilities of water in several normal alkanes from C_7 to C_{16}. *J Phys Chem, 67*, 776–779.

Shibata, A., Ikawa, K., Shimooka, T., & Terada, H. (1994). Significant stabilization of the phosphatidylcholine bilayer structure by incorporation of small amounts of cardiolipin. *Biochim Biophys Acta, 1192*, 71–78.

Shporer, M., & Civan, M. M. (1977). The state of water and alkali cations within the intracellular fluids: the contribution of NMR spectroscopy. *Curr Top Membr Transport, 9*, 1–69.

Solomon, A. K. (1972). Properties of water in red cells and synthetic membranes. In F. Kreuzer, & J. F. G. Slegers (Eds.), *Biomembranes, Vol. 3, Passive Permeability of Cell Membranes* (pp. 299–330). New York: Plenum Press.

Solomon, A. K. (1989). Water channels across the red blood cell and other biological membranes. *Meth Enzymol, 173*, 192–222.

Solomon, A. K., Chasan, B., Dix, J. A., Lukacovic, M. F., Toon, M. R., & Verkman, A. S. (1983). The aqueous pore in the red cell membrane: band 3 as a channel for anions, cations, nonelectrolytes, and water. *Ann NY Acad Sci, 414*, 97–124.

Somero, G. N. (1986). Protons, osmolytes, and fitness of internal milieu for protein function. *Am J Physiol, 251*, R197–R213.

Starke, L. C., & Jennings, M. L. (1993). K-Cl cotransport in rabbit red cells: further evidence for regulation by protein phosphatase type 1. *Am J Physiol, 264*, C118–C124.

Stein, W. D. (1976). An algorithm for writing down flux equations for carrier kinetics, and its application to co-transport. *J Theor Biol, 62*, 467–478.

Strange, K. (1994). *Cellular and Molecular Physiology of Cell Volume Regulation*. Boca Raton: CRC Press.

Suleymanian, M. A., & Baumgarten, C. M. (1996). Osmotic gradient-induced water permeation across the sarcolemma of rabbit ventricular myocytes. *J Gen Physiol, 107*, 503–514.

Suleymanian, M. A., Clemo, H. F., Cohen, N. M., & Baumgarten, C. M. (1995). Stretch-activated channel blockers modulate cell volume in cardiac ventricular myocytes. *J Mol Cell Cardiol, 27*, 721–728.

Tanford, C. (1961). *Physical Chemistry of Macromolecules*. New York: John Wiley.

Tosteson, D. C., & Hoffman, J. F. (1960). Regulation of cell volume by active cation transport in high and low potassium sheep red cells. *J Gen Physiol, 44*, 169–194.

Trauble, H. (1971). The movement of molecules across lipid membranes: a molecular theory. *J Memb Biol, 4*, 193–208.

Uchida, S., Kwon, H., Yamauchi, A., Preston, A., Marumo, F., & Handler, J. (1992). Molecular cloning of the cDNA for an MDCK cell Na^+ and Cl^--dependent taurine transporter that is regulated by hypertonicity. *Proc Natl Acad Sci USA, 89*, 8230–8234.

Uchida, S., Kwon, H., Yamauchi, A., Preston, A., Kwon, H., & Handler, J. (1993). Medium tonicity regulates expression of the Na^+- and

Cl^--dependent betaine transporter in Madin-Darby canine kidney cells by increasing transcription of the transporter gene. *J Clin Invest, 91*, 1604–1607.

Umenishi, F., Verkman, A. S., & Gropper, M. A. (1996). Quantitative analysis of aquaporin mRNA expression in rat tissues by RNase protection assay. *DNA Cell Biol, 15*, 475–480.

Vandenberg, J. I., Rees, S. A., Wright, A. R., & Powell, T. (1996). Cell swelling and ion transport pathways in cardiac myocytes. *Cardiovasc Res, 32*, 85–97.

van Hoek, A. N., Hom, M. L., Luthjens, L. H., de Jong, M. D., Dempster, J. A., & van Os, C. H. (1991). Functional unit of 30 kDa for proximal tubule water channel as revealed by radiation inactivation. *J Biol Chem, 266*, 16633–16635.

van Hoek, A. N., Luthjens, L. H., Hom, M. L., van Os, C. H., & Dempster, J. A. (1992). A 30 kDa functional size for the erythrocyte water channel determined by in situ radiation inactivation. *Biochem Biophys Res Commun, 184*, 1331–1338.

van't Hoff, J.H. (1887). Die Rolle des osmotischen Druckes in der Analogie zwischen Lösungen und Gasen. Z. Physik. Chemie. 1, 481–493 [Translated by G.L. Blackshear (1979). In (G.R. Kepner, ed.) Cell Membrane Permeability and Transport. Dowden, Hutchinson and Ross, Stroudsburg, PA.]

Verkman, A. S. (1993). *Water Channels*. Austin: R. G. Landis Co.

Verkman, A. S., van Hoek, A. N., Ma, T., et al. (1996). Water transport across mammalian cell membranes. *Am J Physiol, 270*, C11–C30.

Villars, F. M., & Benedek, G. B. (1974) *Physics with Illustrative Examples from Medicine and Biology. Statistical Physics, Vol. 2*. Reading: Addison-Wesley.

Walz, T., Smith, B. L., Agre, P., & Engel, A. (1994). The three-dimensional structure of human erythrocyte aquaporin CHIP. *EMBO J, 13*, 2985–2993.

Walz, T., Hirai, T., Murata, K., et al. (1997). The three-dimensional structure of aquaporin-1. *Nature, 387*, 624–627.

Watson, P. A. (1991). Function follows form: generation of intracellular signals by cell deformation. *FASEB J, 5*, 2013–2019.

Wolfe, J., Dowgert, M. F., & Steponkus, P. L. (1986). Mechanical study of the deformation and rupture of the plasma membranes of protoplasts during osmotic expansions. *J Memb Biol, 93*, 63–74.

Wolff, S. D., & Balaban, R. S. (1990). Regulation of the predominant renal medullary organic solutes in vivo. *Annu Rev Physiol, 52*, 727–746.

Wright, A. R., & Rees, S. A. (1998). Cardiac cell volume: crystal clear or murky waters? A comparison with other cell types. *Pharmacol Ther, 80*, 89–121.

Yamauchi, A., Uchida, S., Kwon, H., et al. (1992). Cloning of a Na^+ and Cl^- dependent betaine transporter that is regulated by hypertonicity. *J Biol Chem, 267*, 649–652.

Yancey, P. H. (1994). Compatible and counteracting solutes. In K. Strange (Ed.), *Cellular and Molecular Physiology of Cell Volume Regulation* (pp. 81–177). Boca Raton: CRC Press.

Yancey, P. H., Clark, M. E., Hand, S. C., Bowlus, R. D., & Somero, G. N. (1982). Living with water stress: evolution of osmolyte systems. *Science, 217*, 1214–1222.

Zeidel, M. L., Ambudkar, S. V., Smith, B. L., & Agre, P. (1992). Reconstitution of functional water channels in liposomes containing purified red cell CHIP28 protein. *Biochemistry, 31*, 7436–7440.

Zhang, R., Skach, W., Hasegawa, H., van Hoek, A. N., & Verkman, A. S. (1993). Cloning, functional analysis and cell localization of a kidney proximal tubule water transporter homologous to CHIP28. *J Cell Biol, 120*, 359–369.

Zimmermann, S. B., & Harrison, B. (1985). Macromolecular crowding accelerates the cohesion of DNA fragments with complementary termini. *Nucl Acids Res, 13*, 2241–2249.

Zimmerman, S. B., & Trach, S. (1991). Estimation of macromolecular concentrations and excluded volume effects for the cytoplasm of Escherichia coli. *Mol Biol, 222*, 599–620.

Chapter 17

Intracellular pH Regulation

Robert W. Putnam

Chapter Outline

I. SUMMARY

Virtually all of the H^+ ions within a cell are buffered by reversible binding to weak acids and bases, resulting in a low free H^+ ion activity. Therefore, the activity of free H^+ ions within the cytoplasm is usually expressed as cytoplasmic pH (pH_i), defined as $pH = -\log(a_H)$, which is a more convenient scale for molecules at low activities.

Cytoplasmic pH is an important aspect of the intracellular milieu and can affect nearly all aspects of cell function. In most cells, pH_i is maintained at a value of about 7.0, well alkaline with respect to the equilibrium pH_i, calculated on the assumption that H^+ ions are at equilibrium across the membrane. The fact that pH_i is alkaline to its equilibrium value creates a passive acidifying influx of H^+. In fact, most cells face a continuous acid load due not only to this acidifying influx but to metabolic acid production and leakage from internal acidic compartments as well. Such challenges to a stable pH_i can be blunted by cellular buffers, but the only way to regulate pH_i fully is through the activity of membrane-bound transporters. These transporters fall into five categories: (1) cation-H^+ exchangers, such as the alkalinizing Na^+-H^+ exchanger and the acidifying K^+-H^+ exchanger; (2) HCO_3^--dependent transporters, such as the (Na^++ HCO_3^-)-Cl^- and the Cl^--HCO_3^- exchangers and Na^+-HCO_3^- co-transporters; (3) H^+-ATPases or proton pumps; (4) Na^+-organic anion co-transporters; and (5) Cl^--organic anion exchangers.

Changes in pH_i can affect many cellular functions. Cell metabolism can be affected by changes in pH, predominantly because of pH-sensitive metabolic enzymes, such as phosphofructokinase. Changes of pH_i have also been shown to affect the cross-linking and polymerization of cytoskeletal elements such as actin and tubulin. The loss of the ability of muscle cells to generate tension (muscle fatigue) has been correlated with a decrease of pH_i. Cell pH is also believed to have a modulatory role in gap junctions and many ion-selective channels. Further, changes of pH_i,

Cell Physiology Sourcebook. DOI: 10.1016/B978-0-12-387738-3.00017-2

mediated by activation of the Na^+-H^+ exchanger, may serve as an intracellular signal for the promotion of cell growth and proliferation. It is significant that changes in pH_i can affect other intracellular signals, such as cellular Ca^{2+} and cAMP levels, suggesting a complex interaction among cellular signaling systems.

Many pH-regulating transporters move an osmotically active ion, such as Na^+ or Cl^-, in exchange for a buffered (and thus osmotically "invisible") ion like H^+ or HCO_3^- and thereby mediate the net movement of solute into or out of the cell. This net movement of solute will be accompanied by a net water flow and result in a change in cell volume. Thus, many pH-regulating transporters, in addition to contributing to pH_i regulation, can mediate the regulation of cell volume.

The pH of certain organellar compartments can differ from the value of pH_i and these differences in pH are important for organellar function. For example, mitochondria maintain an internal pH of 7.5, about 0.5 unit more alkaline than pH_i. This pH gradient across the mitochondrial membrane is essential for the major function of mitochondria, the production of ATP. Further, several intracellular organelles in the vacuolar system (e.g. endosomes, lysosomes and storage granules) maintain an internal pH of 5–6, well below pH_i. These organelles contribute to the movement of membranes, membrane-bound proteins and soluble proteins around the cell and their acidic pH is essential for this function.

Given the importance of pH to so many cellular functions, it is not surprising that cells have elaborated highly regulated mechanisms to control pH_i.

II. INTRODUCTION

Intracellular pH is an important aspect of the intracellular environment. Changes in intracellular pH can potentially affect virtually all cellular processes, including metabolism, membrane potential, cell growth, movement of substances across the surface membrane, state of polymerization of the cytoskeleton and ability to contract in muscle cells. Changes of intracellular pH are also often one of the responses of cells to externally applied agents, including growth factors, hormones and neurotransmitters. Further, many organelles, such as lysosomes, mitochondria and endosomal vesicles, maintain an organellar pH that is different from the cytoplasmic pH (pH_i) and these pH differences have important functional consequences for those organelles. It is thus not surprising to find that cells have elaborated a variety of mechanisms that enable them to regulate their intracellular pH. In this chapter, we will discuss the pH level in the cytoplasm and various compartments of a cell, the variety of mechanisms available to a cell to regulate its pH_i and the functional consequences of changes in pH_i.

III. pH AND BUFFERING POWER

The concept of pH was first introduced in 1909 by Sörenson and defined as $-\log [H^+]$. This term was a more convenient way to express the concentration of an ion that is present at very low concentrations. Incorporating the concept of activity, pH is defined as:

$$pH = -\log\ (a_H) = -\log(\gamma_H[H^+]) \qquad (17.1)$$

where a_H is the activity of H^+ and γ_H is the activity coefficient of H^+. At normal intracellular ionic strength, γ_H is about 0.83.

Protons tend to bind to macromolecules and thus are usually present at very low concentrations in biological solutions. This property is the basis for buffering power. A variety of weak acids and bases can bind H^+ through reversible equilibrium binding reactions. Thus, a weak acid in solution obeys the equilibrium reaction:



$$HA\{=\}H^+ + A^- \qquad (17.2)$$

where HA is the weak acid (e.g. lactic acid) and A^- is the conjugate weak base (e.g. lactate). This equilibrium is described by an apparent equilibrium constant, K'_a, as:

$$K'_a = a_H \cdot \frac{[A^-]}{[HA]} \qquad (17.3)$$

This equation is more familiar in its logarithmically transformed expression,

$$pH = pK'_a\ \log \frac{[A^-]}{[HA]} \qquad (17.4)$$

where pK'_a is $-\log\ K'_a$. This equation, better known as the Henderson–Hasselbalch equation, describes the thermodynamic equilibrium that holds for a weak acid in a solution of constant pH. The Henderson–Hasselbalch equation is most commonly used in its specialized form for the total reaction of the hydration of CO_2 and the dissociation of the resulting carbonic acid into H^+ and bicarbonate as:

$$pH = pK'_a + \log \frac{[HCO_3^-]}{\alpha \cdot P_{CO_2}} \qquad (17.5)$$

where a is the solubility coefficient of CO_2 in a given solution and P_{CO_2} is the partial pressure of CO_2 in that solution. Two important facts can be deduced from the Henderson–Hasselbalch equation. First, in any weak acid solution, there will be a finite amount of both A^- and HA. For example, if HCO_3^- is added to a solution, CO_2 will be generated and thus be present. Conversely, if CO_2 is bubbled through a solution, HCO_3^- will be produced. Second, this equation can be used to calculate any of the variable parameters if the other three are known. For instance, if a solution is equilibrated with a gas of known P_{CO_2}, the HCO_3^- in that solution can be calculated from

Equation 17.5 once the pH has reached a stable value (values for pK'_a are readily available).

On addition of H^+ (or OH^-) to a solution, the pH will change. However, if the solution contains weak acids (or bases), many of the added protons (or hydroxyl ions) will be bound up, thus minimizing the change in the concentration of free H^+ and thereby minimizing the change in pH. Since these substances minimize the change in pH upon addition of acid or base, weak acids and bases are referred to as buffers. The definition of the buffering power (β) of a solution is:

$$\beta = \frac{d[B]}{dpH} \tag{17.6}$$

where d[B] is the amount of base added to the solution and dpH is the change in pH of the solution due to that base addition. The addition of acid to the solution is equivalent to a negative addition of base, $-d$[B]. The units of β are mM/pH unit.

An example will indicate the importance of buffering power to maintaining the pH of a solution. If 1 mM NaCl is added to a solution, $[Na^+]$ and $[Cl^-]$ increase by 1 mM (for simplicity, the effects of the non-ideal activity coefficients will be ignored). However, the addition of 1 mM HCl to a solution that has a pH of 7.0 and a buffering power of 10 mM/pH unit will cause that $[Cl^-]$ to increase by 1 mM, but will cause the pH to decrease by only about 0.28 pH unit, to 6.72. Thus, of the added 1 mM of H^+, only 0.091% remain free, i.e. only 1 out of every 11 000 added H ions remains free. The rest are bound to the weak acid buffers. If the buffers had not been present, the same addition of 1 mM HCl would have changed the solution pH by about 4 units to pH 3. This clearly demonstrates that the presence of buffers in a solution markedly blunts the effects of added acid or base.

A buffer can act as either a *closed buffer* or an *open buffer*. A closed buffer is one in which the total buffer concentration remains constant. Most of the commonly used laboratory buffers, such as Hepes or Tris, operate as closed buffers in solution. If a buffer is a weak acid (HA {=}A^-+H^+), then it operates as a closed buffer when the concentration of the total acid ($[A]_T$ = $[HA]+[A^-]$) remains constant. Such a buffer can become protonated or deprotonated, but the total amount of buffer does not change. The following is a mathematical expression for the buffering power of a weak acid acting as a closed buffer:

$$\beta_{closed} = \frac{2.303[A]_T \; K'_a a_H}{(K'_a + a_H)^2} \tag{17.7}$$

where K'_a is the apparent dissociation constant of the weak acid. Several conclusions can be derived from this equation. When pH is very high ($a_H \rightarrow 0$) or very low ($a_H \rightarrow \infty$), β_{closed} approaches 0. β_{closed} reaches a maximum when $a_H = K'_a$ (i.e. when pH = pK'_a) and = $0.58[A]_T$. The relationship between pH and β_{closed} for a theoretical closed buffer is shown in Fig. 17.1.

In contrast to the conditions for a closed buffer, if the protonated (or uncharged) form of a buffer remains constant (i.e. [HA] = constant), then the buffer operates as an open buffer. The most common example of an open buffer in solution is CO_2/ HCO_3^-. Such a solution contains HCO_3^- and is equilibrated with gaseous CO_2 (usually by bubbling). If acid is added to such a solution, H^+ combines with HCO_3^- and forms additional CO_2. Since the solution is in equilibrium with a fixed P_{CO_2}, the additional CO_2 diffuses from the solution and is removed. Thus, under these conditions, the amount of the uncharged form of the buffer (CO_2) remains constant, whereas the total buffer amount goes down because the HCO_3^- has decreased. The buffering power of an open buffer is given by:

$$\beta_{open} = 2.303 \; [A^-] \tag{17.8}$$

where $[A^-]$ = HCO_3^- for the open buffering power of CO_2/HCO_3^-. The relationship between pH and β_{open} for a theoretical open buffer is shown in Fig. 17.1.

Open buffers differ from closed buffers in two important respects. First, unlike closed buffers, the buffering power of open buffers is not maximal at their pK'_a values. In fact, open buffers become better buffers at the more extreme values of pH (see Fig. 17.1). β_{open} becomes larger with alkalinization for weak acids and with acidification for weak bases. Second, open buffers have a much higher buffering power than closed buffers under similar conditions (see Fig. 17.1). Note, however, that neither Equation 17.7 nor Equation 17.8 includes any indication of the nature of the buffer. Thus, all closed buffers are equally potent when the pH is at their pK'_a and all open buffers are equally potent when they have the same $[A^-]$.

Since most uncharged substances are substantially more permeant through cell membranes than charged species, *almost all weak acids and bases can act as open buffers in cells*. For example, a weak acid that has a pK'_a of 4.0 acts like a closed buffer in solution and, since its pK'_a is 4.0, it would be a poor buffer at pH 7.0. However, inside a cell at pH 7.0, this weak acid acts like an open buffer. Any added H^+ will bind to the anionic form of the buffer. The uncharged buffer molecule formed will readily diffuse from the cell and be removed by the blood. Thus, although this weak acid is a poor buffer in the medium, it can contribute substantially to the buffering power inside a cell if present at sufficient concentration.

Complex solutions, like cytoplasm, contain multiple buffers. The *total buffering power* (β_{total}) of such solutions

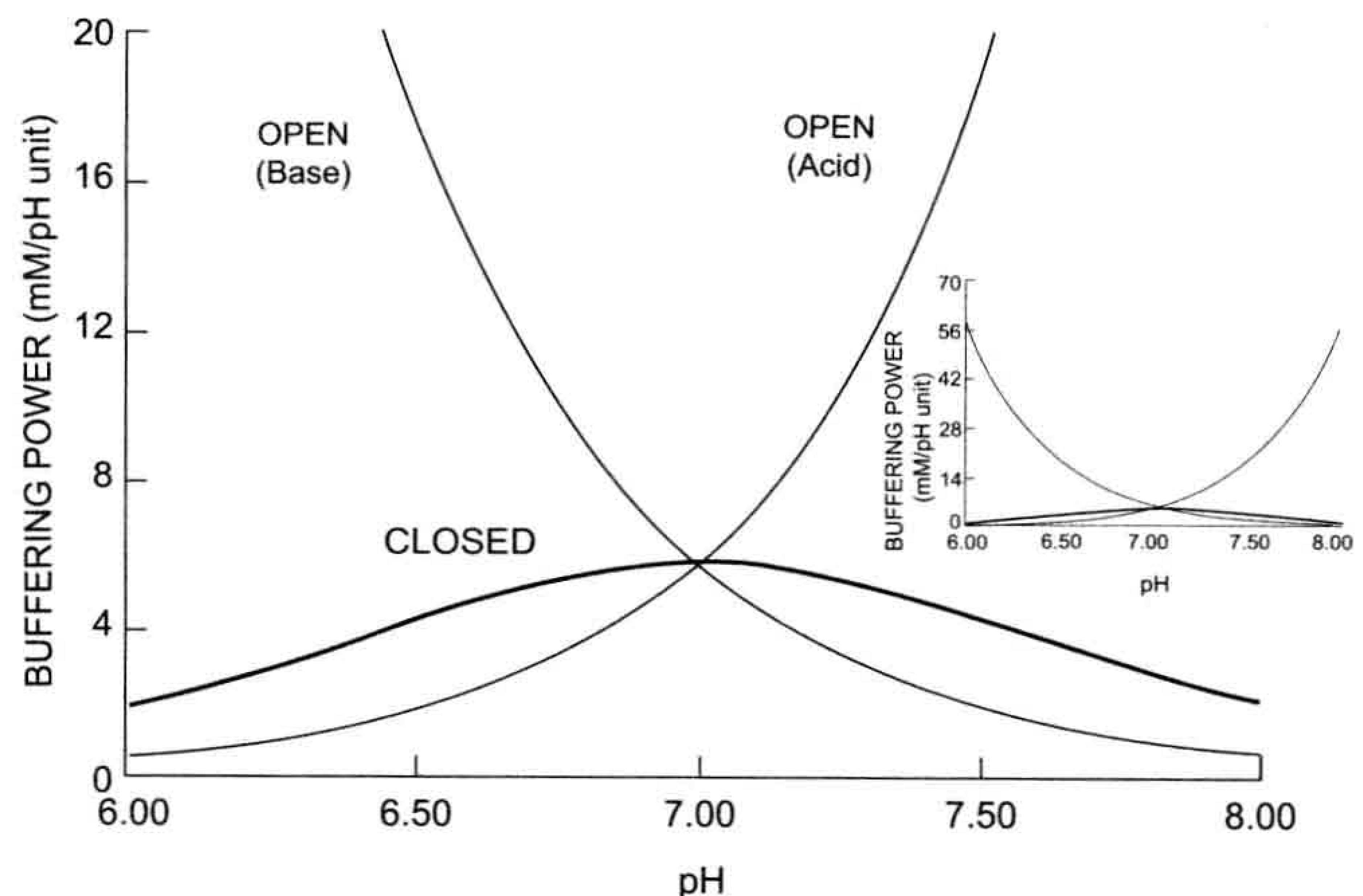


FIGURE 17.1 The pH dependence of a buffer operating as a closed or open buffer. The buffering powers for both a weak acid buffer (H^++A^-{ReversReact}HA) and weak base buffer (H^++B{ReversReact}BH^+) are plotted. The buffers are assumed to have a pK'_a of 7.0 and to have the same buffering power at pH 7.0 whether operating as an open or closed buffer. Note that while closed buffers have maximal buffering power when pH= pK'_a, the buffering power for an open buffer is higher at pH values higher than pK'_a (for weak acid buffers) or at pH values lower than pK'_a (for weak base buffers). Inset: the same plot with a different scale for the ordinate. Note how much higher the open buffering power is compared with the closed buffering power at pH values well above (weak acid) or below (weak base) the value of pK'_a.

will be the sum of the various buffers; i.e. buffers operate independently in solution. Thus,

$$\beta_{\text{total}} = \sum \beta_{\text{closed}} + \sum \beta_{\text{open}} \qquad (17.9)$$

Finally, it is inherent in the definition of buffering power (Equation 17.6) that buffering power is a coefficient that can be used to convert a change of pH into a change in the amount of proton equivalents moved. This relationship has practical application. For instance, in the study of the regulation of intracellular pH, the activity of a transporter that moves H^+ across the surface membrane (such as the Na^+-H^+ exchanger, see Section VIIA) is determined by measuring the rate of change of pH_i (dpH_i/dt). The movement of H^+ on this transporter is accompanied by Na^+, whose movement is measured as a radioisotopic flux (amount of Na^+ influx per unit time). To compare the flux of Na^+ with the flux of H^+, the rate of change of pH_i needs to be converted to the amount of H^+ moved per unit time. This is accomplished by the following equation:

$$J_H = \frac{dpH}{dt} \cdot \beta_{\text{total}} \qquad (17.10)$$

where J_H is the flux of protons and has units of mM H^+ per unit time. Using this equation, the flux of H^+, calculated from the measured rate of pH change, can be directly compared to the flux of another ion determined with radioisotopes.

IV. INTRACELLULAR pH

Protons are just like any other cation, except for three distinguishing characteristics: (1) H ions are a dissociation product of water molecules (H_2O{=}H^++OH^-) and thus are always present in aqueous solutions; (2) H ions are present at very low concentrations in most solutions; and (3) H ions have much higher mobility than other cations. However, the equilibrium distribution and movement of H^+ across biological membranes are governed by the same principles that govern the movement of all other ions across biological membranes.

Originally, protons were assumed to be at equilibrium across biological membranes because of their very high mobility. Assuming an extracellular pH (pH_o) of 7.4, a V_m of −60 mV (inside negative) and assuming that H ions are passively distributed across the membrane (i.e. at equilibrium), pH_i would be 6.4 (calculated from the Nernst equation). However, at such an intracellular pH, metabolism and a variety of other cellular functions would be impaired. With the advent of modern reliable techniques for measuring intracellular pH, including *pH-sensitive glass microelectrodes* and *pH-sensitive fluorescent dyes*, it was shown that, in the majority of cells, pH_i was between 6.8 and 7.2, well above the calculated value for equilibrium pH. It is now clear that for most cells (with the notable exception of red blood cells), pH_i is considerably more alkaline than it would be if protons were at passive equilibrium across the cell membrane.

The question still remains how pH_i can be well above its equilibrium value, since H^+ should be highly permeant to most cell membranes. In fact, the *permeability of H^+* across biological membranes has been estimated to be between 10^{-4} and 10^{-2} cm/s, about four orders of magnitude higher than typical K^+ permeability. However, it is the conductance and not the permeability of H^+ that is crucial. *Conductance* is a measure of ion flux and is a function of both the permeability and the free concentration of an ion. H ions have low conductance across biological membranes despite their high permeability, because they are present in such low concentrations (10^{-7} M free concentration for H^+

versus 10^{-1} M free concentration for K^+). Thus, the acidifying influx of H ions (down their electrochemical gradient) will be small and these H ions can easily be removed from the cell by membrane transport systems (see Section VII).

In summary, most cells have a cytoplasmic pH that is more alkaline than the value calculated assuming equilibrium of H^+ across the cell membrane, and pH_i for most cells is about 6.8–7.2.

V. ORGANELLAR pH

Several intracellular organelles independently control their internal pH, which differs from the cytoplasmic pH (Fig. 17.2). These organelles include *mitochondria* and *acidic intracellular organelles.*

VA. Mitochondria

One of the major roles of mitochondria is the production of ATP. A proton gradient across the inner mitochondrial membrane is required for the production of ATP. The electron transport chain translocates protons from the mitochondrion to the cytoplasm across the inner mitochondrial membrane. This proton extrusion creates an electrical and chemical gradient for proton influx into the mitochondrion. This H^+ influx occurs through a membrane-bound ATPase that produces ATP upon passive proton flux back into the mitochondrion. This is known as the *chemiosmotic hypothesis.*

The extrusion of H^+ to establish a proton gradient renders mitochondria alkaline relative to the cytoplasm by about 0.3–0.5 pH unit. Thus, intramitochondrial pH can be between 7.5 and 8.0. In addition, this pH gradient is maintained in the face of considerable acid loads, indicating that mitochondria may well be able to regulate their internal pH independently of cytoplasmic pH.

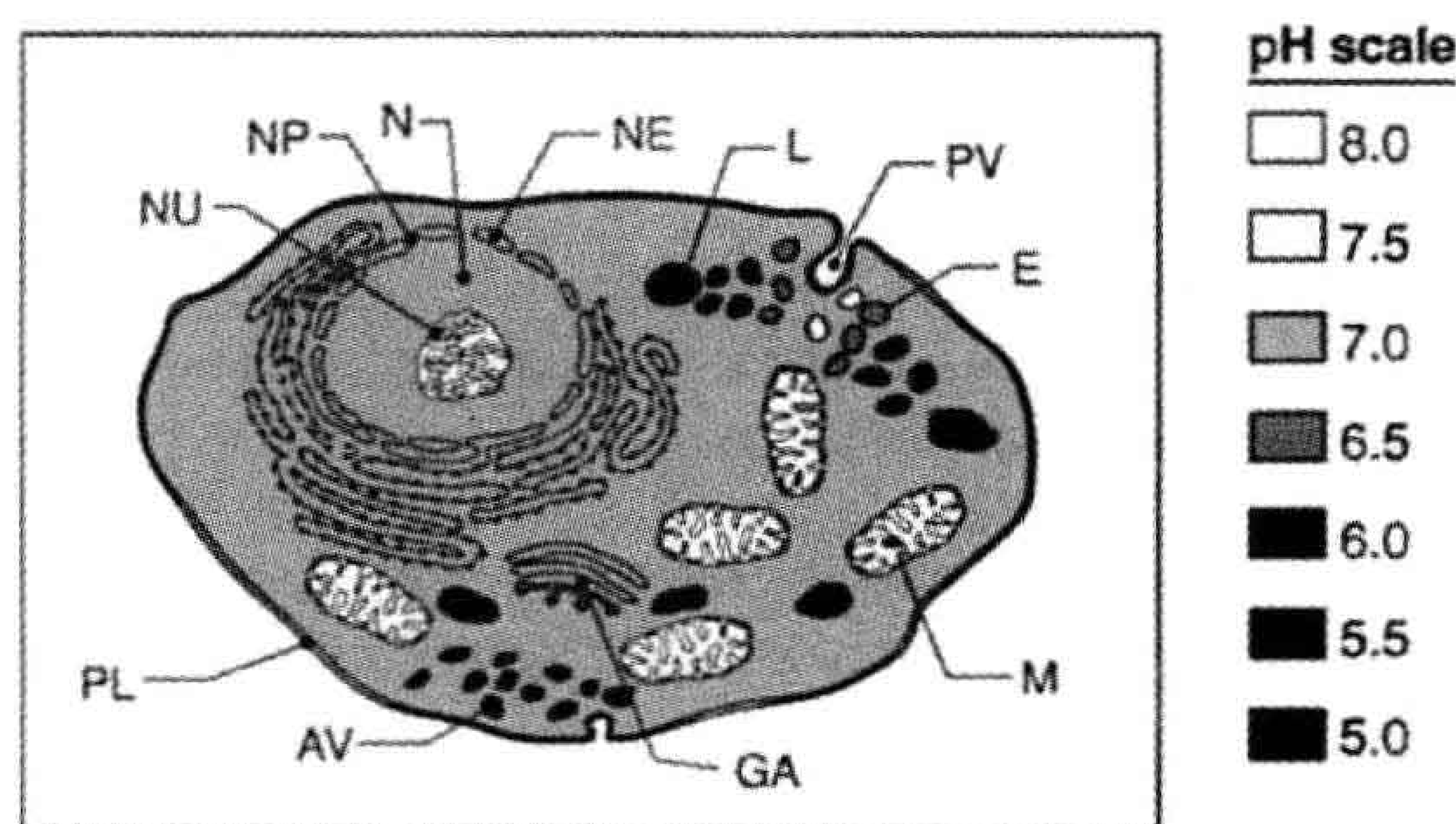


FIGURE 17.2 A diagram of an idealized cell with the gray scale representing different values of pH (note calibration scale on the right). The cytoplasm has a fairly uniform pH of about 7.0, but note the alkaline mitochondria, the increasing acidification in the Golgi apparatus and in the endosomes and the very acidic lysosomes. AV: acidic vesicles; E: endosomes; GA: Golgi apparatus; L: lysosomes; M: mitochondria; N: nucleus; NE: nuclear envelope; NP: nuclear pore; NU: nucleolus; PL: plasmalemma; PV: pinocytotic vesicle.

VB. Acidic Intracellular Organelles

Organelles with a markedly acidic interior are those involved in either the endocytic pathway or the secretory pathway. The acidic organelles involved in endocytosis include *coated pits*, *endosomes* (i.e. prelysosomal endocytic vesicles) and *lysosomes*. Acidic vesicles in the secretory pathway include the *Golgi apparatus* (or at least part of it) and *storage granules* for amines (e.g. chromaffin granules involved in catecholamine secretion) and peptides (e.g. secretory granules in the endocrine pancreas). The pH is not known for all of these compartments, but can be as low as 4.5–5.0 in lysosomes and 5.0–5.7 in endosomes and secretory granules. The pH in the Golgi apparatus seems to fall the farther the compartment is from the nucleus, with values of 6.2–6.4 in the medial Golgi and values as low as 5.9 in the trans Golgi network (TGN).

The acidic internal environment of these various organelles is believed to be necessary for their function. For example, the primary function of lysosomes is the biochemical degradation of macromolecules and these organelles contain a large number of hydrolytic enzymes whose pH optima are about pH 5.0. This serves as protection for the cell. If the lysosomes should leak, the hydrolytic enzymes would be inactivated by the high cytoplasmic pH, thus preventing the indiscriminate degradation of important macromolecules. Receptor-mediated endocytosis involves the internalization of ligand-receptor complexes in endocytic vesicles, or endosomes. Acidification of these vesicles is essential for the dissociation of the ligand from the receptor within the endosome. Once the ligand has dissociated, the internalized receptor is recycled to the surface membrane, while the ligand is delivered to the lysosome. Finally, secretory granules (and perhaps part of the Golgi) serve to accumulate macromolecules to be secreted and often mediate processing or modification of these substances. The maintenance of an acidic environment in these granules can be crucial to both of these functions. There is evidence that the large outward H^+ gradient is used to accumulate biogenic amines in amine secretory granules. This accumulation may be mediated by an H^+-amine exchanger in the granule membrane. These accumulated substances can be biochemically modified into their final form and the enzymes responsible for these modifications often have low pH optima or depend on the availability of organic compounds that will accumulate only in acidic compartments. For all of these acidic compartments, then, it is clear that their proper functioning depends on the maintenance of a low internal pH.

VC. Nucleus

The nucleus is separated from the cytoplasm by a double membrane system that has large nuclear pores. Large macromolecules (up to 5 kDa) readily permeate the nuclear pores and rapidly come to equilibrium between the nucleus and cytoplasm. Given this high degree of permeability of the nuclear membrane, it was believed that nuclear pH could not differ much from cytoplasmic pH. However, measurements clearly show that nuclear pH is from 0.1 to 0.5 pH unit more alkaline than cytoplasmic pH. This is consistent with the findings that the nuclear envelope contains Na^+-H^+ exchangers, indicating active pH regulation across the nuclear membrane.

VI. MAINTENANCE OF A STEADY-STATE pH_i

If a cell is maintaining a *steady-state* pH_i (i.e. the pH of the cytoplasm is constant over time), the rate of acid loading must be equal to the rate of acid extrusion from the cell (in these terms it is exactly equivalent if an acid molecule moves in one direction or a base molecule moves in the opposite direction) (Fig. 17.3). Several processes can contribute to acid loading of a cell, including metabolic production of acid, passive influx of H^+ across the cell membrane, leakage of H^+ from acidic internal compartments, pumping of H^+ from alkaline internal compartments and active influx of H^+ or active extrusion of base. Conversely, acid extrusion includes metabolic consumption of H^+, sequestration of H^+ in internal compartments, and active extrusion of acid or active influx of base.

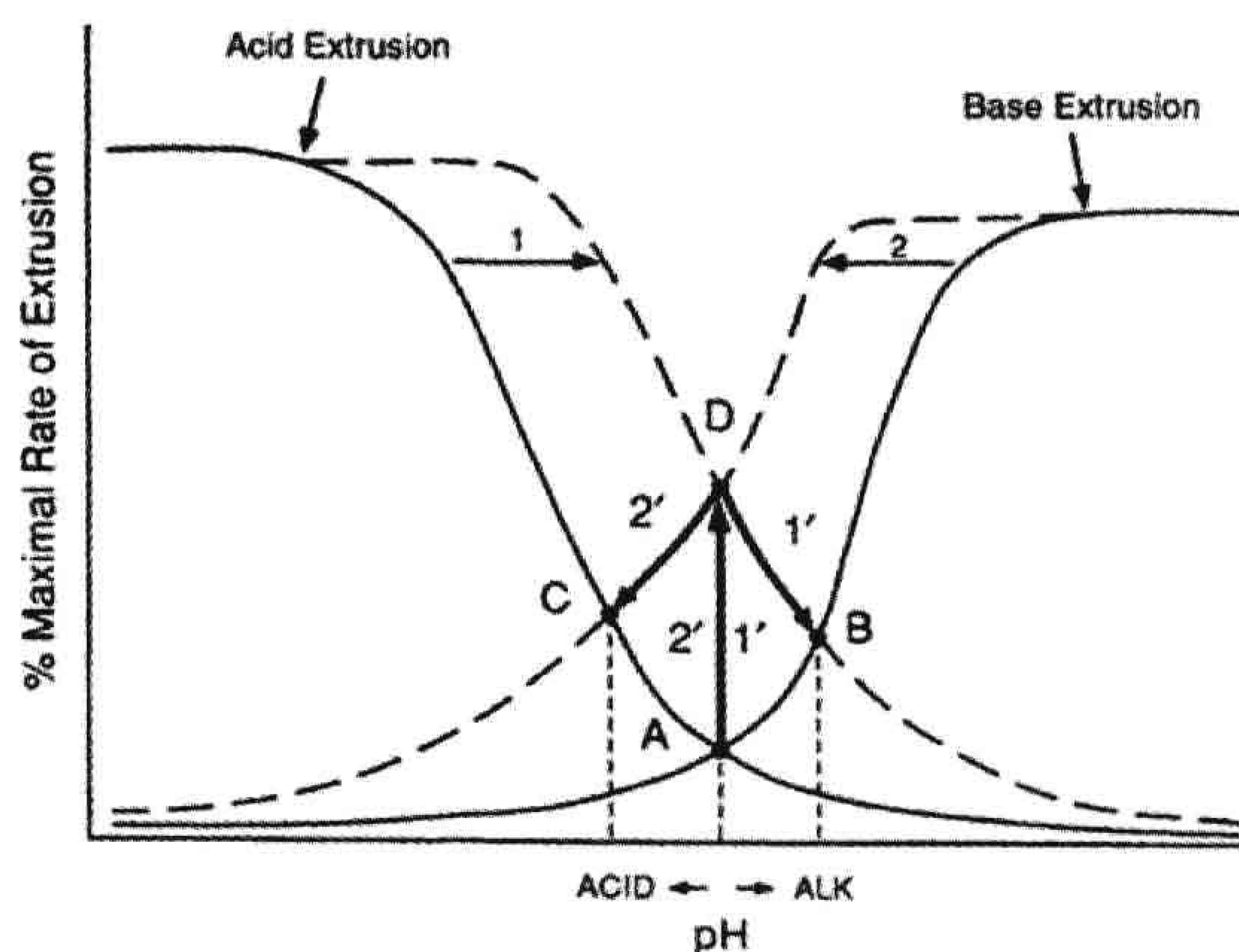


FIGURE 17.3 A model for the regulation of steady-state pH_i. In the cell, steady-state pH_i is determined as the point where acid-extruding processes are balanced by base-extruding (or acid influx) pathways (point A). If acid-extruding processes are activated (arrow 1 – represented as a shift to the right of the pH versus % maximal rate curve), as occurs when growth factors activate Na^+-H^+ exchange, the rate of acid extrusion exceeds the rate of base extrusion and the cell alkalinizes (arrows 1′). Eventually, the cell alkalinizes to the point where acid and base extrusion are again equal and a new alkaline steady state pH_i is reached (point B). In contrast, if base extrusion is activated (arrow 2 – represented as a shift to the left of the pH versus % maximal rate curve), as occurs with an increase in the activity of Cl^--HCO_3^- exchange, the rate of base extrusion exceeds acid extrusion and the cell will acidify (arrows 2′). Eventually, the cell acidifies to the point where acid and base extrusion are again equal and a new acidic steady-state pH_i is reached (point C). If acid and base extrusion are activated to the same extent, the steady state pH_i will remain unchanged (point D).

VIA. Metabolic Production and Consumption of Acids

Several metabolic reactions involve the production of H^+ (Table 17.1). These processes include the production of CO_2, glycolysis (through the generation of lactic and pyruvic acids), formation of creatine phosphate, ATP hydrolysis, lipolysis, triglyceride hydrolysis, the generation of superoxide and the operation of the hexose monophosphate shunt. Obviously, when these reactions run in the opposite direction (e.g. creatine phosphate hydrolysis, ATP formation or consumption of CO_2), there is a net consumption of H^+ and the cell will alkalinize.

When the cell is at steady state, these reactions must be balanced and thus the levels of cellular metabolites such as ATP, creatine phosphate, CO_2 and lactate will also be at steady state. However, during transient periods, these metabolic reactions can result in net changes in metabolite concentrations and thus contribute markedly to changes in pH_i. For instance, during periods of ischemia, cellular lactate and CO_2 may accumulate while ATP will be

TABLE 17.1 Examples of Various Metabolic Reactions that Involve the Generation or Consumption of H^+

Glycolysis[a]	$Glucose + 2MgADP^- + 2P_i^{2-} \rightarrow 2(lactate)^- + 2MgATP^{2-} 2MgATP^{2-} \rightarrow 2MgADP^- + 2P_i^{2-} + 2H^+$
Glycogenolysis[b]	$Glycogen + 3P_i^{2-} + 3MgADP^{-+} \rightarrow 3MgATP^{2-} + 2(lactate)^- + glycogen$
Creatine phosphate hydrolysis	$H^+ + creatine\ phosphate^{2-} + MgADP^- \rightarrow MgATP^{2-} + creatine$
Lipolysis	$Triglyceride \rightarrow 3(palmitate)^- + 3H^+$ $3(palmitate)^- + 3MgATP^{2-} + 3CoA^{4-} \rightarrow 3(palmitoyl\ CoA)^{4-} + 3AMP^{2-} + 6P_i^{2-} + 3H^+ + 3Mg^{2+}$
Superoxide formation	$NADPH + 2O_2 \rightarrow 2O^- + NADP^+ + H^+$
Hexose-monophosphate shunt	$G6P^- + 12NADP^+ + 6H_2O \rightarrow NADPH + P^- + 12H^+ + 6CO_2$

[a]*At pH 7.2 and high [Mg^{2+}], $2H^+$ are always generated but the balance of H^+ produced by the two reactions varies with pH and Mg.*
[b]*Net H^+ production when hydrolysis of the 3MgATP is taken into account.*

hydrolyzed. All of these reactions can contribute to the observed cellular acidification. The hydrolysis of creatine phosphate during ischemia consumes H^+ and will blunt the cellular acidification. Another example of a transient effect of metabolism on cellular pH is the initial acidification seen upon activation of neutrophils with phorbol esters. In this case, stimulation of the production of superoxide and activation of the hexose monophosphate shunt results in increased production of H^+.

VIB. Passive Transmembrane Flux of H^+

Although the H^+ permeability of most biological membranes is quite high ($P_H \approx 10^{-3}$ cm/s), the actual H^+ flux across the membrane is quite low because of the low free H^+ concentration. For example, the putative H^+ flux across a frog muscle fiber can be calculated. Assuming a constant electric field across the membrane, $P_H = 10^{-3}$ cm/s, $V_m = -90$ mV, $pH_i = 7.2$, $pH_o = 7.35$ and $\beta_{otal} = 26$ mM, passive H^+ influx would result in a cellular acidification of only 0.02 pH unit/hour. Although negligible, this does represent a continued acid load on the cell and, if mechanisms do not exist to remove these H ions, the cell will eventually acidify toward its equilibrium pH_i value.

H^+ currents associated with *proton channels* have been reported in several cells, such as snail neurons, salamander oocytes and a number of mammalian cells, including neutrophils, B cells, spermatozoa and airway epithelial cells. All of these channels are activated by depolarization and the resulting H^+ currents alkalinize the cell. Other characteristics of these channels include inhibition by divalent cations (such as Zn^{2+} and Cd^{2+}), gating by both intracellular and extracellular pH and low single-channel conductance. These channels are also purely selective for H ions and they have a very high temperature dependence, both rare features for an ion channel. The proton channel has recently been cloned and shown to contain four transmembrane domains, a large N terminal and a somewhat smaller C terminal domain. The channel often functions as a dimer. These channels have been implicated in the regulation of NADPH oxidase activity during phagocytosis, the facilitation of histamine release from basophils, the activation of sperm and the regulation of pH in airway epithelia. Proton channels may also contribute to the maintenance of pH in restricted submembrane spaces within the cell or contribute to pH_i regulation in cells undergoing prolonged depolarization, such as the prolonged depolarizing fertilization potential in oocytes.

VIC. Internal Compartments

If the pH values of intracellular compartments, such as mitochondria and lysosomes, are at steady state, then they should have no impact on cytoplasmic pH. However, under pathological conditions where mitochondria or acidic intracellular compartments are rendered leaky or mitochondria take up cytoplasmic Ca^{2+} in exchange for H^+, these compartments could influence pH_i. Under normal conditions, though, these compartments should contribute little to the maintenance of a steady-state pH_i, especially owing to their relatively small volume compared with total cell volume.

It is clear that, at the very least, cells face a continual acid load from passive H^+ influx. In addition, under many conditions of metabolic stress, cells also experience a metabolic acid load. Thus, cells must possess active extrusion mechanisms to maintain a steady-state pH_i well above the equilibrium value for pH_i.

VII. ACTIVE MEMBRANE TRANSPORT OF ACIDS AND BASES

To study the ability of cells to actively extrude acid or base from the cell, techniques must be available to alter intracellular pH experimentally. In some large cells, this has been achieved directly by injecting acid into cells, by passing current through microelectrodes, or by internal dialysis through tubing threaded through the cytoplasm of the cell. Changes in pH_i have been accomplished by internal perfusion of cells using whole-cell patch-clamp electrodes. However, the most commonly used experimental method to modify pH_i is by external exposure of cells to weak acids or bases. One of the most popular of such techniques is the *NH_4Cl prepulse technique*. Cells are exposed to an external solution containing NH_4Cl. External NH_3, being uncharged, enters the cell (arrow 1 in Fig. 17.4A) far more rapidly than external NH_4^+. In the cell, the NH_3 combines with an H ion to form NH_4^+ (arrow 2 in Fig. 17.4A), thereby alkalinizing the cell. This alkalinization will continue until the internal and external concentrations of NH_3 are the same, at which time no more NH_3 will enter and the pH_i will reach a new steady-state value alkaline relative to the original pH_i. If NH_4^+ is unable to enter the cell, no further change in pH_i will occur until external NH_4Cl is removed, at which time cytoplasmic NH_4^+ will dissociate to NH_3 and H^+ and all the NH_3 will diffuse from the cell, returning pH_i back to its original value (top pH trace in Fig. 17.4A). However, if NH_4^+ has some membrane permeability, it will enter the cell (arrow 3 in Fig. 17.4A), largely driven by the negative internal membrane potential. The NH_4^+ that enters will dissociate into NH_3 and H^+. The newly formed NH_3 will diffuse from the cell, leaving H^+ in the cell. Thus, a shuttle is established whereby NH_4^+ enters the cell and NH_3 leaves the cell (arrows 3, 2, 1 and 4 in Fig. 17.4A). For each cycle of the shuttle, an H ion is added to the cell and so the cell slowly acidifies in the maintained presence of external NH_4Cl

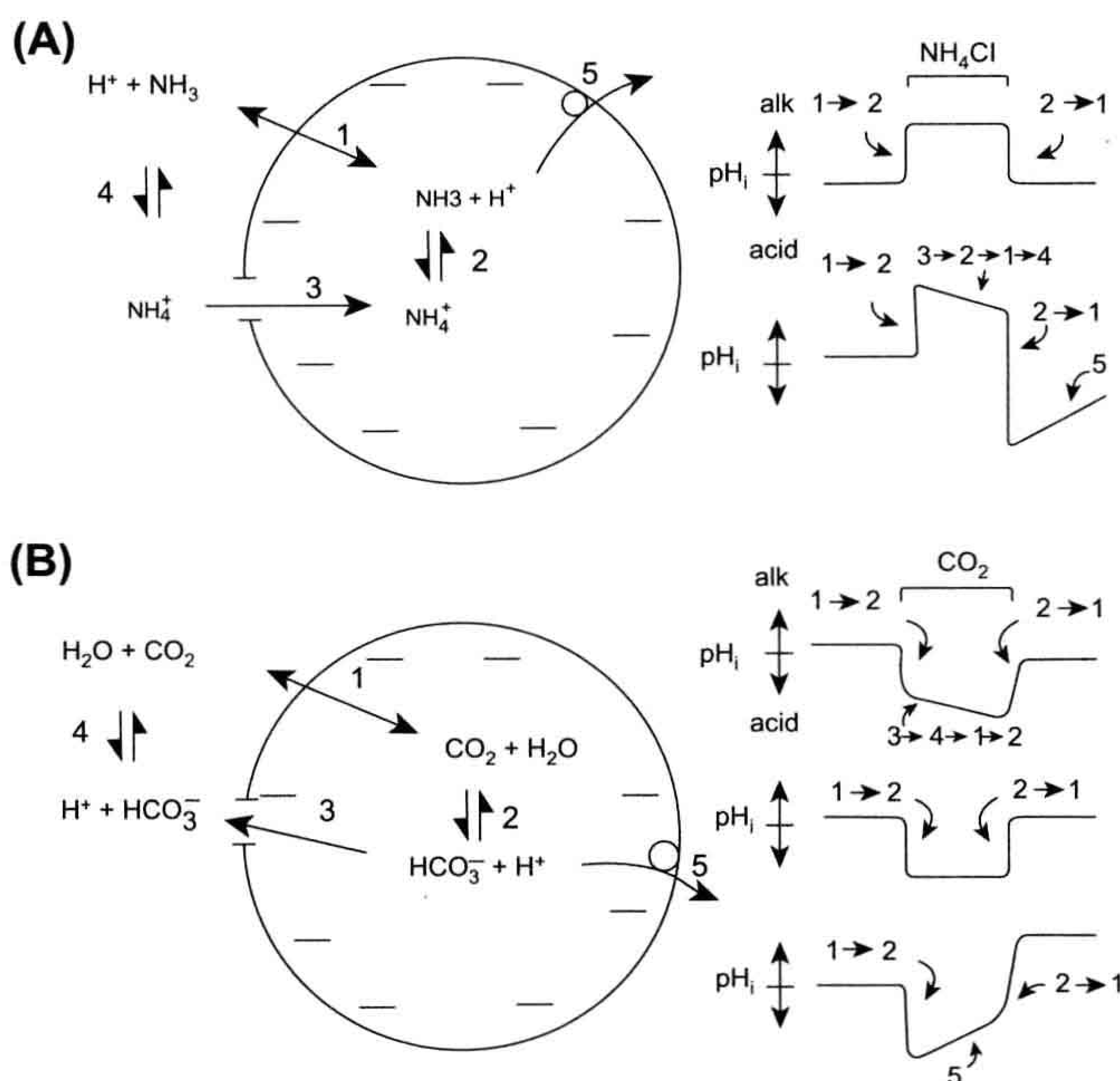


FIGURE 17.4 (A) A diagram of the effects on intracellular pH of a transient exposure of a cell to external NH_4Cl. (B) A diagram of the effects on intracellular pH of a transient exposure of a cell to external CO_2 and HCO_3^-. The meaning of the various numbers and the pH traces to the right are given in the text.

(termed *plateau acidification*). Upon removal of external NH_4Cl, all the original NH_4^+ formed upon exposure will dissociate and regenerate NH_3 (which diffuses from the cell) and H^+. However, the cell will contain extra H^+ due to the operation of the shuttle and thus pH_i will undershoot its initial value, achieving a more acid pH_i than it had before the NH_4Cl exposure. The degree of this undershoot is dependent on the amount of NH_4Cl initially added, the membrane permeability to NH_4^+ and the duration of exposure to NH_4Cl. The net effect of an NH_4Cl prepulse is to acidify the cell and it is entirely analogous to an injection of acid. If a cell possesses membrane transport systems for active H^+ extrusion (arrow 5 in Fig. 17.4A), pH_i will return toward its initial pH value, a process termed *pH recovery* (lower pH trace in Fig. 17.4A).

The other common way to alter pH_i is by exposure of cells to weak acids. The most common weak acid is carbonic acid, in the form of CO_2. This process is analogous to the NH_4Cl prepulse. Upon exposure to a solution containing CO_2 and HCO_3^-, CO_2 rapidly enters the cell (arrow 1 in Fig. 17.4B), hydrates and dissociates to form internal HCO_3^- and H^+ (arrow 2 in Fig. 17.4B). The addition of H^+ internally acidifies the cell. The cell will continue to acidify until internal and external CO_2 are equal. At this point, if HCO_3^- is impermeant, no further change in pH will occur, and pH will return to its initial value upon removal of extracellular CO_2 (middle pH trace in Fig. 17.4B). However, if HCO_3^- can move across the membrane, a shuttle will be established. HCO_3^- will leave the cell (arrow 3 in Fig. 17.4B), mostly driven by the negative membrane potential, internal CO_2 will hydrate and dissociate, and more CO_2 will enter the cell. Thus, HCO_3^- will leave the cell and CO_2 will enter the cell, adding an internal H^+ for every cycle of the shuttle (arrows 3, 4, 1 and 2 in Fig. 17.4B). The cell will slowly acidify (top pH trace in Fig. 17.4B). If, however, the cell possesses transmembrane H^+ extrusion mechanisms (arrow 5 in Fig. 17.4B), pH will recover back toward the initial pH_i value because of active extrusion of internal H^+ even in the maintained presence of CO_2. If external CO_2 is removed after recovery, the H^+ initially formed upon CO_2 exposure will recombine with HCO_3^- and leave the cell as H_2O and CO_2, thereby alkalinizing the cell. However, the cell pH will overshoot, reaching an alkaline value of pH (bottom pH trace in Fig. 17.4B), because of the removal of internal H^+ during pH recovery. Thus, exposure to or removal of weak acids can induce cellular acidification or alkalinization, respectively.

Several integral proteins within the surface membrane of cells are specialized for the active transport of acids and bases across the membrane. Because of their importance to cellular pH regulation, these transport pathways have been extensively studied and can be divided into five groups: (1) those that move H^+ directly in exchange for another

cation; (2) those that move HCO_3^- or an associated species like CO_3^{2-}; (3) H^+-ATPases (proton pumps) that use energy from ATP hydrolysis to transport H^+; (4) those that co-transport anionic weak bases with Na^+; and (5) those that transport anionic weak bases in exchange for Cl^-. Many of the pH-regulating transporters can be derived from genes from one of three gene superfamilies. Na^+/H^+ exchangers (group 1) belong to the SLC9 (solute carrier) gene family, while HCO_3^--dependent transporters belong mainly to the SLC4 superfamily (anion exchanger like Cl^-/HCO_3^- exchangers and Na^+-HCO_3^- co-transporters).

VIIA. Cation-H^+ Exchangers

The best characterized of the cation-H^+ exchangers is the *Na^+-H^+ exchanger (NHE)* (model 1 in Fig. 17.5A). This exchanger responds to cellular acidification by extruding one H^+ in exchange for the influx of one Na^+ (1:1 stoichiometry means that the exchanger is *electroneutral*, i.e. it does not involve net charge movement). There are now known to be at least eight isoforms of the Na^+-H^+ exchanger in mammalian cells. NHE-1 is found in virtually all cells, is inhibited by the loop diuretic amiloride and its analogs, can be activated by a variety of agents and has a molecular weight of 91 000. NHE-2, which has only 50% amino acid homology with NHE-1, is found predominantly in the gastrointestinal tract (GI tract), kidney and skeletal muscle, is much less sensitive to inhibition by amiloride analogs than NHE-1 and has a molecular weight of about 91 000. NHE-3 has about 40% amino acid homology with NHE-1, has a molecular weight of 93 000, is expressed largely in the GI tract and kidney and is not readily inhibited by amiloride. NHE-4 also has about 40% amino acid homology with NHE-1, is the smallest NHE isoform with a molecular weight of 81 000, is largely expressed in the GI tract (with some expression in the uterus, brain, and kidney) and is not very sensitive to inhibition by amiloride. NHE-5 is most similar to NHE-3 (≈53% amino acid homology), but has a larger molecular weight, 99 000, than any of the other NHE isoforms. This isoform is not very sensitive to inhibition by amiloride analogs. NHE-5 is largely expressed in the brain, especially in neuronal cell bodies. Other NHE isoforms undoubtedly exist in mammalian cells. Isoforms NHE-6 and -7 are highly homologous and differ considerably (≈25% homology) from NHE-1. NHE-6 are largely associated with recycling endosomes and NHE-7 are largely associated with the trans-Golgi network. NHE-7 has a high affinity for K^+ and may function largely as a K^+/H^+ exchanger. NHE-8 is at most 25% homologous with the other NHEs and is therefore the most distinct. Its distribution is uncertain, some studies suggesting that it resides mostly on the surface membrane while others indicate a largely intracellular localization.

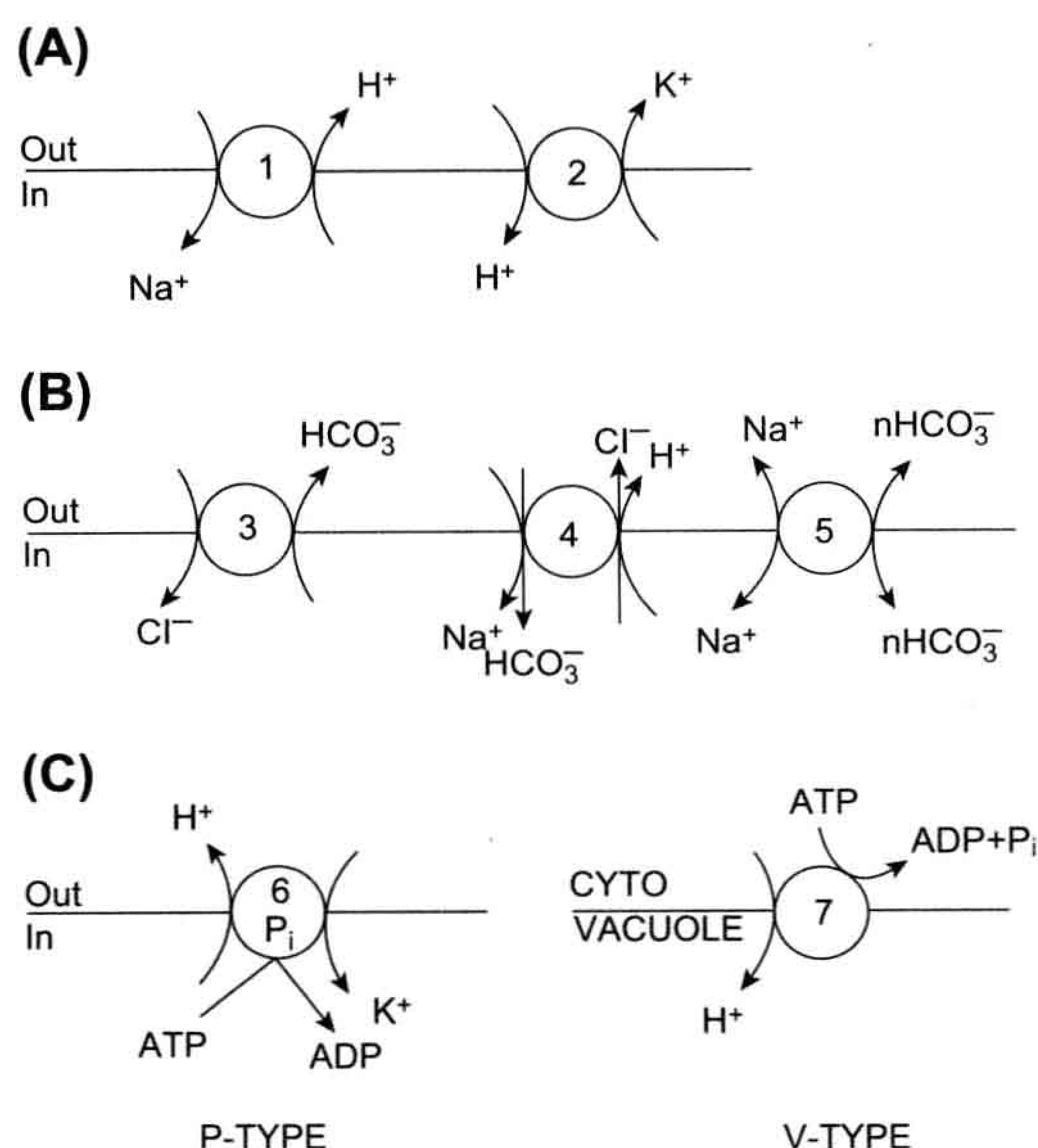


FIGURE 17.5 Models of several different types of pH-regulating transporters. (A) Cation-H^+ exchangers. Included in this group are the alkalinizing Na^+-H^+ exchanger (1) and the acidifying K^+-H^+ exchanger (2). (B) HCO_3^--dependent transporters. This group includes the Cl^--HCO_3^- exchanger (band 3 from red blood cells) (3). Another transporter in this group is the (Na^++HCO_3^-)-Cl^- exchanger (4). Shown here is merely one possible model for this exchanger. This transporter could involve the influx of two HCO_3^- instead of the influx of one HCO_3^- and the efflux of an H^+. Alternatively, one CO_3^{2-} or two $NaCO_3^-$ could be transported in. These four different variants have the same effect on pH, but can be partially distinguished kinetically. The Na^+-HCO_3^- co-transporter is shown as model 5. This transporter is electrogenic, mediating the movement of n HCO_3^- for each Na^+ and is thus sensitive to membrane potential (V_m). The direction of co-transport depends on the value of V_m. (C) Two different types of H^+-ATPases. The P-type H^+-ATPase (6), typified by the electroneutral gastric H^+, K^+-ATPase, involves a phosphorylated intermediate. The V-type H^+-ATPase (7), typified by the vacuolar H^+-ATPase, does not produce a phosphorylated intermediate.

Other NHE isoforms also exist in cells from lower vertebrates, invertebrates, plants and bacteria. For instance, an unusual isoform, β-NHE, that is 50–75% homologous to NHE-1 and is activated by cAMP (unlike NHE-1) has been described in trout red blood cells. The significance of these different isoforms is still largely unclear, but given the variety of functions performed by NHE in cells, it is not surprising that multiple forms have arisen.

The basic structure of the mammalian plasma membrane NHE isoforms is similar (Fig. 17.6A), containing two major domains, a transmembrane domain and a cytoplasmic domain. In NHE-1 the transmembrane domain (N-terminal ≈500 amino acids) is believed to have 12 membrane-spanning regions with an N-linked glycosylation site on the first external loop. This means that NHE

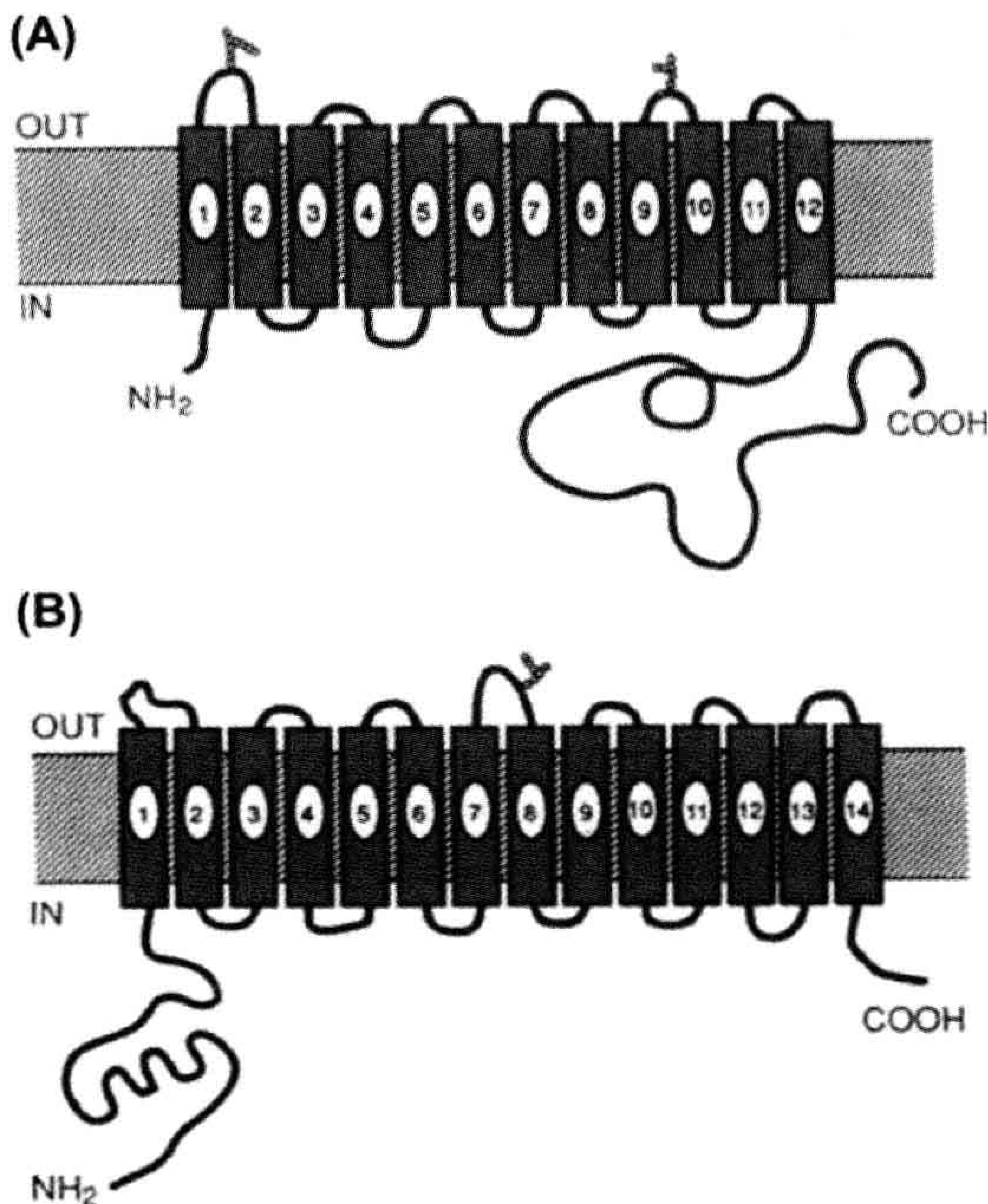


FIGURE 17.6 Models of (A) the structure of the Na^+-H^+ exchanger (NHE-1) and (B) the Cl^--HCO_3^- exchanger (AE 1). The Na^+-H^+ exchanger is believed to have 12 membrane-spanning regions with a large cytoplasmic domain at the C-terminal end. This cytoplasmic domain contains several potential phosphorylation sites that are important to the regulation of the Na^+-H^+ exchanger. The N-terminal end is also cytoplasmic. Two potential glycosylation sites are shown. The Cl^--HCO_3^- exchanger is believed to have 14 membrane-spanning regions and both terminal ends are cytoplasmic. The large cytoplasmic domain is on the N-terminal end in the Cl^--HCO_3^- exchanger. This cytoplasmic domain (in red blood cells at least) contains many binding sites, including those for the cytoskeletal element ankyrin, for hemoglobin, and for some glycolytic enzymes.

is a glycoprotein. The cytoplasmic domain (C-terminal $\approx$300 amino acids) represents a large cytoplasmic region with available serine phosphorylation sites. Both the N- and C-terminal ends of NHE are cytoplasmic. It is believed that the cytoplasmic C-terminal end is involved in the regulation of NHE while the membrane-spanning regions are responsible for Na^+ and H^+ transport. This is borne out by the expression of NHE mutants that lack the C-terminal end in fibroblasts that do not have NHE. In these cells, Na^+-H^+ exchange activity is seen, but can no longer be activated by growth factors. Some variation in this basic structure is seen in other isoforms but the main pattern is the same.

A wide variety of substances have been shown to activate NHE, including hormones, neurotransmitters, growth factors and the extracellular matrix. Many of these factors are believed to activate the NHE by phosphorylating residues on the C-terminal end. These factors may also affect the NHE through the binding of a regulatory protein with the exchanger and/or by binding of a Ca^{2+}—calmodulin complex to a putative autoinhibitory domain on the exchanger. Activation often involves an increase in the affinity of the exchanger's internal binding site for cytoplasmic H^+ (see arrow 1, Fig. 17.3). In some cases, activation of NHE may also involve interaction between the exchanger and the cell cytoskeleton. There is accumulating evidence that NHE isoforms may function best as homodimers. The functional significance of dimerization is unclear. Cell acidification also dramatically activates NHE. This activation is due to an internal allosteric H^+-binding site on NHE (distinct from the H^+ transport site) that increases exchange when occupied. Finally, decreased cell volume (cell shrinkage) also activates NHE. This activation does not involve phosphorylation of NHE and appears to be mediated by a unique activation pathway.

Many signaling pathways can activate NHE, depending on the stimulus. For example, growth factor activation of NHE is usually mediated by an elevation of intracellular Ca^{2+} and/or by an increased activity of protein kinase C. These pathways commonly involve phosphoinositide breakdown. Activation of NHE by cell shrinkage appears to involve ATP- and GTP-dependent pathways.

Much progress has been made to correlate NHE function with structure. As stated above, the transmembrane domain contains the Na^+ and H^+ transport sites. In addition, this domain contains the external amiloride binding site and the internal H^+ allosteric binding site, although the pK for this latter site is markedly acid in the absence of the C-terminal cytoplasmic domain. The C-terminal cytoplasmic domain contains several putative phosphorylation sites and is involved in the regulation of NHE. This region also contains the autoinhibitory domain, the calmodulin binding site, and a possible binding site for the putative cytoplasmic regulatory factor. The C-terminal domain may also contain sites able to interact with cytoskeletal proteins.

Transgenic mice now exist that lack various NHE isoforms such as NHE-1, NHE-2 and NHE-3. All three types of mice are viable, but mice lacking NHE-1 have slowed postnatal development and by 14 days exhibit neurologic symptoms (primarily gait problems and seizures). These mice usually die before weaning. In contrast, high levels of NHE-1 activity, as seen with transient ischemia, result in excessive cellular Na^+ levels and increased intracellular Ca^{2+} which is especially damaging for cardiac and neural cells. Mice lacking NHE-2 are apparently normal, but show long-term gastric changes, including a small decrease in acid secretion and degeneration of parietal cells. Mice lacking NHE-3 also have long-term viability but exhibit gastrointestinal (GI) and renal defects. These defects cause diarrhea, mild acidosis and lowered blood pressure. These symptoms are consistent with a role for NHE-3 in GI and

renal HCO_3^- and fluid absorption. The use of transgenic mice should be helpful in further defining the role of various other NHE isoforms.

The other major cation-H^+ exchanger is the *K^+-H^+ exchanger* (see model 2 in Fig. 17.5A). This transporter exchanges intracellular K^+ for extracellular H^+ and results in cellular acidification. K^+-H^+ exchange has been found in nucleated red blood cells and mediates solute efflux during regulatory volume decrease (see Section VIIIH). It has also been observed in retinal pigment epithelial cells, where it enables the cell to regulate pH_i in the face of an alkaline load.

VIIB. HCO_3^--Dependent Transporters

These transporters are actually a superfamily of related transport proteins (SLC4) that affect pH_i and are characterized by their ability to transport HCO_3^- (or a related species like CO_3^-) and by the ability of disulfonic stilbene derivatives to inhibit them. The three major types of HCO_3^--dependent transporters are Cl^--HCO_3^- exchangers (band 3 from red blood cells, termed AE for anion exchanger), (Na^++HCO_3^-)-Cl^- exchangers (often termed NDCBE for Na^+-dependent or Na^+-driven Cl^--HCO_3^- exchange) and Na^+-HCO_3^- co-transporters (termed NBC for Na^+ bicarbonate co-transport), both electrogenic (NBCe) and electroneutral (NBCn).

The operation of *Cl^--HCO_3^- exchange* (AE) (see model 3 in Fig. 17.5B) has been studied most extensively in red blood cells. This electroneutral transporter involves a 1:1 exchange of Cl^- for HCO_3^- (although many other ions, such as $SO4^-$, can also be transported under specific conditions). As with the Na^+-H^+ exchanger, the Cl^--HCO_3^- exchanger has several isoforms, denoted AE 1, 2 and 3. These various isoforms have about 80–90% homology. AE 1 is widely distributed and is best known as the band 3 transporter from red blood cells. It is the smallest isoform (M_r = 115 000). This protein has as many as 14 (or 13 with a re-entrant loop) membrane-spanning domains (helices) and a large N-terminal cytoplasmic domain that contains various binding sites, including one for ankyrin (see Fig. 17.6B). AE 2 and 3 are larger (M_r = 145 000–165 000). AE 2 appears to be the housekeeping anion exchanger and is the most widely distributed, but is especially prevalent in the choroid plexus and throughout the GI tract. It is activated by cellular alkalinization and returns pH_i to normal by extruding base (HCO_3^-) and thereby re-acidifying the cell. This exchanger may also possess an internal allosteric regulatory site that activates the exchanger at *alkaline* values of pH_i (see the base extrusion curve in Fig. 17.3). In addition to its role in the regulation of pH_i, Cl^--HCO_3^- exchange may also play a role in regulating intracellular Cl^-. The function of AE 3 is not yet clear but it has a far more restricted distribution than AE 2, being found largely in the heart and the central nervous system.

The *(Na^++HCO_3^-)-Cl^- exchanger* (see model 4 in Fig. 17.5B) was originally described as the pH-regulating transport system in invertebrate nerve and muscle preparations, but has since been found in a wide variety of cells. Because it transports Na^+, it operates in the opposite way than Na^+-independent Cl^--HCO_3^- exchange (i.e. the anion exchangers described above). Thus, the (Na^++HCO_3^-)-Cl^- exchanger exchanges one external Na^+ for one internal Cl^- and neutralizes the equivalent of two internal protons. As such, this exchanger is electroneutral and mediates the alkalinization of the cell in response to an acid load. The ability of this exchanger to neutralize two acid equivalents could be achieved by the influx of two HCO_3^-, the influx of one HCO_3^- in exchange for the efflux of one H^+, the influx of one CO_3^{2-}, or the influx of an ion pair ($NaCO_3^-$). In squid axon, this exchanger has been suggested to involve $NaCO_3^-Cl^-$exchange whereas, in barnacle muscle fibers, it must be another variant, suggesting that this exchanger also has at least two isoforms.

The *Na^+-HCO_3^- co-transporter* (NBC) (see model 5 in Fig. 17.5B) was originally identified in renal epithelial cells but has since been found in a number of other cell types as well. It mediates the movement of one Na^+ with one, two or three HCO_3^-, depending on the cell type in which the transporter is located, and can thus be either electroneutral (NBCe) or electrogenic (NBCn). This transporter differs from the other HCO_3^--dependent transporters in that it does not require Cl^- and, in the case where the stoichiometry is 1:2 or 1:3, it is electrogenic. In proximal tubule epithelial cells, NBC is involved in HCO_3^- reabsorption by mediating HCO_3^- efflux across the basolateral membrane. In other cells, the co-transporter is proposed to mediate HCO_3^- influx and contribute to the regulation of intracellular pH in the face of an acid load. The renal co-transporter (1:3 stoichiometry) has been suggested to involve the co-transport of one Na^+ with one HCO_3^- and one CO_3^{2-}. NBCn transporters are widely expressed and play a role in maintaining pH_i and in the secretion of cerebrospinal fluid.

The NBC and several of its variants have been cloned. The first mammalian NBC to be cloned is from rat kidney (rkNBC). This is a glycoprotein consisting of 1035 amino acids (M_r $\approx$130 000). Its structure is similar to other members of the Na^+-HCO_3^--coupled transporters (NCBT: NBCs and NDCBE), includes 12–14 membrane-spanning domains, a large extracellular loop between membrane-spanning segments 5 and 6 that can be glycosylated and large cytoplasmic domains (one each at the N- and C-terminal ends), with the N-terminus domain being the largest. These cytoplasmic domains are probably the site of co-transport regulation and contain putative phosphorylation sites for protein kinases A and C, casein kinase II and tyrosine kinase. A human kidney clone (hkNBC), with 97%

homology to rkNBC, has also been described. These kidney NBCs are electrogenic, with a stoichiometry of one Na^+ transported for every three HCO_3^- ions.

An NBC from human heart (hhNBC) has been described. This clone (along with an identical one from human pancreas) is identical to rkNBC, except that hhNBC has a longer N-terminus (by 44 amino acids); hhNBC is also electrogenic, but with a stoichiometry of 1:2. A similar clone has been isolated from rat brain (rbNBC). This clone has longer C- and N-terminal ends, a stoichiometry of 1:2 and is predominantly localized to cortical neurons but not astrocytes. Finally, a novel clone has been isolated from vascular smooth muscle cells (also found in testis and spleen cells). This clone (NBCn1) has a very large N-terminus, is electroneutral (stoichiometry of 1:1) and is apparently not inhibited by DIDS. These NBC clones are about 30–35% identical to AE transport proteins, indicating that these transporters are indeed part of the SLC4 superfamily.

VIIC. H^+-ATPases (Proton Pumps)

There are at least three known varieties of *H^+-ATPases*: (1) F_0-F_1-type ATPase; (2) E_1-E_2 or P-type ATPase; and (3) vacuolar or V-type ATPase. The *F_0-F_1-type ATPase* is found in mitochondria. This ATPase has also been called the ATP synthase, since it functions to produce ATP when H^+ moves down its electrochemical gradient. F_0-F_1-type ATPase has a lollipop shape and a membrane-spanning region, F_0, that forms the putative H^+ pore through the membrane as well as an extrinsic head region, F_1, that contains the ATPase activity. The F_0 subunit is quite large, with five subunits and a molecular weight of about 380 000. The F_1 region has four subunits and a molecular weight of about 100 000. These two regions are connected by a stalk that contains several subunits, one of which confers sensitivity to oligomycin. The F_0-F_1-type ATPase can be inhibited by azide and N, N'-dicyclohexylcarbodiimide (DCCD) in addition to oligomycin.

The *P-type ATPases* (see model 6 in Fig. 17.5C) are characterized by forming a phosphorylated intermediate upon ATP hydrolysis. The classic example of such an ATPase is the Na^+, K^+-ATPase. An example of a P-type H^+-ATPase is the H^+, K^+-ATPase, best characterized from the apical membrane of gastric glands, where it is responsible for acid secretion into the stomach. This ATPase has also been implicated in the acidification of the urine and reabsorption of K^+ by the kidney and in the establishment of an H^+ gradient across yeast plasma membrane. In contrast to the F_0-F_1-ATPase, the H^+, K^+-ATPase exchanges one K^+ for one H^+ and is thus electroneutral. The H^+, K^+-ATPase has a molecular weight of about 110 000 and has a structure similar to those of other membrane-bound ATPases with several membrane-spanning regions and a large cytoplasmic domain containing the ATP hydrolysis site. Inhibition by vanadate is characteristic for P-type ATPases.

The third type of H^+-ATPase is the vacuolar, or V-type, ATPase (see model 7 in Fig. 17.5C) which is found in yeast and plant vacuoles as well as in several eukaryotic cells (e.g. kidney cells, osteoclasts and macrophages) and organelles (e.g. endosomes, lysosomes, secretory granules and Golgi apparatuses). *V-type ATPases* are more like the F_0-F_1-type ATPase than the P-type ATPase in that they do not form phosphorylated intermediates, are quite large (>400 kDa), assume a lollipop shape and are electrogenic. The major function of V-type ATPases is the acidification of intracellular organelles (see Section VB), which is important for proper protein targeting and handling. These ATPases are characterized by their lack of sensitivity to vanadate and oligomycin and by their inhibition by N-ethylmaleimide (NEM), DCCD and bafilomycin. While P- and F_0-F_1-type ATPases are found in both prokaryotes and eukaryotes, the V-type ATPases are only found in eukaryotes and, therefore, presumably evolved more recently.

VIID. Na^+-Organic Anion Co-transport

In a variety of organisms, renal proximal tubule cells have been shown to have *Na^+-organic anion co-transporters* (model 1 in Fig. 17.7). These co-transporters mediate the influx of a Na^+ with the conjugate base of an organic weak acid, such as lactate or acetate. Such co-transport would cause cellular alkalinization due to the entry of base. The base would bind a proton upon entry and alkalinize the cell. These transport systems are likely to be part of a mechanism designed for the transepithelial movement of organic molecules and should be considered to *affect* pH_i rather than *regulate* it.

VIIE. Chloride-Organic Anion Exchange

Another class of organic anion transporters has been described in renal proximal tubule cells. These transporters involve the exchange of organic anions for inorganic anions such as Cl^- or OH^-. For example, as part of the mechanism for NaCl reabsorption, an exchanger that mediates Cl^- influx (from the lumen) in exchange for formate efflux resides in the apical membrane of proximal tubule epithelia. This *Cl^--formate exchanger* (model 2 in Fig. 17.7) can be inhibited by disulfonic stilbene derivatives and is functionally similar to the Cl^--HCO_3^- exchanger. However, the Cl^--formate exchanger is distinct from the Cl^--HCO_3^- exchanger. The operation of this transporter during NaCl reabsorption should result in epithelial cell acidification. Other transporters involve the movement of organic anions including urate and oxalate. When these

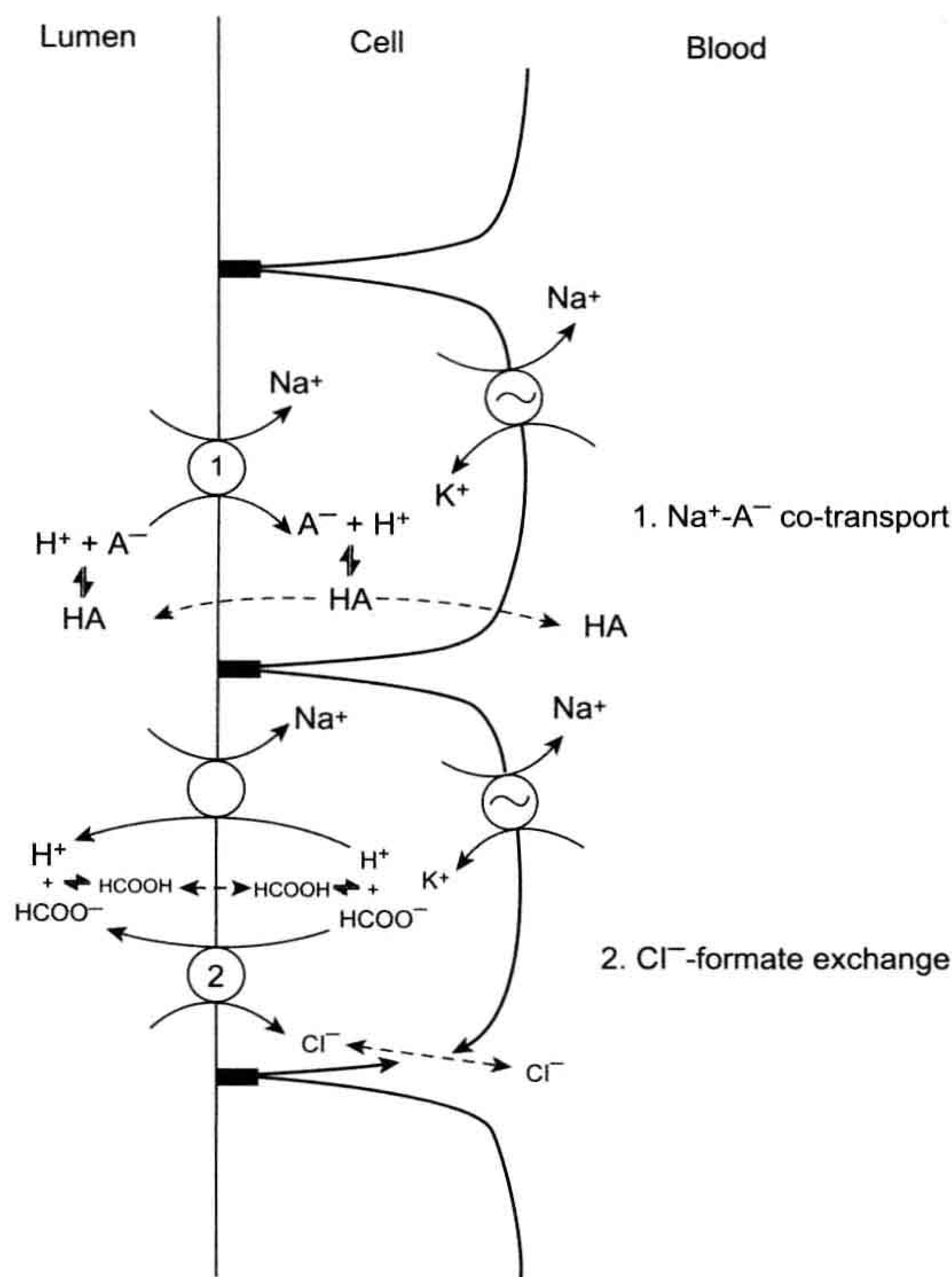


FIGURE 17.7 A model of anionic weak base fluxes in the renal proximal tubule mediated by either co-transport with Na^+ (1) or in exchange for Cl^- (2). An example of 1 is the Na^+-acetate co-transporter. The Cl^--formate exchanger is depicted by 2. These transporters are apparently involved in the luminal entry of Na^+ or Clin NaCl-reabsorbing epithelia like the renal proximal tubule. Solid lines represent ion fluxes mediated by membrane transporters. Dotted lines represent passive diffusion of molecules across the membrane. Cl^- movements across the basolateral membrane are mediated by an ion-selective Cl^- channel.

anions are transported into the cell, they will result in cellular alkalinization.

VIII. CELLULAR FUNCTIONS AFFECTED BY INTRACELLULAR pH

A wide variety of cellular processes and properties are affected by intracellular pH and perhaps in some way all cell functions are influenced by the level of pH_i. It is impossible to discuss all of the various effects, but many of the most important will be highlighted in the following sections (Fig. 17.8).

VIIIA. Cellular Metabolism

The fact that cellular metabolism can affect pH_i was discussed previously (see Section VIA). It has been appreciated for many years that the converse is also true; i.e. changes of pH_i can affect cellular metabolism. Theoretically, because pH will affect the charge on ionizable groups in proteins, it would be anticipated that changes in pH_i could change the configuration of proteins and affect their activity. Such an effect of pH_i has been well documented for two key metabolic enzymes. Phosphofructokinase, a key glycolytic enzyme that converts fructose 6-phosphate (F6P) to fructose 1,6-diphosphate (FDP), has an exquisite pH sensitivity in the physiological range (6.5–7.5), its activity decreasing with a decrease of pH_i. The actual pH sensitivity is dependent on the cellular levels of F6P and 5′-AMP. Similarly, the conversion of phosphorylase (which catalyzes the metabolism of glycogen) from its inactive to active form is inhibited by a decrease in pH_i.

Two observations can be made from these findings. First, the pH dependence of enzyme activity is often affected by the concentrations of other factors, including substrates and other effectors. Thus, caution must be exercised in relating the in vitro pH profile of an enzyme to cellular conditions. Second, the general reaction of metabolic enzymes to a decrease in pH is a reduction in activity. This suggests that a decrease in pH_i could be used to prevent growth or to put a cell in a dormant state, as has been observed for many cells (see Section VIIIG).

VIIIB. Cytoskeleton

Changes in pH_i have been shown to affect the cytoskeleton, which can lead to changes in cell shape or motility. One example of such an effect on the cytoskeleton is the pH dependence of *actin filament* cross-linking to form gels. This cross-linking is mediated by actin-binding proteins whose ability to interact with actin is pH dependent. In some cases, cell alkalinization increases the actin cross-linking to form a gel state in the cytoplasm or to form networks of microfilament bundles. In other cells, alkalinization reduces the cross-linking of actin filaments. The cell-specific responses of cytoskeletal cross-linking are probably due to different pH profiles of actin-binding proteins from different cells.

Changes in cellular pH can also affect the polymerization of cytoskeletal elements, such as *tubulin*. It has been shown that, in some cells, alkalinization can cause depolymerization of tubulin and disaggregation of microtubules within the cell. There are probably many other pH-dependent components to cytoskeletal assembly and function. It should be pointed out, however, that the conditions that lead to a change in pH_i are often accompanied by changes in intracellular calcium concentration and by phosphorylation of the cytoskeleton and it is not always clear which is the predominant effector of cytoskeletal changes. Nevertheless, it is clear that changes in

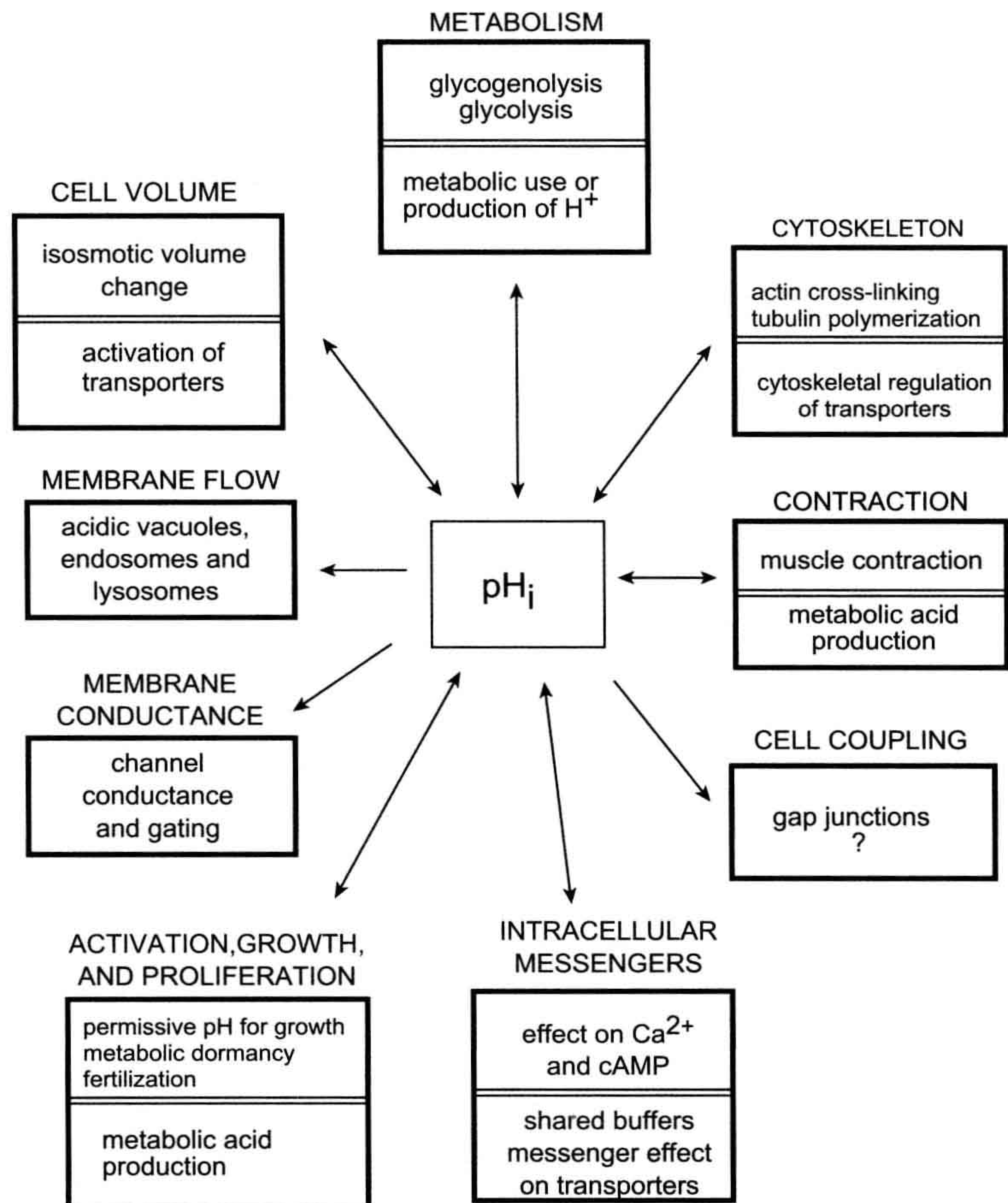


FIGURE 17.8 A summary of the cellular processes affected by intracellular pH. Each box represents a different cellular process. A two-headed arrow indicates that pH_i affects the process and that the process can also affect pH_i. Single-headed arrows suggest that pH affects that cellular function but that the cellular process probably does not have a major impact on pH_i. Within a box, the top half indicates the cellular processes affected by pH_i, while the bottom half indicates the mechanisms by which the process can affect pH_i.

pH_i can play a major modulatory role in at least some alterations of the cytoskeleton.

VIIIC. Muscle Contraction

Intracellular acidification is known to reduce the ability of contractile cells to generate tension. This effect is particularly marked in cardiac muscle, but skeletal muscle also shows a reduced contractility at acidic values of pH_i. There are several possible ways by which cellular acidification could influence contractility: changes in surface channels could reduce cellular excitability, low pH could prevent calcium release from the sarcoplasmic reticulum through the calcium release channel, protons could compete with calcium for binding to the regulatory protein troponin, protons could inhibit the myofibrillar ATPase, or acidification could impair the ability of the cell to generate ATP. The effect of pH on muscle contraction could also be indirect. For example, during intense muscle activity, inorganic phosphate (P_i) accumulates in the cell. A reduced pH will increase the diprotonated form of P_i ($H_2PO_4^-$), which has been shown to be particularly effective in inhibiting muscle force development during muscle fatigue.

VIIID. Cell–Cell Coupling

The coupling of cells through *gap junctions* is apparently affected by intracellular pH. Several studies have suggested that a fall in pH_i uncouples gap junctions, thereby eliminating cell–cell coupling. The direct role of pH_i in the uncoupling process has been questioned and it appears that

changes in intracellular Ca^{2+} levels are responsible for uncoupling in some cells. The control of gap junction conductance may differ from cell to cell, but even in cells where Ca^{2+} is the primary regulator, changes in pH_i probably still have a modulatory effect on gap junction conductance.

VIIIE. Membrane Conductance

Ion-selective channels require the presence of charges within the channel proteins for proper ion conduction and channel gating. If these charges have p*K* values within the physiological range, these channels could well be affected by changes in pH. Indeed, the conductances of many channels are affected by changes in either pH_o or pH_i, including the tetrodotoxin-sensitive Na^+ channel, the delayed-rectifying and inward-rectifying K^+ channels and Cl^- channels. Through the effect on conductance of membrane channels, changes in pH can affect the excitability of nerve and muscle cells and alter the membrane potential in all cells.

One interesting pH-sensitive K^+ channel has been described, the TASK channel (for TWIK-related acid-sensitive K^+ channel). The TASK channel exhibits rectification in asymmetric K^+ solutions that is consistent with the Goldman–Hodgkin–Katz equation, is non-inactivating, is not voltage sensitive and is highly sensitive to changes in *external* pH, with channel conductance falling with decreased pH_o. This type of leak channel is believed to be partly responsible for the resting membrane potential (especially in pancreas, placenta and brain cells) and could explain the relationship between changes of pH_o and membrane potential in these cells.

VIIIF. Intracellular Messengers

Changes in pH_i can affect the levels of important intracellular signaling molecules, such as Ca^{2+} and cAMP. There are several possible ways by which pH can affect intracellular Ca^{2+}. An elevation of cytoplasmic H^+ can activate mitochondrial Ca^{2+}-H^+ exchange, resulting in a sequestering of H^+ within the mitochondria and an elevation of cytoplasmic $[Ca^{2+}]$. A decreased pH_i can reduce Ca^{2+} entry across the plasmalemma. The most direct interaction between cytoplasmic H^+ and Ca^{2+} ions, however, results from shared buffers. Many molecules that buffer H^+ will also bind, and thus buffer, Ca^{2+}. Depending on the relative affinities, an elevation of cytoplasmic $[H^+]$ can elevate intracellular $[Ca^{2+}]$ by displacing Ca^{2+} ions from intracellular buffer sites.

The interaction between changes of pH_i and $[Ca^{2+}]_i$ can also be indirect. An example of such an interaction is the pH-dependence of the binding of Ca^{2+} to calmodulin. Under certain conditions, a decrease in pH can be shown to reduce the binding of Ca^{2+} to calmodulin. Another example of the interaction between pH and Ca^{2+} is the pH-dependence of the interaction of the Ca^{2+}–calmodulin complex with other proteins, the direction of which depends on the protein being considered. Thus, the potential exists for changes of pH_i to alter the effect of Ca^{2+} on cellular function.

Changes of pH_i could affect another important intracellular signaling pathway as well, that involving cAMP. The proposed effects of pH_i on cAMP are based on the pH dependence of adenylyl cyclase (AC – the enzyme that synthesizes cAMP) and the cyclic nucleotide phosphodiesterase (PDE – the enzyme that hydrolyzes cAMP). In most cells, PDE apparently has a rather constant activity over the physiological range of pH (6.5–7.5). However, depending on the cell, an increase in pH can either markedly increase or decrease AC activity. Thus, alkalinization can result in either an increase or a decrease in cellular cAMP levels.

Given the pervasive effect of changes of pH_i on proteins, it is likely that pH_i effects on other signaling pathways, such as those mediated by cGMP or phosphoinositide metabolism, also exist. It should be noted, however, that the physiological significance of these pH_i effects on signaling pathways is often not clear, especially for cells that normally should see only small fluctuations of pH_i.

Some cells in the body function to sense changes in external pH, either in direct response to external acid (acid-sensing taste bud cells) or to elevated external CO_2 (glomus cells of the carotid body and central chemosensitive neurons). In these cells, extracellular acidification results in a *maintained* intracellular acidification, with pH recovery mechanisms being inhibited (most likely by decreased pH_o). It is believed that this decrease in pH_i inhibits K^+ channels, resulting in cell depolarization and increased generation of action potentials. Thus, in these chemosensitive cells, a decrease in pH_i apparently acts as an intracellular signal.

VIIIG. Cell Activation, Growth and Proliferation

One of the most active areas of research on the role of intracellular pH in cell function has been the study of the role of changes of pH_i early in cell proliferation. These studies grew out of early observations that, shortly after fertilization of sea urchin eggs, egg pH increased markedly (roughly 0.4 pH unit) and this rise in pH was necessary for the initiation of growth by fertilization. These observations were followed by others on mammalian cells showing that a variety of growth-promoting agents, including epidermal growth factor (EGF), platelet-derived growth factor (PDGF), insulin, vasopressin and serum albumin, similarly

induced a cellular alkalinization (of about 0.1–0.2 pH unit) shortly after exposure. All of these alkalinizing effects are mediated by activation of Na^+-H^+ exchange. These growth-promoting agents activate the exchanger by activating cellular signaling pathways, which increase the affinity of the exchanger for internal H^+ ions and increase its activity, thereby alkalinizing the cell (see arrow 1 in Fig. 17.3).

It was initially hypothesized that the growth factor-induced increase in pH was part of a suite of early signals that are required for initiation of cell growth and proliferation. Cellular alkalinization was believed to contribute to the initiation of growth by activating key cellular enzymes that were then either direct effectors of growth (e.g. metabolic enzymes) or activators of other systems.

The direct signaling role of increases of pH_i in cell activation has been questioned. Changes in pH_i by themselves do not promote cell growth or division. Further, it has been shown that a number of cells have a higher pH_i in the presence of 5% CO_2 than in its absence. However, most of the initial experiments on the pH_i responses to growth factors had been done in the absence of CO_2. Upon repeating a number of these experiments under conditions more similar to physiological conditions (presence of 5% CO_2), the initial alkalinization upon exposure to stimulatory factors was not always seen and, in some cells, the initial response was indeed an *acidification*. Thus, the current view of the role of pH_i in cell activation, growth and proliferation is that pH_i plays a permissive role. That is, cells will only grow and proliferate if pH_i is above a certain critical value, regardless of how that value is obtained. If a cell had a pH_i above the critical value before exposure to a stimulatory agent, no change in pH_i would be required for cell growth. In fact, the cell could acidify and still grow as long as its pH_i stays above the critical value.

In reality, the role of pH_i as a signal to initiate cell growth may depend on the cell and the activating agent. It is likely that a rapid and marked rise in pH_i is one of the critical early steps necessary for the initiation of growth in fertilized sea urchin eggs. Even more dramatic is the nearly 1-pH-unit increase of pH_i in *Artemia* (brine shrimp) embryos upon arousal from anaerobic dormancy by exposure to oxygen. Undoubtedly, this large rise in pH_i is crucial for the transition from metabolic dormancy in these organisms. On the other hand, in many mammalian cells, the rather modest increase in pH_i on exposure to an activating agent is probably of limited physiological significance, especially given the variability in the degree and direction of pH changes observed in different experimental conditions.

Finally, even under conditions where a change of pH_i is not observed in response to a stimulatory agent, pH-regulating transport systems can still be shown to be activated. It has been hypothesized that, although a change of pH_i may not be crucial for the stimulation of cell growth, the initiation of this growth may confront the cell with an acid or alkaline load. In this regard, activation of the pH-regulating transport systems by growth-promoting agents could be viewed as preparatory, enabling the cell better to maintain a constant pH_i during a period of high metabolic activity.

VIIIH. Cell Volume Regulation

Most pH-regulating transporters move ions such as Na^+ and Cl^- in exchange for a proton equivalent (H^+ or HCO_3^-). Because the transported proton equivalents are buffered (H^+ by HCO_3^- and protein buffers and HCO_3^- by formation of CO_2), they are osmotically "invisible". For example, virtually all of the H^+ transported by the Na^+-H^+ exchanger derive from internal buffers and upon efflux from the cell are buffered by external buffers. Thus, the Na^+-H^+ exchanger mediates the net import of one osmotically active particle (Na^+) and this import of osmolytes will be accompanied by the influx of water and cell swelling. Therefore, the Na^+-H^+ exchanger, in addition to contributing to pH_i regulation, can mediate the regulation of cell volume.

Other pH-regulating transporters can similarly mediate cell volume changes. For example, the Cl^-- HCO_3^- exchanger transports Cl^- into the cell. The HCO_3^- that leaves combines with an H^+ and is removed as CO_2. Thus, like Na^+-H^+ exchange, Cl^--HCO_3^- exchange contributes to cell swelling. In fact, these two exchangers often act in concert to result in the net influx of NaCl (and therefore water) into the cell. The Na^+-HCO_3^- and Na^+-anionic weak base co-transporters would be ideally suited to mediate net solute transfer and therefore cell volume change. Finally, the (Na^++HCO_3^-)-Cl^- exchanger should not contribute to cell volume regulation because it mediates the entry of one osmotically active ion (Na^+) for the efflux of another (Cl^-).

Cell volume can be rapidly changed by exposure to anisosmotic media, with hypertonic media causing cell shrinkage and hypotonic media causing cell swelling. Many cells respond to shrinkage with a *regulatory volume increase* (RVI) that involves the net uptake of solutes, and therefore water, so that cells swell back toward the initial cell volume (Fig. 17.9). In several different types of cells, RVI has been shown to involve an activation of Na^+-H^+ exchange. This exchanger, often in association with the Cl^--HCO_3^- exchanger, results in NaCl influx and a regulatory volume increase. The mechanism by which cell shrinkage activates the Na^+-H^+ exchanger is not fully understood but, interestingly, unlike most other activation pathways, cell shrinkage apparently does not result in phosphorylation of the exchanger. It is possible that the cell cytoskeleton is involved in activating the Na^+-H^+ exchanger upon cell shrinkage.

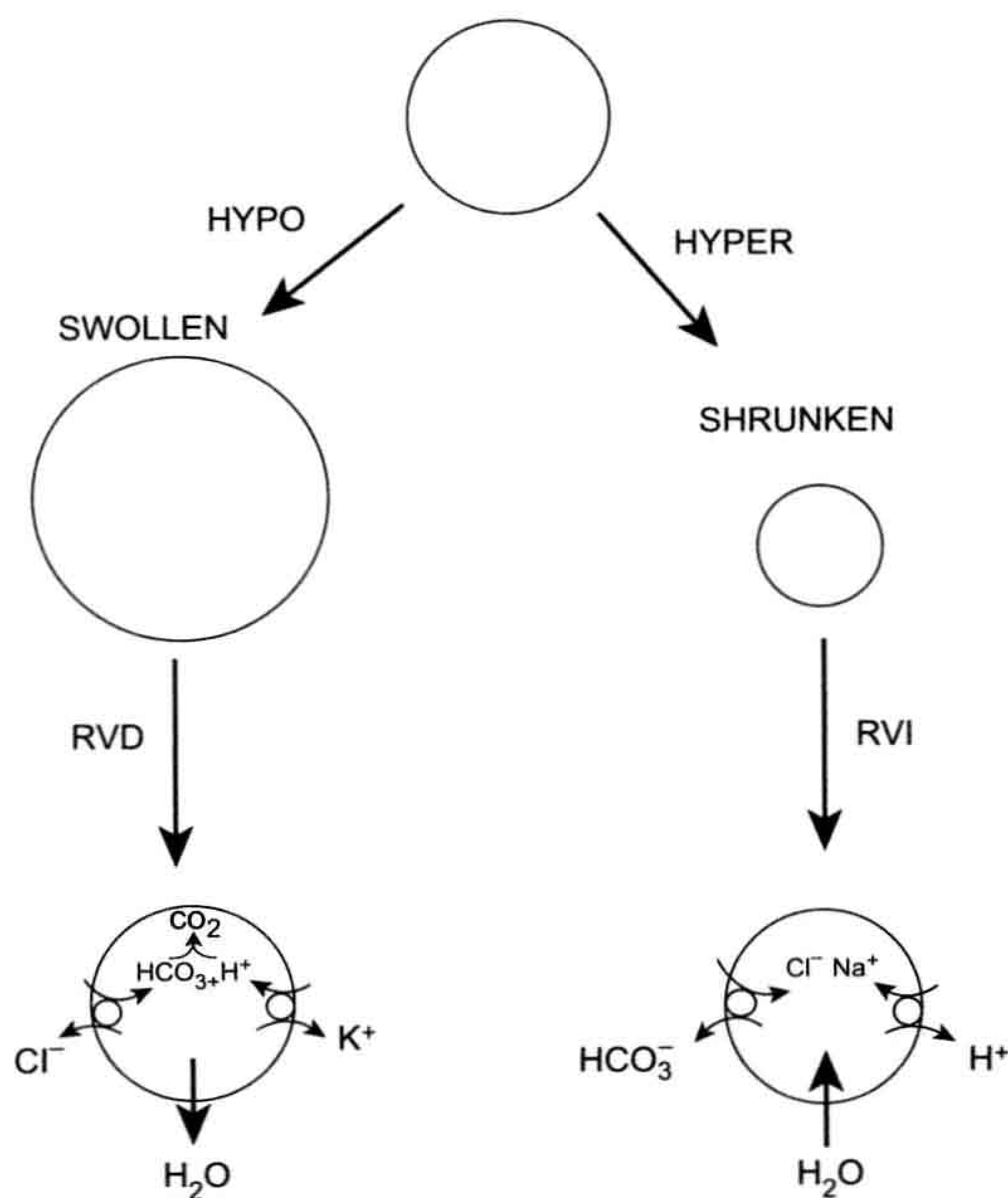


FIGURE 17.9 The role of pH-regulating transporters in cellular volume regulation. Upon cell swelling in hypotonic media, KCl has been shown to be removed from nucleated red blood cells by functionally coupled operation of the K^+-H^+ and the Cl^--HCO_3^- exchangers. The removal of KCl from the cell causes a loss of water from the cell and thus cell shrinkage in a process called regulatory volume decrease (RVD). Upon cell shrinkage in hypertonic media, NaCl enters the cell by parallel operation of Na^+-H^+ and Cl^--HCO_3^- exchangers. The NaCl entry results in water influx and cell swelling in a process called regulatory volume increase (RVI).

Recently, it has been shown that shrinkage can also activate (Na^++ HCO_3^-)-Cl^- exchange in some cells. This observation is interesting since, as stated previously, this exchanger does not mediate any net solute movement and thus should not directly contribute to cell volume regulation. This activation of (Na^++HCO_3^-)-Cl^- exchange by cell shrinkage suggests that pH-regulating transporters may be activated by shrinkage to alkalinize the cell regardless of whether they contribute to volume regulation. It is not clear what benefit a shrunken cell derives from becoming alkaline, but it may involve pH-dependent cytoskeletal rearrangements (see Section VIIIB).

In response to swelling, most cells exhibit a *regulatory volume decrease* (RVD). RVD involves the efflux of solutes accompanied by water and therefore cell shrinkage back toward the initial cell volume (see Fig. 17.9). In at least one cell type, the nucleated red blood cell, RVD has been shown to be mediated by K^+-H^+ exchange (K^+ efflux and H^+ influx) in association with Cl^--HCO_3^- exchange (Cl^- efflux and HCO_3^- influx).

Cell volume can also be altered under isosmotic conditions by an imbalance of solute influx and efflux. For instance, during periods of active pH recovery from acidification, the Na^+ influx mediated by the Na^+-H^+ exchanger could result in cell swelling. Thus, changes in pH_i and the response to them could result in an alteration of cell volume.

It is clear that the regulation of intracellular volume and intracellular pH are highly linked in most cells. This linkage is due in part to the use of many of the same membrane transport systems for the regulation of cell pH and volume. In any given cell type, these transporters may respond predominantly either to changes in pH_i or to changes in cell volume.

VIIII. Intracellular Membrane Flow

The intracellular flow of membranes is affected by changes of pH within acidic vacuolar compartments. In cells, these vacuolar compartments are often involved in the movement of membranes, membrane-bound proteins and soluble proteins around the cell. In addition, components of the vacuolar system are involved in the synthesis, processing and degradation of various proteins. This system includes the endoplasmic reticulum, the Golgi apparatus, lysosomes and endosomes. Movement of materials through this system can be divided into the endocytic and exocytic pathways. The endocytic pathway is involved in the uptake of external macromolecules, the degradation or delivery to the cell of these macromolecules and the downregulation of surface proteins; it includes coated pits, endosomes and lysosomes. The exocytic pathway delivers newly-synthesized proteins to a variety of sites, including the surface membrane or extracellular space. Many of the compartments within this vacuolar system are acidic (see Section VB) and the maintenance of an acidic interior is critical for the functioning of these compartments. This criticality has been shown by the marked disturbance of endocytic and exocytic pathways by a number of agents, such as chloroquine and ammonia, which alkalinize these compartments. In addition, inhibition of vacuolar H^+-ATPase results in alkalinization of the acidic compartments and can lead to inhibition of endocytosis and exocytosis. Thus, the maintenance of a proper pH in acidic intracellular compartments is crucial for continued and proper intracellular membrane flow.

BIBLIOGRAPHY

Al-Awqati, Q. (1986). Proton-translocating ATPases. *Annu Rev Cell Biol, 2*, 179–199.

Alper, S. L. (2009). Molecular physiology and genetics of Na^+-independent SLC4 anion exchangers. *J Exp Biol, 212*, 1672–1683.

Ammann, D., Lanter, F., Steiner, R. A., Schulthess, P., Shijo, Y., & Simon, W. (1981). Neutral carrier based hydrogen ion selective

microelectrode for extra- and intracellular studies. *Anal Chem, 53*, 2267–2269.

Aronson, P. S. (1989). The renal proximal tubule: a model for diversity of anion exchangers and stilbene-sensitive anion transporters. *Annu Rev Physiol, 51*, 419–441.

Aronson, P. S., & Boron, W. F. (Eds.), (1986). *Na^+-H^+ Exchange, Intracellular pH, and Cell Function, Vol. 26 in Current Topics in Membranes and Transport*. New York: Academic Press.

Aronson, P. S., Nee, J., & Suhm, M. A. (1982). Modifier role of internal H^+ in activating the Na^+-H^+ exchanger in renal microvillus membrane vesicles. *Nature, 299*, 161–163.

Attaphitaya, S., Park, K., & Melvin, J. E. (1999). Molecular cloning and functional expression of a rat Na^+/H^+ exchanger (NHE5) highly expressed in brain. *J Biol Chem, 274*, 4383–4388.

Baird, N. R., Orlowski, H., Szabo, E. Z., et al. (1999). Molecular cloning, genomic organization, and functional expression of Na^+/H^+ exchanger isoform 5 (NHE5) from human brain. *J Biol Chem, 274*, 4377–4382.

Bell, S. M., Schreiner, C. M., Schultheis, P. J., et al. (1999). Targeted disruption of the murine Nhe1 locus induces ataxia, growth retardation, and seizures. *Am J Physiol, 276*, C788–C795.

Bidani, A., & Brown, S. E. S. (1990). ATP-dependent recovery in lung macrophages: evidence for a plasma membrane H^+-ATPase. *Am J Physiol, 259*, C586–C598.

Bock, G., & Marsh, J. (1988). *Proton Passage across Cell Membranes. Ciba Foundation Symposium 139*. New York: Wiley.

Boron, W. F. (1986). Special topic: acid/base physiology. *Annu Rev Physiol, 48*, 347–413.

Boron, W. F., & Boulpaep, E. L. (1983). Intracellular pH regulation in the renal proximal tubule of the salamander. Basolateral H cotransport. *J Gen Physiol, 81*, 53–94.

Boron, W. F., & De Weer, P. (1976). Intracellular pH transients in squid giant axons caused by CO_2, NH_3, and metabolic inhibitors. *J Gen Physiol, 67*, 91–112.

Boron, W. F., Chen, L., & Painter, M. D. (2009). Modular structure of sodium-coupled bicarbonate transporters. *J Exp Biol, 212*, 1697–1706.

Busa, W. B., & Nuccitelli, R. (1984). Metabolic regulation via intracellular pH. *Am J Physiol, 246*, R409–R438.

Cala, P. M. (1980). Volume regulation by Amphiuma red blood cells. The membrane potential and its implications regarding the nature of the ion-flux pathways. *J Gen Physiol, 76*, 683–708.

Capasso, M., DeCoursey, T. E., & Dyer, M. J. S. (2011). pH regulation and beyond: unanticipated functions for the voltage-gated proton channel, HVCN1. *Trends Cell Biol, 21*, 20–28.

Chamberlin, M. E., & Strange, K. (1989). Anisosmotic cell volume regulation: a comparative view. *Am J Physiol, 257*, C159–C173.

Chesler, M. (2003). Regulation and modulation of pH in the brain. *Physiol Rev, 83*, 1183–1221.

Counillon, L., & Pouysségur, J. (1995). Structure-function studies and molecular regulation of the growth factor activatable sodium-hydrogen exchanger (NHE-1). *Cardiovasc Res, 29*, 147–154.

DeCoursey, T. E., & Cherney, V. V. (1994). Voltage-activated hydrogen ion currents. *J Membr Biol, 141*, 1994.

Duprat, F., Lessage, F., Fink, M., Reyes, R., Heurteaux, C., & Lazdunski, M. (1997). TASK, a human background K^+ channel to sense external pH variations near physiological pH. *EMBO J, 16*, 5464–5471.

Durham, J. H., & Hardy, M. A. (Eds.), (1989). *Bicarbonate, Chloride, and Proton Transport Systems, Vol. 574*. New York: New York Academy of Sciences.

Edmonds, B. T., Murray, J., & Condeelis, J. (1995). pH regulation of the F-actin binding properties of Dictyostelium elongation factor 1a. *J Biol Chem, 270*, 15222–15230.

Gevers, W. (1977). Generation of protons by metabolic processes in heart cells. *J Molec Cell Cardiol, 9*, 867–874.

Grinstein, S. (1996). Non-invasive measurement of the luminal pH of compartments of the secretory pathway. *Physiologist, 39*, 144.

Grinstein, S. (Ed.), (1988). *Na^+/H^+ Exchange*. Boca Raton: CRC Press.

Grinstein, S., & Rothstein, A. (1986). Mechanisms of regulation of the Na^+/H^+ exchanger. *J Membr Biol, 90*, 1–12.

Häussinger, D. (Ed.), (1988). *pH Homeostasis. Mechanisms and Control*. New York: Academic Press.

Hille, B. (1992). *Ionic Channels of Excitable Membranes*. Sunderland, MA: Sinauer Associates.

Hochachka, P. W., & Mommsen, T. P. (1983). Protons and anaerobiosis. *Science, 219*, 1391–1397.

Hoffmann, E. K., & Simonsen, L. O. (1989). Membrane mechanisms in volume and pH regulation in vertebrate cells. *Physiol Rev, 69*, 315–382.

Karniski, L. P., & Aronson, P. S. (1985). Chloride/formate exchange with formic acid recycling: a mechanism of active chloride transport across epithelial membranes. *Proc Natl Acad Sci USA, 82*, 6362–6365.

Kopito, R. R., & Lodish, H. F. (1985). Primary structure and transmembrane orientation of the murine anion exchange protein. *Nature, 316*, 234–238.

Kotyk, A., & Slavik, J. (1989). *Intracellular pH and Its Measurement*. Boca Raton: CRC Press.

Llopis, J., McCaffery, J. M., Miyawaki, A., Farquhar, M. G., & Tsien, R. Y. (1998). Measurement of cytosolic, mitochondrial, and Golgi pH in single living cells with green fluorescent proteins. *Proc Natl Acad Sci USA, 95*, 6803–6808.

Lowe, A. G., & Lambert, A. (1983). Chloride-bicarbonate exchange and related transport processes. *Biochim Biophys Acta, 694*, 353–374.

Madshus, I. H. (1988). Regulation of intracellular pH in eukaryotic cells. *Biochem J, 250*, 1–8.

Masuda, A., Oyamada, M., Nagaoka, T., Tateishi, N., & Takamatsu, T. (1998). Regulation of cytosol-nucleus pH gradients by K^+/H^+ exchange mechanism in the nuclear envelope of neonatal rat astrocytes. *Brain Res, 807*, 70–77.

Murer, H., Hopfer, U., & Kinne, R. (1976). Sodium/proton antiport in brush-border membranes isolated from rat small intestine and kidney. *Biochem J, 154*, 597–604.

Noël, J., & Pouysségur, J. (1995). Hormonal regulation, pharmacology, and membrane sorting of vertebrate Na^+/H^+ exchanger isoforms. *Am J Physiol, 268*, C283–C296.

Nosek, T. M., Fender, K. Y., & Godt, R. E. (1987). It is diprotonated inorganic phosphate that depresses force in skinned skeletal muscle fibers. *Science, 236*, 191–193.

Nuccitelli, R., & Deamer, D. W. (Eds.), (1981). *Intracellular pH: its Measurement, Regulation, and Utilization in Cellular Function*. New York: A. R. Liss.

Orlowski, J., & Grinstein, S. (2004). Diversity of the mammalian sodium/proton exchanger SLC9 gene family. *Pflügers Arch, 447*, 549–565.

Palokangas, H., Metsikkö, K., & Väänänen, K. (1994). Active vacuolar H^+ ATPase is required for both endocytic and exocytic processes during viral infection of BHK-21 cells. *J Biol Chem, 269*, 17577–17585.
Pouysségur, J., Sardet, C., Franchi, A., L'Allemain, G., & Paris, S. (1984). A specific mutation abolishing Na^+/H^+ antiport activity in hamster fibroblasts precludes growth at neutral and acidic pH. Proc Natl. *Acad Sci USA, 81*, 4833–4837.
Putnam, R. W. (2010). CO_2 chemoreception in cardiorespiratory control. *J Appl Physiol, 108*, 1796–1802.
Putnam, R. W., Filosa, J. A., & Ritucci, N. A. (2004). Cellular mechanisms involved in CO_2 and acid signaling in chemosensitive neurons. *Am J Physiol Cell Physiol, 287*, C1493–C1526.
Reusch, H. P., Lowe, J., & Ives, H. E. (1995). Osmotic activation of a Na^+-dependent Cl^-/HCO_3^- exchanger. *Am J Physiol, 268*, C147–C153.
Rink, T. J., Tsien, R. Y., & Pozzan, T. (1982). Cytoplasmic pH and free Mg^{2+} in lymphocytes. *J Cell Biol, 95*, 189–196.
Ritucci, N. A., Chambers-Kersh, L., Dean, J. B., & Putnam, R. W. (1998). Intracellular pH regulation in neurons from chemosensitive and nonchemosensitive areas of the medulla. *Am J Physiol, 275*, R1152–R1163.
Ritucci, N. A., Dean, J. B., & Putnam, R. W. (1997). Intracellular pH response to hypercapnia in neurons from chemosensitive areas of the medulla. *Am J Physiol, 273*, R433–R441.
Romero, M. F., & Boron, W. F. (1999). Electrogenic Na^+/HCO_3^- cotransporters: cloning and physiology. *Annu Rev Physiol, 61*, 699–723.
Roos, A., & Boron, W. F. (1980). The buffer value of weak acids and bases: origin of the concept, and first mathematical derivation and application to physicochemical systems. The work of M. Koppel and K. Spiro (1914). *Respir Physiol, 40*, 1–32.
Roos, A., & Boron, W. F. (1981). Intracellular pH. *Physiol Rev, 61*, 296–434.
Sardet, C., Counillon, L., Franchi, A., & Pouysségur, A. (1990). Growth factors induce phosphorylation of the Na^+/H^+ antiporter, a glycoprotein of 110 kD. *Science, 247*, 723–726.
Sardet, C., Franchi, A., & Pouysségur, J. (1989). Molecular cloning, primary structure, and expression of the human growth factor-activatable Na^+/H^+ antiporter. *Cell, 56*, 271–280.
Schultheis, P. J., Clarke, L. L., Meneton, P., Nieman, M. L., Riddle, T. M., Flagella, M., Duffey, J. J., Doetschman, T., Miller, M. L., & Shull, G. E. (1998). Renal and intestinal absorptive defects in mice lacking the NHE3 Na^+/H^+ exchanger. *Nat Genet, 19*, 282–285.
Schultheis, P. J., Clarke, L. L., Meneton, P., Harline, M., Boiven, G. P., Stemmermann, G., Duffey, J. J., Doetschman, T., Miller, M. L., & Shull, G. E. (1998). Targeted disruption of the murine Na^+/H^+ exchanger isoform 2 gene causes reduced viability of gastric parietal cells and loss of net acid secretion. *J Clin Invest, 101*, 1243–1253.
Seksek, O., & Bolard, J. (1996). Nuclear pH gradient in mammalian cells revealed by laser microspectrofluorimetry. *J Cell Sci, 109*, 257–262.
Seksek, O., Biwersi, J., & Verkman, A. S. (1995). Direct measurement of trans-Golgi pH in living cells and regulation by second messengers. *J Biol Chem, 270*, 4967–4970.
Soleimani, M., & Aronson, P. S. (1989). Ionic mechanism of Na^+-HCO_3^- cotransport in rabbit renal basolateral membrane vesicles. *J Biol Chem, 264*, 18302–18308.
Svichar, N., Esquenazi, S., Chen, H. Y., & Chesler, M. (2011). Preemptive regulation of intracellular pH in hippocampal neurons by a dual mechanism of depolarization-induced alkalinization. *J Neurosci, 31*, 6997–7004.
Thomas, J. A., Buchsbaum, R. N., Zimniak, A., & Racker, E. (1979). Intracellular pH measurements in Ehrlich ascites tumor cells utilizing spectroscopic probes generated in situ. *Biochemistry, 18*, 2210–2218.
Thomas, R. C. (1974). Intracellular pH of snail neurones measured with a new pH-sensitive glass micro-electrode. *J Physiol (London), 238*, 159–180.
Thomas, R. C. (1978). *Ion-sensitive Intracellular Microelectrodes. How to Make and Use Them.* New York: Academic Press.
Trivedi, B., & Danforth, W. H. (1966). Effect of pH on the kinetics of frog muscle phosphofructokinase. *J Biol Chem, 241*, 4110–4111.
Wakabayashi, S., Ikeda, T., Iwamoto, T., Pouysségur, J., & Shigekawa, M. (1997). Calmodulin-binding autoinhibitory domain controls "pH-sensing" in the Na^+/H^+ exchanger NHE1 through sequence-specific interaction. *Biochemistry, 36*, 12854–12861.
Wakabayashi, S., Shigekawa, M., & Pouysségur, J. (1997). Molecular physiology of vertebrate Na^+/H^+ exchangers. *Physiol Rev, 77*, 51–74.
Yun, C. H. C., Tse, C.-M., Nath, S. K., Levine, S. A., Brant, S. R., & Donowitz, M. (1995). Mammalian Na^+/H^+ exchanger gene family: structure and function studies. *Am J Physiol, 269*, G1–G11.

Section III

Membrane Excitability and Ion Channels

Chapter 18

Cable Properties and Propagation of Action Potentials

Nicholas Sperelakis

Chapter Outline

I. SUMMARY

Although the *biological cable* (i.e. nerve fiber or skeletal muscle fiber) is the best possible, it is a relatively poor cable with a short *length constant* and relatively long *time constant*. Therefore, for faithful and rapid signal transmission over long distances, energy must be put into the system at each point along the way. The system evolved is that of action potential (AP) generation, which are *all-or-none signals* of constant amplitude and constant propagation velocity, in addition to having refractory periods and sharp thresholds. This is a *frequency-modulated* system, in which increasing strength of sensation or motor response follows from an increase in frequency of the AP signals.

AP propagation occurs by means of *local-circuit currents*. The transmembrane current has three phases: outward, inward and outward. The internal and external longitudinal currents have two phases: forward and backward (for internal) or backward and forward (for external). The external currents use the path of least resistance, enabling *electrograms* (e.g. ECG, EMG) to be recorded from the body surface. The compound AP is graded in amplitude, reflecting the summation of the external currents generated from each fiber that is activated; i.e. the more fibers simultaneously activated, the greater the amplitude of the electrogram signal.

Propagation velocity is faster when (1) the diameter of the fiber is larger, (2) the length constant is longer, and (3) the time constant and capacitance are lower. The *myelin sheath* evolved by vertebrates enables much faster propagation velocity and at a lower energy cost. Myelination raises the effective membrane resistance and lowers the effective capacitance. Excitability occurs only at the short *nodes of Ranvier* that periodically interrupt the myelin sheath. Therefore, the AP signal jumps from node to node in a saltatory pattern of conduction.

Cell Physiology Sourcebook. DOI: 10.1016/B978-0-12-387738-3.00018-4

II. INTRODUCTION

The resting potential (RP) of cells enables the electrogenesis of *action potentials* and excitability. In this chapter, we examine the mechanism for propagation of the APs and excitability from one part of a neuron or muscle to a distal part.

It is imperative that the body be able to transmit a signal from one point to another very rapidly. The only way that this can be accomplished is by an electrical mechanism. Blood flow and diffusion and signaling molecules are much too slow to allow rapid signaling. In contrast, electricity flows very quickly, at the speed of light (3×10^8 m/s) in a copper wire or about one-ninth the speed of light in a water solution (like the composition of the body). (The velocity of electricity in solution is equal to the velocity of light (c) divided by the square root of the dielectric constant of water [which is 81].) Therefore, the body makes use of electricity for rapid signaling in the nervous system, skeletal muscle, heart and smooth muscles. Propagation velocity is about 120 m/s in our fastest nerve fibers, about 6 m/s in skeletal muscle, about 0.5 m/s in heart and about 0.05 m/s in smooth muscle (Table 18.1).

One example of the need for very fast communication or signaling is the process of walking. Very rapid signals must travel from the motor cortex of the brain, down to the lower spinal cord region and out the motor axons to the skeletal muscles of the lower extremities (Fig. 18.1). In this process, the signal crosses one or more *synapses*, which are regions in which one neuron ends and the next one begins and in which a special chemical neurotransmitter signal is involved (Fig. 18.2). At the termination of each branch of a motor nerve axon on the skeletal muscle fiber, there is another synapse, known as the *neuromuscular junction* or *motor end-plate* (see Fig. 18.1). The signal crosses the neuromuscular junction and gives rise to an AP in the muscle fiber that propagates in both directions from the motor end-plate. The muscle AP elicits contraction. Receptors in the muscles (e.g. stretch receptors) transmit information (in the form of propagating APs) back into the central nervous system (CNS). Thus, in walking, there is a continuous rapid flow of information and instructions to the muscles in both directions: out of the CNS and into the CNS. Therefore, even a relatively simple skeletal activity such as walking would not be possible without a very rapid signaling system. To illustrate, in various demyelinating diseases (e.g. caused by some viruses, heavy metals, autoimmune reactions), loss of the myelin sheath around the myelinated nerve fibers causes propagation to become slowed and impaired in the affected nerve fibers, with associated incoordination and partial paralysis.

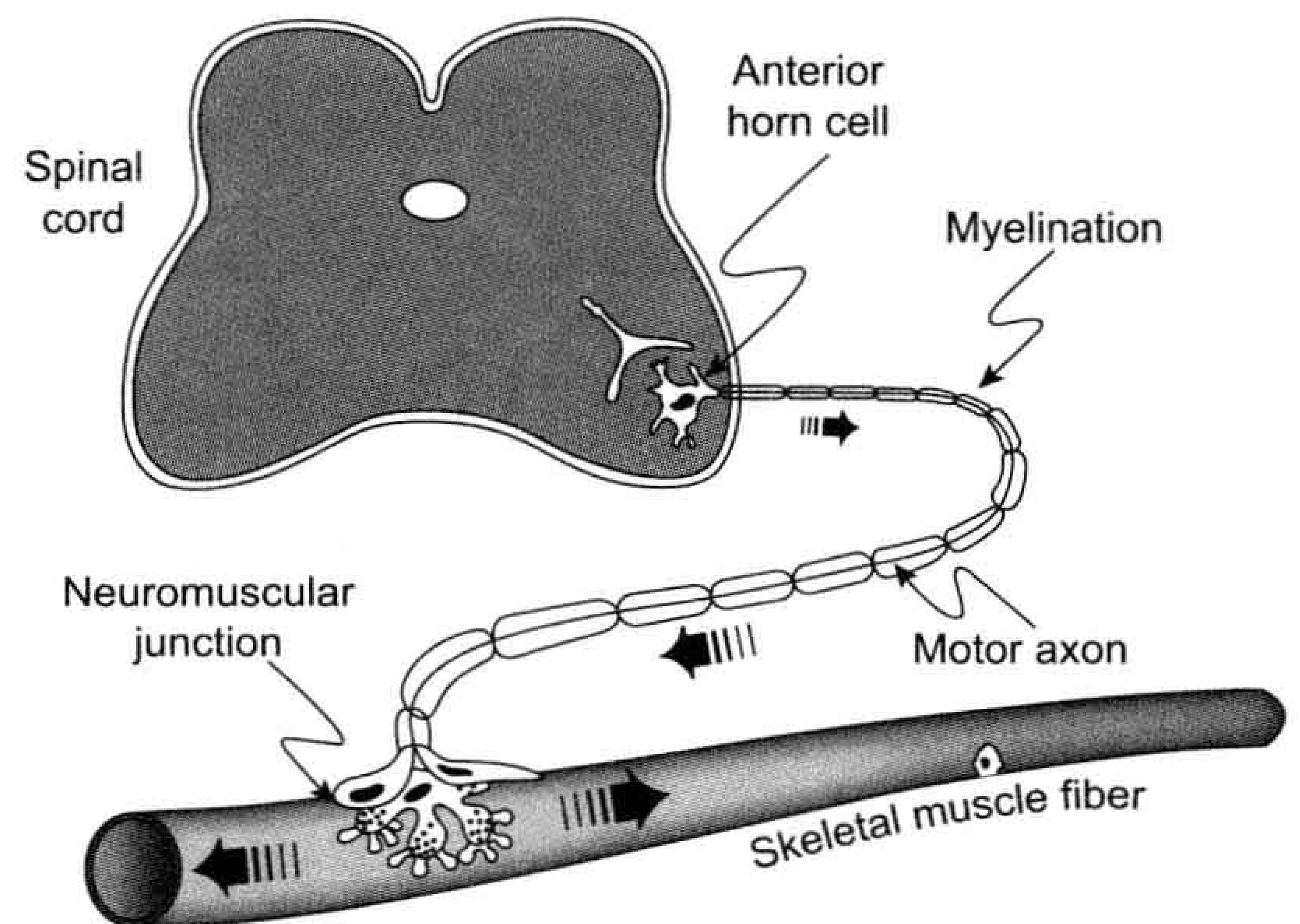


FIGURE 18.1 Schematic diagram of a motor axon, with the cell body (soma) in the anterior horn of the spinal cord and its terminal branches ending on skeletal muscle fibers (only one muscle fiber depicted) to form the neuromuscular junctions (motor end-plates). Each motor axon with its attached skeletal muscle fibers is known as the motor unit. The motor axons are of large diameter (e.g. 20 μm) and are myelinated and therefore propagate at fast velocities (e.g. 120 m/s). As a consequence of the chemical synaptic transmission process at the neuromuscular junction, an AP is initiated in the muscle fiber and propagates in both directions, bringing about contraction.

TABLE 18.1 Conduction Velocity as a Function of Fiber Diameter in Nerve Axons and Muscle Fibers

Fiber Type	Fiber Diameter (μm)	Propagation Velocity (m/s)	Velocity/Diameter (m/s/μm)
Myelinated axons	20	120	6.0
	12	70	5.8
	5	30	6.0
Non-myelinated axons	1.5	2.0	1.3
	1.0	1.3	1.3
Squid giant axons (20°C)	500	25	0.05
Skeletal muscle fibers	50	6	0.12
Cardiac muscle fibers	15	0.5	0.03
Smooth muscle fibers	5	0.05	0.01

III. FREQUENCY-MODULATED SIGNALS

Because propagating all-or-none APs are all very similar to each other (in shape, duration, amplitude, rate of rise and propagation velocity), to make the signal stronger or weaker,

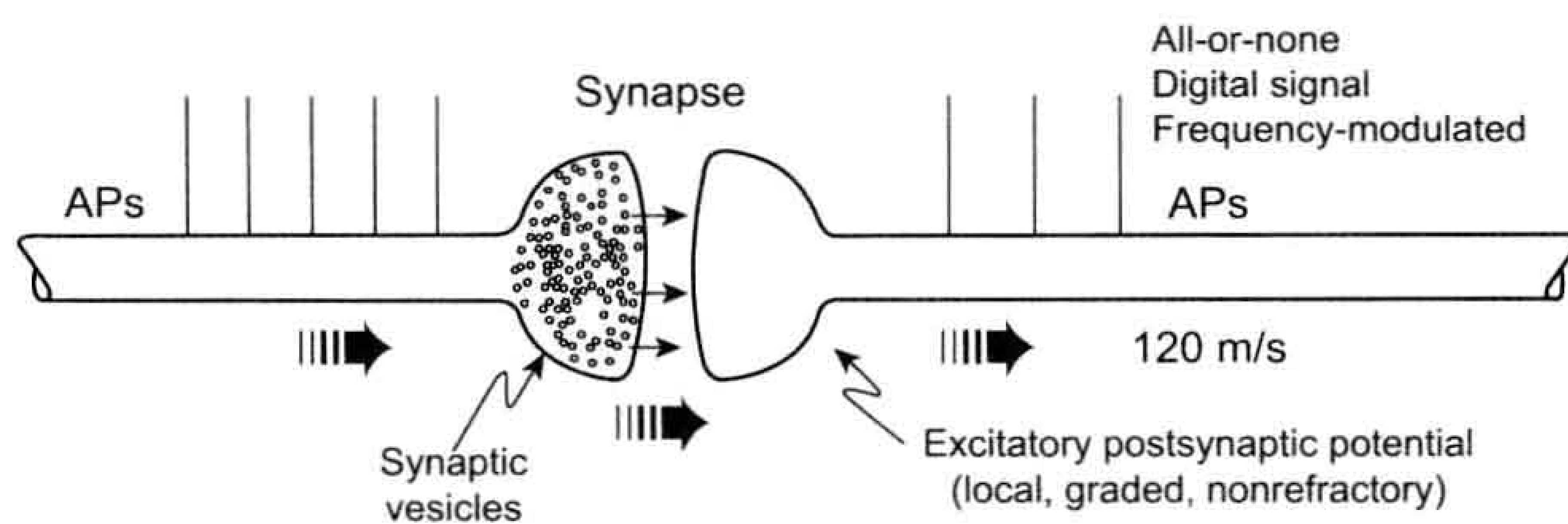


FIGURE 18.2 Diagram of a chemical excitatory synapse between two nerve fibers. An AP in the presynaptic fiber (left) brings about the release of the neurotransmitter at its nerve terminal. The transmitter molecules rapidly diffuse the short distance (e.g. 0.1 μm) across the synaptic cleft, bind to receptor sites on the postsynaptic membrane and open the associated non-selective ion channels (Na^+, K^+ mixed conductance) complexed to the receptor (i.e. these are ligand-gated ion channels). The associated synaptic current depolarizes the postsynaptic membrane, producing the excitatory postsynaptic potential (EPSP); this depolarization spreads passively into the adjacent conductile membrane (excitable) because of cable properties, thereby triggering one or more APs in the postsynaptic axon. The EPSPs are local, graded in amplitude and non-refractory whereas the APs are all-or-none (maximal), refractory and propagated actively. Thus, the AM synaptic process gives rise to an FM or digital signal. The strength of a biological response (e.g. contraction, secretion, sensation) is a function of the frequency of the signal. That is, higher AP frequency corresponds to stronger contraction or stronger sensation.

the body increases or decreases, respectively, the frequency of the APs. That is, the body uses a *frequency-modulated (FM) system*, rather than an amplitude-modulated (AM) system (see Fig. 18.2). It is a digital system composed of on-off identical signals. At each synapse, the signal becomes graded in amplitude rather than all-or-none: the greater the amplitude and duration of the local *postsynaptic potential*, the higher the frequency of APs triggered. The same is true of the local graded *receptor potential* generated at some sensory organs/receptors. Stronger signals translate into a higher frequency of impulses, and weaker signals correspond to a lower frequency of impulses.

IV. CABLE PROPERTIES

IVA. Biological Fiber as a Cable

An *electrical cable* consists of two parallel conductors separated by insulation material, e.g. two copper wires separated by rubber. Usually one of the conductors is arranged as a tubular sleeve surrounding a central solid rod (wire), as depicted in Fig. 18.3A. The equivalent electrical circuit for a cable is shown in Fig. 18.3B: two parallel conductors (wires) separated by a transverse resistance (R) shown distributed along the length of the cable. The resistance of the conductors is so small, compared with the transverse insulation resistance, that it is assumed to be zero. In the case of the *biological cable* (a long narrow nerve fiber or skeletal muscle fiber), one parallel conductor is the inside fluid (cytoplasm) and the second parallel conductor is the outside fluid surrounding (bathing) the cell (the interstitial fluid). Because the conductivity of biological fluid is much less (i.e. much higher resistance) than that of copper wire and because the cross-sectional area of the cell is so small, the inside longitudinal resistance is high and cannot be ignored (Fig. 18.3C). The outside longitudinal resistance is relatively small, as compared with the inside, because of the larger volume (cross-sectional area) of fluid available to carry the outside current, and therefore is assumed to be negligible (Taylor, 1963).

In addition, there is a *stray capacitance* distributed along the length of the cable (see Fig. 18.3D), because a capacitance occurs when two parallel conductors ("plates") are separated by a high-resistance dielectric material. The dielectric constant of materials is related to vacuum, which is assigned a value of 1.0000; air has a value very close to vacuum, oils have a value of 3–6 and that of pure water is 81. The biological membrane, which has a matrix of phospholipid molecules, has a dielectric constant of about 5, typical of oils. The higher the dielectric constant, the higher the capacitance. The closer the parallel plates, the higher the capacitance. Because the biological membrane is so thin (approx.70 Å or 7 nm), its capacitance is relatively high. All cell membranes have a membrane capacitance (C_m) of about 0.7–1.0 μF/cm^2 (where F stands for *farads* (Cole KC, 1965)).

IVB. Length Constant

In the electric cable depicted in Fig. 18.3A and B, a voltage (or signal) applied at one end would be transmitted to the distant end with little or no *decrement* (diminution or attenuation) and the so-called *length constant* would be very long or nearly infinite. In the biological cable (see Fig. 18.3C and D), however, a signal applied at one end rapidly falls off (decays) in amplitude as a function of distance, with a relatively short length constant (λ). This decay in voltage is exponential (Fig. 18.4A). An exponential process gives a straight line on a semilogarithmic plot (log V versus distance) (Fig. 18.4B). In a cable, the relationship between the voltage at any distance (x) from the applied voltage (V_0) is:

$$V_x = V_o\, e^{-x/\lambda} \tag{18.1}$$

Thus, when $x = \lambda$

$$\begin{aligned} V_x &= V_o \frac{1}{e} \\ &= V_o \frac{1}{2.718} \\ &= 0.368\, V_o \end{aligned} \tag{18.2a}$$

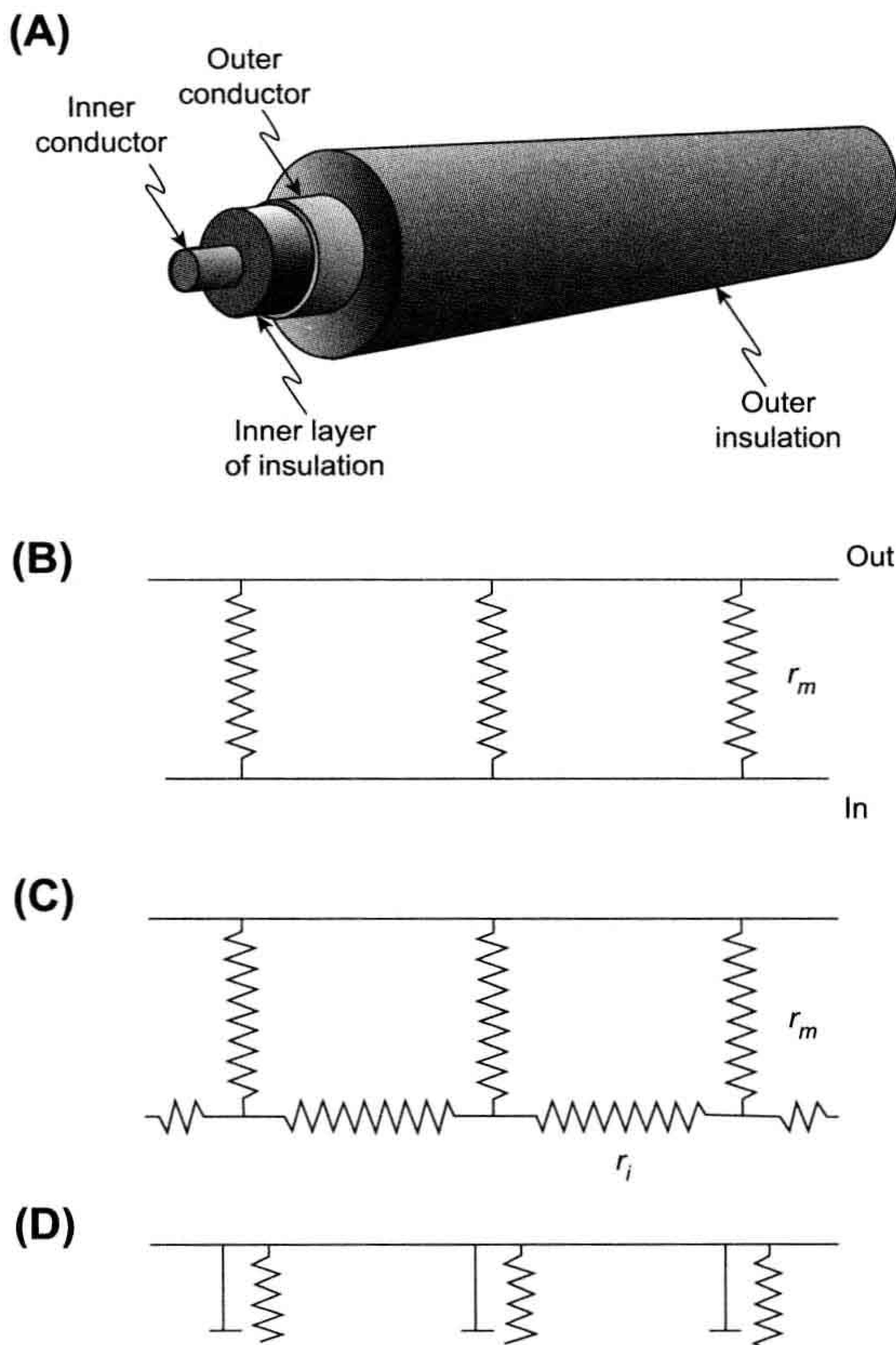


FIGURE 18.3 A coaxial cable and associated electrical equivalent circuit (A, B) and the electrical equivalent circuit for a biological cable (C, D). (A) The coaxial cable consists of an inner conductor (e.g. copper wire) and an outer concentric conductor separated by a layer of insulation (e.g. rubber). (B) The equivalent circuit for a coaxial cable. The inner and outer conductors are depicted as having nearly zero resistances and the transmembrane insulation resistance is shown distributed along the length of the cable. (C) In the biological cable, the inner conductor is the cytoplasm (axoplasm or myoplasm), which is not of negligible resistivity and therefore is depicted as r_i distributed along the length of the fiber. The transverse insulation resistance is the cell membrane resistance (r_m). (D) Addition of the capacitance elements to the biological cable (c_m), which arise due to the lipid bilayer matrix of the cell membrane.

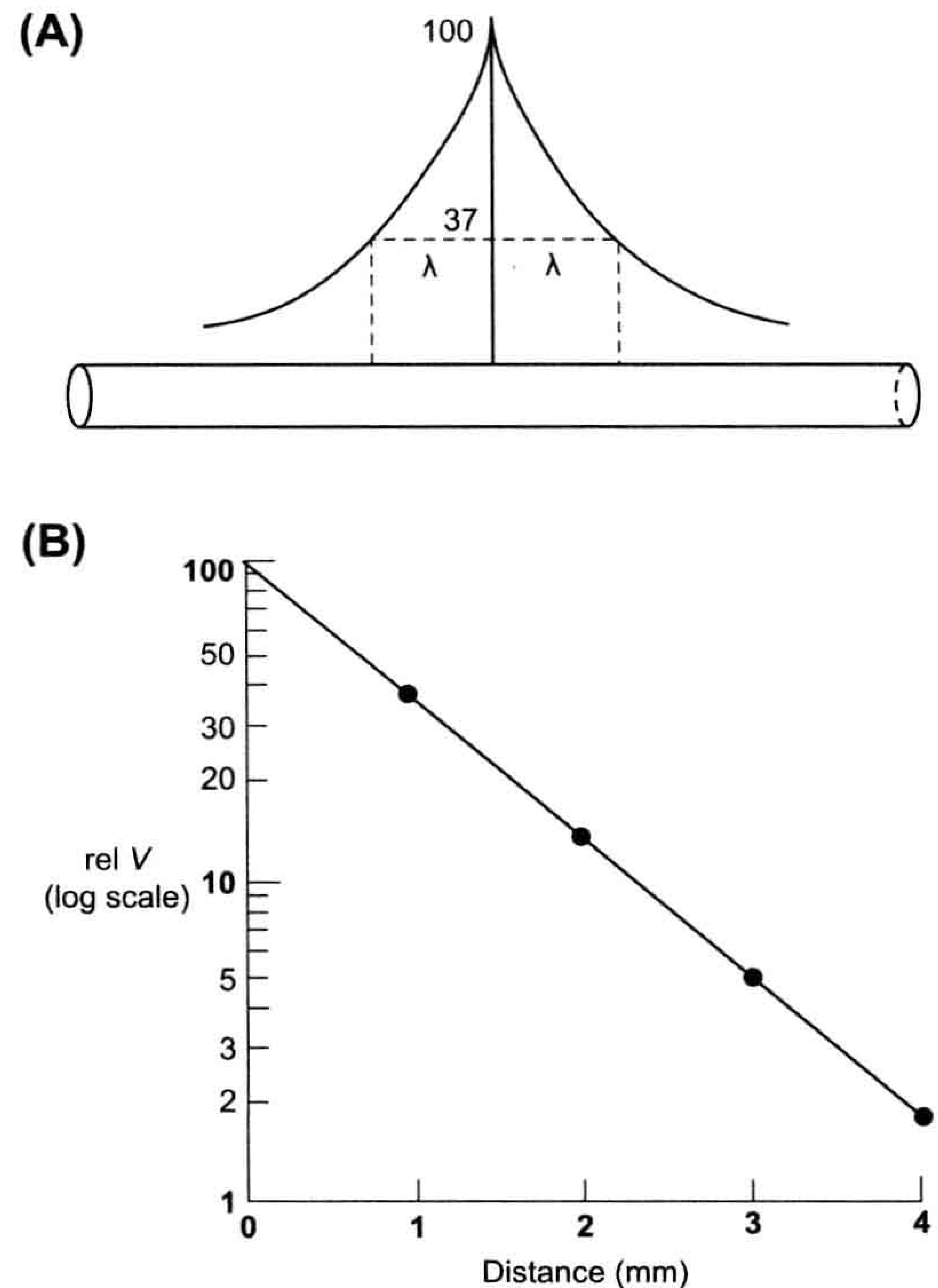


FIGURE 18.4 Length constant of the biological cable (fiber). (A) The exponential decay of voltage on both sides of an applied current (voltage) as a function of distance is diagrammed. The distance at which the voltage falls to 1/e or 36.8% of initial voltage (at $x = 0$), gives the λ value. (B) When the voltage is plotted on a log scale against distance, a straight line is obtained.

The mathematical solution to Equation 18.1 is:

$$V_x = \text{antiln}\left(\ln V_o - \frac{x}{\lambda}\right) \tag{18.2b}$$

$$V_x = \text{antilog}\,\frac{2.303\log V_o - (x/\lambda)}{2.303} \tag{18.2c}$$

Hence, the distance at which the voltage decays to 36.8% of the initial value gives the length constant, λ. In nerve fibers and skeletal muscle fibers, λ has a value of only about 1–3 mm.

Therefore, the relatively short λ, compared with the length of the neuron (e.g. over 1.0 m for a lumbar anterior horn cell motor neuron) or skeletal muscle fiber, means that a signal applied at one end (or midpoint) would fall off very quickly with distance along the fiber (Fig. 18.5). If the length constant were 1.0 mm, then at 4 mm, the signal would become negligibly small. Hence, the electrical signal cannot be conducted passively in the biological cable, because it would decrement and disappear over relatively short distances. The AP (signal) is amplified to a constant value at each point (or each node) in the membrane, as discussed in the following chapter. That is, conduction is active, not passive, with energy being put into the signal at each point to prevent any decay of the signal.

The parameters that determine the length constant of a cable are the square root of the ratio of the transverse

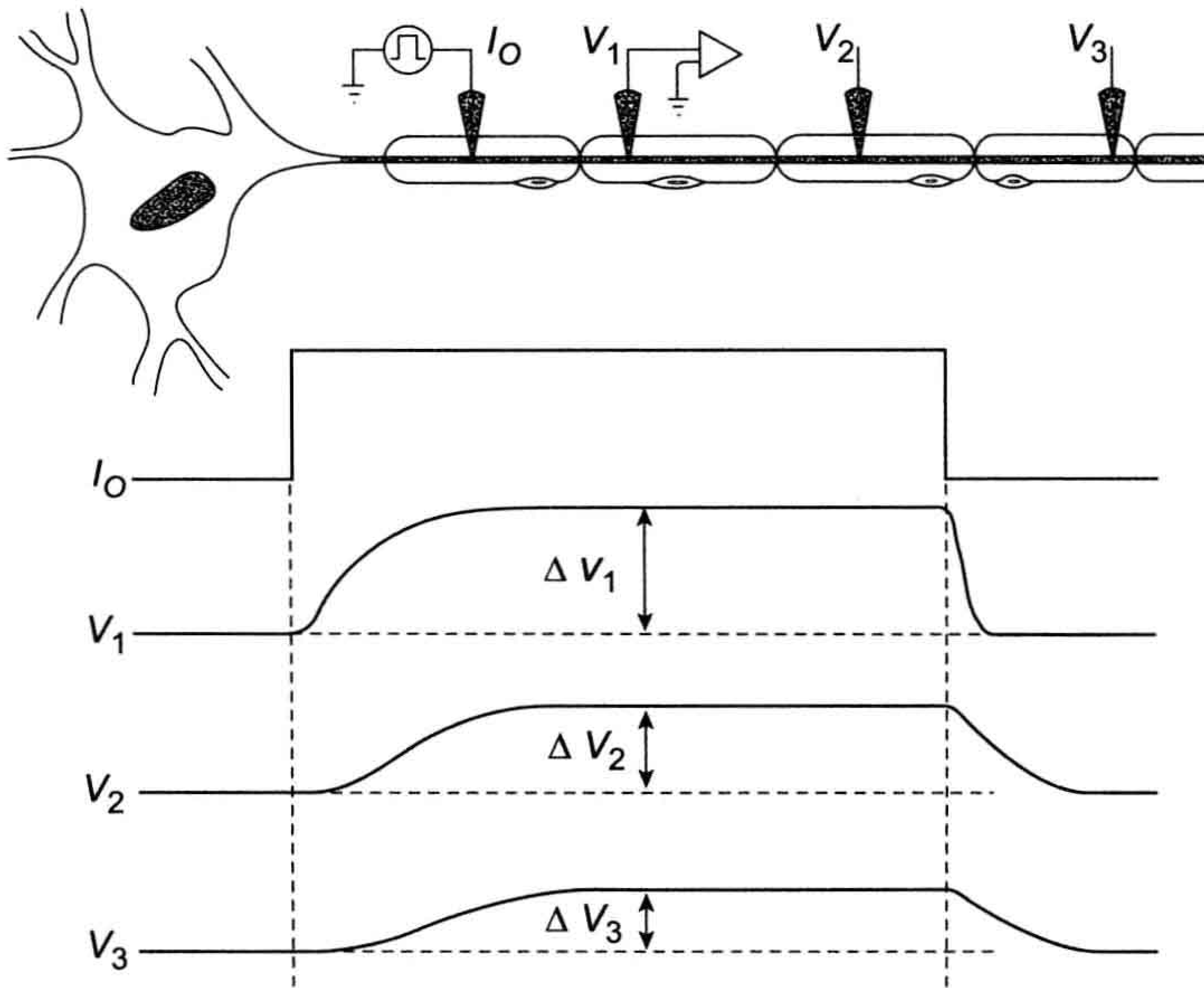


FIGURE 18.5 Diagram of a motor axon and how the voltage signal would decay with distance if the neuron were only a passive cable (non-excitable). The voltage traces illustrate the voltage signals that would be simultaneously recorded at three different points along the axon (V_1, V_2, and V_3) from the site of injection of a rectangular current pulse (I_o). As depicted, the amplitude of the steady-state voltage pulse rapidly falls off with distance, because the length constant (λ) of the biological cable is short (e.g. 1 mm) compared with the length of the axon (e.g. 1000 mm). Therefore, an active response of the cell membrane at each point is required faithfully to propagate the signal. The voltage recorded at point V_1 (ΔV_1) also illustrates that the membrane potential changes in an exponential manner, both at the beginning of an applied rectangular current pulse and at the end. This exponential change results from the capacitance of the cell membrane, the time constant (τ) being a product of the resistance and capacitance ($R_m C_m$). The time it takes for the voltage to decay to 1/e (36.8%) of the initial (maximal) value at the end of the pulse, or to build up to 63.2% (1−1/e) of the maximal value at the beginning of the pulse, gives the τ value.

resistance (r_m) to the sum of the inside (r_i) and outside (r_o) longitudinal resistances:

$$\lambda = \sqrt{\frac{r_m}{r_i + r_o}} \tag{18.3}$$

$$\text{cm} = \sqrt{\frac{\Omega \cdot \text{cm}}{\frac{\Omega}{\text{cm}} + \frac{\Omega}{\text{cm}}}} = \text{cm}$$

where r_m, r_i and r_o are the resistances normalized for a unit length (1.0 cm) of fiber.

For surface fibers of a nerve or a muscle bundle bathed in a large volume conductor, r_o is negligibly small and Equation 18.3 reduces to:

$$\lambda = \sqrt{\frac{r_m}{r_i}} \tag{18.4a}$$

Equation 18.4a is the same as:

$$\lambda = \sqrt{\frac{R_m}{R_i}\frac{a}{2}} \tag{18.4b}$$

$$\text{cm} = \sqrt{\frac{\Omega \cdot \text{cm}^2 \cdot \text{cm}}{\Omega \cdot \text{cm}}} = \text{cm}$$

where a is the fiber radius and R_m and R_i are the membrane resistance and longitudinal cytoplasmic resistance, respectively, normalized for both length (1.0 cm) and cell diameter. Thus, the greater the membrane resistance and the smaller the internal longitudinal resistance (larger cell diameter), the greater the λ value. We will see later that the propagation velocity is a function of λ; i.e. larger diameter fibers propagate faster. We will also see that myelination increases the effective membrane resistance (R_m) and lowers the effective capacitance, thereby increasing propagation velocity.

IVC. Time Constant

Because of the high capacitance of the cell membrane (C_m), the membrane potential (E_m) cannot change instantaneously upon application of a step current pulse. Instead, E_m changes in an exponential (negative) manner (see Fig. 18.5) on both the charge and the discharge. The *membrane time constant* (τ_m) is a product of the resistance (R_m) and capacitance of the membrane and can be expressed as:

$$\tau_m = r_m c_m \tag{18.5a}$$

$$= R_m C_m$$
$$\text{s} = \Omega \cdot \text{F} \tag{18.5b}$$

where R_m is the resistance in ohms (Ω-cm^2), and C_m is the capacitance in farads (F/cm^2).

The discharge of the membrane (parallel RC network) is given by:

$$V_t = V_{\max}\, e^{-t/\tau} \tag{18.6}$$

where V_t is the voltage at any time t (at the site of current injection) and V_{max} is the final maximum voltage attained during the pulse. When $t = \tau$,

$$V_t = V_{max}\frac{1}{e} \tag{18.7a}$$

$$= V_{max}\frac{1}{2.718}$$

$$= 0.368\ V_{max}$$

Hence, the time at which the voltage decays to 36.8% of the initial (maximal) value gives the *time constant*, τ (see Fig. 18.5). In nerve fibers and skeletal muscle fibers, τ_m has a value of about 1.0 ms.

When the membrane is charging, there is a similar *exponential (negative) process*, with the identical time constant (see Fig. 18.5). The corresponding relationship is given by:

$$V_t = V_{max}\ (1 - e^{-t/\tau}) \tag{18.7b}$$

The time it takes for the voltage to build up to 63.2% of its final value gives the time constant. When $t = \tau$,

$$V_t = \left(1 - \frac{1}{e}\right) V_{max} \tag{18.7c}$$

$$= (1 - 0.368)\ V_{max}$$

$$= 0.632\ V_{max}$$

Thus, the time constant can be measured on the build-up of the pulse (time to reach 63.2% of the final voltage) or on the decay (time to decay to 36.8% of the initial voltage).

IVD. Input Resistance

The *input resistance* (R_{in}) of a muscle or nerve fiber is essentially the resistance that an intracellular microelectrode "looks" into when a small current (DC pulse) is injected. Thus, R_{in} is determined by the change in membrane potential (V_o or $V_{x=0}$) at steady-state produced at the site of injection ($x = 0$) by the injection of a known (measured) amount of current (I_o or $I_{x=0}$), based on *Ohm's law.*

$$R_{in} = \frac{V_o}{I_o} \tag{18.8}$$

If the microelectrode is near the middle of a very long fiber (or "infinite" cable), then R_{in} is related to the other cable parameters (e.g. to the internal longitudinal resistance r_i and the DC length constant λ_{DC}):

$$R_{in} = 0.5\ r_i\ \lambda_{DC}$$

$$\Omega = \frac{\Omega}{cm}\cdot cm \tag{18.9}$$

The factor of 0.5 is present because current flows in both directions from the microelectrode. If the microelectrode is at one end of the long fiber, then the factor of 0.5 is removed. Equation 18.9 indicates that the R_{in} is greater when r_i and/or λ_{DC} are greater. Combining Equations 18.8 and 18.9 gives:

$$\frac{V_a}{I_o} = 0.5\ r_i\ \lambda_{DC} \tag{18.10a}$$

or

$$V_o = I_o 0.5\ r_i\ \lambda_{DC} \tag{18.10b}$$

This equation indicates that the change in membrane potential at $x = 0$ is equal to the applied current (I_0) times the input resistance.

To obtain the change in membrane potential at any point x along the fiber cable (V_x), then an exponential term ($e^{-x/\lambda}$) must be added to account for the exponential decay of voltage over distance:

$$V_x = I_o\ 0.5\ r_i\ \lambda_{DC}\ e^{-x/\lambda} \tag{18.11}$$

This equation is identical to Equation 18.1, because the I_o 0.5 r_i λ_{DC} term is equal to V_o (Equation 18.10b):

$$V_x = V_o\ e^{-x/\lambda}$$

Further discussion is given in Appendix 18.1.

IVE. Local Potentials

In contrast to the active propagation of APs, *synaptic potentials* and sensory *receptor potentials* are not actively propagated. Such potentials decay exponentially (from their source of initiation) along the fiber cable, as described previously. Therefore, postsynaptic potentials and receptor potentials are *local potentials.* When local potentials are in the depolarizing direction, they can give rise to APs, which are propagated; when hyperpolarizing, they act to inhibit production of APs. These local potentials are similar to the *local excitatory response* (see following chapter), in that both are confined to a local region; however, the electrogenesis of the two is different. As stated before, the neuromuscular junction is an excitatory type of chemical synapse and produces *excitatory postsynaptic potentials* (EPSPs), also known as *end-plate potentials* (EPPs).

Most synaptic potentials are *graded,* i.e. they can add on to one another, both in time and in space (*temporal summation* and *spatial summation*), to produce larger responses. Larger synaptic potentials exert a greater stimulatory or inhibitory effect on the production of APs.

V. CONDUCTION OF ACTION POTENTIALS

VA. Local-Circuit Currents

The generation of APs is described in the subsequent chapter. This section examines the mechanism for their rapid propagation (conduction). *Propagation* occurs by means of the *local-circuit currents* that accompany the propagating APs, as depicted in Fig. 18.6. Such currents exist because, when two points are at a different potential (voltage) in a conducting medium, current (I) will flow between the two points, as governed by Ohm's law ($I = V/R$).

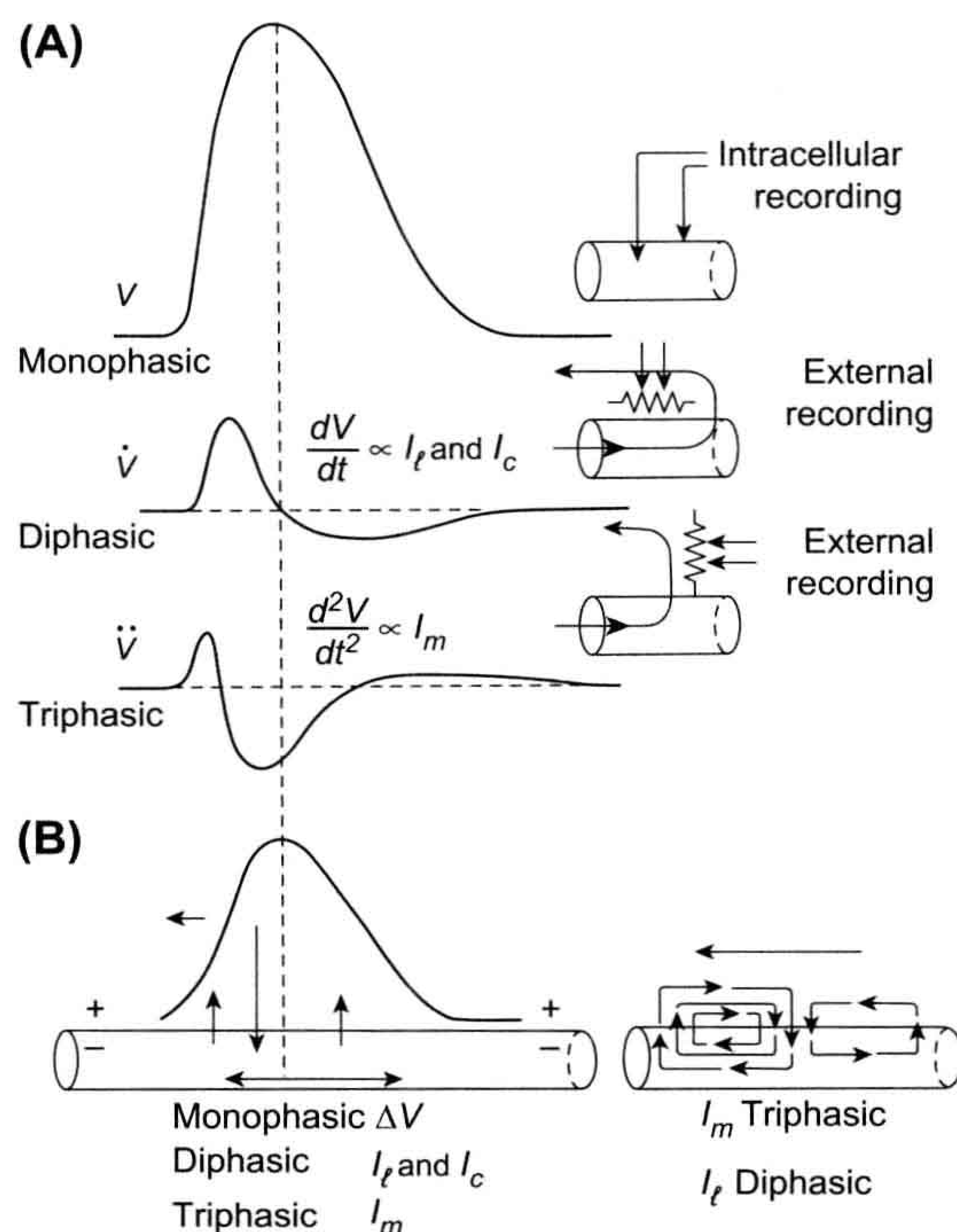


FIGURE 18.6 (A) Schematic representation of the first ($\dot{V}$) and second ($\ddot{V}$) time derivatives of the AP spike and the longitudinal and radial currents associated with the propagating spike. The first derivative (*dV/dt* or $\dot{V}$) is proportional to the capacitive current ($I_c = C_m\, dV/dt$) and to the longitudinal (axial) current and is *diphasic*, having an intense forward phase and a less intense backward phase, as depicted in the diagram at the lower right. The second derivative (d^2V/dt^2 or $\ddot{V}$) is proportional to the radial transmembrane current (I_m), and is *triphasic*, having a moderately intense initial outward phase, then a very intense inward phase (the "current sink"), followed by a least intense second outward phase, as depicted in the lower diagrams. (B) The arrows at the lower left also depict the three phases of the membrane current and the two phases of the axial current. *dV/dt* can be recorded externally by a pair of closely-spaced (relative to the spike wavelength) electrodes arranged parallel to the fiber axis, as illustrated. d^2V/dt^2 can be recorded by a pair of electrodes arranged perpendicular to the fiber axis, as depicted. The vertical dashed line indicates that when the slope of the spike goes to zero at the peak of the spike, *dV/dt* is zero; *dV/dt* is maximum at about the middle of the rising phase of the spike.

At the peak of the AP in one region of the fiber, the inside of the membrane at that region becomes positive with respect to the outside. The inside is also positive with respect to the inside cytoplasm at a region downstream from the active region. Therefore, current flows through the cytoplasm from the active region (*current source*) to the adjacent inactive region, then out of the fiber across the cell membrane, then through the interstitial fluid back to the active region (current "sink") and, finally, through the membrane of the active region. This completes the *closed loop* for the current.

The outward current through the membrane of the inactive region produces an *IR* voltage drop (Ohm's law), positive inside to negative outside. This acts to depolarize this region, because the polarity of the voltage drop is opposite to that of the RP (negative inside, positive outside). When the depolarization exceeds the *threshold potential*, an AP is triggered. Thus, the inactive region becomes converted to an active region. This process is repeated in each segment of fiber, thus resulting in movement (propagation) of the impulse sequentially down the fiber.

If we examine a propagating AP in the middle region of a fiber (see Fig. 18.6), we see that there is also a small backflow of current internally, coupled with a corresponding small forward flow externally, associated with the repolarizing phase of the AP. Thus, as the AP propagates down the fiber, from right to left, there is a simultaneous double flow of local-circuit current: clockwise flow associated with the rising phase of the AP and counterclockwise flow associated with the repolarizing phase of the AP.

The internal longitudinal current, sweeping past a transverse plane of the fiber, has two phases, first forward (right to left) and then reverse (left to right). The external longitudinal current also has two phases: first left to right and then right to left.

The transverse membrane current, flowing outward in a plane perpendicular to the membrane, has three consecutive phases: first outward (still passive membrane), then inward (active membrane) and, finally, outward again (still active membrane).

It is the local-circuit current flow that enables the *electrocardiogram* (ECG), *electromyogram* (EMG), *electroencephalogram* (EEG) and *electroretinogram* (ERG) to be recorded from the body surface over the tissue of interest (heart, skeletal muscle, brain and eye). The internal longitudinal current is confined to the cytoplasm of the fiber, but the external current can use whatever conducting fluid is available (e.g. the entire torso *volume conductor*) because of the principle that parallel resistors give a lower total resistance (or current takes the path of least

resistance). Thus, this external local-circuit current causes the skin to be at different potentials, and these differences can be recorded (as the ECG, etc.).

VB. Propagation Velocity Determinants

The factors that determine active velocity of propagation (θ) include: (1) fiber diameter, (2) length constant (λ), (3) time constant (τ_m), (4) local-circuit current intensity, (5) threshold potential and (6) temperature. Some of these factors are interrelated, such as fiber diameter and length constant (since λ is proportional to the square root of the radius) and length constant and time constant (since both have a dependence on R_m). Propagation velocity is directly proportional to length constant and inversely proportional to time constant as:

$$\theta \propto \frac{\lambda}{\tau_m} \tag{18.12a}$$

By substituting Equation 18.4a for λ and Equation 18.5a for τ_m, we have:

$$\theta \propto \frac{1}{C_m}\sqrt{\frac{a}{R_m R_i}} \tag{18.12b}$$

Thus, propagation velocity is directly proportional to the square root of fiber diameter or radius (a) and inversely proportional to *membrane capacitance* (C_m). The larger the fiber diameter, the lower the absolute longitudinal resistance of the intracellular cytoplasm (principle of resistors in parallel) and therefore the greater the amount of local-circuit current flowing longitudinally and the greater the length constant. For example, it is well known that the larger the diameter of nerve fibers, the faster they propagate (see Table 18.1). Equation 18.12b shows that if C_m can be reduced (by myelination), then θ should increase in proportion. This is discussed in Section IVC.

In addition, θ depends on the intensity of the local-circuit current, and hence on the rate of rise of the AP. The greater the AP rate of rise (max dV/dt), the greater the longitudinal current and the transmembrane *capacitive current* (I_c). Therefore, all other factors being constant, faster-rising APs propagate faster. The AP rate of rise depends on the density of the fast Na^+ channels that carry inward current, on C_m and on temperature. Max dV/dt decreases with increased C_m, with cooling and with partial depolarization (due to the h_∞ versus E_m relationship discussed in the following chapter). Cooling slows the rate of all chemical reactions, particularly those with a high Q_{10} (activation energy), such as the ion conductance changes in activated membrane.

Finally, the *threshold potential* (V_{th}) affects propagation velocity. If the threshold were to be shifted to a more positive voltage (more depolarized), then it would take longer for a given point in the membrane to reach threshold (and explode) during propagation of an AP from upstream. A greater *critical depolarization* (difference between RP and V_{th}) would be required to bring the membrane to threshold. Therefore, propagation velocity would be slowed.

As stated earlier, some of these factors are interrelated and some actually exert opposing effects.

The foregoing discussion applies to non-myelinated nerve axons and skeletal muscle fibers. An electron micrograph of small bundles of non-myelinated nerve fibers enveloped by *Schwann cells* is shown in Fig. 18.7. In myelinated nerve fibers, propagation velocity is greatly increased by the *myelin sheath*, as discussed in the following section.

VC. Saltatory Conduction

The nerve cable has been vastly improved by the evolutionary development of *myelination* in vertebrates. An electron micrograph of a myelinated nerve fiber is shown in Fig. 18.8. The *myelin sheath* improves the cable by increasing the effective R_m by about 100-fold and decreasing the effective C_m by about 100-fold. This increases the length constant, λ. Although τ_m tends to increase with the increase in effective R_m (due to the myelin sheath), the decrease in C_m counteracts this effect, thus acting to hold τ_m almost constant. Thus, Equations 18.12a and 18.12b predict that propagation velocity should increase with myelination.

One consequence of myelination, therefore, is that propagation velocity is greatly increased (see Table 18.1). Another consequence is that the *energy cost of signaling* is

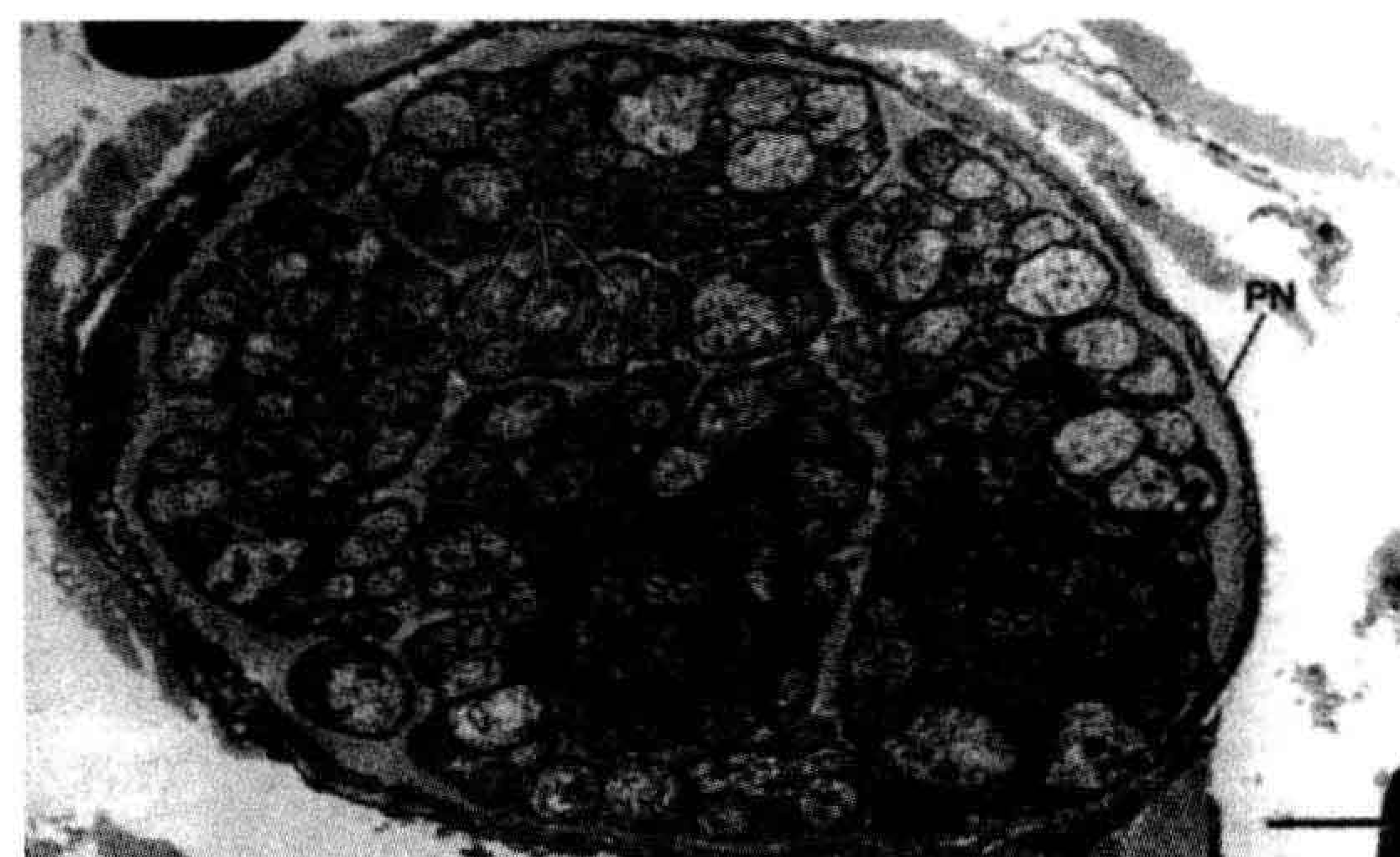


FIGURE 18.7 Electron micrograph of an autonomic nerve of mouse heart cut in transverse section. The unmyelinated axons (Ax) are arranged in small groups (bundles) that are engulfed by the cytoplasm of a Schwann cell. That is, the non-myelinated axons are embedded in, and surrounded by, a Schwann cell. Two Schwann cell nuclei (Sch) can be seen. The axon bundles are separated and surrounded by a collagenous matrix. The entire nerve is surrounded by a perineurial sheath (PN). The scale bar at lower right equals 2 μm. *(Micrograph courtesy of Dr Mike Forbes, University of Virginia.)*

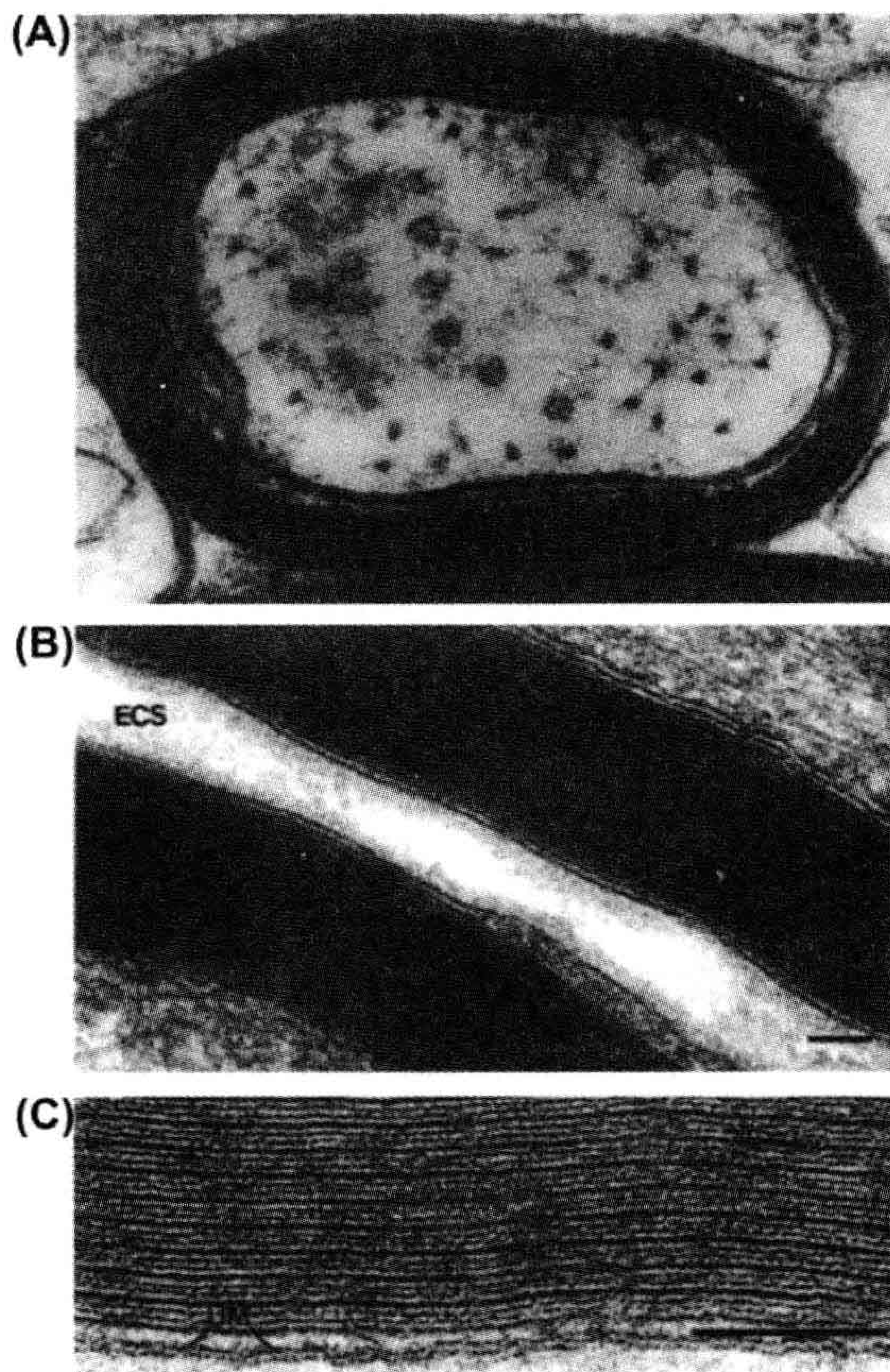


FIGURE 18.8 Myelin sheath of myelinated nerve fibers. (A) Myelinated nerve fiber in spinal cord of rat cut in cross-section. There are about seven wrappings of the Schwann cell around the axon, thus giving about 14 membranes in series with the cell membrane of the axon (axolemma). The internal *mesaxon* is visible at the left side (lower) of the axon and represents the beginning of the spiraling of the Schwann cell membranes (cytoplasm squeezed out) to form the myelin sheath surrounding the axon. On the upper left side, a process of an oligodendrocyte abuts on the myelin sheath. The axon shown is closely plastered up against the myelin sheath of a neighboring axon (bottom of figure). *Microtubules* and *neurofilaments* are visible in the cytoplasm of the axon. Magnification of 168 000×. (From J. Rhodin, An Atlas of Histology, Oxford University Press, New York, 1975.) (B) Higher magnification of two adjacent nerves fibers (in phrenic nerve of rat) cut in longitudinal section to illustrate an axon with a thicker myelin sheath (approx. 23 wrappings=46 membranes). Note that between the thicker (dense) lines are two thinner lines, which can be seen more clearly in (C). The extracellular space (ECS) between the two axons is labeled. The calibration bar at the lower right equals 0.1 μm. (C) Still higher magnification of a portion of one of the myelin sheaths shown in the middle panel better to illustrate the periodicity of the myelin membranes. The dense lines alternate with a pair of thin lines. The space in between the pair of thin lines is extracellular space. The dense lines represent the intracellular (cytoplasmic) region of the Schwann cell process, with the cytoplasm extruded, thus allowing the inner (cytoplasmic face) leaflets of the cell membrane of the Schwann cell to come into close contact. The outer (extracellular face) leaflets of the Schwann cell membrane are seen as the thin lines. Thus, each cell membrane has the appearance of a double line, representing the hydrophilic surfaces of the cell membrane; the hydrophobic region of the membrane is the clear region between the dense line and the contiguous thin line on either side. UM; unit cell membrane. The scale bar on the lower right represents 0.1 μm. *(Micrographs (B) and (C) courtesy of Dr Mike Forbes, University of Virginia.)*

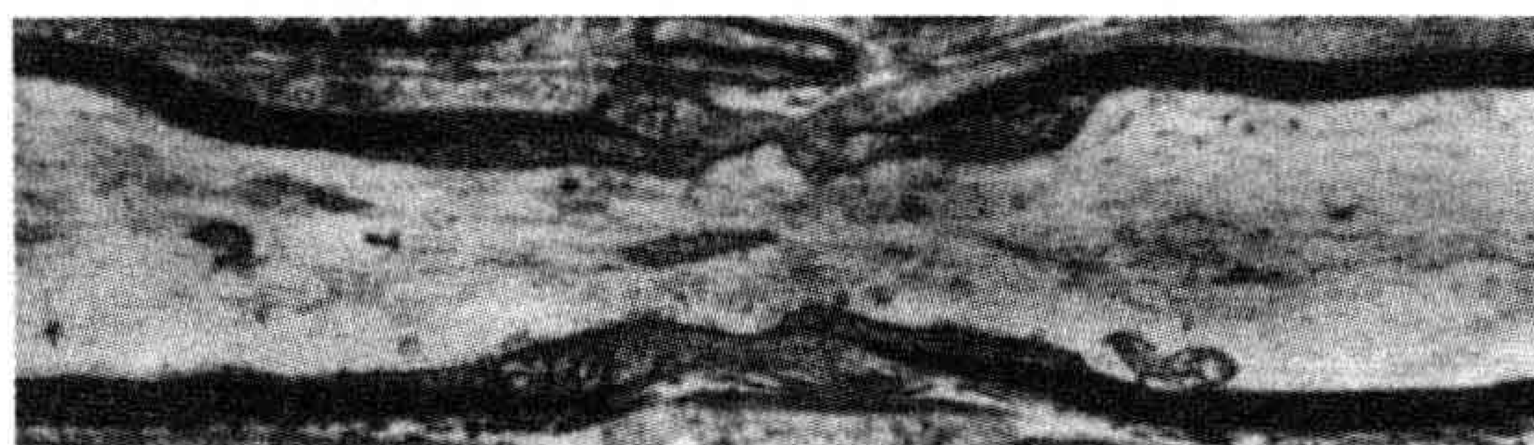


FIGURE 18.9 Electron micrograph of one node of Ranvier in a single myelinated nerve axon of rat sciatic nerve cut in longitudinal section. Dark myelin bordering the axon on each side is interrupted near the middle of the micrograph, leaving the neuronal cell membrane nude of myelin at the node region. However, cytoplasmic processes of the Schwann cells cover the nodal membrane. Collagenous fibrils of the endoneurium are visible at the region of the node. The myelin tapers and thins as it approaches the node and there is a frayed appearance caused by the successive laminae of the myelin sheath terminating as cytoplasmic swellings. The axoplasm contains neurofilaments and microtubules. Magnification of 9000×. *(From J. Rhodin, An Atlas of Histology, Oxford University Press, New York, 1975.)*

greatly decreased, because passive ion leaks are limited and active current losses are restricted to the small nodes of Ranvier, which are spaced relatively far apart. An electron micrograph of a node of Ranvier is shown in Fig. 18.9. At each node, the length of exposed (naked) cell membrane is very short. The node forms an annulus around the entire perimeter of the fiber. The *internodal distance* is about 0.5–2.0 mm (depending on fiber diameter) and the width (length) of each node is only about 0.5–3 μm. Therefore, the degree of energy-requiring active ion transport (Na^+-K^+ and Ca^{2+}) required to maintain the steady-state ion distributions and to hold the system in a state of high potential energy is greatly reduced. For example, the amount of Na^+ gained and K^+ lost per impulse is reduced as a result of myelination. The low rate of oxidative metabolism in myelinated fibers reflects this lowered energy requirement.

The *myelin sheath* is produced by the wrapping of the Schwann cell repeatedly around the nerve fiber in a spiral, forming 20–200 wrappings, depending on axon diameter. That is, the larger axons have a thicker myelin sheath. For the purpose of our discussion, we will assume an average of 100 wrappings. The myelin sheath covers the nerve axon as a coat sleeve and is interrupted at each node. The cytoplasm of the Schwann cell in the region of the myelin sheath is nearly completely extruded during its formation, so that the sheath consists essentially of 100 cell membranes stacked in series. Because resistors in series are added to calculate the total resistance, the effective transmembrane resistance

is increased 100-fold, but the effective capacitance is reduced 100-fold (because the total capacitance of capacitors in series is calculated like resistors in parallel). Since λ is directly proportional to $\sqrt{R_m}$, λ is increased accordingly. The greater λ and lowered C_m increase θ.

Myelinated nerves usually have an *optimal amount of myelin*, which is an amount such that the ratio of diameter of axon cylinder (naked axon) to total fiber (including myelin sheath) is about 0.6−0.8. Assuming a maximal total diameter feasible (the body must pack many circuits within a limited space, e.g. sciatic nerve bundle), a greater fraction of myelin, by infringing on the diameter of the axis cylinder, would raise r_i too high, causing θ to decrease. Thus, there are two opposing factors in determining the degree of optimal thickness of the myelin sheath. The more the myelin, the greater the decrease in C_m and increase in effective R_m, but then the smaller diameter of the axis cylinder causes a higher r_i.

In *saltatory conduction* (Latin *saltare*, to jump), the impulse jumps from one node to the next. The internodal membrane *does not fire* an AP. This is due to two reasons: (1) the internodal membrane is much less excitable (e.g. much fewer fast Na^+ channels); and (2) the depolarization of the neuron cell membrane at the internodal region is only about 1/100th of that at the node. The latter occurs because the *IR* voltage drop across the internodal cell membrane is only 1/100th of that across the entire series resistance network (neuron cell membrane plus 100 layers of Schwann cell membrane) (*Kirchhoff's laws* dealing with voltage drops across resistors in series). Even though the internal potential in the internodal region swings positive (e.g. to +30 mV) when the adjacent nodes fire, the potential at the outer surface of the internodal membrane also swings nearly as positive (e.g. to +29 mV). Therefore, the depolarization of the neuronal membrane at the internode is only about 1 mV, which is well below threshold and so the internodal membrane does not fire. The potential that controls the membrane conductances (activates the voltage-dependent ion channels) is the pd (potential difference) directly across the membrane and not the absolute potential on either side.

As stated previously, the internodal membrane has only a few fast Na^+ channels, whereas the nodal membrane has a very high density. Since the cell membrane is fluid and proteins can diffuse (float) laterally in the lipid bilayer matrix, what keeps the fast Na^+ channel proteins confined (at high density) in the nodal region? There are *special anchoring proteins* (e.g. *ankyrin*) that anchor the ion channel proteins to the cytoskeletal framework, thus preventing their lateral movement into the internodal membrane.

The effect of myelin and saltatory propagation is to make propagation much faster. For example, a 20-μm-diameter myelinated nerve fiber conducts even faster than a 700-μm (0.7 mm) diameter non-myelinated nerve fiber (e.g. the *giant axon* in squid, lobster, earthworm): 120 m/s versus 25−50 m/s. Thus, invertebrates, to achieve fast conduction in some essential circuits, must resort to *giant neurons*, resulting in a lower r_i and hence fast conduction. Because of space/size limitations, only a few critical neurons can be made giant in diameter. In vertebrates, on the other hand, a large fraction of the nerve fibers in the peripheral nerves are myelinated for fast propagation.

We saw earlier that, in non-myelinated axons and skeletal muscle fibers, θ should vary with the square root of the cell diameter or radius ($a^{0.5}$). In myelinated axons, θ varies with the first power of the cell radius (a^1) because θ varies with λ^2 as indicated by:

$$\theta \propto \frac{\lambda^2}{\tau_m} = \frac{a}{2R_iC_m} \qquad (18.13)$$

The dependence of conduction velocity on diameter of nerve fibers is summarized in Table 18.1.

VD. Wavelength of the Impulse

We can calculate the wavelength of the AP, which is the length of the axon simultaneously undergoing some portion of the AP. The wavelength is equal to propagation velocity (θ) times the duration of the AP (APD100); thus,

$$\text{wavelength} = \theta \times \text{APD}_{100} \qquad (18.14)$$

$$\text{cm} = (\text{cm/s}) \times \text{s}$$

$$\text{distance} = \text{velocity} \times \text{time}$$

Note the similarity of this relationship to that for the wavelength of an electromagnetic radiation: wavelength = velocity of light/frequency of the radiation. The reciprocal of frequency is the period (duration of one cycle). The wavelength in a large myelinated nerve axon is about 12 cm: 120 m/s × 1.0 ms. In a skeletal muscle fiber, it is about 1.8 cm (6 m/s × 3.0 ms). In a smooth muscle bundle, the wavelength is only about 1.5 mm (5 cm/s×30 ms).

VI. EXTERNAL RECORDING OF ACTION POTENTIALS

VIA. Monophasic, Diphasic and Triphasic Recording

As discussed previously, local-circuit currents accompany the propagating AP in each fiber. The intracellular and extracellular longitudinal currents are diphasic; i.e. initially they travel in the forward direction intracellularly and then in the reverse direction. The forward direction current is intense (high current density) and the reverse direction

current is weak (low current density). The transmembrane radial currents are triphasic; i.e. the first phase is outward (moderate intensity), the second phase is inward (high intensity) and the third phase is outward (low intensity). The first phase (outward) gives rise to the passive exponential foot of the AP and is due to the passive cable spread of voltage and current. The second phase (inward) corresponds to the large inward fast Na^+ current, which occurs during the later portion of the rising phase and peak of the AP. The third phase (outward) corresponds to the net outward current (K^+), which occurs during the repolarizing phase.

These longitudinal and radial currents can be recorded by suitably-placed external electrodes. The extracellular longitudinal currents can be recorded by two electrodes (bipolar) placed close together along the length of the fiber. If the interelectrode distance is short (relative to the wavelength), an approximate first (time) derivative of the AP is obtained (see Figs. 18.6 and 18.10C). The extracellular radial currents can be recorded by two electrodes placed close together in a plane perpendicular to the fiber axis. This gives an approximation of the second (time) derivative of the AP (see Fig. 18.6).

The internal axial currents are confined to the cytoplasm, whereas the external longitudinal currents can use the entire interstitial fluid space of the nerve bundle or muscle or even the entire torso (volume conductor), since current takes the path of least resistance (resistors in parallel). As mentioned in Section IVA, this allows the recording of the ECG from the body surface and the EMG from the skin overlaying an activated skeletal muscle. The ECG and EMG consist essentially of diphasic potentials, reflecting the external longitudinal currents during propagation of APs.

When the two external electrodes are placed far apart (with respect to the wavelength) along a nerve or muscle fiber, the diphasic recording has two phases that are about equal (Fig. 18.10A). The proximal electrode records the wave of negativity (associated with the propagating AP) first and then returns to isopotential. When the wave reaches the second electrode, the wave is recorded by it in reversed polarity (because current flow through the voltmeter is reversed). If the AP were now prevented from reaching the second (distal) electrode by crushing this region of the fiber or elevating $[K^+]_o$ to depolarize it, then a monophasic recording would be obtained (Fig. 18.10B). This monophasic recording would most resemble the true AP recorded by a microelectrode impaled into a fiber to record the transmembrane potential, but would be much smaller in amplitude.

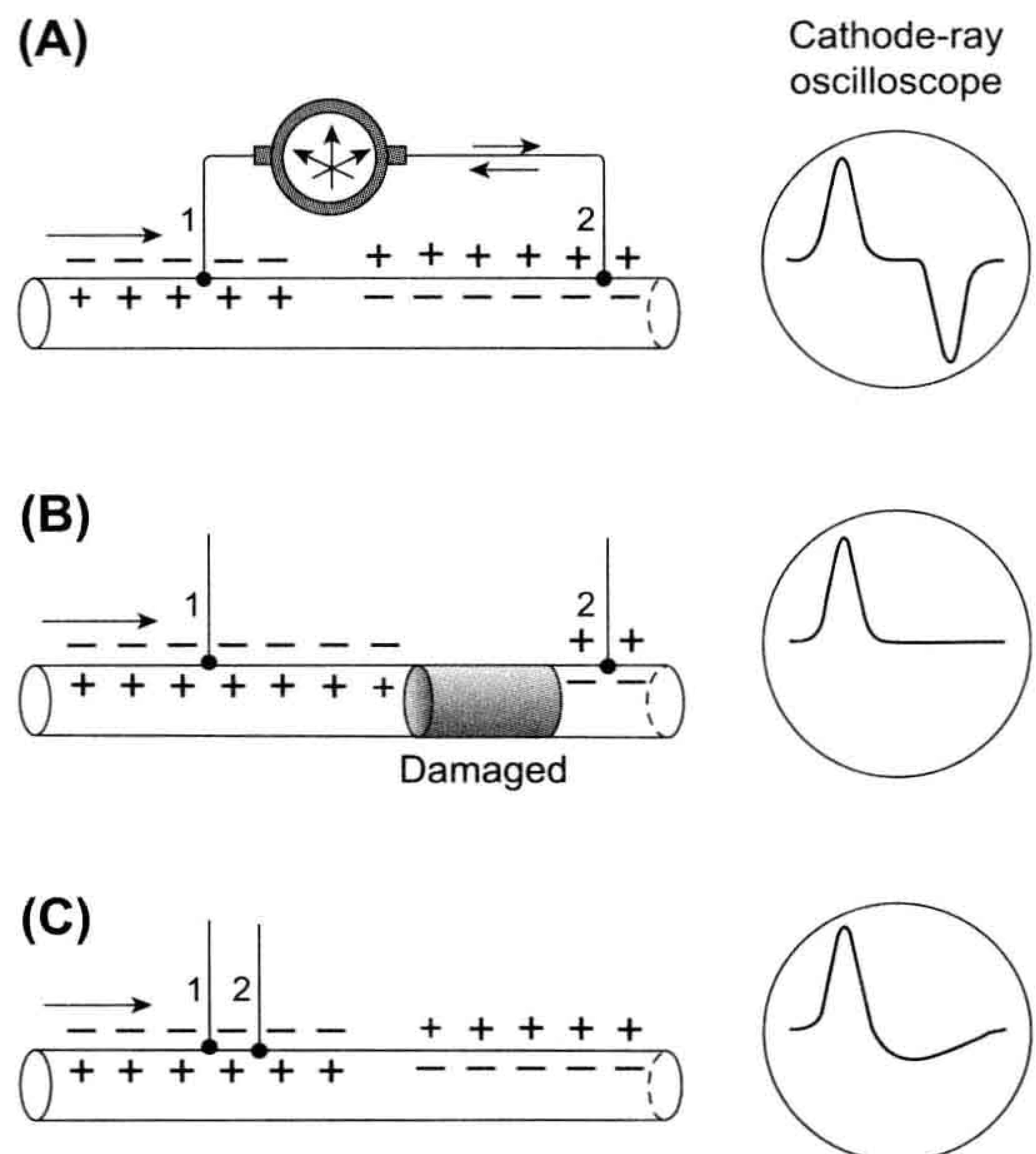


FIGURE 18.10 Diagram of the waveforms that would be recorded externally during propagation of an AP in a single fiber. (A) When the two electrodes are far apart (relative to the AP wavelength), a diphasic recording is obtained, with the two phases being symmetrical and separated by an isopotential segment. The two phases are due to the current flow through the voltmeter recorder being first in one direction and then in the opposite direction. (B) If the fiber between these two electrodes is damaged (e.g. by crushing) or depolarized (by elevated $[K^+]_o$), so the AP cannot sweep past the second electrode (2), then this second phase is prevented and the recording is monophasic. (C) If the two electrodes depicted in (A) are brought progressively closer, then the isopotential segment would shorten and disappear. If electrode 2 is brought very close to electrode 1, so that the interelectrode distance is short relative to the wavelength, then the second phase is smaller than the first phase, and the record resembles the first derivative of the true AP.

VIB. Compound Action Potential

When one records the APs externally, the records are graded and not all-or-none. (In contrast, in the case of the true APs recorded intracellularly from single fibers [see following chapter], the APs are all-or-none.) That is, the signal recorded becomes larger and larger, up to a maximum amplitude as the intensity of stimulation is increased. This is the so-called compound action potential. It is graded because, as a greater and greater fraction of the fibers are activated, the external longitudinal currents associated with the all-or-none AP in each fiber cut across the recording electrodes, thereby producing a larger signal. The AP in each individual fiber is always all-or-none. The amplitude of the signal is determined by the resistance between the electrodes multiplied by the amount of current flowing through this resistance ($V = IR$). The recording of compound action potentials is diagrammed in Fig. 18.11.

The compound action potentials can be demonstrated by recording the EMG from a human subject when one

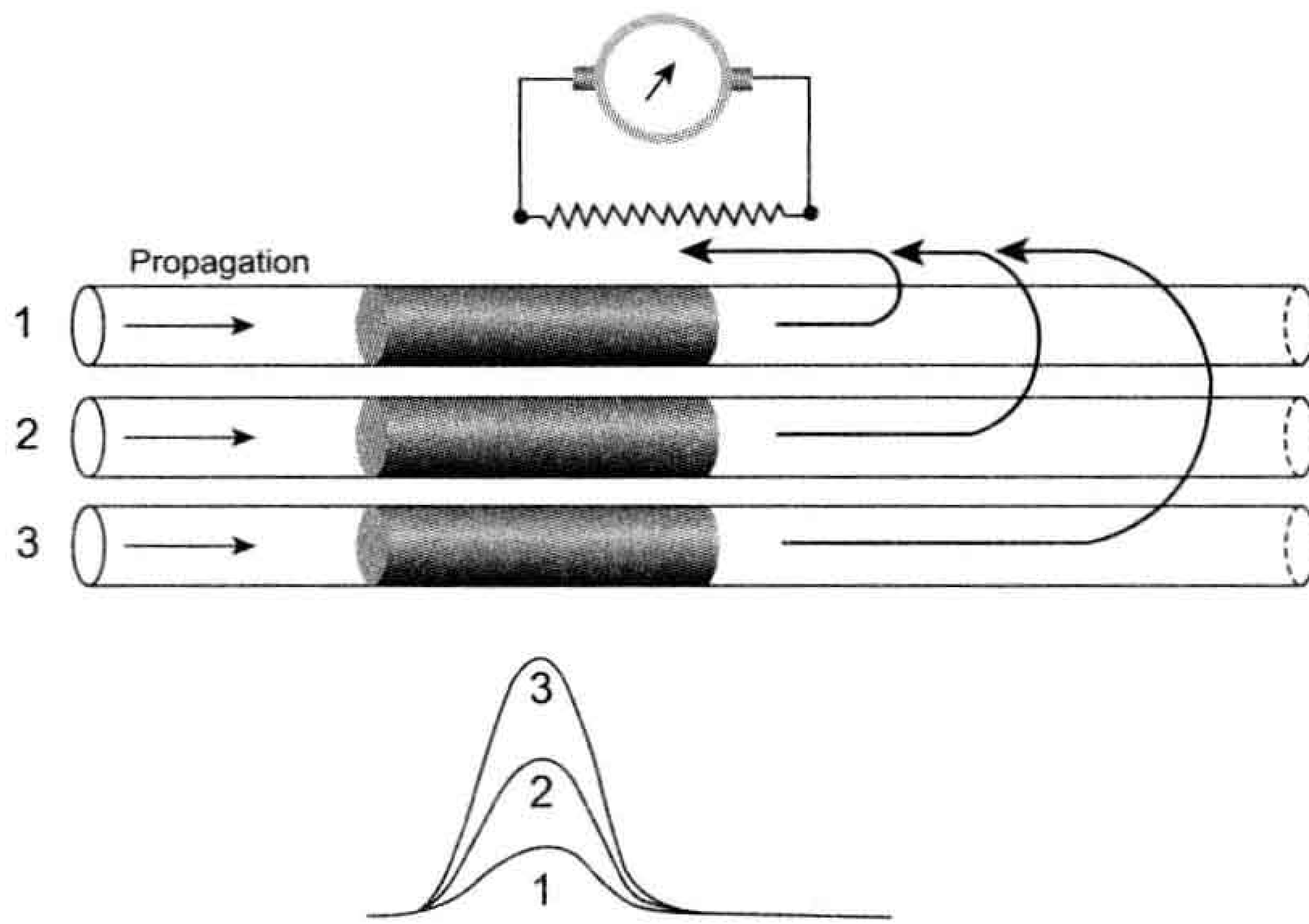


FIGURE 18.11 Diagram of a compound action potential in an isolated nerve trunk, such as the frog sciatic nerve, recorded externally by a pair of longitudinal electrodes. The voltmeter (oscilloscope) records the voltage (*IR*) drop across the resistance (fluid) between the two electrodes. If only fiber 1 is activated, the current passing between the electrodes is small and the voltage recorded is small. If fiber 2 is simultaneously activated with fiber 1, then the amount of current is doubled and the voltage is doubled. When all three fibers are simultaneously activated, the current is tripled, and the voltage is tripled. Therefore, the externally recorded compound action potential is graded because it reflects the electrical activity of numerous fibers, each of which produces an all-or-none AP.

electrode is placed on the skin of the ventral forearm and the other (reference) electrode on the wrist of the same arm. Then, as the subject voluntarily produces stronger and stronger contraction to flex the hand, the electrical signals picked up become greater and greater in amplitude and frequency. The amplitude becomes larger because more muscle fibers are simultaneously activated. This is known as **fiber recruitment**. The frequency also increases, because the motor nerves fire at a higher frequency, causing the muscle fibers to fire at a higher frequency and thus producing a more powerful tetanic contraction.

APPENDIX 1 ADDITIONAL DISCUSSION OF INPUT RESISTANCE AND IMPEDANCE

Because: $\lambda_{DC} = \sqrt{r_m/r_i}$ (Equation 18.4a), Equation 18.9 can be given as:

$$R_{in} = 0.5\, r_i\sqrt{\frac{r_m}{r_i}} = 0.5\sqrt{r_m r_i} \tag{18A.1}$$

and Equation 18.11 can also be given as:

$$V_x = I_o 0.5\sqrt{r_m r_i}e^{-x/\lambda} \tag{18A.2}$$

Thus, input resistance is proportional to $\sqrt{r_m r_i}$. This indicates that the higher the longitudinal resistance of the fiber's axoplasm (or myoplasm), which is a function of the resistivity of the axoplasm and fiber diameter, and the higher the membrane resistance, the higher the input resistance. The input resistance also can be calculated from the electrical equivalent circuit for a cable.

The input impedance can also be given in terms of R_m and R_i, the specific resistance of the cell membrane and resistivity of the axoplasm, respectively. Since $R_m = 2\pi a r_m$ and $R_i = \pi a 2 r_i$, then Equation 18.12 can be converted to:

$$R_{in} = 0.5\sqrt{\frac{R_m}{2\pi a}\frac{R_i}{\pi a^2}} \tag{18A.3a}$$

$$= 0.5\sqrt{\frac{R_m R_i}{2\pi^2 a^3}} \tag{18A.3b}$$

Thus, the input resistance is directly proportional to the square root of the membrane specific resistance and the resistivity of the axoplasm and inversely proportional to the square root of the fiber radius raised to the third power.

Calculation of the input impedance (Z_{in}) is more complicated because it also depends on the membrane capacitance (C_m) and on the frequency (*f*) of the alternating current (AC) used. According to Katz (1966), the input impedance of a long fiber (current injected at one end) is given by:

$$Z_{in} = \sqrt{\frac{R_m R_i}{2\pi^2 a^3\sqrt{1 + 4\pi^2 f^2 R_m^2 C_m^2}}} \tag{18A.4}$$

$$\Omega = \sqrt{\frac{(\Omega\cdot \mathrm{cm}^2)(\Omega\cdot \mathrm{cm})}{\mathrm{cm}^3\sqrt{(\mathrm{s}^{-2})(\mathrm{s}^2)}}}$$

A discussion of the AC length constant (λ_{AC}) is beyond the scope of this chapter.

APPENDIX 2 PROPAGATION IN CARDIAC MUSCLE AND SMOOTH MUSCLES

AI. BACKGROUND

Chapter 18 discusses propagation in cells that are long cables, such as nerve fibers and skeletal muscle fibers. Propagation is more complex in tissues composed of assemblies of short cells, such as cardiac muscle and visceral smooth muscles. These short cells may be considered to be short or truncated cables. In such a truncated cable cell, its true length constant λ is much longer than the cell's length. Therefore, there is relatively little voltage fall-off (decay) over the length of each cell. It follows that the entire cell undergoes an action potential (AP) nearly simultaneously. Yet propagation velocity θ is much slower in cardiac muscle (ca. 0.5 m/s) and smooth muscles (ca. 0.05 m/s) than in skeletal muscle (ca. 5–6 m/s) or non-myelinated nerve fibers

(ca. 2 m/s). Part of the reason for the slower θ concerns fiber diameter (i.e. diameter of cardiac muscle fiber is about 15 μm compared to about 60 μm for skeletal muscle fibers). Equation 16b in Chapter 18 indicates that in a simple cable, θ is a function of $\sqrt{a}$ (where a is the fiber radius). The fact that skeletal muscle also has a much higher max *dV/dt* (rising phase of the AP) than cardiac muscle and smooth muscle is another factor that contributes to the lower than expected θ in cardiac muscle and smooth muscle. The max *dV/dt* in cardiac muscle is ca. 200 V/s and in smooth muscle ca. 5 V/s, as compared with skeletal muscle ca. 600 V/s. In addition, the higher the extracellular resistance, which depends on the tightness of packing of the fibers in the muscle tissue, the slower the velocity.

Another factor that determines velocity in cardiac muscle and smooth muscle is the high resistance of the junctional membranes (the intercalated disk membranes in the case of cardiac muscle). It is still controversial as to exactly how high the junctional resistance is. When gap junctions are present, the gap junction channels span the intercellular junction, and so serve to lower the cell-to-cell resistance (see chapter on gap junctions). However, the hearts of lower vertebrates (e.g. fish, amphibians, reptiles) either have no gap junctions or they are very sparse and tiny. In addition, even parts of mammalian hearts and some visceral smooth muscles (e.g. longitudinal muscle layer of intestine) do not appear to contain gap junctions. If so, another mechanism may be involved for cell-to-cell propagation in those muscles in which there is a virtual absence of gap junctions. One of the mechanisms proposed is known as the *electric field model* (Sperelakis and Mann, 1977; Sperelakis et al., 1979). This mechanism is discussed in this appendix.

Since the short cardiac muscle cell shows no voltage decay, the entire length of the cell should undergo the AP nearly simultaneously (i.e. nearly infinite propagation velocity within each cell). Yet, the overall propagation velocity in the tissue is relatively slow. Clearly, a large time delay must occur at each cell junction. In fact, most of the propagation time is consumed at the cell junctions. This has been demonstrated experimentally. Propagation in cardiac muscle has been shown to be actually *discontinuous* or *saltatory* in nature (Spach et al., 1981; Cole et al.,1988; Sperelakis et al., 1983). Therefore, the presence of a few gap-junction channels is insufficient to reduce the junctional resistance enough to allow a chain of cells to behave as a simple cable. This relatively high junctional resistance may have relevance to heart block and fibrillation.

AII. SOME EXPERIMENTAL FACTS

Some of the key experimental facts relevant to the transmission of excitation from one cell to the next in cardiac muscle and visceral smooth muscle can be summarized as follows. These tissues can be enzymatically separated into their individual cells and the individual single cells are viable and functional. Gap junctions are absent in the hearts of lower vertebrates and in some regions of mammalian hearts, as well as in some visceral smooth muscles, as stated previously. The length constant λ of cardiac muscle and smooth muscle tissues, when measured properly, is relatively short, i.e. less than 0.3 mm (i.e. not much more than about one cell length). The input resistance (R_{in}) of cardiac muscle and smooth muscle, when measured properly, is relatively high, about 5−40 MΩ. The short λ and high R_{in} suggest that the cells are not profusely connected by low-resistance pathways (e.g. by gap-junction channels). Thus, even when gap junctions are present, the junctional membranes still constitute a substantial barrier to current flow from one cell to the next (Tarr & Sperelakis, 1964).

As stated above, there is almost no voltage decay in a single cell and the entire cell fires an AP nearly simultaneously. Therefore, most of the propagation time is consumed at the cell junctions and propagation in these tissues is a discontinuous process. Propagation velocity in cardiac muscle and smooth muscle is slower than what can be accounted for by the smaller fiber diameter and lower max *dV/dt*. The cell-to-cell transmission process is quite labile, somewhat like that in synaptic transmission.

Considerable data have been published concerning the degree of spread of electrotonic current between neighboring cells in cardiac muscle and visceral smooth muscles. Only one example is presented here for frog cardiac (ventricular) muscle. In these experiments, electrode 1 was used to record voltage and to inject current (using a Wheatstone bridge circuit), whereas electrode 2 recorded voltage only. As illustrated in Fig. 18A.1, using a pair of microelectrodes whose tips were spaced 11 μm apart, in some double impalements there was no electrotonic current spread between the two electrodes (e.g. panel A in Fig. 18A.1), whereas in other impalements there was substantial spread of current (e.g. panel B). In one unusual case (panels C, D), the double impalement first showed good spread (i.e. interaction) between the electrodes (C), but then due to muscle contraction, one electrode left that cell and impaled a neighboring cell having a normal RP (right portion of panel C); then there was no significant interaction between the two electrodes residing in neighboring cells (D). In the impalements in which there was substantial interaction between the electrodes (e.g. panels B, C), it was proposed that the two electrodes had impaled the same cell (e.g. both electrodes recorded low RPs (perhaps due to damage caused by the two electrodes impaling one cell). In the impalements in which there was little or no interaction (e.g. panels A, D), it was proposed that the electrodes had impaled neighboring cells. This interpretation is most clear in panel D, in which the two

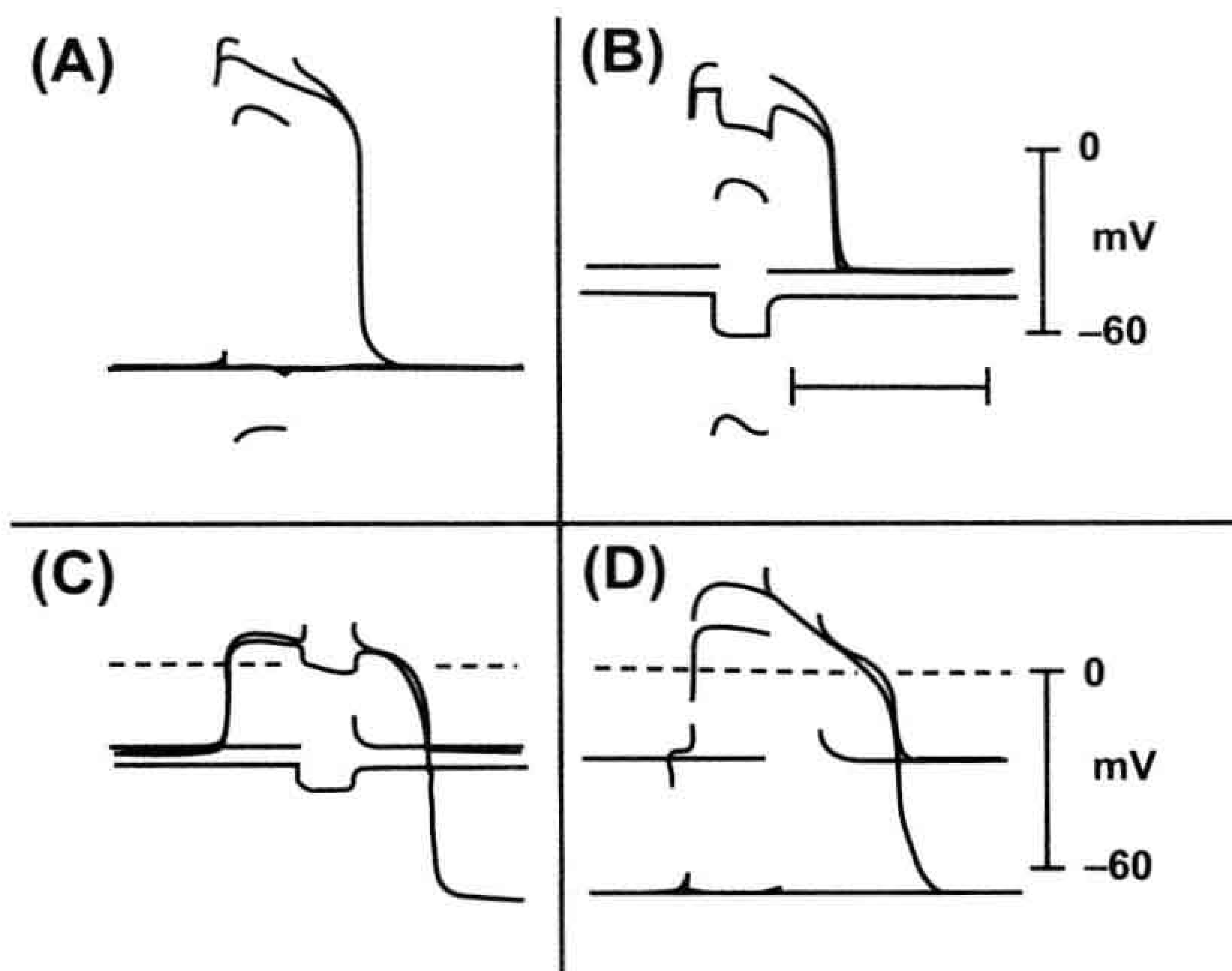


FIGURE 18A.1 Three typical experiments (A, B and C, D) measuring the spread of electrotonic current between two closely spaced intracellular microelectrodes in intact frog ventricular trabeculae at rest and during the plateau of the action potential. The interelectrode distance was 11 μm. Rectangular hyperpolarizing current pulses (approx. 150 ms in duration) were applied. Two successive sweeps of the oscilloscope are superimposed in each panel. (A) Interaction at rest and during the plateau was nearly 0%. Capacitive transients are only seen on the trace from electrode 2, whereas a large maintained hyperpolarization occurred at electrode 1. (B) In another impalement in which the cell was injured by the two electrodes, the resting potential was low and the degree of interaction was high. (C, D) In another impalement in which the cell was damaged, the resting potential was low and the degree of interaction was high (electrode I deflection not shown because of bridge imbalance). The contraction accompanying the action potential caused one of the electrodes to become dislodged from that cell and penetrate into a neighboring cell that had a normal resting potential; the degree of interaction then became nearly zero. *(Reproduced with permission from Tarr, M. and Sperelakis, N. (1964). Am J Physiol. 207, 691-700.)*

electrodes recorded markedly different RPs. Thus, there appears to be little or no spread of current between neighboring cells in frog cardiac muscle. If so, then propagation of excitation must occur by some other means.

AIII. ELECTRIC FIELD MODEL

AIIIA. Electric Field Effect

Sperelakis and colleagues developed an electric field (EF) hypothesis for propagation of APs in cardiac muscle for situations in which there were no functioning gap junction channels. A computer simulation model for cell-to-cell propagation in cardiac muscle was developed and progressively improved since the mid-1970s (Sperelakis and Mann, 1977; Sperelakis et al., 1983; Sperelakis, 1987; Picone et al., 1991). The model allows electrical transmission to occur between adjacent excitable cells by means of the EF effect in the very narrow junctional cleft between the contiguous cells (Sperelakis and Mann, 1977). This EF model does not require low-resistance channels (gap junctions) between cells. The major requirements of the model are that the pre- and post-junctional membranes (pre-JM and post-JM) be ordinary excitable membranes and that these membranes be very closely apposed to one another (i.e. the junctional cleft be very narrow, about 10 nm). When the pre-JM fires, the cleft between the cells becomes negative with respect to ground (the interstitial fluid surrounding the cells) and this negative cleft potential (about −40 mV) acts to depolarize the post-JM by an equal amount (namely, 40 mV) and brings it to threshold. (The inner surface of the post-JM remains at nearly constant potential with respect to ground.) This, in turn, brings the surface membrane of the post-junctional cell to threshold.

Figure 18A.2A illustrates propagation of an AP along a chain of 10 cells by the EF effect. In this computer simulation of cardiac muscle, propagation of overshooting APs occurred at a constant velocity of 32 cm/s and the maximum rate of rise of the AP averaged 209 V/s. As can be seen, the upstroke of each AP exhibited a *break* or *step*, reflecting the junctional transmission process.

In the model, a plot of propagation time as a function of distance along a chain of cells has a **staircase shape**, indicating that almost all propagation time is consumed at the cell junctions and that excitation of each cell is virtually instantaneous (Picone et al., 1991; Sperelakis et al., 1983) (see Fig. 18A.2B). In this figure, it can also be seen that the prejunctional membrane fires a fraction of a millisecond *before* the surface membrane of the same cell, as required by the EF model. Propagation was found to be strongly dependent on radial cleft resistance (R_{jc}) and the junctional membrane properties. There was an optimal R_{jc} for maximum propagation velocity under any given conditions. This model is consistent with many experimental facts about propagation in cardiac muscle, and provides an alternative mechanism for AP propagation that does not require low-resistance pathways to transfer excitation directly between adjacent cells. The EF model can also account for the fact that propagation in cardiac muscle is actually discontinuous or saltatory in nature (Spach et al., 1981).

AIIIB. High Density of Fast Na^+ Channels at Intercalated Disks

For this mechanism to work efficiently, there is a requirement for the prejunctional membrane to fire an AP a fraction of a millisecond before the contiguous surface membrane (Sperelakis and Mann, 1977). That is, the prejunctional membrane should be more excitable than the surface membrane, which would cause it to reach threshold first. This situation would be achieved if there were a greater density of fast Na^+ channels in the junctional membranes (intercalated disks, IDs) than in the contiguous

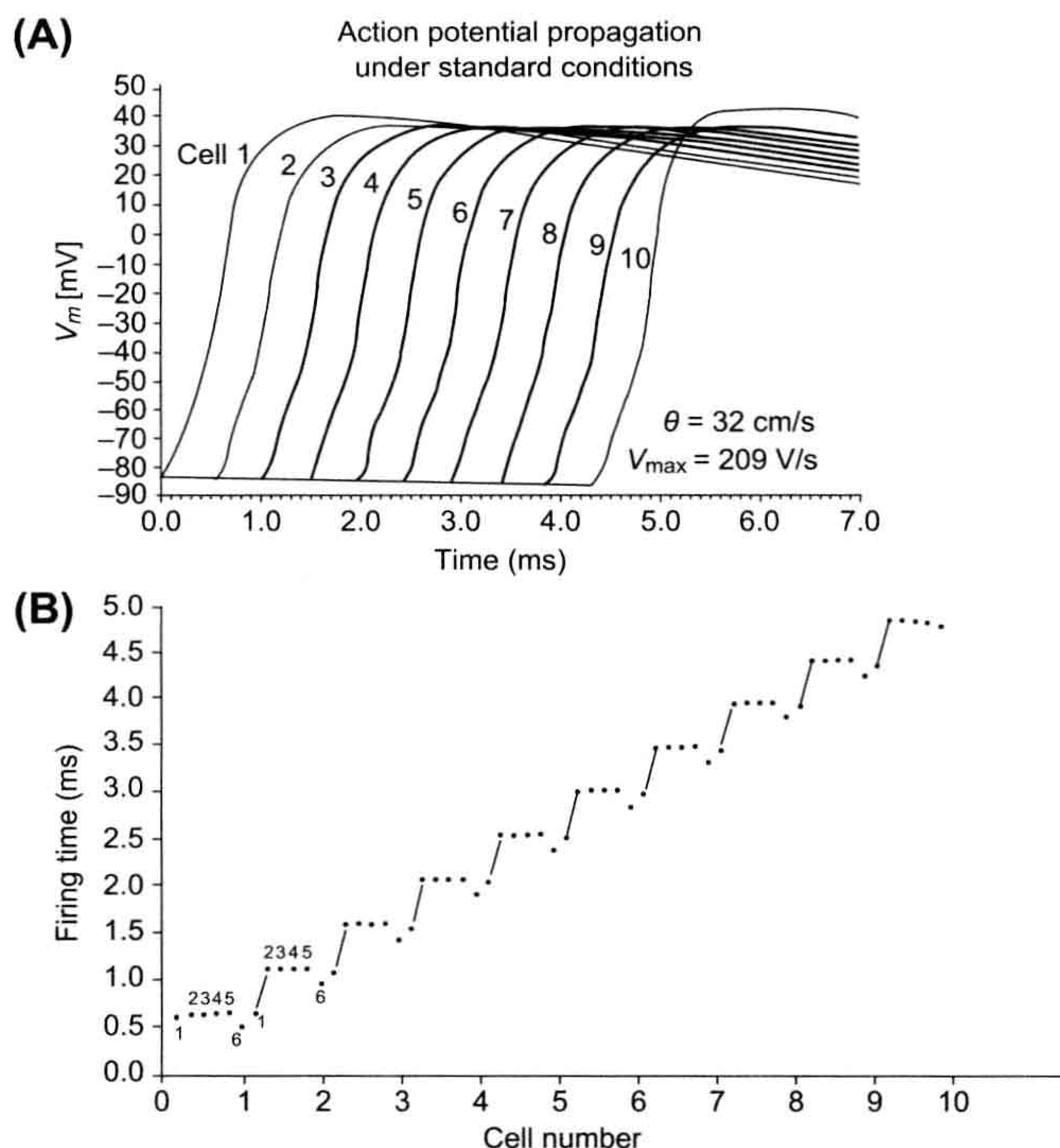


FIGURE 18A.2 Electric field model for propagation in cardiac muscle using a computer simulation. (A) Successful propagation of an AP at constant velocity along a chain of 10 cells under standard conditions. Propagation velocity was 32 cm/s; max dV/dt was 209 V/s. Note the small step, or prepotential, on the AP upstroke. (B) Plot illustrating that junctional delays occupy most of the propagation time. Firing time for an AP to spread along the chain of 10 cells under standard conditions (corresponding to part A) is plotted against distance. Within each cell, the units are numbered 1 through 6 from left to right, 1 corresponding to the post-JM (input), 2–5 the surface membrane and 6 the pre-JM (output). The AP travels along the surface membrane at a high velocity. At the junctions between cells, there is a significant conduction delay as the AP "jumps" across the cleft. This clearly demonstrates the discontinuous nature of AP propagation. *(Adapted with permission from Figs. 2 and 3 of Sperelakis, N., Ortiz-Zuazaga, H. and Picone, J.B. (1991). Innov Tech Biol Med. 12, 404-414.)*

surface membranes (Sperelakis and Mann, 1977). This would make the IDs more excitable and give them a lower threshold than the surface membrane. To examine this possibility, a polyclonal antibody raised against fast Na^+ channels (from rat brain) was used to immunolocalize the fast Na^+ channels in rat atrial and ventricular tissues. In immunofluorescence examination, intense labeling was observed associated with the IDs of both atrial and ventricular cells (Ferguson, D., Sperelakis, N., and Angelides, K. J., 1991 (unpublished) (Fig. 18A.3). This fluorescence was more intense than that of the cell surface membrane. These findings are in agreement with results reported by Cohen and Levitt (1993).

Therefore, it is likely that, not only are fast Na^+ channels present at the ID membranes, they are present in a higher concentration (density) than in the surface cell membrane. A higher density of fast Na^+ channels in the junctional membrane would cause it to have a lower threshold than the surface membrane and so it would reach threshold and discharge first. This would be analogous to the initial segment of the axon of the anterior horn neuron having a lower threshold and therefore discharging before the soma or proximal dendrites (where the excitatory synapses are actually located). Consistent with these

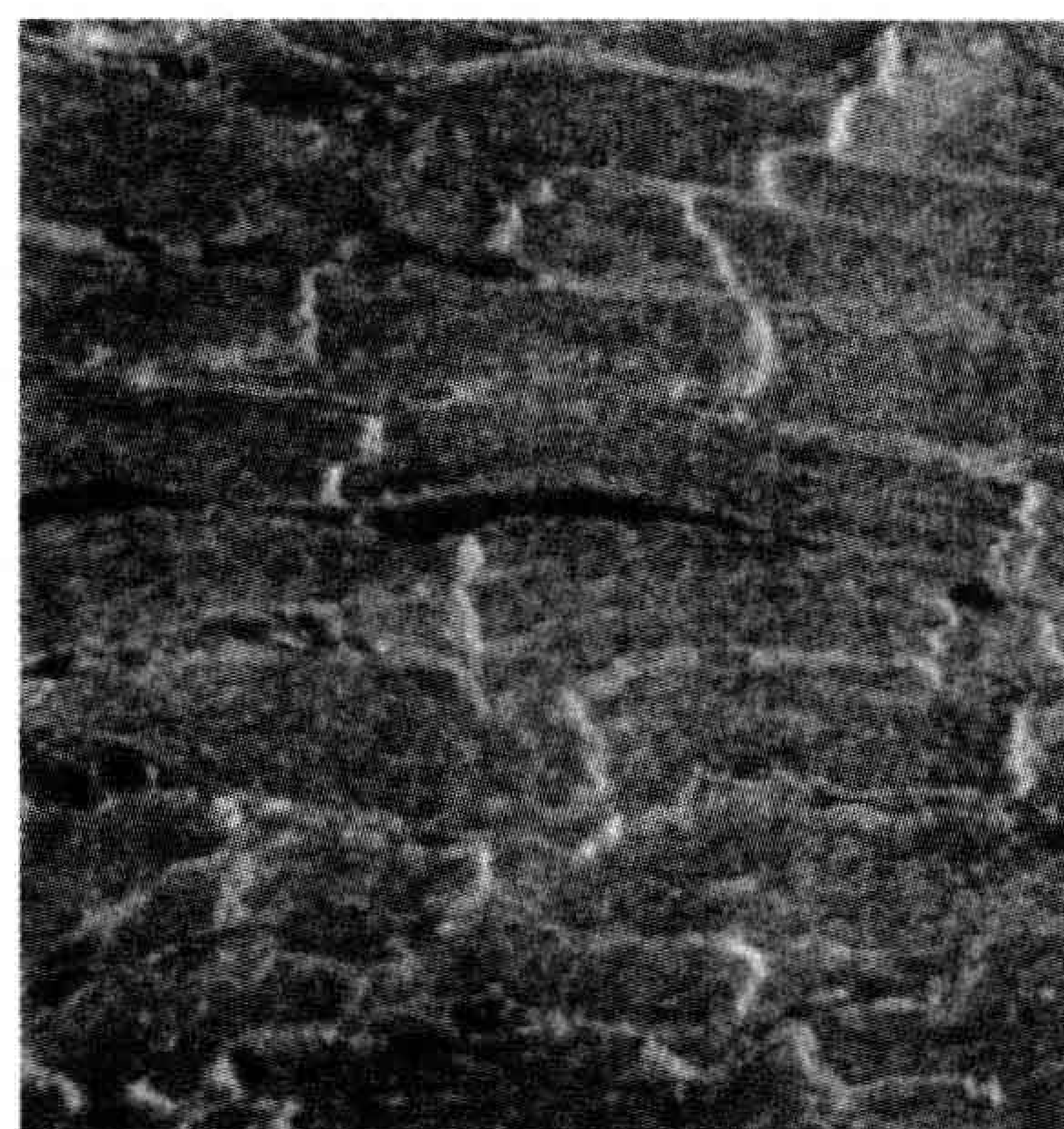


FIGURE 18A.3 Immunofluorescence localization of Na^+ channels in adult rat cardiac muscle (ventricle) using polyclonal antibody to the fast Na^+ channels of rat brain. The antibody is most densely localized at the cell junctions (intercalated disks), but also stained the surface cell membrane. These results suggest that the intercalated disks are highly excitable membranes, even more excitable than the surface cell membrane, consistent with the requirement of the electric field model for propagation between cells not connected by low-resistance tunnels (gap junction connectons). *(From Ferguson, D., Sperelakis, N. and Angelides, K.J., unpublished observations.)*

findings, it was reported that K^+ channels are also localized at the IDs (Mays et al., 1995). Therefore, the EF model is a plausible mechanism for cell-to-cell transmission of excitability in cardiac muscle and in visceral smooth muscle. EF effects may also occur between closely spaced contiguous neurons in the central nervous system.

AIV. ELECTRONIC MODEL FOR SIMULATION OF PROPAGATION

Sperelakis and colleagues (1990) constructed an electronic model to simulate an excitable membrane and this model was used to examine propagation. Four such circuits were successfully made to interact with one another through capacitive coupling to simulate propagation over four cells. Adjustment of one parameter either slightly depolarized and caused repetitive spontaneous APs, or hyperpolarized slightly and depressed excitability, causing partial block (e.g. 2:1, 3:1, 4:1) or complete block of propagation from cell to cell at the cell junctions. When four such cells were connected head to tail in a closed loop, re-entry of excitation occurred and could keep going for many seconds before dying out (due to failure at one of the labile junctions).

In a subsequent study (Ge et al., 1993), 12 such units were arranged to model two adjacent cells: four units for each surface membrane and one for each junctional membrane. The first unit was stimulated to threshold and AP propagation spread over the two cells was recorded (Fig. 18A.4). In this example, the first cell was set to be

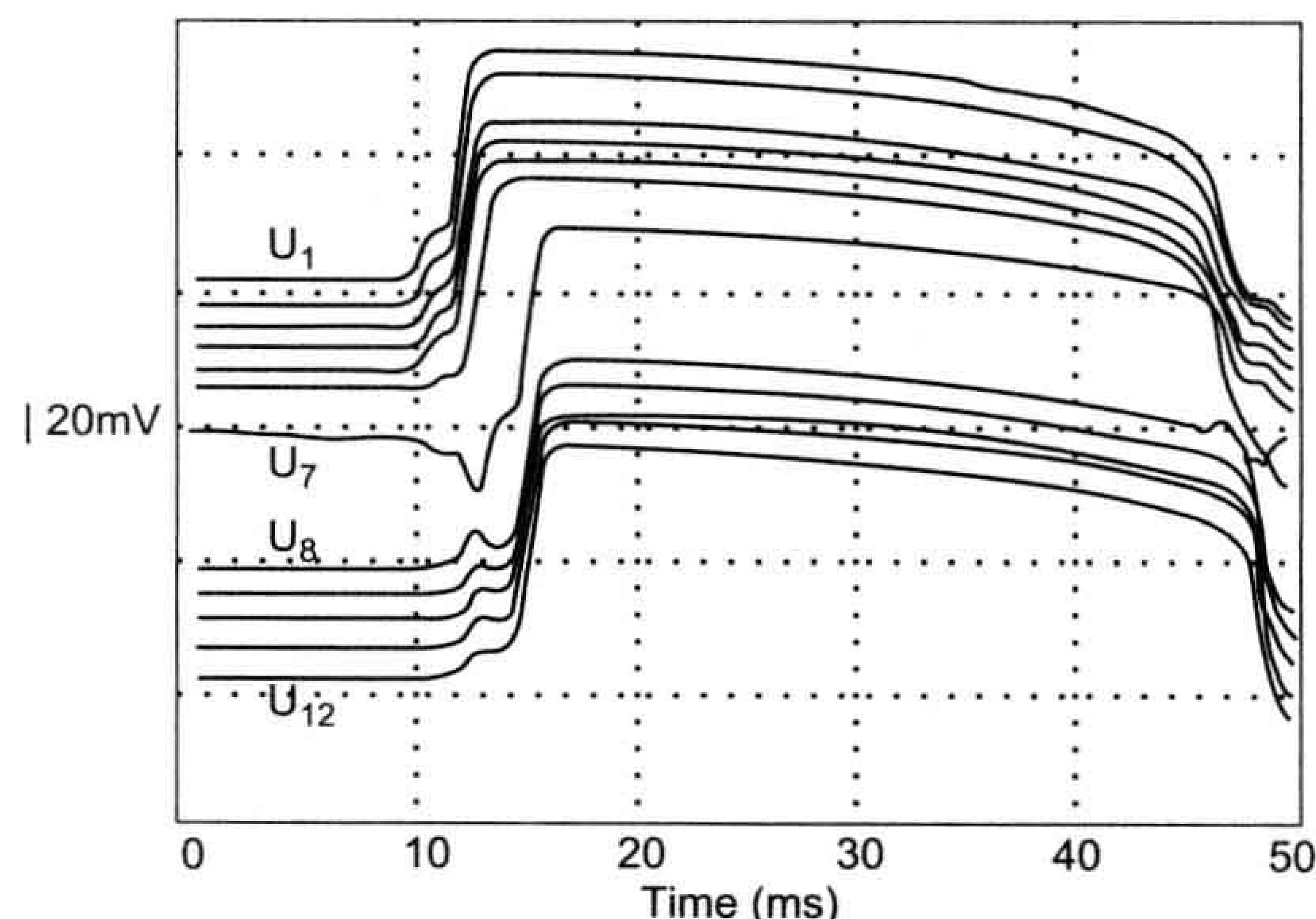


FIGURE 18A.4 Action potentials produced in an electronic model of two heart cells with a cell junction between them. There were six excitable-circuit units in each cell: four representing the surface cell membrane (U2, 3, 4, 5 and U8, 9, 10, 11) and one for each junctional membrane (U1, 6 and U7, 12). The parameters in the first cell (cell 1) were adjusted so that it fired spontaneously in response to pacemaker potential depolarization. Note the nearly simultaneous firing of all units in cell 1 and, after a slight junctional delay time, the nearly simultaneous firing of all units of cell 2. *(Reproduced with permission from Fig. 5A of Ge, J., Sperelakis, N. and Ortiz-Zuazaga, H. (1993). Innov Tech Biol Med. 14, 404-420.)*

spontaneously active and fire a spontaneous cardiac-like AP. All four surface-membrane units in cell 1 (U2, 3, 4, 5) fired an AP nearly simultaneously. However, there was a short delay (e.g. ca. 0.5 ms) in the firing of the unit (U6) representing the prejunctional membrane (at the ID). Firing of U6 led to the firing of all units (U7, 8, 9, 10,11, 12) of cell 2 after a junctional delay of about 2 ms. The firing of the pre-junctional membrane (U6) drove inward hyperpolarizing current through the post-junctional membrane (U7) and outward depolarizing current through the other units (U8, 9, 10, 11, 12) of cell 2 due to current flow (prior to triggering an AP). The time delay was 1−2 ms at the junction. Raising the effective coupling resistance (R_c) between the two cells *and lowering* C_j increased the conduction delay. Propagation was blocked when R_{jc}, the radial shunt resistance at the cell junction, was below 10 KΩ. The post-JM (unit 7) only fired an AP when unit 6 was active, reflecting the EF effect across the junction. Both local-circuit current and the EF effect play roles in the transfer of excitation in this model.

AV. PSPICE MODEL FOR SIMULATION OF PROPAGATION

PSpice is an electrical engineering software program for circuit design and analysis. The appropriate differential equations are built into PSpice. We recently modeled propagation of APs of cardiac muscle using the PSpice program (Sperelakis and Ramasamy, 2002). Like the mathematical simulation and the electronic model, we found that the EF developed in the junctional clefts (negative V_{JC}) was large and sufficient to allow transfer of excitation to the contiguous cell, without the requirement of gap-junction (gj) channels. In the absence of gj channels, transmission of excitation from one cell to the next occurs by means of the intense EF that develops in the narrow junctional cleft (IDs) when the pre-junctional membrane fires an AP. This cleft potential is negative (with respect to ground (interstitial fluid bathing the cells)), and thus acts to depolarize the post-junctional membrane to its threshold potential. This causes the surface sarcolemma of the post-junctional cell to fire an AP and the process is repeated at the next junction. For this EF mechanism to work, the pre-junctional membrane must fire slightly before the surface sarcolemma of the pre-junctional cell (Sperelakis and Mann, 1977). The fact that the density of fast Na^+ channels is greater at the ID membranes than in the surface sarcolemma (Sperelakis N., 1995; Cohen SA and Levitt LK, 1993) means that the excitability of the junctional membranes should be greater than that of the surface sarcolemma.

The myocardial cells were assumed to be cylindrical in shape, 150 μm in length and 16 μm in diameter. The cleft width of the cell junctions (IDs) was assumed to be 100 Å.

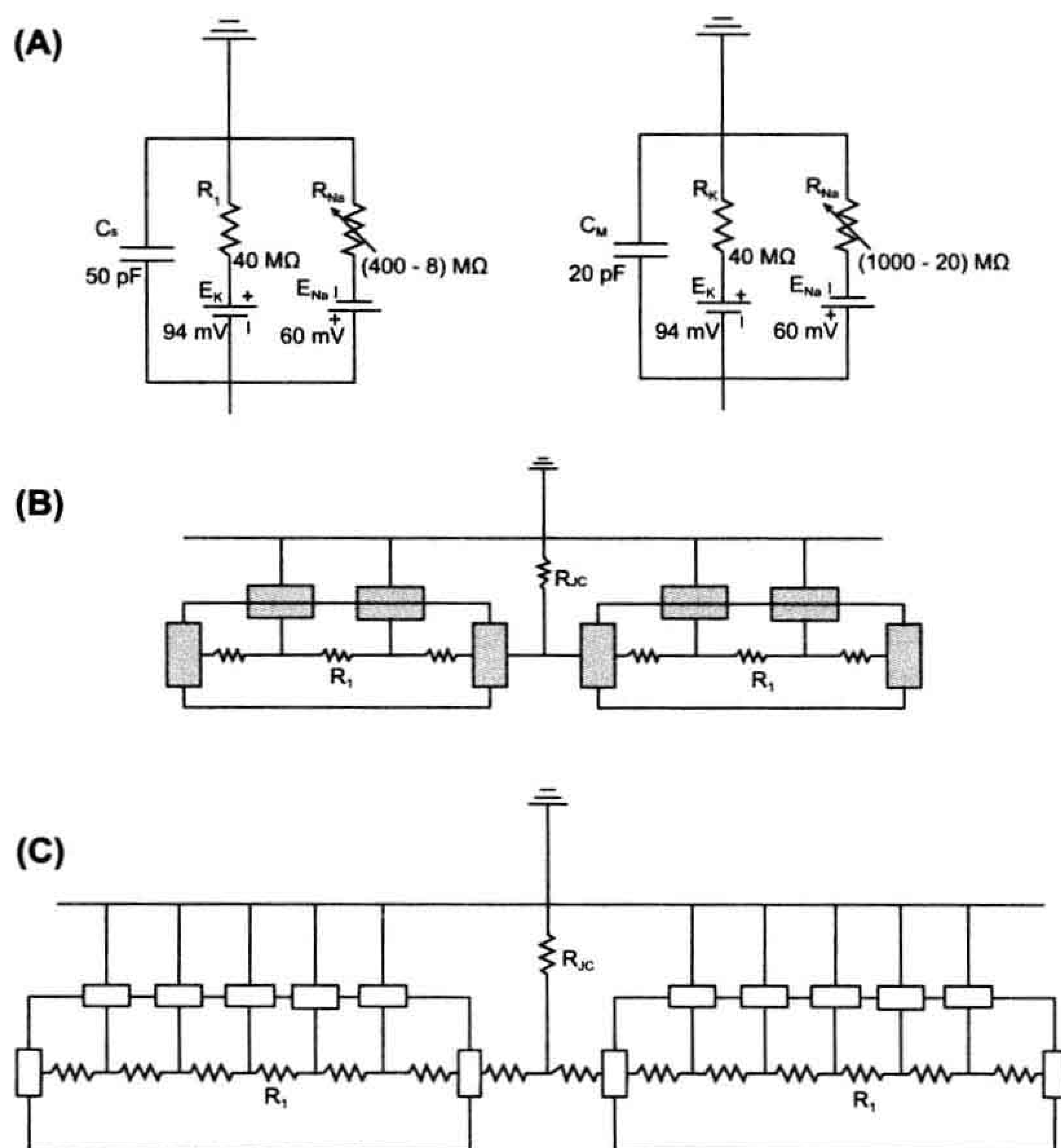


FIGURE 18A.5 (A) Depiction of the basic circuit components in the PSpice model representing a patch of surface membrane of a myocardial cell and a patch of junctional membrane. (B) Four units/cell, two in surface membrane and one in each of the two junctional membranes at the ends of the cell. (C) Seven units/cell.

Each cell was simulated by four basic circuit units; two for the surface sarcolemma and one for each junctional membrane at the two ends of the cell (Fig. 18A.5). The cell junctions contained a transverse resistance, the radial resistance of the junctional cleft (R_{JC}). The standard value used for R_{JC} was 25 MΩ (two 50 MΩ resistors in parallel). The basic units were connected internally by the intracellular longitudinal resistance (r_i) and externally by the extracellular resistance (R_O). The chain of cells was assumed to be bathed in a large volume of Ringer solution connected to ground. The values of the capacitive and the resistive elements in each basic unit were set to reflect an input resistance of 20 MΩ and input capacitance of 100 pF for the individual cells and the junctional units were prorated, based on relative areas represented. At rest, the resistance of K^+ compared to Na^+ was set to give RPs of −80 mV. During excitation, the APs overshot to +34 mV.

To make the circuit as simple as possible, all other types of ion channels were not entered. We focused only on those channels that set the RP and predominate during the rising phase of the AP. That is, we only wanted to inscribe the rising phase of the APs in a chain of cells to study the mechanism of longitudinal propagation. The longitudinal resistance in each junctional cleft was calculated to be 14 Ω (see Fig. 18A.5C). Increasing the longitudinal cleft resistance over a very wide range had no effect on propagation velocity, because there is almost no local-circuit current across the cell junctions. A shunt resistance (R_{gj}, resistance of the gap junction channels) was placed across each cell junction, i.e. from one cell interior to the next (Fig. 18A.6). It was assumed that each gj-channel had a conductance of 100 pS, so R_{gj} was 100 MΩ when 100 gj-channels were inserted. The possibility that the gj-channels are rectifying was ignored for the present purposes. In the current presentation, the data with variation in R_{gj} are not given.

A stimulating current pulse was applied to the inside of unit 1 of cell 1. The values for the rectangular current pulse were 0.50 ms duration and 0.5 nA amplitude. The longitudinal average propagation velocity (θ) was calculated from the measured total propagation time (TPT), assuming a cell length of 150 μm.

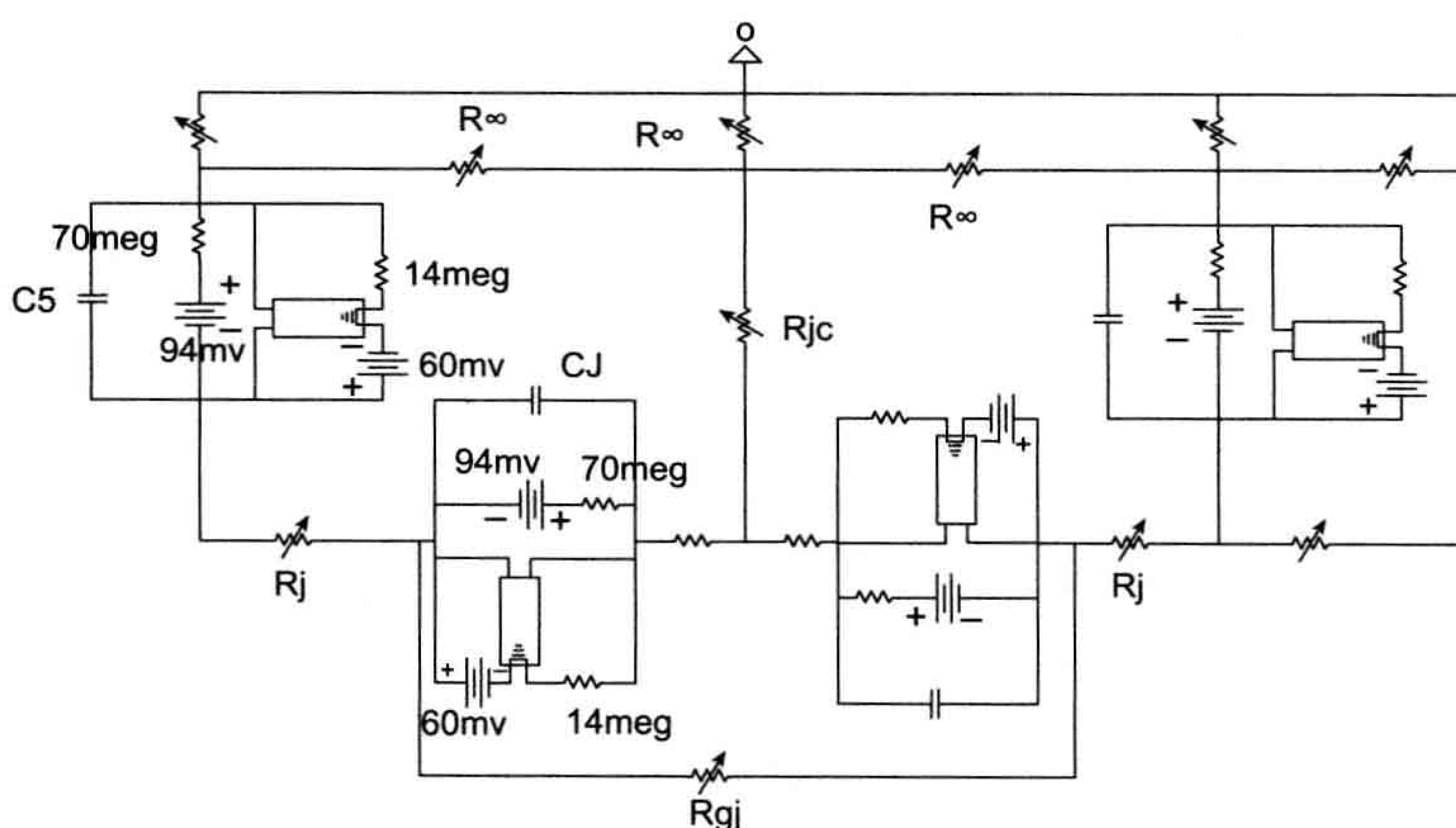


FIGURE 18A.6 A typical cell junction of circuit used for PSpice simulation of propagation of action potentials. A gap-junction shunt resistance (R_{gj}) is inserted across the cell junction and is in parallel with the electric field (EF) mechanism.

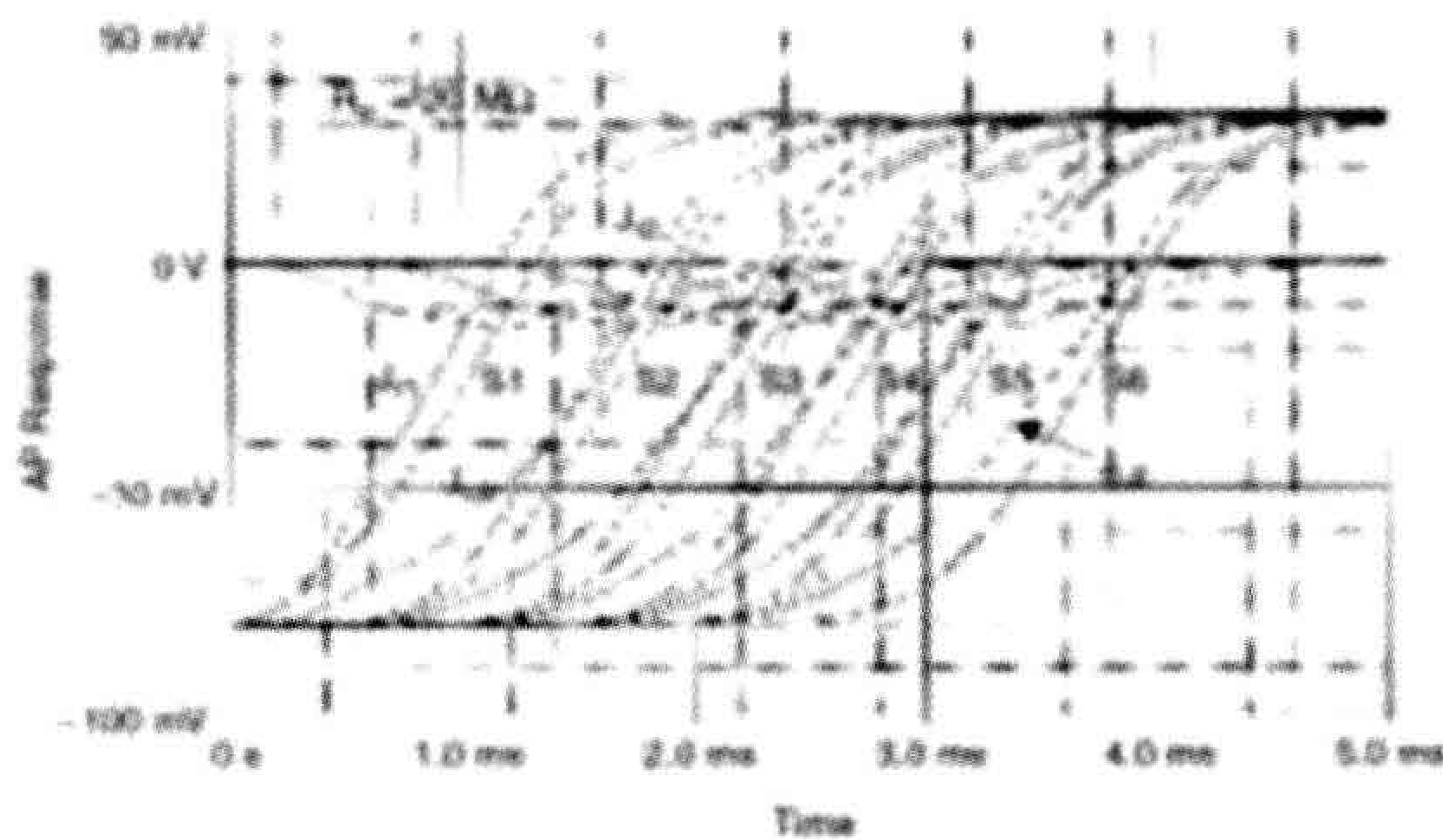


FIGURE 18A.7 Staircase propagation and firing sequences. Absence of gap junctions. Graph plots total propagation time (TPT) as a function of distance along the six-cell chain in membrane units. Total of 42 units: 7 U/cell × 6 cells. Each cell is assumed to be 150 μm long. The surface membrane of each cell is represented by five units and the two junctional membranes by one unit each. The units were numbered consecutively: 1–7 (cell 1), 8–14 (cell 2), 15–21 (cell 3), 22–28 (cell 4), 29–35 (cell 5) and 36–42 (cell 6). The junctional units fired before the surface units. *Taken from Sperelakis and Ramasamy, 2002.*

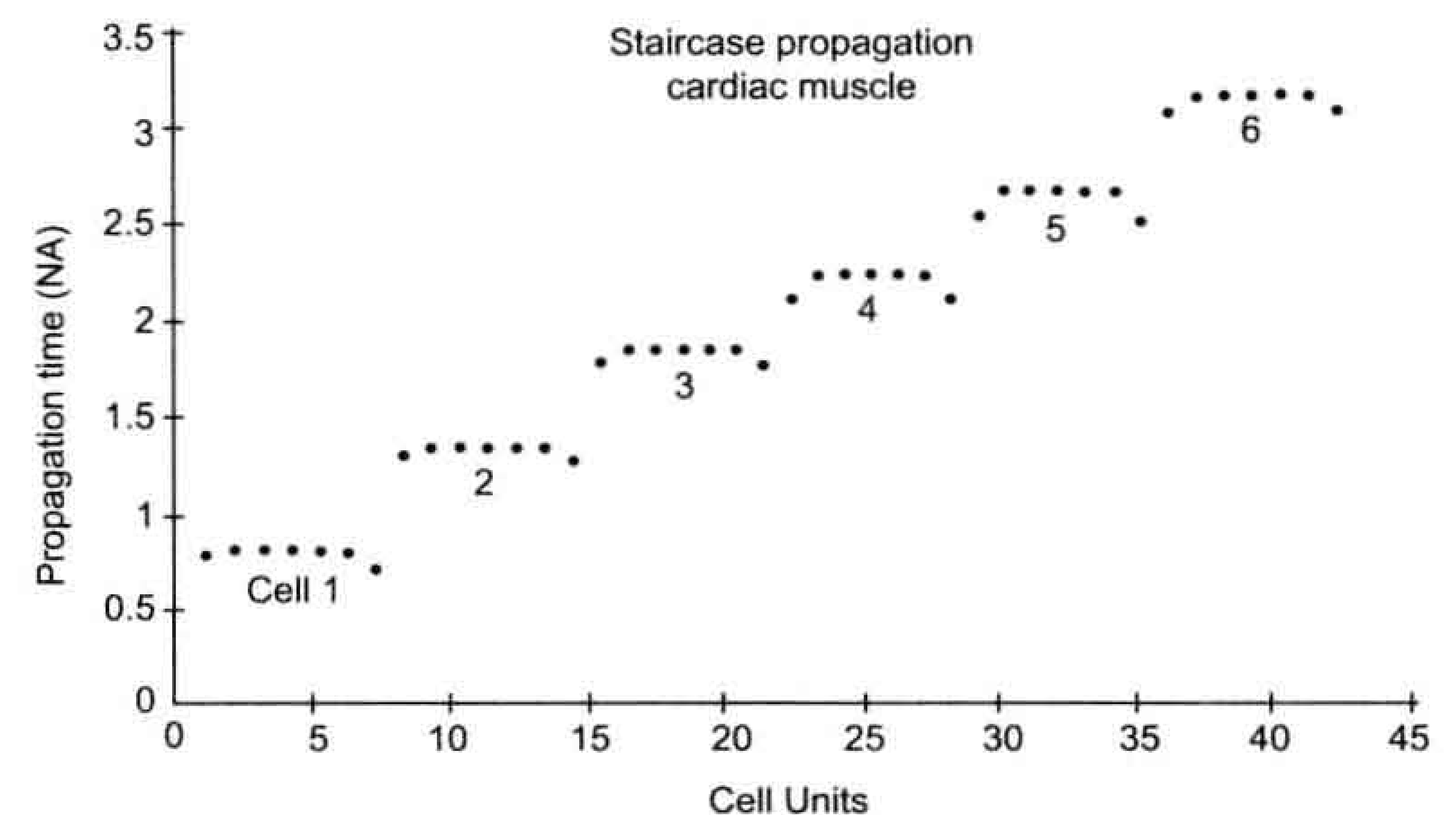


FIGURE 18A.8 Action potential (AP) responses of the six-cell chain of myocardial cells. Absence of gap junctions. At −50 mV, the first trace (of each group of three) is the post-JM (left end of cells), whereas at −10 mV, the leading trace is the pre-JM (right end of cells); i.e. the first two traces criss-cross between −40 and −20 mV). Thus, the post-JM starts to depolarize first because of the cleft potential, but the pre-JM on the far end of the cell reaches the overshoot potential first. The surface membrane units (S1–S6) fire last. *Taken from Sperelakis and Ramasamy, 2002.*

The basic response of the circuit for the six-cell chain under standard conditions is illustrated in Fig. 18A.7. In this experiment, a rectangular current pulse was applied to interior of cell 1 at 0 time. The voltages directly across each of the 42 units (7 U/cell × 6 cells) and the voltage across R_{JC} (the cleft potential) were measured.

The rising phase of the AP response in each of the six cells can be seen. Because the five surface units in each cell fired virtually simultaneously, only three voltage traces can be seen for each cell: (a) post-JM, (b) pre-JM and (c) surface membrane. The RP of the cells was −80 mV and the AP overshoot potential was +34 mV (see Fig. 18A.7), thus giving an AP amplitude of 114 mV. The cleft potential went from 0 mV at rest to a peak of about −12 mV during excitation of the pre-JM in each cell (see Fig. 18A.7). The maximum rate of rise of the APs (max *dV/dt*) was about 110 V/s, the junctional delay time was about 0.3–0.6 ms and propagation velocity (θ) was about 30 cm/s. In general, the transmission delay was reduced when R_{JC} and the cleft potential were increased and when C_j and C_s were decreased. Total propagation time (TPT) was measured between when the APs of the first cell and last cell crossed a V_m of −20 mV.

The firing sequence of the seven units of each cell is shown in Fig. 18A.8. As can be seen, in cell 1, the pre-JM (unit 7) fired before the post-JM (unit 1), which fired before the surface units (units 2–6). As stated earlier, all surface units fired virtually simultaneously. The lead time of the pre-JM became less and less in cells 2–6. This behavior pattern of the pre-JM (right end of cell) firing slightly before the post-JM (left end of cell) was also observed in the mathematical model (Picone et al., 1991). The graphic plot of propagation time as a function of distance along the chain of six cells also illustrates the *staircase propagation* (Fig. 18A.8). That is, the shape of the plot is like a *staircase*. The flat part of each step represents the long surface membrane of each cell. The sharp rise of each step represents the very short (e.g. 100 Å) cell junction gap. The overall propagation time consists almost entirely of the junctional delay times summed. That is, almost all of the propagation time is due to the junctional transmission process. The surface sarcolemma along the cell's entire length fires simultaneously.

The cleft potential occurs during the rising phase of the AP in the pre-JM. The shape of the cleft potential is an approximation of the first time derivative of the AP upstroke (see Fig. 18A.5). In general, the cleft potential is larger when R_{JC} is increased and when C_j and C_s are decreased. When R_{JC} was increased from the standard 20 MΩ to 50 MΩ and 100 MΩ, the cleft potential increased from −12 mV to −27 mV and to −47 mV. The cleft potential instantly depolarizes the post-JM by an equal amount because of its patch-clamp-like action. The amplitude of the depolarization (step) on the rising phase of the AP of the post-JM is proportional to the amplitude of the cleft potential. The value of R_{JC} for minimum junctional delay, and hence maximal propagation velocity, had a broad optimum of 20–30 MΩ. The value of R_{JC} reflects the degree of closeness of the two junctional membranes.

In summary, it was found that propagation of excitation can occur by the EF mechanism alone, even when the excitability of the cells was low. Therefore, the EF mechanism alone can account for propagation of excitation in cardiac muscles that do not possess gap junctions. In those cases in which gap junctions do exist and are functioning, the EF mechanism would act in parallel and thereby increase the safety factor for conduction.

BIBLIOGRAPHY

Cohen, S. A., & Levitt, L. K. (1993). Partial characterization of the rHl sodium channel protein from rat heart using subtype-specific antibodies. *Circ Res, 73*, 735–742.

Cole, K. S. (1968). *Membranes, Ions and Impulses: a Chapter of Classical Biophysics*. Berkeley: University of California Press.

Cole, W. C., Picone, J. B., & Sperelakis, N. (1988). Gap junction uncoupling and discontinuous propagation in the heart: a comparison of experimental data with computer simulations. *Biophys J, 53*, 809–818.

Ge, J., Sperelakis, N., & Ortiz-Zuazaga, H. (1993). Simulation of action potential propagation with electronic circuits. *Innov Tech Biol Med, 14*, 404–420.

Katz, B. (1966). *Nerve, Muscle, and Synapse*. New York: McGraw-Hill.

Mann, J. E., Jr., Sperelakis, N., & Ruffner, J. A. (1981). Alterations in sodium channel gate kinetics of the Hodgkin-Huxley equations on an electric field model for interaction between excitable cells. *IEEE Trans Biomed Eng, 28*, 655–661.

Mays, D. J., Foose, J. M., Philipson, L. H., & Tamkun, M. M. (1995). Localization of the Kv1.5K^+ channel protein in explanted cardiac tissue. *J Clin Invest, 96*, 282–292.

Picone, J. B., Sperelakis, N., & Mann, J. E., Jr. (1991). Expanded model of the electric field hypothesis for propagation in cardiac muscle. *Math Comp Mod, 15*, 17–35.

Rail, W. (1977). In J. M. Brookhart, & V. B. Mounteastle (Eds.), *Handbook of Physiology, Vol. 1* (pp. 39–97). Bethesda: American Physiological Society.

Spach, M. S., Miller, W. T., III, Geselowitz, D. B., Barr, R. C., Kootsey, J. M., & Johnson, E. A. (1981). The discontinuous nature of propagation in normal canine cardiac muscle. Evidence for recurrent discontinuity of intracellular resistance that affects the membrane currents. *Circ Res, 48*, 39–54.

Sperelakis, N. (1987). Electrical field model for electric interactions between myocardial cells. In S. Sideman, & R. Beyar (Eds.), *Activation, Metabolism, and Perfusion of the Heart – Simulation and Experimental Models* (pp. 77–113). Dordrecht: Martinus Nijhoff.

Sperelakis, N. (1992). Cable properties and propagation mechanisms. In N. Sperelakis, & R. O. Banks (Eds.), *Essentials of Physiology* (pp. 83–97). Boston: Little, Brown.

Sperelakis, N. (2001). Cable properties and propagation of action potentials. In *Cell Physiology Sourcebook*, (3rd ed., chapt 24). San Diego: Academic Press.

Sperelakis, N. (2002). Editorial: An electric field mechanism for transmission of excitation between myocardial cells. *Circ Res., 91*, 985–987.

Sperelakis, N., & Mann, J. E., Jr. (1977). Evaluation of electric field changes in the cleft between excitable cells. *J Theor Biol, 64*, 71–96.

Sperelakis, N., & Ramasamy, L. (2002). Modeling electric field transfer of excitation at cell junctions. *IEEE Eng Med Biol, 22*, 130–143.

Sperelakis, N., Marschall, R., & Mann, J. E. (1983). Propagation down a chain of excitable cells by electric field interactions in the junctional clefts: effect of variation in extracellular resistances, including a "sucrose gap" simulation. *IEEE Trans Biomed Eng, 30*, 658–664.

Sperelakis, N., Rollins, C., & Bryant, S. H. (1990). An electronic analog simulation for cardiac arrhythmias and reentry. *J Cardiovasc Electrophysiol, 1*, 294–302.

Tarr, M., & Sperelakis, N. (1964). Weak electronic interaction between contiguous cardiac cells. *Am J Physiol, 207*, 691–700.

Taylor, R. E. (1963). Cable theory. In W. L. Nastuk (Ed.), *Physical Techniques in Biological Research, Vol. 6* (pp. 219–262). New York: Academic Press.

Chapter 19

Electrogenesis of Membrane Excitability

Nicholas Sperelakis

Chapter Outline

I. SUMMARY

Membrane excitability is a fundamental property of nerve and muscle cells (skeletal, cardiac and smooth), as well as certain other cell types, such as some endocrine cells. An excitable cell is one that, in response to certain environmental stimuli (electrical, chemical or mechanical), generates an all-or-none electrical signal or *action potential* (AP). The AP is sometimes called an "impulse", e.g. a *nerve impulse*. The AP is triggered by a depolarization of the membrane, which is produced by the applied stimulus. The depolarization initiates an increase in the membrane permeability to Na^+ ions, which then flow into the cell, causing a transient reversal in the membrane potential (i.e. the *spike*). A slower increase in the permeability of the membrane to K^+ ions contributes to the repolarization of the membrane, in addition to the spontaneous inactivation of the Na^+ channels. Some cells display the property of *automaticity*; i.e. they produce APs spontaneously without any externally-applied stimulus.

In some excitable cell types (such as cardiac), a slow inward Ca^{2+} current contributes to the long plateau of the AP and, in others (such as smooth muscle), the Ca^{2+} current itself generates the upstroke. The membrane currents that contribute to the AP can be studied by the *voltage-clamp method*, which allows isolation and characterization of each membrane current as a function of membrane potential and time. Ionic currents flow across the membrane by means of numerous ion-specific protein channels. Each channel molecule has a region that senses the transmembrane potential and acts as a gate to open or close the channel to ion passage through its *central water-filled pore*.

Some types of channels (i.e. Na^+ channels) have a *second gating system* that closes (or inactivates) the

Cell Physiology Sourcebook. DOI: 10.1016/B978-0-12-387738-3.00019-6

channel during a maintained depolarization. The pattern of minute currents that flow through individual voltage-dependent ion channels can be studied using the patch-clamp method. *Single-channel current measurement* and structural information have given a greater understanding of the molecular basis of membrane excitability.

The APs in vertebrate nerve fibers consist of a spike followed by a hyperpolarizing afterpotential. A large fast inward Na^+ current, passing through *fast Na^+ channels*, is responsible for electrogenesis of the spike, which rises rapidly (ca 1000 V/s). Subsequently, a small inward Ca^{2+} current, passing through kinetically-slower channels, is involved in *excitation–secretion coupling* at the nerve terminals. The nerve cell membrane has voltage-dependent K^+ channels which allow K^+ ions to pass readily outward down the electrochemical gradient for K^+. This is responsible for repolarization. This K^+ channel, which opens more slowly than g_{Na} upon depolarization, is called the *delayed rectifier*. The activation of this channel produces the large increase in total g_K that terminates the AP.

The nerve AP amplitude is about 110 mV, from a resting potential (RP) of −70 mV to a peak overshoot potential of about +40 mV. The duration of the AP (at 50% repolarization) ranges between 0.5 and 1 ms, depending on the species and temperature. The threshold potential (V_{th}) for triggering of the fast Na^+ channels is about −55 mV; a critical depolarization of about 15 mV is required to reach V_{th}. The turn-on of the fast Na^+ conductance is very rapid (within 0.2 ms) and E_m is brought rapidly toward E_{Na}. There is an explosive (positive exponential initially) increase in g_{Na} caused by a *positive-feedback relationship between g_{Na} and E_m*.

In certain nerve cells, as well as muscle cells, as E_m depolarizes it crosses V_{th} (about −35 mV) for the slow Ca^{2+} channels. Turn-on of the slow Ca^{2+} conductance (g_{Ca}) and I_{Ca} is slow and tends to bring E_m toward E_{Ca}. The peak I_{Ca} is considerably smaller than the peak fast I_{Na}. The currents decrease at more depolarized E_m levels because of the diminution in electrochemical driving force, even though the conductance remains high. At the reversal potential (E_{rev}) for the current, the driving force goes to zero and reverses direction with greater depolarization. In some smooth muscle cells, the slow Ca^{2+} current itself is sufficient to depolarize the membrane and generate a regenerative slowly-rising AP in the absence of any fast Na^+ current.

II. INTRODUCTION

Excitability is an intrinsic membrane property that allows a cell to generate an electrical signal or AP in response to stimuli of sufficient magnitude. The elongated nerve axon serves to transmit information in the form of APs over long distances. The AP mechanism is required to propagate a uniform signal in a non-decremental manner. In muscle cells, the AP serves to spread excitation over the entire cell surface and is involved in triggering cell contraction.

The energy source for the generation of the AP is stored in the excitable cell itself. An initial depolarization is produced by a stimulus and triggers the intrinsic AP mechanism. The immediate source of energy for the AP comes from the transmembrane ionic gradients for K^+ and Na^+, which act like a battery. The K^+ ion concentration gradient is mainly responsible for the generation of the resting potential (RP), which causes an excess of negative charge to build up on the inner surface of the membrane. Upon depolarization to threshold, the Na^+ ion electrochemical driving force, which is directed inward, causes a large and rapid inward Na^+ current that generates the AP upstroke. Over a longer time frame, the Na^+-K^+ pump is responsible for the generation of the Na^+ and K^+ ionic gradients and for their maintenance and restoration after repetitive AP activity. The Na^+-K^+ pump derives chemical energy from the hydrolysis of ATP. The bases of the RP and active ion transport have been discussed in earlier chapters.

Important technological improvements have led to significant advances in the understanding of the basis of membrane excitability. In the early 1900s, several theories were proposed to explain the mechanism that produces the AP. Julius Bernstein (1902, 1912) proposed that the excitable cell membrane, at rest, was selectively permeable to K^+ ions (producing the RP) and that during excitation the membrane became permeable to all ions (producing the AP). About the same time, Overton (1902) had demonstrated that Na^+ ions were essential for excitability.

By the 1940s, improvements had been achieved in electronic instrumentation, especially in the high-input impedance amplifiers necessary to record bioelectric phenomena using tiny intracellular microelectrodes. In addition, biophysicists began to study the squid giant axon (500–1000 μm in diameter), which permitted insertion of relatively large intracellular electrodes, yielding the first measurements of the true transmembrane potential. The transmembrane potential is recorded as the difference between an intracellular and an extracellular electrode (Fig. 19.1). The findings from the squid giant axon were successfully applied to the smaller diameter (1–20 μm) neurons found in the vertebrate nervous system (Fig. 19.2).

III. ACTION POTENTIAL CHARACTERISTICS

APs in a given fiber (e.g. myelinated nerve fiber) have the properties of being *all-or-none*, and they have a *sharp threshold* and a *refractory period*. All impulses look alike, being very similar in shape, amplitude and duration. Thus, they constitute a *digital system*. Strength of the signal is conveyed by changing the frequency of the impulses, as discussed in the preceding chapter on propagation. The all-or-none property means that the single signal is not

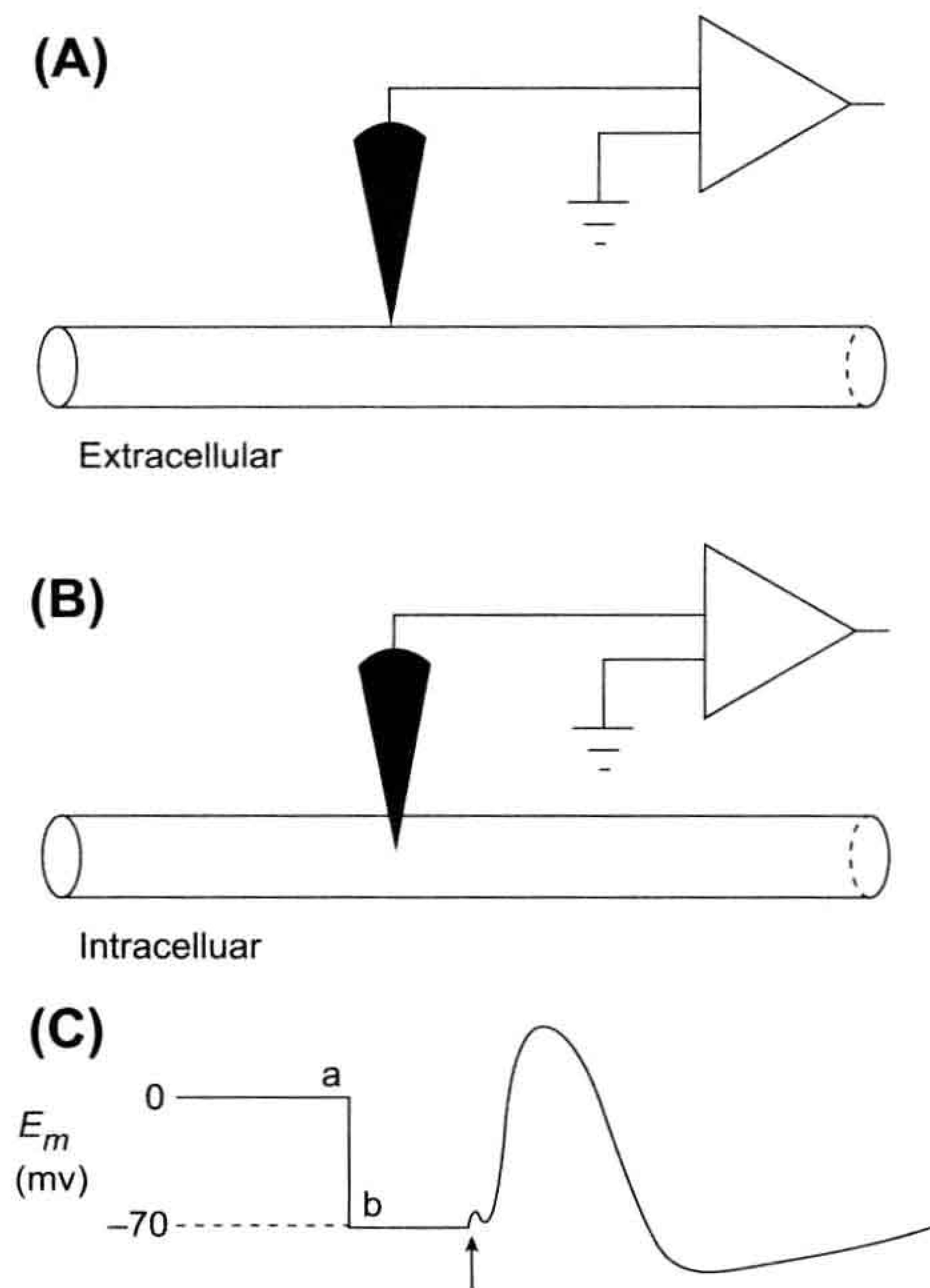


FIGURE 19.1 Recording the transmembrane potential of a squid giant nerve axon. The transmembrane potential is measured as the potential difference between the intracellular and extracellular electrodes. (A) The microelectrode is outside the axon and measures 0 mV (segment a in panel C). (B) As the electrode is advanced and crosses the membrane, the RP of −70 mV is measured (segment b in C). The cell membrane makes a tight seal around the glass electrode. (C) The membrane potential (E_m) is depicted. Stimulation (at arrow) elicits an AP.

graded in amplitude (i.e. not an amplitude-modulated system) and that the signal is either zero ("off" or "no") or maximum ("on" or "yes"). These characteristics of the AP are discussed in the next sections.

IIIA. Local-Circuit Currents

During propagation of an AP down a nerve fiber, current flow accompanies the propagating change in membrane voltage. This current is called the *local-circuit current* and has both longitudinal and radial (transverse) components that make a complete circuit (Fig. 19.3A,B). Propagation and local-circuit currents have been thoroughly discussed in the preceding chapter. For our purpose here, we focus on the longitudinal component. The intracellular and the extracellular (external) longitudinal current are exactly equal in amplitude, but flow in opposite directions (Fig. 19.3A,B). The intracellular current is, of course, confined to the cross-sectional area of the nerve fiber (neuroplasm), whereas the extracellular current can use the entire extracellular volume (so-called *volume conductor*). If a single nerve fiber or nerve bundle is mounted in air, then the extracellular action current is confined to the surface film of fluid adhering to the single fiber or the interstitial fluid space between fibers in the bundle.

To illustrate the principles involved, let us record externally with a pair of electrodes from a single nerve fiber (e.g. squid giant axon) bathed in air (see Fig. 19.3C). The fluid between the two electrodes constitutes a resistance (R) and longitudinal current (I) flowing through this resistance produces an IR voltage drop (Ohm's law: $V = IR$). As the AP moves from left to right past the pair of recording electrodes, the first electrode becomes negative with respect to the second electrode. Therefore, the voltmeter swings in one direction (an upward deflection is defined as negative in extracellular recording) due to the potential difference (pd). When the wave moves to a position between the two electrodes, the voltmeter will record almost zero voltage. When the AP reaches the second electrode, the voltmeter will swing in the opposite direction, because the second electrode is now negative with respect to the first. Thus, the electrodes will record a biphasic change in voltage as the AP sweeps past. When recording externally, the AP is a *wave of negativity* sweeping down the fiber; when recording internally, the AP is a wave of positivity.

Propagation velocity is a function of axon diameter and myelination, such that the larger the diameter, the greater the velocity. *Myelinated axons* conduct much faster than *non-myelinated axons*. The factors that determine propagation velocity and the mechanism of saltatory conduction were discussed in the preceding chapter.

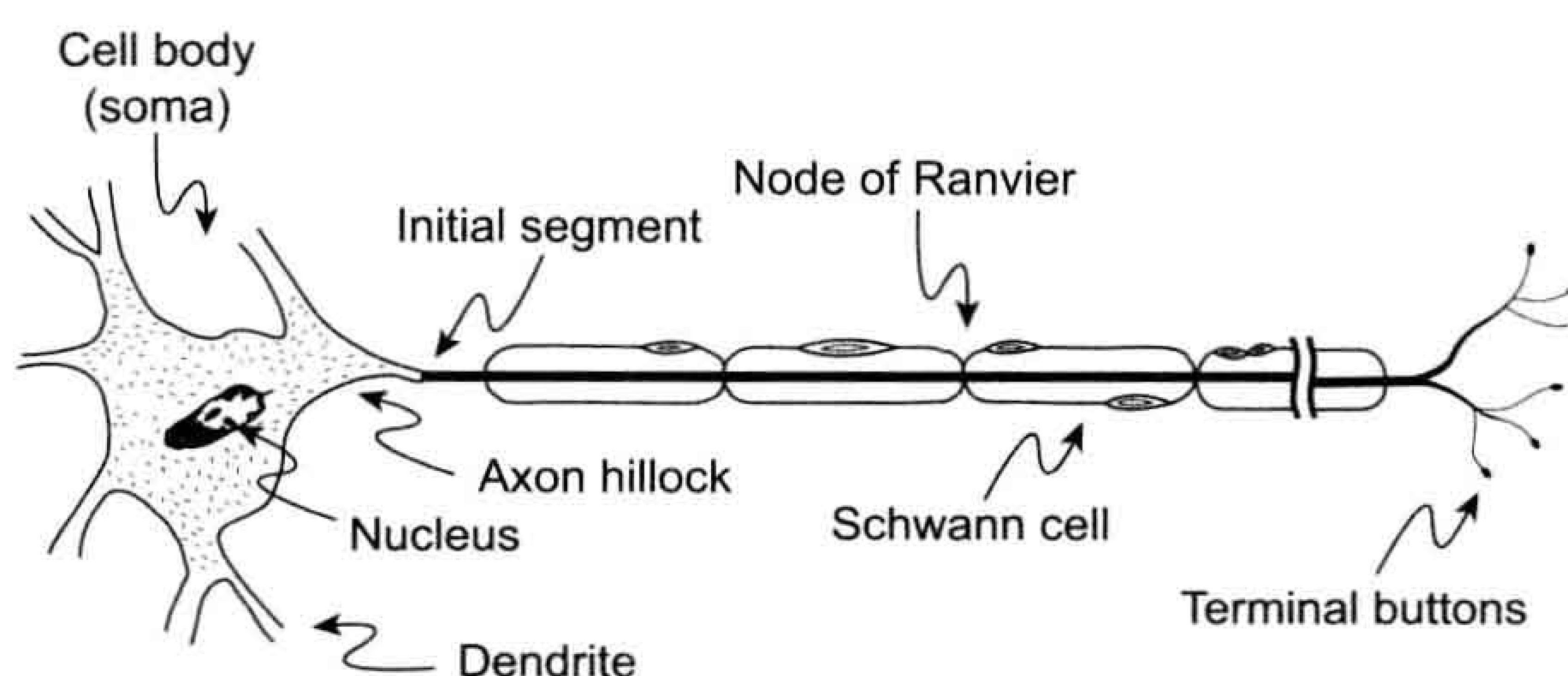


FIGURE 19.2 Diagram of a motor neuron with a myelinated axon. The major structural elements are diagrammed, including the cell body, initial segment, Schwann cell and node of Ranvier.

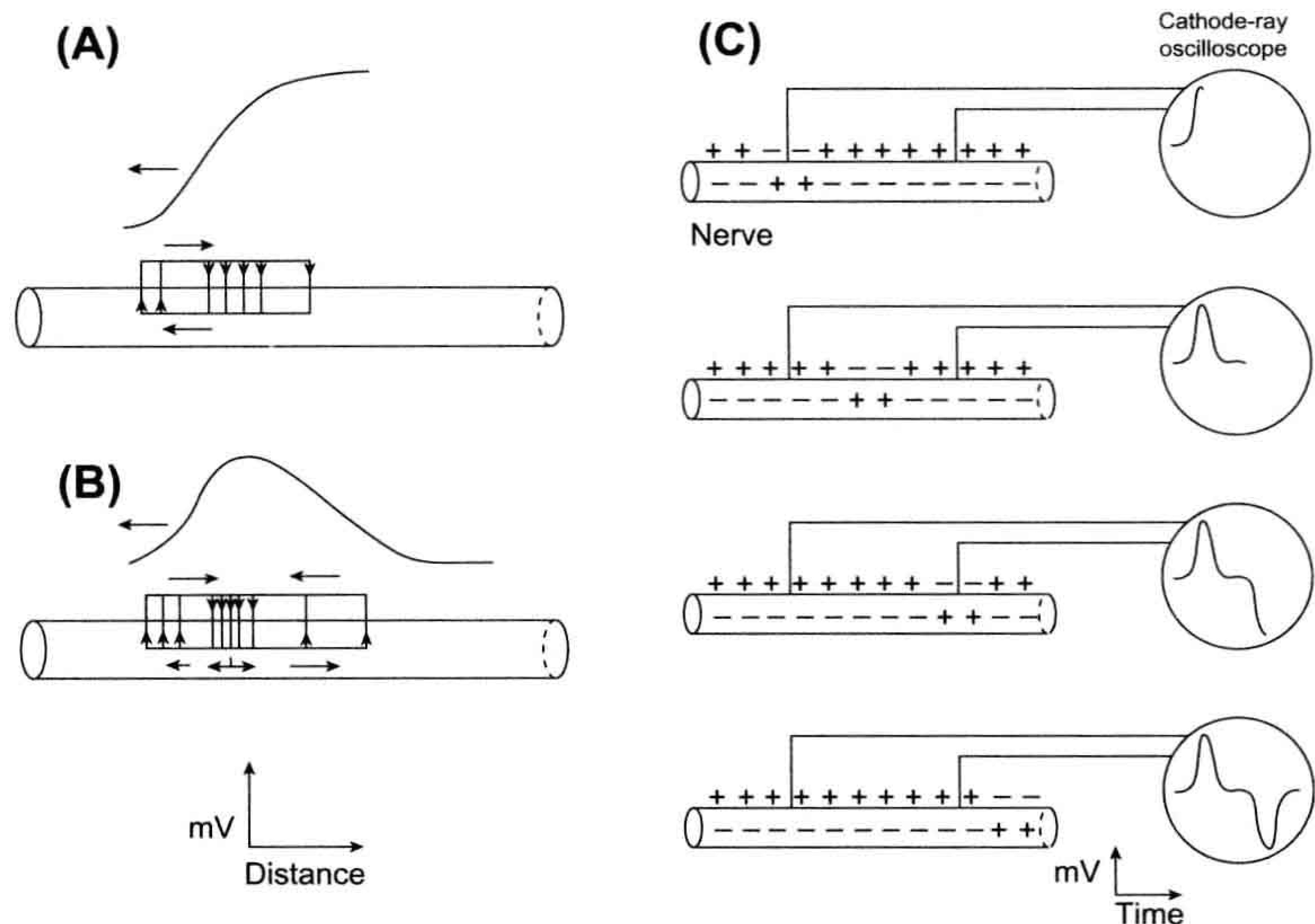


FIGURE 19.3 Diagram of the local-circuit current in a nerve fiber during an AP. (A) The current during the rising phase. (B) The current during the entire AP. The AP is depicted as propagating from right to left. (C) The actual registration of the signal is depicted for an AP propagating from left to right past a pair of electrodes spaced relatively far apart.

IIIB. Threshold and All-or-None Property

Nerve membrane responses near the site of application of brief current pulses vary depending on the magnitude and direction of the pulses (Fig. 19.4). Anodal (inward) currents produce hyperpolarization and cathodal (outward) currents produce depolarization. Hyperpolarizing and subthreshold depolarizing responses are graded in magnitude according to the stimulus current. However, as can be seen, a somewhat higher intensity outward current produces a depolarizing response with a different waveform and a longer duration. This condition is referred to as the *local excitatory state* (Fig. 19.4A, B). It occurs when a small area of the membrane near the stimulus electrode comes close to threshold, but it does not generate an AP. This local membrane activity is not propagated and decays with distance along the axon. A slightly stronger stimulus is, however, sufficient to bring the membrane potential of a large enough membrane area to the *threshold potential*, thereby initiating an all-or-none AP. At the threshold potential, a large inward (depolarizing) current is initiated and the membrane continues to depolarize.

In regard to the applied stimulus, outward current depolarizes the resting membrane (*IR* drop across the membrane is positive inside, negative outside), whereas inward current hyperpolarizes (*IR* drop is negative inside). In contrast, for the active membrane, inward currents are depolarizing (bringing positive charge inside the cell) and outward currents are hyperpolarizing. That is, when the membrane is behaving passively, applied inward current is hyperpolarizing and outward current is depolarizing; this is equivalent to a circuit external to a battery. In contrast, when the membrane is behaving actively, inward current generated is depolarizing and outward current is hyperpolarizing; this is equivalent to the internal current within a battery. This difference is because current flows from positive to negative in the external circuit and from negative to positive within the battery itself.

A subthreshold depolarization is defined as one that does not reach threshold to elicit an AP. It is proportional to the applied stimulus and it decrements with distance along the nerve axon cable. If a stimulus current is of sufficient magnitude, then the resulting membrane depolarization reaches a critical value, called the *threshold potential*, at which an AP is initiated (see Fig. 19.4).

The AP parameters, including overshoot, duration and rate of rise, are characteristic for each type of excitable cell. For example, the duration of the AP of the squid giant axon is about 1 ms, whereas the cardiac AP lasts over a hundred milliseconds. These differences in the APs subserve the functions performed by the different excitable tissues. The overshoot and a hyperpolarizing afterpotential (following the spike) are illustrated in Fig. 19.4C.

IIIC. Refractoriness

Once an AP is initiated, a finite and characteristic time must elapse before a second AP can be generated. This time interval is called the *refractory period* and its value depends on the type of excitable cell. Cells with long-duration APs (e.g. myocardial cells) have long refractory periods; cells

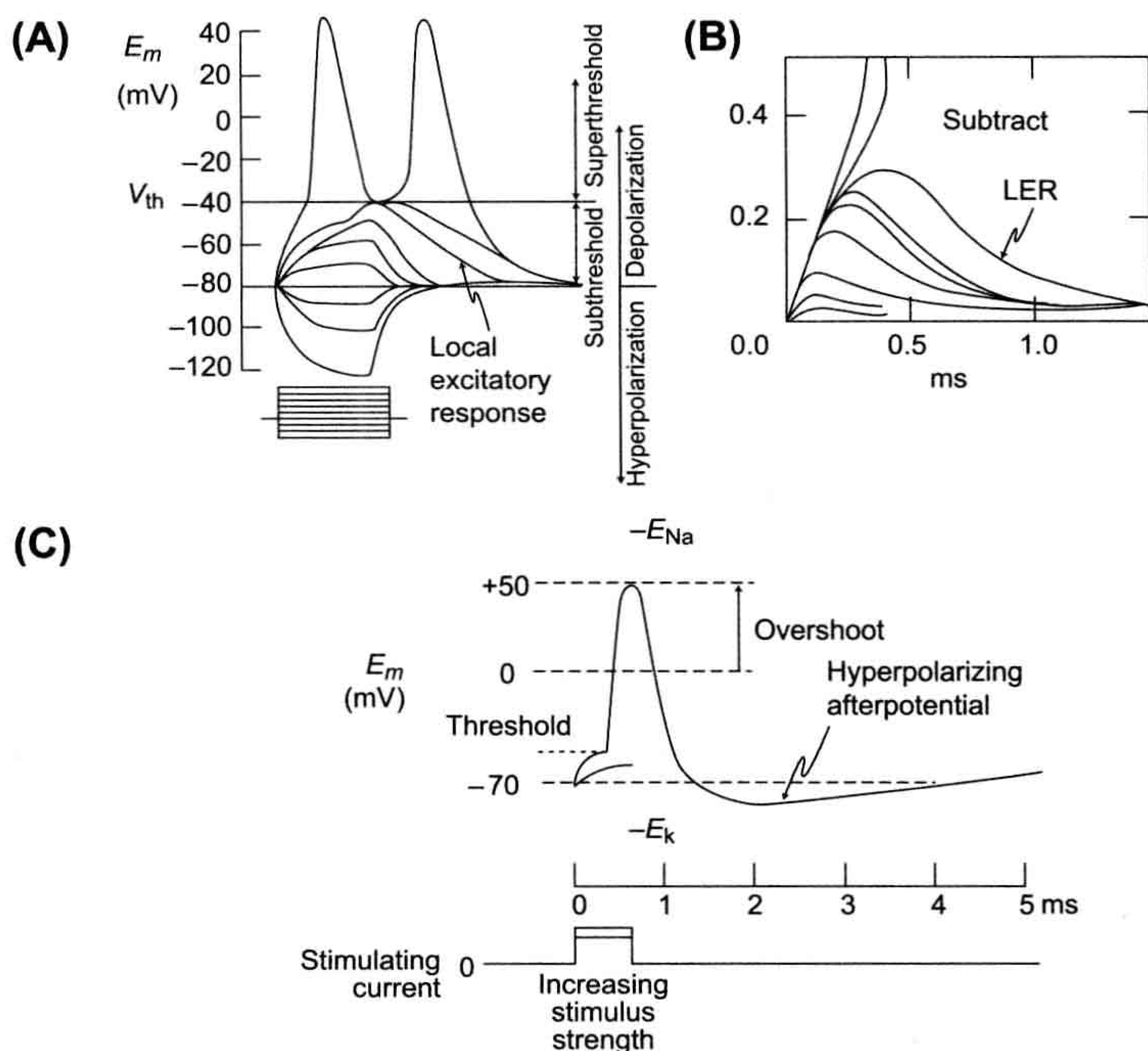


FIGURE 19.4 Diagrammatic sketches depicting initiation of the nerve impulse by membrane depolarization. (A) Membrane responses to depolarizing and hyperpolarizing current pulses are shown. The non-linear local excitatory response (LER) occurs just below the threshold for the all-or-none AP. (B) Illustration of the LER obtained by subtraction of the membrane responses to hyperpolarizing current pulses (passive only) from the responses to depolarizing pulses (passive plus active). (C) A nerve AP is depicted, illustrating the sharp threshold, overshoot and hyperpolarizing afterpotential.

with brief APs (e.g. neurons) have short refractory periods. That is, the refractory periods are related to the AP duration.

Two types of refractory periods are usually defined: an *absolute refractory period* and a *relative refractory period* (Fig. 19.5). The absolute refractory period denotes the interval during which a second AP cannot be elicited, regardless of the intensity of the applied stimulus. During the relative refractory period, a second AP may be elicited, provided that a greater than normal stimulus is applied. The second AP often is subnormal in amplitude and rate of rise. Therefore, the physiologically important refractory period is the *functional (effective) refractory period*, which is defined by the highest frequency of APs that the excitable cell can propagate. For example, if a myelinated nerve axon can propagate impulses up to 1000/s, then the functional refractory period is 1.0 ms. Since the triggering of a second impulse at a given point (or node of Ranvier) is limited by the amount of action current available from an active point (or node) upstream, the functional refractory period encompasses all of the absolute refractory period and part of the relative refractory period.

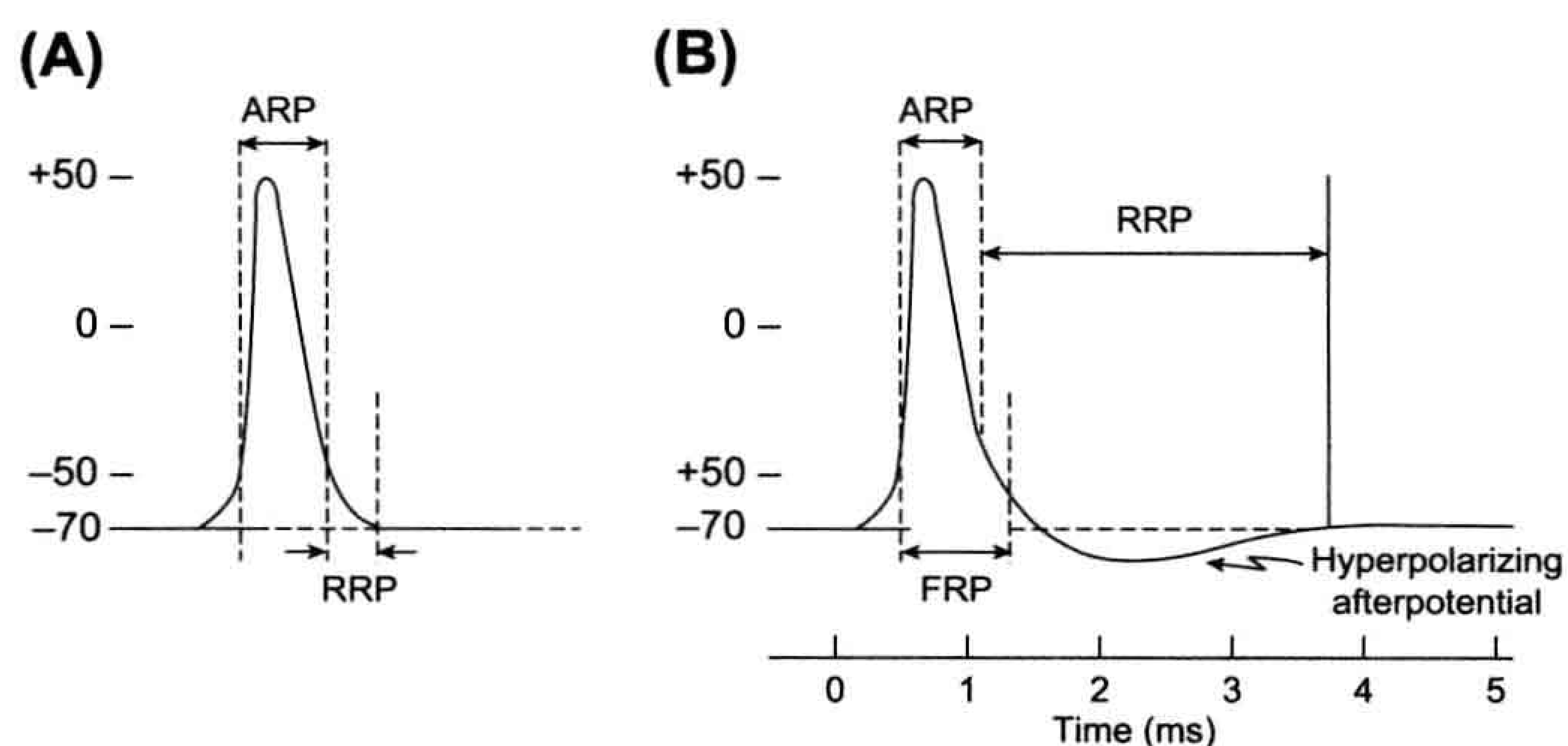


FIGURE 19.5 Refractory periods of nerve APs, both without (A) and with (B) a hyperpolarizing afterpotential. The absolute (ARP), relative (RRP) and functional (FRP) refractory periods are labeled.

The absolute refractory period extends from when threshold (V_{th}) is reached at the initial portion of the rising phase of the AP to when repolarization has reached a level of about −50 mV. During further repolarization beyond −50 mV (e.g. to −70 mV), a larger and larger fraction of the fast Na^+ channels recovers from inactivation and so more fast channels are again available to be reactivated to produce another AP. This is the period that inscribes the relative refractory period. The greater the degree of repolarization (toward the RP), the larger the subsequent AP.

In addition to voltage, time is a factor in the recovery of the ion channels. Therefore, the absolute and relative refractory periods persist briefly beyond the theoretical voltages and the relative refractory period actually slightly exceeds the AP duration.

Membrane excitability is greatly altered during the refractory periods. Excitability is zero during the absolute refractory period and is depressed during the relative refractory period, becoming less and less depressed as the membrane repolarizes back towards the RP.

The afterpotentials that many cells exhibit also affect membrane excitability: hyperpolarizing afterpotentials depress excitability (greater critical depolarization required to reach V_{th}) and depolarizing afterpotentials enhance excitability. A depolarizing afterpotential produces a *supernormal period of excitability*. In contrast, a hyperpolarizing afterpotential blends into and extends the relative refractory period. Thus, for example, since neurons usually exhibit hyperpolarizing afterpotentials, the functional refractory period actually includes part of the afterpotential.

Propagation velocity is slowed during the relative refractory period, achieving the normal value at the end of the relative refractory period. Propagation velocity is slightly faster than normal during the supernormal period of excitability.

IIID. Strength–Duration Curve

Whether the threshold potential is reached depends on the amount of charge transferred across the membrane. Figure 19.6 shows that the total charge transfer across the membrane required to produce excitation is approximately constant ($k = xy$ or $Q = IT$). It is an approximate rectangular hyperbola ($xy = k$) over the sharply-bending region of the curve. The strength–duration (S-D) curve can be derived from the equation for the exponential charge of the membrane capacitance.

The S-D curve deals only with the stimulus parameters (i.e. strength and duration of the applied current pulses) necessary to bring the membrane to threshold. It shows that the greater the duration of the applied pulse, the smaller the current intensity required to just excite the fiber. The asymptote parallel to the x-axis is the *rheobase*, which is the lowest intensity of current capable of producing excitation, even when the current is applied for infinite time (practically, >10 ms for myelinated nerve fibers). The asymptote parallel to the y-axis is the *minimal stimulation time*, which is the shortest duration of stimulation capable of producing excitation, even when huge currents are applied.

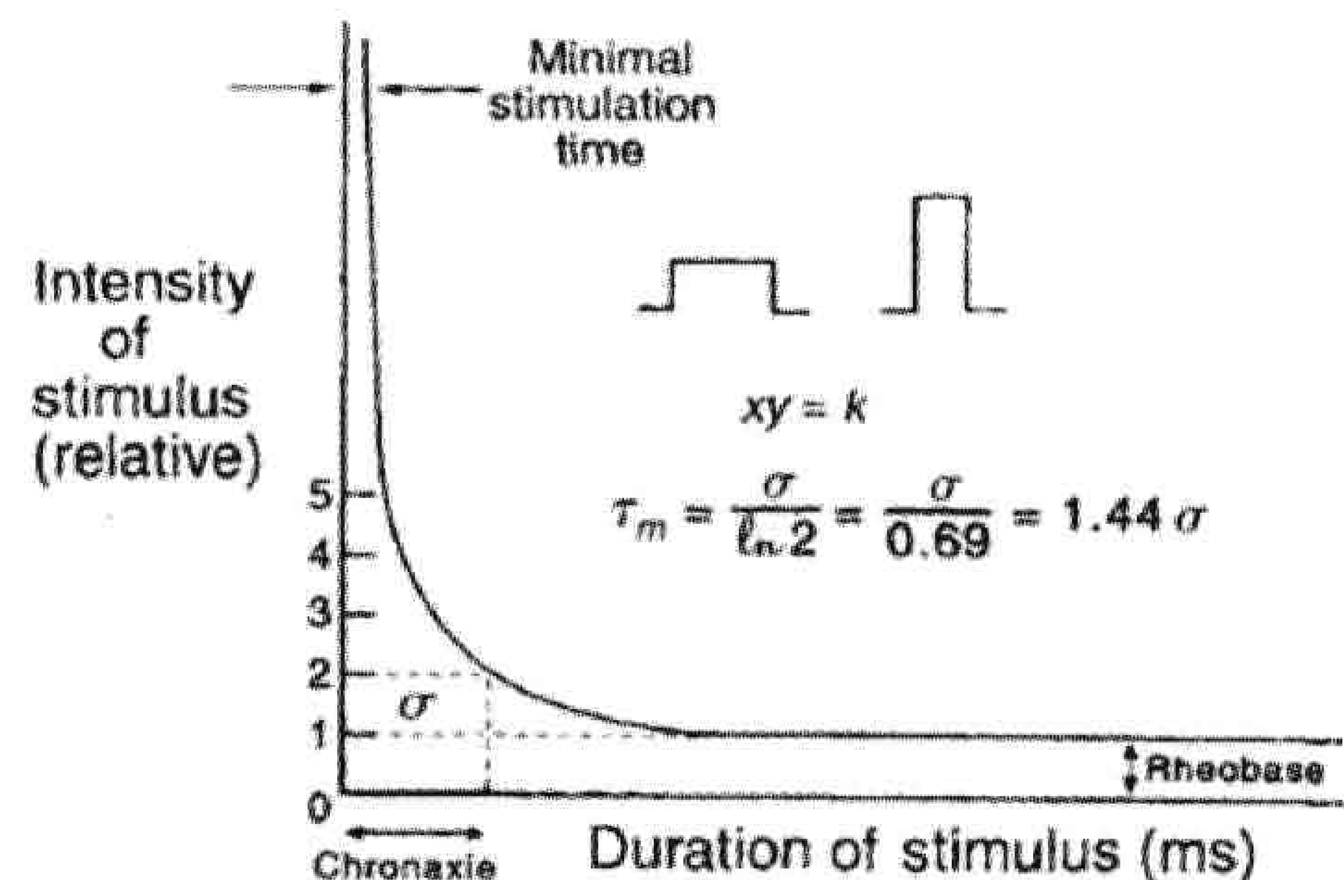


FIGURE 19.6 Strength–duration curve for AP initiation in excitable membranes. The intensity of rectangular stimulating pulses is plotted against their duration for stimuli that are just sufficient to elicit an AP. The rheobase current and chronaxie (σ) are indicated.

The usefulness of the rheobase is limited when comparing the excitability of one nerve with another because only the relative current intensity is meaningful. Furthermore, it is difficult to measure the stimulation time of a current with the intensity of the rheobase because it is an asymptote. Thus, a graphic measurement is made of the time during which a stimulus of double the rheobasic strength must act in order to reach threshold. This time is the *chronaxie*. Chronaxie values tend to remain constant regardless of geometry of the stimulating electrodes. The shorter the chronaxie, the more excitable the fiber. The chronaxie value for normal myelinated nerve fibers is about 0.7 ms. Some nerve pathologies in humans can be detected early by changes in their chronaxies.

Measurement of chronaxie in the laboratory is also valuable because it provides an easy method for measuring the value of the membrane time constant τ_m (see Chapter 18). In brief, the relationship between chronaxie (σ) and time constant (τ_m) is:

$$\tau_m = \frac{\sigma}{\ln 2} = \frac{\sigma}{0.69} = 1.44\sigma \qquad (19.1)$$

Thus, τ_m is 1.44 times the value of σ. Therefore, σ is analogous to a half-time for a first-order reaction, whose rate constant is the reciprocal of the τ_m ($k = 1/\tau_m$).

The S-D curve indicates that current pulses of very short duration (e.g. <0.1 ms) are less effective for stimulation. Thus, sinusoidal alternating current (AC) at frequencies above 10 000 Hz is less capable of stimulation. Another way to view this is that, because the membrane impedance decreases greatly at high frequencies (since the cell

membrane is a parallel RC network), the pd that can be produced across the membrane by current flow across it (IR or IX drops) is very small. Hence, AC of very high frequency has less tendency to electrocute and the energy of such currents can be dissipated as heat in body tissues and thus may be used in diathermy for therapeutic warming of injured tissues.

IIIE. Accommodation

Accommodation, in electrophysiology, refers to the loss of sensitivity of a cell to an applied stimulus. Sensory organs exhibit the property of accommodation, as do many neurons and other excitable membranes, such as skeletal muscle fibers. When a rectangular (square-wave) current pulse is used to depolarize a quiescent motor neuron (step depolarization) from the RP (e.g. −70 mV) to the threshold potential (V_{th}) or beyond, the neuron quickly responds with an all-or-none AP. However, if the applied pulse is ramp-shaped (triangular), the neuron may or may not respond, even if the normal V_{th} is exceeded, depending on the slope of the ramp. If the slope of the ramp is steep, the neuron will respond, but at a higher V_{th} level (more critical depolarization is required). If the slope is shallow, the neuron will fail to fire an AP, regardless of the level to which it is depolarized. This is accommodation. That is, when the membrane is depolarized gradually, the stimulus is ineffective in producing an AP response (Fig. 19.7A).

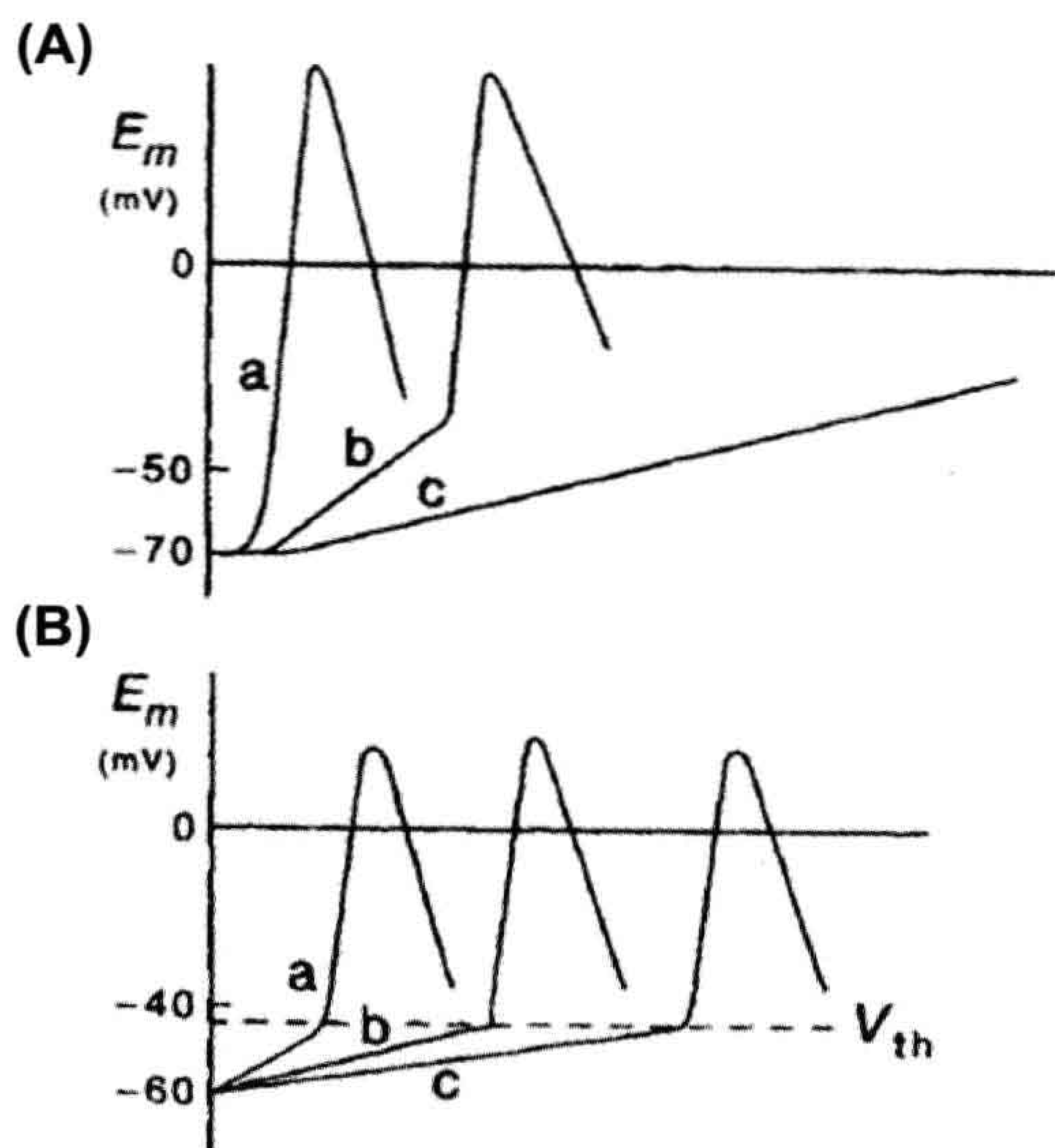


FIGURE 19.7 Sketches of accommodation and non-accommodation. (A) Accommodation in response to a ramp stimulus in a motor neuron and (B) lack of accommodation in a nodal pacemaker cell from the heart. In (A), as the slope of the ramp stimulus is decreased (from a to c), the AP response is delayed (b) and then fails completely (c). V_{th}, threshold potential.

This is not true of pacemaker cells (see Fig. 19.7B). Automatic (spontaneously-discharging) cells (e.g. nodal pacemaker cells of the heart and some sensory neurons) do not exhibit accommodation. Such cells will discharge an AP no matter how gradually the membrane is brought to the V_{th} point. In fact, the pacemaker potential in cardiac nodal cells is of the ramp type, producing depolarization to V_{th} over a period of about 200−800 ms.

The explanation for the phenomenon of accommodation is as follows. As the membrane is slowly depolarized toward V_{th}, the positive feedback cycle between E_m, Na^+ conductance (g_{Na}) and I_{Na} begins to operate (beginning at about 80% of the critical depolarization). Therefore, some of the fast Na^+ channels are turned on (activated), only to inactivate spontaneously (I-gates close) within 1−2 ms. If a critical number (critical mass) of fast Na^+ channels are not activated simultaneously, then the positive feedback cycle does not become explosive and a regenerative AP is not produced. That is, the slow depolarization does not allow a critical number of fast Na^+ channels to be simultaneously in the open conducting state. The channels that opened and spontaneously inactivated cannot be reactivated until they return to the resting state, which requires repolarization to near the RP. Hence, they are lost from the pool of available channels.

Added to this is the fact that K^+ channels (delayed rectifier type) will open during the slow depolarization, thus increasing K^+ conductance (g_K). Whenever g_K is increased, excitability becomes depressed, because it tends to repolarize and keep the membrane from depolarizing (to produce an AP). The g_K increase lowers R_m and so lowers the effectiveness of the depolarizing current.

Therefore, accommodation to low-slope stimuli occurs for two reasons: (1) spontaneous inactivation of fast Na^+ channels that have been activated, and therefore lack of a simultaneously-open critical mass, and (2) increase in g_K, which depresses excitability.

The lack of accommodation in automatic cells (e.g. SA nodal cells of the heart) then may be due to (1) less spontaneous ion channel inactivation and (2) less g_K increase during the applied ramp stimulus or natural ramp pacemaker potential. Both of these conditions apparently apply to cardiac nodal cells. The inward current responsible for the rising phase of the AP is not a fast Na^+ current, but rather a slow Ca^{2+} current, which inactivates very slowly and the kinetics of the turn-on of the delayed-rectifier K^+ current is also very slow.

As stated previously, accommodation also occurs in sensory organs. For example, some stretch receptors accommodate to a sustained stretch. When the stretch is first applied, there is a burst of APs. But the bursting frequency of discharge gradually slows down and then stops, even though the stretch is maintained.

IIIF. Anodal-Break Excitation

Excitation occurs on the make (the beginning) of a square-wave depolarizing stimulus. If the applied stimulus duration is very long (relative to the AP duration), repetitive firing of APs will occur if the membrane is of the non-accommodating type. If the membrane is of the accommodating type, then only the initial AP is produced, because accommodation occurs.

If the cathode (negative) and anode (positive) electrodes are placed directly on an isolated single nerve axon (e.g. squid giant axon), then an AP will be triggered at the cathode region on the make of the square-wave stimulus. This happens because, as depicted in Fig. 19.8A, depolarization occurs under the cathode, whereas hyperpolarization occurs under the anode. However, something unexpected occurs under the anode on the break of the stimulating pulse; namely, an AP is triggered from this hyperpolarized region of the axon (Fig. 19.8B). The explanation for this is that ion channel changes occur during the hyperpolarization, such that the excitability of that membrane is transiently increased (lower V_{th} point) immediately following cessation of the applied pulse.

The increase in excitability is due to two factors: (1) there is an increase in h_∞ during the hyperpolarization, reflecting that almost 100% of the fast Na^+ channels have their I-gates open, and hence are capable of conducting (open state) when the membrane is depolarized on cessation of the hyperpolarizing pulse ($g_{Na} = \max g_{Na}\, m^3 h$); and (2) there is a decrease in n during the hyperpolarization, hence decreasing g_K ($g_K = \max g_K\, n^4$). These equations are discussed in the following section. The changes in the h and n parameters persist for a short period after termination of the applied pulse and hence increase membrane excitability during this brief period and trigger an AP. This is called *anodal-break excitation* and post-anodal enhancement of excitability (due to the post-anodal depolarization).

In contrast, under the cathode, after termination of the applied pulse, an opposite change occurs in E_m and excitability. The membrane is hyperpolarized transiently and excitability is depressed. This is known as post-cathodal hyperpolarization and *post-cathodal depression of excitability*. In Hodgkin–Huxley terms, this phenomenon also is due to two factors: (1) decrease in h_∞ during the depolarization, reflecting a smaller fraction of fast Na^+ channels having their I-gates open and hence incapable of conducting and thereby decreasing g_{Na}; and (2) increase in n_∞, hence increasing g_K. The increased g_K and decreased g_{Na} produce hyperpolarization (refer to Chapter 9), and thereby depress excitability.

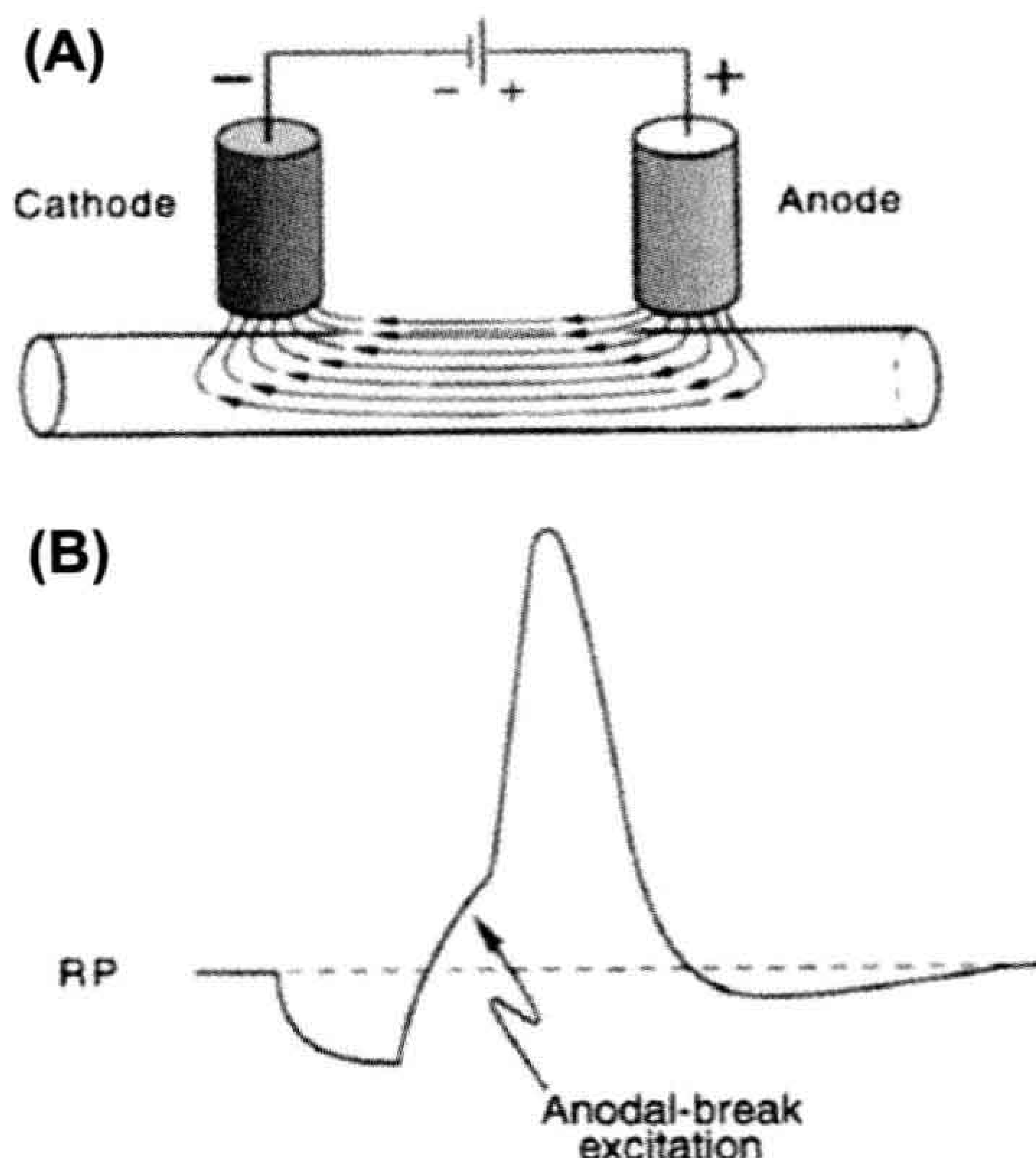


FIGURE 19.8 Current flow under the anode and cathode during extracellular stimulation (A) and anodal-break stimulation of an AP (B). (A) Excitation occurs under the cathode on the make of a current pulse and under the anode at the break of the rectangular pulse. (B) An intracellularly-applied hyperpolarizing current pulse produces an anodal-break response. RP, resting potential.

IV. ELECTROGENESIS OF ACTION POTENTIALS

Early experimentation in electrophysiology focused on determining the mechanism for the generation of the AP. One important finding by Cole and Curtis (1939) was that during the AP, the membrane resistance (but not the capacitance) changed dramatically (Fig. 19.9). The large reduction in membrane resistance during the AP supported the hypothesis that the AP resulted from a large increase in the ionic permeability of the membrane.

To determine which ionic species might be involved in generating the AP, subsequent experimentation was directed toward varying the concentrations of the different ions bathing the axon. When the concentration of Na^+ ions bathing the squid axon was lowered, it was found that the overshoot and the rate of rise of the AP were reduced. This result was the first indirect demonstration that the AP resulted from an increase in the membrane permeability to Na^+ ions. Several years later, this hypothesis was confirmed directly by the voltage-clamp method, as discussed in the next section.

IVA. Voltage-Clamp Method

The membrane current (I_M) that generates the AP is composed of ionic current (Ii) and capacitive current (Ic) according to the relationship:

$$I_M = Ii + Ic \tag{19.2}$$

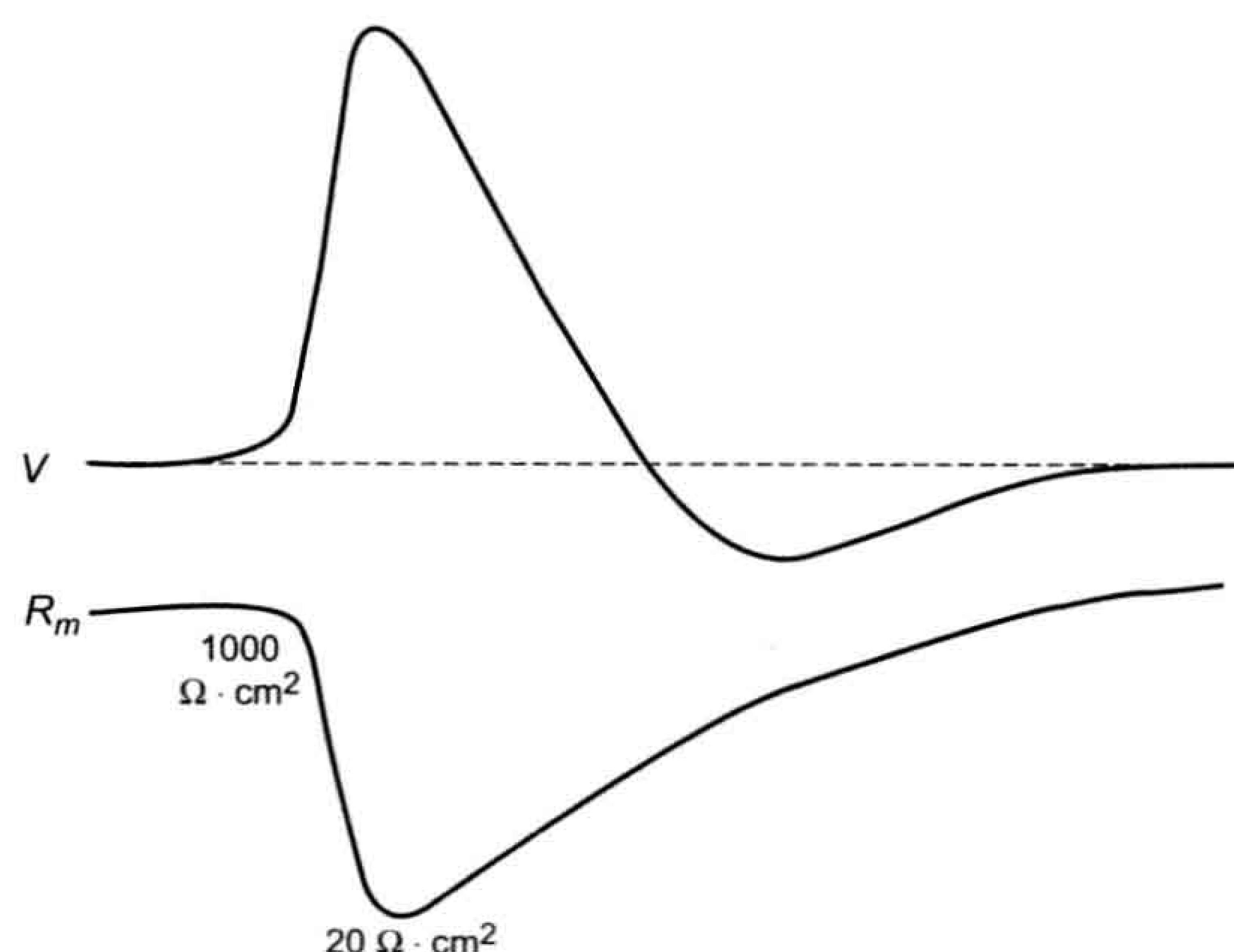


FIGURE 19.9 Time course for the decrease in membrane resistance (R_m) to the passage of current measured during the AP (V) in a nerve axon. R_m falls from about 1000 $\Omega \cdot cm^2$ at rest to about 20 $\Omega \cdot cm^2$ near the peak of the AP. *(Adapted from Cole, K.S. and Curtis, H.J. (1939). J Gen Physiol. 22, 649–687.)*

The flow of ionic currents across their respective resistive membrane pathways (or channels) causes a change in the membrane potential (from Ohm's law: $V = IR$). The change in membrane voltage causes an I_C also to flow as:

$$I_C = C_m \, dV/dt \qquad (19.3)$$

where dV/dt is the rate of change of the AP. Substituting Equation 19.3 into Equation 19.2 yields:

$$I_M = I_i + C_m \, dV/dt \qquad (19.4)$$

Since the membrane potential during an AP is constantly changing, it is difficult to separate the contributions of these ionic and capacitive components. In addition, the total ionic current is composed of multiple individual currents carried by specific ions. To analyze and separate the membrane currents into their capacitive and ionic components, a revolutionary method, called voltage clamping, was introduced in the early 1950s by Cole and then by Hodgkin and Huxley. A diagram of the voltage-clamp method is shown in Fig. 19.10. During a voltage-clamp experiment, the membrane potential is held constant (clamped) by a negative-feedback amplifier and the amount of current that is necessary to perform this task is recorded. Since the membrane potential (V_m) is held constant, the capacitive current is equal to zero. However, at the very beginning of the depolarizing clamp pulse, there is a large transient capacitive current that occurs and again at the "off" of the pulse; these can be electronically subtracted and thus removed by a special procedure. Since V_m is constant during the clamp pulse,

$$dV/dt = 0$$

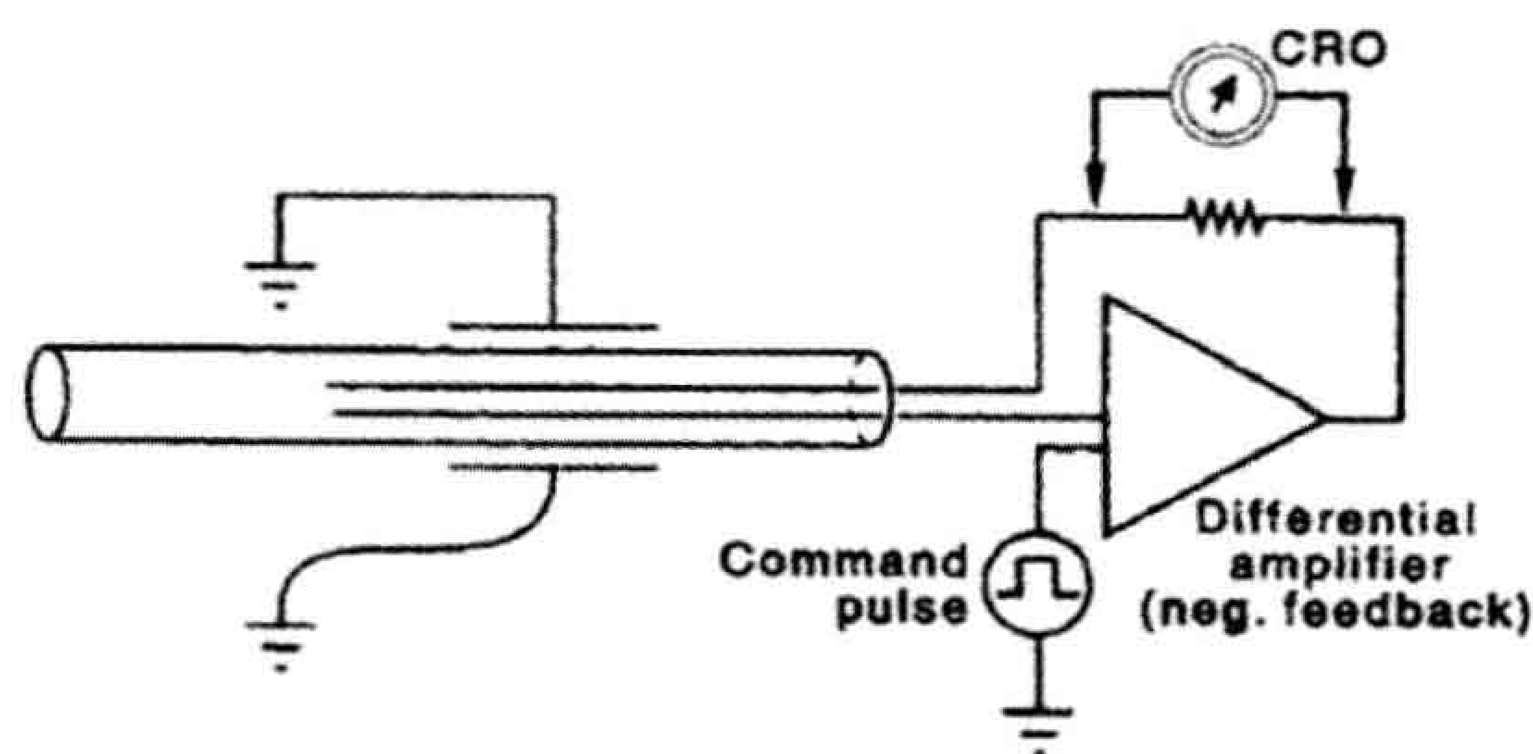


FIGURE 19.10 The voltage-clamp method used in a squid giant axon. The two wires inserted into the axon are used to measure membrane potential (V) and to pass current (I). The high-gain negative-feedback amplifier compares the command pulse with the membrane potential and outputs the amount of current necessary to hold the membrane potential constant (clamped). The magnitude of the feedback current can be measured as the IR voltage drop across a resistor and displayed on a cathode-ray oscilloscope (CRO).

and

$$I_c = 0$$

Therefore,

$$I_M = I_i$$

The voltage-clamp experiment gives the magnitude and time course of the ionic currents at a given clamp potential. By clamping the membrane to many different potentials, information about the flow of ionic currents and the underlying conductance changes during the AP is obtained.

IVB. Voltage-Clamp Analysis

In the voltage-clamp experiments, the various ion currents (such as Na^+, Ca^{2+} or K^+ currents) can be isolated from the total ionic current and analyzed individually. For example, in the squid axon experiments, the total ionic current consists of an early inward current followed by a delayed outward current (Fig. 19.11). By varying $[Na^+]_o$, the early inward current can be shown to be carried by Na^+ ions. Similarly, by changing $[K^+]_o$, the delayed outward current can be shown to be carried by K^+ ions. The Na^+ and K^+ currents can also be separated by blocking their pathways through the membrane. Na^+ channels can be blocked with *tetrodotoxin* (TTX), derived from the ovaries of Japanese puffer fish. K^+ channels can be blocked by several inorganic ions and organic compounds, including tetraethylammonium ions (TEA^+) and 4-aminopyridine (4-AP). The current remaining can then be subtracted from the total ionic current to reveal the time course for the current that was blocked.

The *current–voltage relationship* is obtained from measurements of the peak inward Na^+ current and peak outward K^+ current during a series of voltage clamp steps

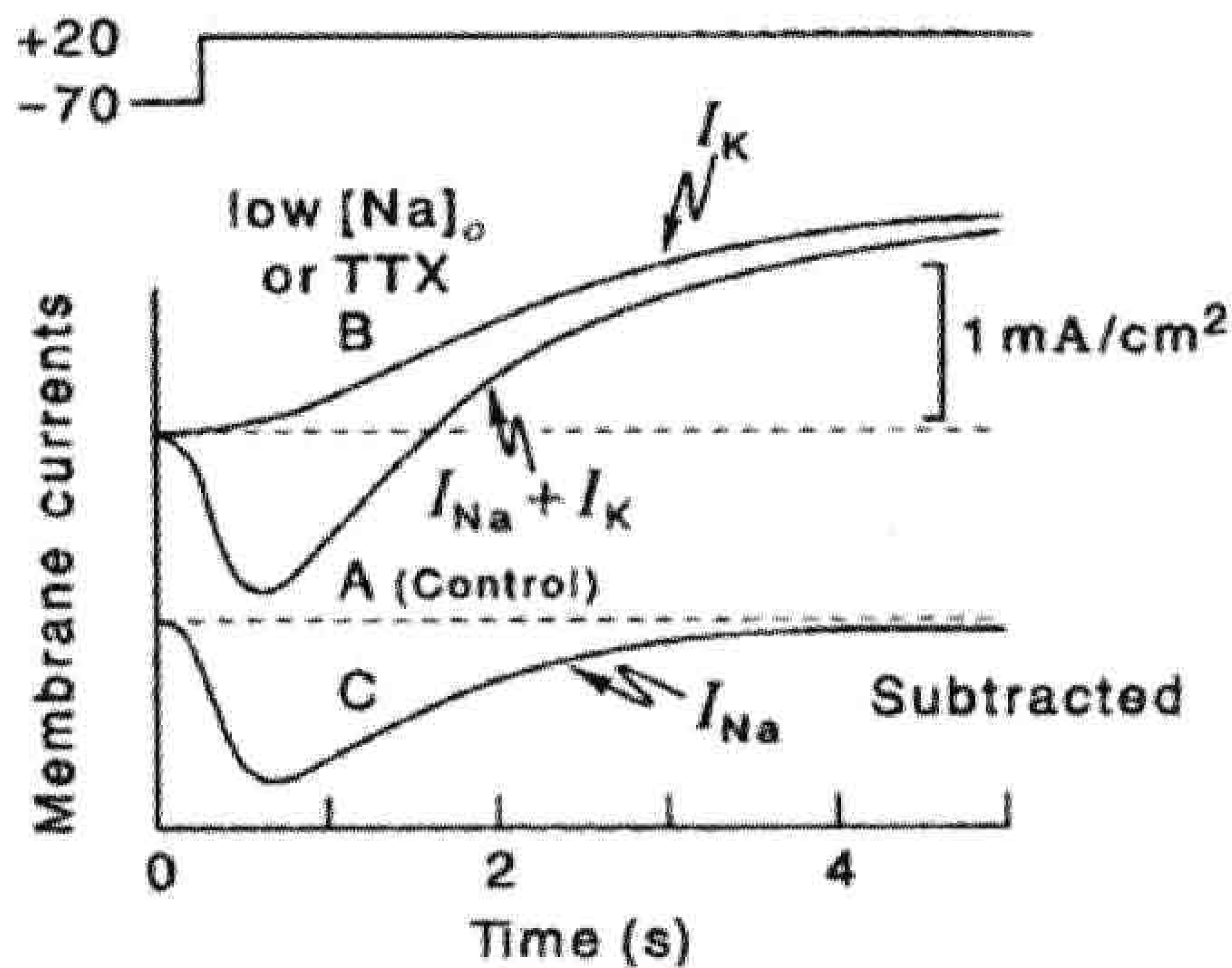


FIGURE 19.11 The ionic currents that flow when a squid giant axon is clamped from its RP (−70 mV) to a transmembrane potential of +20 mV. Trace A shows the net inward Na^+ current (I_{Na}) and outward K^+ current (I_K) in normal medium. Trace B shows the net ionic current when the axon is placed in artificial seawater with most of the Na^+ replaced by choline$^+$ (an impermeant cation), so that the intracellular and extracellular Na^+ concentrations are now equal. This current is due to K^+ only. TTX also can be used to block I_{Na}. Trace C shows the difference between curves A and B, which represents I_{Na}. *(Redrawn from Hodgkin, A.L. and Huxley, A.F. (1952a). J Physiol (London). 116, 449.)*

(Fig. 19.12). Depolarizing voltage steps to just above the RP first produce a small outward current. In this voltage region, the membrane behaves in an ohmic fashion. With greater depolarization, the inward I_{Na} is activated and the *I-V* relationship displays a negative slope or *negative resistance* region. At potentials above the peak current of the *I-V* curve, a positive slope is seen and the current magnitude decreases as E_{Na} is approached (and actually becomes outward at voltages above E_{Na}). The voltage at which the current reverses in direction is the *reversal potential*. The reason that the current diminishes and reverses at potentials approaching E_{Na} and beyond is that the net electrochemical driving force for Na^+ ions first becomes smaller and smaller and then outwardly directed, whereas the conductance for Na^+ ions remains constant and high over this entire voltage range, as indicated by:

$$I_{Na} = g_{Na}\,(E_m - E_{Na}) \qquad (19.5)$$

The outward K^+ current activates above about −40 mV (in squid axon) and increases with further depolarization as:

$$I_K = g_K\,(E_m - E_K) \qquad (19.6)$$

The voltage-clamp experiments have revealed the most fundamental property of the ionic conductances of excitable membrane: namely, that they are both voltage dependent and time dependent (Fig. 19.13). Both g_{Na} and g_K activate with depolarization, but with different time courses (Figs. 19.13 and 19.14). With time, g_{Na} spontaneously turns off, or inactivates. That is, the I_{Na} current shuts off within 1−2 ms.

A number of biological toxins that act on specific ion channels have been discovered. For example, TTX, mentioned previously, has a very high affinity for the fast Na^+ channel of nerve and some types of muscle cells. It

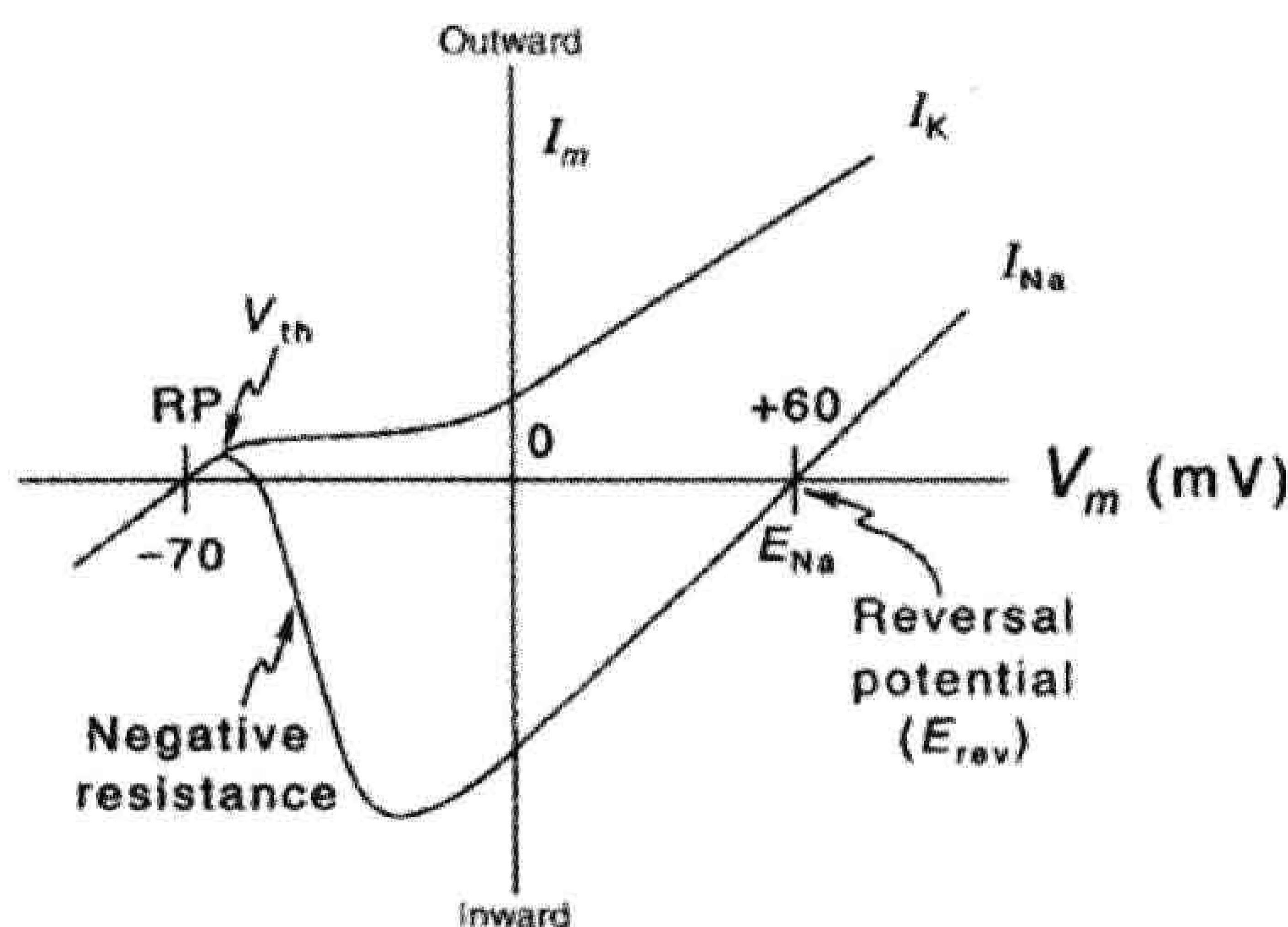


FIGURE 19.12 Current-voltage relationship for the peak early inward current and delayed outward current obtained from a squid axon under voltage-clamp. The inward current is carried by Na^+ (I_{Na}), the outward current by K^+ (I_K). The reversal potential for I_{Na} is the voltage at which the current changes from inward to outward. The region of the I_{Na} curve that has a negative slope is known as negative resistance. RP, resting potential; V_{th}, threshold; E_{Na}, Na^+ equilibrium potential; I_m, total membrane current; V_m, membrane potential. *(Redrawn from Hodgkin, 1964.)*

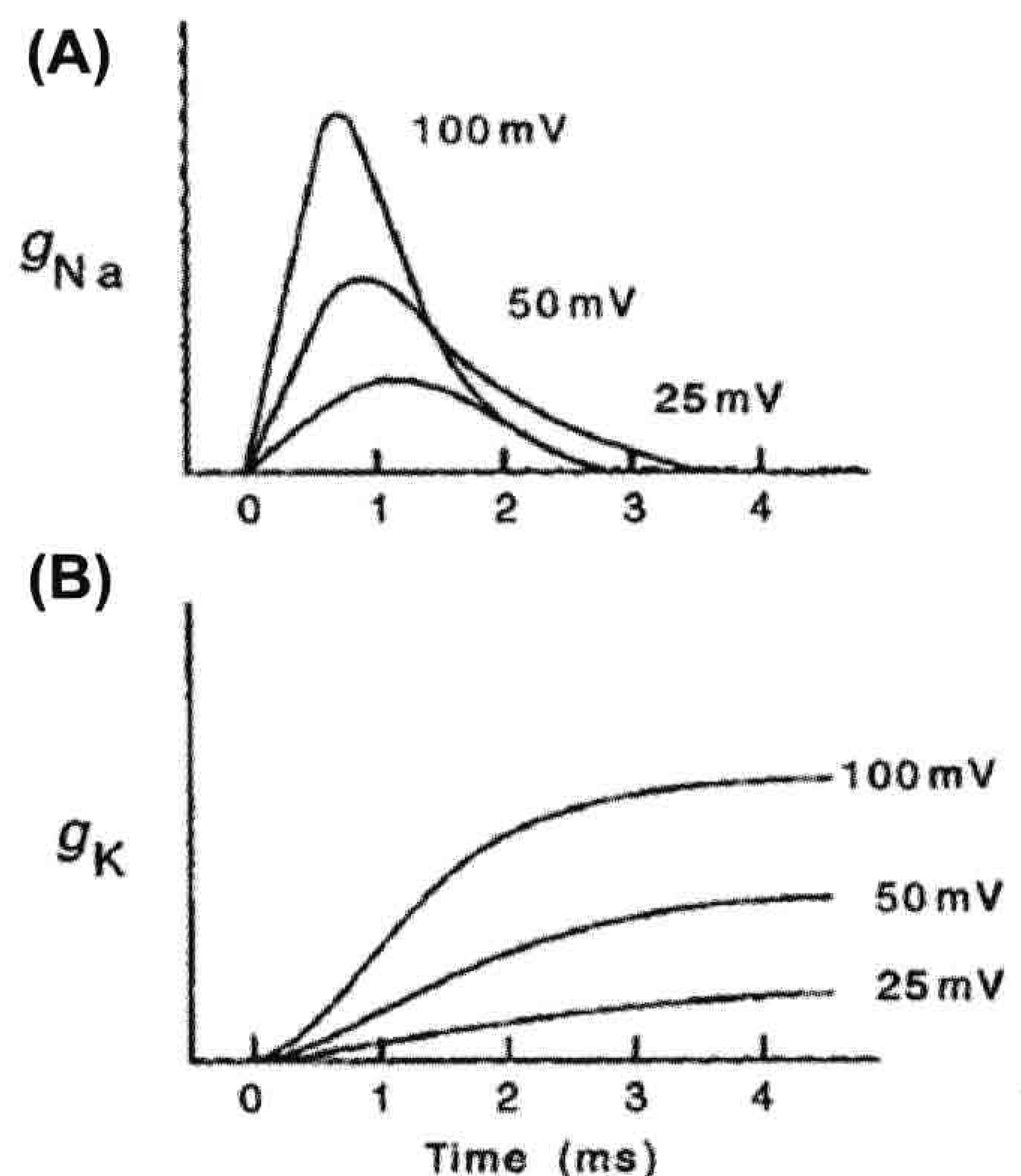


FIGURE 19.13 Voltage dependence and time dependence of the changes in Na^+ conductance (g_{Na}) and K^+ conductance (g_K) during voltage-clamp of the squid giant axon. The numbers refer to the magnitude of depolarization (in mV) from the RP. (A) g_{Na} turns on rapidly and then spontaneously declines over a brief time period. (B) g_K turns on more slowly and is sustained in amplitude during the entire clamp pulse. *(Redrawn from Hodgkin, 1964).*

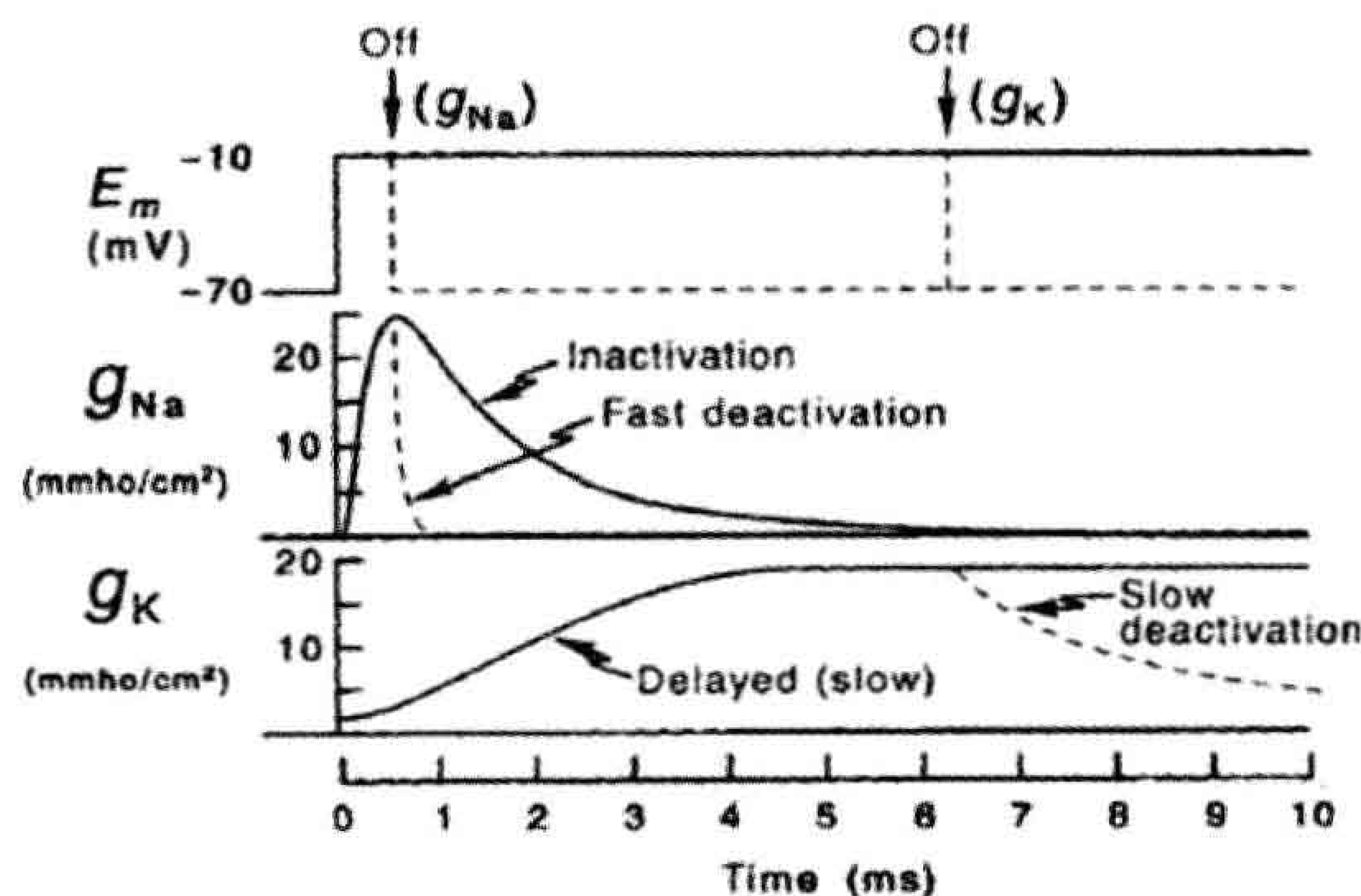


FIGURE 19.14 Na^+ conductance (g_{Na}) and K^+ conductance (g_K) changes are shown in response to voltage-clamp of the squid giant axon from the RP to a membrane potential (E_m) of -10 mV. g_{Na} inactivates after a short time, even when the voltage-clamp is maintained. In contrast, g_K remains elevated until the clamp is released. When the clamp pulse is terminated early, the g_{Na} increase is quickly turned off (deactivated); the turn-off of g_K is considerably slower. *(Redrawn from Hodgkin, A.L. (1958). Proc R Soc London (Biol). B148, 1.)*

binds to the fast Na^+ channel and blocks the passage of Na^+ ions through the channel. Several different types of toxins, including *batrachotoxin* (BTX), inhibit the inactivation process of the Na^+ channel, so that the Na^+ currents are greatly prolonged once activated. Such toxins have proven to be valuable tools in analyzing voltage-clamp currents and understanding ion channel function. The ion channel toxins are discussed in great detail in a later chapter.

IVC. Whole-Cell Voltage-Clamp

A newer electrophysiological method, the whole-cell voltage-clamp technique, has enabled researchers to examine the basis of excitability at the single cell level, e.g. in single myocardial cells or smooth muscle cells. The method allows the recording of the macroscopic currents that flow through the assembly of ion channels in the cell membrane. More information is given in Appendix III to this chapter. In addition, the details of this method are given in the following chapter.

IVD. Overview of Action Potential Generation

The increase in g_{Na} and resulting increase in inward I_{Na} cause the regenerative depolarization of the AP. The depolarization is limited by the approach of the membrane potential toward E_{Na} and by the Na inactivation process. As the membrane is depolarized, both g_K and the driving force for I_K increase and the outward I_K repolarizes the membrane. The increase in g_K is *self-limiting*; i.e. the increase in g_K produces repolarization which, in turn, shuts off the increase in g_K.

The slow kinetics of the turn-off of g_K result in a transient hyperpolarization, the *hyperpolarizing afterpotential.* During the hyperpolarizing afterpotential, the membrane potential is brought closer to E_K than at rest.

The membrane conductance changes that occur during the nerve AP are shown in Fig. 19.15 and the time course for the resultant ionic currents is shown in Fig. 19.16. The total ionic current (I_i) is separated into its two major components, I_{Na} and I_K. Since I_K is slower to activate than I_{Na}, the inward I_{Na} predominates initially, giving rise to the fast upstroke of the AP. Later, I_K dominates, causing a net outward current that repolarizes the membrane, i.e. it is partly responsible for the downstroke of the AP.

As stated in Equations 19.5 and 19.6, the specific ionic currents are a product of the membrane conductance for the ionic species and the electrochemical driving force exerted on the ion. Thus, the driving forces on Na^+ and K^+ ions continually change during the time course of the AP, as diagrammed in Fig. 19.17. At the RP, there is a large driving force for Na^+ to flow into the cell, since ($E_m - E_{Na}$) is large. Conversely, at the peak of the AP, ($E_m - E_{Na}$) is at its lowest value and the driving force for Na^+ entry is small. In contrast, the driving force for K^+ efflux is largest at the peak of the AP, when ($E_m - E_K$) is maximal. It is important to remember that ionic current flow depends on both conductance and driving force. There is no net current if only one, but not the other, is present.

The biological elements of the excitable membrane may be represented in terms of an electrical equivalent circuit model, as shown in Fig. 19.18. Currents flow through the individual conductance pathways for each type of ion. The

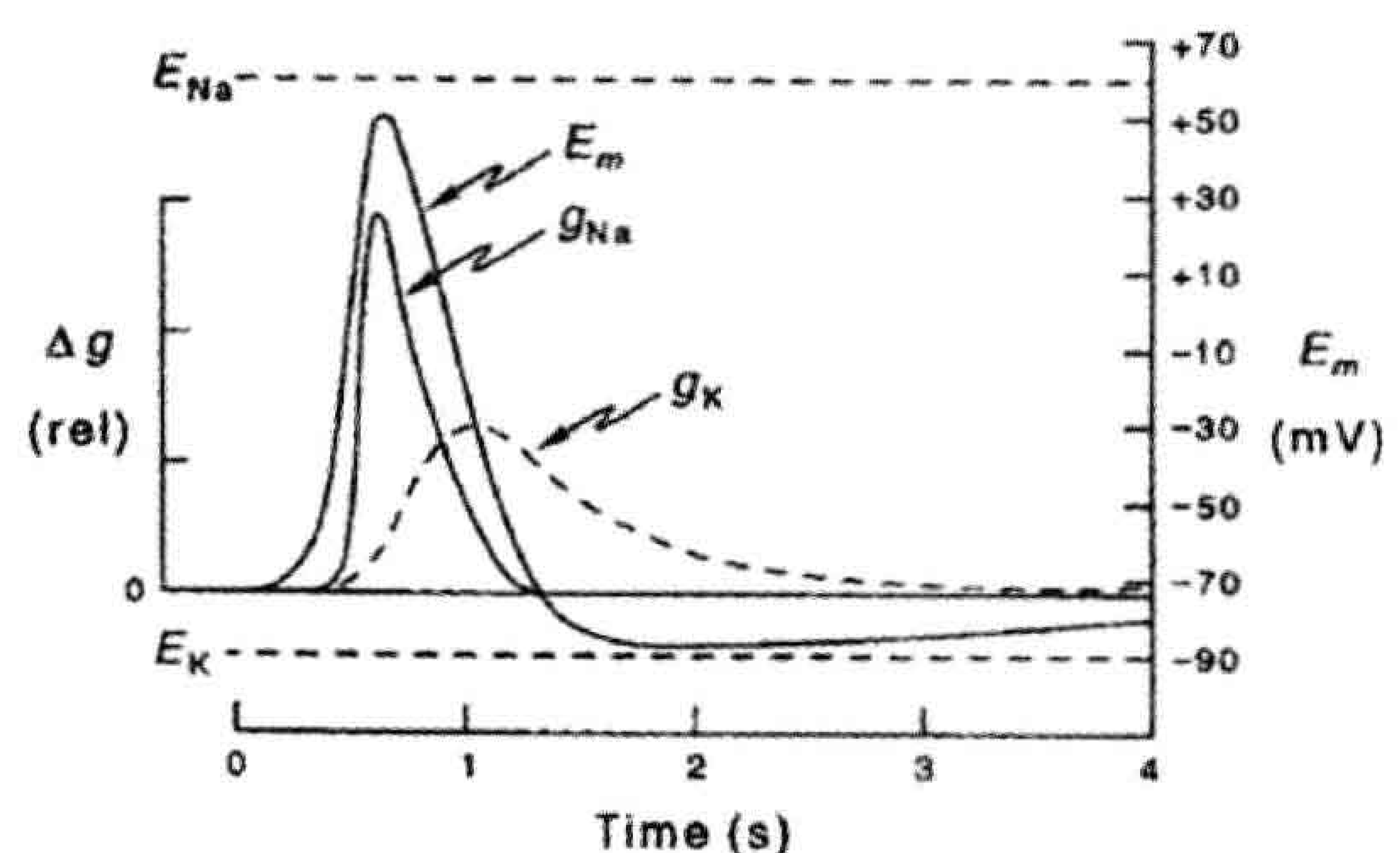


FIGURE 19.15 The relative conductance for Na^+ (g_{Na}) and K^+ (g_K) during an AP in a nerve fiber. The rising phase of the AP is caused by an increase in g_{Na}. The falling phase is due to the rise of g_K (delayed rectification) and to the decrease in g_{Na} (Na^+ inactivation). The hyperpolarizing afterpotential is explained by g_K remaining elevated for a short time following repolarization, tending to hold the membrane potential (E_m) near E_K. Δg, change in conductance. *(Redrawn from Hodgkin, A.L. and Huxley, A.F. (1952d). J Physiol. 117, 500–544.)*

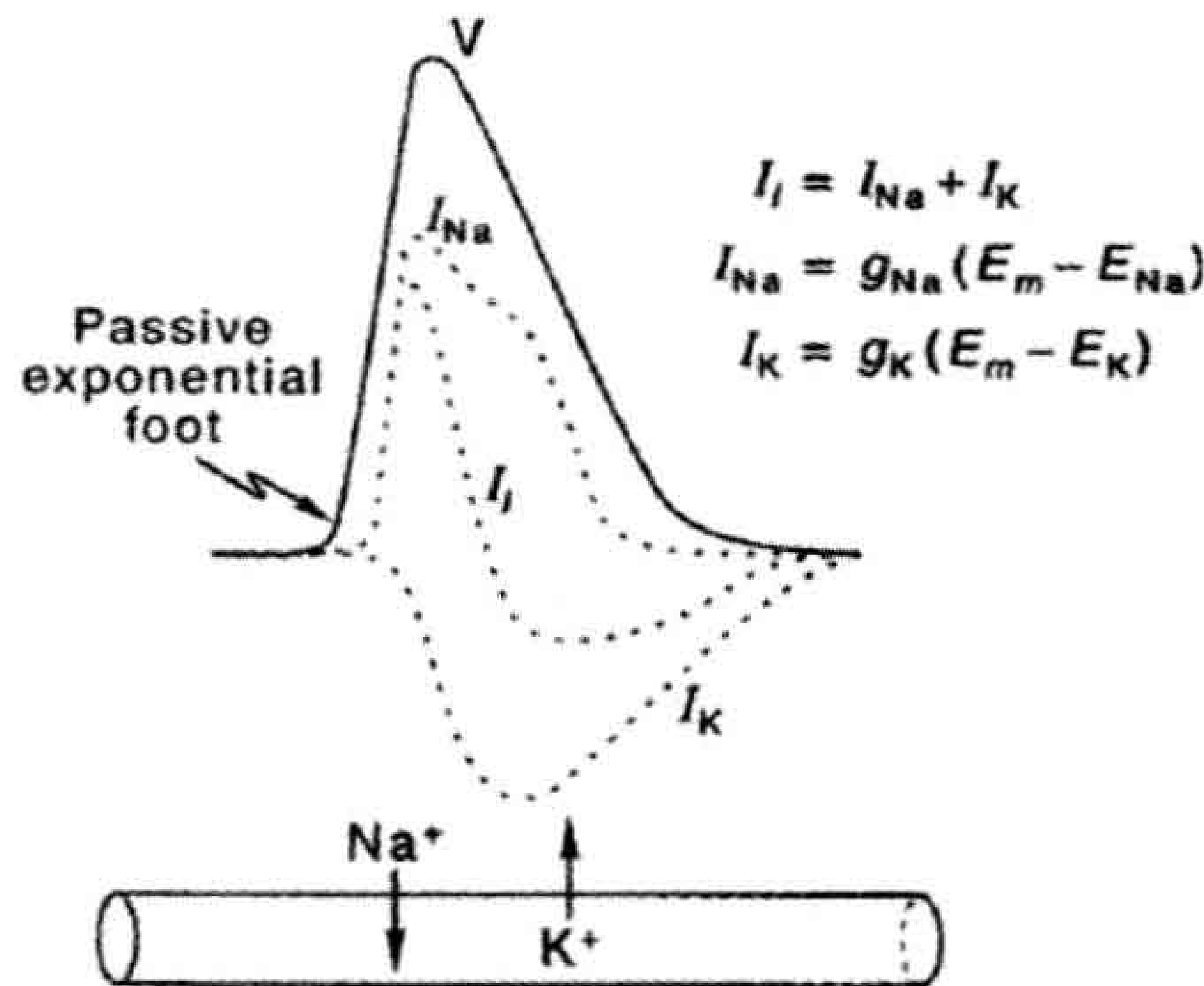


FIGURE 19.16 Ionic currents that flow during the nerve AP. The total current (I_i) is separated into an inward Na^+ current (I_{Na}) and an outward K^+ current (I_K). I_i is the algebraic sum of I_{Na} and I_K. The appropriate equations for I_i, I_{Na} and I_K are given. Also depicted is the fact that a net inward Na^+ flux occurs during the rising phase of the AP and a net K^+ efflux occurs during the repolarizing phase. *(Redrawn from Hodgkin and Huxley, 1952a.)*

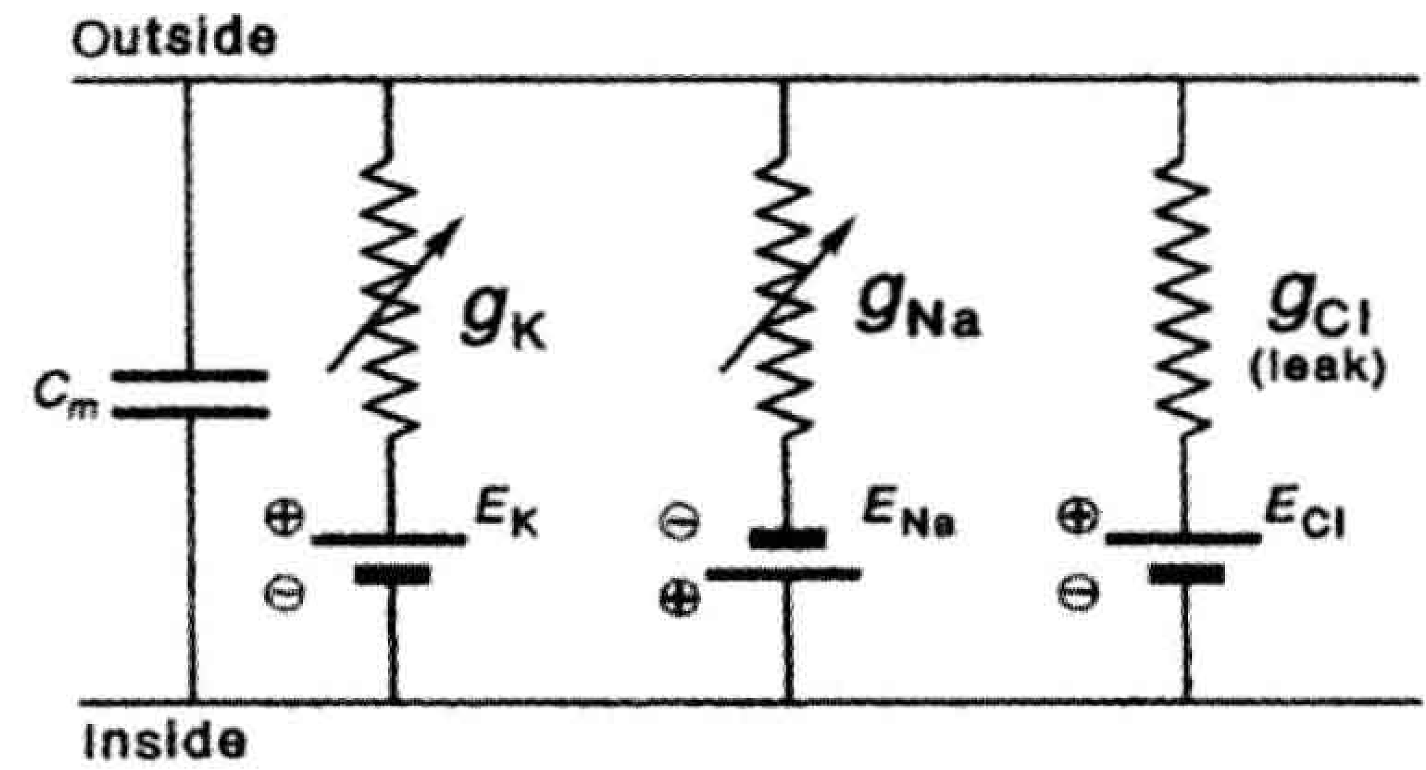


FIGURE 19.18 Hodgkin–Huxley electrical equivalent circuit for the squid giant nerve axon. The K^+ conductance (g_K) is in series with E_K and g_{Na} is in series with E_{Na}. The arrows indicate that g_{Na} and g_K vary with voltage and time. The low conductance for Cl^- (g_{Cl}) was termed the leak conductance. C_m, membrane capacitance. *(Redrawn with permission from Hodgkin, A.L. (1964). The Conduction of the Nervous Impulse. Charles C. Thomas, Springfield.)*

conductances for Na^+ and K^+ ions are variable and depend on the transmembrane potential and time. Batteries (positive pole directed inwardly for Na^+ ions and outwardly for K^+ ions) provide the driving forces for current flow. A passive leak conductance for Cl^- ions is also included in the model. If the correct values for the elements are incorporated and varied over time, the model circuit will generate an AP.

IVE. Fast Na^+ Channel Activation

During an AP, the increase in g_{Na} is related to the membrane potential E_m in a *positive-feedback* fashion, or "vicious cycle" (Fig. 19.19A). That is, a small depolarization leads to an increase in g_{Na}, which allows a larger inward I_{Na}, which causes further depolarization. This greater depolarization produces a greater increase in g_{Na}. This positive feedback process is "explosive," with a sharp trigger point (threshold) resulting from the exponential relationship (initially positive) between g_{Na} and E_m (Fig. 19.19B). It is this positive-feedback relationship that accounts for the *negative resistance* (slope) in the current–voltage curve (see Fig. 19.12). As Fig. 19.19B shows, g_{Na} reaches a maximum (saturates) at positive potentials that gives maximal activation of the population of fast Na^+ channels.

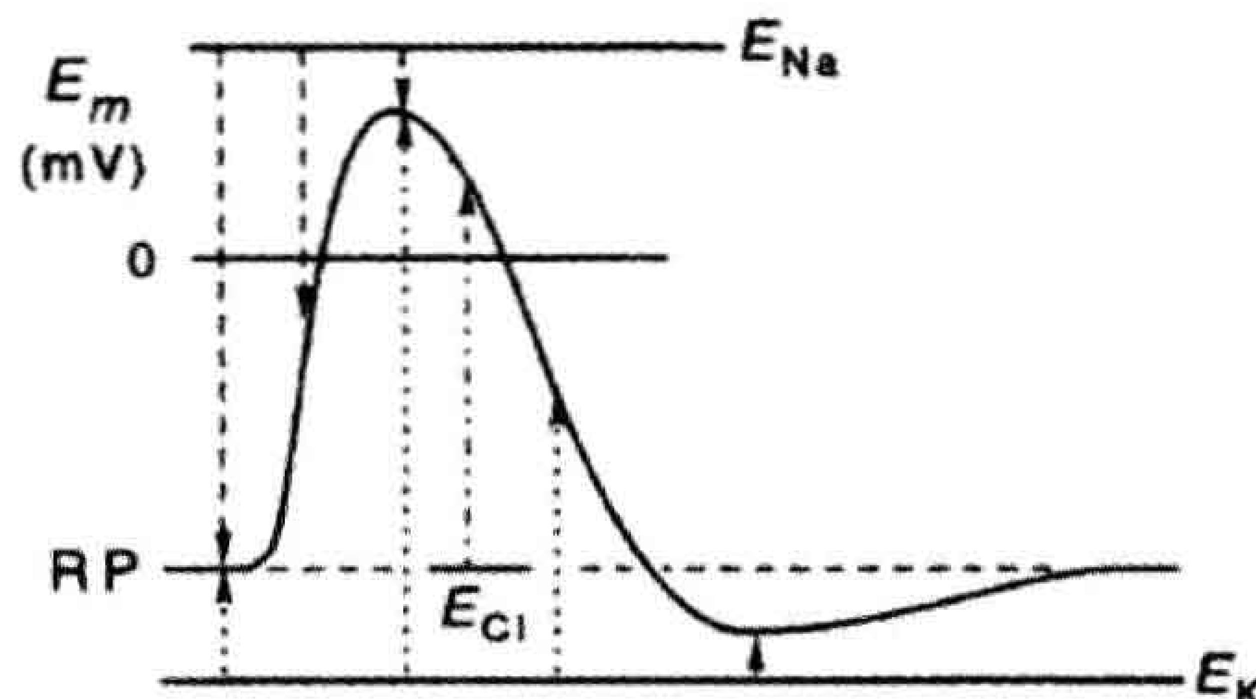


FIGURE 19.17 Driving forces for Na^+ and K^+ currents during the AP. The total electrochemical driving force is equal to membrane potential (E_m) minus the equilibrium potential for the ion (E_i):(E_m–E_i). As depicted, the driving force for the Na^+ current decreases during the AP, whereas that for K^+ increases. Even when Cl^- is passively distributed, a net driving force for Cl^- influx (outward Cl^- current) occurs during the AP.

The fast Na^+ channels (and the slow Ca^{2+} channels) have a double gating mechanism: an inactivation gate (I-gate) and an activation gate (A-gate) (Fig. 19.20). For a channel to be conducting, both the A-gate and the I-gate must be open; if either one is closed, the channel is nonconducting. The A-gate is located somewhere near the middle of the channel; it is not at the outer surface because even TTX does not prevent the movement of this gate and it is not at the inner surface because proteases perfused internally do not affect it. The A-gate is closed at the resting E_m and opens rapidly on depolarization; in contrast, the I-gate is open at the resting E_m and closes slowly on depolarization.

In the Hodgkin–Huxley (1952) analysis, the opening of the A-gate requires simultaneous occupation of three negatively-charged sites by three positively-charged (m^+) particles. The activation variable, m, is the probability of one site being occupied and m^3 is the probability that all three sites are occupied; therefore,

$$g_{Na} = \bar{g}_{Na} m^3 h \tag{19.7}$$

where h is the inactivation variable and $\bar{g}_{Na}$ is the maximum conductance.

Hodgkin and Huxley found that, in squid giant axon, there was an *e*-fold increase in g_{Na} per 4–6 mV of depolarization. To convert to ln from $\log_{10}$, the 2.303 RT/zF

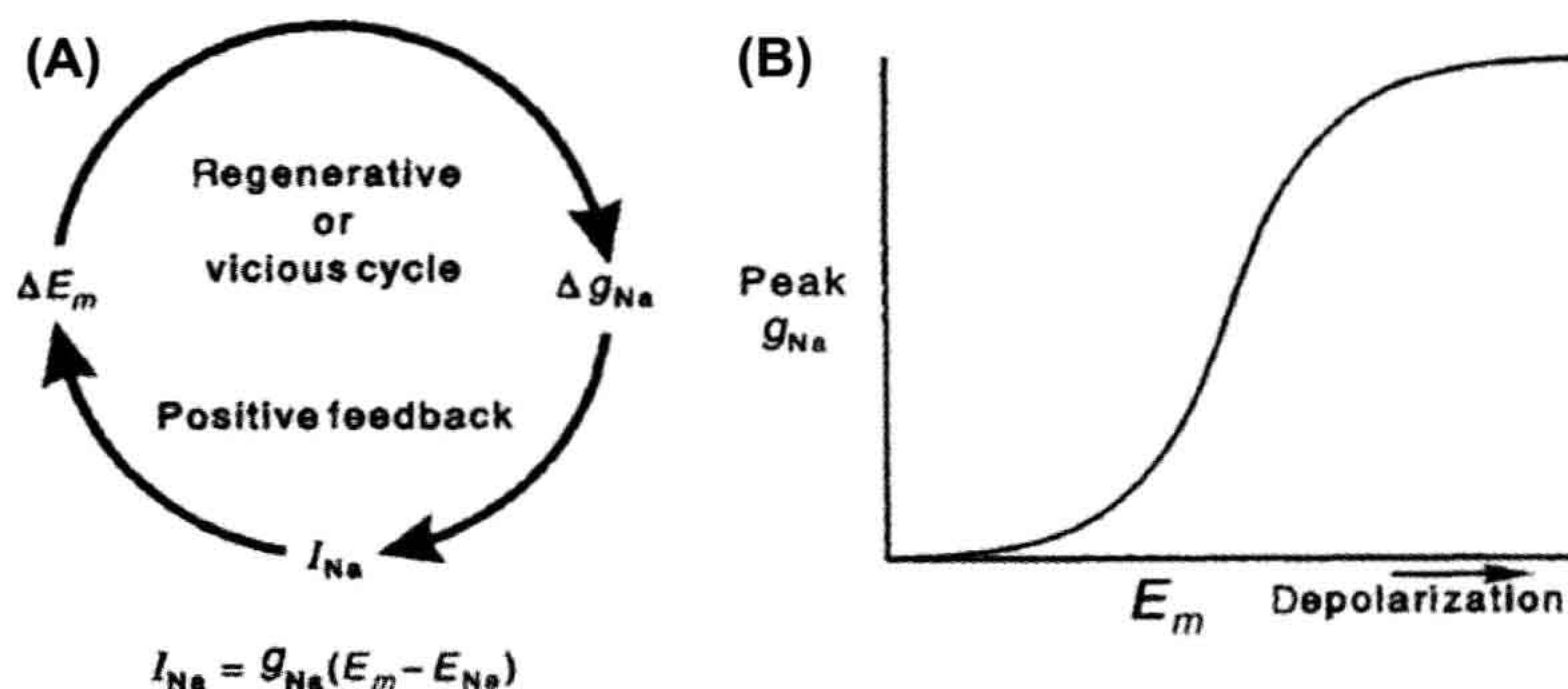


FIGURE 19.19 The positive-feedback relationship between Na^+ conductance (g_{Na}) and membrane potential E_m, leading to the all-or-none AP. (A) The increase in g_{Na} allows an increase in the inward Na^+ current, $I_{Na} = g_{Na}(E_m - E_{Na})$, which is depolarizing and so triggers a further increase in g_{Na}. This explosive feedback cycle is caused by the voltage dependency of the gated fast Na^+ channels. (B) Plot of g_{Na} versus depolarization, showing the initial exponential (positive) increase in g_{Na} as a function of voltage, followed by saturation at greater depolarization, thus giving a sigmoidal relationship. *(Adapted from Hodgkin, A.L. (1964). The Conduction of the Nerve Impulse. Charles C. Thomas, Springfield.)*

factor of 58 mV (at 20°C) becomes 58 mV/2.303, or 25.2 mV. Therefore, they concluded that the voltage-sensitive activation gate must have about 4 to 6 unitary charges (25/6 to 25/4).

IVF. Gating Current

Since the gating of the ionic channels is voltage dependent, a part of the channel protein contains a charged group or dipole that can sense the electric field across the membrane and move in response to a change in transmembrane voltage. When the gating region moves, it causes a shift in the overall conformation of the channel, which allows it to conduct ions. A *gating current* (I_g) that corresponds to the movement of the charged m^+ particles (or rotation of an equivalent dipole) has been measured. The gating current is very small in intensity and is measured by subtracting the linear capacitive current (from a hyperpolarizing clamp step) from the total capacitive current (linear plus non-linear) that occurs with a depolarizing clamp step beyond threshold. The outward I_g precedes the inward I_{Na}. Tetrodotoxin does not block I_g, although it does block I_{Na}. Thus, the gating current is a non-linear outward capacitive current (not an ionic current) obtained during depolarizing clamps that reflects movement of the A-gates from the closed to the open configuration, i.e. the charge movement associated with the A-gates. The linear capacitive current results mainly from the lipid bilayer matrix.

Specific charged residues are located along the primary sequence of amino acids that comprise the channel polypeptide and they can "sense" the transmembrane electric field and move in response to changes in it. The movement of these voltage-sensing or gating residues initiates a conformational change in the channel structure, which then permits ions to flow through the central pore region of the alpha subunit of the channel. Gating currents have been recorded from several types of ion channels.

IVG. Na^+ Inactivation

The fast I_{Na} lasts only for 1–2 ms because of the spontaneous inactivation of the fast Na^+ channels. That is, the fast Na^+ channels inactivate quickly, even if the membrane

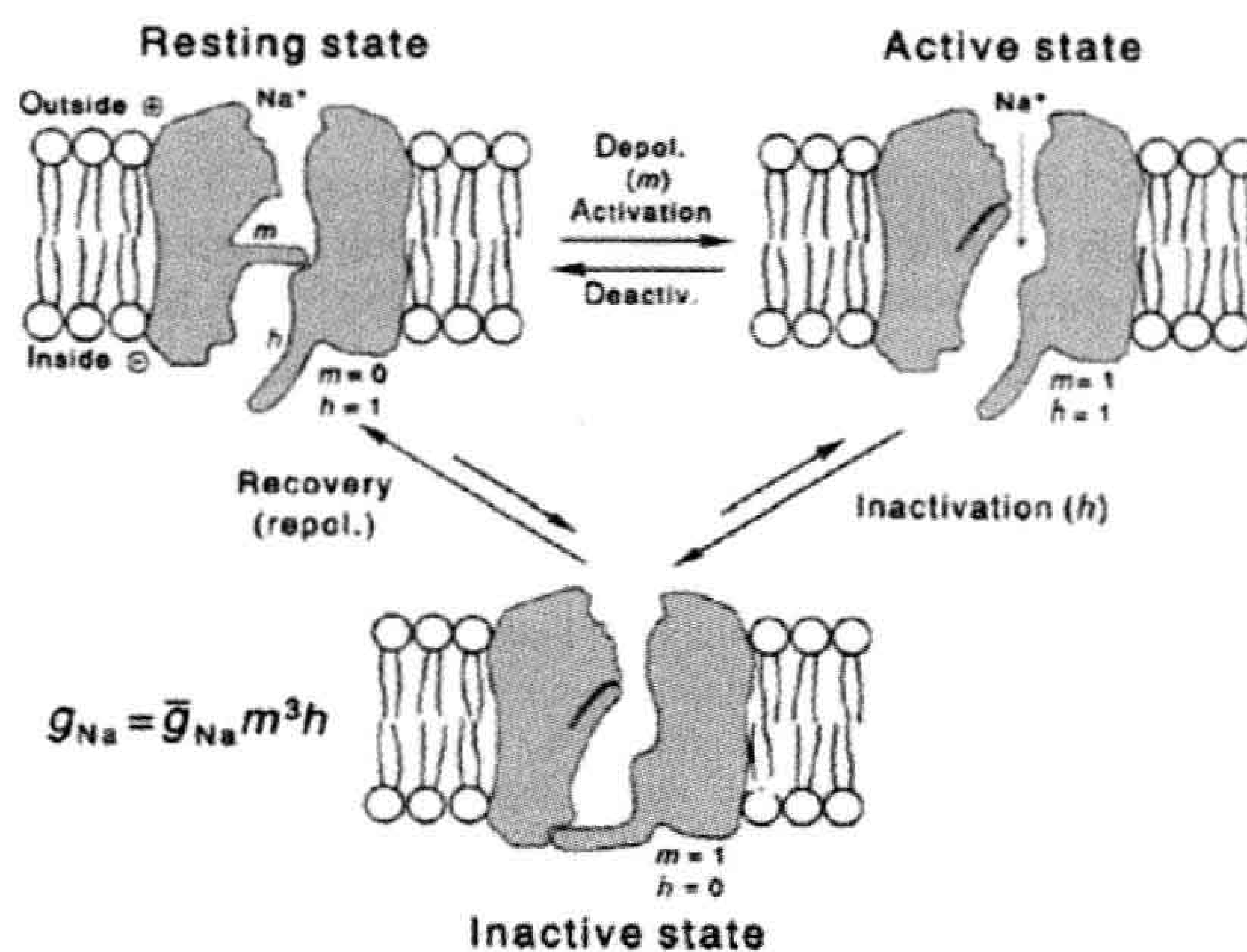


FIGURE 19.20 The three hypothetical states of the fast Na^+ channel, based on the Hodgkin–Huxley model. In the resting state, the activation gate (A or *m*) is closed and the inactivation gate (I or *h*) is open: $m = 0$, $h = 1$. Depolarization to the threshold or beyond activates the channel to the active state, the A-gate opening rapidly and the I-gate still being open: $m = 1$, $h = 1$. The activated channel spontaneously inactivates to the inactive state because of delayed closure of the I-gate: $m = 1$, $h = 0$. The recovery process on repolarization returns the channel from the inactive state to the resting state, thus making the channel again available for reactivation. Na^+ is depicted as being bound to the outer mouth of the channel and poised for entry down its electrochemical gradient when both gates are open (active state of channel). The reaction between resting state and the active states is reversible, whereas the other reactions may be less reversible. The Ca^{2+} slow channels pass through similar states.

were to remain depolarized. (In contrast, the slow Ca^{2+} channels inactivate slowly.) Inactivation is produced in the fast Na^+ channels (and in the slow Ca^{2+} channels) by the voltage-sensitive slow closing of the inactivation gate (I-gate) (see Fig. 19.20). The I-gate is located near the inner surface of the membrane, as evidenced by the fact that addition of proteolytic enzyme to the inside of a perfused giant axon chops off the I-gate and eliminates inactivation. (Protease added outside does not have this effect.) The I-gate is presumably charged positively to allow it to move with changes in the membrane potential. During depolarization, the inside of the membrane becomes less negative or more positive and this causes the I-gate to close. At the normal RP, the I-gate is open (but the A-gate is closed).

The voltage dependency of inactivation is given by the h_∞ versus E_m curve (Fig. 19.21). The inactivation variable h (probability function) varies between 0 and 1.0, perhaps reflecting occupation of a negatively-charged site by a positively-charged h particle; h_∞ is the value of h at infinite time (>10 ms) or at steady state. When $h = 1.0$, the I-gates of all of the fast Na^+ channels are in the open configuration; conversely, when $h = 0$, all the I-gates are closed. Since g_{Na} at any time is equal to the maximal value ($\bar{g}_{Na}$) times m^3h (see Equation 19.7), when $h = 0$, $g_{Na} = 0$. When $h = 1.0$, $g_{Na} = \bar{g}_{Na}$ (if $m = 1.0$). At the normal RP, h_∞ is nearly 1.0 and it diminishes with depolarization, becoming zero at about −30 mV in squid axon (Fig. 19.21A). The maximal rate of rise of the AP (max dV/dt) is directly proportional to the net inward I_{Na}, which is directly proportional to g_{Na}. The decrease in h_∞ is the cause of decrease in g_{Na}. Therefore, depolarization by any means (e.g. elevated $[K^+]_o$ or applied depolarizing current) decreases g_{Na} and excitability disappears at about −50 mV (Fig. 19.21B). The AP disappears at −50 mV (rather than −30 mV) because of a minimum current density requirement for a regenerative and propagating response.

A plot of the inactivation curve along with the activation curve is given in Fig. 19.21C to illustrate the overlap in these curves, giving rise to a so-called *window current* (or steady-state inward current) over a certain voltage region. The presence of the window current means that, over the voltage range of about −50 to −30 mV, there is a steady inward Na^+ current passing through about 10–20% of the fast Na^+ channels that are open (on a rotating population basis).

The slow Ca^{2+} channels behave much the same way as the fast Na^+ channels with respect to activation and inactivation, with one main difference being the voltage range over which the slow channels operate. For example, inactivation occurs between −50 and 0 mV for the slow channels, compared with between −100 and −30 mV for the fast Na^+ channels. Another major difference is that slow channels inactivate much more slowly than the fast channels; i.e. they have a long inactivation time constant (τ_{inact}). In myocardial cells, the h variable for the slow channel is referred to as the f variable and the m variable as the d variable and the exponent is 2.0:

$$g_{Ca} = \bar{g}_{Ca} d^2 f \tag{19.8}$$

The amino acid sequences of Na^+ and Ca^{2+} channels are known, as well as their putative tertiary structure (Fig. 19.22). Na^+ and Ca^{2+} channels consist of several subunits, one of which contains the water-filled pore through which the ions pass. Ion channels have one or more sites that can be phosphorylated, and phosphorylation alters

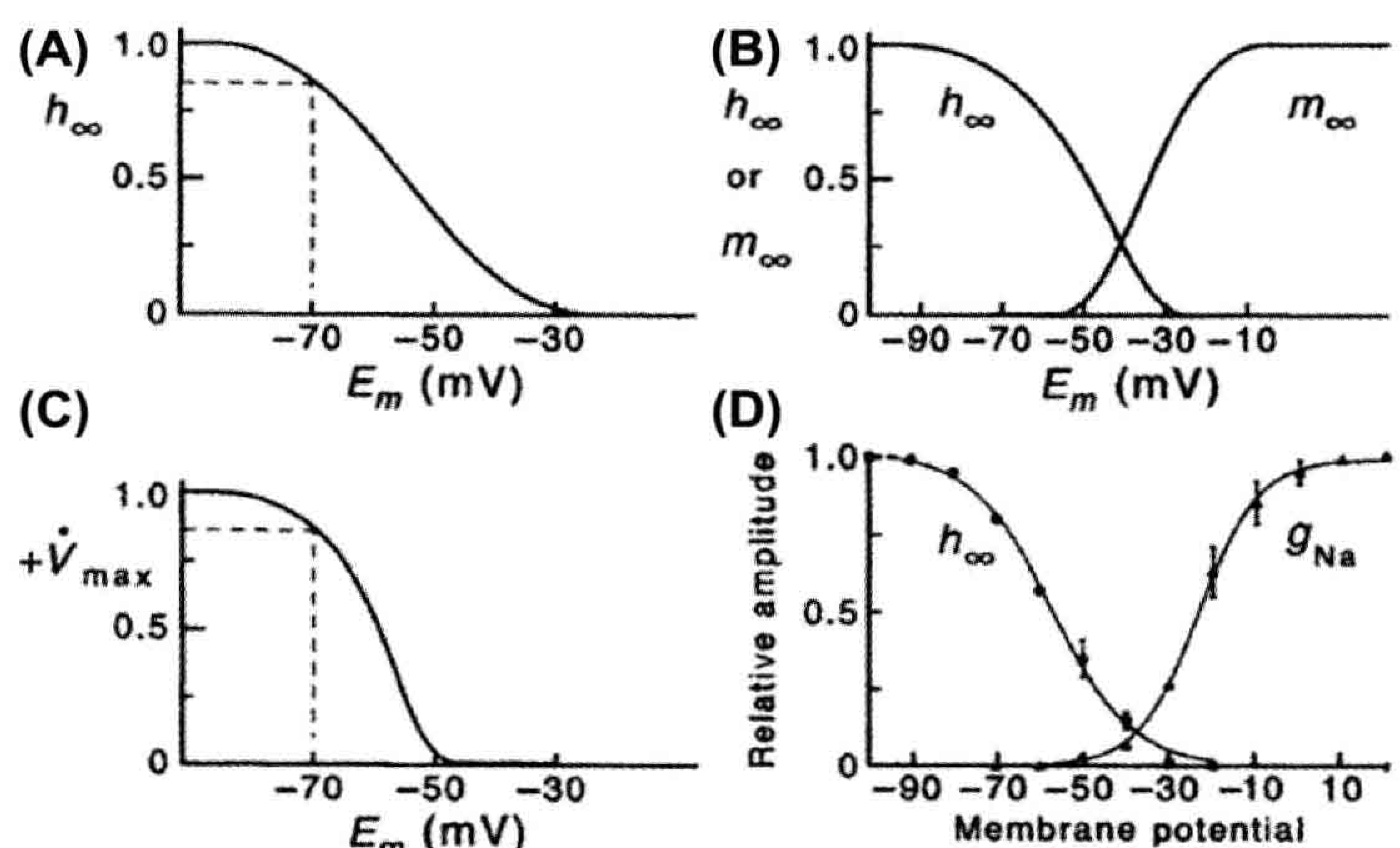


FIGURE 19.21 Voltage inactivation of the fast Na^+ channels as a function of the membrane potential (E_m). (A) h_∞ plotted against E_m, where h is the inactivation factor of Hodgkin–Huxley. The h_∞ represents h at infinite time or steady state. This graph illustrates that fast Na^+ channels begin to inactivate at about −75 mV and nearly complete inactivation occurs at about −30 mV. (B) Maximal rate of rise of the AP (max dV/dt) as a function of resting E_m. Max dV/dt is a measure of the inward current intensity, which is dependent on the number of channels available for activation. Therefore, max dV/dt decreases as h_∞ decreases. (C) Plot of both steady-state inactivation (h_∞) and activation (m_∞) against E_m to illustrate the overlap of the two curves, depicting the window current region. (D) Steady-state activation and inactivation curves for the fast Na^+ current ($I_{Na(f)}$) recorded, using the whole-cell voltage-clamp technique, from uterine smooth muscle cells isolated from late-pregnant (18-day) rats. Note the overlap between the activation and inactivation curves, resulting in a steady-state window current between about −50 and −30 mV. *(Data from Y. Inoue and N. Sperelakis, unpublished observations.)*

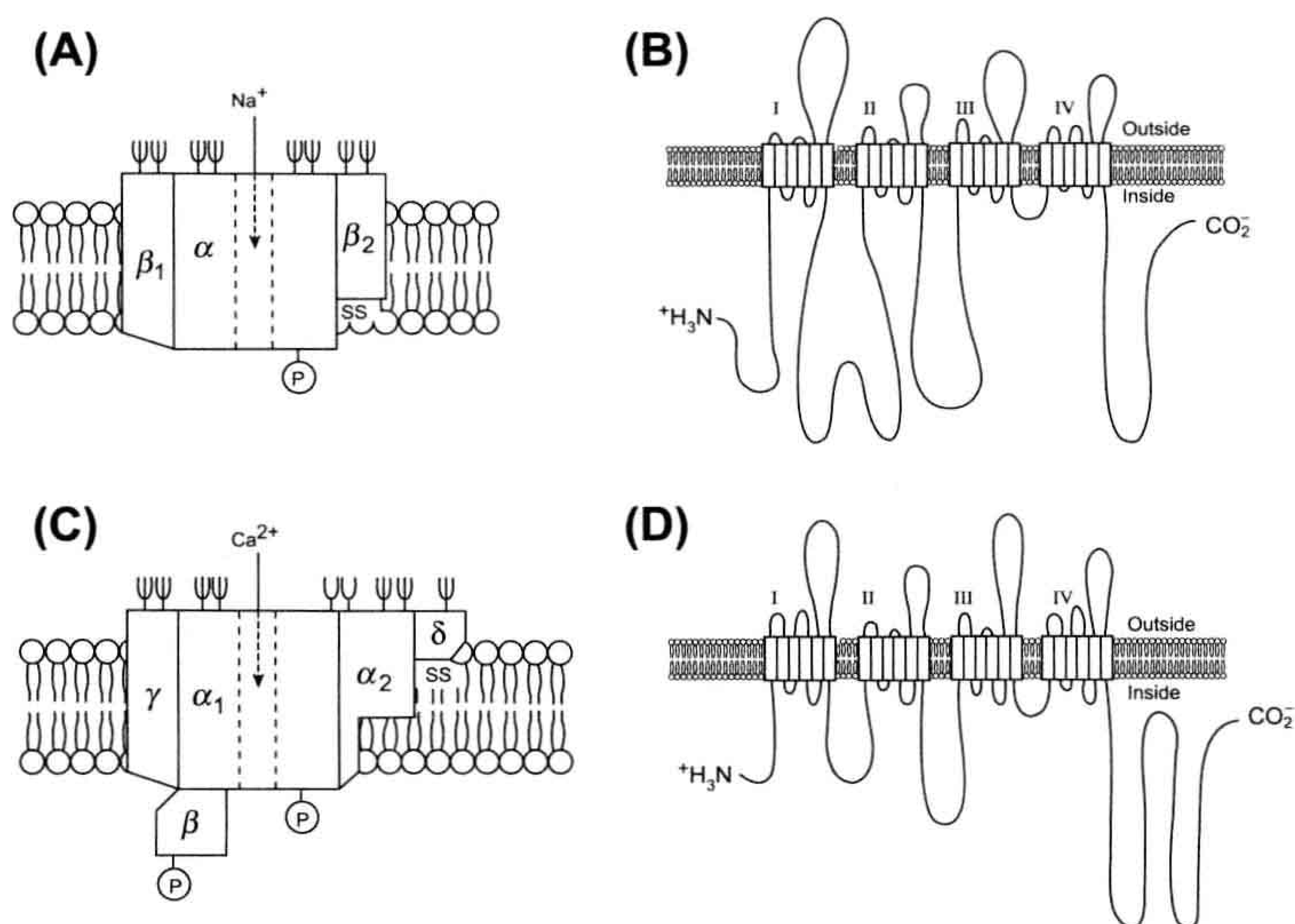


FIGURE 19.22 Models of the fast Na^+ channel and the slow Ca^{2+} channel proteins. (A) The Na^+ channel has multiple protein subunits, labeled α, β_1 and β_2. The α subunit is the one that contains the water-filled pore through which Na^+ passes. One site that can be phosphorylated by cyclic AMP–dependent protein kinase (cAMP-PK) is present on the α subunit which contains the pore. The β_2 subunit has a disulfide bond (SS). (B) In the α subunit, there are four homologous intramembrane polypeptide repeat domains, connected by intracellular polypeptide segments or loops, arranged into a circular structure within the plane of the membrane to form a channel. Each domain consists of six units that span the membrane, as depicted. (C) The Ca^{2+} channel also is composed of several subunits: α_1, α_2, β, γ and δ. The α_1 subunit contains the pore pathway. Two sites can be phosphorylated by the cAMP-PK, one on the α_1 subunit and the other on the β subunit. The β and δ subunits do not span the lipid bilayer and the δ subunit possesses a disulfide bond. (D) The polypeptide structure of the α_1 subunit of the Ca^{2+} channel is similar to that for the fast Na^+ channel, with four repeat membrane-spanning domains connected by intracellular and extracellular loops. *(Reprinted with permission from Catterall, W. (1988). Science. 242, 50–61.)*

their behavior. For example, in cardiac muscle, the slow Ca^{2+} channel activity is increased by epinephrine (adrenaline), a hormone that increases the cyclic AMP level and leads to Ca^{2+} channel phosphorylation (see subsequent chapter). The molecular structure of ion channels is discussed in more detail in a later chapter.

IVH. Recovery

Any Na^+ or Ca^{2+} channel that has been activated and then spontaneously inactivated must go through a recovery process before it can return to the resting state from which it can be reactivated (see Fig. 19.20). The recovery process is dependent on voltage and time. The membrane must be repolarized beyond about −50 mV before the recovery process can begin. At any given E_m, time is necessary for the recovery process to occur, namely, the time required for the charged A-gates and I-gates to move back to their resting configuration (A-gate closed, I-gate open) with the electric field. The recovery process is rapid for fast Na^+ channels (e.g. 1–10 ms) and less rapid for the slow Ca^{2+} channels. The recovery process of the slow channels is slowed by organic calcium antagonist drugs.

IVI. K^+ Activation

The K^+ channel (outward-going delayed rectifier) is generally believed to have only an A-gate, because it does not inactivate. This gate is thought to be located near the inner surface of the membrane, because TEA^+ blocks the K^+ channel more readily from the inner surface. The block is *use dependent* or *frequency dependent*: as the A-gate opens, the TEA^+ molecule can bind in the channel behind the gate. The A-gate is believed to be positively charged and depolarization (inside going positive) opens the gate. In the Hodgkin–Huxley analysis of squid giant axon, the A-gate opens when four positively-charged n^+ particles simultaneously occupy four negatively-charged sites. If n is the probability that one site is occupied, then n^4 is the probability that all four sites are occupied; therefore,

$$g_K = \bar{g}_K n^4 \tag{19.9}$$

The power to which n is raised varies in different tissues.

IVJ. Types of K^+ Channels

The cell membrane of some cells (e.g. myocardial cells) has at least five separate K^+ channels. Some information on these K^+ channels is given in Appendix II to this chapter.

IVK. Model for Activation and Inactivation of Na^+ and K^+ Channels

As stated previously, in the Hodgkin–Huxley analysis, the Na^+ conductance g_{Na} is controlled by three charged activating m particles and one blocking h particle, which move with changes in the electric field across the membrane either to occupy or unoccupy certain sites on the Na^+ channel protein. If m is the probability of one favorable site

being occupied, then $m \times m \times m$ or m^3 is the probability that all three sites are occupied simultaneously. The A-gate cannot be fully opened unless all three sites are occupied. A simplistic variant is to consider that the A-gate actually consists of three separate subgates or subdoors, as illustrated in Fig. 19.23. For an Na^+ ion to pass through the channel, all three subdoors must be open.

The value of h is the probability of one favorable site being occupied that opens the I-gate and this site is already occupied at the normal RP (I-gate open) and becomes unoccupied with depolarization. Therefore, g_{Na} is given by Equation 19.7.

The K^+ conductance g_K is controlled by four charged activating n particles which move with depolarization to occupy four sites on the K^+ channel protein. If n is the probability of one favorable site being occupied, then $n \times n \times n \times n$ or n^4 is the probability that all four sites will be occupied simultaneously. There is no inactivation variable for the K^+ channel, because g_K does not exhibit a major decrease during a short depolarizing voltage-clamp pulse (e.g. 20 ms). Therefore, g_K is given by Equation 19.9. Additional details of the Hodgkin–Huxley analysis are given in Appendix I to this chapter.

IVL. Mechanisms of Repolarization

The AP is terminated primarily by the turn-on of g_K, the *delayed rectification*. It is called the delayed rectifier because its turn-on is slower and delayed with respect to the turn-on of the fast Na^+ channels. The increase in g_K acts to bring E_m toward E_K (about −90 mV), since the membrane potential at any time is determined mainly by the ratio of g_{Na}/g_K (see Chapter 9). This type of g_K channel is activated by depolarization and turned off by repolarization. Therefore, this g_K channel is *self-limiting*, in that it turns itself off as the membrane is repolarized by its action.

In addition to the g_K turn-on, there is also some turn-off of g_{Na}, which contributes to repolarization. Two reasons for g_{Na} turnoff are (1) spontaneous inactivation of fast Na^+ channels that had been activated, i.e. closing of their I-gate (inactivation τ of 1–3 ms); and (2) a reversible shifting of activated channels directly back to the resting state because of the rapid repolarization occurring due to the g_K mechanism. Theoretically, it would be possible to have an AP that would repolarize (but more slowly) even if there were no g_K mechanism, because the g_{Na} channels would spontaneously inactivate and so the g_{Na}/g_K ratio and E_m would slowly be restored to their original resting values. Turn-on of g_K acts to sharpen repolarization of the AP and allows higher frequency of impulses.

IVM. Skeletal Muscle Repolarization

The two mechanisms for sharp repolarization of the AP discussed previously for neurons also apply to skeletal muscle. But there is an important *third factor* involved in repolarization of the skeletal muscle AP, the *Cl^- current*. The Cl^- permeability (P_{Cl}) and conductance (g_{Cl}) are very high in skeletal muscle. In fact, P_{Cl} of the surface membrane is much higher than P_K, the P_{Cl}/P_K ratio being about 3–7. However, as discussed in Chapter 9, the Cl^- ion is passively distributed, or nearly so, and thus cannot determine the RP. However, net Cl^- movements inward (hyperpolarizing) or outward (depolarizing) can and do affect E_m transiently until re-equilibration occurs. There is

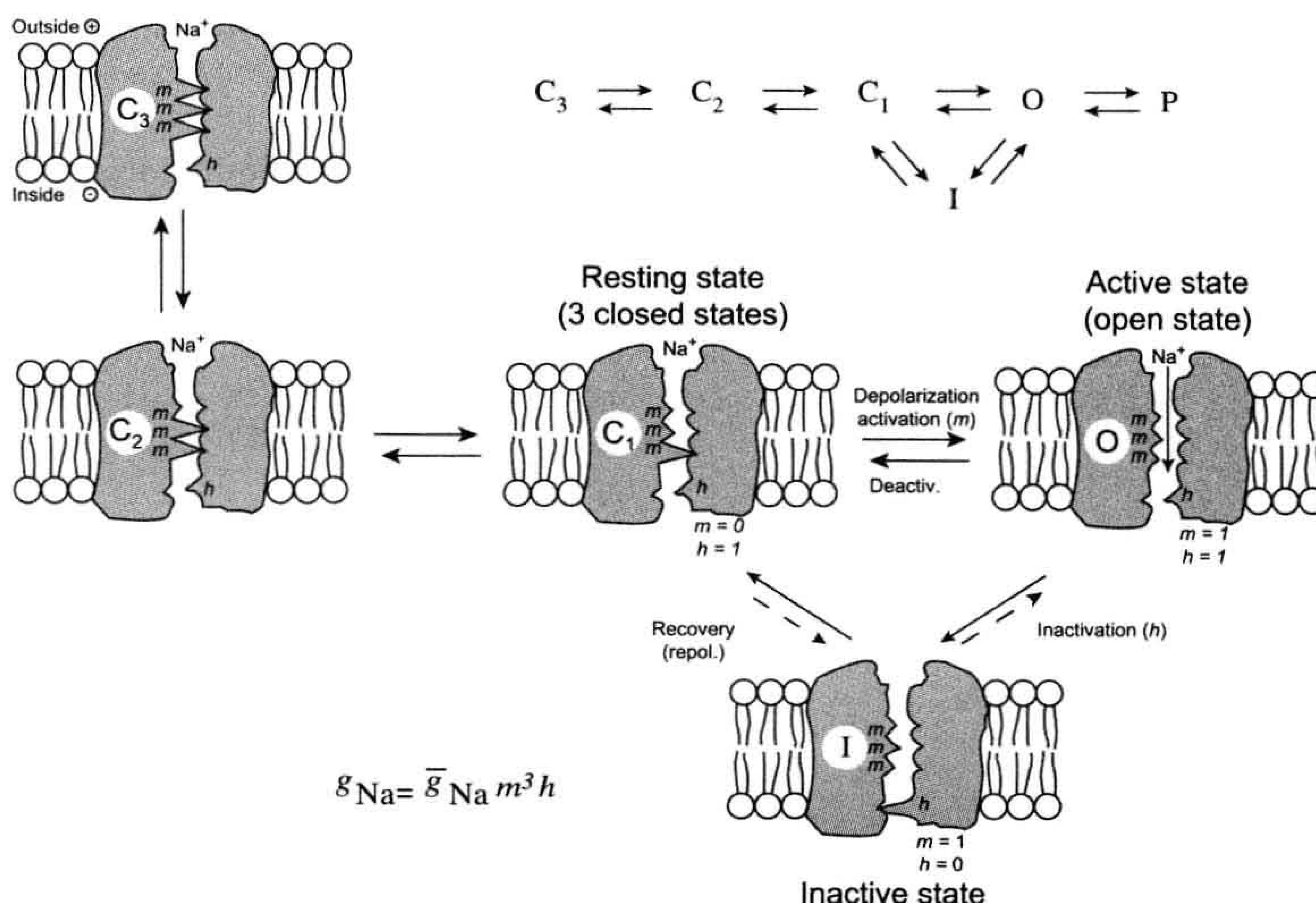


FIGURE 19.23 Diagram depicting the modified Hodgkin–Huxley view of the three states of the fast Na^+ channel. As shown, there is evidence for the existence of three closed states of the channel (C_3, C_2 and C_1). The activation gate (A-gate) is depicted as consisting of three parts, each one being controlled by one m^+ particle. For the A-gate to be open to allow Na^+ ions to pass, all three subgates must be open and therefore all m sites must be occupied. The C_3 closed state is depicted as having all three subgates closed, the C_2 closed state with two subgates closed (one open) and the C_1 closed state with one subgate closed (two open). For the open state (O), all three subgates must be open. P, plugged channel; I, inactive.

no net electrochemical driving force for Cl^- current (I_{Cl}) at the RP, since:

$$E_m = E_{Cl} \quad (19.10a)$$

and

$$(E_m - E_{Cl}) = 0 \quad (19.10b)$$

However, during AP depolarization, there is a larger and larger driving force for outward I_{Cl} (i.e. Cl^- influx), since:

$$I_{Cl} = g_{Cl}(E_m - E_{Cl}) \quad (19.11)$$

where E_{Cl} is the Cl^- equilibrium potential calculated from the Nernst equation (see Fig. 19.17). In other words, the large electric field that was keeping Cl^- out (i.e. $[Cl^-]_i << [Cl^-]_o$) is diminishing during the AP and so Cl^- ions enter the fiber. This Cl^- entry is hyperpolarizing and, therefore, tends to repolarize the membrane more quickly than would otherwise occur. That is, repolarization of the AP is sharpened by the Cl^- mechanism. The higher the g_{Cl}, the greater this effect.

To illustrate some of the above points, if skeletal muscle fibers are placed into Cl^--free Ringer's solution (e.g. methanesulfonate substitution), depolarization and spontaneous APs and twitches occur for a few minutes until most or all of the Cl^- is washed out. After equilibration, the resting E_m then returns to the original value (ca. -90 mV for frog muscle), clearly indicating that Cl^- does not determine the RP and that net Cl^- efflux produces depolarization. Re-addition of Cl^- to the bath produces a rapid large hyperpolarization (e.g. to -120 mV) due to net Cl^- influx and E_m then slowly returns to the original value (-90 mV) as Cl^- re-equilibrates (i.e. redistributes itself passively). These same effects would occur in cardiac muscle, smooth muscle and nerve, but to a lesser extent, because P_{Cl} is much lower in these tissues.

V. EFFECT OF RESTING POTENTIAL ON ACTION POTENTIAL

Any agent that affects the RP has important repercussions on the AP. Depolarization reduces the rate of rise of the AP and thereby also slows its velocity of propagation. A slow spread of excitation throughout the nerve or muscle will interfere with its ability to act efficiently. This effect is progressive as a function of the degree of depolarization. If nerve, skeletal muscle fibers or cardiac muscle cells are depolarized to about -50 mV by any means, then all excitability is lost.

Hyperpolarization usually produces only a small increase in the rate of rise. Larger hyperpolarization may actually slow the velocity of propagation, because the critical depolarization required to bring the membrane to its threshold potential is increased and it can cause propagation block.

The explanation for the effect of resting E_m (or take-off potential) on maximum rate of rise (max dV/dt) of the AP is based on the sigmoidal h_∞ versus E_m curve (see Fig. 19.21A). The I (h)-gates are open in a resting membrane and close with depolarization. As discussed previously, h, the inactivation variable for the fast Na^+ conductance, is a probability factor that deals with the open ($h = 1.0$) versus closed ($h = 0$) positions of the inactivation gate of the channel (see Fig. 19.20). At the RP of -80 mV, h_∞ is 0.9–1.0 and diminishes with depolarization, becoming nearly zero at about -30 mV.

The RP also affects the duration of the AP. With use of polarizing current, depolarization lengthens the AP, whereas hyperpolarization shortens it. This occurs because of anomalous rectification (i.e. g_K decreases with depolarization and increases with hyperpolarization). In contrast, when elevated $[K^+]_o$ levels are used to depolarize the cells, the AP is shortened. One important determinant of the AP duration is g_K. Agents or conditions that increase g_K, such as elevation of $[K^+]_o$, tend to shorten the duration. In contrast, agents that decrease g_K or slow its activation, such as Ba^{2+} ion or TEA^+, tend to lengthen the AP duration. Other factors are also important in determining the AP duration. For example, agents that slow the closing of the I-gates of the fast Na^+ channels, such as veratridine, prolong the AP.

VI. ELECTROGENESIS OF AFTERPOTENTIALS

The APs of nerve and muscle cells usually consist of two components: an initial spike followed by an *early afterpotential* (Fig. 19.24A, B). The early afterpotentials may be of two types: *depolarizing* or *hyperpolarizing*. In addition, *late afterpotentials*, both depolarizing or hyperpolarizing, may appear following a brief train of spikes (Fig. 19.24C, D). The electrogenesis of the early and late afterpotentials is different. The early afterpotentials are due to a conductance change, whereas the late afterpotentials may be due to K^+ accumulation or depletion in restricted diffusion spaces and to electrogenic pump stimulation.

VIA. Early Depolarizing Afterpotentials

The AP spike in skeletal muscle fibers is immediately followed by a prominent depolarizing afterpotential (also called a negative afterpotential, based on the terminology used in external recording) (see Fig. 19.24A). The early depolarizing afterpotential of frog skeletal fibers is about 25 mV (immediately after the spike component) and gradually decays to the RP within 10–20 ms. It results from the fact that the delayed rectifier K^+ channel that opens during depolarization to terminate the spike is less selective

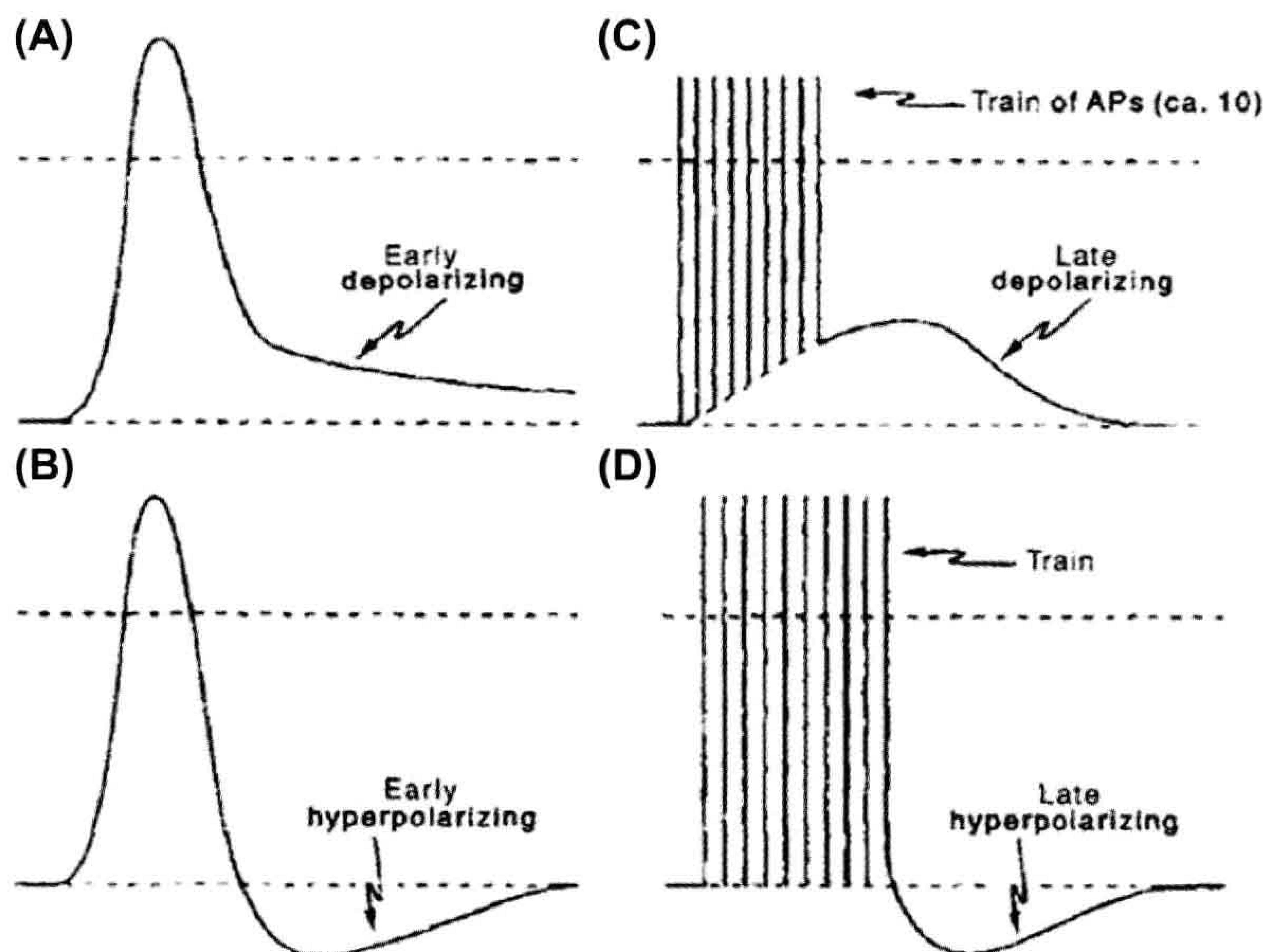


FIGURE 19.24 Examples of the different types of afterpotentials. (A) Early depolarizing (negative) afterpotential recorded after a single AP in a skeletal muscle fiber. (B) Early hyperpolarizing (positive) afterpotential recorded after a single AP in a nerve fiber. (C) Late depolarizing afterpotential recorded after a train (e.g. 10) of APs in a skeletal muscle fiber. (D) Late hyperpolarizing afterpotential recorded following a train of APs in a nerve terminal.

for K^+ (ca. 30:1, K^+:Na^+) than is the K^+ channel in the resting membrane (ca. 100:1, K^+:Na^+). Therefore, from the constant-field equation (see Chapter 9), one can predict that the membrane should be partly depolarized when the membrane is dominated by this delayed rectifier K^+ conductance. Thus, the early depolarizing afterpotential is due to the persistence of, and slow decay of, this less selective K^+ conductance.

VIB. Early Hyperpolarizing Afterpotentials

Neurons, heart pacemaker cells and vascular smooth muscle cells often exhibit early hyperpolarizing (positive) afterpotentials (see Fig. 19.24B). These are due to the delayed rectifier K^+ conductance increase (which terminates the spike) persisting after the spike, thereby bringing E_m closer to E_K. The maximum amplitude possible for the afterpotential is the difference between E_K and the normal RP. The time course of this afterpotential is determined by the decay of the K^+ conductance increase.

VIC. Late Depolarizing Afterpotentials

The *late depolarizing afterpotential* of skeletal muscle fibers results from *accumulation of K^+ ions in the transverse (T) tubules* (see Fig. 19.24C). During the AP depolarization and turn-on of the g_K (delayed rectifier), there is a large driving force for K^+ efflux from the myoplasm coupled with a large K^+ conductance, resulting in a large outward K^+ current ($I_K = g_K\ (E_m - E_K)$) across all surfaces of the fiber, namely, the surface sarcolemma and T-tubule walls. The K^+ efflux at the fiber surface membrane can rapidly diffuse away and mix with the relatively large interstitial fluid (ISF) volume, whereas the K^+ efflux into the T-tubules is trapped in this *restricted diffusion space*. The resulting high $[K^+]_{TT}$ decreases E_K across the T-tubule membrane and thereby depolarizes this membrane. Because of cable properties, part of this depolarization is transmitted to the surface sarcolemma and is recorded by an intracellular microelectrode. The K^+ accumulation in the T-tubules can only be dissipated relatively slowly by diffusion out of the mouth of the T-tubules and by active pumping back into the myoplasm across the T-tubule wall. Thus, the decay of the late afterpotential will be a function of these two processes.

The amplitude and duration of the late depolarizing afterpotential of frog skeletal fibers are functions of the number of spikes in the train and their frequency. That is, the greater the spike activity, the greater the amplitude and duration of the late depolarizing afterpotential. If the

train consists of 20 spikes at a frequency of 50/s, a typical value for the amplitude of the afterpotential is about 20 mV. When the diameter of the T-tubules is increased by placing the fibers in hypertonic solutions, the amplitude of the afterpotential decreases, as expected, because of the greater dilution of the K^+ ions accumulating in the T-tubule lumen. When the T-tubular system is disrupted and disconnected from the surface membrane by the glycerol osmotic shock method, the late depolarizing afterpotential disappears (whereas the early depolarizing afterpotential persists).

VID. Late Hyperpolarizing Afterpotentials

Some cells, such as non-myelinated neurons, exhibit *late hyperpolarizing afterpotentials* following a train of spikes (see Fig. 19.24D). These hyperpolarizing afterpotentials are due to the Na^+-K^+ pump, because inhibition of the pump by any means (such as ouabain) abolishes them. Two mechanisms have been proposed for the hyperpolarization. (1) Hyperpolarization occurs because there is an increased *electrogenic Na^+ pump potential* (V_p), stimulated both by an increase in the $[Na^+]_i$ (since these neurons are small in diameter, and hence have a large surface area/volume ratio) and by an increase in $[K^+]_o$ (since these axons are surrounded by Schwann cells and hence have a narrow intercellular cleft and restricted diffusion space). (2) Hyperpolarization occurs due to an increased E_K caused by K^+ depletion in the intercellular cleft because of the stimulated Na^+-K^+ pump overpumping the K^+ back in. It is generally believed that the first mechanism is the most probable.

VIE. Importance of Afterpotentials

All afterpotentials have physiological importance because they alter the excitability and propagation velocity of the cell. A depolarizing afterpotential enhances excitability (lower threshold) and a hyperpolarizing afterpotential depresses excitability to a subsequent AP. This is because the critical depolarization required to reach the threshold potential would be decreased or increased, respectively. A large late depolarizing afterpotential, such as that due to K^+ accumulation in the T-tubules, can trigger repetitive APs under certain pathological conditions.

The effect of afterpotentials on velocity of propagation is complex because there are two opposing factors: (1) the change in critical depolarization required and (2) the change in maximal rate of rise of the AP, which is a function of the takeoff potential (h_∞ versus E_m curve). For example, during a depolarizing afterpotential in skeletal muscle fibers, the critical depolarization required is decreased, but the maximal rate of rise of the AP is also decreased. Therefore, these two factors exert opposing effects.

APPENDIX

AI. ADDITIONAL HODGKIN–HUXLEY ANALYSIS

Based on the preceding analysis, Hodgkin and Huxley (1952a,b,c) then gave the differential equations that govern the values of n, m and h using a pair of rate constants, α and β, for the forward reaction and reverse reaction, respectively. The subscripts for the α and β rate constants identify which variable they pertain to (i.e. n, m or h). The α and β rate constants depend only on membrane potential (at constant temperature and $[Ca^{2+}]_o$). A schematic model is given in Fig. 19A.1 and the corresponding equations are:

$$\frac{dn}{dt} = \alpha_n(1-n) - \beta_n n \qquad (19A.1)$$

$$\frac{dm}{dt} = \alpha_m(1-m) - \beta_m m \qquad (19A.2)$$

$$\frac{dh}{dt} = \alpha_h(1-h) - \beta_h h \qquad (19A.3)$$

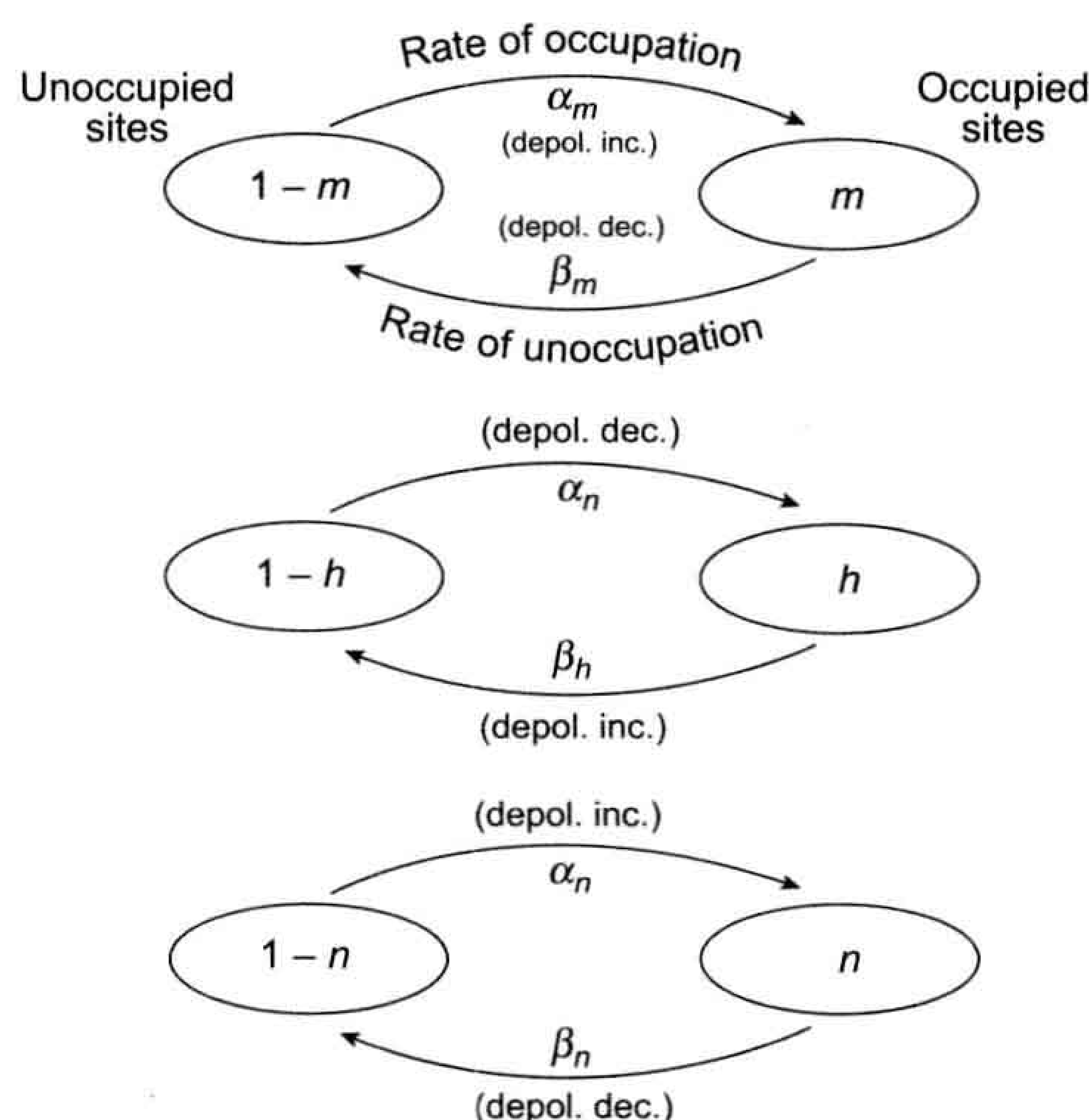


FIGURE 19A.1 Schematic diagram based on the Hodgkin–Huxley model for activation and inactivation of Na^+ channels and K^+ channels. α and β are the rate constants for occupation and unoccupation, respectively, of sites on the channel protein by the m^+, h^+ and n^+ particles. See text for further explanation.

where n is the fraction of sites occupied and, therefore, $(1-n)$ is the fraction of sites unoccupied. Therefore,

$$\text{rate of occupation} = \alpha\,(1-n) \qquad (19A.4)$$

$$\text{rate of unoccupation} = \beta_n n \qquad (19A.5)$$

$$\text{rate of change of } n = \text{rate of occupation} - \text{rate of unoccupation} \qquad (19A.6)$$

which is the same as Equation 19A.1.

The same analysis can be applied to the m and h factors. The effect of making the inside of the fiber more positive (i.e. depolarizing) is to increase α_n, α_m and β_h and to decrease β_n, β_m and α_h. One must remember that the h particles occupy the favorable site at the RP (I-gate open) and this site becomes unoccupied with depolarization (I-gate closes). This is opposite to the situation for the m and n particles (and A-gate).

In voltage-clamp experiments, at a given clamp step, the membrane potential is fixed and the differential equations (Equations 19A.1, 19A.2 and 19A.3) lead to exponential expressions for n, m and h, and the K^+ and Na^+ conductances can then be calculated. When this was done, there was a good fit of the calculated curves with the experimental data points for the changes in g_{Na} and g_K with time at various clamp steps (see Fig. 19.13).

AII. ADDITIONAL INFORMATION ON K^+ CHANNELS

As discussed previously, one type of voltage-dependent K^+ channel is the usual K^+ channel found in many types of excitable membranes. This channel slowly opens (increasing total g_K) on depolarization and is the so-called *delayed rectifier* [I_K or $I_{K(del)}$]. This channel allows K^+ to pass readily outward down the usual electrochemical gradient for K^+ and so is also known as the *outward-going rectifier*. This delayed rectifier channel in myocardial cells turns on much more slowly than in nerve, skeletal muscle or smooth muscle and, therefore, accounts for the long duration of the AP. The activation of this channel produces the increase in total g_K that terminates the cardiac AP plateau (so-called phase 3 repolarization) (see chapter on cardiac AP).

A second type, known as the I_{K1} channel, allows K^+ ion to pass more readily inward than outward, the so-called *inward-going rectifier* or *anomalous rectification*.[1] This kinetically fast channel is responsible for the rapid decrease in K^+ conductance on depolarization (and increase in conductance with repolarization), helps to set the RP and helps bring about the terminal repolarization of the cardiac AP (phase 3). The I_{K1} channel was found to appear at a certain stage of heart development.

A third type of K^+ channel is activated by elevation of $[Ca^{2+}]_i$ and is therefore known as the *Ca^{2+}-activated K^+ channel* or $I_{K(Ca)}$. With Ca^{2+} influx and internal release of Ca^{2+} during the AP and contraction, these channels are activated and help the $I_{K(del)}$ channels to repolarize the AP, i.e. to bring the membrane back to the RP. The presence of this type of K^+ channel has been reported for many types of excitable cells. In actuality, two subtypes of $I_{K(Ca)}$ channel have been found: one that has a high conductance of about 400 pS (big or maxi-K channel) and one that has a lower conductance of about 120 pS (small or mini-K channel).

A fourth type of K^+ channel present in some types of cells, such as myocardial cells, is kinetically fast (compared to $I_{K(del)}$) and provides a rapid outward K^+ current that produces a small amount of initial repolarization, known as phase 1 repolarization in cardiac cells. This occurs immediately following the rapidly-rising spike portion of the AP and is known as the *transient outward current* (I_{to}) in myocardial cells and I_A in neurons. There is some evidence that Cl^- current may contribute to I_{to} (Cl^- influx provides an outward I_{Cl}, which is repolarizing).

A fifth type of K^+ channel is sensitive to ATP, the *K_{ATP} channel* and provides a current known as $I_{K(ATP)}$. This channel is regulated by ATP such that, in normal myocardial cells, this K^+ channel is inhibited (masked or silent). However, in ischemic or hypoxic conditions, when the ATP level is lowered, the $I_{K(ATP)}$ channels become unmasked and provide a large outward I_K that prematurely shortens the cardiac AP. This channel provides a protection mechanism for the heart; namely, the ischemic region of the heart develops very-abbreviated APs and hence contraction is greatly depressed. This effect acts to conserve ATP in the affected cells, enabling full recovery when the blood flow returns to normal after a short time period.

AIII. WHOLE-CELL VOLTAGE CLAMP

To record the whole-cell current, a small-tipped glass pipette, known as a *patch pipette*, is pressed against the cell membrane and negative pressure is applied to the interior of the pipette to draw a small patch of membrane into its tip. A *high-resistance seal* (e.g. $10^{10}\,\Omega$) spontaneously forms (Fig. 19A.2). Then, strong suction is applied to the patch pipette to blow out the membrane patch and allow the lumen of the pipette to be continuous with the lumen of the cell. This technique allows recording of the *whole-cell current* and a complete voltage-clamp analysis can be done for small cells. This technique also allows some control over the intracellular content of the cell; e.g. a substance can be introduced into the cell by diffusion from the patch pipette solution.

[1] It is anomalous in the sense that this channel turns off with depolarization and turns on with hyperpolarization.

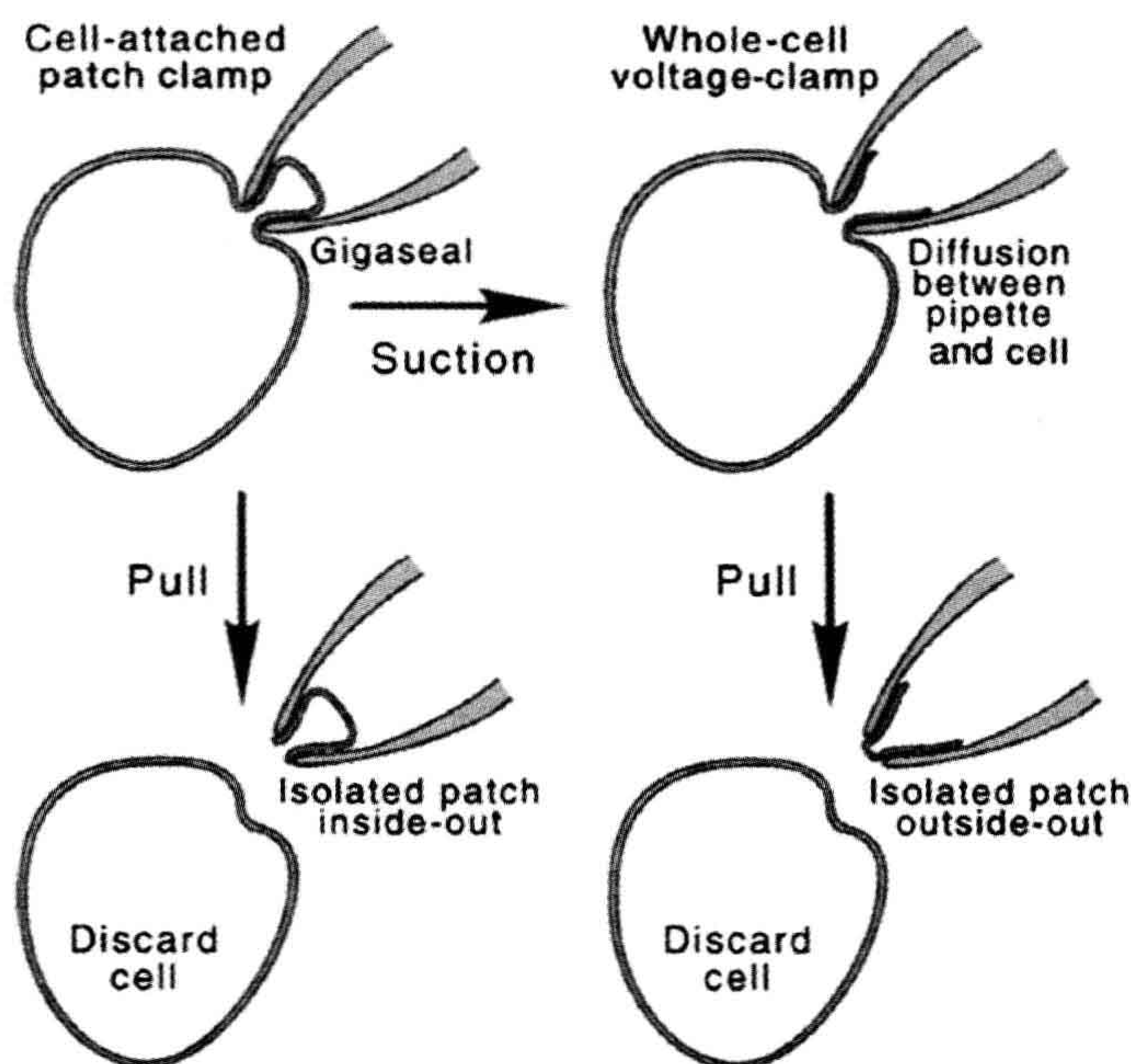


FIGURE 19A.2 The whole-cell voltage-clamp technique in isolated single cells to record the macroscopic current (e.g. I_{Na}, I_{Ca} or I_K) from the entire cell membrane. (Upper left) Cell-attached patch mode, produced by applying light suction to the patch pipette to produce a gigaseal ($10^9\ \Omega$). This mode is used to record the microscopic currents from only one channel or from a few channels. (Upper right) Whole-cell clamp mode produced by applying strong suction to the patch pipette to blow out the membrane patch and allowing the lumen of the pipette to be continuous with the lumen of the cell. This mode is used to record the macroscopic currents from the entire complement of ion channels in the cell membrane. (Bottom) Preparation of isolated membrane patches. *(Reprinted with permission from Hamill, O.P. and Sakmann, B. (1981). Nature. 294, 462–464.)*

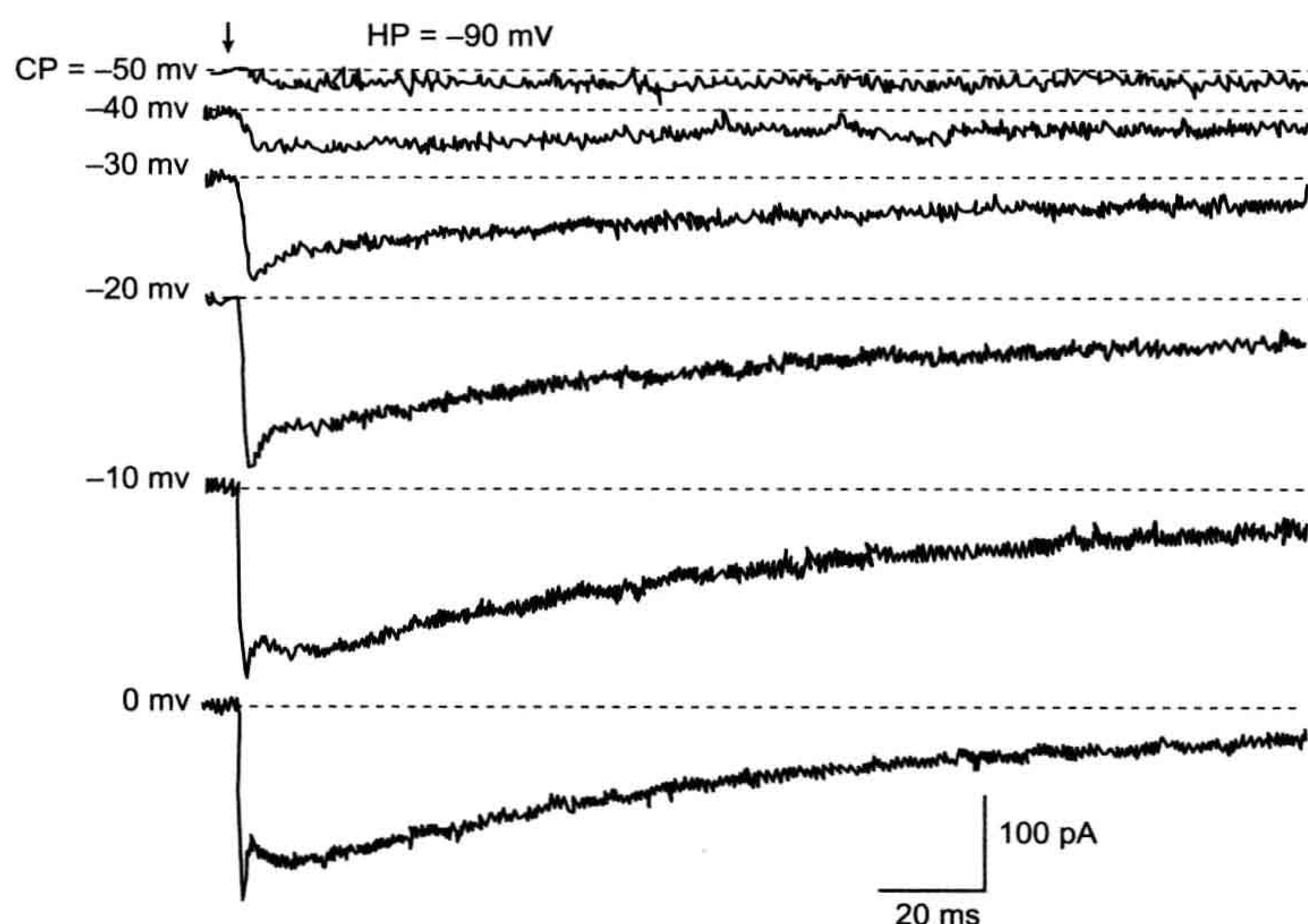


FIGURE 19A.3 Two types of inward current recorded from isolated single myometrial cells from pregnant rat using whole-cell voltage-clamp with a patch-pipette technique. Depolarizing potential steps (−50 to 0 mV) were applied from a holding potential (HP) of −90 mV. The arrow indicates the beginning of a voltage step that continues to the end of the trace. The bath contained K^+-free solution with 150 mM Na^+ and 2 mM Ca^{2+}. The pipette solution contained high Cs^+. Cell capacitance was 80 pF. CP, command potential. *(Reproduced with permission from Ohya, Y. and Sperelakis, N. (1989). Am J Physiol. 257, C408–C412.)*

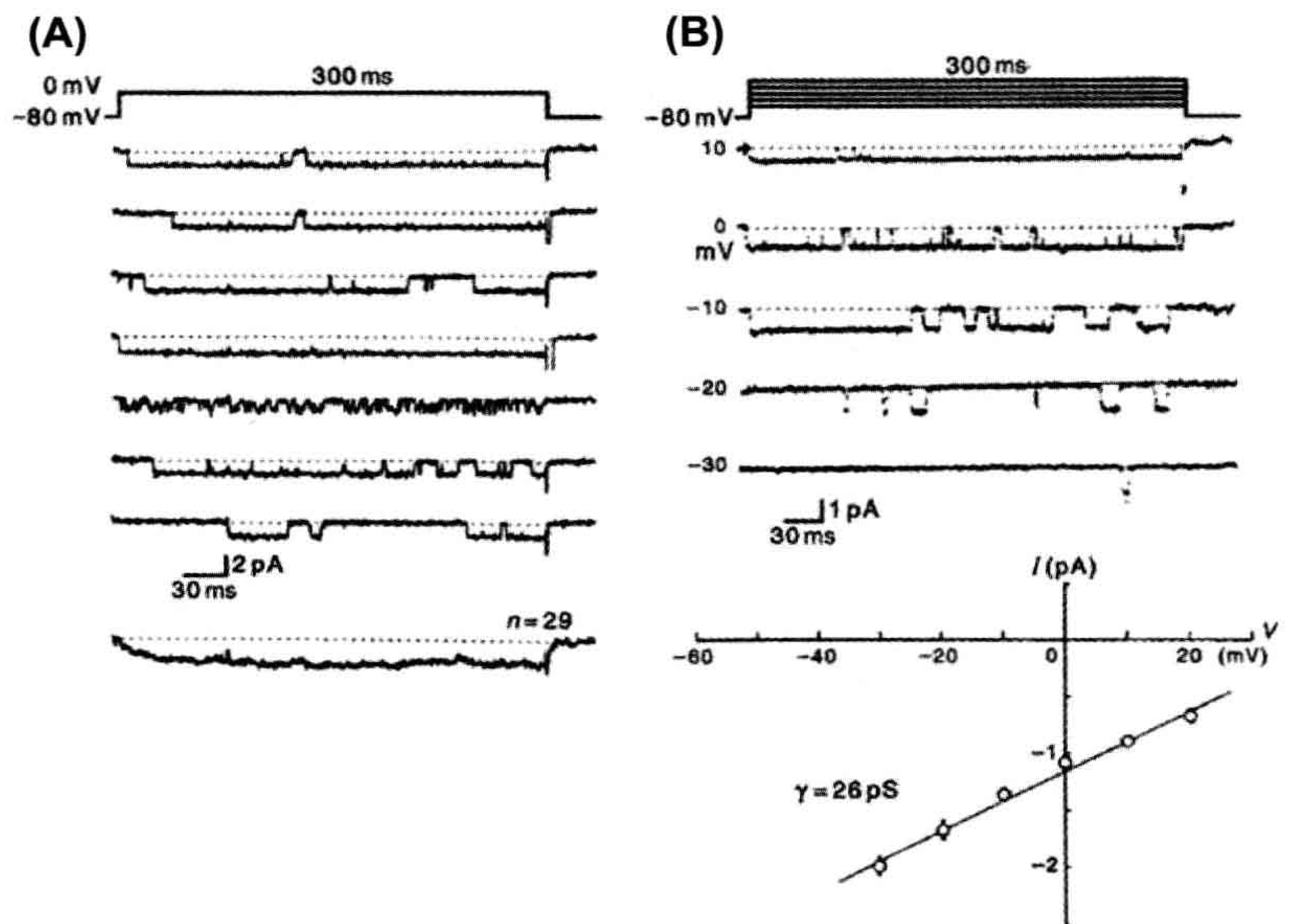


FIGURE 19A.4 Single-channel currents recorded from a slow (L-type) Ca^{2+} channel, using the cell-attached patch-clamp technique, in a single cardiomyocyte isolated from a young (3-day-old) embryonic chick heart. These Ca^{2+} channels in young embryonic/fetal chick and rat heart cells exhibit a high incidence of long openings. Recordings in a cell illustrating the inward currents recorded at five different command step potentials (−30, −20, −10, 0 and +10 mV) from an HP of −80 mV. Note the presence of numerous long openings. The amplitude of the unitary current became smaller at the higher (more positive) command potentials. The current amplitudes are plotted below in the current−voltage curve (each point being the mean ± SE of 5−10 experiments). The data points were fitted by a straight line giving a slope conductance of 26 pS for the single-channel conductance. *(Modified from Tohse, N. and Sperelakis, N. (1990). Am J Physiol. 259, H639−H642.)*

Whole-cell voltage-clamp records obtained from isolated single uterine smooth muscle cells (18-day pregnant rat) are illustrated in Fig. 19A.3. The outward K^+ currents were blocked (by high Cs^+ concentration in the patch pipette) and any inward currents carried by Ca^{2+} or Na^+ ions can be recorded. As shown, there are two inward currents: an initial fast current and a later slow current. The *initial fast current is carried by* Na^+ *ion*, and this Na^+ current is blocked by TTX; the later slow current is carried by Ca^{2+} ions. The presence of functional fast Na^+ channels is unusual for most smooth muscles and it was discovered that such channels developed during pregnancy and reached their maximum density close to term.

The information gained from such whole-cell voltage-clamp experiments, performed on a variety of excitable cell types, has greatly increased our knowledge of the properties and regulation of the many types of ionic currents. The macroscopic or whole-cell current (I) is the product of the number of functional channels in the cell membrane (N) times the probability that the "average" channel is open during the clamp step (p_o) times the single-channel current (i), giving:

$$I = i\,N\,p_o \qquad (19A.7)$$

The single-channel current (in pA), open probability (p_o) and single-channel conductance (γ) are obtained from patch-clamp experiments, in which the activity of a single channel (or a few channels) can be monitored in a small patch of membrane (e.g. 1−10 μm^2) that is electrically isolated from the rest of the cell membrane (cell-attached patch) or excised (isolated patch). Opening and closing of the gates of the single channel reflect conformational changes in the channel protein. This sophisticated technique, which earned the Nobel Prize in physiology and medicine in 1991 for E. Neher and B. Sakmann, allows the biophysical study of the behavior of a single protein molecule and thus represents electrophysiology at the molecular level. An illustration of actual records, obtained from young embryonic chick heart cells, is given in Fig. 19A.4. This patch-clamp technique and analysis is discussed in detail in the following chapter.

BIBLIOGRAPHY

Bernstein, J. (1902). Untersuchengen zür Thermodynamik der bioelektrischen Ströme. *Pflügers Arch, 92*, 521.

Bernstein, J. (1912). *Elektrobiologie*. Braunschweg: Vieweg.

Catterall, W. A. (1988). Structure and function of voltage-sensitive ion channels. *Science, 242*, 50−61.

Cole, K. S. (1949). Dynamic electrical characteristics of the squid axon membrane. *Arch Sci Physiol, 3*, 253−258.

Cole, K. S., & Curtis, H. J. (1939). Electric impedance of the squid giant axon during activity. *J Gen Physiol, 22*, 649−687.

Hamill, O. P., & Sakmann, B. (1981). Multiple conductance states of single acetylcholine receptor channels in embryonic muscle cells. *Nature, 294*, 462−464.

Hamill, O. P., Marty, A., Neher, E., Sakmann, B., & Sigworth, F. J. (1981). Improved patch-clamp technique for high resolution current recording from cells and cell-free membrane patches. *Pflügers Arch, 391*, 85−100.

Hille, B. (1984). *Ionic Channels of Excitable Membrane*. Sunderland: Sinauer Associates.

Hodgkin, A. L. (1964). *The Conduction of the Nervous Impulse*. Liverpool: Liverpool University Press.

Hodgkin, A. L., & Huxley, A. F. (1952a). Currents carried by sodium and potassium ions through the membrane of the giant axon of *Loligo*. *J Physiol (London), 116*, 449–472.

Hodgkin, A. L., & Huxley, A. F. (1952c). The dual effect of membrane potential on sodium conductance in the giant axon of *Loligo*. *J Physiol (London), 116*, 497–506.

Hodgkin, A. L., & Huxley, A. F. (1952d). A quantitative description of membrane current and its application to conduction and excitation in nerve. *J Physiol (London), 117*, 500–544.

Hodgkin, A. L., & Huxley, A. F. (1952b). The components of membrane conductance in the giant axon of *Loligo*. *J Physiol (London), 116*, 473–496.

Hodgkin, A. L., & Katz, B. (1949). The effect of sodium ions on the electrical activity of the giant axon of the squid. *J Physiol (London), 108*, 37–77.

Hodgkin, A. L. (1958). Ionic movements and electrical activity in giant nerve fibres. *Proc Roy Soc B, 148*, 1.

Katz, B. (1966). *Nerve, Muscle and Synapse*. New York: McGraw-Hill.

Ohya, Y., & Sperelakis, N. (1989). Fast Na^+ and slow Ca^{2+} channels in single uterine muscle cells from pregnant rat. *Am J Physiol Cell., 257*, C408–C412.

Overton, E. (1902). Beiträge zur allgemeinen Muskel- und Nervenphysiologie. *Pflügers Arch., 92*, 346.

Tohse, N., & Sperelakis, N. (1990). Long-lasting openings of single slow (L-type) Ca^{2+} channels in chick embryonic heart cells. *Am J Physiol, 259*, H639–H642.

Tohse, N., & Sperelakis, N. (1991). cGMP inhibits the activity of single calcium channels in embryonic chick heart cells. *Circ Res, 69*, 325–331.

Chapter 20

Patch-Clamp Techniques

Laura Conforti

Chapter Outline

I. INTRODUCTION

The patch-clamp technique allows the electrophysiological measurements of currents through ion channels in the cell membrane. Developed in 1976, it has been the technique of choice for measurements of ion-channel activities in cells with resolution up to a single channel (Neher and Sakmann, 1976; Sakmann and Neher, 1984). This technique has wide applications ranging from the recording of the activity of native channels in their natural environment to recombinant channels expressed in heterologous cells.

Historically the patch-clamp technique was based on the work of Alan Hodgkin and Andrew Huxley who, in the 1950s, conducted a series of elegant voltage-clamp experiments that allowed the recording of macroscopic currents in the squid giant axon by controlling the voltage of the membrane (Hodgkin and Huxley, 1952). These studies established the physiological importance of ion fluxes through ion channels in the activity of cells and set the foundation for much of the subsequent work in electrophysiology. In 1963, Hodgkin and Huxley were awarded the Nobel Prize in Physiology or Medicine for this work. A limitation of the technique developed by Hodgkin and Huxley was that it did not have the resolution to measure the current through a single channel. This was made possible in 1976 by Neher and Sackman, who developed the patch-clamp technique. Using this new technique, they succeeded in recording from a tiny area (a patch) of the plasma membrane of frog skeletal muscle the first acetylcholine (ACh)-activated single channel (Neher and Sakmann, 1976). For their discoveries concerning the function of single ion channels in cells, Neher and Sackman were awarded the Nobel Prize in 1991. Since then the patch-clamp technique remains the technique of choice for measuring the activity of ion channels.

This technique and its further refinements represent a major advance in the ability to monitor cell membrane function (Hamill et al., 1981). Sealing a small pipette tip to a clean cell membrane allows recording of the ionic currents through single channels contained in small patches of cell membranes. Together with the method of whole-cell recording, patch-clamp techniques permit the investigation of ion channel conductance and kinetic behavior. This information has led to the discovery of new classes of ion channels and their physiological role in cells too small to be amenable to the standard voltage-clamp techniques and to cells that are not electrically excitable.

In this chapter, we describe the well-established techniques of patch-clamp recording with an extension to newly developed high-throughput applications of this technique. This chapter is divided into five parts: the first part focuses

Cell Physiology Sourcebook. DOI: 10.1016/B978-0-12-387738-3.00020-2

on the applications of the patch-clamp technique. The second section focuses on the basis of the patch-clamp technique with an emphasis on the technical aspects of the recording process including equipment and procedural steps. The third part describes the applications of the different recording configurations to measure single-channel activity and whole-cell currents. The fourth section is on data acquisition and analysis of single-channel and whole-cell data. The last part of this chapter presents the automated patch-clamp system, a newly developed multi-well plate format of the patch-clamp technique that allows high-throughput recording of ion-channel activities.

II. APPLICATIONS OF THE PATCH-CLAMP TECHNIQUE

The patch-clamp technique provides the ability to observe, in real time, the changes in the activity of a single channel including changes in conductance (the rate of ions going through the channel) and kinetic properties (the speed with which a channel opens and closes) in response to a pre-set stimulus. Furthermore, it allows determination of the characteristic sensitivities of specific ion channels to voltage, ions and ligands. Patch-clamp studies have led to the *discovery of a variety of ion-channel types and their classification*. In general, ion channels are functionally classified based on their ion selectivity and their modulation by voltage, ligands, second messengers, phosphorylation and mechanical deformations. *Voltage-gated* (or voltage-sensitive) *channels* are activated by changes in membrane potential. To this family belong the well characterized Na^+, K^+ and Ca^{2+} channels of nerve and muscle (Caterall, 2010). The *extracellular ligand-activated channels* are regulated by ligands such as transmitters. These channels are often named according to the ligand to which they bind, e.g. ACh-sensitive channels of the neuromuscular junction and the GABAA (γ-aminobutyric acid) channels of the inhibitory synapses (Collingridge et al., 2009). The *intracellular ligand-gated ion channels* include channels that are activated indirectly by G-protein-coupled receptors (GPCRs), such as cystic fibrosis transmembrane conductance regulator (CFTR) and other ion channels that are activated by intracellular ligands such as Ca^{2+}, ATP, cyclic AMP and cyclic GMP as well as phosphoinositides (Gadsby et al., 2006). The *mechanosensory and volume-regulated channels* form a rather ubiquitous class of channels that can be activated by mechanical tension of the membrane. To this class belong channels such as transient receptor potential (TRP) and volume-activated Cl^- channels that are important in a variety of key physiological functions ranging from touch sensitivity to regulation of cell volume (Nilius et al., 1996; Sharif-Naeini et al., 2008; Wu et al., 2010). A fifth group includes ion channels that do not have any of the distinct characteristics of the above groups. This group includes the GAP junctions and peptide ion channels like gramicidin (Saez et al., 2003; Kelkar and Chattopadhyay, 2007). There are additional systems of nomenclature which have joined the extracellular- and intracellular-gated channel groups into the "chemically-activated" or just simply "ligand-gated" ion channels. It has been shown by sequence comparison that ion channels within each of the distinct functional groups described above also show the greatest sequence similarity, indicating that they are most likely all descending from a common ancestor. Therefore, within these functional families, ion channels are classified based on the genes encoding their main pore-forming subunits. For the classification of ion channels please refer to the IUPHAR (International Union of Basic and Clinical Pharmacology) database (DB) which provides a cohesive nomenclature and nomenclature guidelines, together with detailed peer-reviewed pharmacological, chemical, genetic, functional and anatomical information on G-protein-coupled receptors, voltage-gated ion channels and ligand-gated ion channels (Harmar et al., 2009). The IUPHAR-DB provides a comprehensive description of the genes encoding these channels and their functions, with information on protein structure and interactions, ligands, expression patterns, signaling mechanisms, functional assays and biologically important channel variants (e.g. single-nucleotide polymorphisms and splice variants). The IUPHAR-DB is freely available at http://www.iuphar-db.org.

Through the patch-clamp technique, the detailed electrical and kinetic properties of a multitude of ion-channel types have been described, giving insight into the physiological modulation of these channels and also their alterations in disease states. Many diseases have been associated with defects in ion channels (Ashcroft, 2000). Ion-channel-associated diseases, i.e. *channelopathies*, often result from a mutation or mutations in the genes encoding the ion channel subunits or associated regulatory subunits. A recent special issue of *Pflügers Archiv European Journal of Physiology* was dedicated to this topic (for relevant websites refer to Nilius, 2010). The patch-clamp technique has been fundamental in discovering the functional implications of mutations in channel protein sequences. Through *structure–function studies*, it is possible to mutate even a single amino acid in a channel protein, express the mutated channel using a heterologous expression system, measure its electrophysiological properties and compare those properties with those of wild-type (native) channels. These studies provide information on how a specific mutation changes the physiological activity of a channel and are thus instrumental in discovering the functional implications of disease-associated mutations. Furthermore, they allow the elucidation of the amino acids associated with specific functional properties of the channels, such as

gating, as well as sensitivity to ligands and second messengers.

Although patch-clamping finds wide application, it still remains a technically challenging method that requires a carefully controlled experimental setting and a skillful experimentalist.

III. PATCH-CLAMP TECHNIQUES

IIIA. Patch-Clamp Set-up

Conventional patch clamping, now also referred to as "manual patch-clamp" to distinguish it from the recently developed "automated patch-clamp" described below (see Section VI), is accomplished by sealing the small tip of a pipette to the surface of the cell membrane in such a way that is possible to isolate a tiny membrane area (patch) from the rest of the membrane and to control its voltage while simultaneously recording the currents through the ion channels in the patch. A typical electrophysiology rig consists of a Faraday cage (which isolates the equipment from electrical noise), a vibration isolation table, a microscope for imaging cells, micromanipulators for moving and positioning the electrodes, low-noise amplifiers, a computer (for generating the stimulus waveform and data acquisition) and a perfusion line. The technique of patch-clamp requires a very steady platform where vibrations are minimized to allow maintaining a stable contact between the pipette and the cell. The first step in reducing vibrations is to find a quiet spot with floors less subject to vibrations. A good anti-vibration table is also used to reduce the problem of vibrations. This table consists of a very heavy tabletop suspended on air cushions. The other main pieces of equipment that are on the table are the microscope and the micromanipulators. The microscope has the optics necessary for the visualization of single cells (ten to one hundred microns in size) and the tip of the patch pipette (a few microns). Usually, phase-contrast and Nomarski (or interference contrast) microscopy allow satisfactory visualization of the membrane. Furthermore, the microscope is an inverted microscope; the objectives are located under the stage. A perfusion (bath) chamber, where the cells are placed for recording, is located on the stage of the microscope. By using an inverted microscope there is sufficient space between the stage and the condenser to place the patch pipette. The schematic of the bath chamber placed on the stage of the microscope is shown in Fig. 20.1. The bath chamber is where the cells are seeded and where the actual patch-clamping procedures occur. The ground electrode in the bath is usually a silver/silver chloride (Ag/AgCl) electrode which has a low junction potential, thus minimizing the development of a solid–liquid junction potential between the electrode and the bath solution (see Section V for description of junction potentials). The patch pipette

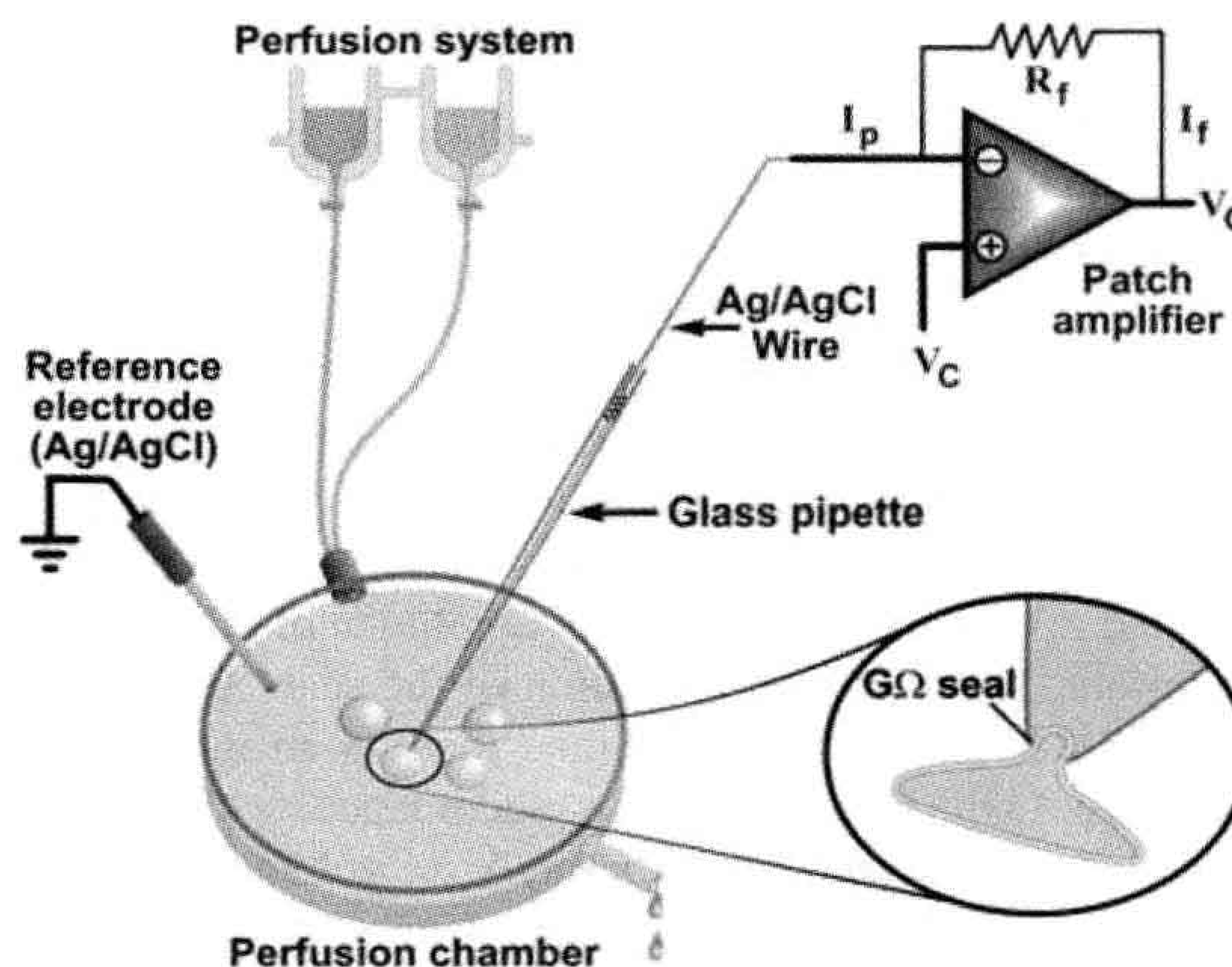


FIGURE 20.1 Schematic of a patch-clamp setting. The cells are plated in the perfusion chamber where solutions of different compositions can be rapidly switched via a perfusion system. The ground (or reference electrode) is made of Ag/AgCl and placed in the perfusion chamber either directly or through an agar bridge (1–3% agar in 0.9% saline) to reduce junction potential. One cell at the time is patched using a glass pipette which comes in contact with the cell membrane and forms the gigaseal (shown in detail in the inset). The glass pipette, filled with a salt solution, is connected to the amplifier via an Ag/AgCl wire. During a voltage-clamp experiment a current is injected through the amplifier so that the recorded voltage (V) (negative junction of the amplifier) is maintained equal to the command V (Vc) in such a way that the output V (Vo) is equal to −Vc. In this condition, $I_f \times R_f = -I_p \times R_f$, where I_f is the feedback current, I_p is the pipette current and R_f is the feedback resistance.

is usually a borosilicate glass pipette with tip diameter of 1–5 μm and is filled with a salt solution. Quartz glass is instead recommended when patch clamping is combined with fluorescence techniques, such as detection of intracellular Ca^{2+} with a fluorescent ion sensitive dye, as this material has better fluorescence properties. For patch pipettes and their fabrication refer to the publications of Rae and Levis (Levis and Rae, 1998; Rae and Levis, 2001). Patch pipettes, especially for single-channel recordings, may be coated with a hydrophobic material to reduce capacitative currents. The patch pipettes are filled with a conducting salt solution (known as pipette solution) in contact with a recording electrode (Ag/AgCl wire) which feeds the signal to a low-noise amplifier. The amplifier, which contains the appropriate measuring and clamping circuits and controls, processes the experimental commands, such as the voltage imposed to the cell membrane, and receives the data from the membrane. Furthermore, the patch-clamp amplifier is designed to minimize the background electrical noise that obscures very small currents in the single-channel experiments.

Once the appropriate equipment is in place, a series of specific steps are followed to make an actual patch-clamp experiment.

IIIB. Patch-Clamp Experiments

The patch-clamp recording is generally performed to measure the electrical properties of the membrane (or portions of it) attached to the pipette. The sequence of events leading to the patch-clamp recording of channel activity can be described as follows. Isolated cells are placed in the perfusion chamber and bathed in the recording solution (see Fig. 20.1). The patch pipette is then moved towards the cell surface while a low-voltage square pulse is applied to the pipette. The current amplitude of this pulse is monitored to follow the formation of the seal. As soon as the pipette touches the membrane there is an increase in resistance which produces, in accordance with Ohm's law ($I = V/R$ where I = current, V = voltage and R = resistance), a decrease in current. Upon gentle suction, a tight seal is formed, allowing the recording of the current through the channels in the patch with very high resolution. The tight seal that is formed between the membrane and the pipette is called a "gigaseal" because it has a resistance greater than one gigaohm ($10^9\ \Omega$). This high-resistance seal allows the reduction of background noise and makes possible high-resolution recordings of single-channel currents of less than 1 pA. The successful achievement of a gigaseal depends on the enzymatic cleaning of the cell membrane, the pipette configuration and solution composition, among other factors. The tight gigaseal makes the connection between the pipette and the membrane mechanically stable and amenable to manipulations that allow the establishment of different recording configurations. Recording configurations are specific architectures of the membrane patch in relationship to the bath and pipette solutions that allow different degrees of control over the channels under investigation. The recording configuration obtained at this point is the *cell-attached configuration* and, while it is used to measure single channels in their most physiological setting, it is also the starting point to reach other recording configurations (Fig. 20.2).

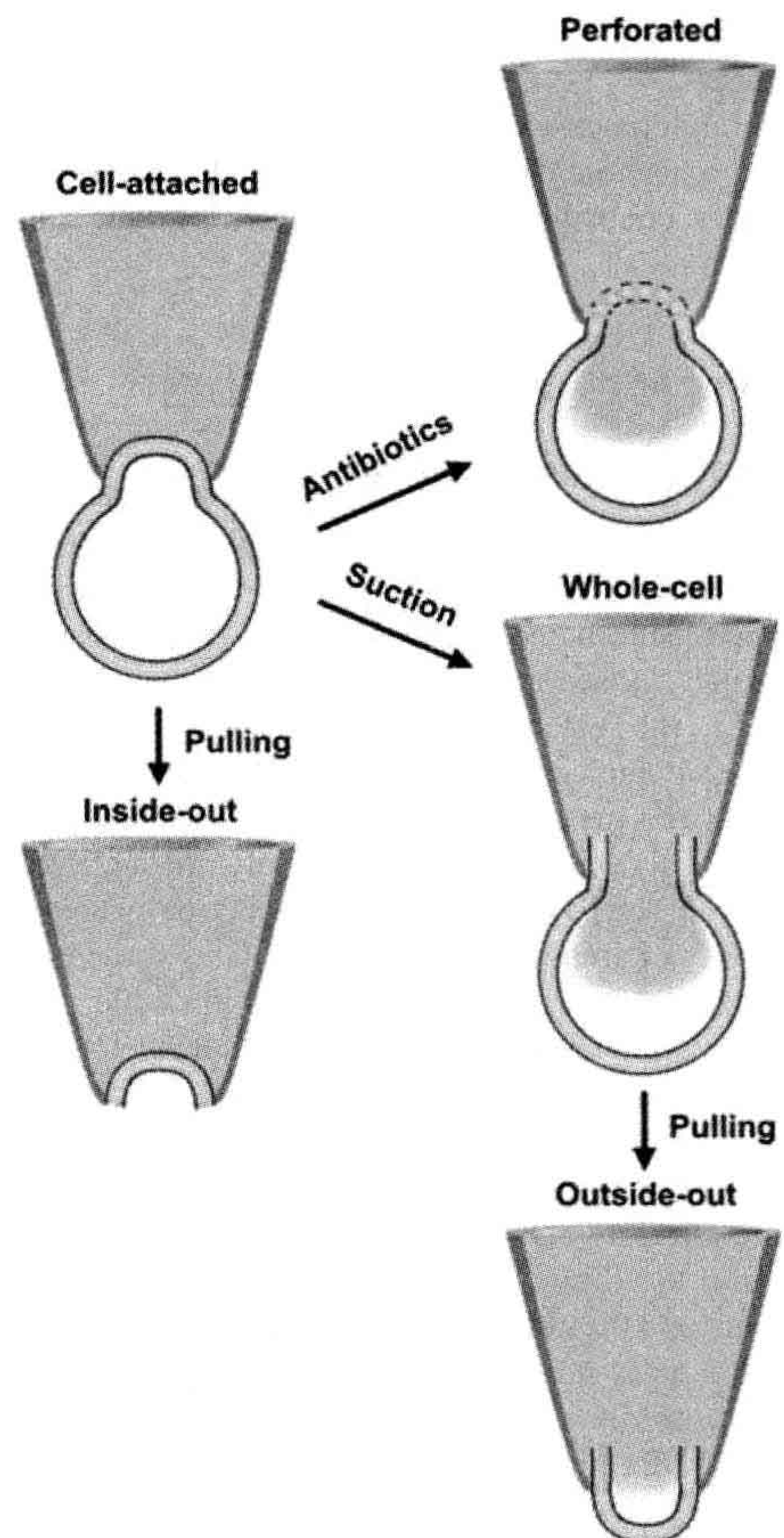


FIGURE 20.2 Patch-clamp recording configurations. The schematic of the recording configurations possible in patch-clamping and the maneuvers necessary to achieve them are shown. Each configuration is described in detail in the text. The patch pipette is labeled in blue and the pipette solution is shown in green.

IIIC. Recording Configurations

Various recording configurations have been used to study ion channels, each with its advantages and disadvantages. These configurations can all be achieved by mechanically manipulating the *cell-attached configuration* described above. The cell-attached configuration itself is ideal to measure the electrophysiological properties of single channels within the patch. The greatest advantage of this configuration is that it is relatively simpler to achieve than other configurations. Moreover, it allows maintaining the most physiological conditions at which to study the channel behavior, as the channel in the patch is in the cell membrane surrounded by the intact membrane microenvironment and intact cytoplasm. Unfortunately, this could be also considered a limitation of this configuration as there is no way to access and control the intracellular environment. Another drawback of this configuration is that the membrane potential is intact, but it is not possible to determine accurately its value. This information is necessary to set the patch potential. Theoretically, it is possible to use another electrode to measure the actual membrane potential, but this is technically quite unpractical. Commonly, it is chosen to use extracellular solutions with high K^+ concentration to "zero" the voltage (the intracellular and extracellular K^+ are made equal so that the equilibrium potential for K^+ (E_K) is set around 0 mV), after which the patch voltage is easily set. These limitations can be overcome by using other recording configurations described below.

When a cell-attached mode is established, the tight seal makes a very strong bond between the membrane and the pipette and the patch of membrane attached to the pipette can be excised from the cell by a variety of methods (see Fig. 20.2). By mechanically pulling the pipette away from the cell, a vesicle is detached. Once exposed to the air the vesicle is destroyed leaving a patch of membrane within the pipette (estimated area of the patch 1–10 μm^2). The patch is detached from the rest of the cell and the intracellular side of the membrane contacts the bath solution. This is known as the *inside-out configuration*. The cytoplasmic side of the membrane is easily accessible because it is immersed in the bath solution, which can be changed to deliver the desired compounds. This is an ideal configuration to study signaling of channels, providing that the lack of the physiological cytoplasmic environment does not modify the activity of the channel and the mechanical breaking of the membrane does not loosen the gigaseal. Other variations of the inside-out configuration are *excised inside-out macro and giant patches* in *Xenopus* oocytes.

The oocytes of the African clawed frog, *Xenopus laevis*, are widely used to study the behavior of ion channels of known molecular identity and have been the expression method of choice for studies of the structure-function relationships of ion channels (Stuhmer, 1998). *Xenopus* oocytes are large cells (ca. 1 mm in diameter) with low expression of endogenous channels. They also have very efficient translation machinery and are easy to use, making them an ideal heterologous expression system. A few days after injection with the messenger RNA of a specific channel, these cells express great quantities of the corresponding channels. Macropatches can be obtained in oocytes using pipettes with an opening 3–8 μm in diameter (Stuhmer et al., 1987). Macropatches allow the recording of macroscopic currents (sum of multiple channels) from a large membrane area, but in an excised configuration that is largely independent of cytosolic factors. Macropatches enable low-noise, fast-clamp patch-recordings of many channels and can be used to study channels with fast kinetics. Furthermore, excised giant membrane patches have also been successfully obtained in *Xenopus* oocytes (Hilgemann, 1995). These giant patches of diameter 12–40 μm allow recordings of transporter currents, charge movements and single-channel recordings of low-density channels. Interestingly, the large size of the oocytes also allows a variation of the inside-out patch that is very useful when studying the regulation of ion channels by cytoplasmic factors. The oocytes offer the unique possibility of reinserting the inside-out patch into the same cell from which the patch was obtained (so-called "*patch cramming*") (Kramer, 1990). It is also possible to introduce the excised patch into another oocyte that has been exposed to different conditions with a technique called "*cross-cramming*" (Parekh et al., 1993).

From the cell-attached configuration it is possible to obtain a second excised patch configuration, *the outside-out configuration* (see Fig. 20.2). First, the gigaseal is broken by applying suction through the glass pipette, reaching the *whole-cell configuration* that will be described in detail below. From this configuration the outside-out configuration is achieved by slowly withdrawing the pipette from the cell. The membrane stretches, eventually breaks and folds back in itself. The electrode thus contains a portion of the membrane with the outside surface facing the bath. This configuration allows making single-channel recordings with easy manipulation of the extracellular milieu while controlling the environment at the intracellular site (with a pipette solution of known composition). Since the external portion of the channel is immersed in the bath solution, it is easily accessible and amenable to manipulations such as exposure to drugs. Still, this remains a difficult configuration to accomplish.

The configurations described so far, with the exception of macro and giant patches in oocytes, allow measurements of the activities of single channels. There are other configurations that are instead used to measure simultaneously the currents through multiple channels on the entire cell membrane: whole-cell and perforated-patch configurations. The *whole-cell configuration* is achieved from a cell-attached configuration by breaking the patch with suction. This allows continuity between the pipette solution and the cytoplasm with dialysis of the cell's content. This can be viewed as an advantage because it provides control over the intracellular ionic concentration and allows delivery of chemicals and peptides to the interior of the cell. However, it is also a disadvantage as it dilutes the cytoplasm. Thus, any response that depends on soluble intracellular second messengers or ionic gradients may be altered. Furthermore, loss of cytoplasmic components essential for maintaining the channel activity can result in progressive decrease or "rundown" of the recorded currents. The *perforated-patch configuration*, like the whole-cell configuration, allows measurement of total currents, but the dialysis of the cytoplasm is reduced. This configuration can be reached from the cell-attached configuration providing that the pipette contains a small amount of an antibiotic, such as amphothericin-B or nystatin (both antifungal drugs) (Horn and Marty, 1988). These compounds form pores in the membrane, providing electrical access to the cell interior. These pores are permeable to ions but do not allow the passage of large molecules, thus reducing the loss of intracellular components. Practically, the pipette tip is filled with antibiotic-free solution and back filled with a solution of the same composition but containing the antibiotic. After the formation of a gigaohm seal, with time, the antibiotic contacts the cell membrane and forms pores. This can take 5 to 15 min, depending on the antibiotic concentration and

the amount of antibiotic-free solution in the pipette. One of the disadvantages of this configuration is that the access resistance (R_{access}) is usually higher (>20 MΩ) than in the whole-cell configuration due to the perforated membrane at the electrode. This decreases voltage-control and current resolution while increasing recording noise. A further disadvantage is that the membrane under the electrode tip is damaged by the perforations and could rupture, in which case the recording will occur in whole-cell mode with antibiotics leaking into the cytoplasm.

Once the desired configuration is achieved, the recording of the activity of a single or multiple channels can begin.

IV. DATA ACQUISITION

Cells express a variety of ion channels, so experimental interventions are made to make sure that recording occurs only from a specific type of channel. The manipulations used are chemical and electrical.

IVA. Chemical Isolation of Specific Channels

When establishing recording configurations, the chemical composition of the bath and the pipette solutions can be controlled. By strategically placing certain ions in the pipette and bath solutions or by replacing certain ions with impermeable ions of equivalent charges, it is possible to isolate specific ionic currents and/or suppress others. Furthermore, it is possible to add drugs that affect the activity of channels such as specific blockers (e.g. intracellular tetraethylammonium to block some potassium channel currents) or drugs that enhance the activity (e.g. Bay K8644 to increase the open probability of L-type calcium channels).

IVB. Voltage-Clamp

The activity of many channels also depends on the membrane voltage and this feature can be used to isolate specific currents from others. The technique used to control the voltage of the membrane is called voltage-clamp and is the most widely used method of recording ion-channel activity associated with the patch-clamp technique. This technique takes advantage of a speedy, low-noise differential patch-clamp amplifier which allows maintaining (clamping), through a feedback circuit, a specified membrane voltage and measuring, at the same time, the current across the membrane. The glass pipette containing a conductive solution is the electrode through which the voltage-clamp is maintained and currents are recorded. In practice, during a voltage-clamp experiment, the electronic feedback system of the amplifier measures the membrane voltage and compares it to a pre-set voltage defined by the experimenter. When a current is activated, the voltage of the membrane changes. To compensate for this change and bring the voltage to the preset value, a current of equivalent magnitude (but opposite direction) is injected through the pipette. In voltage-clamp, different command voltages are applied depending on the channel property under investigation. These command voltages vary in duration and waveform from simple steps to ramps and other complicated waveforms. Most patch-clamp experiments are voltage-clamp experiments. However, it is also possible not to clamp the voltage and to inject a fixed amount of current. This recording technique is called current-clamp.

The concept of voltage-clamp applies to many recording configurations. The electrical parameters involved during a patch-clamp experiment can be described by equivalent electric circuits. These help in understanding the complexity as well as the associated advantages and limitations of each configuration.

IVC. Equivalent Circuits

In every recording mode, the patch pipette and the cell or membrane patch form a complex circuit. The equivalent circuits for the cell-attached, excised-patch and whole-cell configurations are shown in Fig. 20.3.

IVC1. Cell-attached

In this configuration, a patch-pipette is sealed to an intact cell. This configuration allows measuring the current through the channel(s) in the membrane patch within the pipette tip. This is possible because of the high resistance (R) of the patch (R_{patch}). To understand how this technique makes the recording of the patch current possible, we should refer to the associated equivalent circuit. The overall electrical circuit of the cell-attached patch can be viewed as two circuits in series: one at the pipette level and the other at the cell level. The circuit of the intact cell originates from the fact that a cell has a membrane potential (V_m, i.e. the potential difference between the inside and the outside of the cell), a resistance (R_m, the lipid bilayer of the membrane, which acts as a barrier for the movement of charges through the membrane, and any open channels) and a capacitance (C_m, the capacity of the membrane to store charges at a given potential). In the cell-attached configuration, other resistors are present; one at the patch level and another at the pipette level. The latter depends on the opening and length of the pipette and the composition of the pipette solution. Overall, in this recording configuration there are three resistors in series. Since the highest resistance in a series of resistors is the one which dictates the current flow and R_{patch} is higher than R_m and the axial resistance of the pipette (R_p, usually between 1 and 3 MΩ), then, if a voltage (Vp) is applied across the pipette, the circuit effectively monitors current flowing through the ion

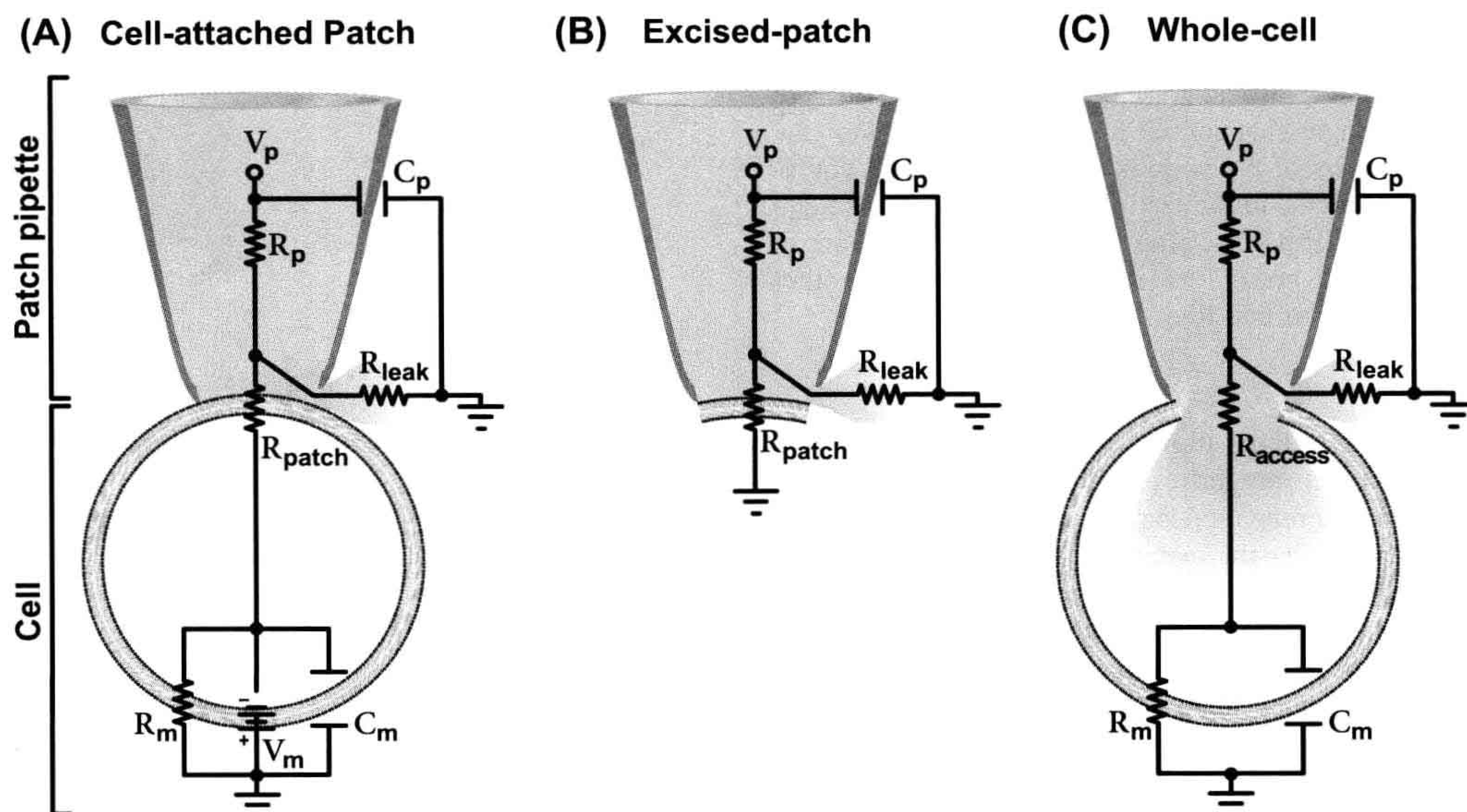


FIGURE 20.3 Recording configuration equivalent circuits. Reported are the equivalent circuitries for the cell-attached patch (A), excised-patch (B) and whole-cell (C) configurations. The patch pipette and cell (or membrane patch) are marked on the left. V_p, R_p and C_p denote the voltage, axial resistance and capacitance of the pipette. V_m, R_m and C_m denote the voltage, resistance and capacitance of the membrane. R_{patch} is the resistance of the patch of membrane which is replaced by the R_{access} in the whole-cell configuration where the patch of membrane is disrupted. R_{leak} denotes the leak resistance which depends on the tightness of the seal between the glass of the pipette and the membrane. Each circuit is described in detail in the text.

channels in the patch. In this circuit there is another resistor in parallel that could drain current away, the leak resistance (R_{leak}), which depends on the quality of the seal between the glass of the pipette and the membrane. A very high R_{leak} means that no significant current will leak away and that the noise is reduced. This explains why the key requirement for a patch-clamp recording is to maintain a high seal resistance, which is the resistance between the pipette solution and the surrounding bath solution. In a low-resistance scenario, there will be a current through the seal that is as high, or higher, than the ionic current to be measured, making the measurement of the actual current impossible. Thus, a gigaohm ($10^9\ \Omega$) seal is necessary for the resolution of ionic currents in the order of picoamperes (10^{-12} A). Three capacitances are present in this circuit: the pipette capacitance (C_p), the whole-cell capacitance (C_m) and the capacitance of the patch of membrane. The latter is very small and thus neglected in the equivalent circuit drawn in Fig. 20.3. The C_p (which depends on the size, shape and material of the patch pipette and also on the height of the bath solution) influences the time-course and the size of the signal, especially when small currents are measured. Patch-clamp amplifiers are equipped with electronics that permit the cancellation of C_p. The whole-cell capacitance C_m is also usually cancelled through the amplifier and/or with the application of a voltage-pulse protocol called positive/negative (P/N) subtraction present in most patch-clamp software. A complication unique to the cell-attached configuration is that the cell is intact; thus the V_m should be factored in unless it is set to 0 mV with a high K^+ extracellular solution as described before (see Section III).

IVC2. Excised-Patch

An excised-patch consists of a small portion of membrane sealed to the patch pipette. This translates into the simplest equivalent circuit (see Fig. 20.3). This circuit is comparable to the one described for the cell-attached configuration without C_m (which is very small for a patch), R_m and V_m. R_{patch} is the dominant resistor and the circuit monitors the current through this resistor. As discussed above for the cell-attached configuration, R_{leak} should be very high to reduce current loss. The R_p is generally very low, but it may vary depending on the size of the pipette tip needed. In some instances, such as when the channels are highly expressed, recording must be done from a small membrane patch. Thus, the pipette has a smaller tip and therefore a higher R_p which must be compensated for. Since the cell is absent in the excised-patch configuration, voltage-clamping is simple. The patch under investigation is clamped at the same voltage as V_p, apart from a very small voltage drop over the R_p. As for cell-attached recordings,

since single-channel currents are very small, on the order of 1 pA or lower, a requisite of this technique is to minimize the background electrical noise that will otherwise obscure the small single-channel current fluctuations. For the detailed analysis of the various components of the equivalent circuits on the minimization of background noise and the features of the patch-clamp amplifiers built in to control for background noise, the reader is referred to other publications (Levis and Rae, 1998).

IVC3. Whole-Cell Recordings

Whole-cell recording allows the measurement of the overall electrical properties of a cell membrane and, specifically, either the total current through all the channels on the membrane or the membrane potential. This configuration is achieved from the cell-attached configuration by breaking the membrane patch within the pipette tip. The equivalent circuit for the whole-cell configuration is simplified compared to that for the cell-attached patch configuration. More importantly, the V_m is disrupted and it can now be controlled by the experimenter. Furthermore, a very small access resistance (R_{access}) replaces the R_{patch} of the cell-attached configuration leaving R_p, R_{access} and R_m as the relevant resistors in series of this circuit. R_m is the largest resistor and thus the one through which the current is monitored. The same considerations described for the other recording configurations should be given to R_{leak}, which must be as high as possible to reduce current loss.

Examples of current measurements through the patch and whole-cell configurations are shown in Fig. 20.4.

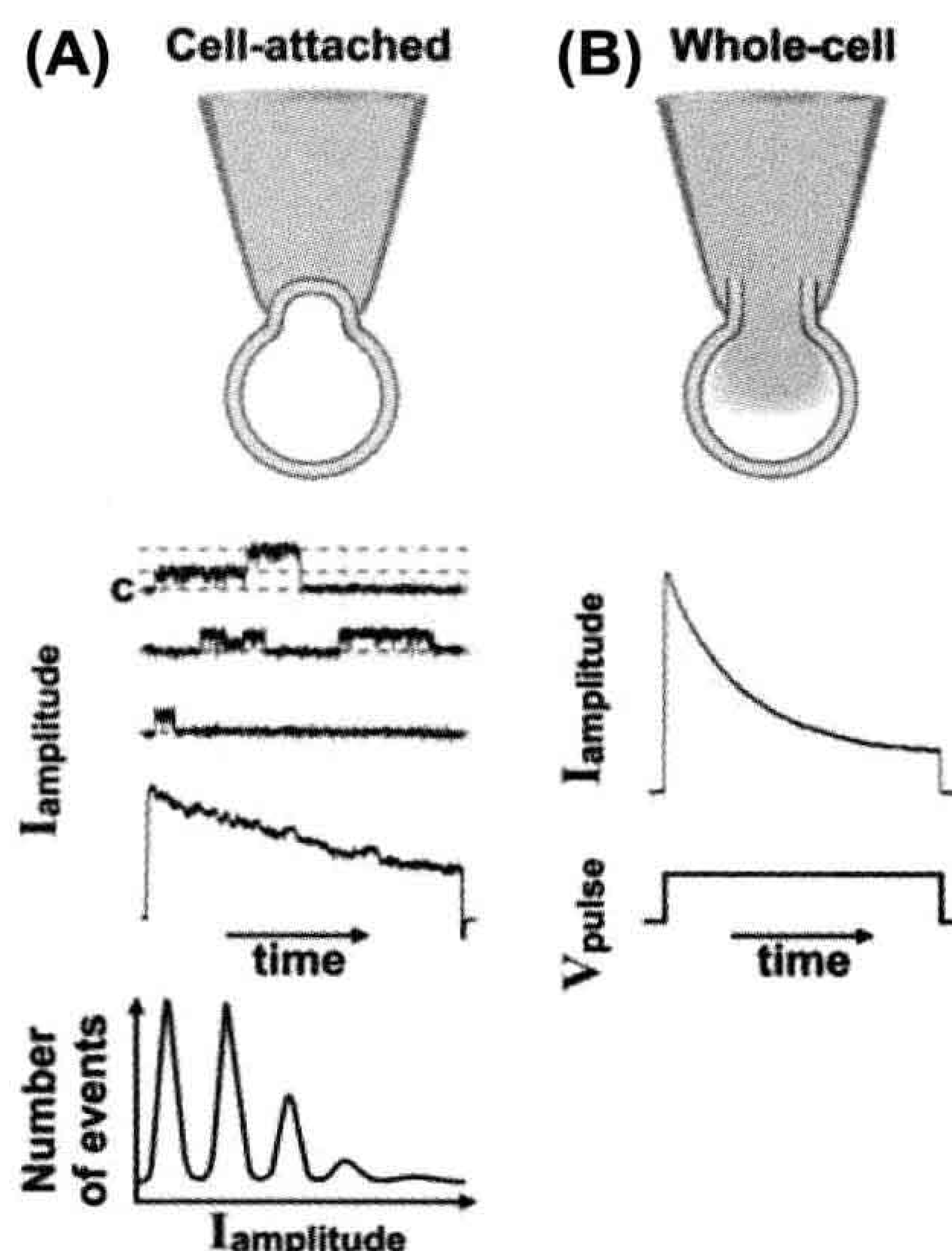


FIGURE 20.4 Current recordings during patch-clamp and whole-cell experiments. (A) Examples of recordings in cell-attached configuration. The cell-attached configuration is reported in the top panel. Middle panel: Single-channel recordings of voltage-dependent outward currents activated by a depolarization step pulse. The voltage pulse is shown in the bottom of panel (B). Three separate recordings of the single-channel fluctuations over time and, below, their corresponding ensemble average current are shown. The closed state (c) and two open states are marked in the upper trace with red and gray dash lines, respectively. Two levels of opening are detectable. Bottom: Amplitude histograms. (B) Example of total current recorded in whole-cell configuration and induced by step depolarization. The whole-cell configuration is reported in the top panel, the outward current in the middle and the pulse protocol in the bottom panel.

V. CURRENT RECORDINGS AND ANALYSIS

VA. Single-Channel Currents

When the appropriate experimental conditions are established, the spontaneous activity of a channel in the patch can be measured. Furthermore, channels can be activated with the appropriate stimulus such as a voltage step/ramp for voltage-gated channels or application of ligands (extracellular or intracellular) for ligand-gated channels. The actual recordings of single-channel activity consist of measurements of the current flowing through an ion channel or a small number of channels over time. Examples of current recordings from a cell-attached patch configuration are shown in Fig. 20.4A. Similar recordings and similar considerations can be applied to excised patches. Basically, recordings of single-channel currents in a patch appear like sudden jumps between current levels and they are generally of small amplitudes (1 pA or less). The jumps correspond to the actual openings and closings of channels which are very rapid stochastic processes due to the protein switching between different conformational states. The small amplitudes and fast kinetics of these events require minimization of the capacitive transients and adequate amplification and filtering to increase the current-to-noise ratio. The noise is reduced using a low-pass filter since the amplitude of noise increases with frequency (Colquhoun and Sigworth, 1995).

Analysis of single-channel data is critical since very little can be concluded from looking at raw recordings due to the random nature of the events. In-depth analyses of single-channel data have been elegantly described elsewhere (Magleby, 1992; Colquhoun and Hawkes, 1995; Colquhoun and Sigworth, 1995). Here we provide a brief description of these methods. The information gained with the analysis of the single-channel recordings are the amplitude(s) of the single-channel currents ($I_{amplitude}$), the durations of the close and open periods (dwell time) and the order in which these events occur. The $I_{amplitude}$ is defined by the difference between two current levels, the close and open states and it is, at least in the simplest cases, nearly constant from one opening to the next. The durations of the open and close events and the order in which they

occur are random. Since the number of channels in a patch can be (and often is) more than one, observation and analysis of the current levels provides information not only of the $I_{amplitude}$ but also of the number and type of channels in the patch. Figure 20.4A shows representative recordings of single currents (middle). Close observation of the uppermost trace indicates that there are at least two channels in the patch. This can be deduced by the two sudden steps from the closed state (C, 0 current) to two open states (indicated by the gray dashed lines) of equal current amplitude. The ensemble average current obtained by averaging a large number of single-channel recordings is shown in the bottom of the traces. A way to display the single-channel data is to report the distribution of amplitudes of each opening separately as *amplitude histograms* (see Fig. 20.4A, bottom). Current levels can be identified by peaks in the histogram: a peak at the closed level and other peaks at each of the open levels. Generally, the number of peaks at the open levels is indicative of the number of channels in the patch (providing that the probability of channel opening allows multiple channel openings to occur within the time of the experiment), but it could also indicate the subconductance states of a channel as some channels undergo multiple conformational changes which are associated with different current levels. In practice, the peaks in the amplitude histograms are fitted by a Gaussian curve using interactive computer algorithms provided in the patch-clamp analysis software. In case of the recording of a single channel in the patch, the area under the open peak is proportional to the fraction of time spent at the open level or *open probability* (Po). Po is one of the parameters that can be measured through the *dwell time analysis* which is applied to study the event transition patterns in single-channel recordings. The Po is the time for which the channel is in the open state relative to the total recording time. The Po is a quick indicator of the activity of the channel and changes in Po are used as measures of the effects of channel activators and blockers. Still, although it can provide such powerful information, the Po does not give any indication of the channel open/closing kinetics. This can be achieved through the analysis of *dwell time distributions*. Ion channels transition through multiple closed and open states. The times a channel dwells (sojourns) in an open or closed state are of different lengths and they can be grouped in dwell time histograms for each current state. This distribution provides information on the stochastic behavior of a channel. Fitting of the distribution of channel open or close dwell times can be done with exponential equations. The exponential terms and the associated time constants are related to the kinetics of the channel transitioning from the open to the closed state and vice versa. Based on these data, it is possible to build mathematical kinetic models that best describe the possible sequence of opening and closing events that lead to the channel behavior observed in response to a certain stimulus (Avdonin and Hoshi, 1998). Because it is very difficult experimentally to determine the behavior of a single channel, even if the single-channel current can be measured with a good degree of resolution, computer modeling is thus an invaluable tool in understanding ion-channel behaviors.

VB. Whole-Cell Currents

While single-channel data can provide a detailed description of the kinetic behavior of a single protein, the sum of the single-channel recordings (the ensemble current) reflects the total current flowing across the channels on the entire membrane surface. The ensemble average current from a series of single-channel recordings is shown in Fig. 20.4A. This current is devoid of contamination of currents from channels other than those in the patch or any current that develops because of the lack of voltage control (described later in this section). The ensemble current is equivalent to the whole-cell currents that can be recorded in whole-cell or perforated-patch configurations (see Fig. 20.4B). Because these configurations measure the currents through all the channels in the membrane, precautions should be taken to isolate the specific channels of interest. This could be achieved through either chemical or electrical interventions as described above in Section IV. Although whole-cell configuration is the configuration of choice for recording macroscopic currents (in the tens to thousands of pA), it presents with a series of limitations that should be considered when establishing and analyzing these types of recordings including rundown, voltage and space control and junction potential.

VB1. Rundown

Rundown is the spontaneous progressive decline of current amplitude over time. In the whole-cell configuration this phenomenon is most likely due to the dilution of regulatory components associated with the channel that occurs with the dialysis of the cytoplasm through the pipette solution. If these factors are known, it is possible to add them to the pipette or bath solution thus maintaining the channel activity. For example, ATP supplementation in the pipette was shown to reduce the rundown rate of Ca^{2+} currents. Similarly, addition of BAYK8644 to the bath prolongs the activity of voltage-dependent Ca^{2+} channels recorded in inside-out patches (Ohya and Sperelakis, 1989). The perforated-patch method, which limits the diffusion of large molecules, is used to minimize rundown (see Section III). This method has been also applied to reduce current rundown in single-channel outside-out recordings. Basically, once the perforated-patch configuration is achieved, the membrane patch is excised with a maneuver similar to that used to

generate outside-out patches (see Fig. 20.2). The only difference is that when the outside-out configuration is achieved the membrane is separated from the pipette via a perforated membrane and contains an intact cytoplasm where the ion composition can be controlled via diffusion of ions through the pores (Levitan and Kramer, 1990).

VB2. Voltage Control and Space-Clamp

The requirement for a successful whole-cell recording under voltage-clamp conditions is that adequate and homogeneous control of the voltage throughout the whole membrane is achieved and maintained. Poor voltage control distorts the kinetics of the current and will give a wrong current-voltage relationship. An inadequate voltage control occurs when the cell membrane is not "space-clamped". According to cable theory, in a linear cable the degree of charge dissipation depends on the electrical properties of the cable. Thus, in the whole-cell circuit (see Fig. 20.3C), when voltage is applied, the actual voltage measured at a point distant from the source (in this case at the membrane) is lower because of the dissipation of charges over the distance. Normally, in round cells the resistance of the cytoplasm is small compared to the R_m. In large cells with long and thin branches, the long volumes of the cytoplasm in the branches can be considered like multiple resistances in series which will add to a significant overall cytoplasmic resistance. Since the voltage is clamped over the dominant resistance in a circuit, poor clamping of the membrane portion far from the pipette will occur. Furthermore, in these large and convoluted cells, the overall C_m is much larger, further delaying the changes in clamp voltage. Inadequate space-clamp is a limitation that should be taken into account when deciding if a cell is suitable for whole-cell experiments. In general, small and electrically tight cells will have a better voltage control than cells with membrane folding and low input R_m, while large cells such as neurons that have formed a dendritic network are unsuitable. Such cells can still be patch-clamped via whole-cell current-clamp recording, which is not subject to space clamping issues. A further consideration to be made regards the type of current recorded: some currents such as voltage-activated Na^+ currents that have a steep voltage-dependent activation and/or inactivation are more prone to space-clamp distortion than others.

VB3. Junction potential

Junction potentials present a problem in voltage-clamp as they can introduce an error in potential, ultimately shifting the actual voltage at which the cell membrane is clamped. Two types of junction potential should be considered during a voltage-clamp experiment. The solid–liquid junction potential is the potential between the surface of the recording electrode and the surface of the ground. Minimization of this potential can be achieved as described in Section III (Neher, 1992). Furthermore, any residual solid–liquid potential can be neutralized after positioning the patch pipette in the bath through the voltage offset compensation of the amplifier. Another source of junction potential for which there is no analog compensation is the liquid–liquid junction potential which occurs when the pipette solution meets the bath solution. Liquid junction potential in general occurs when two solutions of different composition and concentrations are in contact with each other and it is generated by the different mobility of the ions in the two solutions. The rate of diffusion of the ions depends on their size and charge, temperature, hydration, etc. Normally, the pipette and bath solutions include ions with similar mobilities in which case the junction potential is quite small (2–3 mV) and can be ignored. However, when ions are replaced by ions of corresponding charges but of low mobility (such as Na^+ with $Tris^+$ and Cl^- with aspartate$^-$ or glutamate$^-$), the junction potential is fairly large (in the tens of mV) and cannot be ignored. This potential can be assessed experimentally and the actual voltage imposed to the cell should be corrected for this value. Detailed methods for making corrections have been reported (Barry and Lynch, 1991; Neher, 1992).

Overall, manual patch-clamp has been instrumental in understanding the physiology of ion channels. This technique presents with a high degree of flexibility in the recording configuration which provides control over the recording conditions. Furthermore, a highly detailed analysis of channel behavior can be attained. Unfortunately, at the same time, this is a technically challenging method with low throughput. Recently automated high-throughput versions of the patch-clamp technique have been developed.

VI. AUTOMATED PATCH-CLAMP

Conventional patch-clamp has been very effective in measuring, with a great deal of confidence, ionic currents and has supplied invaluable information on ion channels. Unfortunately, this technique is a time-consuming technique of limited throughput. It requires a highly trained patch clamper and, because of the technically challenging steps involved in achieving recording configurations, it only allows recording from a limited number (8–10) of cells during a working day. Multicell-based screening strategies have been developed to increase output. The need for high-throughput is particularly felt in the drug discovery field where screening of a large library of compounds is required. This screening is routinely performed to determine the safety profile of a new compound. It is based on the measurement of its effects on the activity of hERG (human ether-a-go-go-related gene) potassium channels which is indicative of the potential cardiac toxicity of the compound in question (cardiac liability screening). The

hERG channels have been identified as the molecular targets of drugs associated with an increased risk of cardiac arrhythmias (Pollard et al., 2008). Furthermore, it is used to screen libraries of compounds to find new ion-channel blockers/activators. Ion channels are, in fact, arising as attractive targets for new therapeutic agents. Approximately 13% of all marketed drugs have their mechanism of action attributed to modulation of the activity of either ligand- or voltage-gated channels and two out of 18 new compounds approved by the US Food and Drug Administration in 2006 target ion channels (Overington et al., 2006; Dunlop et al., 2008).

Initially, the high-throughput ion-channel assays used were binding, fluorescence and radioactive assays that allowed monitoring ion fluxes and membrane potential simultaneously in a large number of cells. Unfortunately, these assays present with various limitations including a high degree of false-positive and false-negative hits thus requiring verification using conventional patch-clamping. Because of these limitations, several companies have developed automated *patch-clamp systems* that allow testing of hundreds of cells each day. Some of these systems utilize conventional electrodes while others are based on planar arrays (Zhao et al., 2008). The latter have transformed the concept of patch-clamping by switching from the "top-down" access to the cell of conventional patch-clamp technique to a "bottom-up" access in plates or chips (Fig. 20.5). In the manual patch-clamp, the glass electrode approaches cells plated on a dish from above, one cell at the time, and forms a gigaseal with the portion of the membrane that does not make contact with the dish. In the automated system, the cells are suspended on a low-loss dielectric surface partitioning two solutions. This surface is etched with micrometer holes that mimic the conventional glass pipette openings. Application of negative pressure captures the cells on these holes and allows formation of the gigaseals. After this, either through the suction system itself or pore-forming agents, the patch of membrane in the hole is disrupted, allowing access to the interior of the cell and current recording either in whole-cell or in perforated-patch configurations. These new automated systems have integrated features such as fluidic control, suction mechanisms and sophisticated acquisition software that allow the serial execution of the experiment.

The IonWorks platform from Molecular Devices (currently MDS) was the first commercially available automated patch-clamp system, but it used pore-forming agents and did not fully mirror the conventional patch-clamp as it did not form gigaseals (Schroeder et al., 2003). Although this system did not have the low-noise capability of manual patch-clamping and produced lower quality recordings, it was quite effective in reaching high throughput and it has revolutionized the process of screening small compound libraries for ion-channel

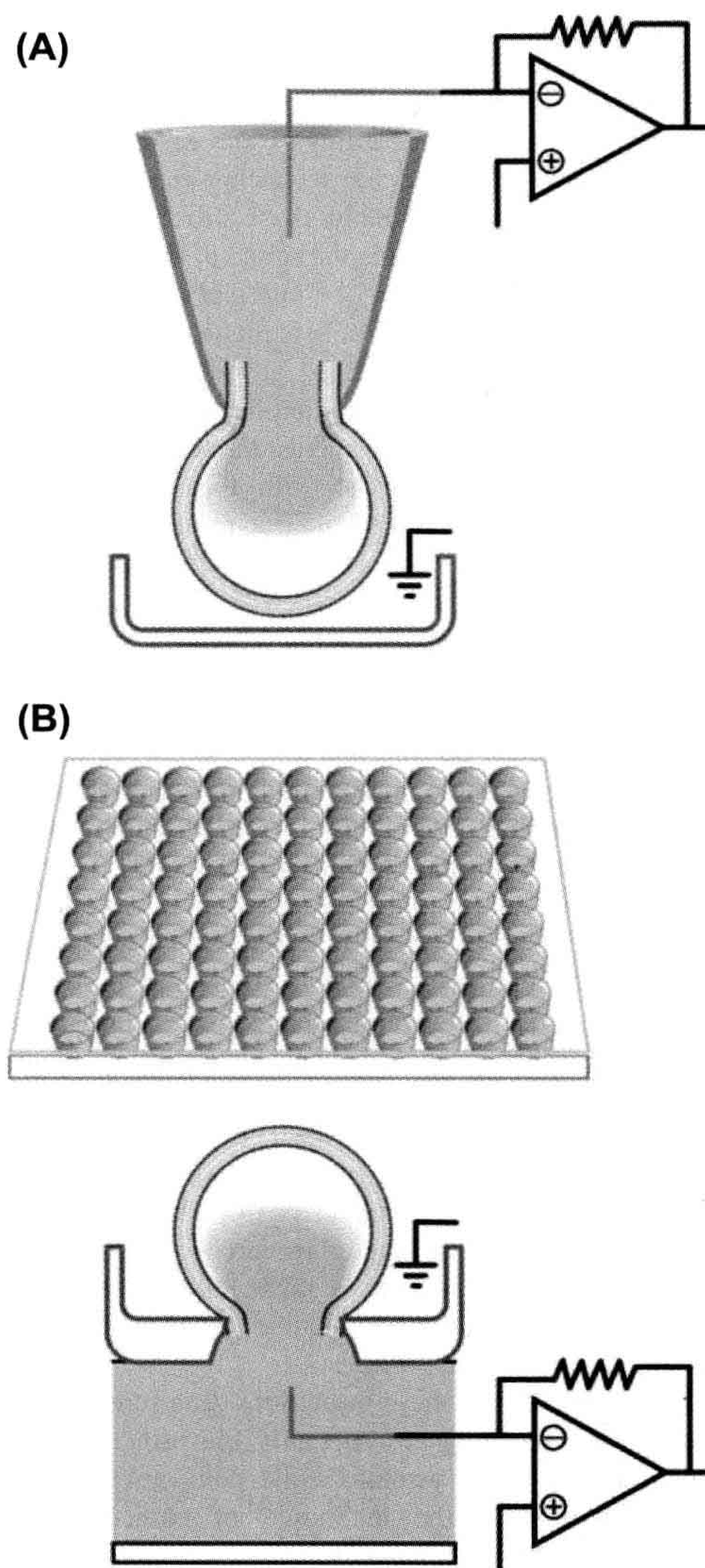


FIGURE 20.5 Comparison of the automated patch and conventional manual patch-clamp settings. (A) Schematic of the "top-down" approach in the conventional patch-clamp. The cell is plated in a dish and contacted by a patch pipette from the top to form the gigaseal and then the whole-cell configuration. (B). Schematic of the automated patch-clamp system performed on a multiwell chip (top). The plates have multiple wells with either single or multiple micrometer holes per well. The cells are seeded in the wells and, upon application of negative pressure, they are sucked in the hole. After this, the portion of the membrane in the hole is disrupted either by further suction or through antibiotics, and the whole-cell configuration is achieved.

targeting (John et al., 2007). After this, a second generation of automated patch-clamp systems followed, including PatchXpress, QPatch, Patchliner and Nanion's Port-a-patch. From single-cell recordings some of these systems have been now optimized for recording from up to 384 cells. A detailed description of these different platforms and their comparison is beside the scope of this chapter (for this please refer to the review of Dunlop et al., 2008) as this field is rapidly changing and new technologies are quickly developing. Our goal here was to introduce the reader to a shift in patch-clamp paradigm that has impacted the way patch-clamping is performed, at least in the pharmaceutical setting. Limitations still exist with these systems that reduce their application in an academic research laboratory.

The major disadvantage of these systems is that they require homogeneous, healthy cells with high expression of the ion channel under investigation which, in reality, only applies to stably transfected cell lines expressing high levels of the ion channels of interest. Primary cell cultures, such as neuronal or cardiac preparations, do not fit these criteria, although robotic multiwell planar patch-clamp has begun to be applied successfully to record native currents from primary cell cultures (Milligan et al., 2009). There are other issues associated with the automated systems that limit their use in an academic research setting where more technically demanding experiments are usually performed. Importantly, since the automated systems only allow limited flexibility, single-channel recordings are still limited to manual patch-clamp and require skilled electrophysiologists. Last, but not least, the costs associated with the platform itself and related consumables such as chips and plates have an impact on the choice of patch-clamp equipment by academic researchers. Future platforms are expected to address these limitations and be useful in both academic and industry settings with a relatively low cost per data point.

Overall, because of these limitations drug screening and cardiac safety profiling are currently the principal applications of these new systems, while conventional patch-clamp still remains the technique of choice for the academic research setting.

ACKNOWLEDGMENTS

My thanks go to Dr Steven Kleene who has critically revised and edited this chapter.

BIBLIOGRAPHY

Ashcroft, F. (2000). *Ion Channels and Disease: Channelopathies*. Boston: Academic Press.

Avdonin, V., & Hoshi, T. (1998). Kinetic models and simulation: practical approaches and implementation notes. In P. M. Conn (Ed.), *Ion Channels part B, Vol. 293* (pp. 724–740). New York: Academic Press.

Barry, P. H., & Lynch, J. W. (1991). Liquid junction potentials and small cell effects in patch-clamp analysis. *J Membr Biol, 121*, 101–117.

Catterall, W. A. (2010). Ion channel voltage sensors: structure, function, and pathophysiology. *Neuron, 67*, 915–928.

Collingridge, G. L., Olsen, R. W., Peters, J., & Spedding, M. (2009). A nomenclature for ligand-gated ion channels. *Neuropharmacology, 56*, 2–5.

Colquhoun, D., & Hawkes, A. G. (1995). The principles of the stochastic interpretation of ion channel mechanisms. In B. Sackman, & E. Neher (Eds.), *Single-channel Recordings* (pp. 397–482). New York: Plenum Press.

Colquhoun, D., & Sigworth, F. J. (1995). Fitting and statistical analysis of single-channel records. In B. Sackman, & E. Neher (Eds.), *Single-channel Recordings* (pp. 483–587). New York: Plenum Press.

Dunlop, J., Bowlby, M., Peri, R., Vasilyev, D., & Arias, R. (2008). High-throughput electrophysiology: an emerging paradigm for ion-channel screening and physiology. *Nat Rev Drug Discov, 7*, 358–368.

Gadsby, D. C., Vergani, P., & Csanady, L. (2006). The ABC protein turned chloride channel whose failure causes cystic fibrosis. *Nature, 440*, 477–483.

Hamill, O. P., Marty, A., Neher, E., Sakmann, B., & Sigworth, F. J. (1981). Improved patch-clamp techniques for high-resolution current recording from cells and cell-free membrane patches. *Pflügers Arch, 391*, 85–100.

Harmar, A. J., Hills, R. A., Rosser, E. M., et al. (2009). IUPHAR-DB: the IUPHAR database of G protein-coupled receptors and ion channels. *Nucl Acids Res, 37*, D680–D685.

Hilgemann, D. W. (1995). The giant membrane patch. In B. Sakmann, & E. Neher (Eds.), *Single-channel Recording* (2nd ed.). (pp. 307–327) New York: Plenum Press.

Hodgkin, A. L., & Huxley, A. F. (1952). A quantitative description of membrane current and its application to conduction and excitation in nerve. *J Physiol, 117*, 500–544.

Horn, R., & Marty, A. (1988). Muscarinic activation of ionic currents measured by a new whole-cell recording method. *J Gen Physiol, 92*, 145–159.

John, V. H., Dale, T. J., Hollands, E. C., et al. (2007). Novel 384-well population patch clamp electrophysiology assays for Ca2+-activated K+ channels. *J Biomolec Screen, 12*, 50–60.

Kelkar, D. A., & Chattopadhyay, A. (2007). The gramicidin ion channel: a model membrane protein. *Biochim Biophys Acta, 1768*, 2011–2025.

Kramer, R. H. (1990). Patch cramming: monitoring intracellular messengers in intact cells with membrane patches containing detector ion channels. *Neuron, 4*, 335–341.

Levis, R. A., & Rae, J. L. (1998). Low-noise patch-clamp techniques. *Meth Enzymol, 293*, 218–266.

Levitan, E. S., & Kramer, R. H. (1990). Neuropeptide modulation of single calcium and potassium channels detected with a new patch clamp configuration. *Nature, 348*, 545–547.

Magleby, K. L. (1992). Preventing artifacts and reducing errors in single-channel analysis. In B. Rudy, & L. E. Iverson (Eds.), *Ion Channels, Vol. 207*. New York: Academic Press.

Milligan, C. J., Li, J., Sukumar, P., et al. (2009). Robotic multiwell planar patch-clamp for native and primary mammalian cells. *Nat. Protocols, 4*, 244–255.

Neher, E. (1992). Correction for liquid junction potentials in patch clamp experiments. *Meth Enzymol, 207*, 123–131.

Neher, E., & Sakmann, B. (1976). Single-channel currents recorded from membrane of denervated frog muscle fibres. *Nature, 260*, 799–802.

Nilius, B. (2010). A special issue on channelopathies. *Pflügers Arch Eur J Physiol, 460*, 221–222.

Nilius, B., Eggermont, J., Voets, T., & Droogmans, G. (1996). Volume-activated Cl- channels. *Gen Pharmacol Vasc Syst, 27*, 1131–1140.

Ohya, Y., & Sperelakis, N. (1989). Modulation of single slow (L-type) calcium channels by intracellular ATP in vascular smooth muscle cells. *Pflügers Arch, 414*, 257–264.

Overington, J. P., Al-Lazikani, B., & Hopkins, A. L. (2006). How many drug targets are there? *Nat Rev Drug Discov, 5*, 993–996.

Parekh, A. B., Terlau, H., & Stuhmer, W. (1993). Depletion of InsP3 stores activates a Ca2+ and K+ current by means of a phosphatase and a diffusible messenger. *Nature, 364*, 814–818.

Pollard, C. E., Valentin, J. P., & Hammond, T. G. (2008). Strategies to reduce the risk of drug-induced QT interval prolongation: a pharmaceutical company perspective. *Br J Pharmacol, 154*, 1538–1543.

Rae, J. L., & Levis, R. A. (2004). Fabrication of patch pipets. *Curr Prot Neurosci, John Wiley & Sons, Inc.*, 6.3.1–6.3.32.

Saez, J. C., Berthoud, V. M., Branes, M. C., Martinez, A. D., & Beyer, E. C. (2003). Plasma membrane channels formed by connexins: their regulation and functions. *Physiol Rev, 83*, 1359–1400.

Sakmann, B., & Neher, E. (1984). Patch clamp techniques for studying ionic channels in excitable membranes. *Annu Rev Physiol, 46*, 455–472.

Schroeder, K., Neagle, B., Trezise, D. J., & Worley, J. (2003). IonWorks™ HT: a new high-throughput electrophysiology measurement platform. *J Biomolec Screen, 8*, 50–64.

Sharif-Naeini, R., Dedman, A., Folgering, J., et al. (2008). TRP channels and mechanosensory transduction: insights into the arterial myogenic response. *Pflügers Arch Eur J Physiol, 456*, 529–540.

Stuhmer, W. (1998). Electrophysiologic recordings from Xenopus oocytes. *Meth Enzymol, 293*, 280–300.

Stuhmer, W., Methfessel, C., Sakmann, B., Noda, M., & Numa, S. (1987). Patch clamp characterization of sodium channels expressed from rat brain cDNA. *Eur Biophys J, 14*, 131–138.

Wu, L.-J., Sweet, T.-B., & Clapham, D. E. (2010). International Union of Basic and Clinical Pharmacology. LXXVI. Current progress in the mammalian TRP ion channel family. *Pharmacol Rev, 62*, 381–404.

Zhao, Y., Inayat, S., Dikin, D. A., Singer, J. H., Ruoff, R. S., & Troy, J. B. (2008). Patch clamp technique: review of the current state of the art and potential contributions from nanoengineering. *Proc Inst Mech Eng J Nanoeng Nanosyst, 222*, 1–11.

Chapter 21

Structure and Mechanism of Voltage-Gated Ion Channels

Simon Rock Levinson and William A. Sather

Chapter Outline

I. SUMMARY

The structure, mechanism and expression of ion channels are currently intense areas of research interest. The first advances in these areas were made by the application of biochemical techniques to the problems of channel purification. Such studies have told us the size of intact channels and their subunit composition and have yielded clues regarding functionally important domains (such as pores, gates, modulation sites and non-protein modifications). For Na^+ and Ca^{2+} channels, attention has been focused on a large polypeptide (so-called α peptide) found in each purified preparation. These α proteins apparently have all the molecular apparatus required for channel operation, while smaller associated subunits may play other roles in channel modulation, synthesis or cellular localization. Purified material has also been important in the construction of probes to identify clones of channel-encoding DNA fragments.

Cell Physiology Sourcebook. DOI: 10.1016/B978-0-12-387738-3.00021-4

Recent work has applied recombinant DNA technology to determine the primary amino acid sequence of channels through cloning. These sequences have revealed widespread sequence homology among the superfamily of voltage-gated ion channels, e.g. between Na^+ and Ca^{2+} channel α polypeptides. Furthermore, the large α proteins have four domains of homology within their sequences, suggesting that pore formation occurs via a common "staves of a barrel" architecture. K^+ channel sequences, determined via a genetic approach, are relatively shorter and they partially correspond to a single internal repeat of the larger α peptides. Hence, K^+ channels are thought to consist of tetramers with each subunit contributing to the pore wall. Other analyses of amino acid sequences have given clues regarding the mechanistically and structurally important domains of ion channels. One analysis was based on thermodynamic (hydropathy) considerations to identify possible membrane-spanning domains. In addition, the sequences were subjected to an empirical analysis that predicts regions of secondary structure, such as helices and sheets. From such predictions detailed models of channel structure and function have been developed. These models have been tested using immunological and mutagenesis approaches and candidate domains for ion selectivity, pore wall formation, gating and modulation have been identified. However, detailed knowledge of the molecular mechanisms of channel function is still limited.

Finally, molecular studies have revealed an astonishing diversity of ion channels at all levels of organization. In particular, the genome of most organisms can express multiple channel isotypes, sometimes coexisting within the same living cell. Much remains to be learned about channel function and the role of channel isotypes in the biology of both simple and complex organisms.

II. INTRODUCTION: HOW IS ION CHANNEL STRUCTURE STUDIED?

Previous chapters have described how the flow of ions across cell membranes is the basis for electrical excitability and signaling in the nervous system. These flows are controlled by a special class of macromolecules known as *ion channels* that form gated pores in the cell membrane. The structure of ion channels and the current thinking about how these structures form transmembrane pores that gate to open and closed states in response to changes in membrane voltage are discussed in this chapter. Subsequent chapters will describe other important aspects of ion channels, such as interactions with drugs and toxins, modulation by intracellular messengers and specific ion channel types found in intracellular organelles and involved in synaptic transmission.

What are the questions that should be addressed in this chapter? Most fundamentally, we wish to know how these macromolecular structures give rise to the important functional properties of ion channels, namely, the formation of transmembrane pores, the selective transport of specific ions and the ability to open and close the pore; i.e. how do ion channels function as molecular mechanisms? As we will see, these considerations also lead into a brief consideration of the structural diversity among ion channels and the origin and possible purposes of such diversity.

Cellular ion channels are basically proteins. In the earliest structural studies, biochemical methods were employed to purify channel molecules from excitable tissues. This approach has been essential to the current state of knowledge of ion channel structure. However, ion channels have certain physicochemical properties that have limited the amount of information obtained solely through biochemical characterization. This bottleneck has been broken recently through the application of recombinant DNA methodologies, which have uncovered the primary structures of numerous ion channel types, while providing a powerful means to study higher order structure and function. However, this latter approach has its own limitations and, ultimately, we will need to "see" more directly the actual structure of the channels to understand more fully their molecular mechanisms of action. In this regard, it is encouraging that significant progress has been made recently in elucidating the structure of purified channels using x-ray crystallographic techniques.

III. BIOCHEMISTRY OF ION CHANNELS: PURIFICATION AND CHARACTERIZATION OF VOLTAGE-GATED CHANNELS

Before the advent of recombinant DNA methods, ion channels were extensively studied by first purifying channels from an excitable tissue and then characterizing the purified molecules by a combination of chemical and physical techniques. While this biochemical approach has fallen somewhat out of use in favor of DNA cloning techniques, it seems certain to re-emerge as a necessary adjunct to structural studies that now seem feasible (see Section VH). Thus, a brief introduction to channel biochemistry seems appropriate here. The first voltage-gated channel to be purified was the Na^+ channel from the electric eel, *Electrophorus electricus*, and the account of how this was achieved will serve to illustrate the basic rationale for the biochemical approach (see Miller et al., 1983).

The basic procedure for purification of membrane-associated proteins (Fig. 21.1) is as follows. First, an enriched fraction of membranes is usually prepared by disrupting the tissue and its cells mechanically and subsequently separating the insoluble fraction containing membranes and connective tissue components from the soluble fraction consisting of cytoplasmic protein.

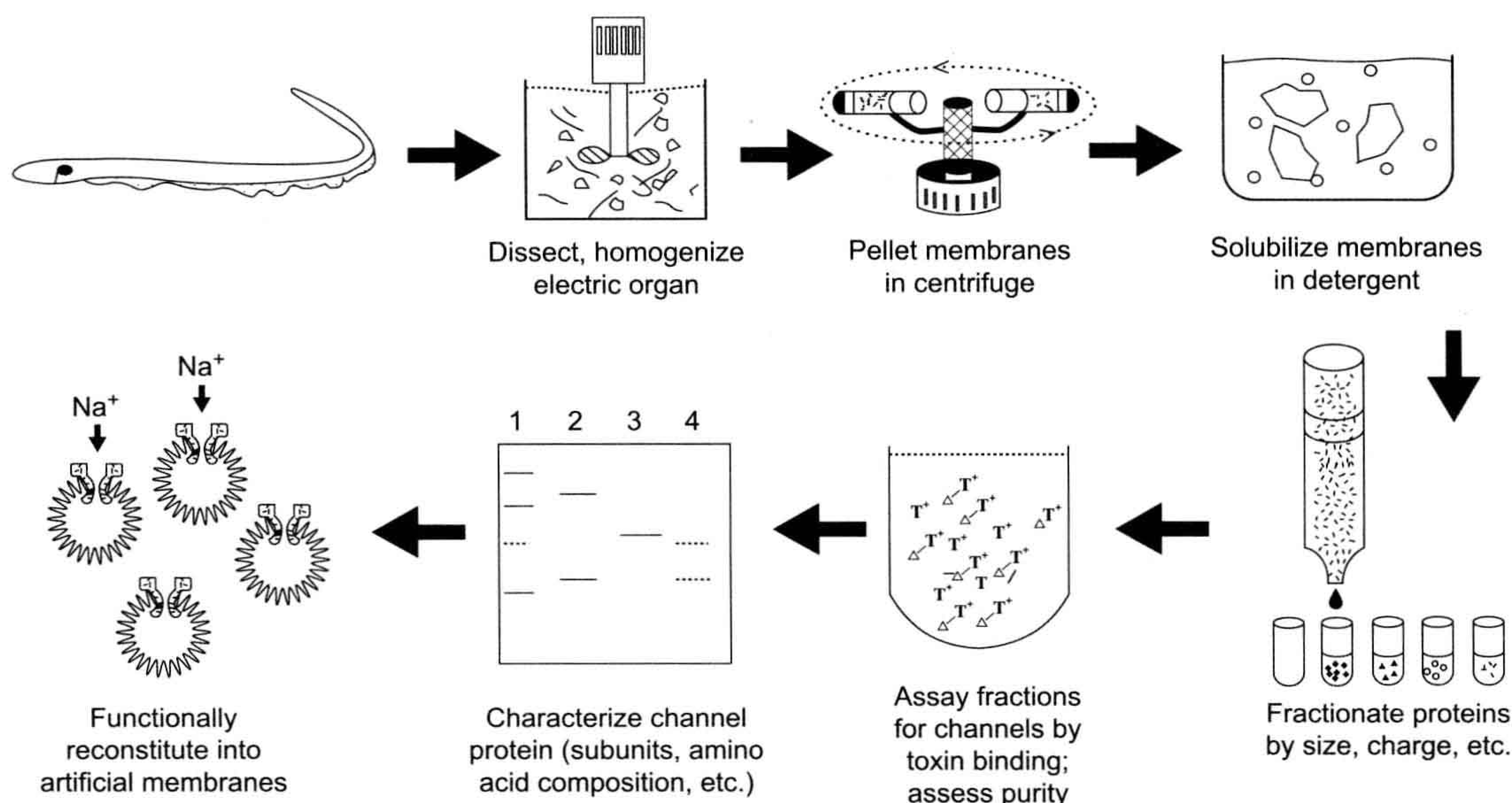


FIGURE 21.1 Scheme used for the biochemical isolation of Na^+ channels from electric tissue of the eel *Electrophorus electricus*. Purification protocols devised for other ion channels utilize similar general principles but differ in details.

Although relatively non-specific, this step also often gives substantial enrichment of ion channel preparations. Next, the membranes are solubilized through the use of detergents. This step disperses the membranes into minute droplets of lipid, protein and detergent known as micelles. This is often the most problematic step of a purification, because the micellar fraction must be dispersed well enough so that no more than one protein molecule is present in each micelle. Too much detergent often results in irreversible denaturation of channels, hence preventing their identification during the purification process. Thus, the solubilization process must be optimized and often many different detergents at various concentrations are tested under a plethora of conditions before the right combination is found. Finally, the dispersed micelles are fractionated based on their physical properties or affinities for certain compounds until a pure sample of channel protein is isolated.

IIIA. Electric Fish Are a Rich Source of Ion Channels

The first requirement for purification of any protein is to have a rich source. Actually, this can be a serious difficulty, since ion channels are present in very small amounts in most excitable tissues. The rarity of channels might at first seem paradoxical in view of the ubiquity of excitability phenomena in nearly all cell membranes. However, the reader should recall that only minute numbers of channels are needed to mediate the flow of ions required to cause the changes in transmembrane voltage during electrical excitation (Table 21.1).

Fortunately, there exist some highly specialized "freaks" of nature that use large ionic currents for purposes other than signaling and stimulus transduction. These are the strongly electric fish, which are capable of generating powerful electrical discharges to stun prey and defend themselves. The electric organs of these animals contain large numbers of ion channels that are present at high density on the surface of the excitable cells of the electric organ (see Chapter 48). As a result, the first two ion channels to be purified were the acetylcholine receptor channel of the electric ray *Torpedo* and the Na^+ channel of the electric eel *Electrophorus*.

IIIB. Toxins and Drugs as Markers for Ion Channels during Purification

Having a rich source of channels does not guarantee a successful isolation of channels. One must also have a very specific and sensitive assay for the presence of solubilized channels to follow the process of fractionation. Unfortunately, unlike enzymes or other chemically

TABLE 21.1 Sodium Channel Densities in Selected Excitable Tissues

Tissue	Surface Density Channels/μm^2	Tissue Density (μg channel/g tissue)
Mammalian		
Vagus nerve (unmyelinated)	110	28
Node of Ranvier	2100	—
Skeletal muscle (various)	2066–557	6–14
Other Animals		
Squid giant axon	166–533	≈1
Frog sartorius muscle	280	6
Electric eel electroplax (excitable surface)	550	38
Garfish olfactory nerve	35	96
Lobster walking leg nerve	90	24

active proteins, the activity of ion channels is to transport ions across membranes. Since this barrier is disrupted during the first stage of purification, the compartments essential to channel function no longer exist and hence the electrically detectable flow of ions through channels no longer occurs. Instead, one may use the binding of powerful neurotoxins to channels to assess the degree of purity attained during fractionation.

For Na^+ channels, there exist highly selective inhibitors of sodium transport known as guanidinium toxins. The most commonly used of these are tetrodotoxin (TTX), obtained from certain species of toxic puffer fish, and saxitoxin (STX), a product of certain dinoflagellates that "bloom" during oceanic "red tides". Either toxin may be radioactively labeled and these substances very specifically interact with Na^+ channels from a wide variety of sources with high affinity. To assess purity, one may thus compare the number of toxin-binding sites in a fraction with the amount of protein present.

IIIC. Isolation of Channel Molecules Based on Fractionation Procedures

With a good source of channels, efficient solubilization procedures and a specific and sensitive assay, one may proceed to attempts at purification. For Na^+ channels, fractionation based on charge, followed by size fractionation of the mixed channel/lipid/detergent micelle, has resulted in highly purified preparations of Na^+ channels. Alternatively, in some protocols, channel proteins have been specifically purified using affinity chromatography, in which channels are selectively retained by a column to which channel-binding substances, such as drugs, toxins or antibodies, are attached.

Skeletal muscle Ca^{2+} channels have also been extensively purified and characterized using much the same approaches as those described for Na^+ channels. In this case, it has been the L-type channels that were isolated, using radiolabeled drugs of the dihydropyridine class to tag channels irreversibly in the intact muscle membrane. This allowed the investigators to isolate the channel protein by following the fractionation of the bound radiolabeled drug (Sharp et al., 1987).

IIID. Information about Channel Structure from Channel Purification

There is much to be learned about channel structure from the physicochemical characteristics of the purified molecule. Some of this information forms the basis for separating the molecule from others in membrane extracts (such as size or charge differences), as described previously, whereas other measurements may be done on the purified material itself. Thus, for Na^+ channels, it was found that the channel is very negatively charged. Furthermore, in detergent solution, the channel appears quite large; in micellar form, its size is on the order of several million molecular weight. Both characteristics are important clues regarding the chemical composition of Na^+ channels.

The subunit composition of a channel is an especially important characteristic to be determined from the purified material. For a number of enzymes, separate functions have been attributed to different subunits; hence breaking down the structural entities represents an important basis for further structure–function correlations. In brief, one usually determines the subunit composition of the purified material by analyzing it using denaturing electrophoresis, in which the intersubunit bonds are broken and each

subunit separated according to size in an electric field. The most commonly used technique is sodium dodecyl sulfate–polyacrylamide gel electrophoresis (SDS-PAGE), in which each polypeptide species appears as a separate band on staining the polyacrylamide sieve used to separate polypeptides. Unfortunately, this is often more difficult than it appears, since (1) one is often not sure whether different bands on a gel are contaminants or true subunits and (2) the stoichiometry of subunits is difficult to establish because of variations in the intrinsic staining intensity among various polypeptides. As a result, considerable effort is expended by various researchers to determine (and argue about!) subunit composition using a wide variety of approaches. For the voltage-gated Na^+ channel, a single large polypeptide apparently accounts for pore formation, ion selectivity and gating. This protein appears on SDS-PAGE as a broad band at high molecular weight.

Given the large size of the eel electric organ, enough protein can be purified to allow study of its chemical composition. Not too surprisingly, Na^+ channels have an elevated proportion of hydrophobic amino acids compared to soluble globular proteins, likely reflecting domains of the channel that insert into the lipid membrane. However, the channel molecule appears to be much more hydrophobic than can be accounted for from its amino acid composition. Thus, further chemical analysis has found that a large number of lipid molecules are bound to the eel protein. Finally, it has been found that Na^+ channels are modified by the presence of extensive domains of carbohydrate. This glycosylation makes up about 30% of the molecule (by weight).

Na^+ channels have also been purified from mammalian brain and muscle tissue. Like the eel channel, they consist primarily of heavily glycosylated large polypeptides. However, unlike the electric organ channel, they are found in association with one or several smaller polypeptides that have been thought to be channel subunits (Table 21.2). The large polypeptide common to Na^+ channels from all sources is referred to as alpha (α) while smaller subunits have been designated as beta (muscle) or $\beta1$ and $\beta2$ (brain). At present, the role of these accessory polypeptides in channel function is not certain, although recent evidence suggests that they may aid in channel expression and modulate channel gating (Isom et al., 1992).

For the skeletal muscle L-type Ca^{2+} channel, it was found that although a single large polypeptide ($\alpha1$) was affinity labeled by the dihydropyridine (DHP) marker, at least four other polypeptides – $\alpha2$, β, gamma (γ), delta (δ)–copurified with the DHP label. As with the Na^+ channel, $\alpha1$ seems to have the mechanisms required for ion channel operation. However, there is evidence that the other subunits are important accessory proteins that may be involved in the key role of this channel as the voltage sensor in excitation–contraction coupling, which is described in Chapter 45.

TABLE 21.2 Subunit Composition of Voltage-Gated Cation Channels

Channel/tissue	Subunit	Molecular Weight[a]
Na^+		
Eel electric organ	α	260 (208)
Rat brain	α	260 (220)
	$\beta1$	36 (23)
	$\beta2$	33
Rat skeletal muscle	α	260 (209)
	β	36
Chick heart	α	235
Ca^{2+}		
L-type, rabbit skeletal muscle	α-1	170 (212)
	α-2	143 (125)[b]
	β	54 (58)
	γ	30 (25)
	δ	24–27 (27)[b]
K^+ Channel		
Drosophila Shaker A	—	65–85 (70)
Rat drk1	—	130 (95)

[a]First set of values is the apparent molecular weight determined biochemically (SDS-PAGE); weights in parentheses were obtained from cloned DNA sequences.
[b]The biochemically observed calcium channel α-2 and δ subunits are derived from proteolysis of a full-length α-2 translation product during biosynthesis.

Also shown in Table 21.2 are data for voltage-gated K^+ channels. The characterization of K^+ channel subunits was achieved primarily through molecular genetic means, as discussed in Section IVF.

IIIE. Reconstitution of Purified Proteins Confirms their Identity as Channels

An important criterion for purification was the reconstitution of the isolated material into artificial membranes and the demonstration that voltage-gated, sodium-selective, toxin-inhibitable channels were formed (see Miller, 1986). Thus, these experiments showed that purified toxin-binding material could be reinserted into small artificial lipid vesicles (liposomes) or planar lipid films (lipid bilayers) where they retained their ability to transport sodium selectively in response to voltage changes. These reconstituted channels had the same ability to respond to

different pharmacological compounds, such as toxins and anesthetics, as the channels in natural tissue (reviewed in Catterall, 1992). Similar experiments have demonstrated that purified DHP receptors can form functional Ca^{2+} channels in bilayers (Catterall, 1988).

IIIF. Limitations of Biochemical Characterization of Channels

The biochemical approach to channel purification thus gave important information about the size, chemical composition and polypeptide makeup of Na^+ and L-type Ca^{2+} channels. Classically, the next steps would be to sequence the purified material and attempt to obtain a high-resolution structure from crystallographic approaches. However, although these techniques have worked well with a small number of soluble globular proteins, for several reasons they have been relatively unsuccessful with membrane proteins in general and voltage-gated channels in particular. First, sequencing a large polypeptide requires that it be enzymatically or chemically cleaved into overlapping smaller fragments amenable to Edman degradation techniques (which can only sequence from 25 to 50 residues at a time). In such an approach, each small fragment must be separately purified from the fragmented preparation. For the large polypeptides of Na^+ and Ca^{2+} channels, the number of fragments generated by such cleavages is just too great for all of them to be purified separately. Furthermore, many of the interesting membrane-spanning segments do not fragment or isolate well because of their high degree of hydrophobicity ("fears water"). Finally, the amphipathic (i.e. polarized hydrophilic/hydrophobic) nature of membrane proteins prevents their crystallization; instead, in the absence of lipids or detergents, such purified preparations usually form amorphous aggregates or precipitates with little intrinsic order. Hence, the elaboration of detailed structure of biochemically purified channels has been hampered by the unfavorable physical properties of membrane proteins.

IV. CHANNEL STRUCTURE INVESTIGATION THROUGH MANIPULATION OF DNA SEQUENCES ENCODING CHANNEL POLYPEPTIDES

Fortunately, the limitations of classic biochemistry may be partly overcome by the application of techniques that allow one to identify and sequence DNA that encodes channel peptides. The next three subsections describe how the powerful methods of molecular biology are being applied to questions of interest to the cell physiologist. These approaches have given important insights into the structure of channels and how they work. This aspect of channel biology is considered in Sections IVA and IVB. However, molecular biology has also shown us that voltage-gated channels exist in a rich diversity of forms even within a single organism. This aspect of channel biology is described in Section IVC. First, a brief description of how recombinant DNA methods are used in such studies is provided for the novice reader (Fig. 21.2).

IVA. Primary Structure of Ion Channels Determined Using Recombinant DNA Technology

One starts with the same tissues shown to be enriched in channel protein because these are also probably enriched in messenger RNAs (mRNAs) encoding these channels. Using the retroviral enzyme reverse transcriptase, one may then make *complementary DNA copies* (cDNAs) of the mRNAs. Using enzymatic "scissors" (called restriction enzymes), one may then insert each cDNA obtained into a circular DNA *plasmid*. These plasmids have the ability to be replicated along with other genetic material in bacteria and also they encode an enzyme that will destroy certain antibiotics that would otherwise kill their bacterial hosts. The recombinant plasmids are next introduced into a bacterial host so that each bacterium will contain no more than a single plasmid with its unique cDNA insert. The bacteria are then diluted and spread over a plate of agar containing an antibiotic. Thus, bacteria without a plasmid are killed, whereas plasmid-containing bacteria can survive and replicate to form visible colony plaques. Since each such colony arises from a single original plasmid-transformed cell, they are known as *clones*. Each agar plate may contain many thousands of such clones, each clone having many cells with plasmids containing the identical cDNA insert.

The problem is to identify which of the many colonies has a particular cDNA that encodes for the channel protein of interest, among all of the cloned cDNAs that encode the myriad proteins of the original tissue. The severity of this problem can be appreciated from the fact that even highly enriched tissues such as eel electric organ may have at most only one message out of 10 000 or so that encodes a Na^+ channel. Hence, there must be a rapid method for screening the colonies to identify the channel cDNA clones. This is where information from biochemical purification proves to be vital.

Despite the near impossibility of totally sequencing large Na^+ or Ca^{2+} channel polypeptides, from a proteolytic digest one can readily purify a homogeneous preparation of a particular fragment. This fragment may then be partially sequenced using standard Edman degradation techniques. In practice, one only needs a few (perhaps six or so) residues of sequence to be reasonably sure that a unique segment of the protein is encoded. From this short amino acid segment, one can then synthesize (by automated

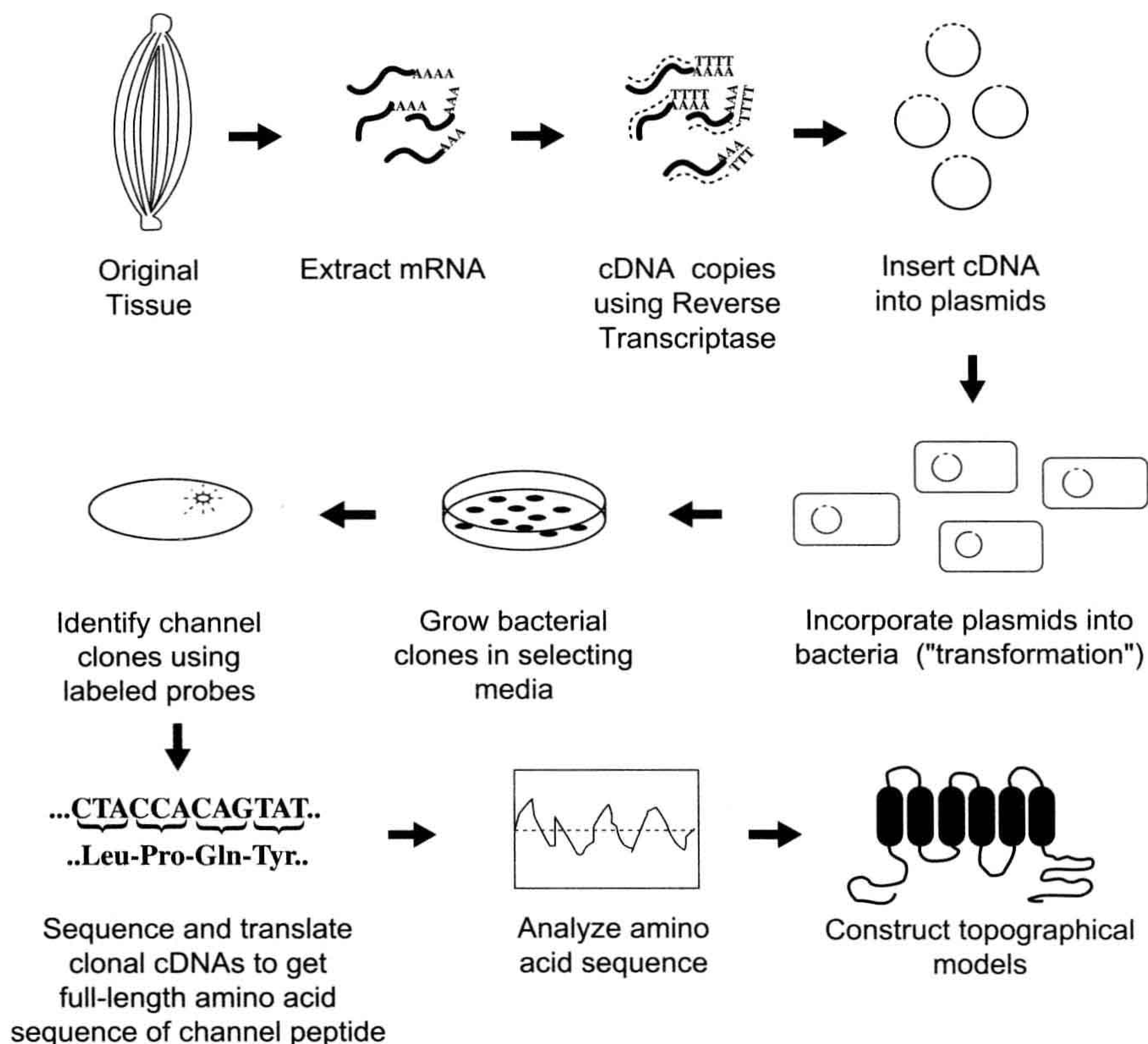


FIGURE 21.2 General strategy used to determine ion channel structure using recombinant DNA approaches.

means) a short DNA fragment, called an *oligonucleotide*, that encodes the segment. Further, this synthetic DNA may be radiolabeled and thus becomes a binding probe to identify cDNA inserts. Identification is done by placing a piece of special paper briefly on top of the agar plate and lifting off a few bacteria from each colony plaque onto the paper. The paper is then placed in a special solution that lyses the bacteria but binds the released DNA immediately on the surface. The radiolabeled synthetic probe may then be washed over the paper; it will bind by complementary interactions to the antisense strand of clonal plasmids encoding the channel protein containing the original sequence. After unbound probe is washed away, the paper is overlaid in the dark with x-ray film. Channel clones are thus identified as dark spots (usually only a few) on the film and may be traced back to the plaque on the original agar plate. This plaque is then lifted from the plate with a toothpick and grown in a nutrient broth to produce many bacteria. This technique provides enough cells from which the plasmids are purified by simple chemical means and the cDNA insert may be readily sequenced. Once the cDNA sequence is known, the genetic code is applied to derive the primary amino acid sequence of the channel protein.

This description of clonal sequencing omits many details. For example, the length of DNA that one may clone or sequence at one time is limited and complex strategies are often required to sequence the entire length of long channel polypeptides. In addition, ion channels that are heteromeric complexes will require that each subunit polypeptide be separately sequenced. Despite these apparent complexities, an organized group of researchers using automated equipment can screen hundreds of thousands of clones and sequence thousands of bases of interesting cDNA inserts in a relatively short time.

IVB. Analysis of the Primary Structure of Large Polypeptide Voltage-Gated Channels

The electroplax Na^+ channel was the first voltage-gated channel to be sequenced (Noda et al., 1984). As

suggested by the biochemistry, it was found to be a long polypeptide of 1820 amino acids (Fig. 21.3). Subsequent cloning of mammalian channels showed them to be similar in size and sequence (see Numa and Noda, 1986). What can one learn about channel structure from such primary sequence data? Typically, one subjects the primary sequence data to several forms of analysis to derive a model of the appearance of the higher order structure. The first striking characteristic revealed in the Na^+ channel sequence was the presence of four repeats (of about 200 amino acids each) that were highly (but not completely) homologous to one another. Furthermore, these internal repeats were found to have great potential for forming membrane-spanning domains of the channel. From such analyses, the model shown later in Fig. 21.6 was obtained.

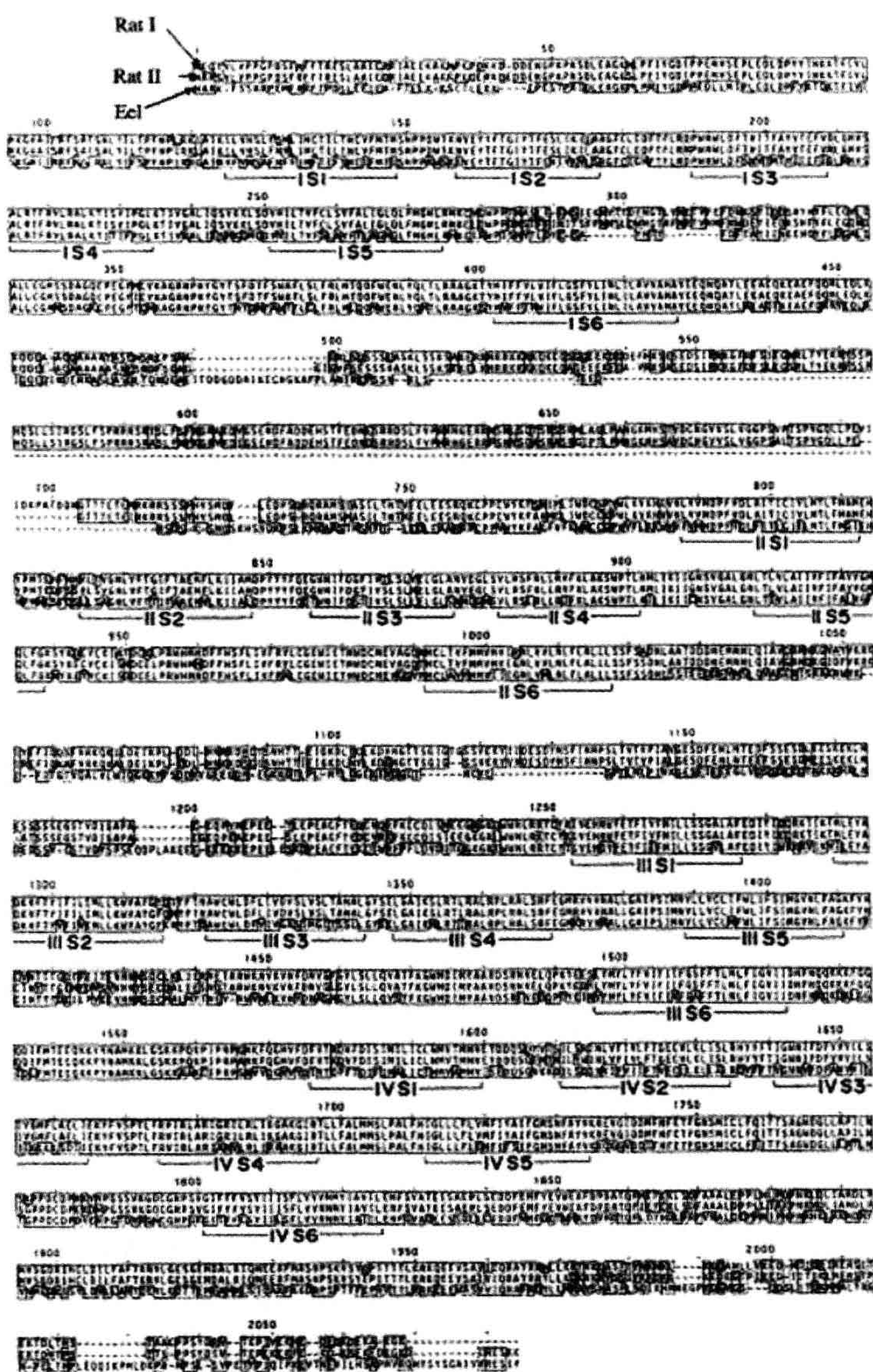


FIGURE 21.3 Amino acid sequences of three Na^+ channels obtained by cDNA cloning techniques. Rat I and II were obtained from rat brain cDNA libraries, while the eel Na^+ channel is that expressed in the electric organ of *Electrophorus electricus*. Boxed residues show homology among the three channels, while dashed lines designate absent segments. Labeled brackets underneath the sequences refer to parts of the highly conserved putative transmembrane repeats (see text and Figs 21.6 and 21.7 for details). *(From Numa and Noda, 1986.)*

How are such analyses performed? Basically, the analyses occur in two or three separate steps. First, one analyzes the sequence of the peptide for regions of high hydrophobicity, on the expectation that membrane-spanning regions should have a high proportion of hydrophobic amino acids. To do this, hydropathy values that reflect its relative hydrophobicity are assigned to each amino acid residue. The assignment of such values is based largely on indirect physical measurements of the hydrophobicity, such as the ability of a given residue to partition from an aqueous solution to an oil phase. Such values may or may not reflect the chemical behavior of a residue in a long polypeptide chain, where chemical properties may be further influenced by neighboring residues. As a result, a number of such hydropathy tables have been developed by various investigators who have significant differences in the way they assign hydropathy weights to a given residue. One of the most popular tables is that of Kyte and Doolittle (1982) shown in Fig. 21.4. In most cases, the assignments are qualitatively obvious, especially for expected hydrophobic groups (e.g. the hydrocarbon chains or leucine or valine) or hydrophilic groups (e.g. the charged residues such as glutamate or lysine).

Figure 21.5 shows hydropathy plots for the Na^+ channel sequences given in Fig. 21.3. The plot is obtained by averaging the hydropathy values of a fixed segment (perhaps 7–15 residues). Starting with the first residues at the N-terminal end, this average is computed and the value is plotted versus the number of the residue in the middle of the segment. This averaging "frame" is then shifted by one residue toward the carboxyl end, the new hydropathy average is recomputed (i.e. the change due to the loss of the

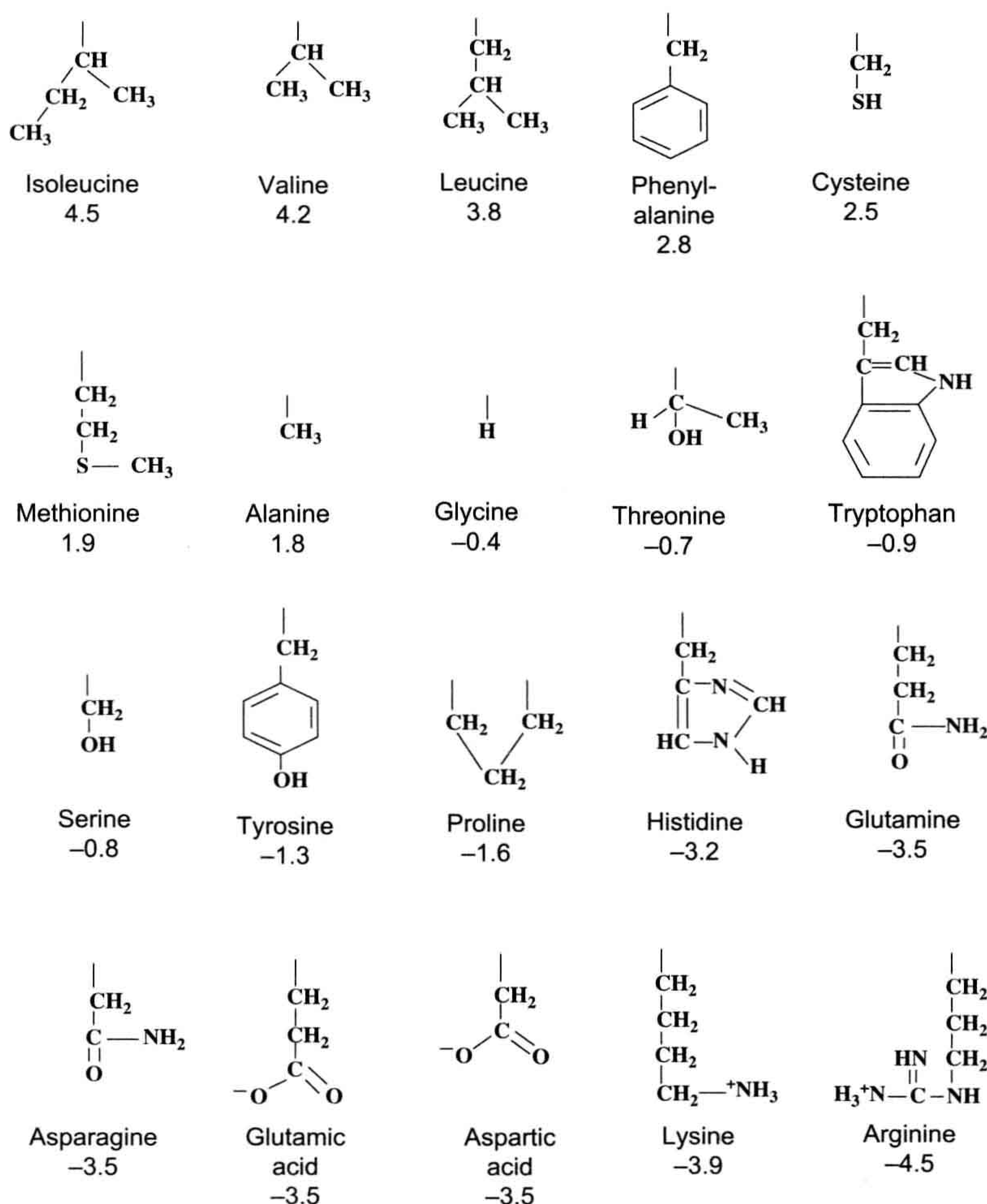


FIGURE 21.4 Structure and hydropathy values of amino acid residues. Arranged from most hydrophobic to most hydrophilic according to relative values assigned by Kyte and Doolittle (1982). Only side groups are shown with hydropathy values underneath.

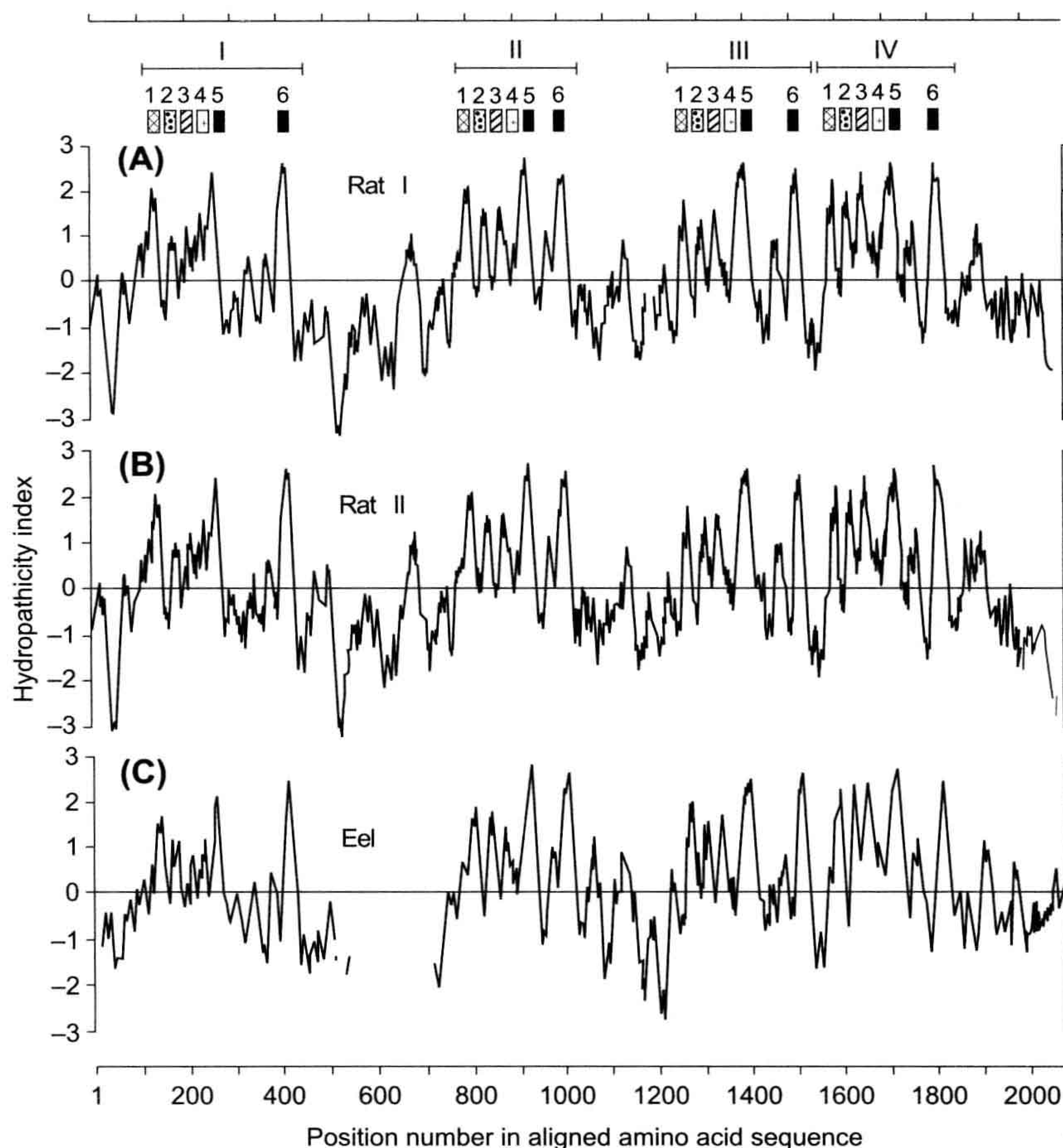


FIGURE 21.5 Hydropathy plots for the three Na^+ channel sequences of Fig. 21.3. Brackets and numbered patterns at top refer to the locations of homologous repeats and transmembrane segments (see text and Fig. 21.7). *(From Numa and Noda, 1986.)*

N-terminal side residue and the gain of the next C-terminal side residue in the sequence) and the value is plotted by incrementing the residue number by one. This *frame-shift* average is thus continued until the end of the protein is reached. The purpose of using the averaging frame is to smooth out sharp variations in hydropathy, so that a pattern may be more readily seen.

As can be seen in Fig. 21.5, there is a repeated pattern of hydropathy for Na^+ channels that reflects the conserved homology of the four internal repeat domains I−IV. Within each domain, there are five or six peaks of hydrophobicity that are each about 20 amino acids long. This is significant because such a length is considered optimal to span the hydrophobic interior of the lipid bilayer. However, hydrophobicity alone is not sufficient to predict a membrane-spanning region; instead, the residues must assume a favorable secondary structure, most commonly assumed to be an α-helix. In the helical conformation, the hydrophobic side chains project radially away from the axis of the helix and presumably into the surrounding lipid. Such a configuration prevents the very hydrophilic peptide backbone of the protein from exposure to the hydrophobic lipid environment and thus represents a favorable low free energy arrangement of the protein−lipid interface.

How are such secondary structures predicted from primary sequence? This too is a highly empirical process (Chou and Fasman, 1978). Basically, investigators have analyzed in detail a number of proteins for which there are high-resolution x-ray structures available at the amino acid level. By cataloging the frequencies with which given amino acids or short combinations of residues are found in helices, β-sheets, or turns, a set of empirical rules has been

developed to predict the secondary structures that a given sequence of amino acids will most probably form (see Fig. 21.5). Although the general accuracy of such predictions has been debated, when combined with hydropathy information the method is apparently rather accurate for the prediction of membrane-spanning domains in membrane proteins. This is probably because of the severe thermodynamic constraints confronting polypeptides needing to cross a boundary of high hydrophobicity while interfacing with a highly hydrophilic aqueous phase on either side of the membrane and in the aqueous channel pore.

IVC. How Is Channel Structure Formed?

In any case, such primary sequence analyses suggest that each internal domain has six α-helical membrane-spanning segments (see Numa and Noda, 1986). The question to consider next is how such an arrangement might form a transmembrane pore for the passage of ions. The answer is that the four transmembrane regions probably contribute equally to the pore walls in a "staves of a barrel" configuration (Fig. 21.6; see Guy and Seetharamulu, 1986). In fact, such a model was comforting to the original investigators, because a similar arrangement had previously been shown to exist among the separate subunits of the synaptic acetylcholine-gated channel, the first ion channel to be purified and sequenced via cDNA cloning.

IVD. Sequence Homology among the Transmembrane Domains of Ion Channels

Analysis of the DHP-sensitive Ca^{2+} channel α-1 peptide revealed that it also has four internal homologous repeats (Fig. 21.7; see Tanabe et al., 1987). Furthermore, these repeats (but not the intervening loops) were found to be highly homologous to the Na^+ channel repeats. The "staves of a barrel" configuration in which either homologous internal repeats (for Na^+ and L-type Ca^{2+} channels) or highly homologous subunits (as in the case of transmitter-gated and K^+ channel—see Section IVG) form a pore seems to be a widespread architecture among ion channels in general.

IVE. How Are Topographical Predictions for Channel Structure Tested?

The modeling approach based on primary structure is highly uncertain and needs to be empirically confirmed for each channel. One of the most popular ways this has been done is through the use of site-directed antibodies raised to synthetic peptides encoding a short stretch (i.e. 10–20 residues) of the channel of which one wishes to know the topographical orientation. These antibodies may be applied to channels in their native membranes or intact cells and the relative sidedness of the epitope may be determined from the side of the membrane to which the antibody is bound. The approach has been used for Na^+ channels in several laboratories and the topographical model shown in Fig. 21.6 has largely been confirmed (see Catterall, 1992). Similar approaches can be used in which impermeant group-reactive chemical reagents are applied to either intact cells or liposomes with oriented channels, followed by some method to identify the site of interaction on the protein (e.g. sequencing of proteolytic fragments). Alternatively, a synthetic, but highly antigenic, short epitope may be recombinantly inserted into the channel sequence and the mutant expressed in cultured cells. In this case, the same antibody may be used in all

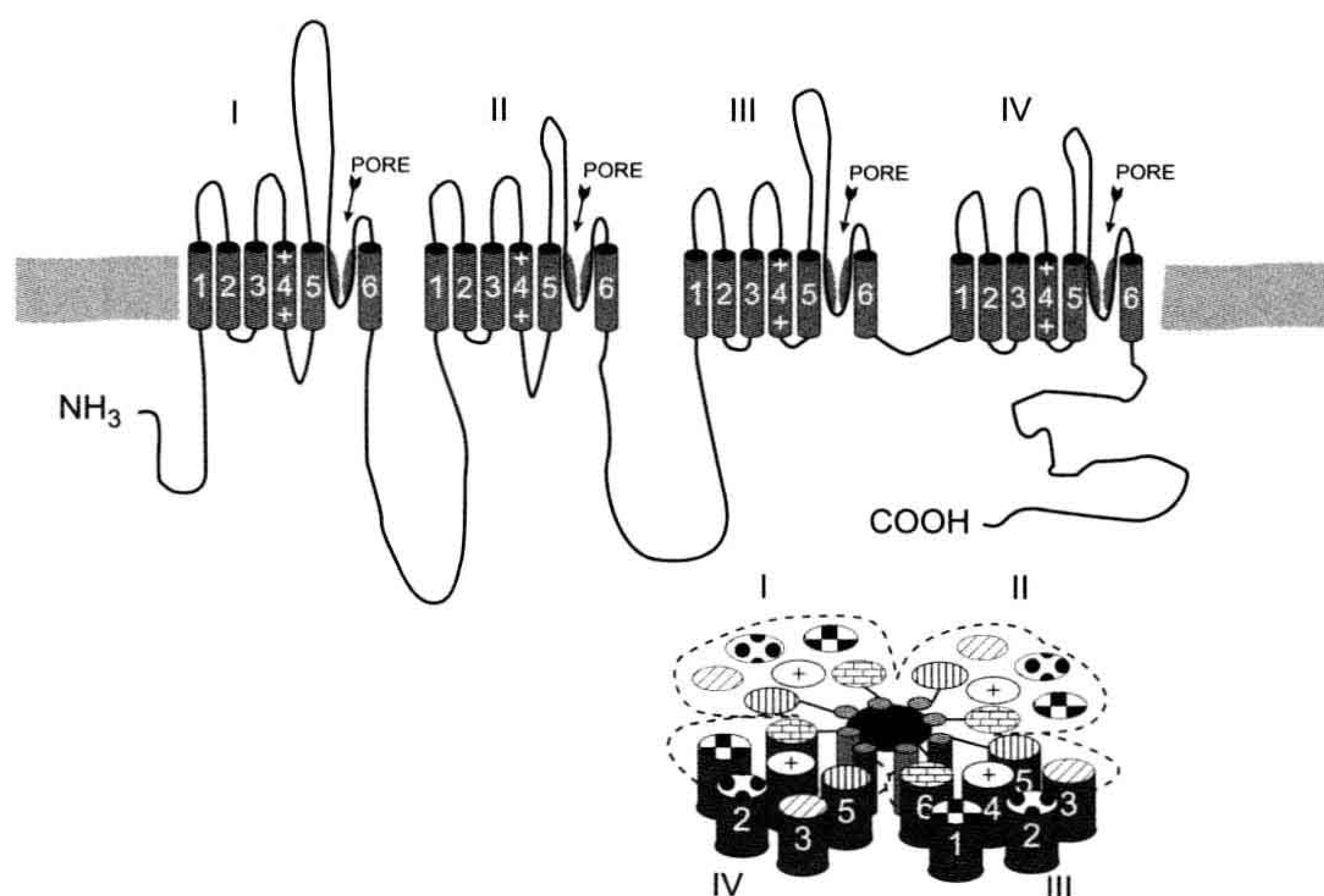


FIGURE 21.6 Model of Na^+ channel structure based on analysis of primary sequence data. The top drawing shows linear placement of four homologous domains, loops and termini (outer surface of membrane is at the top). Possible pore and selectivity regions are labeled and shown as the angled segments between transmembrane segments 5 and 6. The drawing on the bottom right shows a hypothetical arrangement of homology repeats in the "staves of a barrel" configuration to form a pore (placement of transmembrane segments 1–6 is somewhat arbitrary).

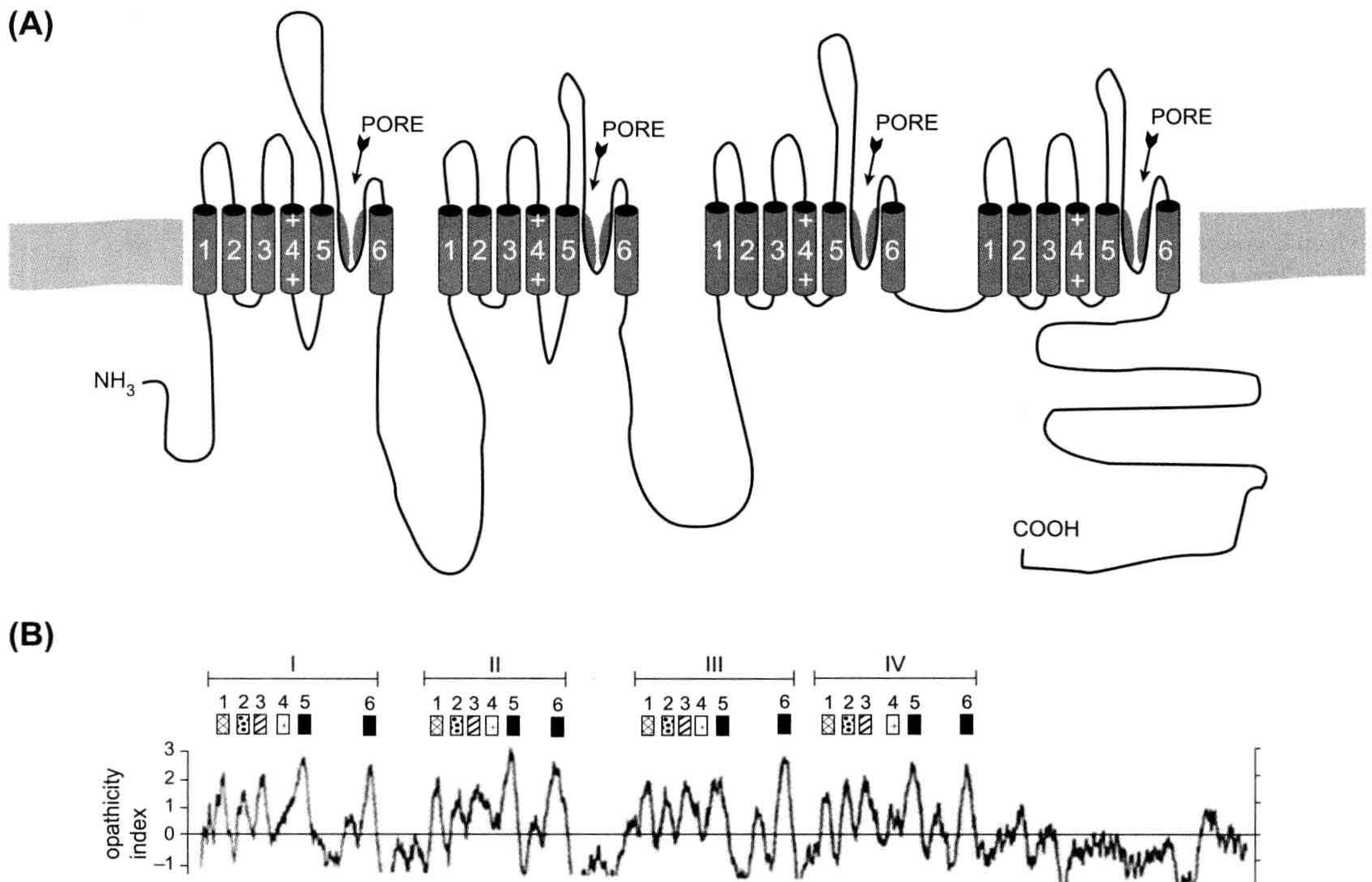


FIGURE 21.7 Model and hydropathy plot (bottom) of L-type skeletal muscle Ca^{2+} channel α-1 subunit. Compare to Figs. 21.5 and 21.6.

experiments to determine on which side of the membrane the epitope tag is located as a function of its position in the native channel sequence.

IVF. The Genetic Approach Used to Identify Nucleic Acid Clones Coding for K^+ Channels

K^+ channels are extremely important in excitation and transduction phenomena. Partly because of the way these channels were cloned and partly because their structure is a simplified version of the long Na^+ and Ca^{2+} channels, they are very valuable systems with which to study the general structures and mechanisms of the voltage-gated ion channel class. Such channels were not originally cloned via the usual biochemical purification–oligonucleotide probe approach described previously because there were few good chemical labels like tetrodotoxin or DHP.

A highly creative, yet complex, approach was taken independently by several laboratories that used behavioral mutants of the fruit fly *Drosophila* (e.g. see Papazian et al., 1987). In brief, mutant strains that had uncontrolled shaking when exposed to ether were identified. Electrophysiology then established that the muscles and certain neurons of such flies had missing or altered K^+ currents of a specific type known as A-type currents that, like sodium currents, inactivate on depolarization. The locus of the genetic defect causing this behavior could be seen as an actual physical defect (translocation) in the polytene salivary chromosomes of these so-called *Shaker* mutants. Since extensive libraries of cloned identified chromosomal DNA fragments of *Drosophila* have long been available (called genomic clones), the investigators were able to obtain the DNA fragment of normal flies on which the mutant defect occurred. This allowed them to sequence such fragments and, by comparison with *Shaker* mutant sequences and by the identification of homologous cDNA fragments (derived as described earlier), the sequence of the A-type K^+ channel could be inferred. Since the *Shaker* mutation allowed a completely genetic elucidation of the channel primary amino acid sequence, the A-current it manifests has become known as the *Shaker*-type K^+ channel.

IVG. K^+ Channels are Homologous to a Single Internal Repeat of Na^+ Channels

An initially surprising finding when the *Shaker* A-type channel sequence was analyzed was that the length of the

sequence was much shorter than that of the other voltage-gated channels, but contained a single domain that was reminiscent of (but strictly speaking not very homologous to) the internal repeat domains of the Na^+ or Ca^{2+} channels (Fig. 21.8; see Pongs, 1992). An obvious hypothesis for channel structure for the *Shaker* channel was that four molecules of this sequence (i.e. subunits) combined to form the "staves of a barrel" structure postulated for the long-channel polypeptides. This tetrameric assembly model has recently received strong support from several elegant experiments (MacKinnon, 1991).

V. MOLECULAR MECHANISMS OF CHANNEL FUNCTION: HOW DOES ONE INVESTIGATE THEM?

We now discuss the methods that can be used to determine which parts of an elucidated channel sequence are involved in the basic channel properties of pore formation, ion selectivity and voltage-dependent gating. Here, too, the methods of recombinant DNA technology have proved to be of great use in that they allow the investigator to change the nucleic acid sequence encoding a channel in the manner desired. Using such mutagenesis techniques, the basic idea is to alter the amino acid sequence via deletion, addition, or change in the primary sequence in specific locations and then to test how such changes affect the function of the mutant channels. The hope is that by obtaining many such structure–function correlations, one might not only infer the part of the sequence that underlies, for example, channel activation, but also infer how this structure works as a mechanism.

VA. Choosing Interesting Sites and Segments as Targets for Mutagenesis

How does one decide which of the many amino acids in a channel polypeptide to change? This is where the modeling approach described previously is so important, for it provides clues or testable hypotheses that focus mutagenesis attempts on reasonable guesses. For example, one might assume that a highly conserved sequence in channels from phylogenetically distant animals might reflect a functionally essential part of the molecule that cannot withstand evolutionary alteration without being deleterious. Another strategy might be to compare the regions of divergence in the sequence of the various voltage-gated channels in the hope of finding candidate regions involved in different functions among channels. For example, the difference in ion selectivity among Na^+, K^+ and Ca^{2+} channels must lie somewhere in the variations in their amino acid sequence. Both approaches have had

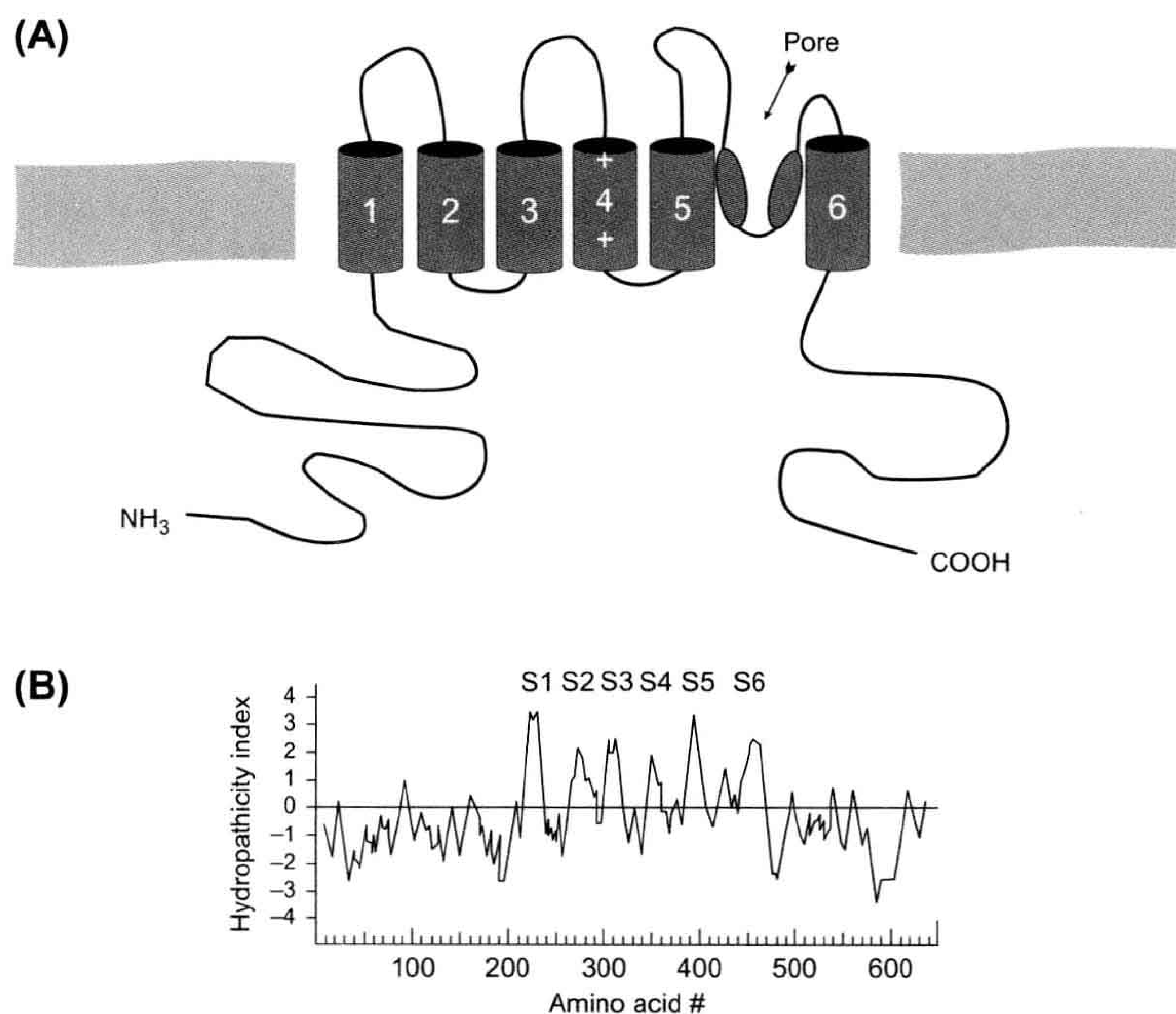


FIGURE 21.8 (A) Model and (B) hydropathy plot of *Shaker* B-type K^+ channel. Compare to Figs. 21.5, 21.6 and 21.7.

a certain degree of success, although "homology" is a relative term and, in reality, large areas of channels are highly variable, even among isotypes of channels from the same organism (see Section VI). This makes it difficult to guess which of these many differences relates to specific functions.

Another approach is to take advantage of certain genetic disorders in which mutations in channel structure occur naturally with functional consequences. A number of human diseases and animal models have been shown to be caused by channel defects. The sequence of such channels can give important clues into structure–function relationships in channels, while directing artificial mutagenesis experiments.

VB. Use of Expression Systems in Mutagenesis Studies

Another essential part of mutagenesis experimentation is the ability to introduce artificially altered genetic material into a cell that is capable of translating it into a protein molecule, processing the molecule appropriately (i.e. folding the polypeptide, assembling subunits, adding sugars or lipids) and inserting the protein into the cell surface. The protein then may be functionally characterized using the biophysical methods described in other chapters. The most popular such *expression system* is the oocyte of the South African frog *Xenopus laevis* (Fig. 21.9; Leonard and Snutch, 1991). In this system, one prepares mRNA from clones of the mutant channel and injects this message into the large (1–2 mm in diameter) oocytes with a micropipette. After waiting a few days for channel synthesis and membrane insertion to occur in sufficient numbers, one observes the expressed ionic currents via voltage-clamp methods, using large microelectrodes to impale the cell. Alternatively, one may also use a very large diameter electrode to patch-clamp a large area of membrane; such macropatch methods give better voltage control than the impaled electrode technique while allowing macroscopic current characterization. Finally, conventional single-channel analysis may be done in all the usual modes using standard patch pipettes. Thus, the oocyte allows the investigator to compare both the macroscopic and single-channel properties of the mutants with the normal wild-type channel.

Although other expression systems in which the altered genetic material may be introduced into cells transiently via

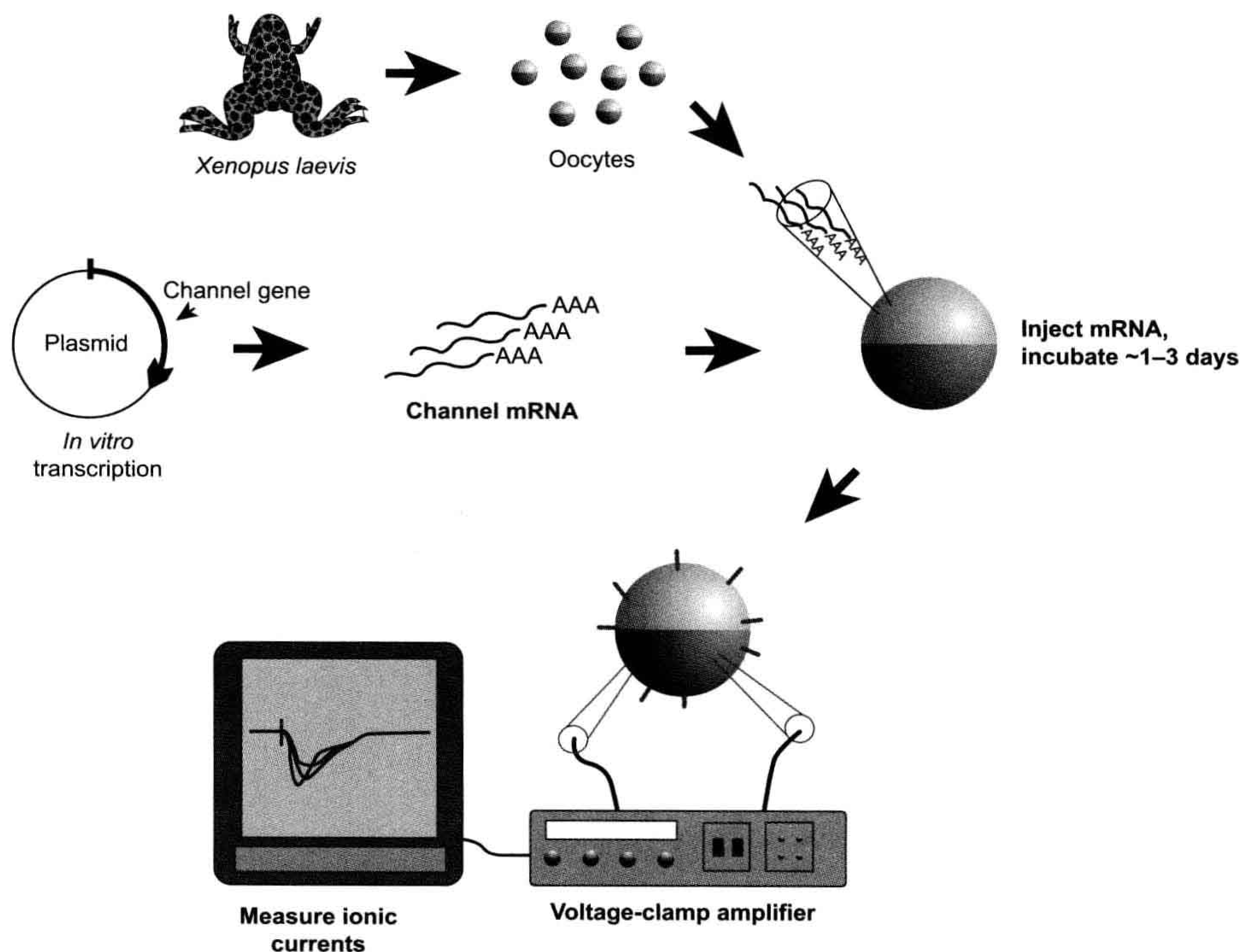


FIGURE 21.9 *Xenopus* oocyte expression system. For details, see text.

viruses or integrated permanently into the host genome (stable transfection) have been developed more recently, the use of such systems is beyond the scope of this chapter. Suffice it to say that the frog oocyte is currently the most popular and productive expression system with which to study structure–function relationships.

Because of its great potential in elucidating channel mechanisms, mutagenesis is being used by a large number of investigators. As a result, both new and altered concepts of channel function appear frequently in the scientific literature. In the brief account that follows, we can only summarize some of the fairly firm basics of gating, pore formation and ion selectivity.

VC. Domains Involved in Voltage-Dependent Activation

The ability to respond to changes in transmembrane potential is a hallmark of voltage-gated channels. Thus investigators looked for common motifs in channel sequences suggestive of voltage sensor domains that might target mutagenesis among the large number of residues in cloned voltage-gated channels. In comparing Na^+, DHP-sensitive Ca^{2+} and *Shaker*-type K^+ channels, the fourth predicted helix in the repeat/subunit motif was seen to display a highly conserved sequence pattern (see Figs. 21.6, 21.7 and 21.8). This segment, known as S4, consists of a repeated triad of a positively charged residue (Arg or Lys), followed by two highly hydrophobic residues (such as Val, Leu, Ile; Fig. 21.10). While the number of such triads in the various S4 segments ranges from three to eight, its structure of both charged and hydrophobic residues suggests an element capable of responding to transmembrane voltage changes (see Catterall, 1992). Accordingly, a number of experiments have now been done in which both the charged and hydrophobic elements have been changed.

In brief, S4 mutagenesis usually causes significant changes in the steady-state activation behavior of the affected channel (Fig. 21.11; Papazian et al., 1991; Lopez et al., 1991). Thus, shifts of the steady-state activation curve along the voltage axis occur with most changes to either charged or hydrophobic residues. In addition, changes in activation slope are frequently seen.

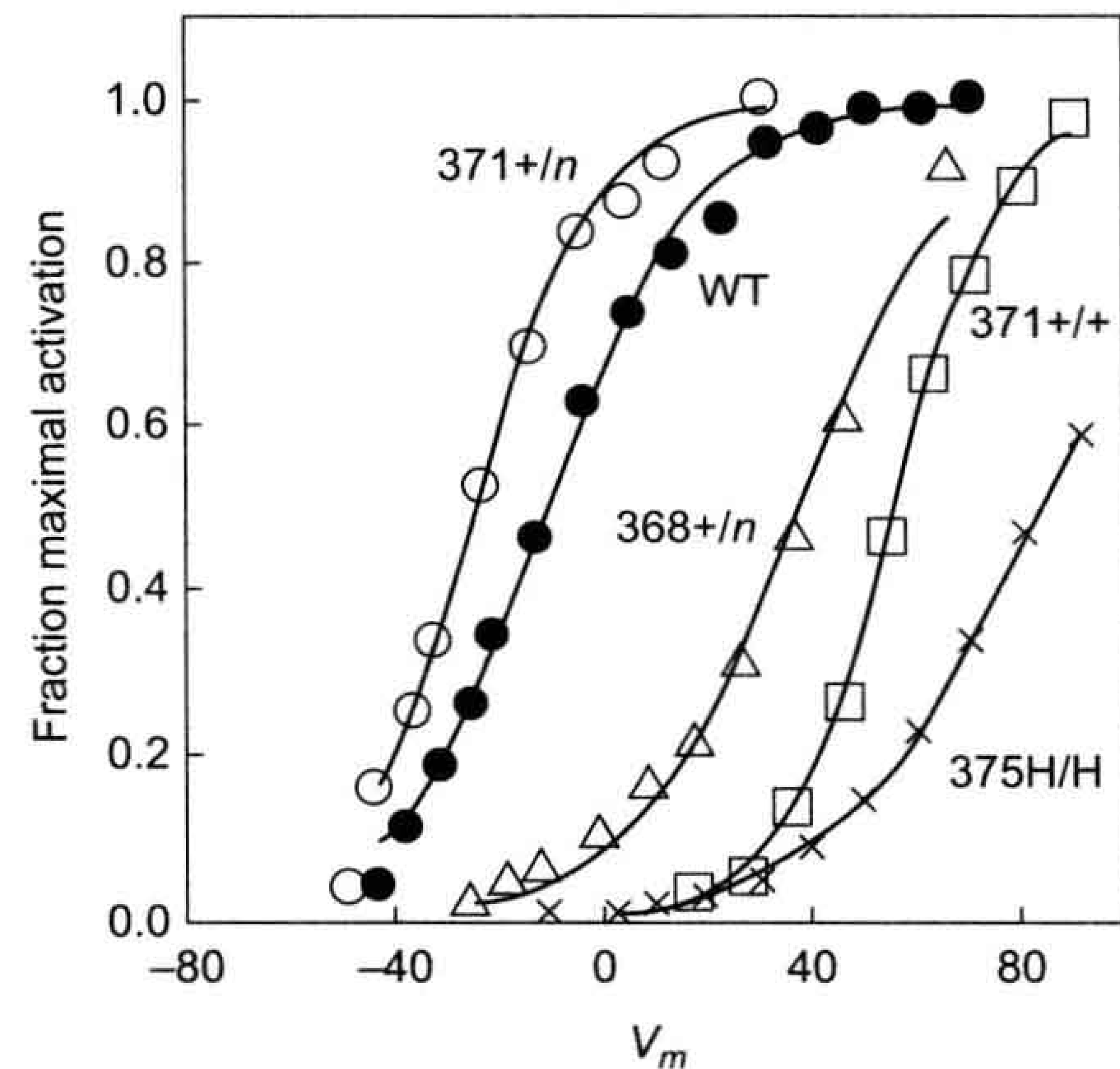


FIGURE 21.11 Effect of S4 mutations on *Shaker* K^+ channel activation expressed in oocytes. Shown are steady-state activation curves for wild-type (WT) and various single amino acid changes. +/n, change from a positively charged residue to a neutral one; +/+, a change of positively charged residue for an other charged residue; H/H, replace one hydrophobic residue with another hydrophobic residue. *(Data redrawn from Papazian et al., 1991 and Lopez et al., 1991.)*

The question is whether the observed changes can be explained in terms of a mechanism by which S4 participates in gating (instead of the general hypothesis that S4 is some part of a gating structure). Unfortunately, to date the results obtained from mutagenesis do not discriminate very well among the various possible roles for S4 in gating, for example, as a gating sensor, a part of the transduction linkage to a gating element, or simply an unrelated part of channel structure. Thus, the magnitude or direction of changes in activation behavior does not systematically correlate with changes to S4 charge or sequence. In addition, others have questioned whether the charged groups in the S4 segments can completely account for all the gating charge that moves when channels activate (see Sigworth, 1995). In general, the mutagenesis approach is inherently

	+	+	+	+	+	+	+	+
Electric eel NaCh IV-S4	LFR	VIR	LAR	IAR	VLR	LIR	AAK	GIR
Rat brain NaCh IV-S4	LFR	VIR	LAR	IGR	ILR	LIK	GAK	GIR
Rat skeletal muscle NaCh IV-S4	LFR	VIR	LAR	IGR	VLR	LIR	GAK	GIR
Drosophila NaCh S4	LLR	VVR	VFR	IGR	ILR	LIK	AAK	GIR
Rabbit skel. muscle CaCh IV-S4	SSA	FFR	LFR	VMR	LIK	LLS	RAE	GVR
Mouse brain KCh S4	ILR	VIR	LVR	VFR	IFK	LSR	HSK	
Drosophila Shaker S4	ILR	VIR	LVR	VFR	IFK	LSR	HSK	

FIGURE 21.10 Comparison of S4 segments from different voltage-gated channels. Note the repeating triadic motif of positive charge (R, Arg; K, Lys) followed by two hydrophobic residues. Hatched areas show conservation of charge among channels; all amino acids designated by single letter codes.

limited in its ability to distinguish between alterations that directly affect a mechanistically important part of the molecule and those that indirectly cause functional effects through structural changes that propagate from mechanistically unrelated domains. This problem arises because protein structures are notoriously sensitive to long-range effects of such alterations, generically known as allosteric ("other site") effects.

VD. Limitations of Mutagenesis in the Study of Channel Mechanisms

The naive reader can understand the problem from a crude analogy in which many of us as children tried to understand the workings of a mechanical watch by a similar approach using simple tools. The child understands the function of the mechanism only by the movement of the hands. However, as we all know, a mechanical watch is quite a delicate machine. Thus, even the act of carelessly opening the case may cause the mechanism to cease working. Are we to conclude that the case is therefore part of the mechanism? Given access to the mechanism itself, the situation is highly complex, since the movement of many parts is required for the ultimate movement of the hands. For example, the result of stopping the second hand by interfering with a given gear tells one very little of the role that gear plays in how the watch operates.

For some time it has been known that the interactions of chemical substances or structural alterations with a site on one side of a protein can dramatically affect the function of another site at some distance, for example, on the other side of the protein. This concern and the potentially complex nature of channel-gating mechanisms should motivate the responsible practitioner of mutagenesis to display caution in interpreting results in mechanistic terms.

How, then, in the face of such limitations does one make progress in elucidating the mechanisms of channel function? In fact, the approach is philosophically identical to the way one attempts to prove any hypothesis, namely, to establish a circumstantial case by as many independent tests as possible. In the example of S4 and mutagenesis, for example, one might wish to demonstrate that mutations to any other part of the molecule have no effect on voltage-dependent activation as a sufficient (but not necessary) test. Unfortunately, mutations to other parts of channel sequence can have equally profound effects as S4 alterations (for example, to the pore-forming region described previously; see Yool and Schwarz, 1991). Thus, while these other mutations do not disprove a role for S4 as a sensor (or any other role), they do suggest, as in the mechanical watch, that a number of segments of the sequence are either directly involved in a complex mechanism of voltage gating or indirectly affect a gating process through allosteric/structural influences.

VE. The Mechanism of Channel Inactivation

Genetic engineering studies of the inactivation process currently provide a better example of what one may learn mechanistically from the mutagenesis approach. Some of the most important such studies have involved the *Shaker* A-type channel. Here early workers found important clues to the segment involved in the inactivation process by comparing naturally occurring variants of the channel (*isotypes*; see Section VI). Thus, Fig. 21.12 shows the pattern of four such isotypes, called A, B, C and D (Timpe et al., 1988). *Shaker* B, C and D were identified from further testing of cDNA clones using probes constructed from the original *Shaker* A sequence as described earlier. When expressed in oocytes, these isotypes displayed very different kinetics of inactivation. Analysis of the regions of homology and differences among the isotypes shown in Fig. 21.12 indicates that fast inactivation properties correlate most strongly with the nature of the N-terminal segment (thought to be cytoplasmic; see Fig. 21.8).

Further evidence for the role of this segment in inactivation was obtained by constructing channel chimeras in which the *Shaker* A clone was modified by replacing its N-terminal segment with those from other isotypes. In each case, the mutant channel assumed the inactivation properties of the isotype donating the N-terminal segment, despite the fact that the rest of the molecule had the sequence of the fast-inactivating *Shaker* isotype (Aldrich et al., 1990).

Finally, investigators mutagenized specific regions of the fast-inactivating *Shaker* B segment to localize those residues involved in the inactivation process (Hoshi et al., 1990). Both by deleting small segments and by replacing others it was found that the crucial part of the molecule was a stretch of residues from the positions 6–83 (i.e. the N-terminal tail of the molecule seen in Fig. 21.8). In this segment there were distant effects of the alterations. Thus, mutations to the residues in the 23–83 residue region tended to produce changes in inactivation kinetics, whereas changes to those in the N-terminal side (6–22) of the segment tended to destroy inactivation completely (see Fig. 21.14).

What might be the mechanism of *Shaker* inactivation? Much earlier, Armstrong and coworkers had reported that internal perfusion of proteases in the squid destroyed the ability of Na^+ channels to inactivate. On the basis of this and other experiments, Armstrong proposed that the inactivation mechanism is a cytoplasmic ball attached to a peptide tether that swings into an open channel to block it from the inside (Fig. 21.13; Armstrong and Bezanilla, 1977). In this hypothesis, the ball blocks the channel by binding to a receptor in the inside of the pore that is accessible only when the channel has opened (activated). The reader may recall the evidence that inactivation is coupled to activation and hence may be intrinsically

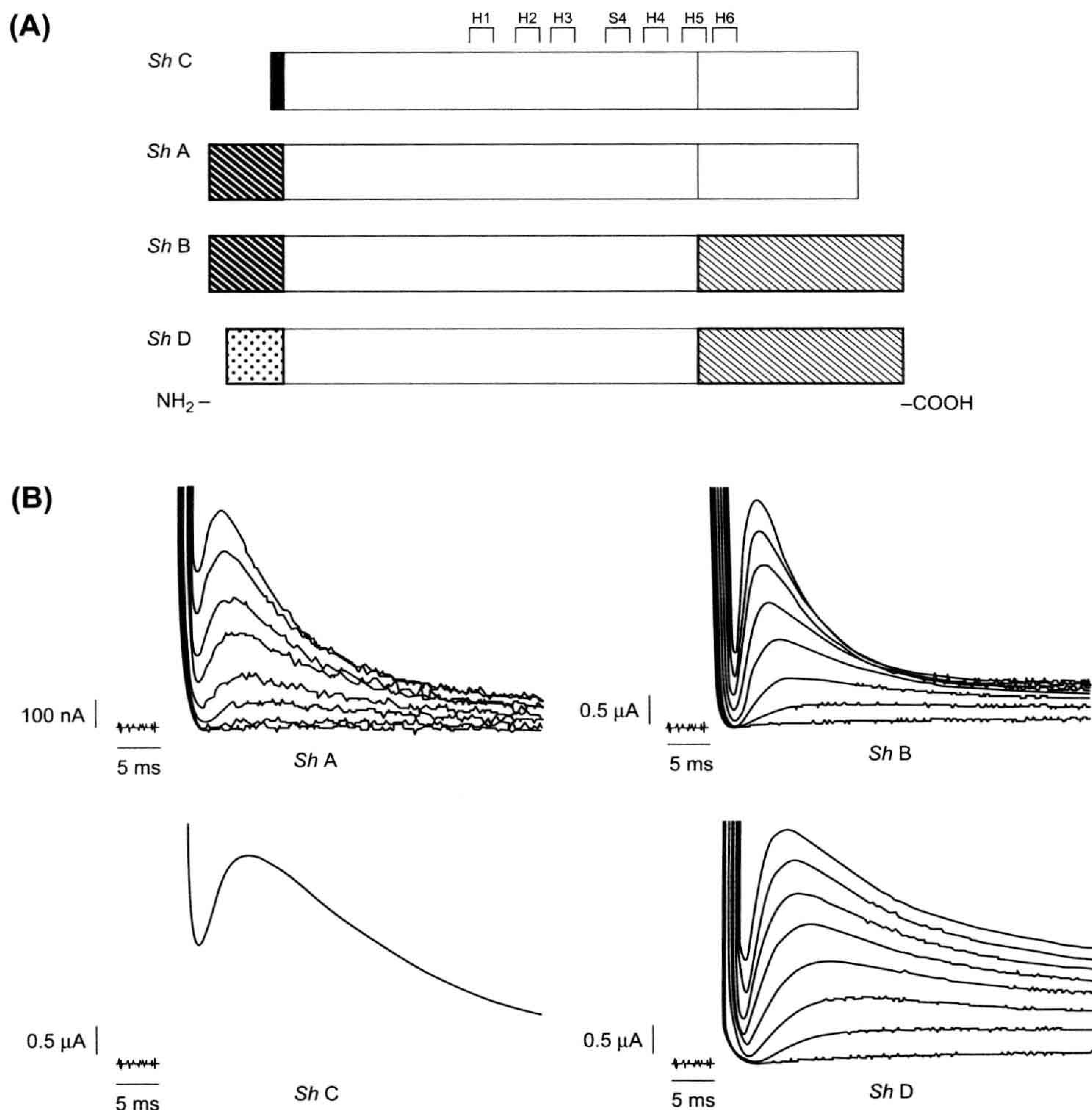


FIGURE 21.12 Gating kinetics of alternatively spliced *Shaker* isoforms expressed in oocytes. (A) Comparison of sequences, with patterned regions representing alternatively spliced domains that are different among isoforms (other unpatterned regions are identical in sequence). (B) Both current traces obtained from oocyte voltage-clamp show currents resulting from each isoform. *(From Timpe et al., 1988. Copyright 1988 by Cell Press.)*

voltage independent. Thus, the ball-and-chain model also explains these properties since the cytoplasmic ball would experience little of the transmembrane field but could swing into the channel only after it had activated and revealed its receptor (hence the coupling properties).

In the case of the *Shaker* channel, Aldrich and colleagues proposed that the N-terminal segment that they identified was just such a mechanism, since changes to the length of the 23–83 segment affected kinetics (as might be expected from changing the length of the chain), while changes to the N-terminal segment (such as alterations of charge) that eliminated inactivation were postulated to prevent the ball from binding to its receptor in the activated channel.

How might such a model be further tested? Here the investigators performed a particularly elegant experiment (Fig. 21.14; Zagotta et al., 1990). First they constructed a mutant *Shaker* channel in which inactivation had been eliminated by a deletion of its own N-terminal segment. Next, a synthetic peptide that had the exact sequence of the deleted region was prepared. The mutant channel was then expressed in oocytes, where both excised macropatch and single-channel observations could be made. The investigators found that when the peptide was applied to the

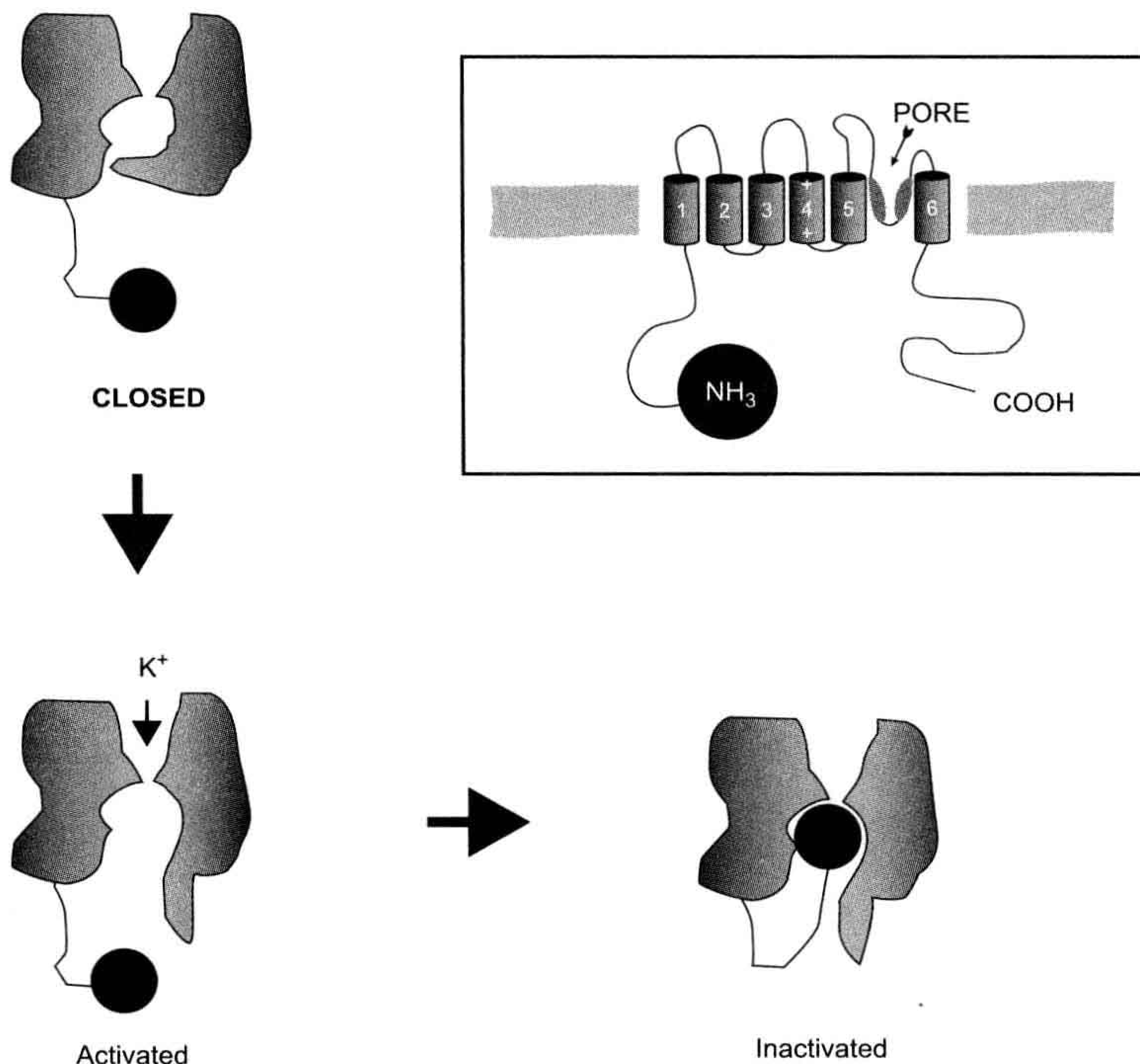


FIGURE 21.13 Ball-and-chain model of inactivation. Not shown are the three other balls that the other subunits of the channel will contribute.

solution bathing the inside surface of the membrane, inactivation was restored to these mutant channels. Furthermore, the kinetics of the restored inactivation depended on the concentration of the peptide in the bath and the inactivation could be reversed by washing away the peptide-containing solution. These observations are thus consistent with a direct blocking interaction of the peptide with a site in the open channel and constitute strong evidence for the ball-and-chain mechanism of inactivation in A-type K^+ channels.

VF. Other Gating-Related Domains in Voltage-Sensitive Channels

Analysis of the homology of the various cloned Na^+ channels revealed that the longest segment of conservation lay in the postulated internal loop between repeats III and IV, even among animals of some phylogenetic distance (see Fig. 21.3). This high degree of conservation suggested a functionally important role for the segment. This idea was initially tested by constructing mutant Na^+ channels in which the channel was expressed in oocytes in two pieces, with the genetic "cut" within this segment (Stuhmer et al., 1989). Interestingly, such artificial dimeric channels were assembled and expressed in the oocyte and displayed relatively normal activation and conductance; however, such channels did not inactivate. Further, site-directed antibodies raised to a synthetic peptide encoding this segment were found to slow or eliminate inactivation when they were applied to the cytoplasmic surface of cells expressing normally inactivating channels (Vassilev et al., 1989). Finally, mutagenesis directed to this segment produced channels with altered inactivation (Catterall, 1992).

However, the sequence of this segment has little resemblance to the N-terminal ball-and-chain *Shaker* domain and it is additionally tethered at both ends. Nonetheless, several lines of evidence now suggest that this domain operates analogously to the *Shaker* ball-and-chain in producing Na^+ channel inactivation. Most notably, via mutagenesis to the III–IV loop, one can produce "inactivationless" sodium channels; in such mutants, inactivation can be restored with the internal application of the same synthetic *Shaker* peptide that restored inactivation to non-inactivating potassium channels in the experiments described above.

For DHP-sensitive Ca^{2+} channels, an isotype of the originally cloned skeletal muscle channel has been cloned from the heart. In the parent tissues, these channels share some characteristics, but differ greatly in the speed by which their calcium currents activate (heart channel currents being much more rapid in responding to voltage).

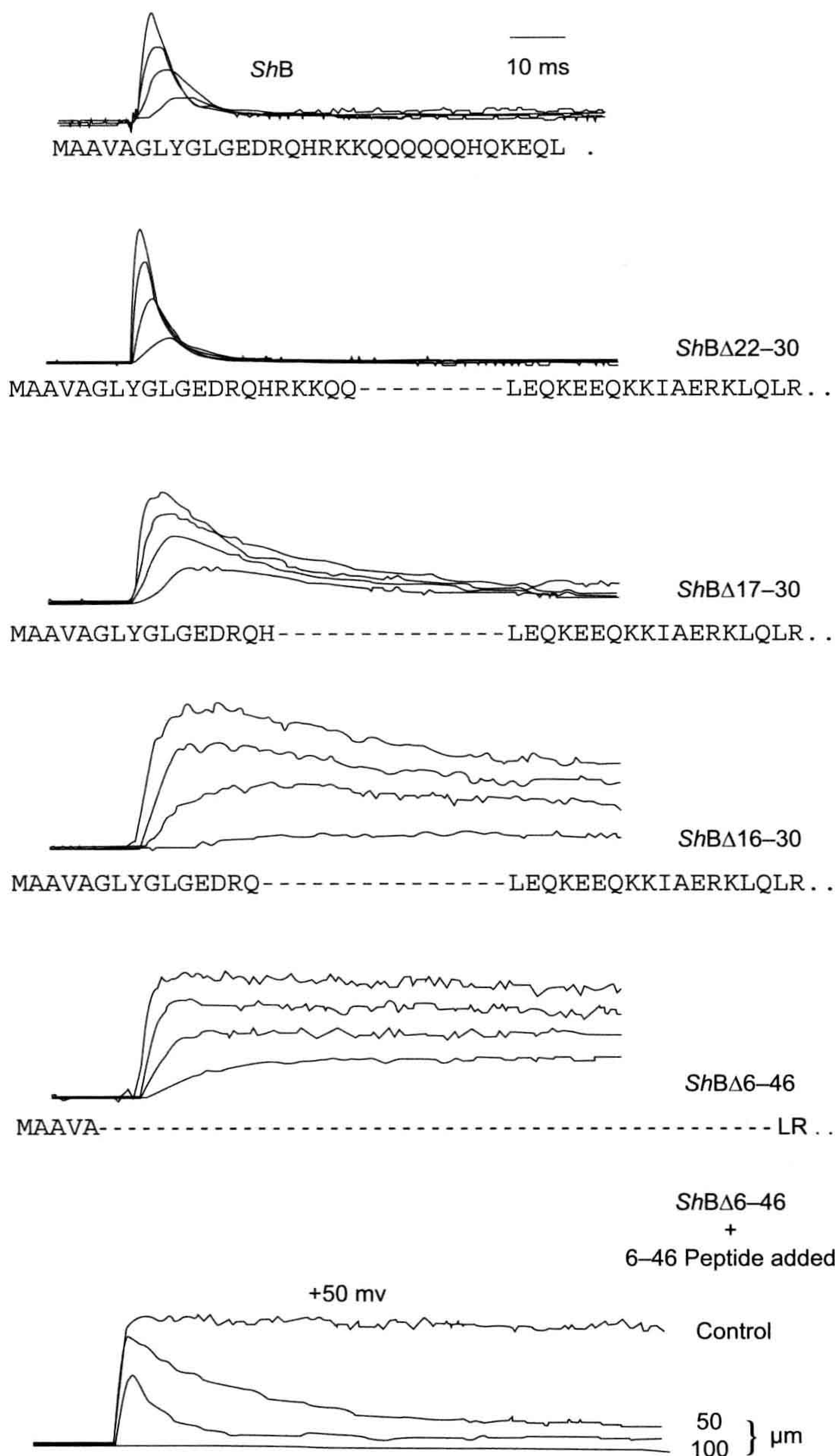


FIGURE 21.14 Identification of a putative ball and chain in *Shaker* B channels expressed in oocytes. Panels 2–5 from the top show the effect of deleting increasing lengths of a segment near the N terminus of the *Shaker* protein. Note that the deletion of residues 6–46 results in a non-inactivating K^+ current. The bottom panel shows that inactivation properties of this latter mutant may be restored by application of the synthetic 6–46 peptide to the inner channel surface in a dose-dependent fashion. *(Reorganized from Hoshi et al., 1990, and Zagotta et al., 1990.)*

Although the isotypes share considerable homology, there is still enough difference in the sequences to make it difficult to guess which residues might be responsible for activation kinetics. This problem was elegantly addressed by Beam, Tanabe and coworkers, who made chimeras of the two channels (Fig. 21.15; Tanabe et al., 1991). To focus the mutagenesis, it was reasoned that only the predicted transmembrane repeats should be involved in voltage-gated activation. Thus, the chimeras swapped the homologous repeats among constructs. As shown in

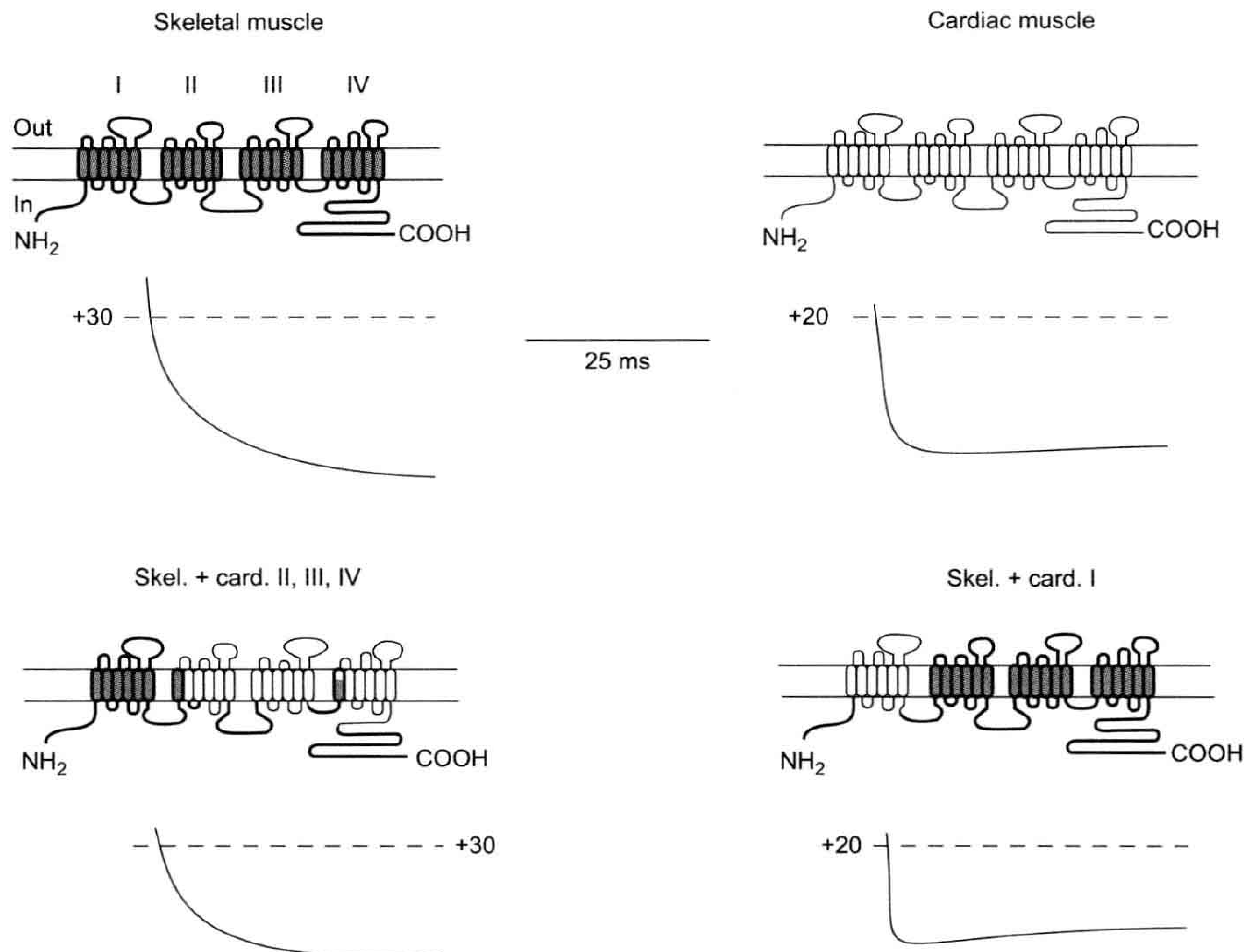


FIGURE 21.15 Identification of regions determining activation kinetics in L-type Ca^{2+} channels from skeletal muscle and heart. In these experiments, hybrids (chimeras) of skeletal muscle and cardiac channels were made in various combinations to localize the domains responsible for the differences in Ca^{2+} current activation kinetics in heart and skeletal muscle. cDNA encoding each construct was injected in cultured muscle cells (myotubes) from mutant mice unable to synthesize active L-type channels. Thus, these mutant cells would express only currents resulting from the genetically engineered DNA introduced into them. The top two panels show the current kinetics resulting from DNA encoding the wild-type skeletal muscle and cardiac channels. The bottom panels show two chimeras in which current kinetics correlate with the donor of repeat domain I. Most of the other possible combinations of channels were also made, with the same correlation of kinetics with domain I. *(Redrawn from Tanabe et al., 1991.)*

Fig. 21.15, the kinetics of activation correlate almost completely with the kinetics of the donor of the first (I) repeat. This finding suggests that despite their approximate homology, the repeats in a given channel contribute differently to gating properties. This is perhaps expected from the observation that the S4 regions among these domains in different channels have somewhat different structures and numbers of charges (e.g. see Fig. 21.10). Having identified the domain responsible, these investigators have been able to narrow their search to shorter segments and, ultimately, will identify the residues involved in this activation phenomenon (Nakai et al., 1994).

VG. Pore Formation and Ion Selectivity

Pores are the defining structures of all ion channels. As such, they provide both an aqueous pathway for ions to traverse the membrane as well as a means for discriminating among ions for access to this path. Studies of the mechanisms of pores provide an especially vivid example of the integration of theoretical modeling, mutagenesis and molecular structural approaches.

Even before the advent of structural studies, Hille hypothesized that ion selectivity and pore formation were performed by the same parts of the channel structure. Experimental evidence also indicated that charged or polar oxygen groups lined the narrowest region of the pore, where cation recognition occurs (see Hille, 1992). This latter finding was a sensible one considering the chemistry of cations in solution. In aqueous solution, metal cations such K^+, Na^+ and Ca^{2+} are stabilized by electrostatic interaction with the electronegative oxygen atoms of water molecules. In the narrowest region of the pore, water molecules must be removed in order for the channel to recognize the preferred cation; lining this narrow region with oxygen-bearing groups provides a chemically favorable *selectivity filter*.

Based on this early work, investigators sought short protein segments that might line the aqueous pore with oxygen atoms. A candidate sequence was initially identified using sophisticated analysis of primary sequence information (Guy and Seetharamulu, 1986). This sequence is 20–25 amino acids long and forms part of the loop connecting the fifth and sixth predicted transmembrane helices in the voltage-gated cation channels (see Figs. 21.6, 21.7 and 21.8). Tests of this putative pore-lining loop's (P-loop) role in pore formation were soon forthcoming.

One type of test was to determine whether site-directed mutations in the P-loop sequence affected the action of known pore-blocking agents on heterologously expressed mutant channels. Among the agents tested in this way were the K^+ channel-blockers tetraethylammonium and charybdotoxin and the Na^+ channel-blocker tetrodotoxin (MacKinnon and Yellen, 1990; MacKinnon et al., 1990; Terlau et al., 1991). Block by the externally effective agents tetrodotoxin or charybdotoxin was specifically affected by mutations at the extracellular end of the P-loop. Tetraethylammonium block of K^+ channels, which occurs by blocker binding at either end of the narrow pore, was altered by mutations at both ends of the P-loop. Results such as these confirmed that the P-loop does indeed form at least part of the pore in voltage-gated ion channels. Does the P-loop also form the ion selectivity filter?

The answer to this question also comes from site-directed mutagenesis studies. In *Shaker*-type K^+ channels, point mutations introduced into the P-loop profoundly altered the channel's preference for K^+ over Rb^+ or NH_4^+ as shown in Fig. 21.16 (Yool and Schwarz, 1991). However, non-conducting channels were produced whenever mutations were introduced into one stretch of eight amino acids in K^+ channel P-loops. This so-called *K^+ channel signature sequence* is highly conserved in K^+ channels found in bacteria to humans and it was therefore suspected of forming the narrow selectivity filter in K^+ channels.

Site-directed mutations in the P-loops of Na^+ channels and Ca^{2+} channels also affect ion selectivity (Heinemann et al., 1992; Yang et al., 1993). In Na^+ channels, a locus of four residues has been identified that confers selectivity for Na^+ over Ca^{2+} (Fig. 21.17). Each of the four P-loops of

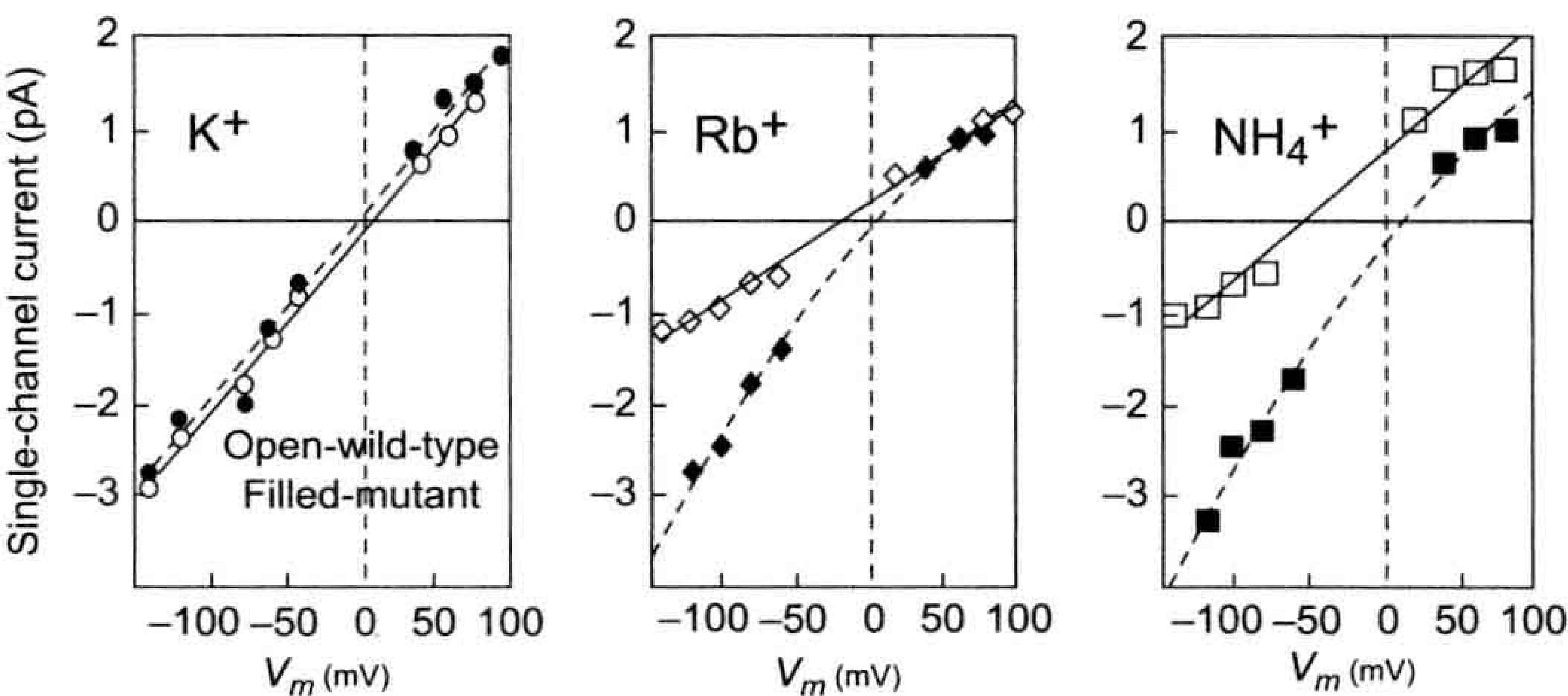


FIGURE 21.16 Alteration of *Shaker* B K^+ channel ion selectivity caused by a mutation in the putative pore-forming region. In these experiments, Phe 433 was mutated to Ser. The oocyte system used to express both wild-type and mutant channels is described in the text. Single-channel currents were measured using patch-clamp methods in which the ion indicated in each panel was applied to the external surface of the channel with K^+ on the inside in all cases. In these bi-ionic conditions, inward (negative) currents will be carried mainly by the test ion, while outward (positive) currents will be mostly K^+ ion fluxes. As can be seen from the increased inward currents, permeability of the channel to Rb and NH_4 ions was greatly enhanced in the mutants, while K^+ was unaffected. *(Data redrawn from Yool and Schwarz, 1991.)*

	Motif I					*Motif II*					*Motif III*					*Motif IV*				
	−2	−1	0	1	2	−2	−1	0	1	2	−2	−1	0	1	2	−2	−1	0	1	2
CaCh	T	M	E	G	W	T	G	E	D	W	T	f	E	G	W	T	G	E	A	W
NaCh	T	Q	D	X	W	C	G	E	-	W	T	F	K	G	W	T	S	A	G	W

FIGURE 21.17 Alignment of Ca^{2+} and Na^+ channel pore sequences. Position 0 in the alignments (shaded) marks the critical residues in the selectivity filter (EEEE locus in Ca^{2+} channels; DEKA locus in Na^+ channels). High-voltage–activated calcium channels are identical to one another in these pore sequences, except at the ñ1 position in motif III: the "f" indicates that this position is occupied by either Phe (F) or Gly (G). In sodium channels, the residue at the +1 position in motif I (x) varies depending on channel isoform. Na^+ channel sensitivity to tetrodotoxin depends partly on the residue present at this position.

a Na^+ channel contributes one residue to the locus, which includes two carboxylate-bearing residues (Asp, Glu) and two non-carboxylate residues (Lys, Ala). Substitution of Glu residues for the Lys and Ala residues dramatically reduces Na^+ selectivity and allows significant amounts of Ca^{2+} to permeate this mutant Na^+ channel. The analogous locus in Ca^{2+} channels is comprised of four Glu residues. Functional analysis of the effects of mutations in this locus has shown that these four Glu residues form the core of the selectivity filter in Ca^{2+} channels (Ellinor et al., 1995).

As described above, oxygen atoms have long been thought to line the selectivity filter in voltage-gated, cation-selective channels. The presence of multiple carboxylate groups in the selectivity filters of Ca^{2+} and Na^+ channels is consonant with the earlier work although, in principle, the carboxylates may either project into the pore or away from it. In fact, Ca^{2+} channel carboxylate groups apparently project into the aqueous pore and thereby provide the electronegative oxygen atoms needed to stabilize Ca^{2+} there. Evidence supporting this picture of selectivity filter structure derives from the fact that protonation of these carboxylate groups blocks current through Ca^{2+} channels; mutational replacement of the carboxylates by non-protonatable groups predictably alters proton block. Orientation of selectivity filter side chains has also been investigated using a technique called the "substituted cysteine accessibility method". In this method, a sulfhydryl-containing Cys residue is substituted for the wild-type residue and a sulfhydryl-modifying agent is bath-applied to the mutant channel. If the side-chain of the substituted Cys projects into the pore, where it may be accessible to the sulfhydryl-modifying agent, then the modifying agent will attach itself to the Cys sulfhydryl and obstruct ion flow. Interruption of channel current thus reports that a particular side chain is oriented into the aqueous pore, whereas absence of block indicates that the side chain faces away from the pore. Application of this method to Na^+ and Ca^{2+} channels indicates that the side chains in the carboxylate-containing loci of these channels all project into the pore (Chiamvimonvat et al., 1996). The extreme narrowness of K^+ channel pores has prevented this technique from being effectively employed with these channels. However, the selectivity filter of K^+ channels may be structurally distinct from that of Ca^{2+} channels and perhaps Na^+ channels.

VH. Crystal Structure of a Bacterial K^+ Channel Pore Region

Results of these site-directed mutagenesis studies have been strikingly confirmed by the first x-ray crystallographic structure obtained for a member of the family of voltage-gated ion channels (Doyle et al., 1998). This structure was solved for a bacterial K^+ channel, which though not in fact voltage-gated, is nevertheless a member of the family of voltage-gated ion channels: most significantly, it possesses the hallmark of all K^+ selective channels, the K^+ channel signature sequence. The crystal structure reveals that the selectivity filter is formed by part of the P-loop, with two K^+ ions stabilized therein, probably by main-chain carbonyl oxygen atoms (Fig. 21.18). That uncharged carbonyl oxygens apparently line the selectivity filter in the bacterial K^+ channel actually agrees with predictions, based on mutagenesis studies, for other K^+ channels.

Why might K^+ channels have evolved a selectivity structure that employs neutral, main-chain carbonyl oxygen atoms, whereas their evolutionary descendants, Ca^{2+} channels, apparently line their selectivity filter with negatively charged, side-chain carboxylate oxygens? Perhaps the negative charge of carboxylate oxygens is necessary in selecting for Ca^{2+}, a charge-dense divalent cation, whereas uncharged carbonyl oxygen atoms are ideal in selecting for certain monovalent cations, such as K^+. How then to account for Na^+ channel selectivity structure? Na^+ channels have evolved from Ca^{2+} channels and the Na^+ channel selectivity filter apparently includes two side-chain carboxylate oxygens. K^+ and Na^+ have the same ionic charge but Na^+ has a higher charge density owing to its smaller ionic radius. As in the case for Ca^{2+}, the relatively high charge density of Na^+ may require carboxylate oxygens for selectivity, though only two rather than the four present in the Ca^{2+} channel selectivity filter.

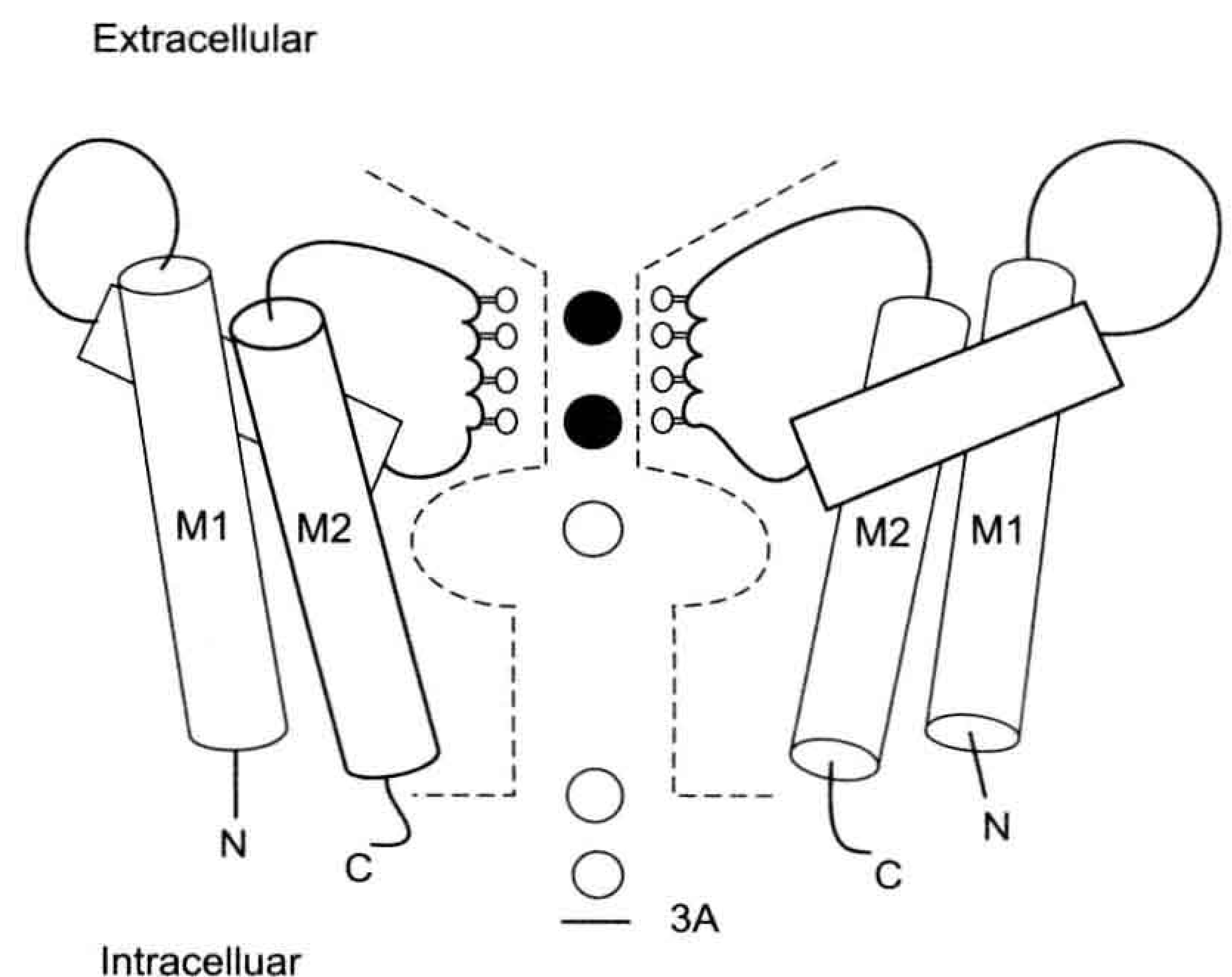


FIGURE 21.18 Cartoon illustration of the bacterial K^+ channel structure. Only two of the four subunits of the channel are shown. Each subunit has a P-loop and two helices (M1, M2), similar to the structure of inwardly rectifying K^+ channels. The segment of the P-loop that lines the ion permeation pathway projects carbonyl oxygen atoms into the pore. A pair of K^+ ions is shown stabilized in the selectivity filter by the rings of carbonyl oxygens. *(Adapted with permission from Choe, S. and Robinson, R. (1998). An ingenious filter: the structural basis for ion channel selectivity. Neuron. 20, 821–823. Copyright 1998 Cell Press.)*

VI. ISOFORMS OF VOLTAGE-GATED CHANNELS AS PART OF A LARGE SUPERFAMILY

One of the most striking results of recombinant DNA analysis of channel clones has been the discovery of numerous channel *isoforms* expressed within the same organism and even within the same cell. Naturally, some degree of homology among channels of different organisms was expected and electrophysiological recordings showed that channels could be functionally diverse at the cellular level. Even a structural similarity among Na^+, Ca^{2+} and K^+ channels had been predicted by some investigators. However, the number and diversity of channels within a single organism revealed by molecular biology were rather unexpected. Channels of a functionally similar class (usually based on ion selectivity) are now called *isotypes* or *isoforms* by analogy to the phenomenon of isoenzymes.

We have previously discussed the *Shaker* isotypes. *Shaker*-derived sequences have also been used to construct probes that have discovered other families of K^+ channels in flies, mammals and other species (Salkoff et al., 1992). These families are so extensive that they challenge investigators to develop appropriate nomenclature for their classification (Table 21.3; Chandy and Gutman, 1995). In any case, although they are all to some degree homologous with the original *Shaker* family, they have much higher degrees of sequence homology among members of their class. Functionally, they run the gamut from inactivating A-type channels to non-inactivating channels of the classic delayed rectifier sort. Interestingly, there is usually a much higher degree of sequence homology among channels of the same class from different animals than there is between channels of separate classes in the same animal. For example, *Shaker* channels from *Drosophila* are much more homologous to *Shaker* channels of mouse brain than they are to the *Drosophila Shab*-type channels.

Recently, several other subfamilies of K^+ channels have been discovered in mammalian and invertebrate genomes. Two of these, the *erg* and KQT subfamilies, are important in mammalian cardiac function. Mutants of these channels have been associated with serious inherited heart and nervous system disorders in humans, in particular the long QT syndrome discussed in other chapters in this book. In any case, in mammals the number of K^+ channel isoforms is already quite large: currently there are 12 known potassium channel subfamilies totaling over 100 isoforms, with more being discovered at frequent intervals (see Coetzee et al., 1999).

Considerable diversity is also found among Na^+ and Ca^{2+} channels (Agnew and Trimmer, 1989; Hofmann et al., 1994). For the main channel-forming α subunits (see Figs. 21.6 and 21.7), there are thought to be at least 10 Na^+ channel and nine Ca^{2+} channel genes in the mammalian genome. Some of these isoforms are expressed very selectively in certain tissues, such as brain, or in only certain cells types or at very specific stages of development.

The term "isoform" is rather non-specific in that it does not convey a sense of relative relatedness among channels. An evolving system of classification refers to the set of voltage-gated channels as a *superfamily*, while the selectivity types (i.e. Na^+, Ca^{2+} or K^+ channels) form families. Because of the impressive degree of diversity found for K^+ channels (see Table 21.3), investigators have formally proposed a uniform system of nomenclature in which the closely related isoforms such as *Shaker* are referred to as subfamilies. A separate nomenclature for isoforms of Ca^{2+} channel subunits has also been developed. Further consideration of channel classification will undoubtedly be useful in understanding the process of channel evolution.

VIA. How Do Isoforms Arise?

In general, two separate mechanisms that create such diversity have been identified. First, there is the expected situation in which distinctly separate genes encode different channels in the same beast. Such is largely the situation for mammalian Na^+ channel and Ca^{2+} channel

TABLE 21.3 Properties of Major Potassium Channel Subfamilies in Fruit Flies and Mammals

Drosophila Gene	Homologous Mammalian Genes (no.)	Properties
Shaker	Kv1.1–1.7 (7)	Extensively spliced in fly; inactivation fast to slow
Shab	Kv2.1, 2.2 (2)	Limited splicing in fly; intermediate inactivation kinetics
Shaw	Kv3.1–3.4 (4)	Limited splicing in fly and mammal; slow inactivation, delayed rectifier characteristics
Shal	Kv4.1–4.3 (3)	Limited splicing in fly; slow inactivation, delayed rectifier characteristics
eag	h-erg (3)	Limited splicing in fly and mammals; slow-activation delayed rectifier

isoforms. However, a second mechanism has been found, called *alternative splicing*, in which a given segment of a channel polypeptide may be encoded in several different stretches of genomic DNA known as *exons*. This is the case for *Shaker* in *Drosophila;* thus, in Fig. 21.12, the various *Shaker* isoforms are generated by mixing and matching the transcripts of different exons. During transcription, some sort of regulatory mechanism exists that decides which one of the alternative coding RNAs for a given segment will be incorporated in the final mRNA. The other undesired homologous segments are then excised from the transcript and the desired RNA segments are spliced together. Currently, there is evidence for the operation of both mechanisms in vertebrates and invertebrates. However, most mammalian systems studied to date appear to rely more heavily on separate genes than alternative splicing whereas, in the fruit fly, both mechanisms appear common.

Finally, for all multisubunit channels there is the possibility of diversification through various combinations of each set of subunit isotypes. The best-studied examples are the heteromeric formation of channels by different K^+ channel subunit isotypes (Salkoff et al., 1992). For example, if the same cell synthesized *Shaker* A and *Shaker* B channel subunits, one might find heteromeric complexes of A and B types as well as the homomeric types. In fact, experiments with the oocyte expression system into which both types of mRNA have been injected show that such heteromeric assembly can occur, yielding functional channels with characteristics different from homomultimers of either channel type. Thus, it is theoretically possible that distinct channel properties may be generated by heteromeric assembly of K^+ channel subunits. Whether this occurs in nature is currently being investigated.

On the other hand, oocyte experiments show that heteromeric association among subunits from different families (e.g. *Shaker* and *Shal*) does not occur. Apparently different families have unique structural domains that allow only homomeric assembly among members of their family. This discovery has led to a recent set of chimeric experiments in which domains among a fly *Shaker* channel and a distantly related mammalian delayed rectifier channel (*drkl*) were exchanged in an attempt to identify the segments specifying assembly specificity (Li et al., 1992). Such a segment was found on the N-terminal part of the peptide. Thus, substitution of the *Shaker* segment into the *drkl* cDNA produced a channel *drkl* subunit that was able to co-assemble with native *Shaker.*

VIB. Why Are Channels So Diverse in a Given Organism?

One obvious reason for the presence of so many channel isotypes in the same animal is that each isotype has different functional properties that are appropriate to the function of its host cell. For example, high-frequency, repetitive firing requires short-duration action potentials that could be created by rapidly gating Na^+ channels and fast-inactivating A-type K^+ channels. In addition, isotypes may be differentially sensitive to intracellular modulators that allow cellular mechanisms to alter the properties of specific channels selectively in response to physiological effectors. On the other hand, many of the discovered isotypes have no significant functional differences among them. In this case, it is possible that it is not the differences in the channels themselves that are important, but rather the way the isotypes are expressed. Thus, in a number of cases it has been shown that expression of one isotype over another occurs developmentally or in response to a physiological stimulus (Ribera and Spitzer, 1992). Such specific expression is thought to be controlled by genetic elements outside the coding region for the channel, known as regulatory elements. These stretches of DNA respond specifically to one of many possible soluble factors by increasing (in the case of promoters and enhancers) or inhibiting (silencers) transcription of the channel gene (see Maue et al., 1990). Separate genes, then, potentially allow the cell to express selectively a given channel in response to a given stimulus or at a specific time during development. Finally, there is the possibility that a given isotype sequence encodes information used by the cellular machinery to localize or cluster it in very discrete locations, such as the nodes of Ranvier in myelinated nerve fibers (Dugandzija-Novakovic et al., 1995), neuronal cell bodies, or dendrites (Maletic-Savatic et al., 1994). The study of the diversity of channels and their biological purpose will continue to be a highly active area of cell biology for some time.

VII. FUTURE DIRECTIONS

The current molecular biological approaches will no doubt be productive for some time. However, it is likely that better understanding of channel mechanism will require more direct and precise resolution of the higher order structure of channel molecules. The problems inherent in a crystallographic approach have been discussed. However, the problem is currently being solved by recombinantly synthesizing smaller segments of channel proteins that may be amenable to crystal formation. To be useful, these small segments must retain a significant part of the structure they have in the original protein (a serious concern). Alternatively, small segments may be structurally studied using advanced spectroscopic techniques, such as magnetic resonance. Finally, some important information has been obtained by direct imaging of purified channels using electron microscopy and modern instruments that promise greatly improved resolution at the molecular level are being developed. Finally, the study of the genetic regulation of channel expression will be expanded through the further

study of regulatory domains in the DNA. This will undoubtedly increase our appreciation of ion channels as important elements in the metabolism of the entire organism.

BIBLIOGRAPHY

Agnew, W. S., & Trimmer, J. (1989). Molecular diversity of voltage-sensitive sodium channels. *Annu Rev Physiol, 51*, 401–418.

Aldrich, R. W., Hoshi, T., & Zagotta, W. N. (1990). Differences in gating among amino terminal variants of Shaker potassium channels. *Cold Spring Harbor Symp Quant Biol, 55*, 19–27.

Armstrong, C. M., & Bezanilla, F. (1977). Inactivation of the sodium channel. II. Gating current experiments. *J Gen Physiol, 70*, 567–590.

Catterall, W. A. (1988). Molecular properties of dihydropyridine sensitive calcium channels in skeletal muscle. *J Biol Chem, 263*, 3535–3538.

Catterall, W. A. (1992). Cellular and molecular biology of voltage-gated sodium channels. *Physiol Rev*, (Suppl. 72), S15–S48.

Chandy, K. G., & Gutman, G. A. (1995). Voltage-gated K^+ channel genes. In R. A. North (Ed.), *CRC Handbook of Receptors and Channels* (pp. 1–71). Boca Raton: CRC Press.

Chiamvimonvat, N., Perez-Garcia, M. T., Ranjan, R., Marban, E., & Tomaselli, G. F. (1996). Depth asymmetries of the pore-lining segments of the Na^+ channel revealed by cysteine mutagenesis. *Neuron, 16*, 1037–1047.

Chou, P. Y., & Fasman, G. D. (1978). Empirical predictions of protein conformation. *Annu Rev Biochem, 47*, 251–276.

Coetzee, W. A., Amarillo, Y., Chiu, J., et al. (1999). Molecular diversity of K^+ channels. *Ann NY Acad Sci., 868*, 233–285.

Doyle, D. A., Cabral, J. M., Pfuetzner, R. A., et al. (1998). The structure of the potassium channel: molecular basis of K^+ conduction and selectivity. *Science, 280*, 69–77.

Dugandzija-Novakovic, S., Koszowski, A. G., Levinson, S. R., & Shrager, P. (1995). Clustering of K^+ channels and node of Ranvier formation in remyelinating axons. *J Neurosci, 15*, 492–503.

Ellinor, P. T., Yang, J., Sather, W. A., Zhang, J.-F., & Tsien, R. (1995). Ca^{2+} channel selectivity at a single locus for high affinity Ca^{2+} interactions. *Neuron, 15*, 1121–1132.

Guy, H. R., & Seetharamulu, P. (1986). Molecular model of the action potential sodium channel. *Proc Natl Acad Sci, USA, 83*, 508–512.

Heinemann, S. H., Terlau, H., Stuhmer, W., Imoto, K., & Numa, S. (1992). Calcium channel characteristics conferred on the sodium channel by single mutations. *Nature, 356*, 441–443.

Hille, B. (1992). *Ionic Channels of Excitable Membranes*. Sunderland: Sinauer Associates.

Hofmann, F., Biel, M., & Flockerzi, V. (1994). Molecular basis for Ca^{2+} channel diversity. *Ann Rev Neurosci, 17*, 399–418.

Hoshi, T., Zagotta, W. N., & Aldrich, R. W. (1990). Biophysical and molecular mechanisms of Shaker potassium channel inactivation. *Science, 250*, 533–538.

Isom, L. L., De Jongh, K. S., Patton, D. E., et al. (1992). Primary structure and functional expression of the β_1 subunit of the rat brain sodium channel. *Science, 256*, 839–842.

Kyte, J., & Doolittle, R. F. (1982). A simple method for displaying the hydropathic character of a protein. *J Mol Biol, 157*, 105–132.

Leonard, J., & Snutch, T. P. (1991). The expression of neurotransmitter receptors and ion channels in Xenopus oocytes. In D. M. Glover, & B. D. Hanes (Eds.), *Molecular Neurobiology: a Practical Approach* (pp. 161–182). New York: Oxford University Press.

Li, M., Jan, Y. N., & Jan, L. Y. (1992). Specification of subunit assembly by the hydrophilic amino-terminal domain of the Shaker potassium channel. *Science, 257*, 1225–1230.

Lopez, G. A., Jan, Y. N., & Jan, L. Y. (1991). Hydrophobic substitution mutations in the S4 sequence alter voltage-dependent gating in Shaker K^+ channels. *Neuron, 7*, 327–336.

MacKinnon, R., Heginbotham, L., & Abramson, T. (1990). Mapping the receptor site for charybdotoxin, a pore-blocking potassium channel inhibitor. *Neuron, 5*, 767–771.

MacKinnon, R., & Yellen, G. (1990). Mutations affecting TEA blockade and ion permeation in voltage-activated K^+ channels. *Science, 250*, 276–279.

MacKinnon, R. (1991). Determination of the subunit stoichiometry of a voltage-activated potassium channel. *Nature, (London), 350*, 232–235.

Maletic-Savatic, M., Lenn, N. J., & Trimmer, J. S. (1994). Differential spatiotemporal expression of K^+ channel polypeptides in rat hippocampal neurons developing in situ and in vitro. *J Neurosci, 15*, 3840–3851.

Maue, R. A., Kraner, S. D., Goodman, R. H., & Mandel, G. (1990). Neuron-specific expression of the rat brain type II sodium channel gene is directed by upstream regulatory elements. *Neuron, 4*, 22–231.

Miller, C. (Ed.), (1986). *Ion Channel Reconstitution*. New York: Plenum.

Miller, J. A., Agnew, W. S., & Levinson, S. R. (1983). Principal glycopeptide of the tetrodotoxin/saxitoxin binding protein from *Electrophorus electricus*: isolation and partial physical and chemical characterization. *Biochemistry, 22*, 462–470.

Nakai, J., Adams, B. A., Imoto, K., & Beam, K. G. (1994). Critical roles of the S3-segment and S3–S4 linker of repeat I in activation of L-type calcium channels. *Proc Natl Acad Sci, USA, 91*, 1014–1018.

Noda, M., Shimizu, S., Tanabe, T., et al. (1984). Primary structure of *Electrophorus electricus* sodium channel deduced from cDNA sequence. *Nature, 312*, 121–127.

Numa, S., & Noda, M. (1986). Molecular structure of sodium channels. *Ann NY Acad Sci, 479*, 338–355.

Papazian, D. M., Timpe, L. C., Jan, Y. N., & Jan, L. Y. (1987). Cloning of genomic and complementary DNA from Shaker, a putative potassium channel gene from Drosophila. *Science, 237*, 749–753.

Papazian, D. M., Timpe, L. C., Jan, Y. N., & Jan, L. Y. (1991). Alteration of voltage- dependence of Shaker potassium channel by mutations in the S4 sequence. *Nature, 349*, 305–310.

Pongs, O. (1992). Molecular biology of voltage-dependent potassium channels. *Physiol Revs*, (Suppl. 72), S69–S88.

Ribera, A. B., & Spitzer, N. C. (1992). Developmental regulation of potassium channels and the impact on neuronal differentiation. In T. Narahashi (Ed.), *Ion Channels, Vol. 3* (pp. 1–38). New York: Plenum Press.

Salkoff, L., Baker, K., Butler, A., Covarrubias, M., Pak, M. D., & Wei, A. (1992). An essential set of K^+ channels conserved in flies, mice, and humans. *TINS, 15*, 161–166.

Sharp, A. H., Imagawa, T., Leung, A. T., & Campbell, K. P. (1987). Identification and characterization of the dihydropyridine-binding subunit of the skeletal muscle dihydropyridine receptor. *J Biol Chem, 262*, 12 309–12 315.

Sigworth, F. J. (1995). Charge movement in the sodium channel. *J Gen Physiol, 106*, 1047–1051.

Stuhmer, W., Conti, F., Suzuki, H., et al. (1989). Structural parts involved in the activation and inactivation of sodium channels. *Nature, 339*, 597–603.

Tanabe, T., Adams, B. A., Numa, S., & Beam, K. G. (1991). Repeat I of the dihydropyridine receptor is critical in determining sodium channel activation kinetics. *Nature, 352*, 800–803.

Tanabe, T., Takeshima, H., Mikami, A., et al. (1987). Primary structure of the receptor for calcium channel blockers from skeletal muscle. *Nature, 328*, 313–318.

Terlau, H., Heinemann, S. H., Stuhmer, W., et al. (1991). Mapping the site of block by tetrodotoxin and saxitoxin of sodium channel II. *FEBS Lett, 293*, 93–96.

Timpe, L. C., Jan, Y. N., & Jan, L. Y. (1988). Four cDNA clones from the Shaker locus of Drosophila induce kinetically distinct A-type potassium currents in Xenopus oocytes. *Neuron, 1*, 659–667.

Vassilev, P., Scheuer, T., & Catterall, W. A. (1989). Inhibition of inactivation of single sodium channels by a site-directed antibody. *Proc Natl Acad Sci, USA, 86*, 8147–8151.

Yang, J., Ellinor, P. T., Sather, W. A., Zhang, J.-F., & Tsien, R. W. (1993). Molecular determinants of Ca^{2+} selectivity and ion permeation in L-type Ca^{2+} channels. *Nature, 366*, 158–161.

Yool, A. J., & Schwarz, T. L. (1991). Alteration of ionic selectivity of a K^+ channel by mutation of the H5 region. *Nature, 349*, 700–704.

Zagotta, W. N., Hoshi, T., & Aldrich, R. W. (1990). Restoration of inactivation in mutants of Shaker potassium channels by a peptide derived from ShB [see comments]. *Science, 250*, 568–571.

Chapter 22

Biology of Gap Junctions

Richard D. Veenstra

Chapter Outline

I. INTRODUCTION

In the late 1950s and early 1960s, physiologists who had been poking fine glass current-injecting and current-recording electrodes into neighboring cells within a variety of tissues made an interesting discovery. They found that while the injection of current into a cell caused a predictable shift in its non-junctional membrane potential, it also caused a similar shift in the non-junctional membrane potential of immediately adjacent cells (Fig. 22.1).

One interpretation of this finding was that the ions emanating from the injection electrode were able to flow freely from the injected cell to the adjacent cell and did so in preference to pathways leading to the extracellular medium or to the intercellular space. Moreover, several studies demonstrated that fluorescent dyes were selectively transferred from cell to cell when injected into the cytoplasm through glass injection pipettes. Many observations such as these led to the hypothesis that some cells were coupled (electrically or with respect to dye transfer) by *permeable cell junctions*.

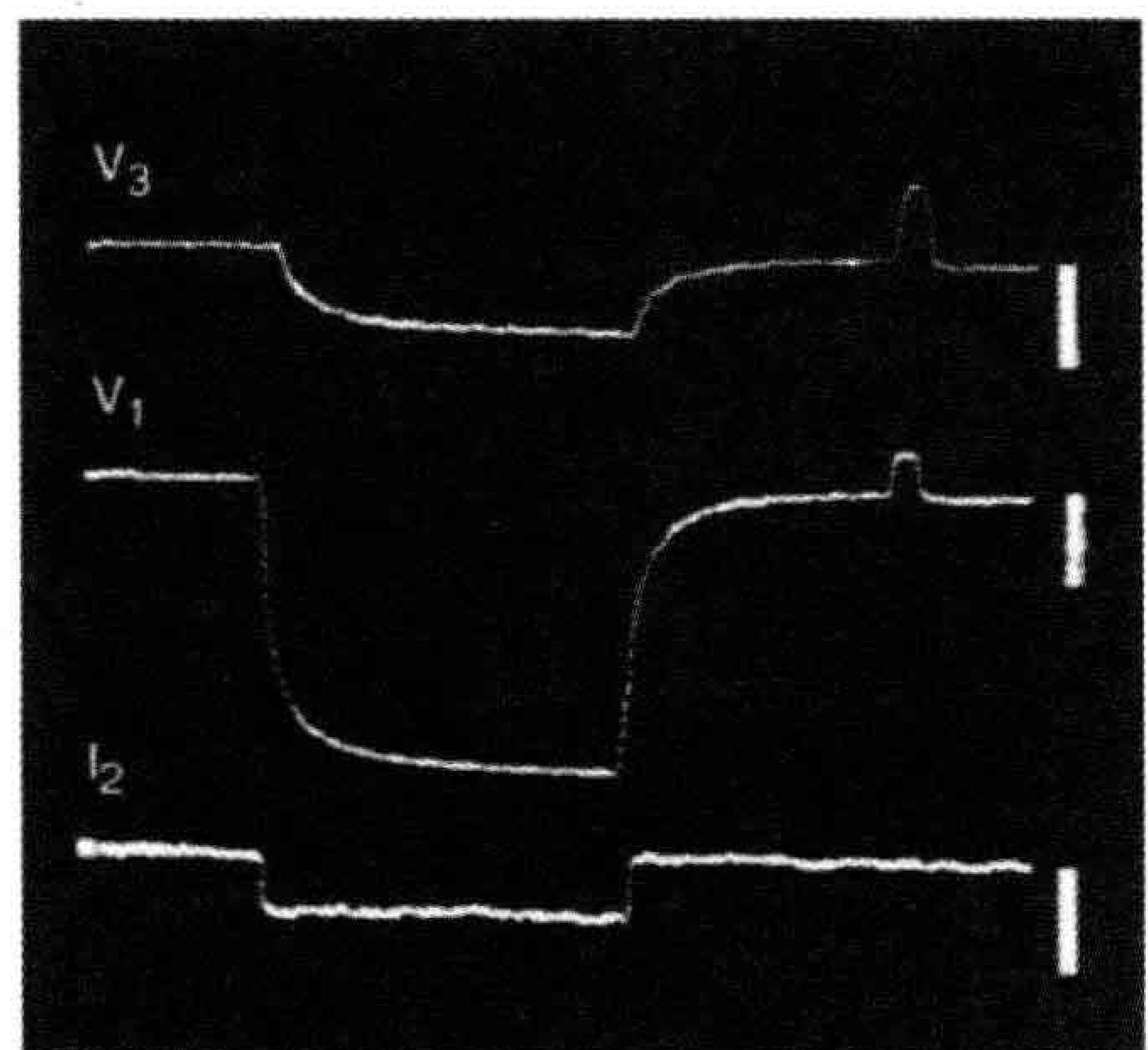


FIGURE 22.1 The injection of current into one cultured WI-26 cell (I2) within a monolayer produces a shift in potential within the injected cell (V1) and in a cell two or three cells removed from the injected cell (V3), indicating that ions may move freely between contacting cells. *(From Furshpan, E.J. and Potter, D D. (1968). Low-resistance junctions between cells in embryos and tissue culture. Curr Top Dev Biol. 3, 95, with permission.)*

Cell Physiology Sourcebook. DOI: 10.1016/B978-0-12-387738-3.00022-6

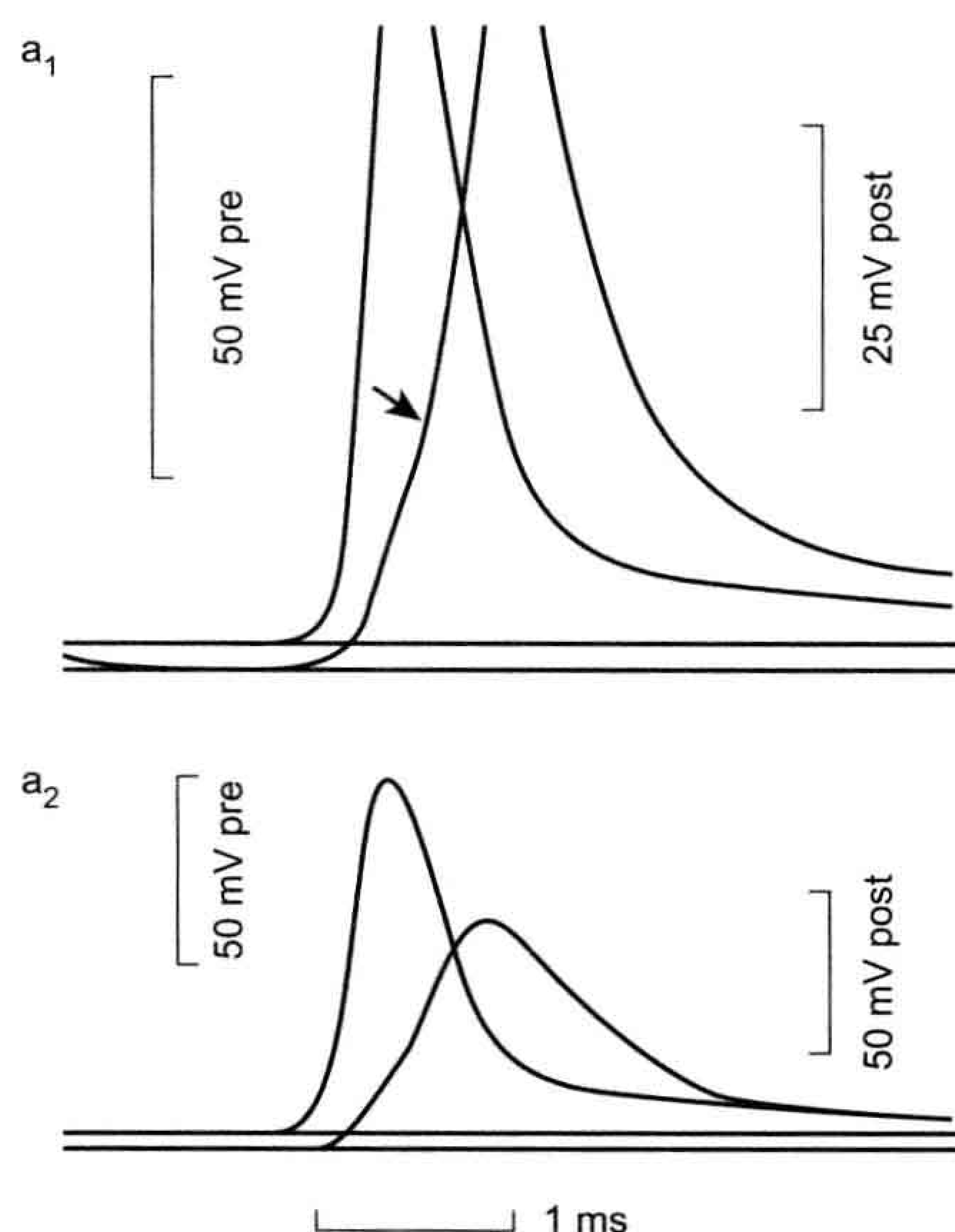


FIGURE 22.2 The upper trace is an AP in the presynaptic element of a crayfish septate axon; the lower trace shows the subsequent AP in the postsynaptic element. The short lag of the latter following the former is typical of electrical synapses. The top and bottom traces were recorded at the same synapse at different amplifications. *(From Furshpan, E.J. and Potter, D.D. (1959). Transmission at the giant motor synapses of the crayfish. J. Physiol. 145, 289, with permission.)*

Additionally, in the neuronal tissues in which this phenomenon had first been witnessed, it was found that action potentials generated in a presynaptic element could be passed to a postsynaptic element much faster than would occur if the presynaptic and postsynaptic elements were connected by chemical synapses (Fig. 22.2). Ironically, this evidence for the presence of permeable cell junctions that could serve as *electrical synapses* in the nervous system came to light soon after the common acceptance of Otto Loewi's findings that supported the idea that neuronal synapses were probably chemical in nature and not electrical as traditionally believed.

II. ADVANTAGES OF ELECTRICAL SYNAPSES IN EXCITABLE CELLS

The utility of electrical synapses in excitable cells is apparent. They may pass action potentials or subthreshold electrical activity more rapidly from one neuronal element to another than can their chemical counterparts. This advantage is especially obvious in neuronal pathways that serve as *escape mechanisms*, such as those in the tail muscles of crayfish and lobsters and those in the pectoral fins of fishes. In these cases, the rapidity of the animal's response to imminent danger has selective value. On the other hand, such permeable junctions connecting smooth muscle cells of the uterus or cardiac muscle cells of the heart wall, provide a mechanism for the systematic cell-to-cell spread of depolarization that is required for *coordinated and effective contractile activity.*

III. UBIQUITOUS MEMBRANE PERMEABLE JUNCTIONS

Numerous studies published in the 1960s and 1970s supported the idea that virtually all cells in normal tissues (even those in inexcitable tissues) were coupled by permeable cell junctions. Based on studies with native biological molecules and with tracers of different sizes, it was also suggested that the pores within vertebrate cell-to-cell junctions were approximately 1.2 nm in diameter and that molecules larger than about 1 kDa were excluded. Thus, it was suggested that the biological molecules capable of freely moving from cell to cell in normal tissues would include a wide range of ions and small metabolites including sugars, nucleotides and nucleosides and possible signaling molecules such as cyclic adenosine monophosphate (cAMP).

Since the pores initially appeared to select molecules only with respect to size, it was suggested that one function of permeable cell junctions was to buffer the concentrations of small metabolites throughout the tissue. Direct evidence for the cell contact-mediated exchange of metabolites, for example, was provided by metabolic cooperation experiments in which it was shown that a normal wild-type cell, able to incorporate thymidine into DNA, could transfer DNA precursor molecules (probably the nucleoside triphosphate form of thymidine) to mutant thymidine kinase-deficient cells only if the wild-type and mutant cell were in contact. In these "kiss-of-life" experiments, the mutant cells were then able to incorporate this nucleoside into DNA required for continued proliferation and survival.

IV. STRUCTURAL CANDIDATES FOR THE PERMEABLE CELL JUNCTION

As electron microscopes first came into common use in the late 1950s, several different kinds of cell–cell junctions were discovered. The *tight junction*, or *occludens-type junction*, was characterized by the fusion of membranes of adjacent cells and so held some appeal as a potential permeable cell junction. *Septate junctions* were also good candidates for the permeable cell junction since they were characterized by cell-to-cell bridges or septa covering a large region of cell–cell apposition in many of the invertebrate tissues shown to be well coupled by

electrophysiological or dye-tracing techniques. The basic argument against their function as permeable cell junctions, however, was that their distribution among tissues and organisms was significantly more limited than was the coupling phenomenon. The septate junction, for example, could not be identified in coupled vertebrate cells. The apparent fusion of plasmalemma between juxtaposed cells in mammalian smooth and cardiac muscle was termed the *nexus* in the early 1960s and was demonstrated to be the site of action potential propagation when hypertonic solutions that separated the nexal membranes also blocked action potential propagation.

V. ULTRASTRUCTURAL CHARACTERIZATION OF GAP JUNCTIONS AND CORRELATIONS WITH CELL COUPLING

In a pioneering study, Revel and Karnovsky (1967) infiltrated the intercellular spaces of heart and liver with an electron opaque dye (lanthanum hydroxide) and then examined these preparations in the electron microscope. They found regions where the membranes of adjacent cells were apposed to one another across a uniform lanthanum-infiltrated intercellular space about 2–4 nm in width (Fig. 22.3B). In addition, in cross-section, they observed small unstained structures bridging the stain-filled gap between adjacent cells in these regions (Fig. 22.3A) and, in en face views, these bridges were packed hexagonally within the intercellular space. Ultimately, freeze-fracture studies provided evidence that these intercellular bridges were in continuity with structures that spanned the lipid bilayers of both cells and thereby could theoretically provide the structural foundation for the cell-to-cell conduit implied by earlier electrophysiological studies.

It was also very important that this cell–cell junction, which Revel and Karnovsky called the *gap junction*, was found in many tissues which were ion- or dye-coupled, including both inexcitable and excitable cells. While well-coupled inexcitable cells, such as liver hepatocytes, possessed large numbers of gap junctions, it was especially satisfying to find that these structures were prominent features of the cell–cell contact regions of excitable cells, such as cardiac myocytes, and were prominent in neuronal systems that had been shown to possess electrical synapses. In addition, in the metabolic cooperation experiments described above, DNA precursor molecules were transferred between test cells only if they were capable of forming gap junctions in regions of cell–cell contact. Moreover, a large body of ultrastructural evidence indicated that gap junctions were components of virtually all tissues in multicellular organisms of the animal kingdom (See Fig. 22.3C–J).

VI. MOLECULAR AND STRUCTURAL STUDIES OF GAP JUNCTION PROTEINS

Application of biochemical and molecular approaches to the study of gap junctions proved to be more perplexing than originally envisioned, but tenacious investigators in a number of laboratories were able to overcome initial obstacles. It is now known that proteins that make up gap junctions in vertebrate tissues are basic and contain significant stretches of hydrophobic sequence. This is not surprising given the fact that these are integral membrane proteins. For these reasons, they proved difficult to isolate and purify. Extraction of tissues with boiling sodium dodecyl sulfate (SDS) proved to be the only reliable method for obtaining morphologically pure fractions of gap junction membranes for many years, but the proteins extracted from these fractions ran at variable molecular weights on polyacrylamide gels. It was controversial as to whether some of these bands were breakdown products or other proteins associated with gap junctions in the cell membrane.

It was not until gentler, non-detergent extraction procedures were developed in the early 1980s that a consistent band on polyacrylamide gels with a predicted molecular weight of 26 kDa could be routinely isolated from rodent livers. Once this native protein was obtained and purified, it was possible to produce a polyclonal antibody. This antibody was used to screen an expression cDNA library to isolate and sequence its gene. This first sequence was published in 1986. Hydropathy analysis of the deduced amino acid sequence of this cDNA revealed a 32-kDa protein which could be interpreted as possessing four potential transmembrane regions, two extracellular loops and an internal loop and amino and carboxyl termini that extended into the cytoplasm (Fig. 22.4). The mapping of these proteins with antibodies directed against specific sequences and their cutting with specific proteases have largely confirmed this initial interpretation of the relationships of gap junction protein segments to the membrane. It was also postulated that six gap junction protein molecules, called *connexins*, constitute each gap junction intramembrane particle (IMP) or *connexon*, thus providing a molecular basis for models of the permeable membrane junction deduced from earlier physiological and structural studies (Figs. 22.4 and 22.5). Indeed, more recent electron cryomicroscopy studies of frozen, rehydrated 2D crystals of a recombinant C-terminal truncated form of Cx43 has revealed even more detail regarding the relationship of connexins to the connexon and the relationship of their specific transmembrane domains to the plasma membrane. These studies show that each connexin subunit contributes a transmembrane α-helix that lines the aqueous pore and an additional α- helix adjacent to the surrounding membrane lipids. In addition, the images

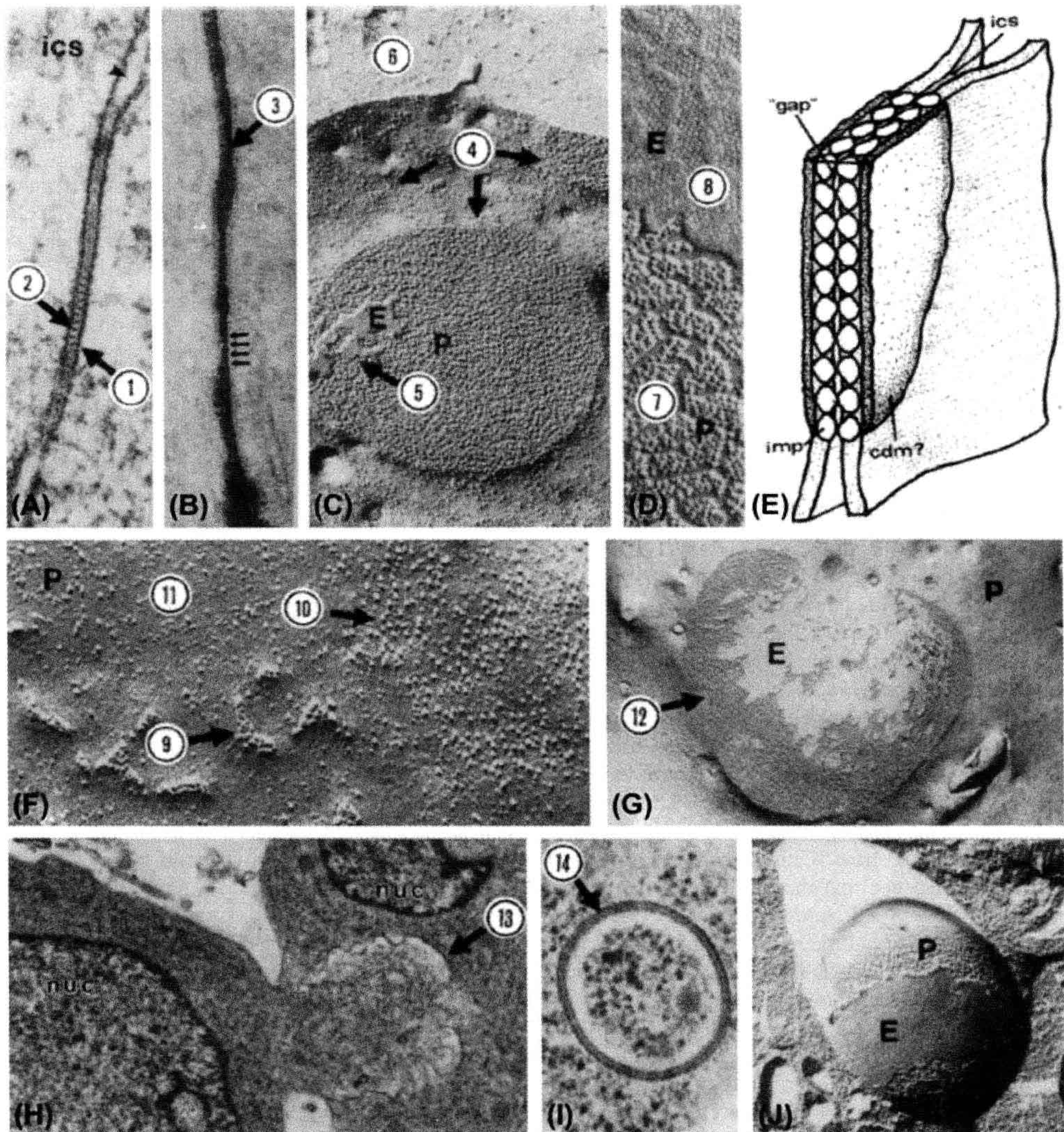


FIGURE 22.3 (A) Thin section of typical gap junction. The entire width of both apposed membranes and the intercellular space is about 18 nm. Dense material is often associated with cytoplasmic surface of gap junction (1). Some gap junctions are characterized by stained periodicites evident at level of "gap" (2). Magnification, 157 500×. *(From Larsen, W.J., Skowron-Lomneth, C. and Carron, C. (1988). Gap junction modulation: possible role in tumor cell behavior. In (H.A. Milman and E. Elmore, eds), Biochemical Mechanisms and Regulation of Intercellular Communication, Vol. 14, p. 151. Princeton Scientific Publ. Co., Princeton, NJ, with permission.)* (B) Lanthanum infiltrated gap junction. The lanthanum infiltrated intercellular "gap" (3) is about 2–4 nm. Magnification, 212 400× *(Reproduced from The Journal of Cell Biology, 1975, vol. 67, p. 801, by copyright permission of the Rockefeller University Press.)* (C) Freeze-fracture image of a gap junction. Each junctional membrane contains a set of particles and a set of pits. In vertebrate tissues, the particles adhere to the protoplasmic leaflet of the lipid bilayer (protoplasmic fracture face, P), whereas the pits remain associated with the extracellular leaflet (extracellular fracture face, E). Gap junction particles aggregate within particle-poor zones (4). The fracture may jump between the two membranes, resulting in adhesion of bits of the E-fracture face from the membrane of the adjacent cell (5) on the P-fracture face or vice versa. Occasionally, the fracture plane leaves the membrane and cuts into the cytoplasm (6). Magnification, 64 800×. *(From Larsen, W.J. (1977). Structural diversity of gap junctions: a review. Tissue Cell, 9, 373, with permission.)* (D) Enlargement of P- and E-fracture faces showing details of gap junction particles (7) and corresponding pits (8). Magnification, 139 000×. *(From Larsen, W.J. (1977). Structural diversity of gap junctions: a review. Tissue Cell, 9, 373, with permission.)* (E) Simple model of gap junction showing particle-particle (imp) contact within the "gap" at the level of the intercellular space (ics). Cytoplasmic dense material (cdm) is particularly apparent in gap junctions in excitable tissues. *(From Larsen, W.J. (1977). Structural diversity of gap*

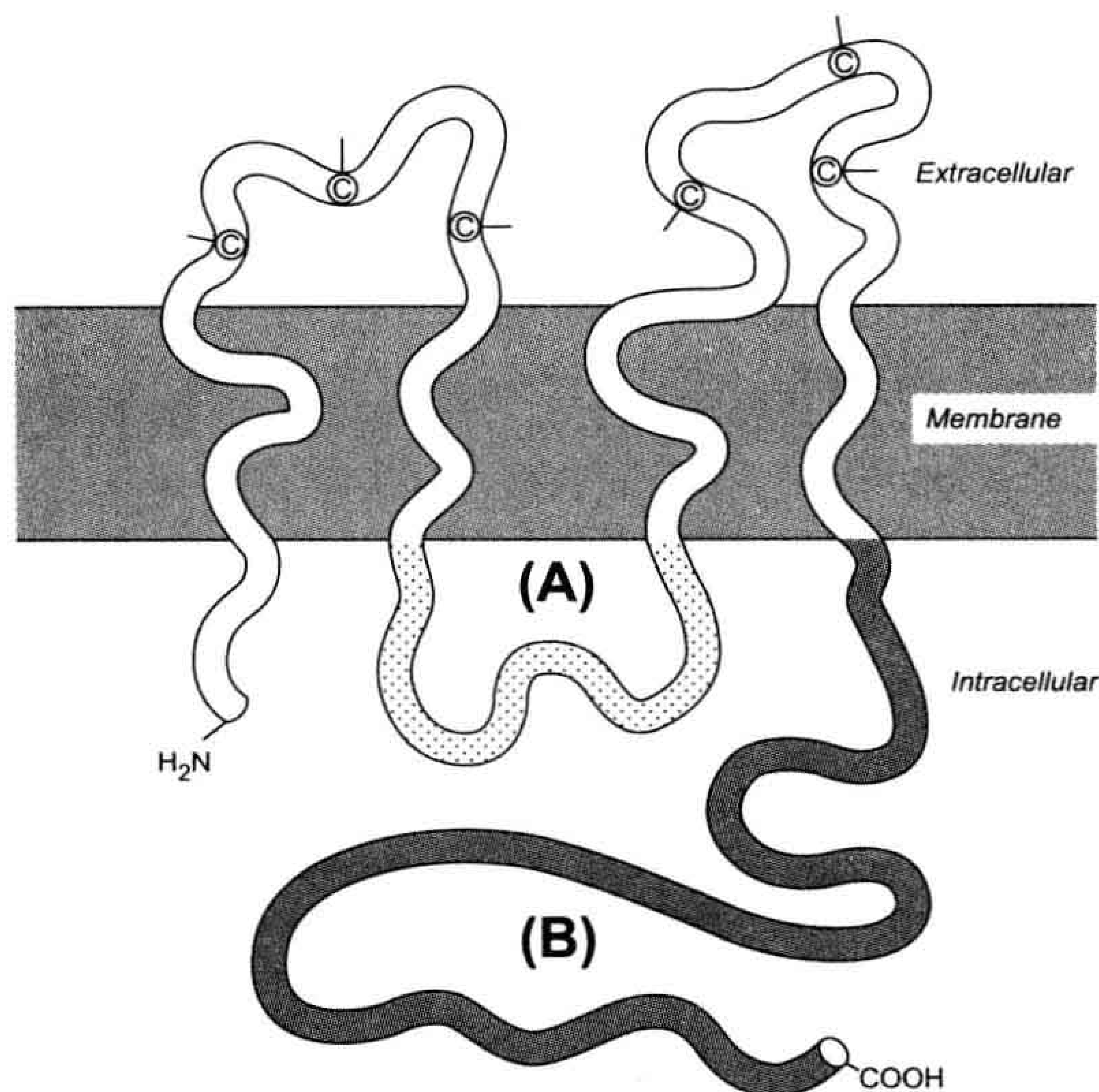


FIGURE 22.4 Structure and topology of a connexin. Both amino and carboxyl termini (B) are located in the cytoplasm along with an intermediate loop (A). Every connexin contains four membrane-spanning regions and two extracellular loops containing highly conserved cyteine residues (C). *(From Beyer, E.C., Paul, D.L. and Goodenough, D.L. (1990). Connexin family of gap junction proteins. J. Membr. Biol., 116, 187, with permission.)*

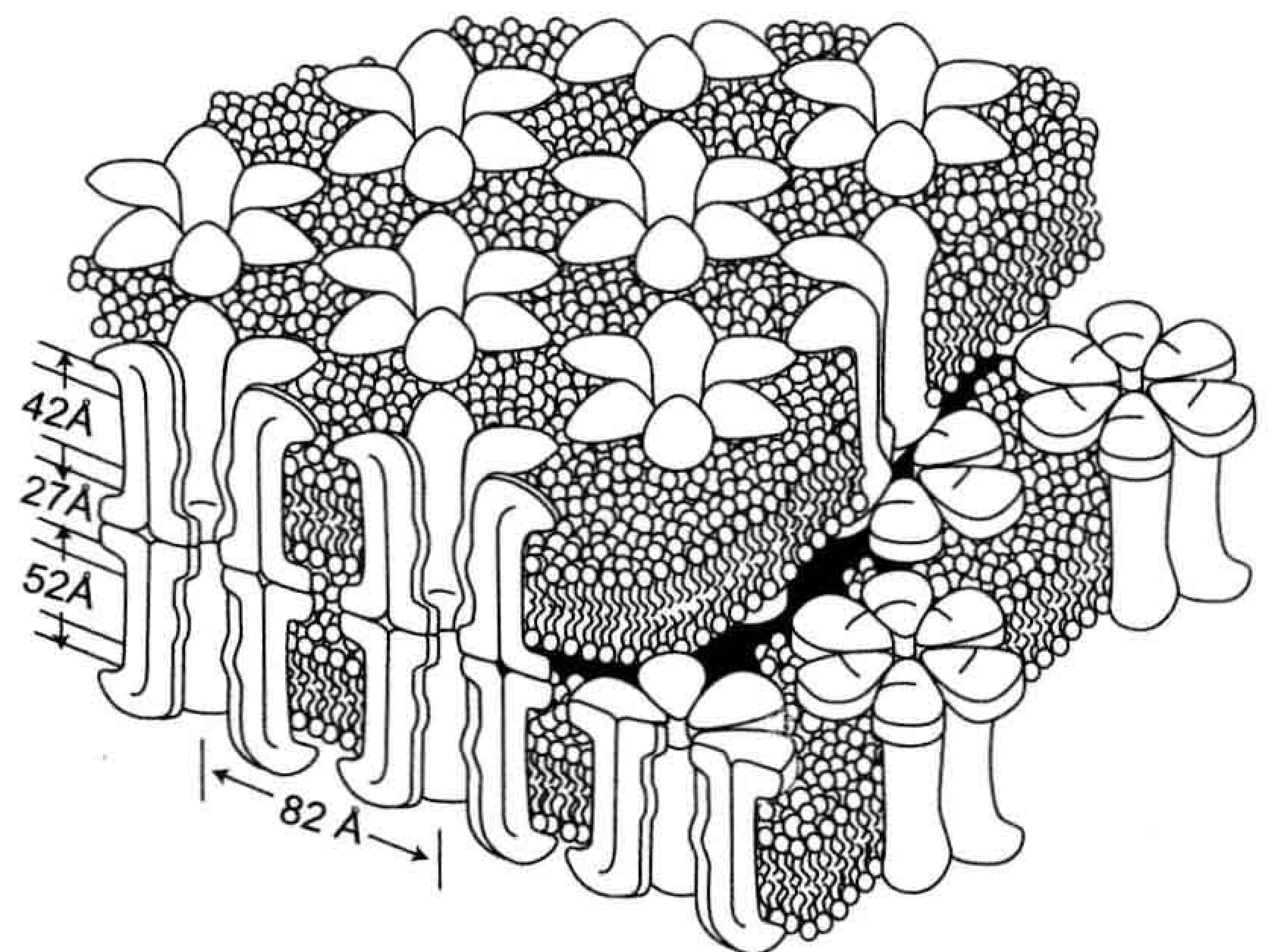


FIGURE 22.5 This diagram of a region of a gap junction isolated from mouse liver is based on electron microscope images and x-ray diffraction data. Each gap junction particle or connexon is composed of six gap junction protein molecules called connexins. Connexons in apposed membranes meet within the intercellular space. *(Reproduced from The Journal of Cell Biology, 1977, 74, p. 449, by copyright permission of the The Rockefeller University Press.)*

reveal that the apposing connexons that form each channel are staggered by about 30°.

VII. TWO LARGE FAMILIES OF GAP JUNCTION PROTEINS

Early structural studies, particularly those utilizing the freeze-fracture technique, demonstrated structural diversity among gap junctions distributed throughout the animal kingdom and within a variety of different tissues. The phylogenetic or species variability in some of these structural features was shown to depend upon the tissue in which the gap junction was identified. This variability in the detailed gap junction structure and composition was not initially understood, although it is now known that gap junctions in different tissues, phyla and species are formed by different protein isoforms within two large families of gap junction proteins. The gap junctions in vertebrate tissues are formed by members of the *connexin family* of gap junction proteins. The gap junctions of invertebrate tissues appear to be formed by members of an analogous *innexin family* of gap junction proteins.

Members of the connexin family of gap junction proteins range in molecular weight from 23 kDa to 62 kDa (Table 22.1). Each connexin is named for its deduced molecular weight in kilodaltons so that the 26-kDa connexin in humans, for example, is called human connexin 26 (human Cx26), while the 30.3-kDa connexin in mice is called mouse connexin 30.3 (mouse Cx30.3). Sequence analysis supports the possibility that at least two major phylogenetic subfamilies of connexins

junctions: a review. Tissue Cell, 9, with permission.) (F) Gap junctions form by the aggregation (9) of single 11-nm particles (10) in particle-poor regions of the membrane (11). Magnification, 222 300×. *(From Larsen, W.J. and Risinger, M.A. (1985). The dynamic life histories of intercellular membrane junctions. In (B. Satir, ed.), Modern Cell Biology, Vol. 4, p. 151. John Wiley & Sons, New York. Copyright 1985 John Wiley & Sons. Reprinted by permission of Wiley-Liss, Inc., a subsidiary of John Wiley & Sons, Inc.)* (G) Very large gap junctions (12) containing thousands of gap junction particles may represent terminal gap junction gaps. Magnification, 21 600×. *(From Larsen, W.J. (1977). Structural diversity of gap junctions: a review. Tissue Cell, 9, 373, with permission.)* (H) The large gap junction caps may invaginate into the cell (13) through an endocytotic mechanism. Magnification, 14 400×. *(From Larsen, W.J. and Tung, H. (1978). Origin and fate of gap junction vesicles in rabbit granulosa cells. Tissue Cell, 10, 585, with permission.)* (I) Bimembranous gap junction vesicles (14) may pinch off from the invaginating junction to fuse with lysosomes before undergoing degradation. Magnification, 52 200×. *(From Larsen, W.J. and Tung, H. (1978). Origin and fate of gap junction vesicles in rabbit granulosa cells. Tissue Cell, 10, 585, with permission.)* (J) Freeze-fracture planes within the cytoplasm may reveal the P-face particles (P) and E-face pits (E) within cytoplasmic gap junction vesicles. Magnification, 38 700×. *(From Larsen, W.J. and Tung, H. (1978). Origin and fate of gap junction vesicles in rabbit granulosa cells. Tissue Cell, 10, 585, with permission.)*

TABLE 22.1 The Connexin Gene and Protein Family[1]

Human Protein Name	Human Gene Name	Mouse Protein Name	Mouse Gene Name
CX43	*GJA1*	Cx43	*Gja1*
CX46	*GJA3*	Cx46	*Gja3*
CX37	*GJA4*	Cx37	*Gja4*
CX40	*GJA5*	Cx40	*Gja5*
—	—	Cx33	*Gja6*
CX50	*GJA8*	Cx50	*Gja8*
CX59	*GJA9*	—	—
CX62	*GJA10*	Cx57	*Gja10*
CX32	*GJB1*	Cx32	*Gjb1*
CX26	*GJB2*	Cx26	*Gjb2*
CX31	*GJB3*	Cx31	*Gjb3*
CX30.3	*GJB4*	Cx30.3	*Gjb4*
CX31.1	*GJB5*	Cx31.1	*Gjb5*
CX30	*GJB6*	Cx30	*Gjb6*
CX25	*GJB7*	—	—
CX45	*GJC1 (GJA7)*	Cx45	*Gjc1*
CX47	*GJC2 (GJA12)*	Cx47	*Gjc2*
CX30.2/CX31.3	*GJC3*	Cx29	*Gjc3*
CX36	*GJD2*	Cx36	*Gjd2*
CX31.9	*GJD3*	Cx30.2	*Gjd3*
CX40.1	*GJD4*	Cx39	*Gjd4*
CX23	*GJE1*	Cx23	*Gje1*

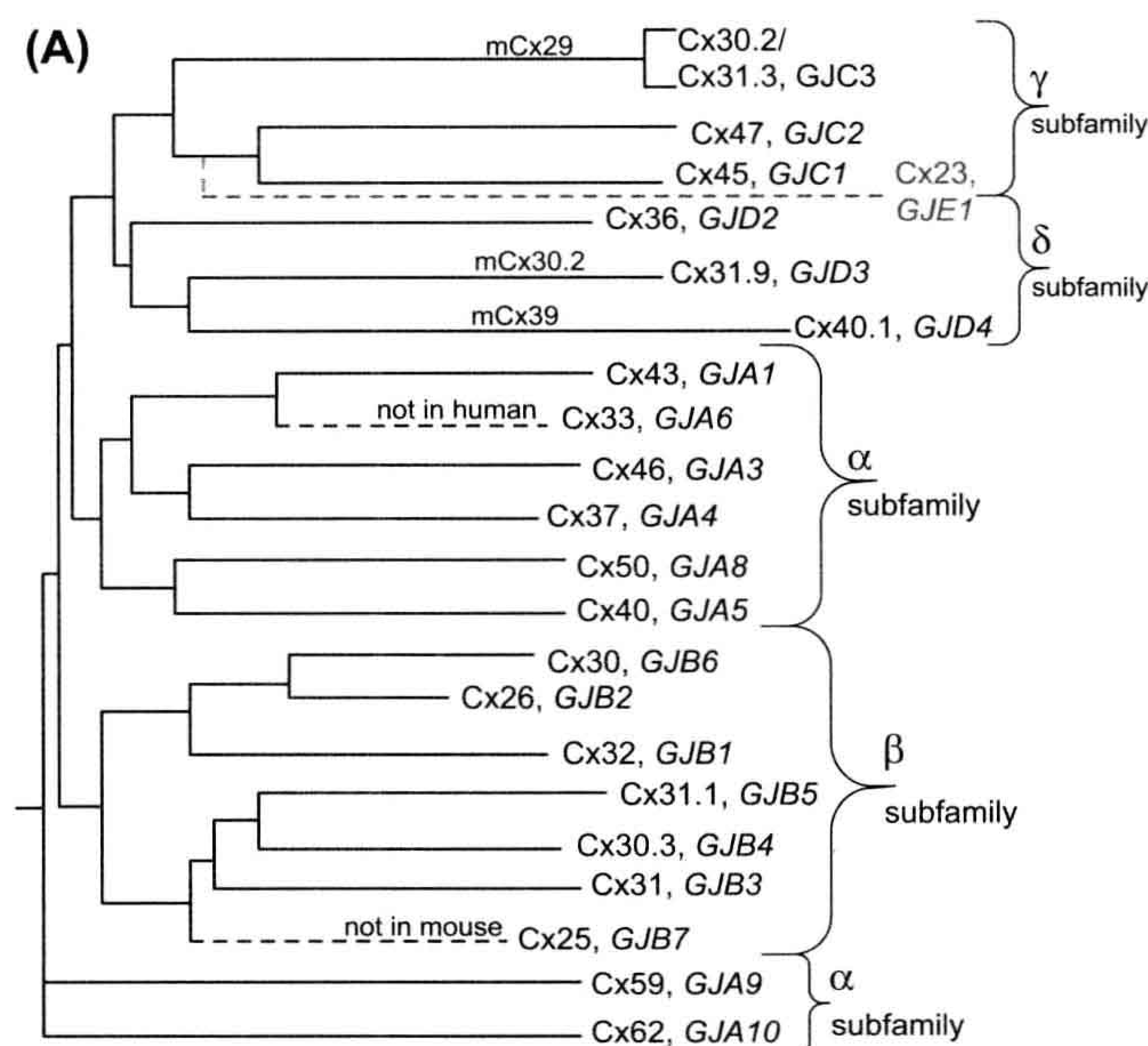
[1]Adapted from Beyer, E.C. and Berthoud, V.M. (2009). The family of connexin genes. In Connexins: A Guide, p. 8, with permission. Copyright 2009 Humana Press.

diverged from each other between 1.3 and 1.9 billion years ago; one group ranging in size from about 26 kDa to 32 kDA (β-group), another from about 33 kDa to 62 kDa (α-group) (Fig. 22.6A). Some lesser divergent connexin subfamilies are also indicated (δ/γ/ε). Twenty different connexin genes have been identified in rodents (e.g. mice), 21 in humans, although transcription of the Cx23 gene has not been demonstrated in humans or mice and the functional expression of some connexins have yet to be described (e.g. Cx25, Cx33).

Typically, it appears that two or more connexins comprise the gap junctions within any given tissue. For example, Cx26 and Cx32 constitute gap junctions of mammalian liver and have been shown to coexist within the same gap junction aggregates. On the other hand, the Cx32 and Cx43 documented in thyroid epithelium, appear to be segregated into separate gap junctions formed in different regions of the lateral cell membrane. Likewise, the distribution of three different connexins (Cx40, Cx43 and Cx45) within the human heart appears to be non-random. For example, Cx45 is the first connexin to appear in the embryonic mouse heart. Ultimately, however, its expression is restricted to the region of the sinoatrial (SA) node, while Cx40 is localized in the atrioventricular (AV) node and in myocytes of the atrium and conductive myocardium. In contrast, Cx43 expression occurs within the crista terminalis and other cardiomyocytes of the heart. As many as six different connexin genes (Cx30.1, Cx31, Cx31.1, Cx40, Cx43 and Cx45) are transcribed and translated in mouse embryos as early as the eight-cell stage. These studies imply differential functions for gap junctions composed of different connexins and consequently stimulate the following question: what part of the connexin molecule encodes functional specificity and how do these specificities differ from connexin to connexin?

In general, the amino termini, transmembrane helicies and extracellular loop cysteine-containing regions of the connexins are highly conserved (see Figs. 22.4 and 22.6B). However, the cytoplasmic loops and cytoplasmic carboxyl termini vary significantly in length and amino acid sequence from one connexin to another. The two triple cysteine-containing segments form the two identified connexin signature sequences less Cx23 which contains only two Cys residues within each extracellular loop (see Fig. 22.6C). Heterotypic gap junctions can be formed only with connexons made of particular connexins, suggesting that sequence specificity within the extracellular domains may be relevant to gap junction assembly. Recent studies, therefore, have focused on the potential functional relevance of specific differences in amino acid sequences within the various domains of the connexin proteins (see Sections IX–XIV).

In invertebrates, proteins of the innexin family are able to form gap junctions based on ultrastructural criteria. In addition, studies with a *Xenopus* oocyte expression system have shown that some of the innexin proteins are able to form permeable cell-to-cell channels that may be voltage- or pH-sensitive. As many as 24 innexin genes have been identified in the nematode, *Caenorhabditis elegans*, while six innexin genes have been described in *Drosophila*. While the innexins bear no sequence homology to the connexin family of proteins, the structural similarities of innexins and connexins are dramatically similar. For example, like the connexins, the innexin proteins have four transmembrane domains, two extracellular loops and cytoplasmic N- and C-termini. Moreover, the functions of the innexin proteins in invertebrates parallel functions of the connexins in



(B)

MXDWXFLXXLLXXXVXXHSTXXGKXWLTVLFIFRILVLXVAAEXVWGDEQ
SXFXCNTXQPGCXNVCYDXXFPISHIRXWVLQIIFVSTPSLLYXGHXXYX
XXXXEXXXXXXXXXXXXXXXXXXXXXXXXXXXXXXXXXXXXXXXXXXXXX
XXXXXXXXXXXXXXXXXXXXXXXXXXXXXXXXXXXXXXXXXXXXXXXXXX
XXXXXGXLXXTYVXSXXXRXXXEXXFLXGQYXLYGXFXXXPLXXCXRXXP
CPNXVDCFVSRPTEKTIFXXFMXXVSXXCLLLNXXELXHLGXKXXXR...

Key: Bold = identical, black ≥ 50% conservation, *italic = transmembrane*

(C)

Connexin signature 1:
C-[D/N/H]-[T/L]-X-[Q/T]-P-G-C-X-X-[V/A/I/L]-C-[F/Y]-D
Connexin signature 2:
C-X-X-X-X-P-C-X-X-X-[L/I/V/M/T/A]-[D/E/N/T]-C-[F/Y/N]-[L/I/V/M/Q]-[S/A]-[K/R/H]-P

FIGURE 22.6 (A) Dendrogram of the mammalian (human, mouse) connexin family tree constructed by aligning the protein sequences for the known connexins using the nomenclature adapted at the 2007 International Gap Junction Conference (see Table 22.1). *(Adapted from Sáez, J.C., Berthoud, V.M., Brañes, M.C., Martínez, A.D. and Beyer, E.C. (2003). Plasma membrane channels formed by connexins: their regulation and functions. Physiol. Rev., 83, 1363, with permission. Copyright 2003 American Physiological Society.)* (B) Consensus sequence for the 20 human connexins (excluding Cx23) illustrating the 50 to 100% conservation of amino acids residues within the amino terminal, first and second extracellular loop and four transmembrane domains with limited sequence homology within the cytoplasmic loop and carboxyl terminal domains. (C) The two connexin signature sequences derived from the consensus sequence underlined in panel B. Cx31 and Cx23 do not match these signature sequences. *(Adapted from Beyer, E.C. and Berthoud, V.M. (2009). The family of connexin genes. In Connexins: a Guide, p. 8, with permission. Copyright 2009 Humana Press.)*

vertebrate tissues. For example, the innexin encoded by the shal-B(neural) locus forms electrical synapses of the *Drosophila* nervous system, while the innexin encoded by the *eat*-5 locus forms permeable junctions responsible for synchronization of pharyngeal musculature in *Drosophila*. There is no signature consensus amino acid sequence common to the Arthropoda, Nematoda, Annelida and other invertebrate phylogeny as there is for the connexins. The innexin extracellular loops contain only two cysteine residues each, in contrast to three for the connexins. Three innexin-related genes are found in the vertebrate genome and these are now referred to as the *pannexins* (*panx1*, *panx2*, *panx3*). Only pannexin1 is capable of forming homologous intercellular channels in *Xenopus* oocytes, suggesting the possibility that pannexins do not form vertebrate gap junctions. Alternatively, it was hypothesized that pannexins form ATP-releasing hemichannels in complex with the purinergic P2X7 receptor. Evidence for functional panx1/P2X7 *hemichannels* in astrocytes and other mammalian cells has received considerable support in recent years, suggesting a more patho/physiological role for pannexins in paracrine signaling pathways than conventional gap junctional communication.

VIII. CHANNELS WITHIN GAP JUNCTIONS

Following the identification of the gap junction as the site of cell-to-cell transfer of ions and small hydrophilic molecules, a hypothesis developed that the pathway for this exchange consisted of an array of parallel aqueous channels. The central aqueous pore resides in each IMP particle in the freeze-fracture images or hexagonal bridge in the negatively stained micrographs of a gap junction plaque. An aqueous pore 16 nm in length with a channel diameter of approximately 14 Å should have a unitary conductance of $10^{-10}\,\Omega$ (=100 pS). Such a relatively high conductance should produce a detectable electrical signal in support of the channel hypothesis for gap junction permeability. Small stepwise changes in the electrical coupling between paired *Xenopus* embryonic cells provided evidence for the existence of discrete coupling elements, but the low input resistance owing to the large cell size limited the resolution of the electrical signals. Adaptation of the two-cell voltage clamp to cell pairs of high input resistance achieved precise determination of unitary gap junction channel conductance. Concomitant current records from both voltage-clamped cells always appear as mirror images since each cell resides on opposite sides of the junction (Fig. 22.7). This *equal amplitude and opposite polarity* is the criterion used to define junctional current signals in the dual whole cell recording configuration. Channel conductance values of 120 and 160 pS were close to the original predicted value and provided supportive evidence for the existence of relatively large non-selective aqueous channels. Conductance values range from 10 to 300 pS for different gap junction channels under essentially physiological salt conditions. For an aqueous diffusion limited pore, the channel conductance will increase in direct proportion to $2\pi r^2$. For a long pore of 16 nm in length, a 300-pS gap junction channel requires a 26-Å diameter right cylindrical pore. It follows that higher conductance gap junction channels should exhibit less ionic selectivity and a higher molecular permeability than channels with smaller conductance values.

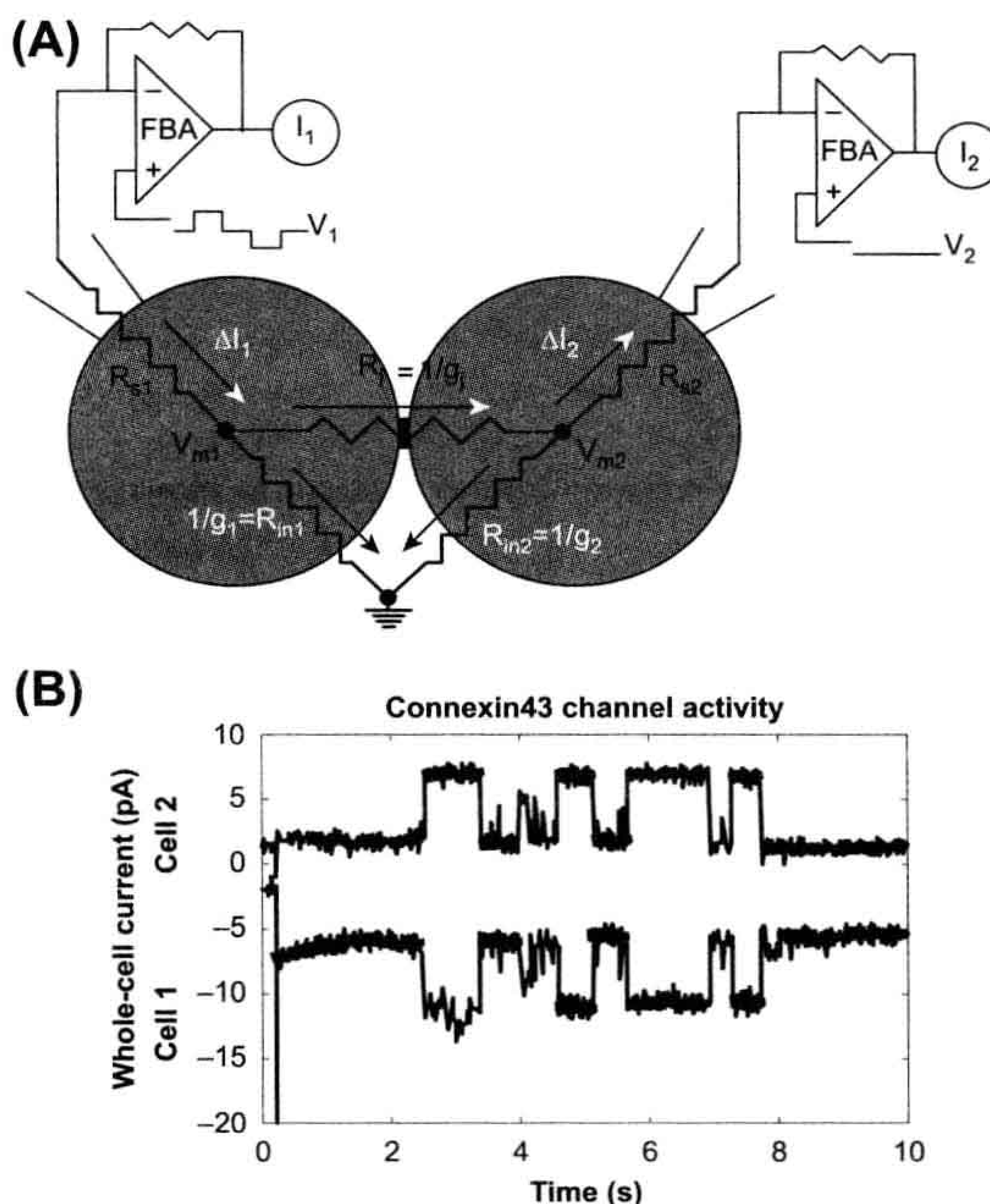


FIGURE 22.7 (A) Dual whole-cell recording configuration. Equivalent resistive circuit for the whole-cell patch-clamp recording configuration from two coupled cells. The voltage command potentials (V_1 and V_2) are applied via each negative feedback patch-clamp amplifier (FBA) through whole-cell patch electrodes. The difference between the command potentials and the cell membrane potentials (V_{m1} and V_{m2}) is minimized by reducing the series resistance (R_{s1} and R_{s2}) to less than 5% of the cell input resistance (R_{in1} and R_{in2}) and junctional resistance (R_j). Accurate junctional current signals are achieved when a majority of the applied current flows across the junction (white arrowheads) instead of the cell membrane (black arrowheads). This condition is readily obtained by using high input resistance cells (R_{in}>1 GΩ). Conductances (g) are the reciprocal of the corresponding resistance element. (B) The whole-cell currents for each amplifier (I_1 and I_2) appear as simultaneous signals of opposite sign. These are unaltered whole-cell currents obtained from a Cx43-transfected N2A cell pair digitized at 1 kHz after low-pass filtering at 100 Hz. The transjunctional voltage was −30 mV.

IX. EVIDENCE FOR CHARGE SELECTIVITY

The apparent permeability to a variety of water-soluble (hydrophilic) molecules (ions, cAMP, sugars, ATP, nucleosides, etc.) suggests the presence of a large-diameter aqueous pore with minimal selectivity based on electrical charge (equivalent valence at physiological pH). Several permeability studies on mammalian cell and invertebrate gap junctions were instrumental in assigning the commonly accepted molecular permeability limit of 1 kDa or diameter <14 Å. However, two of these same studies used tagged fluorescent tracers with different valences and demonstrated that the molecular permeability limit was lower for molecules with higher negativity. Selective permeability of molecules >600 Da and approximately 10 Å in diameter is not surprising since the size of the permeant molecule is approaching the estimated diameter of the pore. Placing any charged surfaces of the pore and the permeable molecule in close proximity to each other would enhance any electrostatic attractive or repulsive forces that might be present. This suggests that the pore of the gap junction channel contains fixed electronegative sites within the pore which reduce the permeability of large negatively charged molecules relative to their neutral or less negative counterparts.

Evidence for selectivity at the ionic level did not exist until the patch-clamp methodology was adapted to the recording of gap junction channel currents. In two cellular preparations, the junctional membranes of the earthworm septate axon and rat lacrimal gland cells were found to be less permeable to Cl^- relative to K^+ by ratios of 0.52 and 0.69, respectively. This modest selectivity among ions with nearly identical aqueous mobilities and diameters of less than 4 Å suggests that there are weak interactions between the permeant ion and the wall of the pore. In a simple diffusion-limited pore, ions interact with water molecules but not with other ions. Observations from four different homotypic connexin hemichannels or gap junction channels reported K^+ to Cl^- permeability ratios of approximately 10:1 with selectivity among monovalent cations in alignment with their relative aqueous mobility sequence. These observations suggest a common theme to the structure of the selectivity filter within the connexin channel pore. This proposed selectivity filter readily permits the passage of hydrated cations while restricting the simultaneous passage of similar aqueous anions by 10-fold. These observations provide direct evidence for cation–anion interactions within the gap junction pore that contradict aqueous diffusion theory. The observed permeability to atomic and large organic cations is consistent with a pore diameter of 10–14 Å for mammalian connexin channels.

The ability to transfer these electrical and chemical signals from cell to cell is important to tissue function. The most direct comparison of connexin-specific molecular permeability differences comes from the use of structurally similar molecules of varying size and valence. Two fluorescein derivatives with varying valences but essentially constant physical dimensions (=10 Å), 2′,7′-dichlorofluorescein (diCl-F) and 6-carboxyfluorescein (6-CF), were readily permeable through rat Cx43 channels. In contrast, both dyes were less permeable through chicken Cx43, human Cx37 and rat Cx40 gap junctions. Chicken Cx45 gap junctions were permeable to diCl-F, but not 6-CF. This indicates that the more anionic 6-CF is restricted in its junctional permeability relative to diCl-F in a connexin-specific manner. Since Cx43 has a lower channel conductance than Cx40 and Cx37, no correlation between the maximum conductance and molecular permeability of the connexin channels exists. This lack of correlation between charge selectivity and channel conductance suggests that pore size and conductance are not directly related. Alternatively, recent channel theory proposes that the pore with the smaller diameter and same electrostatic (fixed structural) charge will exhibit the higher channel conductance due to the increased charge density. This updated charged membrane theory can explain the conductance and selectivity properties of known ion channels, including gap junctions.

X. CHANNEL PROPERTIES OF DIFFERENT CONNEXINS

The functional expression of different connexins, either by mRNA injection into *Xenopus* oocytes or stable expression in communication-deficient cell lines derived from mammalian tumors, has yielded tantalizing results. Single-channel unitary conductance values (the ease with which current flows) are connexin-specific. Channel conductance values vary by 30-fold, from 10 to 300 picosiemens ($pS = 1/10^{12}\,\Omega$), while observed ionic selectivities vary by approximately 10-fold. The reporting of channel conductance became more complicated due to the presence of multiple conductance states for several of the connexin channels. The ability of some connexins to form heterotypic (two connexons of different connexin composition) or heteromeric (two different connexins within the same connexon) gap junction channels adds another level of complexity to the function of channel conductance. The physiological relevance of these conductance differences is poorly understood, but several observations now indicate that connexin composition can modulate gap junction channel molecular permeability limits. For example, rat hepatocyte gap junctions contain almost exclusively Cx32 while mouse hepatocyte gap junctions are composed of a mixture of Cx26 and Cx32. Isolated mouse liver gap junctions exhibited a lower size limit to uncharged sugar molecules and cAMP than rat liver gap junctions, consistent with a smaller pore size, and they exhibited possible charge selectivity, contributed by Cx26 to otherwise Cx32-containing gap junctions. Connexin composition and mutations can affect gap junction selectivity in detrimental ways (e.g. disease-causing mutations), although the molecular basis for these permeability alterations remain to be determined.

The regulation of gap junction conductance by intracellular pH, intracellular calcium, protein kinases and transjunctional (cell-to-cell) voltage are also connexin-specific. The most significant differences in the amino acid sequences of the connexins occur within the cytoplasmic loop and carboxyl-terminal domains. These two cytoplasmic domains provide the basis for distinct conductance and regulatory properties upon the assembled multimeric connexin channels. Since a specific gene encodes for each connexin, tissue- and developmental-specific patterns of expression exist. Limited comparisons of the channel conductance and regulatory properties of the connexin channels to gap junctions in native cell types demonstrate the presence of at least two distinct connexin channel types. The presence of multiple connexin channels can explain the properties of the gap junctions found in many cell types. In one study, the expression of three embryonic chicken heart connexins, Cx42, Cx43 and Cx45, demonstrated that each connexin

exhibited unique conductance properties, which coincided with the observance of multiple conductance states in cultured cardiac myocytes. Furthermore, mixing these three connexins in different proportions modeled the response to transjunctional voltage during different stages of cardiac development. Thus, the observed decline in Cx45 expression could significantly explain the decrease in the transjunctional voltage sensitivity of junctional conductance in the developing chicken heart. Developmental and hormonal changes in connexin expression occur in other tissues, suggesting a possible role for this mechanism in the modulation of gap junction communication in a variety of tissues.

XI. GATING BY IONS AND SECOND MESSENGERS

Perhaps of greater physiological relevance than transjunctional voltage is the modulation of junctional communication by highly buffered intracellular cations (protons and calcium) and organic second messengers such as cAMP, diacylglycerol and inositoltrisphosphate. Whether cations directly bind to a regulatory site (or sites) on the connexin or act through intermediate accessory proteins is unknown. This issue remains an important topic for investigation since it has been observed that interventions that lower intracellular pH also increase intracellular free calcium. Conversely, there is direct evidence that several of the connexins are substrates for phosphorylation by protein kinases such as protein kinase A (PKA) and PKC. Protein kinase-dependent phosphorylation often increases or decreases junctional communication, depending on the connexins expressed in each tissue. Physiological correlates at the channel level are rare, owing to the difficulty of observing channel activity under distinct ionic or phosphorylation conditions. Transjunctional voltage (V_j) gating and Cx43 phosphorylation by PKC have both been shown to decrease the channel conductance and increase the ionic/molecular selectivity of gap junctions by inducing the formation of a subconductance state. Generally, cAMP increases junctional conductance and PKC has the opposite effect, at least in Cx43-containing cells. PKA and PKC may both phosphorylate the same serine residue (S233) of Cx32. In contrast, tyrosine phosphorylation by pp60$^{v\text{-}src}$ produces a rapid and reversible uncoupling of Cx43 gap junctions but has no effect on Cx32 gap junctions. Cx43 contains specific v-src SH2- and SH3-binding domains near a tyrosine phosphorylation site (Y265) by pp60^{v-src} (Fig. 22.8A). Cx32 lacks these binding and tyrosine phosphorylation sites. There is increasing evidence that the diversity in the cytoplasmic loop and carboxyl-tail domains of different connexins confers different conductance and regulatory properties on the connexin-specific gap junctions in response to protein kinases and intracellular ions.

XII. REGULATION OF FUNCTIONS OF CONNEXIN-BASED GAP JUNCTIONS AT MULTIPLE LEVELS

As suggested above, a likely reason for differences in the sequence of the carboxyl tail of connexins may be in the regulation of gap junction-mediated tissue-specific or cell-specific biological activities. Indeed, gap junction regulatory mechanisms described so far appear to fall into one of two general categories. On the one hand, rapid changes in cell coupling that occur within seconds or minutes may reflect regulation of gating of pre-existing pores. On the other hand, long-term changes which occur within minutes or a few hours to days are likely to involve the modulation of synthesis, assembly or degradation of connexins (see Fig. 22.8B). Existence of this latter scheme of modulation is supported by studies that show that the half-lives of several different connexins are relatively short, ranging from 1 to 3 hours, and by more recent direct videomicrography of living cells expressing green fluorescent protein tagged connexins. In these latter studies, connexins have been observed as they concentrate within the developing Golgi; as they move to the surface to form plaques in regions of cell—cell contact; and as large fragments of the connexin-positive plaques are internalized as apparent vesicles (see Figs. 22.3H, I and 22.8B). Moreover, a variety of studies supports the idea that gap junctions may be regulated at virtually any stage of their formation, maturation and degradation.

For example, the possible effect of cAMP on transcription of connexin mRNA and its ultimate translation is supported by studies which show that cAMP-mediated increases in coupling or in junction formation in some cells can be blocked by inhibitors of mRNA or protein synthesis. The potential for control at the level of transcription of connexins is also implied by the characterization of their 5′ flanking sequences. For example, the 5′ flanking sequence of the myometrial Cx43 gene has been shown to possess several consensus activator protein-1 (AP-1) binding sites as well as half-palindromic estrogen response elements. Since the AP-1 proteins, Fos and Jun, are expressed in response to increased estrogen, transcription of Cx43 may be indirectly upregulated through its AP-1, *cis*-acting elements. In vascular smooth muscle, the transcription of Cx43 may be upregulated by mechanical load induced by stretch, presumably via an upregulation of *c-fos,* which may act in turn on AP-1 binding sites or upon other sites in the 5′ flanking region of the Cx43 gene. Promoter analysis of other connexin genes has shown that their transcription may also be regulated by

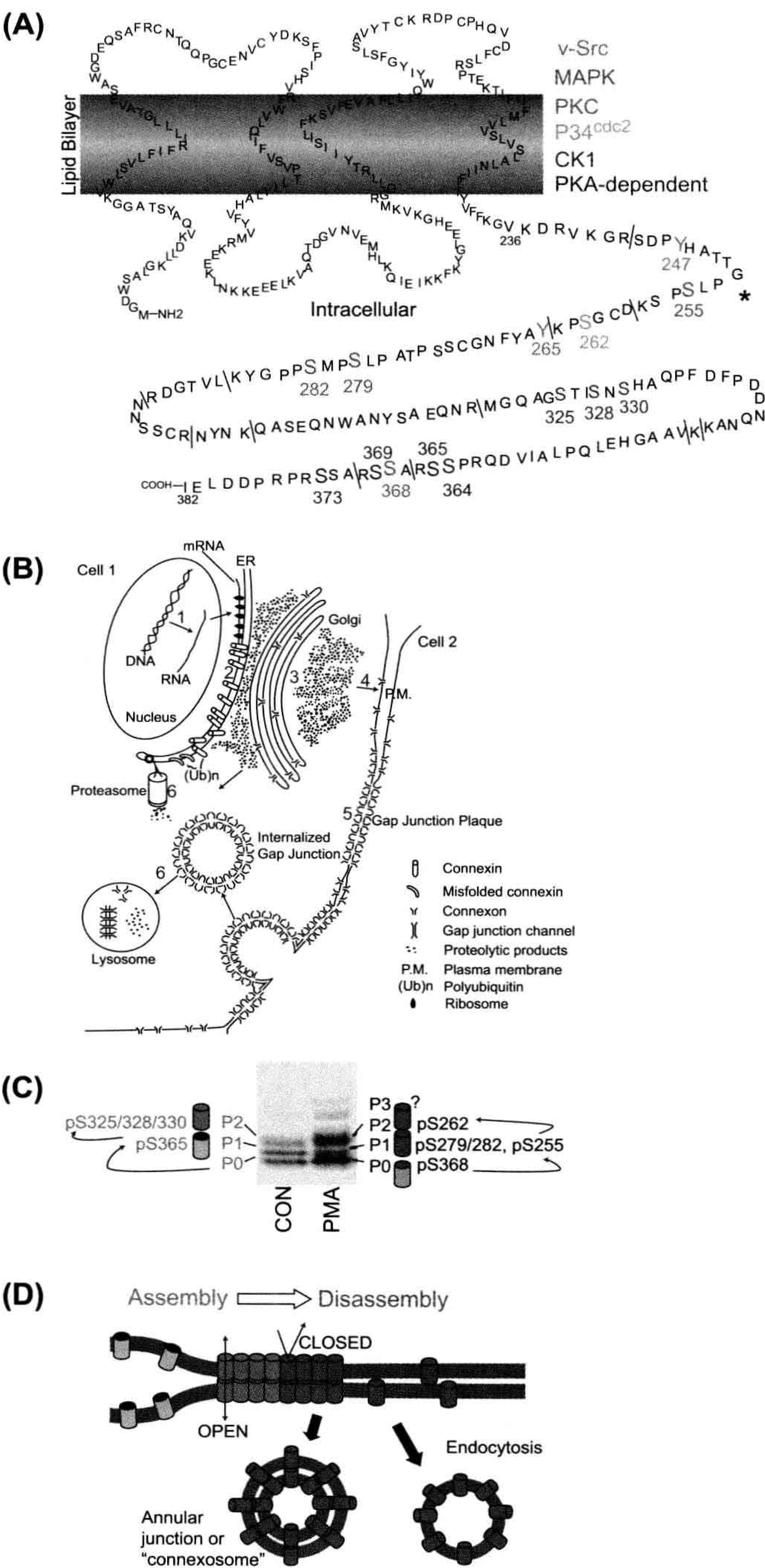


FIGURE 22.8 (A) Graphical illustration of the known protein kinase phosphorylation sites on the carboxyl domain of Cx43 (purple: PKA; blue: PKC; green: CK1; red: MAPK; orange: $p34^{cdc2}$; lime green: v-src, brackets: trypsin cleavage sites). *(Reprinted from Solan, J.L., and Lampe, P.D. (2005). Connexin phosphorylation as a regulatory event linked to gap junction channel assembly. Biochim Biophys Acta, 1711, 155 with permission. Copyright 2005 Elsevier Press.)* (B) Illustration of the life cycle of the connexins beginning with mRNA transcription (*1*), translation and protein folding (*2*), oligomerization and intracellular transport (*3*), hemichannel insertion into the plasmalemma (*4*), hemichannel docking and gap junction formation (*5*), and degradation by the proteasome and lysosome (*6*). *(Reprinted from Beyer, E.C. and Berthoud, V.M. (2009). The family of connexin genes. In Connexins: a Guide, p. 17, with permission. Copyright 2009 Humana Press.)* (C and D) Association of Cx43 phosphorylation-dependent bands on an SDS/PAGE gel with the PO, PI, P2, or P3 isoforms correlated with the protein kinase phosphorylation sites implicated in the assembly (green) or disassembly (red) of gap junctions. Assembled gap junctions are internalized as a double membrane bounded "connexosome" while unassembled hemichannels appear in endocytotic vesicles. *(Reprinted from Solan, J.L. and Lampe, P.D. (2007) Connexin43 phosphorylation: structural changes and biological effects. Biochem. J., 419, 262, with permission. Copyright 2007 Biochemical Society.)*

transcription factor binding sites. For example, two GC boxes, two GT boxes, a TTAAAA box, a YY1-like binding site and a mammary gland factor binding site have been identified in the proximal promoter region of the human Cx26 gene. Likewise AP-1, AP-2, SP-1, TRE and p53 transcription factor binding sites have been identified in the 5′ flanking sequence of the mouse Cx40 gene, while Cx-B2 and P1 and P2 promoters are implicated in the transcriptional regulation of Cx32.

Yet another level of control of gap junction function is revealed by studies that show the upregulation of coupling or gap junction formation in the absence of transcription or translation, perhaps at a post-translational level of control. The direct application of dibutyryl cAMP (dbcAMP) to mammary tumor cells in culture, for example, increases the number of gap junctions as well as cell–cell coupling in the absence of an increase in Cx43 mRNA or protein. Likewise, connexin 43 trafficking within several cultured cell lines appears to be regulated by post-translational mechanisms. Specifically, the trafficking of Cx43 from the cytoplasm to the plasma membrane and its assembly into functional gap junction aggregates may require phosphorylation of two serine phosphorylation consensus sites in the carboxyl tail of this connexin (see Fig. 22.8C, D). For example, two cell lines were studied that could not form gap junctions or become coupled, but were able to synthesize significant amounts of Cx43, which was stored within vesicles in the cytoplasm. The Cx43 in these cells was phosphorylated at only one of its serine residues. When one of these lines was transfected with a gene for a cell adhesion molecule, L-CAM, the Cx43 in the transfected line was phosphorylated again, translocated to the plasma membrane and assembled into gap junctions. Further evidence for the phosphorylation-dependent trafficking and assembly of Cx43 in cardiomyocytes has been obtained in experiments with monensin, a reagent that inhibits translocation of proteins between Golgi cisternae. These studies suggest that phosphorylation of Cx43 to the mature form occurs in a compartment of the cell between the Golgi apparatus and the plasma membrane. Similar results are obtained in studies of effects of brefeldin A, which blocks both Cx43 phosphorylation and trafficking to the plasma membrane in a mammary tumor cell line. Finally, it has also been suggested that the process of connexon clustering that gives rise to functional gap junction plaques may be facilitated by the action of microfilaments. Thus, the increase in Cx43-positive gap junctions and coupling in the absence of Cx43 mRNA synthesis following treatment of cultured prostatic cells with forskolin may be explained by effects of cAMP on post-translational processing of Cx43, namely their assembly into functional plaques and their translocation from the cytoplasm to the membrane.

Numbers of functional gap junctions within the plasma membrane may also be affected by regulation of their removal and degradation. For example, the treatment of some cells with phorbol esters such as 12-*o*-tetradecanoylphorbol-13-acetate (TPA) may stimulate the removal and degradation of gap junctions through phosphorylation of connexins by protein kinase C. Similarly, it is thought that the phosphorylation of mitogen-activated protein (MAP) kinase serine phosphorylation sequences in cultured rat liver cells treated with epidermal growth factor, may mediate the loss of functional gap junctions from the cell membrane. In another example, it has been shown that massive endocytosis of gap junctions in granulosa cells of the ovary is stimulated by high titers of follicle stimulating hormone; that endocytosis is facilitated by clathrin and microfilaments; and that the internalized gap junction vesicles fuse with lysosomes prior to degradation (see Fig. 22.8B). Alternatively, it has been suggested that gap junction plaques and their connexins may be disposed of via a ubiquitin-mediated proteasomal proteolytic pathway. This mechanism is supported by studies showing that connexins accumulate in cells treated with proteasomal inhibitors and by immunogold studies that demonstrate the association of ubiquitin with gap junction plaques (Fig. 22.9).

In summary, it appears that the amount of functional gap junction membrane at the cell surface may be controlled at virtually any point in the gap junction's life history; namely through regulation of (1) transcription of connexin mRNA,



FIGURE 22.9 Image of gap junction in cultured HeLa cell transfected with Cx40 and Cx43. The replica was immunostained with antibodies to Cx40, Cx43, and ubiquitin. The 6-nm gold particles indicate Cx40, the 10-nm gold particles stain for Cx43, and the 15-nm gold particles indicate epitopes for ubiquitin.

(2) translation of connexin protein, and then through post-translational modifications, which affect the (3) assembly of functional plaques, (4) gating of junctional channels, (5) channel conductance and (6) degradation of functional gap junctions.

XIII. SPECIFIC BIOLOGICAL FUNCTIONS OF GAP JUNCTIONS

Early speculations regarding the general functional significance of gap junctions, such as the electrical coupling of some neurons and the buffering of metabolites within a tissue mass, have not been seriously challenged for the past three decades (see Sections I, II and IX). Several recent studies, however, have begun to establish even more specific functional relationships between gap junctions and tissue activities and behaviors, most notably with respect to the regulation of smooth muscle contraction and ligand-mediated secretory activity.

Perhaps one of the best-studied cases is that of the myometrial connexin, Cx43. It is known, for example, that the myometrium of the non-pregnant uterus in a variety of species is virtually devoid of gap junctions and expresses very little, if any myometrial Cx43 mRNA or protein. In contrast, however, Cx43 mRNA is rapidly synthesized and translated and then gap junctions appear coincident with rising estrogen and declining progesterone titers just prior to parturition. Experimental manipulations of these hormones also predictably induce or inhibit the appearance of gap junctions in experimental models of preterm labor or tocolysis respectively (effective labor coincides with their induction while myometrial quiescence parallels their inhibition). For example, removal of the ovaries or the injection of RU-486 during the latter part of pregnancy effectively increases the estrogen:progesterone ratio, the expression of Cx43 mRNA and protein, the assembly of myometrial gap junctions and concomitant preterm labor. Conversely, the injection of progesterone several days prior to term inhibits the formation of gap junctions and onset of labor. Thus, it is likely that transcription and translation of Cx43 are required for gap junction formation and coordinated myometrial contractions in humans. Moreover, the evidence for the presence of AP-1 binding sites in 5′ flanking sequences of the myometrial Cx43 gene and the estrogen-mediated expression of Jun and Fos described above (see Section XII) is consistent with this notion. The function of myometrial gap junctions and contractility may also be regulated at the level of post-translational processing. For example, high levels of myometrial Cx43 appear a full day prior to delivery in rats (Fig. 22.10) but most of the Cx43 in these cells is located within perinuclear vesicles which also stain with an antibody against a Golgi-associated protein (Fig. 22.10B). Six to 12 hours prior to onset of delivery, however, Cx43 immunopositive plaques are observed in the plasma membrane (Fig. 22.10C). Conversely, cessation of delivery is accompanied by the loss of gap junctions from the cell surface by a process of endocytosis (Fig. 22.10E).

Gap junctions have also been implicated in the process of secretion and other ligand-mediated functions in many different kinds of cells. For example, gap junctions are well developed in differentiated endocrine and exocrine cells and are typically sparse or absent in proliferating stem cells. Moreover, the induction of secretory activity itself appears to be correlated with increased numbers of gap junctions in luteal cells, adrenal cortical cells, pancreatic exocrine cells, mammary alveolar cells and thyroid cells. Studies of osteoblasts have demonstrated a close correlation between the effects of hormones on the generation of a second messenger, formation of gap junctions and cell function. In addition, gap junctions appear to be more abundant in cultured confluent osteoblasts than proliferating cells and osteoblast cell coupling in culture and cAMP production are enhanced by the application of parathyroid hormone (PTH). Conversely, an analog of PTH which binds to PTH receptors but attenuates cAMP accumulation, results in a decrease in cell coupling. Finally, transfection of osteoblasts with antisense Cx43 mRNA results in significant concomitant reductions in coupling and in cAMP synthesis in response to PTH.

It has been suggested that the development of gap junctions may enhance the sensitivity of hormonally responsive cells to their specific ligand as a consequence of the transfer of cAMP through gap junctions. Thus, cells not receiving direct stimulation by binding of the secretogogue to its receptor may also respond to the ligand-mediated production of cAMP in neighboring cells which possess the appropriate receptor. Such a hypothesis has been invoked to explain the maintenance of meiotic arrest of mammalian primary oocytes. These germ cells initiate the first meiotic division during embryonic life but are then almost immediately arrested at the first meiotic prophase stage. Typically, a primary oocyte does not resume meiotic maturation until it responds to an ovulatory surge of gonadotropic hormones following puberty. However, since meiosis spontaneously resumes when the oocyte is removed from the follicle and cultured in medium-lacking hormones, it has been postulated that the follicular environment is inhibitory to resumption of meiotic maturation. Meiotic arrest may be maintained by follicle cell-generated cAMP which enters the oocyte through a well-developed network of gap junctions. Conversely, it has been suggested that meiotic resumption may be signaled by the LH-mediated disruption of the gap junction pathway within the cumulus mass (following an ovulatory surge of gonadotropins), thus preventing cAMP manufactured within the follicle cells

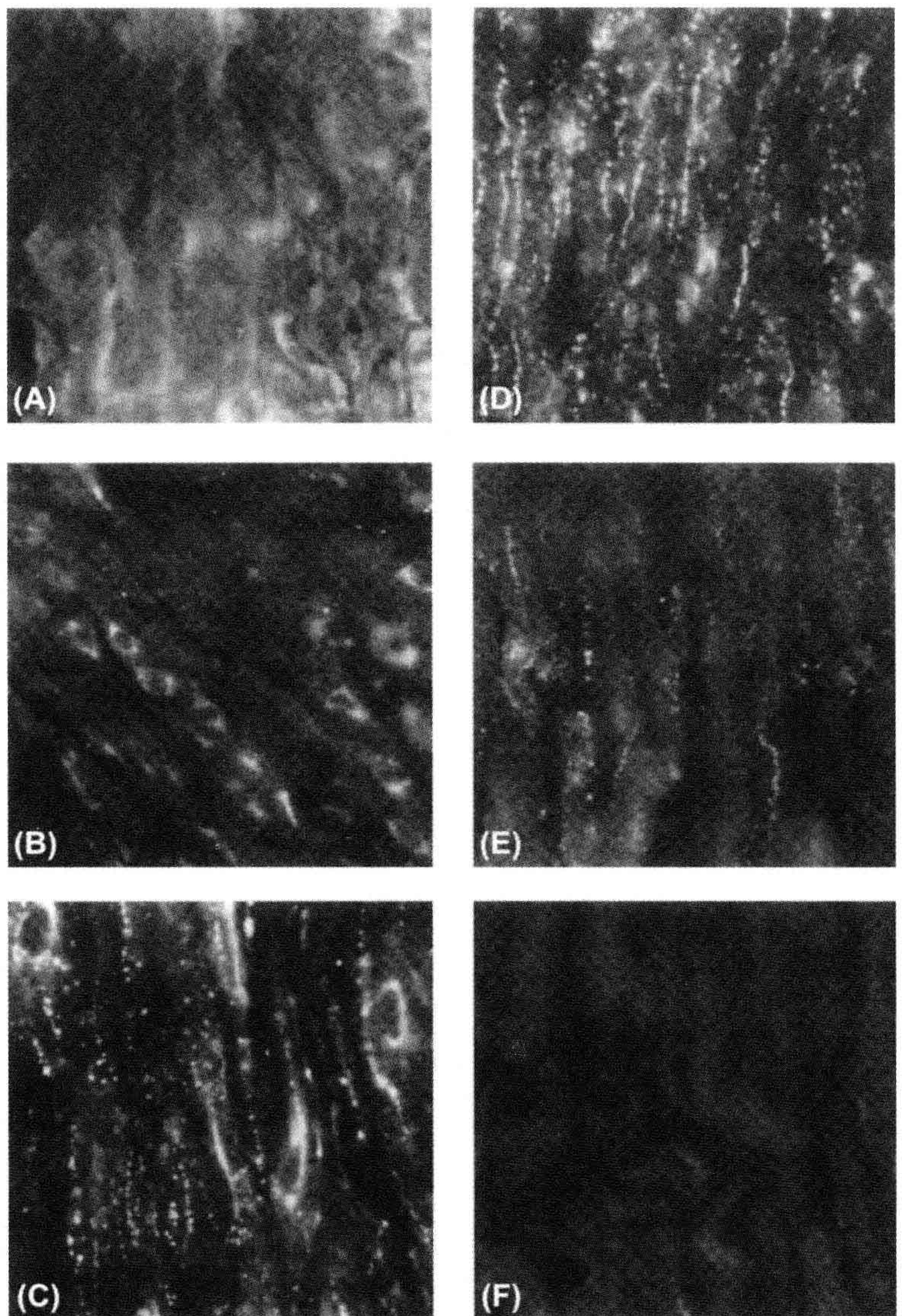


FIGURE 22.10 Immunofluorescent staining of myometrium sections incubated with site-specific antibodies to the carboxyl terminus of Cx43 from pregnant rat sacrificed on day 19 (A) or day 21 (B), at midnight on day 21 (C), during delivery on day 22 (D), 6 h after delivery (E) or 24 h after delivery (F). Magnification, 500×. *(From Hendrix, E.M., Mao, S.J.T., Everson, W. and Larsen, W.J. (1992). Myometrical connexin 43 trafficking and gap junction assembly at term and in preterm labor. Mol. Reprod. Dev., 33, 27, with permission. Copyright 1992 Wiley-Liss, a division of John Wiley & Sons, Inc.)*

from entering the oocyte. Other hypotheses of both negative and positive regulation of meiotic resumption have also been proposed.

It has recently been proposed that gap junction connexins (specifically Cx43) may function in a role somewhat different than those described above; namely in protein trafficking. It has been shown, for example, that the second PDZ domain (of three) of the tight junction-associated protein ZO-1 binds to the extreme C-terminal end of the Cx43 molecule typically resulting in cell membrane colocalization of Cx43 and ZO-1 in cells that co-express these proteins. In support of the possibility that Cx43 is required for shuttling of ZO-1 to the cell membrane, it was found that both ZO-1 and Cx43 fail to accumulate at the cell membrane in Cx43 knockout astrocytes.

XIV. GAP JUNCTIONS IN HUMAN DISEASE AND IN MURINE MODELS OF HUMAN DISEASE

The first hypothesis for a direct link between connexin gap junction function and a human disease was formulated in the 1970s based on the positive correlation between the loss of gap junction function and uncontrolled cell growth as exhibited in carcinogenesis. Over the last two decades, hereditary links to central and peripheral neuropathies, deafness, skin disorders, cataracts, cardiac arrhythmias and multisyndromic craniofacial dysplasias have been identified for 10 different connexins to date. Essentially, all of the known connexin mutations are loss-of-function mutations, either by rendering the resultant gap junction communication-deficient or by preventing the assembly of gap junctions due to connexin misfolding and/or trafficking defects. The precise molecular mechanisms by which a particular connexin mutation produces a communication or trafficking defect are not fully understood but may include alterations in channel permeability, regulatory gating or critical structural components key to correct protein assembly/trafficking and function. A graphical summary of many known connexin-linked human diseases is provided in Fig. 22.11. It should be noted that genetic mutations in *tight junction* and *desmosome* intercellular junction protein constituents are also known to occur.

XIVA. Carcinogenesis

Studies that compared the presence or absence of coupling or gap junctions in normal cells and in several tumors and cancer cell lines initially supported this hypothesis. For example, coupling or gap junctions were found to be deficient in certain hepatoma cells and in L-cell derivatives such as the clone-1D cell line in contrast to their normal counterparts. Indeed, more recent studies support these early observations. For example, an extensive study has examined the role of gap junctions in tumor progression in rat liver following initiation by diethylnitrosamine (DEN) and promotion by either phenobarbitol (PB) or 2,3-dichloro-7,8-dibenzo-*p*-dioxin (TCDD). Transcripts and protein levels of Cx26, Cx32 and Cx43 were measured and reductions in Cx26- and Cx32-positive gap junctions were observed in all resulting neoplasms. However, it was also demonstrated that these decreases were not always associated with reductions in specific m-RNA transcripts for these connexins, suggesting that the loss of junctions could result from the modulation of transcription or translation or from post-translational modification affecting assembly or degradation (see Section XII). Consistent with these observations, the transfection of HeLa cells with cDNA encoding Cx26, but not Cx40 or Cx43, results in inhibition of tumor formation in nude mice, suggesting that Cx26 gap junctions play a pivotal role in growth control. Similarly, the transfection of communication-deficient hepatoma cells (SKHep1) with cDNA encoding Cx32 results in slowing of the growth rate of tumors in nude mice, compared with tumors arising from communication-deficient parental SKHep1 cells.

In conflict with these findings, however, other highly malignant tumor cells have been shown to be well coupled or to possess large numbers of gap junctions. These include Novikoff hepatoma cells, human SW-13 adrenal cortical carcinoma cells and murine B16 melanoma cells.

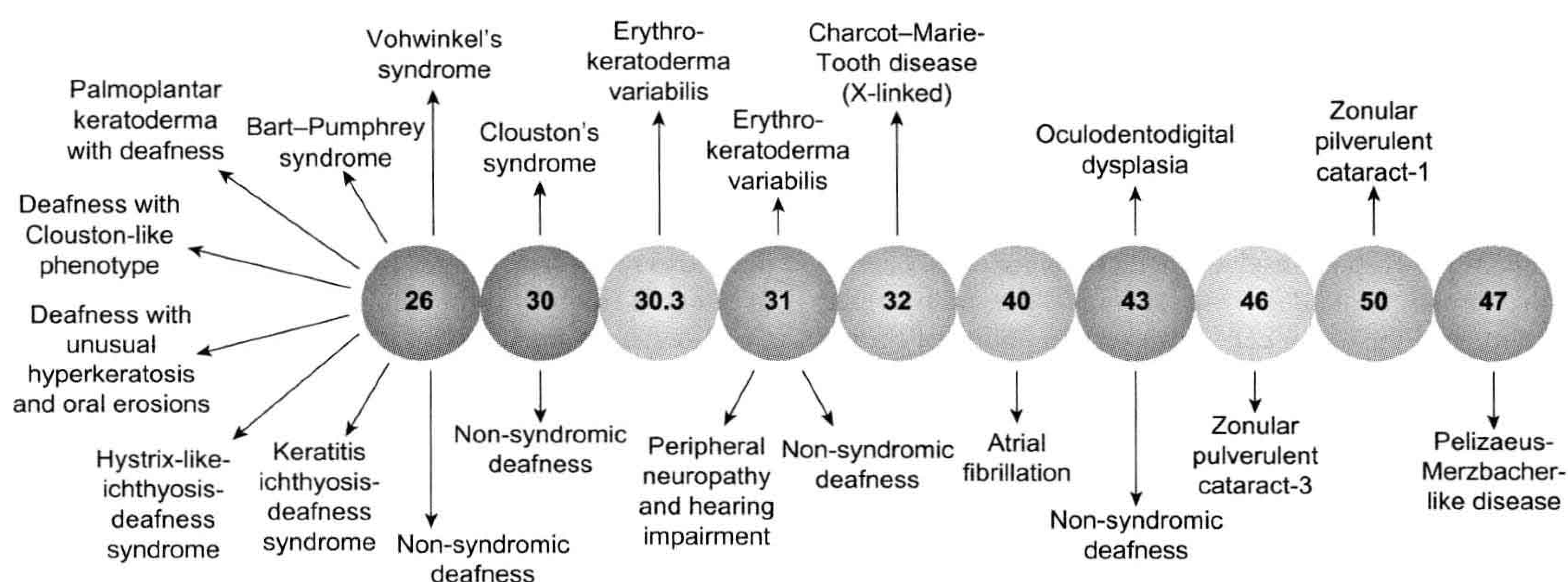


FIGURE 22.11 An illustration of the relationship between inherited connexin mutations and human disease phenotypes. The majority of inherited connexin disorders are autosomal dominant and all involve a loss-of-function due to improper protein folding and trafficking or deficits in gap junction communication. *(Adapted from Lai-Chong, J.E., Arita, K. and McGrath, J.A. (2007). Genetic diseases of junctions. J. Invest. Dermatol., 127, 2715, with permission. Copyright 2007 The Society for Investigative Dermatology.)*

Moreover, other studies have analyzed gap junctions during tumor progression in skin tumors and in hepatocarcinoma and have found that, while gap junctions or coupling may disappear during the transformation of normal cells by cancer-causing agents (such as tumor promoters), their loss seems to follow, rather than lead the changes which transform these normal cells to tumor cells. In response to results such as these, a modified *defective communication* hypothesis was proposed to include cancer cells which might not necessarily exhibit an absence of, or obvious structural defect in the gap junction itself, but which might be defective with respect to some other part of the gap junction communication mechanism, for example, lack of ability of the cell to synthesize the postulated regulatory message or defects in the receptor which translates the cell's activity. Other modifications of the hypothesis have also been advanced, proposing, for example, that some cancer cells (e.g. cultured human SW13 cells and diethylstilbestrol-induced tumors of the proximal tubule in the Syrian hamster) are not able to maintain a steady-state gap junction level through a regulated balance of synthesis or degradation of gap junctions. Under some circumstances, these cells possess normal or even excessive gap junction complements and are mitotically quiescent while, under other conditions, the cells lose most or all of their junctions, resulting in cancerous growth. A temporal relationship between gap junction formation and degradation and the rate of proliferation is also exhibited by normal liver cells in partially hepatectomized rats. Normal rat liver cells remaining after partial hepatectomy initially lose their gap junctions and proliferate rapidly. By 40 hours after partial hepatectomy, the liver cells regain their gap junctions coincident with a reduction in the rate of DNA synthesis and cell division.

Another variation of the hypothesis is based upon a series of experiments that demonstrate that normal cells may have the ability to suppress tumor cell behavior in some normal tumor cell co-cultures as long as the tumor cells can also form gap junctions with the co-cultured normal cells. Other tumor cells may not be able to form gap junctions with normal cells but may be able to form gap junctions between themselves. In these tumor cells, contact with normal cells does not suppress the transformed phenotype of the tumor cell. However, the ability of certain tumor cells to make gap junctions with one another may result in more efficient killing by antitumor agents by allowing the cell-to-cell movement of lethal metabolites formed in some, but not all of the tumor cells within the interconnected network. This phenomenon is called *the bystander effect*. Apoptotic signals may also be propagated by the bystander effect.

In conclusion, despite decades of research, a direct causal link between cancerous growth and deficiencies in gap junction intercellular communication remains elusive. In numerous instances, there is a positive correlation between the development or progression of cancerous tumors and the loss of gap junction communication, but this is not always the case. It is also unlikely that mechanisms of gap junction-mediated growth control will be identical in all cells or tumors where the activity of gap junctions can be demonstrated to play a pivotal role due to the differential expression of connexins.

XIVB. Demyelinating Neuropathies of Cx32 and Cx47 Mutations

Spontaneous mutations of Cx32 result in a common peripheral neuropathy in humans, Charcot-Marie-Tooth disease, which affects one of every 2500 individuals. While this demyelinating disease may arise as a consequence of mutations of a peripheral myelin protein PMP22 (on chromosome 17) or of the myelin constituent Po (on chromosome 1), numerous families have been identified with an X-linked dominant form of the disease characterized by as many as 150 different mutations of Cx32 (CMTX). Mutations may involve single-base substitutions, formation of a premature stop codon, frame-shift or elimination of an amino acid residue. They may occur in amino or carboxyl termini, cytoplasmic or extracellular loops, or in transmembrane regions of the connexin. The causal relationship between these diverse mutations of Cx32 and demyelination of peripheral nerves is obviously varied since the mutations are quite diverse and may or may not affect channel properties. In some cases, it seems possible that mutations may directly affect the function of Cx32 gap junctions in peripheral myelin by interfering with their possible function as ATP-sensitive hemichannels, their function in the exchange of nutrients between the perinuclear region of the Schwann cell and the Schmidt–Lantermann incisures and paranodal processes at the node of Ranvier, or their possible function in signaling between internodes. In other cases, it is thought that the mutations may indirectly affect Cx32 function through effects on Cx32 synthesis and trafficking within the cell. Targeted knockout of connexin 32 in mice also results in changes in liver enzyme activities and in glucose mobilization but, most interestingly, these Cx32-deficient mice have an increased susceptibility to hepatocarcinogenesis. Otherwise, they are vital and fertile. There are >300 *GJB1* mutations thus far identified. A list of these CMTX mutations can be found at http://www.molgen.ua.ac.be/CMTMutations/Mutations/MutByGene.cfm. Oligodendrocytes in the central nervous system also develop a demyelinating neuropathy, Pelizaeus–Merzbacher–like disease (PLMD1) owing to mutations in Cx47 (*GJC2,* formerly *GJA12*). For additional information go to http://www.ncbi.nlm.nih.gov/omim/608804.

XIVC. Cataract Formation and Mutations of Cx50 and Cx46

The maintenance of junctional communication between lens fiber cells is necessary for the homeostatic maintenance of normal transparency of the lens since it is an avascular tissue and the cells are devoid of intracellular organelles. Targeted knockout in mice or mutations in Cx50 lead to development of zonular pulverulent cataracts of the lens but also results in microphthalmia. These results thus implicate Cx50 not only in the maintenance of lens transparency but also in the growth of the eye. Cx46 null mice or mutations in Cx46 produce a more severe form of autosomal dominant zonular pulverulent cataracts, but not microphthalmia. Substituting Cx46 for Cx50 prevents the cataract phenotype but does not rescue the microphthalmia, indicative of differential roles for the two lens connexins in the maintenance of lens homeostasis and crystalline solubility, but not developmental growth control. Additional information can be found at http://www.ncbi.nlm.nih.gov/omim/116200 or /601885.

XIVD. Deafness and Mutations of Cx26, Cx30, Cx31 and Cx43

A variety of mutations of Cx26 including missense mutations and mutations resulting in frameshifts and formation of premature stop codons have been linked to both autosomal recessive and autosomal dominant hearing loss in humans. It is known that deletion of the Cx26 gene leads to the progressive degeneration of the outer hair cells, supporting cells in the outer and middle organ of Corti and spiral ganglion neurons, presumably by disruption of the gap-mediated ion and endolymph circulation in the cochlea. Greater than 100 total *GJB2* mutations have now been identified to cause syndromic (dominant) or non-syndromic (recessive) deafness. Anywhere from two to five non-sydromic deafness mutations have also been identified in the *GJA1* (Cx43), *GJB3* (Cx31) and *GJB6* (Cx30) genes. A database of connexin-linked inherited deafness mutations can be found at http://davinci.crg.es/deafness/index.php?seccion=mut_db&db=synd&synd=cx26synd, or _db&db=nonsynd&nonsynd=cx26mut, ...=cx31mut, ...=cx30mut, and ...=cx43mut. Germline knockout of Cx26 resulted in embryonic lethality as a consequence of placental dysfunction but conditional Cx26 (cCx26) knockout and Cx30 null mice are viable and recapitulate the deafness phenotype.

XIVE. Skin Disorders

Several of the Cx26 mutations associated with syndromic deafness also cause ectodermal skin disorders such as palmoplantar keratoderma, hyperkeratosis, ectodermal dysplasia keratitis-ichthyosis and mutilating keratoderma (Vohwinkel's syndrome). Deafness and non-deafness mutations in Cx31 are known to produce erythrokeratoderma variabilis. Cx30.3 (*GJB4*) also cause erythrokeratoderma variabilis and non-deafness mutations in Cx30 produce autosomal dominant hidrotic ectodermal dysplasia (Clouston syndrome).

XIVF. Oculodentodigital dysplasia (ODDD)

Within the last decade, a multisymptom human disorder including bilateral microphthalmia, microcornea, glaucoma, hypertelorism, narrow nose, microdontia, syndactyly of the fourth and fifth fingers and various neurological and cardiac anomalies were linked to mutations in Cx43. Sixty-two *GJA1* mutations are already known and the vast majority are autosomal dominant but exhibit phenotypic variability for unknown reasons (see http://www.ncbi.nlm.nih.gov/omim/164200). Some mutations result in Cx43 trafficking defects while others form non-communicating or communication-deficient gap junctions, the common theme being a loss-of-function. Already, three murine models of Cx43 ODDD mutations (G60S, I130T, G138R) have been demonstrated to exhibit an increased susceptibility to cardiac arrhythmias, whereas clinically cardiac abnormalities are observed in only 3% of human ODDD patients, 10-fold less than the observed rate for neurological disorders and >20 times less frequent than the observed syndactyly. Perhaps the low incidence of cardiac abnormalities observed with Cx43 mutations is that severe defects likely result in embryonic or neonatal lethality.

XIVG. Heart Function and Mutations of Cx43 and Cx40

While few specific heart defects related to mutations of Cx43 have been observed in humans, a series of studies with animal models of ischemia support a role for Cx43 gap junctions in recovery from injuries to the myocardium. For example, the number of gap junction plaques within the intercalated disk has been shown to decrease in the region of the border of the healing infarct. In addition, the spatial distribution of gap junctions is also abnormal in these areas. These observations, along with studies that show the critical role of Cx43 in conduction (particularly in the ventricle), have led to suggestions that alterations in Cx43 levels and distributions may play an important role in development of infarct-mediated arrhythmias. Targeted knockouts of Cx43 and mice overexpressing Cx43 are characterized by abnormal development of the pulmonary (right ventricular) outflow tract resulting in their death immediately following birth. Enlargement of the right ventricle with thinning of the wall, attenuation of the ductus

arteriosus and formation of one or two abnormal pouches at the base of the pulmonary outflow tract were also observed. It has been suggested that these defects of conotruncal development may result from disruption of the cardiac neural crest. In addition, Cx43 knockout mice of both sexes have small gonads, resulting in part from deficiencies in germ cell development. Since these mice die shortly after birth, the gonads were cultured to determine their capacity for folliculogenesis. It was found that follicles in these ovaries develop only to the primary follicle stage. Targeted knockout of Cx40 results in defects consistent with its localization in the AV node and in conductive myocardium. Electrocardiography of Cx40 knockout animals was characterized by reduced conduction velocities and abnormalities characteristic of first-degree atrioventricular block with associated bundle branch block.

At least half a dozen mutations in Cx40 have been identified in human patients suffering from chronic atrial fibrillation (AF) in recent years and Cx40 polymorphisms have been linked to atrial standstill as well as AF. Conditional Cx43 knockout and Cx43 ODDD mutation mouse models have further revealed that heterogeneous loss of Cx43 from the myocardium increases the susceptibility to atrial or ventricular arrhythmias to a greater extent than uniform reductions in Cx43 expression. Many of these Cx40 or Cx43 mutations again result in a loss-of-function, although the underlying precise molecular mechanisms are poorly understood. Chronic AF and myocardial ischemia or infarction cause cardiac remodeling of gap junctions that sustain AF or increase susceptibility to ventricular arrhythmias due to increased heterogeneity and reductions in the safety margin for conduction disturbances especially during rapid stimulation rates. Our understanding of acute and chronic changes in cardiac gap junction distribution and function will likely evolve through further investigations of Cx40/Cx43 mutations and the molecular mechanisms involved in their redistribution and function.

XIVH. Fertility and Targeted Knockout of Cx37

While no human syndrome resulting from mutations of Cx37 (the human ortholog of *Xenopus* oocyte Cx38 [*GJA2*]) is known, the targeted knockout of Cx37 in mice has been shown to result in the disruption of folliculogenesis. Follicles develop only to early antral stages, the oocytes fail to acquire meiotic competence and ovulation does not occur. Cx43 is essential to (antral) follicular maturation.

IN MEMORIAM

This chapter is dedicated to the memory of William J. Larsen who previously co-authored this chapter before losing his life to cancer soon after publication of the 3rd edition in 2001.

BIBLIOGRAPHY

Alcolea, S., Theveniau-Ruissy, M., Jarry-Gnichard, T., et al. (1999). Downregulation of connexin 45 gene products during mouse heart development. *Circ Res, 84*, 1365–1379.

Bai, S., Schoenfeld, A., Pietrangelo, A., & Burk, R. D. (1995). Basal promoter of the rat connexin 32 gene: identification and characterization of an essential element and its DNA-binding protein. *Mol Cell Biol, 15*, 1439–1445.

Barr, L., Dewey, M. M., & Berger, W. (1965). Propagation of action potentials and the structure of the nexus in cardiac muscle. *J Gen Physiol, 48*, 797–823.

Bevans, C. G., Kordel, M., Rhee, S. K., & Harris, A. L. (1998). Isoform composition of connexin channels determines selectivity among second messengers and uncharged molecules. *J Biol Chem, 272*, 2808–2816.

Beyer, E. C., & Berthoud, V. M. (2009). The family of connexin genes. In *Connexins: A Guide* (pp. 3–26). New York: Humana Press.

Beyer, E. C., Paul, D. L., & Goodenough, D. L. (1990). Connexin family of gap junction proteins. *J Membr Biol, 116*, 187–194.

Brink, P. R., & Dewey, M. M. (1980). Evidence for fixed charge in the nexus. *Nature, 285*, 101–102.

Brink, P. R., & Fan, S.-F. (1989). Patch clamp recordings from membranes which contain gap junction channels. *Biophys J, 56*, 579–593.

Budunova, I. V., Carbajal, S., Viaje, A., & Slaga, T. J. (1996). Connexin expression in epidermal cell lines from SENCAR mouse skin tumors. *Mol Carcinog, 15*, 190–201.

Bukauskas, F. F., Bukauskiene, A., & Verselis, V. K. (2002). Conductance and permeability of the residual state of connexin43 gap junction channels. *J Gen Physiol, 119*, 171–185.

Chiba, H., Sawada, N., Oyamada, M., et al. (1993). Relationship between the expression of the gap junction protein and osteoblast phenotype in a human osteoblastic cell line during cell proliferation. *Cell Struct Func, 19*, 419–426.

Coppen, S. R., Kodama, I., Boyett, M. R., et al. (1999). Connexin45, a major connexin of the rabbit sinoatrial node, is co-expressed with connexin43 in a restricted zone at the nodal-crista terminalis border. *J Histochem Cytochem, 47*, 907–918.

Cowan, D. B., Lye, S. J., & Langille, B. L. (1998). Regulation of vascular connexin43 gene expression by mechanical loads. *Circ Res, 82*, 786–793.

Dahl, G., & Locovei, S. (2006). Pannexin: to gap or not to gap, is that a question? *IUBMB Life, 58*, 409–419.

Darrow, B. J., Laing, J. G., Lampe, P. D., Saffitz, J. E., & Beyer, E. C. (1995). Expression of multiple connexins in cultured neonatal rat ventricular myocytes. *Circ Res, 76*, 381–387.

Donahue, H. J., McLeod, K. J., Rubin, C. T., et al. (1995). Cell-to-cell communication in osteoblastic networks: cell line-dependent hormonal regulation of gap junction function. *J Bone Min Res, 10*, 881–889.

Ek-Vitorin, J. F., King, T. J., Heyman, N. S., Lampe, P. D., & Burt, J. M. (2006). Selectivity of connexin43 gap junction channels is regulated through protein kinase C-dependent phosphorylation. *Circ Res, 98*, 1498–1505.

Ewart, J. L., Cohen, M. F., Meyer, R. A., et al. (1997). Heart and neural tube defects in transgensis mice overexpressing the Cx43 gap junction gene. *Development, 124*, 1281–1292.

Filson, A. J., Azarnia, R., Beyer, E. C., Loewenstein, W. R., & Brugge, J. A. (1990). Tyrosine phosphorylation of a gap junction protein correlated with inhibition of cell-to-cell communication. *Cell Growth Diff, 1*, 661–668.

Flagg-Newton, J., Simpson, I., & Loewenstein, W. R. (1979). Permeability of the cell-to-cell membrane channels in mammalian cell junction. *Science, 205*, 404–407.

Forge, A., Becker, D., Casalotti, S., et al. (1999). Gap junctions and connexin expression in the inner ear. *Novartis Found Symp, 219*, 134–150.

Furshpan, E. J., & Potter, D. D. (1959). Transmission at the giant motor synapses of the crayfish. *J Physiol, 145*, 289–325.

Furshpan, E. J., & Potter, D. D. (1968). Low-resistance junctions between cells in embryos and tissue culture. *Curr Top Dev Biol, 3*, 95–127.

Gerido, D. A., & White, T. W. (2004). Connexin disorders of the ear skin, and lens. *Biochim Biophys Acta, 1662*, 159–170.

Giepmans, B. N., & Moolenaar, W. H. (1998). The gap junction protein connexin43 interacts with the second PDZ domain of the zona occludens-1 protein. *Curr Biol, 8*, 931–934.

Goldberg, G. S., Martyn, K. D., & Lau, A. F. (1994). A connexin 43 antisense vector reduces the ability of normal cells to inhibit the foci formation of transformed cells. *Mol Cytogen, 11*, 106–114.

Gollob, D. A., Jones, D. L., Krahn, A. D., et al. (2006). Somatic mutations in the connexin 40 gene (GJA5). *N Engl J Med, 354*, 2677–2688.

Goodenough, D. A., Simon, A. M., & Paul, D. L. (1999). Gap junctional intercellular communication in the mouse ovarian follicle. *Novartis Found Symp, 219*, 226–235.

Gutstein, D. E., Morley, G. E., Vaidya, D., et al. (2001). Heterogeneous expression of gap junction channels in the heart leads to conduction defects and ventricular dysfunction. *Circulation, 104*, 1194–1199.

Harris, A. L. (2007). Connexin channel permeability to cytoplasmic molecules. *Prog Biophys Molec Biol, 94*, 120–143.

Hauer, R. N. W., Groenewegen, W. A., Firouzi, M., Ramanna, H., & Jongsma, H. J. (2006). Cx40 polymorphisms in human atrial fibrillation. *Adv Cardiol, 42*, 284–291.

Hendrix, E. M., Mao, S. J. T., Everson, W., & Larsen, W. J. (1992). Myometrial connexin 43 trafficking and gap junction assembly at term and in preterm labor. *Mol Reprod Develop, 33*, 27–38.

Hendrix, E. M., Myatt, L., Sellers, S., Russell, P. T., & Larsen, W. J. (1995). Steroid hormone regulation of rat myometrial gap junction formation: effects on Cx43 levels and trafficking. *Biol Reprod, 53*, 547–560.

Hille, B. (1992). *Ionic Channels of Excitable Membranes* (2nd ed.). Sunderland: Sinauer Assoc.

Huelser, D. F., Rehkopf, B., & Traub, O. (1997). Dispersed and aggregated gap junction channels I identified by immunogold labeling of freeze-fractured membranes. *Exp Cell Res, 233*, 240–251.

Iglesias, R., Locovei, S., Roque, A., et al. (2008). P2X7 receptor-Panenxin1 complex: pharmacology and signaling. *Am J Physiol (Cell Physiol), 295*, C752–C760.

Jordan, K., Solan, J. L., Dominguez, M., et al. (1999). Trafficking, assembly, and function of a connexin 43-green fluorescent protein chimera in live mammalian cells. *Mol Biol Cell, 10*, 2033–2050.

Juneja, S. C., Barr, K. J., Enders, G. C., & Kidder, G. M. (1999). Defects in the germ line and gonads of mice lacking connexin43. *Biol Reprod, 60*, 1263–1270.

Kalcheva, N., Qu, J., Sandeep, N., et al. (2007). Gap junction remodeling and cardiac arrhythmogenesis in a murine model of oculodentodigital dysplasia. *Proc Natl Acad Sci USA, 104*, 20512–20516.

Kamibayashi, Y., Oyamada, Y., Mori, M., & Oyamada, M. (1995). Aberrant expression of gap junction proteins (connexins) is associated with tumor progression during multistage mouse skin carcinogenesis. *Carcinogen, 16*, 1287–1297.

Kanemitsu, M. Y., Loo, L. W. M., Simon, S., Lau, A. F., & Eckhart, W. (1997). Tyrosine phosphorylation of connexin 43 by v-src is mediated by SH2 and SH3 domain interactions. *J Biol Chem, 272*, 22824–22831.

Kanter, H. L., Saffitz, J. E., & Beyer, E. C. (1992). Cardiac myocytes express multiple gap junction proteins. *Circ Res, 70*, 438–444.

Kenne, K., Fransson-Steen, R., Honkasalo, S., & Warngard, L. (1994). Two inhibitors of gap junction intercellular communication, TPA and endosulfan: different effects on phosphorylation of connexin 43 in the rat liver epithelial cell line, IAR 20. *Carcinogen, 15*, 1161–1165.

Khan-Dawood, F. S., Yang, J., & Dawood, M. Y. (1996). Expression of gap junction protein connexin-43 in the human and baboon corpus luteum. *J Clin Endocrinol Metab, 81*, 835–842.

Kiang, D. T., Jin, N., Tu, Z. J., & Lin, H. H. (1997). Upstream genomic sequence of the human connexin26 gene. *Gene, 199*, 165–171.

Kirchhoff, S., Nelles, E., Hagendorff, A., Kruger, O., Traub, O., & Willecke, K. (1998). Reduced cardiac conduction velocity and predisposition to arrythmias in connexin40-deficient mice. *Curr Biol, 8*, 299–302.

Lai-Chong, J. E., Arita, K., & McGrath, J. A. (2007). Genetic diseases of junctions. *J Invest Dermatol, 127*, 2713–2725.

Laird, D. W. (2007). Closing the gap on autosomal dominant connexin-26 and connexin-43 mutants linked to human disease. *J.Biol Chem, 283*, 2997–3001.

Laird, D. W., Puranam, K. L., & Revel, J.-P. (1991). Turnover and phosphorylation dynamics of connexin43 gap junction protein in cultured cardiac myocytes. *Biochem J, 273*, 67–72.

Laird, D. W., Castillo, M., & Kasprzak, L. (1995). Gap junction turnover, intracellular trafficking and phosphorylation of connexin 43 in brefeldin A-treated rat mammary tumor cells. *J Cell Biol, 131*, 1193–1203.

Landesman, Y., White, T. W., Starich, T. A., Shaw, J. E., Goodenough, D. A., & Paul, D. L. (1999). Innexin-3 forms connexin-like intercellular channels. *J Cell Sci, 112*, 2391–2396.

Larsen, W. J., Wert, S. E., & Brunner, G. D. (1987). Differential modulation of follicle cell gap junction populations at ovulation. *Dev Biol, 122*, 61–71.

Lo, C. W., Cohen, M. F., Huang, G. Y., et al. (1997). Cx43 gap junction gene expression and gap junctional communication in mouse neural crest cells. *Dev Genet, 20*, 119–132.

Loewenstein, W. R. (1979). Junctional intercellular communication and control of growth. *Biochim Biophys Acta, 560*, 1–65.

Loewenstein, W. R. (1985). Regulation of cell-to-cell communication by phosphorylation. *Biochem Soc Symp, 50*, 43–58.

Loewenstein, W. R., Kanno, Y., & Socolar, S. J. (1978). Quantum leaps of conductance during formation of membrane channels at cell-cell junction. *Nature, 274*, 133–136.

Loo, L. W., Berestecky, J. M., Kanemitsu, M. Y., & Lau, A. F. (1995). pp60src-mediated phosphorylation of connexin 43, a gap junction protein. *J Biol Chem, 270*, 12751–12761.

Maestrini, E., Korge, B. P., Ocana-Sierra, J., et al. (1999). A missense mutation in connexin26, D66H, causes mutiliating keratoderma with sensorineural deafness (Vohwinkel's syndrome) in three unrelated families. *Hum Mol Genet, 8*, 1237–1243.

Makowski, L., Caspar, D. L. D., Phillips, W. C., & Goodenough, D. A. (1977). Gap junction structures. II. Analysis of the x-ray diffraction data. *J Cell Biol, 74*, 629–645.

Mesnil, M., Crespin, S., Avanzo, J. L., & Dagli, M. L. (2005). Defective gap junctional intercelluar communication in the carcinogenic process. *Biochim Biophys Acta, 1719*, 125–145.

Mesnil, M., Krutovskikh, V., Piccoli, C., et al. (1995). Negative growth control of HeLa cells by connexin genes: connexin specificity. *Cancer Res, 55*, 629–639.

Moennikes, O., Buchmann, A., Ott, T., Willecke, K., & Schwarz, M. (1999). The effect of connexin32 null mutation on hepatocarcinogenesis in different mouse strains. *Carcinogenesis, 20*, 1379–1382.

Musil, L. S., & Goodenough, D. A. (1990). Gap junctional intercellular communication and the regulation of connexin expression and function. *Curr Opin Cell Biol, 2*, 875–880.

Neuhaus, I. M., Bone, L., Wang, S., Ionascescu, V., & Werner, R. (1996). The human connexin32 gene is transcribed from two tissue-specific promoters. *Biosci Rep, 16*, 239–248.

Neveu, M. J., Hully, J. R., Babcock, K. L., et al. (1994). Multiple mechanisms are responsible for altered expression of gap junction genes during oncogenesis in rat liver. *J Cell Sci, 107*, 83–95.

Neyton, J., & Trautmann, A. (1985). Single-channel currents of an intercellular junction. *Nature, 317*, 331–335.

Nonner, W., & Eisenberg, B. (1998). Ion permeation and glutamate residues linked by Poisson-Nernst-Planck Theory in L-type calcium channels. *Biophys J, 75*, 1287–1305.

Orsino, A., Taylor, C. V., & Lye, S. J. (1996). Connexin-26 and connexin-43 are differentially expressed and regulated in the rat myometrium throughout late pregnancy and the onset of labor. *Endocrinology, 137*, 1545–1553.

Pal, J. D., Berthoud, V. M., Beyer, E. C., Mackay, D., Shiels, A., & Ebihara, L. (1999). Molecular mechanism underlying a Cx50-linked congenital cataract. *Am J Physiol, 276*, c1443–c1446.

Paznekas, W. A., Karczeski, B., Vermeer, S., et al. (2009). GJA1 mutations, variants, and connexin43 dysfunction as it relates to the oculodentodigital dysplasia phenotype. *Hum Mutat, 30*, 724–733.

Peters, N. S. (1996). New insights into myocardial arrythmogenesis: distribution of gap junctional coupling in normal ischaemic and hypertrophied human hearts. *Clin Sci, 90*, 447–452.

Phelan, P. (2005). Innexins: members of an evolutionarily conserved family of gap junction proteins. *Biochim Biophys Acta, 1711*, 225–245.

Piersanti, M., & Lye, S. J. (1995). Increase in messenger ribonucleic acid encoding the myometrial gap junction protein, connexin-43, requires protein synthesis and is associated with increased expression of the activator protein-1, c-fos. *Endocrinology, 136*, 3571–3578.

Qu, Y., & Dahl, G. (2002). Function of the voltage gate of gap junction channels: selective exclusion of of molecules. *Proc Natl Acad Sci USA, 99*, 697–702.

Reaume, A. G., de Sousa, P. A., Kulkarni, S., et al. (1995). Cardiac malformation in neonatal mice lacking connexin43. *Science, 267*, 1831–1834.

Revel, J.-P., & Karnovsky, M. J. (1967). Hexagonal array of subunits in intercellular junctions in the mouse heart and liver. *J Cell Biol, 38*, C7–C12.

Revel, J.-P., Hoh, J. H., John, S. A., Laird, D. W., Puranam, K., & Yancey, S. B. (1992). Aspects of gap junction structure and assembly. *Sem Cell Biol, 3*, 21–28.

Sáez, J. C., Berthoud, V. M., Brañes, M. C., Martínez, A. D., & Beyer, E. C. (2003). Plasma membrane channels formed by connexins: their regulation and functions. *Physiol Rev, 83*. 13659–1400.

Saez, J., Nairn, A. C., Czernik, A. J., et al. (1990). Phosphorylation of connexin32, a hepatocyte gap junction protein, by cAMP-dependent protein kinase, protein kinase C and Ca^{2+}/calmodulin-dependent protein kinase II. *Eur J Biochem, 192*, 263–273.

Seul, K. H., Tadros, P. N., & Beyer, E. C. (1997). Mouse connexin40: gene structure and promoter analysis. *Genomics, 46*, 120–126.

Simon, A. M., Goodenough, D. A., & Paul, D. L. (1998). Mice lacking connexin40 have cardiac conduction abnormalities characteristic of atriventricular block and bundle branch block. *Curr Biol, 8*, 295–298.

Simpson, I., Rose, B., & Loewenstein, W. R. (1977). Size limit of molecules permeating the junctional membrane channels. *Science, 195*, 294–296.

Solan, J. L., & Lampe, P. D. (2005). Connexin phosphorylation as a regulatory event linked to gap junction channel assembly. *Biochim Biophys Acta, 1711*, 154–163.

Solan, J. L., & Lampe, P. D. (2007). Connexin43 phosphorylation: structural changes and biological effects. *Biochem J, 419*, 261–272.

Spray, D. C., & Dermietzel, R. (1995). X-linked dominant Charcot-Marie-Tooth disease and other potential gap junction diseases of the nervous system. *TINS, 18*, 256–262.

Sun, Y., Tang, W., Chang, Q., Wang, Y., Kong, W., & Lin, X. (2009). Connexin30 null and conditional mice connexin26 null mice display distinct pattern and time course of cellular degeneration in the cochlea. *J Comp Neurol, 516*, 569–579.

Swenson, K. I., Piwnica-Worms, H., McNamee, H., & Paul, D. L. (1990). Tyrosine phosphorylation of the gap junction protein connexin43 is required for the pp60v-src-induced inhibition of communication. *Cell Reg, 1*, 989–1002.

Tu, Z. J., & Kiang, D. T. (1998). Mapping and characterization of the basal promoter of the human connexin26 gene. *Biochim Biophys Acta, 1441*, 169–181.

Unger, V. M., Kumar, N. M., Gilula, N. B., & Yeager, M. (1999). Three-dimensional structure of a recombinant gap junction membrane channel. *Science, 283*, 1176–1180.

Veenstra, R. D. (2000). Ion permeation through connexin gap junction channels: effects on conductance and selectivity. In C. Perrachia (Ed.), *Current Topics in Membranes*, Vol. 49, pp. 95–129.

Veenstra, R. D., & DeHaan, R. L. (1986). Measurement of single channel currents from cardiac gap junctions. *Science, 233*, 972–974.

Veenstra, R. D., Wang, H.-Z., Beblo, D. A., et al. (1995). Selectivity of connexin-specific gap junctions does not correlate with channel conductance. *Circ Res, 77*, 1156–1165.

Veenstra, R. D., Wang, H.-Z., Westphale, E. M., & Beyer, E. C. (1992). Multiple connexins confer distinct regulatory and conductance properties of gap junctions in developing heart. *Circ Res, 71*, 1277–1283.

Waldo, K. L., Lo, C. W., & Kirby, M. L. (1999). Connexin43 expression reflects neural crest patterns during cardiovascular development. *Dev Biol, 208*, 307–323.

Warn-Cramer, B. J., Lampe, P. D., Kurata, W. E., et al. (1996). Characterization of the mitogen-activated protein kinase phosphorylation sites on the connexin-43 gap junction protein. *J Biol Chem, 271*, 3779–3786.

White, T. W., Goodenough, D. A., & Paul, P. L. (1998). Targeted ablation of connexin 50 in mice results in micropthalmia and zonular pulverulent cataracts. *J Cell Biol, 143*, 815–825.

Yamaguchi, D. T., Huang, J. T., & Ma, D. (1995). Regulation of gap junction intercellular communication by pH in MC3T3-E1 osteoblastic cells. *J Bone Min Res, 10*, 1891–1899.

Yamasaki, H. (1991). Aberrant expression and function of gap junctions during carcinogenesis. *Env Health Prosp, 93*, 191–197.

Yang, Y. Q., Liu, X., Zhang, X. L., et al. (2010). Novel connexin40 missense mutations in patients with familial atrial fibrillation. *Europace, 12*, 1421–1427.

Yu, W., Dahl, G., & Werner, R. (1994). The connexin43 gene is responsive to oestrogen. *Proc Roy Soc (London) Series B Biol Sci, 255*, 125–132.

Chapter 23

Regulation of Cardiac Ion Channels by Cyclic Nucleotide-Dependent Phosphorylation

Gordon M. Wahler and Nicholas Sperelakis

Chapter Outline

I. SUMMARY

Ion channels in the heart are regulated by many physiological mechanisms. One of the most important mechanisms is the regulation by cyclic nucleotide protein kinases. Calcium channels in the heart play a central role in excitation–contraction coupling and the physiological modulation of these channels is crucial to the functioning of the heart under differing conditions. Phosphorylation–dephosphorylation reactions regulate the cardiac calcium channel activity. Activation of the cyclic AMP-dependent protein kinase stimulates the channel activity, whereas activation of the cyclic GMP-dependent protein kinase inhibits the channel activity. Both synthesis and degradation of the cyclic nucleotides are regulated by a large number of physiological and pathophysiological first messengers. There is considerable compartmentalization of the components of the cyclic nucleotide pathways and there are significant interactions between the two cyclic nucleotides. The complexities of these two cyclic nucleotide systems allows for fine control of calcium channel activity in the heart.

II. INTRODUCTION

Phosphorylation of ion channel proteins by various protein kinases is one of the primary mechanisms for physiological modulation of ion channel activity. One of the most widely-studied examples of this regulatory mechanism is cyclic nucleotide-dependent phosphorylation of the calcium channels in the heart.

There exist several different subtypes of voltage (V)-dependent Ca^{2+} channels in excitable cells. In cardiac muscle cells, the primary channels responsible for entry of Ca^{2+} ions into the cell during an action potential (AP) are the V-dependent "L-type" (i.e. "long-lasting") Ca^{2+} channels responsible for the L-type Ca^{2+} current (I_{Ca}). This chapter will focus on the L-type Ca^{2+} channel of cardiac myocytes and modulation of I_{Ca} by the cyclic nucleotide-dependent phosphorylation, in order to illustrate some important principles that are involved in ion channel regulation.

The L-type channels play a central role in excitation–contraction (E-C) coupling. During an AP, Ca^{2+} influx through the L-type channels leads to: (1) direct activation

Cell Physiology Sourcebook. DOI: 10.1016/B978-0-12-387738-3.00023-8

of the myofilaments; (2) Ca^{2+} loading of the sarcoplasmic reticulum (SR); and (3) release of Ca^{2+} from the SR ("calcium-induced calcium release"). Thus, controlling the amount of Ca^{2+} influx through the L-type channels is a key mechanism for regulation of myocardial contractility.

The L-type Ca^{2+} channels have some special properties, including functional dependence on metabolic energy, selective blockade by acidosis and regulation by intracellular second messengers. Because of these special properties of these channels, Ca^{2+} influx into the myocardial cell can be controlled by both extrinsic factors (such as autonomic nerve stimulation or circulating hormones) and intrinsic factors (such as intracellular pH or ATP levels). Thus, there are many sites for physiological and pathophysiological modulation of I_{Ca}.

III. REGULATION OF THE CARDIAC L-TYPE Ca^{2+} CHANNELS BY CYCLIC AMP

IIIA. Evidence for Cyclic AMP Modulation of L-Type Ca^{2+} Channel Function

A major physiological modulator of ion channels and E-C coupling in the heart is the β-adrenergic pathway. It has long been known that the β-adrenergic-cAMP pathway modulates the functioning of the L-type Ca^{2+} channels (Shigenobu and Sperelakis, 1972; Tsien et al., 1972) (Fig. 23.1). Every step in the pathway has been shown to alter I_{Ca}. Stimulation of cardiac β-adrenergic receptors (e.g. in response to the release of norepinephrine from sympathetic nerves) causes adenylate cyclase activation. This results in increase of intracellular cyclic AMP (cAMP) levels and enhanced activation of the cAMP-dependent protein kinase (PK-A). The activated PK-A phosphorylates a number of proteins, including several involved in E-C coupling (e.g. Stojanovic et al., 2001).

Thus, induction of Ca^{2+}-dependent slow APs, an indirect measure of I_{Ca}, was observed with exposure to direct activators of adenylate cyclase (forskolin, Gpp(NH)p) (Josephson and Sperelakis, 1978; Wahler and Sperelakis, 1986). These effects have been repeatedly confirmed by direct measurement of adenylate cyclase activators on I_{Ca} (e.g. Ziolo et al., 2003; Fig. 23.2). Additionally, direct injection of cAMP into ventricular muscle cells was shown rapidly to (within seconds) induce Ca^{2+}-dependent slow APs (Vogel and Sperelakis, 1981; Li and Sperelakis, 1983; Bkaily and Sperelakis, 1985) and enhance I_{Ca} (Irisawa and Kokubun, 1983). Similarly, rapid enhancement of I_{Ca} was observed with intracellular photochemical activation of cAMP in ventricular myocytes (Nargeot et al., 1983). Other neurotransmitters, hormones and autacoids that stimulate cAMP production (e.g. histamine) also enhance I_{Ca}.

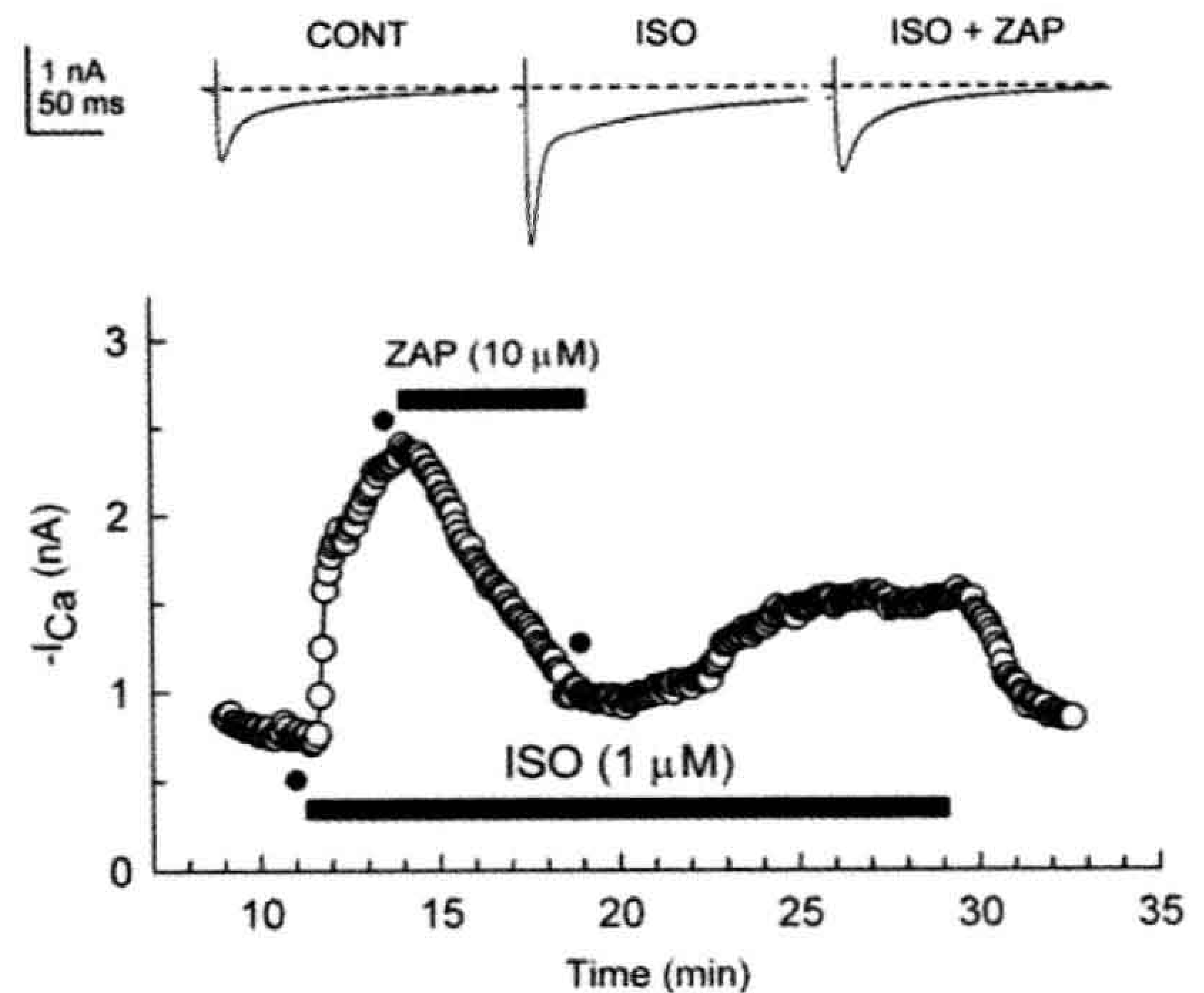


FIGURE 23.1 Zaprinast inhibited the isoproterenol-stimulated I_{Ca}. Shown are the original currents (upper panel) and the amplitude of I_{Ca} at 0 mV over time (lower panel) during superfusion of the cells with control (CONT), 1 μM isoproterenol-containing (ISO), or isoproterenol plus 10 μM zaprinast-containing (ISO + ZAP) solutions. Superfusion of the cell with 1 μM isoproterenol caused a large stimulation of I_{Ca}. Subsequent superfusion of the cell with 10 μM zaprinast caused a substantial inhibition of the isoproterenol-induced stimulation of I_{Ca}. Upon washout of zaprinast there was a partial recovery of the isoproterenol-stimulated I_{Ca}. Standard whole-cell recording (calcium-free pipette solution) was used. Individual current traces were obtained at time points indicated by the filled circles in the lower panel. *(From Ziolo et al., 2003; used with permission).*

Since PK-A phosphorylation of the L-type Ca^{2+} channels leads to an increase in I_{Ca} and enhanced Ca^{2+} influx during the plateau phase of the AP, this causes a direct increase in the amount of Ca^{2+} available to the contractile proteins. It also indirectly increases the Ca^{2+} available to the contractile proteins due to effects of increased Ca^{2+} influx on Ca^{2+} cycling and release by the SR. The direct and indirect effects of the phosphorylated L-type Ca^{2+} channel, together with the effects of PK-A-phosphorylated SR proteins, mediate the vast majority of the positive inotropic effects of β-adrenergic stimulation on the heart.

Single-channel analysis indicates that β-adrenergic stimulation causes an increase in the mean open time of Ca^{2+} channels and increases the probability of opening (largely by decreasing interval between bursts of openings), whereas the single-channel conductance is unaffected (Reuter et al., 1982; Klein et al., 2000). These effects on the channels lead to an increased I_{Ca} during the AP.

IIIB. The Phosphorylation Hypothesis

Because of the relationship between cAMP and the number of available L-type Ca^{2+} channels and because of the metabolic dependence of the functioning of these

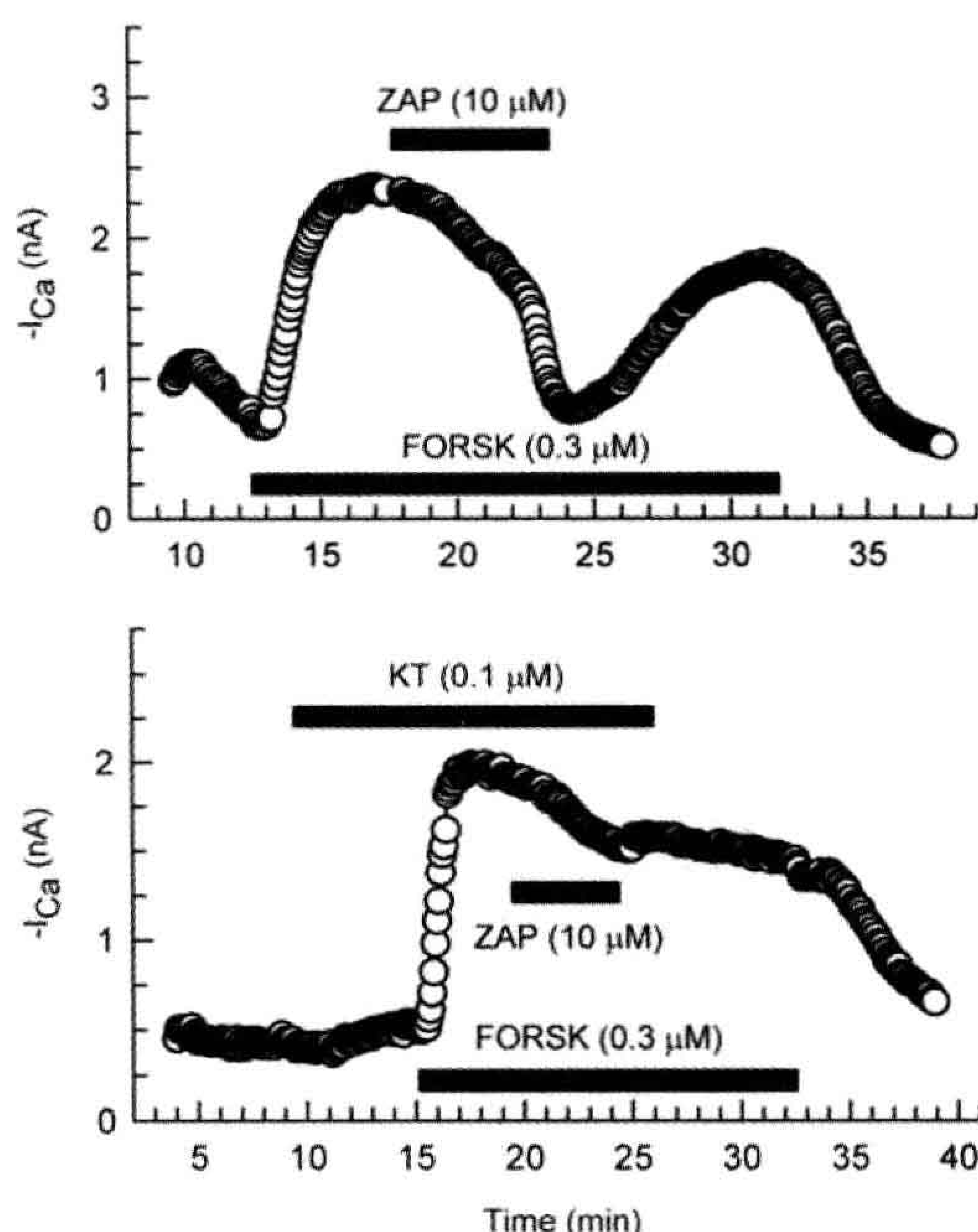


FIGURE 23.2 Zaprinast inhibition of the forskolin-stimulated I_{Ca} in the absence and presence of an inhibitor of PK-G (KT5823). Superfusion of a cell with 0.3 μM forskolin (FORSK), a direct activator of adenylate cyclase, caused a large stimulation of I_{Ca}. Upper panel: under control conditions, subsequent superfusion of the cell with 10 μM zaprinast (ZAP) caused a substantial reversible inhibition of the forskolin-induced stimulation of I_{Ca}. Lower panel: in contrast, in the presence of 0.1 μM KT5823 (KT), the inhibitory effect of zaprinast was greatly attenuated. Standard whole-cell recording was used. *(Modified from Ziolo et al., 2003; used with permission).*

channels, it was hypothesized that one of the proteins that is phosphorylated is the L-type Ca^{2+} channel protein (or a contiguous regulatory protein). That is, the L-type channel must be phosphorylated for it to become available for voltage activation (Shigenobu and Sperelakis, 1972; Tsien et al., 1972). According to the phosphorylation hypothesis (Fig. 23.3), agents that elevate cAMP increase the fraction of the channels that are in the phosphorylated form and hence readily available for voltage activation. Whatever the precise molecular mechanism for the effect phosphorylation has on channel activity, in the phosphorylation model, the phosphorylated form of the L-type channel is the active (operational) form and the dephosphorylated form is the inactive (inoperative) form. The dephosphorylated channels are virtually silent electrically (i.e. their opening probability approaches zero). Phosphorylation increases the probability of channel opening with depolarization. An equilibrium should exist between the phosphorylated and dephosphorylated forms of the channel under a given set of conditions.

IIIC. Protein Kinase-A (PK-A) Activation

Over the years, considerable evidence has accumulated that supports the phosphorylation hypothesis. For example, intracellular injection of the catalytic subunit of PK-A induces and increases the slow Ca^{2+}-dependent APs and potentiates I_{Ca} (Osterreider et al., 1982; Bkaily and Sperelakis, 1984). Injection of a PK-A inhibitor protein into heart cells inhibits slow Ca^{2+}-dependent APs and I_{Ca} (Bkaily and Sperelakis, 1984; Kameyama et al., 1986). These results verify that the regulatory effect of cAMP on I_{Ca} is mediated by PK-A and phosphorylation.

Also consistent with the phosphorylation hypothesis, L-type Ca^{2+} channel activity disappears within 90 s in isolated membrane inside-out patches, but can be restored (in neurons) by applying the catalytic subunit of PK-A together with MgATP (Armstrong and Eckert, 1987). This is consistent with the washing away of regulatory components of the Ca^{2+} channels or of the enzymes necessary to phosphorylate the channel. Even in whole-cell voltage-clamp, there is a progressive run-down of the Ca^{2+} current, which is slowed or partially reversed by conditions that enhance PK-A phosphorylation.

IIID. Phosphatases

While much research has been done on the role of phosphorylation in the regulation of ion channels, much less is known about the reverse reaction, i.e. the role of dephosphorylation of ion channels by phophatases. Based on the rapid decay of the response to microinjected cAMP, the mean life span of a phosphorylated channel is probably only a few seconds at most. Agents that affect or regulate the phosphatase that dephosphorylates the channel would affect the life span of the phosphorylated channel. Thus, channel stimulation can be produced either by increasing the rate of phosphorylation (by PK-A activation) or by decreasing the rate of dephosphorylation (inhibition of the phosphatase).

In ventricular cells, several phosphatases have been shown to inhibit I_{Ca} (e.g. Kameyama et al., 1986; duBell and Rogers, 2004), consistent with the phosphorylation hypothesis. Additionally, phosphatase inhibitors, such as okadaic acid and microcystin, cause large increases in I_{Ca} (Hescheler et al., 1987, 1988; Frace and Hartzell, 1993). There is some disagreement about the relative effectiveness of specific phosphatases (particularly type 1 versus type 2A) in reducing I_{Ca} and whether basal I_{Ca} is significantly inhibited by phosphatases, or if only the cAMP-stimulated I_{Ca} (e.g. by a β-adrenergic agonist) is affected.

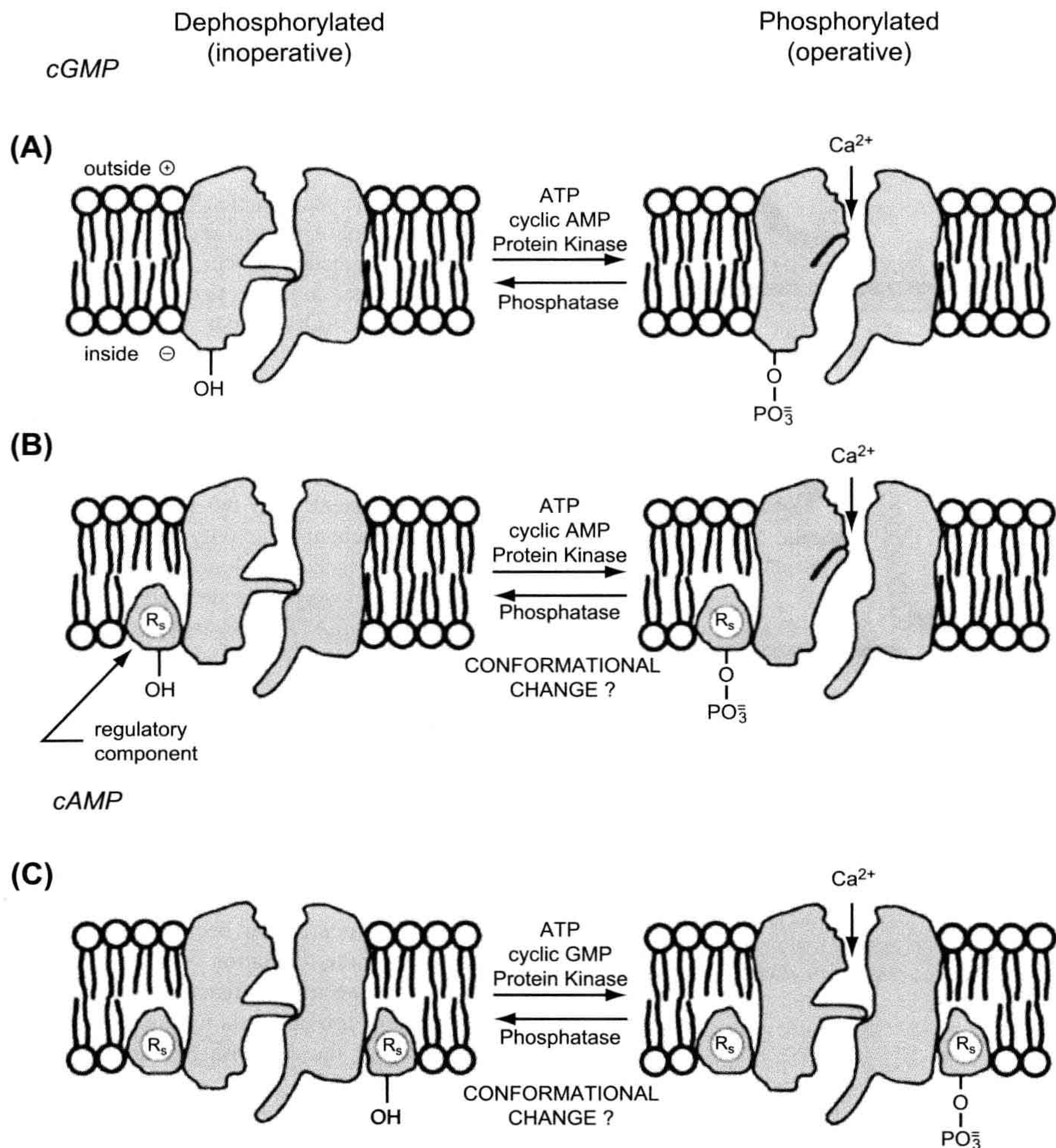


FIGURE 23.3 The phosphorylation hypothesis. Schematic model for an L-type Ca^{2+} channel in myocardial cell membrane in two hypothetical forms: dephosphorylated (or electrically silent) form (left diagrams) and phosphorylated form (right diagrams). The two gates associated with the channel are an activation gate and an inactivation gate. The phosphorylation hypothesis states that a protein constituent of the Ca^{2+} channel itself (A) or a regulatory protein associated with the channel (B) must be phosphorylated for the channel to be in a state available for voltage activation. Phosphorylation of a serine (or threonine) residue occurs by PK-A in the presence of ATP. Phosphorylation may produce a conformational change that effectively allows the channel gates to operate. The L-type channel (or an associated regulatory protein) may also be phosphorylated by PK-G (C), thus mediating the inhibitory effects of cGMP on the Ca^{2+} channel. *(Adapted from Sperelakis and Schneider, 1976).*

Protein phosphatase-type 1 activity is inhibited by (at least) two low-molecular-weight proteins, protein phosphatase inhibitor-1 (PPI-1) and protein phosphatase inhibitor-2 (PPI-2). PPI-1 is present in ventricular myocytes and it may be an important additional component of the modulation of the phosphorylation–dephosphorylation cycle of the L-type channel. The activity of PPI-1 is enhanced by phosphorylation with PK-A (Ahmad et al., 1989; Gupta et al., 1996). Thus, PK-A not only phosphorylates the Ca^{2+} channel, it also decreases the rate of channel dephosphorylation. Both actions stimulate channel activity.

In contrast to the effects of other phosphatases examined to date, calcineurin has been shown to enhance I_{Ca} (Tandan et al., 2009). Calcineurin binds to the L-type Ca^{2+} channel near the site where PP2A binds and

dephosphorylates the channel but, unlike PP2A, calcineurin upregulates channel activity. Additionally, calcineurin inhibitors inhibit I_{Ca}. Thus, while dephosphorylation of the Ca^{2+} channel does not always inhibit I_{Ca}, it does appear that phosphatases are an additional important determinant of the amplitude of I_{Ca}. Alternatively, there may be more than one site on the channel that can be phosporylated.

IV. REGULATION OF THE L-TYPE Ca^{2+} CHANNELS BY CYCLIC GMP

IVA. Cyclic GMP Effects

The physiological role played by cyclic GMP (cGMP) on cardiac function appears to be more complex than that of cAMP. It was originally proposed that cGMP plays a role antagonistic to that of cAMP (Goldberg et al., 1975) and, in most instances, but not all, this appears to be the case. Thus, considerable evidence has accumulated demonstrating cGMP inhibition of I_{Ca}. For example, 8-Br-cGMP, a more permeable and hydrolysis-resistant analog of cGMP, has been shown to shorten the AP duration in rat atria (accompanied by a negative inotropic effect) (Nawrath, 1977) and to inhibit Ca^{2+}-dependent slow APs (Kohlhardt and Haap, 1978; Wahler and Sperelakis, 1985) and accompanying contractions (Wahler and Sperelakis, 1985). Intracellular injection of cGMP into atrial, ventricular and Purkinje fiber preparations was also shown rapidly to depress or abolish slow APs (Mehegan et al., 1985; Wahler and Sperelakis, 1985).

In whole-cell voltage-clamp experiments on single cardiomyocytes from a variety of species, it has been directly shown that cGMP regulates I_{Ca} (e.g. Fischmeister and Hartzell, 1987; Levi et al., 1989, 1994; Wahler et al., 1990; Mery et al., 1991; Wahler and Dollinger, 1995; Sumii and Sperelakis, 1995; Ziolo et al., 2003) (Fig. 23.4). For example, in voltage-clamp experiments on single ventricular cardiomyocytes from embryonic chicks or neonatal rats, stimulation of I_{Ca} produced by 8-Br-cAMP added to the bath could be completely reversed by the addition of 8-Br-cGMP (Masuda and Sperelakis, unpublished observations; Fig. 23.5). The ratio of cAMP/cGMP apparently determines the degree of stimulation of I_{Ca}.

In some instances, the cGMP inhibition of I_{Ca} is dependent on prior stimulation of I_{Ca} by cAMP. However, it has also been directly demonstrated that, under some conditions, 8-Br-cGMP inhibits basal I_{Ca} (i.e. unstimulated by cAMP) in voltage-clamped ventricular myocytes (e.g. Wahler et al., 1990; Haddad et al., 1995) (see Fig 23.4). Inhibition of basal Ca^{2+} channel activity by cGMP has also been demonstrated at the single-channel level in embryonic chick heart (Tohse and Sperelakis, 1991) (Fig. 23.6), under conditions in which the intracellular environment is likely to be more normal than during

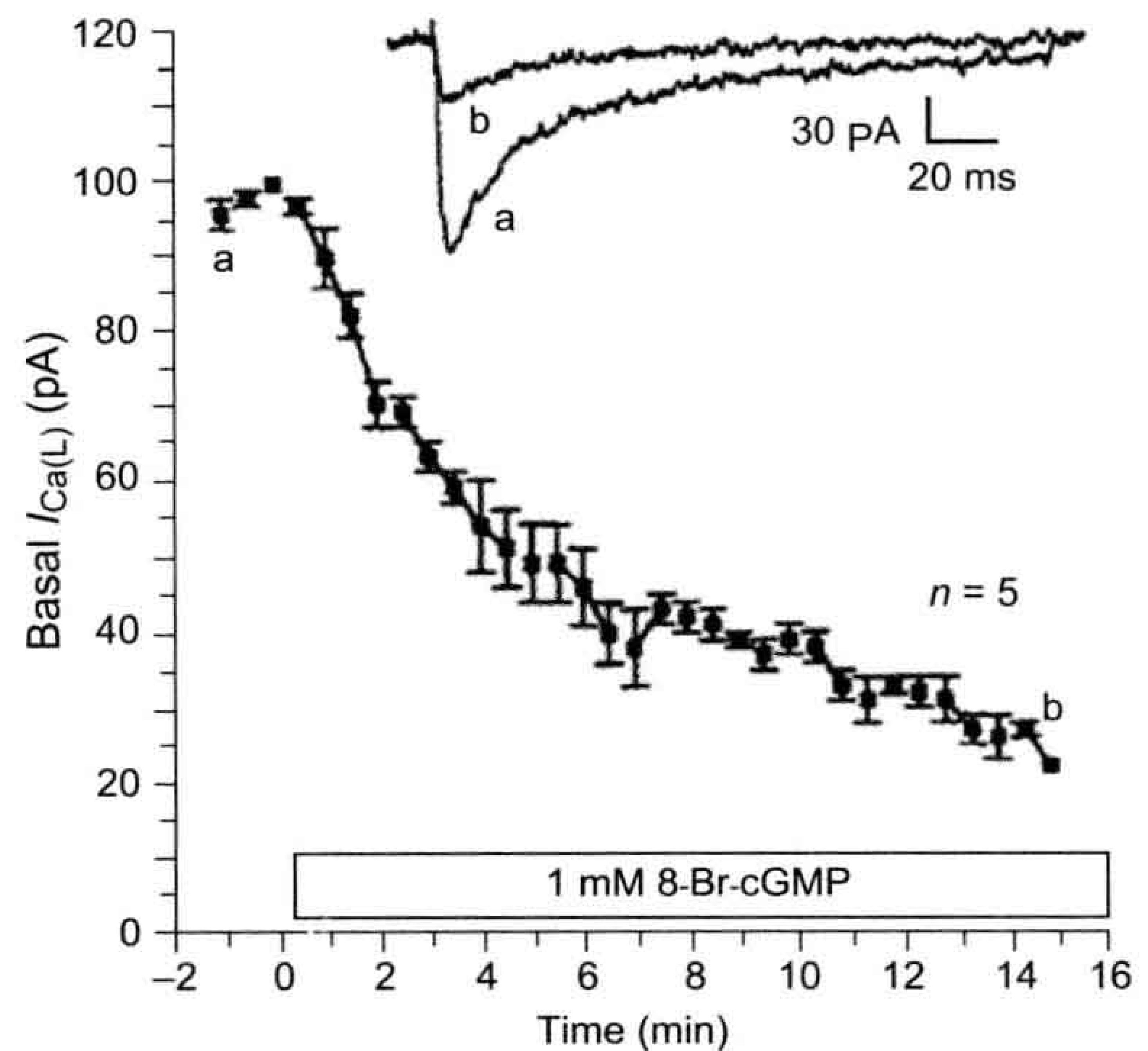


FIGURE 23.4 Time course of the inhibition of the basal I_{Ca} by 8-Br-cGMP (1 mM) in 17-day-old embryonic chick heart cells. Data points plotted are the mean ± standard error. The upper two traces show the original current recordings of I_{Ca} taken at the time points shown by the corresponding letters in the graph. I_{Ca} was elicited by 200 ms depolarizing pulses to +10 mV from a holding potential of −45 mV. Experiments conducted at room temperature. *(From Haddad et al., 1995.)*

whole-cell voltage clamp experiments. Addition of 8-Br-cGMP to the bath completely inhibited Ca^{2+} channel activity. Cyclic GMP did not change the conductance of the Ca^{2+} channel, but prolonged the closed times and shortened the open times. In contrast, 8-Br-cGMP had no effect on the basal Ca^{2+} single-channel activity in mouse ventricular myocytes, but did reverse all the stimulatory effects of the β-adrenergic agonist isoproterenol (Klein et al., 2000). However, the debate about whether basal I_{Ca} is inhibited by cGMP is likely more of academic than physiological importance, since in vivo there would consistently be tonic activation of β-adrenergic receptors due to sympathetic nerve activity and adrenal release of catecholamines. Under such conditions, no true "basal" (i.e. unstimulated by cAMP) I_{Ca} would exist.

IVB. Mechanisms for cGMP Inhibition of I_{Ca}

As noted above, cGMP regulates the functioning of the L-type Ca^{2+} channels in a manner that is antagonistic to that of cAMP. It was hypothesized that the Ca^{2+} channel protein has a second site that can be phosphorylated by the cGMP-dependent protein kinase (PK-G) and that, when phosphorylated, inhibits the Ca^{2+} channel (Wahler and Sperelakis, 1985). Another possibility is that there is a second type of regulatory protein that is inhibitory when phosphorylated (see Fig. 23.3). Subsequently, it was shown that, similar to activated PK-A, activated

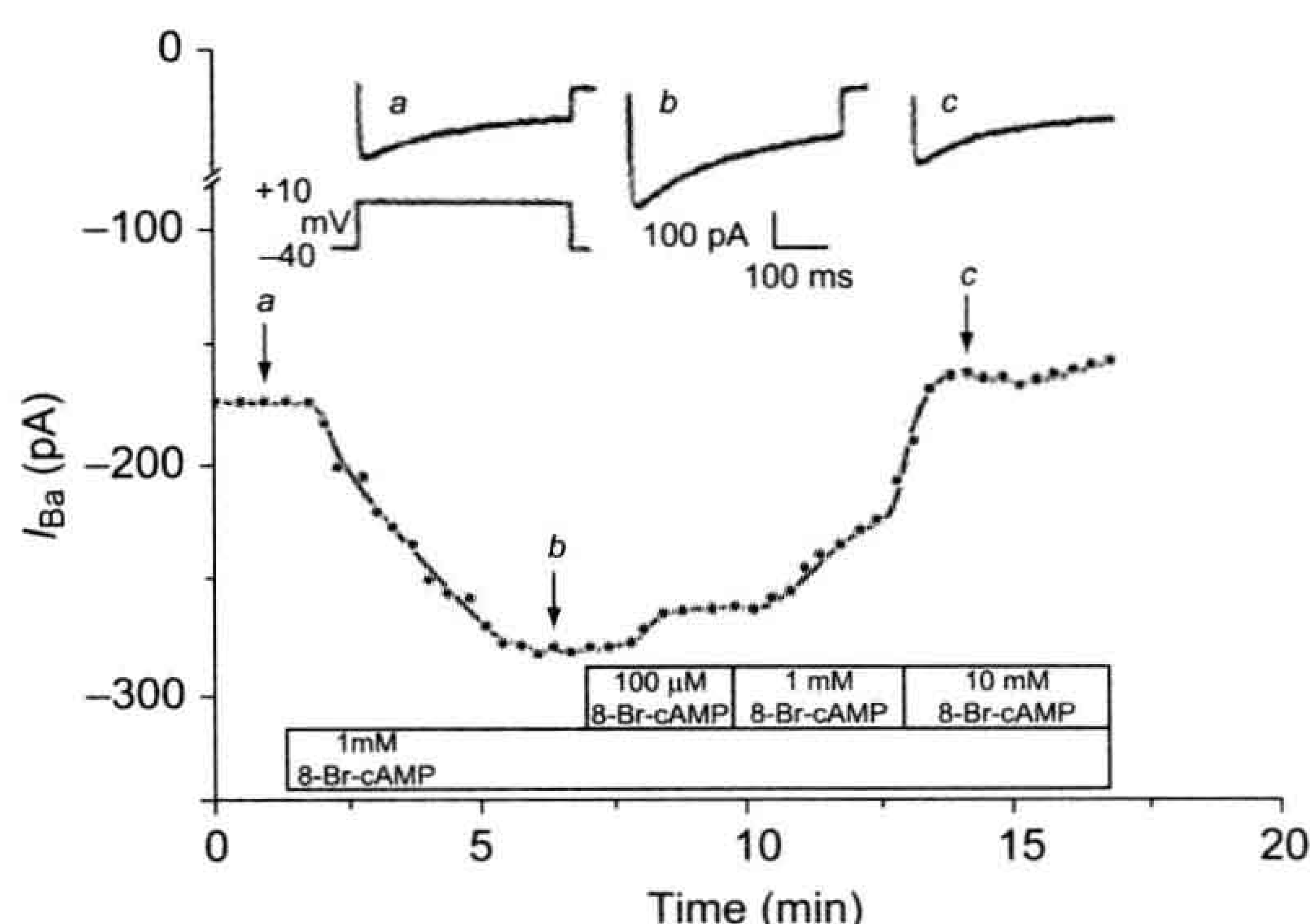


FIGURE 23.5 Antagonism of the stimulating effect of 8-Br-cAMP on I_{Ca} by 8-Br-cGMP in a single 2-day rat ventricular myocyte. Upper tracings show three original current recordings of I_{Ca} corresponding to the three time points labeled in the lower graph. I_{Ca} was elicited by 300 ms depolarizing pulses to +10 mV from a holding potential of −40 mV. Ba^{2+} (20 mM) was used as the charge carrier. Experiments conducted at room temperature of 25°C. *(From Masuda and Sperelakis, unpublished.)*

PK-G phosphorylates a number of proteins involved in E-C coupling (e.g. Stojanovic et al., 2001), including the L-type Ca^{2+} channel (Schröder et al., 2003; Yang et al., 2007).

There is considerable evidence that the PK-G-mediated phosphorylation of the L-type Ca^{2+} channel is functionally significant, i.e. that the reduction of I_{Ca} observed with cGMP is mediated by this phosphorylation (at least in mammalian and avian ventricular myocytes; see below). Observation of inhibition of I_{Ca} by 8-Br-cGMP (see Figs. 23.4–23.6), which is a potent activator of PK-G, supports the view that PK-G is responsible for the inhibitory effect of cGMP on I_{Ca}.

In some preparations (e.g. embryonic chick, neonatal rat), when PK-G is directly added to the patch pipette for diffusion into the cell during whole-cell voltage clamp, basal I_{Ca} is inhibited markedly and rapidly, with maximum inhibition reached in about 3–5 min (Fig. 23.7). Note that inhibition of basal I_{Ca} began about 80 s after breaking into the cell. Similar effects of PK-G infusion were observed in early neonatal rat ventricular myocytes, as illustrated in Fig. 23.8 (Sumii and Sperelakis, 1995). As can be seen, there is a rapid and prominent inhibition of basal I_{Ca} by PK-G. Addition of H-8 (a blocker of both PK-A and PK-G) to the bath often causes a rapid restoration of I_{Ca} to about the original basal level. Addition of 1 mM 8-Br-cAMP can produce only a small stimulation of I_{Ca} in the continued presence of PK-G (see Fig. 23.8). Therefore, these findings indicate that the inhibitory effects of cGMP on I_{Ca} in mammalian and avian ventricular myocytes are mediated by activation of PK-G and resultant phosphorylation. Because 8-Br-cGMP is a potent activator of PK-G and does not stimulate cAMP hydrolysis, cGMP-induced inhibition of the basal activity of the Ca^{2+} channels (not prestimulated by cAMP) is likely also to be mediated by PK-G.

In ventricular muscle from wild-type mice, 8-Br-cGMP inhibited contractility, consistent with observations in other cardiac preparations. In addition, in the same study (Wegener et al., 2002), 8-Br-cGMP had no effect on contractility in PK-G-1 knockout mice, supporting the view that PK-G mediated the inhibition of contractility caused by 8-Br-cGMP. In contrast, muscarinic cholinergic stimulation reduced myocyte contractility, not only in wild-type, but also in the PK-G-1 knockout mouse, suggesting that muscarinic inhibition of contractility may be independent of PK-G-1 activation.

In single-channel recordings in mouse ventricular myocytes, 8-Br-cGMP has no effect on basal single Ca^{2+}

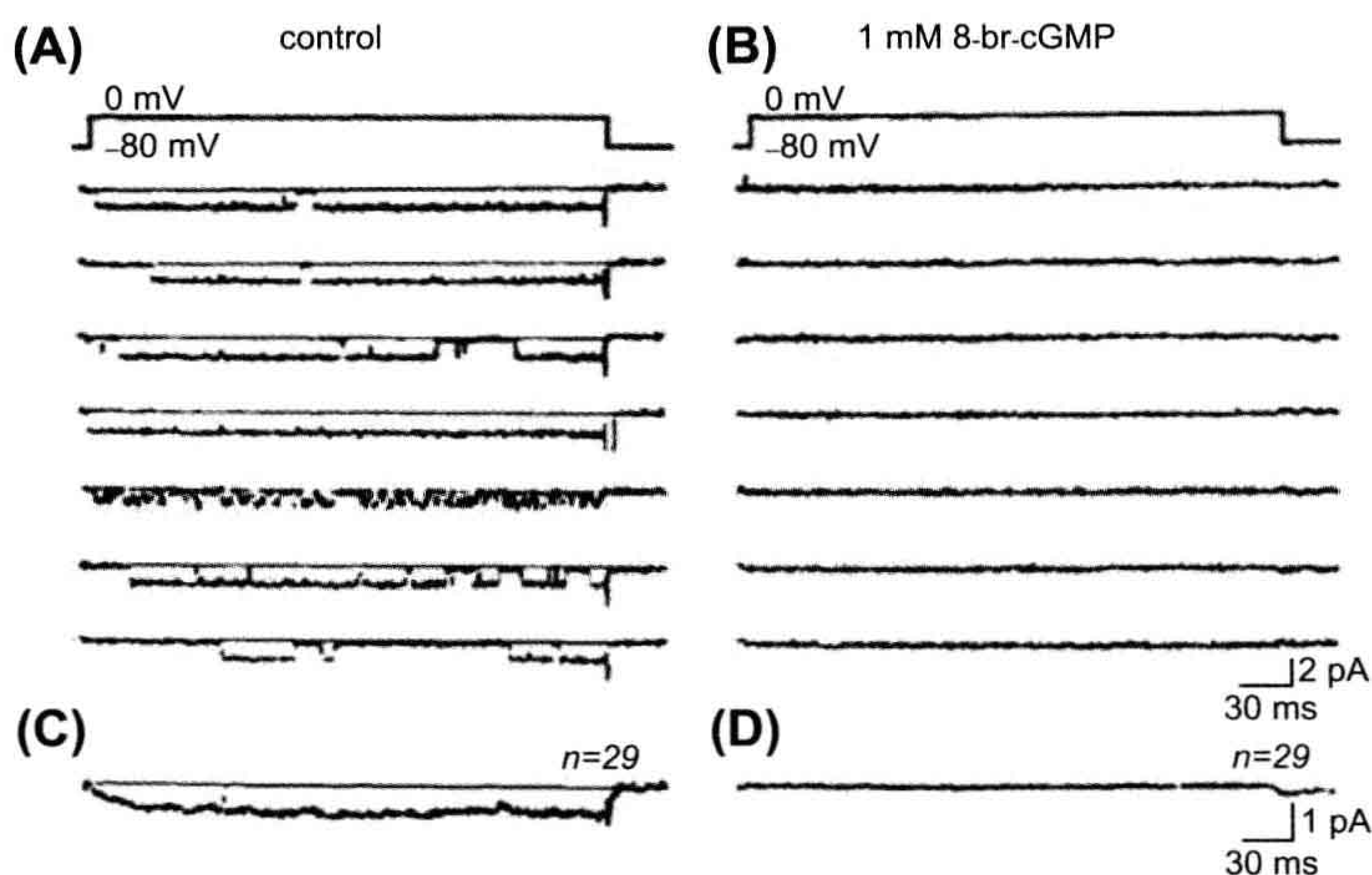


FIGURE 23.6 Current recordings from a cell-attached patch showing the effect of 8-Br-cGMP on the Ca^{2+} channel activity in a single myocardial cell isolated from a 3-day-old embryonic chick heart. Single channel currents were evoked by depolarizing voltage pulses to 0 mV from a holding potential of −80 mV, at a duration of 300 ms and stimulation frequency of 0.5 Hz. (A and B) Examples of original current recordings from the same patch, before (A) and after (B) superfusion with 1.0 mM 8-Br-cGMP. (C and D) Ensemble-averaged currents calculated from the current recordings (n = 29 traces). *(Data from Tohse and Sperelakis, 1991.)*

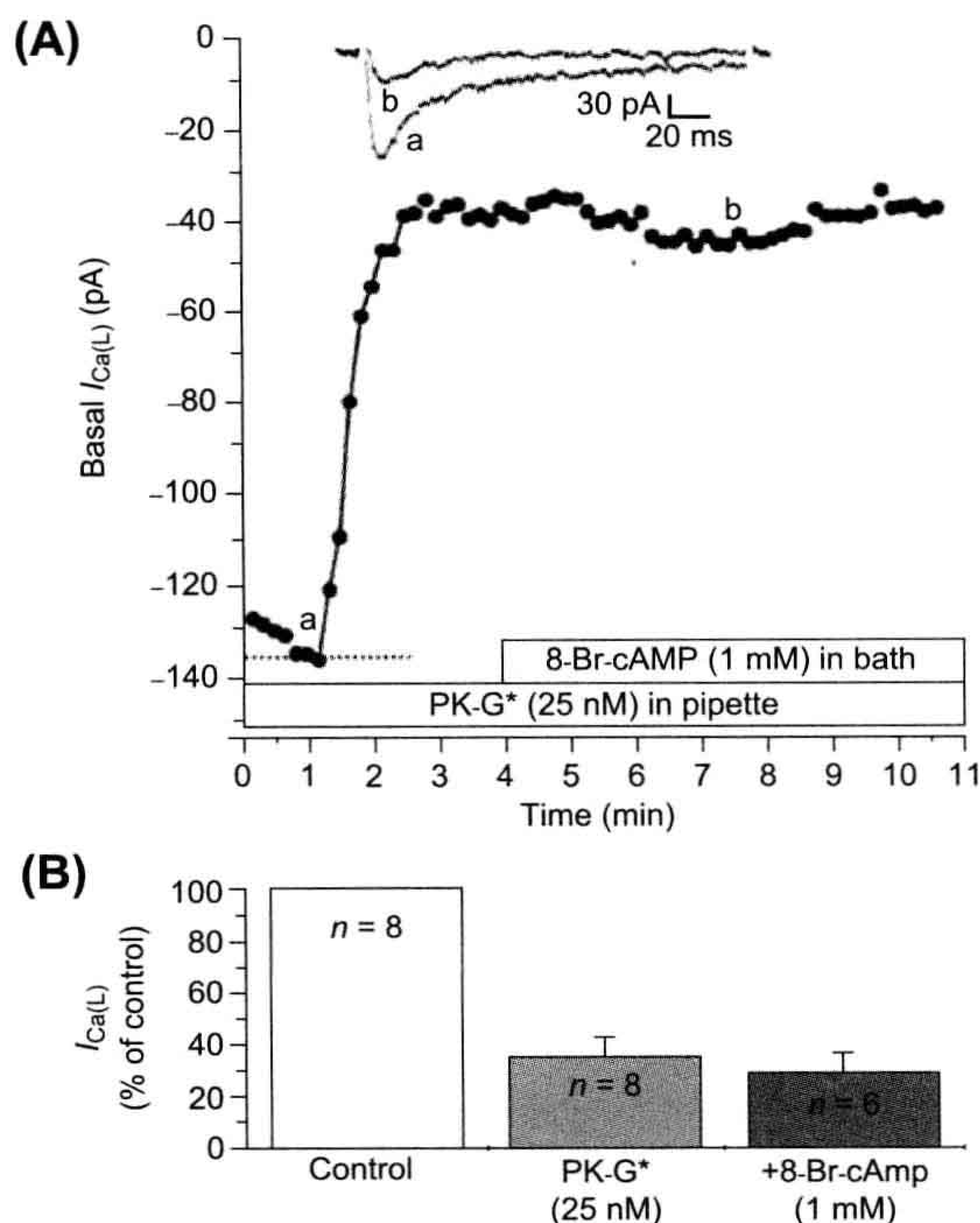


FIGURE 23.7 Inhibition of basal I_{Ca} of 17-day-old embryonic chick cardiomyocytes by PK-G. (A) PK-G (25 nM) was present in the patch pipette for diffusion into the cell during whole-cell voltage clamp. Inhibition of I_{Ca} began within 70 s after breaking into the cell and reached maximum at about 2.5 min. Addition of 1 mM 8-Br-cAMP into the bath failed to reverse the inhibition produced by PK-G. The two current traces illustrated at the top correspond to the time points labeled a and b in the graph. (B) Bar graph summary of the inhibition of basal I_{Ca} by PK-G in eight cells, and the lack of reversal by 8-Br-cAMP in six cells. Experiments were done at room temperature. *(From Haddad et al., 1995.)*

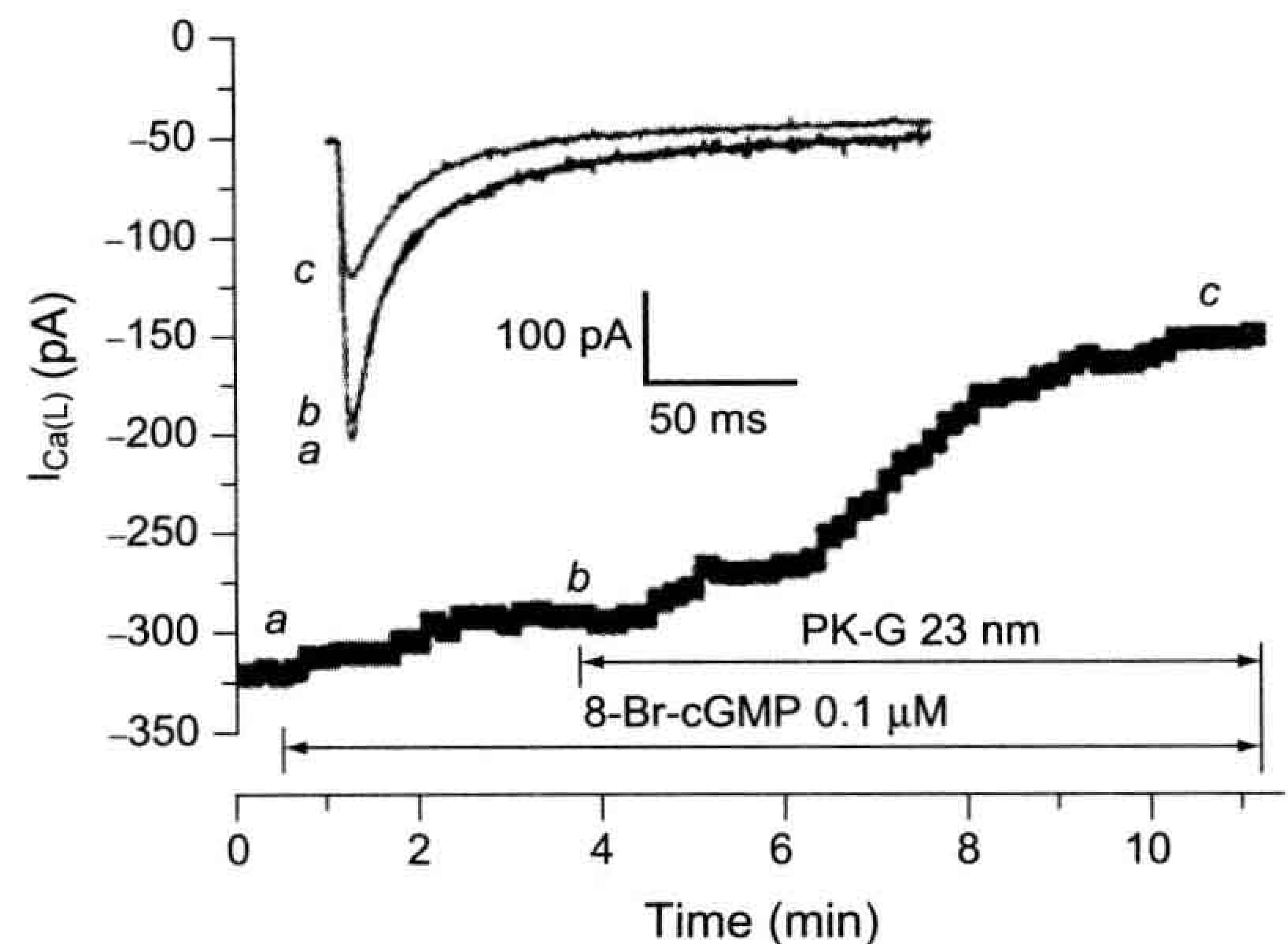


FIGURE 23.8 Inhibition of basal I_{Ca} by PK-G (25 mM) in a ventricular myocyte from an early (4 day) neonatal rat heart. Time course of the effect of low doses of 8-Br-cGMP (0.1 μM) and PK-G (25 nM) on basal (not stimulated) I_{Ca}. 8-Br-cGMP and PK-G were applied using the perfusion patch-pipette technique. As shown, when 8-Br-cGMP was applied in advance of PK-G, it had only a little effect, whereas subsequent addition of PK-G produced rapid inhibition (inset). Selected current traces of I_{Ca} (a, b, and c) at points denoted on the time course curve. *(Reproduced with permission from Sumii and Sperelakis, 1995.)*

channel activity, but reverses all the stimulatory effects of the β-adrenergic agonist isoproterenol (Klein et al., 2000). This inhibitory effect of 8-Br-cGMP is also blocked by a PK-G inhibitor, indicating that the effect is mediated by PK-G.

The effects of cardiac myocyte-selective overexpression of PK-G 1 (the primary isoform of PK-G in cardiac myocytes) on the Ca^{2+}-channel response to cGMP have also been investigated at the single-channel level (Schröder et al., 2003). 8-Br-cGMP, DEA-NO (an NO donor) and carbachol (a muscarinic agonist) all inhibited the β-adrenergic stimulation of L-type Ca^{2+} activity in wild-type mouse ventricular myocytes. This inhibition of channel activity was dramatically enhanced for 8-Br-cGMP and DEA-NO (but not carbachol) in the myocytes from mice that overexpressed PK-G 1. Furthermore, while none of the three agents had any effect on the basal L-type Ca^{2+} channel activity in myocytes from wild-type mice, in myocytes overexpressing PK-G 1, 8-Br-cGMP and DEA-NO (but not carbachol) had a dramatic inhibitory effect on basal L-type channel activity. These data again support the hypothesis that the inhibitory effects of 8-Br-cGMP and NO are mediated by PK-G 1, but not the inhibitory effects of muscarinic agonists.

There is another mechanism for cGMP inhibition of I_{Ca} that has been reported for some preparations. This indirect mechanism involves cGMP stimulation of PDE 2, leading to an anti-adrenergic effect due to a reduction in cAMP levels. Evidence for this mechanism comes primarily from frog ventricular myocytes, in which intracellular application of cGMP inhibited I_{Ca} only after the cAMP levels had been increased and EHNA (a selective PDE 2 inhibitor) blocked the cGMP inhibition (Hartzell and Fischmeister 1986; Fischmeister and Hartzell, 1987). It was concluded that cGMP activates PDE 2 (a cGMP-stimulated isoform of phosphodiesterase), resulting in degradation of cAMP. This cGMP-stimulated PDE mechanism for inhibition of I_{Ca} was also found to occur in human atrial cells (Rivet-Bastide et al., 1997).

However, this mechanism (cGMP stimulation of PDE) for cGMP inhibition of I_{Ca} does not appear to be present in mammalian ventricular myocytes. For example, EHNA has no effect on basal or β-stimulated I_{Ca} in mammalian ventricular myocytes (Rivet-Bastide et al., 1997). In mammalian and avian ventricular myocytes, the inhibition of I_{Ca} by cGMP is not mediated by PDE 2, but rather by

PK-G (Levi et al., 1989; Wahler et al., 1990; Mery et al., 1991; Wahler and Dollinger, 1995). 8-Br-cGMP (which does not stimulate PDE 2), not only inhibits slow APs in mammalian cardiac muscle, but it does so without decreasing cAMP levels (Thakkar et al., 1989). Additionally, the inhibitory effect on I_{Ca} of agents that elevate cGMP is maintained when there is a general inhibition of PDEs, including PDE 2, with a non-specific PDE inhibitor (IBMX) (Fig. 23.9). In contrast, the anti-adrenergic action of cGMP is blocked by KT5823, a selective inhibitor of PK-G (Wahler and Dollinger, 1995; Ziolo et al., 2003; see Figs. 23.2 and 23.9).

IVC. Effects of Nitric Oxide on I_{Ca}

Nitric oxide (NO) is known to be an important regulator of a variety of cellular functions, including contractility of the heart. Many (though not all) of the effects of NO are mediated through stimulation of soluble guanylate cyclase (G-cyclase) activity and the resulting enhanced cGMP production. As numerous studies have shown that cGMP inhibits I_{Ca} in cardiac myocytes, the depression of contractility by NO may be in large part due to a cGMP-mediated inhibition of I_{Ca}.

Due to the highly labile nature of NO, NO donors are often used to examine the effect of NO. The NO donor SIN-1 has been shown to have an anti-adrenergic effect on I_{Ca} in both frog and mammalian ventricular myocytes (Mery et al., 1993; Wahler and Dollinger, 1995), similar to the effects of cGMP. The spontaneous breakdown of SIN-1 in solution, not only generates NO, but also generates superoxide anions which can inactivate NO and lead to formation of peroxynitrite, a strong oxidizing agent. Thus, SIN-1 is also used as a peroxynitrite donor and the effects of SIN-1 observed on I_{Ca} could be caused by peroxynitrite, rather than by NO. The addition of superoxide dismutase and catalase, which should degrade superoxide (thereby protecting NO and minimizing peroxynitrite formation) enhanced the effects of SIN-1 on I_{Ca} (Wahler and Dollinger, 1995). Furthermore, LY83583, which blocks cGMP formation by G-cyclase (Kontos and Wei, 1993), or KT5823, which inhibits PK-G, nearly abolished the I_{Ca} response to SIN-1 (see Fig. 23.9). Together these results strongly suggest that NO, rather than peroxynitrite, mediates the effects of SIN-1 on I_{Ca} and that this occurs through enhanced activity of PK-G.

Although in the virtual absence of intracellular (pipette) Ca^{2+}, SIN-1 was reported to have no effect on ventricular I_{Ca}, when a physiological concentration of Ca^{2+} (pCa = 6.85) was present in the pipette solution, SIN-1 did reduce basal I_{Ca} (Matsumoto, 1997). Thus, it is clear that cGMP can also inhibit basal I_{Ca} at least in some preparations under physiological intracellular conditions.

SIN-1, in addition to producing a prominent inhibitory (anti-adrenergic) effect, can occasionally cause an

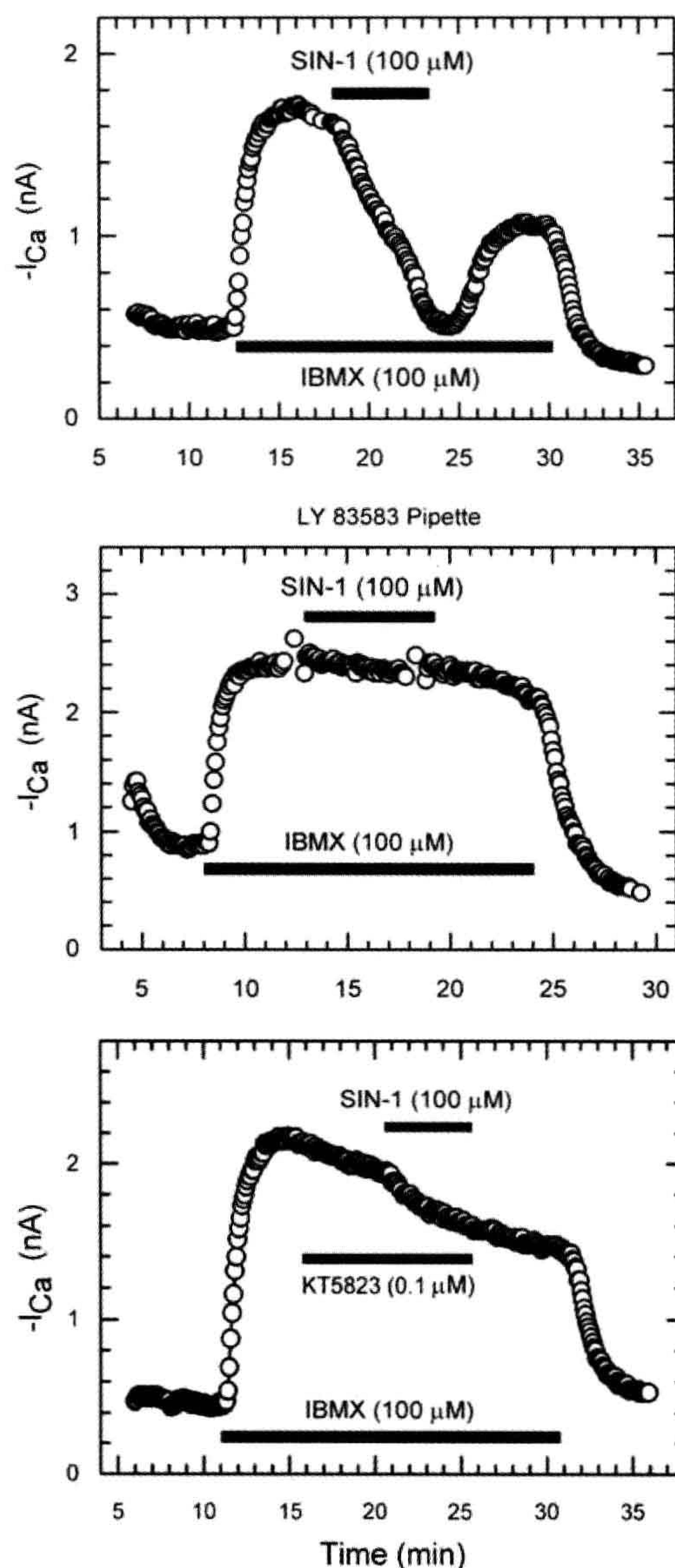


FIGURE 23.9 Blockade of SIN-1 inhibition of I_{Ca} by LY-83583 or KT5823. Top panel: shown is an example of SIN-1 (100 μM) inhibition of IBMX-enhanced I_{Ca} under control conditions. Central panel: inclusion of 10 μM LY-83583 in the pipette solution virtually abolished the response to SIN-1. Bottom panel: superfusion of the cell with 0.1 μM KT5823 had little effect on IBMX-stimulated ICa, but greatly reduced the effect of SIN-1. *(Modified from Wahler and Dollinger, 1995; used with permission.)*

enhancement of I_{Ca} in frog and mammalian ventricular myocytes (Mery et al., 1993; Wahler and Dollinger, 1995). Thus, in cells in which the response to β-agonists was relatively small, low doses of SIN-1 sometimes caused a stimulation of I_{Ca} rather than an inhibition (Fig. 23.10). A similar enhancement of β-stimulated I_{Ca} by low doses of pipette cGMP had been reported previously (Ono and Trautwein, 1991). Thus, while NO and cGMP generally have an inhibitory effect on I_{Ca}, in some instances, they can actually enhance the response to β-stimulation of I_{Ca}. The stimulatory effect of SIN-1 occasionally observed is likely to be mediated by the same mechanism thought to be responsible for cGMP stimulation of cAMP-enhanced I_{Ca} previously described for guinea pig ventricular myocytes, i.e. cGMP inhibition of the cGMP-inhibited PDE (Ono and Trautwein, 1991).

IVD. Pathophysiological Effects of Nitric Oxide/cGMP

Nitric oxide is synthesized by nitric oxide synthase (NOS) from L-arginine. NOS exists in three isoforms, neuronal nitric oxide synthase (NOS-1 or nNOS), inducible nitric oxide synthase (NOS-2 or iNOS), and endothelial nitric oxide synthase (NOS-3 or eNOS) (Alderton et al., 2001). The constitutive isoforms of NOS (NOS-1 and NOS-3) produce relatively small amounts of NO in a Ca^{2+}-dependent fashion (Xie and Nathan, 1994). In cardiac myocytes, constitutive NOS (primarily eNOS) is normally present and functional (Schulz et al., 1992). In contrast, iNOS (which produces much more NO than the constitutive isoform and for longer periods of time) is not normally present in most types of cells, including cardiac myocytes. However, it is expressed in cardiac myocytes under pathological conditions that involve exposure of the cells to cytokines. Thus, it may be that NO produced by constitutive NOS mediates the physiological effects of NO, whereas the much higher levels of NO produced by iNOS may mediate the pathophysiological actions of NO in a number of pathological conditions of the heart. For example, pre-exposure of guinea pig ventricular myocytes to IL-1β for several hours has an anti-adrenergic effect on I_{Ca} that is L-arginine-dependent and NO-mediated (Rozanski and Witt, 1994).

Transplanted hearts are exposed to a variety of cytokines during rejection and have an increased NO production and depressed contractility. Myocytes isolated from rejecting hearts exhibit parallel increases in NO (and cGMP) production (due to the expression of the inducible form of nitric oxide synthase) (Yang et al., 1994; Ziolo et al., 1998) and both a reduced basal contraction and inotropic response to β-adrenergic stimulation (Pyo and Wahler, 1995; Ziolo et al., 1998). The reduced contractile function is due to an NO/cGMP-mediated inhibition of I_{Ca}. Thus, I_{Ca} is reduced in myocytes from rejecting transplanted rat hearts (allografts) compared to myocytes from non-rejecting transplanted control hearts (isografts) (Ziolo et al., 2001). This reduction in I_{Ca} in the allograft myocytes is dependent on L-arginine (the precursor of NO). Additionally, aminoguanidine (a selective inhibitor of the inducible nitric oxide synthase) and KT5823 (a selective inhibitor of PK-G) rapidly reversed the elevated NO and cGMP production, the inhibition of I_{Ca} and the contractile depression in allograft myocytes, but had no effect on I_{Ca} or contraction of isograft myocytes (Ziolo et al., 1998, 2001). In human transplant patients, expression of iNOS in rejecting hearts correlates with increased cGMP levels and

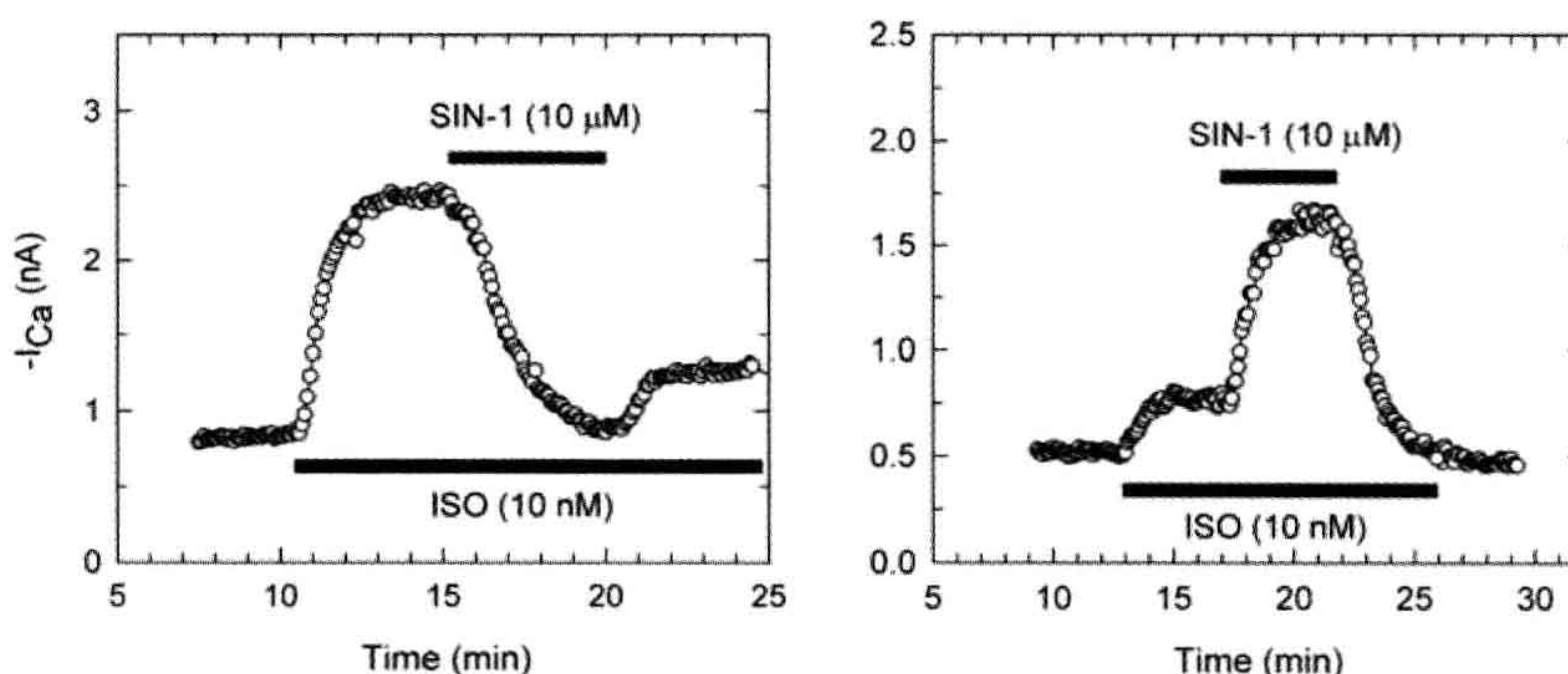


FIGURE 23.10 SIN-1 inhibition and stimulation of isoproterenol (ISO)-enhanced calcium current (I_{Ca}). Shown are time courses of I_{Ca} response during superfusion of cells with control (CONT), 10 nM ISO, and ISO plus 10 μM SIN-1 (ISO + SIN-1) bath solutions. Currents were recorded at 0 mV. Left panel: in this cell, 10 nM ISO had a large effect on I_{Ca}, and subsequent exposure to 10 μM SIN-1 caused a considerable inhibition of ISO-enhanced I_{Ca}. I_{Ca} partially recovered following washout of SIN-1 with ISO solution. Right panel: in another cell, the response to 10 nM ISO was quite small, compared with the left panel example, and exposure to 10 μM SIN-1 substantially increased ISO-enhanced I_{Ca}. *(Modified from Wahler and Dollinger, 1995; used with permission.)*

depressed contractility (Lewis et al., 1996; Paulus et al., 1997).

V. PHOSPHODIESTERASES

VA. cAMP PDEs

The hydrolysis of cyclic nucleotides occurs via phosphodiesterases (PDEs). There are 11 isoform families of these enzymes that hydrolyze cAMP and/or cGMP, of which PDEs 2-5 seem to be the most important ones for cyclic nucleotide regulation in cardiac myocytes (for review see Fischmeister et al., 2006). Previous studies have found that inhibitors of PDEs, not only can increase basal I_{Ca}, they can also potentiate the effect of β-adrenergic stimulation on I_{Ca} (e.g. Fischmeister and Hartzell, 1991; Mubagwa et al., 1993; Kawamura and Wahler, 1994; Wahler and Dollinger, 1995; Kajimoto et al., 1997; Verde et al., 1999). Thus, it is clear that both the synthesis and the rate of hydrolysis of cAMP are important in regulating I_{Ca}.

It should be noted that cGMP interacts with several isoforms of PDE that preferentially hydrolyze cAMP. Thus, the activity PDE 2 (the PDE responsible for the anti-adrenergic effects of cGMP in frog ventricular myocytes) is stimulated by cGMP. In addition, PDE 3 is a cGMP-inhibited PDE and it is this PDE which appears to mediate the positive (stimulatory) effect of cGMP on I_{Ca}.

VB. cGMP PDE

Of the multiple isoforms of PDE, some preferentially degrade cAMP, whereas others hydrolyze both cAMP and cGMP equally. One family of isoforms (PDE 5) preferentially hydrolyzes cGMP (for review, see Francis et al., 2010). The inhibitory action of exogenous cGMP on I_{Ca} can be mimicked by reducing cGMP hydrolysis through inhibition of PDE 5. A commonly used inhibitor of PDE 5 is zaprinast, which has been shown to be a specific inhibitor of this PDE isoform in the heart (Prigent et al., 1988; Kotera et al., 1998). Zaprinast has been shown to have an anti-adrenergic effect on I_{Ca} similar to exogenous cGMP (Ziolo et al., 2003). That is, zaprinast inhibited the I_{Ca} of cardiac myocytes following stimulation by isoproterenol or forskolin (see Figs. 23.1 and 23.2). The inhibitory effect of zaprinast was blocked by the PK-G inhibitor, KT5823 (see Fig. 23.2) and it was accompanied by an approximately threefold increase in intracellular cGMP levels and no change in cAMP levels. Since cAMP levels were not altered by zaprinast at the concentrations used in this study, significant non-specific inhibition of other PDE isoforms does not appear to occur with zaprinast at this concentration. These results also suggest that the effects of zaprinast were unlikely to be due to indirect effects of cGMP-induced decreases in cAMP levels caused by stimulation of PDE 2.

In standard whole-cell recording, in which intracellular Ca^{2+} concentration is unphysiologically low, zaprinast did not significantly alter basal (unstimulated) I_{Ca}. In contrast, zaprinast did inhibit basal I_{Ca} when the perforated-patch technique was used (which maintains a more physiological intracellular environment) or when whole-cell recording was used with free Ca^{2+} concentration maintained at a more physiological level (pCa = 7) (Ziolo et al., 2003). These results indicate that, under more physiological intracellular conditions, increases in endogenous cGMP can inhibit both the basal and cAMP-stimulated I_{Ca} via a mechanism that involves PK-G.

Intracellular Ca^{2+} modulates the activity of several isoforms of the enzymes that synthesize and hydrolyze cyclic nucleotides. As a result, the overall effects of the unphysiologically low levels of intracellular Ca^{2+} often used in standard whole-cell voltage clamp recording on modulation of I_{Ca} by different steps in the cAMP and/or cGMP pathways can be unpredictable. For example, perforated-patch recording enhances the I_{Ca} response to β-adrenergic stimulation, but reduces the I_{Ca} response to the non-specific PDE inhibitor IBMX (Kawamura and Wahler, 1994). Perhaps one reason that, with cGMP elevation, the basal response of I_{Ca} is typically small or non-existent while there is a much greater response of the cAMP-enhanced I_{Ca}, is that increased cAMP levels typically lead to an increase in intracellular Ca^{2+} levels, which then may upregulate one or more steps in the cGMP—PK-G pathway. As noted earlier, basal Ca^{2+} channel activity can be inhibited by PK-G under some circumstances (e.g. following overproduction of PK-G 1 in cardiac myocytes; Schröder et al., 2003) in which PK-G levels and/or activity are enhanced.

VI. COMPARTMENTALIZATION OF CYCLIC NUCLEOTIDES

The cyclic nucleotide signaling pathways are known to demonstrate a substantial amount of compartmentation. For example, although both particulate and soluble G-cyclases synthesize cGMP, the two cyclases respond to different agonists (natriuretic peptides for the particulate enzyme and NO for the soluble one) and their responses are mediated by different effectors. Additionally, there are clearly localized microdomains in which synthesizing enzymes, PDEs and effectors are in close proximity and act as a functional unit. What has only recently begun to be appreciated is that the spatial distribution of components of the system is not always fixed (not solely due to physical constraints).

Some of the isoforms of the enzymes involved in synthesizing and degrading cyclic nucleotides are substrates for cyclic nucleotide-dependent kinases. Thus, cAMP exerts a negative feedback control of its own concentration and localization due to PK-A stimulation of

PDE activity (Fischmeister et al., 2006). Similarly, PDE 5 (which is co-localized with soluble G-cyclase) is a substrate for PK-G and its activity is increased by PK-G phosphorylation. PK-G decreases the accumulation of soluble G-cyclase-generated cGMP by enhancing PDE 5 activity. On the other hand, PK-G increases the accumulation of particulate G-cyclase-generated cGMP by stimulating particulate G-cyclase activity. As a result, the distribution of cGMP within the cell is altered in response to PK-G activation. Additionally, when PDE activity is largely eliminated with a non-specific PDE inhibitor (IBMX), cGMP compartmentalization disappears and cGMP diffusion is no longer restricted, suggesting that cGMP diffusion within the cell is restricted primarily by the activity of PDEs, rather than by physical barriers (Castro et al., 2010).

Such regulation of cyclic nucleotide compartmentalization is not limited to feedback regulation of a cyclic nucleotide by its own effectors. That is, there is considerable cross-talk between the cAMP and cGMP systems. For example, the contractile response to β-adrenergic stimulation has been shown to be modulated by the soluble cGMP pool (i.e. the cGMP synthesized by soluble G-cyclase and degraded by PDE 5), but not the particulate cGMP pool, even though stimulation of particulate G-cyclase causes a larger global increase in cGMP levels than stimulation of soluble G-cyclase (Takimoto et al., 2007).

BIBLIOGRAPHY

Ahmad, Z., Green, F. J., Subuhi, H. S., & Watanabe, A. M. (1989). Autonomic regulation of type 1 protein phosphatase in cardiac muscle. *J Biol Chem, 264*, 3859–3863.

Alderton, W. K., Cooper, C. E., & Knowles, R. G. (2001). Nitric oxide synthases: structure, function and inhibition. *Biochem J, 357*, 593–615.

Armstrong, D., & Eckert, R. (1987). Voltage-activated calcium channels that must be phosphorylation to respond to membrane depolarization. *Proc Natl Acad Sci USA, 84*. 2518–1522.

Bkaily, G., & Sperelakis, N. (1984). Injection of protein kinase inhibitor into cultured heart cells blocks calcium slow channels. *Am J Physiol, 248*, H745–H749.

Bkaily, G., & Sperelakis, N. (1985). Injection of cyclic GMP into heart cells blocks the Ca^{2+} slow channels. *Am J Physiol, 248*, H745–H749.

Castro, L. R. V., Schittl, J., & Fischmeister, R. (2010). Feedback control through cGMP-dependent protein kinase contributes to differential regulation and compartmentation of cGMP in rat cardiac myocytes. *Circ Res, 107*, 1232–1240.

duBell, W. H., & Rogers, T. B. (2004). Protein phosphatase 1 and an opposing protein kinase regulate steady-state L-type Ca^{2+} current in mouse cardiac myocytes. *J Physiol, 556*, 79–93.

Fischmeister, R., & Hartzell, H. C. (1987). Cyclic guanosine 3′,5′-monophosphate regulates the calcium current in single cells from frog ventricle. *J Physiol, 387*, 455–472.

Fischmeister, R., & Hartzell, H. C. (1991). Cyclic AMP phosphodiesterases and Ca^{2+} current regulation in cardiac cells. *Life Sci, 48*, 2365–2376.

Fischmeister, R., Castro, L. R. V., Abi-Gerges, A., et al. (2006). Compartmentation of cyclic nucleotide signaling in the heart. The role of cyclic nucleotide phosphodiesterases. *Circ Res, 99*, 816–828.

Frace, A. M., & Hartzell, H. C. (1993). Opposite effects of phosphatase inhibitors on L-type calcium and delayed rectifier currents in frog ventricular myocytes. *J Physiol, 472*, 305–326.

Francis, S. H., Busch, J. L., & Corbin, J. D. (2010). cGMP-dependent protein kinases and cGMP phosphodiesterases in nitric oxide and cGMP action. *Pharmacol Rev, 62*, 525–563.

Goldberg, N. D., Haddox, M. K., Nicol, S. E., et al. (1975). Biological regulation through opposing influences of cyclic GMP and cyclic AMP: the Yin Yang hypothesis. *Adv Cyclic Nucleotides, 5*, 307–330.

Gupta, R. C., Neumann, J., Watanabe, A. M., Lesch, M., & Sabbah, H. N. (1996). Evidence for presence and hormonal regulation of protein phosphatase inhibitor-1 in ventricular cardiomyocytes. *Am J Physiol, 270*, H1159–H1164.

Haddad, G. E., Sperelakis, N., & Bkaily, G. (1995). Regulation of calcium channel by cyclic GMP-dependent protein kinase in chick heart cells. *Mol Cell Biochem, 148*, 89–94.

Hartzell, H. C., & Fischmeister, R. (1986). Opposite effects of cyclic GMP and cyclic AMP on Ca2+ current in single heart cells. *Nature, 323*, 273–275.

Hescheler, J., Kameyama, M., Trautwein, W., Mieskes, G., & Soling, H. D. (1987). Regulation of the cardiac calcium channel by protein phosphatases. *Eur J Biochem, 165*, 261–266.

Hescheler, J., Mieskes, G., Ruegg, J. C., Takai, A., & Trautwein, W. (1988). Effects of a protein phosphatase inhibitor, okadaic acid, on membrane currents of isolated guinea-pig cardiac myocytes. *Pflügers Arch, 412*, 248–252.

Irisawa, H., & Kokubun, S. (1983). Modulation of intracellular ATP and cyclic AMP of the slow inward current in isolated single ventricular cells of the guinea-pig. *J Physiol, 338*, 321–327.

Josephson, I., & Sperelakis, N. (1978). 5′Guanylimidophosphate stimulation of slow Ca^{2+} current in myocardial cells. *J Molec Cell Cardiol, 10*, 1157–1166.

Kajimoto, K., Hagiwara, N., Kasanuki, H., & Hosoda, S. (1997). Contribution of phosphodiesterase isozymes to the regulation of the L-type calcium current in human cardiac myocytes. *Br J Pharmacol, 121*, 1549–1556.

Kameyama, M., Hoffman, F., & Trautwein, W. (1986). On the mechanism of β-adrenergic regulation of the Ca^{2+} channel in the guinea pig heart. *Pflügers Arch, 405*, 285–293.

Kawamura, A., & Wahler, G. M. (1994). Perforated-patch recording does not enhance effect of 3-isobutyl-l-methylxanthine on cardiac calcium current. *Am J Physiol, 266*, C1619–C1627.

Klein, G., Drexler, H., & Schröder, F. (2000). Protein kinase G reverses all isoproterenol induced changes of cardiac L-type calcium channel gating. *Cardiovasc Res, 48*, 367–374.

Kohlhardt, M., & Haap, K. (1978). 8-Bromo-guanosine-3′, 5′-monophosphate mimics the effect of acetylcholine on slow response action potential and contractile force in mammalian atrial myocardium. *J Mol Cell Cardiol, 10*, 573–578.

Kontos, H. A., & Wei, E. P. (1993). Hydroxyl radical-dependent inactivation of guanylate cyclase in cerebral arteries by methylene blue and LY83583. *Stroke, 24*, 427–433.

Kotera, J., Fujishige, K., Akatsuka, H., et al. (1998). Novel alternative splice variants of cGMP-binding cGMP-specifc phosphodiesterase. *J Biol Chem, 273*, 26982–26990.

Levi, R. C., Alloatti, G., & Fischmeister, R. (1989). Cyclic GMP regulates the Ca-channel current in guinea pig ventricular myocytes. *Pflügers Arch, 413*, 685–687.

Levi, R. C., Alloatti, G., Penna, C., & Gallo, M. P. (1994). Guanylate cyclase-mediated inhibition of cardiac I_{Ca}, by carbachol and sodium nitroprusside. *Pflügers Arch, 426*, 419–426.

Lewis, N. P., Tsao, P. S., Rickenbacker, P. R., et al. (1996). Induction of nitric oxide synthase in human cardiac allograft is associated with contractile dysfunction of the left ventricle. *Circulation, 93*, 720–729.

Li, T., & Sperelakis, N. (1983). Stimulation of slow action potentials in guinea pig papillary muscle cells by intracellular injection of cAMP, Gpp(NH)p, and cholera toxin. *Circ Res, 52*, 111–117.

Matsumoto, S. (1997). Effect of molsidomine on basal Ca^{2+} current in rat cardiac cells. *Life Sci, 50*, 383–390.

Mehegan, J. P., Muir, W. W., Unverferth, D. V., Fertel, R. H., & McGuirck, S. M. (1985). Electrophysiological effects of cyclic GMP on canine cardiac Purkinje fibers. *J Cardiovasc Pharmacol, 7*, 30–35.

Mery, P. F., Lohmann, S. M., Walter, U., & Fischmeister, R. (1991). Ca^{2+} current is regulated by cyclic GMP-dependent protein kinase in mammalian cardiac myocytes. *Proc Natl Acad Sci USA, 88*, 1197–1201.

Mery, P. F., Pavoine, C., Belhassen, L., Pecker, F., & Fischmeister, R. (1993). Nitric oxide regulates cardiac Ca^{2+} current. Involvement of cGMP-inhibited and cGMP-stimulated phosphodiesterases through guanylyl cyclase activation. *J Biol Chem, 268*, 26286–26295.

Mubagwa, K., Shirayama, T., Moreau, M., & Pappano, A. J. (1993). Effects of phosphodiesterase inhibitors and carbachol on the L-type calcium current in guinea pig ventricular myocytes. *Am J Physiol, 264*, H1353–H1363.

Nargeot, J., Nerbonne, J. M., Engels, J., & Lester, H. A. (1983). Time course of the increase in myocardial slow inward current after a photochemically generated concentration jump of intracellular cAMP. *Proc Natl Acad Sci USA, 80*, 2395–2399.

Nawrath, H. (1977). Does cyclic GMP mediate the negative inotropic effect of acetylcholine in the heart? *Nature, 267*, 72–74.

Ono, K., & Trautwein, W. (1991). Potentiation by cyclic GMP of β-adrenergic effect on Ca^{2+} current in guinea-pig ventricular cells. *J Physiol, 443*, 387–404.

Osterreider, W., Brum, G., Hescheler, J., et al. (1982). Injection of subunits of cyclic AMP-dependent protein kinase into cardiac myocytes modulates Ca^{2+} current. *Nature, 298*, 576–578.

Paulus, W. J., Kastner, S., Pujadas, P., et al. (1997). Left ventricular contractile effects of inducible nitric oxide synthase in the human allograft. *Circulation, 96*, 3336–3342.

Pyo, R., & Wahler, G. M. (1995). Ventricular myocytes isolated from rejecting cardiac allografts exhibit a reduced β-adrenergic contractile response. *J Molec Cell Cardiol, 27*, 773–776.

Prigent, A. F., Fougier, S., Nemoz, G., et al. (1988). Comparison of cyclic nucleotide phosphodiesterase isozymes from rat heart and bovine aorta. Separation and inhibition by selective reference phosphodiesterase inhibitors. *Biochem Pharmacol, 37*, 3671–3681.

Reuter, H., Stevens, C.-F., Tsien, R. W., & Yellen, G. (1982). Properties of single calcium channels in cardiac cell culture. *Nature, 297*, 501–504.

Rivet-Bastide, M., Vandecasteele, G., Hatem, S., et al. (1997). cGMP-stimulated cyclic nucleotide phosphodiesterase regulates the basal calcium current in human atrial myocytes. *J Clin Invest, 99*, 2710–2718.

Rozanski, G. J., & Witt, R. C. (1994). IL-1 inhibits β-adrenergic control of cardiac calcium current: role of L-arginine/nitric oxide pathway. *Am J Physiol, 267*, H1753–H1758.

Schröder, F., Klein, G., Fiedler, B., et al. (2003). Single L-type Ca^{2+} channel regulation by cGMP-dependent protein kinase type 1 in adult cardiomyocytes from PKG 1 transgenic mice. *Cardiovasc Res, 60*, 268–277.

Schulz, R., Nava, E., & Moncada, S. (1992). Induction and potential biological relevance of a Ca^{2+}-independent nitric oxide synthase in the myocardium. *Br J Pharmacol, 105*, 575–580.

Shigenobu, K., & Sperelakis, N. (1972). Ca^{2+} current channels induced by catecholamines in chick embryonic hearts whose fast Na^{+} channels are blocked by tetrodotoxin or elevated K^{+}. *Circ Res, 31*, 932–952.

Stojanovic, M. O., Ziolo, M. T., Wahler, G. M., & Wolska, B. M. (2001). Anti-adrenergic effects of nitric oxide donor SIN-1 in rat cardiac myocytes. *Am J Physiol, 281*, C342–C349.

Sumii, K., & Sperelakis, N. (1995). Cyclic GMP-dependent protein kinase regulation of the L-type calcium current in neonatal rat ventricular myocytes. *Circ Res, 77*, 803–812.

Takimoto, E., Belardi, D., Tocchetti, C. G., et al. (2007). Compartmentalization of cardiac β-adrenergic inotropy modulation by phosphodiesterase type 5. *Circulation, 115*, 2159–2167.

Tandan, S., Wang, Y., Wang, T. T., et al. (2009). Physical and functional interaction between calcineurin and the cardiac L-type Ca^{2+} channel. *Circ Res, 150*, 51–60.

Thakkar, J., Tang, S. B., Sperelakis, N., & Wahler, G. M. (1989). Inhibition of cardiac slow action potentials by 8-bromo-cyclic GMP occurs independent of changes in cyclic AMP levels. *Can J Physiol Pharmacol, 66*, 1092–1095.

Tohse, N., & Sperelakis, N. (1991). Cyclic GMP inhibits the activity of single calcium channels in embryonic chick heart cells. *Circ Res, 69*, 325–331.

Tsien, R. W., Giles, W., & Greengard, P. (1972). Cyclic AMP mediates the action of adrenaline on the action potential plateau of cardiac Purkinje fibers. *Nature, 240*, 181–183.

Verde, I., Vandecasteele, G., Lezoualc'h, F., & Fischmeister, R. (1999). Characterization of the cyclic nucleotide phosphodiesterase subtypes involved in the regulation of the L-type Ca^{2+} current in rat ventricular myocytes. *Br J Pharmacol, 127*, 65–74.

Vogel, S., & Sperelakis, N. (1981). Induction of slow action potentials by microiontophoresis of cyclic AMP into heart cells. *J Molec Cell Cardiol, 13*, 51–64.

Wahler, G. M., & Dollinger, S. J. (1995). Nitric oxide donor SIN-1 inhibits mammalian cardiac calcium current through cGMP-dependent protein kinase. *Am J Physiol, 268*, C45–C54.

Wahler, G. M., & Sperelakis, N. (1985). Intracellular injection of cyclic GMP depresses cardiac slow action potentials. *J Cyclic Nucleotide Protein Phosphorylation Res, 10*, 83–95.

Wahler, G. M., & Sperelakis, N. (1986). Cholinergic attenuation of the electrophysiological effects of forskolin. *J Cyclic Nucleotide Protein Phosphorylation Res, 11*, 1–10.

Wahler, G. M., Rusch, N. J., & Sperelakis, N. (1990). 8-Bromo-cyclic GMP inhibits the calcium channel current in embryonic chick ventricular myocytes. *Can J Physiol Pharmacol, 68*, 531–534.

Wegener, J. W., Nawrath, H., Wolfsgruber, W., et al. (2002). cGMP-dependent protein kinase I mediates the negative inotropic effect of cGMP in the murine myocardium. *Circ Res, 90*, 18–20.

Xie, Q., & Nathan, C. (1994). The high-output nitric oxide pathway: role and regulation. *J Leukocyte Biol, 56*, 572–582.

Yang, X., Chowdhury, N., Cai, B., et al. (1994). Induction of myocardial nitric oxide synthase by cardiac allograft rejection. *J Clin Invest, 94*, 714–721.

Yang, L., Liu, G., Zakharov, S. I., et al. (2007). Protein kinase G phosphorylates Cav1.2 alpha1c and beta2 subunits. *Circ Res, 101*, 465–474.

Ziolo, M. T., Dollinger, S. J., & Wahler, G. M. (1998). Myocytes isolated from rejecting transplanted hearts exhibit reduced basal shortening which is reversible by aminoguanidine. *J Molec Cell Cardiol, 30*, 1009–1017.

Ziolo, M. T., Harshbarger, C. H., Roycroft, K. E., et al. (2001). Myocytes isolated from rejecting transplanted rat hearts exhibit a nitric oxide-mediated reduction in the calcium current. *J Molec Cell Cardiol, 33*, 1691–1699.

Ziolo, M. T., Lewandowski, S. J., Smith, J. M., Romano, F. D., & Wahler, G. M. (2003). Inhibition of cyclic GMP hydrolysis with zaprinast reduces basal and cyclic AMP-elevated L-type calcium current in guinea pig ventricular myocytes. *Br J Pharmacol, 138*, 986–994.

Chapter 24

Direct Regulation of Ion Channels by GTP-Binding Proteins

Atsushi Inanobe and Yoshihisa Kurachi

Chapter Outline

I. INTRODUCTION

Various extracellular stimuli can initiate physiological processes by changing membrane potentials. These stimuli regulate ionic flows by controlling the opening and closing of ion channel pores. A cluster of membrane receptors that are coupled to heterotrimeric GTP-binding proteins (G proteins) provide the largest contribution to these signaling pathways. This type of receptor is called a G-protein-coupled receptor (GPCR) and it regulates a relatively small number of different enzymes and ion channels. Because sequential protein interactions mediate GPCR signaling, the signaling pathways cause the temporal range of cellular responses to vary from milliseconds to hours. The responses are obviously slower than those evoked by ionotropic neurotransmitter receptors, which operate within milliseconds. Many ion channels are under direct or indirect control by G proteins. One example of the regulation of an ion channel by the direct action of G proteins is that of activation by acetylcholine (ACh) of the muscarinic K^+ channel in the heart (Kurachi, 1995). This action is responsible for the deceleration of the heartbeat upon stimulation of the vagus nerve (Fig. 24.1A) (Loewi, 1921). This K^+ channel is also responsible for the formation of the slow inhibitory postsynaptic potential in the central nervous system (Fig. 24.1B) (Lüscher and Slesinger, 2010). Furthermore, it is also known that this system is responsible for inhibition of presynaptic Ca^{2+} channels (Dolphin, 1998; Currie, 2010). Direct regulation of ion channels by G proteins is therefore an important cell signaling system.

II. G-PROTEIN-COUPLED RECEPTORS

G-protein-coupled receptors (GPCRs) are encoded by over 900 genes and they constitute the largest family of

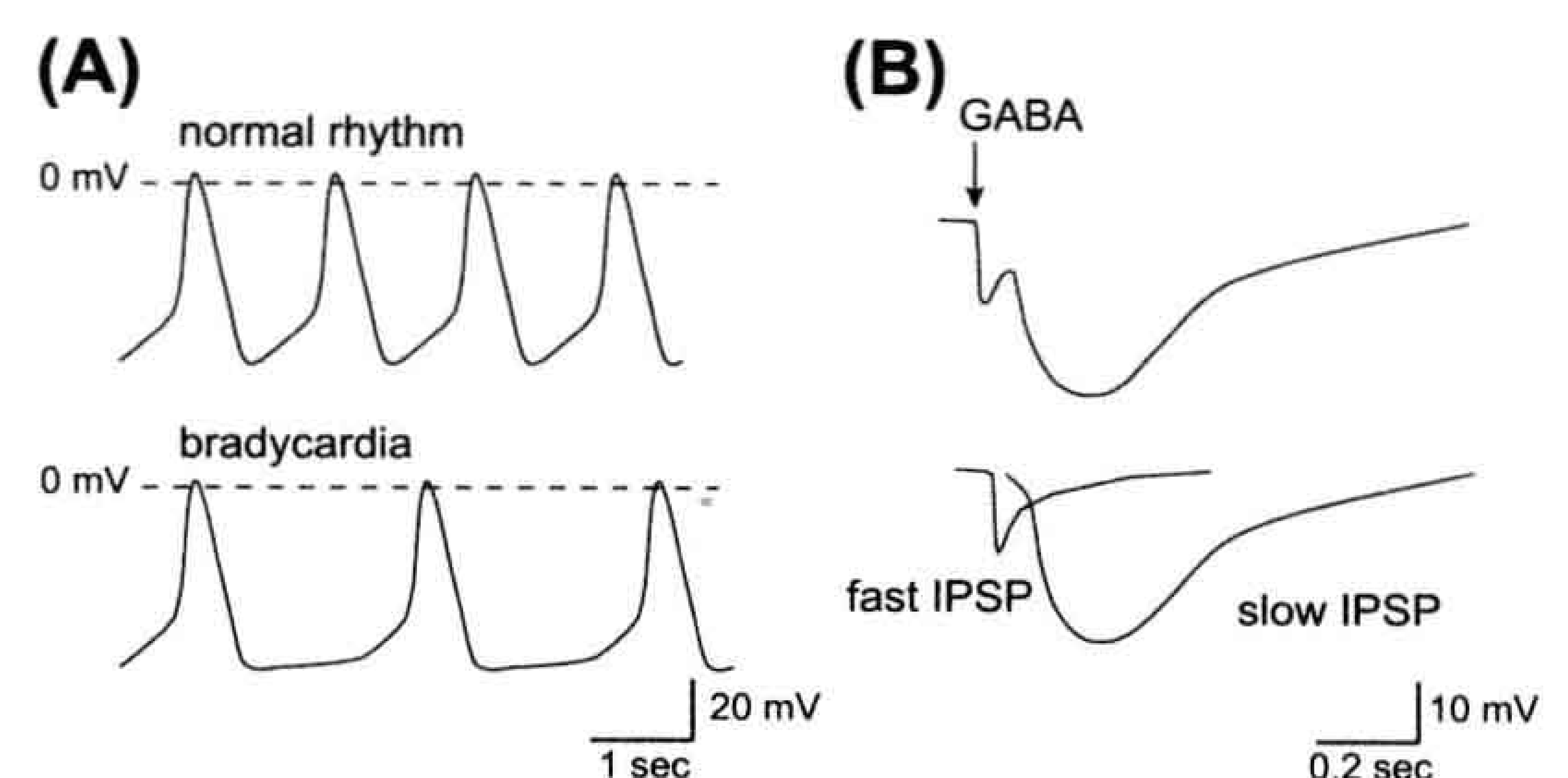


FIGURE 24.1 Physiological implications of the control of cell excitability by K_G channels. (A) Control of cell excitability in the sinoatrial nodal cells. Vagus nerve stimulation augments K^+ conductance at potentials near the equilibrium potential of K^+ and prolongs the interval between action potentials without affecting the action potential configuration. (B) The control of excitability at the inhibitory postsynaptic membranes. γ-Amino butyric acid (GABA) released at the synaptic cleft elicits biphasic changes in the postsynaptic membrane potential of inhibitory synapses (IPSP). While ionotropic $GABA_A$ receptors carrying Cl^- influx mediate the fast response, metabotropic $GABA_B$ receptors increase the K^+ efflux via G proteins.

Cell Physiology Sourcebook. DOI: 10.1016/B978-0-12-387738-3.00023-8

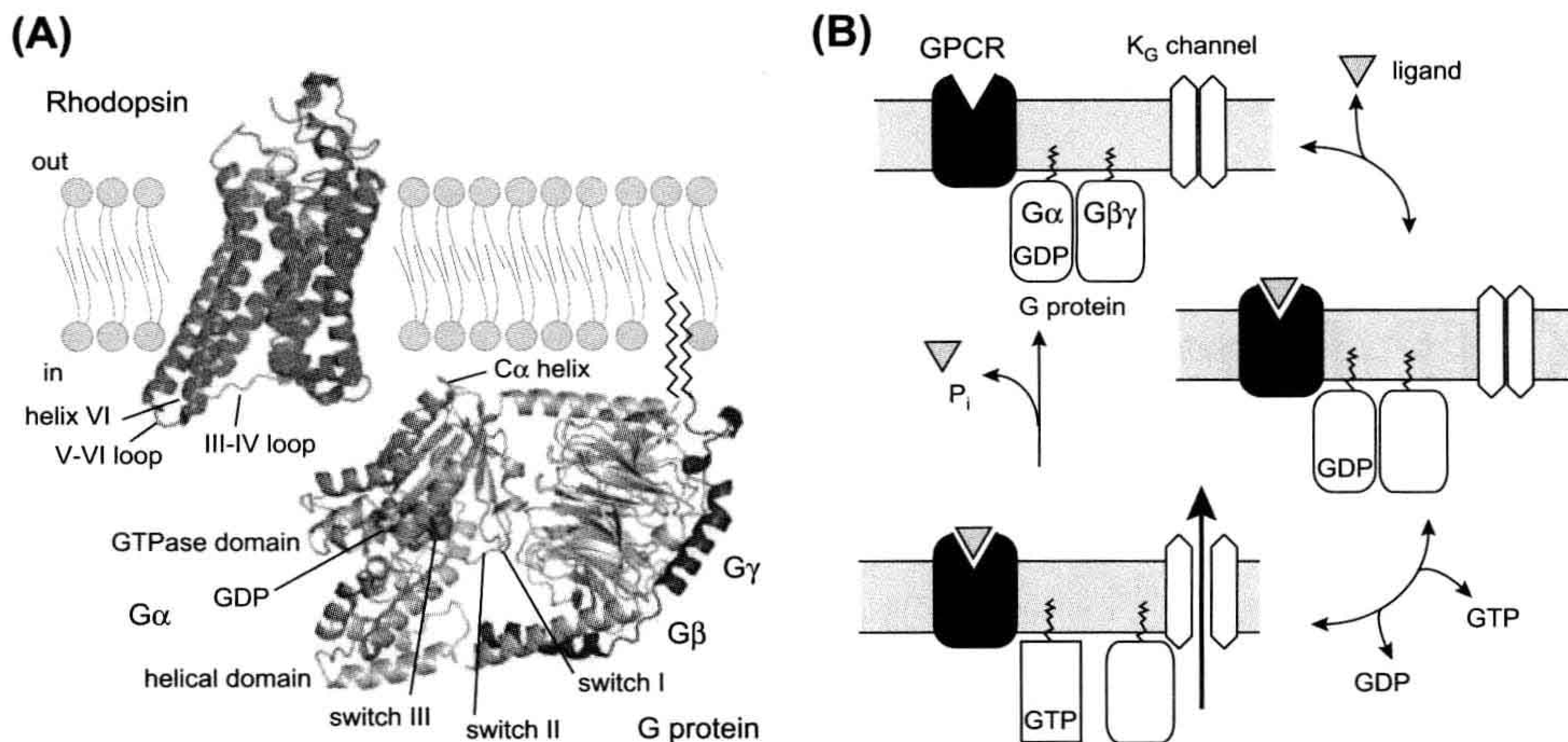


FIGURE 24.2 Molecular architectures of GPCR and G proteins and the G-protein cycle. (A) Molecular architectures of rhodopsin and G protein. The structures of retinal-free rhodopsin (Protein Data Bank identifier 3DQB) is colored in green and the trimeric complexes containing the $G\alpha_t/G\alpha_i$ chimera and the $G\beta\gamma_t$ subunits (1GOT) are colored in blue-gray and pink, respectively. The bound nucleotide on Gα is represented as a sphere. Palmitoylation and myristoylation are common post-transcriptional modifications at the N-terminus of Gα and the C-terminus of Gγ, respectively. (B) Schematic representation of the G-protein cycle. GPCR: G-protein-coupled receptor; Gα and Gβγ: α and βγ subunits of trimeric G protein, respectively; K_G channel: G-protein-gated inwardly rectifying K^+ channel.

membrane-embedded proteins in the mammalian genome (Fredriksson et al., 2003; Bjarnadottir et al., 2006). GPCRs are important targets for drugs in all therapeutic areas, and they form the sites for the effects of 25–30% of existing drugs (Overington et al., 2006). GPCRs possess heptahelical transmembrane segments and their N- and C-termini are exposed to the extracellular and intracellular sides of the membrane, respectively (Fig. 24.2A). The GPCRs in the human genome can be divided into five subfamilies that have diverse N-terminal extracellular architectures at the sites where ligands bind and trigger activation of the receptor (Fredriksson et al., 2003). Although the ligands interact with sites differently positioned within GPCRs, they ultimately evoke conformational changes at the cytoplasmic interface to activate G proteins. The most significant conformational change is probably an outward movement of helix VI and subsequent reorientation of the cytoplasmic end of the helix (Fig. 24.2A). This may be linked with the opening of a crevice within the intracellular surface of the receptor and it could allow Gα proteins to interact at their C-termini (Scheerer et al., 2008).

III. THE G-PROTEIN CYCLIC REACTION MEDIATES RECEPTOR-TO-CHANNEL SIGNAL TRANSMISSION

G proteins consist of Gα, Gβ and Gγ subunits (Gilman, 1987; Sprang, 1997; Oldham and Hamm, 2008). To date, at least 16 Gα, 5 Gβ and 12 Gγ genes have been identified. Gα has been subclassified into four groups ($G\alpha_s$, $G\alpha_i$, $G\alpha_q$ and $G\alpha_{12}$) on the basis of sequence similarity, coupling effectors and sensitivity to toxins. The crystal structures of Gα and Gαβγ have revealed the presence of two preserved domain architectures: the GTPase domain and the helical domain. The former is conserved among all members of G proteins and it hydrolyzes GTP. The latter is specific for Gα, which interacts with the GTPase domain by covering the nucleotide-binding pocket. Under physiological conditions, Gβ and Gγ associate tightly to form a dimer (Gβγ). Gβ is in the form of a seven-bladed propeller, each blade of which is a four-stranded anti-parallel β–sheet. The N-terminus of Gβ possesses an α-helix that forms a coiled-coil with the N-terminus of Gγ. The physiological significance of the possible heterogeneity of Gβγ has been a matter of debate.

In the absence of agonists, Gα exists predominantly in an inactive GDP-bound state (Gα-GDP) (see Fig. 24.2B) (Gilman, 1987; Oldham and Hamm, 2008). Gα-GDP has a high affinity for Gβγ, forming a heterotrimer. Receptor stimulation allows Gα and GDP to dissociate, which results in marked acceleration of the GDP–GTP exchange reaction. Formation of GTP-bound Gα (Gα-GTP) leads to dissociation of Gβγ from Gα-GTP. The separate components of the G protein (Gα-GTP and Gβγ) are subsequently available to transduce signals to the downstream effectors. Gα hydrolyzes the bound GTP to GDP, thereby returning to its GDP-bound state (Gα-GDP), which re-associates with Gβγ. This reaction terminates effector regulation, and

the agonist-occupied receptor triggers the heterotrimeric G protein to restart the cycle.

The C-terminus of Gα probably binds to the open crevice in a ligand-associated GPCR (Sprang, 1997; Scheerer et al., 2008). Multiple contacts mediate the interaction of Gα with GPCR. Furthermore, Gβ and Gγ stabilize the GPCR-G protein complex. Extensive contact is necessary for a change to occur in the conformation of Gα, leading to the GDP–GTP exchange reaction. The partially overlapped areas are thought to be involved in the specificity of GPCR-coupling on G proteins. Although poor sequence conservation prevents the identification of the source of G-protein-coupling specificity on GPCR, cytoplasmic loops III–IV and the C-terminus are believed to be closely involved.

IV. ELECTROPHYSIOLOGICAL EVIDENCE FOR K^+ CHANNEL ACTIVATION BY G PROTEINS

On stimulation of vagus nerves, ACh released from synaptic terminals decelerates the heartbeat and decreases atrioventricular conduction (see Fig. 24.1A) (Loewi, 1921). ACh causes membrane hyperpolarization in the heart (Del Castillo and Katz, 1955), by increasing K^+ efflux across the cell membrane (Hutter and Trautwein, 1956). A specific population of K^+ channels, the muscarinic K^+ (K_{ACh}) channels, is responsible for this efflux (Trautwein and Dudel, 1958; Noma and Trautwein, 1978) and treatment with a toxin from *Bordetella pertussis* prevents activation of the channel by m_2-muscarinic and A_1-adenosine receptors (Kurachi et al., 1986a). In cell-free inside-out membrane patches, internal GTP (in the presence of extracellular agonists) and non-hydrolyzable analog of GTP, GTPγS, activate the K_{ACh} channel (Kurachi et al., 1986b). These observations led to the proposal that the channel is directly activated by G proteins in a membrane-delimited manner. Subsequently, it was found that Gβγ, but not Gα, was the subunit responsible for activating the K_{ACh} channel (Logothetis et al., 1987). Because G-protein-sensitive K^+ (K_G) channels in neurons and endocrine cells are also regulated by Gβγ like cardiac K_{ACh} channels, we refer to these types of channel as "K_G channels" henceforth.

V. ELECTROPHYSIOLOGICAL PROPERTIES OF K_G CHANNELS

The difference between the membrane potential (V_m) and the equilibrium potential of K^+ (E_K) drives K^+ ions through K_G channels (Trautwein and Dudel, 1958; Noma and Trautwein, 1978; Kurachi, 1995; Yamada et al., 1998). The manner of K^+ conduction through K_G channels is unique, involving a large K^+ conductance at potentials negative relative to E_K, but less outward current flow at potentials positive relative to E_K (Fig. 24.3A). Blocking of the outward K^+ flow by intracellular Mg^{2+} and polyamines is responsible for this diode-like conduction and this property is similar to that originally observed as "anomalous" rectifier K^+ currents in skeletal muscles of the frog (Katz, 1949). The unidirectional conduction permits a prolongation of the interval of action potential with little effect on the action potential configuration (see Fig. 24.1A). Therefore, the inward rectification property of K_G channels is fundamental to their physiological function.

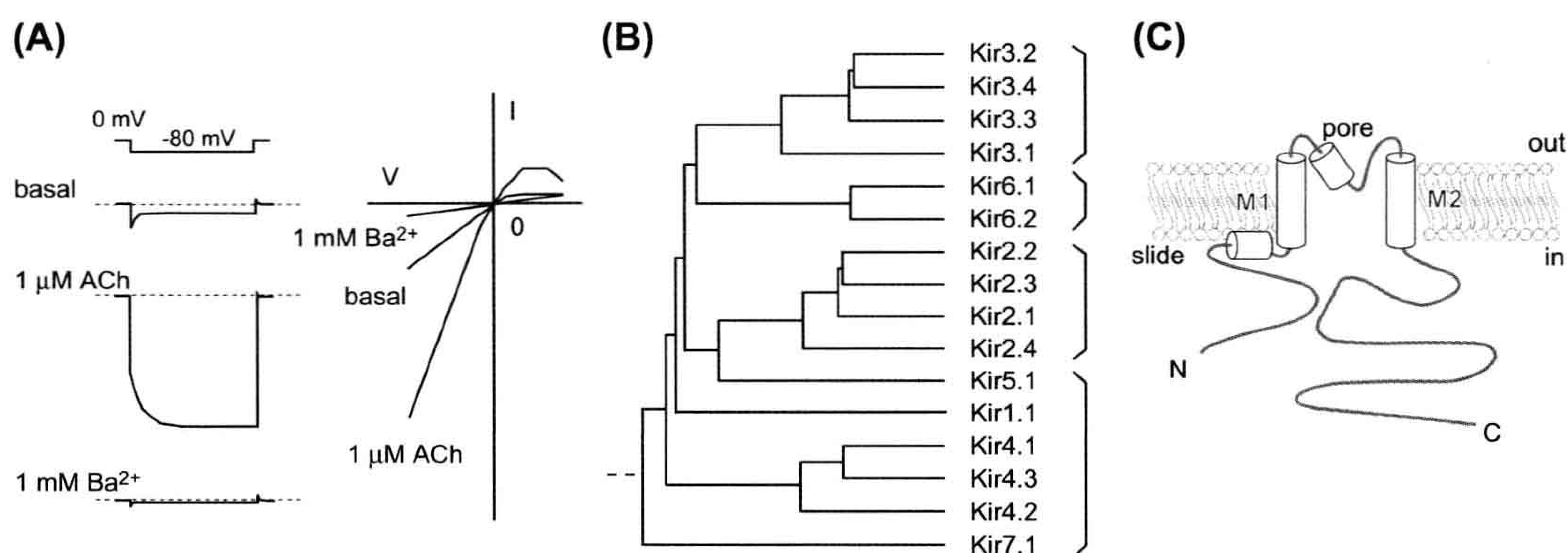


FIGURE 24.3 Kir channel members and their structural description. (A) Representative current response of the K_G channel. The reconstituted K_G channel with Kir3.1, Kir3.4 and m_2-muscarinic receptor shows a rapid change in current followed by a gradual increase on application of hyperpolarizing voltage steps from E_K. External Ba^{2+} practically blocks most Kir channels. (B) Phylogenic tree of Kir channels. The Kir channel members can be classified into four groups: G: protein-gated Kir (K_G) channels, Kir3.x; ATP-sensitive Kir channels, Kir6.x; classical Kir channels, Kir2.x; K^+ transport-Kir channels, Kir1.1, Kir4.x, Kir5.1 and Kir7.1. (C) Simple representation of Kir channels. Each subunit contains a transmembrane domain that flanks cytoplasmic N- and C-termini.

The activity of the K_G channel increases in response to GPCR activation. As discussed below, direct interactions with Gβγ and the K_G channel are responsible for this response. How does Gβγ augment the channel activity? The macroscopic current amplitude (I) of the K_G channels can be defined as follows:

$$I = N \times P_o \times i = N \times P_o \times \gamma \times (V_m - {}_EK) \quad (24.1)$$

where N is the number of channels in the patch membrane, P_o is the probability of the channel being open, i is the single-channel current amplitude and γ is the single-channel conductance. Therefore, the changes in macroscopic current amplitude during continuous recording can be explained in terms of changes in P_o and γ. The single-channel conductance of either a native or a recombinant K_G channel is dependent on the difference between V_m and ${}_EK$ and is independent of receptor stimulation, thereby showing that the increase in current amplitude caused by Gβγ is the result of an increase in the P_o of the channels.

VI. DIRECT COUPLING OF K_G CHANNEL SUBUNITS TO Gβγ

Mammalian K_G channels form a subgroup of inward rectifier K^+ (Kir) channels (see Fig. 24.3B) (Yamada et al., 1998; Hibino et al., 2010). Each channel consists of four Kir3.x subunits: Kir3.1, Kir3.2, Kir3.3 and Kir3.4 (Kubo et al., 2005). Kir3.1/GIRK1 was the first K_G channel subunit to be isolated from rat atrium (Kubo et al., 1993). Subsequently, Kir3.2–Kir3.4 were isolated from brain and atrial cDNA libraries (Krapivinsky et al., 1995). These gene transcripts are translated into several splicing variants. Four individual Kir3.x subunits assemble to form functional channels. The primary combination of subunits for the I_{kach} is Kir3.1 and Kir3.4 (Krapivinsky et al., 1995). In neural tissues, the K_G channels consist mainly of a heteromeric Kir3.1/Kir3.2 channel and a homomeric Kir3.2 channel. Kir3.3 also assembles to form neuronal K_G channels with Kir3.1 and/or Kir3.2. The primary amino acid sequences of Kir channels show that they possess common transmembrane segments (TM1 and TM2), flanked by a pore-forming region that has a signature motif (T-X-G-Y/F-G) for K^+-selective ion channels (see Fig. 24.3C) (Jan and Jan, 1997). Furthermore, it has been speculated that the unique cytoplasmic N- and C-termini to Kir channels play roles in ion conduction and regulation of gating specific to Kir channels.

Proof of the regulation of K_G channel activity by direct interactions of Gβγ has been provided by several experiments. First, the co-expression of m_2-muscarinic receptor with K_G channel subunits in host cells yielded ACh-dependent channel activity (see Fig. 24.3A) (Reuveny et al., 1994). Secondly, further expression of Gβγ resulted in a constitutively active channel, an effect that could be cancelled by additional expression of the Gβγ-binding domain of β-adrenergic receptor kinase 1 (Reuveny et al., 1994). Thirdly, Gβγ directly bound purified cytoplasmic N- and C-termini of K_G channel subunits, as well as purified recombinant and native K_G channels composed of Kir3.1 and Kir3.4 (Yamada et al., 1998; Bichet et al., 2003). The potential sites for Gβγ binding were thus narrowed down to two distinct regions in the N- and C-termini and several amino acids (the corresponding His57, Leu262, Leu333, and Gly336 in Kir3.1) appear to be critically involved in the Gβγ-dependent activation process.

Because all Kir channels require phosphatidylinositol 4,5-bisphosphate [PtdIns(4,5)P_2] for activation, the lipid is a prerequisite for opening of the K_G channel (Logothetis et al., 2007; Hibino et al., 2010). However, Gβγ and PtdIns(4,5)P_2 cannot activate the channel by themselves. How then do Gβγ and PtdIns(4,5)P_2 regulate the activity of the K_G channel? Electrophysiological and biochemical experiments have shown that the association of Gβγ probably strengthens the channel–PtdIns(4,5)P_2 interactions (Hilgemann and Ball, 1996). Differences in the turnover rate of PtdIns(4,5)P_2 or in the membrane property of lateral diffusion of PtdIns(4,5)P_2 may account for differences in the sensitivity of K_G channels to PtdIns(4,5) P_2 in different cell lines.

VII. STRUCTURAL BASIS OF THE REGULATION OF K_G CHANNEL ACTIVITY

The crystal structures of the isolated cytoplasmic domain of Kir3.1 (Nishida and MacKinnon, 2002) and of the entire bacterial Kir channel homolog KirBac1.1 (Kuo et al., 2003) revealed the structural features of Kir channels (Fig. 24.4A). The Kir channel consists of two functionally and structurally distinct domains: the transmembrane domain and cytoplasmic domain (Bichet et al., 2003; Kuo et al., 2003). The former has a significant degree of similarity with those in other K^+ channels and consists primarily of two long helices (TM1 and TM2), two short helices (slide and pore helices) and a selectivity filter (see Figs. 24.3C and 24.4B). The ion-conduction pathway is located at the center of this assembly. The pore starts at the external vestibule and connects to the selectivity filter. In the middle of the membrane, there is a widening in space, called the central cavity. The C-terminal end of the pore helix is oriented toward the midpoint of the cavity and this is presumed to play a role in the positioning of K^+. The TM2 helix from each subunit makes a physical constraint at the area closed to the cytoplasm. The slide helix located at the internal surface of membrane is connected to the cytoplasmic N-terminus through a short portion consisting of about 10 amino acids.

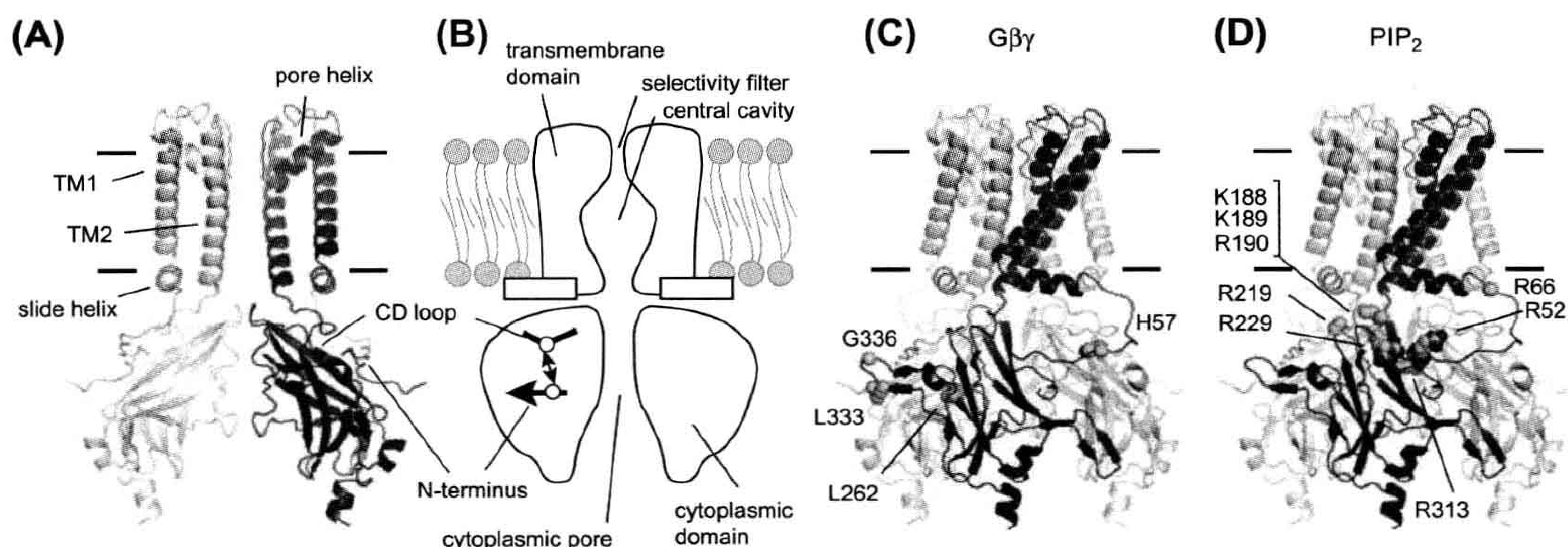


FIGURE 24.4 Structural features of K_G channels. (A) Molecular architecture of K_G channels. The K_G channel has an ion-conduction pathway at the center of a tetrameric assembly. The front and back subunits are omitted for clarity. (B) A schematic representation of K_G channels. The channels consist of two structurally distinct domains: a transmembrane domain and a cytoplasmic domain. The inter-subunit ionic bond between the N-terminus and the CD loop lowers the sensitivity to PtdIns(4,5)P_2 and stabilizes a closed conformation (Inanobe et al., 2010). (C) Residues involved in Gβγ-interaction. Several residues in the K_G channel subunits have been reported to mediate Gβγ-dependent activation. The equivalent residues in Kir3.1 are shown by spheres. (D) Mapping of residues participating in PtdIns(4,5)P_2-dependent activation. Many residues in Kir channels have been identified as being involved in PtdIns(4,5)P_2-dependent activation. The corresponding residues in Kir3.1 are indicated by spheres.

The cytoplasmic N- and C-termini contribute to a domain folding (see Fig. 24.4A). The domain consists of four individual subunits, each of which has an immunoglobulin-like β-sandwich fold. There is a water-filled pore at the fourfold symmetry axis perpendicular to the membrane. Because the residues involved in the inward rectification are distributed on the internal surface of the pore, the cytoplasmic pore extends the distance that K^+ must travel to cross the membrane. The N-terminus of one subunit interacts with the C-terminus of an adjacent subunit.

The residues involved in association with Gβγ and PtdIns(4,5)P_2 can be mapped onto the three-dimensional model (see Figs. 24.4C and D). Among the residues involved in Gβγ-dependent channel activation in Kir3.1, His57 is located on the N-terminus, whereas Leu333 and Gly336 are positioned on a loop between the βL and βM strands (see Fig. 24.4C) (Bichet et al., 2003; Logothetis et al., 2007; Hibino et al., 2010). In addition, the regions involved in the binding to Gβγ are clustered at the outer edge of a tetrameric assembly where the sites permit interaction with Gβγ. PtdIns(4,5)P_2-sensitive residues are widely distributed in the cytoplasmic domain facing the membrane (see Fig. 24.4D) (Logothetis et al., 2007; Hibino et al., 2010). The cytoplasmic end of TM2 accommodates a cluster of positively charged residues and the linker connecting the cytoplasmic N-terminus to a slide helix and a loop between the βC and βD strands (CD loop) also contains basic amino residues.

What is the mechanism underlying the Gβγ-induced increase in the affinity to PtdIns(4,5)P_2? One hypothesis is that the association of Gβγ induces a conformational change that creates a binding pocket for PtdIns(4,5)P_2. Another hypothesis is that Gβγ disrupts the inhibitory mechanism that hinders association with PtdIns(4,5)P_2. It becomes apparent that, to keep the channel insensitive to PtdIns(4,5)P_2, Kir3.2 forms an inter-subunit ionic bond between His69 on the N-terminus and Asp228 on the CD loop (see Fig. 24.4B) (Inanobe et al., 2010); the former residue is equivalent to the residues that are crucial for Gβγ-dependent activation and the latter residue is mandatory for Na^+-dependent activation. The crevice between the N-terminus and the CD loop serves as a high-affinity binding site for Cd^{2+} and the bound Cd^{2+} tethers the N-terminus and CD loop to inhibit Kir3.2 activity. It seems likely therefore that the mode of action of Gβγ is liberation of the channel from the inactive state to allow the channel to have a high affinity for PtdIns(4,5)P_2. These observations also suggest that the cytoplasmic domain of K_G channel changes its conformation during gating. How does such conformational change lead to opening of the channel? At the transmembrane domain, the pivoting movement of TM2 and restructuring of the selectivity filter appear to be involved in the control of ionic flow (Jin et al., 2002; Bichet et al., 2003). The rotational and rigid conformational changes of the transmembrane domain against the cytoplasmic domain are also predicted to be coupled with gating (Riven et al., 2003). Furthermore, the widening of the cytoplasmic pore and the rearrangement of the domain interface have also been proposed as potential conformational changes in the bacterial Kir channel (Clarke et al., 2010).

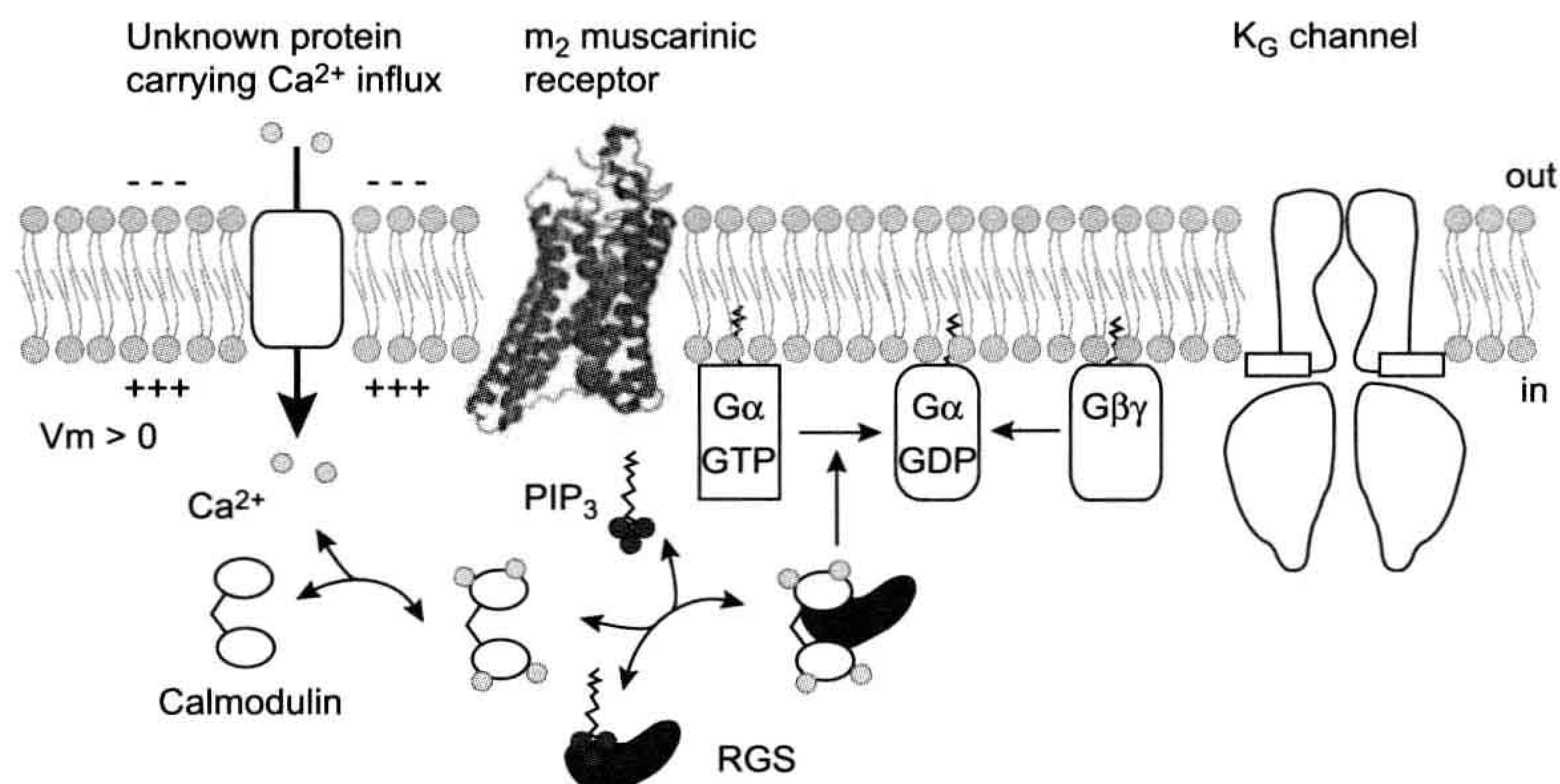


FIGURE 24.5 Regulation of G-protein-mediating channel activation by RGS proteins. Ca^{2+} influx facilitates the formation of Ca^{2+}/CaM, which binds to RGS proteins and competes with PtdIns(3,4,5)P_3. This binding restores the GAP activity and control the G protein cycle negatively.

VIII. RGS PROTEINS CONFER VOLTAGE-DEPENDENT GATING ON K_G CHANNEL

Upon hyperpolarization, the K_G channel current increases progressively after a current jump, whereas the opposite occurs upon depolarization. The slow time-dependent current change is called "relaxation" and is characteristic for the native K_G current (see Fig. 24.3A) (Noma and Trautwein, 1978). The degree of the relaxation varies with the strength of the receptor stimulation, but such relaxation behavior is not observed in cells that express only K_G channels and m_2-muscarinic receptor.

Regulators of G-protein signaling (RGS) proteins function as GTPase-activating proteins (GAP) specific to Gα to terminate G-protein-mediated signaling (Ross and Wilkie, 2000). To date, more than 20 RGS proteins have been identified. They share a conserved structure of 120 amino acids, designated the "RGS domain", which is responsible for their GAP activity. Actually, RGS proteins accelerate the time-course of activation and deactivation of K_G currents induced by agonists (Saitoh et al., 1997). Subsequently, RGS protein has been recognized as the protein that confers depolarization-induced facilitation on the channel by decreasing the K_G channel availability (Fig. 24.5) (Ishii et al., 2001). In the resting state, PtdIns(3,4,5)P_3 binds to the RGS domain and the GAP activity of RGS is inhibited. Depolarization facilitates the influx of Ca^{2+}, resulting in the formation of Ca^{2+}/calmodulin (CaM). This complex binds to the RGS domain, thereby ending the PtdIns(3,4,5)P_3-mediated inhibition and restoring GAP activity. Therefore, at depolarized potentials, the G-protein cycle is negatively regulated by Ca^{2+}/CaM-bound RGS proteins and the number of active K_G channels is decreased by the number of Gβγ moieties available to open the K_G channels. This is the mechanism of the voltage-dependent relaxation behavior of K_G channels.

IX. CONCLUSIONS

Research in the last decade has provided structural insights into the polypeptides that are involved in G-protein signaling at the atomic level. Since available conformations are limited, it is still difficult to address how proteins change their conformation and transduce the signals. Molecular dynamics simulation is a powerful tool to provide statistical mechanics of the proteins. However, restrictions by computational power and its theory hamper the precise corroboration of the ideas about dynamic features of the proteins and signaling. Therefore, multiple structural models for different functional states are necessary to grasp how the molecule operates and transfers signals. Furthermore, a lipid raft, an organization of specialized membrane microdomains in which cholesterol, sphingolipids and membrane proteins are preferentially associated, has the power to modulate this membrane-delimited signal transduction. Such a system may be linked to the idea that GPCR, G proteins, RGS proteins and K_G channels are precoupled, even in the absence of ligands (Lüscher and Slesinger, 2010). In addition, the molecular entity participating in the Ca^{2+} influx should be clarified to permit understanding of the convergence of two different cellular signaling pathways involving the G protein and the membrane potential, respectively (Ishii et al., 2001). We therefore need to achieve greater clarification regarding the regulatory mechanism of ion channels at the molecular level as well as at the cellular level.

BIBLIOGRAPHY

Bichet, D., Haass, F. A., & Jan, L. Y. (2003). Merging functional studies with structures of inward-rectifier K^+ channels. *Nat Rev Neurosci, 4*, 957–967.

Bjarnadottir, T. K., Gloriam, D. E., Hellstrand, S. H., Kristiansson, H., Fredriksson, R., & Schioth, H. B. (2006). Comprehensive repertoire and phylogenetic analysis of the G protein-coupled receptors in human and mouse. *Genomics, 88*, 263–273.

Clarke, O. B., Caputo, A. T., Hill, A. P., Vandenberg, J. I., Smith, B. J., & Gulbis, J. M. (2010). Domain reorientation and rotation of an intracellular assembly regulate conduction in Kir potassium channels. *Cell, 141*, 1018–1029.

Currie, K. P. (2010). G protein modulation of CaV2 voltage-gated calcium channels. *Channels (Austin), 4*, 497–509.

Del Castillo, J., & Katz, B. (1955). Production of membrane potential changes in the frog's heart by inhibitory nerve impulses. *Nature, 175*, 1035.

Dolphin, A. C. (1998). Mechanisms of modulation of voltage-dependent calcium channels by G proteins. *J Physiol, 506*, 3–11.

Fredriksson, R., Lagerstrom, M. C., Lundin, L. G., & Schioth, H. B. (2003). The G-protein-coupled receptors in the human genome form five main families. Phylogenetic analysis, paralogon groups, and fingerprints. *Mol Pharmacol, 63*, 1256–1272.

Gilman, A. G. (1987). G proteins: transducers of receptor-generated signals. *Annu Rev Biochem, 56*, 615–649.

Hibino, H., Inanobe, A., Furutani, K., Murakami, S., Findlay, I., & Kurachi, Y. (2010). Inwardly rectifying potassium channels: their structure, function, and physiological roles. *Physiol Rev, 90*, 291–366.

Hilgemann, D. W., & Ball, R. (1996). Regulation of cardiac Na^+, Ca^{2+} exchange and K_{ATP} potassium channels by PIP_2. *Science, 273*, 956–959.

Hutter, O. F., & Trautwein, W. (1956). Vagal and sympathetic effects on the pacemaker fibers in the sinus venosus of the heart. *J Gen Physiol, 39*, 715–733.

Inanobe, A., Nakagawa, A., Matsuura, T., & Kurachi, Y. (2010). A structural determinant for the control of PIP_2 sensitivity in G protein-gated inward rectifier K^+ channels. *J Biol Chem, 285*, 38517–38523.

Ishii, M., Inanobe, A., Fujita, S., Makino, Y., Hosoya, Y., & Kurachi, Y. (2001). Ca^{2+} elevation evoked by membrane depolarization regulates G protein cycle via RGS proteins in the heart. *Circ Res, 89*, 1045–1050.

Jan, L. Y., & Jan, Y. N. (1997). Cloned potassium channels from eukaryotes and prokaryotes. *Annu Rev Neurosci, 20*, 91–123.

Jin, T., Peng, L., Mirshahi, T., Rohacs, T., et al. (2002). The βγ subunits of G proteins gate a K^+ channel by pivoted bending of a transmembrane segment. *Mol Cell, 10*, 469–481.

Katz, B. (1949). Les constantes electriques de la membrane du muscle. *Arch Sci Physiol, 3*, 285–299.

Krapivinsky, G., Gordon, E. A., Wickman, K., Velimirovic, B., Krapivinsky, L., & Clapham, D. E. (1995). The G-protein-gated atrial K^+ channel I_{KACh} is a heteromultimer of two inwardly rectifying K^+-channel proteins. *Nature, 374*, 135–141.

Kubo, Y., Adelman, J. P., Clapham, D. E., et al. (2005). International Union of Pharmacology. LIV. Nomenclature and molecular relationships of inwardly rectifying potassium channels. *Pharmacol Rev, 57*, 509–526.

Kubo, Y., Reuveny, E., Slesinger, P. A., Jan, Y. N., & Jan, L. Y. (1993). Primary structure and functional expression of a rat G-protein-coupled muscarinic potassium channel. *Nature, 364*, 802–806.

Kuo, A., Gulbis, J. M., Antcliff, J. F., et al. (2003). Crystal structure of the potassium channel KirBac1.1 in the closed state. *Science, 300*, 1922–1926.

Kurachi, Y. (1995). G protein regulation of cardiac muscarinic potassium channel. *Am J Physiol, 269*, C821–C830.

Kurachi, Y., Nakajima, T., & Sugimoto, T. (1986a). Acetylcholine activation of K^+ channels in cell-free membrane of atrial cells. *Am J Physiol, 251*, H681–H684.

Kurachi, Y., Nakajima, T., & Sugimoto, T. (1986b). On the mechanism of activation of muscarinic K^+ channels by adenosine in isolated atrial cells: involvement of GTP-binding proteins. *Pflügers Arch, 407*, 264–274.

Loewi, O. (1921). Über humorale Übertragbarkeit der Herznervenwirkung. *Pflügers Arch, 189*, 239–242.

Logothetis, D. E., Jin, T., Lupyan, D., & Rosenhouse-Dantsker, A. (2007). Phosphoinositide-mediated gating of inwardly rectifying K^+ channels. *Pflügers Arch, 455*, 83–95.

Logothetis, D. E., Kurachi, Y., Galper, J., Neer, E. J., & Clapham, D. E. (1987). The βγ subunits of GTP-binding proteins activate the muscarinic K^+ channel in heart. *Nature, 325*, 321–326.

Lüscher, C., & Slesinger, P. A. (2010). Emerging roles for G protein-gated inwardly rectifying potassium (GIRK) channels in health and disease. *Nat Rev Neurosci, 11*, 301–315.

Nishida, M., & MacKinnon, R. (2002). Structural basis of inward rectification: cytoplasmic pore of the G protein-gated inward rectifier GIRK1 at 1.8 Å resolution. *Cell, 111*, 957–965.

Noma, A., & Trautwein, W. (1978). Relaxation of the ACh-induced potassium current in the rabbit sinoatrial node cell. *Pflügers Arch, 377*, 193–200.

Oldham, W. M., & Hamm, H. E. (2008). Heterotrimeric G protein activation by G-protein-coupled receptors. *Nat Rev Mol Cell Biol, 9*, 60–71.

Overington, J. P., Al-Lazikani, B., & Hopkins, A. L. (2006). How many drug targets are there? *Nat Rev Drug Discov, 5*, 993–996.

Reuveny, E., Slesinger, P. A., Inglese, J., et al. (1994). Activation of the cloned muscarinic potassium channel by G protein βγ subunits. *Nature, 370*, 143–146.

Riven, I., Kalmanzon, E., Segev, L., & Reuveny, E. (2003). Conformational rearrangements associated with the gating of the G protein-coupled potassium channel revealed by FRET microscopy. *Neuron, 38*, 225–235.

Ross, E. M., & Wilkie, T. M. (2000). GTPase-activating proteins for heterotrimeric G proteins: regulators of G protein signaling (RGS) and RGS-like proteins. *Annu Rev Biochem, 69*, 795–827.

Saitoh, O., Kubo, Y., Miyatani, Y., Asano, T., & Nakata, H. (1997). RGS8 accelerates G-protein-mediated modulation of K^+ currents. *Nature, 390*, 525–529.

Scheerer, P., Park, J. H., Hildebrand, P. W., et al. (2008). Crystal structure of opsin in its G-protein-interacting conformation. *Nature, 455*, 497–502.

Sprang, S. R. (1997). G protein mechanisms: insights from structural analysis. *Annu Rev Biochem, 66*, 639–678.

Trautwein, W., & Dudel, J. (1958). [Mechanism of membrane effect of acetylcholine on myocardial fibers]. *Pflügers Arch, 266*, 324–334.

Yamada, M., Inanobe, A., & Kurachi, Y. (1998). G protein regulation of potassium ion channels. *Pharmacol Rev, 50*, 723–760.

Chapter 25

Developmental Changes in Ion Channels

Takeshi Kobayashi, Noritsugu Tohse, Hisashi Yokoshiki and Nicholas Sperelakis

Chapter Outline

I. SUMMARY

Action potentials (APs) and resting potentials (RPs) in excitable cells, such as cardiomyocytes, skeletal muscle fibers and neurons, are greatly altered during development. In general, the RP increases (becomes more negative), the AP rate of rise increases, overshoot increases and duration decreases. These electrophysiological alterations are mainly produced by developmental changes in the ion channels, i.e. by changes in the types, number and kinetic properties of the ion channels.

In cardiomyocytes, the RP at the early embryonic/fetal period is low and there is a gradual hyperpolarization during development. This increase in the RP during development can be accounted for by the increase in the density of inward-rectifier K^+ current (I_{K1}) and the resultant decrease in the permeability ratio for Na^+ to K^+ (P_{Na}/P_K ratio). In contrast, the hyperpolarization-activated inward current (I_h), which may affect automaticity, is dominant in early embryonic chick and mouse cardiomyocytes and disappears during development.

The Na^+ current of cardiomyocytes increases markedly during development. This increase in number (density) of fast Na^+ channels accounts for the large increase in the maximal rate of depolarization of the AP (max dV/dt) during development. The fast Na^+ current in embryonic/fetal hearts has a significant sustained component. The sustained component decreases during development and this decrease contributes, at least in part, to the abbreviation of the AP duration.

Developmental change of Ca^{2+} channels varies with the species. The density of total Ca^{2+} current in chick cardiomyocytes decreases during the developmental period from fetal to neonate. In rat and mouse, however, it increases from the fetal to the neonatal period, followed by a substantial decrease in the adult. In contrast, the current density in the neonatal period is smaller than that in the adult in rabbit and guinea pig.

In fetal heart cells, the role of the sarcoplasmic reticulum (SR) increases with embryonic development. Therefore, Ca^{2+} influx through the Ca^{2+} channels is especially important for the excitation–contraction (E-C) coupling process of immature cardiomyocytes.

The density of the transient outward current (I_{to}) of cardiomyocytes increases during development. An increase in the density of the delayed-rectifier K^+ current (I_K) also occurs during early development and decreases during the

Cell Physiology Sourcebook. DOI: 10.1016/B978-0-12-387738-3.00025-1

postnatal period. The change of these voltage-gated outward currents acts to abbreviate the AP duration during development.

In skeletal muscle fibers, there is an overall trend toward an increase in the density of I_{K1} during the early developmental period. However, there is a transient period during which the current density actually decreases. This transient period parallels the increased incidence of spontaneous firings, presumably due to a less stable RP. The major voltage-gated inward currents, the Na^+ and Ca^{2+} currents, are already present in the early embryonic skeletal myocytes in culture and they increase in intensity during development. These changes contribute to the increases in the AP rate of rise, overshoot and propagation velocity.

The nicotinic acetylcholine receptor/channel (nAChR), which is essential to transmission at the neuromuscular junction, is converted from fetal-type to adult-type and this conversion may be related to innervation of the muscles that occurs during development.

In neuronal cells, there is an overall trend that the ionic dependence of the AP is altered during development from being Ca^{2+}-dependent (prolonged AP duration) to Na^+-dependent (brief AP duration). The pattern of ion channel development varies among different types of neuronal cells, with faster development of Ca^{2+} channels occurring in some cells. Another important factor that determines the ionic dependence of the AP is the developmental increase in I_K. Therefore, the change in the I_K/I_{Ca} ratio during development is the major determinant of the conversion of the AP configuration and influences Ca^{2+} influx. The activities of ligand-gated Ca^{2+} permeable channels (such as NMDA receptor/channels and AMPA-gated receptor/channels) are also altered during development. Therefore, the Ca^{2+} influx through the voltage-gated and the ligand-gated Ca^{2+} channels, and the subsequent effects on intracellular Ca^{2+}, may affect the structural changes of the developing neurons and help the establishment of the neuronal network.

II. INTRODUCTION

Cellular functions and tissue structures change dramatically during development. Ion channels are responsible for cellular signaling and maintenance of the intracellular environment. For example, the Ca^{2+} channels allow Ca^{2+} influx into the cell, which acts as a second messenger that affects several structures: activation of enzymes; activation of some ion channels; and activation of the contractile proteins. The ion channels change in their types, number and kinetic properties during the embryonic/fetal period and the neonatal period. Particularly in excitable cells (i.e. cardiomyocytes, skeletal muscle fibers, neurons), their resting potential (RP) and action potentials (APs) are progressively altered during the developmental stages. For example, the RP increases in amplitude during development and large changes occur in the AP rate of rise, overshoot and duration. In general, the rate of rise increases markedly, the overshoot increases and the duration decreases during development. This chapter focuses primarily on the ion channels of cardiomyocytes, skeletal muscle fibers and neurons, where most is known about the developmental changes.

III. CARDIOMYOCYTES

IIIA. Resting Potential

In the early embryonic period, the heart primordium (the so-called cardiac crescent) begins to contract before the appearance of a linear heart tube (Kobayashi et al., 2011). In the middle embryonic period, the heart tube twists and then the cardiac loop is constructed. In this period, the ventricular portion becomes distinguished from the atrial portion.

The electrophysiological properties are also altered during development. The RP of the ventricular cells in the early embryonic/fetal period is low (e.g. −40 to −55 mV) and there is a gradual hyperpolarization during development. Finally, in the late embryonic period, the RP becomes nearly equal to that of adult cells (around −80 mV) (Bernard, 1975). During this increase of the RP, a decrease in the permeability ratio for Na^+ to K^+ (P_{Na}/P_K ratio) occurs (Sperelakis and Shigenobu, 1972). The developmental changes in the RP cannot be accounted for by changes in the intracellular ion concentrations because $[K^+]_i$ is already high in the early embryonic period. Although the Na^+-K^+ pump specific activity was found to be low in the early embryonic period (Sperelakis and Lee, 1971), the Na^+-K^+ pump is sufficient to maintain a high $[K^+]_i$ and low $[Na^+]_i$ because of the less leaky membrane (i.e. high in resistance) (Sperelakis and Shigenobu, 1972). Therefore, the developmental change in the RP is due to changes in membrane permeability (conductance) for the ions.

In the early embryonic period, the low RP of the ventricular cells is not stable, but exhibits a spontaneous depolarization, the *pacemaker potential* (phase 4 diastolic depolarization). During embryonic development, the *maximum diastolic potential* increases (hyperpolarized) and the slope of the pacemaker potential progressively decreases. When the RP has attained the adult level in the late embryonic period, the pacemaker potential disappears. Thus, automaticity of the ventricular cells is lost by the late embryonic period. One possible factor in the loss of automaticity is the decrease in the P_{Na}/P_K ratio and the resultant hyperpolarization. This factor is closely related to the increase in the inward-rectifier K^+ current (I_{K1}) and the loss of the hyperpolarization-activated inward current (I_h or I_f) (see Sections IIIE and IIIG).

IIIB. Action Potential

The *action potentials* (APs) get larger and rise faster during embryonic development (Couch et al., 1969; Sperelakis and Shigenobu, 1972; Bernard, 1975; Kojima et al., 1990). These changes are accompanied by the hyperpolarization of the RP and by an increase in overshoot to about +30 mV. The maximal rate of depolarization (max *dV/dt*) progressively increases during development, from about 20 V/s to 200 V/s in the late embryonic stage, which is about the adult level. However, the time course of the increase in max *dV/dt* is not parallel to the increase in RP. The increase in RP precedes the increase in max *dV/dt* by several days. Therefore, this increase in max *dV/dt* is not simply due to the hyperpolarization, but is produced by a much greater number (density) of tetrodotoxin (TTX)-sensitive fast Na^+ channels (see Section IIIC).

The duration of the AP (e.g. at 50% repolarization, APD_{50}) hardly changes in the chick during development (Sperelakis and Shigenobu, 1972). The same is true of the guinea pig heart, as well as in many other mammalian species (Sanchez-Chapula et al., 1994; Kato et al., 1996). However, in human atrial cells, the APD_{50} is significantly shortened with development (Wang et al., 2003). The rat also shows a marked decrease in APD_{50} beginning in the late fetal period and extending through the first 3 weeks of the neonatal period, after which adult-like brief APs are attained (Kojima et al., 1990). Several factors contribute to this marked abbreviation of the AP in the rat, including increase in the transient outward current (I_{to}) and loss of the sustained component of the fast Na^+ current (see Section IIIC).

IIIC. Na^+ Channels

Slow Ca^{2+} channel current makes a major contribution to the upstroke of the AP in the early embryonic period (Bernard, 1975). The fast Na^+ current in ventricular cells increases markedly during development by a factor of about 10-fold in chick, rat and murine hearts (Fujii et al., 1988; Sada et al., 1995; 1988; Conforti et al., 1993; Davies et al., 1996). However, in rabbit and canine sinoatrial node cells, the fast Na^+ current actually decreases during development (Baruscotti et al., 1996; Protas et al., 2010). Tetrodotoxin- (TTX, a specific blocker of the fast Na^+ channels) binding studies indicated that a marked increase in density of the fast Na^+ channel protein occurs during development of embryonic chick heart (Renaud et al., 1981, 1983). This increase in number (density) of fast Na^+ channels accounts for the large increase in max *dV/dt* of the AP that occurs. Therefore, the contribution of fast Na^+ channel current to the AP of ventricular cells progressively increases during development.

The heart greatly enlarges in size during development. Thus, the excitation wave must travel over longer distances in the larger hearts during the late embryonic and adult periods. A fast conduction velocity for excitation is required to allow a synchronized contraction of the ventricle, i.e. to allow the heart to serve as an effective pump. The increase in max *dV/dt* during development would contribute to the required increase in conduction velocity. Another factor involved in conduction velocity is that the cell size (i.e. diameter) becomes much greater. It is well known that conduction velocity is a function of the square root of cell diameter (see Chapter 18).

The TTX sensitivity of the fast Na^+ current in avian cardiomyocytes (in the nanomolar range) is about 1000-fold greater than that for adult mammalian hearts (such as guinea pig), which are in the micromolar range (Sada et al., unpublished observation). It is not known whether the high TTX sensitivity of chick embryonic hearts is due to a different isoform of the channel. This finding is in agreement with previous reports of the high sensitivity of embryonic chick hearts to TTX (Iijima and Pappano, 1979; Marcus and Fozzard, 1981; Fujii et al., 1988).

The fast Na^+ channels are completely blocked by 10 μM TTX in fetal rat cardiomyocytes (Conforti et al., 1993) and by 30 μM TTX in adult rat cardiomyocytes (Brown et al., 1981). Binding studies using TTX and saxitoxin (STX, also a specific blocker of the fast Na^+ channels) revealed that fetal and newborn rat ventricular myocytes have only low-sensitivity Na^+ channels. In contrast, adult rat ventricular myocytes have both high-sensitive and low-sensitive to (TTX/STX) Na^+ channels, leading to the discovery of the low-sensitive "cardiac" isoform of the Na^+ channel ($Na_v1.5$) (Renaud et al., 1983; Rogart et al., 1989). In mouse heart, high TTX-sensitive Na^+ channel isoforms ($Na_v1.1$–$Na_v1.4$) increase with development, although the "cardiac" isoform Na^+ channel is always predominantly expressed during development (Haufe et al., 2005; Dominguez et al., 2008).

The fast Na^+ current has a slow inactivating or sustained component. This component is small, but has a larger contribution in the embryonic period than in adult (Conforti et al., 1993). Sustained Na^+ current, which is blocked by 10 μM TTX, is observed in the early embryonic period of chicks. Reopening of some of the fast Na^+ channels during a long depolarizing clamp step is one explanation for the small sustained component (Josephson and Sperelakis, 1989). The sustained component may reflect the *window current* produced by a balance between the activating (m) gate and the inactivating (h) gate (Sada et al., 1995) (see Chapter 19). In rat heart cells, the fast Na^+ current has a slow inactivating component and its time constant decreases in neonatal cells compared to fetal cells (Conforti et al., 1993). Although the slow component of the Na^+ current is small, inward current produced by the slow component helps to maintain the longer duration of the AP plateau in the fetal period. TTX, which is specific for fast

Na^+ channels, shortens the AP duration in rat fetal cardiomyocytes (Fig. 25.1) (Conforti et al., 1993). A key factor that may contribute to the shortening of the AP duration during development of rat heart is the loss of the slow component of the Na^+ current. However, in adult hearts, it appears that the sustained component of the Na^+ current persists in the Purkinje fiber, because its AP plateau is substantially shortened by TTX (Morikawa et al., 1987). Another factor responsible is an increase in I_{to} carried primarily by K^+ (see Section IIIF).

IIID. Ca^{2+} Channels

Changes in the slow (L-type) Ca^{2+} current also occur during development of the heart. However, the direction of the change is opposite in avian versus mammalian hearts (Fig. 25.2). In rat hearts, the L-type Ca^{2+} current increases during development (Masuda et al., 1995), whereas in chick hearts it actually decreases (Tohse et al., 1992b). In the chick early embryonic period, the current density of the L-type channels is 8 $\mu A/cm^2$ which is comparable to that in other adult animals (about 10 $\mu A/cm^2$). The current density decreased during development to about 5 $\mu A/cm^2$ in the late embryonic period (Fig. 25.2B). However, the current density of the L-type Ca^{2+} channels of rat cardiomyocytes increases through the middle fetal, late fetal and neonatal period (Masuda et al., 1995) (Fig. 25.2A). In mouse, the current density of L-type Ca^{2+} channels increases with development (Davies et al., 1996; Liu et al., 2002; Nguemo et al., 2007). Another investigation demonstrated that the current density in the neonatal period is actually larger than that in adult rat (Cohen and Lederer, 1988). That is, in the development of rat heart, the current density increases, followed by a decrease. In contrast, in rabbit (Osaka and Joyner, 1991; Huang et al., 2006) and guinea pig (Kato et al., 1996) cardiomyocytes, the current density in the neonatal period is smaller than that in adults. Thus, the changes in the L-type Ca^{2+} channel density that occur during development are complex and vary from one species to another.

Other types of Ca^{2+} channels are also observed during development. In chick embryonic heart cells, it has been reported that the T-type channel is dominant in the early embryonic period, but that the L-type current is dominant in the late embryonic period (Kawano and DeHaan, 1991; Kitchens et al., 2003). However, other reports indicate that the L-type current is also dominant in the early chick embryonic period (Tohse and Sperelakis, 1990; Tohse et al., 1992b). In rat and mouse fetal cardiomyocytes, although L-type current is always dominant, T-type current is observed during the embryonic and postnatal periods and decreases with development (Leuranguer et al., 2000; Ferron et al., 2002; Niwa et al., 2004). However, another report shows that embryonic rat ventricle myocytes have a substantial fraction of the total Ca^{2+} current that is resistant to nifedipine (a relatively selective blocker of L-type Ca^{2+} channels) shown in Fig. 25.3 (Tohse et al., 1992a). This nifedipine-resistant current is not blocked by ω-conotoxin (N-type Ca^{2+} channel-blocker), tetramethrine (T-type Ca^{2+}

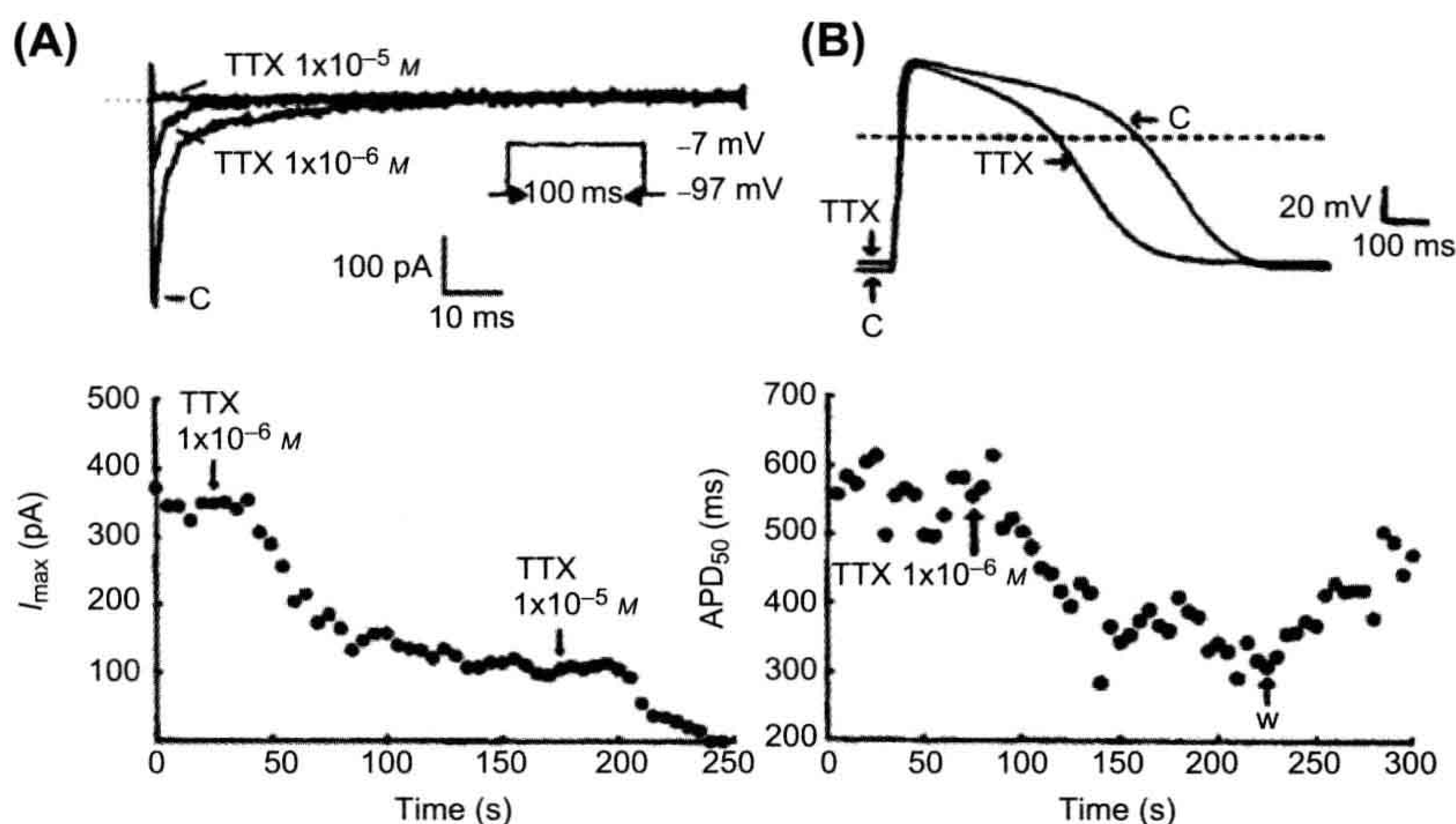


FIGURE 25.1 Effect of TTX on the Na^+ current and the AP configuration recorded from a fetal rat cardiomyocyte. (A) Top panel: superimposed current traces showing the Na^+ current recorded before (C, Control) and after 90-s exposure to 1 and 10 μM TTX. Holding potential (HP) was −97 mV and the test potential was −7 mV. Bottom panel: time course of the TTX effect. Steady-state responses were attained at about 1−2 min. (B) Effect of TTX on the AP configuration of a fetal cell recorded in current-clamp mode. Top panel: superimposed traces (averaged from 10 consecutive records) showing APs before (C, Control) and after a 90-s exposure to 1 μM TTX. Bottom panel: time course of the change in APD_{50} produced by TTX. Arrows indicate points of introduction and washout (w) of TTX. *(Reproduced with permission from Conforti et al., 1993.)*

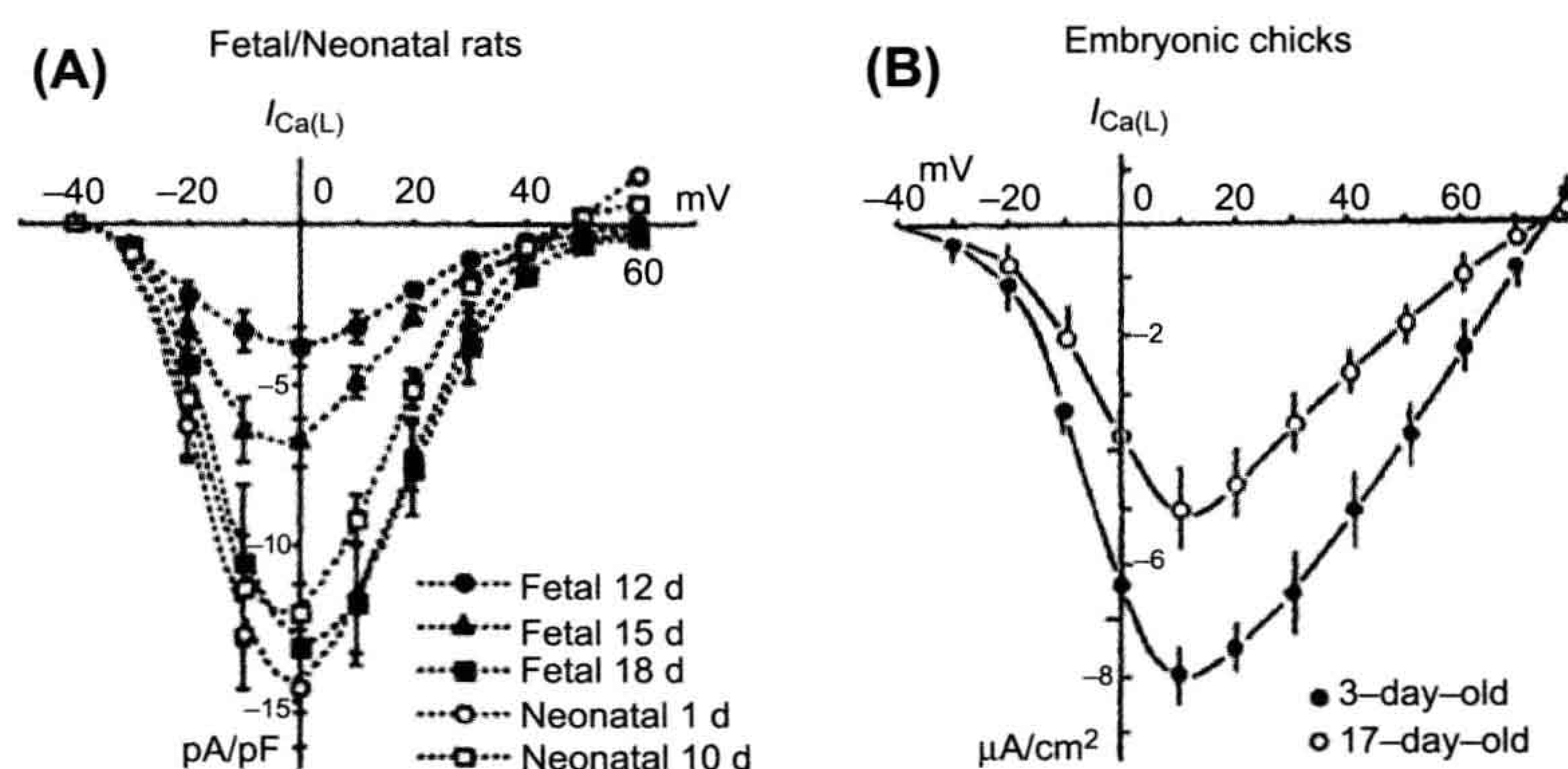


FIGURE 25.2 Developmental changes of $I_{Ca(L)}$ in (A) fetal/neonatal rats and (B) embryonic chicks. (A) Ba^{2+} currents through L-type Ca^{2+} channels ($I_{Ca(L)}$) were elicited by depolarizing steps from an HP of −40 mV (22°C). Current−voltage curves (normalized as current density (in pA/pF)(mean ± SE)) are shown for the different developmental stages (from day 12 fetal to day 10 neonatal). (B) Changes in the density of $I_{Ca(L)}$ in isolated embryonic chick heart cells; 1.8 mM $[Ca^{2+}]_o$, 35°C. *((A) modified with permission from Masuda et al. (1995). Long openings of calcium channels in fetal rat ventricular cardiomyocytes. Pflügers Arch. 429, 595−597, copyright Springer-Verlag. (B) Tohse et al. (1992b). Developmental changes in long-opening behavior of L-type Ca^{2+} channels in embryonic chick heart cell. Circ. Res. 71, 376−384. Reproduced with permission* Circulation Research. *Copyright 1992 American Heart Association.)*

channel-blocker) and is only partially inhibited by 30 µM Ni^{2+}, which is a blocker of T-type Ca^{2+} channels. Therefore, this channel is called a *fetal-type* (F-type) Ca^{2+} channel. The F-type Ca^{2+} current is absent in adult heart cells. That is, in the fetal period, the total Ca^{2+} current has two main components: L-type current, which is blocked by nifedipine and the F-type current, which is not blocked by nifedipine.

In chick embryonic heart, unit conductance of the L-type Ca^{2+} channel is 26 pS (using 50 mM Ba^{2+} in the pipette), which is comparable to that in adult heart cells (Tohse and Sperelakis, 1990). The single-channel activity of the L-type Ca^{2+} channel in the embryonic cells was completely blocked by nifedipine.

The kinetics of opening of the L-type Ca^{2+} channels in embryonic heart cells is different from that in adult heart cells. Long-lasting openings of the channels occur relatively frequently, in addition to the more usual brief bursting openings observed in adult heart cells (Fig. 25.4). These long-lasting openings are similar to the mode 2 openings produced by Ca^{2+} agonists, such as the dihydropyridine Bay-K-8644. For example, Fig. 25.4 shows long openings that persist over the entire duration of the clamp pulse (i.e. 300 ms); the long openings are sometimes punctuated by brief closures. As can be seen, in many sweeps, the open probability (P_0) is close to 1.00. The long-lasting openings gradually disappear during development (Tohse et al., 1992b; Masuda et al., 1995).

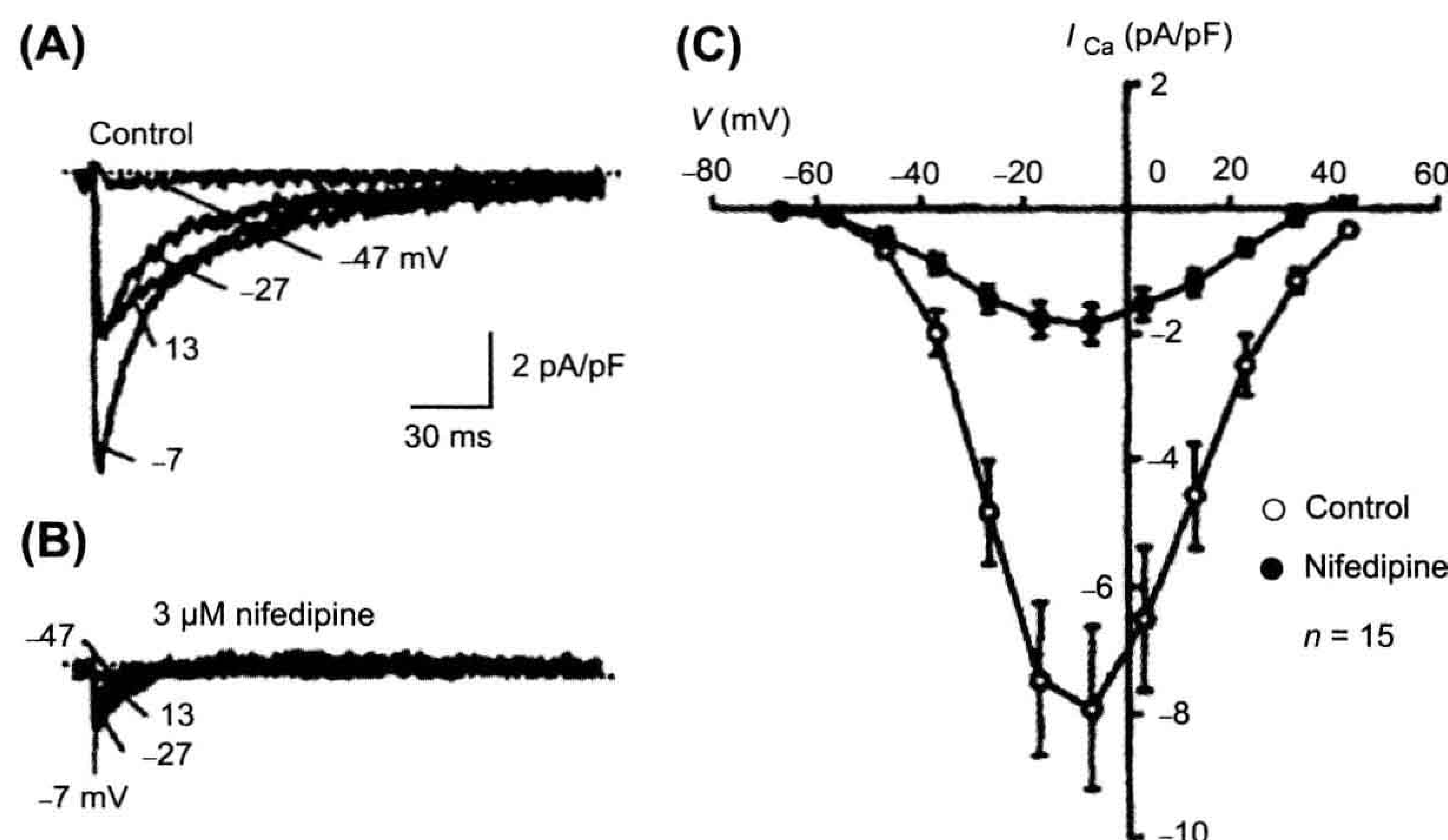


FIGURE 25.3 Presence of fetal-type Ca^{2+} channels in fetal (18-day) rat cardiomyocytes. (A) Currents elicited by 300-ms (only 150 ms shown) depolarizing pulses to −47, −27, −7 and 13 mV from an HP of −87 mV. (B) In the presence of 3 µM nifedipine, a significant inward current remained at each potential. (C) Current-voltage relationship; data points given as mean ± SE. Nifedipine did not completely block the Ca^{2+} current, indicating the presence of a nifedipine-resistant Ca^{2+} current. *(Reproduced with permission from Tohse et al., 1992a.)*

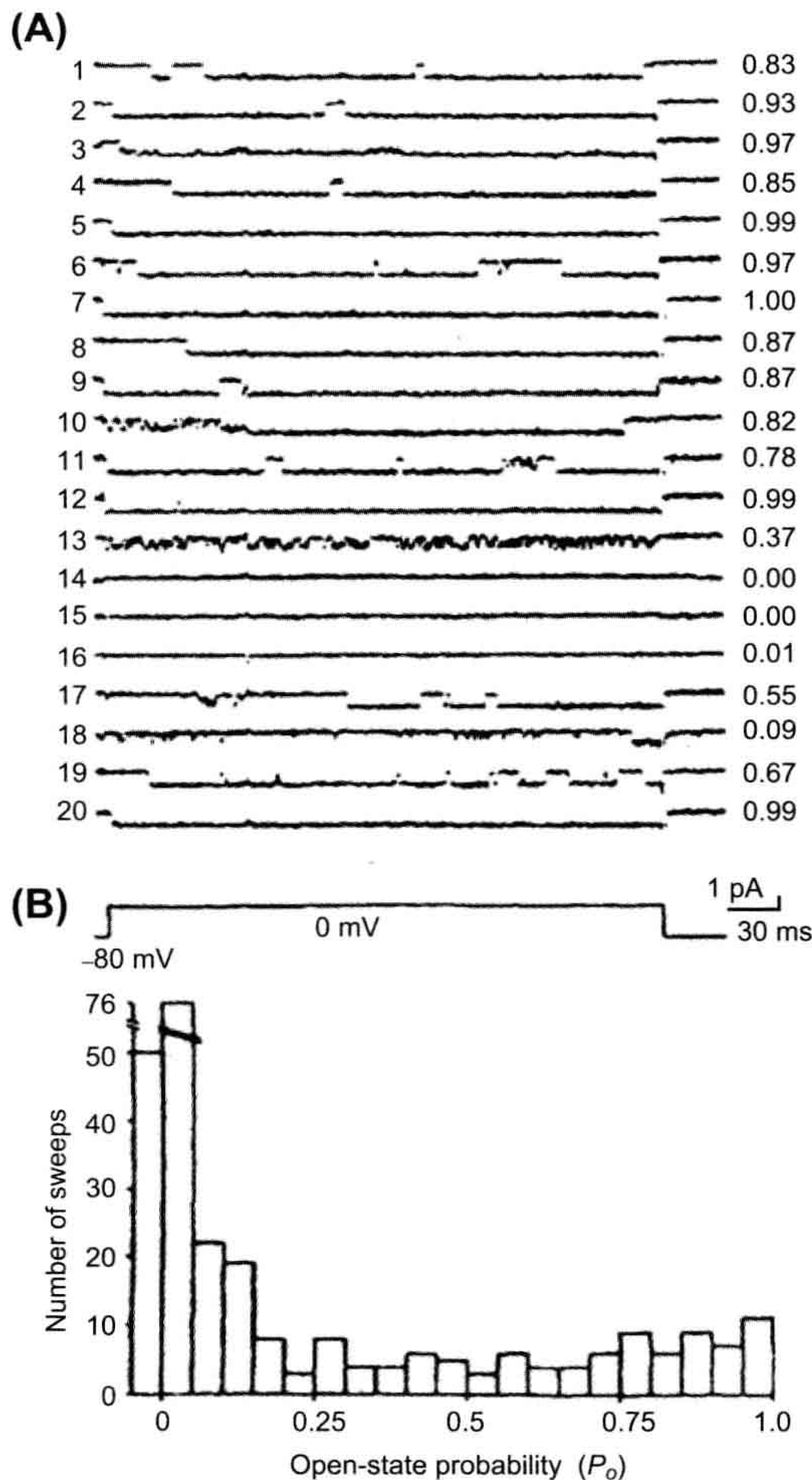


FIGURE 25.4 Presence of long openings of the slow (L-type) Ca^{2+} channels in young embryonic (3-day) chick heart cell. (A) Single-channel activity elicited by consecutive command pulses to 0 mV (from an HP of −80 mV) every 2 s. Sweep-to-sweep variations of the probability of the channel opening (P_0) are given in the right-hand column. (B) A histogram of P_0 data from nine cells (30 sweeps each). Note that many sweeps showed long openings and high P_0. *(Reproduced with permission from Tohse and Sperelakis, 1990.)*

IIIE. Inward-Rectifier K$^+$ Channels

It has been demonstrated that the inward-rectifier K^+ current (I_{K1} or $I_{K(IR)}$) of ventricular cells increases markedly during development of rabbit (Huynh et al., 1992; Sanchez-Chapula et al., 1994) and embryonic chick heart (Josephson and Sperelakis, 1990). In rat ventricle, I_{K1} increases from the embryonic to neonatal period, whereas some gradual decrease (due to an increase in cell membrane capacitance) is evident in myocytes from neonate to adult period (Kilborn and Fedida, 1990; Masuda and Sperelakis, 1993; Xie et al., 1997; Nagashima et al., 2001). In mouse atrial and ventricular myocytes, I_{K1} substantially increases with development, although it is still controversial whether the current density of I_{K1} increases or not during the embryonic period (Davies et al., 1996; Trepanier-Boulay et al., 2004; Grandy et al., 2007; Liu et al., 2010).

The increase in I_{K1} is likely to be a major factor responsible for the increase in the RP (hyperpolarization) that occurs during development, concomitant with a decrease in membrane resistivity and in the membrane time constant ($\tau_m = R_mC_m$). The increase in I_{K1} channels can also account for the decrease in the P_{Na}/P_K ratio that occurs during development (Sperelakis and Shigenobu, 1972); namely, it results in an increase in the K^+ permeability (P_K). Similar change in the P_{Na}/P_K ratio during development is shown in the skeletal muscle fibers (see Section IVA).

The increase in I_{K1} during development may be due to two factors: (1) an increase in the number of channel molecules and (2) an increase in single-channel conductance (Masuda and Sperelakis, 1993). The single-channel conductance in young fetal rats is much less than that in old fetuses and neonates (Fig. 25.5). However, the mean open time of the channels is longer in young fetal cells than in old fetal and neonatal cells. These observations suggest that the structure (i.e. a different isoform) of the inward-rectifier K^+ channel changes dramatically during development. On the other hand, a later study (Xie et al., 1997) suggests that the small conductance events in young fetal heart are sublevels of the large conductance channels in old fetal hearts. The developmental changes of the molecular correlate of I_{K1} (Kir2.1−2.3) were evaluated in rat and mouse heart. During development of the rat embryonic ventricle, the expression of Kir 2.1 and 2.2 mRNA increases, whereas Kir2.3 is not detected (Nagashima et al., 2001). In mouse atrial and ventricular myocytes, it has been demonstrated that the expression of Kir 2.1 and 2.2 increase during development, whereas Kir2.3 decreases (Nakamura et al., 1999; Trepanier-Boulay et al., 2004; Grandy et al., 2007; Liu et al., 2010).

IIIF. Voltage-Gated K$^+$ Channels

Transient outward current (I_{to}) density, mainly carried by K^+ ion, has been reported to increase during development. A substantial amount of I_{to} has been observed in early embryonic chick heart cells (Satoh, 1995). In rat ventricular myocytes, the density of I_{to} was reported to increase with development (Kilborn and Fedida, 1990; Wahler et al., 1994; Kobayashi et al., 2003). In mouse (Wang and Duff, 1997), rabbit (Sanchez-Chapula et al., 1994) and canine ventricular cells (Jeck and Boyden, 1992), a postnatal increase of I_{to} was

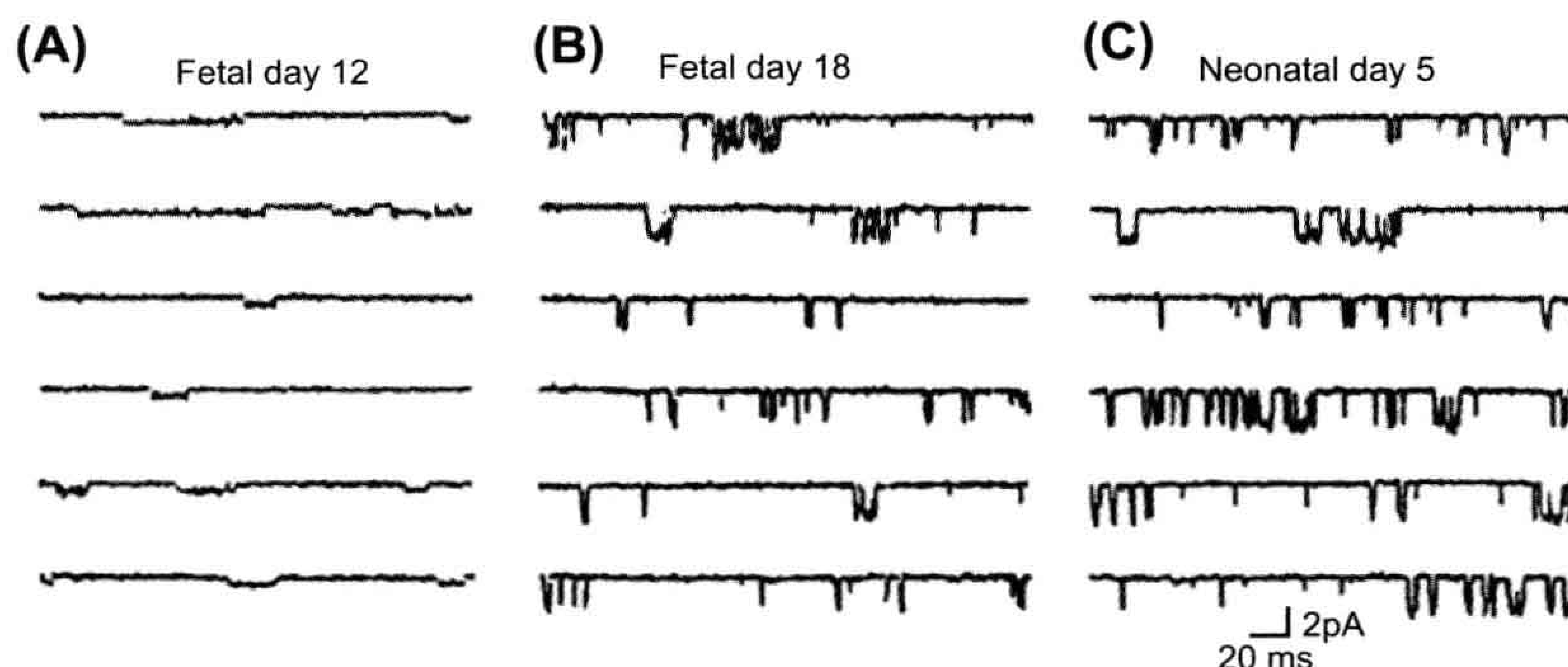


FIGURE 25.5 Developmental increase in I_{K1} in maturing rats. Single-channel activities illustrated for (A) 12-day fetal, (B) 18-day fetal and (C) 5-day neonatal ventricular myocytes. Single-channel activities were recorded at −80 mV. *(Reproduced with permission from Masuda and Sperelakis, 1993.)*

also observed. This increase in I_{to} contributes to the abbreviation of the AP that occurs in the neonatal period.

In the mammalian ventricular myocytes, I_{to} is composed of at least two components; one is characterized by a relatively fast recovery from inactivation ($I_{to,f}$) and another by a slow recovery from inactivation ($I_{to,s}$). The molecular correlate of $I_{to,f}$ is thought to be Kv4.2/4.3 and that of $I_{to,s}$ is Kv1.4. In rat ventricular myocytes, Kv4.2 protein levels increase during postnatal development, whereas Kv1.4 decreases (Matsubara et al., 1993; Xu et al., 1996). Therefore, the developmental increase in I_{to} was thought to be associated with the increase in $I_{to,f}$. However, there is a mismatch in the expression of Kv4.2 and I_{to} between postnatal days 5 and 30 (Xu et al., 1996). Recently, it has been demonstrated that the expression of voltage-gated K^+ channel-interacting proteins 2 (KChIP2) increases from embryonic day 12 to postnatal day 10, whereas Kv4.2 and Kv4.3 do not increase (Kobayashi et al., 2003). Therefore, KChIP2 is thought to be crucial to induce $I_{to,f}$ during development.

Between postnatal days 8 and 20, rat plasma thyroid hormone (T3) level increases (Shimoni et al., 1997). T3 stimulation enhanced Kv4.2 and Kv4.3 expression and decreased Kv1.4 transcription, while KChIP2 remained unaffected (Wickenden et al., 1997; Guo et al., 1998; Gassanov et al., 2009). Therefore, it has been suggested that T3 plays a role in postnatal upregulation of $I_{to,f}$. In addition, basic fibroblast growth factor (bFGF), which has tyrosine kinase activity, may also promote the expression of I_{to} during development (Guo et al., 1995).

As I_{to} in neonatal rat ventricular cells is smaller than that in adult cells, an ultrarapidly activating delayed-rectifier K^+ current (I_{Kur}) predominates I_{to} only during the early neonatal period (Guo et al., 1997b). In cultured neonatal rat ventricular cells, IGF-I promotes the expression of I_{Kur} as well as Kv1.5 protein (Guo et al., 1997a). I_{Kur} in ventricular cells decreases during postnatal development, which is associated with a reduction of the Kv1.5 expression. However, no substantial change in Kv1.5 protein is also reported from neonate to adult in the same preparation (Xu et al., 1996). Recently, it has been demonstrated that co-expression of KChIP2 decreases Kv1.5-encoded K^+ currents (Li et al., 2005). Therefore, KChIP2 is thought to be crucial to the decreased I_{Kur} during development.

In mouse fetal ventricular cells, a rapidly activating delayed-rectifier K^+ current (I_{Kr}) is the dominant component of delayed-rectifier I_K, whereas a slowly activating delayed-rectifier K^+ current (I_{Ks}) becomes dominant in early postnatal period (day one to three). However, both components disappear in adult mouse ventricular cells (Davies et al., 1996; Wang et al., 1996). Similarly, I_{Kr} in rat ventricular cells functions during the fetal period, but is negligible in adults. The main molecular correlates of I_{Kr} are thought to be ERG and MiRP1, whereas those of I_{Ks} are KvLQT1 and minK. ERG expression is observed in mouse ventricle in the embryonic period, whereas MiRP1 expression is not observed (Franco et al., 2001). Evaluating the expression of mRNAs of mouse heart during the embryonic and postnatal periods revealed that KvLQT1 decreases during development, whereas minK increases until late embryonic period and then decreases (Mai et al., 2004).

The density of I_K (the sum of I_{Kr} and I_{Ks}) in guinea pig ventricles is smaller in fetal cells than in neonatal and adult cells, suggesting a developmental increase in I_K (Kato et al., 1996). No substantial changes in the kinetics and voltage dependency of I_K are observed during development.

IIIG. Hyperpolarization-Activated Inward Current

The hyperpolarization-activated inward current (I_h or I_f), which is mainly carried by Na^+ and K^+ ions, is observed in sinoatrial node and early embryonic cardiomyocytes. In the

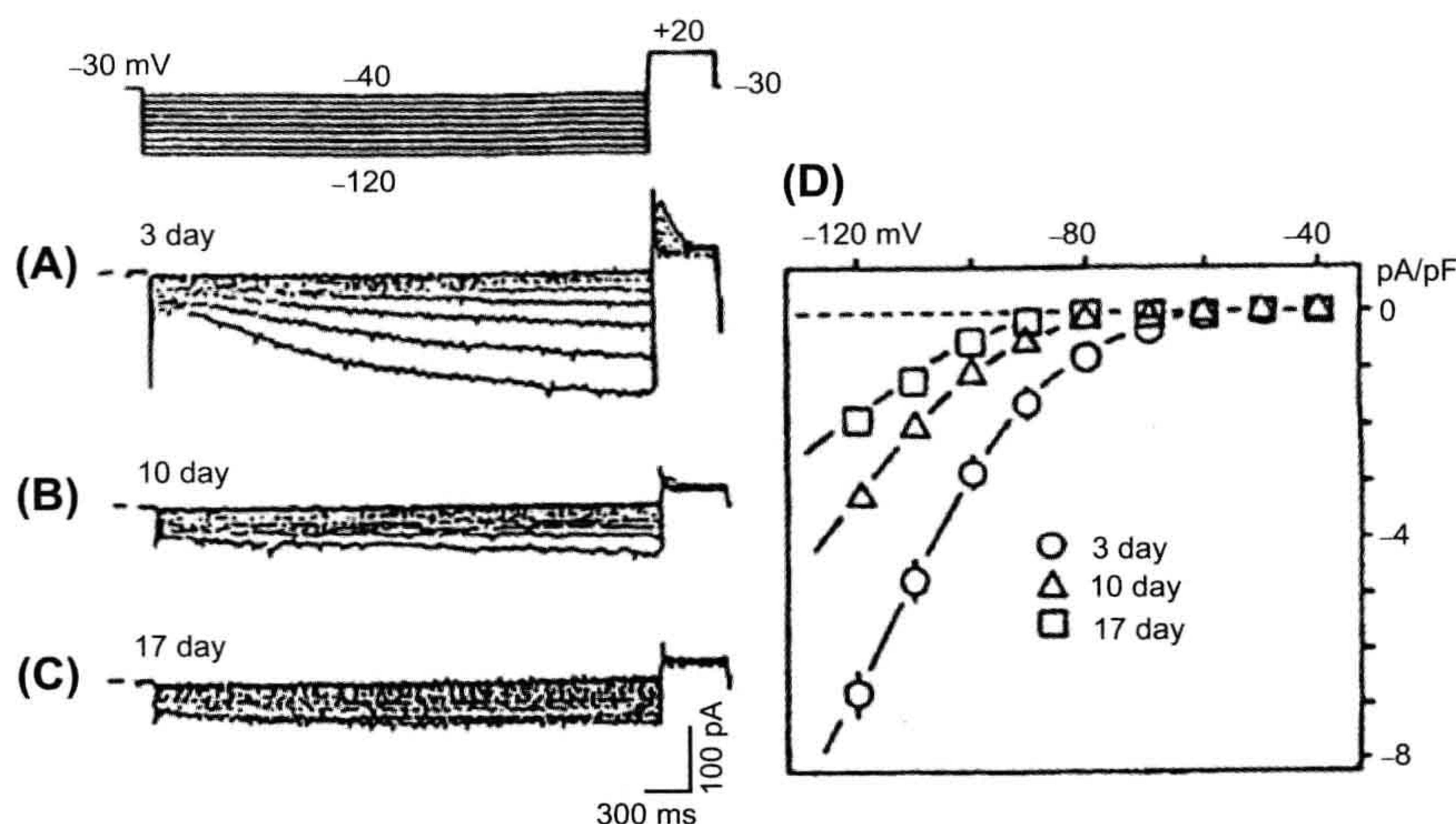


FIGURE 25.6 Developmental changes of the hyperpolarization-activated inward current (I_h) in young embryonic chick ventricular cells. Test pulses were applied between −40 mV and −120 mV, in 10-mV increments, from an HP of −30 mV. (A) A large inward current was slowly activated by hyperpolarization in a 3-day-old cell. (B) Smaller I_h in a 10-day-old cell. (C) Further reduced I_h in a 17-day-old cell. (D) Current-voltage relations for I_h current density at the three developmental stages (mean ± SE). *(Reproduced from Satoh, H. and Sperelakis, N. (1993). Hyperpolarization-activated inward current embryonic chick cardiac myocytes: developmental changes and modulation by isoproterenol and carbachol. Eur J Pharmacol, 240, 283–290, Copyright 1993. With permission from Elsevier Science.)*

chick ventricular myocytes, I_h progressively decreased during development and essentially disappears in the late embryonic period (Fig. 25.6) (Satoh and Sperelakis, 1993). In rabbit sinoatrial node, a slope conductance of I_h in neonatal cells is larger than that in the adult cells (Accili et al., 1997). In the rat ventricular myocytes, it is still controversial whether the current density of I_h decreases or not during the postnatal period (Robinson et al., 1997; Cerbai et al., 1999). In the mouse cardiomyocyte, I_h increases at the early embryonic period (between embryonic day 8.5 to 9.5) and then decreases (between embryonic day 9.5 and 18) (Yasui et al., 2001; Stieber et al., 2003).

The I_h is called the *pacemaker current* in adult cardiomyocytes. In Purkinje fibers, I_h plays a key role in pacemaker depolarization during the diastolic phase. In sinoatrial node cells, the contribution of I_h to pacemaker potential is still controversial for two reasons (Irisawa et al., 1993): the time course of activation of I_h is too slow to account for the high frequency of the pacemaker and the threshold potential for activation of I_h (close to −70 mV) is beyond the maximum diastolic potential (−60 to −70 mV) for the nodal cells. In chick embryonic cardiomyocytes, although the time course of decrease in I_h parallels the disappearance of the pacemaker potential, the contribution of I_h to the pacemaking may still be small (Satoh and Sperelakis, 1993).

Recently, it has been demonstrated that the I_h current is mediated by hyperpolarization-activated and cyclic nucleotide-gated (HCN) channels. In the early embryonic period, HCN4 mRNA is highly expressed in mouse ventricle and then the expression decreases with development (Yasui et al., 2001). Mice with a selective deletion of HCN4 in cardiomyocytes die between embryonic days 9.5 and 11.5 (Stieber et al., 2003). In mouse heart, although small I_h current could be detected in HCN4 knockout mice, it has been suggested that the HCN4 channel plays a key role in pacemaker depolarization during the diastolic phase.

IIIH. Excitation–Contraction Coupling

Changes in the excitation–contraction coupling process also occur during development of the heart. In particular, the source of Ca^{2+} for producing contraction is altered during development (Fig. 25.7) (Nakanishi et al., 1988; Kitchens et al., 2003; Seki et al., 2003; Tohse et al., 2004; Kobayashi et al., 2011). In fetal heart cells, the role of the sarcoplasmic reticulum (SR) is none at first and increases with embryonic development. Therefore, most of the Ca^{2+} required for contraction of embryonic cells is derived from Ca^{2+} influx through the voltage-dependent Ca^{2+} channels (L-type and T-type), i.e. originates from the extracellular space. In neonatal heart cells, the SR matures and plays a main role as the source of Ca^{2+} for contraction. Therefore, the Ca^{2+}-induced Ca^{2+} release from the SR compartment (Fabiato and Fabiato, 1978) becomes the more important system for contraction. That is, in adult heart cells, most of the Ca^{2+} for

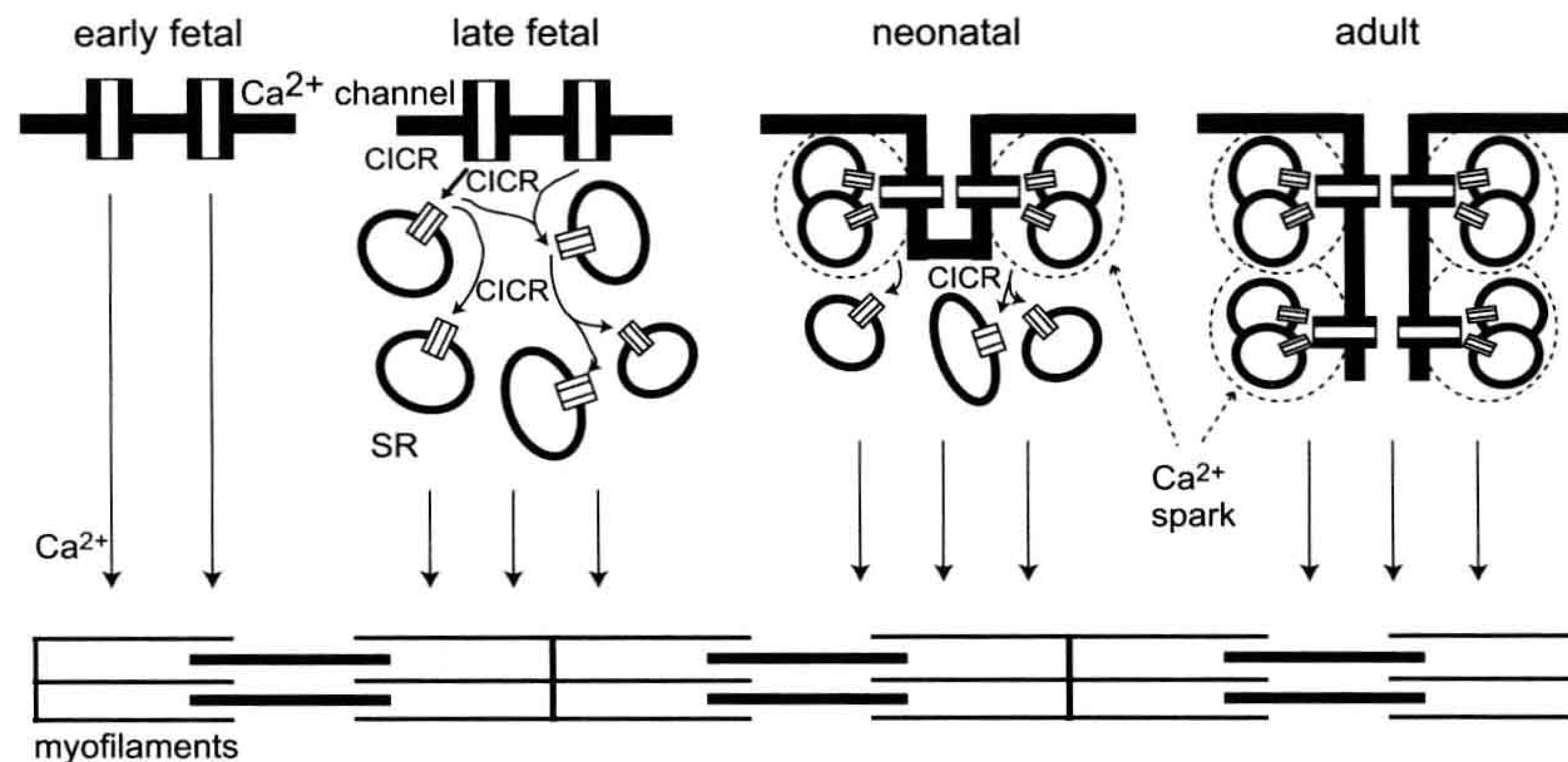


FIGURE 25.7 Schematic model of excitation–contraction (E-C) coupling during heart development. In the early fetal period at which the heart begins to contract, Ca^{2+} entering the cell through the sarcolemmal Ca^{2+} channels directly activates the myofilaments. During embryonic development, Ca^{2+} release from the sarcoplasmic reticulum (SR) through the ryanodine receptor (RyR) increases. This released Ca^{2+} from SR also stimulated another SR, as shown in "late fetal" panel. In the neonatal period, the formation of the T-tube system starts. A few L-type Ca^{2+} channels are close to RyRs and can evoke the Ca^{2+} spark in the periphery of cardiomyocytes. In the center of cardiomyocytes, the slow cascade of CICR still evokes. In the adult period, the T-tube system is established in all areas of cardioymyocytes. Each L-type Ca^{2+} channel is close to RyRs. The Ca^{2+} sparks simultaneously evoke in the periphery and centers of cells, producing fast and large Ca^{2+} transient in adulthood. *(Reproduced in modified form, with permission, from Tohse et al., 2004.)*

contraction comes from the internal SR stores. However, Ca^{2+} influx through the sarcolemma remains the determining factor for contractile force, because the Ca^{2+} influx controls the amount of Ca^{2+} released.

IV. SKELETAL MUSCLE FIBERS

IVA. Resting Potential and Action Potential

In skeletal muscle fibers, the RP also increases during development and differentiation from the individual myoblast stage to the multinucleated myotube stage to the mature fiber. (The myoblasts fuse end to end to form the myotubes which get progressively larger in length and diameter.) For example, the RP of cultured chick embryonic skeletal myocytes is low in the immature stage (short mononucleated myoblasts) and is dramatically hyperpolarized during differentiation (to long myotubes or mature fibers) (Fig. 25.8A) (Fischbach et al., 1971; Spector and Prives, 1977). The mature fibers in older cultures consist of multinucleated myotubes with cross-striations (i.e. aligned myofibrils). In the immature myoblasts, the RP generally is about −40 mV. However, the RP of the maturing myotubes is about −60 mV, which is approximately equal to that of adult skeletal muscles bathed in the same culture medium (Fig. 25.8A). A similar change in the RP occurs in rat skeletal myoblasts/myotubes during development (Ritchie and Fambrough, 1975). A progressive decrease in the P_{Na}/P_K ratio, which sets the RP closer to the equilibrium potential for K^+ (E_K), accounts for the developmental changes in the RP (Fig. 25.8B). The family of curves shown in Fig. 25.8B is similar to that reported in developing chick heart (Sperelakis and Shigenobu, 1972).

In human skeletal muscle (from biopsy), the RP increases (hyperpolarization) during culture. Fetal and postnatal myocytes exhibit RPs of about −8 to −35 mV in the early period of culture and then hyperpolarize to about −50 to −74 mV in later culture (Iannaccone et al., 1987; Liu et al., 1998, 2003). This hyperpolarization, which is due to the sequential expression of I_K and I_{K1}, induces an increase in intracellular Ca^{2+} concentration, which is essential for myoblast differentiation and fusion to occur (Bijlenga et al., 2000; Fischer-Lougheed et al., 2001; Konig et al., 2006).

The AP configuration of skeletal muscle fibers also changes during development and differentiation. For example, in one study of chick embryonic myotubes, prolonged APs that persist for more than 500 ms, with prolonged contraction, were exhibited on day 5 in culture (Spector and Prives, 1977). By culture day 7, the myotubes exhibited primarily brief APs (less than 10 ms) and brief twitch contraction. (On day 5, small regions of the myotubes sometimes displayed brief APs with localized twitches in those regions.) Thus, the brief AP becomes more dominant during development that proceeds in culture.

A second study on cultured chick skeletal myoblast/myotubes is depicted in Fig. 25.9. As can be seen, at the early stage, the AP is small and does not overshoot (the zero membrane potential level) (Fig. 25.9A, upper record). In the myotubes formed by fusion of myoblasts after a few

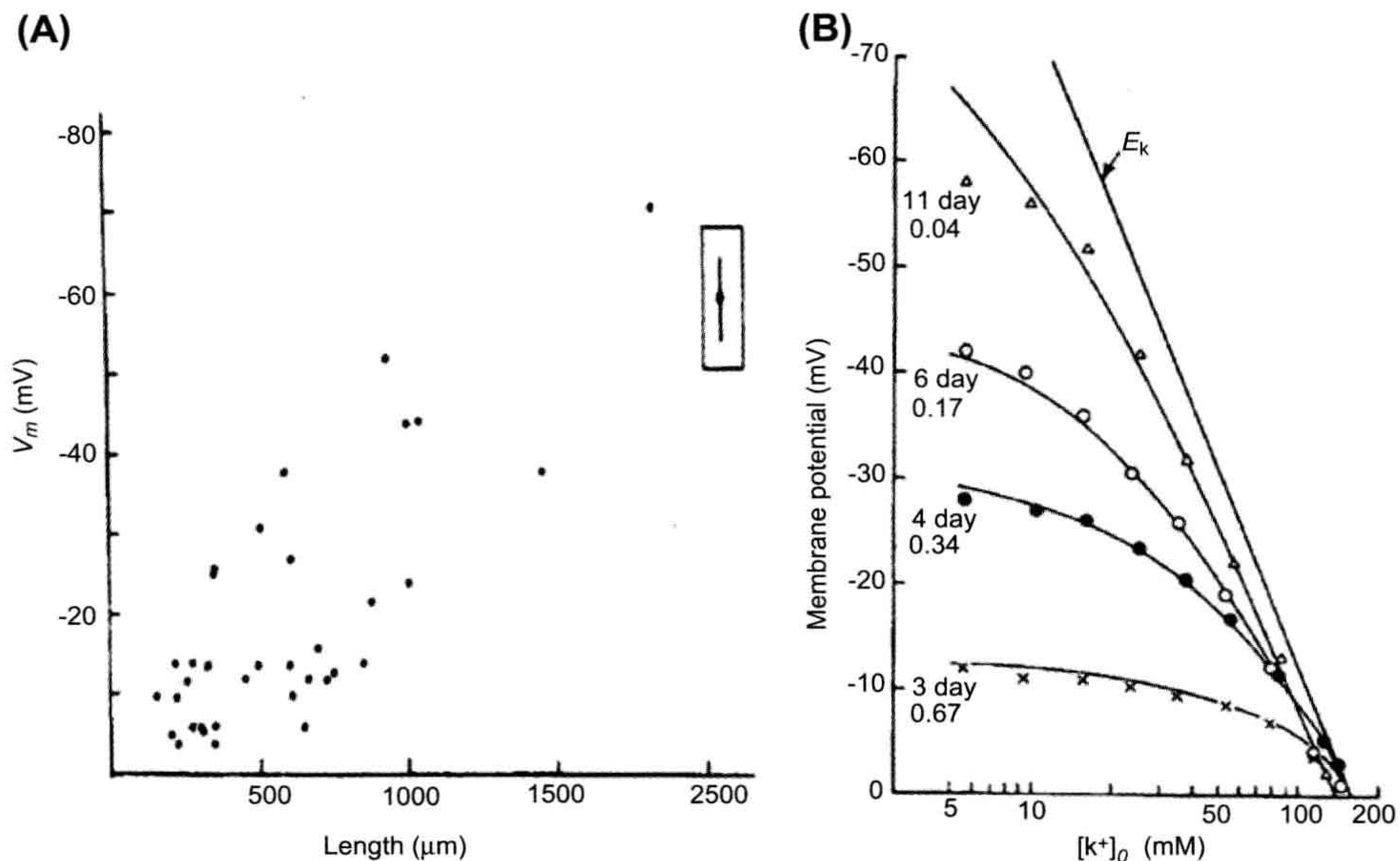


FIGURE 25.8 Developmental changes of resting potential in the skeletal myoblasts/myotubes from (A) embryonic chick and (B) fetal rat. (A) The relation between the RP and length of the chick skeletal myoblasts/myotubes in culture. The filled circle enclosed within the box is the mean (± 2SE) resting potential of 20 myotubes. (B) The relationship between the RP and external K^+ ion concentration ($[K^+]_o$) for rat skeletal myotubes of different periods in culture. The Nernst equilibrium potential for K^+ is indicated by the straight line labeled E_K. The solid line for each myotube is the theoretical curve predicted by the Goldman equation for the P_{Na}/P_K ratios given at the left and the extrapolated $[K^+]_i$ value. *(Reproduced with permission from (A) Fischbach et al. (1971). J. Cell. Physiol. 78, 289–300. Copyright 1971 John Wiley & Sons, Inc. Reprinted by permission of Wiley-Liss, Inc., a subsidiary of John Wiley & Sons, Inc. and (B) Ritchie and Fambrough, 1975. Reproduced from The Journal of General Physiology, by copyright permission of The Rockefeller University Press.)*

more days in culture (day 7 and 11), the amplitude and maximum rate of the spikelike APs increased markedly during development while in culture (Fig. 25.9A, middle and lower records, and Fig. 25.9B). A plot of max dV/dt versus the number of days in culture is given in Fig. 25.9B. Since the APs were blocked by TTX in almost all myotubes tested (Fig. 25.9A, right side, and Fig. 25.9B), differentiation of the spike-like APs is due to progressively increased intensity of inward current through fast Na^+ channels (Kano and Yamamoto, 1977). That is, an increase in the number (density) of fast Na^+ channels allows a regenerative AP to be produced, and the maximum rate of rise to become faster and faster.

In myocytes of a marine tunicate (ascidian), AP duration abbreviates during the embryonic period (Greaves et al., 1996). There is a progressive decrease in AP duration from the middle embryonic to the late embryonic period and a corresponding increase in the rate of rise and fall of the AP. Spontaneous firing of APs is observed in most ascidian myocytes in the middle embryonic period. The automaticity progressively disappears during development.

IVB. Inward-Rectifier K^+ Channels

The RP of maturing myotubes gets closer to E_K because the P_{Na}/P_K ratio is gradually decreased during development (see Fig. 25.8B). These characteristics are also observed in chick embryonic cardiomyocytes during development (Sperelakis and Shigenobu, 1972) and are produced by marked expression of the inward-rectifier K^+ channels in the surface membrane of the myocytes (Shin et al., 1997). Therefore, it seems likely that the hyperpolarization of the RP of skeletal myocytes in culture is produced by a similar developmental change of inward-rectifier K^+ channels.

The I_{K1} is present in skeletal muscle cells from early embryonic amphibian (Linsdell and Moody, 1995). Although there is a brief period (approximately 4 h) during which its density decreases, the overall trend is an increase during development.

In ascidian myocytes, I_{K1} exhibited dramatic changes during development (Fig. 25.10C) (Greaves et al., 1996). In the ascidian, the inward-rectifier K^+ current is gained after fertilization of the egg. (The same change also occurs in other species.) When gastrulation ends (at 16 h after

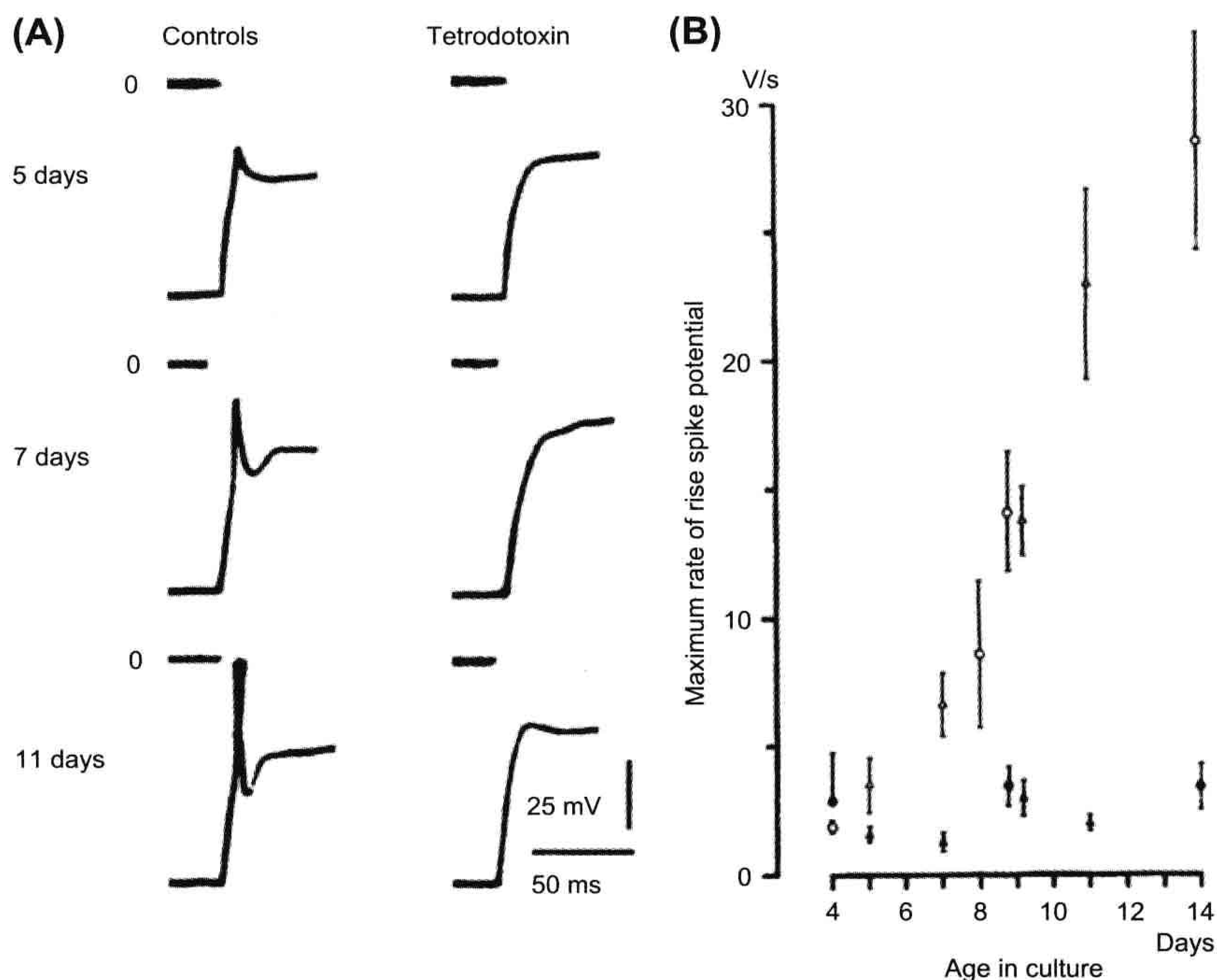


FIGURE 25.9 Spike-like APs and their maximum rate of rise in maturing skeletal myotubes from chick embryo. (A) Responses of three myotubes at different ages in culture: 5 days (upper), 7 days (middle) and 11 days (lower). Each pair of records is taken from the same myotube before (left) and after (right) application of TTX (10^{-7} M). Depolarizing current pulses were applied after the membrane potential was hyperpolarized to a standard level of −80 mV. The zero potential level is indicated. (B) Maximum rate of rise of spike potentials as a function of the age in culture (mean ± SE). Circles and triangles represent two different batches of culture; filled symbol indicates presence of TTX. *(From Kano and Yamamoto (1977). Development of spike potentials in skeletal muscle cells differentiated in vitro from chick embryo. J. Cell. Physiol. 90, 439–444. Copyright © 1977 Journal of Cellular Physiology. Reprinted by permission of Wiley-Liss, Inc., a subsidiary of John Wiley & Sons, Inc.)*

fertilization), the current density suddenly decreases from 4 to 0.5 pA/pF. After the tailbud stage (22 h after fertilization), the current density progressively increases again and reaches a value of 5 pA/pF before hatching. Because I_{K1} is one of the most important resting conductances (which stabilizes and helps to set the RP), this transient decrease and subsequent increase in the current density parallels the generation of spontaneous APs.

Evaluating the human myoblast fusion revealed that the I_{K1} increases during differentiation (Liu et al., 1998). In addition, inhibition of Kir 2.1 expression with an antisense-Kir2.1-RNA reduced the endogenous I_{K1} and blocked fusion (Fischer-Lougheed et al., 2001). Therefore, it seems likely that the increase in I_{K1} is required for human muscle differentiation.

IVC. Delayed-Rectifier K^+ Channels

The delayed-rectifier K^+ current (I_K) in skeletal myocytes of early embryonic amphibian progressively increases during development in culture (Linsdell and Moody, 1995). A similar increase in I_K occurs in ascidian myocytes after the neurula stage (16 h postfertilization) (see Fig. 25.10B) (Greaves et al., 1996). However, $I_{K(Ca)}$ progressively increases after 26 h postfertilization. The increase in $I_{K(Ca)}$ closely parallels the increase in sustained L-type Ca^{2+} current (see Figs. 25.10A,B). These developmental changes in K^+ channels contribute to the abbreviation of AP duration during the late developmental period.

Evaluating the human myoblast fusion revealed that I_K increases during differentiation (Bijlenga et al., 1998; Fischer-Lougheed et al., 2001). It seems likely that I_K contributes to the RP, because the cells were depolarized by 5 μM dofetilide, a class III antiarrhythmic agent known selectively to inhibit ERG channels. However, it remains unknown whether I_K is a prerequisite for myoblast fusion to occur, because the inhibition of I_K accelerates the rate of human myoblast fusion (Liu et al., 2003). Further experiments are necessary to reveal the precise roles of I_K during differentiation.

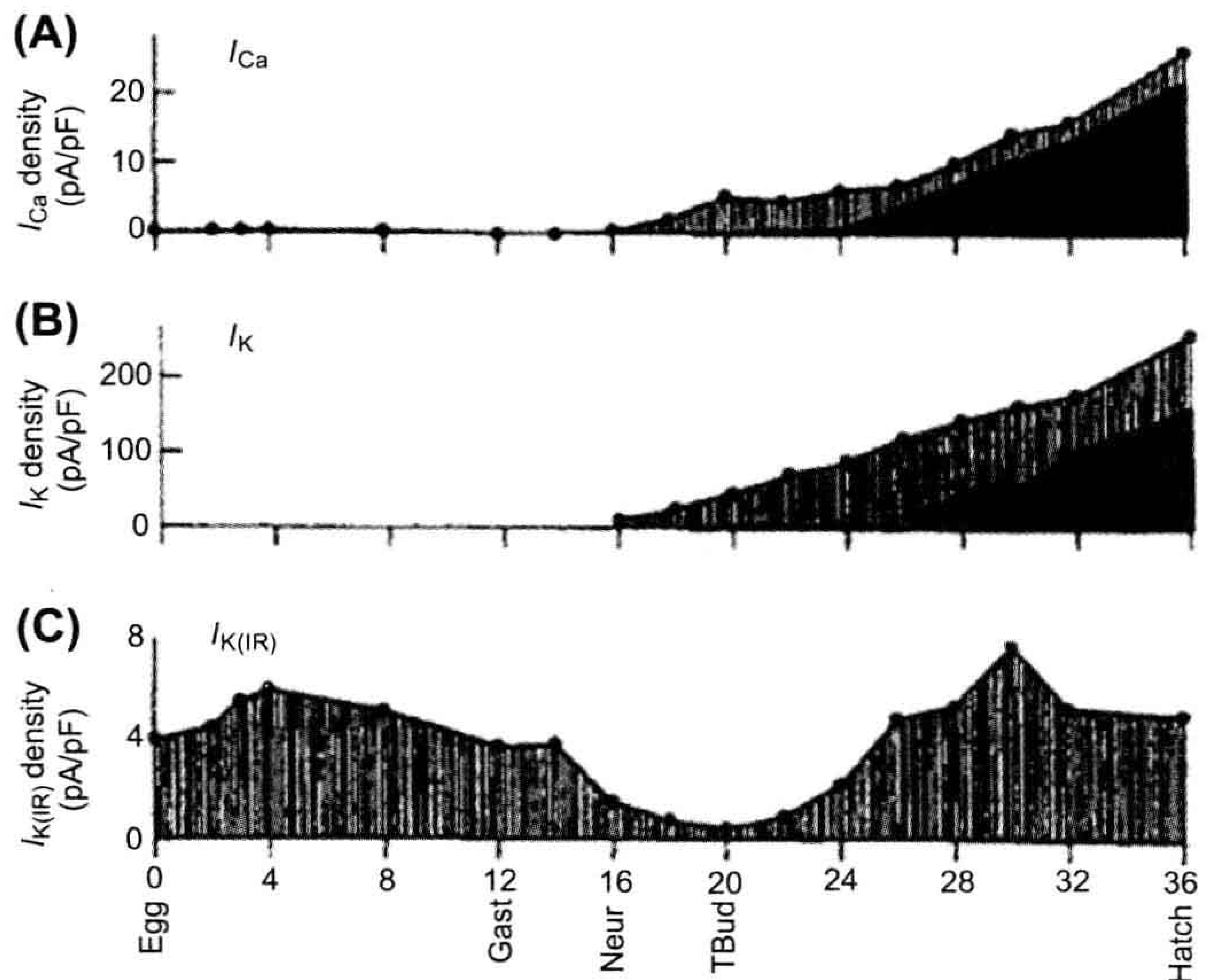


FIGURE 25.10 Development of Ca^{2+} and K^+ currents in skeletal muscle of a marine tunicate (ascidian). The plots start at fertilization (0 h). (A) Total Ca^{2+} current density (filled circles), with inactivating (hatched) and sustained (solid) components. (B) Total K^+ current density (filled circles), with voltage-dependent (hatched) and Ca^{2+}-dependent (solid) components. (C) Inward-rectifier K^+ current (I_{K1} or $I_{K(IR)}$) density. Gast, Neur and Tbud indicate the stages of gastrula, neurula and tailbud, respectively. *(Modified with permission from Greaves et al., 1996.)*

IVD. Ca^{2+} Channels and Na^+ Channels

High-voltage-activated Ca^{2+} channels have also been observed in the ascidian embryo (see Fig. 25.10A) (Greaves et al., 1996). These Ca^{2+} channels exhibit inactivation and may be an N-type Ca^{2+} channel because the current is blocked by conotoxin. The channels increase after the neurula stage (16 h after fertilization). After the tailbud stage, sustained Ca^{2+} channel activity (probably L-type) begins to increase and dominates at the time of hatching. Low voltage-activating, rapidly inactivating Ca^{2+} channels (T-type) are detected in about 50% of the cells at each stage of development. The contribution of the T-type channels to total Ca^{2+} influx is relatively small in comparison with L-type and N-type channels.

In early embryonic amphibian skeletal myocytes, substantial Ca^{2+} current and Na^+ current appeared almost at the same time (after 10–12 h in culture) (Linsdell and Moody, 1995). These channel currents continued to increase steadily over an observation period of 10–28 h in culture.

In mouse skeletal muscle, L-type Ca^{2+} current increases during embryonic development, whereas T-type Ca^{2+} current increases until embryonic day 16 followed by a decrease until birth (Shimahara and Bournaud, 1991; Strube et al., 2000; Berthier et al., 2002). It seems likely that this developmental change of T-type Ca^{2+} current is involved in the early stages of muscle differentiation via the increase in the intracellular Ca^{2+} concentration, because the inhibition of T-type Ca^{2+} current by 100 μM amiloride, 200 μM Ni^{2+} or antisense oligonucleotides directed against the α1H subunit suppresses fusion of myoblasts (Bijlenga et al., 2000).

IVE. Acetylcholine Receptor/Channel

The nicotinic acetylcholine receptor/channel (nAChR) is essential to transmission at the neuromuscular junction (see chapter on synaptic transmission). During development, the nAChR channels in embryonic muscles are converted to adult-type nAChR channels around the time of birth (Mishina et al., 1986). The fetal nAChR channel is composed of α-, β-, γ- and δ-subunits and, in the adult channel, the γ-subunit is substituted by an ε-subunit. In functional characteristics, the fetal channel exhibits a low conductance and long openings compared with those of the adult channel. This conversion of the nAChR channel may be related to innervation of the muscles that occurs during development, because the substitution of the fetal-type nAChR channels with an adult-type nAChR channels substantially alters the innervation pattern of mouse muscle by the motor nerve (Koenen et al., 2005).

In the early embryonic period, nAChR channels are present at a moderate level throughout the myotube surface. In adult muscle, nAChR channels are highly concentrated in the neuromuscular junction (Sanes and Lichtman, 2001). A recent study has revealed the coordinated activities of Wnt3 and agrin, which are both secreted by motoneurons, in clustering nAChR channels at the neuromuscular junction (Henriquez et al., 2008).

IVF. Regulation of Expression of Ion Channels

It has been well analyzed that several humoral factors regulate expression of ion channels during development. Activin, a member of the TGFβ family, has proved to be a particularly potent inducing agent to form different mesodermal cell types from animal cap cells. In vitro induction of animal cap *Xenopus* cells under culturing with activin triggers a whole cascade of developmental events, resulting in the differentiation of skeletal muscle (Currie and Moody, 1999). The developmental pattern of ion channel expression in muscle induced in vitro by activin is close to that of normal muscle. First, the same currents (I_K, I_{K1}, I_{Na}, I_A, I_{Ca}) are expressed over a similar time course during differentiation. The sequence in which the currents are expressed is also maintained, with I_K and I_{K1} being expressed first, followed by I_{Na}, I_A and I_{Ca} at slightly later stages. This study indicates that activin is very important for development of electrical activity in skeletal muscle.

V. NEURONS

VA. Action Potential

The ionic dependence of the neuronal AP is altered during the early stages of embryonic development (Spitzer and Baccaglini, 1976; Spitzer et al., 1994). Initially, the AP exhibits a prominent Ca^{2+} dependence (i.e. Ca^{2+}-dependent AP) and its duration is prolonged. Later in development, the AP duration becomes brief and most of the inward current during the depolarizing phase is carried by Na^+ (i.e. Na^+-dependent AP). The Na^+-dependent APs continue until maturation of the neuron. For example, in embryonic amphibian neurons in vivo, the AP is prolonged and the rate of rise is slow at a relatively early stage (Fig. 25.11A). Removal of Na^+ ion does not affect the AP configuration at this stage, whereas it is almost abolished by Co^{2+} ion, an inorganic blocker of voltage-dependent Ca^{2+} channels. In the late embryonic stage, the AP becomes greatly abbreviated and loses the shoulder on its falling phase (Fig. 25.11B). This AP is completely blocked by removal of Na^+ ion (or by TTX), but is unaffected by Co^{2+} (Spitzer and Baccaglini, 1976).

In rat spinal motoneurons at embryonic day 16, the AP upstroke may be dependent upon Na^+ ion, although maximum rate of rise of the AP is slow (about 20 V/s) (Gao and Ziskind-Conhaim, 1998). Duration of the AP at day 16 is prolonged (about 10 ms). At postnatal day 3, the AP upstroke is very fast (about 70 V/s) and duration of the AP is very short (2–3 ms).

In mouse cortical neurons at embryonic day 14, the AP duration is prolonged. During development, the AP duration becomes brief. This developmental change is mainly due to the increase in Na^+ current density, while outward K^+ current density remains almost unchanged (Picken Bahrey and Moody, 2003).

VB. Ca^{2+} Transient

Spontaneous transient elevation of intracellular Ca^{2+} is observed in developing neurons. The spontaneous Ca^{2+} transient (recorded by use of fluorescent dyes, e.g. FURA-2, fluo-3, indo-1, etc.) is exclusively dependent on Ca^{2+} influx because it is abolished either by removal of extracellular Ca^{2+} or by agents that block Ca^{2+} channels (Holliday and Spitzer, 1990; Spitzer, 1994). Therefore, the observed intracellular Ca^{2+} transient is due to Ca^{2+} influx from the extracellular space.

Two classes of spontaneous Ca^{2+} transients have been detected: rapid events, termed Ca^{2+} *spikes* (Gu et al., 1994) and slow events, termed Ca^{2+} *waves*. The incidence of

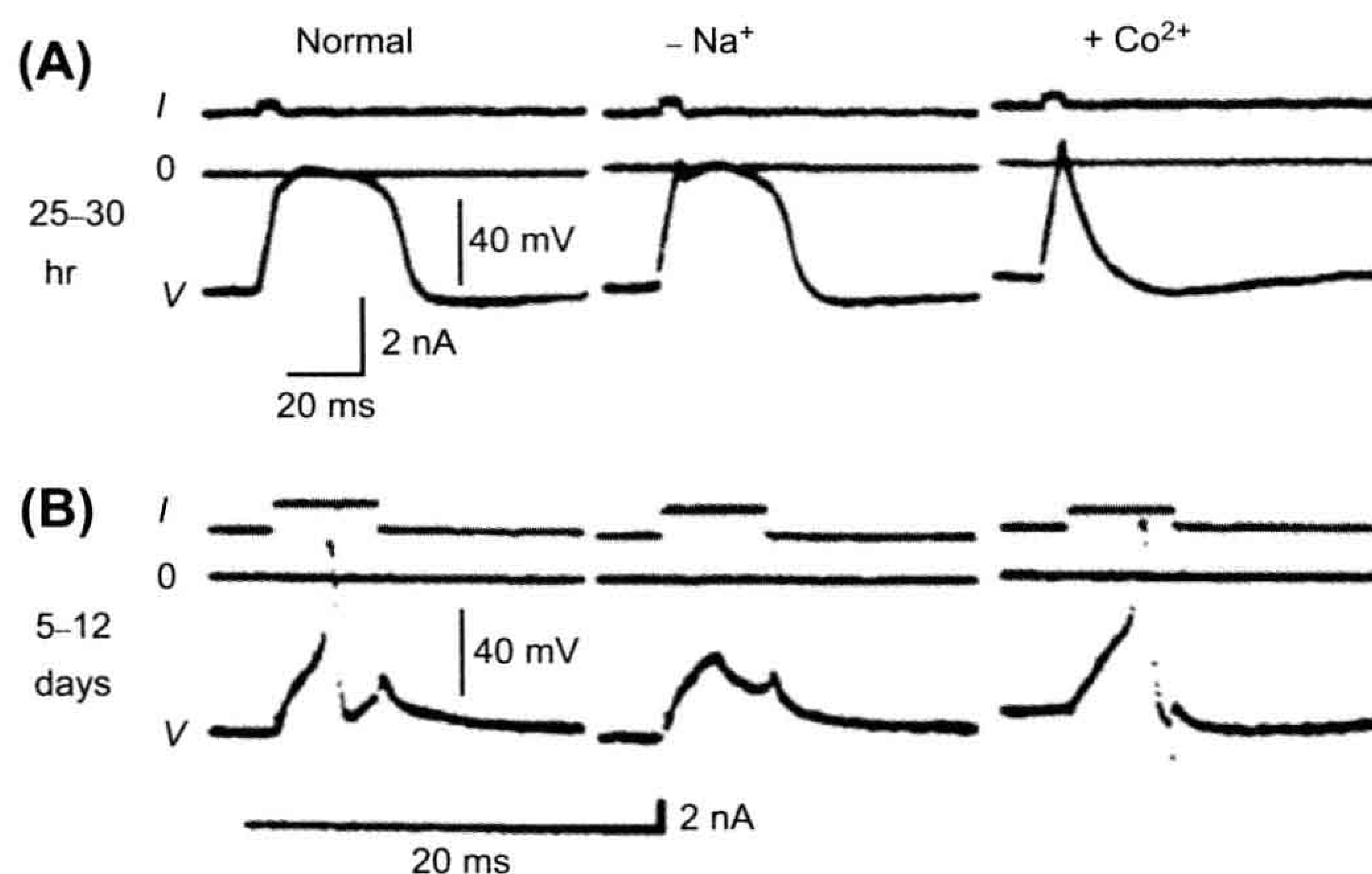


FIGURE 25.11 Developmental changes in APs of embryonic amphibian neurons at two different stages: (A) 25–30 h and (B) 5–12 days after fertilization of the egg. Depolarizing current (*I*) is applied to evoke the AP (*V*). The zero potential is shown by a solid line (0). (A) The AP is of long duration and the rate of rise is slow at this early stage. This AP is little affected by removal of Na^+, but is abolished by Co^{2+}. (B) The AP at this late stage is brief and its amplitude is large. This AP is blocked by removal of Na^+ and is unaffected by Co^{2+}. *(Modified from Spizer, N.C. and Baccaglini, P.I. (1976). Development of the action potential in embryo amphibian neurons in vivo, Brain Res. 107, 610–616, Copyright 1976, with permission from Elsevier Science.)*

these Ca^{2+} transients changes during development in culture. Ca^{2+} spikes in the cell body (soma) are triggered by spontaneous APs and are rapidly propagated to the growth cone. Ca^{2+} spikes also use the intracellular Ca^{2+} store because depletion of the store with caffeine substantially reduces their amplitude. Ca^{2+} spikes may be required for the normal appearance of the transmitter γ-aminobutyric acid (GABA), since blocking of Ca^{2+} spikes by a Ca^{2+} channel-blocker prevents the acquisition of GABA immunoreactivity (Spitzer et al., 1993). The normal developmental increase in the activation kinetics of K^+ currents is also prevented by the blocking of Ca^{2+} spikes.

Ca^{2+} waves occur often (about 10/h) in the growth cone and they are not generally propagated to the soma. The Ca^{2+} waves in the soma occur at a lower frequency (about 2/h). Therefore, the Ca^{2+} waves are local and occur independently in separate growth cones of the same neuron. Because there seems to be some relation between external Ca^{2+} and the length of the neurite, Ca^{2+} waves in growth cones are likely to regulate neurite extension (Gu et al., 1994; Spitzer, 1994; Spitzer et al., 1994).

The recent evaluation of Ca^{2+} signaling in gastrula stage embryos revealed that not only Ca^{2+} transients (Ca^{2+} spikes and Ca^{2+} waves) but also a slow increase in $[Ca^{2+}]_i$ was observed during early gastrulation of *Xenopus* and zebrafish (Gilland et al., 1999; Leclerc et al., 2000; Webb et al., 2005). Inhibition of these Ca^{2+} signalings decreases the expression of neuralising genes, *Zic3* and *geminin*, and proto-oncogene, *c-fos* and FOS-related protein (Leclerc et al., 1999, 2000). Furthermore, the activators of L-type Ca^{2+} channel (ConA and Bay-K-8644) trigger neural induction (Moreau et al., 1994). Although the precise downstream targets of the Ca^{2+} signaling cascades remain to be elucidated, Ca^{2+} might be a key central regulator in the process of neural induction (Webb et al., 2005).

VC. Voltage-Gated Ion Channels

In mature excitable cell membranes, the major inward currents consist of two ions, Na^+ and Ca^{2+}, which are carried through voltage-gated Na^+ channels and Ca^{2+} channels, respectively. Na^+ and Ca^{2+} channels exhibit two patterns of development (Gottmann et al., 1988; O'Dowd et al., 1988). In the first pattern, Ca^{2+} channels appear earlier and develop faster than Na^+ channels. This explains, at least in part, the conversion of the Ca^{2+}-dependent AP to the Na^+-dependent one discussed earlier.

In the second pattern, Ca^{2+} channels and Na^+ channels become expressed almost at the same time. For example, in cultured embryonic amphibian neurons, Ca^{2+} currents are large even at the early stage of development and the peak current density does not change from the early stage to the late stage (Fig. 25.12A). Na^+ currents are also present, but the current density is small at the early stage. The peak

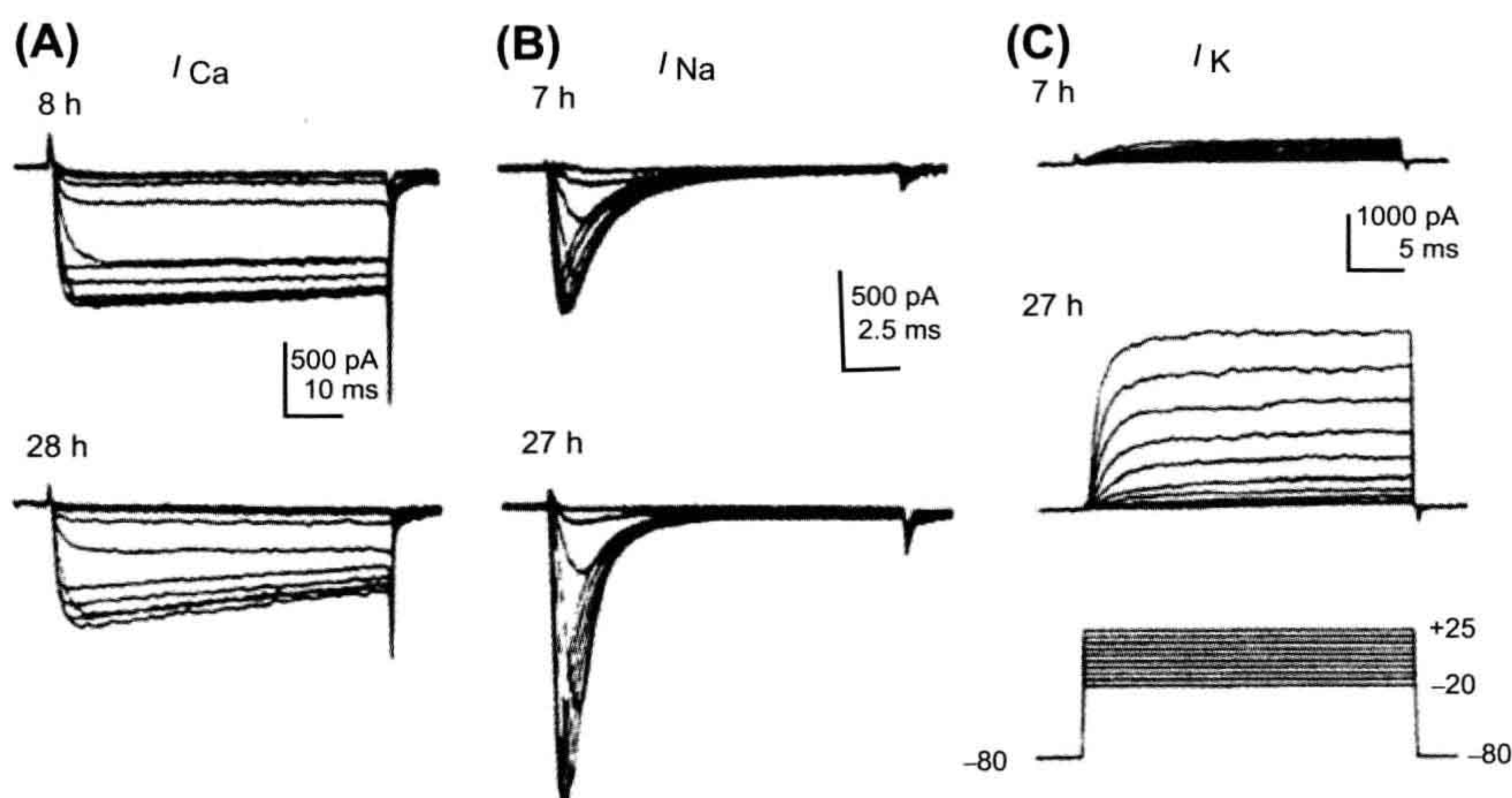


FIGURE 25.12 Developmental changes in ionic currents of cultured maturing neurons of embryonic amphibian. Records from cells in the early stage (7−8 h in culture)(upper traces) and the late stage (27−28 h)(lower traces). Records in (A) and (B) were obtained in presence of Cs^+ (internal solution) and TEA (external solution) to block outward K^+ currents. (A) Ca^{2+} current (I_{Ca}) recorded in Na^+-free solution. The amplitude of I_{Ca} was nearly equal at early and late stages. (B) Na^+ current (I_{Na}) recorded in presence of Co^{2+} to I_{Ca} block. I_{Na} was smaller at the early stage than at the late stage. (C) K^+ current (I_K) recorded in the presence of Co^{2+} and TTX to block the inward currents (I_{Ca} and I_{Na}). I_K is small at the early stage and gets larger in amplitude and faster in rate of activation at the late stage. Pulse protocols for (A), (B) and (C) are given at the bottom of (C). *(Modified with permission from O'Dowd et al. (1988). Development of voltage-dependent calcium, sodium and potassium currents in* Xenopus *spinal neuron. J. Neurosci. 8, 792−805, Copyright 1988 by the Society for Neuroscience.)*

density of the Na^+ current approximately doubles between the early and late stages of development in culture (Fig. 25.12B).

In ascidian embryos, Na^+ channels in neural cells dramatically change during the early developmental stage (Takahashi and Okamura, 1998). In unfertilized eggs, a small amount of Na^+ current (type A) is already observed. However, the type A Na^+ current is almost abolished after fertilization. After fertilization, fast-activating and inactivating Na^+ current (type C) with slow-inactivating Na^+ current (type B) is markedly increased. However, in the blastomere, which develops into neurons, the type B current is abolished in a moment. Finally, the type C current, corresponding to neural-specific *TuNa I* gene, increases further and becomes responsible for the neural Na^+ spike.

Patch-clamp experiments with acute sliced preparation of brain revealed that Na^+ current densities of neurons increase during development of mouse cortical plate of neocortex (Picken Bahrey and Moody, 2003), mouse cerebellum (Fry, 2006) and rat spine (Gao and Ziskind-Conhaim, 1998). On the other hand, Na^+ current densities remain almost unchanged in the intermediate zone of mouse neocortex (Picken Bahrey and Moody, 2003) and layers III–V of rat neocortex (Wang et al., 2009).

As described earlier, the Ca^{2+} channel allows Ca^{2+} influx and is responsible for the spontaneous Ca^{2+} transient in developing neurons. However, regulation of Ca^{2+} influx during development is not always due to change in the density of the Ca^{2+} channels, because some neurons show no increase in the Ca^{2+} current density (Salgado et al., 2005). The ratio of the K^+ current to the Ca^{2+} current (I_K/I_{Ca}) affects the configuration of the APs, because the inward I_{Ca} is deactivated earlier when the outward I_K is augmented, resulting in a decrease in the net inward current. In other words, any outward (K^+) current subtracts from the inward (Ca^{2+}) current to give a lower net inward current. In addition, the change in the amplitude and the kinetics of I_K that occurs during development greatly affects the AP configuration and apparent ionic dependence (Barish, 1986; Lockery and Spitzer, 1992). Therefore, the I_K/I_{Ca} ratio determines whether Ca^{2+}-independent APs are exhibited as well as influences the Ca^{2+} influx.

It is well known that Ca^{2+} channels are classified by their threshold voltage (low-voltage activated, LVA; high-voltage activated, HVA) or specific blockers (T-, L- and N-type). In rat cortical neurons of neocortex and phrenic motoneurons of cervical spine, the major Ca^{2+} channel subtype shifts from the LVA (T-type) Ca^{2+} current to the HVA Ca^{2+} current during development (Tarasenko et al., 1998; Martin-Caraballo and Greer, 2001). In mouse brainstem neurons, the density of LVA Ca^{2+} currents increases during the first postnatal week, while the density of HVA Ca^{2+} currents increases after the first postnatal week (Zhang et al., 1999).

The developmental increase in K^+ currents and change in their activation kinetics have been investigated in amphibian neurons in intact (isolated) spinal cord (Desarmenien et al., 1993) and in dissociated cell culture (see Fig. 25.12C) (Barish, 1986; O'Dowd et al., 1988). The general rule regarding the order of appearance of ionic conductances in developing neurons is that K^+ currents appear first before functional expression of the voltage-dependent inward currents (Spitzer et al., 1994). However, the types of K^+ currents regulating the AP duration and the order of their maturation vary among different neuronal cells at early stages of development. In some neurons, delayed-rectifier K^+ current precedes the appearance of the transient outward K^+ current (I_A or I_{to}). In contrast, in other neurons, the inactivating K^+ current (I_A) precedes expression of the delayed-rectifier K^+ current (Bader et al., 1985; Aguayo, 1989; Beck et al., 1992).

The Ca^{2+}-activated K^+ channels play a pivotal role for afterhyperpolarization and regulation of repetitive firing in neurons. In rat spinal motoneurons, the Ca^{2+}-activated K^+ current is markedly increased from the embryonic period to the postnatal period (Gao and Ziskind-Conhaim, 1998). The increase in this current shortens the duration of the action potential and produces the afterhyperpolarization. In addition, the Ca^{2+}-activated K^+ current reduces the frequency of action potential repetitive firing after birth. In rat Purkinje cells of cerebellum, the large-conductance Ca^{2+}-activated K^+ channels (BK) increase during development, whereas the small-conductance Ca^{2+}-activated K^+ channels (SK) decrease (Muller et al., 1998; Muller and Yool, 1998; Cingolani et al., 2002).

VD. Ligand-Gated Channels

Ionotropic glutamate receptors (iGluRs) are heteromeric ligand-gated ion channels. Based on their pharmacological and electrophysiological properties, iGluRs can be subdivided into three families: AMPA (α-amino-3-hydroxy-methyl-4-isoxazolepropionic acid) receptor; NMDA (N-methyl-D-aspartate) receptor and KA (kinate) receptor.

In Purkinje and granule cells of cerebellum, NMDA receptors are expressed transiently during early stages of development, resulting in the increase in intracellular Ca^{2+} which could lead to neuronal differentiation (Garthwaite et al., 1987).

AMPA receptors in immature neurons produce Ca^{2+} influx and elevation of intracellular Ca^{2+}. The Ca^{2+} permeability of iGluRs is governed by their subunit composition as well as by single amino acid substitutions generated by RNA editing; both factors may be developmentally regulated (Hume et al., 1991; Burnashev et al., 1992). It has been reported that AMPA receptors express in

the early stage of differentiation of *Xenopus* spinal neurons. Ca^{2+} influx to regulate the neural differentiation mainly flows through AMPA receptors soon after neurite initiation and before expression of NMDA receptors (Gleason and Spitzer, 1998).

The evaluation of long-term potentiation (LTP) in hippocampus revealed an increase in the ratio of current carried by AMPA receptors relative to NMDA receptors during development (Hsia et al., 1998; Abrahamsson et al., 2008). It may be presumed that such developmental change is due to, not only the developmental change in the expression of iGluRs subunits, but also to the change of molecules that associate/regulate iGluRs subunits (Petralia et al., 2005; Hall and Ghosh, 2008).

VI. CONCLUDING REMARKS

Action potentials (APs) and resting potentials (RPs) in excitable cells, such as cardiomyocytes, skeletal muscle fibers and neurons, are greatly altered during development. In general, the RP increases (becomes more negative), the AP rate of rise increases, overshoot increases and duration decreases. These electrophysiological alterations are mainly produced by developmental changes in the ion channels, i.e. by changes in the types, number and kinetic properties of the ion channels.

In cardiomyocytes, the density of inward-rectifier K^+ currents (I_{K1}) usually increases during development. This increase may result from changes in the single-channel conductance, as well as in the number and open probability of the channel, because the conductance of early fetal myocytes is much smaller than those of neonatal myocytes. The hyperpolarization of the RP during development can be accounted for by the increase in the density of I_{K1} and the resultant decrease in the P_{Na}/P_K ratio. In contrast, the hyperpolarization-activated inward current (I_h), which may affect automaticity, is dominant in early embryonic chick and mouse cardiomyocytes and disappears during development.

The Na^+ current also increases markedly during development. That is, there are few or no functional fast Na^+ channels present at the earliest stages, and the density of these channels increases progressively during development. The fast Na^+ current is responsible for the increase in the AP rate of rise (independent of the hyperpolarization of RP). The max dV/dt increases dramatically during development, e.g. in chick heart, from 20 to 200 V/s.

The fast Na^+ current in embryonic/fetal hearts has a significant sustained (i.e. slow-inactivating or steady-state) component. The sustained component of the embryonic/fetal Na^+ current decreases during development and this decrease contributes, at least in part, to the abbreviation of the AP duration.

Development of Ca^{2+} channels seems more complex. The density of total Ca^{2+} current in chick cardiomyocytes decreases during the developmental period from fetal to neonate. In rat and mouse, however, it increases from the fetal to the neonatal period, followed by a substantial decrease in the adult. In rabbit and guinea pig cardiomyocytes, the current density in the neonatal period is smaller than that in the adult. The total Ca^{2+} current is composed of currents through several different types of channels: L-type, T-type, and F-type. (1) The proportion of the T-type Ca^{2+} channel current in immature cells is generally more than that in mature cells and it may actually disappear in adults. That is, the L-type Ca^{2+} channel current becomes more dominant in mature cells. (2) A nifedipine-resistant F-type Ca^{2+} channel current is also present in early fetal cardiomyocytes of rats. (3) Long-lasting openings of the L-type Ca^{2+} channels are relatively frequently observed in embryonic chick and fetal rat cardiomyocytes, but are quite unusual in adult cells.

Ca^{2+} influx through the Ca^{2+} channels is especially important for the excitation–contraction coupling process of fetal cardiomyocytes. This is because the SR function and/or the essential component for Ca^{2+} release from the SR is immature and so Ca^{2+} influx from the extracellular space is the main source of Ca^{2+} for contraction.

The density of the transient outward current (I_{to}) increases during development. An increase in the density of the delayed-rectifier K^+ current (I_K) also occurs during early development and decreases during the postnatal period. The change of these voltage-gated outward currents (i.e. I_{to} and I_K) helps to abbreviate the AP duration during development.

In skeletal muscle fibers, there is an overall trend toward an increase in the density of I_{K1} during the early developmental period. However, there is a transient period during which the current density decreases. This transient period parallels the increased incidence of spontaneous firings, presumably due to a less stable RP. The major voltage-gated inward currents, the Na^+ and Ca^{2+} currents, are already present in the early embryonic skeletal myocytes in culture and they increase in intensity during development. These changes contribute to the increases in the AP rate of rise, overshoot and propagation velocity. Prolonged APs and brief APs can be elicited in chick embryonic skeletal myotubes, depending on the stage of development. The prolonged APs are associated with long-lasting contractions of the myotubes. The brief APs become more dominant during development in culture and are associated with myotube twitches. The nicotinic acetylcholine receptor/channel, which is essential to transmission at the neuromuscular junction, is converted from fetal-type to adult-type and this conversion may be related to innervation of the muscles that occurs during development. Activin, a member of the TGFβ family, is important for development of ion channels in skeletal muscles. Activin stimulates the expression of the same ion channels (I_K, I_{K1}, I_{Na}, I_A, I_{Ca}) in cultured skeletal

myoblasts. The sequence in which currents are expressed is also maintained (I_K and I_{K1} are expressed first).

In neuronal cells, there is an overall trend that the ionic dependence of the AP is altered from Ca^{2+}-dependent (prolonged AP duration) to Na^{+}-dependent (brief AP duration) during development. The pattern of ion channel development varies among different types of neuronal cells, with faster development of Ca^{2+} channels in some cells. Another important factor that determines the ionic dependence of the AP is the developmental increase in I_K. Therefore, the I_K/I_{Ca} ratio is the major determinant of the conversion of the AP configuration and influences Ca^{2+} influx during development. Two types of Ca^{2+} transients, Ca^{2+} spikes and Ca^{2+} waves, are present in developing neurons. Ca^{2+} spikes in the cell body (soma) are generated by spontaneous APs and propagate to the growth cone. The incidence of these Ca^{2+} transients changes in developing neurons in culture. In addition to Ca^{2+} transients, a slow increase in $[Ca^{2+}]_i$ is observed during neural induction. The activities of ligand-gated Ca^{2+}-permeable channels (such as NMDA receptor/channels and AMPA-gated receptor channels) are also altered during development. Therefore, the Ca^{2+} influx through the voltage-gated (LVA or HVA channels) and the ligand-gated Ca^{2+} channels, and the subsequent effects on intracellular Ca^{2+}, may affect the structural changes of the developing neurons and help the establishment of the neuronal network.

As described earlier, ion channels exhibit dramatic changes during development in their type, structure, function and distribution. These dynamic alterations are controlled by expression of genes coding ion channels and may be essential to cellular growth and differentiation by affecting intracellular Ca^{2+} concentration and excitability. Thus, molecular biology, combined with electrophysiology, has enabled large advances in our understanding of cell function.

BIBLIOGRAPHY

Abrahamsson, T., Gustafsson, B., & Hanse, E. (2008). AMPA silencing is a prerequisite for developmental long-term potentiation in the hippocampal CA1 region. *J Neurophysiol, 100*, 2605–2614.

Accili, E. A., Robinson, R. B., & DiFrancesco, D. (1997). Properties and modulation of If in newborn versus adult cardiac SA node. *Am J Physiol, 272*, H1549–H1552.

Aguayo, L. G. (1989). Post-natal development of K+ currents studied in isolated rat pineal cells. *J Physiol, 414*, 283–300.

Bader, C. R., Bertrand, D., & Dupin, E. (1985). Voltage-dependent potassium currents in developing neurones from quail mesencephalic neural crest. *J Physiol, 366*, 129–151.

Barish, M. E. (1986). Differentiation of voltage-gated potassium current and modulation of excitability in cultured amphibian spinal neurones. *J Physiol, 375*, 229–250.

Baruscotti, M., DiFrancesco, D., & Robinson, R. B. (1996). A TTX-sensitive inward sodium current contributes to spontaneous activity in newborn rabbit sino-atrial node cells. *J Physiol, 492*, 21–30.

Beck, H., Ficker, E., & Heinemann, U. (1992). Properties of two voltage-activated potassium currents in acutely isolated juvenile rat dentate gyrus granule cells. *J Neurophysiol, 68*, 2086–2099.

Bernard, C. (1975). *Establishment of Ionic Permeabilities of the Myocardial Membrane during Embryonic Development of the Rat. Developmental and Physiological Correlates of Cardiac Muscle.* New York: L.M. and S. T. Raven Press.

Berthier, C., Monteil, A., Lory, P., & Strube, C. (2002). Alpha(1H) mRNA in single skeletal muscle fibres accounts for T-type calcium current transient expression during fetal development in mice. *J Physiol, 539*, 681–691.

Bijlenga, P., Liu, J. H., Espinos, E., et al. (2000). T-type alpha 1H Ca2+ channels are involved in Ca2+ signaling during terminal differentiation (fusion) of human myoblasts. *Proc Natl Acad Sci USA, 97*, 7627–7632.

Bijlenga, P., Occhiodoro, T., Liu, J. H., et al. (1998). An ether -a-go-go K+ current, Ih-eag, contributes to the hyperpolarization of human fusion-competent myoblasts. *J Physiol, 512*, 317–323.

Brown, A. M., Lee, K. S., & Powell, T. (1981). Sodium current in single rat heart muscle cells. *J Physiol, 318*, 479–500.

Burnashev, N., Monyer, H., Seeburg, P. H., & Sakmann, B. (1992). Divalent ion permeability of AMPA receptor channels is dominated by the edited form of a single subunit. *Neuron, 8*, 189–198.

Cerbai, E., Pino, R., Sartiani, L., & Mugelli, A. (1999). Influence of postnatal-development on I(f) occurrence and properties in neonatal rat ventricular myocytes. *Cardiovasc Res, 42*, 416–423.

Cingolani, L. A., Gymnopoulos, M., Boccaccio, A., Stocker, M., & Pedarzani, P. (2002). Developmental regulation of small-conductance Ca2+-activated K+ channel expression and function in rat Purkinje neurons. *J Neurosci, 22*, 4456–4467.

Cohen, N. M., & Lederer, W. J. (1988). Changes in the calcium current of rat heart ventricular myocytes during development. *J Physiol, 406*, 115–146.

Conforti, L., Tohse, N., & Sperelakis, N. (1993). Tetrodotoxin-sensitive sodium current in rat fetal ventricular myocytes – contribution to the plateau phase of action potential. *J Mol Cell Cardiol, 25*, 159–173.

Couch, J. R., West, T. C., & Hoff, H. E. (1969). Development of the action potential of the prenatal rat heart. *Circ Res, 24*, 19–31.

Currie, D. A., & Moody, W. J. (1999). Time course of ion channel development in Xenopus muscle induced in vitro by activin. *Dev Biol, 209*, 40–51.

Davies, M. P., An, R. H., Doevendans, P., et al. (1996). Developmental changes in ionic channel activity in the embryonic murine heart. *Circ Res, 78*, 15–25.

Desarmenien, M. G., Clendening, B., & Spitzer, N. C. (1993). In vivo development of voltage-dependent ionic currents in embryonic Xenopus spinal neurons. *J Neurosci, 13*, 2575–2581.

Dominguez, J. N., de la Rosa, A., Navarro, F., Franco, D., & Aranega, A. E. (2008). Tissue distribution and subcellular localization of the cardiac sodium channel during mouse heart development. *Cardiovasc Res, 78*, 45–52.

Fabiato, A., & Fabiato, F. (1978). Calcium-induced release of calcium from the sarcoplasmic reticulum of skinned cells from adult human, dog, cat, rabbit, rat, and frog hearts and from fetal and new-born rat ventricles. *Ann NY Acad Sci, 307*, 491–522.

Ferron, L., Capuano, V., Deroubaix, E., Coulombe, A., & Renaud, J. F. (2002). Functional and molecular characterization of a T-type Ca(2+) channel during fetal and postnatal rat heart development. *J Mol Cell Cardiol, 34*, 533–546.

Fischbach, G. D., Nameroff, M., & Nelson, P. G. (1971). Electrical properties of chick skeletal muscle fibers developing in cell culture. *J Cell Physiol, 78*, 289–299.

Fischer-Lougheed, J., Liu, J. H., Espinos, E., et al. (2001). Human myoblast fusion requires expression of functional inward rectifier Kir2.1 channels. *J Cell Biol, 153*, 677–686.

Franco, D., Demolombe, S., Kupershmidt, S., et al. (2001). Divergent expression of delayed rectifier K(+) channel subunits during mouse heart development. *Cardiovasc Res, 52*, 65–75.

Fry, M. (2006). Developmental expression of Na+ currents in mouse Purkinje neurons. *Eur J Neurosci, 24*, 2557–2566.

Fujii, S., Ayer, R. K., Jr., & DeHaan, R. L. (1988). Development of the fast sodium current in early embryonic chick heart cells. *J Membr Biol, 101*, 209–223.

Gao, B. X., & Ziskind-Conhaim, L. (1998). Development of ionic currents underlying changes in action potential waveforms in rat spinal motoneurons. *J Neurophysiol, 80*, 3047–3061.

Garthwaite, G., Yamini, B., Jr., & Garthwaite, J. (1987). Selective loss of Purkinje and granule cell responsiveness to N-methyl-D-aspartate in rat cerebellum during development. *Brain Res, 433*, 288–292.

Gassanov, N., Er, F., Michels, G., et al. (2009). Divergent regulation of cardiac KCND3 potassium channel expression by the thyroid hormone receptors alpha1 and beta1. *J Physiol, 587*, 1319–1329.

Gilland, E., Miller, A. L., Karplus, E., Baker, R., & Webb, S. E. (1999). Imaging of multicellular large-scale rhythmic calcium waves during zebrafish gastrulation. *Proc Natl Acad Sci USA, 96*, 157–161.

Gleason, E. L., & Spitzer, N. C. (1998). AMPA and NMDA receptors expressed by differentiating Xenopus spinal neurons. *J Neurophysiol, 79*, 2986–2998.

Gottmann, K., Dietzel, I. D., Lux, H. D., Huck, S., & Rohrer, H. (1988). Development of inward currents in chick sensory and autonomic neuronal precursor cells in culture. *J Neurosci, 8*, 3722–3732.

Grandy, S. A., Trepanier-Boulay, V., & Fiset, C. (2007). Postnatal development has a marked effect on ventricular repolarization in mice. *Am J Physiol Heart Circ Physiol, 293*, H2168–H2177.

Greaves, A. A., Davis, A. K., Dallmanm, J. E., & Moody, W. J. (1996). Co-ordinated modulation of Ca2+ and K+ currents during ascidian muscle development. *J Physiol, 497*, 39–52.

Gu, X., Olson, E. C., & Spitzer, N. C. (1994). Spontaneous neuronal calcium spikes and waves during early differentiation. *J Neurosci, 14*, 6325–6335.

Guo, W., Kada, K., Kamiya, K., & Toyama, J. (1997a). IGF-I regulates K(+)-channel expression of cultured neonatal rat ventricular myocytes. *Am J Physiol, 272*, H2599–H2606.

Guo, W., Kamiya, K., Hojo, M., Kodama, I., & Toyama, J. (1998). Regulation of Kv4.2 and Kv1.4 K+ channel expression by myocardial hypertrophic factors in cultured newborn rat ventricular cells. *J Mol Cell Cardiol, 30*, 1449–1455.

Guo, W., Kamiya, K., Liu, W., & Toyama, J. (1997b). Developmental changes of the ultrarapid delayed rectifier K+ current in rat ventricular myocytes. *Pflügers Arch, 433*, 442–445.

Guo, W., Kamiya, K., & Toyama, J. (1995). bFGF promotes functional expression of transient outward currents in cultured neonatal rat ventricular cells. *Pflügers Arch, 430*, 1015–1017.

Hall, B. J., & Ghosh, A. (2008). Regulation of AMPA receptor recruitment at developing synapses. *Trends Neurosci, 31*, 82–89.

Haufe, V., Camacho, J. A., Dumaine, R., et al. (2005). Expression pattern of neuronal and skeletal muscle voltage-gated Na+ channels in the developing mouse heart. *J Physiol, 564*, 683–696.

Henriquez, J. P., Webb, A., Bence, M., et al. (2008). Wnt signaling promotes AChR aggregation at the neuromuscular synapse in collaboration with agrin. *Proc Natl Acad Sci USA, 105*, 18812–18817.

Holliday, J., & Spitzer, N. C. (1990). Spontaneous calcium influx and its roles in differentiation of spinal neurons in culture. *Dev Biol, 141*, 13–23.

Hsia, A. Y., Malenka, R. C., & Nicoll, R. A. (1998). Development of excitatory circuitry in the hippocampus. *J Neurophysiol, 79*, 2013–2024.

Huang, J., Xu, L., Thomas, M., et al. (2006). L-type Ca2+ channel function and expression in neonatal rabbit ventricular myocytes. *Am J Physiol Heart Circ Physiol, 290*, H2267–H2276.

Hume, R. I., Dingledine, R., & Heinemann, S. F. (1991). Identification of a site in glutamate receptor subunits that controls calcium permeability. *Science, 253*, 1028–1031.

Huynh, T. V., Chen, F., Wetzel, G. T., Friedman, W. F., & Klitzner, T. S. (1992). Developmental changes in membrane Ca2+ and K+ currents in fetal, neonatal, and adult rabbit ventricular myocytes. *Circ Res, 70*, 508–515.

Iannaccone, S. T., Li, K. X., & Sperelakis, N. (1987). Transmembrane electrical characteristics of cultured human skeletal muscle cells. *J Cell Physiol, 133*, 409–413.

Iijima, T., & Pappano, A. J. (1979). Ontogenetic increase of the maximal rate of rise of the chick embryonic heart action potential. Relationship to voltage, time, and tetrodotoxin. *Circ Res, 44*, 358–367.

Irisawa, H., Brown, H. F., & Giles, W. (1993). Cardiac pacemaking in the sinoatrial node. *Physiol Rev, 73*, 197–227.

Jeck, C. D., & Boyden, P. A. (1992). Age-related appearance of outward currents may contribute to developmental differences in ventricular repolarization. *Circ Res, 71*, 1390–1403.

Josephson, I. R., & Sperelakis, N. (1989). Tetrodotoxin differentially blocks peak and steady-state sodium channel currents in early embryonic chick ventricular myocytes. *Pflügers Arch, 414*, 354–359.

Josephson, I. R., & Sperelakis, N. (1990). Developmental increases in the inwardly-rectifying K+ current of embryonic chick ventricular myocytes. *Biochim Biophys Acta, 1052*, 123–127.

Kano, M., & Yamamoto, M. (1977). Development of spike potentials in skeletal muscle cells differentiated in vitro from chick embryo. *J Cell Physiol, 90*, 439–444.

Kato, Y., Masumiya, H., Agata, N., Tanaka, H., & Shigenobu, K. (1996). Developmental changes in action potential and membrane currents in fetal, neonatal and adult guinea-pig ventricular myocytes. *J Mol Cell Cardiol, 28*, 1515–1522.

Kawano, S., & DeHaan, R. L. (1991). Developmental changes in the calcium currents in embryonic chick ventricular myocytes. *J Membr Biol, 120*, 17–28.

Kilborn, M. J., & Fedida, D. (1990). A study of the developmental changes in outward currents of rat ventricular myocytes. *J Physiol, 430*, 37–60.

Kitchens, S. A., Burch, J., & Creazzo, T. L. (2003). T-type Ca2+ current contribution to Ca2+-induced Ca2+ release in developing myocardium. *J Mol Cell Cardiol, 35*, 515–523.

Kobayashi, T., Maeda, S., Ichise, N., et al. (2011). The beginning of the calcium transient in rat embryonic heart. *J Physiol Sci, 61*, 141–149.

Kobayashi, T., Yamada, Y., Nagashima, M., et al. (2003). Contribution of KChIP2 to the developmental increase in transient outward current of rat cardiomyocytes. *J Mol Cell Cardiol, 35*, 1073–1082.

Koenen, M., Peter, C., Villarroel, A., Witzemann, V., & Sakmann, B. (2005). Acetylcholine receptor channel subtype directs the innervation pattern of skeletal muscle. *EMBO Rep, 6*, 570–576.

Kojima, M., Sada, H., & Sperelakis, N. (1990). Developmental changes in beta-adrenergic and cholinergic interactions on calcium-dependent slow action potentials in rat ventricular muscles. *Br J Pharmacol, 99*, 327–333.

Konig, S., Beguet, A., Bader, C. R., & Bernheim, L. (2006). The calcineurin pathway links hyperpolarization (Kir2.1)-induced Ca2+ signals to human myoblast differentiation and fusion. *Development, 133*, 3107–3114.

Leclerc, C., Duprat, A. M., & Moreau, M. (1999). Noggin upregulates Fos expression by a calcium-mediated pathway in amphibian embryos. *Dev Growth Differ, 41*, 227–238.

Leclerc, C., Webb, S. E., Daguzan, C., Moreau, M., & Miller, A. L. (2000). Imaging patterns of calcium transients during neural induction in Xenopus laevis embryos. *J Cell Sci, 113*, 3519–3529.

Leuranguer, V., Monteil, A., Bourinet, E., Dayanithi, G., & Nargeot, J. (2000). T-type calcium currents in rat cardiomyocytes during postnatal development: contribution to hormone secretion. *Am J Physiol Heart Circ Physiol, 279*, H2540–H2548.

Li, H., Guo, W., Mellor, R. L., & Nerbonne, J. M. (2005). KChIP2 modulates the cell surface expression of Kv 1.5-encoded K(+) channels. *J Mol Cell Cardiol, 39*, 121–132.

Linsdell, P., & Moody, W. J. (1995). Electrical activity and calcium influx regulate ion channel development in embryonic Xenopus skeletal muscle. *J Neurosci, 15*, 4507–4514.

Liu, A., Tang, M., Xi, J., et al. (2010). Functional characterization of inward rectifier potassium ion channel in murine fetal ventricular cardiomyocytes. *Cell Physiol Biochem, 26*, 413–420.

Liu, J. H., Bijlenga, P., Fischer-Lougheed, J., et al. (1998). Role of an inward rectifier K+ current and of hyperpolarization in human myoblast fusion. *J Physiol, 510*, 467–476.

Liu, J. H., Konig, S., Michel, M., et al. (2003). Acceleration of human myoblast fusion by depolarization: graded Ca2+ signals involved. *Development, 130*, 3437–3446.

Liu, W., Yasui, K., Opthof, T., et al. (2002). Developmental changes of Ca(2+) handling in mouse ventricular cells from early embryo to adulthood. *Life Sci, 71*, 1279–1292.

Lockery, S. R., & Spitzer, N. C. (1992). Reconstruction of action potential development from whole-cell currents of differentiating spinal neurons. *J Neurosci, 12*, 2268–2287.

Mai, W., Janier, M. F., Allioli, N., et al. (2004). Thyroid hormone receptor alpha is a molecular switch of cardiac function between fetal and postnatal life. *Proc Natl Acad Sci USA, 101*, 10332–10337.

Marcus, N. C., & Fozzard, H. (1981). Tetrodotoxin sensitivity in the developing and adult chick heart. *J Mol Cell Cardiol, 13*, 335–340.

Martin-Caraballo, M., & Greer, J. J. (2001). Voltage-sensitive calcium currents and their role in regulating phrenic motoneuron electrical excitability during the perinatal period. *J Neurobiol, 46*, 231–248.

Masuda, H., & Sperelakis, N. (1993). Inwardly rectifying potassium current in rat fetal and neonatal ventricular cardiomyocytes. *Am J Physiol, 265*, H1107–H1111.

Masuda, H., Sumii, K., & Sperelakis, N. (1995). Long openings of calcium channels in fetal rat ventricular cardiomyocytes. *Pflügers Arch, 429*, 595–597.

Matsubara, H., Suzuki, J., & Inada, M. (1993). Shaker-related potassium channel, Kv1.4, mRNA regulation in cultured rat heart myocytes and differential expression of Kv1.4 and Kv1.5 genes in myocardial development and hypertrophy. *J Clin Invest, 92*, 1659–1666.

Mishina, M., Takai, T., Imoto, K., et al. (1986). Molecular distinction between fetal and adult forms of muscle acetylcholine receptor. *Nature, 321*, 406–411.

Moreau, M., Leclerc, C., Gualandris-Parisot, L., & Duprat, A. M. (1994). Increased internal Ca2+ mediates neural induction in the amphibian embryo. *Proc Natl Acad Sci USA, 91*, 12639–12643.

Morikawa, Y., Rosen, M. R., Meiri, H., & Robinson, R. B. (1987). Developmental changes in the response of cardiac Purkinje fibers to SC-72-14. *Am J Physiol, 252*, H771–H776.

Muller, Y. L., & Yool, A. J. (1998). Increased calcium-dependent K+ channel activity contributes to the maturation of cellular firing patterns in developing cerebellar Purkinje neurons. *Brain Res Dev Brain Res, 108*, 193–203.

Muller, Y. L., Reitstetter, R., & Yool, A. J. (1998). Regulation of Ca2+-dependent K+ channel expression in rat cerebellum during postnatal development. *J Neurosci, 18*, 16–25.

Nagashima, M., Tohse, N., Kimura, K., et al. (2001). Alternation of inwardly rectifying background K+ channel during development of rat fetal cardiomyocytes. *J Mol Cell Cardiol, 33*, 533–543.

Nakamura, T. Y., Lee, K., Artman, M., Rudy, B., & Coetzee, W. A. (1999). The role of Kir2.1 in the genesis of native cardiac inward-rectifier K+ currents during pre- and postnatal development. *Ann NY Acad Sci, 868*, 434–437.

Nakanishi, T., Seguchi, M., & Takao, A. (1988). Development of the myocardial contractile system. *Experientia, 44*, 936–944.

Nguemo, F., Fleischmann, B. K., Schunkert, H., Hescheler, J., & Reppel, M. (2007). Functional expression and inactivation of L-type Ca2+ currents during murine heart development – implications for cardiac Ca2+ homeostasis. *Cell Physiol Biochem, 20*, 809–824.

Niwa, N., Yasui, K., Opthof, T., et al. (2004). Cav3.2 subunit underlies the functional T-type Ca2+ channel in murine hearts during the embryonic period. *Am J Physiol Heart Circ Physiol, 286*, H2257–H2263.

O'Dowd, D. K., Ribera, A. B., & Spitzer, N. C. (1988). Development of voltage-dependent calcium, sodium, and potassium currents in Xenopus spinal neurons. *J Neurosci, 8*, 792–805.

Osaka, T., & Joyner, R. W. (1991). Developmental changes in calcium currents of rabbit ventricular cells. *Circ Res, 68*, 788–796.

Petralia, R. S., Sans, N., Wang, Y. X., & Wenthold, R. J. (2005). Ontogeny of postsynaptic density proteins at glutamatergic synapses. *Mol Cell Neurosci, 29*, 436–452.

Picken Bahrey, H. L., & Moody, W. J. (2003). Early development of voltage-gated ion currents and firing properties in neurons of the mouse cerebral cortex. *J Neurophysiol, 89*, 1761–1773.

Protas, L., Oren, R. V., Clancy, C. E., & Robinson, R. B. (2010). Age-dependent changes in Na current magnitude and TTX-sensitivity in the canine sinoatrial node. *J Mol Cell Cardiol, 48*, 172–180.

Renaud, J. F., Kazazoglou, T., Lombet, A., et al. (1983). The Na+ channel in mammalian cardiac cells. Two kinds of tetrodotoxin receptors in rat heart membranes. *J Biol Chem, 258*, 8799–8805.

Renaud, J. F., Romey, G., Lombet, A., & Lazdunski, M. (1981). Differentiation of the fast Na+ channel in embryonic heart cells: interaction of the channel with neurotoxins. *Proc Natl Acad Sci USA, 78*, 5348–5352.

Ritchie, A. K., & Fambrough, D. M. (1975). Electrophysiological properties of the membrane and acetylcholine receptor in developing rat and chick myotubes. *J Gen Physiol, 66*, 327–355.

Robinson, R. B., Yu, H., Chang, F., & Cohen, I. S. (1997). Developmental change in the voltage-dependence of the pacemaker current, if, in rat ventricle cells. *Pflügers Arch, 433*, 533–535.

Rogart, R. B., Cribbs, L. L., Muglia, L. K., Kephart, D. D., & Kaiser, M. W. (1989). Molecular cloning of a putative tetrodotoxin-resistant rat heart Na+ channel isoform. *Proc Natl Acad Sci USA, 86*, 8170–8174.

Sada, H., Ban, T., Fujita, T., Ebina, Y., & Sperelakis, N. (1995). Developmental change in fast Na channel properties in embryonic chick ventricular heart cells. *Can J Physiol Pharmacol, 73*, 1475–1484.

Sada, H., Kojima, M., & Sperelakis, N. (1988). Fast inward current properties of voltage-clamped ventricular cells of embryonic chick heart. *Am J Physiol, 255*, H540–H553.

Salgado, H., Tecuapetla, F., Perez-Rosello, T., et al. (2005). A reconfiguration of CaV2 Ca2+ channel current and its dopaminergic D2 modulation in developing neostriatal neurons. *J Neurophysiol, 94*, 3771–3787.

Sanchez-Chapula, J., Elizalde, A., Navarro-Polanco, R., & Barajas, H. (1994). Differences in outward currents between neonatal and adult rabbit ventricular cells. *Am J Physiol, 266*, H1184–H1194.

Sanes, J. R., & Lichtman, J. W. (2001). Induction, assembly, maturation and maintenance of a postsynaptic apparatus. *Nat Rev Neurosci, 2*, 791–805.

Satoh, H. (1995). Identification of and developmental changes in transient outward current in embryonic chick cardiomyocytes. *Reprod Fertil Dev, 7*, 1369–1374.

Satoh, H., & Sperelakis, N. (1993). Hyperpolarization-activated inward current in embryonic chick cardiac myocytes: developmental changes and modulation by isoproterenol and carbachol. *Eur J Pharmacol, 240*, 283–290.

Seki, S., Nagashima, M., Yamada, Y., et al. (2003). Fetal and postnatal development of Ca2+ transients and Ca2+ sparks in rat cardiomyocytes. *Cardiovasc Res, 58*, 535–548.

Shimahara, T., & Bournaud, R. (1991). Barium currents in developing skeletal muscle cells of normal and mutant mice foetuses with 'muscular dysgenesis'. *Cell Calcium, 12*, 727–733.

Shimoni, Y., Fiset, C., Clark, R. B., et al. (1997). Thyroid hormone regulates postnatal expression of transient K+ channel isoforms in rat ventricle. *J Physiol, 500*, 65–73.

Shin, K. S., Park, J. Y., Kwon, H., Chung, C. H., & Kang, M. S. (1997). A possible role of inwardly rectifying K+ channels in chick myoblast differentiation. *Am J Physiol, 272*, C894–C900.

Spector, I., & Prives, J. M. (1977). Development of electrophysiological and biochemical membrane properties during differentiation of embryonic skeletal muscle in culture. *Proc Natl Acad Sci USA, 74*, 5166–5170.

Sperelakis, N., & Lee, E. C. (1971). Characterization of (Na+, K+)-ATPase isolated from embryonic chick hearts and cultured chick heart cells. *Biochim Biophys Acta, 233*, 562–579.

Sperelakis, N., & Shigenobu, K. (1972). Changes in membrane properties of chick embryonic hearts during development. *J Gen Physiol, 60*, 430–453.

Spitzer, N. C. (1994). Spontaneous Ca2+ spikes and waves in embryonic neurons: signaling systems for differentiation. *Trends Neurosci, 17*, 115–118.

Spitzer, N. C., & Baccaglini, P. I. (1976). Development of the action potential in embryo amphibian neurons in vivo. *Brain Res, 107*, 610–616.

Spitzer, N. C., Debaca, R. C., Allen, K. A., & Holliday, J. (1993). Calcium dependence of differentiation of GABA immunoreactivity in spinal neurons. *J Comp Neurol, 337*, 168–175.

Spitzer, N. C., Gu, X., & Olson, E. (1994). Action potentials, calcium transients and the control of differentiation of excitable cells. *Curr Opin Neurobiol, 4*, 70–77.

Stieber, J., Herrmann, S., Feil, S., et al. (2003). The hyperpolarization-activated channel HCN4 is required for the generation of pacemaker action potentials in the embryonic heart. *Proc Natl Acad Sci USA, 100*, 15235–15240.

Strube, C., Tourneur, Y., & Ojeda, C. (2000). Functional expression of the L-type calcium channel in mice skeletal muscle during prenatal myogenesis. *Biophys J, 78*, 1282–1292.

Takahashi, K., & Okamura, Y. (1998). Ion channels and early development of neural cells. *Physiol Rev, 78*, 307–337.

Tarasenko, A. N., Isaev, D. S., Eremin, A. V., & Kostyuk, P. G. (1998). Developmental changes in the expression of low-voltage-activated Ca2+ channels in rat visual cortical neurones. *J Physiol, 509*, 385–394.

Tohse, N., Masuda, H., & Sperelakis, N. (1992a). Novel isoform of Ca2+ channel in rat fetal cardiomyocytes. *J Physiol, 451*, 295–306.

Tohse, N., Meszaros, J., & Sperelakis, N. (1992b). Developmental changes in long-opening behavior of L-type Ca2+ channels in embryonic chick heart cells. *Circ Res, 71*, 376–384.

Tohse, N., Seki, S., Kobayashi, T., et al. (2004). Development of excitation-contraction coupling in cardiomyocytes. *Jap J Physiol, 54*, 1–6.

Tohse, N., & Sperelakis, N. (1990). Long-lasting openings of single slow (L-type) Ca2+ channels in chick embryonic heart cells. *Am J Physiol, 259*, H639–H642.

Trepanier-Boulay, V., Lupien, M. A., St-Michel, C., & Fiset, C. (2004). Postnatal development of atrial repolarization in the mouse. *Cardiovasc Res, 64*, 84–93.

Wahler, G. M., Dollinger, S. J., Smith, J. M., & Flemal, K. L. (1994). Time course of postnatal changes in rat heart action potential and in transient outward current is different. *Am J Physiol, 267*, H1157–H1166.

Wang, K., Cui, J., Cai, Y., et al. (2009). Critical roles of voltage-dependent sodium channels in the process of synaptogenesis during the postnatal cortical development of rats. *Cell Mol Neurobiol, 29*, 1131–1142.

Wang, L., & Duff, H. J. (1997). Developmental changes in transient outward current in mouse ventricle. *Circ Res, 81*, 120–127.

Wang, L., Feng, Z. P., Kondo, C. S., Sheldon, R. S., & Duff, H. J. (1996). Developmental changes in the delayed rectifier K+ channels in mouse heart. *Circ Res, 79*, 79–85.

Wang, Y., Xu, H., Kumar, R., et al. (2003). Differences in transient outward current properties between neonatal and adult human atrial myocytes. *J Mol Cell Cardiol, 35*, 1083–1092.

Webb, S. E., Moreau, M., Leclerc, C., & Miller, A. L. (2005). Calcium transients and neural induction in vertebrates. *Cell Calcium, 37*, 375–385.

Wickenden, A. D., Kaprielian, R., Parker, T. G., Jones, O. T., & Backx, P. H. (1997). Effects of development and thyroid hormone on K+ currents and K+ channel gene expression in rat ventricle. *J Physiol, 504*, 271–286.

Xie, L. H., Takano, M., & Noma, A. (1997). Development of inwardly rectifying K+ channel family in rat ventricular myocytes. *Am J Physiol, 272*, H1741–H1750.

Xu, H., Dixon, J. E., Barry, D. M., et al. (1996). Developmental analysis reveals mismatches in the expression of K+ channel alpha subunits and voltage-gated K+ channel currents in rat ventricular myocytes. *J Gen Physiol, 108*, 405–419.

Yasui, K., Liu, W., Opthof, T., et al. (2001). I(f) current and spontaneous activity in mouse embryonic ventricular myocytes. *Circ Res, 88*, 536–542.

Zhang, W., Elsen, F., Barnbrock, A., & Richter, D. W. (1999). Postnatal development of GABAB receptor-mediated modulation of voltage-activated Ca2+ currents in mouse brain-stem neurons. *Eur J Neurosci, 11*, 2332–2342.

Chapter 26

Regulation of Ion Channel Localization and Activity Through Interactions with the Cytoskeleton

Stephen Lambert

Chapter Outline

I. SUMMARY

The physiological function of a variety of cell types is dependent upon their ability to organize and cluster ion channels into specialized areas of the plasma membrane. Studies over the last 20 years have indicated a role for interactions between ion channels and the cellular cytoskeleton in achieving this complex organization. A variety of adaptor/scaffolding proteins that tether ion channels to the cytoskeleton has been identified. In addition to localizing ion channels, interactions with the cytoskeleton may also regulate channel activity. This could be through direct binding to the channel by actin or scaffolding molecules, or by the co-recruitment of signaling molecules that regulate channel activity into a macromolecular complex by scaffolding proteins.

In this chapter, we will review three examples of specialized membrane domains: the axon initial segment and node of Ranvier; the postsynaptic membrane; and the apical domain of the epithelial cell. We will examine the unique adaptor/scaffolding systems found in each of these domains and how they have evolved in response to their particular physiological requirements.

Cell Physiology Sourcebook. DOI: 10.1016/B978-0-12-387738-3.00026-3

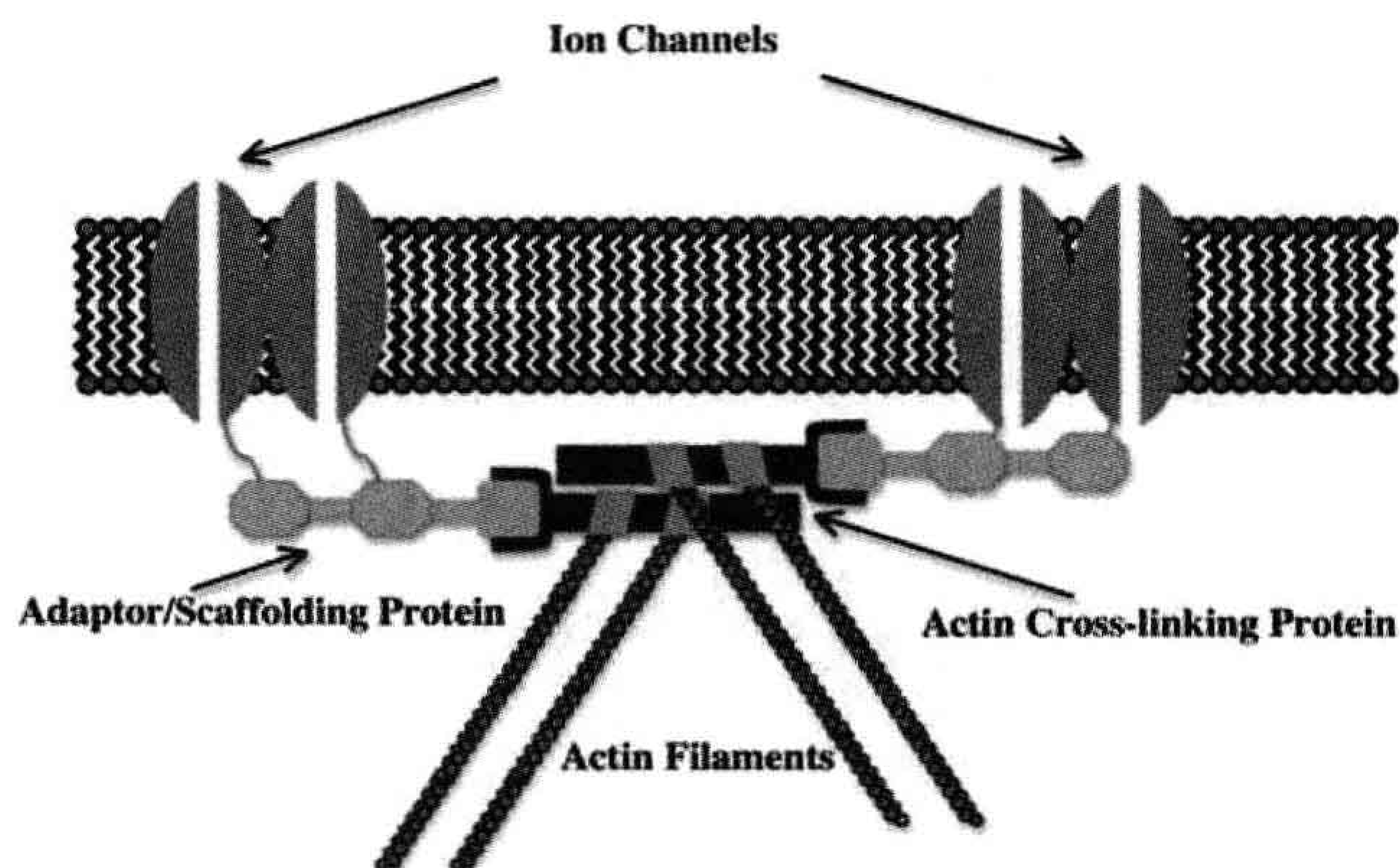


FIGURE 26.1 Conceptual model of a general mechanism for the interaction of ion channels with the cytoskeleton.

II. GENERAL INTRODUCTION

Ion channels are selective "pores" for the passage of ions across the hydrophobic barrier of the plasma membrane. The physiological activity of a number of cell types is dependent upon their ability to organize integral membrane proteins and, in particular, ion channels, into functionally specialized domains of the plasma membrane. This organization underlies a wide range of cellular functions including the propagation and integration of electrical signals in the nervous and muscular system by "excitable" membranes. A general mechanism whereby ion channels become organized into these membrane domains is shown in Fig. 26.1 and reflects an interaction between the ion channel and the cellular cytoskeleton, particularly the actin microfilament system. This mechanism localizes the lateral mobility of ion channels to a membrane domain through direct tethering of the ion channel to the cytoskeleton utilizing adaptor or scaffold proteins.

As well as restricting the localization of ion channels, interactions with the cytoskeleton and adaptor proteins can also regulate their activity. This could result from direct interactions between actin or adaptor proteins with functional domains of the channel and/or the organization of functional microdomains, whereby ion channels through the activity of scaffold proteins, are brought into close proximity with molecules that can regulate their activity. Conversely, several lines of evidence, particularly from the nervous system, have shown that it is possible for ion channel activity to activate signaling pathways that remodel the actin cytoskeleton.

In this chapter, we will examine a number of different examples of ion channel–cytoskeleton interactions illustrating some of the important concepts in this area. The rapid development of knowledge in this field over the last decade makes it impossible to list all of the known examples of these types of interactions. For example, we have not included discussion of the neuromuscular junction, which is a well-characterized example of the role of the cytoskeleton in the immobilization of postsynaptic receptors or the rapidly growing area of mechanosensory transduction. Apologies are therefore offered to all colleagues where space limitations have prevented mention of their work.

III. MECHANISMS FOR INTERACTIONS BETWEEN THE CYTOSKELETON AND ION CHANNELS

IIIA. The Spectrin-Based Membrane Skeleton

IIIA1. Characteristics of the Spectrin-Based Membrane Skeleton

Originally described in the human erythrocyte, where it plays a major role in maintaining cell shape (reviewed in Bennett and Gilligan, 1993), the spectrin-based membrane skeleton is perhaps the best characterized complex of proteins linking ion channels to the actin cytoskeleton. As shown in Fig. 26.2, at the heart of this complex of proteins is the filamentous protein spectrin, which exists as a 200 nm flexible rod composed of a heterotetramer of α and β subunits. Beta subunits are characterized by the possession of an actin-binding domain at their N-terminus. Heterotetramers and other higher ordered structures form through head to head association of the heterodimer to yield a molecule capable of cross-linking actin through binding sites at opposite ends. In the red cell membrane, short actin oligomers (10–14 monomers) are cross-linked in this fashion to yield a series of pentameric or hexameric structures with actin at the junction (termed the junctional complex) and spectrin filaments organized like spokes of a wheel. Stretched

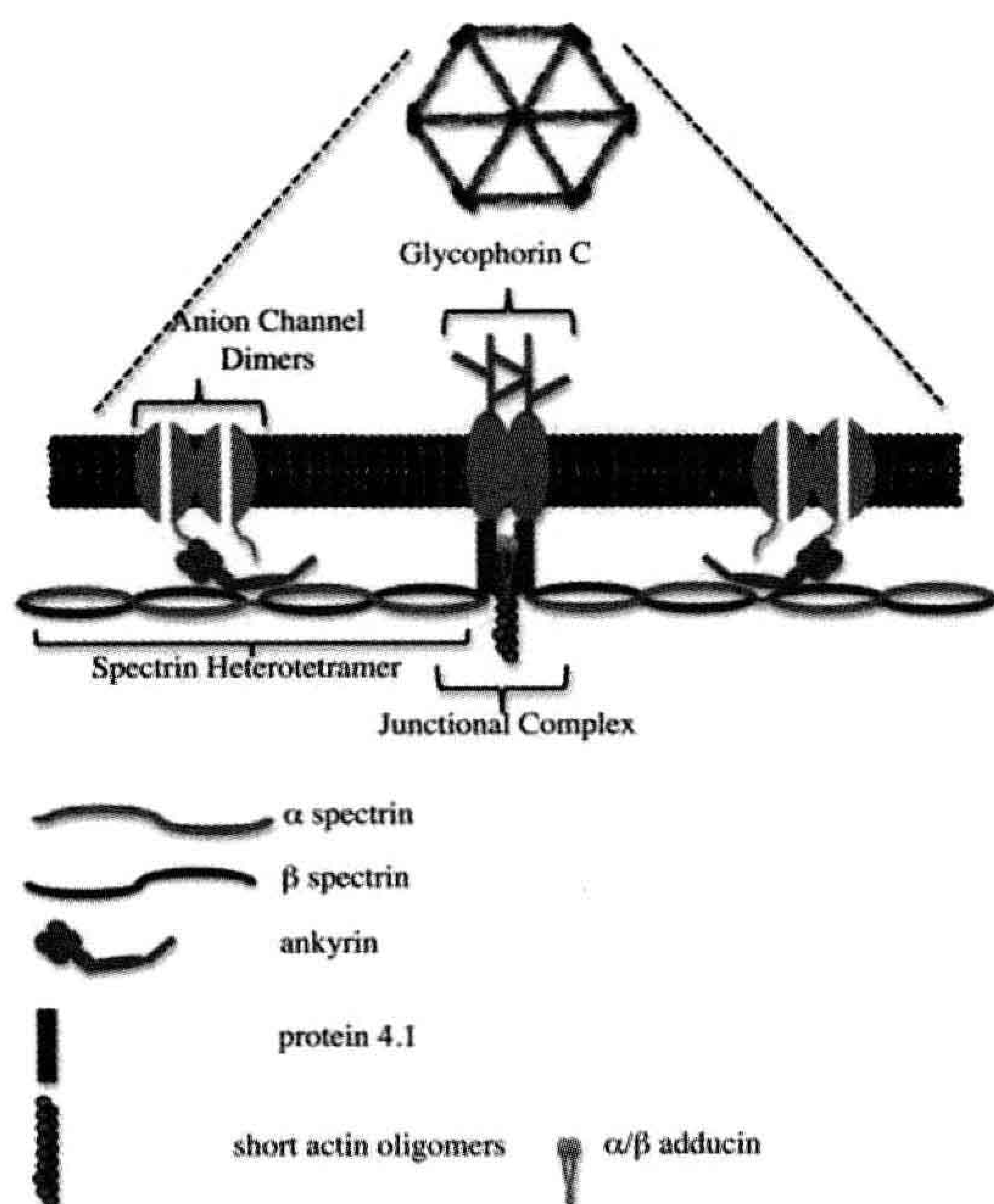


FIGURE 26.2 Cartoon of the major features of the spectrin-based membrane skeleton. Spectrin heterotetramers are arranged around an actin-based junctional complex to generate a hexagonal/pentagonal lattice that can be viewed under the electron microscope when the membrane skeleton is stretched. This lattice is laminated to the bilayer through the interactions of ankyrin with the anion channel and β-spectrin, in addition to interactions between protein 4.1, spectrin and glycophorin C at the junctional complex.

examples of this structure have been visualized by electron microscopy (Byers and Branton, 1985). The molecules protein 4.1 and adducin facilitate the interaction of spectrin with actin at these junctional complexes (Bennett and Gilligan, 1993).

The spectrin-based membrane skeleton forms an electron dense subplasmalemmal undercoating, which can be visualized by electron microscopy and is associated with a number of specialized plasma membrane domains. In red cells, the skeleton is laminated to the bilayer through two major sites of interaction: an association between protein 4.1 which binds both to the β subunit of spectrin and the integral membrane protein glycophorin C and through the molecule ankyrin, which binds both to the β spectrin subunit and to the cytoplasmic domain of the anion channel band 3 (AE1). Mutations that affect the anion channel–ankyrin–spectrin association in red cells result in a loss of membrane lamination, destabilization of the lipid bilayer and a loss of plasma membrane resulting in a shift in cell morphology from discocytes to spherocytes (Palek and Lambert, 1990). In this system, the lateral mobility of the anion channel is restricted in two ways: (1) through the direct interaction of the anion channel with ankyrin and the spectrin bilayer; and (2) through the "corralling" of anion channels within compartments demarcated by the spectrin lattice (Kodippili et al., 2009). However, for the purposes of this review we shall focus on the direct interactions of ankyrins with integral proteins and how this mechanism is used to localize ion channels to specialized plasma membrane domains.

IIIA2. The Ankyrins and their Binding Partners

As shown in Fig. 26.2, the ankyrins are multifunctional adaptors characterized by domains that associate with the β subunit of spectrin and with the cytoplasmic domains of a wide variety of integral membrane proteins, including cell adhesion molecules, transporters and ion channels (Bennett and Healy, 2009). The domain that associates with integral proteins (the membrane-binding domain) consists of 24 copies of the ANK repeat motif now identified in a large number of polypeptides. These repeats are stacked in an array with four basic subdomains such that protein–protein interactions may involve the participation of contact sites from multiple different repeats (Michaely and Bennett, 1993). Binding sites within integral membrane proteins for this domain of ankyrin have arisen independently a number of times during evolution. Hence, it is not easily possible to identify ankyrin-binding sequences within integral proteins from simple analysis of primary sequence. For example, the amino acid sequence associated with ankyrin binding in the family of voltage-gated sodium channels (Garrido et al., 2001; Lemaillet et al., 2003), bears no homology to that identified for members of the L1 family of cell adhesion molecules that also bind ankyrin (Davis and Bennett, 1994). Intriguingly, the same ankyrin-binding sequence that is found in voltage-gated sodium channels is also found in the voltage-gated potassium channels KCNQ2/3 (Pan et al., 2006), responsible for the so-called M-type current. These sequences in KCNQ2/3 appear to have evolved independently and at a later stage in evolution than that of the sodium channels, as one of the first examples of convergent molecular evolution (Hill et al., 2008).

In addition to the membrane and spectrin-binding domains that are highly conserved among different members of the ankyrin family, ankyrins also exhibit an unstructured C-terminal regulatory domain, which is less conserved. The function of this domain is still relatively unclear but it has been implicated in the regulation of the activity of the membrane and spectrin-binding domains (Hall and Bennett, 1997; Abdi et al., 2006). This may well be important as conservation between the various ankyrin membrane-binding domains leads to the question as to how specific ankyrins and their integral

partners are associated within specialized membrane domains.

The vertebrate ankyrin gene family consists of three members, ankyrin$_R$ (encoded by the ANK1 gene), ankyrin$_B$ (ANK2) and ankyrin$_G$ (ANK3) reflecting the distribution of these isoforms within tissues (ankyrin$_R$ being the isoform initially identified in red cells). Many tissues, such as the nervous system, express variants of all three family members. Diversity in ankyrin structure is also achieved through alternative mRNA processing and the use of alternate promotors. The most prominent of these is the insertion of a large sequence between the ankyrin spectrin-binding and C-terminal regulatory domains to produce the "giant" ankyrin molecules, ankyrin$_G$ 480 kDa (Kordeli et al., 1995) and ankyrin$_B$ 440 kDa (Otto et al., 1991). These isoforms are almost twice the size of the originally characterized red cell ankyrin (Lambert et al., 1990). The functions of these large inserted sequences remains unknown, although they appear to be mainly associated with isoforms of ankyrin that are targeted to axonal membrane domains (Chan et al., 1993; Kordeli et al., 1995). As the inserted sequences appear to have an extended conformation, they have the potential to link integral proteins in the axonal membrane with structures deep within the axoplasm. "Giant" isoforms of ankyrin have also been reported in *Drosophila* where the inserted sequences interact with microtubules at the presynaptic neuromuscular junction (Bennett and Healy, 2009).

IIIA3. The Spectrin-Based Membrane Skeleton at the Axon Initial Segment and Nodes of Ranvier

The axon initial segment (AIS) represents a physiologically specialized area of the axon adjacent to the cell body and enriched in cytoplasmic and integral membrane proteins (reviewed in Grubb and Burrone, 2010). It is credited with two major functions in the neuron: (1) the initiation of action potentials; and (2) the formation of a molecular barrier that separates axonal and somatodendritic compartments of the cell to establish and maintain their identity. Key to the organization of this specialized membrane domain is an isoform of ankyrin$_G$ (ankyrin$_G$ 480 kDa) that has been localized to this area of the axon (Kordeli et al., 1995), although other smaller isoforms of ankyrin$_G$ may also be present within this domain. A specialized form of spectrin (β-IV) is also found at the AIS (Grubb and Burrone, 2010). This molecule appears to be important in maintaining or stabilizing integral membrane concentrations at the AIS, as its knockdown does not prevent the initial recruitment of ankyrin$_G$ and its membrane-binding partners to the AIS in cultured neurons. The recruitment of ankyrin$_G$ to the AIS occurs early in development of the axon, although how this molecule is specifically targeted to the AIS is still unknown. This may reflect the nature of the microtubules in this region of the axon which, in some ways, resemble those of dendrites (Gomis-Ruth et al., 2008). Such microtubules could potentially interact with the ankyrin$_G$ 480 kDa inserted region.

Ankyrin$_G$ is thought to establish and maintain the localization of a large number of integral proteins from ion channels to cell adhesion molecules at the AIS and it is thought that this high density of integral proteins forms a diffusion barrier that inhibits the migration of non-ankyrin-associated integral proteins between somatodendritic and axonal compartments of the cell (Winckler et al., 1999). It has also been shown that a barrier exists at the AIS for movement within the axonal cytoplasm (Song et al., 2009) and that this selectivity filter is dependent upon the presence of ankyrin$_G$. Knockdown of ankyrin$_G$ function in cultured hippocampal neurons not only has been found to dismantle the AIS, but also causes the axon to acquire dendritic characteristics including the formation of spine-like protrusions associated with excitatory synapses (Grubb and Burrone, 2010).

The AIS is the main site of action potential initiation. This is achieved through the establishment of high concentrations of both voltage-gated sodium (vgsc) and potassium channels (vgpc) in the AIS membrane, through interactions with ankyrin$_G$. Vgsc consist of an α subunit composed of 24 transmembrane segments divided into four subdomains that generate an ion-selective pore and an auxillary β subunit that regulates channel activity and membrane expression (Goldin, 1999). There are nine different genes that encode α subunits and proteins encoded by these genes all share an ankyrin-binding sequence within the cytoplasmic domain linking domains II and III (Lemaillet et al., 2003). This sequence is also conserved in the KCNQ2/3 (also referred to as Kv7.2 and Kv7.3) subunits of the M-type potassium channel, responsible for stabilizing the resting membrane potential and preventing repetitive action potentials (Pan et al., 2006). The AIS localization of both vgsc and KCNQ2/3 channels is missing in ankyrin$_G$ knockout animals (Zhou et al., 1998; Pan et al., 2006). Consequently, Purkinje neurons from these animals exhibit deficiencies in their ability to initiate action potentials (Zhou et al., 1998).

Ankyrin has also been reported to bind to the accessory β subunits of the voltage-gated sodium channel (Malhotra et al., 2000), although this finding was not supported in alternative studies (Lemaillet et al., 2003). This difference may reflect a requirement for tyrosine phosphorylation within the cytoplasmic domain of the β1 subunit to facilitate ankyrin-binding (Malhotra et al., 2002). Finally, the identification of a di-leucine motif in the C-terminus of the Nav1.2 sodium channel suggests a mechanism whereby

voltage-gated sodium channels not bound to ankyrin at the AIS can be selectively removed from the membrane by endocytosis (Garrido et al., 2003) thereby helping to concentrate molecules retained by $ankyrin_G$ at the AIS.

Physiologically related to the AIS, the nodes of Ranvier are enriched in ion channels (particularly vgsc) necessary for the propagation of the saltatory action potential (Fig. 26.3). Vgsc densities here are typically 25-fold compared to those observed in the internodal area (Salzer et al., 2008). Nodes are small gaps (1 μM) in the myelin sheath between adjacent myelinating glia. Unlike the AIS whose formation is intrinsic to the neuron, node formation in the PNS requires glial cell contact (Ching et al., 1999). Clustering of sodium channels in the CNS is less understood but at the very least requires soluble factors released from the oligodendrocyte (Kaplan et al., 1997).

Key to the formation of the nodes of Ranvier is the binding of ankyrin to members of the L1 family of cell adhesion molecules (CAMs) through a conserved sequence regulated by phosphorylation (Garver et al., 1997; Bennett and Healy, 2009). Both NrCAM and neurofascin 186 kDa from this family are present at both the AIS and nodes of Ranvier and co-localize with $ankyrin_G$ 480 kDa and vgsc (Bennett and Healy, 2009). The function of these CAMs at the AIS is unclear, but may be important for the formation of GABAergic synaptic inputs that target the AIS (Grubb and Burrone, 2010). However, at the nodes of Ranvier these CAMs have a clear role in facilitating contacts between the myelinating Schwann cell and the axolemma. Schwann cell microvilli, identified by the presence of ERM (ezrin, radixin, moesin) proteins (Melendez-Vasquez et al., 2001; Gatto et al., 2003) express a unique extracellular matrix that contains multimers of the soluble protein gliomedin complexed with heparin sulphate proteoglycans (HSPGs) (Salzer et al., 2008). Gliomedin binds to the extracellular domain of neurofascin 186 kDa and NrCAM, hence clustering it at the tips of myelinating Schwann cells (Salzer et al., 2008). This results in the recruitment of $ankyrin_G$ (Lambert et al., 1997) providing a platform for the immobilization of vgsc and KCNQ2/3 molecules in the nodal membrane. Theoretically, $ankyrin_G$ can simultaneously associate with both the CAM and vgsc allowing Schwann cells to regulate directly the clustering of ion channels in the nodal membrane. In addition, the β subunit of the sodium channel has been shown to interact in a *cis*-like fashion with neurofascin 186 kDa to further promote this clustering (Ratcliffe et al., 2001). As myelination progresses, clusters of nodal complexes associated with the adjoining Schwann cells are brought together to form the mature nodal membrane (Lambert et al., 1997).

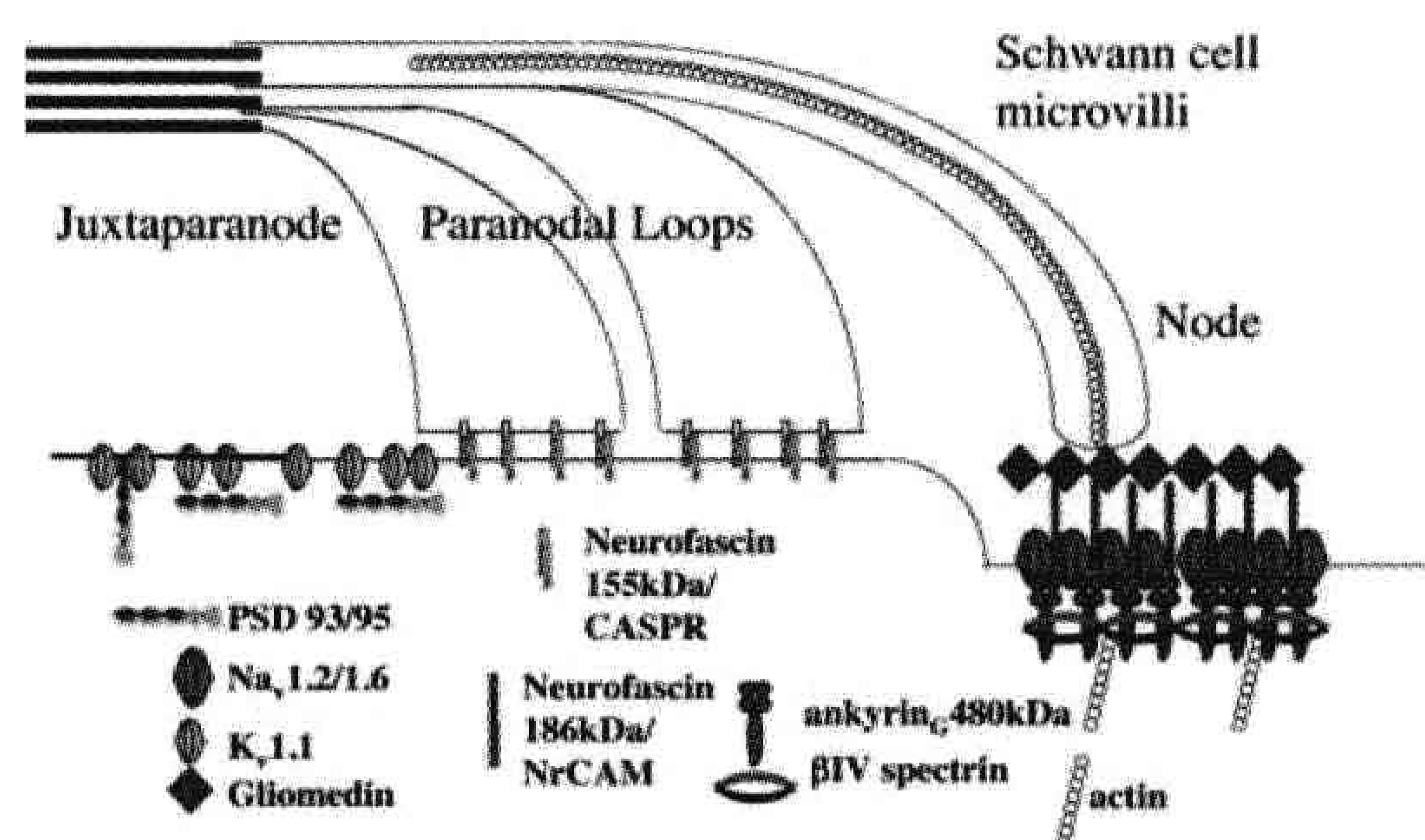


FIGURE 26.3 Mechanisms involved in the localization of ion channels at the nodes of Ranvier. A specialized isoform of ankyrin, $ankyrin_G$ 480 kDa binds to voltage-gated sodium channels Nav1.2/1.6 at the nodal membrane along with the cell adhesion molecule neurofascin 186 kDa. This molecule is associated with a specialized isoform of spectrin, β-IV. The release of gliomedin from the myelinating Schwann cell causes neurofascin 186 kDa to cluster, which leads to the recruitment of the $ankyrin_G$ 480 kDa and associated Nav1.2/1.6 voltage-gated sodium channels into these clusters. The voltage-gated potassium channel Kv1.1 is able to bind to the PDZ domain containing proteins PSD 93/95 and co-localizes with them in the juxtaparanode.

Further maintenance of the nodal membrane comes from the formation of the flanking paranodal junctions that act as diffusion barriers to prevent the movement of proteins between nodal and internodal compartments of the axonal membrane (Salzer et al., 2008). Paranodal junctions composed of glial loops anchored to the axolemma through the interactions of the axonal contactin/caspr complex with Schwann cell neurofascin 155 kDa (Salzer et al., 2008). This results in a very close apposition (3–5 nm) between the Schwann cell and the axonal membrane that limits the diffusion of ions between the nodal and internodal areas. The definitive roles of alternatively spliced neurofascin isoforms in nodal development are clearly demonstrated by specific rescues of these isoforms in neurofascin knockout mice (Zonta et al., 2008). Interestingly, the presence of isoforms of neurofascin in the nodal membrane also prevents the invasion of paranodal loops into the nodal membrane domain (Thaxton et al., 2011).

In the juxtaparanodal region of the axon, insulated from the nodal membrane by the paranodal junctions, lie concentrations of vgpc composed of the Kv1 channel subunits Kv1.1, 1.2 and 1.4 (reviewed in Rasband, 2010). As these channels lie under the myelin sheath where they are electrically insulated, their function is somewhat controversial. However, they are thought to modulate action potential propagation and dampen the repetitive firing properties of early myelinating axons. As with ankyrins at the nodal membrane, these proteins exist in a complex that includes both CAMs and adaptors that link them to the cytoskeleton. In this case, an important *trans* interaction between axon and glial cell is established through an interaction between axonal Caspr2 and glial TAG-1. Caspr2 can also associate with protein 4.1B, a homolog of the molecule characterized in red cells, that

links this complex to the spectrin-based membrane skeleton and actin cytoskeleton. Caspr2 also has the ability to link up with multiple PDZ domain containing proteins through its C-terminus. Two of these proteins, PSD-95 and PSD-93 (to be discussed in more detail in the next section), are able to bind to Kv1.1 and 1.2 and have been localized to the juxtaparanodes. However, current observations suggest their activity is not required for vgpc localization (Rasband et al., 2002). Recently, the metalloprotease ADAM22, originally identified as a Kv1 binding partner, has been observed at the juxtaparanode and has been shown to play a role in the clustering of PSD-95 and PSD-93 (Ogawa et al., 2010).

IIIA4. The Spectrin-Based Membrane Skeleton in Muscle Physiology

The wide variety of integral binding partners for ankyrin facilitates its use in the establishment of a range of specialized membranes within a variety of cell types. Studies from the Bennett laboratory in the last decade have shown a range of functions for ankyrin molecules in muscle physiology. As found in other "excitable" cells, ankyrin$_G$ is crucial to the localization of vgsc to allow the propagation of action potentials. In cardiomyocytes, this involves the localization and surface expression of Nav1.5 to the intercalated disk, to allow propagation of the action potential between adjoining cells (Mohler et al., 2004).

As well as the intercalated disk, Nav1.5 is also found with ankyrin$_G$ in the plasma membrane of the t-tubule (Mohler et al., 2004). T-tubules are extensive invaginations of the plasma membrane that allow it to be brought into close proximity with the sarcoplasmic reticulum at various points along its length. This proximity is crucial for facilitating excitation–contraction coupling in the cardiomyocyte. The t-tubule system consists of a number of specialized microdomains that strictly regulate the movement of calcium between these different membrane compartments to initiate contraction. Key to this activity is a complex between L-type voltage-gated calcium channels in the plasma membrane with ryanodine receptors in the sarcoplasmic reticulum. The localization of Nav1.5 by ankyrin$_G$ in microdomains adjacent to this complex is thought to be responsible for activating the voltage-gated calcium channels in this complex. This allows for the passage of small amounts of calcium which, in turn, mobilize calcium stores from the sarcoplasmic reticulum (Bennett and Healy, 2009; Orchard et al., 2009).

A third specialized microdomain within the t-tubule system is enriched in the Na/Ca exchanger (NCX1), which allows for the passage of calcium back across the t-tubule membrane. NCX1 binds to and co-localizes with ankyrin$_B$ in these microdomains (Bennett and Healy, 2009). In addition, the Na/K ATPase and the IP3 receptor, which are also known to bind ankyrin, co-localize with ankyrin$_B$ in these areas (Mohler et al., 2005). Animals lacking ankyrin$_B$ expression in their cardiomyocytes exhibit aberrant localization of these three integral proteins (Mohler et al., 2005) with deficient cardiomyocytes showing increased contractility and increased calcium transients (Mohler et al., 2003, 2005). This suggests an attractive model whereby ankyrin$_B$ brings together a functional coupling between the NCX1 and Na/K ATPase with sodium ions entering the cell in exchange for calcium ions. The IP3 receptor in this scenario could be coupled to allow the passage of Ca ions directly from the sarcoplasmic reticulum through NCX1 (Mohler et al., 2005). It would be interesting to determine if ankyrin$_B$ is capable of simultaneously associating with both NCX1 and the Na/K ATPase to facilitate formation of a functional macromolecular complex.

Cardimyocytes derived from the ankyrin$_B$ knockout mouse also show defects in sodium channel currents suggesting a role for ankyrin$_B$ in vgsc activity (Chauhan et al., 2000). These defects include changes in sodium current density detected using whole cell voltage clamp techniques. This suggests a role for ankyrin$_B$ in the trafficking and/or stabilization of vgsc on the plasma membrane. Interestingly, changes were also observed in the activation kinetics of the sodium currents suggesting that the binding of ankyrin may also exert functional changes in channel activity.

IIIA5. Mutations Affecting Ankyrin Interactions in Human Cardiac Pathology

Knockout animals have proven invaluable to understanding the role of ankyrins in organizing potentially complex plasma membrane systems such as the t-tubules. Of interest, however, is that some of the same phenotypes can be observed in humans with inherited cardiac disorders and that these phenotypes can be traced to mutations in components of the ankyrin–spectrin based membrane skeleton (reviewed in Ackerman and Mohler, 2010). For example, the E1053K mutation in Nav1.5 is associated with Brugada syndrome, a disorder characterized by cardiac arrhythmia. This mutation falls within the defined ankyrin$_G$ binding site (Lemaillet et al., 2003) and abolishes the ability of Nav1.5 to associate with ankyrin$_G$ which, in vitro, perturbs the surface expression of the molecule and its localization to intercalated disks.

As well as ankyrin$_G$ mutations, mutations within ankyrin$_B$ have been associated with cardiac arrhythmias (Ackerman and Mohler, 2010). LQT4 (type 4 long QT syndrome), a disease characterized by prolonged QTc, catecholaminergic polymorphic ventricular arrhythmia and sudden death, was localized to human chromosome 4q25-27 in a large four generation French kindred. This lies within the same region as the ANK2 gene. Further

examination of the original kindred showed a missense mutation localized to the regulatory domain of $ankyrin_B$ resulting in a loss of function. Subsequent studies have now identified a number of kindreds with similar arrhythmias due to mutations in the ANK2 gene. Phenotypes associated with these individuals range from severe to mild with sinus node dysfunction and atrial fibrillation as hallmarks of this disease. This disease has now been renamed ankyrin-B syndrome (Mohler et al., 2007). These findings illustrate the tip of a potential iceberg in which a number of "channelopathies" might be traced to defects in the adaptor system used to localize them to specific membrane domains or regulate their activity.

IIIA6. Regulation of the Association Between Ankyrin and its Integral Partners

Despite the static nature of the AIS and nodes of Ranvier, evidence has been presented for the dynamic regulation of the ankyrin-integral protein interaction that may be important in the formation or maintenance of these structures. It may also explain one of the conundrums of ankyrin activity. How does a specific ankyrin isoform become targeted to these domains and associate in a non-redundant fashion with its integral partner, given that the ankyrin membrane-binding domains are highly conserved? For example, both $ankyrin_G$ and $ankyrin_B$ are expressed in axons and both can bind with equal affinitity to ank-CAMs vgsc and vgpc. However, within the axon, $ankyrin_G$ is found only at the AIS with neurofascin 186 kDa and vgsc (Bennett and Healy, 2009), whereas $ankyrin_B$ is distributed along the length of the axon (Chan et al., 1993). This problem is yet to be fully answered but may lie in the modulation of ankyrin interactions by the divergent regulatory domain (Bennett and Healy, 2009) or control of ankyrin trafficking by the same domain (Mohler et al., 2002). Another possibility is that ankyrin interactions may be regulated by post-translational modifications such as phosphorylation.

Within the cytoplasmic loop between subdomains II and III of the voltage-gated sodium channel are residues phosphorylated by protein kinase CK2 (CK2) (Brechet et al., 2008). Phosphorylation of these residues enhances ankyrin-binding and CK2 is specifically localized to the AIS in neurons through mechanisms currently unknown. Disruption of CK2 activity results in an aberrant localization for voltage-gated sodium channels within the axon (Brechet et al., 2008). This suggests a mechanism whereby the interaction of $ankyrin_G$ with vgsc is locally regulated at the AIS.

The ankyrin-binding site in the cytoplasmic C-terminus of neurofascin (the FIGQY motif) contains a tyrosine residue, which when phosphorylated abolishes ankyrin binding (Garver et al., 1997). In axons, neurofascin phosphorylated in this position is excluded from the node of Ranvier and localized to the paranodes (Bennett and Healy, 2009). In contrast, this post-translational event is required for the binding of neurofascin to the microtubule associated protein doublecortin (Bennett and Healy, 2009), suggesting a "switch" mechanism whereby neurofascin is able to associate with different cytoskeletal systems when needed.

IIIB. PDZ Proteins and the Postsynaptic Density

IIIB1. The Postsynaptic Density and the Dendritic Spine: Dynamic Interactions Between Ion Channel Receptors and the Actin Cytoskeleton

The postsynaptic compartment of excitatory glutamatergic synapses is localized to small, highly dynamic protuberances that emanate from the dendritic shaft known as dendritic spines. These structures, which are up to a few microns in length, contain all of the signaling molecules and organelles necessary for the receipt, integration and propagation of the synaptic chemical signal. In addition, spines assume a range of dynamic morphologies and mounting evidence has supported the idea that changes in spine morphology alter the propagation of postsynaptic signals. These changes in spine morphology are an important component of synaptic plasticity and hence memory and learning. Dendritic spines themselves are enriched in actin filaments that determine the morphology of the spine and provide a scaffold for the immobilization of postsynaptic receptors and signaling molecules. In turn, these signaling molecules, in response to the activity of synaptic receptors, can regulate the actin cytoskeleton to change the morphology of the spine, thereby regulating synaptic strength. In this section, we will examine the molecules present in the spine, which participate in the immobilization of postsynaptic receptors and signaling molecules regulating dendritic spine morphology.

IIIB2. PDZ Proteins and the Immobilization of Postsynaptic Receptors

The NMDA (N-methyl-D-aspartate) and AMPA (α-amino-3-hydroxy-5-methyl-4-isoaxazole propionic acid) receptors are the major receptors for glutamate in the postsynaptic membrane. Both are ionotrophic receptors which behave as ion channels for the influx of calcium ions to invoke a membrane depolarization in response to glutamate binding. Quantitative analysis of the numbers of such receptors present in the postsynaptic density indicates that the number of NMDA receptors stays largely fixed at ≈ 20 molecules/synapse, whereas the AMPA receptor number can

vary from ≈5 to 200 (reviewed in Sheng and Hoogenraad, 2007). The variety in AMPA receptor number is believed to correlate with the size of the spine head and the dynamic nature of AMPA receptor trafficking to and from the postsynaptic density to be an important feature of synaptic plasticity (Shepherd and Huganir, 2007). Both of these channels form heterotetrameric pores in the membrane to allow for the passage of calcium. The NMDA receptor consists of two NR1 subunits and two NR2 subunits. There are eight variants of the NR1 (NR1-1a/b, 2a/b, 3a/b and 4a/b) subunit produced from a single gene by alternative mRNA processing and four distinct isoforms of the NR2 variant (NR2A-D) (Hollmann et al., 1993). It is the differential expression of the NR2 subunit across cells that determines the particular electrophysiological characteristics of a receptor. A third subunit (NR3) is also found, which has an inhibitory affect on receptor function. AMPA receptors consist of four subunits (GluR1–4). The majority of subunits found in these receptor types have PDZ-domain interacting motifs in their C-termini, which facilitate their interactions with scaffolding and signaling molecules.

Canonical PDZ domains are ≈90 amino acid sequences consisting of six β-strands and two α-helices arranged in a barrel-like conformation (reviewed in Feng and Zhang, 2009). These domains function in protein–protein recognition and typically recognize a short stretch of amino acids (5–7 residues) at the C-termini of target proteins. There are currently thought to be 335 non-redundant PDZ domains present in the human genome. Many PDZ domain-containing proteins contain more than one PDZ domain, which may or may not have different recognition sequences. This then allows for the clustering of proteins or co-clustering of proteins that may have interrelated functions. Interactions of the PDZ domain lend themselves to analysis using the yeast 2-hybrid technique, which has allowed for the elucidation of a complex network of interacting proteins starting with the C-terminal domains of the NMDA and AMPA receptors and traveling deep within the postsynaptic density and head of the dendritic spine. Details of this network of proteins that form the postsynaptic density is shown in Fig. 26.4.

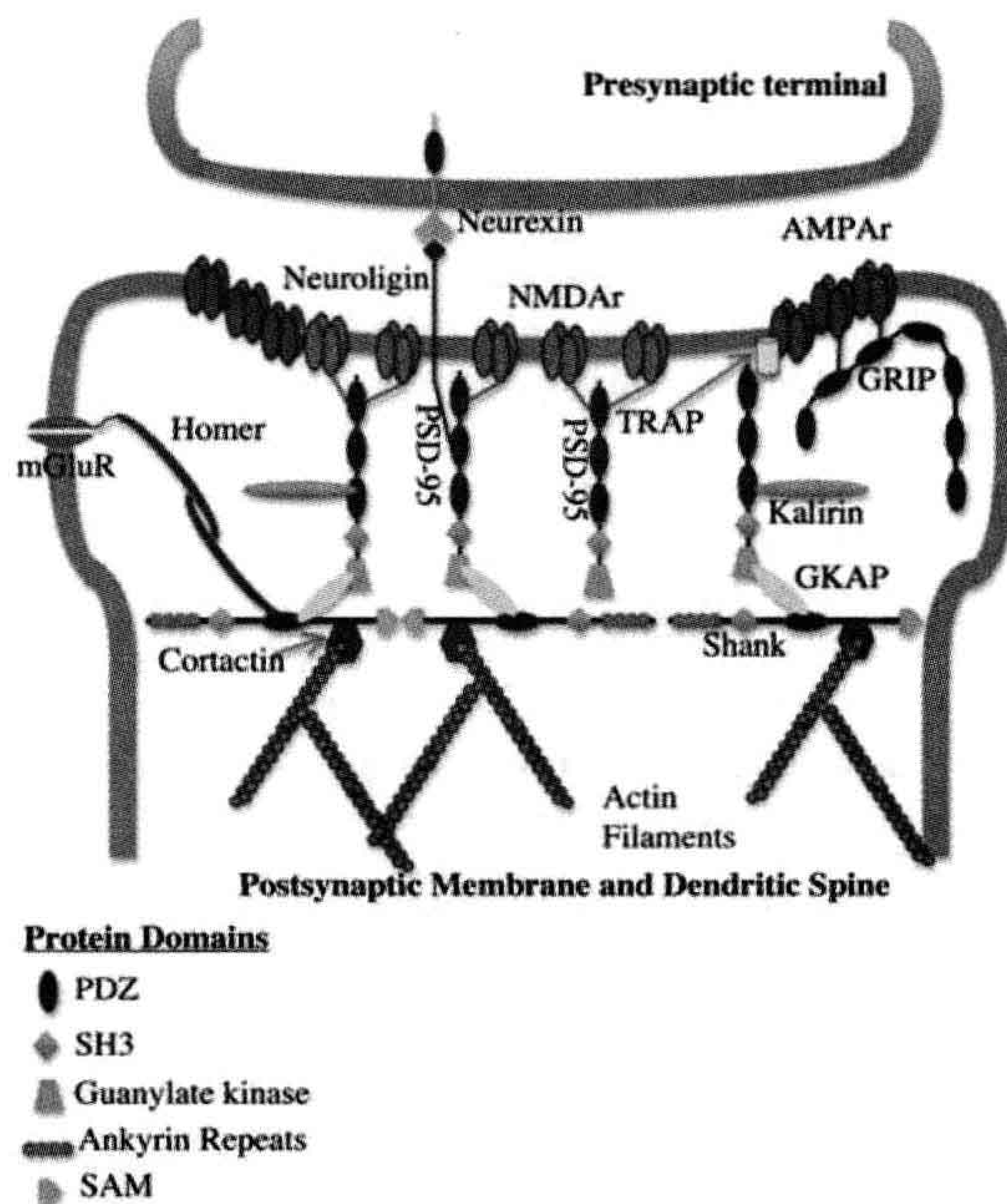


FIGURE 26.4 Interactions of PDZ domain containing proteins at the postsynaptic membrane. NMDA and AMPA receptors at the postsynaptic membrane interact with members of the MAGUK family of scaffolding proteins through their PDZ domains. These scaffolding proteins can also interact with cell adhesion molecules involved in connections with the presynaptic membrane. Interactions with the "higher order" scaffolding proteins (Shanks) link the MAGUKs to the actin cytoskeleton through cortactin. *(Adapted from Feng and Zhang, 2009.)*

IIB3. MAGUKS

Studies to identify proteins interacting with the cytoplasmic C-termini of NMDA receptors, in particular the NR2 subunit, led to the identification of a new family of proteins referred to as the MAGUKs (membrane associated guanylate kinases) (Kornau et al., 1995; Niethammer et al., 1996). The possession of three PDZ domains, an SH3 domain involved in protein–protein interactions, and an inactive guanylate kinase domain characterize this family of proteins (reviewed in Dimitratos et al., 1999). MAGUKS have now been identified in a number of specialized membrane domains in cell types where they appear to have a role in the targeting and/or immobilization of integral proteins. The protein found to associate with NMDA receptor subunits in the postsynaptic density was termed PSD-95 (also known as DLG4) and has been found to exist as a family of proteins at the excitatory synapse with PSD-93, SAP-102 and SAP-97. The multimodular nature of these proteins means that they can cluster multiple integral proteins through their multiple PDZ domains or bring together different proteins within functional microdomains. For example, PSD-95 is theoretically able to associate simultaneously with the CAM neuroligin (which associates in a *trans* fashion with the presynaptic protein neurexin) and the AMPA receptor allowing the presynaptic area to guide development of the postsynaptic density (Feng and Zhang, 2009). Although these proteins are widely expressed throughout the nervous system, their copy number varies according to the neuronal type and developmental stage. The copy number can also vary in accordance with activity-dependent changes underlying synaptic plasticity. It is thought that a typical postsynaptic density contains

≈300–400 copies of MAGUK family members related to PSD-95 (Sheng and Hoogenraad, 2007).

Since the original identification of MAGUKs at the postsynaptic density, a large number of interacting proteins has been identified (see Fig. 26.4). For example AMPA receptors can bind indirectly to PSD-95 family members using the adaptor protein stargazing (Chen et al., 2000) or, alternatively, to the PDZ domain containing protein GRIP (Dong et al., 1997). The development of specific antibodies to these proteins, combined with advances in EM tomography, has allowed a high-resolution anatomical map of the spine head and postsynaptic density to be constructed (Chen et al., 2008). This map divides the postsynaptic density into three layers, the first being at the plasma membrane which encompasses CAMs involved in contact between pre- and postsynaptic areas, ion channels as well as the NMDA and AMPA receptors. Within the spine head the NMDA receptor is observed in the center, whereas AMPA receptors are distributed around the outside of the spine head (Chenet al., 2008). The second layer is enriched in MAGUKs and other scaffolding proteins, arranged such that the N-termini of these molecules are closely associated with the plasma membrane and the C-termini reach down into the density. Finally, the third layer is enriched in large scaffolding proteins termed Shanks (Sh3 domain and Ank repeat domain containing protein).

Shank proteins are large (120–230 kDa) multidomain proteins characterized by the presence of a series of ankyrin repeats, SH3 and PDZ domains, a long proline-rich region and a C-terminal SAM (*sterile alpha*) domain (reviewed in Kreienkamp, 2008). Three Shank genes have been described which give rise to a diverse range of proteins as a result of alternative mRNA processing and promotor usage. It is estimated that approximately 100 Shank molecules are localized deep within the postsynaptic density (Sheng and Hoogenraad, 2007). Shank proteins are thought to function as higher order scaffolding molecules, organizing the postsynaptic density by connecting different scaffold/receptor complexes through their multiple functional domains. Shank molecules also self-assemble through their C-terminal Sam domain in a head-to-head fashion and connect with the actin cytoskeleton indirectly through an interaction with the actin-binding proteins cortactin and/or fodrin (non-erythroid spectrin) (Kreienkamp, 2008). Receptor scaffolding complexes can anchor to Shank proteins through GKAP (also termed SAP-associated proteins or SAPAP) molecules, which can bind both to the guanylate kinase domain of PSD-95/PSD-93 and with the PDZ domains of Shank (Kreienkamp, 2008). Other ion channels and receptors within the postsynaptic density can also associate with Shank. These include the metabotrophic glutamate receptor (mGluR1), which can associate with the Shank complex through the dimeric linker protein Homer (Tu et al., 1999).

IIB4. Regulation of Synaptic Strength through Interactions with Scaffolding Proteins

Activity-dependent changes in synaptic strength define synaptic plasticity and hence, memory and learning. At the electrical level, it is possible to regulate synaptic strength either through changing the ionotrophic characteristics of the receptor, or by altering the expression levels of the channel in the plasma membrane. As mentioned previously, the copy number of the NMDA receptor remains fairly fixed in the postsynaptic membrane, whereas that of the AMPA receptor varies widely (Sheng and Hoogenraad, 2007). In the last few years, there has been increasing evidence suggesting that an important component of synaptic strength is the turnover of AMPA receptors in the postsynaptic membrane. At the same time, evidence has accumulated to say that this turnover to some extent is regulated by interactions between the AMPA receptor and scaffolding proteins (reviewed in Elias and Nicoll, 2007).

Evidence of a role for MAGUK proteins in the regulation of AMPA trafficking to the postsynaptic membrane originally came from overexpression studies of PSD-95 in dissociated neurons and slice cultures (Elias and Nicoll, 2007). In these experiments, a large change in AMPA receptor excitatory postsynaptic currents (epscs) was observed when PSD-95 was overexpressed without a concomitant increase in NMDA epscs. This conclusion however, was not supported in studies of knockout animals lacking either PSD-95 or PSD-93, where epscs were unaffected. This finding may reflect functional redundancy between these two similar proteins (Elias and Nicoll, 2007). Indeed, further studies using RNAi to target specific isoforms of MAGUK proteins, when combined with electrophysiology have now shown that the regulation of AMPA receptor surface expression is complex, with multiple MAGUKs within the same neuron playing a role (Elias and Nicoll, 2007).

Perturbing the activity of MAGUKs has also been found to affect the activity of NMDA receptors. The overexpression of PSD-95 has been shown to reduce sensitization of the NMDA receptor in cultured neurons and increases the NMDA receptor opening probability. In heterologous systems, it also results in increased insertion into the plasma membrane (Aoki et al., 2001; Abel et al., 2004). However, these results remain to be reconciled with those of PSD-95 overexpression studies as mentioned above.

IIB5. Regulation of Dendritic Spine Morphology

Chemical transmission across the glutamergic synapse involving the NMDA and AMPA receptors produces an epsc that is dependent upon the influx of calcium. It is now clear that dendritic spines serve to compartmentalize

calcium changes from the dendritic shaft, where the length and diameter of the spine neck influences the strength and nature of the calcium signal in response to glutamate stimulation (Tada and Sheng, 2006). As increasing lines of evidence indicate that spine morphology can be remodeled by synaptic activity, then spine morphology is closely associated with synaptic plasticity. The morphology of dendritic spines reflects the underlying actin cytoskeleton. Hence, the cytoskeleton not only serves to anchor the ion channels necessary for synaptic activity, but is also remodeled in response to that activity. Not surprisingly then, changes in dendritic spine morphology and numbers has been observed in a number of human neurological disorders ranging from autism (Pickett and London, 2005) to Alzheimer's (Knobloch and Mansuy, 2008).

Although highly varied in their shape, dendritic spines can be roughly classified into three main types: thin, stubby and mushroom, with larger spine heads correlating with increased synaptic strength (Tada and Sheng, 2006). As mentioned earlier, this is thought to reflect increased levels of AMPA receptors in the postsynaptic membrane. Studies using stimuli that induce long-term potentiation (LTP) (Noguchi et al., 2005) and in vivo two-photon microscopy studies of spine turnover (Holtmaat et al., 2005) show that larger spines are more stable and less plastic, whereas smaller spines preferentially undergo LTP. These spines can undergo dramatic changes in their morphology including "splitting" to form two individual postsynaptic areas (Dyson and Jones, 1984). The reason why smaller spines may be susceptible to LTP probably reflects their "neck" geometry, where smaller spines show enhanced elevation of calcium concentrations in the spine head in response to stimuli due to decreased calcium leak through their thinner spine neck (Noguchi et al., 2005).

Dendritic spines are thought to arise from highly dynamic actin-based structures known as filopodia and are induced when these structures contact the nascent presynaptic region (Tada and Sheng, 2006). Finger-like filopodia are associated with a number of motile structures, including the growth cones of neurons and owe their dynamic nature to rapid remodeling of their actin cytoskeleton. Hence, many of the molecules involved in actin remodeling in other cellular structures are also localized in the dendritic spine and play a role in activity-dependent morphological changes. These include molecules that regulate the kinetics of actin polymerization and depolymerization such as profilin, a molecule that associates with actin monomers to limit their availability for the polymerization of actin (Birbach, 2008). Stimulation of NMDA receptors causes the recruitment of profilin to spine heads with the concomitant blocking of actin-related shape changes in the spine (Ackermann and Matus, 2003).

Members of the RhoGTPase family along with proteins that control their activity have also been localized to the spine with their overexpression or inhibition causing major changes in spine morphology (Yoshihara et al., 2009). RhoGTPases act as molecular switches to regulate the actin cytoskeleton (reviewed in Heasman and Ridley, 2008). When associated with GTP, these small G proteins bind to downstream effectors to regulate their activity. A number of proteins are found that cycle RhoGTPases between active (GTP bound) and inactive (GDP bound) states. An example of one of these proteins in dendritic spines is kalirin-7, which is a GEF (guanine-nucleotide exchange factor) that activates the RacGTPase (reviewed in Penzes and Jones, 2008). During synaptogenesis, kalirin-7 activity is induced downstream of signals from the intercellular CAM ephrinB and its receptor. Studies with knockout animals have demonstrated a critical role for kalirin-7 in the regulation of both spine number as well as morphology (Ma, 2010).

Downstream of RacGTPase activity in many cell types is the Lim-kinase cofilin pathway, which is involved in the severing of actin filaments to provide nucleation sites for new actin filament growth. This pathway has also been shown to play a role in synaptic plasticity (Meng et al., 2003). Knockout animals lacking Lim-kinase exhibit dendritic spines with abnormal morphologies and have impaired spatial learning and synaptic plasticity (Meng et al., 2002). As the loss of dendritic spines has been associated with the cognitive defects found in Alzheimer's disease (Tackenberg et al., 2009), it is not surprising to note that changes in this signaling pathway have also been observed in this disorder (Zhao et al., 2006).

Finally, overexpression or knockdown experiments of scaffold proteins such as Shank or PSD-95 have also been shown to alter the morphology of dendritic spines. This may reflect the functions of these proteins in the recruitment of signaling proteins to these structures (Tada and Sheng, 2006). Given the large number of molecules involved in regulating the actin cytoskeleton that have now been localized to the dendritic spine, the challenge is now to elucidate how the function (or localization) of these molecules is regulated in response to synaptic activity.

IIIC. Gephyrin and the Inhibitory Synapse

As described above, the molecules involved in the formation and maintenance of the excitatory synapse, their interactions and localizations have been characterized with a high degree of resolution. Unfortunately, despite its clinical significance, the same cannot be said of the inhibitory synapse. To some extent this may reflect the ease with which the excitatory synapse can be purified compared with its inhibitory counterpart. However, purification of the glycine receptor did yield a binding protein involved in the linkage of these receptor molecules to the microtubule-based cytoskeletal system. This protein has been termed gephyrin (reviewed in Fritschy et al., 2008). Gephyrin has

a predicted molecular mass of 83 kDa and consists of three major structural domains, although multiple isoforms are generated by alternative mRNA processing. Two of these domains are termed G and E. This nomenclature comes about because of sequence homologies between gephyrin and the bacterial Moco (molybdenum co-factor) synthesizing enzymes MogA and MoeA. Indeed, gephyrin is highly conserved between species and mediates Moco biosynthesis in addition to serving as a postsynaptic protein (Feng et al., 1998).

Gephyrin's function in clustering glycine receptors at the inhibitory synapse is based largely on its self-aggregation properties. The protein is thought to form trimers through self-association sites in the G domain and sites in the E domain associate with the large intracellular M3–M4 loops of the pentameric glycine receptor (Fritschy et al., 2008). These trimers are believed to assemble into higher order structures as postulated from aggregation studies of isolated domains in various cell lines (Sola et al., 2001). However, the observation that gephyrin clusters are observed only at the postsynaptic membrane suggests that other factors also regulate this aggregation, including the activation of glycine receptors (Kirsch and Betz, 1998).

As well as binding directly to microtubules, gephyrin associates with the dynein light chain, therefore linking it to motor molecules that utilize the microtubule system for intercellular transport (Fuhrmann et al., 2002). This interaction is supported by live cell imaging studies that show the movement of intracellular complexes of glycine receptor and gephyrin (Maas et al., 2006). In addition, evidence suggests that these complexes may also be able to associate with the actin cytoskeleton as well as providing a second anchorage system for glycine receptor–gephyrin complexes at the inhibitory membrane (Fritschy et al., 2008).

Gephyrin also is found at GABA- (γ-aminobutyric acid) ergic synapses, although interactions between the GABA receptor and gephyrin are currently not well understood (Fritschy et al., 2008). This interaction may be indirect through the protein GABARAP, which has been shown to bind both gephyrin and the GABA receptor (Kanematsu et al., 2007), although it has been shown that this protein is not essential for GABA targeting to the synapse (O'Sullivan et al., 2005). Unlike the glycine receptor, clusters of GABA receptors have been observed independently of gephyrin in neurons. However, gephyrin gene targeting experiments clearly demonstrate a requirement for gephyrin in GABA receptor clustering (Yu et al., 2007), with the recruitment of gephyrin to GABAergic synapses dependent on GABA receptor clustering. This suggests that gephyrin's role may be in the stabilization of GABA receptor clusters at the postsynaptic membrane, rather than in their formation. The role of gephyrin in the recruitment of GABA receptors remains to be elucidated, along with the question of how different GABA receptors with different subunit compositions are targeted to specific synapses and the role gephyrin plays in that selectivity.

IIID. The Interaction of Epithelial Ion Channels with the Cytoskeleton

So far this review has focused on the role of the cytoskeleton in the establishment and maintenance of "excitable" membrane systems such as the AIS and the postsynaptic membrane. In this section, we will now look at how cytoskeleton–ion channel interactions contribute to the polarized nature of epithelial cells. Epithelial cells line cavities and surfaces throughout an organism and form a barrier between the "outside" and the "inside". The use of an array of junctions including adherens and tight junctions on the lateral surface ensures that the passage of solutes between these two compartments occurs through, rather than around the epithelial cell. In this way epithelial cells control processes such as secretion and selective adsorption, as well as play a role in the detection of sensation. In order to achieve this function, epithelial cells become highly polarized during differentiation into two plasma membrane domains associated with the two physiological compartments that they bridge: an apical domain and a basolateral domain that sits on a specialized extracellular matrix (Fig. 26.5). The restriction of ion channels to these two domains is in part due to their interaction with the actin-based cytoskeleton of these cells. In addition, this interaction can help contribute to the function of these ion channels particularly in the area of sensation detection.

Electrophysiology studies of epithelial ion channel activity first suggested a functional link between these molecules and the actin cytoskeleton. Treatment of epithelial cells with cytochalasins, drugs that cause a depolymerization of the actin cytoskeleton, either activated or inactivated epithelial sodium, chloride and potassium channel activity when examined by patch-clamp electrophysiology (reviewed in Mazzochi et al., 2006). However, from these experiments it was impossible to tell whether affects observed were from binding of the channel to the cytoskeleton or the activation of cytoskeleton-associated second messenger systems that affect channel activity. It is now known that a number of channels associate with the actin cytoskeleton using adaptor and scaffolding systems similar to those described for "excitable" membrane domains in the nervous system.

IIID1. CFTR and PDZ Domain Scaffold Proteins in the Apical Membrane

The cystic fibrosis transmembrane conductance regulator (CFTR) is an ion channel of the ABC-transporter class involved in the movement of chloride and thiocyanate ions

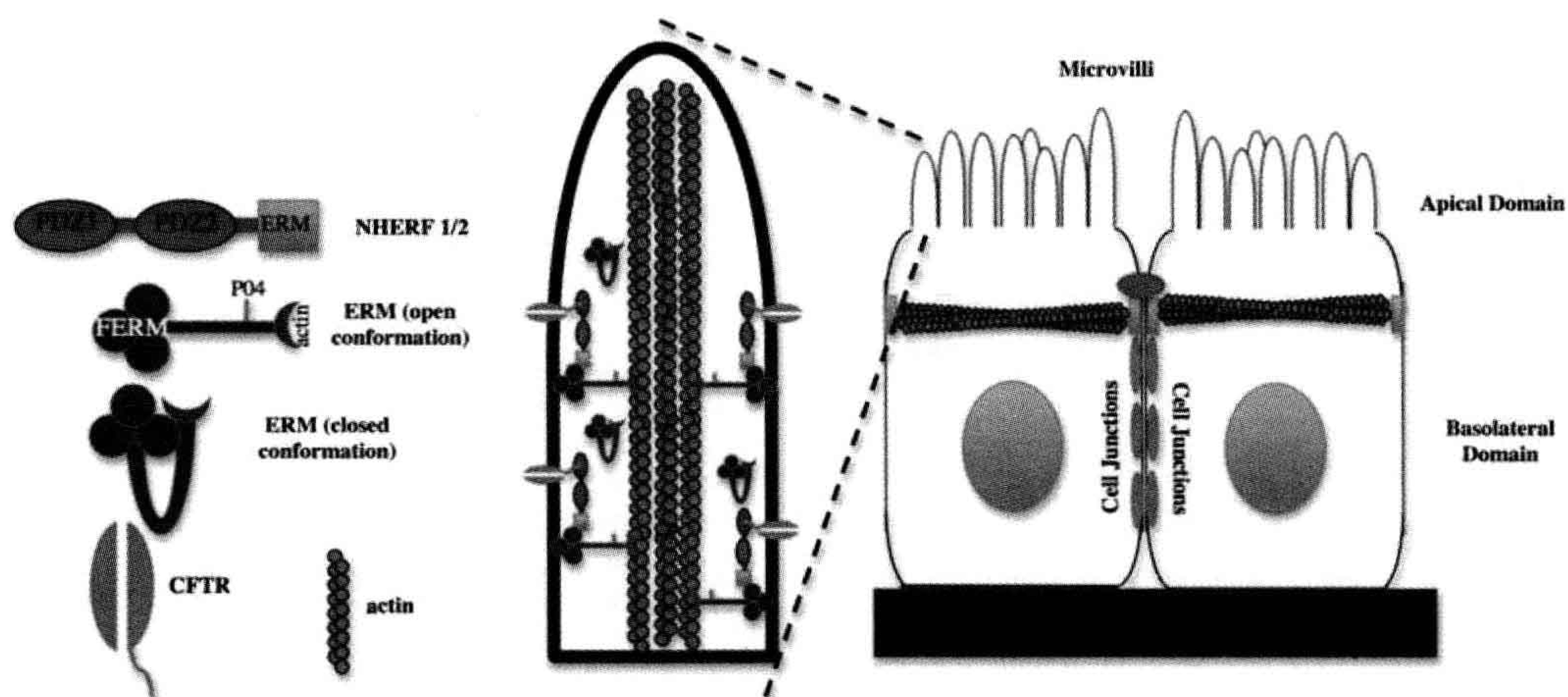


FIGURE 26.5 Interactions that localize CFTR to the apical microvilli of epithelial cells. Epithelial cells are polarized into apical and basolateral domains. The CFTR is localized to the apical compartment of these cells and here is shown localized to apical microvilli. CFTR binds to the PDZ domain of NHERF1/2 which, in turn, binds indirectly to the actin cytoskeleton in the apical domain through an association with ERM (ezrin, radixin, moesin) proteins. As shown, ERM proteins exist in both "open" and "closed" conformations. Binding sites for NHERF1/2 and actin are masked on ERM proteins in the "closed" conformation.

across the apical membrane of epithelial cells (Miller, 2010). Essentially, the channel acts as an ATP-gated anion channel allowing anions such as chloride to flow down their electrochemical gradient in response to cAMP activation. This is in contrast to other ABC transporters where ATP is used to drive the passage of ions against the gradient (Miller, 2010). CFTR is found in a number of epithelia but has been well characterized in the lung where the movement of chloride ions from the epithelial cell to the covering mucus results in the movement of water by osmosis and a more fluid mucus (Kreindler, 2010). The importance of this is clearly seen in mutations of the CFTR that give rise to cystic fibrosis, one of the most common genetic disorders among Caucasians. This disease is characterized by the presence of thick mucus that can block airways and glands and acts as a reservoir for bacterial infections (Kreindler, 2010).

The characterization and identification of C-terminal cytoplasmic sequences in CFTR capable of interacting with PDZ-domain containing proteins led to the idea that CFTR maybe anchored to the apical surface through an interaction with a PDZ-domain scaffolding protein. This protein was found to be a previously identified molecule termed NHERF1 (Na^+/H^+ exchanger regulatory protein) also known as EBP-50 (ezrin-binding protein 50 kDa) (Mazzochi et al., 2006). NHERF proteins are a family of four members that possess either two or four PDZ domains. Family members include the closely related NHERF1 (ebp-50) and NHERF2 (also known as E3KARP) and the four PDZ domain containing proteins NHERF3 (also known as PDZK1, CAP70) and NHERF4 (IKEPP) (Donowitz et al., 2005). As well as their PDZ domains NHERF family members also possess a C-terminal ERM (ezrin-radixin-moesin) binding domain, which therefore indirectly links them to the actin-based cytoskeleton as shown in Fig. 26.5.

NHERF proteins have now been implicated as a major mechanism for the connection of epithelial ion channels to the actin cytoskeleton. These molecules were originally identified as binding partners for the apical membrane Na^+/H^+ exchanger type 3 (NHE3) (Weinman et al., 1995; Yun et al., 1997; Donowitz et al., 2005). They have been shown to be responsible for the localization of the TRPV5/6 epithelial calcium channels (Embark et al., 2004), TRPC4/5 non-selective cation channels (Tang et al., 2000), the β-adrenergic receptor (Hall et al., 1998), CIC-3 chloride channel (Gentzsch et al., 2003) and ROMK potassium channels (Yoo et al., 2004) in addition to their interactions with CFTR. As with other PDZ domain proteins, the possession of multiple PDZ domains allows NHERF proteins to cluster ion channels and/or establish signaling platforms whereby ion channels are brought into close proximity with proteins that regulate their activity. This is clearly illustrated with CFTR, where the molecule has been shown to bind to both PDZ domains of NHERF1 with physiologically relevant affinity (Raghuram et al., 2001). These interactions have been shown to promote dimerization of the CFTR molecule affecting its activity. In addition, CFTR has been localized in a macromolecular complex with the β-adrenergic receptor bound to NHERF2

(Naren et al., 2003). Given that these two molecules are functionally coupled with activation of the receptor stimulating CFTR activity, interactions with NHERF2 represent an important mechanism for regulating CFTR activity in the cell.

Although interactions between CFTR, NHERFs and ERM proteins are necessary for the trafficking and/or stabilization of CFTR in the apical membrane (Mazzochi et al., 2006), these interactions are found to be fairly dynamic and regulated by cell signaling pathways. Interaction of the CFTR with NHERF1 can be regulated by protein kinase C- (PKC-) mediated phosphorylation of a single residue (S162) within PDZ domain 2 of NHERF1 (Raghuram et al., 2001). Phosphorylation of this residue decreases the binding of CFTR to NHERF1. The binding of NHERFs to ERM proteins is also regulated. ERM proteins are characterized by a globular FERM domain and an extended "tail" region that contains an actin-binding site. Within these two domains are sites of self-association that allow the protein to assume a "closed" conformation, where N- and C-termini interact (reviewed in Fehon et al., 2010). Binding sites for actin and NHERF proteins are blocked in this "closed" conformation (see Fig. 26.5). Movement between "closed" and "open" conformations of the ERM proteins is downstream of cell signaling events. These include an interaction between the FERM domain of ERM proteins with PIP2 (phosphatidylinositol 4,5-bisphosphate) synthesized in the membrane in response to G-protein receptor signaling and phosphorylation of ERM proteins in response to activation of RhoGTPases (Fehon et al., 2010). The dynamic nature of the interaction of CFTR with the actin cytoskeleton through NHERF proteins has been demonstrated using a series of FRAP (fluorescence recovery after photobleaching) studies with GFP-labeled CFTR (Haggie et al., 2004). These studies showed that the diffusion of CFTR in the plane of the membrane is dependent on its ability to bind to PDZ-domain-containing proteins, but that this interaction is highly dynamic with these interactions constantly occurring on a time scale of seconds or faster. In support of the dynamic nature of these interactions, it has been reported that NHERF proteins constitute only a small amount ($\approx 2\%$) of proteins found in CFTR-containing macromolecular complexes (Li et al., 2004).

IIID2. Interactions of Epithelial Ion Channels with Actin-Binding Proteins

The epithelial sodium channel (ENaC, also known as the amiloride sensitive sodium channel) is present in the apical membrane of epithelial cells (particularly the kidney) where it plays a major role in the reabsorption of sodium. These channels are also closely related to the degenerins family of proteins in *Caenorhabditis elegans* that are implicated in mechanosensory transduction (Lumpkin et al., 2010). The channel consists of three subunits termed α, β and γ that form a pore with selective permeability for Li^+ and Na^+ ions (Garty and Palmer, 1997). An interaction between the α subunit of the ENaC and the SH3 domain of α spectrin has been reported (Rotin et al., 1994). This interaction maps to a proline-rich sequence present in the cytoplasmic C-terminal region of the subunit. Microinjection of this domain into rat alveolar epithelial cells causes it to co-localize with α-spectrin in the apical domain. This is in contrast to a domain from the N-terminal region of the ENaC which remains diffuse in the cytoplasm (Rotin et al., 1994).

Other members of the spectrin superfamily of proteins, characterized by the presence of the 106 amino acid spectrin repeat (Hartwig, 1994) are also expressed in epithelial cells. α-Actinin, which consists of four spectrin repeat motifs, is arranged as an anti-parallel homodimer to bind and cross-link actin filaments (Sjoblom et al., 2008). This molecule has been shown to bind to PC2 (polycystin-2 also known as TRPP2) through its spectrin repeat domains (Li et al., 2005), thereby cross-linking PC2 to the actin cytoskeleton. PC2 is a member of the TRP (transient receptor potential) superfamily of ion channels and is a Ca^{2+}-permeable cation channel. Mutations in the PKD2 gene that encodes PC2 are associated with autosomal dominant polycystic kidney disease (ADPKD) (Gonzalez-Perrett et al., 2001). Although PC2 is predominantly localized to the cilia, it is also found in the apical plasma membrane of epithelial cells (Ong and Harris, 2005). Interestingly α-actinin was able to stimulate the activity of PC2 when incorporated into lipid bilayers, suggesting that this interaction may also have a direct regulatory role on PC2 activity as well as regulating its subcellular localization (Li et al., 2005).

IIID3. Direct Interactions Between Epithelial Ion Channels and Actin Filaments

We have so far examined examples of a model in which ion channels couple to the actin cytoskeleton through intermediary adaptor or scaffold proteins. However, increasing lines of evidence support the idea that some ion channels in epithelial cells can directly associate with actin. Actin has been shown to interact directly with the ClC-2 chloride channel using actin overlay and co-sedimentation assays (Ahmed et al., 2000). In addition, treatment of *Xenopus laevis* oocytes expressing ClC-2 with cytochalasin D or latrunculin that disrupt the actin cytoskeleton significantly increased channel activity. Similarly, changes in conductance of ENaC channels incorporated into lipid bilayers were observed in the presence of short actin filaments (Berdiev et al., 1996) and these channels were found to be activated by protein kinase A (PKA) only in the presence of actin. The concept that ion channel activity may be regulated by the presence of short actin filaments is supported

by patch-clamp studies in *X. laevis* cells showing an increase in ENaC activity within 5 minutes of applying cytochalasin D to the cells (Cantiello et al., 1991). Further experiments utilizing gelsolin, which preferentially stabilizes the polymerization of actin into short oligomers, have demonstrated that it is the interaction of ENaC with short actin filaments, rather than just with actin itself, that regulates ENaC activity (Prat et al., 1993). Mapping studies have localized a putative actin-binding site to the region between E631 and F644 of the α-ENaC molecule (Copeland et al., 2001).

IV. GENERAL CONCLUSIONS

The localization of ion channels to physiologically specialized membrane domains is crucial to the function of a wide variety of metazoan cell types. This localization is dependent upon interactions, either direct or indirect, between ion channels and the actin or microtubule-based cytoskeleton. In this review, we have examined some examples of these interactions and how they contribute to the physiological function of these specialized membrane domains. As is observed, the interaction between ion channels and cytoskeletal elements not only facilitates channel localization, but also may regulate their activity. Regulation of ion channel activity can reflect the affects of direct interactions of the cytoskeleton or cytoskeletal adaptor/scaffolding proteins with components of the channel. An area where this concept becomes crucial, but not covered in this review, is in the area of mechanosensitive transduction. There, the interaction of ion channels with the cytoskeleton and the extracellular matrix serves to regulate channel activity in response to mechanical changes (Lumpkin et al., 2010). Alternatively, ion channel activity can be regulated by the formation of functional microdomains brought about by scaffolding proteins that bring the channel into close proximity with signaling molecules that regulate its activity.

As evidenced in the dendritic spine, the activity of ion channels can also serve to regulate the cytoskeleton to achieve changes in cell shape. These changes can themselves affect how epscs are propagated to the dendritic shaft and are an important component of synaptic plasticity, a crucial concept underlying memory and learning. Dendritic spines themselves contain molecules that have been demonstrated to have a regulatory affect on their morphology. The challenge in upcoming years will be to try to understand how synaptic activity, with its accompanying ion channel involvement, regulates the function of these molecules to change spine morphologies.

A number of insights have occurred over the last 10 years into how these specialized membrane domains are localized and assembled. However, a significant number of important questions remain to be answered. Are ion channels and their associated trafficking proteins trafficked together to the plasma membrane as macromolecular complexes or is assembly localized to these sites? In the case of the excitatory postsynaptic density, we know that at least some of these proteins are already preassembled prior to reaching the postsynaptic membrane (Naisbitt et al., 1999). Similarly, a role for various motor proteins in synapse assembly has been noted (reviewed in Hirokawa et al., 2010), although mechanisms underlying the specific targeting of protein complexes to these sites have yet to be elucidated. The discovery that certain scaffold proteins simultaneously bind to both CAMs and ion channels suggests a mechanism whereby *trans* interactions between cells could direct ion channel clustering and formation of specialized membrane domains. For example, at the node of Ranvier, gliomedin released from the myelinating Schwann cell clusters the ankyrin-binding molecule neurofascin (Salzer et al., 2008) to direct ankyrin recruitment (Lambert et al., 1997). As ankyrin also binds the vgsc (Lemaillet et al., 2003), a series of molecular interactions allow the Schwann cell to orchestrate directly early assembly of the nodal membrane. However, this model does not explain how these same players are assembled at the AIS, which is an intrinsic feature of the neuron and can be assembled in the absence of cell contacts. Again, the answer to these question lies in understanding mechanisms undergoing the trafficking of these proteins to their specialized membrane domains.

The use of knockout and transgenic animals has been extremely useful in demonstrating the physiological consequences of aberrant interactions between ion channels and the cytoskeleton. However, we have also seen that mutations in these interactions can also be associated with human disease as is seen with ankyrin in the heart (Ackerman and Mohler, 2010) and CFTR in epithelial cells (Kreindler, 2010). In addition, increasing evidence suggests that proteins that affect the dendritic spine cytoskeleton and, hence, its morphology, may be associated with human neurological disorders such as Alzheimer's disease (Knobloch and Mansuy, 2008; Penzes and Jones, 2008). It may well be that these disorders represent only the tip of the iceberg when it comes to channelopathies that result from aberrant interactions with the cytoskeleton.

BIBLIOGRAPHY

Abdi, K. M., Mohler, P. J., Davis, J. Q., & Bennett, V. (2006). Isoform specificity of ankyrin-B: a site in the divergent C-terminal domain is required for intramolecular association. *J Biol Chem, 281*, 5741–5749.

Abel, H. J., Lee, J. C., Callaway, J. C., & Foehring, R. C. (2004). Relationships between intracellular calcium and after hyperpolarizations in neocortical pyramidal neurons. *J Neurophysiol, 91*, 324–335.

Ackerman, M. J., & Mohler, P. J. (2010). Defining a new paradigm for human arrhythmia syndromes: phenotypic manifestations of gene mutations in ion channel- and transporter-associated proteins. *Circ Res, 107*, 457–465.

Ackermann, M., & Matus, A. (2003). Activity-induced targeting of profilin and stabilization of dendritic spine morphology. *Nat Neurosci, 6*, 1194–1200.

Ahmed, N., Ramjeesingh, M., Wong, S., Varga, A., Garami, E., & Bear, C. E. (2000). Chloride channel activity of ClC-2 is modified by the actin cytoskeleton. *Biochem J, 352*, 789–794.

Aoki, C., Miko, I., Oviedo, H., et al. (2001). Electron microscopic immunocytochemical detection of PSD-95, PSD-93, SAP-102, and SAP-97 at postsynaptic, presynaptic, and nonsynaptic sites of adult and neonatal rat visual cortex. *Synapse, 40*, 239–257.

Bennett, V., & Gilligan, D. M. (1993). The spectrin-based membrane skeleton and micron-scale organization of the plasma membrane. *Annu Rev Cell Biol, 9*, 27–66.

Bennett, V., & Healy, J. (2009). Membrane domains based on ankyrin and spectrin associated with cell-cell interactions. *Cold Spring Harb Perspect Biol, 1*, a003012.

Berdiev, B. K., Prat, A. G., Cantiello, H. F., et al. (1996). Regulation of epithelial sodium channels by short actin filaments. *J Biol Chem, 271*, 17704–17710.

Birbach, A. (2008). Profilin, a multi-modal regulator of neuronal plasticity. *Bioessays, 30*, 994–1002.

Brechet, A., Fache, M. P., Brachet, A., et al. (2008). Protein kinase CK2 contributes to the organization of sodium channels in axonal membranes by regulating their interactions with ankyrin G. *J Cell Biol, 183*, 1101–1114.

Byers, T. J., & Branton, D. (1985). Visualization of the protein associations in the erythrocyte membrane skeleton. *Proc Natl Acad Sci USA, 82*, 6153–6157.

Cantiello, H. F., Stow, J. L., Prat, A. G., & Ausiello, D. A. (1991). Actin filaments regulate epithelial Na+ channel activity. *Am J Physiol, 261*, C882–C888.

Chan, W., Kordeli, E., & Bennett, V. (1993). 440-kD ankyrinB: structure of the major developmentally regulated domain and selective localization in unmyelinated axons. *J Cell Biol, 123*, 1463–1473.

Chauhan, V. S., Tuvia, S., Buhusi, M., Bennett, V., & Grant, A. O. (2000). Abnormal cardiac Na(+) channel properties and QT heart rate adaptation in neonatal ankyrin(B) knockout mice. *Circ Res, 86*, 441–447.

Chen, L., Chetkovich, D. M., Petralia, R. S., et al. (2000). Stargazin regulates synaptic targeting of AMPA receptors by two distinct mechanisms. *Nature, 408*, 936–943.

Chen, X., Winters, C., Azzam, R., et al. (2008). Organization of the core structure of the postsynaptic density. *Proc Natl Acad Sci USA, 105*, 4453–4458.

Ching, W., Zanazzi, G., Levinson, S. R., & Salzer, J. L. (1999). Clustering of neuronal sodium channels requires contact with myelinating Schwann cells. *J Neurocytol, 28*, 295–301.

Copeland, S. J., Berdiev, B. K., Ji, H. L., et al. (2001). Regions in the carboxy terminus of alpha-bENaC involved in gating and functional effects of actin. *Am J Physiol Cell Physiol, 281*, C231–C240.

Davis, J. Q., & Bennett, V. (1994). Ankyrin binding activity shared by the neurofascin/L1/NrCAM family of nervous system cell adhesion molecules. *J Biol Chem, 269*, 27163–27166.

Dimitratos, S. D., Woods, D. F., Stathakis, D. G., & Bryant, P. J. (1999). Signaling pathways are focused at specialized regions of the plasma membrane by scaffolding proteins of the MAGUK family. *Bioessays, 21*, 912–921.

Dong, H., O'Brien, R. J., Fung, E. T., Lanahan, A. A., Worley, P. F., & Huganir, R. L. (1997). GRIP: a synaptic PDZ domain-containing protein that interacts with AMPA receptors. *Nature, 386*, 279–284.

Donowitz, M., Cha, B., Zachos, N. C., et al. (2005). NHERF family and NHE3 regulation. *J Physiol, 567*, 3–11.

Dyson, S. E., & Jones, D. G. (1984). Synaptic remodelling during development and maturation: junction differentiation and splitting as a mechanism for modifying connectivity. *Brain Res, 315*, 125–137.

Elias, G. M., & Nicoll, R. A. (2007). Synaptic trafficking of glutamate receptors by MAGUK scaffolding proteins. *Trends Cell Biol, 17*, 343–352.

Embark, H. M., Setiawan, I., Poppendieck, S., et al. (2004). Regulation of the epithelial Ca2+ channel TRPV5 by the NHE regulating factor NHERF2 and the serum and glucocorticoid inducible kinase isoforms SGK1 and SGK3 expressed in Xenopus oocytes. *Cell Physiol Biochem, 14*, 203–212.

Fehon, R. G., McClatchey, A. I., & Bretscher, A. (2010). Organizing the cell cortex: the role of ERM proteins. *Nat Rev Mol Cell Biol, 11*, 276–287.

Feng, G., Tintrup, H., Kirsch, J., et al. (1998). Dual requirement for gephyrin in glycine receptor clustering and molybdoenzyme activity. *Science, 282*, 1321–1324.

Feng, W., & Zhang, M. (2009). Organization and dynamics of PDZ-domain-related supramodules in the postsynaptic density. *Nat Rev Neurosci, 10*, 87–99.

Fritschy, J. M., Harvey, R. J., & Schwarz, G. (2008). Gephyrin: where do we stand, where do we go? *Trends Neurosci, 31*, 257–264.

Fuhrmann, J. C., Kins, S., Rostaing, P., et al. (2002). Gephyrin interacts with Dynein light chains 1 and 2, components of motor protein complexes. *J Neurosci, 22*, 5393–5402.

Garrido, J. J., Fernandes, F., Giraud, P., Mouret, I., et al. (2001). Identification of an axonal determinant in the C-terminus of the sodium channel Na(v)1.2. *EMBO J, 20*, 5950–5961.

Garrido, J. J., Fernandes, F., Moussif, A., Fache, M. P., Giraud, P., & Dargent, B. (2003). Dynamic compartmentalization of the voltage-gated sodium channels in axons. *Biol Cell, 95*, 437–445.

Garty, H., & Palmer, L. G. (1997). Epithelial sodium channels: function, structure, and regulation. *Physiol Rev, 77*, 359–396.

Garver, T. D., Ren, Q., Tuvia, S., & Bennett, V. (1997). Tyrosine phosphorylation at a site highly conserved in the L1 family of cell adhesion molecules abolishes ankyrin binding and increases lateral mobility of neurofascin. *J Cell Biol, 137*, 703–714.

Gatto, C. L., Walker, B. J., & Lambert, S. (2003). Local ERM activation and dynamic growth cones at Schwann cell tips implicated in efficient formation of nodes of Ranvier. *J Cell Biol, 162*, 489–498.

Gentzsch, M., Cui, L., Mengos, A., Chang, X. B., Chen, J. H., & Riordan, J. R. (2003). The PDZ-binding chloride channel ClC-3B localizes to the Golgi and associates with cystic fibrosis transmembrane conductance regulator-interacting PDZ proteins. *J Biol Chem, 278*, 6440–6449.

Goldin, A. L. (1999). Diversity of mammalian voltage-gated sodium channels. *Ann NY Acad Sci, 868*, 38–50.

Gomis-Ruth, S., Wierenga, C. J., & Bradke, F. (2008). Plasticity of polarization: changing dendrites into axons in neurons integrated in neuronal circuits. *Curr Biol, 18*, 992–1000.

Gonzalez-Perrett, S., Kim, K., Ibarra, C., et al. (2001). Polycystin-2, the protein mutated in autosomal dominant polycystic kidney disease (ADPKD), is a Ca2+-permeable nonselective cation channel. *Proc Natl Acad Sci, USA, 98*, 1182–1187.

Grubb, M. S., & Burrone, J. (2010). Building and maintaining the axon initial segment. *Curr Opin Neurobiol, 20*, 481–488.

Haggie, P. M., Stanton, B. A., & Verkman, A. S. (2004). Increased diffusional mobility of CFTR at the plasma membrane after deletion of its C-terminal PDZ binding motif. *J Biol Chem, 279*, 5494–5500.

Hall, R. A., Ostedgaard, L. S., Premont, R. T., et al. (1998). A C-terminal motif found in the beta2-adrenergic receptor, P2Y1 receptor and cystic fibrosis transmembrane conductance regulator determines binding to the Na+/H+ exchanger regulatory factor family of PDZ proteins. *Proc Natl Acad Sci, USA, 95*, 8496–8501.

Hall, T. G., & Bennett, V. (1987). Regulatory domains of erythrocyte ankyrin. *J Biol Chem, 262*, 10537–10545.

Hartwig, J. H. (1994). Actin-binding proteins 1: spectrin superfamily. *Protein Profile, 1*, 706–778.

Heasman, S. J., & Ridley, A. J. (2008). Mammalian Rho GTPases: new insights into their functions from in vivo studies. *Nat Rev Mol Cell Biol, 9*, 690–701.

Hill, A. S., Nishino, A., Nakajo, K., et al. (2008). Ion channel clustering at the axon initial segment and node of Ranvier evolved sequentially in early chordates. *PLoS Genet, 4*, e1000317.

Hirokawa, N., Niwa, S., & Tanaka, Y. (2010). Molecular motors in neurons: transport mechanisms and roles in brain function, development, and disease. *Neuron, 68*, 610–638.

Hollmann, M., Boulter, J., Maron, C., et al. (1993). Zinc potentiates agonist-induced currents at certain splice variants of the NMDA receptor. *Neuron, 10*, 943–954.

Holtmaat, A. J., Trachtenberg, J. T., Wilbrecht, L., et al. (2005). Transient and persistent dendritic spines in the neocortex in vivo. *Neuron, 45*, 279–291.

Kanematsu, T., Mizokami, A., Watanabe, K., & Hirata, M. (2007). Regulation of GABA(A)-receptor surface expression with special reference to the involvement of GABARAP (GABA(A) receptor-associated protein) and PRIP (phospholipase C-related, but catalytically inactive protein). *J Pharmacol Sci, 104*, 285–292.

Kaplan, M. R., Meyer-Franke, A., Lambert, S., et al. (1997). Induction of sodium channel clustering by oligodendrocytes. *Nature, 386*, 724–728.

Kirsch, J., & Betz, H. (1998). Glycine-receptor activation is required for receptor clustering in spinal neurons. *Nature, 392*, 717–720.

Knobloch, M., & Mansuy, I. M. (2008). Dendritic spine loss and synaptic alterations in Alzheimer's disease. *Mol Neurobiol, 37*, 73–82.

Kodippili, G. C., Spector, J., Sullivan, C., et al. (2009). Imaging of the diffusion of single band 3 molecules on normal and mutant erythrocytes. *Blood, 113*, 6237–6245.

Kordeli, E., Lambert, S., & Bennett, V. (1995). AnkyrinG. A new ankyrin gene with neural-specific isoforms localized at the axonal initial segment and node of Ranvier. *J Biol Chem, 270*, 2352–2359.

Kornau, H. C., Schenker, L. T., Kennedy, M. B., & Seeburg, P. H. (1995). Domain interaction between NMDA receptor subunits and the postsynaptic density protein PSD-95. *Science, 269*, 1737–1740.

Kreienkamp, H. J. (2008). Scaffolding proteins at the postsynaptic density: shank as the architectural framework. *Handb Exp Pharmacol*, 365–380.

Kreindler, J. L. (2010). Cystic fibrosis: exploiting its genetic basis in the hunt for new therapies. *Pharmacol Ther, 125*, 219–229.

Lambert, S., Davis, J. Q., & Bennett, V. (1997). Morphogenesis of the node of Ranvier: co-clusters of ankyrin and ankyrin-binding integral proteins define early developmental intermediates. *J Neurosci, 17*, 7025–7036.

Lambert, S., Yu, H., Prchal, J. T., et al. (1990). cDNA sequence for human erythrocyte ankyrin. *Proc Natl Acad Sci USA, 87*, 1730–1734.

Lemaillet, G., Walker, B., & Lambert, S. (2003). Identification of a conserved ankyrin-binding motif in the family of sodium channel alpha subunits. *J Biol Chem, 278*, 27333–27339.

Li, C., Roy, K., Dandridge, K., & Naren, A. P. (2004). Molecular assembly of cystic fibrosis transmembrane conductance regulator in plasma membrane. *J Biol Chem, 279*, 24673–24684.

Li, Q., Montalbetti, N., Shen, P. Y., et al. (2005). Alpha-actinin associates with polycystin-2 and regulates its channel activity. *Hum Mol Genet, 14*, 1587–1603.

Lumpkin, E. A., Marshall, K. L., & Nelson, A. M. (2010). The cell biology of touch. *J Cell Biol, 191*, 237–248.

Ma, X. M. (2010). Kalirin-7 is a key player in the formation of excitatory synapses in hippocampal neurons. *Sci World J, 10*, 1655–1666.

Maas, C., Tagnaouti, N., Loebrich, S., Behrend, B., Lappe-Siefke, C., & Kneussel, M. (2006). Neuronal cotransport of glycine receptor and the scaffold protein gephyrin. *J Cell Biol, 172*, 441–451.

Malhotra, J. D., Kazen-Gillespie, K., Hortsch, M., & Isom, L. L. (2000). Sodium channel beta subunits mediate homophilic cell adhesion and recruit ankyrin to points of cell-cell contact. *J Biol Chem, 275*, 11383–11388.

Malhotra, J. D., Koopmann, M. C., Kazen-Gillespie, K. A., Fettman, N., Hortsch, M., & Isom, L. L. (2002). Structural requirements for interaction of sodium channel beta 1 subunits with ankyrin. *J Biol Chem, 277*, 26681–26688.

Mazzochi, C., Benos, D. J., & Smith, P. R. (2006). Interaction of epithelial ion channels with the actin-based cytoskeleton. *Am J Physiol Renal Physiol, 291*, F1113–F1122.

Melendez-Vasquez, C. V., Rios, J. C., Zanazzi, G., Lambert, S., Bretscher, A., & Salzer, J. L. (2001). Nodes of Ranvier form in association with ezrin-radixin-moesin (ERM)-positive Schwann cell processes. *Proc Natl Acad Sci, SA, 98*, 1235–1240.

Meng, Y., Zhang, Y., Tregoubov, V., et al. (2002). Abnormal spine morphology and enhanced LTP in LIMK-1 knockout mice. *Neuron, 35*, 121–133.

Meng, Y., Zhang, Y., Tregoubov, V., Falls, D. L., & Jia, Z. (2003). Regulation of spine morphology and synaptic function by LIMK and the actin cytoskeleton. *Rev Neurosci, 14*, 233–240.

Michaely, P., & Bennett, V. (1993). The membrane-binding domain of ankyrin contains four independently folded subdomains, each comprised of six ankyrin repeats. *J Biol Chem, 268*, 22703–22709.

Miller, C. (2010). CFTR: break a pump, make a channel. *Proc Natl Acad Sci USA, 107*, 959–960.

Mohler, P. J., Davis, J. Q., & Bennett, V. (2005). Ankyrin-B coordinates the Na/K ATPase, Na/Ca exchanger, and InsP3 receptor in a cardiac T-tubule/SR microdomain. *PLoS Biol, 3*, e423.

Mohler, P. J., Gramolini, A. O., & Bennett, V. (2002). The ankyrin-B C-terminal domain determines activity of ankyrin-B/G chimeras in rescue of abnormal inositol 1,4,5-trisphosphate and ryanodine receptor distribution in ankyrin-B (−/−) neonatal cardiomyocytes. *J Biol Chem, 277*, 10599–10607.

Mohler, P. J., Healy, J. A., Xue, H., et al. (2007). Ankyrin-B syndrome: enhanced cardiac function balanced by risk of cardiac death and premature senescence. *PLoS One, 2*, e1051.

Mohler, P. J., Rivolta, I., Napolitano, C., et al. (2004). Nav1.5 E1053K mutation causing Brugada syndrome blocks binding to ankyrin-G and expression of Nav1.5 on the surface of cardiomyocytes. *Proc Natl Acad Sci USA, 101*, 17533–17538.

Mohler, P. J., Schott, J. J., Gramolini, A. O., et al. (2003). Ankyrin-B mutation causes type 4 long-QT cardiac arrhythmia and sudden cardiac death. *Nature, 421*, 634–639.

Naisbitt, S., Kim, E., Tu, J. C., et al. (1999). Shank, a novel family of postsynaptic density proteins that binds to the NMDA receptor/PSD-95/GKAP complex and cortactin. *Neuron, 23*, 569–582.

Naren, A. P., Cobb, B., Li, C., et al. (2003). A macromolecular complex of beta 2 adrenergic receptor, CFTR, and ezrin/radixin/moesin-binding phosphoprotein 50 is regulated by PKA. *Proc Natl Acad Sci USA, 100*, 342–346.

Niethammer, M., Kim, E., & Sheng, M. (1996). Interaction between the C terminus of NMDA receptor subunits and multiple members of the PSD-95 family of membrane-associated guanylate kinases. *J Neurosci, 16*, 2157–2163.

Noguchi, J., Matsuzaki, M., Ellis-Davies, G. C., & Kasai, H. (2005). Spine-neck geometry determines NMDA receptor-dependent Ca2+ signaling in dendrites. *Neuron, 46*, 609–622.

Ogawa, Y., Oses-Prieto, J., Kim, M. Y., et al. (2010). ADAM22, a Kv1 channel-interacting protein, recruits membrane-associated guanylate kinases to juxtaparanodes of myelinated axons. *J Neurosci, 30*, 1038–1048.

Ong, A. C., & Harris, P. C. (2005). Molecular pathogenesis of ADPKD: the polycystin complex gets complex. *Kidney Int, 67*, 1234–1247.

Orchard, C. H., Pasek, M., & Brette, F. (2009). The role of mammalian cardiac t-tubules in excitation–contraction coupling: experimental and computational approaches. *Exp Physiol, 94*, 509–519.

O'Sullivan, G. A., Kneussel, M., Elazar, Z., & Betz, H. (2005). GABARAP is not essential for GABA receptor targeting to the synapse. *Eur J Neurosci, 22*, 2644–2648.

Otto, E., Kunimoto, M., McLaughlin, T., & Bennett, V. (1991). Isolation and characterization of cDNAs encoding human brain ankyrins reveal a family of alternatively spliced genes. *J Cell Biol, 114*, 241–253.

Palek, J., & Lambert, S. (1990). Genetics of the red cell membrane skeleton. *Semin Hematol, 27*, 290–332.

Pan, Z., Kao, T., Horvath, Z., et al. (2006). A common ankyrin-G-based mechanism retains KCNQ and NaV channels at electrically active domains of the axon. *J Neurosci, 26*, 2599–2613.

Penzes, P., & Jones, K. A. (2008). Dendritic spine dynamics – a key role for kalirin-7. *Trends Neurosci, 31*, 419–427.

Pickett, J., & London, E. (2005). The neuropathology of autism: a review. *J Neuropathol Exp Neurol, 64*, 925–935.

Prat, A. G., Bertorello, A. M., Ausiello, D. A., & Cantiello, H. F. (1993). Activation of epithelial Na+ channels by protein kinase A requires actin filaments. *Am J Physiol, 265*, C224–C233.

Raghuram, V., Mak, D. O., & Foskett, J. K. (2001). Regulation of cystic fibrosis transmembrane conductance regulator single-channel gating by bivalent PDZ-domain-mediated interaction. *Proc Natl Acad Sci USA, 98*, 1300–1305.

Rasband, M. N. (2010). Clustered K+ channel complexes in axons. *Neurosci Lett, 486*, 101–106.

Rasband, M. N., Park, E. W., Zhen, D., et al. (2002). Clustering of neuronal potassium channels is independent of their interaction with PSD-95. *J Cell Biol, 159*, 663–672.

Ratcliffe, C. F., Westenbroek, R. E., Curtis, R., & Catterall, W. A. (2001). Sodium channel beta1 and beta3 subunits associate with neurofascin through their extracellular immunoglobulin-like domain. *J Cell Biol, 154*, 427–434.

Rotin, D., Bar-Sagi, D., O'Brodovich, H., et al. (1994). An SH3 binding region in the epithelial Na+ channel (alpha rENaC) mediates its localization at the apical membrane. *EMBO J, 13*, 4440–4450.

Salzer, J. L., Brophy, P. J., & Peles, E. (2008). Molecular domains of myelinated axons in the peripheral nervous system. *Glia, 56*, 1532–1540.

Sheng, M., & Hoogenraad, C. C. (2007). The postsynaptic architecture of excitatory synapses: a more quantitative view. *Annu Rev Biochem, 76*, 823–847.

Shepherd, J. D., & Huganir, R. L. (2007). The cell biology of synaptic plasticity: AMPA receptor trafficking. *Annu Rev Cell Dev Biol, 23*, 613–643.

Sjoblom, B., Salmazo, A., & Djinovic-Carugo, K. (2008). Alpha-actinin structure and regulation. *Cell Mol Life Sci, 65*, 2688–2701.

Sola, M., Kneussel, M., Heck, I. S., Betz, H., & Weissenhorn, W. (2001). X-ray crystal structure of the trimeric N-terminal domain of gephyrin. *J Biol Chem, 276*, 25294–25301.

Song, A. H., Wang, D., Chen, G., et al. (2009). A selective filter for cytoplasmic transport at the axon initial segment. *Cell, 136*, 1148–1160.

Tackenberg, C., Ghori, A., & Brandt, R. (2009). Thin, stubby or mushroom: spine pathology in Alzheimer's disease. *Curr Alzheimer Res, 6*, 261–268.

Tada, T., & Sheng, M. (2006). Molecular mechanisms of dendritic spine morphogenesis. *Curr Opin Neurobiol, 16*, 95–101.

Tang, Y., Tang, J., Chen, Z., et al. (2000). Association of mammalian trp4 and phospholipase C isozymes with a PDZ domain-containing protein, NHERF. *J Biol Chem, 275*, 37559–37564.

Thaxton, C., Pillai, A. M., Pribisko, A. L., Dupree, J. L., & Bhat, M. A. (2011). Nodes of Ranvier act as barriers to restrict invasion of flanking paranodal domains in myelinated axons. *Neuron, 69*, 244–257.

Tu, J. C., Xiao, B., Naisbitt, S., et al. (1999). Coupling of mGluR/Homer and PSD-95 complexes by the Shank family of postsynaptic density proteins. *Neuron, 23*, 583–592.

Weinman, E. J., Steplock, D., Wang, Y., & Shenolikar, S. (1995). Characterization of a protein cofactor that mediates protein kinase A regulation of the renal brush border membrane Na(+)-H+ exchanger. *J Clin Invest, 95*, 2143–2149.

Winckler, B., Forscher, P., & Mellman, I. (1999). A diffusion barrier maintains distribution of membrane proteins in polarized neurons. *Nature, 397*, 698–701.

Yoo, D., Flagg, T. P., Olsen, O., Raghuram, V., Foskett, J. K., & Welling, P. A. (2004). Assembly and trafficking of a multiprotein ROMK (Kir 1.1) channel complex by PDZ interactions. *J Biol Chem, 279*, 6863–6873.

Yoshihara, Y., De Roo, M., & Muller, D. (2009). Dendritic spine formation and stabilization. *Curr Opin Neurobiol, 19*, 146–153.

Yu, W., Jiang, M., Miralles, C. P., Li, R. W., Chen, G., & de Blas, A. L. (2007). Gephyrin clustering is required for the stability of GABAergic synapses. *Mol Cell Neurosci, 36*, 484–500.

Yun, C. H., Oh, S., Zizak, M., et al. (1997). cAMP-mediated inhibition of the epithelial brush border Na+/H+ exchanger, NHE3, requires an associated regulatory protein. *Proc Natl Acad Sci USA, 94*, 3010–3015.

Zhao, L., Ma, Q. L., Calon, F., et al. (2006). Role of p21-activated kinase pathway defects in the cognitive deficits of Alzheimer disease. *Nat Neurosci, 9*, 234–242.

Zhou, D., Lambert, S., Malen, P. L., Carpenter, S., Boland, L. M., & Bennett, V. (1998). AnkyrinG is required for clustering of voltage-gated Na channels at axon initial segments and for normal action potential firing. *J Cell Biol, 143*, 1295–1304.

Zonta, B., Tait, S., Melrose, S., et al. (2008). Glial and neuronal isoforms of Neurofascin have distinct roles in the assembly of nodes of Ranvier in the central nervous system. *J Cell Biol, 181*, 1169–1177.

Chapter 27

Why are So Many Ion Channels Mechanosensitive?

Catherine E. Morris

Chapter Outline

I. SUMMARY

Reports of stretch-sensitive channels started appearing in the mid-1980s. Briefly, the unidentified mechanosensitive (MS) channels were seen as representatives of a new subclass of channels. There were speculations that "mechano-gating motifs" would soon be discovered. Gradually, however, it emerged that channels showing no mechanosensitivity are the outliers and it became clear that gating energy is supplied by bilayer deformations. Over the last decade, what has been particularly helpful in clarifying the role of bilayer mechanics in the mechanosensitive responses of diverse eukaryotic channels have been converging advances on three fronts: (1) high resolution structure/function data for voltage-gated channels (VGCs); (2) the demonstration that VGCs are inherently mechanosensitive; and (3) experimental and computational data showing how mechanosensitivity emerges from the energetics at the interface of dynamically structured bilayers and dynamically structured proteins. An ongoing task is to establish if and where the reversible mechanosensitive responses of ion channels are physiologically relevant; do they, for instance, contribute to cardiac mechano-electric feedback? Also enormously important, in my view, is to learn what the irreversible MS behaviors of channel reveal about the pathological membrane phenomena associated with trauma, ischemia, inflammation and, in fact, any condition where channel-bearing membranes undergo irreversible structural changes. One likely payoff: "smarter" drugs designed to target not simply channel-X, but channel-X in bilayer-structure-Y – say, leaky sodium channel in nodes of Ranvier where lipid packing has become disorderly and where leaflet asymmetry has been compromised by traumatic brain injury.

II. INTRODUCTION

Even before "channel" entered the physiology lexicon, mechanosensitive (MS) membrane conductances were studied in eukaryotic organisms (Gray and Sato, 1953). Sixty years on, much evidence points to ion channels as the mechanotransducers in vertebrate and invertebrate mechanosensory cells. Transduction channels absorb mechanical gating energy from cytoarchitectural elements arranged to focus and amplify small stimuli; candidates include Peizo1 and Peizo2, proteins with no known homologies (Coste et al., 2010), "TRPs" (transient receptor potentials), multimodal channels with overwhelmingly diverse homologies (Patel et al., 2010) and proteins homologous to "ENaC" (epithelial Na channel) (Cueva et al., 2007). Prokaryotic walled cells express several molecularly unrelated multimeric proteins that, at near-lytic bilayer strain, open as osmolyte channels (Kung et al., 2010); additionally, expanding closed-closed transitions noted for some might serve as membrane spandex, providing tension-relief in high turgor conditions (Boucher et al., 2009). Together, these mechanosensory specialists – unidentified eukaryote mechanotransducers and identified

Cell Physiology Sourcebook. DOI: 10.1016/B978-0-12-387738-3.00027-5

prokayote osmovalves – operate at opposite ends of the mechanostimulus intensity spectrum.

Here I discuss a different phenomenon, that of the many non-specialist ion channels that respond to mechanical stimuli. Non-specialist MS channels, like the prokaryote osmovalve specialists, derive gating energy from bilayer deformation. Eukaryotic mechanotransduction, however, is thought to require stiff vectorial protein assemblies whose gating springs control displacement of a gate (Hudspeth, 2008; Kung et al., 2010) on to a channel that, in stark contrast to the non-specialist MS channels, might be designed to ignore all bilayer "noise".

III. EUKARYOTIC MS CHANNELS – BILAYER STRUCTURE, BILAYER DEFORMATION

Shortly after gigaohm patch-clamp techniques were adopted, reports of stretch-activated cation channels began appearing, first for skeletal muscle, then oocytes (Fig. 27.1A), then everywhere. Early assumptions (Guharay and Sachs, 1984) (1) that these must be MS specialists and (2) that bilayer deformation could not provide sufficient mechano-gating energy to account for the stretch-sensitive activity were dropped (Morris, 1990; Sachs and Morris 1998; Hamill and Martinac, 2001). Interrogated under cell-attached or excised-patch-clamp conditions, it emerged that most channels exhibit mechanosensitivity due, almost certainly, to bilayer deformation (Tabarean and Morris, 2002; Liu et al., 2008). Two reports in 2010 exemplify these points: (1) 20 years after cytic fibrosis transport regulator (CFTR) unitary current was first reported, CFTR was shown to be a "stretch-channel" (Zhang et al., 2010); and (2) a putative cytoplasmic linker protein was shown to be irrelevant, not mandatory, to MS responses of big calcium-activated K channel (BKCa) channels (Wang et al., 2010).

MS cation channels were soon joined by stretch-activated and stretch-inactivated potassium and anion channels, then NMDA-glutamate channels and L-type Ca current (whole-cell recordings were used as well as patches in some cases). Wherever it is sought – from fibroblasts to fish skin to fungi – MS channel activity is found (Morris, 1990, 2001a; Sachs and Morris, 1998; Hamill and Martinac, 2001; Morris and Juranka, 2007a).

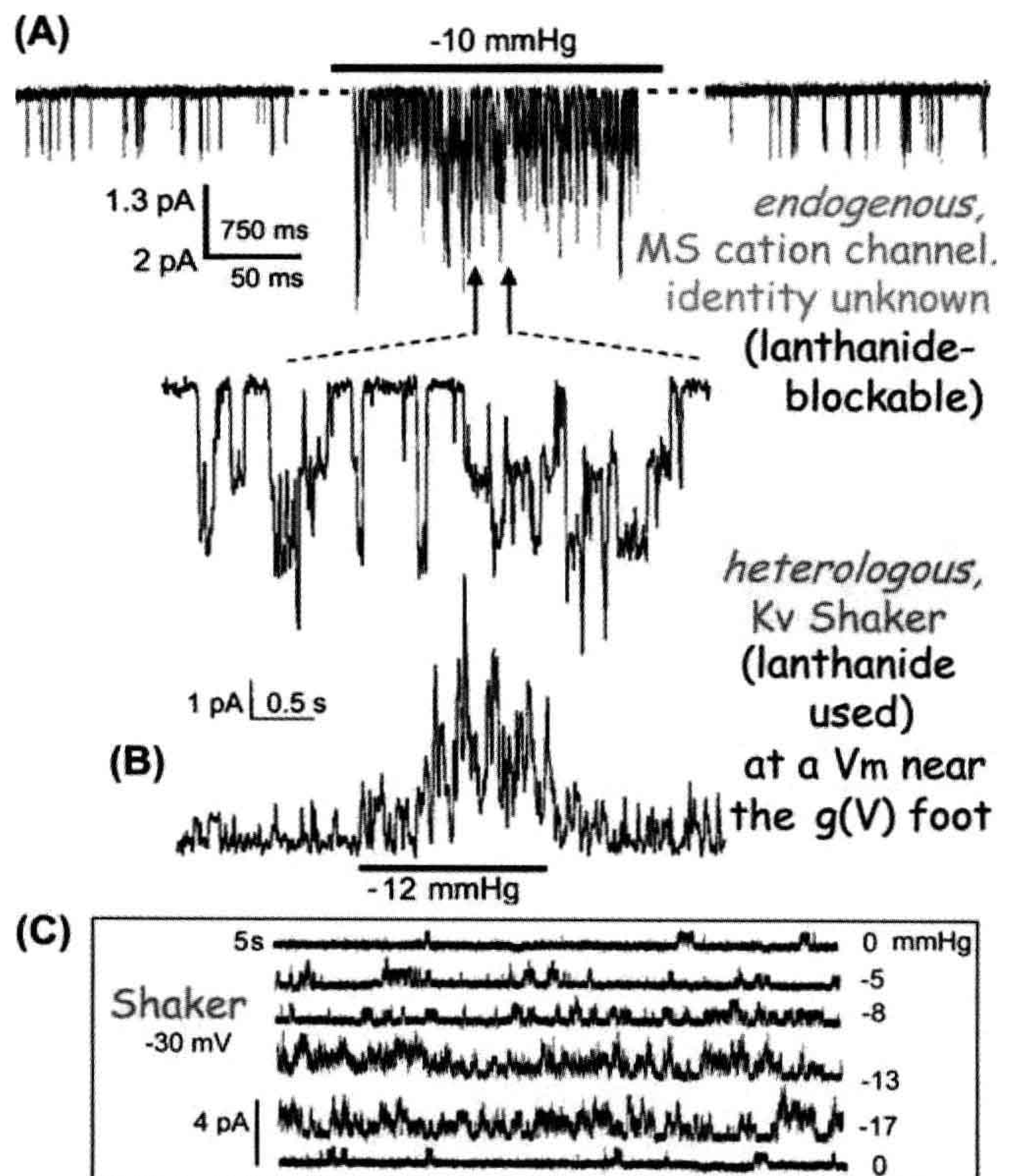


FIGURE 27.1 An unidentified "stretch-activated cation channel" and an equally stretch-sensitive *identified* "stretch-activated" potassium channel (i.e. an archetypical voltage gated K channel, Kv, Shaker WT, inactivation removed) recorded from oocyte patches, before, during and after stretch due to patch suction (A, B) and Shaker current (C) at a fixed voltage near the foot of the Shaker activation Boltzmann, without (0 mmHg), with (−5,−8,−13,−17 mmHg) and again without stretch *(see Gu et al., 2001; Morris and Juranka, 2007a for details).*

Membrane trauma (Fig. 27.2), which implies plastic (irreversible), as opposed to elastic (reversible), changes in membrane structure in response to a mechanical stimulus, can uncover inherent stretch sensitivity in channels normally mechano-protected by a cortical cytoskeleton meshwork (Morris and Horn, 1991; Wan et al., 1999; Hamill and Martinac, 2001; Morris, 2001b; Morris et al., 2006; Liu et al., 2008). Membrane trauma cannot be completely avoided during patch formation and, certainly, patch excision causes plastic changes. Structurally, the plasma membrane becomes a bleb bilayer. During progressive bleb development (Bailey et al., 2009), adhesion to cortical proteins is lost, lateral order in lipids is diminished, lateral mobililty increases and leaflet asymmetry is lost.

In situ, channels could be strongly to weakly mechano-protected, according to the status of the cortical spectrin–actin–myosin membrane skeleton (Morris, 2001b). Local modifications (cellular or subcellular, chronic or transient) might allow for developmentally or physiologically meaningful mechanical signals from channels. To establish convincingly such phenomena, however, identified MS channels with mutant mechano-phenotypes will likely be needed, as will discrete amphiphilic agents that preferentially inhibit (or activate) the identified channels during bilayer deformation (Fig. 27.3).

Disease mutant MS channels in rhythmically active cells (cardiomyocytes, smooth muscle) might provide fertile ground for in situ studies. Consider the contracting, pumping heart. Cardiac rhythm varies with mechanical load and, where causal links exist between mechanical events and cardiac electrophysiology, there is mechano-electric feedback. Voltage-gated channels (VGCs) shape cardiac rhythms and all classes of VGC have proven to be

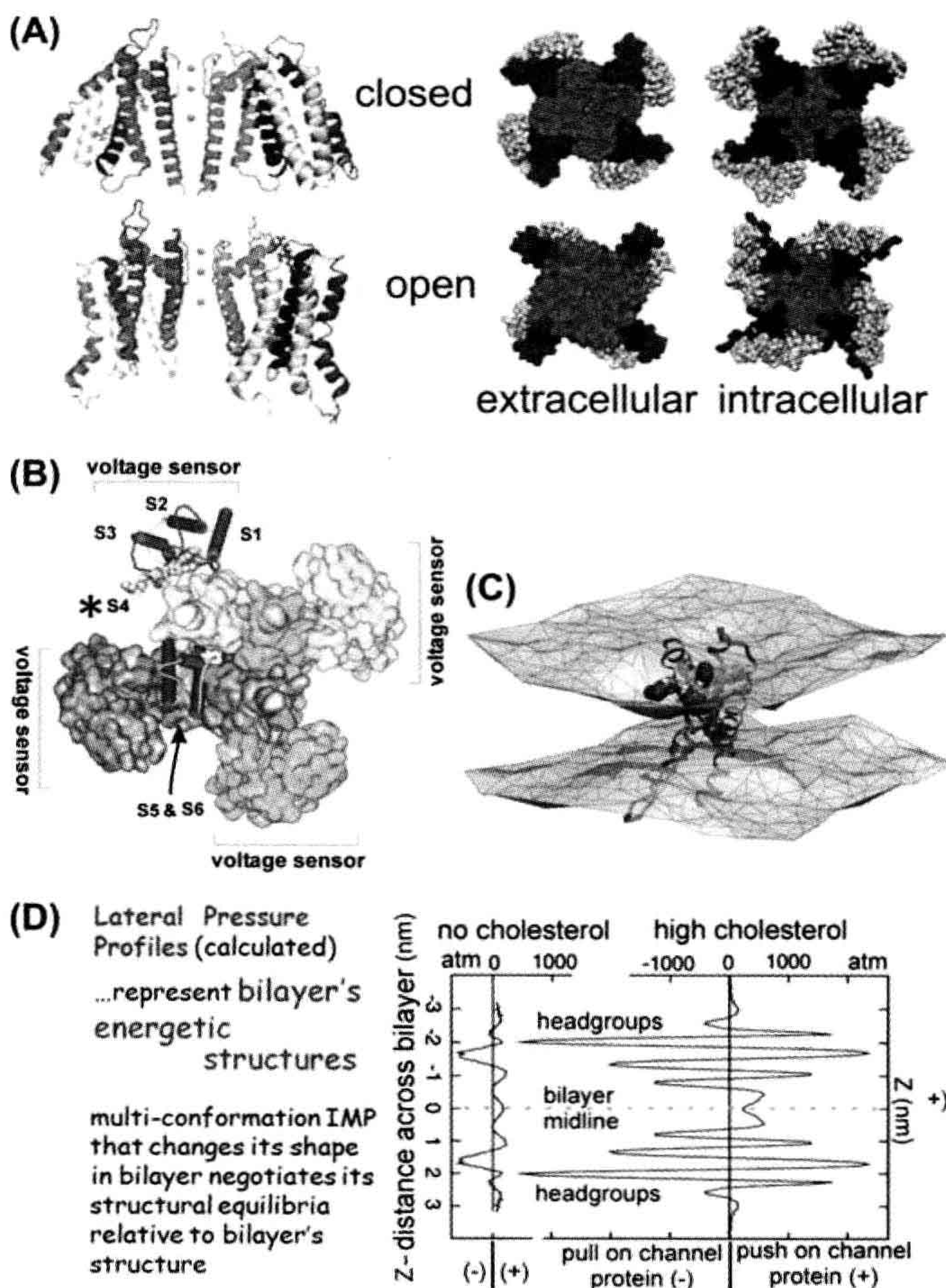


FIGURE 27.2 Protein structure and bilayer structure are interdependent; thence "MS channels". (A) Kv channel, structural models for two conformations. Voltage sensors occupy periphery; note different protein–lipid interfaces and (B) Kv channel indicating peripheral location of S4-based voltage sensors *(A, B modified from Schmidt and MacKinnon, 2008 and references therein).* (C) An activated-state voltage sensor domain locally deforms/thins the bilayer *(modified from Krepkiy et al., 2009).* (D) Different bilayers have composition-dependent structure and energetics. Lateral pressure profiles calculated for symmetric bilayers without/with cholesterol *(see Finol-Urdaneta et al., 2010 for details).*

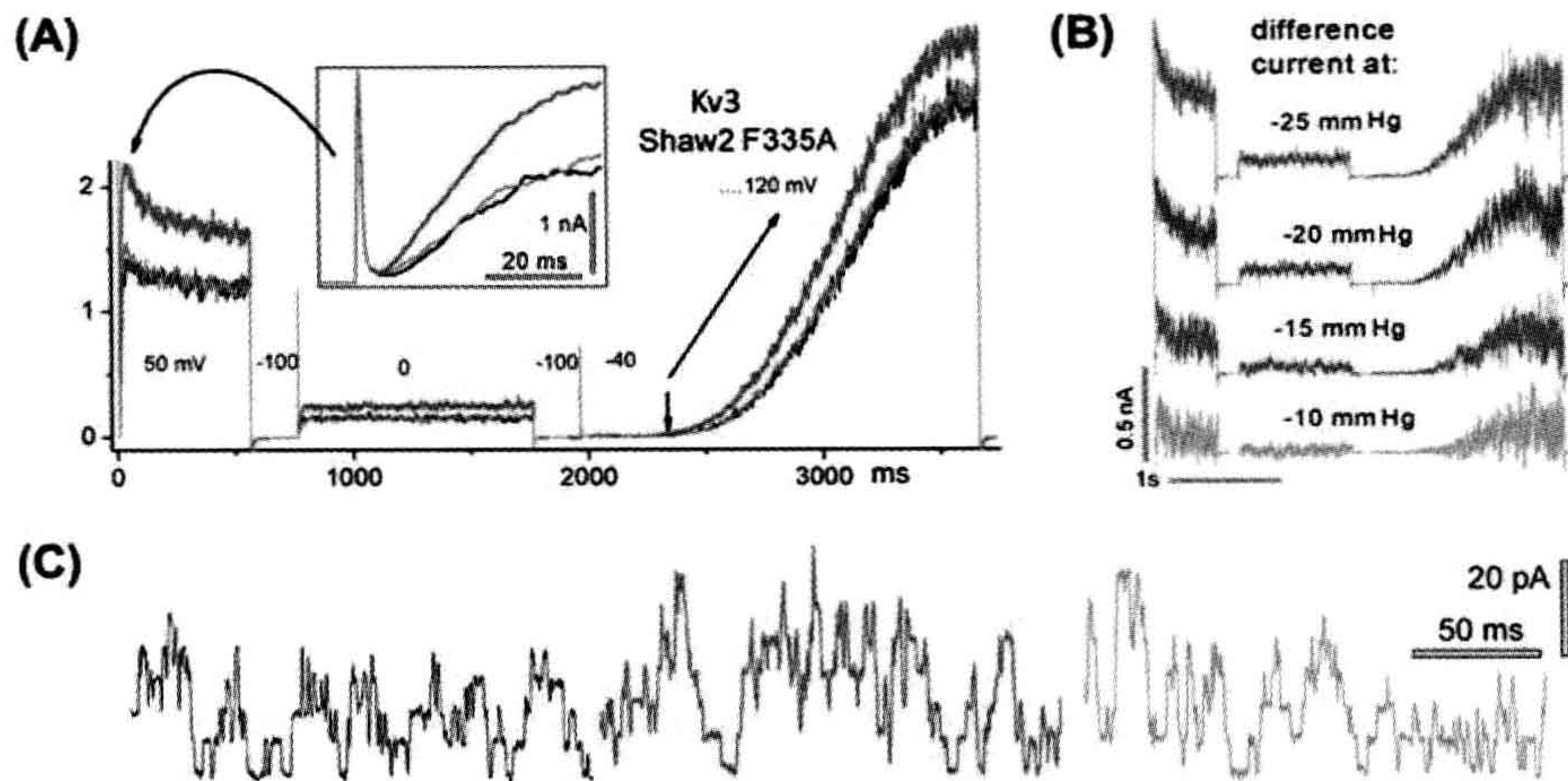


FIGURE 27.3 Kv3 channel activity, before, during and after stretch (black, red and gray traces – same meaning in Figs. 27.6, 27.7, 27.8). (A) Currents during a complex voltage protocol (large then small depolarizing steps followed by a V-ramp); boxed inset, early current); (B) stretch difference currents for different stretch intensities; (C) unitary currents at 0 mV *(see Laitko et al., 2006 for details).*

inherently MS (see Figs. 27.1B,C, 27.4–27.8). To argue a priori that the abundant and ubiquitous VGCs of the myocardium never feel the impacts of shear or stretch forces in the pumping heart would be difficult and yet, evidence showing that any specific MS channel participates in cardiac mechano-electric feedback is lacking. Molecular and genetic tools and modeling approaches now available for VGCs might be usefully exploited to make headway on this question (Morris, 2011a,b).

What can be said, a priori, about ion channel mechanosensitivity? The following: for any structurally dynamic integral membrane protein with >1 bilayer/protein interface conformation, structural deformation of the bilayer will elicit re-equilibration among protein conformations (see Fig. 27.4A). The scope of this simple notion is wide. Consider, for example, voltage-gated sodium channel (Nav) responses in the following circumstances: depletion or addition of membrane cholesterol or fatty acids (Andersen and Koeppe, 2007), traumatic brain injury (Wang et al., 2009), focused ultrasound applied to cortical brain regions (Tufail et al., 2010), stretch of ventricular myocyte sarcolemma (Banderali et al., 2010). Modified

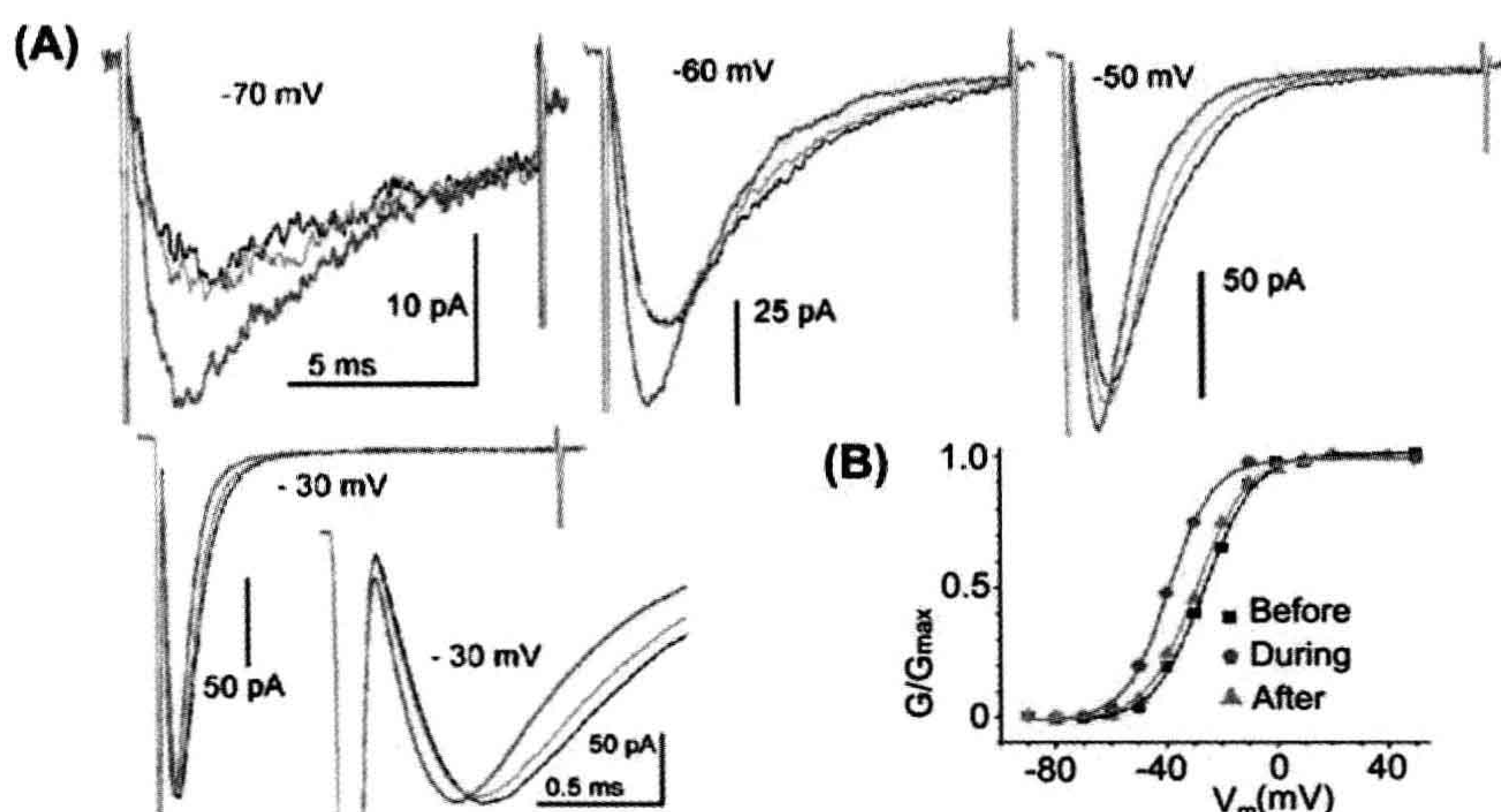


FIGURE 27.4 Nav1.5 currents before during and after stretch. (A) Voltages as labeled; expanded current at −30 mV (which is $\approx g_{max}$) reveals the "purely kinetic" effect of stretch, which is to accelerate current onset and inactivation *(modified from Morris and Juranka, 2007b);* (B) the Nav1.5 g(V) left-shifts reversibly with stretch (due to pipette suction of −30 mmHg) *(modified from Banderali et al., 2010).*

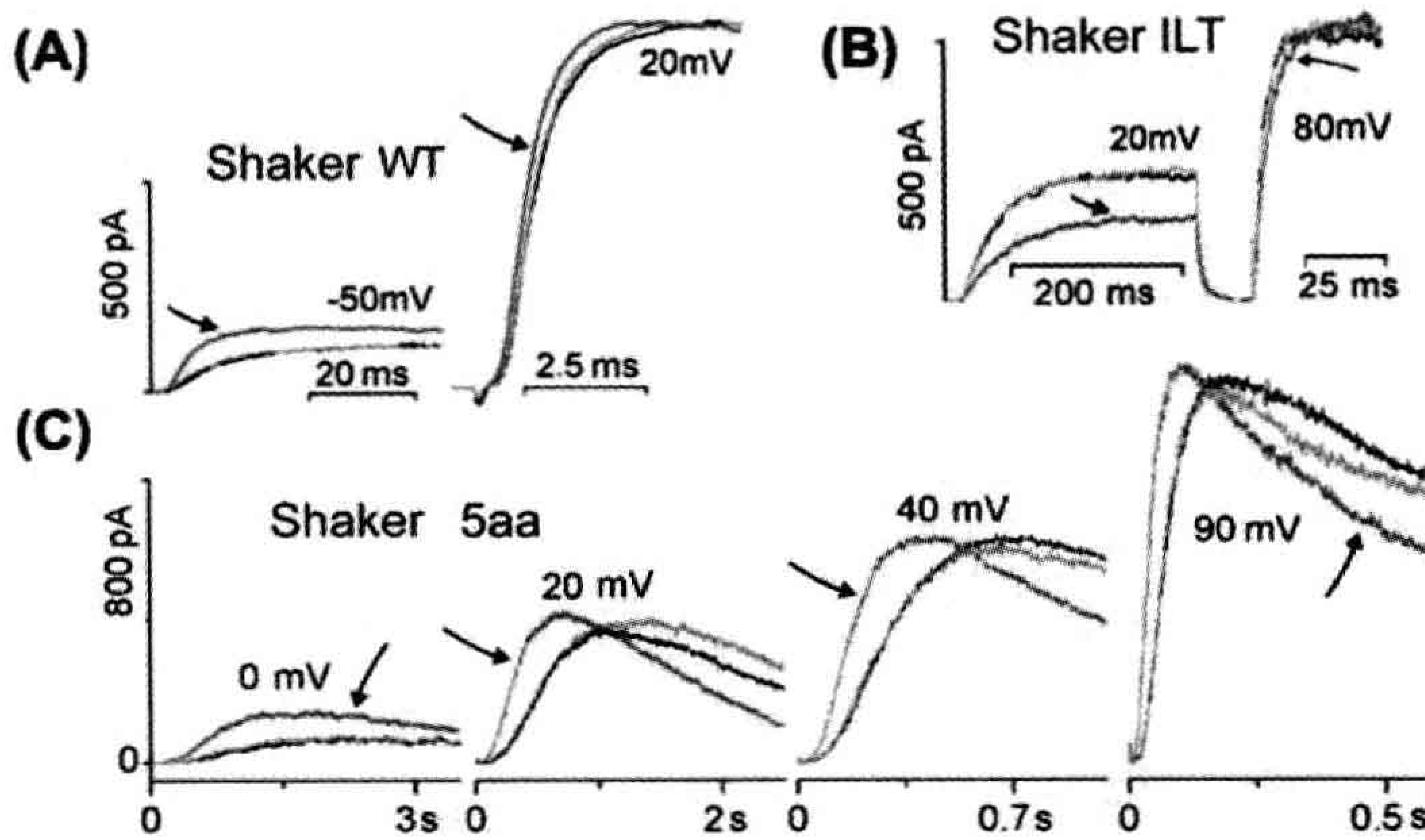


FIGURE 27.5 VGCs are MS channels in which the effects of stretch on particular transitions can be discerned. (A, B, C) Shaker WT and ILT and 5aa as described in the text. Arrows to red traces highlight the during stretch traces. Note that stretch reversibly slows current onset in ILT, while speeding it in WT (as for Nav1.5, the purely kinetic effect is evident at or beyond g_{max}). Not shown, WT g(V) reversibly left-shifts and ILT g(V) reversibly right-shifts with stretch *(see Laitko and Morris, 2004; Laitko et al., 2006 for details).*

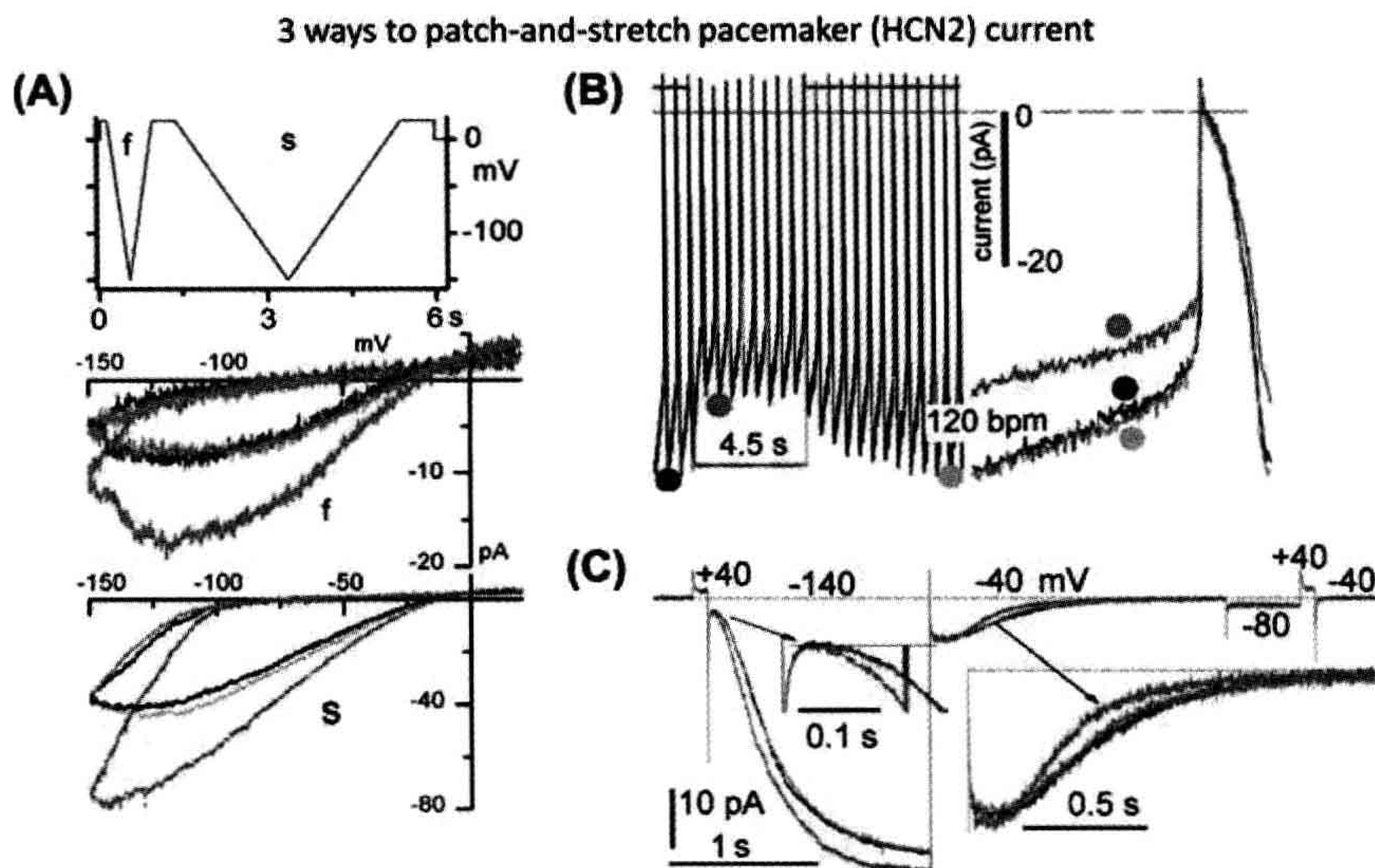


FIGURE 27.6 The pacemaker channel, HCN2, can generate both "SA" and "SI" cation current (*S*tretch-*A*ugmented, *S*tretch-*I*nhibited): (A) V-ramp clamp at two speeds; (B) passive action potential clamp (the net effect under these circumstance: a reversible *stretch-inhibition* of cation current); and (C) V-step clamp reveals stretch acceleration of both HCN2 current onset and turn-off (the turn-off is "equivalent" to Shaker turn-on vis à vis voltage-sensor movements during depolarization). If cells had a background HCN2 conductance, its stretch-accelerated turn-off could be construed as a "SI cation conductance". *(Consult Lin et al., 2007, Morris, 2011a,b, for details.)*

Nav channel activity in each scenario is explained most simply in terms of modified channel/bilayer interactions. This applies generally for VGC channels (Schmidt and MacKinnon, 2008) as well as for Nav channels in particular (Morris and Juranka, 2007a; Wang et al., 2009; Banderali et al., 2010; Morris, 2011b).

"Structure" at the angstroms to tens of nanometers scale encompasses shape, dimensional size and local charge density; together this equates closely to "mechanics". Thus, secondary and tertiary protein structure can be inferred from the set of mechanical forces needed to pull the protein apart from various angles. Applying structure=mechanics thinking to bilayers is fruitful when considering bilayer/membrane protein interfaces (e.g. Butterwick and MacKinnon, 2010). At various depths through the bilayer ("Z"-dimension), bilayer lipids collectively push or pull any embedded protein, with the sign and magnitude of these forces switching dramatically within angstroms (see Fig. 27.4D) and with the Z-dimension integral of push/pull forces in the equilibrated bilayer being zero. For any given

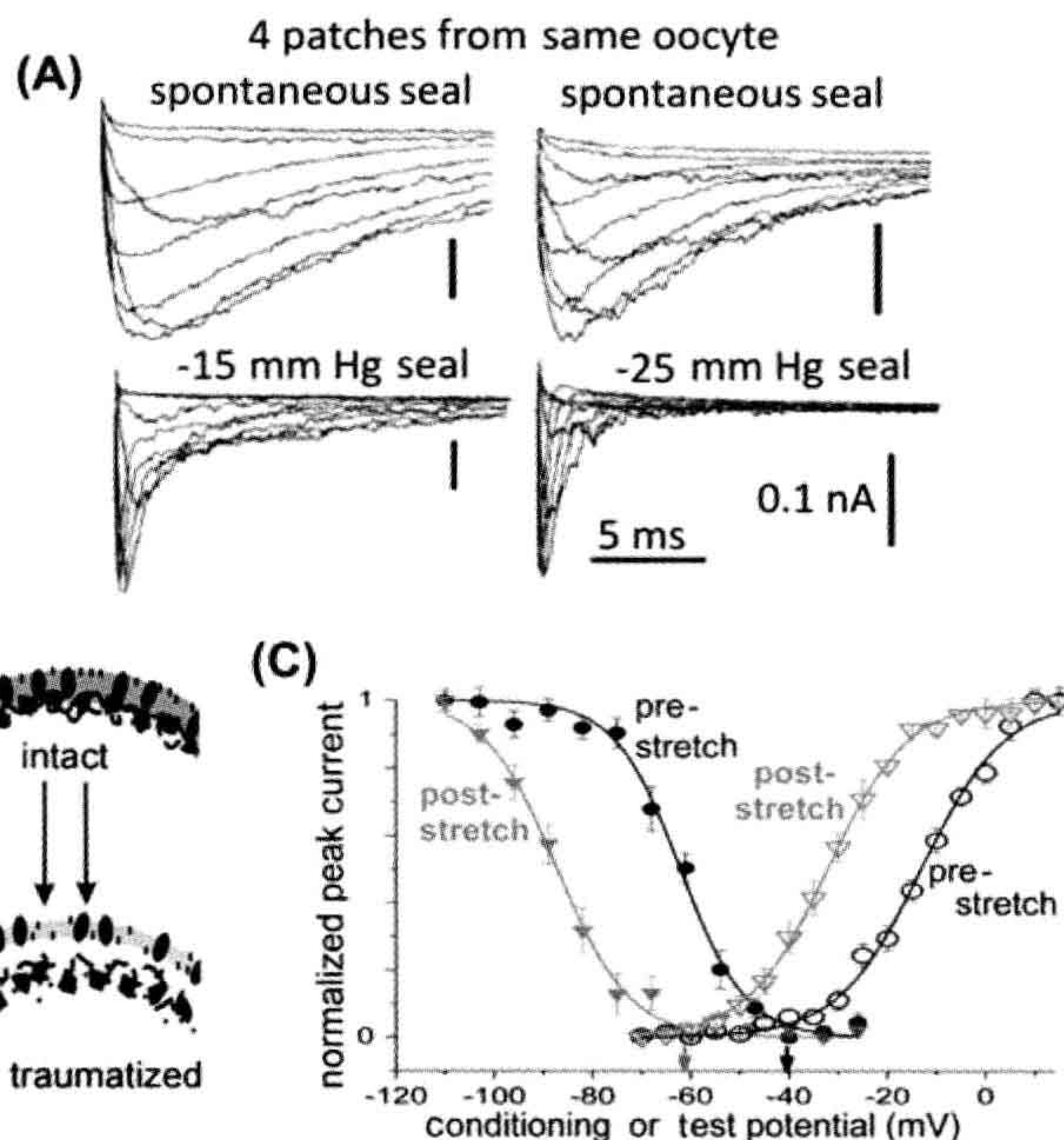


FIGURE 27.7 Membrane trauma can irreversibly alter channel behavior. Trauma here results from gigaohm seal formation accompanied by unintended (A) or intended (C) patch stretch. (A) Four patches, different trauma intensities, same oocyte, Nav1.4 (no beta subunit) current families *(see Morris and Juranka, 2007a; Tabarean et al., 1999).* (B) Membrane trauma that induces bleb formation irreversibly alters the bilayer environment (Δpacking order, Δthickness, Δasymmetry) for channels *(see Wang et al., 2009).* (C) For several VGCs, gating is irreversibly left-shifted by trauma as in this example for Nav1.6 activation and steady-state inactivation *(Wang et al., 2009).*

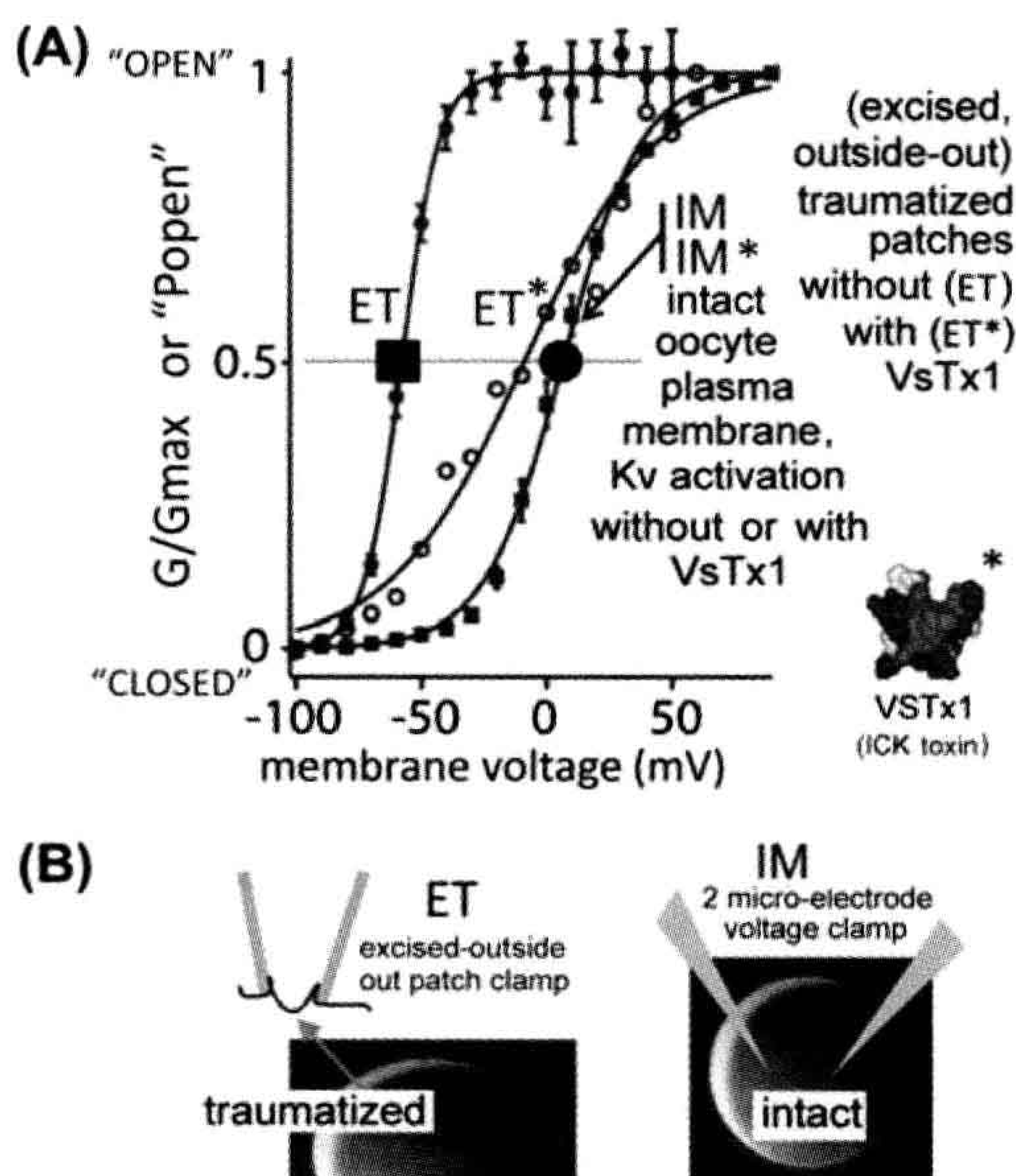


FIGURE 27.8 Bilayer mechanics allows an amphiphilic channel toxin to act like a "silver bullet", targetting only channels in traumatized membrane. A Kv channel that is irreversibly left-shifted by excision trauma (compare g(V) for IM and ET). Kv is unaffected in intact membrane (IM*) by the amphiphilic toxin, VsTx1(*), but is strongly inhibited (right-shifted) by the toxin in traumatized membrane (ET*). *(Modified from Schmidt and MacKinnon, 2008, see further discussion in Morris, 2011a,b).*

bilayer (e.g. Fig. 27.9A,B), this equilibrium "Z-force" summary is its lateral pressure profile (LPP). The prevailing equilibrium (and hence the LPP) can be perturbed by changes in the bilayer's chemical make-up, by applied physical forces (stretch, hydrostatic pressure, enforced curvature) and by temperature changes (Baumgart et al., 2003, 2011; Morris and Juranka, 2007a; Patel et al., 2010; Morris, 2011b).

LPPs are good mnemonics for these ideas, but emerge from calculations, not direct measurements. Channel activity, of course, is exquisitely accessible to measurement. If at least one of a channel's several structural states (i.e. conformations, e.g. open, closed, inactivated, desensitized, partially-open... etc.) differs at the protein/bilayer interface then any bilayer deformation at that interface has the potential to modulate the channel's time-averaged activity and a measurable activity change justifies calling the channel "mechanosensitive".

The first-cloned VGC, Shaker (Kv1), is thus an MS channel based on its response to patch stretch (see Figs. 27.1B,C and 27.7). More generally than just stretch, one can alter bilayer thickness and orderliness by pressure, temperature and by removal/addition of multitudes of different amphiphiles (e.g. fatty acids, cholesterol, sphingomyelin, alkanols, drugs, soluble gases). For "MS-channel-X", each of these bilayer mechanical perturbors could alter the probability of being open (P_{open}) in some fashion. VGCs behave this way (Tilman and Cascio, 2003;

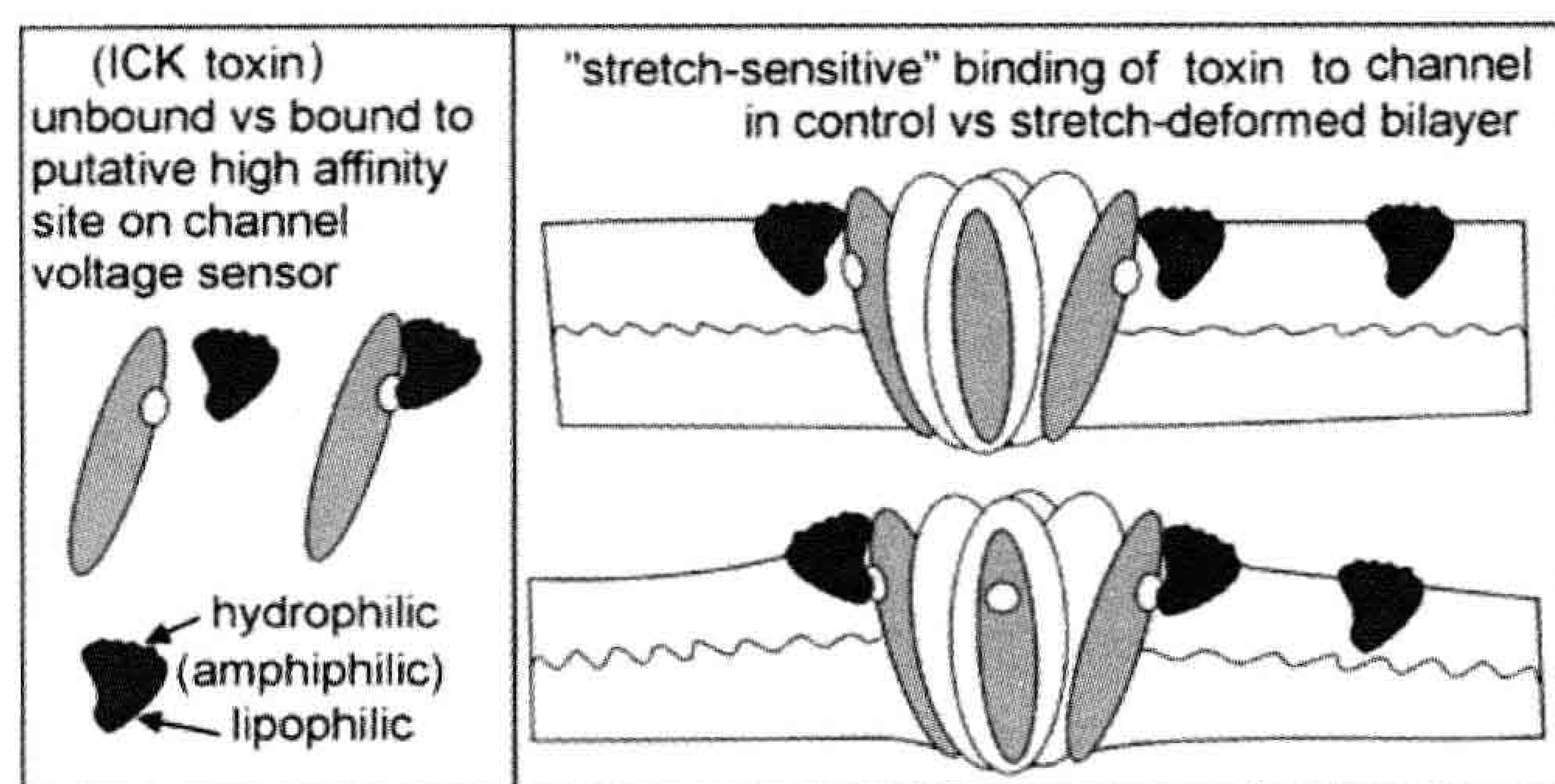


FIGURE 27.9 The efficacy of amphiphilic ICK peptide voltage sensor toxins depends on bilayer mechanics and so some of these toxins might be stretch-sensitive as cartooned here. Other classes of amphiphilic peptide agents with specific binding targets on different classes of channels or non-channel membrane proteins are likely to share this feature *(see Morris, 2011a,b)*.

Andersen and Koeppe, 2007; Morris and Juranka, 2007a; Finol-Urdaneta et al., 2010), but "MS-channel-X" encompasses the whole alphabet soup of channel families, from ATP-binding cassettes (ABCs) to ligand-gated ion channels (LICs) to VGCs. Moreover, any multiconformation membrane protein with >1 lipid/bilayer interface structure could be mechanosensitive even though "read-outs" might be trickier in, say, Na/K pumps or Na/Ca exchangers than in Nav, Cav, Kv channels. Thanks to precision readouts from rhodopsin, G-protein coupled receptor bilayer mechanics are rather well understood (Soubias et al., 2010). At the brutal extreme of cytomechanics, gross perturbation of bilayers embedding rhodopsin and axonal Nav channels might explain "seeing stars" and "knock-out punches" (Wang et al., 2009).

IV. CHANNEL MECHANOSENSITIVITY – TUNING OF CHANNEL BEHAVIOR

Fine-tuning of membrane protein function via bilayer structure can have major implications for development, for physiology and for biomedicine (pathology/pharmacology/anesthesiology). Mass spectrometry-based membrane lipidomics is uncovering enormous diversity among bilayer lipids (Shevchenko and Simons, 2010). Understanding their contributions to general bilayer structure and to particular protein/bilayer interfaces will be a task of many years, but already there are big changes. Until recently, the plasma membrane bilayer was seen mostly as a two-dimensional amphiphilic solvent that reliably orients membrane proteins while simultaneously providing an osmotic barrier to define intra- from extracellular. Lipid imaging, biochemistry (Shevchnko and Simons, 2010; Baumgarten et al., 2011) plus high-resolution channel structures (Schmidt et al., 2009) and computational approaches (Marsh, 2008; Krepkiy et al., 2009; Patel et al., 2010; Baumgarten et al., 2011) have helped bilayers garner respect. No longer are VGCs routinely depicted as cylinders with fixed lateral walls or cartooned with their voltage sensors sequestered from bilayer lipids. Structural models of VGCs now depict protein/lipid interfaces regions for different conformations (e.g. open-like and closed-like for Kv channels (see Fig. 27.4A) with different lateral interfaces.

Bilayers at their most basic are established and maintained by thermally-driven processes; they continually self-organize, minimizing the system's free energy (Boal, 2001). Channel activity too is thermally-driven, as is directly evident from unitary currents, whose stochastics, quantified for different conditions, yield "channel kinetics".

e.g. for a one-Nav-channel membrane patch, step 1000X from −100 mV to 0 mV, make a 1000-item histogram of the random-lengthed times-till-first-opening, from plotted histogram obtain the characteristic "first latency" at 0 mV. Repeat for steps to different voltages, plot voltage-dependence of this kinetic parameter. Likewise for open times and closed times (Horn and Vandenberg, 1984).

Taken together, these susceptibilities to thermal energy predict that the rates at which channel conformation changes occur will vary as bilayer structure is varied. Bilayer structure and protein/bilayer interface structure are both subject to the thermal environment; protein and bilayer will therefore accommodate each other structurally (Marsh, 2008). This mutual accommodation has "real-time" consequences – i.e. consequences on the time scales characteristic for activity in any particular channel, whether P_{open} changes re-equilibrate over hundreds of microseconds or hundreds of milliseconds.

To illustrate this last point, consider how stretch affects fast and ultra-slow variants of a particular VGC channel (Tabarean and Morris, 2002). In both, stretch of a given intensity accelerates activation approximately the same-fold. Not, that is, by the absolute amount, but by the same relative amount (say, 1.6-fold). For both channels, stretch tips the relevant energy landscape the same number of kT units. In a Boltzmann equation for $P_{open}(V)$, i.e. for ([open]/[open+closed])(V), the affected term is that for the

conformational energy difference between the two states, which is "the pre-exponential term" in an Arrhenius equation for thermally-activated exponential behavior. Imagine a generic VGC in a membrane whose voltage corresponds to the activation-Boltzmann midpoint for that channel: by definition, the VGC is equally stable open or closed. Single-channel recordings under such conditions directly reveal thermal energy nudging a Kv channel (say) back and forth between open and closed. Now, change the bilayer structure via stretch (see Fig. 27.1C), for example, or via hyperbaric pressure see Morris and Juranka, 2007a) or via amphiphiles (Fig. 27.10) (Andersen and Koeppe, 2007; Finol-Urdaneta et al., 2010; Patel et al., 2010). Voltage is unchanged but the channel has a new P_{open}. These considerations apply for elastic (reversible) change and also for plastic change, like the irreversible bilayer restructuring that occurs when membranes bleb due to trauma, ischemia and inflammatory conditions (see Fig. 27.2).

Bilayer mechanics operate when a bilayer/protein interface structure impacts channel function. Outside the purview of bilayer mechanics is a lipid (e.g. an inositol phosphate) behaving as a ligand at a discrete binding site in a channel. Nevertheless, like ligands or covalent modifications, bilayer-structure-changing amphiphiles extend or "tune" the behavioral repertoire of a membrane protein (Tillman and Cascio, 2003). One gene product in three quite different bilayers is like three slightly different gene products in one bilayer. Auditory hair cells use structural tuning on many fronts to optimize mechano-electrical signaling over the auditory spectrum frequencies. In outer hair cells, electromechanical signaling involves prestin, a charge-transferring membrane protein whose in-plane expand/contract conformation changes generate cellular motion. Since cholesterol and fatty acid levels affect the rates of those transitions (Nilsen et al., 2011), it is inevitable to wonder if prestin "resonances" occur along the cochlea's low-high frequency axis, associated with a gradient of peri-prestin lipid-packing density.

V. VGCs AND THE MECHANOSENSITIVITY OF DISCRETE TRANSITIONS

Voltage sensor proteins in their activated conformations elicit a local (nanometers) thinning of the bilayer (Krepkiy et al., 2009) so, unsurprisingly, membrane stretch favors activated states of VGCs. This cavalier-sounding sentence could not have been written before late 2009 (see Fig. 27.5C) but it is now evident that applied stretch would relieve a voltage sensor of some of the bilayer-thinning work it must do to go from resting to activated. More than for most other classes of membrane protein, structure/function relations of VGCs, especially for voltage-gated K channels (Kv) (Bezanilla, 2008; Schmidt et al., 2009; Hulse et al., 2010) are getting less mysterious. Fortunately, the message of this section, that protein dynamics and

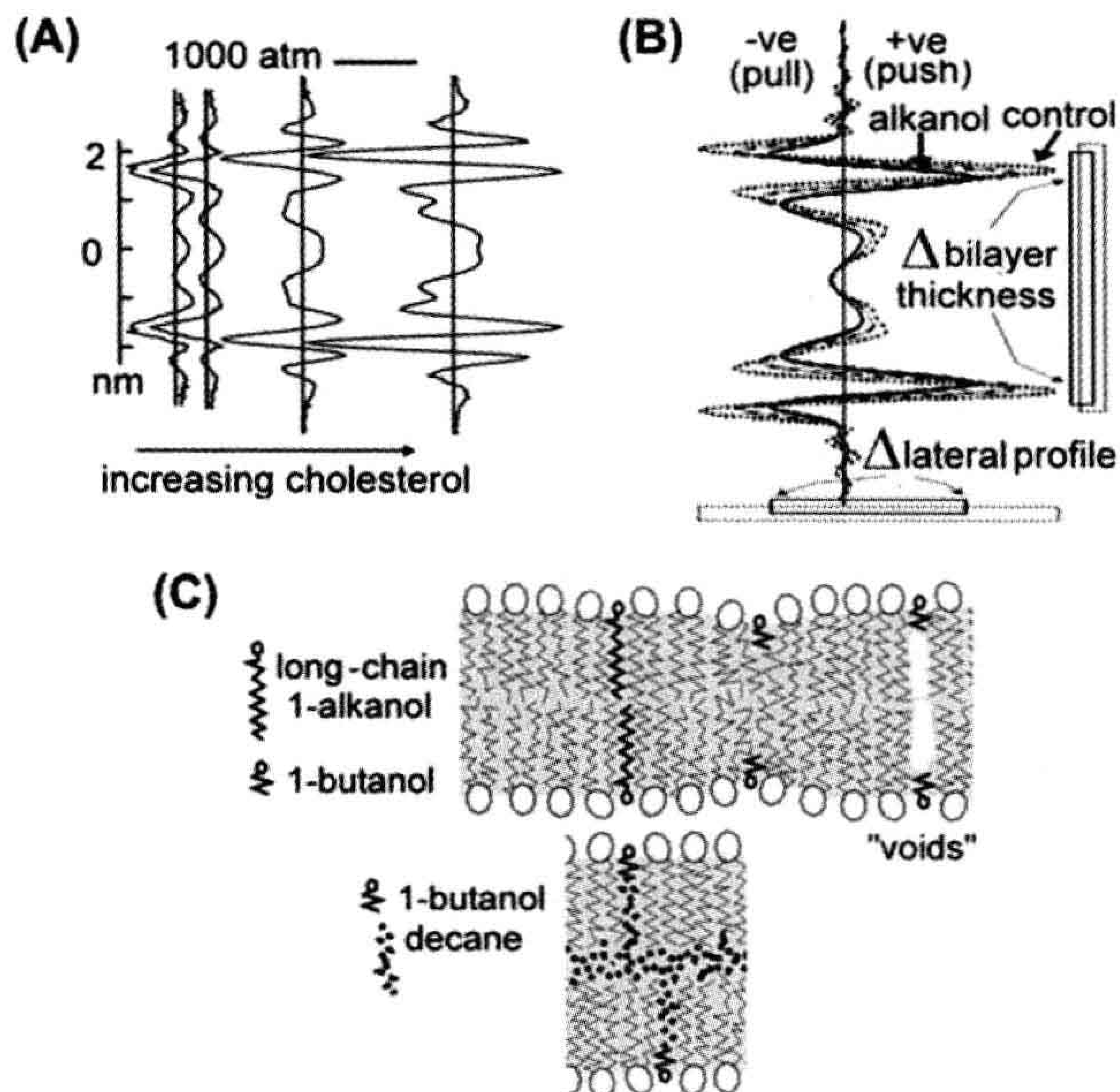


FIGURE 27.10 Calculated LPPs for two different symmetrical bilayers. To each is added increasing abundances of (A) cholesterol and (B) a short chain alkanol. In (C) top, a cartoon depicts impacts of short- and long-chain alkanols in a "bio-bilayer" or any other solvent-free membrane. The planar bilayers from which data in Figure 27.10 were obtained, did have solvent – decane; as cartooned below, a short-chain alkanol can team with decane (which prevents "void collapse") and thus behave like a long-chain alkanol *(see Finol-Urdaneta et al., 2010 for details).*

bilayer structure interdependencies are becoming reasonably explicable, extrapolates to other multiconformation integral membrane proteins (Patel et al., 2010).

Voltage-clamped VGC currents monitored for tens of microseconds to hundreds of seconds allow fast and slow VGC conformation changes to be monitored, yielding gating current, i.e. charge movement associated with voltage sensor motions, and ionic current, i.e. ion flow through a channel's selectivity filter pore or its omega-current pathways. Simultaneously monitored site-directed fluorescence signals provide read-outs about protein movements. Given the resulting database, discrete conformation changes in VGCs can be monitored in conjunction with bilayer mechanical perturbations in cells or artificial bilayers (Schmidt and MacKinnon, 2008; Finol-Urdaneta et al., 2010). Reversible patch stretch is the simplest case to consider. A stretched bilayer will have more disorderly hydrocarbon tails at mid-plane. In a stretched bilayer, the changed propensity for hydrophobic mismatch at any channel/lipid interfaces will have to be compensated.

In Kv1 and in Nav channels, the rate-limiting voltage dependent transition for activation is, it turns out, also a stretch-sensitive transition: in these VGCs, current turn-on accelerates with stretch (Laitko and Morris, 2004; Banderali et al., 2010). In other VGCs, including Cav and Kv3, stretch increases P_{open} without any change in the speed of current turn-on (Calabrese et al., 2002; Morris, 2011a). Since the rate-limiting (*slowest*) transition in the voltage activation pathway of these channels is indifferent to stretch, it probably occurs remote from the bilayer interface.

"ILT" is a mutant Kv1 channel useful because its rate-limiting activation transition happens after the one mentioned above in wild-type (WT) Kv1 channels. In WT-Kv1, each of four identical subunits responds independently to a depolarizing step. Those rate-limiting motions make activation in WT Kv1 current a fourth order process (which, as indicated already, *accelerates* with stretch). In ILT-Kv1, the next step in the activation pathway, a highly cooperative or "concerted" transition (four subunits together) has been rendered so sluggish that it becomes the slowest step. In ILT-Kv1, as a consequence, activation is a first order process and, interestingly, membrane stretch *decelerates* (see Fig. 27.7B) that single-exponential current onset (Laitko et al., 2006; Morris, 2011a).Thus, for Kv1 in a stretch-deformed bilayer, the independent sensor motions become easier to achieve while the concerted transition becomes harder.

These stretch experiments indicate that in Kv1, concerted and independent transitions both "see" the bilayer interface, while the less-understood rate-limiting activation transitions in Kv3 and Cav do not. What of inactivation transitions? In Nav1.5, the cardiac sodium channel, fast inactivation is a "particle-binding" process strongly coupled to activation but not directly affected by stretch either in WT or in disease mutant-Nav1.5 channels with impaired fast inactivation; in both, stretch accelerates fast inactivation only secondarily, via activation (Banderali et al., 2010). By contrast, for Kv1 slow inactivation (a selectivity filter-occlusion process unrelated to Nav inactivation), stretch is a direct accelerator, distinct from its action on activation (Laitko and Morris, 2004).

Short-chain alkanols (e.g. butanol) are excellent chemical agents for reversibly perturbing bilayer mechanics but, over the years, the qualitatively different, albeit comprehensible, behavior of alkanols and cholesterol in solvent-containing (planar) bilayers versus natural membranes has generated confusion (see Fig. 27.9). Recent work shows that, in KvAP channels, gating kinetics and conductance (see Fig. 27.10) respond simultaneously to these surface active agents (Finol-Urdaneta et al., 2010).

VI. BILAYER STRUCTURE IN X, Y AND Z – ONE LPP HERE, ANOTHER LPP THERE

Except in broad biochemical physics terms, plasma membrane bilayer structure in living cells is poorly understood (Shevchenko and Simons, 2010). In the X-Y plane, bilayer structures are non-uniform vis à vis lipid species distribution, leaflet asymmetry, thickness, orderliness and curvature (Baumgart et al., 2010). Sustained high curvature requires protein aggregates, asymmetry requires ATP-flippase activity. Concentrations and arrangements of lipid species of each situation remain to be characterized. Thickness and order differences readily quantified in model systems (Baumgart et al., 2003) are hard to detect in living cells; subdomains in mammalian cells at physiological temperatures are in the 10–200 nm range (Shevchenko and Simons, 2010).

Fluorescent lipid probes like laurdan align parallel to hydrophobic tails of phospholipids in bilayers, emitting at different wavelengths according to nano-environment fluidity/water content. In a fascinating precedent using laurdan, distinctive bilayer heterogeneity is seen in living transparent zebrafish embryos (Owen et al., 2010), poikilotherms for whom lower temperatures are physiological. Gut epithelial cells express transporters and channels differentially along their apical-to-basal axis, so it is fascinating to see, in situ, clear apical-to-basal polarization in the lipid orderliness of living gut cells.

Elevated cholesterol and sphingomyelin typically correlate with thicker more orderly bilayer domains and unsaturated fatty acid with thinner more disorderly bilayers. Large hydrostatic (hyperbaric) pressures increase bilayer thickness by virtue of denser lateral packing (more order), whereas bilayer stretch and elevated temperature both cause thinning and greater disorder. Short-chain

alkanols (e.g. butanol) thin native bilayers and increase mid-plain disorder while reducing surface (interfacial) tension (imposed stretch, by contrast, increases the interfacial tension). Lipid molecules differ in shape, size, internal rigidity, headgroup charge and charge dispersion. These molecular features of lipids collectively determine bilayer structure and hence the energetics (Andersen and Koeppe, 2007; Patel et al., 2010) of bilayer/protein interfaces, collectively, modulating the stability of different membrane protein conformations (Morris and Juranka, 2007a).

Channels have some lipid requirements outside the "bilayer mechanics" repertoire. Kv channel activation, for example, has an absolute requirement for phosphatidylphosphate/S4-arginine interactions (see Schmidt et al., 2009). Stereo-specific binding of amphiphilic voltage sensor toxins occurs at lipid-embedded voltage sensor sites; this, too, is not bilayer mechanics (see Finol-Urdaneta et al., 2010). Nevertheless, the global efficacy of voltage sensor toxins is strikingly sensitive to bilayer mechanics (see Figs. 27.3 and 27.11) (Schmidt and MacKinnon, 2009; see Morris, 2011b).

Specific binding of inner leaflet cholesterol molecules to discrete locations abutting the transmembrane domains of a Kir channel (Rosenhouse-Dannntsker et al., 2011) appears to be an intriguing instance of a channel using its cytoplasmic domains to regulate the LPP at its own bilayer/protein interface. Could "bilayer auto-mechanics" be the appropriate term here? It seems likely that comparable provisions will turn up in other channels.

The idea that healthy plasma membrane bilayer structure represents a controlled disequilibrium has just begun to be contemplated. Bilayers of living cell plasma membranes have asymmetrical leaflets. The exo-leaflet has little phosphatidyl serine or phosphatidyl ethanolamine and abundant phosphatidyl choline. Vice versa for the cyto-leaflet. ATP-dependent lipid flippases generate asymmetry at endomembrane stages. Properly arrayed adherent proteins help maintain the asymmetry. As has long been recognized for apoptotic blebs, the blebbed membrane of cells in traumatized, ischemic and inflamed tissue loses bilayer asymmetry, but the consequences for channel function have received little attention. In mechanically blebbed membrane, some Kv and Nav channels activate at pathologically hyperpolarized potentials (Schmidt and MacKinnon, 2008; Wang et al., 2009) (see Figs. 27.2C and 27.11A). In ischemic tissue, bilayer disorder due to ATP-starved flippases might achieve the same effect.

Having contemplated bilayer asymmetry, we turn back to symmetric spontaneously-formed bilayers and the lateral pressure profile (LPP) summary of Z-dimension energetics. Extensive formation of weak, thermally-labile bonds (van

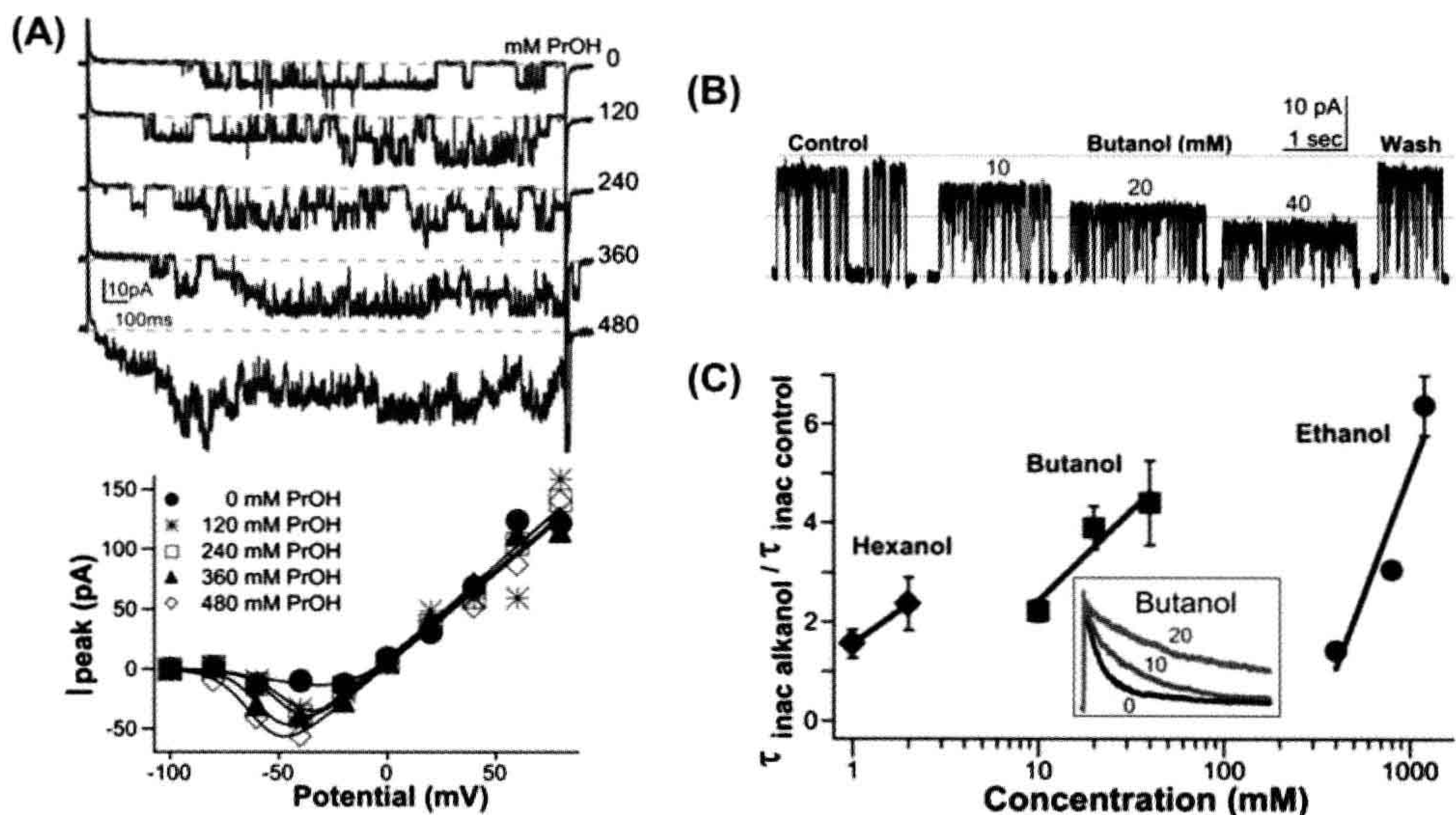


FIGURE 27.11 Surface active agents modulate gating and unitary conductance of a Kv channel in a planar bilayer. (A) KvAP currents traces with increasing abundance of propanol, and below, progressively more left-shifted I/V relations; perhaps short-range bilayer thinning required for voltage sensor activation (see Fig. 27.1C) becomes easier with small alkanols present. (B) Open KvAP in the presence of bilayers of increasing packing order (due to butanol teamed with decane; see Fig. 27.9C) shows a decreasing unitary conductance. (C) Slower entry of KvAP into its slow inactivated state (the state seen in Kv crystal structures) correlates with increased packing order due to alkanols-plus-decane (inset, normalized currents, as labeled) *(see Finol-Urdaneta et al., 2010 for details).*

der Waals, hydrophobic and electrostatic interactions and hydrogen bonds) underlies the free energy minimization that characterizes structural equilibrium. This maximizes the interactions among the lipids' hydrocarbon tails and maximizes water—water interactions. The outcome is minimal contact between water and lipid-"grease", while the lipids' charged-or-polar headgroups are constrained to the two X,Y-plane interfaces separating hydrocarbon from water.

The terms tension, surface tension, interfacial tension, pressure and force are sometimes confusing in bilayer contexts. As in protein structural energetics, forces, in energy units, are what matter. A tension is a force per unit length and pressure is force per unit area. Note that "compression" can take on contradictory context-specific usages. Some speak of a force locally compressing the bilayer where hydrophobic mismatch causes *local thinning*. Others use it for global bilayer compression under hydrostatic pressure, which causes *global bilayer thickening*. In an LPP, "lateral pressures" can be in the ± 1000 atm range; these are forces acting over some infinitisimally small "area" encircling an imaginary cylinder in the Z-axis. "Living" bilayers with metabolically forced leaflet asymmetries and/or curvatures (Marsh, 2008), sustained in part by peripheral and integral membrane proteins, will be non-equilibrium structures whose LPPs need not integrate to zero. Since membrane proteins are evolutionarily "designed" for asymmetric cholesterol-rich bilayers but crystallized without them, accommodations (Marsh, 2008) to those absences can be expected in even the most elegant of high-resolution structures.

In the LPPs of Figs. 27.4 and 27.9, bilayer thickness is defined by the distance between the two strongly negative lateral pressure regions at the bilayer—water interfaces. Just exterior to that, repulsions between polar headgroups create a smaller positive pressure; positive pressures tend to compress circumferentially any embedded protein. Interacting lipid tails exclude water where pressures go negative at the two bilayer edges. These narrow zones of intense negative pressure will tend to pull circumferentially on any embedded protein (think "suction" from any embedded protein's point of view) as the lipids fight successfully to stay together. LPPs can be highly structured along Z or flatter. Whereas cholesterol dramatically increases Z-structure in an LLP, addition of short chain alkanols flattens it out. Most eukaryotic membranes are cholesterol-rich in both leaflets, as well as being asymmetrical and so, presumably, most have considerable "Z-structure". The consequence of adding short alkanols to a membrane is colloquially called "lowering the surface tension" (by analogy to the lowering to air—water interfacial [surface] tension upon addition of alcohol), but in reality, the *entire* LPP is "lowered" (i.e. flattened). I mention this to emphasize that any "surface active agent", even if it does not readily cross the bilayer, acts (energetically) *across the entire LPP* of a bilayer.

LPPs for biological (asymmetrical) bilayers would differ among cell types and among subdomains in a given cell. If membrane protein X occurs where there are different LPPs, both its basic behavior and its responses to amphiphiles will vary whenever the LPP varies. Imagine Channel-X (or GCPR-Z) in diverse neurons with different LPPs. Add amphiphile-A (e.g. propofol) or cocktail-Y (e.g. ethanol + resveratrol + tetrahydrocannabinol + dimethyletcetera). Channel-X (or GCPR-Z) will surely show LPP-dependent "side-effects" when confronted with amphiphile-A or cocktail-Y in quantities sufficient to alter LPPs. Membrane proteins whose conformation changes do not occur at bilayer interfaces could avoid amphiphile modulation but, for VGCs and GCPRs, at least, as well as for all the other MS channels, this is not an option.

VII. PHYSIOLOGY? READ WITH CAUTION. PROCEED WITH CAUTION

When it comes to physiology and MS channels, the arena is littered with flawed reports in the highest impact journals and elsewhere. An amazing dynamic range of a few centimeters of water (pipette aspiration pressure) for MS channel activity... surely that indicates exquisitely stretch-sensitive channels? No, it indicates that the so-called "manometer" was corked. Or, readily evident cut-and-paste errors at four points in a report claiming to have cloned an MS calcium-permeant channel – retracted, surely? No, just a "report clarification". The irreproducible "cloning" of ENaC and of TRPC1 as calcium-permeant MS-channels – retracted? No, but at least the latter effort was "revisited". A fundamental problem has been lack of proper controls. In our attempt to clone the stretch-activated cation channel of *Xenopus* oocytes, candidates were tested using blinded stereotyped protocols. After much effort, the dismal conclusion was that none of our clones expressed in mammalian cells yielded more MS current than is seen in controls (Wan et al., 1999; Juranka et al., 2001). Endogenous MS channels tend to activate more readily upon repeated stretch trials; in the absence of blinded stereotyped procedures, this evidently generates the results one expects/wants. Exacerbating problems in this arena have been misuse of gadolinium as a blocker and assertions that GsMTx4 is a specific inhibitor of MS cation channels (see Morris, 2011a,b).

Piezo1 and Piezo2 and CFTR, new entries to the field, and perhaps VGCs, might revitalize the cellular physiology of ion channel mechanosensitivity, though Piezos are probably mechanotransducer specialist proteins. VGCs, the best understood of the identified non-specialist MS channels, generate rhythmic signals in myocardium and smooth muscle. Perhaps arrhythmia-inducing VGC mutants with

distinctive mechano-phenotypes, plus the MS actions of voltage sensor toxins (Morris, 2011a,b) will provide leverage for assessing their possible contributions to mechanophysiology.

BIBLIOGRAPHY

Andersen, O. S., & Koeppe, R. E., 2nd (2007). Bilayer thickness and membrane protein function: an energetic perspective. *Annu Rev Biophys Biomol Struct, 36*, 107–130.

Bailey, R. W., Nguyen, T., Robertson, L., Gibbons, E., Nelson, J., Christensen, R. E., Bell, J. P., Judd, A. M., & Bell, J. D. (2009). Sequence of physical changes to the cell membrane during glucocorticoid-induced apoptosis in S49 lymphoma cells. *Biophys J, 96*, 2709–2718.

Banderali, U., Juranka, P. F., Clark, R. B., Giles, W. R., & Morris, C. E. (2010). Impaired stretch modulation in potentially lethal cardiac sodium channel mutants. *Channels (Austin), 4*, 12–21.

Baumgart, T., Capraro, B. R., Zhu, C., & Das, S. L. (2011). Thermodynamics and mechanics of membrane curvature generation and sensing by proteins and lipids. *Annu Rev Phys Chem, 62*, 483–506.

Baumgart, T., Hess, S. T., & Webb, W. W. (2003). Imaging coexisting fluid domains in biomembrane models coupling curvature and line tension. *Nature, 425*, 821–824.

Bezanilla, F. (2008). Ion channels: from conductance to structure. *Neuron, 60*, 456–468.

Boal, D. (2001). Mechanics of the Cell. Cambridge University Press.

Boucher, P. A., Morris, C. E., & Joós, B. (2009). Mechanosensitive closed-closed transitions in large membrane proteins: osmoprotection and tension damping. *Biophys J, 97*, 2761–2770.

Butterwick, J. A., & MacKinnon, R. (2010). Solution structure and phospholipid interactions of the isolated voltage-sensor domain from KvAP. *J Mol Biol, 403*, 591–606.

Calabrese, B., Tabarean, I. V., Juranka, P., & Morris, C. E. (2002). Mechanosensitivity of N-type calcium channel currents. *Biophys J, 83*, 2560–2574.

Coste, B., Mathur, J., Schmidt, M., Earley, T. J., Ranade, S., Petrus, M. J., Dubin, A. E., & Patapoutian, A. (2010). Piezo1 and Piezo2 are essential components of distinct mechanically activated cation channels. *Science, 330*, 55–60.

Cueva, J. G., Mulholland, A., & Goodman, M. B. (2007). Nanoscale organization of the MEC-4 DEG/ENaC sensory mechanotransduction channel in Caenorhabditis elegans touch receptor neurons. *J Neurosci, 27*, 14089–14098.

Finol-Urdaneta, R. K., McArthur, J. R., Juranka, P. F., French, R. J., & Morris, C. E. (2010). Modulation of KvAP unitary conductance and gating by 1-alkanols and other surface active agents. *Biophys J, 98*, 762–772.

Gray, J. A., & Sato, M. (1953). Properties of the receptor potential in Pacinian corpuscles. *J Physiol, 122*, 610–636.

Gu, C. X., Juranka, P. F., & Morris, C. E. (2001). Stretch-activation and stretch-inactivation of Shaker-IR, a voltage-gated K+ channel. *Biophys J, 80*, 2678–2693.

Guharay, F., & Sachs, F. (1984). Stretch-activated single ion channel currents in tissue-cultured embryonic chick skeletal muscle. *J Physiol, 352*, 685–701.

Hamill, O. P., & Martinac, B. (2001). Molecular basis of mechanotransduction in living cells. *Physiol Rev, 81*, 685–740.

Horn, R., & Vandenberg, C. A. (1984). Statistical properties of single sodium channels. *J Gen Physiol, 84*, 505–534.

Hudspeth, A. J. (2008). Making an effort to listen: mechanical amplification in the ear. *Neuron, 9*, 530–545.

Hulse, R. E., Li, Q., & Perozo, E. (2010). Up a hydrophobic creek with a short paddle. *Cell, 142*, 515–516.

Juranka, P. F., Haghighi, A. P., Gaertner, T., Cooper, E., & Morris, C. E. (2001). Molecular cloning and functional expression of Xenopus laevis oocyte ATP-activated P2X4 channels. *Biochim Biophys Acta, 1512*, 111–124.

Krepkiy, D., Mihailescu, M., Freites, J. A., Schow, T. V., Worcester, D. L., Gawrisch, K., Tobras, D. J., White, S. H., & Swartz, K. J. (2009). Structure and hydration of membranes embedded with voltage-sensing domains. *Nature, 462*, 473–479.

Kung, C., Martinac, B., & Sukharev, S. (2010). Mechanosensitive channels in microbes. *Annu Rev Microbiol, 64*, 313–329.

Laitko, U., & Morris, C. E. (2004). Membrane tension accelerates rate-limiting voltage-dependent activation and slow inactivation steps in a Shaker channel. *J Gen Physiol, 123*, 135–154.

Laitko, U., Juranka, P. F., & Morris, C. E. (2006). Membrane stretch slows the concerted step prior to opening in a Kv channel. *J Gen Physiol, 127*, 687–701.

Lin, W., Laitko, U., Juranka, P. F., & Morris, C. E. (2007). Dual stretch responses of mHCN2 pacemaker channels: accelerated activation, accelerated deactivation. *Biophys J, 92*, 1559–1572.

Liu, X., Huang, H., Wang, W., Wang, J., Sachs, F., & Niu, W. (2008). Stretch-activated potassium channels in hypotonically induced blebs of atrial myocytes. *J Membr Biol, 226*, 17–25.

Lundbaek, J. A., Koeppe, R. E., 2nd, & Andersen, O. S. (2010). Amphiphile regulation of ion channel function by changes in the bilayer spring constant. *Proc Natl Acad Sci USA, 107*, 15427–15430.

Marsh, D. (2008). Protein modulation of lipids, and vice-versa, in membranes. *Biochim Biophys Acta, 1778*, 1545–1575.

Morris, C. E. (1990). Mechanosensitive ion channels. *J Membr Biol, 113*, 93–107.

Morris, C. E. (2001a). Mechanosensitive ion channels in eukaryotic cells. In N. Sperelakis (Ed.), *Cell Physiology Sourcebook* (3rd ed.). (pp. 745–760) Academic Press.

Morris, C. E. (2001b). Mechanoprotection of the plasma membrane in neurons and other non-erythroid cells by the spectrin-based membrane skeleton. *Cell Mol Biol Lett, 6*, 703–720.

Morris, C. E. (2011a). Pacemaker, potassium, calcium, sodium: stretch modulation of the voltage-gated channels. In P. Kohl, F. Sachs, & M. Franz (Eds.), *Cardiac Mechano-Electric Coupling and Arrhythmias: from Pipette to Patient* (2nd ed.). (pp. 43–49) Elsevier Saunders.

Morris, C. E. (2011b). Voltage gated channel mechanosensitivity. Fact or friction? *Front Physiol.* 2:25.

Morris, C. E., & Horn, R. (1991). Failure to elicit neuronal macroscopic mechanosensitive currents anticipated by single-channel studies. *Science, 251*, 1246–1249.

Morris, C. E., & Juranka, P. F. (2007a). Lipid stress at play: mechanosensitivity of voltage-gated channels. In O. Hamill, S. Simon, & D. Benos (Eds.), *Mechanosensitive Ion Channels, Part B. Curr Top Membr, 59* (pp. 297–337).

Morris, C. E., & Juranka, P. F. (2007b). Nav channel mechanosensitivity: activation and inactivation accelerate reversibly with stretch. *Biophys J, 93*, 822–833.

Morris, C. E., Juranka, P. F., Lin, W., Morris, T. J., & Laitko, U. (2006). Studying the mechanosensitivity of voltage-gated channels using oocyte patches. *Methods Mol Biol, 322*, 315–329.

Nilsen, N., Brownell, W. E., Sun, S. X., & Spector, A. A. (2011). Effect of membrane mechanics on charge transfer by the membrane protein prestin. *Biomech Model Mechanobiol*, Mar 2.

Owen, D. M., Magenau, A., Majumdar, A., & Gaus, K. (2010). Imaging membrane lipid order in whole, living vertebrate organisms. *Biophys J, 99*, L7–9.

Patel, A., Sharif-Naeini, R., Folgering, J. R., Bichet, D., Duprat, F., & Honoré, E. (2010). Canonical TRP channels and mechanotransduction: from physiology to disease states. *Pflügers Arch, 460*, 571–581.

Phillips, R., Ursell, T., Wiggins, P., & Sens, P. (2009). Emerging roles for lipids in shaping membrane-protein function. *Nature, 459*, 379–385.

Rosenhouse-Dantsker, A., Logothetis, D. E., & Levitan, I. (2011). Cholesterol sensitivity of KIR2.1 is controlled by a belt of residues around the cytosolic pore. *Biophys J, 100*, 381–389.

Sachs, F., & Morris, C. E. (1998). Mechanosensitive ion channels in nonspecialized cells. *Rev Physiol Biochem Pharmacol, 132*, 1–78.

Schmidt, D., & MacKinnon, R. (2008). Voltage-dependent K+ channel gating and voltage sensor toxin sensitivity depend on the mechanical state of the lipid membrane. *Proc Natl Acad Sci USA, 105*, 19276–19281.

Schmidt, D., Cross, S. R., & MacKinnon, R. (2009). A gating model for the archeal voltage-dependent K(+) channel KvAP in DPhPC and POPE: POPG decane lipid bilayers. *J Mol Biol, 390*, 902–912.

Shevchenko, A., & Simons, K. (2010). Lipidomics: coming to grips with lipid diversity. *Nat Rev Mol Cell Biol, 11*, 593–598.

Soubias, O., Teague, W. E., Jr., Hines, K. G., Mitchell, D. C., & Gawrisch, K. (2010). Contribution of membrane elastic energy to rhodopsin function. *Biophys J, 99*, 817–824.

Tabarean, I. V., & Morris, C. E. (2002). Membrane stretch accelerates activation and slow inactivation in Shaker channels with S3-S4 linker deletions. *Biophys J, 82*, 2982–2994.

Tabarean, I. V., Juranka, P., & Morris, C. E. (1999). Membrane stretch affects gating modes of a skeletal muscle sodium channel. *Biophys J, 77*, 758–774.

Tillman, T. S., & Cascio, M. (2003). Effects of membrane lipids on ion channel structure and function. *Cell Biochem Biophys, 38*, 161–190.

Tufail, Y., Matyushov, A., Baldwin, N., et al. (2010). *Transcranial pulsed ultrasound stimulates intact brain circuits. Neuron, 66*, 681–694.

Wan, X., Juranka, P., & Morris, C. E. (1999). Activation of mechanosensitive currents in traumatized membrane. *Am J Physiol, 276*, C318–C327.

Wang, J. A., Lin, W., Morris, T., Banderali, U., Juranka, P. F., & Morris, C. E. (2009). Membrane trauma and Na+ leak from Nav1.6 channels. *Am J Physiol Cell Physiol, 297*, C823–C834.

Wang, W., Huang, H., Hou, D., Liu, P., Wei, H., Fu, x., & Niu, W. (2010). Mechanosensitivity of STREX-lacking BKCa channels in the colonic smooth muscle of the mouse. *Am J Physiol Gastrointest Liver Physiol, 99*, G1231–G1240.

Zhang, W. K., Wang, D., Duan, Y., Loy, M. M., Chan, H. C., & Huang, P. (2010). Mechanosensitive gating of CFTR. *Nat Cell Biol, 12*, 507–512.

Section IV

Ion Channels as Targets for Toxins, Drugs, and Genetic Diseases

Chapter 28

Ion Channels as Targets for Toxins

Kenneth M. Blumenthal

Chapter Outline

I. SUMMARY

Neurotoxins have proven to be invaluable tools in the purification of many of the best-characterized cation channels and, in addition, have contributed significantly to our understanding of how these macromolecules function in excitable tissues. This collection of molecules displays a great deal of diversity in both a chemical and a functional sense. Although many of the compounds are cationic, additional unifying structural themes are conspicuous by their absence. Even within the subgroup of polypeptide toxins, the most well-studied groups (i.e. anemone, scorpion, snail, spider and snake toxins) fail to display any intergroup relatedness at the level of primary structure. Indeed, this is rather surprising in view of the ability of (e.g.) anemone and α-scorpion toxins to compete for a common receptor. While all of the polypeptides do share a cationic character and are rich in disulfide bonds, it remains to be proven that the former property is intimately related to their activity. The latter property is almost certainly a consequence of the necessity for stabilizing small peptides in an extracellular environment. Perhaps the most striking observation is the relatedness between charybdotoxin and the Na^+ channel-directed scorpion toxins at the level of their three-dimensional structures. This clearly raises the possibility of common binding mechanisms having evolved.

Given the vast diversity of the venoms from which each of these toxins is derived and the growing array of ion channels purified and/or channel activities characterized, it is likely that new and interesting toxins will continue to emerge in the future and that their characterization will add significantly to our knowledge of channels and receptors in excitable tissues. Two areas of research that might prove especially fruitful involve using existing (or newly discovered) toxins to probe for specific channel isoforms in different tissues and using behavioral assays to identify new venom components likely to have neuronal activities. This latter approach has already been applied to components of *Conus geographus* venom with very intriguing results, among them being the discovery of the so-called "sleeper" and "King Kong" peptides. It is likely that this surface has as yet only been scratched and that future studies will unveil additional toxins that interact with new, and perhaps presently unknown, target sites.

II. INTRODUCTION

A wide variety of neurotoxins has served as potent tools used by biochemists, biophysicists, physiologists or pharmacologists interested in identifying, purifying and characterizing voltage-sensitive ion channels of excitable membranes and in understanding the molecular details of their structure and function for several decades. This

Cell Physiology Sourcebook. DOI: 10.1016/B978-0-12-387738-3.00028-7

chapter provides brief descriptions of some of these toxins, focusing on their chemical natures, similarities and differences, target macromolecules and effects on transmembrane ionic fluxes. In this chapter, the ion channels are used as an organizational framework and, in those cases where multiple-toxin binding sites have been demonstrated with a single channel, the relationships among these sites are discussed. A number of excellent reviews on this subject have been published in recent years, including a volume of *Toxicon* (49(2), pp. 123-292; Catterall, 2000; Escoubas and Rash, 2004; Olivera, 2006; Catterall et al, 2007; Nicholson, 2007; Swartz, 2007) devoted to gating modifiers.

Toxins are diverse both chemically and functionally. They include an ever-expanding array of polypeptides derived from marine invertebrates and terrestrial arthropods, alkaloids of diverse structures, heterocyclic compounds of the tetrodotoxin family and synthetic insecticides. Functionally, these molecules are equally diverse. Toxins have been characterized that modify the voltage dependence of activation and inactivation gating or block ion fluxes and a growing number have multiple actions. Thus, in addition to being useful probes for purification of channel constituents, they have contributed significantly to our understanding of how these various processes are coupled to one another.

III. VOLTAGE-GATED SODIUM CHANNELS (VGSCS; $Na_V1.x$)

The neuronal sodium channel consists of three polypeptides having molecular masses of 260 (α), 36 (β_1), and 33 kDa (β_2) (Catterall, 2000); whether the smaller subunits are present in all channel isoforms remains unresolved. All of the toxin binding sites characterized to date appear to be associated with the α subunit, reconstitution of which into planar lipid bilayers restores most of the activities of the native channel. Microinjection of mRNA encoding this subunit into *Xenopus* oocytes results in expression of sodium channels which are functionally similar, though not identical, to their natural counterparts and the same is true for mammalian cell lines which stably express the α subunit.

The α subunit is organized into four repeated structurally homologous domains, each containing 300–400 amino acid residues. Each domain includes six transmembrane helices (designated S1–S6) as well as a seventh region (the P-loop), whose length varies among the four domains, that lies at least partially within the membrane. P-loop sequences provide the channel's outer vestibule and selectivity filter and also contribute to the inner lining of the conducting pore. Although no crystal structures have been solved for VGSCs, the MacKinnon laboratory has provided several structures for potassium channels to which they are homologous (Doyle et al, 1998; Jiang et al 2003a; Long et al, 2005), all showing the presence of a non-transmembrane pore helix in this region, followed by a turn and β-strand. Several models of the VGSC pore region which include such a structure have been described (Lipkind and Fozzard, 1994, 2000; Penzotti et al 1998; see below). Several classes of toxin binding sites have been identified on the α subunit by both biochemical and mutagenic analyses, pore blockers interacting with all four channel domains while gating modifiers appear to bind primarily to domains I, II, and IV. Figure 28.1 depicts the putative transmembrane organization of the α subunit of this channel; as described in subsequent sections, this organization is shared by known K^+ channels and the α_1 subunit of the Ca^{2+} channel as well.

A series of elegant analyses, carried out mainly by Catterall, clearly established the presence of four independent classes of neurotoxin binding sites on the rat brain $Na_V1.2$ channel (Catterall, 2000; also, see Summary, Table 28.1). These include sites for: (1) the classic channel inhibitors tetrodotoxin and saxitoxin; (2) activating alkaloids, such as batrachotoxin and veratridine; (3) polypeptide (α) toxins from scorpion and sea anemone venoms, which delay channel inactivation; and (4) a distinct set of scorpion (β-toxins) and tarantula toxins that alter the voltage dependence of channel activation and inactivation. Each class is discussed below.

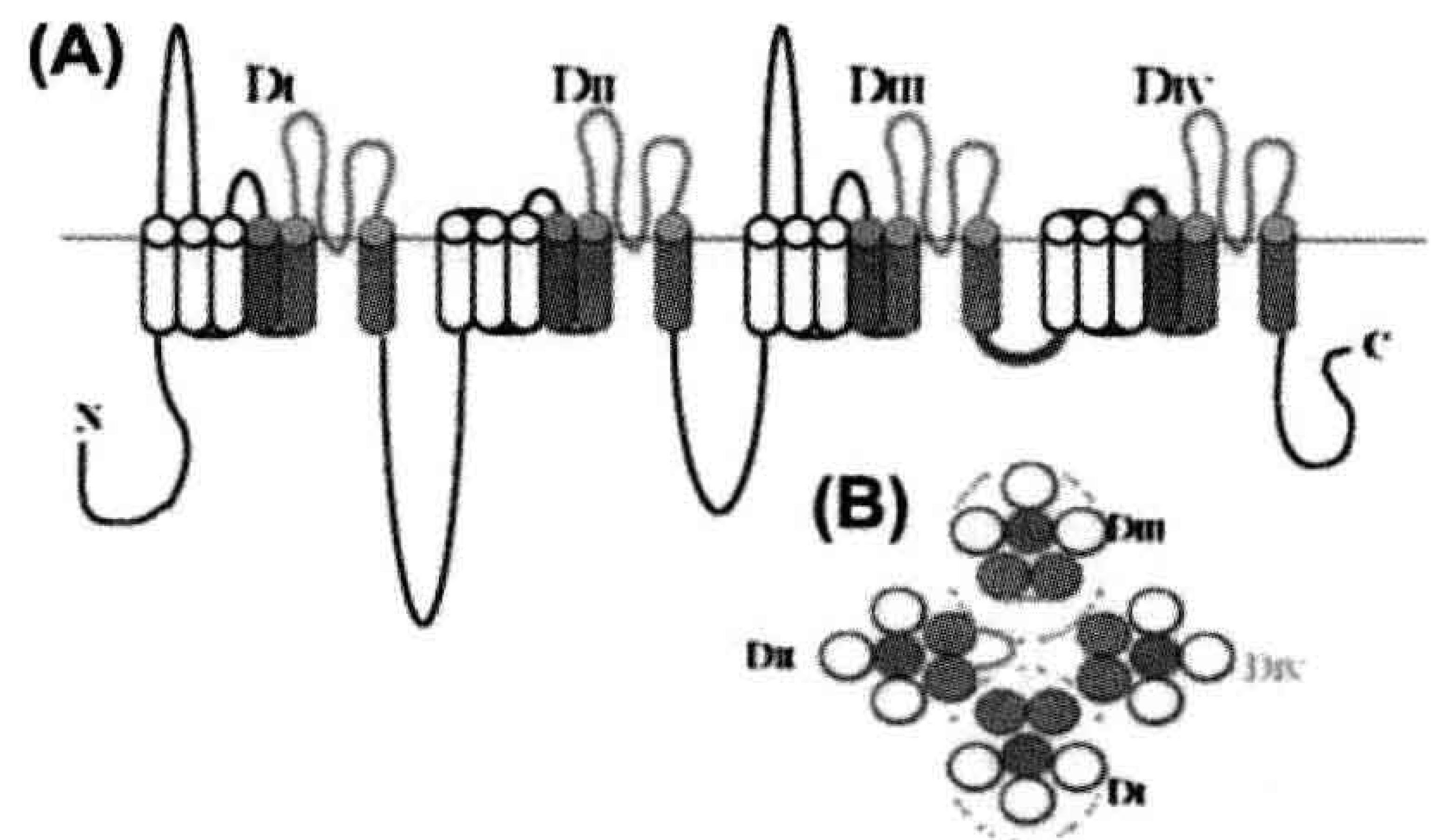


FIGURE 28.1 (A) Transmembrane topology of the voltage-sensitive sodium channel. The channel consists of four homologous domains, each containing six transmembrane segments in addition to a P-loop which contains the channel's outer vestibule. Segments S5 and S6 of each domain, shown in blue, comprise the inner lining of the channel, while S4, shown in red, represents the main voltage sensor. The intracellular linker connecting domains III and IV has been shown to be involved in fast inactivation of the channel. The binding site for tetrodotoxin (site 1) contains elements of all four P-loops; batrachotoxin binding (site 2) determinants are found in the C-terminal portions of the S6 segments of domains I and IV; α-scorpion and anemone toxins bind (site 3) to the S3–S4 loop of domain IV; and β-scorpion toxins (site 4) to the corresponding loop of domain II. (B) Proposed arrangement of the four domains, looking down, with the pore in the center.

TABLE 28.1 Toxin Effectors of Voltage-Sensitive Sodium Channels

Toxin	Binding Affinity	Functional Effect
Tetrodotoxin	1−5 nM (Nerve)	Blockade
	1−10 μM (Heart)	Blockade
Saxitoxin	1 nm (Nerve)	Blockade
	100 nM (Heart)	Blockade
Alkaloids		
Batrachotoxin	0.25 μM	Persistent activation
Grayanotoxin	>1 mM	Persistent activation
Veratridine	50 μM	Persistent activation
Polypeptides		
α-Scorpion toxins	1−2 nM	Delayed inactivation
β-Scorpion toxins	0.5 nM	Modified activation gating
Anemone toxins	10−1000 nM	Delayed inactivation
Tarantula toxins	0.1−100 nM	Multiple
Dinoflagellate Toxins		
Brevetoxin	μM range	Shifts activation
Ciguatoxin	μM range	Depolarization
Goniopora	50 νM	Delayed inactivation

IIIA. Site 1: Tetrodotoxin, Saxitoxin and μ-Conotoxin

The presence of a paralytic toxin in newts, pufferfish and other organisms has been known for well over 50 years and the structure of this compound (Fig. 28.2), called tetrodotoxin, was first described in 1964. Narahashi, Moore and collaborators demonstrated that the toxicity of tetrodotoxin (TTX) was attributable to its ability to block the rapid increase in sodium conductance associated with the rising phase of the action potential in frog muscle. Because TTX and the structurally related dinoflagellate-derived saxitoxin (STX) bind to the channel with high affinity (1−5 nM for the neuronal isoform), a property that is essentially unaltered by detergent solubilization, their discovery provided biochemists with an essential probe for purification of the channel protein. Because of the availability of TTX and STX, purification, biochemical characterization and molecular cloning of voltage-dependent sodium channels from a variety of sources have been accomplished over the past two decades.

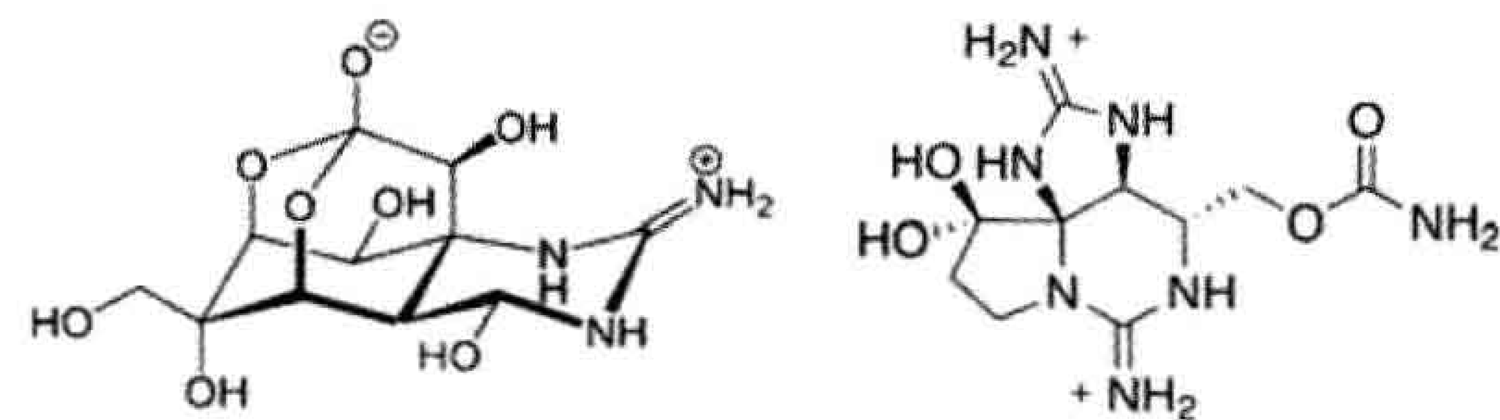


FIGURE 28.2 Structures of the guanidinium channel blockers tetrodotoxin (left) and saxitoxin (right). The guanidinium groups of both compounds are essential for binding to site 1, as are hydrogen bonds contributed by several of the axial hydroxyl groups.

Tetrodotoxin and saxitoxin are heterocyclic guanidinium compounds that bind reversibly and with high affinity ($K_d = 1 - 5$ nM) to a site accessible from the external face of neuronal and muscle Na^+ channels. This K_d agrees well with that obtained from analysis of the effects of these toxins on Na^+ currents in these tissues. Binding of TTX and STX to cardiac Na^+ channels is of much lower affinity, with K_d values on the order of 0.1−1 μM. The cardiac channels are thus defined as being TTX-resistant. Analyses of channels by site-directed mutagenesis (Noda et al., 1989; Satin et al., 1992) have implicated Cys-374 and Arg-377 of the cardiac channel as being important for their decreased TTX sensitivity.

Binding of TTX and STX blocks Na^+ currents and was originally thought to involve interaction of toxin with the ionized form of a channel carboxyl group, which Hille proposed was associated with the channel *selectivity filter.* However, the notion that the carboxylate(s) important in TTX binding was also a part of the selectivity filter was abandoned when it was shown that chemical modification of channel carboxylates, which abolished binding, had no effect on ion selectivity. Subsequent structure−function analysis of TTX and STX, using both natural and synthetic analogs (Mosher, 1986; Shimizu, 1986), clearly delineated the importance of the guanidinium group of TTX (and the corresponding 7, 8, 9 guanidinium of the bifunctional STX) for activity. In addition, the C4, C9 and C10 hydroxyl groups of TTX and the C12 hydroxyl of STX are required. It is assumed that these hydroxyl groups form hydrogen bonds to as yet unknown acceptor sites on the channel. The TTX binding site is located near the external face of the channel and may lie outside of the transmembrane field.

Site-directed mutagenesis of both Na^+ channels and K^+ channels indicates that this region is important both for ion selectivity and binding of channel-specific toxins. Replacement of Arg 377 of the TTX-resistant cardiac ($Na_V1.5$) channel by asparagine results in a small increase in TTX-sensitivity (Noda et al., 1989), whereas the mutation of Cys 374 to tyrosine renders the channel approximately 700-fold more sensitive to TTX (Satin et al., 1992). This latter result raises the possibility that TTX and STX owe their affinity not to ion pairing between their positively charged guanidinium groups and channel carboxylates but rather to interactions with the π-clouds contributed by a cluster of electron-rich aromatic residues located near the

channel mouth. Analogous models have been proposed to account for acetylcholine binding to the nicotinic acetylcholine receptor and tetraethylammonium binding to a variety of potassium channels. However, it is clear that interaction with aromatic residues is not the *sole* binding determinant, since mutagenesis has also identified a carboxyl group, Glu 387, essential for high-affinity TTX binding in the brain $Na_V1.2$ channel. Like Cys 374 and Arg 377, this residue is also located in the SS2 region of the P-loop.

The corresponding S5–S6 linker regions from domains III and IV are also important determinants of ionic selectivity, as shown by the finding that the mutations Lys 1422 to glutamate and Ala 1714 to glutamate give the $Na_V1.2$ channel an ionic selectivity similar to that of a Ca^{2+} channel. Interestingly, mutagenesis has also been used to show that the S5–S6 region of *shaker* K^+ channels is directly involved in both ion transit and interaction of inhibitors such as tetraethylammonium (TEA) and charybdotoxin. Tyr 379 of the K^+ channel RBK-1 has been identified as an important determinant of tetraethylammonium (TEA) binding (MacKinnon and Yellen, 1990), while the introduction of a tyrosine at position 449 of the *shaker* H4 channel greatly increases its sensitivity to TEA. Thus, a leitmotif stressing the importance of aromatic residues in the binding of cationic ligands to ion channels is emerging.

As already noted, the three-dimensional structure of $Na_V1.x$ channels is unknown. However, several modeling studies based on K-channel structures and/or on effects of mutagenesis on toxin binding affinities have predicted elements of the pore structure. Based on the structure of the KcsA channel, Lipkind and Fozzard (2000) have postulated the importance of a hydrophobic core involving residues Leu-396, Gln-399 and Trp-402 ($Na_V1.4$), in addition to the carboxylates and aromatic residues already mentioned, in stabilizing tetrodotoxin binding.

A structurally unrelated peptidic toxin, designated μ-conotoxin or geographutoxin, is a competitive inhibitor of STX binding to muscle, but not nerve, Na^+ channels ($K_d < 100$ nM in muscle versus >1 µM in brain; Cruz et al., 1985; Ohizumi et al., 1986). μ-Conotoxin is a 22-residue, hydroxyproline-containing peptide, tightly cross-linked by three disulfide bonds. Its three-dimensional structure, based on two-dimensional nuclear magnetic resonance (NMR) measurements and simulated annealing protocols, has been described. The overall structure includes a series of tight turns in the N-terminal region and a short stretch of right-handed helix, while the core of the peptide encompasses what the authors refer to as a disulfide cage. A key feature of the structure is that the cationic side chains of arginines 1, 13 and 19, and lysines 8 and 16 all project into solution, away from the core of the molecule as defined by the disulfide bonds. Analysis of synthetic variants of μ-conotoxin has shown that Arg 13 is essential for activity: even conservative replacement by lysine reduces potency by about 10-fold. In contrast, Arg 19 can be replaced by lysine with essentially no change in activity, while substitution at Arg 1 yields an intermediate result (Cruz et al., 1989). It is interesting that binding of both TTX/STX and the μ-conotoxins is at least partially dependent on guanidinium functions, suggestive of a dispersed positive charge being more effective than a point charge in this respect.

Unlike TTX and STX, the binding of μ-conotoxin is dependent on membrane potential, with K_d decreasing *e*-fold for every 34 mV depolarization (Cruz et al., 1989). TTX/STX-resistant (i.e. cardiac) channels are likewise resistant to μ-conotoxins. More recently, a mutated form of μ-conotoxin has been used as a monitor of distance between the voltage sensor and channel pore (French et al., 1996).

IIIB. Site 2: Batrachotoxin, Grayanotoxin, Veratridine and Related Compounds

The existence of low molecular weight hydrophobic compounds having dramatic effects on the gating properties of voltage-sensitive Na^+ channels has been known for over 20 years. The most commonly used of these alkaloids are batrachotoxin, grayanotoxin and veratridine (Fig. 28.3). Despite their differing biological origins (respectively, skin secretions of the frog *P. aurotaenia*, *Lilaceae* and *Ericaceae* species) and dose–response curves (IC_{50}s are approximately 0.25, 10 and 50 μM for

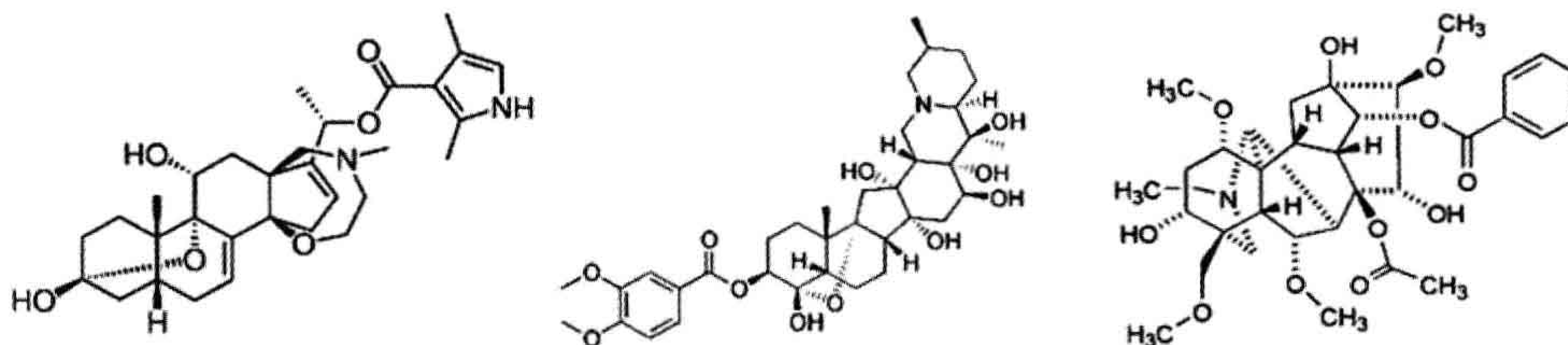


FIGURE 28.3 Structures of some major alkaloid agonists of the voltage-sensitive sodium channel. Left, batrachotoxin; center, veratridine; right, aconitine.

batrachotoxin, grayanotoxin and veratridine), these molecules have very similar effects on channel function. All appear to interact at a common binding site, which is allosterically coupled to both the TTX binding site described in the previous section and the α-scorpion toxin site to be discussed later (Catterall, 1977). Binding of any of the alkaloids to this site causes persistent activation of the channel, leading to membrane depolarization. In addition, alkaloid-treated channels display a more relaxed ionic selectivity than do their naive counterparts. Thus, while the permeability order of untreated Na^+ channels is Na^+: guanidinium:K^+: $Rb^+ = 1{:}0.13{:}0.09{:}0.01$, veratridine increases the relative permeability for guanidinium, K^+ and Rb^+ by factors of 2.7, 4.5, and 10, respectively. Qualitatively similar results are obtained with the other alkaloids of this class and with combinations of alkaloid and polypeptide toxins from scorpion or sea anemone venoms.

The steroidal alkaloid batrachotoxin (BTX) was purified and characterized by Witkop, Daly and their coworkers. In collaboration with Albuquerque, the effects of BTX were measured in a variety of tissues including axons, brain slices and isolated synaptosomes, neuromuscular junctions, heart papillary muscle and cardiac Purkinje fibers. Batrachotoxin binding has been measured directly in rat brain synaptosomes using a tritiated derivative and the measured density of binding sites correlates well with that for TTX and STX. Binding of BTX to this site is competitively inhibited by veratridine with a K_i very similar to the $K_{0.5}$ for veratridine's activation of the channel. Because BTX acts from either side of the membrane, it had been speculated that its binding site might lie within the lipid bilayer and a photoactivatable derivative of batrachotoxin has been demonstrated to specifically label a site within the S6 transmembrane segment of domain I of the rat brain channel (Trainer et al., 1996). Site-directed mutagenesis of $Na_V1.2$ has identified F1764 as an important binding determinant (Linford et al., 1998) and additional mutations in the same domain IV S6 segment have similar effects (Wang and Wang, 1999). Thus, the BTX binding site, which also interacts with local anesthetics, is most likely composed of residues in the C-terminal portions of channel S6 segments.

As discussed later, fluorescent derivatives of BTX have also been important for measuring distances between the various toxin-binding sites by resonance energy transfer experiments. Because the effects of BTX on membrane potential are dependent on the presence of extracellular Na^+ and are blocked by treatment with TTX, they are attributed to the toxin's ability to cause voltage-dependent Na^+ channels to activate at the resting potential and to persist in the activated state. BTX also causes increased permeability to larger cations, consistent with allosteric coupling between the BTX binding site and the selectivity filter of the Na^+ channel.

Other alkaloids that appear to interact with the BTX site with similar functional effects include veratridine, grayanotoxin (GTX) and aconitine. While structurally distinct from one another, these highly hydrophobic compounds do have certain common features, such as the bridged ring systems and esterified aromatic moieties found in BTX, veratridine and aconitine (see Fig. 28.3). In the case of BTX, both the bridge and the esterified group are essential for activity.

For all of these toxins, the available data strongly suggest that interaction of a single toxin molecule per channel is sufficient for activation. The known biological effects of these toxins are ascribed to their ability to interact with the voltage-dependent Na^+ channel, although only BTX binding has been measured directly. Catterall proposed that the alkaloids bind preferentially to the activated conformation of the Na^+ channel, shifting a preexisting equilibrium between active and inactive states toward the former. Thus, toxin action would best be approximated by the allosteric model of Monod, Wyman and Changeaux, in which the binding energy for a given toxin is expressed as a shift in the voltage dependence for channel activation. As will be discussed later, conformational changes in the channel induced by binding of toxins have been directly demonstrated, thus supporting this model.

IIIC. Sites 3 and 4: Scorpion, Sea Anemone and Spider Toxins

An effect of scorpion venom on frog Na^+ channels was first demonstrated about 40 years ago and individual toxins from *Androctonus* venom were purified and sequenced beginning in the mid-1970s. Subsequently, scorpion toxins active on the sodium channel have been purified from the venoms of *Androctonus*, *Leiurus*, *Centruroides*, *Tityus* and *Buthus* species. While these toxins exhibit certain common structural features, the pharmacology of the *Androctonus* and *Leiurus* toxins is quite distinct from that of the corresponding polypeptides from *Centruroides* and *Tityus*. Toxins from the former (α-toxin) group delay or abolish channel inactivation and thus delay repolarization of the membrane via binding to neurotoxin site 3, while the latter (β-toxin) group shifts the voltage dependence of activation to more negative potentials as a result of binding to site 4 (in the Catterall nomenclature), thereby yielding spontaneous activity. α-Toxin binding is dependent on membrane potential, with K_d values in the nanomolar range at the resting potential. In contrast, β-toxin binding is potential-independent and generally of slightly lower affinity. The pharmacologic distinction between the α- and β-toxins is somewhat unexpected in view of the close relationship among these toxins at the level of covalent and tertiary structure. Moreover, recent data raises the possibility that

Representative α-toxins

```
AaH-1      KRDGYIVYPN NCVYHCVPP- -CDGLCKKNG GSSGSSCFLV -PSGLACWC- KDLPDNVPIK
AsH-2      VKDGYIVDDV NCTYFCGRNA YCNEECTKLK GESGY-CQWA SPYGNACYCY K-LPDHVRTK
Lqq-V      LKDGYIVDDK NCTFFCGRNA YCNDECKKKG GESGH-CQWA SPYGNACWCY K-LPDRVSIK
BoT-1      GRDAYIAQPE NCVYECAQNS YCNDLCTKNG ATSGY-CSWL GKYGNACWC- KDLPDNVPIR
BoT-XI     VKDGYIVDDV NCTYFCGRNA YCHEECTKLK GESGY-CQWA SPYGNACYCY K-LPDHVRTK

Consensus  N+DGYIUOXX NCβΦXCXOOO YCOOXCOKXO GOSGO-CXUU OXOGXACΦCY KDLPDOVOβ+

AaH-1      DTSRKCT
AsH-2      GPGP-CH
Lqq-V      EKGR-CN
BoT-1      IPGK-CHF
BoT-XI     GSPGRCH

Consensus  OXOO+CO
```

Representative β-toxins

```
CsE1  KEGYLVEKTG CKKTCYKLGE NDFCRECKWK HIGGSYGYCY GFGCYCELGL PDSTQTWPLP -NKCT
TssG  KEGYLMDHEG CKLSCFIRPS -GYCRECGIK K- GSSGYCA WPACYCYGLP NWVKVWDRAT TNKC
```

FIGURE 28.4 Primary structures of representative α- and β-scorpion toxins. Sequences are shown in the single letter code and disulfide bonds link Cys 12 to Cys 63, Cys 16 to Cys 36, Cys 22 to Cys 46 and Cys 26 to Cys 48 in both groups. Numbering is based on the sequence of AaH-II. Highlighted positions are either invariant or occupied by functionally equivalent residues within the α or β subgroup. In the consensus sequence, the coding is: + = Cationic residue; O = Polar residue; X = Character undefined; U = Non-polar residue; Φ = Aromatic residue; β = Branched side chain. AaH, *Androctonus australis* Hector; Lqq, *Leiurus quinquestriatus quinquestriatus*; BoT, *Buthus occitanus Tunetanus*; CsE, *Centruroides sculpturatus* Ewing; TsS, *Tityus serrulatus*.

some site 4 determinants may be found within the membrane (Smith et al., 2005).

The primary structures of representative scorpion toxins are depicted in Fig. 28.4. All scorpion toxins characterized to date are cationic polypeptides of molecular mass approximately 7000 Da and contain four disulfide bonds whose integrity is essential for activity; in addition, they display a significant degree of sequence homology, with approximately 30% of all positions being conserved among the known α-toxins. The β-toxins, exemplified by *Centruroides* toxin 3, are generally similar to those of the α group, but display less extensive homology. It is likely that much of this sequence conservation within a group is essential simply for allowing proper folding of these toxins, similar to results obtained with the conotoxin family, since structure–function analyses of the scorpion toxins have identified relatively few "essential" residues and the three-dimensional structures of representatives of each group show a great deal of similarity in the peptide backbones.

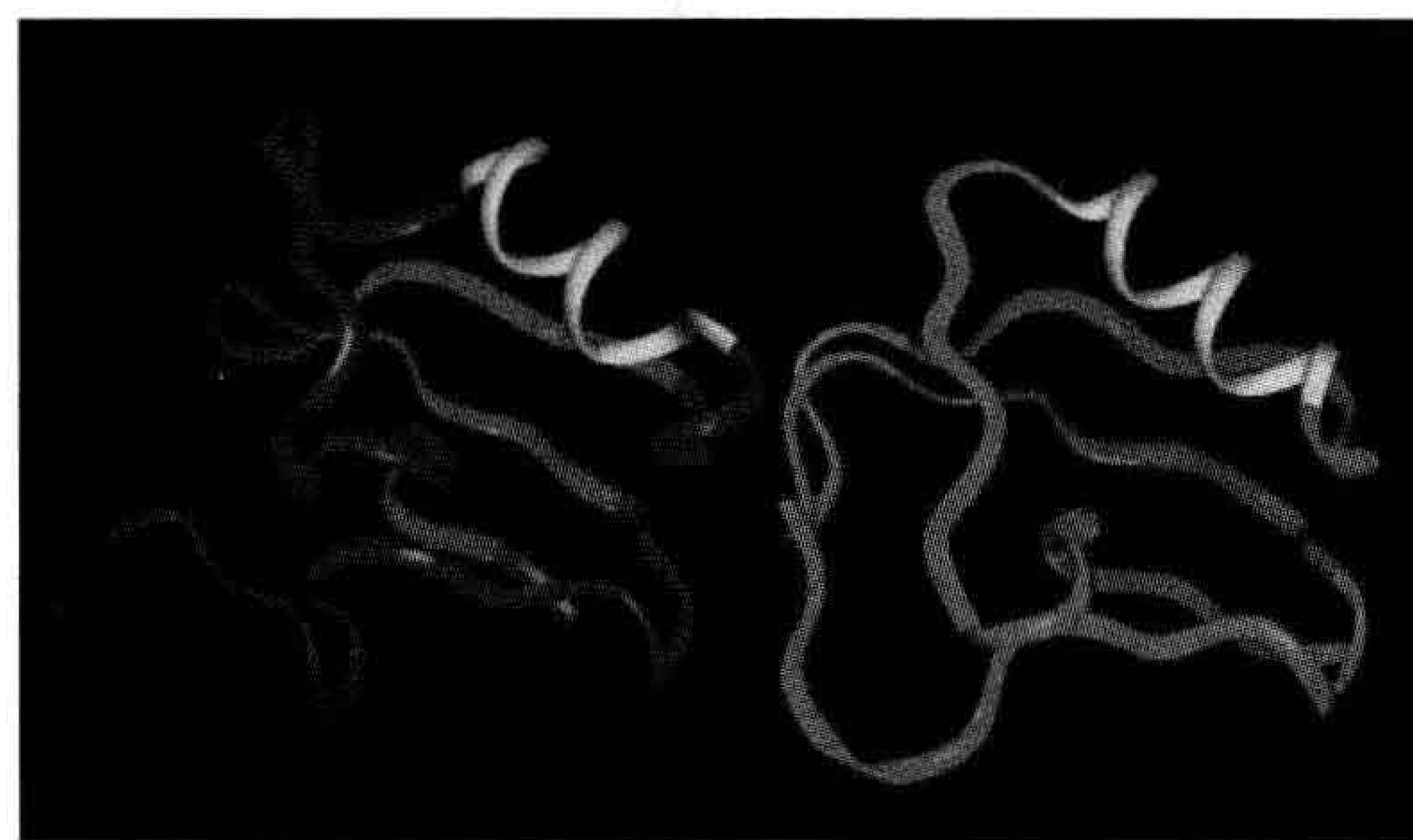


FIGURE 28.5 Comparison of the backbone structures of the site 3 toxin from *Androctonus australis Hector* (right, pdb1PTX) and the site 4 toxin from *Centruroides sculpturatus Ewing* (left, pdb1JZA). The 3-stranded β-sheets of each molecule are colored in red and the single α-helix in yellow. The most divergent portions of these structures are in the loop regions connecting the well-defined core elements.

The three-dimensional structures of many scorpion toxins are now known, including members of both the α- and β-classes (Fig. 28.5). As might be anticipated from the highly cross-linked nature of these proteins, both possess a dense core of secondary structure connected by two of the four disulfides; this core contains three strands of antiparallel β-sheet (residues 1–4, 37–41 and 46–50) and a short strand of α-helix (residues 23–32). In addition to several loops that protrude from this core region, a prominent feature of both structures is a relatively non-polar surface region, which contains a number of conserved aromatic residues. Because chemical modification of sites external to this surface region is, in general, not deleterious to toxin function and because Lys 56, referred to previously, lies within it, Fontecilla-Camps and coworkers first suggested that this region was essential for receptor binding. Interestingly, this surface is fairly well conserved in both the α- and β-toxins, despite their distinct pharmacologies and non-overlapping binding sites. Indeed, all of the structural features discussed here are common amongst scorpion toxins regardless of binding site or species specificity.

With respect to structure–activity correlations, it has been shown that alkylation of Lys 56 of AaH-I is correlated with its inactivation, suggesting the importance of a cationic group at this position in the α-scorpion toxins and that modification of Arg 2 and Arg 60 likewise results in inactivation. However, chemical modification using group-specific reagents has been relatively uninformative, perhaps owing to the fact that these toxins lack the super reactive residues seen in enzymes, for which this approach has been more successful. Site-directed mutagenesis of cloned α-toxin genes has pointed to an amphiphilic binding site containing a central hydrophobic region surrounded by cationic residues (Zilberberg et al., 1997).

Binding determinants for the α-scorpion toxin LqqV have been mapped to the domain I S5–S6 region of $Na_V1.2$ by photoaffinity labeling, and to the S3–S4 linker of domain IV by mutant cycle analysis (Rogers et al., 1996). The latter site has also been shown to bind site 3 anemone toxins (see below) whose pharmacologic effect is identical to that of LqqV (Benzinger et al., 1998). Interestingly, mutations in the domain IV S3–S4 linker give rise to hyperkalemic periodic paralysis, a condition in which channel inactivation is inhibited. The dominantly heritable disorder paramyotonia congenita, which displays an electrophysiologic phenotype identical to that of an anemone or scorpion toxin-treated, wild-type channel, likewise maps to a set of missense mutations in the S3–S4 linker region of domain IV of the muscle sodium channel (Cannon and Corey, 1993; Chahine et al., 1994; Yang et al., 1994).

In addition to the α-scorpion toxins, site 3 also binds a variety of polypeptide toxins derived from marine invertebrates: the best characterized of these is a diverse family of sea anemone toxins derived from *Anemonia*, *Anthopleura*, *Stichodactyla* and *Radianthus* species. Under appropriate conditions, certain of these polypeptides can function as cardiac stimulants. While also basic and rich in disulfides, the anemone toxins differ from those discussed previously in being somewhat smaller (46–50 residues versus 60–65 residues) and having three, rather than four, disulfides. Moreover, despite the wealth of structural information now available, no sequence homology has been found between neurotoxins from scorpions and anemones. Representative anemone toxin sequences are shown in Fig. 28.6.

The solution structures of several anemone toxins have been solved (Fig. 28.7). Examination of these structures, all having a core of twisted, four-stranded, antiparallel β-pleated sheet (residues 2–4, 18–23, 31–34 and 42–47 in anthopleurin A numbering), demonstrate unequivocally that anemone and scorpion toxins are structurally unrelated. Nonetheless, anemone and α-scorpion toxins have very similar pharmacologies and display mutually competitive binding to Na^+ channel site 3, suggesting that at least a limited degree of relatedness may yet remain to be found. It may be significant that all anemone toxins contain a large loop region (approximately residues 9–20) whose solution structure is very poorly defined and which contains at least two of the amino acid residues known to be important determinants of anemone toxin-binding affinity. In addition, biophysical analyses have provided evidence for the exposure of a number of hydrophobic residues on the surface of homologous anemone toxins. In anthopleurin B, the functional roles played by some of these residues have been analyzed using site-directed mutagenesis of a synthetic gene which encodes the toxin polypeptide. These studies have clearly demonstrated that both Leu 18 and Trp 33 play important roles in regulating high-affinity binding of this toxin to both neuronal and cardiac sodium channels and further show that two other exposed hydrophobic sites, Ile 43 and Trp 45, are external to this binding epitope. Thus, the former pair of residues may act as the functional equivalent of the hydrophobic surface implicated in scorpion toxin binding (Dias-Kadambi et al., 1996a,b). Indeed, charge-neutralizing mutations of all the ionizable groups in this toxin reveal that the contribution to affinity made by hydrophobic contacts is far more

```
AsI        GAPCKCKSDG PNTRGNSMSG TIWV— FGCP SGWNNCEGRA - HGYCCKQ
AsII       GVPCLCDSDG PSVRGNTLSG IIWL- AGCP SGWHNCKKHG PTIGWCCKQ
AsV        GVPCLCDSDG PSVRGNTLSG ILWL- AGCP SGWHNCKKHK PTIGWCCK
ApA        GVSCLCDSDG PSVRGNTLSG TLWLYPSGCP SGWHNCKAHG PTIGWCCKQ
ApB        GVPCLCDSDG PRPRGNTLSG ILWFYPSGCP SGWHNCKAHG PNIGWCCKK
ShI        -AACKCDDEG PDIRTAPLTG - TVDLGSCN AGWEKCASYY TIIADCCRKKK
RpII       -ASCKCDDDG PDVRSATGTG - TVDFWNCN EGWEKCTAVY TPVASCCRKK

Consensus  XUXCUCDODG POXROOOUOG βUXUXXXGCP SGWHCKXXXX PβUGΦCC+
```

FIGURE 28.6 Primary structures of representative sea anemone toxins. Sequences are shown in the single letter code, with the numbering based on the sequence of anthopleurin A. Disulfide bonds link Cys 4 to Cys 46, Cys 6 to Cys 36 and Cys 29 to Cys 47. Highlighted positions are either invariant or contain functionally conservative replacements. In the consensus sequence, the coding is + = Cationic residue; O = Polar residue; X = Character undefined; U = Non-polar residue; Φ = Aromatic residue; β = Branched side chain. As, *Anemonia sulcata*; Ap, *Anthopleura xanthogrammica*; Sh, *Stichodactyla helianthus*; Rp, *Radianthus paumotensis*.

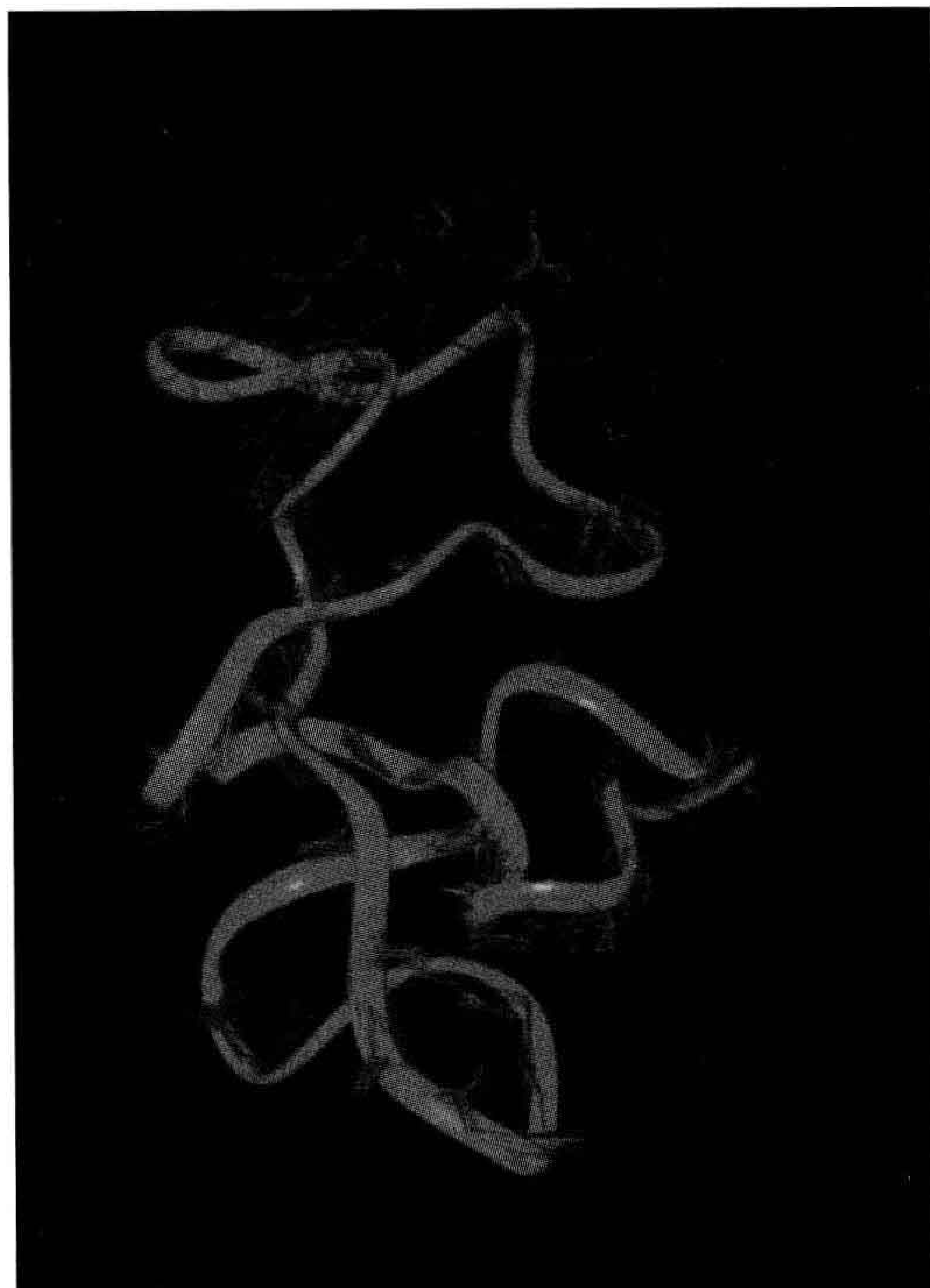


FIGURE 28.7 Solution structure of the site 3 anemone toxin Anthopleurin-B from Protein DataBase file 1APF. Original data from Monks et al. (1995). Structure. 3, 791-803. The backbone ribbon depicts the convergence of 20 NMR models, with individual backbones included to indicate the disorder region (Residues 9–20) in which several residues essential for affinity have been demonstrated. This loop region is conserved in all site 3 anemone toxins of known structure.

significant than any involving electrostatic interactions. Surprisingly, even Arg 14, which is conserved in all known anemone toxins, is revealed by mutagenesis to play at most a minor role in defining binding affinity (Khera and Blumenthal, 1994).

While sea anemone and α-scorpion toxins bind to the channel in a membrane-potential-dependent manner and their binding sites overlap at least in part, β-scorpion toxins bind to a demonstrably distinct site on the same protein and their binding is potential-independent. β-Scorpion toxins are also pharmacologically different from their homologous α-toxin counterparts in that their binding modifies the voltage-dependence of channel activation, rather than inhibiting inactivation. The β-toxin binding site has been mapped by mutagenesis to the S3–S4 linker of domain II, leading to the proposal that these toxins function by trapping the domain II voltage sensor in its deployed conformation (Cestele et al., 1998). Perhaps the most thorough structure–function analysis of the β-toxins has been carried out by alanine scanning mutagenesis of toxin Css4 (Cohen et al., 2005). This work identified a group of aromatic residues (Y24, Y40, Y42, F44 and W58) whose replacement diminishes binding to $Na_V1.2$ by 100–1000 fold without discernible effect on toxin structure. The last four of these residues are located in the second and third β-strands of Css4, forming a surface hydrophobic cluster. In addition to these aromatic sites, mutation of E28 decreases binding affinity by several hundredfold. Both Y24 and E28 are found in the single α-helix of Css4. Somewhat surprisingly, in view of the cationic nature common among scorpion and anemone toxins, no essential positively-charged residues were identified.

Over the past 5–10 years, a number of new polypeptide toxins which modify sodium channel function have been isolated from tarantula venoms and characterized in some detail. These toxins typically contain about 30 amino acid residues and share a three disulfide, cystine-knot (ICK) structural motif and are homologous to other polypeptides which modify K-channel function. Protx-II, the most thoroughly characterized of these toxins, shifts the voltage-dependence of $Na_V1.5$ channel activation in the depolarizing direction and decreases G_{max} at all potentials tested (Edgerton et al., 2008); in the $Na_V1.7$ channel, it appears to delay inactivation as well (Xiao et al., 2010). Mutant cycle analysis of Protx-II binding to $Na_V1.5$ indicates that previously characterized channel sequences required for binding of site 3 or 4 toxins are not important for Protx binding (Smith et al., 2007), although a similar study of $Na_V1.2$ suggests an interaction with the S3–S4 loop of domain II which is known to be essential for binding of site 4 toxins (Sokolov et al., 2008). The interaction of Protx-II with its target channels appears to be dominated by hydrophobic interactions, perhaps suggesting that its binding site lies wholly or partially within the membrane (Smith et al., 2005).

The existence of multiple sodium channel genes that display tissue-specific expression in mammals is well established. It is thus logical to inquire into the isoform selectivity of the toxins discussed above, a question whose answer is of great potential significance in drug design. It is clear, for example, that the cardiac channel $Na_V1.5$ is at least 100 times more sensitive to the sea anemone toxin anthopleurin-B than are the neuronal and muscle channels (Khera et al., 1995) and that the peripheral channel $Na_V1.7$ is two to three orders of magnitude more sensitive than any other Na-channel to the tarantula toxin Protx-II (Smith et al., 2005, 2007). Similarly, μ-conotoxins display a very high selectivity for muscle sodium channels.

IIID. Relationships among Sites 1–4

All of the known polypeptide toxin binding sites are structurally distinct from those for the alkaloid activators

and guanidinium inhibitors. However, it is well-established that these sites communicate with one another. The distances between the various toxin sites have been estimated using resonance energy transfer between fluorescent derivatives of the bound ligands. In addition to confirming that the α- and β-toxin sites are unique and separated by about 22 Å, these studies indicate that the TTX site is some 33 Å removed from that for β-toxins and the BTX site lies about 37 Å distant from that of α-toxins. Both fluorescence resonance energy transfer experiments and direct analyses of binding affinities to the various sites support the existence of allosteric interactions between sites 1 and 2, 1 and 3, and 2 and 3. A very recent study, using mutagenically truncated site 4 toxin, is consistent with allosteric interactions between sites 3 and 4 as well (Cohen et al., 2008).

IIIE. Other Toxins Specific for the Na^+ Channel

A variety of non-proteinaceous substances of diverse (and in some cases, unknown) structure has been shown to interact with the Na^+ channel at sites distinct from those discussed previously. These include lipid-soluble dinoflagellate toxins (brevetoxins, ciguatoxin and maitotoxin), the *Goniopora* toxins and the pyrethroid insecticides. The brevetoxins induce the Na^+ channel to open at membrane potentials of −80 to −160 mV and also abolish rapid inactivation; these effects lead to both generation of repetitive action potentials and ultimately membrane depolarization. Both effects are blocked by TTX. Analyses of brevetoxin binding suggest the existence of a fifth ligand site on the channel, since brevetoxin binding fails to displace toxins bound to sites 1–4. The physiologic effects of ciguatoxin are very similar to those of the brevetoxins, while the mechanism of maitotoxin toxicity is unresolved at this time. *Goniopora* toxins, while not completely characterized, appear to be protein in nature, with molecular weights between 12 000 and 19 000 being reported from different preparations. The mode of action of at least one of these proteins appears to be similar to that of sea anemone toxins, but there is evidence that multiple *Goniopora* toxins with distinct molecular targets exist. Finally, the pyrethroids delay inactivation via interaction with a site distinct from that for polypeptide toxins having the same effect. Physiologic effects of pyrethroids are antagonized by TTX.

IV. VOLTAGE-ACTIVATED AND Ca^{2+}-ACTIVATED POTASSIUM CHANNELS

The use of molecular genetics, electrophysiology and x-ray crystallography has had an enormous impact on our knowledge of the structure, function and diversity of voltage-gated ion channels, and nowhere is this more apparent than in the family of potassium channels ($K_V1.x$–$K_V4.x$). However, despite the enormous power of the genetic approach, the ability of polypeptide toxins specific for this family of channels to distinguish among subtypes is proving an invaluable tool. Both polypeptide and non-proteinaceous blockers, such as tetraethylammonium ions and 4-aminopyridines, were important tools for development of structural models of the K^+ channel pore and the predictions made by these models have been largely borne out by channel crystal structures.

While voltage-dependent Na^+ channels exist in a relatively small number of molecular forms, the diversity seen in K^+ channels is vastly greater: some are ligand-coupled, while others are activated by either Ca^{2+} or depolarization. A large number of channels seem to exist even within this last category. In *Drosophila*, K^+ channels are encoded by genetic loci designated as *shaker*, *shal*, *shab*, *shaw* and *eag* and mammalian counterparts for each of these channel types have been identified. *Shaker* apparently encodes channels of the rapidly inactivating (or A) type and transcripts from this locus display alternative splicing. It seems likely that this gives rise to channel forms that differ with respect to virtually all important properties: pharmacology, voltage-dependence and unit conductance. Multiple transcripts from the *shab* locus have also been observed and the gene products have many of the properties associated with the delayed rectifier channel. The *shal* and *shaw* genes seem to encode A-type and delayed rectifier channels, respectively.

The channels encoded by *shaker* and related genes have many structural features in common with the Na^+ channels discussed above and these proteins display a limited degree of homology at the amino acid level, mostly within their transmembrane regions. In both Na^+ and K^+ channels, the channel "subunit" contains six putative transmembrane helices with the N-terminus being cytoplasmic, and a pore loop located between helices S5 and S6. Helix S4, which contains a series of cationic groups separated by two hydrophobic residues, serves as the main voltage sensor, perhaps with some participation by charged residues in S2 and S3. As with the Na^+ channel, sequences joining the helices designated S5 and S6 are thought to provide the inner lining of the pore and a great deal of evidence that these residues also provide the binding sites for channel-specific toxins has been accumulated over the years. The most obvious structural difference between these channels is that, whereas the Na^+ channel α subunit has a molecular mass of about 260 kDa and contains some 1800 amino acid residues grouped into four homologous domains, the K^+ channel monomer is approximately one-quarter this size. While the monomeric unit of the K^+ channel is thus small relative to its Na^+ and Ca^{2+} counterparts, co-expression of mRNAs encoding distinct channel isoforms in *Xenopus* oocytes results in the appearance of functional channels

having intermediate properties, strongly suggesting that the physiologically relevant form of this channel is a non-covalent tetramer. Crystallographic studies have confirmed this prediction. The possibility of functional diversity arising from both alternative splicing and formation of hetero-oligomeric channels thus arises.

In 1998, MacKinnon's laboratory solved the crystal structure of the *Streptomyces lividans* K^+ channel, KcsA (Doyle et al., 1998) and several other K^+ channel structures, including those from eukaryotes, have since been described (Jiang et al., 2003a; Long et al., 2005). While KcsA is only about 30% as large as the eukaryotic voltage-gated K^+ channels, it displays significant homology within the putative pore-forming regions to (e.g.) the *shaker* and other eukaryotic voltage-gated channels. As a result, the *S. lividans* channel has been useful for modeling the three-dimensional structure of the eukaryotic pore. In the KcsA channel, the pore region contains a 10-residue α-helix (the pore helix) whose C-terminus is oriented toward the center of the pore and is joined to the C-terminal transmembrane helix by a 20-residue linker that lacks regular secondary structure. The helices flanking the pore region are proposed to be analogous to the S5 and S6 helices of eukaryotic K^+ channels. The KcsA-based models of the K^+ channel pore regions were subsequently validated as the structures of archeal and eukaryotic channels were solved.

Most of the known K^+-channel-specific toxins have been purified from scorpion, honeybee, spider and snake venoms (Table 28.2). The first such agent to be characterized was purified by Miller from *Leiurus* venom, and given the colorful, if non-descriptive, name charybdotoxin (Miller et al., 1985). Homologs of this polypeptide have been found in venoms from *Leiurus* (scyllatoxin and agitoxin), *Androctonus* (kaliotoxin), *Buthus* (iberiotoxin) and *Centruroides* (noxiustoxin) species. In addition, the honeybee peptides apamin and mast cell degranulating peptide and a homologous family of snake (*Dendroaspis*) dendrotoxins have been shown to have K^+-channel-blocking activity. Analogous to the case for sodium channels, the potassium channel toxins from scorpion venom comprise a homologous family in which essentially the only *absolutely* conserved residues are involved in disulfide bond formation (Fig. 28.8). Thus, one would reasonably expect these toxins to fold into a generally similar overall structure, but to differ in detail. It is therefore not surprising to realize that at least some of the K^+ channel toxins are able to distinguish among channel subtypes. The honeybee toxins and dendrotoxins display no homology to any of the scorpion polypeptides.

Charybdotoxin (ChTX) was first identified in 1985 as a polypeptide from *Leiurus* venom capable of inhibiting Ca^{2+}-activated K^+ channels from skeletal muscle and is the founding member of a family of structurally homologous peptide blockers of K^+-channels. As such, the following discussion of peptidic K-channel blockers will use ChTX as a paradigm. The three-dimensional structure of ChTX was solved by NMR spectroscopy in 1991 (Fig. 28.9; Bontems et al., 1991a,b; 1992). Its major features include a small, triple-stranded β-sheet encompassing residues 1–2, 25–29 and 32–36 linked by disulfide bonds (Cys 13–Cys 33 and Cys 17–Cys 35) to an α-helix including residues 10–19. Surprisingly, however, this overall fold is quite similar to those of the *Centruroides* and *Androctonus* Na^+-channel-specific toxins for which crystal structures had been obtained during the 1980s. Structural features shared by these toxin families include three disulfide bonds occurring in similar positions and orientations, the triple-stranded β-pleated sheet (residues 1–4, 37–41 and 46–50 of *Centruroides* toxin versus residues 1–2, 25–29 and 32–36 of charybdotoxin), the single strand of α-helix (residues

TABLE 28.2 Polypeptide Blockers of K^+ Channels

Toxin	Channel Type	K_d	Function
Charybdotoxin	Ca^{2+}-activated Voltage-sensitive	Low nM 140 pM	Blocker
Iberiotoxin	Ca^{2+}-activated (BK)	140 pM	Blocker
Kaliotoxin	Ca^{2+}-activated (BK)	250 pM	Blocker
Noxiustoxin	Ca^{2+}-activated (BK)	20 nM	Blocker
Scyllatoxin	Ca^{2+}-activated (SK)	>300 nM	Blocker
Apamin	SK	10–400 pM	Blocker
Dendrotoxins	Voltage-sensitive	100 pM	Blocker
Hanatoxin SgTx1	$K_V1.x$ $K_V2.1$	High nM 2 μM	Gating modifier Gating modifier

(A) Charybdotoxin-like

```
ChTX        QFTNVSCTTS KECWSVCQRL HNTSRGK-CM NKKCRCYS
ScTX             AFCNL- RMCQLSCRSL GLL--GK-CI GDKCECVKH
KaTX        GVEINVKCSGS PQCLKPCKDA GM-RFGK-CM NRKCHCTP
IbTX        QFTDVDCSVS KECWSVCKDL FGVDRGK-CM GKKCRCYQ
NxTX        TIINVKCTSP KQCSKPCKEL YGSSAGAKCM NGKCKCYNN

Consensus   XXβOUOCOXX +XCXXXC+OU XXXOXGO CU OOKCKCΦ
```

(B) ICK Motif Gating Modifiers

```
Hanatoxin      ECRYLFGGCK TTSDCCKHLG ---CKFRDKY CAWDFTFS
Hainatoxin 4   ECLGFGKGCN PSNDQCCKSS NLVCSRKHRW CKYEI
ProTx-1        ECRWLWGGCS AGQT-CCKHL V--CSRRHGW CVWDTGFS
SgTx-1         TCRYLFGGCK TTADCCKHLA ---CRSDGKY CAWDGTF
```

FIGURE 28.8 Primary structures of selected polypeptide toxins specific for K^+ channels. Sequences are depicted in the single letter code, with disulfide bonds linking Cys 7 to Cys 28, Cys 13 to Cys 33 and Cys 17 to Cys 35 in charybdotoxin. Highlighted residues are invariant within a class. In the consensus sequence, the coding is + = Cationic residue; O = Polar residue; X = Character undefined; U = Non-polar residue; Φ = Aromatic residue; β = Branched side chain. ChTX, charybdotoxin; ScTX, scyllatoxin; KaTX, kaliotoxin; IbTX, iberiotoxin; NxTX, noxiustoxin; αDTx, α-dendrotoxin; Dtx_I, dendrotoxin I; kalicludine, K^+ channel blocker from *Anemonia sulcata*. (B) Primary sequences of selected gating modifiers of K_V channels. In the ICK motif to which these toxins conform, disulfide bonds link Cys2–16, Cys9–21 and Cys15–28.

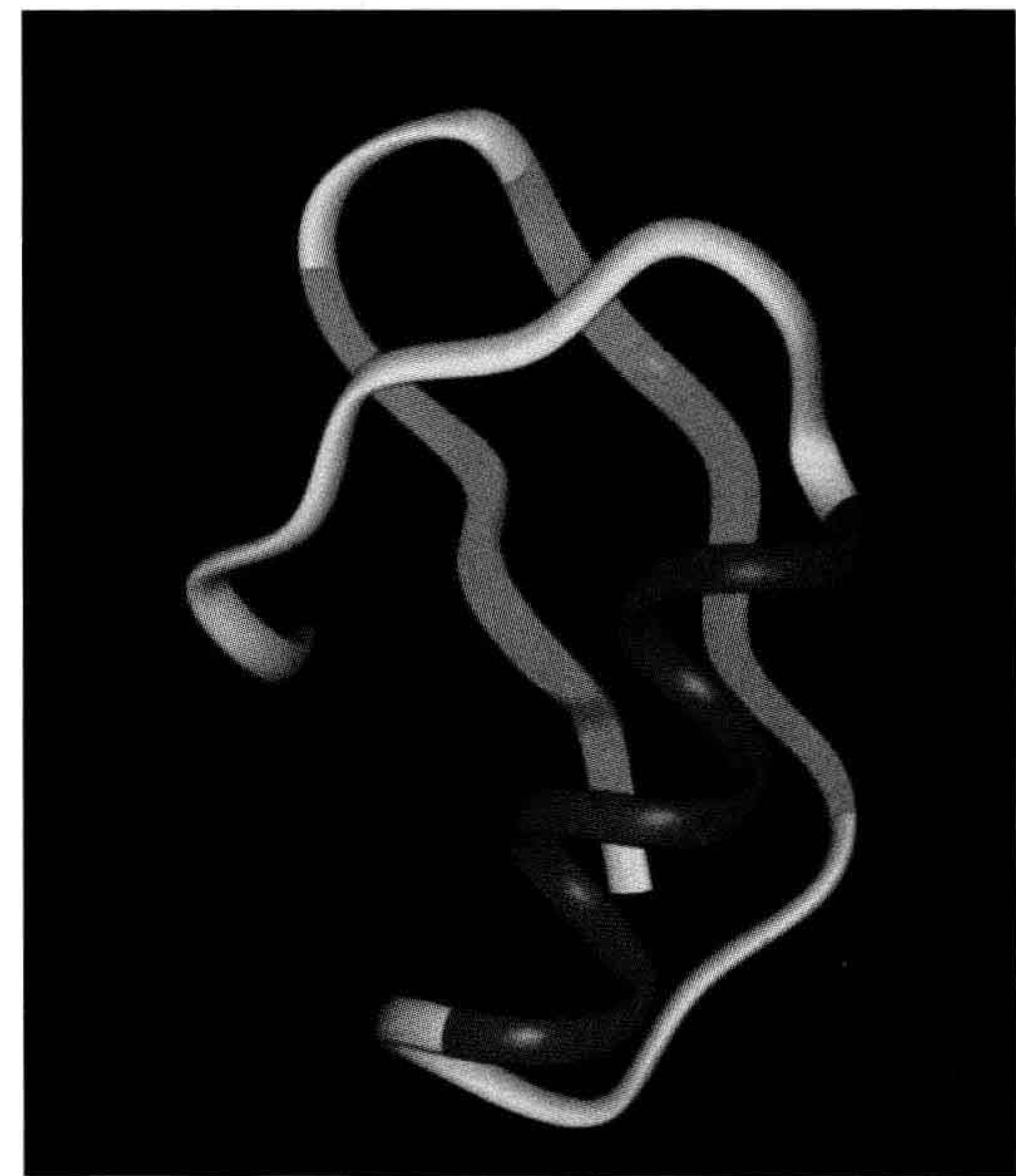


FIGURE 28.9 Solution structure of charybdotoxin. The backbone ribbon depicts the single α-helix (blue) and two strands of the β-sheet (cyan) against which it is docked (pdb2CRD). *(Original data reported in Bontems et al. (1992). Biochemistry. 31, 7756-7764.)*

23–32 versus 10–19) and a significant proportion of extended structure (Fig. 28.10). The differences in comparing the structures of these long and short neurotoxins are most pronounced in loop regions connecting the elements of defined secondary structure. Thus, the scorpion

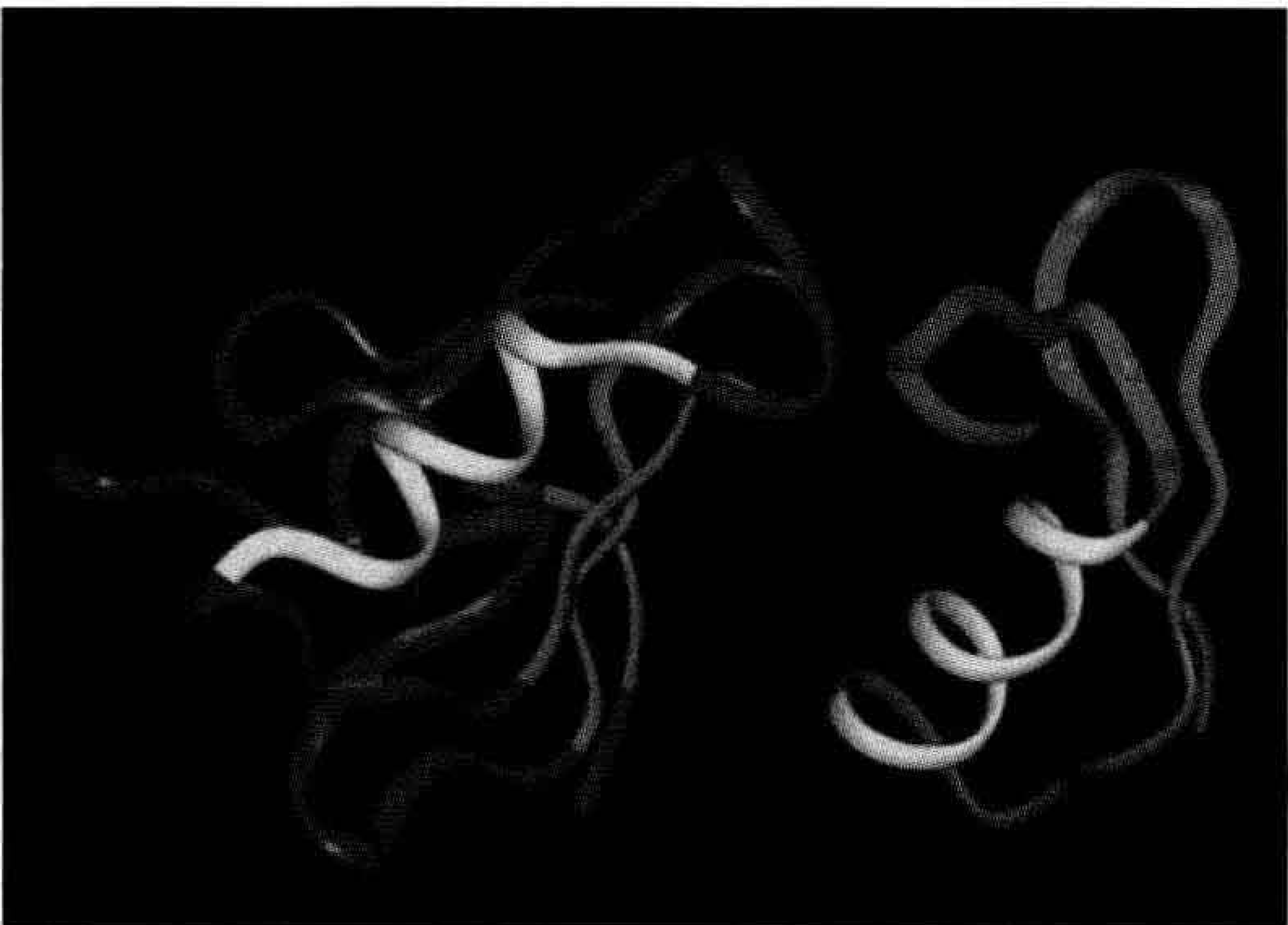


FIGURE 28.10 Comparison of the backbone structures of *Centruroides* toxin (left, pdb2JZA) and charybdotoxin (right, pdb2CRD), color coded to highlight the conservation of a single α-helix (yellow) docked against a three-stranded β-sheet (red).

neurotoxins as a group share a common structural motif, apparent only at the level of three-dimensional structure, regardless of the nature of their target channel. The apparent similarities in channel folding thus seem to be mirrored in the structures of their "ligands". Interestingly, this motif appears to be similar to one observed in insect defensins, small peptides produced in response to injury that are thought to play a role in protecting insects against bacterial infections (Bontems et al., 1992). It seems counterintuitive that the scorpion toxins, despite their vastly different pharmacologies, display conservation of tertiary structure, while anemone and scorpion α-toxins, which show very similar pharmacologies, do not. Perhaps this is simply indicative of the fact that our knowledge of the molecular interactions important for productive binding of

these toxins to their target sites remains incomplete (however, see the following). However, it should be noted that the very recently characterized K^+-channel-blockers from anemones (e.g. kalicludines and kaliseptines), which are functional homologs of charybdotoxin and dendrotoxin, appear to share neither this structural motif, sequence homology, nor even disulfide connectivities.

Because ChTX possesses a net charge of +5, it was predicted that ionic interactions with the channel would be important in its binding. This prediction is supported by the observations that: (1) ChTX binding affinity is decreased 100-fold in media of high ionic strength, owing to decreased toxin association; and (2) chemical modification of the channel with the carboxylate-specific reagent trimethyloxonium (TMO) ion greatly reduces ChTX binding. The structure of the *S. lividans* channel reveals that the binding site for cationic toxins like ChTX is rich in acidic amino acid residues. Affinity also depends on membrane potential, with ChTX preferring the open conformation by approximately sevenfold. More recent studies with charybdotoxin mutants are consistent with hydrophobic interactions between channel sites and Met 29 and Tyr 36 of ChTX as also being important for binding.

In addition to BK channels, charybdotoxin also blocks voltage-dependent K^+ channels in frog ganglia and SK channels from *Aplysia*. However, its best known application has been as a molecular ruler useful for mapping the pore of the *shaker* channel in the days before channel crystal structures were available (Goldstein et al., 1994). Mutant cycle analyses using both ChTX and the homologous agitoxin-2 identified both anionic and hydrophobic channel residues whose mutation diminished binding significantly. This work, and that of others, yielded a low-resolution structural map of the channel's outer vestibule. Although these studies are now largely of only historical interest, it is important to realize that the structural models of the pore which arose from these studies has been largely validated by subsequent crystal structures of archaeal and eukaryotic K^+-channels (Doyle et al., 1998).

Other polypeptide K^+-channel blockers may have more restricted specificities than ChTX. For example, iberiotoxin (IbTX), isolated from *Buthus* venom is 70% homologous to ChTX, but significantly less basic. IbTX inhibits ChTX binding to smooth muscle non-competitively, consistent with it having a distinct binding site, and appears to recognize only Ca^{2+}-activated channels in a variety of tissues (Galvez et al., 1990). Studies with chemically-synthesized chimeras of the two toxins suggest that C-terminal sequences of each toxin dictate channel specificity to a large degree: a construct containing the N-terminal 19 residues of ChTX and the C-terminal 18 from IbTX has IbTX-like properties, and vice versa. Two additional scorpion toxins have been shown to target preferentially the BK-type channel. Kaliotoxin, recently purified and characterized from *Androctonus* venom, is approximately 50% homologous to ChTX, IbTX and noxiustoxin and has been shown to suppress the whole-cell Ca^{2+}-activated K^+ current in mollusk and rabbit sympathetic nerve. The affected channel is insensitive to both apamin and dendrotoxins and is blocked by ChTX and TEA. Noxiustoxin (NxTX), purified from *Centruroides* venom, is 50% identical to ChTX, but due to its relatively low affinity in many systems and its apparent interaction with a multiplicity of channel types, it seems unlikely that NxTX will be widely useful for channel purification and/or discrimination studies.

In recent years, several spider toxins, most notably hanatoxin, versustoxin (VsTX) and SgTx, have become important tools in potassium channel research. This family of structurally homologous gating modifiers all shift the voltage dependence of activation upon interaction with the channel's S3–S4 linker (Swartz and MacKinnon, 1997) and as such have been important probes of channel gating mechanisms. In particular, use of VsTX and hanatoxin has helped demonstrate the commonality of the so-called paddle motif in gating of voltage-sensitive channels (Jiang et al., 2003b; Alabi et al., 2007, Bosmans et al., 2008). Their structures, essentially consisting of a series of loops stabilized by three disulfide bonds, all conform to the ICK motif (Fig. 28.11). Another common feature of these toxins

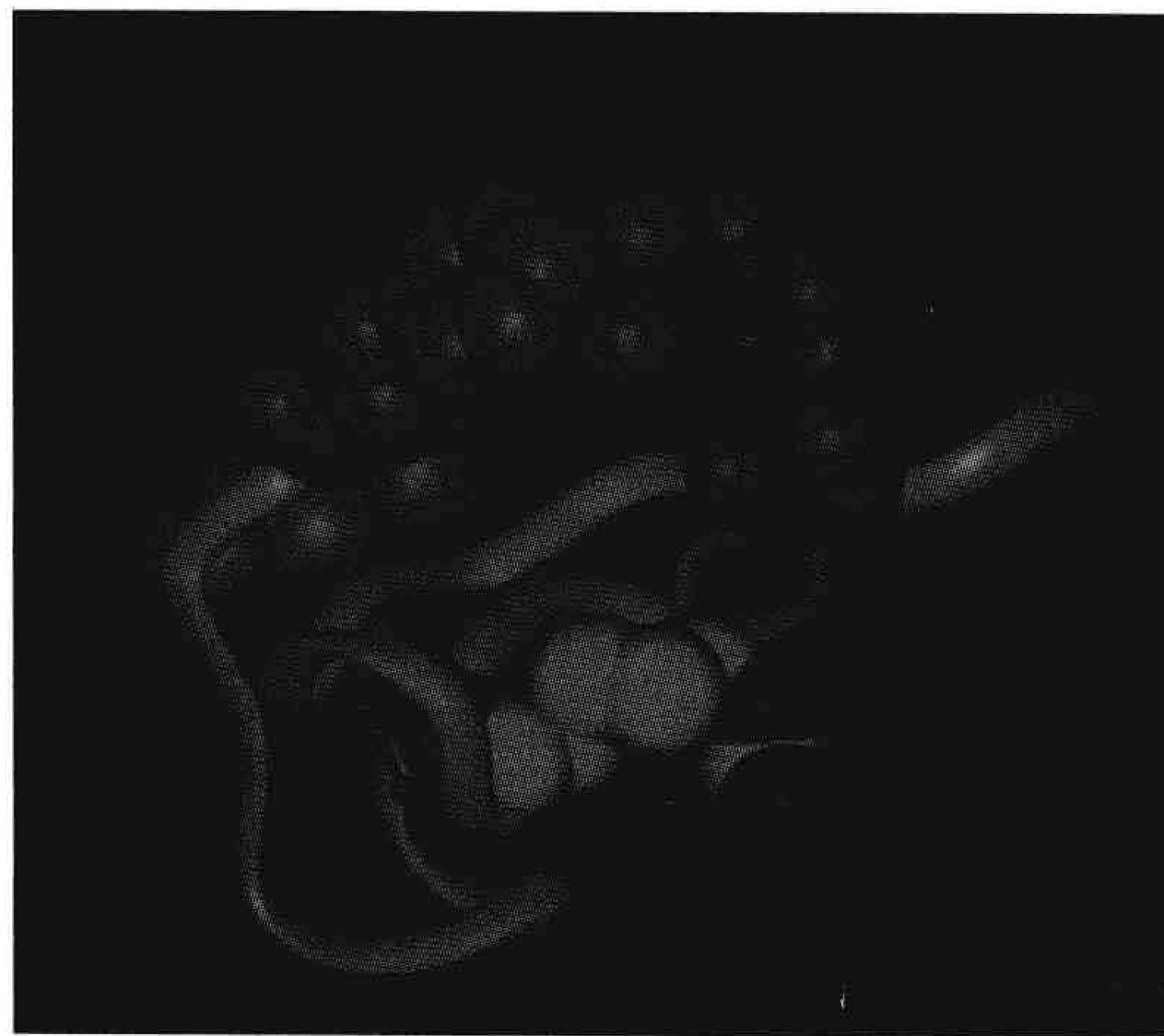


FIGURE 28.11 Solution structure of the ICK-motif K^+-channel gating modifier SgTx-1 (pdb1LA4). The backbone of this polypeptide is largely devoid of regular secondary structure, such that toxin folding is absolutely dependent on the integrity of the three disulfide bonds, shown in ball and stick rendering. Amino acid residues shown in CPK rendering have been shown by Wang et al. (2004) to be essential for binding affinity and include the hydrophobic bulge (Leu5, Phe6 and Trp30) at the top of the molecule plus two cationic residues (Arg3 and Arg22) located on the opposite face. A homologous hydrophobic bulge has been shown to be required for activity in a second ICK toxin, Protx-II. *(Smith et al., 2007)*

is the presence of a hydrophobic bulge protruding from the surface of the molecule (Lee et al., 2004) which contains several residues essential for toxin binding (Wang et al., 2004). These properties have led to the proposal that the spider toxin binding site is at least partially membrane-embedded (Milescu et al., 2007; Lee and MacKinnon, 2004). SgTX-1 is the most thoroughly characterized of these spider toxins in terms of structure–function relationships.

Apamin is an 18-residue polypeptide containing two disulfide bonds; it has an α-helical core comprising residues 9–15 flanked by regions rich in β-turns. Analysis of synthetic analogs of apamin highlights the importance of arginines 13 and 14 for activity. Electrophysiologic analyses and ion flux experiments indicate that apamin is directed against the SK channel in guinea pig hepatocytes, murine neuroblastoma cells and cultured rat muscle cells. Iodinated apamin has been used to demonstrate the existence of high affinity ($K_d = 10 - 400$ pM) receptors in rat brain, with affinity increasing with [K^+]. The chemical nature of the apamin-binding protein has been studied by radiation inactivation and chemical cross-linking, but the results have been inconclusive, with multiple polypeptides being labeled.

Dendrotoxins comprise yet another family of toxins which target the K^+ channel and, at present, are the only snake (*Dendroaspis* species) toxins known to do so. Although larger than the scorpion and spider toxins, dendrotoxins (Dtx; four homologs known) are otherwise grossly similar, being highly cationic molecules containing 57–59 amino acid residues cross-linked by three disulfide bonds. Structurally, the Dtxs are clearly related to the small subunit of β-bungarotoxin and to bovine pancreatic trypsin inhibitor (BPTI). Dendrotoxins were first identified by their ability to stimulate neurotransmitter release at both central and peripheral neurons. Available electrophysiologic data now indicate that α-Dtx recognizes a variety of voltage-dependent K^+ channels. The Dtx sensitivity of RCK channels expressed in *Xenopus* oocytes has been analyzed, showing that rapidly inactivating channels are less sensitive than slowly inactivating ones, although all four types were responsive. Based on immunologic cross-reactivity, the α-Dtx receptor in mammalian brain is likely related to proteins encoded by the *shaker* locus and mutations in the S5–S6 linker of RBK1 have been shown to influence strongly Dtx binding to this *shaker* homolog.

V. VOLTAGE-DEPENDENT CALCIUM CHANNELS

Voltage-dependent Ca^{2+} channels are a good deal more complex than the K^+-channels discussed in Section IV, containing five subunits ranging in size from approximately 30 to 170 kDa (Catterall, 1991). Nonetheless, certain structural features of the Ca^{2+} channel are strikingly similar to those of the Na^+ and K^+ channels. Most importantly, the α_1 subunit of the calcium channel is 29% identical to the α subunit of the rat brain $Na_V1.2$ channel and the two proteins have functionally related but chemically distinct residues at about the same frequency. Application of the usual predictive structural algorithms to the α_1 subunit suggest the protein to be organized into four homologous structural domains, each containing the now-familiar six transmembrane helices and P loop. In addition, the sequence of the S4 helix shows that, like its counterparts in Na^+ and K^+ channels, this region functions as the voltage sensor. Heterologous expression experiments in mammalian cells have shown that the α_1 subunit is essential to the properties of dihydropyridine-sensitive Ca^{2+} channels.

Knowledge of the toxinology of Ca^{2+} channels is less extensive than for Na and K channels, at least as regards polypeptide effectors. There are no known scorpion, anemone or snake toxins directed at this channel molecule. Known peptide blockers of the Ca^{2+} channel are the ω–conotoxins and a family of peptides from funnel web spiders that are structurally unrelated to the conotoxins; both groups prevent transmitter release at presynaptic terminals (Venema et al., 1992). In addition, several gating modifier tarantula toxins have recently been described. At least seven ω-conotoxins have been described; their commonalities include their cationic nature, the presence of three disulfide bonds, amidated C-termini and a large number of hydroxylated amino acids, including in some cases hydroxyproline. Two basic classes of these conotoxins are known and homology across these classes amounts to about 40%. However, it should again be emphasized that this value may be misleading in view of the fact that approximately half the identical residues are involved in disulfide bonds.

ω–Conotoxins irreversibly block stimulus-evoked transmitter release in frog neuromuscular preparations; because the muscle retains the ability to respond to a direct stimulus, a presynaptic target for the toxin is indicated. That this target is the Ca^{2+} channel has since been confirmed in chick dorsal root ganglia (DRG). The effect of this toxin seems to be irreversible: in experiments in which DRG was treated with 100 nM toxin, then washed for 2 hours, no recovery of Ca^{2+} activity was observed.

Because many distinct Ca^{2+} channel subtypes have been characterized electrophysiologically, it is natural to ask whether all are equally susceptible to the ω-conotoxins. Clearly, from the experiments described above, muscle channels are unaffected. However, even among neuronal channels, at least three subtypes are distinguishable by a variety of criteria, including gating kinetics, unit conductance and antagonist pharmacology: Nowycky and coworkers, who studied them in chick DRG, designated these channels as T, N, and L-types. The L-type channel is

distinguished by its sensitivity to dihydropyridines (DHPs), whereas T-types are not affected by these agents. ω-Conotoxins block T-type channels only weakly, whereas inhibition of neuronal L-type channels is essentially complete and irreversible in almost all cases; the irreversibility precludes an accurate determination of K_d.

Binding of ω-conotoxins to a variety of tissues has been analyzed, with K_d values in the subnanomolar range commonly reported. However, the validity of these values may fairly be questioned, given the irreversible nature of the toxin's effects. What is most clear is the lack of competition between the conotoxins and any class of organic channel blockers: dihydropyridine, benzothiazepine and phenylalkylamine binding is unaffected in the presence of high concentrations of any of these drugs. In interpreting the literature on ω-conotoxin binding, it must be remembered that distinct forms of this toxin are made by different *Conus* species and these toxins do not invariably have the same specificity.

Two classes of spider toxin blockers, distinguishable by size and amino acid sequences, are now known and have been designated either as agatoxins (not to be confused with agitoxin, discussed previously) or curtatoxins (Adams, 2004). The shorter group (μ-toxins) contains 36–38 residues and is cross-linked by four disulfides; in addition, these μ-toxins are distinguished from the polypeptides discussed previously in being generally less cationic. A second group of spider toxins (ω–agatoxins) contains 65–75 residues and as many as six disulfides and is more cationic than the shorter group. Comparison of representative sequences spider toxin undescores their lack of relatedness to the conotoxins at the level of primary structure.

Type III and IV ω-agatoxins reduce calcium influx by blockade of vertebrate presynaptic L, N and P/Q-type, voltage-gated calcium channels, thereby limiting synaptic neurotransmitter release. ω-Aga-IIA has been shown to inhibit binding of CgTX GVIA to chick brain membranes, while ω-Aga-IA and-IB do not, suggesting that these spider toxins discriminate among channel subtypes. The type III toxins have molecular weights around 8.5 kDa, while a broader range of sizes is seen for type IV agatoxins. Type IV agatoxins appear to be highly selective for P and Q type Ca^{2+}-channels.

In recent years, it has been discovered in several laboratories that toxins previously thought to target a single channel type are actually much less specific. Surprisingly, this promiscuity extends beyond channel isoforms, encompassing channels having different ion specificities. One example of this is the aforementioned tarantula toxin, Protx-II. Originally isolated as an inhibitor of $Na_V1.5$ channels, (Middleton et al., 2002) and characterized most extensively against $Na_V1.2$, 1.5 and 1.8, Protx-II has recently been discovered to inhibit activation of the T-type channel $Ca_V3.1$ (Edgerton et al., 2010). As is true for its actions on the $Na_V1.5$ channel, the toxin both inhibits $Ca_V3.1$-mediated currents and shifts the voltage dependence of activation in the positive direction without altering single channel currents or gating charge. These effects arise from a slowing of channel activation and a destabilization of the open state. In view of its dual specificity for Na/Ca channels, it is surprising that Protx-II displays little or no activity against the T-channel isoforms $Ca_V3.2$ and 3.3.

VI. OTHER TOXINS AND CHANNELS

VIA. α-Conotoxins and the Nicotinic Acetylcholine Receptor-Associated Channel

Although not targeted directly to ion channels, the α-conotoxins will be briefly discussed in the interest of covering all of the conotoxin classes. The α-conotoxins are the smallest of the conotoxin peptides known, comprising 13–15 amino acid residues, of which four are half-cystines involved in disulfide bonds. All of the known α-conotoxins are cationic, with formal charges of +1.5 to +3.5 at neutral pH. Conservative changes are tolerated at most positions without significant loss of activity, so that relatively little information on structure–function relationships can be derived from synthetic analogs. It is clear that the presence of two disulfides in such a short peptide imposes relatively severe constraints upon its three-dimensional structure. The proposed structure for α-conotoxin, based upon NMR measurements, includes β-turns at residues 5–8 and 9–12.

α-Conotoxins are directed at the nicotinic acetylcholine receptor channel and mechanistically act like the snake toxins exemplified by α-bungarotoxin. In fact, the most widely accepted model for α-conotoxin structure places several of its side-chain functional groups into α-conotoxin is consistent with its observed ability to compete with other nAChR antagonists like *d*-tubocurarine and α-BgTX. On this basis, α-conotoxin is, strictly speaking, not truly directed against the ion channel and will not be discussed further.

BIBLIOGRAPHY

Adam, M. E. (2004). Agatoxins: ion channel specific toxins from the American funnel web spider, Agelenopsis aperta. *Toxicon, 43*, 509–525.

Alabi, A. A., Bahamonde, M. I., Jung, H. J., Kim, J. I., & Swartz, K. J. (2007). Portability of paddle motif function and pharmacology in voltage sensors. *Nature, 450*, 370–376.

Benzinger, G. R., Kyle, J. W., Blumenthal, K. M., & Hanck, D. A. (1998). A specific interaction between the cardiac sodium channel and site-3 toxin anthopleurin B. *J Biol Chem, 273*, 80–84.

Bontems, F., Roumestand, C., Boyot, P., et al. (1991a). Three-dimensional structure of natural charybdotoxin in aqueous solution by ^{1}H-NMR. Charybdotoxin possesses a structural motif found in other scorpion toxins. *Eur J Biochem, 196*, 19–28.

Bontems, F., Roumestand, C., Gilquin, B., Menez, A., & Toma, F. (1991). Refined structure of charybdotoxin: common motifs in scorpion toxins and defensins. *Science, 254*, 1521–1523.

Bontems, F., Gilquin, B., Roumestand, C., Menez, J. A., & Toma, F. (1992). Analysis of side-chain organization on a refined model of charybdotoxin: structural and functional implications. *Biochemistry, 31*, 7757–7764.

Bosmans, F., Martin-Eauclaire, M. F., & Swartz, K. J. (2008). Deconstructing voltage-sensor function and pharmacology in sodium channels. *Nature, 456*, 202–208.

Cannon, S. C., & Corey, D. P. (1993). Loss of Na-channel inactivation by anemone toxin mimics the myotonic state in HPP. *J Physiol, 466*, 501.

Catterall, W. A. (1977). Activation of the action potential Na+ ionophore by neurotoxins: an allosteric model. *J Biol Chem, 252*, 8669–8676.

Catterall, W. A. (1991). Functional subunit structure of voltage-gated calcium channels. *Science*, 253.

Catterall, W. A. (2000). From ionic currents to molecular mechanisms: structure and function of voltage-gated sodium channels. *Neuron, 26*, 13–25.

Catterall, W. A., Cestele, S., Yarov-Yarovoy, V., Yu, F. H., Konoki, K., & Scheuer, T. (2007). Voltage-gated ion channels and gating modifier toxins. *Toxicon, 49*, 124–141.

Cestele, S., Qu, Y., Rogers, J. C., Rochat, H., Scheuer, T., & Catterall, W. A. (1998). Voltage sensor-trapping: enhanced activation of sodium channels by β-scorpion toxin bound to the S3–S4 loop in domain II. *Neuron, 21*, 919–931.

Chahine, M., George, A. L., Jr., Zhou, M., et al. (1994). Na channel mutation in paramyotonia congenita uncouple inactivation from activation. *Neuron, 12*, 281.

Cohen, L., Karbat, I., Gilles, N., et al. (2005). Common features in the functional surface of scorpion β-toxins and elements that confer specificity for insect and mammalian voltage-gated sodium channels. *J Biol Chem, 280*, 5045–5053.

Cohen, L., Lipstein, N., Karbat, I., et al. (2008). Miniaturization of scorpion β-toxins uncovers a putative ancestral surface of interaction with voltage-gated sodium channels. *J Biol Chem, 283*, 15169–15176.

Cruz, L. J., Gray, W. R., Olivera, B. M., et al. (1985). Conus geographus toxins that discriminate between neuronal and muscle sodium channels. *J Biol Chem, 260*, 9280–9288.

Cruz, L. J., Kupryszewski, G., LeCheminant, G. W., Gray, W. R., Olivera, B. M., & Rivier, J. (1989). μ-Conotoxin GIIIA, a peptide ligand for muscle sodium channels: chemical synthesis, radiolabeling and receptor characterization. *Biochemistry, 28*, 3437–3442.

Dias-Kadambi, B. L., Combs, K. A., Drum, C. L., Hanck, D. A., & Blumenthal, K. M. (1996a). The role of exposed tryptophan residues in the activity of the cardiotonic polypeptide anthopleurin B. *J Biol Chem, 271*, 23828–23835.

Dias-Kadambi, B. L., Drum, C. L., Hanck, D. A., & Blumenthal, K. M. (1996b). Leucine-18, a hydrophobic residue essential for high affinity binding of anthopleurin-B to the voltage sensitive sodium channel. *J Biol Chem, 271*, 9422–9429.

Doyle, D. A., Cabral, J. M., Pfuetzner, R. A., et al. (1998). The structure of the potassium channel: molecular basis of K-conduction and selectivity. *Science, 280*, 69–77.

Edgerton, G. B., Blumenthal, K. M., & Hanck, D. A. (2008). Evidence for multiple effects of Protx-II on activation gating in $Na_V1.5$. *Toxicon, 52*, 489–500.

Edgerton, G. B., Blumenthal, K. M., & Hanck, D. A. (2010). Inhibition of the activation pathway of the T-type calcium channel $Ca_V3.1$ by Protx-II. *Toxicon, 56*, 624–636.

Escoubas, P., & Rash, L. (2004). Tarantulas: eight-legged pharmacists and combinatorial chemists. *Toxicon, 43*, 555–574.

French, R. J., Sochaczewski, E. P., Zamponi, G. W., Becker, S., Kularatna, A. S., & Horn, R. (1996). Interactions between a pore-blocking peptide and the voltage sensor of the sodium channel: an electrostatic approach to channel geometry. *Neuron, 16*, 407–413.

Galvez, J. A., Gimenez-Gallego, G., Reuben, J. P., et al. (1990). Purification and characterization of a unique, potent, peptidyl probe for the high conductance calcium-activated potassium channel from venom of the scorpion Buthus tamulus. *J Biol Chem, 265*, 11083–11090.

Goldstein, S. A. N. (1996). A structural vignette common to voltage sensors and conduction pores: canaliculi. *Neuron, 16*, 717–722.

Goldstein, S. A. N., Pheasant, D. J., & Miller, C. (1994). The charybdotoxin receptor of a shaker K^+ channel: peptide and channel residues mediating molecular recognition. *Neuron, 12*, 1377–1388.

Jiang, Y., Lee, A., Chen, J., et al. (2003a). X-ray structure of a voltage-dependent K^+ channel. *Nature, 423*, 33–41.

Jiang, Y., Ruta, V., Lee, A., & MacKinnon, R. (2003b). The principle of gating charge movement in a voltage-dependent K^+-channel. *Nature, 423*, 42–48.

Khera, P. K., & Blumenthal, K. M. (1994). Role of the cationic residues Argenine-14 and Lysine-48 in the function of the cardiotonic polypeptide anthopleurin B. *J Biol Chem, 269*, 921–926.

Khera, P. K., Benzinger, G. R., Lipkind, G., Drum, C. L., Hanck, D. A., & Blumenthal, K. M. (1995). Multiple cationic residues of anthopleuruin B that determine high affinity and channel isoform discrimination. *Biochemistry, 34*, 8533–8541.

Lee, C. W., Kim, S., Roh, S. H., et al. (2004). Solution structure and functional characterization of SGTx1, a modifier of Kv2.1 channel gating. *Biochemistry, 43*, 890–897.

Lee, S. Y., & MacKinnon, R. (2004). A membrane access mechanism of ion channel inhibition by voltage sensor toxins from spider venom. *Nature, 430*, 232–235.

Linford, N. J., Cantrell, A. R., Qu, Y., Scheuer, T., & Catterall, W. A. (1998). Interaction of batrachotoxin with the local anesthetic binding site in transmembrane segment IVS6 of the voltage-gated sodium channel. *Proc Natl Acad Sci USA, 95*, 13947–13952.

Lipkind, G. M., & Fozzard, H. A. (1994). A structural model of the tetrodotoxin and saxitoxin binding site of the Na-channel. *Biophys J, 66*, 1–13.

Lipkind, G. M., & Fozzard, H. A. (2000). KcsA crystal structure as a framework for molecular model of the Na-channel pore. *Biochemistry, 39*, 8161–8170.

Long, S. B., Campbell, E. B., & MacKinnon, R. (2005). Crystal structure of a mammalian voltage-dependent shaker K^+ channel. *Science, 309*, 897–903.

MacKinnon, R., & Yellen, G. (1990). Mutations affecting TEA blockade and ion permeation in voltage-activated K+-channels. *Science, 250*, 276–279.

MacKinnon, R., Cohen, S. L., Kuo, A., Lee, A., & Chait, B. T. (1998). Structural conservation in prokaryotic and eukaryotic potassium channels. *Science, 280*, 106–109.

Middleton, R. E., Warren, V. A., Kraus, R. L., et al. (2002). Two tarantula peptides inhibit activation of multiple sodium channels. *Biochemistry, 41*, 14734–14747.

Milescu, M., Vobecky, J., Roh, S., et al. (2007). Tarantula toxins interact with voltage sensors within lipid membranes. *J Gen Physiol, 130*, 497–511.

Miller, C., Moczydlowski, E., Latorre, R., & Phillips, M. (1985). Charybdotoxin, a protein inhibitor of single Ca-activated K channels from mammalian skeletal muscle. *Nature, 313*, 316–318.

Monks, S. A., Pallaghy, P. K., Scanlon, M. J., & Norton, R. S. (1995). Solution structure of the cardiostimulant polypeptide anthopleurin-A. *Structure, 3*, 791–799.

Mosher, H. S. (1986). The chemistry of tetrodotoxin. *Ann N Y Acad Sci, 479*, 32–43.

Nicholson, G. (2007). Insect-selective spider toxins targeting voltage-gated sodium channels. *Toxicon, 49*, 490–512.

Noda, M., Suzuki, H., Numa, S., & Stuhmer, W. (1989). A single point mutation confers tetrodotoxin and saxitoxin insensitivity on the sodium channel II. *FEBS Lett, 259*, 213–216.

Ohizumi, Y., Nakamura, H., Kobayashi, J., & Catterall, W. A. (1986). Specific inhibition of saxitoxin binding to skeletal muscle sodium channels by geographutoxin II, a polypeptide channel blocker. *J Biol Chem, 261*, 6149–6152.

Olivera, B. M. (2006). Conus peptides, biodiversity-based discovery and exogenomics. *J Biol Chem, 281*, 31173–31177.

Penzotti, J. L., Fozzard, H. A., Lipkind, G. M., & Dudley, S. C. (1998). Differences in saxitoxin and tetrodotoxin binding revealed by mutagenesis of the Na-channel outer vestibule. *Biophys J, 75*, 2647–2657.

Rogers, J. C., Qu, Y., Tanada, T. N., Scheuer, T., & Catterall, W. A. (1996). Molecular determinants of high affinity binding of α-scorpion toxin and sea anemone toxin in the S3-S4 extracellular loop in domain IV of the Na-channel α subunit. *J Biol Chem, 271*, 15950–15962.

Satin, J., Kyle, J. W., Chen, M., et al. (1992). A mutant of TTX-resistant cardiac sodium channels with TTX-sensitive properties. *Science, 256*, 1202–1205.

Shimizu, Y. (1986). Chemistry and biochemistry of saxitoxin analogues and tetrodotoxin. *Ann NY Acad Sci, 479*, 24–31.

Smith, J. J., Alphy, S., Seibert, A. L., & Blumenthal, K. M. (2005). Differential phospholipid binding by site 3 and site 4 toxins: implications for structural variability between voltage-sensitive sodium channel domains. *J Biol Chem, 280*, 11127–11133.

Smith, J. J., Cummins, T. R., Alphy, S., & Blumenthal, K. M. (2007). Molecular interactions of the gating modifier toxin Protx-II with $Na_V1.5$: implied existence of a novel toxin binding site coupled to activation. *J Biol Chem, 282*, 12687–12697.

Sokolov, S., Kraus, R. L., Scheuer, T., & Catterall, W. A. (2008). Inhibition of sodium channel gating by trapping the domain II voltage sensor with Protx-II. *Molec Pharmacol, 73*, 1020–1028.

Stuhmer, W., Conti, F., Suzuki, H., et al. (1989). Structural parts involved in activation and inactivation of the sodium channel. *Nature, 339*, 597–603.

Swartz, K. J. (2007). Tarantula toxins interacting with voltage sensors in potassium channels. *Toxicon*, 49.

Swartz, K. J., & MacKinnon, R. (1997). Mapping the receptor site for hanatoxin, a gating modifier of voltage-dependent K+ channels. *Neuron, 18*, 675–682.

Trainer, V. L., Brown, G. B., & Catterall, W. A. (1996). Site of covalent labeling by a photoreactive batrachotoxin derivative near transmembrane segment IS6 of the sodium channel α subunit. *J Biol Chem, 271*, 11261–11267.

Venema, V. J., Swiderek, K. M., Lee, T. D., Hathaway, G. M., & Adams, M. E. (1992). Antagonism of synaptosomal calcium channels by subtypes of omega agatoxins. *J Biol Chem, 267*, 2610–2615.

Wang, J. M., Roh, S. H., Kim, S., Lee, C. W., Kim, J. I., & Swartz, K. J. (2004). Molecular surface of tarantula toxins interacting with voltage sensors in K_V channels. *J Gen Physiol, 123*, 455–467.

Wang, S., & Wang, G. (1999). Batrachotoxin-resistant Na channels derived from point mutations in transmembrane segment D4-S6. *Biophys J, 76*, 3141–3149.

Xiao, Y., Blumenthal, K., Jackson, J. O., Liang, S., & Cummins, T. R. (2010). The tarantula toxins Protx-II and Huwentoxin-IV differentially interact with human $Na_V1.7$ voltage sensors to inhibit channel activation and inactivation. *Molec Pharmacol, 78*, 1124–1134.

Yang, N., Ji, S., Zhou, M., et al. (1994). Na channel mutations in paramyotonia congenita exhibit similar biophysical phenotypes in vitro. *Proc Natl Acad Sci USA, 91*, 12785.

Zilberg, N., Froy, O., Loret, E., et al. (1997). Identification of structural elements of a scorpion α-neurotoxin important for receptor site recognition. *J Biol Chem, 272*, 14810–14817.

Chapter 29

Ion Channels as Targets for Drugs

Seth Robey, Kevin J. Sampson and Robert S. Kass

Chapter Outline

I. SUMMARY

Many drugs exert their therapeutic effects by acting on the ion channels of various tissues. Electrical activity in the heart is generated by the summation of currents through multiple ion channels (Kass, 1995). The ventricular action potential is characterized by a long-lasting plateau period in which a balance is maintained between small inwardly and outwardly directed exchange of ion channel currents and small changes in this balance can have severe functional consequences. During the past 25 years, a wealth of information has evolved characterizing the molecular structures that form the protein pathways for ion conduction in heart and other excitable cells (Nerbonne and Kass, 2005; Caterall 2010). With the emerging molecular and structural information, pharmacological approaches to disease management are evolving to incorporate rational drug intervention based on specific pathological conditions including genetic defects in cardiac ion channels. As illustrations, we will concentrate on only a few of the ion channels of the cardiac muscle. This chapter will focus on recent progress in the development of a molecular pharmacological approach to targeting two types of cardiac ion channels: voltage-gated calcium (Ca^{2+}) and voltage-gated sodium (Na^+) channels.

II. CALCIUM CHANNELS

At least six types of voltage-gated calcium channels (N-, L-, P-, Q-, R- and T-type) have been identified based on their pharmacological and/or biophysical properties (Caterall, 2000b). In the heart, both T- and L-type channels contribute to cardiac electrophysiology. L-type channels, the targets of organic calcium channel modulators and substrates for several cellular signaling cascades, are highly important in the maintenance of calcium homeostasis because they can be under pharmacological and/or neurohormonal control (Catterall et al., 1991; Tsien et al., 1991; Ma et al., 1992; Sculptoreanu et al., 1993a,b; Gutierrez et al., 1994; Zhao et al., 1994). Skeletal and cardiac muscle L-type calcium channels are heteromultimeric proteins consisting of α_1, β_2, and α_2/δ subunits that are part of a large macromolecular complex including a number of other auxiliary proteins that modulate function (Xu and Colecraft, 2009). Figure 29.1 shows a comparison of the primary putative subunit structures of skeletal and cardiac calcium channels as well as proposed phosphorylation sites.

The functional roles of the channel's individual subunits have been studied by several groups (Dolphin, 2003a; Xu and Colecraft, 2009). The α_1 subunit ($Ca_v1.2$ for L-type and $Ca_v3.2$ for T-type) is the pore-forming peptide and, when expressed in heterologous systems, is sufficient to encode channels with most of the biophysical and pharmacological properties of intact native channels (Mikami et al., 1989; Mori et al., 1991; Hofmann et al., 1993; Welling et al., 1993) (see Fig. 29.1). It is structurally remeniscient of the broader class of voltage-gated ion channels (Caterall, 2010), with four homologous domains of six transmembrane helices and a voltage-sensing S4 helix.

While α_1 provides most of the endogenous biophysical properties, several auxiliary proteins are required for the complete reconstitution of native function (Xu and Colecraft, 2009). Co-expression of α and β subunits is essential for both proper trafficking and the functional reconstitution of channel kinetics in heterologous systems (Dolphin, 2003a). Similarly, α_2/δ subunits increase channel number, increase gating charge and increase ionic current in

Cell Physiology Sourcebook. DOI: 10.1016/B978-0-12-387738-3.00029-9

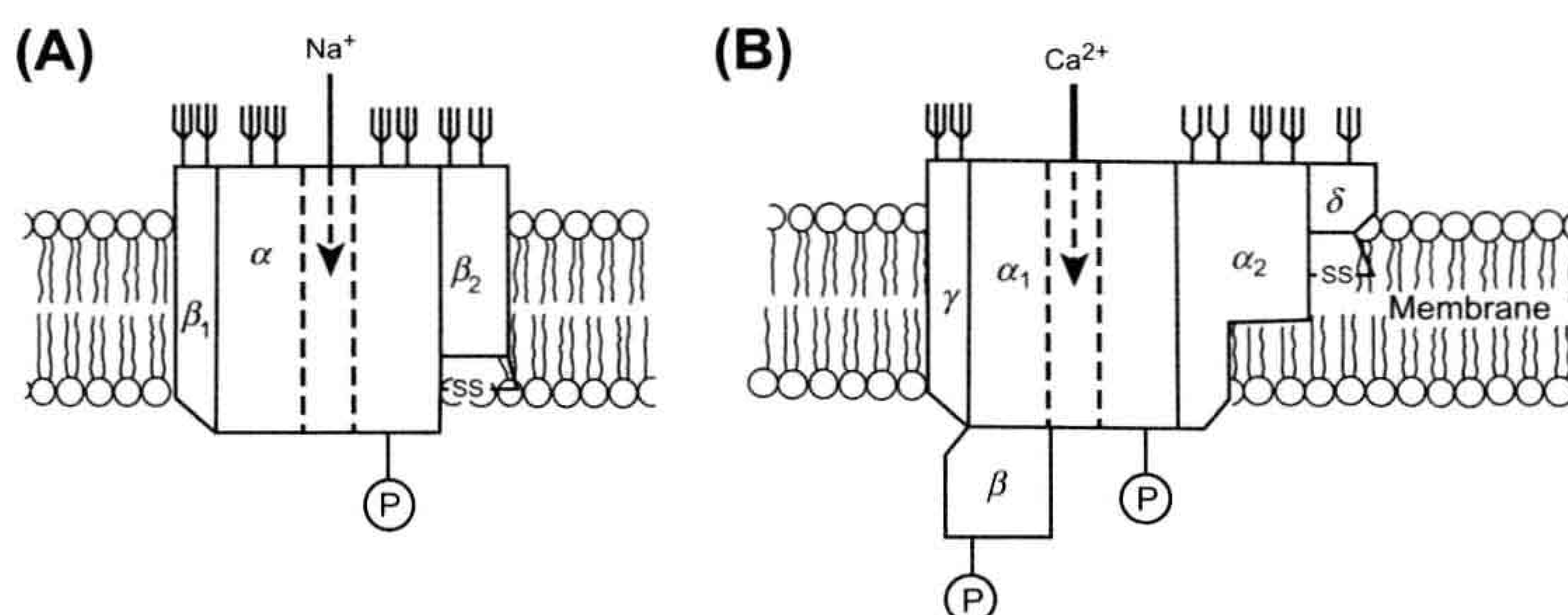


FIGURE 29.1 Block diagram illustrating subunit structures of voltage-gated sodium channels (A) and L-type calcium channels. (B) Sodium channels consist of a central pore-forming subunit (α) and two auxiliary β subunits. L-type calcium channels also contain a pore-forming α subunit and β subunits, but also $\alpha_2\delta$ and γ subunits. *(Catterall, 1988).*

recombinant channels (Bangalore, 1996; Klugbauer et al., 2003). In addition, calmodulin has been shown to associate closely with L-type channels, utilizing its Ca^{2+}-binding capabilities as a feedback regulatory mechanism (Peterson et al., 1999). The γ subunit has been examined less closely than other auxiliary proteins, but appears to have an inhibitory effect on channel function (Xu and Colecraft, 2009). The roles of auxiliary proteins in modulating native channel distribution and function continues to be an area of investigation that will be important in unraveling drug and neurohormonal modulation of L-type calcium channels (Hosey et al., 1996; Dolphin, 2003b).

Functionally, individual L-type calcium channels open, inactivate and close in a voltage- and calcium-dependent manner (Grandi et al., 2010) and their pharmacological and adrenergic modulation has been examined extensively (Triggle, 2007). Perhaps best studied is the marked modulation of L-type calcium channels by the β-adrenergic (β-AR) signaling cascade. Action potentials in the heart are sensitive to catecholamines. Exposure of isolated tissue to norepinephrine increases pacemaker activity (Tsien, 1977), increases the height but decreases the duration of the ventricular action potential plateau and increases the strength of contraction (Reuter and Scholz, 1977). Recent studies have used mass spectometry to identify the precise residues phosphorylated in a protein kinase A (PKA) or CamKII-dependent manner (Emrick et al., 2010).

At a cellular level, calcium entry via L-type channels contributes the localized sparks necessary for initiation of coordinated calcium transients and muscle contraction. Calcium flux across the sarcolemma activates ryanodine receptors (RyR) of the sarcoplasmic reticulum, which are held in close spatial proximity to L-type channels in the plasma membrane. The resulting calcium-dependent calcium release links the excitation of membrane depolarization to the mechanical contraction of the heart (Wier and Balke, 1999; Kushnir and Marks, 2010). In fact, loss of this coupling between sarcolemmal L-type calcium channels and sarcoplasmic RyR has been proposed as a step in the pathogenesis of chronic heart failure (Lyon et al., 2009). Modulation of L-type Ca^{2+} channel activity by calcium channel antagonists has therefore become a key clinical therapeutic approach to the management of hypertension and certain types of cardiac rhythm disturbances (Triggle, 2007; Viola et al., 2009). Several recent reports, however, have raised questions about the effectiveness and safety of some calcium channel antagonists in the treatment of hypertension (Opie 2001). Of particular concern is the widespread distribution of L-type calcium channels in physiologically diverse systems and the resulting potential for dangerous non-specific drug interactions (Xu and Colecraft, 2009). It is clear that an understanding of the precise molecular targets of this important drug family is crucial to improved therapeutic efficacy.

The drugs that have received the most attention belong to three distinct chemical classes: (1) phenylalkylamines (PAAs), including verapamil and D-600; (2) benzothiazepines ((+) *cis* diltiazem); and the 1,4-dihydropyridines (DHPs), such as nitrendipine, nifedipine and nisoldipine (Xu and Colecraft, 2009) (Fig. 29.2). These drugs bind to distinct but allosterically coupled sites on the α_1 subunit (Hockermann et al., 1997b; Striessnig et al., 1998). Studies of the molecular site(s) and mechanisms of action of calcium channel blockers have focused on the biochemical and biophysical role of the binding site within the α_1 subunit and the relationship of that site to modulation of native L-type channels.

Site-directed mutagenesis studies have revealed specific residues that form the binding domains for all three classes of drugs (Hockerman et al., 1997a; Streissnig et al., 1998). Emerging from these studies is the consensus view that domains III and IV of the α_1 subunit are crucial to modulation of L-type Ca^{2+} channels and it is likely that multiple residues on the α_1 subunit interact in an allosteric manner to cause voltage-dependent modulation of channel gating (Tang et al., 1993; Grabner et al., 1996; Peterson et al., 1996, 1997; Schuster et al., 1996; Ito et al., 1997). The most provocative model for the actions of these drugs has been developed by Catterall and his colleagues, who have proposed that DHPs bind at the domain interface

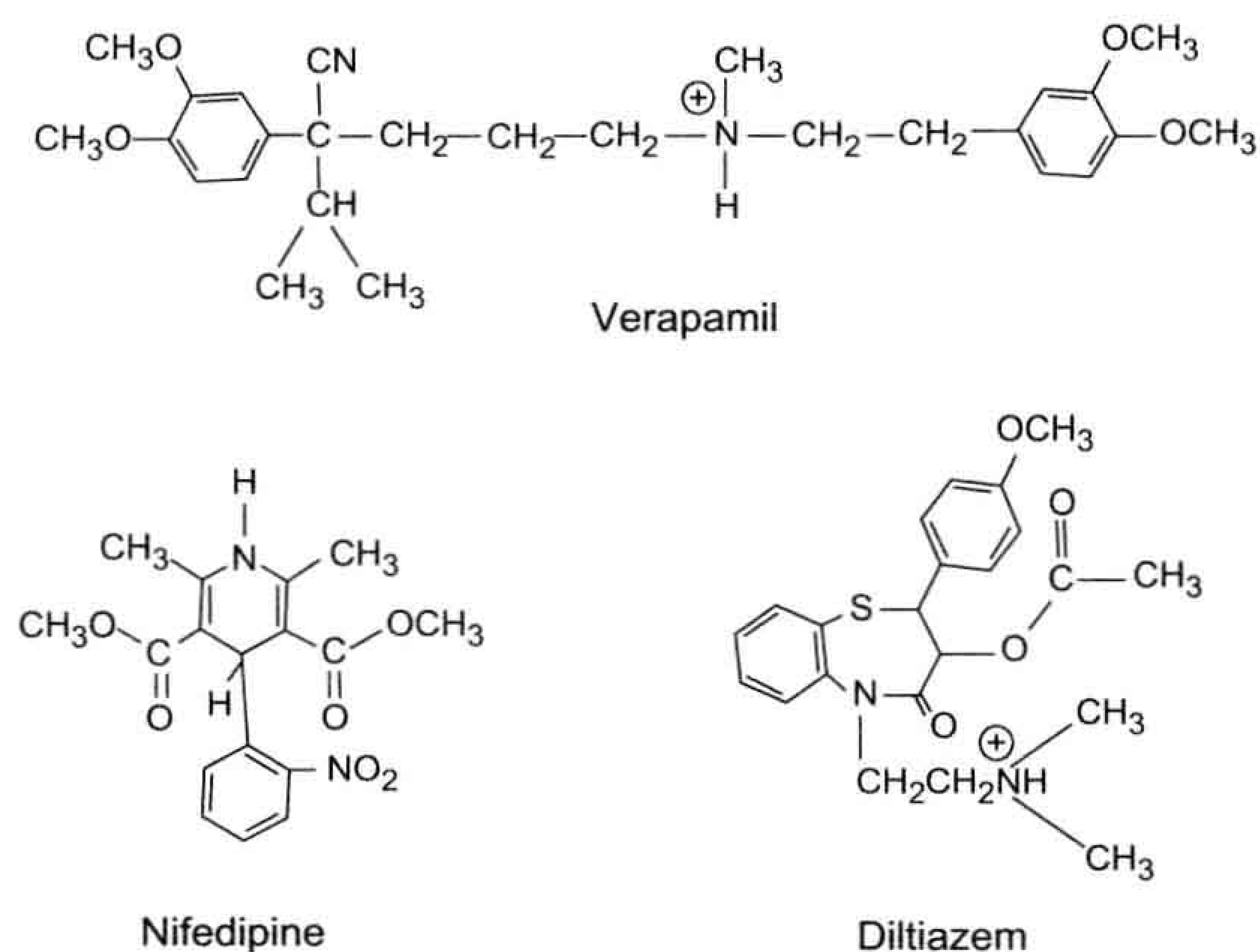


FIGURE 29.2 The major classes of calcium channel blockers: phenylalkylamines (verapamil); dihydropyridines (nifedipine); and benzothiazepines (diltiazem), *(Hille, 1992)*.

allosterically to regulate pore dynamics (Fig. 29.3) (Hockerman et al., 1997b; Tikhonov and Zhorov, 2009). Most importantly in this model, allosteric interactions between bound drug and two domains of the α_1 subunit

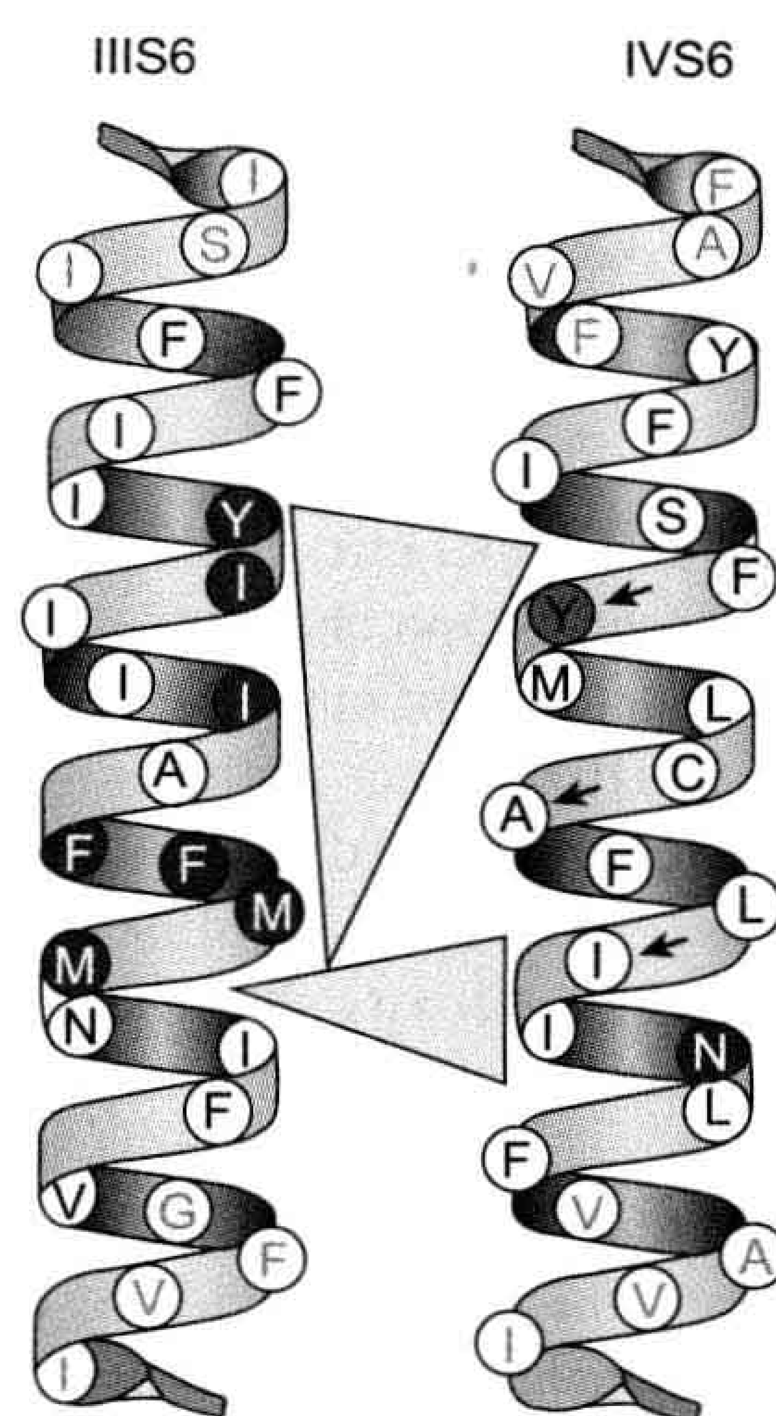


FIGURE 29.3 Domain interface model for dihydropyridine (DHP) binding in the α subunit of the L-type calcium channel. Indicated are key amino acids in domain IIIS6 and domain IVS6 that, when mutated, change dihydropyridine block by factors greater than fivefold. Black letters inside shaded circles represent amino acids that when mutated have significant but less than fivefold reduction in DHP binding. A schematized DHP ligand is illustrated by the triangle contacting the putative key binding residues. It is proposed that channel regulation is a consequence of allosteric interactions between the drug molecule and the two helices IIIS6 and IVS6. *(From Hockermann et al., 1997b.)*

cause conformational changes in the channel, which modify channel gating and control the entry of divalent ions.

Most DHP derivatives previously studied in detail, such as nitrendipine and nisoldipine, are neutral compounds at physiological pH (Rodenkirchen et al., 1982) and inhibit L-type Ca^{2+} channels in a voltage-dependent manner. Repolarization to negative holding potentials readily reverses voltage-enhanced channel inhibition (Sanguinetti and Kass, 1984). The voltage dependence of neutral DHP channel modulation has been interpreted within the general framework of the modulated receptor hypothesis, which accounts for state-dependent allosteric channel block, as in many local anesthetics (see Section III). For DHPs, binding affinity to inactivated channels is high; binding affinity to channels in the resting state is low (Sanguinetti and Kass, 1984; Tikhonov and Zhorov, 2009), consistent with this hypothesis. Interestingly, addition of a charged head-group appears to change this relationship between channel modulation and membrane potential: channel inhibition by charged DHPs is not relieved upon repolarization (Kass, 1994a,b; Lacinova et al., 1999), suggesting the presence of charged salt-bridge partners in the binding pocket.

The interrelationship between the activity of DHPs and divalent ions is also well established (Glossmann et al., 1987). High-affinity DHP labeling of L-type channels in brain, cardiac or smooth muscle membranes depends on the presence of divalent ions (Glossmann and Striessnig, 1990), as does the binding of phenylalkylamines and DHPs to the purified L-type channel (Flockerzi et al., 1986). Ca^{2+} binding to glutamate residues in the putative pore-lining regions (S5–S6) of repeats I–IV in the calcium channel $\alpha_{1C\text{-}a}$ subunit is a critical determinant of ion selectivity and permeation in $\alpha_{1C\text{-}a}$ Ca^{2+} channels (Yang et al., 1993; Tikhonov and Zhorov, 2009). These residues have also been shown to play a significant role in the activity of DHPs and PAAs (Hockerman et al., 1995), suggesting a mechanism by which the drug binding site and ion permeation pathway are allosterically coupled. This notion is supported by the consideration that channel block by charged DHPs is not voltage dependent. Thus, it has been proposed that the binding of Ca^{2+} to the selectivity filter is allosterically coupled to DHP binding via conserved glutamate residues and that stabilization of ions in the permeation pathway makes complete permeation less probable (Peterson and Caterall, 2006).

L-type calcium channels encoded by the smooth muscle splice variant of the α ($\alpha_{1C\text{-}b}$) subunit respond to DHP derivatives differently than channels encoded by the cardiac splice variant ($\alpha_{1C\text{-}a}$) (Zuhlke et al., 1998). In particular, it was found that channels encoded by $\alpha_{1C\text{-}b}$ cDNA were more sensitive to the DHP antagonist nisoldipine than were channels encoded by the $\alpha_{1C\text{-}a}$ splice variant (Fig. 29.4). Subsequent work has shown that this distinct

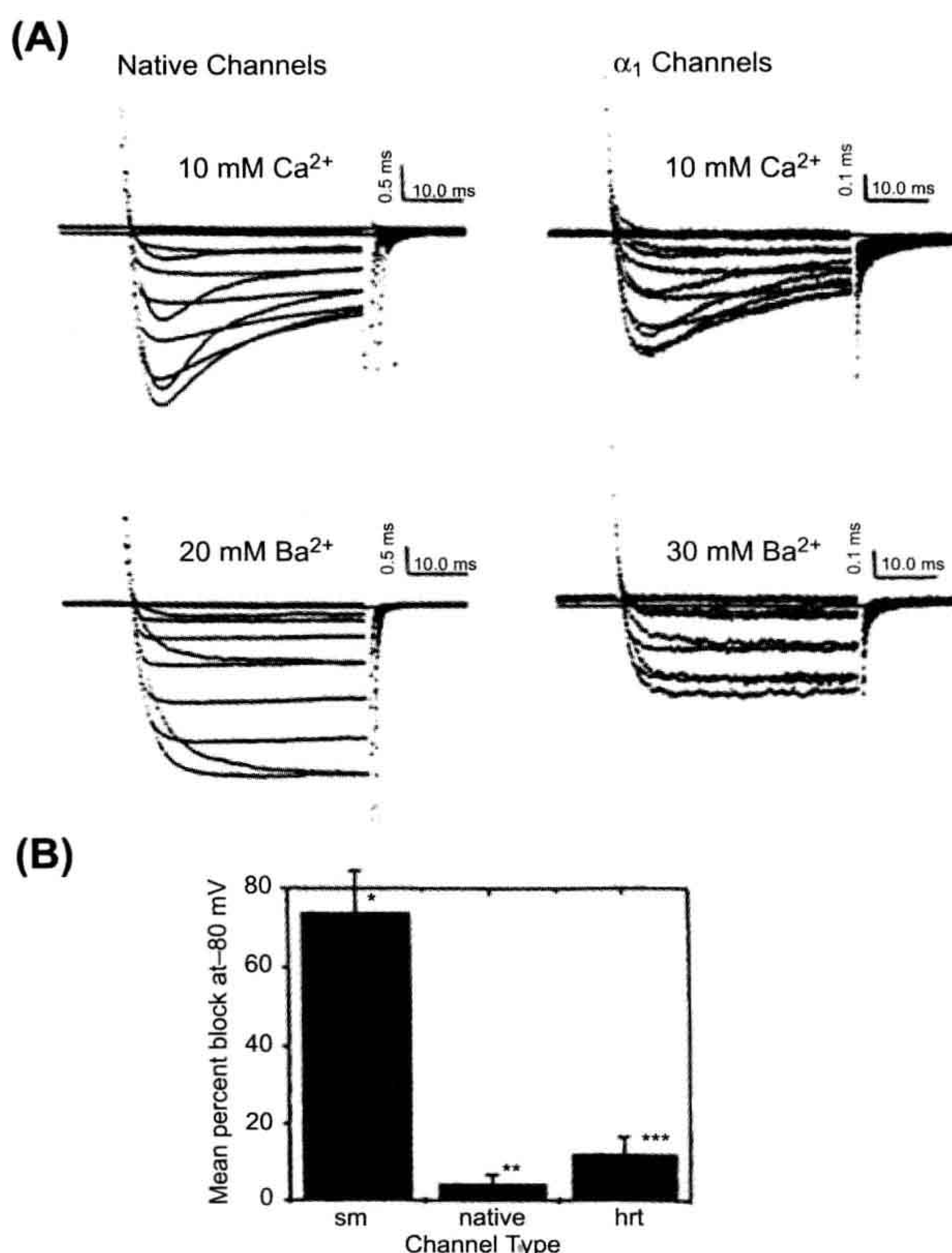


FIGURE 29.4 L-type calcium channels expressed in Chinese hamster ovary (CHO) cells, showing the greater sensitivity of smooth muscle (sm) than heart (hrt) channel variants to dihydropyridine block. (A) Native (left) and recombinant (right) L-type calcium channel activity when calcium (upper row) and barium (lower row) carries the charge. (B) Tonic block of recombinant channel activity by the DHP nisoldipine for $\alpha_{1C\text{-}a}$ (hrt) and $\alpha_{1C\text{-}b}$ (sm) α subunits. *(From Welling et al., 1997.)*

pharmacological profile is due to alternative splicing of the IS6 segments of the 1C gene in cardiac and smooth muscle (Welling et al., 1997). In addition, Welling and colleagues confirmed that $\alpha_{1C\text{-}b}$ is expressed in smooth muscle, but not cardiac, cells, linking the molecular pharmacology to the physiology of the tissues. These experimental results are important because they show that regions of the 1C subunit distinct from the DHP-binding domain influence drug activity, most likely through allosteric interactions. These results for DHP antagonists have been confirmed by others (Hu and Marban, 1998; Zuhlke et al., 1998); however, differences in DHP agonist modulation of smooth muscle versus cardiac muscle L-type calcium channels has not yet been systematically addressed.

T-type calcium channels (Perez-Reyes et al., 2006) have voltage-dependent kinetics, ion permeability and pharmacological properties that distinguish them from L-type calcium channels. They are resistant to block by dihydropyridines, inactivate in a voltage-dependent manner and, most importantly, activate at voltages much more negative than L-type calcium channels (Bean, 1989; Nilius et al., 2006; Xu and Colecraft, 2009). Because of the voltage dependence of T-type channels and the relatively small size of T-channel current in the ventricle (Bean, 1985; Ono and Iijima, 2010), direct activation of contractile proteins and/or calcium-induced release of calcium from the SR is not likely (Balke et al., 1993; Cannell et al., 1995). T-type channel activity has been suggested to contribute to pacemaker activity in nodal cells (Irisawa and Hagiwara, 1991; Vassort et al., 2006), which may be particularly important in the Purkinje fibers in the conduction system of the heart. The cloning of the neuronal T-type channel has opened the possibility of determining the molecular basis for these differences (Perez-Reyes et al., 1998).

III. SODIUM (Na^+) CHANNELS

Voltage-gated Na^+ channels are integral membrane proteins (Catterall, 2000a) that not only control the movement of Na^+ and underlie the spread of excitation in ventricular and atrial muscle cells and in the Purkinje fiber

network throughout the heart, but also can contribute so-called "late" current, which prolongs action potential duration (Attwell et al., 1979). The electrocardiogram can therefore give some insight into channel activity: the QRS interval reflects conduction time through the ventricle and hence the number of available Na^+ channels and the QT interval represents the time to ventricular repolarization. For example, when peak sodium current is diminished in the presence of tetrodotoxin (TTX; an Na^+ channel-blocking toxin) or after sodium removal (Colatsky, 1982; Hiraoka et al., 1986), the rate of action potential initiation is slowed. The consequential slowing of electrical propagation through the myocardium manifests itself as a prolongation of the QRS interval. Conversely, inherited mutation in the cardiac Na^+ channel can impinge upon channel inactivation and cause a substantial non-inactivating, or "late", sodium current. This enhanced depolarizing current prolongs the action potential and can lead to long-QT syndrome (Balser, 1999; Clancy and Rudy, 1999; Zimmer and Surber, 2008). Cardiac sodium channels therefore serve as an important target of antiarrhythmic agents.

In most tissues, the voltage-gated Na^+ channel is a heterotrimeric protein consisting of α (33 kDa), β_1 (36 kDa) and/or β_2 (33 kDa) subunits (Catterall et al., 1992; Catterall, 2000), but only the α subunit (primarily $Na_v1.5$ in the heart) is needed for expression of recombinant channels, particularly for heart channels (Suzuki et al., 1988; Stuhmer et al., 1989a; Noda et al., 1989; Abriel and Kass, 2005). Like the L-type calcium channel α_{1c} subunit, the Na^+ channel α subunit maintains the classical four-domained structure, with S4 serving as a voltage sensor in each domain (Balser, 1999; Abriel and Kass, 2005).

The selective pore of Na^+ channels is responsive to changes in the voltage-sensing domains and, as a first approximation, gating follows the simplified Hodgkin and Huxley model (Hodgkin and Huxley, 1952). At resting membrane potentials, Na^+ channels are in a resting state with the pore closed. Membrane depolarization induces conformational changes in the S4 helix that open the gate (Abriel and Kass, 2005), resulting in conduction of Na^+ ions through the pore and inward Na^+ current. Continued depolarization triggers closure of an inactivation gate, occlusion of the channel pore and termination of the Na^+ current. Membrane repolarization returns the channel to the resting state by allowing S4 to relax, shutting the gate and relieving inhibition.

The molecular determinants of inactivation of the voltage-gated Na^+ channel have been well studied (Caterall, 2000a) and have been shown to be interrelated to the actions of local anesthetics (LAs) in modulating sodium channels (Ragsdale and Avoli, 1998; Kambouris et al., 1998). Multiple groups have provided molecular and biophysical evidence that fast inactivation of this channel occurs by the binding of an intracellular inactivation gate, the loop connecting homologous domains III and IV of the Na^+ channel, to regions around the inner mouth of the Na^+ channel pore through hydrophobic interactions (Vassilev et al., 1988; Stuhmer et al., 1989b; Chahine et al., 1997; Rohl et al., 1999). The docking site of the inactivation gate has been less clearly identified, but the short intracellular loops connecting the S4 and S5 segments in each domain of the channel (McPhee et al., 1998) have been revealed as interaction sites and two residues in the S6 segment of domain IV (F1764 and Y1774 in rat brain IIA channel) have been found to be key in modulating inactivation (McPhee et al., 1995). More recently, it has become evident that the structured proximal segment of the C-terminus is crucial in modulating the docking of the inactivation gate to the pore (Kass, 2006; Zimmer and Surber, 2008).

Our present understanding of LA action relies heavily on the state-dependent hypothesis of Hille and Starmer. Hille (1977) proposed the *modulated receptor hypothesis* in which a single LA receptor lies within the pore, between the selectivity filter and channel gate. Receptor occupation leads to cessation of ion flow and promotion of inactivation. Drugs approach the receptor by an aqueous, hydrophilic pathway through the open cytoplasmic mouth and the pore (see Fig. 29.1) and induce small conformational changes that stabilize drug/channel interactions. Alternatively, Starmer and Courtney (1986) proposed that state-dependent affinity of an intrapore receptor arises from a static receptor that is guarded by the channel gate, a *guarded receptor.* Here, the channel gate regulates access to the receptor, so that open channels provide greater receptor access.

Two drugs, lidocaine and flecainide, differ in their modes of action in that each binds preferentially to a different state of the channel. Lidocaine interacts preferentially with the inactivated state of the channel and drug block is not necessarily dependent on channel openings (Bean et al., 1983; Ragsdale et al., 1996). This is evidenced by the hyperpolarizing shift in the voltage dependence of inactivation and by the voltage range over which the drug is active (Ragsdale et al., 1996). Furthermore, mutation of the hydrophobic IFM motif of the III–IV intracellular loop into QQQ removes fast inactivation of brain IIA (West et al., 1992) and cardiac Na^+ channels (Bennett et al., 1995) and strongly decreases lidocaine efficacy (Fig. 29.5) (Bennett et al., 1995). However, recent data suggest that transitions to the active state may play a more important role in the actions of lidocaine block than previously considered (Vedantham and Cannon, 1999; Scheuer, 1999). Conversely, charged, hydrophilic analogs of LAs, such as the drug flecainide, block sodium channels preferentially in the open state. The activity of flecainide requires channels to open and does not require channels to enter the inactivated state to promote block (Anno and Hondeghem, 1990; Ragsdale et al., 1996). Confirmation of this hypothesis has been illustrated in Markov models of state dependent drug interaction that

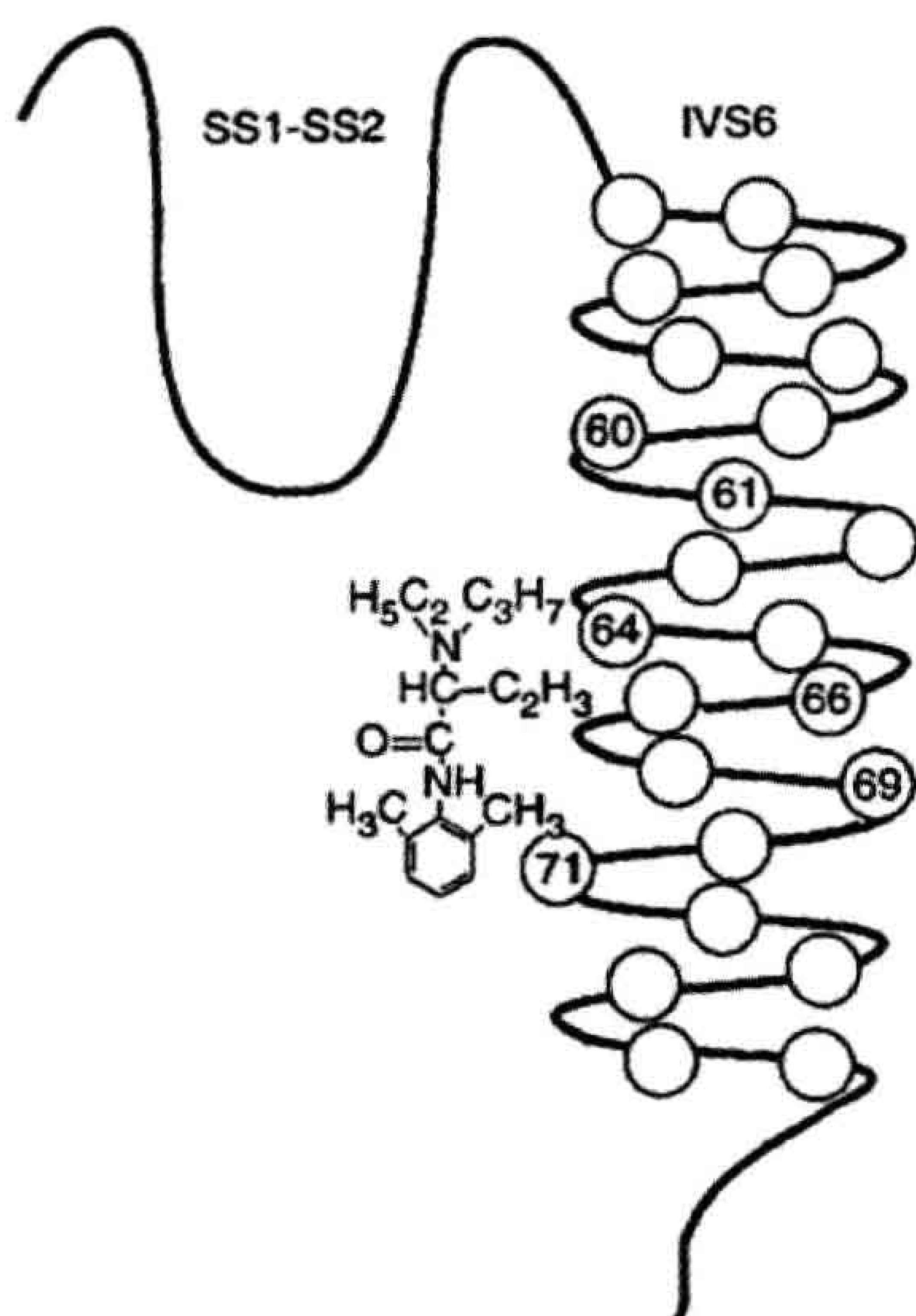


FIGURE 29.5 Schematic diagram of the putative interaction between lidocaine and key residues on domain IV transmembrane segment S6 of the rat brain Na channel. *(Reprinted with permission from Science. Copyright 1994 American Association for the Advancement of Science.)*

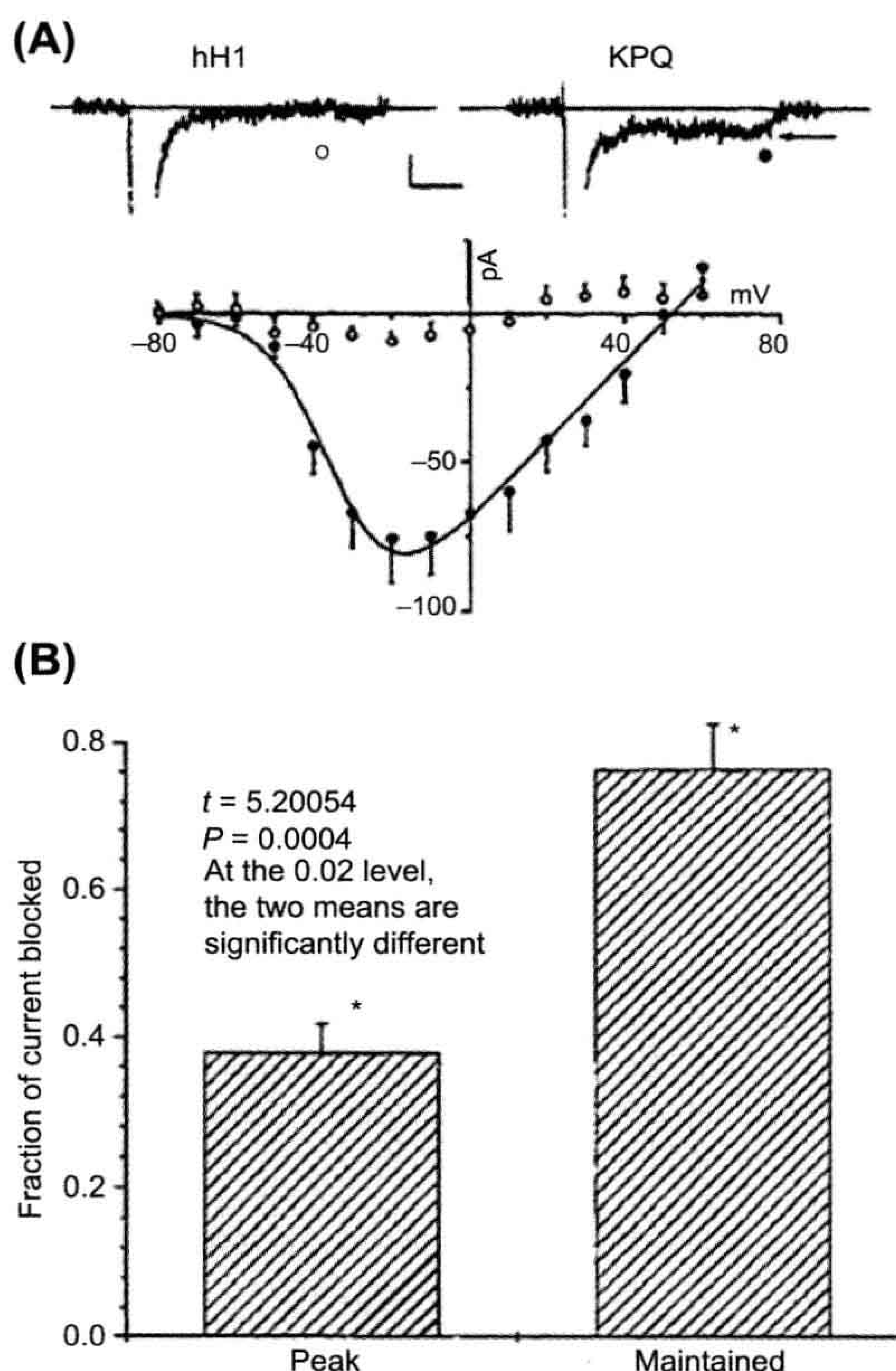


FIGURE 29.6 (A) The ΔKPQ deletion mutation of the cytoplasmic linker between domains III and IV of the human heart Na^+ channel α subunit promotes maintained sodium channel current that is not present in wild-type a (hH1) channels. (B) Summary of experiments in which the fraction of peak inward Na^+ channel current (left bar) was compared with the fraction of late or maintained Na^+ channel current blocked (right bar) by the same concentration of lidocaine (100 μM). The late current is more than twice as sensitive to lidocaine as peak current. *(From An et al., 1996.)*

reproduce the experimental findings for two different classes of LA (Clancy et al., 2007).

IIIA. Mutation-Specific Drug Actions

Multiple mutations of *SCN5A*, the gene that encodes the human heart Na^+ channel α subunit, have been discovered and linked to two inherited cardiac arrhythmias: the long QT syndrome and the Brugada's syndrome. The fact that these mutations cause functional changes in expressed channel activity has created the unique opportunity to develop specific molecular therapeutic approaches to disease management based on specific functional changes in the channel proteins encoded by mutant genes (Keating and Sanguinetti, 1996).

Pharmacological analysis of mutant channels expressed heterologously has provided evidence that Na^+ channel blockers which preferentially interact with the inactivated state of the channel (Hille, 1977; Hondeghem and Katzung, 1977) block in a targeted manner the maintained current conducted by some mutant LQT (ΔKPQ mutant) channels (An et al., 1996; Compton et al., 1996; Dumaine et al., 1996; Priori et al., 1996; Wang et al., 1997; Dumaine and Kirsch, 1998), shorten action potential duration in cellular studies (Schwartz et al., 1995; Shimizu and Antzelevitch, 1997) and correct QT prolongation in patients (Schwartz et al., 1995; Rosero et al., 1997). Figure 29.6B illustrates the maintained current carried by LQT-3 mutant (ΔKPQ) channels and preferential block of this current by lidocaine. Flecainide, which preferentially blocks open but not inactivated channels (Ragsdale et al., 1996), has also been shown to be effective in inhibiting persistent Na^+ channel current in ΔKPQ mutant channels (Nagatomo et al., 1997) and in shortening and normalizing QT intervals in patients carrying this gene mutation (Windle et al., 2001).

Interestingly, clinical data suggest that flecainide might also be effective in controlling arrhythmias caused by the D1790G mutation located in the C-terminal region of the $Na_V1.5$ channel (Benhorin et al., 1999). This mutation decreases the probability of channel inactivation, allowing for late sodium currents and prolonged action potentials. Flecainide is therefore more active in diseased channels than in WT (wild-type) channels, presumably because

deficiencies in inactivation increase the time over which the drug has access to its intrapore binding site (Liu et al., 2003). Recently, one severe mutation in a newborm, F1473C, had a differential response to flecainide and mexilitine in the patient but not in cellular studies (Bankston et al., 2007). This newborn also harbored a polymorphism in a K^+ channel that may play a role in the unique drug response and highlights the importance in understanding the genetic background in which disease-causing mutations exist.

These studies represent the ongoing effort to target selectively ion channels that have been implicated in both acquired and congenital arrhythmias. Further understanding of the normal and pathological gating and pharmaceutical modulation of these ion channels has led and will continue to lead us to more targeted therapies designed on correcting the defect in an individual ion channel. Ultimately, therapeutic strategies will need to take into account the genetic background of the individual patient in addition to the dysfunction in an ion channel.

BIBLIOGRAPHY

Abriel, H., & Kass, R. S. (2005). Regulation of the voltage-gated cardiac sodium channel Nav1.5 by interacting proteins. *Trends Cardiovasc Med, 15*, 35–40.

An, R. H., Bangalore, R., Rosero, S. Z., & Kass, R. S. (1996). Lidocaine block of LQT-3 mutant human Na^+ channels. *Circ Res, 79*, 103–108.

Anno, T., & Hondeghem, L. M. (1990). Interactions of flecainide with guinea pig cardiac sodium channels. Importance of activation unblocking to the voltage dependence of recovery. *Circ Res, 66*, 789–803.

Attwell, D., Cohen, I., Eisner, D., Ohba, M., & Ojeda, C. (1979). The steady state TTX-sensitive ("window") sodium current in cardiac Purkinje fibres. *Pflügers Arch, 379*, 137–142.

Bankston, J. R., Yue, M., Chung, W., et al. (2007). A novel and lethal de novo LQT-3 mutation in a newborn with distinct molecular pharmacology and therapeutic response. *PLoS One, 2*, 1258.

Balke, C. W., Rose, W. C., O'Rourke, B., Mejia-Alvarez, R., Backx, P., & Marban, E. (1993). Biophysics and physiology of cardiac calcium channels. *Circ, 87*(Suppl. 7), VII49–VII53.

Balser, J. R. (1999). Sodium "channelopathies" and sudden death: must you be so sensitive? *Circ Res, 85*, 872–875.

Bangalore, R., Mehrke, G., Gingrich, K., Hofmann, F., & Kass, R. S. (1996). Influence of the L-type Ca-channel α_2/δ subunit on ionic and gating current in transiently-transfected HEK 293 cells. *Am J Physiol, 270*, H1521–H1528.

Bean, B. P. (1985). Two kinds of calcium channels in canine atrial cells. Differences in kinetics, selectivity, and pharmacology. *J Gen Physiol, 86*, 1–30.

Bean, B. P. (1989). Classes of calcium channels in vertebrate cells. *Ann Rev Physiol, 51*, 367–384.

Bean, B. P., Cohen, C. J., & Tsien, R. W. (1983). Lidocaine block of cardiac sodium channels. *J Gen Physiol, 81*, 613–642.

Benhorin, J., Medina, A., Taub, Y., et al. (2000). Effects of flecainide in patients with a new SCN5A mutation: mutation-specific therapy for Long QT Syndrome? *Circulation, 101*, 1698–1706.

Bennett, P. B., Valenzuela, C., Chen, L. Q., & Kallen, R. G. (1995). On the molecular nature of the lidocaine receptor of cardiac Na^+ channels. Modification of block by alterations in the alpha-subunit III–IV interdomain. *Circ Res, 77*, 584–592.

Cannell, M. B., Cheng, H., & Lederer, W. J. (1995). The control of calcium release in heart muscle. *Science, 268*, 1045–1049.

Catterall, W. A. (1988). Structure and function of voltage-sensitive ion channels. *Science, 242*, 50–61.

Catterall, W. A. (2000a). From ionic currents to molecular mechanisms: the structure and function of voltage-gated sodium channels. *Neuron, 26*, 13–25.

Catterall, W. A. (2000b). Structure and regulation of voltage-gated Ca^{2+} channels. *Annu Rev Cell Dev Biol, 16*, 521–555.

Catterall, W. A. (2010). Ion channel voltage sensors: structure, function, and pathophysiology. *Neuron, 67*, 915–928.

Catterall, W. A., Scheuer, T., Thomsen, W., & Rossie, S. (1991). Structure and modulation of voltage-gated ion channels. [Review]. *Ann NY Acad Sci, 625*, 174–180.

Catterall, W. A., Trainer, V., & Baden, D. G. (1992). Molecular properties of the sodium channel: a receptor for multiple neurotoxins. [Review]. *Bull Soc Pathol Exot, 85*, 481–485.

Chahine, M., Deschenes, I., Trottier, E., Chen, L. Q., & Kallen, R. G. (1997). Restoration of fast inactivation in an inactivation-defective human heart sodium channel by the cysteine modifying reagent benzyl-MTS: analysis of IFM-ICM mutation. *Biochem Biophys Res Commun, 233*, 606–610.

Clancy, C. E., & Rudy, Y. (1999). Linking a genetic defect to its cellular phenotype in a cardiac arrhythmia. *Nature, 400*, 566–569.

Clancy, C. E., Zhu, Z. I., & Rudy, Y. (2007). Pharmacogenetics and anti-arrhythmic drug therapy: a theoretical investigation. *Am J Heart Circ Physiol, 292*, H66–H75.

Colatsky, T. J. (1982). Mechanisms of action of lidocaine and quinidine on action potential duration in rabbit Purkinje fibers, an effect on steady state sodium currents? *Circ Res, 50*, 17–27.

Compton, S. J., Lux, R. L., Ramsey, M. R., et al. (1996). Genetically defined therapy of inherited long-QT syndrome – correction of abnormal repolarization by potassium. *Circulation, 94*, 1018–1022.

Dolphin, A. C. (2003a). Beta subunits of voltage-gated calcium channels. *J Bioenerg Biomembr, 35*, 599–620.

Dolphin, A. C. (2003b). G protein modulation of voltage-gated calcium channels. *Pharmacol Rev, 55*, 607–627.

Dumaine, R., & Kirsch, G. E. (1998). Mechanism of lidocaine block of late current in long Q-T mutant Na^+ channels. *Am J Physiol, 274*, H477–H487.

Dumaine, R., Wang, Q., Keating, M. T., et al. (1996). Multiple mechanisms of Na^+ channel linked long-QT syndrome. *Circ Res, 78*, 916–924.

Emrick, M. A., Sadelik, M., Konoki, K., & Catterall, W. (2010). Beta-adrenergic-regulated phosphorylation of the skeletal muscle Ca(V)1.1 channel in the fight-or-flight response. *Proc Natl Acad Sci USA, 107*, 18712–18717.

Flockerzi, V., et al. (1986). Purification of dihydropyridine-binding site from skeletal muscle t-tubules is a functional calcium channel. *Nature, 323*, 66–86.

Glossmann, H., & Striessnig, J. (1990). Molecular properties of calcium channels. *Rev Physiol Biochem Pharmacol, 114*, 1–105.

Glossmann, H., Striessnig, J., Ferry, D. R., Goll, A., Moosburger, K., & Schirmer, M. (1987). Interaction between calcium channel ligands and calcium channels. *Circ Res, 61*, 130–136.

Grabner, M., Wang, Z., Hering, S., Striessnig, J., & Glossmann, H. (1996). Transfer of 1,4-dihydropyridine sensitivity from L-type to class A (BI) calcium channels. *Neuron, 16*, 207–218.

Grandi, E., Morotti, S., Ginsberg, K. S., Severi, S., & Bers, D. M. (2010). Interplay of voltage and Ca-dependent inactivation of L-type Ca current. *Prog Biophys Mol Biol, 103*, 44–50.

Gutierrez, L. M., Zhao, X. L., & Hosey, M. M. (1994). Protein kinase C–mediated regulation of L-type Ca channels from skeletal muscle requires phosphorylation of the alpha 1 subunit. *Biochem Biophys Res Commun, 202*, 857–865.

Hille, B. (1977). Local anesthetics: hydrophilic and hydrophobic pathways for the drug-receptor reaction. *J Gen Physiol, 69*, 497–515.

Hille, B. (1992). *Ionic Channels of Excitable Membranes* (2nd ed.). Sunderland: Sinauer.

Hiraoka, M., Sawada, K., & Kawano, S. (1986). Effect of quinidine on plateau currents of guinea-pig ventricular myocytes. *J Molec Cell Cardiol, 18*, 1097–1106.

Hockerman, G. H., Johnson, B. D., Scheuer, T., & Catterall, W. A. (1995). *Molecular determinants of high affinity phenylalkylamine block of L-type calcium channels, 270*, 22119–22122.

Hockerman, G. H., Peterson, B. Z., Johnson, B. D., & Catterall, W. A. (1997a). Molecular determinants of drug binding and action on L-type calcium channels. [Review]. *Annu Rev Pharmacol Toxicol, 37*, 361–396.

Hockerman, G. H., Peterson, B. Z., Sharp, E., Tanada, T. N., Scheuer, T., & Catterall, W. A. (1997b). Construction of a high-affinity receptor site for dihydropyridine agonists and antagonists by single amino acid substitutions in a non-L-type Ca2+ channel. *Proc Natl Acad Sci USA, 94*, 14906–14911.

Hodgkin, A. L., & Huxley, A. F. (1952). A quantitative description of membrane current and its application to conduction and excitation in nerve. *J Physiol (London), 117*, 500–544.

Hofmann, F., Biel, M., Bosse, E., Flockerzi, V., Ruth, P., & Welling, A. (1993). Functional expression of cardiac and smooth muscle calcium channels. In A. M. Brown, W. A. Catterall, G. J. Kaczorowski, P. S. Spooner, & H. C. Strauss (Eds.), *Ion Channels in the Cardiovascular System: Function and Dysfunction*. Washington: AAAS Press.

Hondeghem, L. M., & Katzung, B. G. (1977). Time- and voltage-dependent interactions of antiarrhythmic drugs with cardiac sodium channels. [Review]. *Biochim Biophys Acta, 472*, 373–398.

Hosey, M. M., Chien, A. J., & Puri, T. S. (1996). Structure and regulation of L-type calcium channels – a current assessment of the properties and roles of channel subunits. *Trends Cardiovasc Med, 6*, 265–273.

Hu, H., & Marban, E. (1998). Isoform-specific inhibition of L-type calcium channels by dihydropyridines is independent of isoform-specific gating properties. *Mol Pharmacol, 53*, 902–907.

Irisawa, H., & Hagiwara, N. (1991). Ionic current in sinoatrial node cells. *J Cardiovasc Electrophys, 2*, 531–540.

Ito, H., Klugbauer, N., & Hofmann, F. (1997). Transfer of the high-affinity dihydropyridine sensitivity from L-type to non–L-type calcium channels. *Mol Pharmacol, 52*, 735–740.

Kambouris, N. G., Hastings, L. A., Stepanovic, S., Marban, E., Tomaselli, G. F., & Balser, J. R. (1998). Mechanistic link between lidocaine block and inactivation probed by outer pore mutations in the rat micro1 skeletal muscle sodium channel. *J Physiol (London), 512*, 693–705.

Kass, R. S. (1994a). Dihydropyridine modulation of cardiovascular L-type calcium channels: molecular and cellular pharmacology. In P. M. Spooner, A. M. Brown, W. A. Catterall, G. J. Kaczorowski, & H. C. Strauss (Eds.), *Ion Channels in the Cardiovascular System: Function and Dysfunction* (pp. 425–440). Armonk: Futura Publishing Co.

Kass, R. S. (1994b). Molecular pharmacology of cardiac L-type calcium channels. In C. Peracchia (Ed.), *Handbook of Membrane Channels: Molecular and Cellular Physiology* (pp. 187–198). Orlando: Academic Press.

Kass, R. S. (1995). Ionic basis of electrical activity in the heart. In N. Sperelakis (Ed.), *Physiology and Pathophysiology of the Heart* (pp. 77–90). Norwell: Kluwer Academic.

Kass, R. S. (2006). Sodium channel inactivation in heart: a novel role of the carboxy-terminal domain. *J Cardiovasc Electrophysiol, 17*, S21–S25.

Keating, M. T., & Sanguinetti, M. C. (1996). Pathophysiology of ion channel mutations. Curr Opin Gen. *Devel, 6*, 326–333.

Klugbauer, N., Marais, E., & Hofmann, F. (2003). Calcium channel alpha2delta subunits: differential expression, function, and drug binding. *J Bioenerg Biomembr, 35*, 639–647.

Kushnir, A., & Marks, A. (2010). The ryanodine receptor in cardiac physiology and disease. *Adv Pharmacol, 59*, 1–30.

Lacinová, L., An, R. H., Xia, J., et al. (1999). Distinctions in the molecular determinants of charged and neutral dihydropyridine block of L-type calcium channels. *J Pharmacol Exp Ther, 289*, 1472–1479.

Liu, H., Atkins, J., & Kass, R. S. (2003). Common molecular determinants of flecainide and lidocaine block of heart Na+ channels: evidence from experiments with neutral and quaternary flecainide analogues. *J Gen Physiol, 121*, 199–214.

Lyon, A. R., MacLeod, K. T., Zhang, Y., et al. (2009). Loss of T-tubules and other changes to surface topography in ventricular myocytes from failing human and rat heart. *Proc Natl Acad Sci USA, 106*, 6854–6859.

Ma, J., Gutierrez, L. M., Hosey, M. M., & Rios, E. (1992). Dihydropyridine-sensitive skeletal muscle Ca channels in polarized planar bilayers. 3. Effects of phosphorylation by protein kinase C. *Biophys J, 63*, 639–647.

McPhee, J. C., Ragsdale, D. S., Scheuer, T., & Catterall, W. A. (1995). A critical role for transmembrane segment IVS6 of the sodium channel alpha subunit in fast inactivation. *J Biol Chem, 270*, 12025–12034.

McPhee, J. C., Ragsdale, D. S., Scheuer, T., & Catterall, W. A. (1998). A critical role for the S4–S5 intracellular loop in domain IV of the sodium channel alpha-subunit in fast inactivation. *J Biol Chem, 273*, 1121–1129.

Mikami, A., Imoto, K., Tanabe, T., et al. (1989). Primary structure and functional expression of the cardiac dihydropyridine-sensitive calcium channel. *Nature, 340*, 230–233.

Mori, Y., Friedrich, T., Kim, M.-S., et al. (1991). Primary structure and functional expression from complementary DNA of a brain calcium channel. *Nature, 350*, 398–402.

Nagatomo, T., Fan, Z., Ye, B., January, C. T., & Makielski, J. C. (1997). Effects of flecainide on the long QT sodium channel syndrome. *Circulation, 96*, 677.

Nerbonne, J. M., & Kass, R. S. (2005). Molecular physiology of cardiac repolarization. *Physiol Rev, 85*, 1205–1253.

Nilius, B., Talavera, K., & Verkhratsky, A. (2006). T-type calcium channels: the never ending story. *Cell Calcium, 40*, 81–88.

Noda, M., Suzuki, H., Numa, S., & Stuhmer, W. (1989). A single point mutation confers tetrodotoxin and saxitoxin insensitivity on the sodium channel II. *FEBS Lett, 259*, 213–216.

Ono, K., & Iijima, T. (2010). Cardiac T-type Ca(2+) channels in the heart. *J Mol Cell Cardiol, 48*, 65–70.

Opie, L. H. (2001). Calcium channel blockers in hypertension: reappraisal after new trials and major meta-analyses. *Am J Hypertens, 14*, 1074–1081.

Perez-Reyes, E. (1998). Molecular characterization of a novel family of low voltage-activated, T-type, calcium channels. *J Bioeng Biomembr, 30*, 313–318.

Perez-Reyes, E., & Lory, P. (2006). Molecular biology of T-type calcium channels. *CNS Neurol Disord Drug Targets, 5*, 605–609.

Peterson, B. Z., & Catterall, W. A. (2006). Allosteric interactions required for high-affinity binding of dihydropyridine antagonists to Ca(V)1.1 Channels are modulated by calcium in the pore. *Mol Pharmacol, 70*, 667–675.

Peterson, S. G., DeMaria, C. D., Adelman, J. P., & Yue, D. T. (1999). Calmodulin is the Ca2+ sensor for Ca2+ -dependent inactivation of L-type calcium channels. *Neuron, 22*, 549–558.

Peterson, B. Z., Johnson, B. D., Hockerman, G. H., Acheson, M., Scheuer, T., & Catterall, W. A. (1997). Analysis of the dihydropyridine receptor site of L-type calcium channels by alanine-scanning mutagenesis. *J Biol Chem, 272*, 18 752–18 758.

Peterson, B. Z., Tanada, T. N., & Catterall, W. A. (1996). Molecular determinants of high affinity dihydropyridine binding in L-type calcium channels. *J Biol Chem, 271*, 5293–5296.

Priori, S. G., Napolitano, C., Cantu, F., Brown, A. M., & Schwartz, P. J. (1996). Differential response to Na^+ channel blockade, beta-adrenergic stimulation and rapid pacing in a cellular model mimicking the SCN5A and HERG defects present in the long-QT syndrome. *Circ Res, 78*, 1009–1015.

Ragsdale, D. S., & Avoli, M. (1998). Sodium channels as molecular targets for antiepileptic drugs. *Brain Res Rev, 26*, 16–28.

Ragsdale, D. S., McPhee, J. C., Scheuer, T., & Catterall, W. A. (1996). Common molecular determinants of local anesthetic, antiarrhythmic, and anticonvulsant block of voltage-gated Na^+ channels. *Proc Natl Acad Sci USA, 93*, 9270–9275.

Reuter, H., & Scholz, H. (1977). The regulation of Ca conductance of cardiac muscle by adrenaline. *J Physiol, 264*, 49–62.

Rodenkirchen, R., Bayer, R., & Mannhold, R. (1982). Specific and nonspecific Ca antagonists: a structure-activity analysis of cardiodepressive drugs. *Progr Pharmacol, 5*, 9–23.

Rohl, C. A., Boeckman, F. A., Baker, C., Scheuer, T., Catterall, W. A., & Klevit, R. E. (1999). Solution structure of the sodium channel inactivation gate. *Biochemistry, 38*, 855–861.

Rosero, S. Z., Zareba, W., Robinson, J. L., & Moss, A. (1997). Gene-specific therapy for long QT syndrome: QT shortening with lidocaine and tocainide in patients with mutation of the sodium channel gene. *Ann Noninvasive Electrocardiol, 2*, 274–278.

Sanguinetti, M. C., & Kass, R. S. (1984). Voltage-dependent block of calcium channel current in the calf cardiac Purkinje fiber by dihydropyridine calcium channel antagonists. *Circ Res, 55*, 336–348.

Scheuer, T. (1999). Commentary: a revised view of local anesthetic action: what channel state is really stabilized? *J Gen Physiol, 113*, 3–6.

Schuster, A., Lacinova, L., Klugbauer, N., Ito, H., Birnbaumer, L., & Hormann, F. (1996). The IVS6 segment of the L-type calcium channel is critical for the action of dihydropyridines and phenylalkylamines. *EMBO J, 15*, 2365–2370.

Schwartz, P. J., Priori, S. G., Locati, E. H., et al. (1995). Long QT syndrome patients with mutations of the SCN5A and HERG genes have differential responses to Na^+ channel blockade and to increases in heart rate: implications for gene-specific therapy. *Circulation, 92*, 3381–3386.

Sculptoreanu, A., Rotman, E., Takahashi, M., Scheuer, T., & Catterall, W. A. (1993a). Voltage-dependent potentiation of the activity of cardiac L-type calcium channel alpha 1 subunits due to phosphorylation by cAMP-dependent protein kinase. *Proc Natl Acad Sci USA, 90*, 10 135–10 139.

Sculptoreanu, A., Scheuer, T., & Catterall, W. A. (1993b). Voltage-dependent potentiation of L-type Ca^{2+} channels due to phosphorylation by cAMP-dependent protein kinase. *Nature, 364*, 240–243.

Shimizu, W., & Antzelevitch, C. (1997). Sodium channel block with mexiletine is effective in reducing dispersion of repolarization and preventing torsade des pointes in LQT2 and LQT3 models of the long-QT syndrome. *Circulation, 96*, 2038–2047.

Starmer, C. F., & Courtney, K. R. (1986). Modeling ion channel blockade at guarded binding sites: application to tertiary drugs. *Am J Physiol, 251*, H848–H856.

Striessnig, J., Grabner, M., Mitterdorfer, J., Hering, S., Sinnegger, M. J., & Glossmann, H. (1998). Structural basis of drug binding to L Ca2+ channels. *Trends Pharmacol Sci, 19*, 108–115.

Stuhmer, W., Conti, F., Suzuki, H., et al. (1989b). Structural parts involved in activation and inactivation of the sodium channel. *Nature, 339*, 597–603.

Stuhmer, W., Conti, F., Suzuki, H., et al. (1989a). Structural parts involved in activation and inactivation of the sodium channel. *Nature, 339*, 597–603.

Suzuki, H., Beckh, S., Kubo, H., et al. (1988). Functional expression of cloned cDNA encoding sodium channel III. *FEBS Lett, 228*, 195–200.

Tang, S., Yatani, A., Bahinski, A., Mori, Y., & Schwartz, A. (1993). Molecular localization of regions in the L-type calcium channel critical for dihydropyridine action. *Neuron, 11*, 1013–1021.

Tikhonov, D. B., & Zhorov, B. S. (2009). Structural model for dihydropyridine binding to L-type calcium channels. *J Biol Chem, 284*, 19006–19017.

Triggle, D. J. (2007). Calcium channel antagonists: clinical uses – past, present, and future. *Biochem Pharmacol, 74*, 1–9.

Tsien, R. W. (1977). Effects of epinephrine on the pacemaker potassium current of cardiac Purkinje fibers. *J Gen Physiol, 64*, 293–319.

Tsien, R. W., Ellinor, P. T., & Horne, W. A. (1991). Molecular diversity of voltage-dependent Ca^{2+} channels. [Rev.]. *TIPS, 12*, 349–354.

Vassilev, P. M., Scheuer, T., & Catterall, W. A. (1988). Identification of an intracellular peptide segment involved in sodium channel inactivation. *Science, 241*, 1658–1661.

Vassort, G., Talavera, K., & Alvarez, J. L. (2006). Role of T-type Ca2+ channels in the heart. *Cell Calcium, 40*, 205–220.

Vedantham, V., & Cannon, S. C. (1999). The position of the fastinactivation gate during lidocaine block of voltage-gated Na^+ channels. *J Gen Physiol, 113*, 7–16.

Viola, H. M., Macdonald, W. A., Tang, H., & Hool, L. C. (2009). The L-type Ca(2+) channel as a therapeutic target in heart disease. *Curr Med Chem, 16*, 3341–3358.

Wang, D. W., Yazawa, K., Makita, N., George, A. L., & Bennett, P. B. (1997). Pharmacological targeting of long QT mutant sodium channels. *J Clin Invest, 99*, 1714–1720.

Welling, A., Kwan, Y. W., Bosse, E., Flockerzi, V., Hofmann, F., & Kass, R. S. (1993). Subunit-dependent modulation of recombinant L-type calcium channels: molecular basis for dihydropyridine tissue selectivity. *Circ Res, 73*, 974–980.

Welling, A., Ludwig, A., Zimmer, S., Klugbauer, N., Flockerzi, V., & Hofmann, F. (1997). Alternatively spliced IS6 segments of the alpha 1C gene determine the tissue-specific dihydropyridine sensitivity of cardiac and vascular smooth muscle L-type Ca^{2+} channels. *Circ Res, 81*, 526–532.

West, J. W., Patton, D. E., Scheuer, T., Wang, Y., Goldin, A. L., & Catterall, W. A. (1992). A cluster of hydrophobic amino acid residues required for fast Na(+)-channel inactivation. *Proc Natl Acad Sci USA, 89*, 10 910–10 914.

Wier, W. G., & Balke, C. W. (1999). Ca(2+) release mechanisms, Ca(2+) sparks, and local control of excitation-contraction coupling in normal heart muscle. *Circ Res, 85*, 770–776.

Windle, J. R., Geletka, R. C., Moss, A. J., & Atkins, D. L. (2001). Normalization of ventricular repolarization with flecainide in patients with the LQT3 form (SCN5A) of long QT syndrome. *Ann Noninvasive Electrocardial, 6*, 153–158.

Xu, X., & Colecraft, H. (2009). Engineering proteins for custom inhibition of Ca(V) channels. *Physiology, 24*, 210–218.

Yang, J., Ellinor, P. T., Sather, W. A., Zhang, J. F., & Tsien, R. W. (1993). Molecular determinates of Ca^{2+} selectivity and ion permeation in L-type Ca^{2+} channels. *Nature, 366*, 158–161.

Zhao, X. L., Gutierrez, L. M., Chang, C. F., & Hosey, M. M. (1994). The alpha 1-subunit of skeletal muscle L-type Ca channels is the key target for regulation by A-kinase and protein phosphatase-1C. *Biochem Biophys Res Commun, 198*, 166–173.

Zimmer, T., & Surber, R. (2008). SCN5A channelopathies – an update on mutations and mechanisms. *Prog Biophys Mol Biol, 98*, 120–136.

Zuhlke, R. D., Bouron, A., Soldatov, N. M., & Reuter, H. (1998). Ca^{2+} channel sensitivity towards the blocker isradipine is affected by alternative splicing of the human alpha1C subunit gene. *FEBS Lett, 427*, 220–224.

Chapter 30

Inherited Diseases of Ion Transport

Robert A. Farley

Chapter Outline

I. SUMMARY

Diseases caused by mutations in genes that encode ion channels or ion transporters affect nearly every organ in the body. This chapter describes the genetic basis for several of these diseases, including the effect of gene mutations on protein structure and function, the biochemical and physiological consequences of the mutant proteins on organ function, the relationship of altered ion transport to disease symptoms and available treatments for the diseases.

II. INTRODUCTION

In 2010, four of the 20 best-selling drugs in the world targeted ion transporters because inhibition of these transporters is an effective way to alleviate the symptoms of many diseases. This should not be surprising since ion transport is a fundamental physiological activity in all tissues of the body and many diseases and pathological conditions are caused by dysfunctions of ion transport. For many diseases, such as type II diabetes, in which the disease pathology is manifest in several different organs, the abnormal ion transport may not be the primary cause of the disease and correction of the ion transport defect may not relieve the symptoms of the disease or cure the patient. In an increasing number of diseases, however, it is known that disease is caused by a mutation in a single gene that codes for an ion transport protein or for a regulator of an ion transport protein. Diseases of this type are found in many different organs in the body and include cystic fibrosis, familial hemiplegic migraine, long QT syndrome, myotonias and periodic paralyses of skeletal muscle, malignant hyperthermia and several different forms of hypertension. This chapter summarizes current knowledge about the origin of several of these inherited diseases of ion transport, the effects of the gene mutations on protein structure and function, the mechanisms whereby alterations in transport function can explain the symptoms of the disease and therapeutic approaches to relieve the symptoms of the disease or cure the patient. The excellent book by Frances Ashcroft (2000) discusses many diseases associated with altered ion channel function as they were understood prior to the year 2000.

III. IDENTIFYING HERITABLE MUTATIONS UNDERLYING DISEASES OF ION TRANSPORT

The most powerful techniques available to identify genes that contain mutations causing symptoms of common diseases such as diabetes, cardiovascular disease and hypertension are genome-wide association techniques. Very large numbers of samples are needed because the symptoms of these diseases are usually caused by mutations in multiple genes and the contribution of any single mutation to the disease symptoms in the population may be small. For diseases of this sort, the "common disease—common variant" hypothesis, that the genetic variations

Cell Physiology Sourcebook. DOI: 10.1016/B978-0-12-387738-3.00030-5

that underlie a disease should be over-represented in individuals with the disease, is assumed.

For rare diseases that occur in a small number of cases, genome-wide association techniques are not applicable, although these techniques are beginning to be applied to study some rare diseases. Most of the diseases of ion transport that are discussed in this chapter are rare diseases that segregate in a Mendelian pattern and the underlying mutations have been identified in genes using positional cloning and linkage analysis. In this approach, individuals from a large family in which several members suffer from the disease are collected and a pedigree is constructed to show how the disease segregates between generations. DNA from both affected family members and those who are not affected is screened with multiple chromosomal markers in order to identify a region on a chromosome that is associated with the inheritance of the disease. Examples of genetic markers that have been used for this type of analysis are restriction fragment length polymorphisms (RFLPs), microsatellite or short tandem repeat polymorphisms (STRs or STRPs) and single nucleotide polymorphisms (SNPs). Once a region of a chromosome has been identified as a candidate for the location of the mutation, the fine structure of the DNA is analyzed by studying the inheritance pattern of several different genes located in this region of the chromosome to identify those that segregate with the disease symptoms and, finally, DNA sequence analysis to identify mutations in the DNA of affected individuals. Using these methods, the gene encoding the protein whose mutations are responsible for cystic fibrosis was identified in 1989 (Riordan et al., 1989). This was the first gene associated with a disease of ion transport in humans to be identified. It is noteworthy that linkage between cystic fibrosis and the DNA marker DOCRI-917 in humans was reported in 1985 and that it took four years to identify the gene after the linkage was established.

IV. FAMILIAL HEMIPLEGIC MIGRAINE

Migraine is a common episodic headache disorder that can occur either with preceding visual or other sensory discomfort (migraine with aura) or without these symptoms (migraine without aura). Migraine attacks are typically characterized by pulsating headache, nausea, vomiting and photo- and phonophobia and may last between 4 and 72 hours. Migraine occurs approximately twice as often in females as in males, with up to 25% of females reporting two or more occurrences. Family, twin or population-based studies indicate that there are genetic factors involved in the susceptibility to migraine, but the complexity of the symptoms reported by different groups indicates that there are likely to be several different physiological mechanisms that contribute to the occurrence of migraine in different populations. Familial hemiplegic migraine is a rare autosomal dominant form of migraine with aura that is associated with paralysis of one side of the body during the attack (ictal hemiparesis) (Gargus, 2009). Unlike other forms of migraine, permanent cerebellar symptoms such as progressive cerebellar ataxia or nystagmus with cerebellar atrophy are observed in some cases of familial hemiplegic migraine. A gene locus for familial hemiplegic migraine on chromosome 19 was identified by positional cloning and, in 1996, mutations in the CACNA1A gene that encodes a calcium channel $\alpha 1$ subunit were identified as causing both familial hemiplegic migraine (FHM1) and episodic ataxia type-2, which is another autosomal dominant paroxysmal cerebral disorder having migraine-like symptoms (Ophoff et al., 1996). Subsequently, mutations in the ATP1A2 gene (Vanmolkot et al., 2003), encoding the $\alpha 2$ subunit of Na^+/K^+-ATPase, and in the SCN1A gene (Dichgans et al., 2005), encoding the α subunit of a voltage-gated sodium channel, have been identified in subpopulations of patients with familial hemiplegic migraine FHM2 and FHM3, respectively. Patients with FHM2 or FHM3 do not have mutations in the CACNA1A gene.

Migraine headache pain is initiated by activation of nociceptive sensory afferents of the trigeminal nerve (Pietrobon, 2005). These neurons release vasoactive neuropeptides at their nerve terminals that activate second-order neurons in the trigeminal nucleus caudalis, with further activation of additional neuronal pathways that are involved in the processing and perception of pain. The mechanisms whereby the trigeminal nociceptors are activated remain incompletely understood at this time; however, studies in animals and humans implicate cortical spreading depression as a possible cause of migraine headache pain. Cortical spreading depression is an electrophysiological occurrence of a wave of depolarization followed by a short-lasting depression of electrical activity that spreads across the cortex at a rate of 2–6 mm/min, a rate similar to the rate of spread of the aura associated with migraine. Cortical spreading depression is also associated with changes in cerebral blood flow that are due to coupling between neuropeptide release and cerebrovascular tone. The changes in blood flow that have been measured during aura are synchronous with increased release of excitatory amino acids and this suggests that the mechanism of cortical spreading depression may underlie migraine aura and headache.

The CACNA1A gene encodes the pore-forming subunit of $Ca_v2.1$, a voltage-gated P/Q-type Ca^{2+}-channel. P/Q-type Ca^{2+}-channels are found in presynaptic terminals and somatodendritic membranes throughout the mammalian brain and spinal cord where they play a prominent role in initiating action potential-evoked neurotransmitter release. They have been identified in all of the brain structures that have been implicated in the pathogenesis of

migraine pain and they are involved in the mechanism of release of vasoactive neuropeptides from terminals of the trigeminal nerve and the release of excitatory neurotransmitters in several different cortical areas. As of 2010, 21 missense mutations had been identified in CACNA1A that produce amino acid substitutions in conserved regions of the $Ca_v2.1$ Ca^{2+}-channel. Analysis of whole cell or single-channel Ca^{2+}-channel currents from different mutants showed that different effects were produced by different mutations, but all of the mutants seemed to show voltage-activation curves that were shifted to more negative voltages. This shift results in a higher open probability and single channel Ca^{2+} influx through open channels. Despite this single channel gain of function effect, whole cell Ca^{2+} current density was reduced in cells overexpressing mutant channels. Analysis of the number of functional channels overexpressed in either HEK293 cells or in $Ca_v2.1^{-/-}$ cells showed that the number of mutant channels on the cell surface was reduced compared to the number of wild-type channels. In knock-in mice, however, in which the mutant channels are expressed at near physiological levels, the effect of the mutations is seen to be consistent with the gain of function seen in the single channel measurements. Gain-of-function mutations in the $Ca_v2.1$ channels lead to increased evoked Ca^{2+}-dependent neurotransmitter release in individuals with familial hemiplegic migraine. Consistent with this mechanism, the induction and propagation of cortical spreading depression were larger in mice containing mutant $Ca_v2.1$ channels than in wild-type mice.

The multiple mutations in the ATP1A2 gene that encodes the $\alpha2$ subunit of Na^+,K^+-ATPase and that have been identified in patients with familial hemiplegic migraine type 2 (FHM2) have been found to cluster in six regions of the protein: the N-domain, which is involved in ATP binding; the A-domain, called the actuator domain; the P-domain, which the site of the aspartate residue that is phosphoryated by ATP during the catalytic cycle; at the interface between the transmembrane domain and the P-domain, which is involved in coupling ATP hydrolysis to ion transport; near the carboxy-terminus of the α subunit; and in the extracellular loops of the α subunit, which may form a pathway for release of transported ions to the extracellular solution (Morth et al., 2009). Only some of the mutants have been characterized for biochemical effects of the mutations and pumps that are either functionally inactive or pumps that are functionally active but have reduced activity have been identified. The functionally active pumps either have altered affinity for Na^+ or K^+, or have reduced catalytic turnover for other reasons. The decrease in Na^+,K^+-ATPase activity associated with these mutants may lead to the symptoms of familial hemiplegic migraine by causing an increase in extracellular K^+ that would depolarize the cell resting membrane potential and induce spontaneous waves of cortical spreading depression. A correlation between extracellular K^+ concentrations and the frequency of waves of spontaneous spreading depression in chicken retina has been reported (Dahlem et al., 2003). On the other hand, the $\alpha2$ isoform of Na^+,K^+-ATPase constitutes only about 10% of the total Na^+,K^+-ATPase activity in the brain and it might seem surprising that mutations in the $\alpha2$ subunit would have such severe effects. This apparent inconsistency might be resolved, however, if the $\alpha2$ isoform of the sodium pump were confined to microdomains of the cell membrane that are associated with other transporters involved in calcium signaling and homeostasis, such as the Na^+/Ca^{2+} exchanger and Ca^{2+} channels, where they could influence neurotransmitter release (see Chapter 14).

The SCN1A gene encodes the pore-forming subunit of the voltage-gated sodium channel $Na_V1.1$ and at least three missense mutations in this gene have been linked to familial hemiplegic migraine type 3 (FHM3). Each of the mutant sodium channels exhibits a different set of functional consequences. Both loss-of-function and gain-of-function phenotypes have been found, as well as a mutant that is defective in the trafficking to the plasma membrane. It has been suggested that the loss-of-function mutants may affect primarily inhibitory GABAergic (γ-aminobutyric acid) neurons whereas gain-of-function mutants may primarily affect the activity of excitatory neurons. Either of these consequences of mutations in the $Na_V1.1$ channel could reduce the threshold for spontaneous action potentials and the initiation of cortical spreading depression in FHM3 patients.

V. CYSTIC FIBROSIS

Cystic fibrosis, the most common lethal genetic disease in Caucasians, was the first inherited disease of ion transport for which the genetic locus was identified. More than 1000 mutations have been identified in a gene on chromosome 7 that encodes the CFTR protein (cystic fibrosis transmembrane conductance regulator) and lead to symptoms of varying severity that characterize the disease. Cystic fibrosis is an autosomal recessive disease that occurs with a frequency of approximately 1 in 2000 Caucasians and it has been estimated that approximately 1 in 20 people of European descent are carriers with a mutation in one allele. Because of the severity of the disease and the availability of information about many of the mutations in the CF gene that cause cystic fibrosis, screening of newborns for CFTR mutations is nearly universal in the USA.

The clinical symptoms of cystic fibrosis include abnormally high concentrations of Na^+ and Cl^- in sweat, persistent pulmonary infection with *Pseudomonas aeruginosa*, thick and viscous mucus, pancreatic insufficiency, muscle weakness and failure to thrive. CFTR is a cAMP-activated Cl^- channel that is present on the apical surface

of many epithelial cells and is involved in Cl^- absorption or secretion. In secretory epithelia, the symptoms of the disease are caused by reduced NaCl transport out of the cells and an associated reduction in hydration of the lumen of the secretory organs. This leads to thickened and dehydrated mucus that blocks motility in organs such as the pancreas, the trachea and the intestinal tract. Pancreatic and intestinal blockage prevent release of digestive enzymes and the efficient absorption of nutrients and explains the muscle weakness and failure to thrive seen in CF children. Obstruction of pancreatic ducts eventually leads to tissue destruction, with fibrotic tissue and fat depositions replacing normal pancreatic parenchyma. Children with cystic fibrosis are routinely treated with oral enzyme replacements to offset this deficiency of pancreatic enzyme secretion. Tracheal blockage is responsible for the persistent coughing of CF patients and also provides a hospitable environment for *Pseudomonas* growth. Persistent bacterial infection and the associated inflammation lead to progressive pulmonary insufficiency due to damaged lung parenchyma and recurrent pneumothoraces. The major cause of morbidity and mortality in CF patients is progressive pulmonary disease. In absorptive epithelia such as the sweat gland, the reduced absorption of NaCl leads to the elevated concentrations of salt that is the characteristic feature of the disease. The diagnostic criterion for cystic fibrosis is the elevated Na^+ and Cl^- concentrations in the sweat. Normal sweat chloride levels are 10–35 mEq/L, whereas patients with cystic fibrosis usually have sweat chloride concentrations of 60 mEq/L or greater. Intermediate levels of 35–60 mEq/L may be found in some CF patients, as well as in the normal population.

The major anion secreted by the pancreas is bicarbonate and there is some uncertainty about whether CFTR transports bicarbonate as well as Cl^- in the pancreas. Evidence supporting this mechanism has been published, but an alternative explanation for pancreatic insufficiency due to mutations in CFTR is that CFTR is the route of Cl^- efflux from pancreatic acinar cells and this extracellular Cl^- is then recycled back into the cell via the Cl^-/HCO_3^- exchanger, with efflux of bicarbonate. Mutations in CFTR that reduce Cl^- efflux would have the effect of also reducing bicarbonate secretion through this mechanism. The trachea has both absorptive and a secretory functions and, in cystic fibrosis, the balance between these two functions shifts toward increased absorption.

Mutations in the CF gene may reduce chloride absorption and secretion by epithelia by different mechanisms. Some mutations are nonsense, frameshift or splicing mutations that prevent the CFTR protein from being synthesized. The most common mutation in cystic fibrosis patients, a deletion of one amino acid (ΔF508) in CFTR, is found in about 70% of cystic fibrosis patients and causes CFTR to fold incorrectly. The biosynthesis of misfolded CFTR is disrupted, trapping the protein in the endoplasmic reticulum and the channel is not delivered to the plasma membrane. Other mutations, such as the missense mutation G551D, result in CFTR channels that reach the plasma membrane but rarely open. Studies in cell cultures suggest the possibility of reversing some of these abnormalities and many trials have been undertaken to correct different defects in CFTR. Among the most promising at this time are efforts to use small molecules to potentiate the activity of mutants, such as the G551D mutant, by increasing the open lifetime of the channel. The most important target, however, remains the ΔF508 mutation, because of its prevalence in the CF population, and high-throughput screening has identified some candidate molecules that improve the processing of this mutant and increase its abundance in the plasma membrane of cells where it functions as a chloride channel.

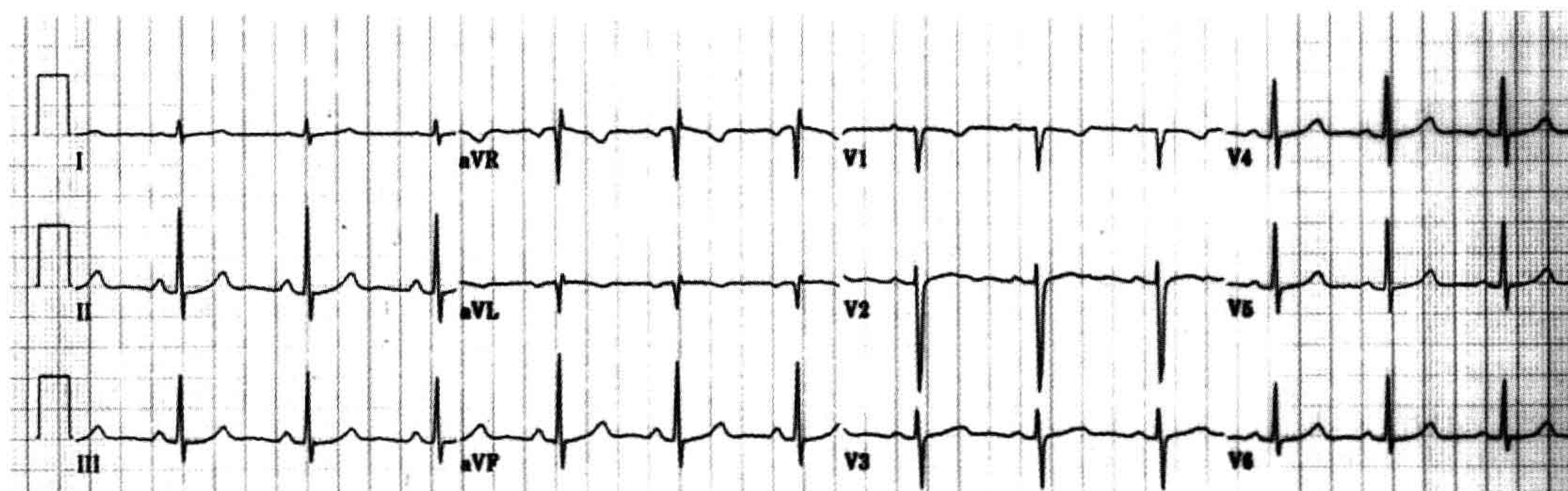
VI. LONG QT SYNDROME

Cardiac contraction is the end result of action potentials that are initiated at the sinoatrial node by the spontaneous depolarization of the nodal cells to threshold and the subsequent transmission of triggered action potentials in different cells of the cardiac conduction pathway to the atrial and ventricular muscle fibers. The amount of charge that moves across cell membranes during action potentials in most cells of the conduction system is small; however, because atrial muscle and ventricular muscle are sufficiently massive, charge movement during contraction and relaxation of these tissues can be detected at the surface of the body. It is the movement of charge during cardiac muscle contraction and relaxation that is measured in the electrocardiogram (EKG; ECG). A 12-lead EKG from a heart showing normal sinus rhythm is shown in Fig. 30.1A. The deflections are most easily identified using lead II, shown in Fig. 30.1B.

The deflections or waves in the EKG correspond to atrial muscle depolarization and contraction (P wave), ventricular depolarization and contraction (QRS complex) and ventricular repolarization and relaxation (T wave). Among the parameters that are measured on an EKG are the times between specific events, such as the beginning of the T wave and the end of the R wave (PR interval) and the beginning of the Q wave and the end of the T wave (QT interval). In the normal population, the PR interval is 0.12–0.20 s. The QT interval is most often reported as a "corrected" QT interval, $QT/\sqrt{RR}$, in recognition of the fact that the QT interval changes as heart rate changes. Corrected QT intervals in the normal population are less than 0.44 s. When the QT interval is longer than 0.44 s, individuals are said to have long QT syndrome.

The presence and timing of the different deflections on the EKG reflect the highly coordinated opening and closing

(A)



(B)

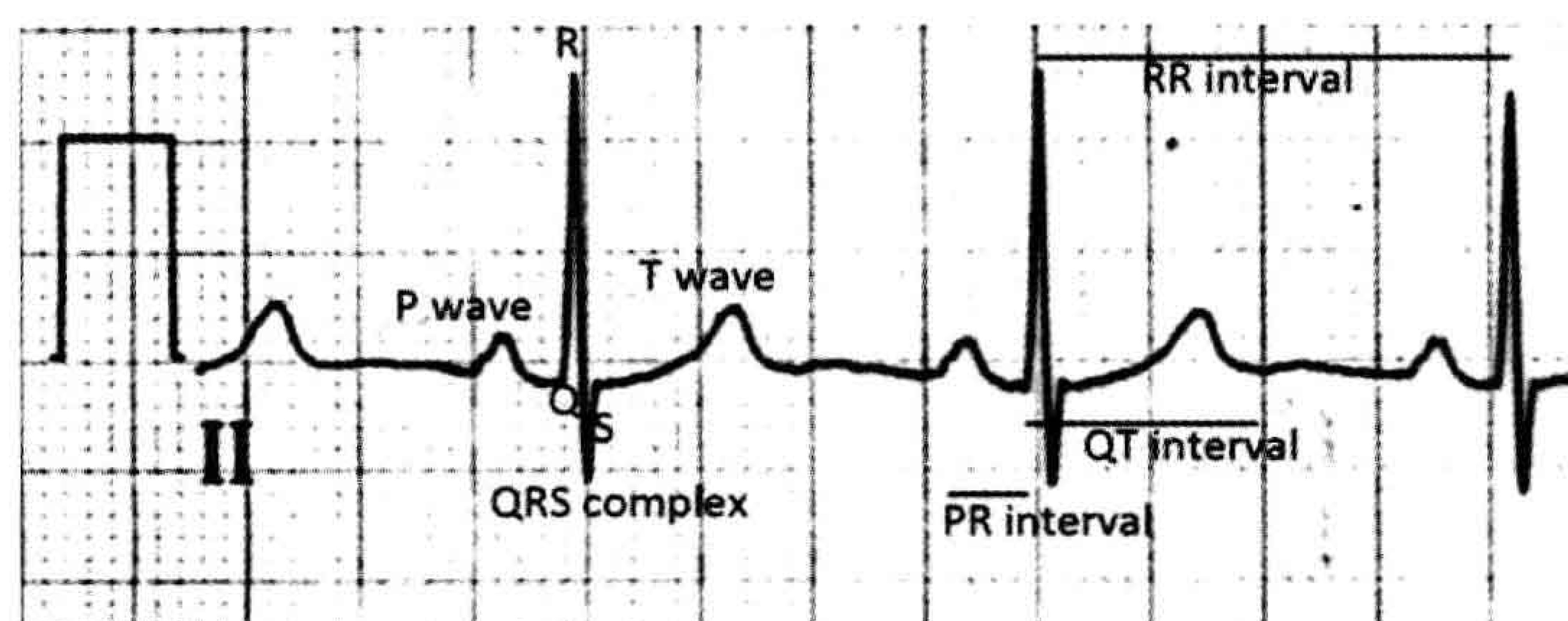


FIGURE 30.1 Electrocardiogram (EKG) showing normal sinus rhythm. (A) 12-lead EKG record. The horizontal axis is time and the vertical axis is voltage. Each lead is identified below the EKG trace that is recorded from that lead. (B) EKG trace from lead II in (A) showing the names of the deflections and intervals. *(See text for details.)*

of ion channels in the cardiac myocytes. A typical action potential in ventricular myocytes is shown in Fig 30.2, with the different phases of the action potential labeled as phases 0–4. In the EKG, the QRS complex corresponds to muscle depolarization and contraction, or phase 0 in the action potential, whereas the T wave corresponds to muscle repolarization and relaxation, or phase 3 of the action potential.

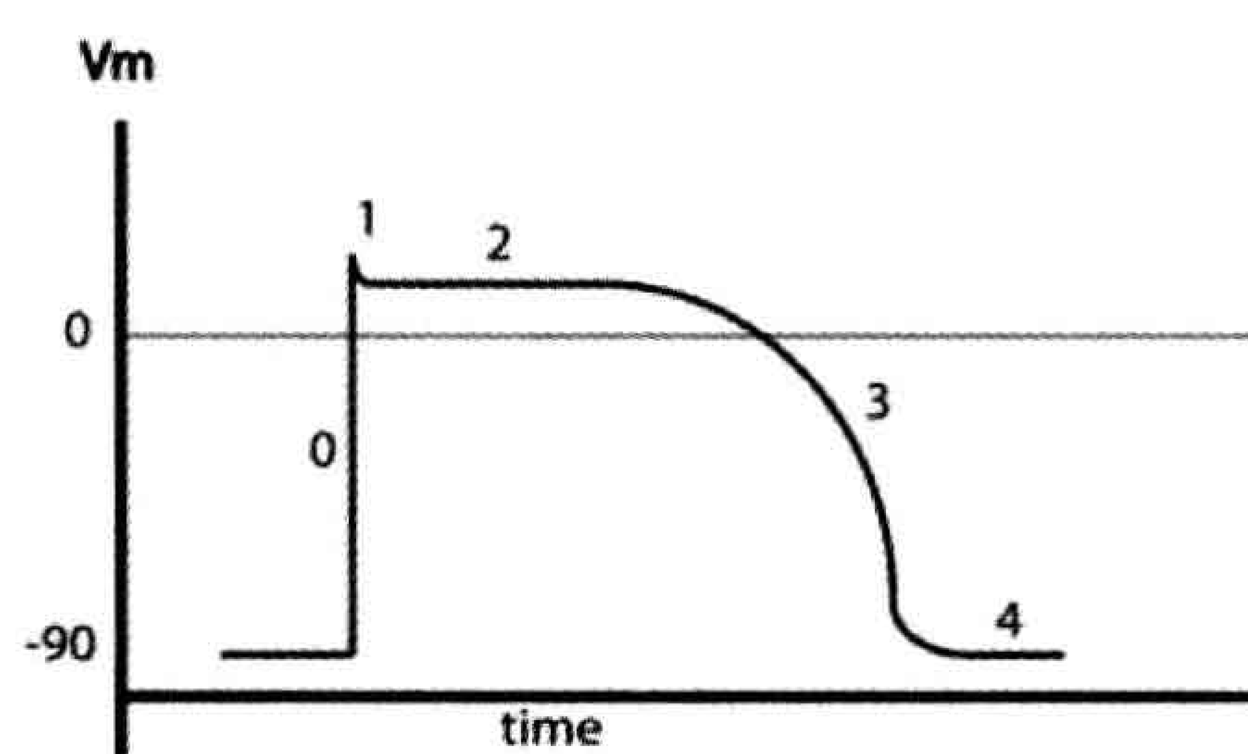


FIGURE 30.2 Drawing of an action potential from a cardiac ventricular myocyte. The phases of the action potential are identified by the numbers 0–4. The value of the membrane potential is shown on the vertical axis as a function of time on the horizontal axis. *(See text for details.)*

The phase 0 depolarization of the action potential is due to the opening of voltage-gated Na^+ channels that are encoded by the SCN5A gene. These channels inactivate toward the end of phase 0 and, in phase 1, the reduction in sodium conductance due to the closure of these channels, together with the delayed opening of transient-open K^+ channels, is responsible for the slight repolarization of the membrane potential that is observed. During phase 2 of the action potential, there is a relative balance between inward current carried primarily by Ca^{2+} and Na^+ ions through voltage-gated L-type Ca^{2+} channels and outward current through delayed rectifier K^+ channels. Toward the end of phase 2, the voltage-gated Ca^{2+} channels close while delayed rectifier K^+ channels continue to activate, shifting the balance of current flow to outward K^+ current. This shift in charge movement repolarizes the membrane potential and triggers muscle relaxation. On the EKG, the QT interval can be understood as a reflection of the balance between the depolarization due to open Na^+ channels and repolarization due to open K^+ channels. Mutations in any

of the channels that affect the action potential duration might be expected to affect the QT interval and at least 10 forms of long QT syndrome have been identified in patients, reflecting underlying mutations in these different channels or other proteins associated with them.

Long QT syndrome type 1 (LQT1) is due to mutations in the KCNQ1 gene that encodes the pore forming α subunit of the slow delayed rectifier K^+ channel. In phase 2 of the action potential, two different delayed rectifier K^+ channels open at different rates, a fast delayed rectifier and a slow delayed rectifier. The slow delayed rectifier channel consists of a pore forming α subunit (K_VLQT1) and a β subunit (MinK) that is encoded by the KCNE1 gene. LQT5 is caused by mutations in the KCNE1 gene. The faster-opening delayed rectifier K^+ channel contains a pore-forming α subunit that is encoded by the HERG gene and a β subunit (MiRP1) encoded by the KCNE2 gene. LQT2 is due to mutations in the HERG gene and LQT6 is caused by mutations in the KCNE2 gene. A different type of K^+ channel, an inward rectifier K^+ channel, plays little or no role during phase 2 of the cardiac action potential, but is important during the phase 3 repolarization phase. The current carried by these channels is called I_{K1} and is due to the inward rectifier Kir2.1 channel that is encoded by the KCNJ2 gene. Reductions in I_{K1} prolong the repolarization phase of the action potential and mutations in KCNJ2 underlie LQT7. As discussed in the next section, Kir2.1 K^+ channels are also expressed in skeletal muscle and mutations in KCNJ2 lead to a form of periodic paralysis in skeletal muscle that is called Andersen's syndrome (Andersen–Tawil syndrome). All of the forms of long QT syndrome that are caused by mutations in genes encoding K^+ channel subunits are loss-of-function mutations that lead to reductions in repolarizing currents. This reduction in repolarization prolongs phase 2 of the action potential, which is manifest as a longer QT interval on the EKG.

In contrast to the loss-of-function mutations in K^+ channels, mutations in the SCN5A gene encoding the voltage-gated Na^+ channel that are associated with LQT5 are gain-of-function mutations. These mutations do not alter the conductance of the channel but rather affect the inactivation of the channel. Electrophysiological measurements and computer simulations of channel activity show that a small fraction of voltage-gated Na^+ channels with LQT5 mutations reopen during phase 2 of the action potential and result in a sustained inward Na^+ current. This inward Na^+ current is depolarizing and opposes the repolarization that is due to opening of K^+ channels.

Other forms of long QT syndrome have been identified in which mutations occur in genes that encode other proteins that influence the action potential, such as voltage-gated Ca^{2+} channels or proteins that affect the subcellular localization of the channels, such as ankyrin. The molecular characterization of the effects of these mutations has not been so well characterized, however, as those described above.

VII. MYOTONIA AND PERIODIC PARALYSIS OF SKELETAL MUSCLE

Mutations in genes that encode voltage-gated sodium channels or potassium channel subunits in the heart are responsible for long QT syndrome and altered myocardial contraction. Inherited mutations in a voltage-gated sodium channel or in any of several potassium channel subunits are also responsible for various forms of paralysis or myotonia in skeletal muscle. Like in the heart, mutations in these channels in skeletal muscle primarily affect the rates of entry into the inactivated state or the recovery from inactivation and have little or no affect on ion selectivity or single channel conductance. The clinical hallmark of periodic paralysis is the episodic occurrence of attacks of flaccid weakness. Periodic paralysis in skeletal muscle is often associated with abnormally high or low serum K^+ concentrations and is called either hyperkalemic periodic paralysis or hypokalemic periodic paralysis, depending on whether ictal serum K^+ concentrations are elevated or depressed compared to normal levels. The changes in serum $[K^+]$ associated with these diseases, however, can be variable. Although mutations in the SCN4A gene encoding the voltage-gated sodium channel in skeletal muscle can lead to either hyperkalemic periodic paralysis or hypokalemic periodic paralysis, most patients who are diagnosed with hypokalemic periodic paralysis have mutations in the CACNA1S gene that encodes an L-type voltage-gated calcium channel. Andersen's syndrome, which is caused by mutations in the KCNJ2 gene that encodes the inward rectifier Kir 2.1 channel and is also called Andersen–Tawil syndrome, is the only form of inherited periodic paralysis in humans that affects tissues other than skeletal muscle. In addition to periodic paralysis of skeletal muscle, patients with Andersen's syndrome often have ventricular arrhythmias and dysmorphic features such as clinodactyly, low-set ears, short stature and hypoplastic mandible.

Myotonia is a state of sustained muscle contraction that is difficult to relax. During myotonic contractions, electrophysiological measurements show that repetitive action potentials fire in muscle cells even in the absence of nervous input. Paramyotonia congenita is a form of myotonia that is caused by mutations in the SCN4A gene. Another form of myotonia, called myotonia congenital, is caused by mutations in the CLCN1 gene that encodes a voltage-gated chloride channel found in the transverse tubules. Myotonia congenita is also called Thomsen's disease for the Danish physician who first described the symptoms in himself. Note that, depending on the nature of

the mutation in SCN4A, amino acid substitutions in the skeletal muscle voltage-gated sodium channel may lead to either paralysis or myotonia. Furthermore, episodes of mytonia may also occur in patients with hyperkalemic periodic paralysis, sometimes within minutes of the paralysis. All of the myotonias and familial periodic paralyses are inherited in an autosomal dominant pattern and are in contrast to a generalized form of myotonia called Becker's type that is inherited in a recessive pattern. Becker's myotonia is also caused by mutations in the CLCN1 gene.

Mutations in SCN4A that lead to hyperkalemic periodic paralysis reduce the rate of inactivation of the voltage-gated Na^+ channels, which are responsible for the initiation of the action potential in the skeletal muscle cells. Furthermore, a small fraction of Na^+ channels (1.5–5%) may remain open after depolarization of the muscle fiber and lead to a persistent inward current and slight depolarization of the skeletal muscle membrane potential (Cannon, 2002). Tonic depolarization of the membrane potential leads to inactivation of sodium channels with the result that there is an insufficient number of channels available to initiate an action potential in response to nervous stimulation. Muscle weakness and paralysis then ensue. The failure of these mutant channels to inactivate normally is exaggerated when serum K^+ concentrations are elevated. In addition, the voltage dependence of opening of the mutant channels is shifted to hyperpolarized potentials, also resulting in a small persistent inward Na^+ current at membrane potentials where wild-type channels are normally closed. Ingestion of a carbohydrate-rich meal can sometimes alleviate the symptoms of hyperkalemic periodic paralysis, because the carbohydrates stimulate insulin release and insulin is an activator of Na^+,K^+-ATPase, which would pump K^+ into cells and reduce plasma K^+ concentrations.

Mutations in SCN4A are responsible for only about 10% of patients with hypokelemic periodic paralysis, whereas about 70% of these patients have been found to have mutations in the CACNA1S gene, which encodes an L-type Ca^{2+} channel that is located in the transverse tubule of the myocyte. The molecular mechanisms responsible for this type of paralysis are not understood and it seems paradoxical that muscle from patients with hypokalemic periodic paralysis will depolarize when serum K^+ concentrations are less than normal. All of the mutations in CACNA1S that are found in patients with hypokelemic periodic paralysis are located in the one of the four S4 segments of the channel, which is part of the voltage-sensor. In vitro studies indicate that the Ca^{2+} current density of muscle fibers from these patients is only about 50% of controls and the channels demonstrate a reduction in the rate of activation in response to a stimulus. Microelectrode recordings from muscle fibers containing sodium channel mutations in SCN4A show a shift in the voltage-dependence of inactivation to hyperpolarized potentials, which would result in an increase in the fraction of inactivated channels at mildly depolarized potentials. There is also some evidence that mutations in the voltage-gated Na^+ channel can lead to a non-selective inward monovalent cation leak through the channel at hyperpolarized potentials, but it has been shown that most cases of hypokalemic periodic paralysis are characterized by mutations in the voltage-sensor segments of either the Na^+ channels or the Ca^{2+} channels. Taken together, the defects in the voltage-gated Na^+ channels and Ca^{2+} channels are consistent with a mechanistic disruption of the coupling between nervous stimulation of the muscle and contraction, and with consequent muscle weakness and paralysis. How hypokalemia induces muscle cell depolarization, however, remains unknown. The reader is referred to Chapter 9 where a roll-over in the RP vs $(K)_o$ curve at low $(K)_o$ levels is shown and discussed.

Patients with paramyotonia congenita are often alerted to the disease by myotonia that is induced by cold weather. Paramyotonia congenita is also aggravated by prolonged exercise and, whereas patients with paramyotonia congenita may also have episodic periods of muscle weakness that is associated with elevated serum $[K^+]$ or prolonged cooling, the aggravation of symptoms with prolonged exercise is not observed in hyperkalemic periodic paralysis. Mutations in SCN4A that are associated with paramyotonia congenita slow inactivation of the sodium channels and increase the rate of recovery from inactivation. Computer simulations (Fig. 30.3) indicate that these effects promote repetitive firing of the muscle fiber followed by decreased excitability due to sustained depolarization of the membrane (Hayward et al., 1996). Like the mutant sodium channels in hyperkalemic periodic paralysis that also show slow inactivation, channels associated with paramyotonia congenita do not inactivate completely and a persistent inward current at the end of depolarization is observed.

Andersen's syndrome is caused by missense or deletion mutations in the KCNJ2 gene that encodes an inward rectifier potassium channel Kir2.1 in humans. Inward rectifier K^+ channels are important for setting the resting membrane potential in many cells. There are multiple inward rectifier channels expressed in skeletal muscle and the contribution of each channel type to the maintenance of resting membrane potential in these cells has not been established. Expression of Kir2.1 channels with any of several missense mutations associated with Andersen's syndrome in *Xenopus* oocytes does not result in measurable K^+ current and it has been shown that this is the result of the failure of the channels to assemble properly and be transported to the cell surface (Bendahhou et al., 2003). Expression of mutant subunits together with wild-type subunits, however, results in assembly of hybrid channels containing both wild-type and mutant subunits. Some of these hybrid channels are transported to the cell surface but

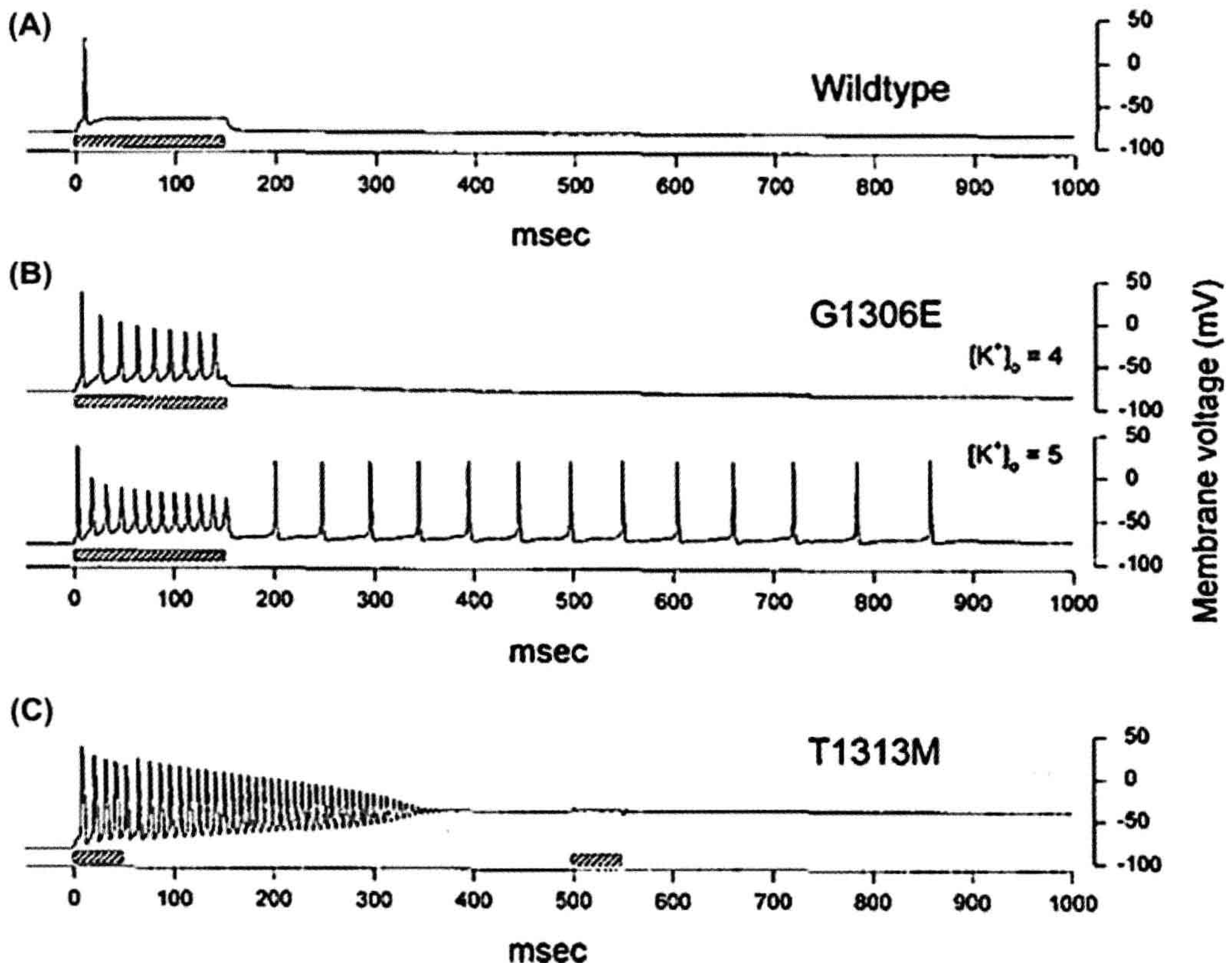


FIGURE 30.3 Simulated membrane potential changes in response to injected current pulses in cells containing G1306E and T1313M mutations in the cardiac voltage gated Na^+ channel gene SCN4A. (A) The wild-type response to a 150 ms stimulus (shaded bar) is a single action potential. (B) The G1306E mutation is found in patients with sodium channel myotonia. The response of cells containing this mutant channel to a 150 ms stimulus is repetitive firing of action potentials (myotonia). At normal $[K^+]$ the action potentials cease once the stimulus is stopped and the membrane potential returns to the baseline. At slightly elevated $[K^+]$, repetitive action potentials continue even after stimulation of the cells has stopped. (C) The T1313M mutation is found in the SCN4A gene of patients with paramyotonia congenita. Repetitive action potentials are observed during and following cessation of a 150 ms stimulus. The membrane potential remains depolarized after cessation of the stimulus, which renders the cell unresponsive to a second stimulus delivered at t = 500 ms. *(Figure reproduced from Hayward et al., 1996 with permission.)*

they are non-functional, indicating that the mutant subunits have a dominant-negative effect on the wild-type subunits. Other mutants fail to assemble with the wild-type subunits or assemble with wild-type subunits but are not transported to the cell surface. In all of these instances, the number of functional inward rectifier channels is reduced and the cell membrane potential will be depolarized. Depolarization will inactivate the sodium channels and make the muscle fiber electrically inexcitable. Because the Kir2.1 channel also contributes to the repolarization of the cardiac action potential, reductions in this component of the K^+ current at the end of the plateau phase will delay repolarization and lead to a long QT interval (LQT7) and increased susceptibility to cardiac arrhythmias. The role of Kir2.1 channels in craniofacial, limb and axial skeletal development has not been completely described, but the K^+ current through these channels must be involved in this process early in development because the targeted disruption of Kir2.1 in knockout mice causes neonatal lethality.

Unlike most mammalian cell membranes, the skeletal muscle plasma membrane is significantly more permeable to Cl^- ions than to K^+ ions. The reader is referred to the Chapter 42 where this is discussed in great detail. During muscle contraction there is a significant increase of $[K^+]$ in the confined space of the transverse tubules and the efflux of Cl^- through voltage-gated ClC-1 Cl^- channels neutralizes this charge buildup, preventing prolonged depolarization of the membrane potential. In myotonia congenita,

mutations in the CLCN1 gene that encodes the ClC-1 channel cause a shift in the voltage-activation of the ClC-1 channel to more positive potentials or result in the reduction of the number of functional channels in the cell membrane (Lossin and George, 2008). Both of these effects on the channel increase the concentration of K^+ in the lumen of the transverse tubules and lead to depolarization of the membrane potential and periods of repetitive action potential initiation. The electrical basis for the myotonia was determined in the laboratory of Shirley Bryant in 1974 from electrophysiological recordings from muscle fibers from myotonic goats (Adrian and Bryant, 1974). Strains of these goats are known to collapse for short periods of time after being startled. Patients with myotonia congenita often find that the muscle stiffness caused by the myotonia is alleviated by periods of mild exercise. This improvement in the symptoms of myotonia congenita, like in hyperkalemic periodic paralysis, may be due to the increased activity of Na^+,K^+-ATPase which will pump K^+ from the tubules into the cells. The reader is referred to the Chapter 42 where myotonia involving a low Cl^- conductance is discussed.

VIII. MALIGNANT HYPERTHERMIA

Malignant hyperthermia is detected as a rapid rise in body temperature in response to volatile anesthetics and depolarizing muscle relaxants, such as succinylcholine, that are administered during surgery. The disease is inherited as an autosomal dominant trait with an incidence in adults undergoing surgery with anesthesia of approximately 1 in 60 000 and 1 in 15 000 in children and adolescents. The increase in body temperature is caused by the uncontrolled release of Ca^{2+} from the sarcoplasmic reticulum, leading to sustained muscle contraction with utilization of ATP and the generation of heat (MacLennan and Zvaritch, 2010). Other symptoms of malignant hyperthermia include hyperkalemia, respiratory and metabolic acidosis and tachycardia. Malignant hyperthermia is potentially fatal and fatalities as high as 80% were reported in the 1960s. Dantrolene sodium is a muscle relaxant that was found to be effective in blocking the progression of a malignant hyperthermia episode and was introduced as a treatment for malignant hyperthermia in 1979. By the 1990s, fatalities had been reduced to less than 10% using this drug. Genetic testing has identified mutations in the RYR1 gene encoding the skeletal muscle ryanodine receptor Ca^{2+} channel in approximately 70% of patients with malignant hyperthermia and dantrolene has been shown to inhibit Ca^{2+} release from the sarcopasmic reticulum by binding to the ryanodine receptor Ca^{2+} release channel and preventing Ca^{2+} release. A small number of patients have mutations in the CACNA1S gene encoding the transverse tubule voltage-gated L-type Ca^{2+} channel. There is a strong correlation between the incidence of malignant hyperthermia and central core disease, another congenital sarcoplasmic myopathy that is characterized by hypotonia and proximal muscle weakness. Linkage between central core disease and mutations in the RYR1 gene has been established and the majority of the mutations in the ryanodine receptor associated with central core disease are located in the carboxy-terminal region of the polypeptide.

Identification of the genetic locus of the malignant hyperthermia mutations was facilitated by the identification of certain lines of pigs that suffered from porcine stress syndrome. Episodes of porcine stress syndrome could be triggered in these animals by exercise, mating, overheating or emotional stress induced during shipping to the slaughterhouse and also by halothane. Breeders of the pigs selecting for large hams and lean muscle mass had identified a single autosomal gene (HAL) that segregated with the porcine stress syndrome/malignant hyperthermia characteristics in these pigs (Fuji et al., 1991). Following the cloning of the large (>15 000 base pairs) cDNAs for human and rabbit ryanodine receptor genes, linkage between the human RYR1 gene on chromosome 19 and malignant hyperthermia susceptibility was shown. The RYR1 gene locus in humans is isologous with the location of the HAL gene on pig chromosome 6 and mutations causing malignant hyperthermia were soon identified in both pigs and humans. Only one mutation in the pig ryanodine receptor has ever been identified in pigs with malignant hyperthermia (R615C), making it possible that all of the affected breeds originate from a single founder animal.

Multiple mutations in the human ryanodine receptor channel have been identified in patients with malignant hyperthermia and there is no simple genetic test to diagnose the disease. Mutations in the RYR1 gene have not been found in all patients with malignant hyperthermia suggesting that other loci must exist. Mutations in the CACNA1S gene encoding the transverse tubule voltage-gated Ca^{2+} channel have been found in some patients with malignant hyperthermia who do not have mutations in the RYR1 gene. This finding is consistent with a disruption in the excitation–contraction coupling mechanism in skeletal muscle as the mechanism for the symptoms of malignant hyperthermia since the Ca^{2+} channel interacts directly with the ryanodine receptor in the sarcoplasmic reticulum membrane to promote Ca^{2+} release through the ryanodine receptor in response to T-tubule depolarization.

The mechanism whereby volatile anesthetics trigger malignant hyperthermia appears to be due to an increase in the sensitivity of the mutant ryanodine receptor channels to activation by the volatile anesthetics, as well as caffeine, and to a decrease in the threshold of the channels to activation by SR luminal $[Ca^{2+}]$ (Jiang et al., 2008). Once the channel is triggered to open by the anesthetic, Ca^{2+} leaves the sarcoplasmic reticulum and activates the contractile

proteins. The SERCA Ca^{2+} pump hydrolyzes ATP as it returns the Ca^{2+} to the SR, but because the channel remains open in the presence of the anesthetic and, because the threshold for activation of the channel by luminal Ca^{2+} is low, the SR [Ca^{2+}] continues to activate the channel and be released into the cytoplasm. Continuous or repetitive cycles of this process contribute to rapid generation of heat and the other symptoms of the disease.

IX. LIDDLE'S SYNDROME

Hypertension is associated with increased susceptibility to stroke, myocardial infarction and renal failure. Evidence from different populations indicates that hypertension can be caused by any of several different physiological disturbances, some of which are genetically determined. Because there are multiple factors that contribute to elevated blood pressure, identification of the underlying causes of inherited hypertension in different individuals must be done in restricted populations. Patients with Liddle's syndrome are an extremely small subset of the hypertensive population, with fewer than 30 pedigrees reported worldwide as of 2008. This restricted population of patients facilitated genetic linkage analysis of these individuals and, in 1994, it was shown that there was complete linkage of the gene encoding the β subunit of the epithelial sodium channel (ENaC) to Liddle's syndrome in Liddle's original kindred (Shimkets et al., 1994). Liddle's syndrome is characterized by elevated blood pressure with serum hypokelemia. Similar symptoms are also seen in pediatric patients with hypertension caused by elevated aldosterone levels (hyperaldosteronism) but, because aldosterone levels are not elevated in Liddle's syndrome patients, this disease is also called pseudoaldosteronism.

ENaC is composed of three homologous subunits (αENaC, βENaC and γENaC), with 30–35% amino acid identity, in a 2α:1β:1γ stoichiometry. Each subunit polypeptide consists of short intracellular amino- and carboxy-terminal sequences, two transmembrane helices and a large extracellular loop connecting the transmembrane helices. The extracellular loop comprises more than 80% of each subunit. Epithelial sodium channels are located in the apical membrane of polarized epithelial cells and Na^+ entry into the epithelial cell through ENaC represents the rate-limiting step in sodium absorption across epithelial barriers. In contrast to the voltage-gated Na^+ channels of excitable membranes, sodium currents through ENaC are not affected by changes in the membrane potential. Despite being insensitive to changes in voltage, ENaC does undergo slow transitions between open and closed states, but the mechanisms underlying these transitions have not been well characterized. Epithelial sodium channels are also more selective for Na^+ over K^+ than are the voltage-gated channels.

Maintenance of fluid and electrolyte balance involves tight regulation of Na^+ absorption via ENaC. Sodium absorption varies widely under conditions of Na^+ excess or depletion and is primarily regulated by the hormones aldosterone and vasopressin, both of which increase renal Na^+ absorption by acting on the principal cells of the kidney. Aldosterone, acting through the mineralocorticoid receptor, increases the transcription of mRNA for several ion transporting proteins including the Na^+,K^+-ATPase and ENaC in target cells in the distal nephron and the collecting duct, with the net effect of increasing the number of these pumps and channels at the cell surface. Hyperaldosteronism resulting from increased aldosterone synthesis and release from adrenal tumors is another rare form of hypertension. Vasopressin promotes the activation of ENaC in the apical membrane of the principal cells in the distal nephron and also insertion of additional channels into this membrane via a cAMP-dependent mechanism. ENaC abundance in the apical membrane of the renal cells is a balance between the insertion of new channels in response to aldosterone or vasopressin release and the degradation of existing channels. In cultured cells, the half-life of ENaC subunits is between 1 and 3 hours, suggesting that the channel is a short-lived protein in cells. The degradation of ENaC at the cell surface is mediated by the E3 ubiquitin-ligase Nedd-4-2, which binds to PY motifs in the carboxy-terminal region of ENaC and catalyzes the ubiquitination of ENaC α, β and γ subunits. Ubiquitinated ENaC subunits are removed from the membrane by endocytosis and degraded in the proteasome and the lysosome.

In patients with Liddle's syndrome, the genes for either the β or the γ subunits of ENaC contain premature termination or frameshift mutations that either truncate the polypeptides and delete the PY motifs or disrupt the PY motifs of these subunits. As a result, Nedd4-2 cannot bind to these ENaC subunits and ubiquitination does not occur (Staub et al., 1996). The result is that there is an increase in the abundance of functional channels at the cell surface that facilitates excess Na^+ uptake and salt and water retention, leading to elevated blood pressure.

X. BARTTER SYNDROME

Approximately two-thirds of the renal reabsorption of Na^+ that is filtered by the glomerulus is done in the proximal tubule and most of the remaining absorption of sodium is done by transporters located in the limb of Henle. In the thick ascending limb of the loop of Henle, mutiple ion channels and transporters cooperate to control salt and water absorption (Fig. 30.4). In the absence of vasopressin, the thick ascending limb and other downstream segments of the kidney are relatively impermeable to water and the combination of NaCl absorption and low water permeability in this region of the nephron enables the kidney to

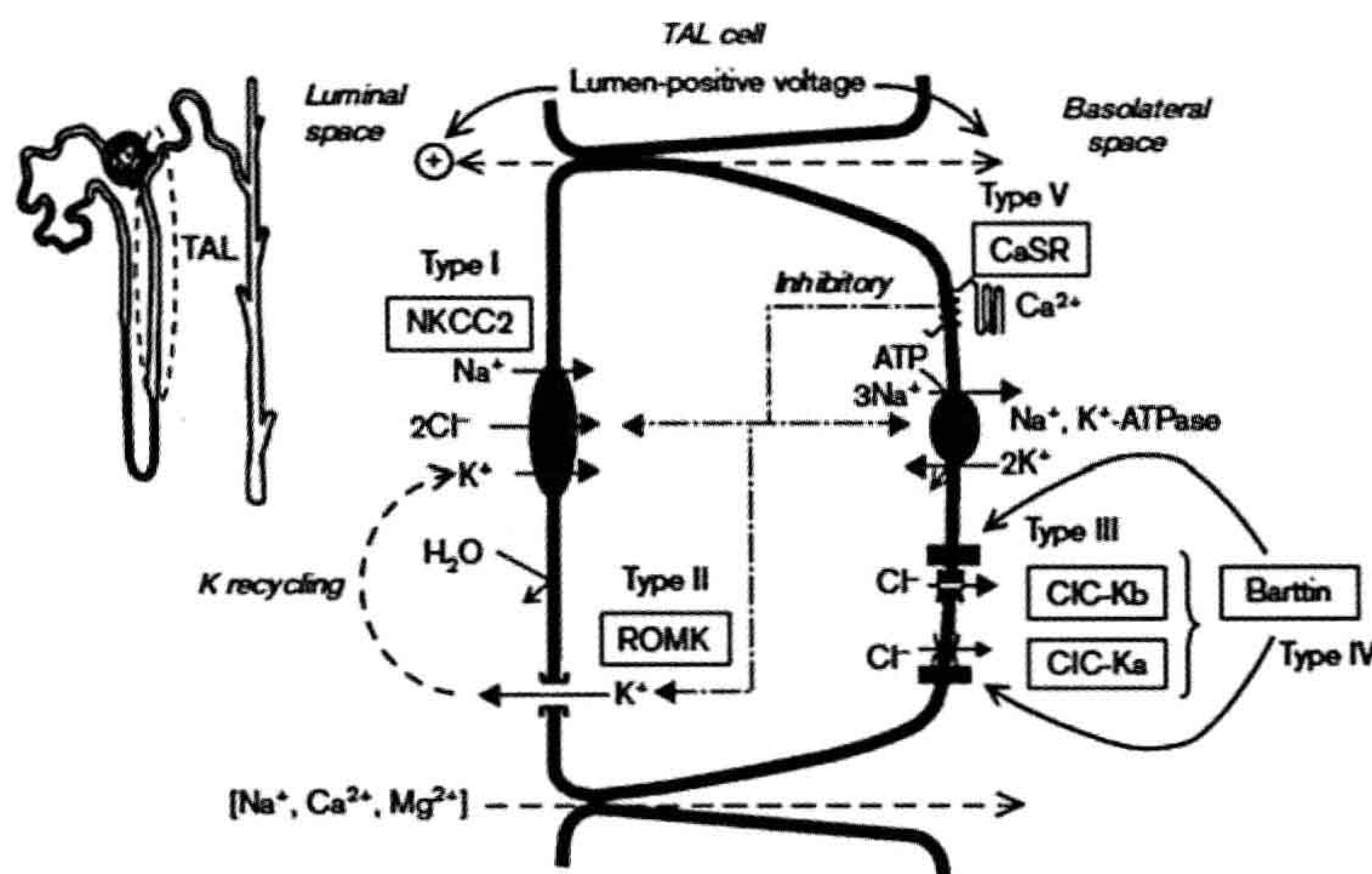


FIGURE 30.4 A model of salt transport by the thick ascending limb of Henle, depicting the five types (I–V) of Bartter syndrome discussed in the text. Each Bartter type is associated with mutations in a specific gene that encodes the protein whose name is indicated in a rectangle. (See text for details.) The insert shows the anatomical organization of the nephron. *(Figure is reproduced with permission from Staub et al., 1996.)*

generate a low luminal [Na^+] and osmolality with respect to the surrounding interstitial fluid. In the thick ascending limb, Na^+ reabsorption occurs both by the transcellular pathway and by the paracellular pathway. In the transcellular pathway, the NKCC2 transporter in the apical membrane of the cells couples the influx of 1 Na^+, 1 K^+ and 2 Cl^- ions in an electroneutral process. NKCC2 is encoded by the SLC12A1 gene in humans and is inhibited by loop diuretics such as furosemide and bumetinide. Sodium also enters the epithelial cells using the NHE3 sodium–proton antiporter. A large fraction of the K^+ that enters the cells through NKCC2 is recycled back to the tubular lumen through apical ROMK potassium channels that are encoded by the KCNJ1 gene. Recycling of K^+ across the luminal membrane is necessary to maintain tubular [K^+] at sufficiently high levels that are necessary for NKCC2 to function. Movement of K^+ into the tubular lumen also creates a lumen-positive potential that serves as the driving force for paracellular Na^+, Ca^{2+} and Mg^{2+} movement from the lumen to the interstium. Na^+ entering cells through NKCC2 is pumped out of the cells at the basolateral membrane by the Na^+,K^+-ATPase. Most of the Cl^- that enters the cells of the thick ascending limb is transported out of the cells through basolateral ClC-Ka and ClC-Kb Cl^- channels. The pore-forming subunit of the ClC-Kb channel is encoded by the CLCNKB gene. The ClC-Ka and ClC-Kb channels also contain a β subunit called barttin, encoded by the BSND gene that is required for translocation of the ClC-Ka and ClC-Kb channels to the plasma membrane from the Golgi.

Bartter syndrome is a group of rare autosomal recessive disorders that are characterized by renal salt loss, chronic hypokalemia and metabolic alkalosis (Herbert, 2003). Renin and aldosterone levels are elevated in patients, but blood pressure is usually normal or low. Many patients with Bartter syndrome also have elevated urinary Ca^{2+} excretion. Mutations in the SLC12A gene (Bartter syndrome type 1), in the KCNJ1 gene (Bartter syndrome type 2), in the CLCNKB gene (Bartter syndrome type 3) and in the BSND gene (Bartter syndrome type 4) have been identified in patients with these symptoms. Patients with Bartter syndrome type 4 also have sensorineural deafness. Bartter syndrome type 5 is associated with mutations in the gene for an extracellular Ca^{2+} sensor (CaSR) that is located on the basolateral membrane of cells of the thick ascending limb. The Ca^{2+} sensor is a G-protein-coupled receptor that is activated by increases in extracellular [Ca^{2+}]. Activation of this receptor inhibits salt uptake and activating gain-of-function mutations in the gene for CaSR are found in individuals with Bartter syndrome type 5. The symptoms of Bartter syndrome types 1–4 can all be understood as arising from loss-of-function mutations in genes encoding the NKCC2 transporter (decreased Na^+, K^+ and Cl^- absorption), ROMK (reduced K^+ recycling that compromises NKCC2 function and transepithelial voltage difference) and ClC-Kb or barttin (reduced number of Cl^- channels in the basolateral membrane that prevents transepithelial Cl^- movement). The symptoms of Bartter syndrome type 4 are typically more severe than those of Bartter syndrome type 3 because mutations in barttin affect all segments of the nephron expressing either ClC-Ka or ClC-Kb, whereas when ClC-Kb function is compromised in Bartter syndrome type 3, Cl^- uptake can still occur through ClC-Ka channels. Furthermore, sensorineural deafness is associated with Bartter syndrome type 4 patients but not type 3 patients because mutations in barttin will similarly reduce the abundance of both types of ClC-K channels in the marginal cells that produce endolymph in the inner ear. The secretion of K^+-rich endolymph by these cells is required for the normal function of the hair cells that mediate transduction of sound

waves into electrical impulses. Cytoplasmic [K^+] is increased in the marginal cells through the activity of the $Na^+/K^+/2Cl^-$-co-transporter NKCC1 located in the basolateral membrane of these cells. K^+ is secreted from the cells through apical K^+ channels and Cl^- is recycled across the basolateral membrane through ClC-K channels. The need for Cl^- recycling across the basolateral membrane of these cells in the inner ear is analogous to the role of K^+ recycling across the apical membrane of epithelial cells in the thick ascending limb of the loop of Henle through ROMK channels. Gain-of-function mutations in the extracellular Ca^{2+} sensor CaSR on the basolateral surface of the cells activate the receptor at concentrations of interstitial Ca^{2+} below those that normally activate the receptor (Riccardi and Brown, 2009). The activated CaSR inhibits salt absorption by inhibiting K^+ recycling through the ROMK channel.

BIBLIOGRAPHY

Adrian, R. H., & Bryant, S. H. (1974). On the repetitive discharge in myotonic muscle fibres. *J Physiol, 240*, 505–515.

Ashcroft, F. M. (2000). *Ion Channels and Disease*. San Diego, CA: Academic Press.

Bendahhou, S., Donaldson, M. R., Plaster, N. M., Tristani-Firouzi, M., Fu, Y.-H., & Ptacek, L. J. (2003). Defective potassium channel Kir2.1 trafficking underlies Andersen-Tawill syndrome. *J Biol Chem, 278*, 51779–51785.

Cannon, S. C. (2002). An expanding view for the molecular basis of familial periodic paralyses. *Neuromusc Disord, 12*, 533–543.

Dahlem, Y. A., Dahlem, M. A., Mair, T., Braun, K., & Müller, S. C. (2003). Extracellular potassium alters frequency and profile of retinal spreading depression waves. *Exp Brain Res, 152*, 221–228.

Dichgans, M., Freilinger, T., Eckstein, G., et al. (2005). Mutation in the neuronal voltage-gated sodium channel SCN1A in familial hemiplegic migraine. *Lancet, 366*, 371–377.

Fuji, J., Otsu, K., Zorzato, F., et al. (1991). Identification of a mutation in porcine ryanodine receptor associated with malignant hyperthermia. *Science, 253*, 448–451.

Gargus, J. J. (2009). Genetic calcium signaling abnormalities in the central nervous system: seizures, migraine, and autism. *Ann NY Acad Sci, 1151*, 133–156.

Hayward, L. J., Brown, R. H., Jr., & Cannon, S. C. (1996). Inactivation defects caused by myotonia-associated mutations in the sodium channel III-IV linker. *J Gen Physiol, 107*, 559–576.

Hebert, S. C. (2003). Bartter syndrome. *Curr Opin Nephrol Hypertens, 12*, 527–532.

Jiang, D., Chen, W., Xiao, J., et al. (2008). Reduced threshold for luminal Ca^{2+} activation of RyR1 underlies a causal mechanism of porcine malignant hyperthermia. *J Biol Chem, 283*, 20813–20820.

Lossin, C., & George, A. L., Jr. (2008). Myotonia congenita. *Adv Genet, 63*, 25–55.

MacLennan, D. H., & Zvaritch, E. (2010). Mechanistic models for muscle diseases and disorders originating in the sarcoplasmic reticulum. *Biochim Biophys Acta*. [Epub ahead of print].

Morth, J. P., Poulsen, H., Toustrup-Jensen, M. S., et al. (2009). The structure of the Na^+, K^+-ATPase and mapping of isoform differences and disease-related mutations. *Phil Trans R Soc B, 364*, 217–227.

Ophoff, R. A., Terwindt, G. M., Vergouwe, M. N., et al. (1996). Familial hemiplegic migraine and episodic ataxia type-2 are caused by mutations in the Ca^{2+} channel gene CACNL1A4. *Cell, 87*, 543–552.

Pietrobon, D. (2005). Migraine: new molecular mechanisms. *Neuroscientist, 11*, 373–386.

Riccardi, D., & Brown, E. M. (2009). Physiology and pathophysiology of the calcium-sensing receptor in the kidney. *Am J Physiol Renal Physiol, 298*, F485–F499.

Riordan, J. R., Rommens, J. M., Kerem, B.-S., et al. (1989). Identification of the cystic fibrosis gene: cloning and characterization of complementary DNA. *Science, 245*, 1066–1073.

Shimkets, R. A., Warnock, D. G., Gositis, C. M., et al. (1994). Liddle's syndrome: heritable human hypertension caused by mutations in the β subunit of the epithelial sodium channel. *Cell, 79*, 407–414.

Staub, O., Dho, S., Henry, P. C., et al. (1996). *EMBO J, 15*, 2371–2380.

Vanmolkot, K. R. J., Kors, E. E., Hottenga, J.-J., et al. (2003). Novel mutations in the Na^+, K^+-ATPase pump gene ATP1A2 associated with familial hemiplegic migraine and benign familial infantile convulsions. *Ann Neurol, 54*, 360–366.